The background of the book cover features a dynamic, radial burst of glowing particles. These particles are primarily blue and orange, resembling stars or energy particles, and they radiate outwards from a central bright yellow-orange source at the bottom center. The overall effect is one of intense energy, motion, and scientific discovery.

Second Edition

CHEMICAL KINETICS

From Molecular Structure to Chemical Reactivity

Luís Arnaut



Chemical Kinetics

From Molecular Structure to Chemical Reactivity

This page intentionally left blank

Chemical Kinetics

From Molecular Structure to Chemical Reactivity

Second Edition

Luis Arnaut

Chemistry Department, University of Coimbra, Coimbra, Portugal



ELSEVIER

Elsevier
Radarweg 29, PO Box 211, 1000 AE Amsterdam, Netherlands
The Boulevard, Langford Lane, Kidlington, Oxford OX5 1GB, United Kingdom
50 Hampshire Street, 5th Floor, Cambridge, MA 02139, United States

Copyright © 2021 Elsevier B.V. All rights reserved.

No part of this publication may be reproduced or transmitted in any form or by any means, electronic or mechanical, including photocopying, recording, or any information storage and retrieval system, without permission in writing from the publisher. Details on how to seek permission, further information about the Publisher's permissions policies and our arrangements with organizations such as the Copyright Clearance Center and the Copyright Licensing Agency, can be found at our website: www.elsevier.com/permissions.

This book and the individual contributions contained in it are protected under copyright by the Publisher (other than as may be noted herein).

Notices

Knowledge and best practice in this field are constantly changing. As new research and experience broaden our understanding, changes in research methods, professional practices, or medical treatment may become necessary.

Practitioners and researchers must always rely on their own experience and knowledge in evaluating and using any information, methods, compounds, or experiments described herein. In using such information or methods they should be mindful of their own safety and the safety of others, including parties for whom they have a professional responsibility.

To the fullest extent of the law, neither the Publisher nor the authors, contributors, or editors, assume any liability for any injury and/or damage to persons or property as a matter of products liability, negligence or otherwise, or from any use or operation of any methods, products, instructions, or ideas contained in the material herein.

British Library Cataloguing-in-Publication Data

A catalogue record for this book is available from the British Library

Library of Congress Cataloging-in-Publication Data

A catalog record for this book is available from the Library of Congress

ISBN: 978-0-444-64039-0

For Information on all Elsevier publications
visit our website at <https://www.elsevier.com/books-and-journals>

Publisher: Susan Dennis
Acquisitions Editor: Anneka Hess
Editorial Project Manager: Lindsay Lawrence
Production Project Manager: Sruthi Satheesh
Cover Designer: Christian Bilbow

Typeset by MPS Limited, Chennai, India



Working together
to grow libraries in
developing countries

www.elsevier.com • www.bookaid.org

Contents

Preface	xi
CHAPTER 1 Introduction	1
1.1 Introduction	1
1.2 Initial difficulties in the development of chemical kinetics in the twentieth century.....	2
1.3 Chemical kinetics: the current view	5
References.....	15
CHAPTER 2 Reaction rate laws	17
2.1 Reaction rates	17
2.2 Factors that influence the velocities of reactions	19
References.....	35
CHAPTER 3 Experimental methods	37
3.1 Application of conventional techniques to study reactions.....	38
3.2 Application of special techniques for fast reactions	54
References.....	90
CHAPTER 4 Reaction order and rate constants.....	93
4.1 Rates of elementary reactions	93
4.2 Rates of complex reactions	100
4.3 Methods for solving kinetic equations.....	109
4.4 Simplification of kinetic schemes.....	128
4.5 Global and target analysis of kinetic data	135
References.....	138
CHAPTER 5 Collisions and molecular dynamics	139
5.1 Simple collision theory	141
5.2 Improved collision theory	146
5.3 Collision cross section	150
5.4 Calculation of classical trajectories	157
5.5 PES crossings	163
5.6 Molecular dynamics	167
References.....	172
CHAPTER 6 Reactivity in thermalised systems	173
6.1 Transition-state theory.....	173
6.2 Semi-classical treatments	186

6.3	Intersecting-state model	198
References.....		221
CHAPTER 7	Relationships between structure and reactivity	225
7.1	Quadratic free-energy relationships.....	225
7.2	Linear free-energy relationships	229
7.3	Other kinds of relationships between structure and reactivity	237
References.....		244
CHAPTER 8	Unimolecular reactions	247
8.1	Lindemann–Christiansen mechanism	247
8.2	Hinshelwood's treatment.....	250
8.3	Rice–Ramsperger–Kassel–Marcus treatment.....	253
8.4	Local random matrix theory	256
8.5	Energy barriers in the isomerisation of cyclopropane.....	258
References.....		261
CHAPTER 9	Elementary reactions in solution	263
9.1	Solvent effects on reaction rates.....	263
9.2	Effect of diffusion	265
9.3	Diffusion constants.....	269
9.4	Spin-statistical factors in diffusion-controlled reactions	275
9.5	Reaction control	277
References.....		293
CHAPTER 10	Reactions on surfaces	295
10.1	Adsorption	295
10.2	Adsorption isotherms	300
10.3	Kinetics on surfaces	303
10.4	Transition-state theory for reactions on surfaces	308
10.5	Model systems.....	312
References.....		315
CHAPTER 11	Substitution reactions.....	317
11.1	Mechanisms of substitution reactions.....	317
11.2	S_N2 and S_N1 reactions.....	318
11.3	Langford–Gray classification.....	320
11.4	Symmetrical methyl group transfers in the gas-phase	324
11.5	State correlation diagrams of Pross and Shaik	327
11.6	Intersecting-state model	329
11.7	Cross-reactions in methyl group transfers in the gas phase	334

11.8 Solvent effects in methyl group transfers	336
References.....	341
CHAPTER 12 Chain reactions	343
12.1 Hydrogen–bromine reaction.....	343
12.2 Reaction between molecular hydrogen and chlorine	346
12.3 Reaction between molecular hydrogen and iodine	347
12.4 Calculation of energy barriers for elementary steps in hydrogen–halogen reactions.....	348
12.5 Comparison of the mechanisms of the hydrogen–halogen reactions.....	351
12.6 Pyrolysis of hydrocarbons.....	353
12.7 Explosive reactions	358
12.8 Polymerisation reactions	366
References.....	368
CHAPTER 13 Acid–base catalysis and proton-transfer reactions	369
13.1 General catalytic mechanisms.....	369
13.2 General and specific acid–base catalysis.....	374
13.3 Mechanistic interpretation of the pH dependence of the rates	377
13.4 Catalytic activity and acid–base strength	386
13.5 Salt effects	389
13.6 Acidity functions	390
13.7 Hydrated proton mobility in water	392
13.8 Proton-transfer rates in solution.....	398
13.9 Proton-transfer model system	406
References.....	407
CHAPTER 14 Enzymatic catalysis	409
14.1 Terminology	409
14.2 Factors that accelerate enzymatic action	412
14.3 Michaelis–Menten equation	418
14.4 Mechanisms with two enzyme–substrate complexes	423
14.5 Inhibition of enzymes.....	424
14.6 Effects of pH	429
14.7 Temperature effects.....	431
14.8 Isomerisation of dihydroxyacetone phosphate to glyceraldehyde 3-phosphate catalysed by triose-phosphate isomerase	433

14.9	Hydroperoxidation of linoleic acid catalysed by soybean lipoxygenase-1	435
14.10	Enzymes in drug design.....	437
	References.....	438
CHAPTER 15 Pharmacokinetics		441
15.1	Origins and current use of pharmacokinetics	441
15.2	Drug administration and absorption	443
15.3	Drug distribution	445
15.4	Drug metabolism and excretion.....	447
15.5	Pharmacokinetics models.....	449
	References.....	461
CHAPTER 16 Transitions between electronic states.....		463
16.1	Mechanisms of energy transfer.....	463
16.2	The “Golden Rule” of quantum mechanics.....	470
16.3	Radiative and radiationless rates	474
16.4	Franck–Condon factors	480
16.5	Radiationless transition within a molecule.....	488
16.6	Triplet energy (or electron) transfer between molecules	492
16.7	Electronic coupling	504
16.8	Triplet energy transfer rates.....	512
	References.....	519
CHAPTER 17 Electron-transfer reactions.....		523
17.1	Rate laws for outer-sphere electron exchanges	523
17.2	Theories of electron-transfer reactions	525
17.3	ISM and electron-transfer reactions.....	540
17.4	Non-adiabatic self-exchanges of transition-metal complexes	548
17.5	Electron self-exchanges of organic molecules	550
17.6	Inverted regions.....	552
17.7	Electron transfer at electrodes	562
	References.....	575
CHAPTER 18 Oscillatory reactions.....		579
18.1	Non-linear systems	579
18.2	Chaos	587
18.3	Oscillatory reactions.....	592
18.4	The Coimbrator	596
	References.....	601

Appendix 1: General data.....	603
Appendix 2: Statistical thermodynamics	605
Appendix 3: Parameters employed in ISM calculations	613
Appendix 4: Semi-classical interacting state model.....	617
Appendix 5: The Lippincott–Schroeder potential	623
Appendix 6: Quantum-mechanical radiationless transition theory	629
Appendix 7: Problems	643
Index	673

This page intentionally left blank

Preface

Chemical Kinetics takes the reader on a journey through the world of chemical changes, guided by explanations of how molecular structures evolve over time. For less-experienced travellers, this book provides the basics: the simplest concepts, the fundamental experiments, and the underlying theories. For seasoned travellers, this book takes them to a viewpoint where sophisticated experimental and theoretical methods combine to offer a panorama of time-dependent molecular phenomena. The second edition of *Chemical Kinetics: From Molecular Structure to Chemical Reactivity* builds on the success of the first edition to provide an understanding of chemical reactions rates and their relations to reactants properties, reaction media, and external factors. The new edition is fully revised and updated, reflecting the latest developments in the field and expanding its scope.

Written in an accessible style, this book is primarily intended for an audience of undergraduate and graduate students in Chemistry, Chemical Engineering, Biochemistry, and Pharmacy, all of whom need to understand how to measure, evaluate, and predict rates of molecular transformations. Beginners, presumed to have a basic knowledge of calculus, are offered a simple rationale for measuring, interpreting, and predicting rates of chemical reactions. This book makes rigour and exactitude accessible by illustrating all the theories and mechanisms with recent examples. Some examples are described with sufficient detail and simplicity to be used in general chemistry and lab courses. The gap for specialists in the field is bridged with sections of increasing complexity in the chapters discussing experimental techniques, theories of reaction dynamics and kinetics in thermalized systems, and rates of prototypical reactions (atom transfer, proton transfer, substitution reactions, and catalysis). Sophisticated rate calculations are made simple with a programme available free of charge at a dedicated website (<http://www.ism.qui.uc.pt:8180/ism/>). The last chapters on energy transfer, electron transfer, and oscillatory reactions satisfy the curiosity and thoroughness of specialists. The second edition contains new chapters on pharmacokinetics and oscillatory reactions. Pharmacokinetics is presented in the sequence of enzyme catalysis to address the interests of researchers working in medicinal chemistry, life, and health sciences. Oscillatory reactions are also of interest to the life sciences, and this new chapter also presents their relevance to ecology, atmospheric phenomena, and climate change.

This book is the product of nearly 40 years of teaching at undergraduate and graduate levels, and of research covering virtually all the subjects addressed in this book's 18 chapters. The author is much indebted to thousands of students, hundreds of reviewers, and many co-workers who over the years provided the feedback needed to refine concepts, improve explanations, and clarify the lessons to be learned. This second edition was unable to benefit from contributions by Prof. Sebastião Formosinho and Prof. Hugh Burrows, who had worked on the first edition. The author had the privilege of being a former student and colleague of

Sebastião Formosinho, who was both an example and a source of inspiration, and this second edition is dedicated to his memory. The path walked with Hugh Burrows in the first edition was similarly much appreciated and helpful in arriving at this second edition.

Luis Arnaut

Chemistry Department, University of Coimbra, Coimbra, Portugal

Introduction

1

1.1 Introduction

It is easy with the hindsight of the twenty-first century to think that chemical kinetics has developed in a logical and coherent fashion. But this was far from the case. However, an understanding of the way we achieved our present ideas on chemical kinetics is a very good basis for truly understanding the subject. In the first chapter, we start by looking at some of the milestones and pitfalls in the development of chemical kinetics. We then consider the relationship between kinetics and thermodynamics and finally, we consider the relationship between the macroscopic world we live in and the microscopic world of molecules.

The great success of Newtonian mechanics in the areas of mechanics and astronomy, which involved the idea of explaining phenomena by simple forces acting between particles, led scientists in the nineteenth century to try to introduce such a mechanical explanation to all areas involving natural phenomena. In chemistry, for example, these concepts were applied to interpret “chemical affinity,” leading to the so-called “chemical mechanics.” We will see that this is not far removed from many of our modern ideas in this area, and we will develop our understanding of chemical kinetics within this context.

In this chapter, we will see that the concepts of chemical kinetics evolved relatively late in terms of the overall studies of reactions and reactivity. The study of chemical kinetics can be traced back to Ludwig Wilhelmy [1], who carried out in 1850 the first study of the inversion of cane sugar (sucrose) in the presence of acids that he formulated in terms of a first-order mathematical expression to interpret the progress of the reaction. Unfortunately, this work went unrecognised until Ostwald [2] drew attention to it some 34 years later. It may seem strange today that such an idea of studying the variation of “chemical affinity” with time had not occurred earlier. Farber [3] had tried to explain this and has shown that, in fact, there were some earlier attempts to study the time evolution of reactions, even before Wilhelmy, but that these tended to be isolated observations. Most probably, the practical importance of such studies did not exist at the end of the eighteenth century, and it was only with the advent of the chemical industry at the beginning of the nineteenth century that chemists, rather late, needed to consider this problem. Eventually, this became of great importance for the development of industrial research at the end of that century. An excellent discussion of this problem is given by Christine King [4–6] in her studies on the *History of Chemical Kinetics*, where

she analyses the impact of the various theoretical, experimental and conceptual works of Berthelot and Péan de St Giles [7–9], Guldberg and Waage [10] and Harcourt and Essen [11–14]. These researchers can truly be considered to be the founders of this new branch of chemistry, chemical kinetics.

1.2 Initial difficulties in the development of chemical kinetics in the twentieth century

One of the major difficulties in the development of chemical kinetics stemmed from the lack of mathematical preparation of chemists of that period. For example, Morris Travers [4,5,15] in his biography of William Ramsay noted that his lack of mathematical preparation was the determining factor that made him decide not to become a physicist. Harcourt also notes his own mathematical weakness and his inability to understand many of the mathematical treatments that were made on his experimental data on chemical reactions. These were due to the mathematician Esson, professor of geometry at Oxford. Such developments were sufficiently complex that they were not even understood by many of his contemporary mathematicians, let alone by the chemists of the period. Also, the work of Guldberg and Waage in this area resulted from a collaboration between a professor of applied mathematics and a chemist, while the extremely promising work of Berthelot and Péan de St Gilles on kinetics was finally abandoned by the premature death of the latter scientist at the age of 31.

Berthelot and St Giles, in their kinetic study of esterification reactions, showed that the amount of ester formed at each instant was proportional to the product of the “active masses” of the reactants and inversely proportional to the volume. Rather inexplicably, these authors did not take into account the role of these factors in defining the rate law of the reaction [4,5,15]. A possible explanation for this can be seen in a note on the life and work on Marcelin Berthelot [16]. In this work, indications are given of Berthelot’s understanding of the role of mathematics in chemistry: “the mathematicians make an incoherent block out of physical and chemical phenomena. For better or for worse, they force us to fit our results to their formulae, assuming reversibility and continuity on all sides, which, unfortunately, is contradicted by a large number of chemical phenomena, in particular the law of definite proportions.”

Guldberg and Waage arrived at the concept of chemical equilibrium during 1864–67 through the laws of classical mechanics: that there are two opposing forces, one owing to the reactants and the other to the products, which act during a chemical reaction to achieve equilibrium. In an analogy with the theory of gravity, such forces will be proportional to the masses of the different substances; actually, they established two separate laws, one relating to the effect of masses and the other to that of volume, and it was only later that they were combined into a single law, involving concentrations or “active masses.”

Guldberg and Waage also initially experienced difficulties in finding the proper exponents involved in the description of the variations in the concentrations of the different substances; this problem was resolved in 1887, in terms of molecular kinetic theory. However, far more importantly, these authors did not manage to distinguish the rate laws (what we would call today the initial conditions) from the derivatives of the equilibrium conditions. This considerably complicated and delayed the future development of chemical kinetics. The dynamic nature of chemical equilibrium was never in doubt. However, the complexity of the systems was far from being considered and the link between equilibrium and kinetics was weak. The works of Harcourt and Esson are models of meticulous experimental and theoretical work, but on reading them, it is also obvious that these authors had to confront many conceptual and technical problems. Their kinetic studies needed fairly slow reactions that could be started and stopped quickly and easily. The reactions that best satisfied these experimental conditions were, in fact, fairly complex in mechanistic terms. In spite of the fact that Harcourt knew that such reactions did not happen in a single step, he was far from being able to recognise all their complexities. It was this difficulty in seeing simplicity in the macroscopic observations and extending it to the corresponding microscopic interpretation that became one of the main obstacles to the proper development of chemical kinetics.

Another area of chemical kinetics that has been the focus of various historical studies, involved the interpretation of the effect of temperature on the rates of chemical reactions. For rates measured under standard concentration conditions, Arrhenius expressed this effect by the equation

$$k = Ae^{-(E_a/RT)} \quad (1.1)$$

where k is the rate under standard conditions and A and E_a constants, which are practically independent of temperature. A is called the *frequency factor* or *pre-exponential factor* and E_a is the *activation energy*.

The Arrhenius law took a long time to become accepted; many other expressions were also proposed to explain the dependence of rate on temperature [17–19]. However, the Arrhenius expression eventually became dominant, as it was the model that was the easiest to relate to in terms of physical significance. Nevertheless, its acceptance did not come quickly and was compounded by great difficulties in scientific communication at the time, with lack of interaction between different research groups often carrying out similar, and often parallel studies, instead of drawing on the progress that had already been achieved in this area.

Many of these conceptual and experimental difficulties would disappear with the brilliant work of van't Hoff [20], who introduced the concept of order of reaction and, through it, the possibility of knowing the mechanism of a chemical reaction just on the basis of chemical kinetics [21]. In fact, van't Hoff used the term *molecularity* for what we would call today reaction *order* (the power to

which a concentration of a component enters into the rate equation). When referring to the actual concept of *molecularity*, this author used the explicit expression “the number of molecules that participate in the reaction” [6]. The term *order* is due to Ostwald. Van’t Hoff received the first Nobel Prize in 1901 for his discovery of the laws of chemical dynamics.

During this period, interest in chemical kinetics remained fairly high until 1890, and then declined “due to the lack of stimulus from kinetic theories which could suggest appropriate experiments, sufficient to stimulate a discussion” [22] and, in essence, it needed something to allow a connection between molecular structure and chemical reactivity. This is true, not just of chemical kinetics: all areas of science suffer in the absence of appropriate theories, which help to guide the development of experiments.

A revival of interest in this area began around 1913 with the “radiation hypothesis,” due to Max Trautz, Jean Perrin and William Lewis. The particular challenge they tackled would probably have escaped notice of the scientific community, except for the fact that Perrin and Lewis were two highly respected scientists. Their developments required a strong mathematical preparation. Lewis was the first chemist to develop a theory of chemical kinetics based on statistical mechanics and quantum theory. It is clear that Lewis was an exception in terms of mathematical background to the majority of British chemists, who even in the 1920s had a mathematical background that was insufficient to address, or even understand such problems.

The “radiation theory,” which was received with enthusiasm, was later seen to be mistaken. However, it was important as it stirred up a lively debate that greatly contributed to the development of the correct theories of chemical kinetics.

In this first phase of development, the theories of chemical kinetics tried to resolve the problem of the calculation of the pre-exponential factor and activation energy in the Arrhenius equation. The difficulties in calculating A stemmed in large part from the confusion that had existed ever since the first quarter of the nineteenth century over the role of molecular collisions on the rates of reaction. Today, we know that molecular collisions lead to the distribution of energy between molecules, but the rate of chemical reactions is determined both by the frequency of these collisions and the factors associated with the distribution of energy.

Max Trautz in 1916 and William Lewis in 1918 developed mathematical expressions that allowed the formulation of a collision theory for pre-exponential factors. In 1936 Henry Eyring, and almost independently, Michael Polanyi and M. G. Evans came to develop the transition state theory, having as its bases thermodynamics and statistical mechanics.

The concept of potential energy surface (PES) was developed to calculate the activation energy. Based on quantum mechanics, the first PES was constructed, at the start of the 1930s by Eyring and Polanyi for the reaction $\text{H} + \text{H}_2$. However, the concept of PES is much more comprehensive because it allows the dynamic study of the rates of elementary reactions. This is based on the study of the forces that cause molecular motions that will lead to chemical reaction.

1.3 Chemical Kinetics: the current view

Chemistry is concerned with the study of molecular structures, equilibria between these structures and the rates with which some structures are transformed into others. The study of molecular structures corresponds to the study of the species that exist at the minima of multidimensional PESs, and which are, in principle, accessible through spectroscopic measurements and X-ray diffraction. The equilibria between these structures are related to the difference in energy between their respective minima and can be studied by thermochemistry, by assuming an appropriate standard state. The rate of chemical reactions is a manifestation of the energy barriers existing between these minima, barriers that are not directly observable. The transformation between molecular structures implies the variable *time* in the study of chemical reactions and is the sphere of chemical kinetics. The “journey” from one minimum to another on the PES is one of the objectives of the study of molecular dynamics, which is included within the domain of chemical kinetics. It is also possible to classify nuclear decay as a special type of unimolecular transformation, and as such, nuclear chemistry can be included as an area of chemical kinetics. Thus, the scope of chemical kinetics spans the area from nuclear processes up to the behaviour of large molecules.

The range of rates of chemical reactions is enormous. Figure 1.1 gives a general panorama of the variety of reaction rates of processes in the world around us. Nuclear transformations and geological processes can be considered to be some of the slowest reactions that we come across. The corrosion of some metals frequently takes place during the life expectancy of a human (80 years = 2.5×10^9 sec). The

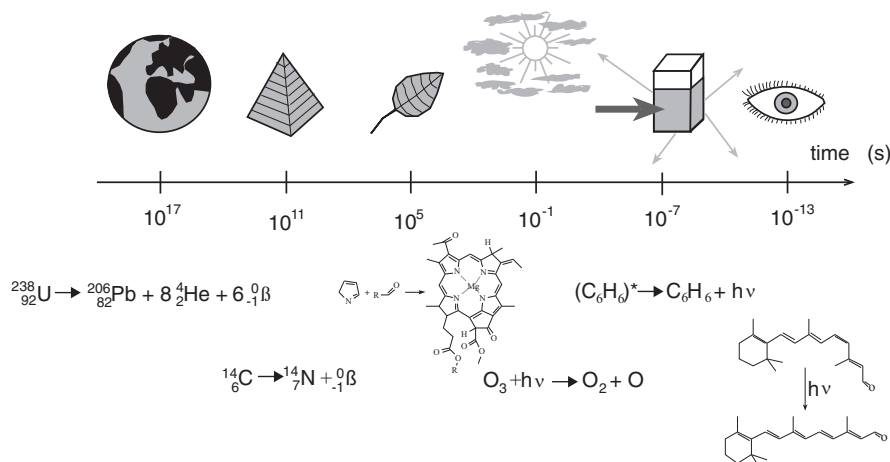


FIGURE 1.1

Range of rates of chemical reactions.

time of cooking food is readily measurable simply by visual observation and extends from minutes to hours. We can contrast this with the case of reactions such as the precipitation of salt or neutralisation of an acid, which occur in <0.1 sec, because visually we can no longer distinguish images on this timescale. There are, however, special techniques that allow much shorter time resolution in our observation window, and which allow study of extremely rapid reactions. The limit of time resolution of interest for chemical kinetics is defined by the movement of nuclei in molecules in their vibrational or rotational motion.

The chemical reaction can be considered as a voyage on a multidimensional PES (Figure 1.2). The definition of the PES has its origin in the separation of the movement of electrons and nuclei. This separation is justified on the basis of the difference in mass between an electron and a proton (the mass of the former is 1/1800 times the rest mass of the second), which means that the movement of electrons is much more rapid than that of the nuclei. Because of this, the electrons can be considered to readjust *instantaneously* to each of the geometries that the nuclei might adopt. The PES results from solving the Schrödinger equation for each of the possible nuclear geometries. The sum of the electronic energy and the nuclear repulsion governs the movement of the nuclei. Ideally, the Schrödinger equation must be solved for a great number of nuclear geometries using only the laws of quantum mechanics and the universal constants, which are given in

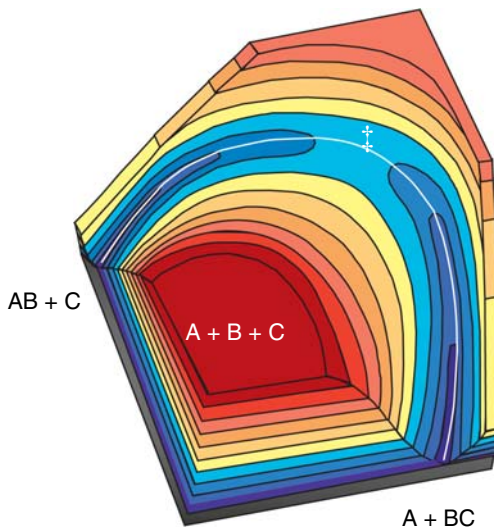


FIGURE 1.2

PES for collinear approach of atom A to the diatomic molecule BC in the triatomic system $A + BC \rightarrow AB + C$, with the most important topographical regions: reactant valley ($A + BC$), transition state (\ddagger), product valley ($AB + C$), dissociation plateau for all bonds ($A + B + C$) and lowest energy pathway from reactants to products (dashed line).

Appendix I. From this, a set of points will be obtained, and the energy determined for each of the possible geometries. This type of calculation, known as *ab initio*, is very time consuming and difficult for polyatomic systems. As a consequence, many PESs include experimental information and are described by more or less complex functions, which are fitted to results of *ab initio* calculations and experimental information on the system.

In a hypersurface of a polyatomic system, there can exist a number of more or less stable structures, which correspond to deeper or shallower potential wells. The separation between these wells is made up of hills, that is, potential barriers with variable heights. The height of the potential barriers determines the energy necessary to convert from one structure into another, that is, for a chemical reaction to occur. In the passage from a reactant well, or valley, to that of products, there is normally one that goes by a path, whose point of highest energy is termed the saddle point, given the topographic similarity to the saddle of a horse. A saddle point corresponds to a maximum energy on the route that leads from reactants to products, but a minimum one on the direction orthogonal to this. The reaction pathway, which goes through the lowest energy path, is called the *minimum energy path*. It is natural that a chemical reaction, which occurs on a single PES will follow preferentially the minimum energy pathway or route. The surface orthogonal to the minimum energy pathway between reactants and product and which contains the saddle point corresponds to a set of nuclear configurations that is designated the *transition state*. Its existence can be considered as virtual or conceptual, because the transition state corresponds to a region on the potential energy hypersurface from which the conversion of reactants to products leads to a decrease in the potential energy of the system. The transition state is, therefore, intrinsically unstable.

The minimum energy pathway for a given reaction can be defined by starting from the transition state as being the path of the largest slope that leads to the reactants valley on one side and the product valley on the other. This minimum energy pathway is shown in [Figure 1.2](#) for a typical reaction that involves breaking one bond in the reactants and forming a new bond in the products. Normally, the PES for a chemical system cannot be determined accurately since for a molecule containing N atoms the PES is a function of $3N$ nuclear coordinates. Some of these coordinates can be separated, in particular the three coordinates that describe translational motion, given the conservation of the movement of the centre of mass, and the coordinates corresponding to rotational motion, given the conservation of angular momentum. After separation of these motions, the PES will be a function of $3N-5$ internal, inter-dependent coordinates for linear configurations and $3N-6$ for non-linear configurations. The complexity of the PES for polyatomic systems justifies the use of simplified models that simulate the variation of the potential energy of the system as a function of a reaction coordinate of the reaction. The reaction coordinate starts to have a particular significance for each model that represents the variation of the energy of the system on the conversion of reactants to products. Given that these models are simplified representations of the PES, the reaction coordinate given by a model may not correspond to the minimum energy pathway.

[Figure 1.2](#) shows the case of a very simple PES. In fact, the topography of the PESs can be very diverse. [Figure 1.3](#) shows an example of a PES, where instead of a maximum (saddle point), there is a minimum (intermediate) in the middle of the minimum energy pathway.

The movement of atoms across the reaction coordinate can, in an elementary approximation, be compared with that of atoms in a bond with a low-frequency vibration. The vibrational frequency ν of a bond between atoms A and B is characteristic of the AB bond and depends, to a first approximation, on the force constant of the bond f and the reduced mass of its atoms, μ

$$\nu = \frac{1}{2\pi} \left(\frac{f}{\mu} \right)^{1/2} \quad (1.2)$$

where the reduced mass is given by

$$\mu = \frac{m_A m_B}{m_A + m_B} \quad (1.3)$$

The energies where vibrations of AB are expected to occur lie between 300 and 3000 cm^{-1} ($4\text{--}40\text{ kJ mol}^{-1}$) such that they can be seen in the infrared. These energies can be related to the corresponding vibrational frequencies by the Planck equation

$$E = h\nu \quad (1.4)$$

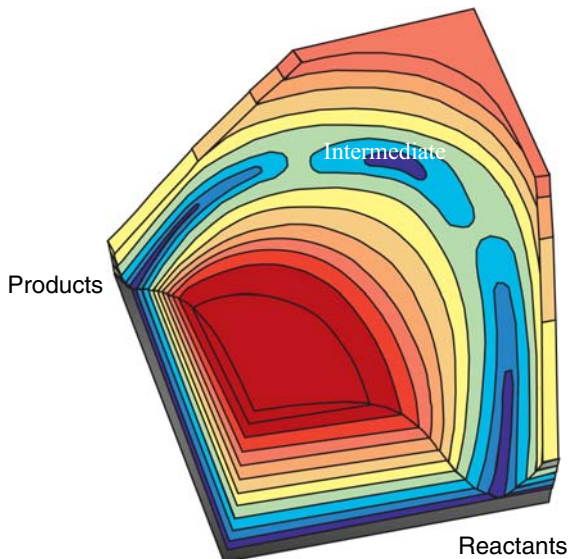


FIGURE 1.3

Reaction occurring on a surface with a potential well separating reactants and products, and corresponding to the formation of a reactive intermediate. The reaction is exothermic.

where Planck's constant, $h = 6.626 \times 10^{-34}$ J sec = 6.626×10^{-34} N m sec. Thus, it is possible to calculate that a bond AB typically will undergo 10^{13} – 10^{14} oscillations per second, or that there will be one vibration for each 100–10 fsec. As the vibrational energy of a bond is given by

$$E_v = \left(v + \frac{1}{2} \right) h\nu, \quad v = 0, 1, 2, 3, \dots \quad (1.5)$$

where v is the vibrational quantum number, the minimum distortion that a diatomic molecule suffers relative to its equilibrium bond length, r_{eq} , can be calculated by considering that the bond is in its lowest vibrational energy, $v = 0$, and using a harmonic oscillator as the model of the variation of energy with the distortion (Figure 1.4). The variation of the energy with the distortion is given by the equation of a parabola

$$V(r) = \frac{1}{2}f(r_{\text{eq}} - r)^2 \quad (1.6)$$

where f is the force constant characteristic of the oscillator. By substituting eq. (1.2) into expression (1.5) with $v = 0$, and equating to (1.6), we obtain

$$r_{\text{eq}} - r = \sqrt{\frac{\hbar}{f}} \sqrt{\frac{f}{\mu}} \quad (1.7)$$

To apply this equation to the real case of the $^{35}\text{Cl}-^{35}\text{Cl}$ bond, it is necessary to know its reduced mass and vibrational frequency. The reduced mass of Cl_2 calculated from the atomic mass of chlorine and eq. (1.3) leads to $\mu = 2.905 \times 10^{-26}$ kg. The

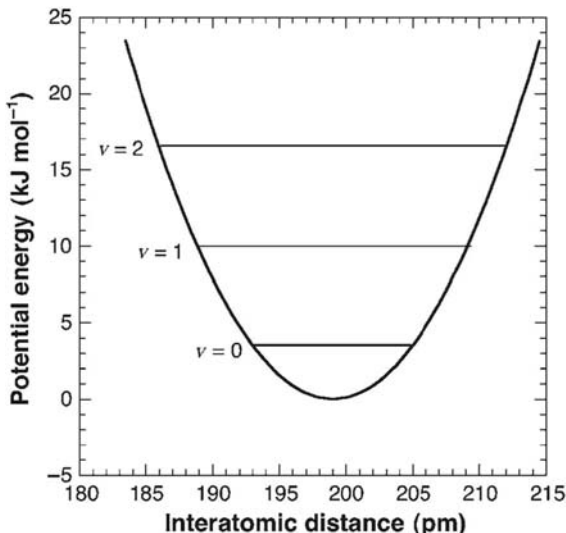


FIGURE 1.4

Harmonic oscillator with the characteristic behaviour of Cl_2 molecule.

Cl–Cl vibration is seen at 559.71 cm^{-1} with $\nu = c\bar{\nu}$, where $c = 2.998 \times 10^8\text{ m sec}^{-1}$ is the speed of light in vacuum and the frequency is $1.68 \times 10^{13}\text{ sec}^{-1}$. Using [eq. \(1.2\)](#), the force constant for this bond is $f = 322.7\text{ N m}^{-1}$, since by definition $1\text{ N} = 1\text{ kg m sec}^{-2}$. Force constants are often expressed in $\text{mdyn}\text{ \AA}^{-1}$, $\text{kcal mol}^{-1}\text{ \AA}^{-1}$ or $\text{J mol}^{-1}\text{ pm}^{-1}$, so that it is useful to know the conversion factors for these units:

$$1\text{ mdyn \AA}^{-1} = 100\text{ N m}^{-1} = 143.8\text{ kcal mol}^{-1}\text{ \AA}^{-2} = 60.17\text{ J mol}^{-1}\text{ pm}^{-2}.$$

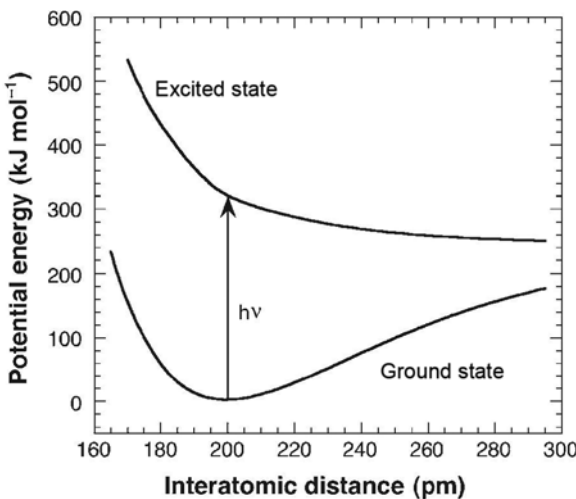
Knowing the values of f and μ , [eq. \(1.7\)](#) gives $(r_{\text{eq}} - r) = 5.87 \times 10^{-12}\text{ m}$. As such, a vibration goes through $1.17 \times 10^{-11}\text{ m}$ in $5.95 \times 10^{-14}\text{ sec}$, or, in other words, the speed at which the atoms undergo vibrational movement is about 200 m sec^{-1} (720 km h^{-1}) in the fundamental vibrational level. It should be noted that the Cl–Cl bond, whose equilibrium bond length is $1.99 \times 10^{-10}\text{ m}$, is distorted by about 3% of its length.

Today, a technique called transition state spectroscopy that uses lasers with pulse widths around 10 fsec facilitates the detection of transient species with extremely short lifetimes. In this time interval, a bond in its fundamental vibration covers a distance of only $2 \times 10^{-12}\text{ m}$. As such, this technique enables one to obtain a sequence of images of vibrational motion of a chemical bond in the act of breaking. However, it is worth remembering that owing to the Heisenberg uncertainty principle:

$$\Delta E \Delta t \geq \frac{1}{2}\hbar \quad (1.8)$$

observations on the time scale 10^{-14} sec correspond to an uncertainty in energy of 3 kJ mol^{-1} . A better time resolution leads to greater uncertainties in energy, which will not be of much use in chemical kinetics, given that, according to [eq. \(1.1\)](#), an uncertainty of 3 kJ mol^{-1} in transition state energy leads to a factor of 3 in the rate of a reaction at 25°C . Nevertheless, these ultrashort pulse techniques do find applications in areas of spectroscopy where one is dealing with broad bands in terms of frequency distribution, and spectral bandwidth is not the limiting factor.

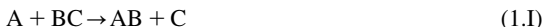
It is anticipated that the most rapid chemical reactions will be those that occur every time there is a bond vibration, that is, when the energy barrier is equal or less than that of the vibrational energy. This corresponds to a purely repulsive PES that could be obtained, for example, by electronic excitation. [Figure 1.5](#) gives a typical example of a reaction of this type. For molecules with more than two atoms, the situation becomes significantly more complicated, because it is necessary to consider energy distribution between the various bonds involved. For a bimolecular reaction, the maximum rate will be achieved for an exothermic reaction that occurs on every collision between reactant molecules. This limit is reached in some reactions of free radicals in the gas phase that occur without any activation barrier. However, even in some of these reactions potential wells are seen instead of barriers separating reactants and products, as in the surface shown in [Figure 1.3](#). In these cases, the rate of the reaction may be limited by the formation of a complex or intermediate with a finite lifetime. In this case, the reaction is no longer elementary, and follows a two-step mechanism: formation of an intermediate, followed by its decay. In fluid solutions, the maximum rate of a

**FIGURE 1.5**

Reaction occurring on a barrier-free surface, obtained by electronic excitation of the reactants.

bimolecular reaction is limited by the rate at which the reactants can diffuse in the medium to achieve the reaction radius.

Beyond the above limiting situation, in a chemical reaction of the general type



energy barriers are always found. The simplest model for the origin of these energy barriers consists in assuming that to break the B–C bond, we need to supply to the BC molecules an energy equal to the energy of this bond. However, frequently, the observed energy barriers of these reactions are only *ca.* 10% of the energy of the bonds being broken. As such, we can see that, in general, the reaction cannot proceed in one step in which the B–C bond is broken followed by a subsequent and independent step in which there is formation of the A–B bond. In all the steps of the reaction, there must be a strong correlation between the bonds, which is broken and that which is being formed. The transition state appears to have an electronic configuration that maximises the bonding in all of the parts (A–B and B–C) of which it is composed. The energy barrier results from two opposing factors: on one hand, the approach between the species A and BC allows the formation of a new bond, AB, which lowers the energy of the system, while on the other, this approach results in an increase in the energy of the system, given the energy penalty associated with stretching a bond and the repulsion between the molecules at short distances. The total energy depends on the correlation between the breaking and formation of the bonds.

The potential energy is a microscopic variable. For any configuration of the reactive system, in principle it is possible to calculate a potential energy. Knowing the potential energy along the minimum energy path, it is possible to define a continuous analytical function that will describe the evolution of the system from reactants to products. The

knowledge of the PES allows estimation of the potential energy of activation of a chemical reaction, that is following classical mechanics, the minimum energy necessary, for the isolated reactants to be transformed to isolated product molecules. To make a comparison between the potential energy of activation calculated from the PES and the experimental activation energy, it is necessary to make the change from the microscopic to the macroscopic domain. The energy of the system, which is observed macroscopically, is a thermodynamic energy. The energy differences between reactants and products in solution are normally measured in terms of their equilibrium constants. As the equilibrium constant of a reaction is related to the free energy

$$\Delta G^0 = -RT \ln K_{\text{eq}} \quad (1.9)$$

the barrier height to be surmounted in the course of a reaction must be expressed in macroscopic terms by a free energy of activation. The variation of potential energy calculated in this way thus corresponds to the variation in free energy when the entropy differences are negligible. The relation between the microscopic models and the experimental macroscopic reality can be made through statistical mechanics. In statistical terms, although a chemical species is a group of particles with a determined range of properties, all the particles of one species have to have the same equilibrium configuration. So, as many species exist as equilibrium configurations that can be statistically defined along the reaction coordinate.

In this context, equilibrium configuration denotes a geometry in mechanical equilibrium, that is, a geometry corresponding to a point for which the derivative of the potential energy function is zero. This derivative is zero for potential maxima and minima. As such, along the reaction coordinate, we can define three configurations that fulfil these requisites: the reactants, the products and the transition state. The first two correspond to minima and are in stable equilibria, while the latter corresponds to a maximum along the reaction coordinate, and is in unstable equilibrium (or pseudo-equilibrium). Then, although the reaction coordinate is continuous, the thermodynamic energy along it is discontinuous, containing only three points. Nevertheless, it is useful to formulate the variation of free energy as a function of the reaction coordinate in terms of a continuous function. It should be noted, however, that the interpolated points between the equilibrium configurations do not have any thermodynamic significance.

In the transformation from the microscopic world to the macroscopic one, we also need to consider the effect of molecular collision on the distribution of molecular velocity or energy in these systems. The majority of molecules will have a velocity close to the mean value for the molecules, but there are always some molecules with a velocity much greater than and others with a velocity much lesser than the mean velocity. The distribution of velocities of gas molecules was first described by Maxwell in 1860. The Maxwell distribution of velocities is given by

$$f(s) = 4\pi \left(\frac{M}{2\pi RT} \right)^{3/2} s^2 \exp\left(-\frac{Ms^2}{2RT}\right) \quad (1.10)$$

The mean velocity can be calculated from the integral

$$\bar{s} = \int_0^{\infty} sf(s)ds = 4\pi \left[\frac{M}{2\pi RT} \right]^{3/2} \int_0^{\infty} s^3 \exp\left[-\frac{Ms^2}{2RT}\right] ds = \sqrt{\frac{8RT}{\pi M}} \quad (1.11)$$

where M is the molar mass of the molecules and $f(s) ds$ is the fraction of molecules which has velocities between s and $s + ds$. Figure 1.6 illustrates the distribution of molecular velocities of a gas at various temperatures.

For the case of N_2 molecules at 298 K, using the constants from Appendix I, General Data, we obtain a mean velocity of 475 m sec⁻¹.

Until now, we have only considered elementary reactions, that is, ones that occur in a single step. These reactions are observed between a certain number (that must be a whole number) of atoms, molecules or ions. The number of species involved in an elementary reaction is designated as the molecularity of an elementary reaction. A chemical reaction is generally described by an equation of the type



where $v_A, v_B, v_X, v_Y, \dots$ are the stoichiometric coefficients of the species A, B, X, Y, These coefficients are also whole numbers, but as the overall reaction can occur with a sequence of elementary steps of molecularity one, two or three, the stoichiometric coefficients will only correspond to the molecularity of the

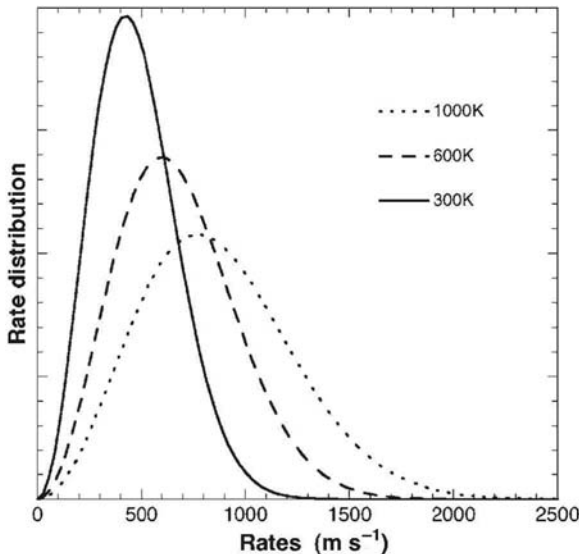


FIGURE 1.6

Distribution of molecular velocities for N_2 at three different temperatures (in Kelvin).

reaction if this is an elementary reaction. The sequence of these microscopic elementary steps is known as the mechanism of the reaction. In any case, the balance of all the microscopic elementary steps has to result in the macroscopic process described by the above general chemical equation, whose equilibrium constant is

$$K_{eq} = \frac{(a_X)^{v_X} (a_Y)^{v_Y} \dots}{(a_A)^{v_A} (a_B)^{v_B} \dots} \quad (1.13)$$

where a_i represents the activity of species i .

The mechanism of a reaction is normally determined experimentally, but although it is possible to disprove a mechanism, it is impossible to confirm that a proposed mechanism is correct simply on the basis of the experimental results available. It is also possible that a reaction can occur by two distinct mechanisms.

In the above explanation, we did not consider the possibility of an elementary process having a molecularity greater than 3. The probability that elementary kinetic processes involve the simultaneous collision of four particles is negligible. When more than three reactant molecules are involved, it is certain that the chemical transformation that occurs does not take place in a single elementary step.

Current practice in chemical kinetics tries to identify the one particular elementary step that has a very large effect on the overall reaction rate. This elementary process is known as the rate-determining step of the reaction. This rate-determining step depends on the relative magnitudes of the energy barriers for each elementary reaction as well as on the concentrations of the reactants and intermediates. When such a step exists, the rate of the overall reaction is either the value for this rate-determining step or it is this value multiplied by some equilibrium constants of steps preceding it (pre-equilibria).

In [Chapters 2 and 3](#), we will consider, respectively, the factors involved in determining the rates of chemical reaction and the techniques that allow the experimental study of their kinetics. In [Chapter 4](#), we will start from empirical knowledge of the variation of concentration of reactants and products with time to establish the rate laws for the corresponding elementary reactions. [Chapters 5–8](#) will consider some theories that allow us to calculate or rationalise the numerical values in the above rate laws. [Chapters 9–14](#) will discuss in detail some of the most important reactions that have been studied using chemical kinetics. [Chapter 15](#) makes a detour from traditional chemical kinetics to explore similarities between the rates of chemical reactions and the time course of medications in the human body, emphasising some of their mathematical similarities. [Chapters 16 and 17](#) focus on some less familiar topics in textbooks in this area, but we believe they will lead to a conceptual awareness of the role of energy and electron transfer in chemical kinetics. Finally, [Chapter 18](#) takes the reader to the exquisite time dependences of non-linear systems and how they can generate chaos and oscillatory reactions with an impact on biological systems and on the environment.

References

- [1] L Wilhelmy, *Pogg. Ann.* **81** (1850) 423.
- [2] W Ostwald, *J. Prakt. Chem.* **29** (1884) 358.
- [3] E Farber, *Chymia* **7** (1961) 135.
- [4] MC King, *Ambix* **29** (1982) 49.
- [5] MC King, *Ambix* **31** (1984) 16.
- [6] MC King, KJ Laidler, *Arch. Hist. Exact. Sci.* **30** (1984) 45.
- [7] M Berthelot, LP Gilles, St., *Ann. Chim.* **65** (1862) 385.
- [8] M Berthelot, LP Gilles, St., *Ann. Chim.* **66** (1862) 5.
- [9] M Berthelot, LP Gilles, St., *Ann. Chim.* **68** (1863) 255.
- [10] J Lamor, *Manchester Mem.* **32** (1908) 10.
- [11] AV Harcourt, W Esson, *Chem. News* **10** (1864) 171.
- [12] AV Harcourt, W Esson, *Proc. Roy. Soc. (London)* **14** (1865) 470.
- [13] AV Harcourt, W Esson, *Philos. Trans.* **156** (1866) 202.
- [14] AV Harcourt, W Esson, *Chem. News* **18** (1868) 13.
- [15] MC King, *Ambix* **28** (1981) 70.
- [16] E Jungfleische, *Bull Soc. Chem.* (1913) 102.
- [17] EW Lund, *J. Chem. Educ.* **45** (1968) 125.
- [18] SR Logan, *J. Chem. Educ.* **59** (1982) 279.
- [19] KJ Laidler, *J. Chem. Educ.* **61** (1984) 494.
- [20] JH van't Hoff, *Études de Dynamique Chimique*, F. Muller & Co., Amsterdam, 1884.
- [21] A Findlay, T William, *A Hundred Years of Chemistry*, University Paperbacks, G. Duckworth, Methuen, London, 1965.
- [22] AJ Ihde, *The Development of Modern Chemistry*, Harper & Row, New York, 1964.

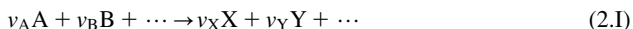
This page intentionally left blank

Reaction rate laws

2

2.1 Reaction rates

The rate of conversion for the general form of a chemical reaction,



where v_A , v_B , v_X and v_Y are the stoichiometric coefficients of the species involved, can be expressed in terms of a single parameter ξ , which is known as the extent of reaction, and is defined by [1]

$$\xi = \frac{|n_i(\xi) - n_i(0)|}{v_i} \quad (2.1)$$

Here, i represents any of the reactants or products, n_i the number of moles of i in the chemical reaction, $n_i(0)$ the amount of i present when $\xi = 0$ (that is before the start of the reaction) and $n_i(\xi)$ the amount of i present at extent of reaction ξ . The absolute value is used because the number of moles of the reactants decreases in the course of the reaction, while that of the products increases, but the extent of the reaction must be a positive quantity.

The rate of conversion in a chemical reaction is defined as the variation of ξ with time, t ,

$$r = \frac{d\xi}{dt} \quad (2.2)$$

Using the definition of ξ from eq. (2.1), we obtain

$$\frac{d\xi}{dt} = \frac{1}{v_i} \left| \frac{dn_i}{dt} \right| \quad (2.3)$$

where, to simplify the notation, we will write n_i instead of $n_i(\xi)$.

The reaction velocity is defined by

$$v = \frac{r}{V} = \frac{1}{v_i V} \left| \frac{dn_i}{dt} \right| \quad (2.4)$$

The distinction between the rate of conversion r and the reaction velocity (rate) v can be made on the basis of the units that are used. Normally, the amount of substance i is given in moles and the rate of conversion is expressed as mol sec^{-1} , while for the case of the volume being given in dm^3 , the reaction velocity is given in $\text{mol dm}^{-3} \text{ sec}^{-1}$. If the volume stays constant during the

reaction, it is more common to give the concentration of i , that is, $[i]$ in mol L $^{-1}$ (1 L = 1 dm 3) in the determination of the rate of conversion of reactions. Thus for a total constant volume V ,

$$\left(\frac{d\xi}{dt}\right)_V = \frac{V}{v_i} \left| \left(\frac{d[i]}{dt}\right)_V \right| \quad (2.5)$$

The experimental determination of the velocity of a reaction in solution is made by measuring the change in the concentration of reactants or products with time, since the volume of the environment in which the reaction occurs does not vary appreciably during the reaction. This is also true of reactions in the gas phase when the reactor is kept at constant volume.

Sometimes for a reaction in the gas phase at constant temperature and volume, it is more convenient to measure the partial pressure P_i of one component i rather than its concentration. Assuming ideal mixing behaviour of the gases, we can express the rate of conversion as a function of partial pressure of any one of the components

$$\left(\frac{d\xi}{dt}\right)_{T,V} = \frac{V}{v_i RT} \left| \left(\frac{dP_i}{dt}\right)_{T,V} \right| \quad (2.6)$$

When there is a change in the total number of moles of gas in the system,

$$\Delta v_i = \sum v_{i,\text{products}} - \sum v_{i,\text{reactants}} \neq 0 \quad (2.7)$$

the total pressure will vary proportionally with the extent of the reaction. From eq. (2.1)

$$\xi = \frac{\sum n_i(\xi) - \sum n_i(0)}{\Delta v_i} \quad (2.8)$$

If all the gases follow ideal behaviour

$$n_i(\xi) = \frac{P_i(\xi)}{RT} V \quad (2.9)$$

and we can write

$$\xi = \frac{V}{RT} \frac{\sum P_i(\xi) - \sum P_i(0)}{\Delta v_i} \quad (2.10)$$

As $\sum P_i(\xi)$ and $\sum P_i(0)$ are the total pressures of the system for the extent of reaction ξ and for the start of the reaction, respectively, the previous equation can be simplified to give

$$\xi = \frac{V}{RT} \left(\frac{P(\xi) - P(0)}{\Delta v_i} \right) \quad (2.11)$$

As a consequence, where there is a change in the total number of moles of gas, the rate of conversion for a reaction at constant volume and temperature will be given by

$$\left(\frac{d\xi}{dt}\right)_{V,T} = \frac{V}{RT\Delta v_i} \left(\frac{dP}{dt} \right)_{V,T} \quad (2.12)$$

where P represents the total pressure of the reaction system.

From the perfect gas equation, if a gas phase reaction in which $\Delta v_i \neq 0$ occurs at constant temperature and pressure, the volume must change. In this case, if all the components follow ideal behaviour

$$n_i(\xi) = \frac{P_i(\xi)V(\xi)}{RT} \quad (2.13)$$

where $V(\xi)$ is the total volume of the system for an extent of reaction ξ . Substituting into eq. (2.8) and considering that the pressure remains constant, $\Sigma P_i(\xi) = \Sigma P_i(0) = P$,

$$\xi = \frac{P}{RT\Delta v_i}[V(\xi) - V(0)] \quad (2.14)$$

and

$$\left(\frac{d\xi}{dt}\right)_{T,P} = \frac{P}{RT\Delta v_i} \left(\frac{dV}{dt}\right)_{T,P} \quad (2.15)$$

It is important to prove that eq. (2.2) defines the rate of conversion in the reaction, that eq. (2.4) defines the velocity of the reaction and that in the expressions (2.5), (2.6), (2.12) and (2.15), the quantities $(d[i]/dt)_{V,T}$, $(dP/dt)_{V,T}$, $(dP/dt)_{V,T}$ and $(dV/dt)_{T,P}$ are proportional to the velocity of the reaction. It must also be emphasised that, generally, the rate can be defined in terms of any of the reactant or product molecules, provided that the stoichiometry of the reaction is included. In other words, eq. (2.16) is valid

$$v = -\frac{1}{v_A V} \left(\frac{dn_A}{dt}\right) = -\frac{1}{v_B V} \left(\frac{dn_B}{dt}\right) = \frac{1}{v_X V} \left(\frac{dn_X}{dt}\right) = \frac{1}{v_Y V} \left(\frac{dn_Y}{dt}\right) \quad (2.16)$$

2.2 Factors that influence the velocities of reactions

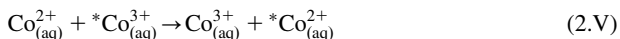
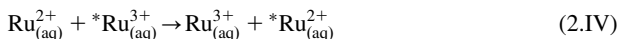
2.2.1 Nature of the reactants

The velocities of elementary chemical reactions depend on a great number of factors, in particular the nature of the reactants, concentrations or pressures, temperature, light, catalysts and the solvent used. The great variation observed in reaction velocities will be related first to the nature of the reagents. Many reactions, such as those between oppositely charged ions in aqueous solution, which do not involve breaking chemical bonds, are very rapid at room temperature.

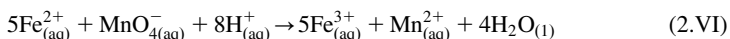


However, reactions involving structurally similar reactant molecules such as exchange reactions of electrons between two isotopically labelled transition metal

complexes, which also do not involve breaking chemical bonds, often show great differences in rates under similar conditions



Reaction (2.IV) is 10^5 times faster than reaction (2.V). In contrast, although reactions involving bond breaking and bond formation are generally slow, there are some extremely fast reactions of this type such as the oxidation of iron (2.VI) by permanganate ion in acid solution:



Thus there appears to be a lack of even qualitative general rules to evaluate the effect of the nature of reactants on the rates of reactions. The success of theoretical calculations of reaction velocities in chemical kinetics without using adjustable parameters has been limited. Even for the simplest reactions in the gas phase, a large amount of computer time is needed with ab initio quantum mechanical calculations to obtain detailed and precise information on the potential energy surface of a reaction system, in addition to requiring the calculation of a large number of trajectories before we can calculate the macroscopic velocity of a reaction. For more complex reactions, such calculations are prohibitive in terms of both computer time and money. In practice, it is more common to base the interpretation and prediction of reaction velocities as a function of the nature of reactants on the development of simplified theoretical models that relate some properties of the reactants with the ease with which their bonds can be broken and/or new bonds formed in the products. In Table 2.1 we give a typical family of chemical reactions, with their respective activation energies, and some appropriate parameters that have been used for the theoretical calculation of their reaction rates [2].

It is useful to define *families of reactions*, in the sense of a series of reactions that occur via the same mechanism and under the same experimental conditions, but where the reactants differ from each other by only small changes in structure, such that they produce only small perturbations in the reaction centre. These small structural changes are normally associated with minor changes in the bonding of substituent groups in the region of the bonds that are broken or being formed during the reaction. Many theoretical models have been suggested for such classes of reactions, leading to empirical correlations between the activation energy and the change in a specific parameter such as reaction enthalpy or electronic or steric parameters. This will be explored further in Chapter 7, Structure–Reactivity Relationships. In Table 2.1, the family of reactions is that of hydrogen-atom transfers in the gas phase.

Table 2.1 is organised to stress the fact that if we keep a series of the parameters constant, it is possible to attribute the change in activation energy, and consequently, the velocity of reaction [eq. (2.4)], to the change in a specific parameter. For example, in the reactions (i) and (ii) the increase in the sum of

Table 2.1 Molecular and kinetic parameters of some elementary gas phase reactions.

Reaction	ΔH^a (kJ mol ⁻¹)	$I_{AB} + I_{BC}$ ^b (Å)	f_{BC} ^b (kJ mol ⁻¹ Å ⁻²)	f_{AB} ^b (kJ mol ⁻¹ Å ⁻²)	I_p ^c (eV)	E_A ^c (eV)	E_a ^d (kJ mol ⁻¹)
(i) $H + H_2 \rightarrow H_2 + H$	0	1.482	3439	3439	13.598	0.7542	32
(ii) $CH_3 + CH_4 \rightarrow CH_4 + CH_3$	0	2.174	3435	3435	9.843	0.08	61
(iii) $C_2H_5 + C_2H_6 \rightarrow C_2H_6 + C_2H_5$	0	2.188	3348	3348	8.117	-0.26	56
(iv) $CH_3 + C_2H_6 \rightarrow CH_4 + C_2H_5$	-19	2.181	3348	3435	8.117	0.08	48
(v) $Cl + CH_4 \rightarrow HCl + CH_3$	+8	2.362	3435	3120	12.968	3.614	11

^aReaction enthalpy.

^bSum of the bond lengths of the bonds broken or formed in the course of the reaction, and force constants of these bonds.

^cIonization energies and electron affinities of the radicals.

^dExperimental activation energies.

bond lengths in reactants and products leads to an increase in activation energy. With reactions (ii) and (iii), the predominant factor in the decrease in activation energy appears to be the decrease in force constants. Comparison between reactions (iii) and (iv) shows, as we may suspect intuitively, that the most exothermic reaction is the fastest one, from which we can say that the predominant factor in this case is the change in enthalpy of the reaction. However, if we compare reactions (ii) and (v), we find a very significant decrease in activation energy, in contrast to what we would expect from the positive enthalpy change, the increase in bond lengths or the decrease in force constants. In this case, what appears to be the dominant factor is the difference in electronic structure between the chlorine atom and the methyl radical, represented here by their ionisation potentials and electron affinities.

2.2.2 Reactant concentration

Almost all reaction rates depend on the concentration of reagents, while for reversible reactions they are also affected by those of products. The mathematical expression that relates the reaction velocity and the concentration of species present is called the law of reaction velocity, the kinetic law, or most simply, the rate law. Assuming that the reaction being considered involves an elementary process,



the corresponding rate law can be written

$$v = k[A]^a[B]^b \quad (2.17)$$

where the powers a and b are known as the partial orders of reaction for components A and B, and the proportionality constant k is called the specific rate constant for the reaction, or simply the rate constant. This constant is independent of the concentrations of the reactants but depends on the temperature, pressure and reaction medium. The partial orders can only be identified with the stoichiometric coefficients when we are dealing with an elementary reaction. The rate law of any reaction always has to be determined experimentally. The formulation of this principle is known as the law of mass action, which can be stated that in dilute solutions the velocity of each chemical reaction is proportional to the product of the concentration of reactants, is independent of the concentration of other species and of the presence of any other reactions.

Treating the case of an elementary reversible reaction



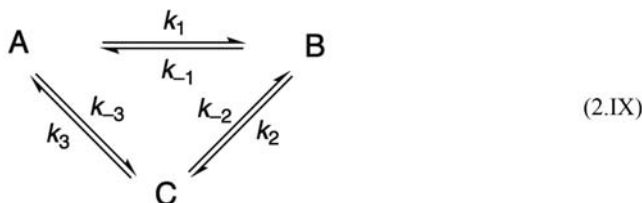
where a , b , x and y are whole numbers, this same law indicates that the velocity of the reaction is given by

$$v = k_d[A]^a[B]^b - k_i[X]^x[Y]^y = v_d - v_i \quad (2.18)$$

At equilibrium $v_d = v_i$, and since, overall, $v = 0$ we obtain

$$\left(\frac{k_d}{k_i}\right) = \frac{[X]_{\text{eq}}^x [Y]_{\text{eq}}^y}{[A]_{\text{eq}}^a [B]_{\text{eq}}^b} = K_{\text{eq}} \quad (2.19)$$

where K_{eq} is the equilibrium constant for the reaction. From eq. (2.19), we can see that only two of the three constants k_d , k_i and K_{eq} are independent. The same reasoning can be applied to more complicated systems such as that described by the following mechanism:



In this cyclic kinetic scheme, there is equilibrium between all the species. As a consequence, we can write the equilibrium constants

$$\begin{aligned} K_1 &= \frac{k_1}{k_{-1}} = \frac{[B]}{[A]} \\ K_2 &= \frac{k_2}{k_{-2}} = \frac{[C]}{[B]} \\ K_3 &= \frac{k_3}{k_{-3}} = \frac{[A]}{[C]} \end{aligned} \quad (2.20)$$

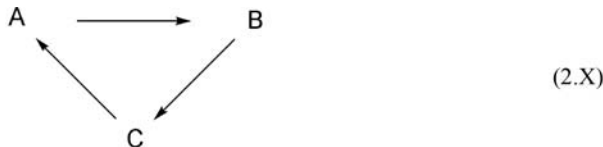
such that $K_1 K_2 K_3 = 1$, from which

$$k_1 k_2 k_3 = k_{-1} k_{-2} k_{-3} \quad (2.21)$$

In this scheme, only five of the six rate constants are independent.

At first sight, it may appear strange that the equilibrium constant expression only depends on the stoichiometry of a reaction when it stems from equating the rate laws for the forward and reverse reactions, where these reactions have an empirical character and, except for the case of elementary reactions, the rate expressions cannot be obtained from the overall equation for the chemical reaction. However, this observation has its basis on an important physical principle, the *principle of microscopic reversibility*. This can be stated in the form that in the state of macroscopic equilibrium each elementary process is in equilibrium, and is reversible at the microscopic level. In other words, the mechanism of a reversible reaction is the same in the forward and reverse directions. The mathematical basis of this principle comes from the fact that the equations of motion are symmetrical relative to time inversion, from which a particle which follows a given trajectory in the time from 0 to t will follow the identical reverse

trajectory in the time from t to 0. We can see, in fact, that at equilibrium, the concentrations of reactants and products are constant and do not oscillate about a mean value. Thus mechanism (2.IX) represents a possible chemical system, which is in agreement with the principle of microscopic reversibility and which will respond promptly to any perturbation from the equilibrium state. The same is not true for mechanism (2.X), where the step for formation of A from B implies an intermediate which is not involved in the formation of B from A, that is the mechanism of formation of B from A is different from that for the formation of A from B. Mechanism (X) cannot represent a real chemical system. If a system evolved spontaneously from A to B, from B to C and then returned to A, and if any of these steps would be exothermic, then the system would spontaneously and perpetually produce heat, which is impossible. However, if one of these reactions is driven by light, then mechanism (2.X) may represent a realistic (photochemical) system.



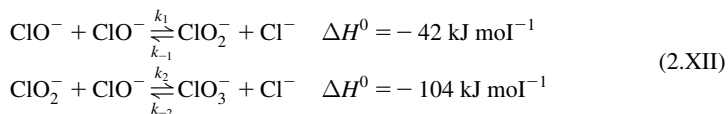
The principle of microscopic reversibility can be applied to the explanation of reaction mechanisms and of rate laws. As an example, we can take the disproportionation of the hypochlorite ion under equilibrium conditions



with the equilibrium constant given by

$$K_{\text{eq}} = \frac{[\text{ClO}_3^-]_{\text{eq}} [\text{Cl}^-]_{\text{eq}}^2}{[\text{ClO}^-]_{\text{eq}}^3} \quad (2.22)$$

and with a reaction mechanism involving the following steps in equilibrium, a slow first step followed by a second fast one



By equating the rates of each elementary process in the forward and reverse direction, we obtain

$$\begin{aligned} k_1[\text{ClO}^-]^2_{\text{eq}} &= k_{-1}[\text{ClO}_2^-]_{\text{eq}} [\text{Cl}^-]_{\text{eq}} \\ k_2[\text{ClO}_2^-]_{\text{eq}} [\text{ClO}^-]_{\text{eq}} &= k_{-2}[\text{ClO}_3^-]_{\text{eq}} [\text{Cl}^-]_{\text{eq}} \end{aligned} \quad (2.23)$$

Eliminating the concentration of the intermediate ClO_2^- , which is not present in the expression for the equilibrium constant, by multiplying both these equations, we obtain

$$k_1[\text{ClO}^-]_{\text{eq}}^2 k_2[\text{ClO}^-]_{\text{eq}} = k_{-1}[\text{Cl}^-]_{\text{eq}}^2 k_{-2}[\text{ClO}_3^-]_{\text{eq}} \quad (2.24)$$

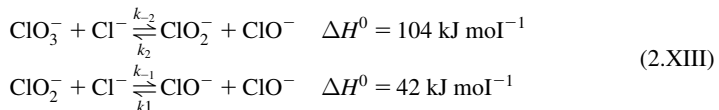
or

$$\frac{k_1 k_2}{k_{-1} k_{-2}} = \frac{[\text{ClO}_3^-]_{\text{eq}} [\text{Cl}^-]_{\text{eq}}^2}{[\text{ClO}^-]_{\text{eq}}^3} \quad (2.25)$$

the expression that gives a relationship between the rate constants, from which we can conclude that for this reaction

$$\frac{k_1 k_2}{k_{-1} k_{-2}} = K_{\text{eq}} \quad (2.26)$$

The equilibrium constant for a reaction arises from the equality of the rates of all the elementary processes. However, it is not possible starting from the rate law for the forward process and the equilibrium constant to obtain the rate law for the reverse process. We will illustrate this with the same reaction. Writing the above reactions in the reverse direction



and considering the values for the change of reaction enthalpies of the elementary processes, it would be expected that the first process would be the slower one, that is, that this will be the rate-determining step of the reaction. The rate law for the reaction written in the direction of eq. (2.XIII) will then be

$$v_1 = k_{-2}[\text{ClO}_3^-][\text{Cl}^-] \quad (2.27)$$

Regarding the rate law in the reverse directions as

$$v_{-1} = k_1[\text{ClO}^-]^2 \quad (2.28)$$

leads to a relation that bears no relationship to the equilibrium constant, or to any power of it, and also does not follow the stoichiometry of the reaction,

$$\frac{k_1}{k_{-2}} = \frac{[\text{ClO}_3^-][\text{Cl}^-]}{[\text{ClO}^-]^2} \neq K_{\text{eq}} \quad (2.29)$$

For a system far from equilibrium, if the reverse reaction follows a distinct mechanism from the forward one, common sense tells us that the ratio of concentrations will be different from that given by the rate laws and the equilibrium constant. The mechanisms of reaction in the forward and reverse directions can only be assumed to be the same close to equilibrium. From the above, it is clear that

both the rate laws for the reaction must be obtained experimentally. The relationship between the rate laws for reactions far from equilibrium is only equal to the equilibrium constant for elementary reactions, or for systems where the forward and reverse reactions have the same rate-determining step.

As the partial orders of reaction are experimentally determined parameters, they can take any value, and the positive integer values we have presented until now are only specific cases. We will show this with some experimental rate laws. The exchange of iodine atoms between iodate ion and molecular iodine has been studied with radioisotopes



and the following rate law obtained:

$$v = k[\text{I}_2]^{3/5}[{\text{IO}}_3^-]^{9/5}[\text{H}^+]^{9/5} \quad (2.30)$$

where the partial orders are all fractions. Another example is the following reaction in aqueous solution, which has a negative partial order



$$v = k[\text{I}^-][\text{ClO}^-][\text{OH}^-]^{-1} \quad (2.31)$$

indicating that the reaction rate decreases with increasing pH. These laws also show that the velocity of a reaction can depend on other species apart from the reactants involved in the chemical equation.

Until now, all the rate laws we have given take the general form of eq. (2.17). However, some reactions show very different forms for their rate laws. One example is the formation of hydrogen bromide from bromine and molecular hydrogen



whose rate law is

$$v = \frac{k'[\text{H}_2][\text{Br}_2]^{1/2}}{k'' + [\text{HBr}]/[\text{Br}_2]} \quad (2.32)$$

For this case, it is not possible to define reaction orders, except over limited concentration regions. In the first stages of reaction, when $[\text{HBr}]$ is small, we can make the approximation

$$\frac{[\text{HBr}]}{[\text{Br}_2]} \ll k'' \quad (2.33)$$

and the previous expression simplifies to

$$v' = k[\text{H}_2][\text{Br}_2]^{1/2} \quad (2.34)$$

with $k = k'/k''$. In this example, the velocity depends on the concentration of a product of the reaction, such that as the reaction progresses, $[\text{HBr}]$ will

increase and toward the end of the reaction we arrive at the situation in which

$$\frac{[\text{HBr}]}{[\text{Br}_2]} \gg k'' \quad (2.35)$$

Under these conditions, eq. (2.32) reduces to

$$v'' = k'[\text{H}_2][\text{Br}_2]^{3/2}[\text{HBr}]^{-1} \quad (2.36)$$

Both eqs. (2.34) and (2.36) represent kinetic laws of the general form of eq. (2.17), but the apparent reaction orders will vary with the extent of the reaction such that we cannot strictly talk about reaction orders. For example, the reaction order of bromine changes from 1/2 at the start of the reaction to 3/2 at the end.

This type of kinetic law illustrates two important points that have to be taken into account in the determination of reaction orders. First, a kinetic law is only strictly valid close to the concentration range where it is studied experimentally; its extrapolation to other concentration regions requires further experimental and theoretical studies. Second, considering the variation in reaction order during a reaction, from this it is important that studies of reaction orders must be limited to periods of relatively small extent of reaction (not $>10\%$), otherwise mean values may be obtained which have no chemical meaning.

Until now, we have only considered chemical reactions in homogeneous systems. However, the study of heterogeneous systems, in which more than one phase is present, are equally important, particularly in the areas of catalysis and corrosion. For example, the oxidation of a metal is faster when its area exposed to the oxidising medium increases. In general, it is seen that the rate of a heterogeneous reaction is directly proportional to the contact area between the reactants, S_c . Thus in the rate law [eq. (2.17)], these reactions are first order relative to S_c .

2.2.3 Temperature

Van't Hoff gave the first description of the effect of temperature on the equilibrium constant of a reaction, K_{eq} , with the relationship

$$\left(\frac{\partial \ln K_{\text{eq}}}{\partial T} \right)_p = \frac{\Delta H^0}{RT^2} \quad (2.37)$$

where ΔH^0 is the change in standard enthalpy for the reaction. In contrast to the spirit of the era, in which attempts were made to relate equilibria and rates in terms of molecular motions and Maxwell's distribution law of molecular velocities, the Swedish chemist Arrhenius considered that the effect of temperature on reaction rates is normally too great to be explained simply in terms of its effect on the translational energy of molecules. As an alternative, he proposed that there will be equilibrium between "normal" molecules and "reactive" ones, and that this has the same temperature dependence given by eq. (2.37). It is implicit in

this work that the energy difference between molecules is independent of temperature. From this, Arrhenius was able to provide the first adequate description of the relationship between the rate constant and the temperature:

$$k = A \exp\left(-\frac{E_a}{RT}\right) \quad (2.38)$$

where A is the pre-exponential (or frequency) factor, E_a the activation energy and T the absolute temperature. Arrhenius received the Nobel Prize in 1903. However, it was not on the basis of his work on chemical kinetics, and the merits of eq. (2.38) remained controversial for many years.

In the Arrhenius equation, the temperature dependence comes basically from the exponential term. However, it should be noted that the pre-exponential factor can also have a weak temperature dependence, and it is more correct to assume that A is proportional to T^m

$$k = A' T^m \exp\left(-\frac{E_a}{RT}\right) \quad (2.39)$$

where A' is independent of temperature. Often, the Arrhenius expression (2.38) is used only over a fairly limited temperature range, but eq. (2.39) is able to describe kinetic data over a wider range of temperatures. The units in which A is expressed are the same as those of the rate constant, while the activation energy is given in the same units as the energy R , normally in kJ mol^{-1} . This leads to the Arrhenius equation in the logarithmic form

$$\ln k = \ln A - \frac{E_a}{RT} \quad (2.40)$$

where the temperature is in Kelvin, k and A are now taken, simply, as their numerical values, and the units in eq. (2.38) cancel out.

Assuming that Arrhenius behaviour is followed, for a first-order process a plot of $\ln(k)$ against $1/T$ leads to a straight line of slope $-E_a/R$. The extrapolation to $1/T = 0$, which is normally significantly outside the temperature range studied and, as such, subject to appreciable errors, gives us $\ln(A)$, where A is given in units $(\text{time})^{-1}$. We must note that when the experimental results are only obtained over a limited temperature range, the accuracy in the values of A and E_a will be low.

The rate constants for second-order reactions can be expressed in $\text{dm}^3 \text{ mol}^{-1} \text{ sec}^{-1}$, or, if the rate is measured from the change of gas pressure at constant volume, as described in eq. (2.12), in $(\text{pressure})^{-1}(\text{time})^{-1}$. The conversion between units of pressure and those of concentration for gas phase reactions which are not first order can be obtained from the perfect gas equation, from which, for the general case of a reaction of order n , the variation in the total gas pressure can be related to the change in the total gas concentration by $p = cRT$

$$k_c = k_p(RT)^{n-1} \quad (2.41)$$

Thus from the rate constants given in the units $(\text{pressure})^{-1}(\text{time})^{-1}$, to obtain the terms A and E_a for reactions other than the first-order case, we must start by converting all the rate constants to be used with expression (2.41) into units of $(\text{concentration})^{-1}(\text{time})^{-1}$ before we can make an Arrhenius plot. If these values were obtained from logarithmic plots of rate constants given as $(\text{pressure})^{-1}(\text{time})^{-1}$ against $1/T$, we will get different numerical values for A and E_a . This is obvious for A , which, for a second-order process, will be given in terms of $(\text{pressure})^{-1}(\text{time})^{-1}$. However, it is equally true for E_a , and we need to take care to correct for the change in dimensionality to avoid the illusion that the values of activation energy are comparable between the two plots, since they are always given in kJ mol^{-1} .

For reactions in solution, the values of E_a typically lie between 40 and 120 kJ mol^{-1} . As a first approximation, these values correspond to an increase in reaction rate by a factor of 2–5 for every 10 K rise in temperature. The empirical rule often given is that the rate doubles for every 10 K rise in temperature.

2.2.4 Light

The effect of light on chemical reactions is well known from natural processes such as photosynthesis and vision, it is exploited in medicine in a therapeutic approach called photodynamic therapy and finds industrial applications such as photopolymerisation (“photocuring”). The general area is known as photochemistry. Normal photosynthesis is a chemical process in which green plants store solar energy through the synthesis of sugars from carbon dioxide and water. This process is catalysed by chlorophyll and requires the presence of light. There are also various types of bacterial photosynthesis, which can use substrates such as H_2S instead of water. However, the basic requirements in terms of light absorption are similar. Human vision requires the absorption of light by a pigment in a photoreceptor cell. There are two types of photoreceptor cells, rod cells (used for night vision) or cone cells (used for colour vision), which harbour pigments called rhodopsin and cone opsins, respectively. In both cases, the light-sensitive molecule is 11-*cis*-retinal but it is bound to different proteins. When light is absorbed, 11-*cis*-retinal isomerises to all-*trans*-retinal and triggers the transduction of light into nerve impulses. Photodynamic therapy employs a photosensitiser molecule that, when electronically excited, transfers electronic energy or an electron to a nearby oxygen molecule to produce reactive oxygen species (ROS). These ROS (singlet oxygen, superoxide ion, hydrogen peroxide, hydroxyl radical, etc.) are short lived but very cytotoxic, and produce local oxidative stress capable of killing cells within the region where they were generated. Photocuring of polymers consists in the photoinduced production of a reactive species (usually a radical or a cation) that initiates reactions with lower molecular weight species to form polymers or networks.

The action of light on a chemical reaction results essentially from the reactants in the presence of light having the possibility of following a different mechanism

that is not possible in the dark. For experimental reasons, the wavelengths (λ) most commonly used for initiating photochemical processes vary between the ultraviolet (200–250 nm) and the near infrared (750–800 nm). Light at these wavelengths has an energy, which is given by

$$E_{\text{photon}} = h\nu = h\frac{c}{\lambda} \quad (2.42)$$

and corresponds roughly to 600–150 kJ mol⁻¹, which is very close to the energies of many chemical bonds. This energy is much greater than the thermal energy at 25°C, which can be estimated from the mean velocity given by eq. (1.11) following the expression:

$$\frac{1}{2}Ms^2 = \frac{M}{2} \int_0^\infty s^2 f(s) ds = 2M\pi \left(\frac{M}{2\pi RT}\right)^{3/2} \int_0^\infty s^4 \exp\left(-\frac{Ms^2}{2RT}\right) ds = \frac{3}{2}RT \quad (2.43)$$

and is ~ 3.7 kJ mol⁻¹.

In the dark, the electrons in a molecule occupy the lowest energy electronic levels, giving rise to the so-called electronic ground state. When irradiated by light whose wavelength corresponds to the energy difference between the ground state and an electronically excited state, a molecule can absorb a photon and be transformed into this electronically excited state. This is a chemically distinct species, with its own structure, properties and reactivity.

The quantitative description of light absorption by a sample is based on the Beer-Lambert (or, more correctly, Beer-Lambert-Bouger) law. In deriving this law, we consider that incident monochromatic light of intensity I_0 crosses an infinitesimal thickness, dl , of an absorbing species of concentration c . The decrease in light intensity, dI , is proportional to the thickness of the sample, the concentration of the absorbing species and the incident light intensity

$$dI = -acl I_0 dt \quad (2.44)$$

where a is a proportionality constant that depends on the sample and wavelength. Integrating this expression over the whole optical path of the light in the sample, l , gives

$$I = I_0 \exp(-acl) \quad (2.45)$$

Expressing the above relationship in the most common form of logarithms to the base 10 gives the normal form of the Beer-Lambert equation

$$I = I_0 10^{-\varepsilon cl} \quad (2.46)$$

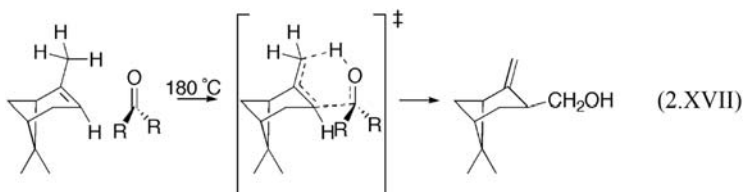
where ε is the molar absorption coefficient (sometimes referred to as extinction coefficient or molar absorptivity), which normally has the units L mol⁻¹ cm⁻¹. The Beer-Lambert law can also be written as

$$A = \log\left(\frac{I_0}{I}\right) = \varepsilon lc \quad (2.47)$$

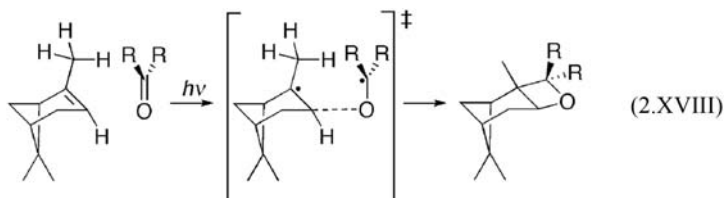
where A is the absorbance, a dimensionless parameter.

The electronic distribution in the electronic excited state formed by absorption of ultraviolet or visible light is different from that of the ground state, but immediately after light absorption, the nuclear configuration is identical to that of the ground state. This is the basis of the Franck-Condon principle. The structural relaxation toward a new nuclear configuration, corresponding to a potential energy minimum in the electronically excited state, occurs very rapidly, with a rate close to that of a molecular vibration. This new electronically excited isomeric form of the ground state can now undergo new reaction pathways, while its high-energy content will also tend to make it more reactive than the ground state. Often, the lifetime of a molecule in its electronically excited state is only a few nanoseconds (10^{-9} sec) in solution at room temperature. Within this lifetime, the excited molecule can follow various competing routes to lose its excess electronic energy, including re-emitting light and returning to the ground state, reacting exothermically either intra-molecularly or inter-molecularly with another molecule, and thus converting part of its electronic energy into potential energy, or decaying to another more stable electronic state, and eventually to the ground state, dissipating its electronic energy as thermal energy (i.e., heat).

A good example of how light absorption can modify the reactivity of molecules is given by cycloaddition to carbon-carbon double bonds. While the ground state process normally involves the reaction [3]



in the excited state, the reaction which is observed is [4,5]



Pericyclic reactions offer remarkable examples of the differences between thermal and photochemical reactions. Such differences were elegantly rationalised by Woodward and Hoffmann in terms of the conservation of orbital symmetry when reactants evolve to products [6,7], and their relevance to the understanding of the course of chemical reactions was acknowledged in the 1981 Nobel Prize in Chemistry.

Increases in reactivity and changes in the mechanism owing to electronic excitation can also be seen in the hydrogen abstraction reactions of ketones. At room temperature, ketones in their ground states do not react with hydrogen atoms bonded to alkanes. However, following light absorption they rapidly abstract hydrogen atoms to produce two radicals



This reactivity has been compared with that of alkoxyl radicals [8]

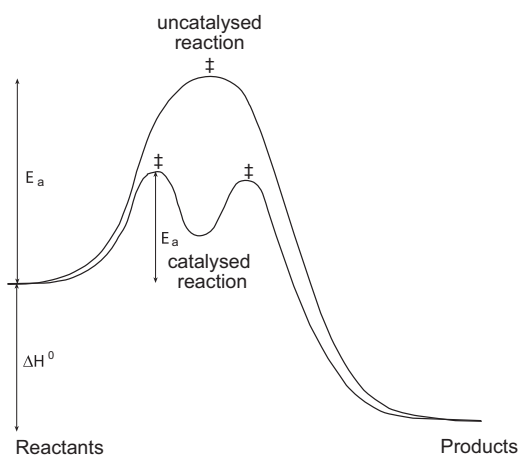


which suggests that light absorption has the effect of breaking the π bonding of the carbonyl group and leaving an unpaired electron on the oxygen atom. This is due to the formation of a so-called n, π^* excited state.

2.2.5 Catalysts

Catalysts are substances that although not included in the overall stoichiometric equation of a process, appear in the rate law with a partial order greater than zero. Occasionally, a reaction can undergo autocatalysis when, under the conditions described, a product of the reaction participates in the rate law of this process. Although caution needs to be used with such a definition, from the above a catalyst may increase the rate of a reaction without being consumed during it. The note of caution comes from the fact that in some processes, for example, Friedel-Crafts alkylations and acylations of aromatic compounds using Lewis acid catalysts, the catalysts are consumed in other steps of the process. Normally, a good catalyst can lead to enormous enhancement in reaction rates even when present in only very small quantities. In any case, the catalyst always has a partial order in the rate law that largely exceeds its stoichiometric coefficient in the overall stoichiometric equation.

It is useful to distinguish between homogeneous catalysis, where reactants, products and catalyst are all in the same phase, and heterogeneous catalyst, where the catalyst is present in a phase different from that of the reactants and products. As an example, we can consider the hydrogenation of carbon-carbon double bonds to transform them into single bonds. This can be carried out homogeneously using the Wilkinson catalyst, which is a complex of the transition metal rhodium, $\text{RhCl}(\text{P}(\text{C}_6\text{H}_5)_3)_3$, *tris*-(triphenylphosphine)rhodium(I) chloride, or heterogeneously, using particularly metallic platinum. This hydrogenation is very important in both the pharmaceutical and food industries, as it leads to the efficient production of saturated products from unsaturated compounds. Partly for his work in developing such homogeneous catalysts through the study of transition metal complexes, Geoffrey Wilkinson received the 1973 Nobel Prize in chemistry. A further example of an important industrial catalytic process involves the synthesis of ammonia from nitrogen and hydrogen using metallic iron or other transition metals as heterogeneous catalysts.

**FIGURE 2.1**

Energy profiles for a catalysed and an uncatalysed reaction showing the appearance of a lower energy pathway in the former case.

Catalysts do not alter the position of equilibrium in a reaction. Their effect, instead, arises from the fact that in their presence a pathway with lower activation energy becomes available to the reactants, as can be seen in Figure 2.1. The uncatalysed route still exists, but this new mechanism becomes kinetically more favourable. As a consequence, in the presence of a catalyst, the form of the rate equation will be changed with the addition of a new term, which becomes more important than the uncatalysed reaction. Returning to the general reaction mechanism (2.VII) and rate law [eq. (2.17)], the new rate law including the effect of catalysts will take the general form

$$v = k[A]^a[B]^b + k_{\text{cat}}[A]^{a'}[B]^{b'}[C]^{c'} \quad (2.48)$$

where C represents the catalyst. When the catalyst is a solid, such as the case of heterogeneous catalysts, its concentration is constant and does not appear as an independent term in this equation. Its effect will be included in the value of k_{cat} . As a general rule, to see the effects of catalysis, if the reaction order is unchanged, it is necessary that $k_{\text{cat}}[C]^c > 0.1 k$. As we will discuss in the next section, we should note that while changes in the reaction medium can lead to increases in rate, this phenomenon is not strictly a catalytic process in kinetic terms.

2.2.6 Reaction medium

More than a century ago, Menschutkin [9] noted that a reaction in solution cannot be separated from the medium in which it occurs. In fact, the effects of solvent on reaction rates can be dramatic. In the reactions studied by Menschutkin, such as



it has been found that the rate increases almost 100,000 times when the solvent is changed from hexane (highly nonpolar) to dimethylsulphoxide (very polar and aprotic). This variation is easy to interpret qualitatively, given that charges are created during the reaction, and that these will be stabilised in the presence of a polar solvent. However, the quantitative interpretation of the solvent's effect on the reaction rate is much more difficult. It must be stressed that the effect of the reaction medium can be seen both on the kinetic and thermodynamic properties of the reactions. Ideally, solvent effects on reaction rates should be studied by comparing the same reactions in the gas phase and in solution. However, such a comparison is not always possible experimentally.

Even for systems given in the same units and over the same temperature range the velocities of reactions in solution and gas phase, do not give directly comparable activation energy barriers. For two molecules, A and B, in the gas phase, initially at large distances there is no interaction, but as they approach one another, van der Waals attractive forces become involved at intermediate distances owing to correlations of the motions of the electrons of the two molecules. On even closer approach, an energy barrier is introduced for the reaction as a result of orbital overlap. This effect is even more marked when one of the reactants is an ion. Figure 2.2 shows an energy profile for a gas-phase reaction of this type. It should be noted that the change in entropy in the course of this reaction tends to counteract the change in potential energy shown in the figure: the formation of a complex leads to a decrease in entropy compared with that of the two isolated molecules, A and B. In solution, it is also necessary to consider the change in entropy and enthalpy associated with solvation of the reagents, transition state and products.

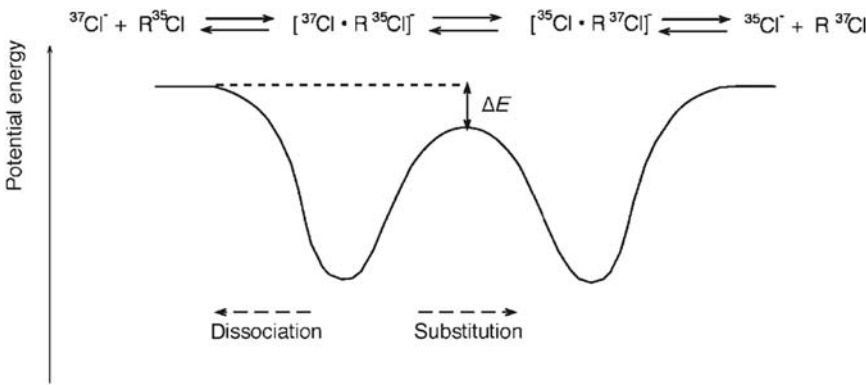


FIGURE 2.2

Potential energy profile for a second-order nucleophilic substitution reaction (S_N2) in the gas phase. The reaction barrier is 25 kJ mol⁻¹ below the energy of the separated reactants when $R = \text{CH}_2\text{CN}$. The substitution reaction is favoured for total energies less than or equal to that of the reactive channel, while a dissociative pathway (S_N1), which is favoured entropically, predominates for higher energies.

Given the existence of a potential energy minimum between the isolated reactants and the transition state, if it is found that $\Delta H_f > \Delta H^\ddagger$, the activation energy for the reaction will be negative although the energy barrier for the reaction could be even bigger than the free energy for the same reaction in solution.

Apart from the effect of solvent on the kinetics of chemical reactions, another significant effect of the reaction medium can come from the ionic strength of solutions. The most important case in which this has to be considered involves the reaction between two ions, A and B, in aqueous solution in the presence of an electrolyte. If A and B have the same charge, there will be an electrostatic repulsion between them, which will inhibit their approach, and, consequently, their reaction rate. The opposite will be true for reactions involving ions with different charges, that is reactions between cations and anions. This effect of ionic strength is known as the *primary salt effect*, and, as we will see in [Chapter 9](#), Reaction in Solution, is extremely useful in obtaining information on mechanisms of reactions involving ions in solution.

If the rate law involves the concentration of a species involved in a pre-equilibrium before the rate-determining step of a reaction, then the concentration of this species may depend upon the ionic strength, from which the reaction rate may also show an ionic strength dependence. This effect is known as the *secondary salt effect*. To some extent, this effect is an artefact, since it does not really affect the rate constant of the reaction, but changes the concentration of the reactants. The correct rate constant can be determined using the true concentration of the species, calculated using the appropriate equilibrium constant for the pre-equilibrium step determined at the experimental ionic strength.

References

- [1] H Maskill, *Educ. Chem.* **21** (1984) 122.
- [2] AACC Pais, LG Arnaut, SJ Formosinho, *J. Chem. Soc. Perkin Trans 2* (1998) 2577.
- [3] JP Bain, *J. Am. Chem. Soc.* **68** (1946) 638.
- [4] E Paterno, G Chieffi, *Gazz. Chim. Ital.* **39** (1909) 3412.
- [5] G Buchi, CG Zuman, ES Lipinsky, *J. Am. Chem. Soc.* **76** (1954) 4327.
- [6] R Hoffmann, RB Woodward, *J. Am. Chem. Soc.* **87** (1965) 395.
- [7] RB Woodward, R Hoffmann, *Angew. Chem. Int. Ed.* **8** (1969) 781.
- [8] SJ Formosinho, LG Arnaut, *Adv. Photochem.* **16** (1991) 67.
- [9] NA Menschutkin, *Z. Phys. Chem. Neue Folge* **5** (1890) 589.

This page intentionally left blank

Experimental methods

3

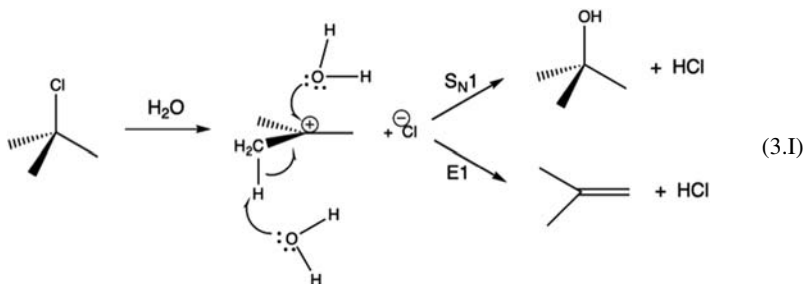
The experimental measurement of a reaction rate requires the use of techniques that allow us to obtain information on the concentration of the species involved for N reaction times: $t_1, t_2, t_3, \dots, t_N$. As the value of N increases, the description of the time evolution becomes more accurate. It is particularly important to study the early part of a reaction, far from equilibrium, as when there is appreciable reaction, the relatively high concentrations of products means that they can participate in other processes, and, as such, they will make the analysis of the results obtained more difficult. In practice, we need a finite time interval to carry out the measurement of a concentration, Δt_{obs} . If we start the reaction by mixing two reactants, there will be a dead time before we can make a measurement of the reactant or product concentration. We can consider this time to be the sum of the time interval necessary to mix the reactants, Δt_{mix} , and the time to obtain a homogeneous distribution of all the chemical species in the solution, Δt_{hom} . Thus the total time lapse before we obtain the first measurement of the concentration will be given by the interval $\Delta t_{\text{obs}} + \Delta t_{\text{mix}} + \Delta t_{\text{hom}}$. If (as is common) we employ spectroscopic methods to analyse for the reactant or product concentrations and use conventional mixing and homogenisation techniques for the reactant solutions, this time interval is usually between 3 and 5 sec. As it is necessary to record various readings of concentration to describe the velocity of a reaction fully, we should try to ensure that during the first 10 sec of reaction, the concentration of the reactants is reduced by less than half of the initial value. We can observe the evolution of these reactions directly and conventional analytical methods can be employed to monitor the concentration changes. We can note in relation to these analytical measurements that human vision has a somewhat faster time response, with the capacity to distinguish visibly changes occurring with a frequency of $<10 \text{ sec}^{-1}$, such that it is easy to see the above reaction directly.

Within certain limits, it is possible to control the rate with which a reaction occurs, for example, through the control of reactant concentrations or temperature. Thus we can study experimentally a considerable number of reactions over a convenient timescale, using conventional analytical methods [1]. However, a number of other reactions, such as the neutralisation of an acid or the precipitation of a salt, appear to occur “instantaneously”. To study the reaction kinetics of these rapid processes, it is necessary to resort to special techniques. We will discuss these later.

3.1 Application of conventional techniques to study reactions

3.1.1 First-order reactions

The solvolysis of 2-chloro-2-methylpropane in water occurs by the mechanism



The first step is the rate-determining one for this reaction, and we will follow the velocity of this reaction. In this step, the haloalkane ionises to produce an intermediate species, in this case a carbocation. Subsequently, the carbocation can be attacked by water to give either 2-methylpropanol or 2-methylpropene. The overall reaction is known as unimolecular nucleophilic substitution, S_N1 , when the nucleophilic attack predominates. Alternatively, if after initially forming the same carbocation elimination of a proton occurs to give 2-methylpropene, the process is termed unimolecular elimination, $E1$. At room temperature, the predominant reaction is S_N1 , but the rate-determining step is the same for both reactions, and both lead to formation of the same amount of HCl. It is not uncommon in chemical kinetics for different pathways to occur via the same intermediate. As the only ionic species formed in either case is HCl, the progress of the reaction can be followed by the increase of the conductance of the solution. If Λ_0 is the conductance of the solvent, Λ_t the conductance of the solution at time t and Λ_∞ the final conductance of the solution ($t = \infty$), then

$$[\text{HCl}]_t \propto \Lambda_t - \Lambda_0 \quad (3.1)$$

$$[\text{HCl}]_\infty \propto \Lambda_\infty - \Lambda_0 \quad (3.2)$$

The proportionality constant can be obtained experimentally using the same conductivity cell by measuring the increase in conductivity in the same solvent or in a mixture of solvents owing to the formation of HCl.

Experiment 3.1. *Experimental determination of the rate constant and reaction order for the solvolysis of 2-chloro-2-methylpropane in ethanol–water mixture [2–4].*

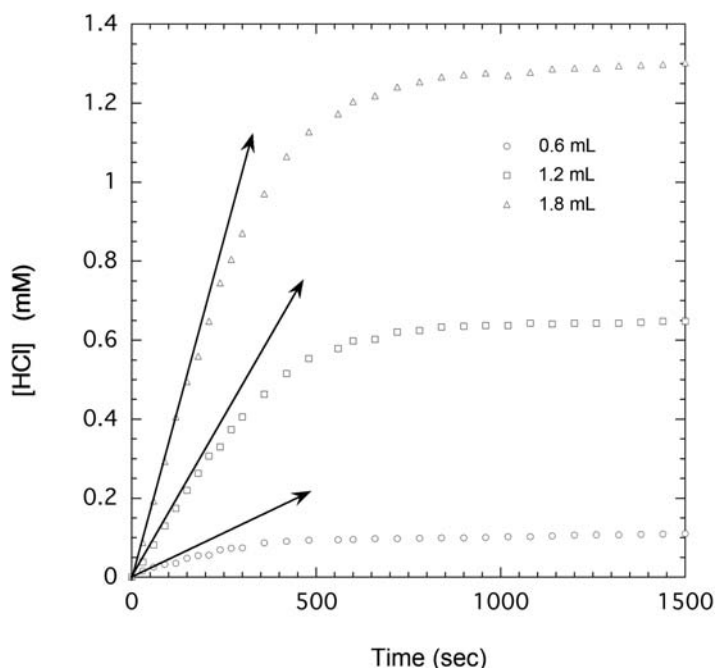
Material. Stopwatch, thermostat bath, conductivity cell, 1 cm^3 pipette (or syringe), 25 cm^3 pipette, 100 cm^3 measuring cylinder, 250 cm^3 Erlenmeyer flask.

Experimental procedure. Prepare a solution of 40% ethanol–water v/v by mixing 40 cm³ of ethanol with 60 cm³ of water. Fill an Erlenmeyer flask with 75 cm³ of this solvent, place in a thermostat bath at 25 °C and introduce the conductivity cell into the Erlenmeyer flask. When thermal equilibrium with the bath has been reached, prepare a stock solution of 2-chloro-2-methylpropane by adding 0.1 cm³ of the haloalkane to approximately 10 cm³ of ethanol. Connect the conductivity bridge and measure the conductivity of the 40% ethanol–water solvent. Inject 0.6 cm³ of the stock solution of the haloalkane and start the stopwatch. Stir the solution in the conductivity cell continuously until measurements are made. Read the conductivity every 30 sec during the first 5 min, and subsequently every minute until the conductivity no longer changes with time (i.e., the reaction is effectively completed). The stirring should be stopped ~5 sec before each conductivity reading is made. Repeat this experimental procedure using different injected volumes of haloalkane solution, for example, 1.2–1.8 cm³, taking care to wash the electrodes before each new experiment. Make a calibration curve for the conductivity bridge using solutions of HCl (0.5, 1.0 and 2.0 mM) in 40% ethanol–water.

Results. Table 3.1 shows typical results obtained by students with this procedure.

Table 3.1 Variation of conductivity with time during the solvolysis of 2-chloro-2-methylpropane in 40% ethanol–water solution.

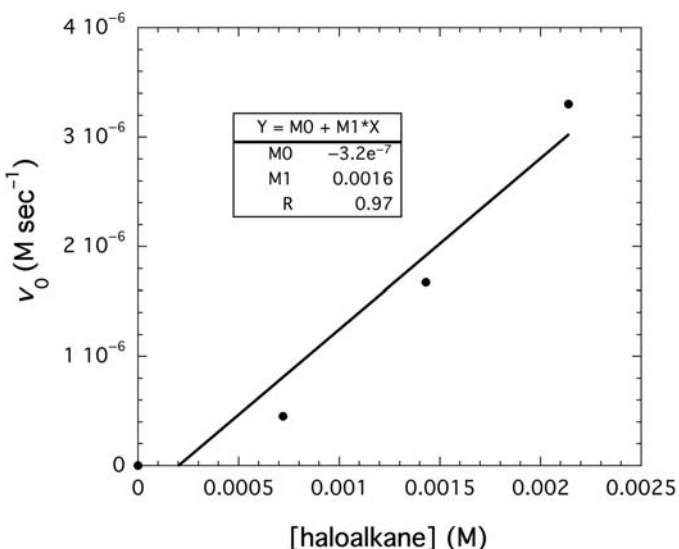
Time (sec)	0.6 cm ³ of haloalkane		1.2 cm ³ of haloalkane		1.8 cm ³ of haloalkane	
	Λ (μS)	[HCl] (mM)	Λ (μS)	[HCl] (mM)	Λ (μS)	[HCl] (mM)
0	39.7	0	40.1	0	40.5	0
30	40.5	0.0157	42.6	0.0377	47.4	0.0880
60	41.4	0.0252	46.8	0.0817	57.4	0.1928
90	42.1	0.0325	51.4	0.1299	66.9	0.2924
120	42.4	0.0356	55.6	0.1739	77.7	0.4055
150	43.6	0.0482	60.0	0.2201	86.2	0.4946
180	44.2	0.0545	64.1	0.2630	92.4	0.5596
210	44.3	0.0555	68.2	0.3059	100.8	0.6476
240	45.6	0.0691	70.5	0.3301	110.1	0.7451
270	46.0	0.0734	74.6	0.3731	115.7	0.8037
300	46.1	0.0744	77.7	0.4055	122.0	0.8698
360	47.3	0.0869	83.2	0.4632	131.6	0.9704
420	47.7	0.0912	88.2	0.5156	140.6	1.0647
480	47.9	0.0933	91.8	0.5533	146.5	1.1265
780	48.4	0.0985	98.6	0.6246	158.6	1.2533
1200	49.1	0.1058	100.4	0.6434	162.0	1.2889
1260	49.2	0.1069	100.4	0.6434	162.0	1.2889
1320	49.2	0.1069	100.5	0.6434	162.5	1.2942
1380	49.3	0.1079	100.5	0.6447	162.7	1.2963
1440	49.4	0.1089	100.8	0.6476	162.9	1.2984

**FIGURE 3.1**

Change in the concentration of HCl with time in the solvolysis of 2-chloro-2-methylpropane in the presence of 40% ethanol–water solution at 20 °C.

From these experimental results, it is possible to plot the changes in HCl concentration with time as shown in Figure 3.1.

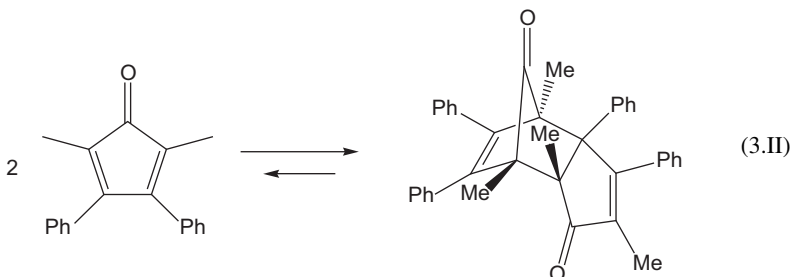
The velocity of this reaction for each time t can be obtained by tracing tangents to the curve of the variation of concentration with time for the particular time t of interest. For the time $t = 0$, we obtain the initial rate for a given initial concentration of haloalkane. The initial concentrations of 2-chloro-2-methylpropane can be calculated from its density (840 kg m^{-3}) and molecular weight (92.57 g mol^{-1}). The stock solution used in this experiment has a concentration of 0.0907 M . The plot of initial rate as a function of the initial concentration of haloalkane gives a straight line that passes through the origin. This means that the reaction is first order in terms of the concentration of haloalkane. The rate constant of the reaction can be obtained from the slope of this plot (Figure 3.2). Alternatively, it is possible to use a function of [HCl] as a function of time to obtain the rate constant of this reaction directly. This is based on the integration of the first-order rate law, as will be discussed in detail in Chapter 4, Reaction Order and Rate Constants.

**FIGURE 3.2**

Dependence of the initial rate of solvolysis of 2-chloro-2-methylpropane with initial concentration of the solute in ethanol–water mixture. The slope of the linear plot gives the rate constant $k = 1.6 \times 10^{-3} \text{ sec}^{-1}$ at 20°C .

3.1.2 Second-order reactions

The dimerisation of 2,5-dimethyl-3,4-diphenylcyclopentadienone



can be followed by colorimetry since the monomer is coloured, while the dimer does not absorb in the visible spectral region. The spectrum of the pure monomer is difficult to obtain since the dimerisation proceeds at an appreciable rate at room temperature. Thus to follow the evolution of the concentration of the monomer with time for this experiment, it is necessary to obtain the molar absorption coefficient (ϵ) of the monomer using data from literature. We note that for a 1 mM solution of the monomer in a 1-cm-pathlength cuvette, the absorbance A_{460} is 0.225 and by applying the Beer–Lambert law, we can calculate ϵ . The

velocity of this reaction is measured by producing the monomer initially by thermolysis of the dimer that is commercially available.

Experiment 3.2. *Experimental determination of the rate constant and reaction order for the dimerisation of 2,5-dimethyl-3,4-diphenylcyclopentadienone in toluene or xylene [5]*

Material. Stopwatch, colorimeter or spectrometer, water bath, ice, 1 cm glass or plastic cuvettes for visible absorption spectra, 10 cm³ measuring cylinder, 100 cm³ Erlenmeyer flask.

Experimental procedure. Dissolve approximately 50 mg of the dimer in 10 cm³ toluene or xylene. Heat the solution in a water bath in a fume cupboard for 10–15 min, until a strongly coloured solution of the monomer is produced. Cool this solution to room temperature in an ice bath. Transfer the solution at room temperature to the cuvette, introduce it in the colorimeter and measure the absorption at 460 nm. When the absorbance of the solution is within the scale of the colorimeter, make the first reading and start the stopwatch. Measure the absorbance every 5 min during the first 1/2 h of the reaction. After this, take readings at longer time intervals until the reaction is completed (~ 2 h).

Results. Table 3.2 presents typical results obtained by students while following this experimental procedure.

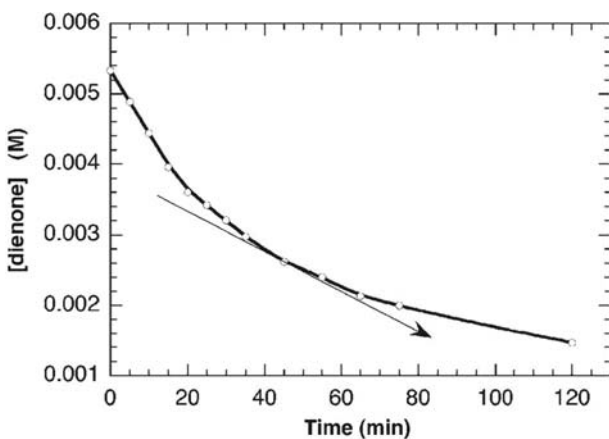
Figure 3.3 presents the variation of concentration of the dienone as a function of time, assuming a molar absorption coefficient of $\varepsilon = 225 \text{ M}^{-1} \text{ cm}^{-1}$. The velocity of the reaction at time t can be obtained from the slope of the curve corresponding to the point t on the abscissa. Taking logarithms of eq. (2.17) and noting that the only reactant for this bimolecular process is the monomer, we obtain

$$\log v = \log k + a \log[A] \quad (3.3)$$

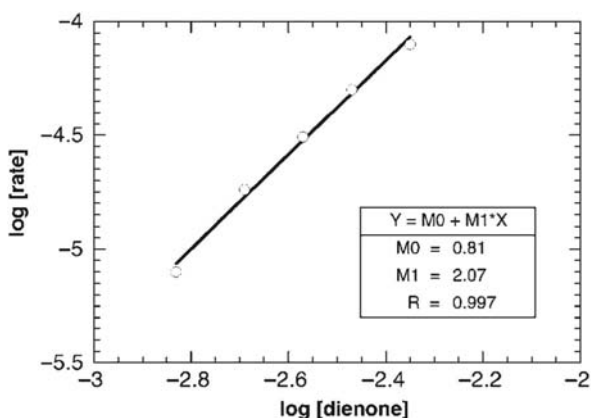
from which we can observe that the graph of the logarithm of the rate as a function of the logarithm of the concentration of the monomer (Figure 3.4) is a straight line, whose slope is the order of the reaction in terms of the monomer and whose intercept gives the logarithm of the rate constant. Alternatively, if we assume second-order kinetics in terms of the monomer, we can plot a graph of velocity as a function of [monomer]² and observe that we obtain a straight line, which passes through the origin and whose slope is the rate constant. The presentation of integrated laws for second-order reactions will be given in Chapter 4, Reaction Order and Rate Constants.

Table 3.2 Variation of monomer absorbance at 460 nm as a function of reaction time (in min).

t (min)	0	5	10	15	20	25	30	35	45	55	65	75	120
A_{460}	1.2	1.1	1.0	0.89	0.81	0.77	0.72	0.67	0.59	0.54	0.48	0.45	0.33

**FIGURE 3.3**

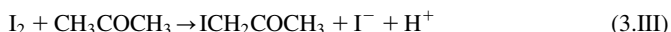
Change in concentration of dienone with time.

**FIGURE 3.4**

Logarithm of the rate of dimerisation as a function of the logarithm of the concentration of the monomer.

3.1.3 Complex reactions

Iodination of acetone in water



can be followed by colorimetry since one of the reactants, I_2 , is coloured, while all the other species involved in the reaction are colourless [6]. Alternatively, as we will see later, this reaction is accelerated by the presence of an acid and can be stopped (or quenched) by making the medium more basic. Following this

quenching, we can proceed to carry out the analysis of the concentrations of the reactants or products at leisure by titration at any specified reaction time interval.

Experiment 3.3. *Determination of the rate constant and kinetic order of iodination of acetone in water*

Materials. Stopwatch, graduated pipettes, burette, volumetric flask, Erlenmeyer flasks.

Experimental procedure. Prepare the following in water: 100 cm³ each of solutions 0.01 M iodine and 1 M in sulphuric acid, 500 cm³ of an aqueous sodium acetate solution (1 M) and 1000 cm³ of a standardised solution of sodium thiosulphate (0.01 M). As iodine is sparingly soluble in water, the solution of 0.01 M I₂ is prepared by dissolving the appropriate mass of iodine in an aqueous solution of 0.01 M KI. Also prepare a solution of starch indicator in water as follows: mix 1 g of starch and 1 cm³ of hot water to form a paste, add 1 cm³ of the 1.0 M H₂SO₄ solution and 0.1 g NaHSO₃ and finally dilute to 250 cm³. To a 250 cm³ Erlenmeyer flask, add the following quantities of the above solutions:

Solution	CH ₃ COCH ₃ (mL)	H ₂ SO ₄ (mL)	H ₂ O (mL)
1	20	10	150
2	15	10	155
3	10	10	160
4	20	15	145
5	20	5	155

Add 20 cm³ of the solution of iodine and start the stopwatch. Withdraw 20 cm³ aliquots every 5 min and add them to an Erlenmeyer flask containing 10 cm³ of the sodium acetate solution. Titrate this solution with the standardised solution of sodium thiosulphate, using the starch indicator.

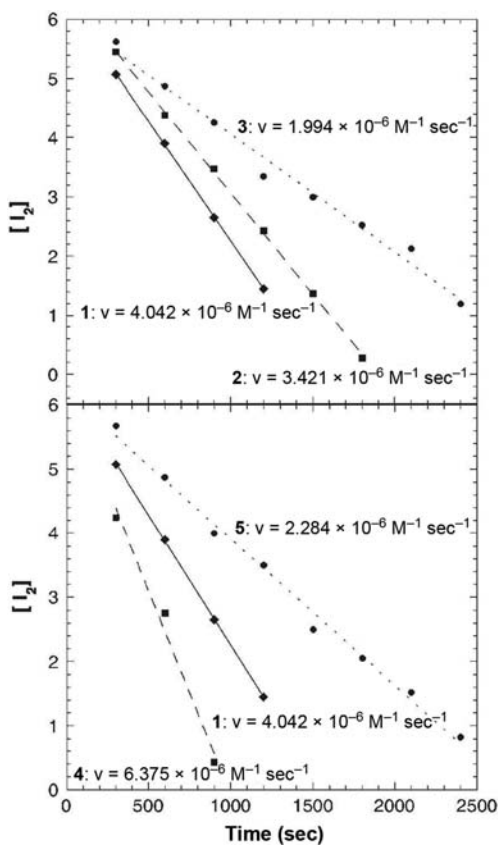


Results. By titrating with the standardised solution, calculate the concentration of iodine for each of the kinetic experiment presented in [Table 3.3](#).

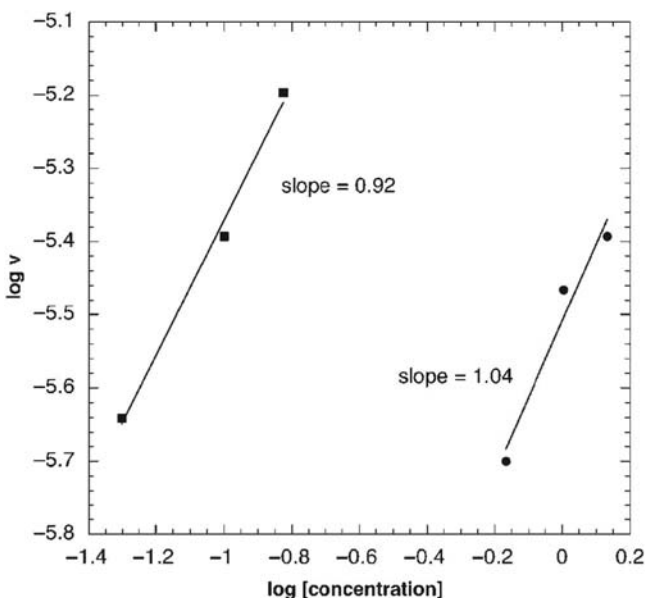
[Figure 3.5](#) shows that, for the extent of reaction studied, the iodine concentration varies linearly with time. That is, the velocity of the reaction is constant and independent of the concentration of iodine, that is, the rate is zero order in terms of the iodine concentration. However, the reaction mechanism is complex, and the participation of I₂ as reactant occurs after the rate-determining step of the reaction. From the slopes of the lines in [Figure 3.5](#), we can obtain the velocities of the reactions, $v = -d[\text{I}_2]/dt$, for the corresponding concentrations of acid and acetone. The plot of the logarithm of the reaction velocity versus the logarithm of the concentration of acetone has a slope close to one, as does the logarithm of rate versus the logarithm of the H⁺ concentration

Table 3.3 Variation of iodine concentration with time.

Time (sec)	Solution 1 [I_2] (mM)	Solution 2 [I_2] (mM)	Solution 3 [I_2] (mM)	Solution 4 [I_2] (mM)	Solution 5 [I_2] (mM)
300	6.175	5.30	5.60	5.80	5.65
600	4.125	4.70	5.10	4.725	5.275
900	3.25	4.05	4.675	3.275	4.725
1200	2.525	3.425	4.20	2.00	4.40
1500	1.50	2.875	3.875	0.625	4.025
1800	0.875	2.325	3.375	0.25	3.475
2100	0.25	1.65	3.025		3.025
2400		1.075	2.725		2.65

**FIGURE 3.5**

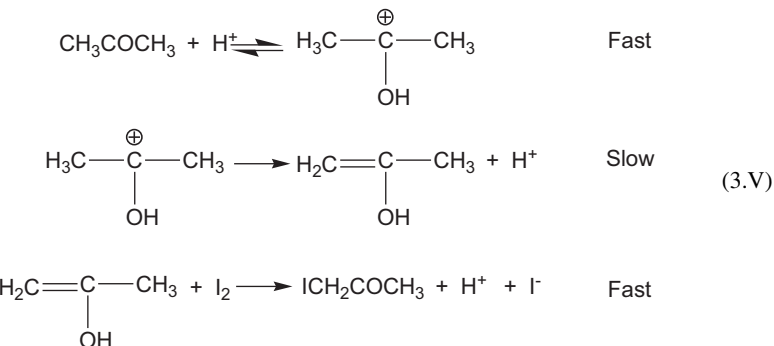
Variation of the concentration of iodine with time for the five solutions studied in the iodination of acetone.

**FIGURE 3.6**

Determination of the reaction orders for acetone (circles) and H⁺ (squares) in the iodination of acetone.

(Figure 3.6). The rate law is thus first order in terms of concentrations of acetone as well as acid. Using the velocities indicated in Figure 3.5 and the orders of reaction, the rate constant of the reaction can now be determined. The mean value obtained for this group of experiments is $k = 3.1 \times 10^{-5} \text{ M}^{-1} \text{ sec}^{-1}$.

The appearance of H⁺ in the rate law, but not in the stoichiometry of the reaction suggests an acid-catalysed step preceding the slowest step in the kinetic scheme. A mechanism that is in agreement with this rate law is



It should be noted that this mechanism requires the presence of two intermediates that have not been detected in this reaction. However, although it is acceptable to

propose mechanisms involving intermediates that are not detected experimentally, evidence should be given to support the existence of these species on the basis of structural, thermochemical and/or kinetic evidence available for related systems.

3.1.4 Activation energy

Iodide ion reacts with persulphate to produce iodine and sulphate ion [7,8].



The amount of iodine formed can be determined by titration with thiosulphate in reaction (3.IV) using starch as indicator, since this process as well as the complexation of the iodine produced with iodide ion is fast



The species I_3^- forms a complex with starch giving an intense blue colour. Thus by taking aliquots at various time intervals and determining the iodine concentration by titration, the order and rate of reaction (3.VI) can be determined. Alternatively, instead of taking aliquots, the reaction can be carried out in a single reaction vessel containing the same concentrations of I^- and $\text{S}_2\text{O}_8^{2-}$ ($y \text{ mol dm}^{-3}$), together with a known quantity of $\text{S}_2\text{O}_3^{2-}$ ($2x \text{ mol dm}^{-3}$, where $2x < y$) and starch indicator. Under these conditions, the appearance of the blue colour, owing to the complex formed between I_3^- and starch, only occurs when reaction (3.VI) produces more than $x \text{ mol dm}^{-3}$ of I_2 . The first $x \text{ mol dm}^{-3}$ of I_2 formed by reaction (3.VI) will be consumed by the $2x \text{ mol dm}^{-3}$ of $\text{S}_2\text{O}_3^{2-}$ in the reaction flask. This will be followed by reaction (3.IV), and since the rate of this reaction as well as our capacity for seeing the changes is much faster than that of reaction (3.VI), the time that we observe the appearance of the blue colour corresponds to the time of formation of $x \text{ mol dm}^{-3}$ of I_2 in reaction (3.VI).

If the initial $\text{S}_2\text{O}_8^{2-}$ concentration is kept constant for a series of experiments, the time needed to produce the blue colour is a measure of the velocity of the reaction, $\Delta[\text{I}_2]/\Delta t$. To be more specific, the reciprocal of the time interval up to the appearance of the blue colour is proportional to the rate of the reaction

$$\frac{1}{t} = c[\text{I}^-]^a [\text{S}_2\text{O}_8^{2-}]^b \quad (3.4)$$

where c is a constant proportional to the rate constant of the reaction.

Experiment 3.4. Experimental determination of activation energies

Material. Stopwatch, thermostat bath, 10 and 1 cm^3 pipettes, 250 cm^3 Erlenmeyer flasks, 250 cm^3 volumetric flasks, thermometer, ice.

Experimental procedure. Prepare aqueous solutions of H_2SO_4 (1.0 M), KI (0.2 M), $\text{K}_2\text{S}_2\text{O}_8$ (0.2 M) and $\text{Na}_2\text{S}_2\text{O}_3$ (0.01 M). Prepare starch indicator as follows: mix 1 g of starch with 1 cm^3 of hot water to form a paste, add 1 cm^3 of the H_2SO_4 solution and 0.1 g of NaHSO_3 and, finally, dilute to 250 cm^3 . Transfer to

a 100 cm^3 Erlenmeyer flask (solution A) 20 cm^3 of KI and 10 cm^3 of $\text{Na}_2\text{S}_2\text{O}_3$ solutions. Transfer 20 cm^3 of $\text{K}_2\text{S}_2\text{O}_8$ and 1 cm^3 of the starch indicator to another 100 cm^3 Erlenmeyer flask (solution B). Place the two Erlenmeyer flasks in a thermostat bath at $20\text{ }^\circ\text{C}$. When the solutions have achieved thermal equilibrium, add the contents of one flask into the other, start the stopwatch and homogenise the mixture. Note the time taken for the appearance of the blue colour. Repeat the experiment at different temperatures.

Results. Table 3.4 presents the reaction time obtained for each of the temperature studied.

The logarithmic form of the Arrhenius law [eq. (2.40)] shows that the slope of the plot of $\ln(1/t_r)$ as a function of $1/T$ is equal to $-E_a/R$ (Figure 3.7), from which the activation energy can be easily obtained. From the above data, the value $E_a = 56\text{ kJ mol}^{-1}$ was obtained. Unfortunately, we cannot apply the same method for the pre-exponential factor, since, in this experiment, we do not

Table 3.4 Reaction times at different temperatures.

$T\text{ (}^\circ\text{C)}$	2	10	20	25	35	40
$T\text{ (K)}$	275	283	293	298	308	313
$t_r\text{ (sec)}$	79.5	58.5	49.5	36.5	36.0	26.5
$t^{-1}\text{ (sec)}^{-1}$	0.0126	0.017	0.020	0.027	0.028	0.038

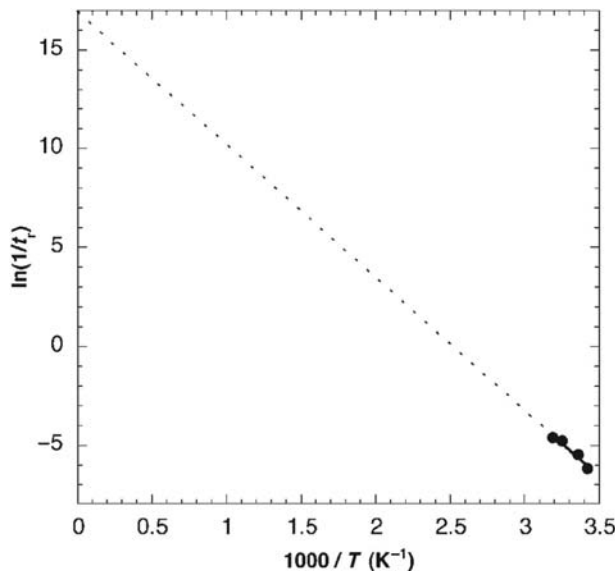


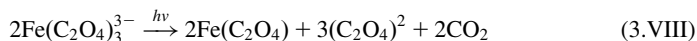
FIGURE 3.7

Arrhenius plot for the reaction between iodate and bisulphite ions.

determine the rate of the reaction, but quantities that are proportional to it. In addition, Figure 3.7 shows that the pre-exponential factor is obtained by extrapolation over a range far from the experimental results, which will introduce considerable errors. To estimate the pre-exponential factor, we can repeat the kinetic experiment at one temperature using colorimetry or spectroscopy, and from the measured rate constant and calculated activation energy, use eq. (2.38).

3.1.5 Dependence of light intensity

When molecules absorb visible or ultraviolet light, they are transformed from their ground state to the electronically excited states with high-energy contents. At room temperature, electronically excited molecules have short lifetimes and the study of their reactivity cannot be made simply using conventional analytical methods. However, it is possible to devise and carry out simple experiments that show quantitatively the dependence between the intensity of light absorbed and the quantity of products formed. For example, the ferrioxalate anion when exposed to light of wavelength <590 nm, decomposes according to the reaction



Such solutions, which are used to measure light intensities, are known as actinometers. At pH *ca.* 3.5, the Fe(II) formed reacts with 1,10-phenanthroline to form the well-known red complex $[\text{Fe}(\text{phen})_3]^{2+}$ (ferroin), whose molar absorption coefficient at 510 nm is well established ($\varepsilon = 11,100 \text{ M}^{-1} \text{ cm}^{-1}$).

Experiment 3.5. Experimental determination of the effect of light exposure on the photo-decomposition of potassium ferrioxalate [9]

Material. Stopwatch, colorimeter, 1 cm glass or plastic cuvettes, 1 dm³ volumetric flask, 250 cm³ Erlenmeyer flask, 1 cm³ graduated pipette.

Experimental procedure. Prepare potassium ferrioxalate by adding, with stirring, a solution of potassium oxalate (1.5 M) to iron(III) chloride (1.5 M) in the volume ratio 3:1. Recrystallise the precipitate obtained from water, and dry the potassium ferrioxalate crystals obtained and store in the dark. Prepare a 0.006 M solution of this actinometer in a 1 dm³ flask by dissolving 2.847 g of the crystals obtained in 800 cm³ water and adding sufficient 2 M sulphuric acid to bring to the 1 dm³ mark on the flask. This solution absorbs more than 99% of the incident light with $\lambda > 390 \text{ nm}$ in a 1 cm cell. Irradiate 3 cm³ of this solution in a 1 cm cuvette at 405 nm in the colorimeter or spectrometer for 30 min. At the end of this time, take the cell out of the colorimeter and add 0.5 cm³ of a solution of sodium acetate (1.8 M) and sulphuric acid (2.16 M) containing 0.1% (m/v) of 1,10-phenanthroline. After 30 min, measure the absorbance at 510 nm. Repeat with a reference solution that has been kept in the dark. Convert the difference in absorbance between the irradiated sample and the reference into concentration of Fe^{2+} produced in the irradiated solution, knowing that

Table 3.5 Relation between the irradiation time and the concentration of Fe^{2+} produced photochemically.

Time (min)	Absorbance (A)	$A - A_0$	$[\text{Fe}^{2+}] (\text{M})$
0	0.0083	0	0
30	0.0223	0.0140	1.26×10^{-6}
45	0.0353	0.0270	2.43×10^{-6}
60	0.0496	0.0413	3.72×10^{-6}

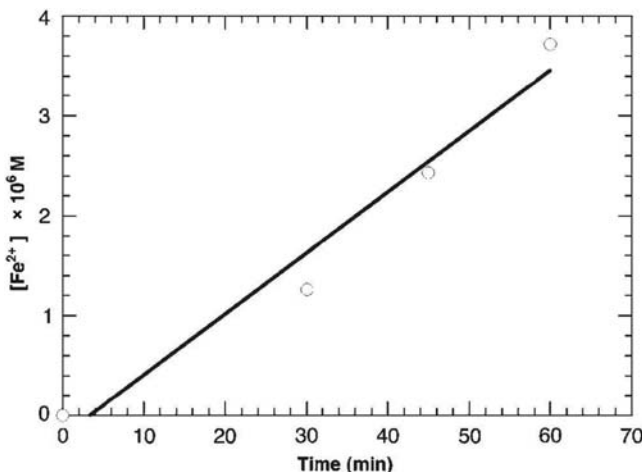


FIGURE 3.8

Dependence of the concentration of product formed on the irradiation time.

the iron(II)-phenanthroline complex in a 0.1 mM solution in a 1 cm cell has an absorbance of 1.11. Repeat the experiment, irradiating for 45 and 60 min.

Results. Table 3.5 summarises the results obtained.

Figure 3.8 shows $[\text{Fe}^{2+}]$ as a function of the irradiation time. The quantum yield for formation of iron(II) (that is the ratio of product formed to photons absorbed) when a 0.006 M solution of ferrioxalate is irradiated at 405 nm is 1.14 [10]. This allows us to calculate the intensity of light absorbed by the ferrioxalate solution, which is why this solution is called an actinometer. Assuming that all the incident light is absorbed by the solution, the intensity of this light, in Einstein min^{-1} , is given by

$$I = \frac{A_{510}V}{\varepsilon_{510}d\Phi_\lambda t} \quad (3.5)$$

where A_{510} is the absorbance of the irradiated solution at 510 nm, corrected by the absorbance of the reference solution, d the optical path of the absorption cell measured

in centimetre, $\varepsilon_{510} = 1.11 \times 10^4 \text{ M}^{-1} \text{ cm}^{-1}$, Φ_λ the quantum yield of production of Fe^{2+} at the wavelength (λ) used in the photolysis, t the irradiation time and V the volume in dm^3 of the solution used in the determination of the absorbance. For the experiment shown in [Table 3.5](#), $V = 3.5 \times 10^{-3} \text{ cm}^3$ and the mean intensity of the incident light is $1.6 \times 10^{-10} \text{ Einstein min}^{-1}$, that is, $1.5 \times 10^{12} \text{ photons sec}^{-1}$.

3.1.6 Enzyme catalysis

Enzymes are the most efficient and versatile catalysts known. They are able to increase the rates of some reactions by up to 21 orders of magnitude, with a high degree of specificity, such that they cannot only distinguish between substrates, but also between two optical isomers of the same substrate. In addition, in biological systems they are normally subject to the regulatory action of cellular metabolites, such that they carry out diverse tasks while maintaining the overall chemical balance relatively constant. The reaction centre in the enzyme where the major chemical processes occur is known as the *active site*. The reactants involved in reactions catalysed by enzymes are known as substrates, and the compounds that increase or decrease the rates of these reactions are known as activators or inhibitors, respectively.

The most relevant parameters that can be obtained from a kinetic study of enzymatic catalysis are the dependence of the velocity of catalysis on the concentration of the substrates, in particular in the early stages of reaction, and the maximum rate at which the enzyme can accelerate the reaction.

A simple experiment in which these parameters can be obtained by conventional experimental methods uses papain as the enzyme and Azocoll as the substrate. Papain is a sulphhydryl protease that can be isolated from the fruit papaya (paw-paw), and which is used for tenderising meat. Azocoll is insoluble ground cowhide to which a red dye has been covalently bonded. When the peptide bonds of the collagen are hydrolysed by the papain, the dye is liberated into the solution and the increase in its concentration as a function of time can be studied spectrophotometrically at 520 nm.

Experiment 3.6. Experimental determination of the kinetics of hydrolysis of Azocoll by papain [11]

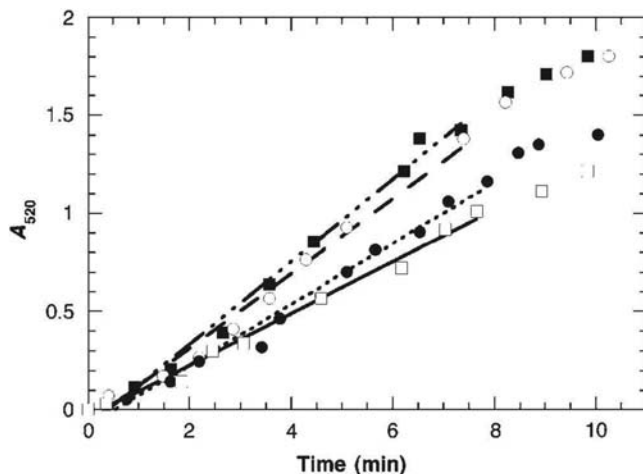
Material. Stopwatch, colorimeter (or spectrometer), 1 cm^3 spectroscopy cuvette, 10 cm^3 measuring cylinder, test tube.

Experimental procedure. At room temperature, dissolve an enzyme tablet (Allergan Soflens) in 10 cm^3 of doubly distilled or deionised water. This will give a solution with an enzyme concentration of $\sim 0.5 \text{ mg cm}^{-3}$. Add 12.5 mg of Azocoll to the spectroscopy cuvette. Add 2 cm^3 of the enzyme solution to this cell, start the stopwatch and invert the cell to homogenise the solution. Introduce the cell in the colorimeter (or spectrophotometer) and 30 sec later record the first absorbance reading at 520 nm. Invert the cell again, leave for a further 30 sec and read the absorbance. Repeat this procedure for a duration of 10 min. Repeat the experiments with the following amounts of Azocoll: 7.1, 4.1 and 3.4 mg.

Results. Typical results obtained with this procedure are shown in [Table 3.6](#).

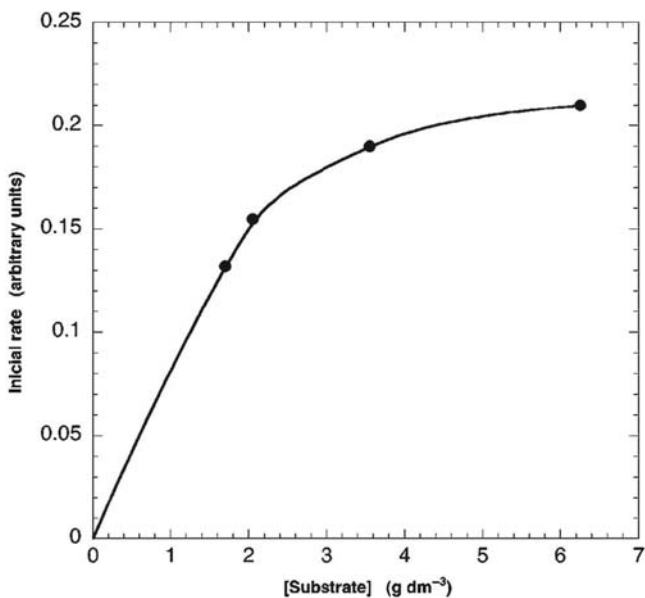
Table 3.6 Time evolution of the absorbance (A) at 520 nm for various initial concentrations of Azocoll.

Time (sec)	A , Azocoll (12.5 mg)	Time (sec)	A , Azocoll (7.1 mg)	Time (sec)	A , Azocoll (4.1 mg)	Time (sec)	A , Azocoll (3.5 mg)
55	0.113	24	0.072	45	0.0520	21	0.031
98	0.206	88	0.173	97	0.144	110	0.144
159	0.392	131	0.268	131	0.247	146	0.299
214	0.639	171	0.412	205	0.320	183	0.340
266	0.856	214	0.567	226	0.464	275	0.567
373	1.22	257	0.763	306	0.701	370	0.722
392	1.38	306	0.928	339	0.814	422	0.918
441	1.42	443	1.38	391	0.907	459	1.01
496	1.62	492	1.57	425	1.06	535	1.11
542	1.71	566	1.72	471	1.16	590	1.22
591	1.80	615	1.80	507	1.31		
				532	1.35		
				602	1.40		

**FIGURE 3.9**

Variation of absorbance with time for the hydrolysis of Azocoll by papain.

Since the variation of absorbance with time is proportional to the reaction velocity, we can estimate quantities proportional to the velocity of the reaction from the tangents of the curves in [Figure 3.9](#) at $t = 0$, and follow them as functions of the initial concentration of the substrate ([Figure 3.10](#)).

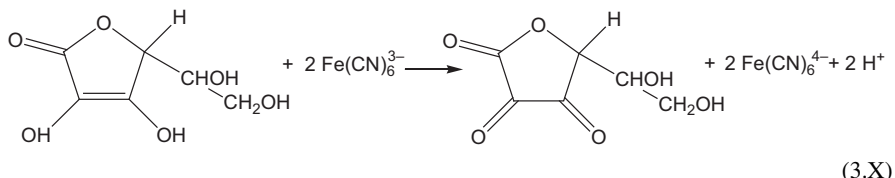
**FIGURE 3.10**

Relative rates as a function of initial concentration of Azocoll.

Knowing the molar absorption coefficient of the dye at 520 nm, it is possible, from Figure 3.9, to determine the maximum rate for this catalysis [12].

3.1.7 Dependence on ionic strength

Ascorbic acid is oxidised by hexacyanoferrate(III) to produce dehydroascorbic acid



As aqueous solutions of $[\text{Fe}(\text{CN})_6]^{3-}$ have a maximum absorption at 418 nm with a molar absorption coefficient $1012 \text{ M}^{-1} \text{ cm}^{-1}$ and the other reactants and products are colourless, it is possible to follow the progress of this reaction by visible absorption spectroscopy. The concentration of $\text{Fe}(\text{CN})_6^{3-}$ at time t is given by

$$[\text{Fe}(\text{CN})_6^{3-}] = [\text{Fe}(\text{CN})_6^{3-}]_0 \frac{A}{A_0} \quad (3.6)$$

where $[\text{Fe}(\text{CN})_6^{3-}]_0$ is the initial concentration of hexacyanoferrate(III), A_0 the initial absorbance and A the absorbance at time t .

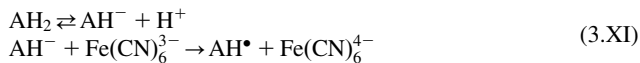
Experiment 3.7. Experimental determination of the effect of ionic strength [13]

Material. Stopwatch, colorimeter or spectrophotometer, 1 cm spectroscopy cuvette, 100 cm³ volumetric flasks, 25 cm³ pipettes, 100 cm³ Erlenmeyer flasks.

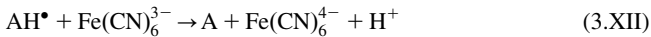
Experimental procedure. Prepare four solutions of potassium hexacyanoferrate(III) (1.0×10^{-3} M) in water containing sodium nitrate of different concentrations (e.g., 0.02, 0.05, 0.1 and 0.2 M). Prepare a 0.010 M solution of nitric acid, 0.001% of the disodium salt of EDTA and 2.5×10^{-4} M ascorbic acid. In the preparation of this solution, ascorbic acid must be the last solution to be added. Pipette 25 cm³ of one of the solutions of K₃[Fe(CN)₆]/NaNO₃ into an Erlenmeyer flask and add 25 cm³ of the solution of ascorbic acid/nitric acid. Start the stopwatch and shake for a few seconds. Transfer the solution to the cuvette and measure the absorbance at 418 nm every minute for 20 min. To obtain the absorbance corresponding to $t = 0$, add 25 cm³ of water and 25 cm³ of the solution of K₃[Fe(CN)₆]/NaNO₃ and record the absorbance. Repeat the process for all the solutions over the whole range of NaNO₃ concentrations.

Results. Table 3.7 presents the results obtained by students for this experiment.

Figure 3.11 shows that the concentration of [Fe(CN)₆]³⁻ decreases more rapidly for solutions containing a higher concentration of NaNO₃, that is, the velocity of the reaction increases with the ionic strength. This is what is expected for reactions between two ions of the same charge. One mechanism proposed for the reaction involves initial ionisation of the ascorbic acid (AH₂), which rapidly and reversibly forms an ascorbate anion intermediate (AH⁻), which then subsequently transfers an electron to the hexacyanoferrate(III) in the slowest step in the mechanism:



Finally, there is another rapid step in which the ascorbate-free radical (AH[•]) transfers an electron to the hexacyanoferrate(III) to give dehydroascorbate (A)

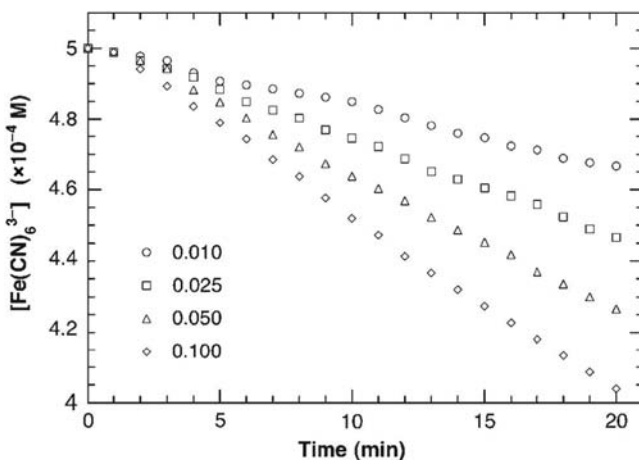


3.2 Application of special techniques for fast reactions

In conventional kinetic methods in which the reactants are mixed and homogenised by simple addition and shaking, and the progress of the reaction measured by analytical or physical methods, the time of mixing has to be short relative to that of the reaction. For fast reactions, these experimental conditions are not met, so these methods cannot be used. To overcome this problem, various routes can be followed: (1) we can decrease the rate of the reaction by decreasing the concentration of reagents or the temperature; (2) we can decrease the time interval of mixing, using flow methods; (3) we can rapidly perturb the equilibrium, and follow the subsequent

Table 3.7 Effect of sodium nitrate concentration on the kinetics of oxidation of ascorbic acid.

Time	[NaNO ₃] = 0.010 M		[NaNO ₃] = 0.025 M		[NaNO ₃] = 0.050 M		[NaNO ₃] = 0.100 M	
	A ₄₁₈	[Fe(CN) ₆ ³⁻] (10 ⁻⁴ M)	A ₄₁₈	[Fe(CN) ₆ ³⁻] (10 ⁻⁴ M)	A ₄₁₈	[Fe(CN) ₆ ³⁻] (10 ⁻⁴ M)	A ₄₁₈	[Fe(CN) ₆ ³⁻] (10 ⁻⁴ M)
0	0.434	5.000	0.431	5.000	0.429	5.000	0.427	5.000
1	0.433	4.988	0.430	4.988	0.428	4.988	0.426	4.988
2	0.432	4.977	0.428	4.965	0.426	4.965	0.422	4.941
3	0.431	4.965	0.426	4.942	0.424	4.942	0.418	4.894
4	0.428	4.931	0.424	4.919	0.419	4.883	0.413	4.836
5	0.426	4.908	0.421	4.884	0.416	4.848	0.409	4.789
6	0.425	4.896	0.418	4.849	0.412	4.802	0.405	4.742
7	0.424	4.885	0.416	4.826	0.408	4.755	0.400	4.684
8	0.423	4.873	0.414	4.803	0.405	4.772	0.396	4.637
9	0.422	4.862	0.411	4.768	0.401	4.673	0.391	4.578
10	0.421	4.850	0.409	4.745	0.398	4.638	0.386	4.520
11	0.419	4.827	0.407	4.721	0.395	4.604	0.382	4.473
12	0.417	4.804	0.404	4.687	0.392	4.569	0.377	4.414
13	0.415	4.781	0.401	4.652	0.388	4.522	0.373	4.367
14	0.413	4.758	0.399	4.629	0.385	4.487	0.369	4.321
15	0.412	4.746	0.397	4.605	0.382	4.452	0.365	4.274
16	0.410	4.723	0.395	4.582	0.379	4.417	0.361	4.227
17	0.409	4.712	0.393	4.559	0.375	4.370	0.357	4.180
18	0.407	4.689	0.390	4.524	0.372	4.335	0.353	4.133
19	0.406	4.677	0.387	4.489	0.369	4.300	0.349	4.086
20	0.405	4.666	0.385	4.466	0.366	4.266	0.345	4.040

**FIGURE 3.11**

Dependence of the variation in concentration of hexacyanoferrate(III) with time and sodium nitrate concentration.

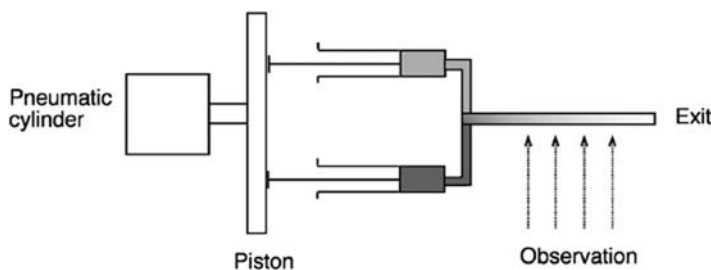
chemical changes occurring in the relaxation of the system until the same or a new equilibrium is established; (4) we can observe the competition between the reaction of interest and another fast process, whose rate is known.

From the experimental point of view, the biggest challenge is to choose the technique, which is best adapted to the system that we are trying to study, considering parameters such as the nature of the reactants, rate constants, temperature, solvent, etc. For the reaction under study, it is important to clarify whether this leads to equilibrium between reactants and products, or if it is, effectively, irreversible. In addition, is the product formed stable or not, and what type of reactants, intermediates and products are involved (ions, free radicals, excited states, etc.)? The choice of the experimental method will also depend on the order of magnitude expected for the rate constant, the type of solvent used and the analytical techniques available to study reactants, products, etc. In addition, since some of these techniques use rather expensive apparatus, this will also depend upon the availability of the equipment.

3.2.1 Flow methods

3.2.1.1 Continuous flow

Flow methods were first introduced by Hartridge and Roughton [14] in their study of the reaction between haemoglobin and oxygen. The application of these techniques is fairly general; they have been used to study the kinetics of reactions in liquid and gas phases and reactions with small and large equilibrium constants. The basis of this technique involves the injection of two reactants A and B in a

**FIGURE 3.12**

Scheme of an apparatus to measure the kinetics of reactions using continuous flow.

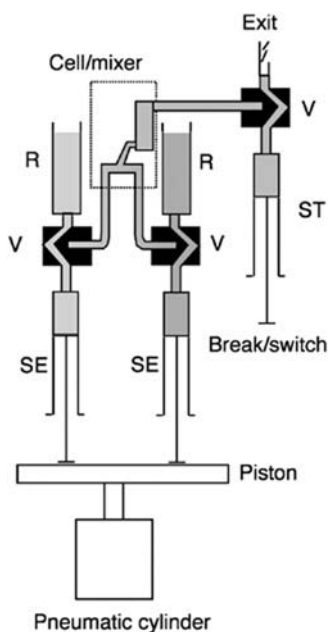
mixing chamber, followed by the determination of their concentration, or that of the products, at a certain distance from the mixing chamber (Figure 3.12). In this continuous flow method, the reactants are injected continuously into the mixing chamber, leading to a profile of concentration of reactants and products along the detection tube, which does not change with time. Knowing the rate of flow, the reaction time can be related to the distance between the mixing chamber and the place where the reactants or products of the reaction are observed by whatever analytical technique is used. Typically, either a spectroscopic or electrochemical technique is used for analysis. For a flow rate of 10 m sec^{-1} , a distance of 1 cm corresponds to a reaction time of 1 msec. With the attainment of a stationary state in the concentration of the species involved, the time resolution of the detection method does not generally limit the time resolution of this technique, which normally depends upon only the mixing time. For conventional injection systems involving laminar flow, this is typically about 1 msec. It should be remembered that for all fluids the flow rate and hence the minimum time for mixing will have a limit, since the flow becomes turbulent when the Reynolds number is >2300 .

$$\text{Re} = \frac{ud\rho}{\eta} > 2300 \quad (3.7)$$

where u is the flow rate, d the diameter of the tube, ρ the density of the reaction medium and η its specific viscosity. Given these limitations, the flow method only enables the study of reactions with half-lives $>10^{-3}$ sec. In addition, to maintain steady-state conditions throughout the experiment, this technique requires the use of large quantities of reactants.

3.2.1.2 Stopped flow

Another common flow technique is the so-called stopped-flow method. This has the advantage of using much smaller amounts of reactants than those in continuous flow. As in the previous method, the solutions containing the reactants are kept in separate syringes, whose pistons are pushed rapidly by the same mechanical system. The reactants are, thus, injected simultaneously into the mixing chamber, where the reaction

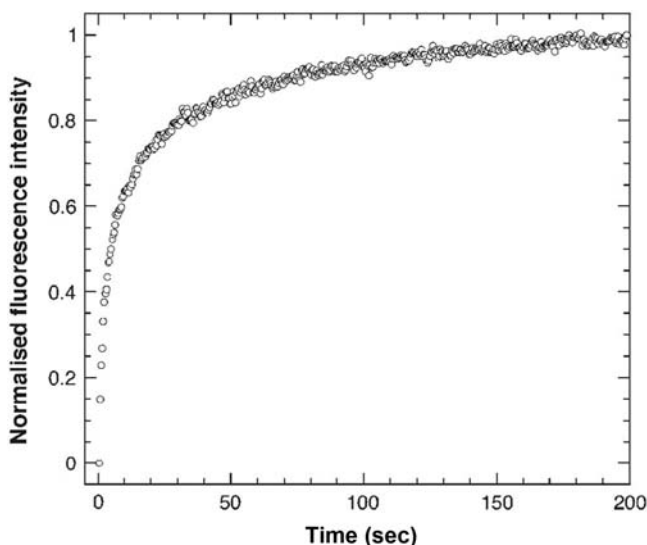
**FIGURE 3.13**

Schematic diagram of an apparatus to measure the kinetics of reactions using stopped flow. The pressure of the pneumatic cylinder controls the rate at which the pistons can be moved to mix the reagents. Detection is made in the mixer/cell, using light absorption or fluorescence emission. *R*, reactant solution reservoir; *V*, valve; *SE*, reactant syringes; *ST*, stopping syringe.

starts. The whole reaction mixture is then transferred into the observation cell. The flow is interrupted by a stop syringe, which will control the reaction volume studied. This syringe is stopped mechanically by a rigid brake which leads to a rapid slowing of the flow, and which starts the measurement of time for the reaction. The reaction between the well-mixed reactants continues and the changes in the concentrations of reactants and products are followed in real time, normally using spectroscopic methods. The crucial aspect of this technique (Figure 3.13) stems from the fact that small quantities of reactants are mixed rapidly and efficiently, and the kinetics followed electronically using techniques with good time resolution. This technique allows us to follow changes in optical or other properties of solutions with a time resolution in the range of milliseconds to seconds. Figure 3.14 shows a set of results obtained with this method.

3.2.2 Relaxation methods

The development of relaxation methods is due principally to Eigen, who was awarded the Nobel Prize for this in 1967. Relaxation methods can be used in the

**FIGURE 3.14**

Results obtained by stopped flow for a mixture of bovine serum albumin (BSA) labelled with a fluorescent probe (a rhodamine derivative) with a solution of BSA (without label) and rhodamine green at 35 °C. In the mixture there is energy transfer from the rhodamine green to the labelled protein, when it is irradiated at $\lambda_{\text{exc}} = 530 \text{ nm}$. The increase in fluorescence in the labelled protein is followed using $\lambda_{\text{em}} > 530 \text{ nm}$.

Courtesy of Magda Abreu: Results were obtained in the Coimbra Chemistry Centre using a Hi-Tech SF-61 apparatus.

kinetic study of reversible reactions, and are based on the perturbation of a system initially in equilibrium. This perturbation can be induced by rapid variation of any of the parameters that affect the equilibrium constant. These include temperature, pressure, electric field, pH and chemical potential.

3.2.2.1 Temperature jump

The most commonly used relaxation technique is based on a temperature jump, using the relationship between temperature and equilibrium constant given by the van't Hoff equation. For efficient perturbation of the equilibrium by this method, the change in the standard enthalpy of solution should be significant. In addition, we need to use a method that heats the system faster than its chemical relaxation time. Normally, this heating is produced by discharge of a high voltage condenser, assuming that the reaction medium does not have a high electrical resistance. This heating method is restricted to solutions in polar solvents of high ionic strength (such as aqueous solutions). The time resolution that can be achieved is around 10^{-6} sec .

Alternatively, it is possible to heat the reaction medium using a high-intensity near-infrared laser pulse (typically, >200 mJ), which will be preferentially absorbed by the solvent—usually in one of its vibrational overtone bands. The time resolution of this technique is limited by the resistance of the cell where the reaction is studied to the high-intensity laser pulse, by the laser pulse and by the relaxation time of the vibrational and rotational states of the solvent in the near-infrared region. For example, for water this relaxation time is $<10^{-12}$ sec. However, we also have to consider thermal equilibration in the region under study, and, consequently, the time resolution of this technique is of the order of tens of picoseconds.

3.2.2.2 Pressure jump

Pressure affects equilibrium constants in a way similar to temperature:

$$\left(\frac{\partial \ln K_{\text{eq}}}{\partial P} \right)_T = - \frac{\Delta V^0}{RT} \quad (3.8)$$

in which the change in molar volume of the reaction is given by $\Delta V^0 = \sum v_i V_i^0$, where v_i is the stoichiometric coefficient and V_i^0 is the partial molar volume of the species i present in equilibrium in the standard state. The majority of reactions in solution involve changes in volume induced by conformational changes or changes in solvation of the reactants or products, so that they can be affected by change in the pressure. The most common method of inducing a rapid jump in the pressure involves breaking a diaphragm that separates a reaction vessel at atmospheric pressure from one at a much higher pressure. With this, it is possible to increase the pressure by 100 atm in 100 μsec .

3.2.2.3 Electric field jumps

Rapid changes in electric field can also be used to perturb chemical equilibria. As high electric fields favour the production of ions from neutral species, it is possible to increase rapidly the dissociation of weak electrolytes. In the most common application of this technique, a high voltage discharge of a few microseconds' duration is applied and the transient species produced are followed by electrical conductivity measurements.

If the electric field applied is small, dielectric relaxation is obtained. Dielectric relaxation is observed if there is a change in the polarisability of the medium under the influence of an applied electric field. This rule suggests that dielectric relaxation can only be detected in polar media. However, this effect can also be observed in some non-polar materials, since there are contributions to the polarisability owing to collisional effects, that is, when two non-polar molecules collide, there will be a distortion of the electron clouds and formation of a transient dipole. Dielectric relaxation has a limited application in chemical kinetics, since it reflects the re-orientation of dipoles that occur on a timescale determined by the motions of all the molecules and not specifically those involved in

chemical reactions. To obtain chemical information it is necessary to suppress the molecular motions using, for example, rigid matrices as supporting media for the molecules whose reactivity we are trying to study. As such, dielectric relaxation has been used to measure the rate of re-orientation of a whole molecule in simple fluids or the relaxation of segments of polymers.

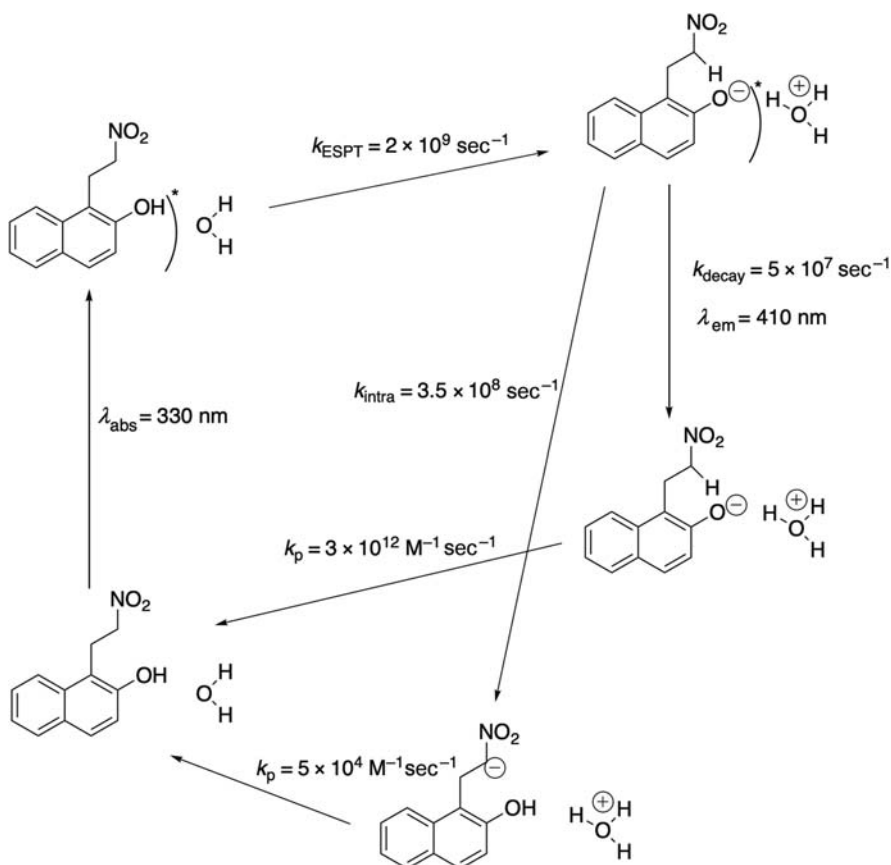
3.2.2.4 Ultrasonic absorption

The observation that a system in chemical equilibrium can absorb ultrasounds dates back to the 1930s. During this period, Bazulin attributed the absorption of ultrasounds by acetic acid to the existence of hydrogen bonds. When an acoustic wave is made to cross a medium, alternate regions of compression and depletion of the particles that comprise it are produced. Eventually, this acoustic wave is attenuated within the space covered, in the same way that an electromagnetic wave is attenuated, because no medium is completely transparent. If species in chemical equilibrium that absorb ultrasound at the frequency used are added to this medium, and if the relaxation for the equilibrium situation is slower than that in the ultrasonic frequency, the regions of compression and depletion will not occur with the same phase or amplitude as the pure solvent. By comparison of the two situations it is possible to obtain the velocity of relaxation of the system in equilibrium. The time resolution of the system depends upon the frequency of ultrasound used, and can reach 10^{-11} sec.

3.2.2.5 pH jump

Acid-base equilibria can be perturbed by a rapid change in the pH of the medium. To induce this change we need to use a species that responds rapidly to a short-duration external stimulus, either transferring a proton to the medium or capturing one from it. Given the extremely high time resolution that can be achieved with pulsed lasers, it is convenient to use these as sources for the external perturbation of the system. To induce the pH jump, we need to introduce into the medium under study a chromophore that has a lesser ionisation constant in its excited state than that in the ground state. Thus light absorption by the laser pulse will rapidly produce the chromophore excited state which will transfer a proton to the solvent, rapidly increasing the pH of the medium. These conditions are met, for example, by 2-naphthol-6-sulphonate in water, whose pK_a in the ground state is 9.1, and in the excited state is 2, and whose pseudo-first-order rate constant for transferring a proton to water is 10^9 sec^{-1} . Using laser pulses with high photon fluxes (*ca.* $10^{27} \text{ photons cm}^{-2} \text{ sec}^{-1}$) it is possible in 10 nsec to increase the H_3O^+ concentration with 2-naphthol-6-sulphonate to 10^{-4} M , that is, to decrease the pH of an aqueous solution from pH 7 to ~ 4 . However, 2-naphthol systems have the intrinsic limitation that the excited state lifetimes 2-naphtholates anions are also in the nanosecond range and that once back in the ground state, 2-naphtholates re-protonate very rapidly and severely limits the time window of the pH jump.

Figure 3.15 shows a system devised to enable persistent pH jumps that combines the photoacid properties of 2-naphthol with the slow proton transfer rates of

**FIGURE 3.15**

Proton transfer rates in a strong photoacid with intra-molecular proton transfer to generate a carbanion with slow recombination rates in aqueous solutions, where the rates were estimated from experimental data and a semi-empirical kinetic model.

nitroalkanes [15]. The 2-naphtholate moiety generated by excited-state proton transfer to water molecules can undergo fast intra-molecular proton transfer to generate a carbanion. The intra-molecular reaction is faster than the decay of 2-naphtholate, and the generation of the carbanion occurs with a quantum yield of 0.63. The interesting aspect of this system is that the re-protonation on the carbanion is slow and the reversible pH jump lasts for 1 sec at pH 6.

3.2.3 Competition methods

All spectroscopic techniques involve production or deactivation of excited states, normally by the interaction between electromagnetic radiation and molecules. The

excited states have finite lifetimes, determined by radiative and non-radiative relaxation to the ground state. Kinetic information can be obtained by comparison of the rates of these processes with those of chemical reactions in competition with them. We will consider two of these processes, involving nuclear spin and electronic excited states. However, the same ideas are applicable to other types of spectroscopic transition.

3.2.3.1 Nuclear magnetic resonance

Nuclear magnetic resonance (NMR) is one of the most powerful methods to study the structure and time evolution of species involved in chemical reactions. This spectroscopic method is based on the fact that nuclei with spin (such as ^1H) in a magnetic field selectively absorb electromagnetic radiation in the radio frequency region owing to change in the spin orientation. Following this, the excited nuclei can relax to the spin ground state, with emission of energy to the medium. The measurement of these radio frequencies (most commonly given as a chemical shift relative to some reference) and of the rate with which nuclei relax to the ground state, constitute the information available by NMR about the molecular structure and dynamics of the sample under study. The energies involved in these nuclear spin transitions are very small and depend upon the magnetic field strength. For example, the ^1H nucleus in a magnetic field of 4.7 T (Tesla) absorbs radiation of frequency around 200 MHz, which, by the Planck relation $E = h\nu$ is equivalent to an energy of 0.08 J mol^{-1} . As the energy levels involved in these nuclear spin transitions are very close, the probability of relaxation by spontaneous emission to the ground state is very small. Nevertheless, under normal experimental conditions, we do not obtain equal population of the spin levels, which would lead to saturation of the excited state and loss of the resonance signal, because there are non-radiative transitions induced by the fluctuating magnetic field that lead to a loss of this excess energy as thermal energy of the medium. This spin-lattice relaxation has a relaxation time T_1 , known as the longitudinal or spin-lattice relaxation time. Further, when a molecule is subjected to a homogeneous external magnetic field in an NMR experiment, its electrons also respond to this field. If there are unpaired electrons, the magnetic moments of the spins of these electrons are polarised and the magnetic field in the interior of the sample is greater than the applied field. This phenomenon is known as paramagnetism. In contrast, if all the electrons are paired, the external field induces electric currents in the molecule, leading to a polarisation of the electrons in their orbitals, which counteracts the effect of the applied magnetic field. Under these conditions, the magnetic field inside the sample is less than the external field, a phenomenon known as diamagnetism. In either case, the local microscopic magnetic environment for the nuclei of these molecules will be different, and when they enter into resonance with the external field, such that different values of applied field will be required, it leads to the chemical shift in its NMR spectrum. Further effects on the spectra are obtained by the coupling between the nuclear spins of two adjacent nuclei, which leads to splitting of the NMR signals (spin–spin coupling). Apart

from these effects, when the oscillating field produced by a nucleus is in phase with that of a neighbour in an identical chemical environment, there can be energy transfer from one nucleus to the other. This leads to deactivation of one of the spin excited states without decreasing the total population of excited states in the process called spin–spin relaxation, given by a relaxation time T_2 known as transversal or spin–spin relaxation time. It is worth noting that all spectroscopic transitions have similar longitudinal and transverse relaxation processes which are responsible for the homogeneous broadening and linewidth of the transitions of isolated molecules, although the experimentally observed spectral linewidths result from inhomogeneous broadening.

A chemical reaction in which there is exchange of one nucleus between two magnetically non-equivalent sites of the reactant can be followed by NMR, provided that the rate of exchange is not so fast relative to T_1 and T_2 that, on the macroscopic scale, we only observe the average of the frequencies of the two sites. Consider a proton NMR experiment in which the difference in resonance frequencies is typically of the order 10² Hz, corresponding to lifetimes of the order 10⁻² sec. If the lifetime of the reactant is much longer than this, we will see the NMR signals of both reactant and product without any effect of the exchange, and the NMR experiment corresponds to a conventional kinetic study where we observe the time dependence of the spectra of the reactant and product separately at different phases of the reaction, and so can follow the transformation. However, it is more interesting to study reactions whose rates lie between this limit and that of fast exchange where we see a single signal. In this intermediate case, we see a progressive broadening of the signal as the rate increases, until in the limit the two signals collapse into one, that is, we are in the fast exchange limit.

From the Heisenberg uncertainty principle, a magnetic nucleus will always give an NMR absorption band with finite width, even if it is not involved in a chemical exchange reaction. The minimum bandwidth can be related to the spin-lattice relaxation time, T_1 , since the mean lifetime of the excited spin state cannot exceed T_1 ,

$$\Delta\nu = \frac{1}{2\pi T_1} \quad (3.9)$$

However, normally the bandwidth at half maximum can be related to the spin–spin relaxation time, T_2 ,

$$\Delta\nu_{1/2} = \frac{1}{\pi T_2} \quad (3.10)$$

In the intermediate chemical exchange condition, the total relaxation frequency is given by the sum of the spin–spin relaxation, as above, together with the relaxation owing to chemical exchange, τ , given by,

$$\frac{1}{\tau} = \frac{1}{\tau_A} + \frac{1}{\tau_B} \quad (3.11)$$

where τ_A and τ_B are the lifetimes of the magnetic nuclei in the magnetically non-equivalent sites A and B, or in other words the reciprocal of their exchange rate constants. In the presence of this exchange, the experimentally observed bandwidth at half maximum will be

$$\Delta\nu'_{1/2} = \Delta\nu_{1/2} + \frac{1}{\pi\tau} \quad (3.12)$$

Thus knowing the value of $\Delta\nu_{1/2}$, which can be obtained by cooling the system such that the exchange becomes slower, and using the value of $\Delta\nu'_{1/2}$ obtained experimentally, we can obtain τ . If the fractional occupation of the sites is

$$x_A = \frac{\tau_A}{\tau_A + \tau_B} \quad x_B = \frac{\tau_B}{\tau_A + \tau_B} \quad (3.13)$$

we get $\tau = \chi_A\tau_B = \chi_B\tau_A$. As was already indicated, the time resolution of the application of the NMR technique is limited by the difference between the resonance frequencies of the magnetic nuclei when the velocity of exchange is very slow, which for protons is not normally >100 MHz; from this, the lifetime of relaxation processes experimentally accessible must be $>10^{-4}$ sec.

In the limit of fast exchange between two species of resonance frequencies v_d and v_p , $k[\text{reagents}] \gg 2\pi|v_p - v_d|$, where k is the exchange rate constant, it is still possible, in certain circumstances, to determine the exchange rate constant. We will consider the case of a process in the presence of a paramagnetic species, which is of particular importance to electron transfer reactions. When the mean lifetimes of a paramagnetic species (p) and a diamagnetic one (d) are considerably greater than their relaxation times T_1 , the system can be treated as a two-site system. In the particular case of a first-order electron transfer reaction relative to each of the reactants, the mean bandwidth for the mixture of reactants

$$(\Delta\nu_{1/2})_{dp} = \frac{1}{\pi(T_2)_{dp}} \quad (3.14)$$

where the width at half-height in Hertz for an absorption band of Lorenzian shape, is related to the rate constant for electron exchange, k_{ex} , by

$$(\Delta\nu_{1/2})_{dp} = x_p(\Delta\nu_{1/2})_p + x_d(\Delta\nu_{1/2})_d + x_p x_d \frac{4\pi(v_p - v_d)^2}{k_{\text{ex}}([p] + [d])} \quad (3.15)$$

where x_p and x_d indicate the mole fractions of the paramagnetic and diamagnetic species, respectively. This expression can be written as

$$k_{\text{ex}} = \frac{4\pi x_p x_d (v_p - v_d)^2}{\left((\Delta\nu_{1/2})_{dp} - x_p(\Delta\nu_{1/2})_p - x_d(\Delta\nu_{1/2})_d \right) ([p] + [d])} \quad (3.16)$$

from which it can be shown that from the resonance frequencies of the diamagnetic and paramagnetic species and the respective widths at half-height

$$(\Delta\nu_{1/2})_p = \frac{1}{\pi(T_2)_p} \quad (\Delta\nu_{1/2})_d = \frac{1}{\pi(T_2)_d} \quad (3.17)$$

and information on the bandwidth measured for the mixture of reactants, we can calculate the rate constant for electron exchange. [Figure 3.16](#) shows some results obtained using the technique of NMR line broadening [16] for the system

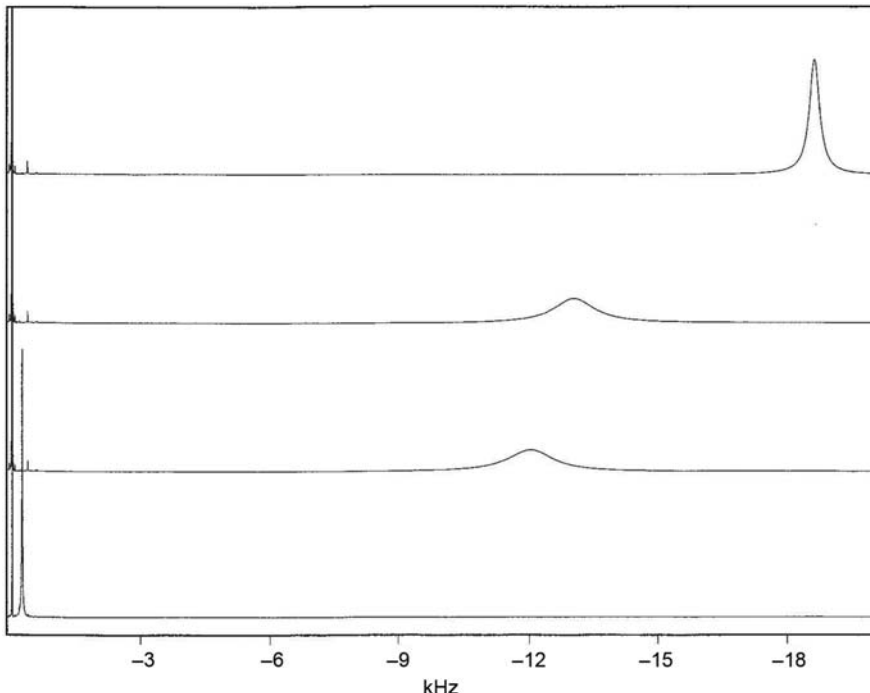
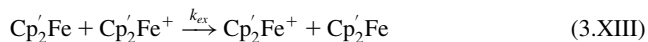


FIGURE 3.16

NMR spectra obtained for reaction (3.XIII) for $\text{Cp}_2'\text{Fe}^+$ (upper spectrum), $\text{Cp}_2'\text{Fe}$ (lower spectrum, while the intermediate spectra show mixtures of these reactants) obtained on a Varian-Unity 500 MHz NMR spectrometer of the Faculty of Science and Technology, University of Coimbra.

Courtesy of M.I. Silva, J.R. Rodrigues, R. Brito.

Table 3.8 Experimental parameters and rate constants for the self-exchange between decamethylferrocinium hexafluorophosphate and decamethylferrocene in acetone-d₆ at 37 °C.

Concentration ^a (mM)	ν_d (Hz)	$(\Delta\nu_{\nu_d})_{dp}$ (Hz)	x_p ^b	x_d ^b	k_{ex} (mol ⁻¹ dm ³ sec) ⁻¹
38.55	-12,020	1120.4	0.6484	0.3516	2.80×10^7
39.09	-12,042	1118.0	0.6496	0.3504	2.80×10^7
39.87	-13,068	1042.0	0.7038	0.2962	2.78×10^7

^aTotal concentration, $[Cp'_2Fe^+] + [Cp'_2Fe]$.

^bMole fraction, calculated from the corresponding chemical shifts: $x_p = |\nu_{dp} - \nu_p|/|\nu_d - \nu_p|$ or $x_d = |\nu_{dp} - \nu_d|/|\nu_d - \nu_p|$.

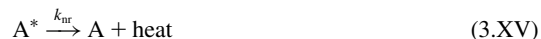
where Cp' represents the methylated cyclopentadienyl ligand. It should be noted that this technique can be applied because the decamethylferrocinium ion, Cp'₂Fe⁺, is paramagnetic, with $\nu_p = -18,667.0$ Hz with $(\Delta\nu_{\nu_d}) = 274.9$ Hz under the experimental conditions used, while the decamethylferrocene, Cp'₂Fe, is diamagnetic and, under the same conditions, has $\nu_d = 238.4$ Hz with $(\Delta\nu_{\nu_d})_d = 17.3$ Hz.

From the NMR spectra shown in Figure 3.16 it is possible to extract the data presented in Table 3.8 and obtain the exchange rate constants indicated. The exchange rate constant obtained for reaction (3.XIII) is $k_{ex} = 2.8 \times 10^7$ mol⁻¹ dm³ sec⁻¹ at 37 °C, which is in agreement with the values of 2.9×10^7 mol⁻¹ dm³ sec⁻¹ and 1.8×10^7 mol⁻¹ dm³ sec⁻¹ determined by Wahl and co-workers [17] at 35 °C and by Weaver *et al.* [18] at 25 °C, respectively.

3.2.3.2 Luminescence quenching

Another technique that is based on competition in the measurement of lifetimes in the absence and presence of chemical reactions is luminescence quenching. Luminescence refers to light emission by electronically excited molecules. When this emission is between states of the same spin multiplicity, it is called fluorescence, while when it is between states of different spin multiplicity, it is termed phosphorescence. The technique of luminescence quenching can be applied to either of these processes, although it is more common with the former. We will only treat explicitly the case of fluorescence quenching. The fluorescence intensity is directly proportional to the number of electronically excited species that emit light in their transition from the electronically excited state to the ground state in the same way that light absorption by the ground state leading to an electronically excited state (A*) is proportional to the concentration of the species in the ground state. The ratio between the number of photons emitted and the number of photons absorbed defines the quantum yield of fluorescence of the system,

$\Phi = I_{\text{em}}/I_{\text{abs}}$. In addition to emitting light, the electronically excited state has various other competing pathways available to lose its excitation energy that have been previously mentioned: non-radiative transitions to the ground state or to another state of lower energy with the partial or total conversion of its electronic energy into thermal energy, or chemical reaction with another species:



In the absence of quencher, the quantum yield of emission is

$$\Phi_0 = \frac{k_F}{k_F + k_{\text{nr}}} \quad (3.18)$$

In the presence of quencher the quantum yield is reduced due to the presence of an additional competing pathway

$$\Phi = \frac{k_F}{k_F + k_{\text{nr}} + k_Q[\text{Q}]} \quad (3.19)$$

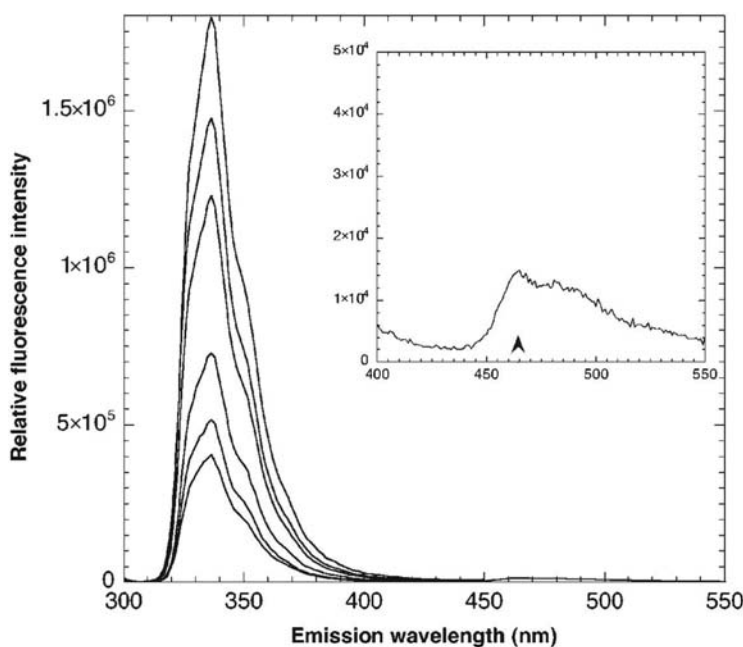
As the concentration of the quencher is normally much greater than that of the electronically excited species, $[\text{Q}]$ can be treated as a constant. The ratio between the emission quantum yields in the absence and presence of quencher is equal to the ratio between the emission intensities under the same conditions

$$\frac{I_0}{I} = \frac{k_F + k_{\text{nr}} + k_Q[\text{Q}]}{k_F + k_{\text{nr}}} \quad (3.20)$$

This expression is similar to that which will be deduced in the next chapter for the yields of products of parallel first-order (or pseudo-first-order) reactions, such as reactions (3.XIV)–(3.XVI). From the definition of experimental molecular fluorescence lifetimes $\tau_0 = 1/(k_F + k_{\text{nr}})$, the previous equation reduces to

$$\frac{I_0}{I} = 1 + \tau_0 k_Q[\text{Q}] \quad (3.21)$$

which is the expression obtained in 1919 by Stern and Volmer. Through readings of the fluorescence intensities in the absence of the quencher and the presence of known concentrations of quencher, it is possible to obtain k_Q knowing τ_0 or vice versa. This method allows us to obtain rate constants of very fast photochemical reactions, including ones close to or above the diffusion-controlled limits in liquid solution. In Figure 3.17 results are presented for the decrease in naphthalene fluorescence at 337 nm upon increasing the concentration of biacetyl. In this figure, we can also see the appearance of biacetyl fluorescence at 470 nm, whose S_1 state is formed by energy transfer.

**FIGURE 3.17**

Quenching of fluorescence of a solution of naphthalene (0.01 M) in benzene by biacetyl (<0.01 M). Under these conditions, irradiation at 300 nm leads to negligible light absorption by biacetyl. Results obtained on a SPEX Fluorolog 3 at the Coimbra Chemistry Centre. Accompanying the decrease in the naphthalene emission at 337 nm, an increase is observed in the biacetyl emission at 470 nm.

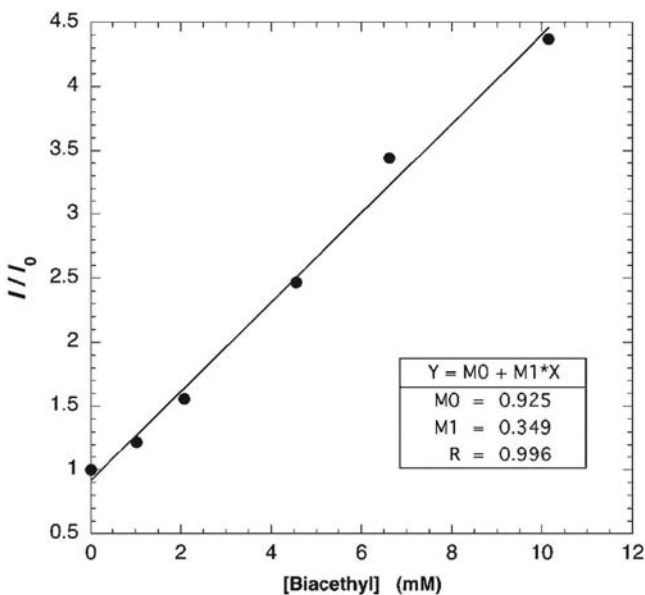
Courtesy of Marta Piñeiro.

Figure 3.18 shows the corresponding Stern–Volmer plot obtained for energy transfer from the lowest energy singlet state of naphthalene ($E_{S1} = 385 \text{ kJ mol}^{-1}$) to biacetyl ($E_{S1} = 267 \text{ kJ mol}^{-1}$) [19]. From the slope of the Stern–Volmer plot the product $k_Q\tau_0 = 268 \text{ M}^{-1}$ is obtained, from which, using the experimental fluorescence lifetime $\tau_0 = 18.2 \text{ nsec}$ for naphthalene in benzene, we determine $k_Q = 1.5 \times 10^{10} \text{ M}^{-1} \text{ sec}^{-1}$.

3.2.4 Methods with enhanced time resolution

3.2.4.1 Flash photolysis

The development of flash photolysis is due mainly to the work of Norrish and Porter. However, it was the development of the laser in 1960 that allowed this technique to attain its full potential. The contributions of Norrish and Porter

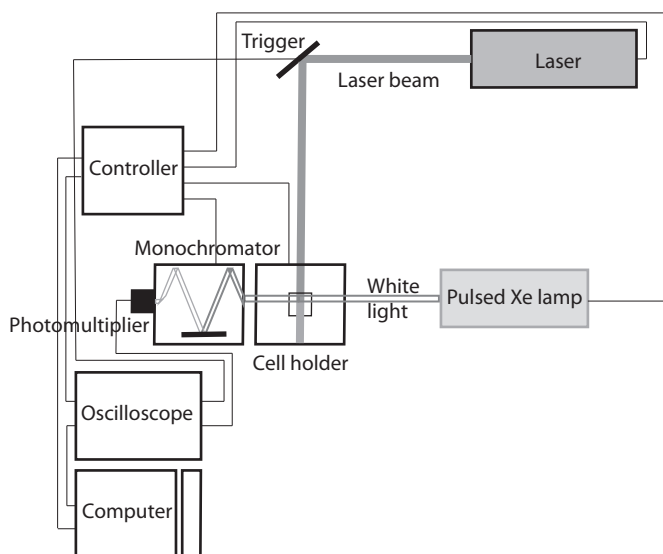
**FIGURE 3.18**

Stern–Volmer plot for energy transfer between naphthalene and biacetyl under the conditions of Figure 3.17.

earned them the Nobel Prize in chemistry in 1967. In fact, this technique has great versatility and has been used to study short-lived transients such as radicals, biradicals, electronically excited states, carbenes, exciplexes, radical ions, organic and inorganic species in unstable oxidation states, etc.

The conditions which determine whether flash photolysis can be used to study a given chemical system are: (1) a precursor of the species of kinetic interest has to absorb light (normally from a pulsed laser); (2) this species is produced on a timescale that is short relative to its lifetime in the system. Current technical developments make it easy to study timescales of nanoseconds for production and analysis of species. The last part of this chapter shows that the related technique of transient absorption extends this timescale to few femtoseconds. Once the species of interest has been produced, it is necessary to use an appropriate rapid detection method. The most common technique involves transient optical absorption spectroscopy. In addition, luminescence has been frequently used to detect transients, and other methods such as time-resolved resonance Raman spectroscopy and electrical conductivity have provided valuable information in certain cases.

Figure 3.19 shows a set-up for flash photolysis using absorption spectroscopy to detect transients formed on photolysis.

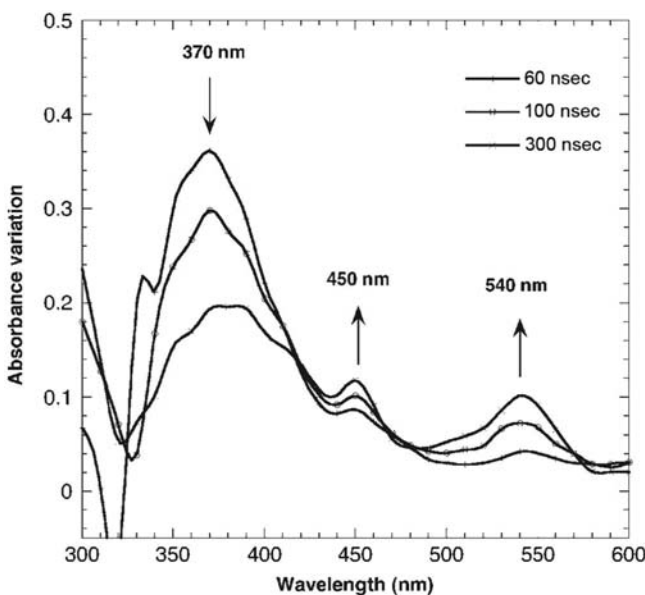
**FIGURE 3.19**

Schematic diagram of a flash photolysis system. The white light illuminates the sample in the cell holder while the laser is fired, and the nanosecond laser pulse produces a photochemical change in the composition of the sample that is observed as a change ΔA in the absorption of the sample. The change in ΔA is followed as a function of time in the nanosecond and microsecond time window.

To obtain the decay of a transient, the analysing white light from the xenon lamp is focussed on the sample contained in a cuvette. The initial intensity of the analysing light, I_0 , is detected at the analytical wavelength λ by a photomultiplier. The laser is then discharged. A small part of the laser beam is diverted to a detector that triggers a transient digitiser to start measurement of time and signal acquisition. The rest of the light is absorbed by the sample. The signal registered by the digitiser is the light intensity of wavelength λ transmitted in the presence of the transient, $I(\lambda, t)$, which depends upon time owing to its decay in the reaction of interest. The signal recorded by the digitiser is transferred to the computer and the time profile of the absorbance of the transient at wavelength, λ , is calculated

$$A(\lambda, t) = \log \frac{I_0(\lambda)}{I(\lambda, t)} \quad (3.22)$$

In these experiments, the decay curve of transient absorbance at a given wavelength is studied in real time. It is also possible to obtain time-resolved

**FIGURE 3.20**

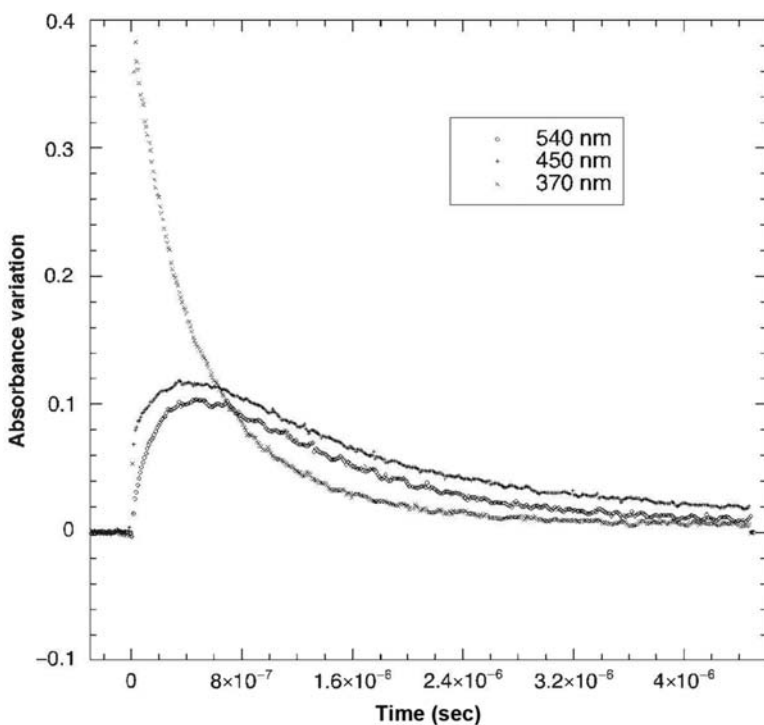
Time-resolved spectra for the system anthraquinone + trimethoxybenzene in acetonitrile, excited at 355 nm, under conditions where the quinone absorbs. The spectra were recorded 60, 100 and 300 nsec after irradiation with the laser pulse. Results obtained on an Applied Photophysics LKS 60 flash photolysis apparatus in the Coimbra Chemistry Centre.

Courtesy of Carlos Serpa.

absorption spectra of transients, recording their absorbance at pre-determined times: t_1, t_2, \dots, t_n .

Figure 3.20 shows transient absorption spectra obtained following excitation of anthraquinone (5.1×10^{-4} M) at 355 nm in the presence of trimethoxybenzene (1.3×10^{-4} M). Note the disappearance of the absorption of the triplet state of the anthraquinone at 370 nm, formed following excitation at 355 nm with the 8 nsec laser pulse, with the simultaneous formation of two new bands at 450 and 540 nm.

It is possible to follow the disappearance of the initial intermediates at one analytical wavelength and the formation of new ones at other wavelengths, as can be seen in Figure 3.21. The instrumentation involved requires using a sequence generator for coordination of the various steps which proceed the signal acquisition: triggering the transient digitiser, opening the shutters, starting a pulsed analysing lamp (to increase sensitivity), reading I_0 , pulsing the laser, reading $I(\lambda, t)$ and then closing the shutters.

**FIGURE 3.21**

Kinetic traces of signals observed at 370, 450 and 540 nm, corresponding to the anthraquinone triplet state, trimethoxybenzene radical cation and anthraquinone radical anion, respectively. The decay of the triplet state is pseudo-first-order, and has the same lifetime as formation of the radical ions. Subsequently, these compounds decay by slower processes.

Courtesy of Carlos Serpa.

3.2.4.2 Pulse radiolysis

In flash photolysis, transient species are produced by absorption of light, normally from a pulsed laser. This specifically excites the solute. The interaction of high-energy radiation such as X-rays, γ -rays or high-energy electron beams with matter is termed radiation chemistry. High-energy radiation induces ionisation, which can subsequently lead to formation of either free radicals or excited states. Absorption of high-energy radiation is not specific, and will be predominantly by the species present in the greatest amount. For solutions, this is the solvent. Thus radiation chemistry depends upon the solvent, and provides a route to specifically generate either charged species or excited states, depending upon the solvent used. Pulse radiolysis is the

radiation chemistry equivalent of flash photolysis, and provides a valuable complementary technique. Normally, a pulsed beam of high-energy electrons (energies of several MeV) produced by a linear accelerator (electron gun) is used as the radiation source and, as in flash photolysis, transient absorption spectroscopy is used to characterise reactive intermediates both in terms of their spectra and kinetics. The basic techniques are similar, the main differences stem from the fact that we are considering reactions of solvent-derived transients with solutes, and that, owing to the need for large-scale equipment, there are relatively few places where these experiments can be carried out. However, these are compensated for by the fact that many of the experiments cannot be easily carried out by other fast reaction methods.

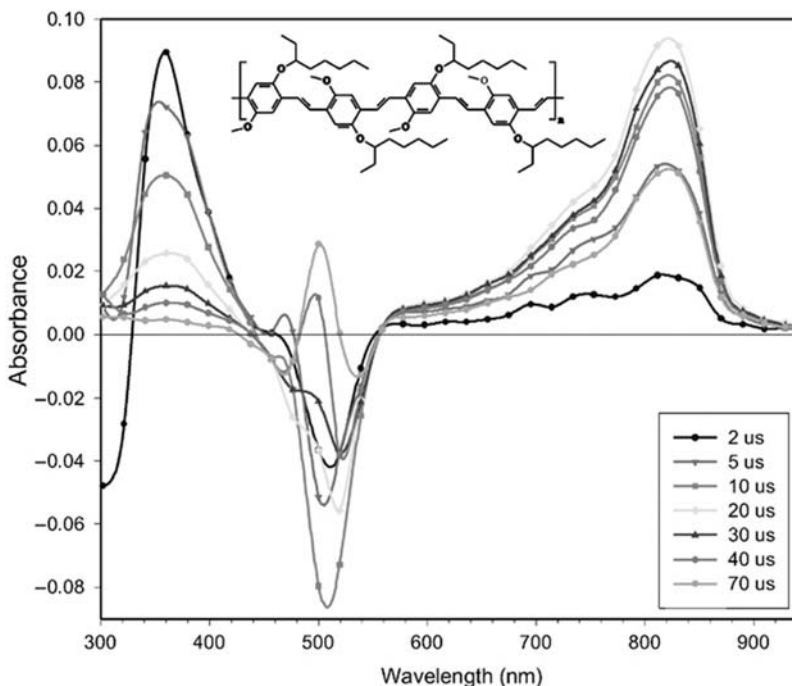


FIGURE 3.22

Time evolution of the transient absorption spectra following pulse radiolysis of argon-saturated solutions of MEH-PPV in benzene in the presence of biphenyl sensitiser.

Reprinted from AP Monkman, HD Burrows, MG Miguel, I Hamblett, ES Navaratnam, Measurement of the S_0-T_1 energy gap in poly(2-methoxy,5-(2 ethylhexoxy)- ρ -phenylenevinylene), MEH-PPV, by triplet-triplet energy transfer, Chem. Phys. Lett. 307 (1999) 303–309. (Copyright 1999, with permission from Elsevier.)

As an example, we will consider the characterisation of triplet states of conjugated organic polymers. Pulse radiolysis of aromatic solvents such as benzene produces mainly excited triplet and singlet states in the ratio 3:1. By incorporating an appropriate energy acceptor with high-inter-system crossing yields, it is possible to capture this excitation energy and specifically produce excited triplet states. This species can then act as triplet donor and populate triplet states of other species by energy transfer, even though these may not be readily accessible by photochemical routes because of low yield of inter-system crossing from singlet states.

Figure 3.22 shows the transient spectra observed following pulse radiolysis of an argon-saturated solution of biphenyl (10 mM) and the conjugated polymer MEH-PPV in benzene solution. In this experiment, the triplet state of biphenyl (${}^3\text{Ph}_2^*$) is initially formed by energy transfer from the solvent (Bz) leading to the absorption around 360 nm. Biphenyl then transfers its triplet energy to the polymer, leading to a new absorption at 830 nm owing to the triplet state of the polymer, and depletion of the

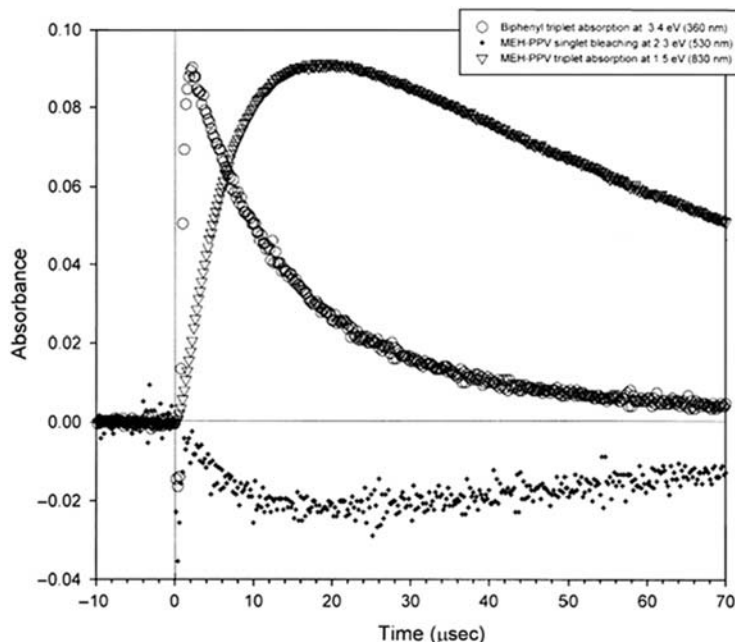
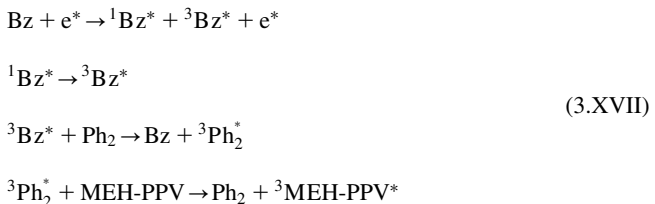


FIGURE 3.23

Decay and grow-in of the various spectral features seen in Figure 3.22.

Reprinted, with permission, from the same source.

ground-state absorption band of the polymer at 530 nm. The overall kinetic scheme is



while the kinetic traces for decay of the biphenyl triplet at 360 nm and formation and decay of the polymer triplet at 830 nm and bleaching at 530 nm are shown in Figure 3.23.

3.2.4.3 Time-resolved photoacoustic calorimetry

Time-resolved photoacoustic calorimetry (PAC) is a technique complementary to flash photolysis. In flash photolysis we study transient species through their radiative processes (light absorption or emission) in the wavelength region analysed. In contrast, in PAC we study the non-radiative transitions (vibrational relaxation, physical quenching of excited states or chemical reactions), again normally induced by excitation with a pulsed laser. These transitions correspond to the conversion of absorbed light energy into thermal energy, leading to production of thermal pulses (or heat waves) within the sample. The heat liberated by the transient species is directly proportional to the increase in temperature of the sample [20]

$$H_{\text{ther}} = C_p V_{\text{irr}} \rho \Delta T \tag{3.23}$$

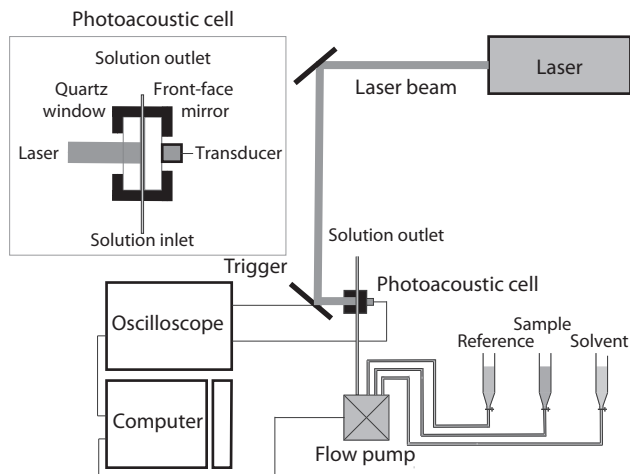
where C_p is the heat capacity of the solution at constant pressure, V_{irr} is the volume irradiated by the laser pulse and ρ is the density of the solution. At constant volume, the pressure and temperature are related

$$\Delta P = \frac{\alpha}{k_T} \Delta T \tag{3.24}$$

Here, α is the coefficient of thermal expansion and k_T is the adiabatic compressibility of the solution. The ratio α/k_T is also known as the coefficient of thermal pressure or internal pressure of the solvent. From Eqs. (3.23) and (3.24) we obtain the transient pressure produced by the conversion of absorbed light into thermal energy

$$\Delta P = \frac{1}{C_p A l \rho k_T} H_{\text{ther}} \tag{3.25}$$

where A is the area of the sample irradiated and l its thickness. The acoustic wave produced in this process can be detected by coupling a high-frequency transducer to the irradiated sample cell, using the set-up given in

**FIGURE 3.24**

Schematic diagram of the photoacoustic calorimetry equipment developed in the Coimbra Chemical Centre. The laser beam from a Q-switched Nd:YAG laser (EKSPLA NL301G), optionally pumping an optical parametric oscillator (EKSPLA PG/122/SG), is directed to a photoacoustic calorimetry flow cell. A detail of the flow cell is given in the inset rectangle. The optical path of the solution is *ca.* 0.2 mm. The photoacoustic wave generated in the solution travel through the front-face mirror and reaches the ultrasound transducer coupled to the rear of the cell. Transducers with resonance frequencies between 0.5 and 100 MHz (Olympus Panametrics contact transducers) are selected to cover the expected lifetimes of the species to be investigated [22]. Automatic injection using a Kloehn syringe pump allows for the successive collection of photoacoustic waves generated by the sample, reference and solvent.

Figure 3.24. The transducer or microphone converts the pressure that acts on it into a voltage

$$V_t = c_t \frac{1}{C_p A l \rho} \frac{\alpha}{\kappa T} H_{\text{ther}} \quad (3.26)$$

where c_t is an experimental constant.

In photoacoustic experiments, low absorbances must be used for all for solutions to ensure homogeneous light absorption within the sample volume V_{irr} . In the first experiment, an acoustic wave is measured for a solution containing a photoacoustic reference material, which converts all the light energy absorbed into thermal energy in a short time compared to the frequency of the transducer. Following this, the acoustic wave of the solution containing the sample under study is measured. This sample must have a lifetime similar to the frequency of the transducer and also the same absorbance

as the reference solution at the laser wavelength. Finally, the acoustic wave of the solvent used is determined. This solvent wave is subtracted from those of the reference and the sample.

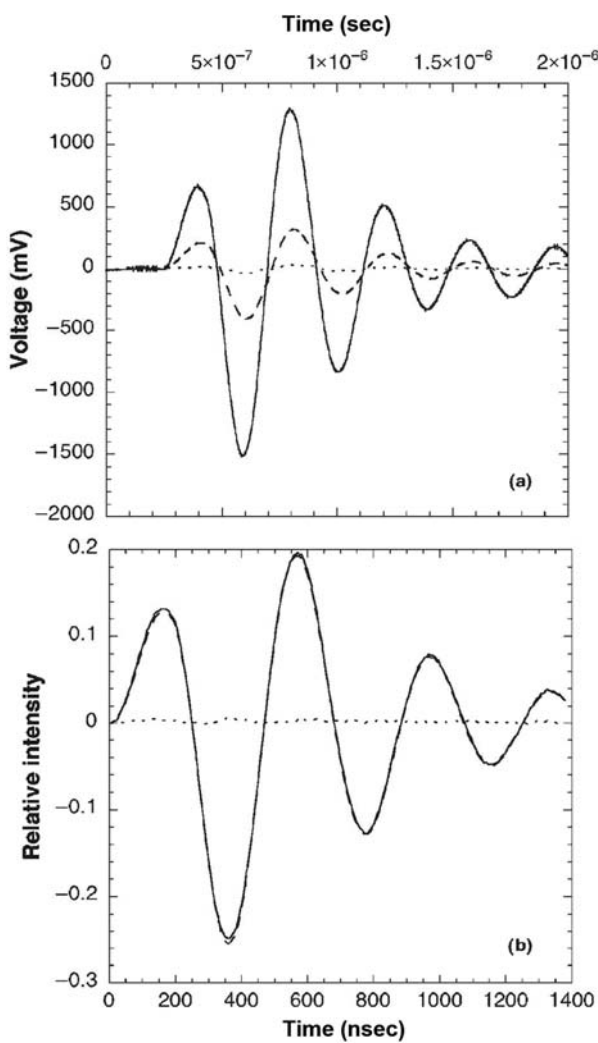
[Figure 3.25](#) shows acoustic waves for a reference and a sample, both corrected for solvent absorption. The sample consists of benzophenone (Bp) and benzhydrol (Bh) in benzene. When benzophenone is electronically excited, it abstracts a hydrogen atom from benzhydrol to give a pair of identical ketyl radicals (K^\bullet)



Inter-system crossing to form ${}^3\text{Bp}^*$ is very fast. Hence the first heat decay is associated with the formation of ${}^3\text{Bp}^*$, and the first transient detected is ${}^3\text{Bp}^*$. The bimolecular reaction with Bh is done in conditions where $[\text{Bh}] \gg [{}^3\text{Bp}^*]$ and the hydrogen abstraction reaction proceeds with the kinetics of a first-order reaction. This reaction leads to a second heat decay and the second transient detected is the ketyl radical. From the computational analysis of these waves, it is possible to calculate, from the differences in the phase and amplitude, the lifetime of the species under study together with the enthalpy of the reaction involved [\[21,22\]](#). The calculation from this calorimetric data requires the quantum yields of the processes involved. In mechanism (3.XVIII), this is simplified because it is known that the benzophenone triplet quantum yield is unity and for sufficiently high concentrations of benzhydrol the quantum yield of the hydrogen abstraction is also unity. The biggest limitation of this technique stems from the fact that it does not allow identification of the transients whose heats of reaction and lifetimes are being measured.

3.2.4.4 Single photon counting

Time-resolved fluorescence spectroscopy is one of the most widely used techniques for studying the structure, function and reaction dynamics of macromolecules in chemistry and biology. Fluorescence measurements can reveal ligand-induced conformational changes in proteins, the origins of charge transfer reactions, solvent relaxation phenomena and local conformational changes. Most fluorescence decays occur in the time window of ~ 100 fsec to nanoseconds, so measurements require short light pulses and high temporal resolution instrumentation. The lifetime of a fluorescent species can be determined from the decay of its fluorescence intensity as a function of time. The technique of time-correlated single photon counting (TCSPC), used to determine fluorescence lifetimes, is based on the fact that the probability of time distribution of a single emitted photon follows the statistical distribution of all the photons emitted. If we study a large number of experiments in which we observe only a single photon emitted in each case, the probability distribution for the

**FIGURE 3.25**

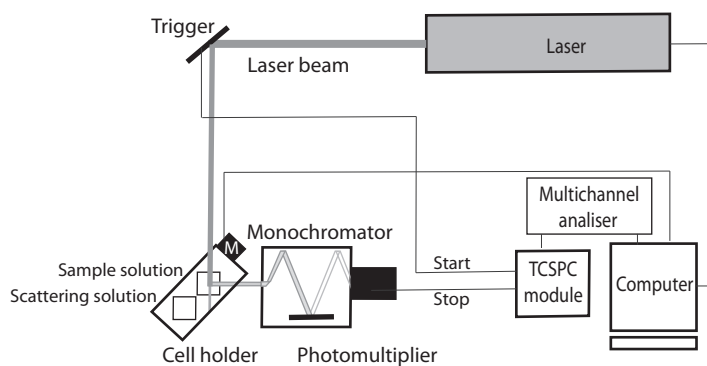
- (a) Photoacoustic waves of references (solid line) and sample (dashed line) containing benzophenone and benzhydrol in benzene (dotted line), measured by a 2.25 MHz transducer following excitation by a pulse from a nitrogen laser ($\lambda_{\text{irr}} = 337$ nm).
- (b) Comparison between the calculated and experimental waves when two consecutive exponentials are used to describe this process. The dotted line is the difference between the experimental and calculated waves. The first exponential corresponds to the rapid formation of the triplet state of benzophenone, and the second to the abstraction of a hydrogen atom from benzhydrol by benzophenone triplet. Results obtained with the photoacoustic calorimeter in the Coimbra Chemistry Centre.

Courtesy of Monica Barroso.

emission of all the single-photon events provides the distribution of intensity, over time, for all the photons emitted. This method has a high time resolution, allows averaging over many events, and so can be used with relatively weak fluorophores, and allows time resolution in the nanosecond and picosecond range. TCSPC works even when the emitted light is too weak to create an analogue voltage representing the optical flux because it uses multiple cycles of excitation and emission. It relies on the repetitive and precisely time registration of single photons coming from a fluorescent sample. This means that the excitation source must have a high photon repetition rate. Pulse repetition rates are usually between 1 and 100 MHz and pulse durations are typically in the range of femtoseconds to about 100 psec. Another valued characteristic of TCSPC is that it is able to cover an extremely large dynamic range. Unlike analogue techniques, TCSPC is not limited by the linearity range of the detector. A fluorescence decay function can be followed over more than three orders of magnitude. Hence TCSPC is an excellent method for studying multi-exponential or non-exponential processes.

A TCSPC equipment consists in a pulsed laser source (alternatively, more affordable NanoLEDs can be employed, taking advantage of pulsed laser diodes and LED technology), a monochromator, a single photon detector (e.g., multi-channel photomultiplier or single-photon avalanche diodes) and fast TCSPC electronics. The TCSPC module includes a constant fraction discriminator (CFD) to extract precise timing information from trigger and detector, and is usually based on the time-to-amplitude converter/analogue-to-digital converter principle (TAC/ADC). The TAC provides an accurate measure of the time between two events, such as START and a STOP pulses, and generates an analogue output pulse proportional to the measured time. This pulse is sent to the ADC that gives a value corresponding to the time difference between the photon emitted and the excitation pulse. Each time difference is made correspond to a different channel of a multi-channel analyser (MCA), and the signals are distributed and accumulated in the various channels of the MCA according to their time differences. Provided that the light level of the emission is low, and this can be achieved by attenuation of the light level at the sample if needed, only one photon per cycle (one count) is registered in one channel of the MCA. After many counts, this generates a histogram of photon arrivals per channel, where each channel is selected according to the time difference between the START and STOP pulses of each photon. A sufficient statistical distribution of counts as a function of channel number is obtained after n repetitions/cycles (typically 10,000 counts), to allow an accurate analysis of the decay time.

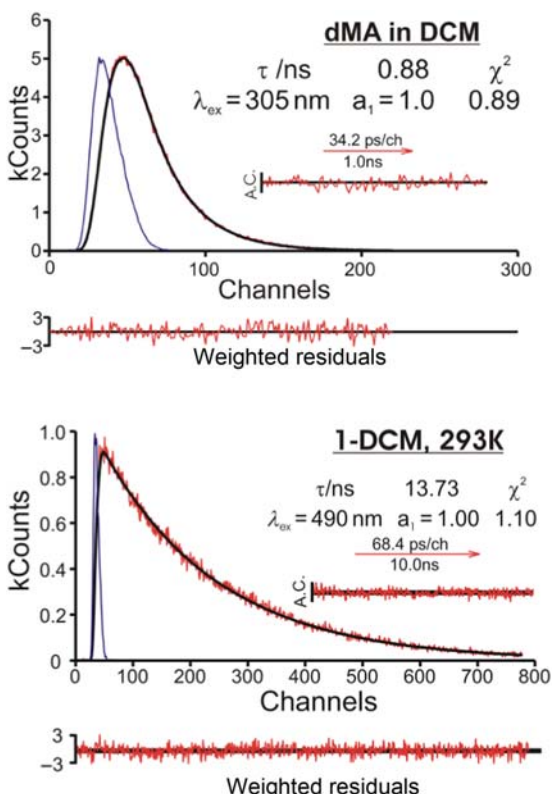
Figure 3.26 shows the main components of a typical TCSPC equipment. In this case, the excitation source consists of a picosecond Spectra Physics mode-lock Tsunami laser (Ti: sapphire) model 3950 (repetition rate of about 82 MHz, tuning range 700–1000 nm), pumped by a Millennia Pro-10s, frequency-doubled continuous wave (CW), diode-pumped, solid-state laser ($\lambda_{\text{em}} = 532$ nm). A harmonic generator model GWU-23PS (Spectra-Physics) can be used to produce the

**FIGURE 3.26**

Setup for the picosecond TCSPC apparatus in the Coimbra Chemical Centre. A laser or a NanoLED can be used for excitation. Emission from sample or scattering solutions is collected in alternation, with the repositioning of the cells with motor M. The TCSPC module includes CFD and TAC/ADC components. (CFD, Constant fraction discriminator; TAC/ADC, time-to-amplitude converter/analogue-to-digital converter; TCSPC, technique of time-correlated single photon counting).

second and third harmonic from the Ti:sapphire laser exciting beam frequency output. The sample and scattering solutions are placed in a motorised (M) cell holder. This allows for alternate collection of the emission from the sample and of the light scattered by the scattering solution (e.g., LUDOX). This scattered light is treated in the same way as the emitted light to obtain the instrumental response function (IRF). Emission at 90 degrees geometry is detected at a magic angle (to avoid anisotropy effects) through a double subtractive Oriel Cornerstone 260 monochromator by a Hamamatsu microchannel plate photomultiplier (R3809U-50). Signal acquisition and data processing employs a Becker & Hickl SPC-630 TCSPC module. Fluorescence decays and IRF are collected using 4096 channels. The scale of the channels is selected to enable the detection of the emission over three or more decay lifetimes. In this equipment, the fastest scale possible is 0.814 psec/channel scale. The full width at half-maximum (FWHM, also named linewidth) of the IRF is about 22 psec and is highly reproducible with identical system parameters. The analysis of the decays is conveniently made deconvoluting the IRF from the signal and using the method of modulating functions described by Striker [23]. The quality of each fit is judged by the χ^2 value, weighted deviations, and their autocorrelations.

Scheme (3.XIX) shows a system featuring molecule **1** designed to study intramolecular electron transfer reactions. The chromophore of molecule **1** is appropriately represented by 3,4-dimethylanisole (dMA), which fluoresces at 305 nm. In addition to this chromophore, molecule **1** has a good electron acceptor group that allows for photo-induced electron transfer. The charge-separated state, ${}^1\text{I}^\pm$, is stabilised by the solvent, which in this case is dichloromethane, and emits at

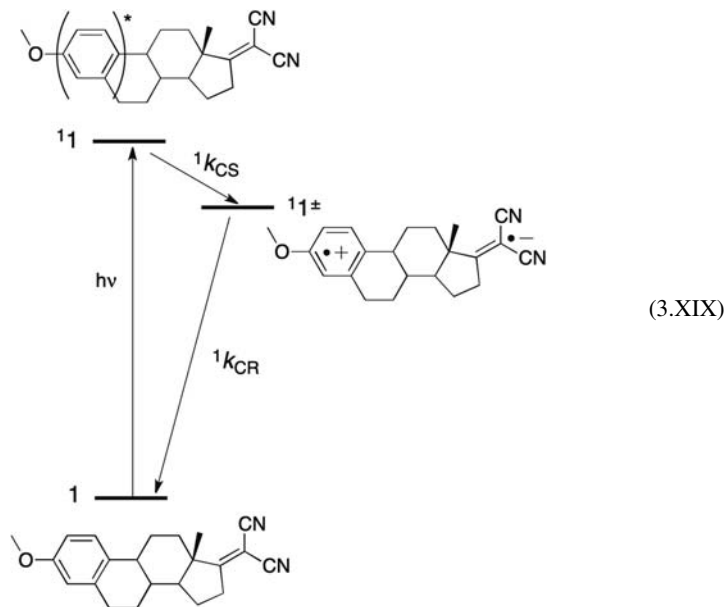
**FIGURE 3.27**

TCSPC decays of dMA (model of the chromophore of molecule 1) and of 1 in dichloromethane, represented in Scheme (3.XIX). The fluorescence of dMA was collected at 305 nm and that of $^1\text{I}^\pm$ was collected at 490 nm. The narrower trace in the decays is the IRF, which is needed for the deconvolution of the signal. Convolution of the IRF with a single exponential decay (first-order reaction) gives the calculated decay that overlaps with the experimental data. The lower part of the decays shows the difference between the experimental signal and the calculated decay (using the lifetime indicated), convoluted with the IRF. The autocorrelation (AC) shows a narrow and unbiased distribution and the χ^2 is close to unit, indicating that high quality of the fit. Results obtained with the TCSPC system in the Coimbra Chemical Centre. (IRF, Instrumental response function; TCSPC, technique of time-correlated single photon counting)

Courtesy of Kamila Mentel.

490 nm. Figure 3.27 shows TCSPC of dMA and molecule 1. The lifetime of $^1\text{I}^\pm$ (13.73 nsec), measured by following the emission at 490 nm, is much longer than that of the singlet state of dMA (0.88 nsec), measured from the fluorescence at 305 nm. The lifetime of the locally excited state of 1, ^1I , is too short to be

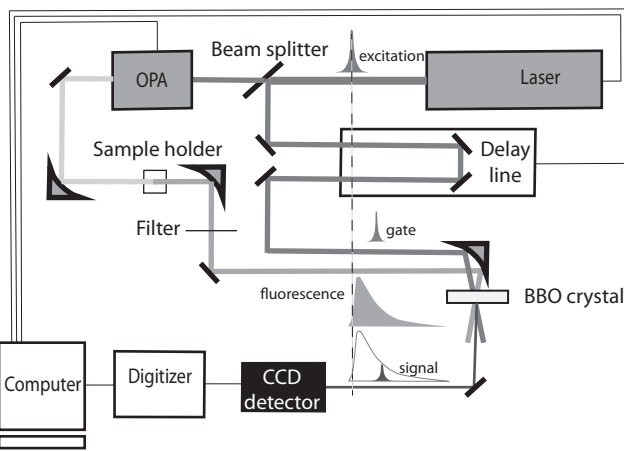
measured in this experiment because the intra-molecular charge separation is very fast. This ultra-fast intra-molecular electron transfer benefits from the short separation between the limits of the aromatic ring (donor group) and C = C(CN)₂ (acceptor group), which is about 5.9 Å [24]. This lifetime is presented in the description of ultra-fast transient absorption.



3.2.4.5 Fluorescence upconversion

Short laser pulses, fast electronics and low radio frequency noise contribute to short IRFs. Deconvolution of the signals further increases the time resolution of TCSPC. However, TCSPC cannot go beyond a resolution of a few picoseconds. Alternatively, fluorescence upconversion enables spectroscopic studies of biological and chemical systems with a time resolution limited only by the pulse width of ultra-fast lasers, which can operate on the femtosecond timescale.

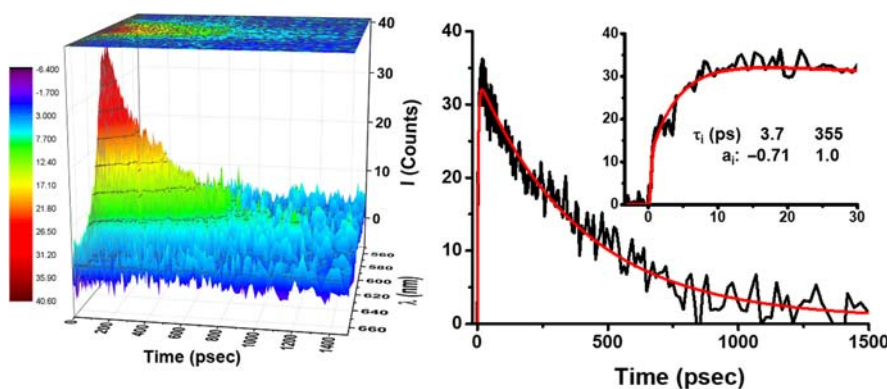
The fundamental principles of fluorescence upconversion were established in the 1970s. They are based on the mixing in a non-linear optical crystal of fluorescence excited with an ultra-fast laser pulse with a delayed portion of that laser pulse (the gate pulse). The non-linear crystal allows for sum-frequency generation (SFG) or for difference-frequency generation (DFG) of the pumped fluorescence with the gate pulse. The mixing process takes place only when the gate pulse overlaps with the fluorescence and provides a time resolution comparable with the pulse width. Variable delays of the gate laser pulse with respect to the fluorescence excitation pulse, which are readily achieved by increasing or decreasing the optical path length of the gate pulse, allow for probing the mixing at sequences of

**FIGURE 3.28**

Schematic diagram of fluorescence upconversion measurements. The beam of a femtosecond laser is split in two, to generate an excitation pulse and a gate pulse. The excitation pulse is first directed to an OPA to allow for the generation of a wavelength that matches an absorption band of the sample, and then is used to excite the sample. The fluorescence from the sample is focused with an appropriate angle on a BBO crystal where it meets phase matching conditions that optimise the sum frequency generation with the gate pulse to give the upconversion signal. (*BBO*, β -barium borate; *OPA*, optical parametric amplifier).

very short and precise time intervals. The upconverted signal generated is proportional to the fluorescence intensity at the moment the gate pulse arrives. The time-resolved decay is obtained by measuring the intensity of the upconverted signal as the delay time of the gate pulse is varied [25].

Figure 3.28 presents an equipment to measure fluorescence upconversion. In this equipment, a femtosecond ultra-fast amplifier Spectra Physics Solstice Ace HP delivers 100 fsec pulses with 7 mJ per pulse at 800 nm and a repetition rate of 1 kHz. The 800 nm laser pulses are used to pump the TOPAS Prime-F optical parametric amplifier (OPA) that converts the pump pulse into pulses with wavelengths selected in the range 240–2600 nm. The sample holder, delay line, β -barium borate (BBO) crystal and multi-wavelength charge-coupled device (CCD) camera are all integrated in the Halcyone Fire spectrometer of Ultrafast Systems. In order to maximise the upconverted signal intensity the BBO crystal needs to be rotated to a certain angle with respect to the fluorescence and gate beams. The SFG process is efficient only if conditions for phase matching between gating and fluorescence pulses are satisfied; this happens only for a narrow band of wavelengths centred at a wavelength determined by the phase-matching angle. While the CCD itself can detect a fluorescence signal in the

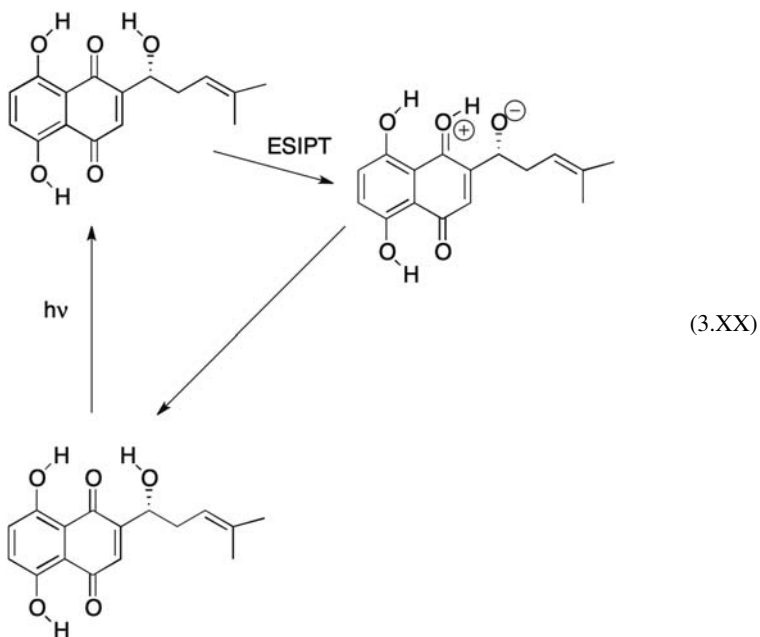
**FIGURE 3.29**

Time-resolved fluorescence emission spectra together with the representative kinetic trace at 615 nm for shikonin in cyclohexane collected with excitation at 450 nm. The purported mechanism is represented in [Scheme \(3.XX\)](#). The best-fit results and pre-exponential values (a_i) are presented as inset. Results obtained with the fluorescence upconversion system in the Coimbra Chemical Centre.

Courtesy of João Pina.

400–800 nm range, the non-linear crystal has a rather limited spectral bandwidth at each phase matching angle. Therefore in order to measure a full fluorescence spectrum, one needs to rotate the non-linear crystal over a range of angles corresponding to the spectral window of interest. In the Halcyone Fire spectrometer, this is achieved by putting the non-linear crystal on a computer-controlled rotation stage that optimises the crystal angles automatically.

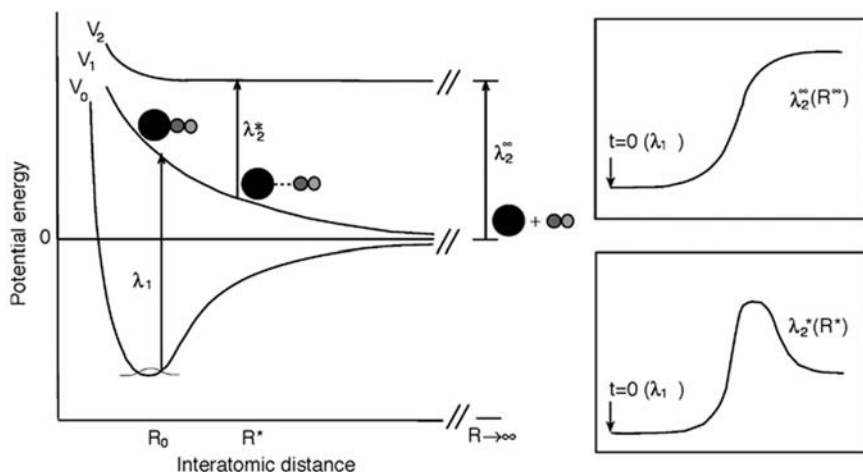
[Figure 3.29](#) presents the transient fluorescence emission spectra obtained with the Coimbra upconversion spectrometer described in [Figure 3.28](#) for shikonin (a hydroxy-1,4-naphthoquinone derivative naturally occurring in plants) collected with excitation at 450 nm. [Scheme \(3.XX\)](#) presents a possible mechanism associated with electronic excitation of shikonin. Global fit analysis (i.e., simultaneous analysis of all kinetics in the 575–640 nm range) using the principal component analysis methodology to be described in [Chapter 4](#), Reaction Order and Rate Constants, was performed after singular value decomposition. The decays were best fitted with a bi-exponential decay law, with lifetimes of 3.7 and 355 psec. Worth mention that the longer lifetime is in good agreement with the value obtained by TCSPC while the shorter lifetime was not resolved in the TCSPC system. The shortest time component, 3.7 psec, is associated to a negative pre-exponential factor, a_i , (rise-time) which is usually ascribed to the occurrence of an excited state dynamic process. Indeed, this lifetime was assigned to excited state intra-molecular proton transfer (ESIPT), while the 355 psec decay component was attributed to the decay of the ESIPT product.



3.2.4.6 Femtochemistry

In the first chapter, it was indicated that, intrinsically, the transition state has a virtual existence, since by definition it corresponds to a maximum, at infinitesimally small times, of potential energy on the pathway that separates the reactants and the products. To obtain information on the reaction process, close to the region of the transition state, it is necessary to resort to a technique with an extraordinarily high time resolution. Some idea of this time resolution can be obtained by considering that the separation of the fragments of a photo-induced molecular cleavage occurs typically with a velocity 1000 m sec^{-1} . Thus to determine the positions of the fragments when these are separated by 10 pm, which corresponds to 10% of a bond length, it is necessary to make measurements with a time resolution better than 10^{-14} sec . Although experiments are in progress with attosecond lasers, the most reliable technology currently available produces laser pulses with duration of $\sim 5\text{--}6 \text{ fsec}$. This provides possibilities for “transition state spectroscopy”. The development of femtochemistry to map the reaction coordinate and the spectroscopy of the transition state is mainly due to A. Zewail, who was awarded the Nobel Prize in chemistry for this work in 1999 [26,27].

A good illustration of the spectroscopy of the transition state is given by the photo-dissociation of ICN. A low-density beam of ICN molecules is irradiated with a 307 nm laser pulse, exciting the molecules to a repulsive electronic excited state. In this state, each molecule dissociates into I and CN. The production of

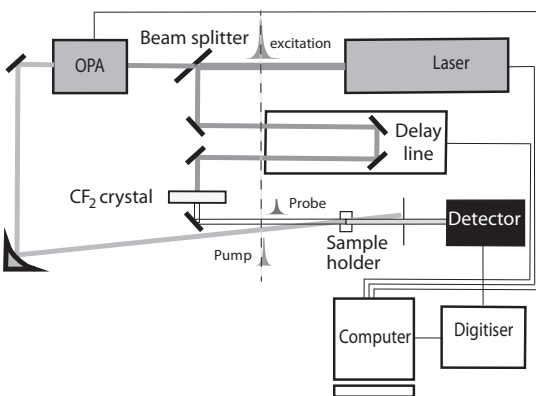
**FIGURE 3.30**

Dissociation of the molecule of ICN by excitation with a $\lambda_1 = 307$ nm laser pulse, and its analysis in real time by excitation with an analysing pulse of variable wavelength, λ_2 , for an emissive state of fragment CN. Detection is made by the intensity of the emission of CN with time, using analysing pulses with different values of λ_2 . Values are also shown of the emission expected for analysing pulses that excite the CN fluorescence when this is isolated and when it is still partially bound to the iodine atom [27].

CN can be followed by its fluorescence, induced by an analysing laser pulse at 388.9 nm, which is in resonance at this wavelength with the energy separation between the CN ground state and a fluorescence-excited state. The analysing pulse is delayed relative to the photolysis pulse by variable time intervals, which are controlled by modifying the distance covered by the pulses. This so-called “pump-probe” technique is very commonly used to study ultra-fast processes on the picosecond and sub-picosecond timescale. We should remember that with the velocity of light *in vacuo* (2.998×10^8 m sec $^{-1}$) light travels about 0.3 mm in a picosecond, and that this distance will depend on the medium used. The intensity of the induced fluorescence of CN is equal to zero until this fragment is separated by ~ 600 nm from the iodine atom. The analysing pulse can be tuned to a slightly longer wavelength, 389.5 nm, to see what happens when the bond is only partially broken. The intensity of the induced fluorescence at this longer wavelength pulse increases with time, reaching a maximum and subsequently decaying when the wavelength of the analysing pulse is out of resonance with the fluorescent electronic state (Figure 3.30).

3.2.4.7 Transient pump–probe spectroscopy

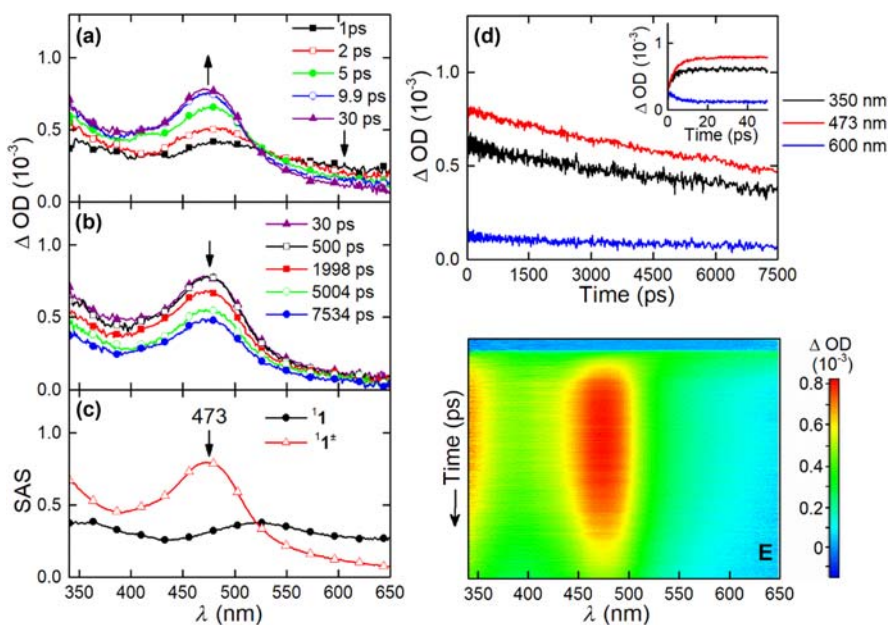
Today, chemical and physical processes that take place in the femtosecond timescale are often studied by fluorescence upconversion when they involve

**FIGURE 3.31**

Schematic diagram of a femtosecond transient absorption spectrometer. The beam of a femtosecond laser is split in two. One part goes through an OPA to generate a wavelength appropriate for the excitation of the sample, and is called the pump pulse. The other one, called probe beam, goes to a delay line and is then focused on a CF_2 crystal or sapphire plates to generate white light. The probe beam arrives at the sample at a precise time interval Δt after the pump beam and is absorbed by the transients generated by the pump beam. The detector registers the absorption spectrum at Δt , which is imposed by the delay line. Changing the length of the path of the probe beam in the delay line allows for the selection of different Δt . (OPA, Optical parametric amplifier)

fluorescent species, or by transient pump–probe absorption when changes in the absorption of reactants and short-lived intermediates are of interest.

Figure 3.31 offers a schematic presentation of a femtosecond transient absorption spectrometer. Following the same principle presented above for fluorescence upconversion, the laser beam is split in two, to obtain pump and probe beams. Sending the pump beam through an OPA allows for the selection of a pump wavelength that matches an absorption band of the sample. The probe beam is a small fraction of the laser beam. It goes through a delay line and is focused in a vertical translating CaF_2 crystal or in sapphire plates of different thicknesses. The crystal or the sapphire plates induce high order non-linear optical process to produce a white-light continuum in the 350–750 nm or in the 450–800 nm and 800–1600 nm range, respectively. Thus the probe pulse is white light that can be absorbed at specific wavelengths by the transient generated by the pump pulse. Selecting different delays between pump and probe allows for the collection of transient spectra at different time intervals. Plotting the changes in absorption at a given wavelength as a function of the time intervals yields the decay(s) of transient(s) that absorbs at that wavelength. Negative changes in absorption at a given wavelength correspond to the recovery of a species (usually the chromophore) bleached by the pump pulse, because its absorption increases with time. When very short times are of interest, the differences in the velocity of light at different

**FIGURE 3.32**

Transient absorption spectra of the processes illustrated in Scheme (3.XIX) for molecule 1 in dichloromethane at 293K, in short- (a) and long-time scales (b), and calculated species-associated spectra (c). Time profile of selected decays (d). 2D image of collected data (e). All the spectra presented were subject to the subtraction of the solvent response and chirp correction. Results obtained with the ultra-fast transient absorption spectrometer in the Coimbra Chemical Centre.

Courtesy of Kamila Mentel.

wavelengths in the material (quartz, glass) of the cell, due to their differences in refractive index, must be taken into account because not all wavelengths reach the sample at the same time (chirp). Chirp correction requires the measure of the transient signal obtained in the same cell with the solvent of interest.

Figure 3.32 presents the transient absorption of molecule 1 shown in Scheme (3.XIX) and in the example of TCSPC. The experimental setup employed in this experiment consists of a broadband (350–1600 nm) HELIOS pump-probe femtosecond transient absorption spectrometer from Ultrafast Systems, equipped with an amplified femtosecond Spectra-Physics Solstice-100F laser (displaying a pulse width of 128 fsec and 1 kHz repetition rate), coupled with a Spectra-Physics TOPAS Prime F optical parametric amplifier (195–22,000 nm) for pulse pump generation. The probe beam is a small portion of the 800 nm light from the Solstice-100F laser that goes through a computerised optical delay (with a time window of up to 8 nsec) and is then focused in a vertical translating CaF₂ crystal

or in sapphire plates of different thicknesses to produce white-light continuum. To avoid photo-degradation, the 2 mm quartz cuvette containing the sample solution is kept in movement using a motorised translating sample holder and/or the solution is stirred. The detector for the UV–VIS and NIR regions is a CCD sensor. The instrumental response function of the system is assumed to be equal to that of the pump–probe cross correlation determined from the measurement of the instantaneous stimulated Raman signal from the pure solvent (in a 2 mm cuvette). Typical values for the IRF of the system are below 250 fsec. Figure 3.32 shows that there is an increase in absorption at 473 nm followed by a slower decrease. This is assigned to the formation of the singlet excited-state of **1** (${}^1\text{I}$), followed by its decay to generate the charge-separated species (${}^1\text{I}^\pm$). Fitting this change in absorption with time gives a lifetime for the decay of ${}^1\text{I}$ (or generation of ${}^1\text{I}^\pm$) of 6.6 psec. This decay was too short to be accurately measured by TCSPC. The discussion of analysis of all the decays at all wavelengths using the Surface Xplorer PRO programme from Ultrafast Systems and the global analysis of the data is postponed to Chapter 4, Reaction Order and Rate Constants. The result is that the spectrum of ${}^1\text{I}^\pm$ can be identified and its transient decay is 14.7 nsec. The value obtained by TCSPC was 13.7 nsec. There is a very good consistency between the two measurements, but the value obtained by TCSPC is more accurate because this relatively long decay is in the upper limit of the time window of the femtosecond transient absorption equipment.

References

- [1] J Liebermann, Jr., *J. Chem. Educ.* **65** (1988) 1067.
- [2] JP Lorimer, TJ Mason, *Educ. Chem* **21** (1984) 151.
- [3] JP Lorimer, TJ Mason, *Educ. Chem* **22** (1985) 19.
- [4] A Allen, AJ Haughey, Y Hernandez, S Ireton, *J. Chem. Educ.* **68** (1991) 609.
- [5] HM Weiss, K Touchette, *J. Chem. Educ.* **67** (1990) 707.
- [6] JP Birk, DL Walters, *J. Chem. Educ.* **69** (1992) 585.
- [7] JP Lorimer, TJ Mason, *Educ. Chem* **23** (1986) 75.
- [8] H Elias, AP Zipp, *J. Chem. Educ.* **65** (1988) 737.
- [9] SL Murov, I Carmichael, GL Hug, *Handbook of Photochemistry*, Marcel Dekker, New York, 1993.
- [10] CG Hatchard, CA Parker, *Proc. Roy. Soc. A* **235** (1956) 518.
- [11] AA Rowe, M Brown, *J. Chem. Educ.* **65** (1988) 548.
- [12] O Moe, R Cornelius, *J. Chem. Educ.* **65** (1988) 137.
- [13] KW Watkins, JA Olson, *J. Chem. Educ.* **57** (1980) 158.
- [14] H Hartridge, FJW Roughton, *Proc. R. Soc. A* **104** (1923) 376.
- [15] RMD Nunes, M Pineiro, LG Arnaut, *J. Am. Chem. Soc.* **131** (2009) 9456.
- [16] DL Jameson, R Anand, *J. Chem. Educ.* **77** (2000) 88.
- [17] ES Yang, M-S Chan, AC Wahl, *J. Phys. Chem.* **84** (1980) 3094.
- [18] RM Nielson, GE McManis, LK Safford, MJ Weaver, *J. Phys. Chem.* **93** (1989) 2152.
- [19] JB Birks, MSSCP Leite, *J. Phys. B* **3** (1970) 417.

- [20] LG Arnaut, RA Caldwell, JE Elbert, LA Melton, *Rev. Sci. Instrum.* **63** (1992) 5381.
- [21] FA Schaberle, MJ Francisco de Assis, LA Reis, LG Arnaut, *Photochem. Photobiol. Sci.* **15** (2016) 204.
- [22] FA Schaberle, RMD Nunes, M Barroso, C Serpa, LG Arnaut, *Photochem. Photobiol. Sci.* **9** (2010) 812.
- [23] G Striker, V Subramaniam, CAM Seidel, A Volkmer, *J. Phys. Chem. B* **103** (1999) 8612.
- [24] KK Mentel, A Serra, PE Abreu, LG Arnaut, *Nature Commun.* **9** (2018) 2903.
- [25] H Chosrowjan, S Taniguchi, F Tanaka, *FEBS J* **282** (2015) 3003.
- [26] AH Zewail, *Angew. Chem. Int. Ed.* **39** (2000) 2587.
- [27] A Zewail (Ed.), *The Chemical Bond*, Academic Press, San Diego, 1992, p. 223.

This page intentionally left blank

Reaction order and rate constants

4

4.1 Rates of elementary reactions

The dependence of the rate of a chemical reaction upon the concentration of reactants must be obtained experimentally. For any time instant, the reaction velocity can be calculated from the tangent to the curve of the variation of concentration of reactants or products as a function of time. Since the rate law may change during the course of a reaction, in principle, this should be determined experimentally at various times of reaction, either to confirm that it is constant or to identify any changes. However, although this is possible, such a procedure is very time consuming and is not normally used, except for the initial phase of the reaction. The determination of rates of reactions using this method of tangents is known as the differential method of determination of rate laws.

Alternatively, descriptions of the time evolution of concentration can be obtained by mathematical integration of the kinetic laws rather than from the study of the variation of concentration with time. From this, it is possible to predict the concentrations of reactants or products from the initial rate at any instant during the reaction. These can be compared with the experimental results. We should note, however, that there are cases in which the kinetic law is very complex, such that its analytical integration is very difficult or even impossible. In these cases, it is still possible to resort to numerical integration.

Although kinetic methods based on differential laws are more exact and more generally applicable, integrated rate laws have the advantage of being more rapid. In addition, in some cases, the integrated rate equations can be used to describe the entire course of a chemical reaction.

4.1.1 First-order reactions

We return to the solvolysis of 2-chloro-2-methylpropane in water discussed in [Chapter 3](#), Experimental Methods (Section 3.1). The rate-determining step of this reaction is the ionisation of the haloalkane, such that the reaction follows first-order kinetics. Thus, we can write

$$-\frac{d[A]}{dt} = k_1[A] \quad (4.1)$$

Separating the variables and integrating, using the initial condition that for $t = 0$, $[A] = [A]_0$, gives

$$-\int_{[A]_0}^{[A]} \frac{d[A]}{[A]} = k_1 \int_0^t dt \quad (4.2)$$

from which

$$-\ln[A] + \ln[A]_0 = k_1 t \quad (4.3)$$

or

$$\log[A] = -\frac{k_1 t}{2.303} + \log[A]_0 \quad (4.4)$$

These equations show that for a first-order reaction, the logarithm of the concentration is directly proportional to time and that the proportionality constant is the rate constant. These equations are often given in the exponential form

$$[A] = [A]_0 \exp(-k_1 t) \quad (4.5)$$

Using the relationship

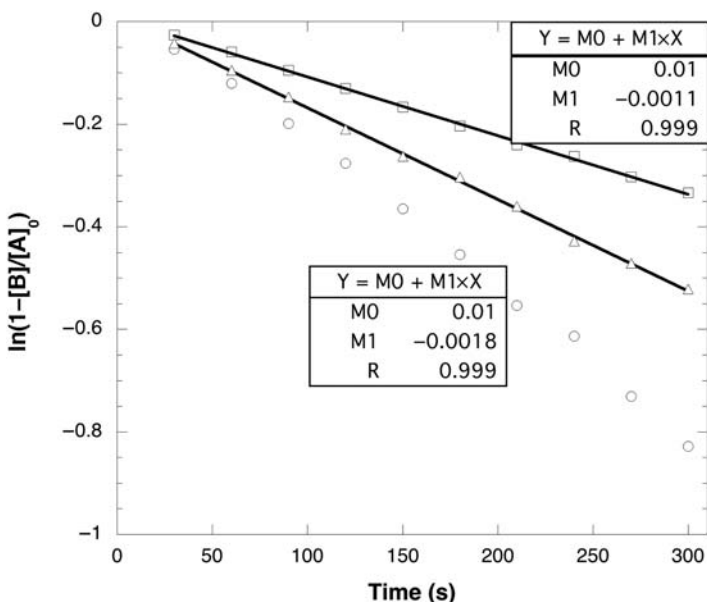
$$[A]_0 = [A] + [B] \quad (4.6)$$

we can describe the variation of product concentration with time

$$[B] = [A]_0 [1 - \exp(-k_1 t)] \quad (4.7)$$

The confirmation of the reaction order is obtained by noting that for a first-order process, the rate is directly proportional to the concentration. This dependence can be shown using the initial velocity for various well-defined concentrations. The initial rate for each concentration is obtained from the tangent at time $t = 0$ of the experimental concentration-time curve. For the solvolysis of 2-chloro-2-methylpropane in water, the initial velocities obtained for different concentrations show a linear dependence on the initial concentration that passes through the origin, with a slope k_1 , confirming that the reaction is first order (see [Figure 3.2](#)).

The analysis of the kinetic data following the differential law of [eq. \(4.1\)](#) requires the initial determination of the tangents to the curve of time dependence versus concentration, which can be somewhat subjective, followed by the graph of initial velocity as a function of the initial concentration. The combination of these steps can lead to errors. Alternatively, the same kinetic data can be analysed more quickly and securely using the integrated rate law of [eq. \(4.4\)](#) for the reactants or the equivalent of [eq. \(4.7\)](#) for the products. The use of the time dependence of the products concentration requires the knowledge of $[A]_0$. The stock solution prepared in Experiment 3.1 has a concentration of 0.0907 M and the experiments with additions of 0.6, 1.2 and 1.8 cm³ have $[A]_0 = 0.72, 1.43$ and 2.14 mM, respectively. [Figure 4.1](#) shows the application of the integrated rate law using $[H^+]$ generated in the solvolysis of 2-chloro-2-methylpropane, [Table 3.1](#). Provided that one is reasonably far from the end of the reaction, the

**FIGURE 4.1**

Dependence of the logarithm of the concentration of product upon time for the solvolysis of 2-chloro-2-methylpropane.

logarithm of $(1 - [B]/[A]_0)$ is a linear function of the reaction time. The slopes of these plots (using natural logarithms) give the rate constant. If logarithms to the base 10 are used, they need to be multiplied by $\ln(10) = 2.303$. For the set of data shown in Figure 4.1, the lowest concentration of 2-chloro-2-methylpropane does not give a linear plot. This is likely to be caused by experimental error in the measurement of small changes in conductivity at these low concentrations. The rate constants given by the other plots, 1.8×10^{-3} and $1.1 \times 10^{-3} \text{ sec}^{-1}$, are in reasonable agreement with the rate constant obtained in Figure 3.2, $k = 1.6 \times 10^{-3} \text{ sec}^{-1}$.

Another parameter commonly used to characterise the rates of a first-order reaction is the half-life, $t_{1/2}$. For any kinetic process, this is defined as the time taken for the concentration of reactant to be reduced to half its initial value. For a first-order process, we can write from eq. (4.5)

$$\frac{[A]_0/2}{[A]_0} = \exp(-k_1 t_{1/2}) \quad (4.8)$$

from which

$$t_{1/2} = \frac{\ln 2}{k_1} = \frac{0.693}{k_1} \quad (4.9)$$

We can see from the above equation that for a first-order process the half-life does not depend upon the initial concentration. This means that the time necessary for the concentration of the reactant to be reduced from $[A]_0/2$ to $[A]_0/4$, is the same as the initial half-life. Similarly, all subsequent half-lives must be the same. This provides an excellent technique for confirming the reaction order, and, as a working definition, it is normally accepted that if the integrated rate plot of the logarithm of change in concentration as a function of time is linear for three half-lives (which corresponds to 87.5% of the reaction, and implies that the first three half-lives are identical), the kinetics can be considered to follow good first-order behaviour. One area where the concept of half-lives is commonly used is in the decay of radioactive nuclei. All such reactions follow first-order kinetics.

4.1.2 Second-order reactions

Returning to the dimerisation of 2,5-dimethyl-3,4-diphenylcyclopentadienone, discussed in [Chapter 3](#), Experimental Methods, the second-order rate law in this case is of the type

$$-\frac{d[A]}{dt} = k_2[A]^2 \quad (4.10)$$

Separating the variables, and integrating with the initial conditions that for $t = 0$, $[A] = [A]_0$, we get

$$-\int_{[A]_0}^{[A]} \frac{d[A]}{[A]^2} = k_2 \int_0^t dt \quad (4.11)$$

from which

$$\frac{1}{[A]} = k_2 t + \frac{1}{[A]_0} \quad (4.12)$$

The experimental data presented in [Chapter 3](#), Experimental Methods, allow us to analyse the kinetics of this reaction using the differential law of [eq. \(4.10\)](#) and to obtain the dependence of the dienone concentration upon time. To confirm the reaction order, we can take the logarithms of [eq. \(4.10\)](#) to give

$$\log\left(-\frac{d[A]}{dt}\right) = \log(k_2) + 2\log([A]) \quad (4.13)$$

This predicts that a plot of logarithm of rate as a function of logarithm of monomer concentration will give a straight line whose slope gives the order of the reaction ([Figure 3.4](#)), while the intercept gives the rate constant. However, since this value is derived from extrapolation over a wide range, which is likely to reduce the precision of the value, it is normally better to obtain the rate constant by plotting rate as a function of $[\text{dienone}]^2$.

An alternative treatment uses the integrated law, eq. (4.12), to study the kinetics of this reaction. The graph of the reciprocal of concentration as a function of time gives a straight line whose slope is k_2 (Figure 4.2). Again, the integrated rate method is quicker and less subjective than the differential form.

The half-life can also be calculated from eq. (4.12), using

$$\frac{2}{[A]_0} = k_2 t_{1/2} + \frac{1}{[A]_0} \quad (4.14)$$

from which

$$t_{1/2} = \frac{1}{k_2 [A]_0} \quad (4.15)$$

The half-life of a reaction of this type depends upon the initial concentration of the reagents.

Another type of second-order reaction involves two different reactants:



from which

$$-\frac{d[A]}{dt} = -\frac{d[B]}{dt} = k_2[A][B] \quad (4.16)$$

Using the condition of mass balance, we obtain

$$\begin{aligned} [A] - [A]_0 &= [B] - [B]_0 \\ [A] - [B] &= [A]_0 - [B]_0 \end{aligned} \quad (4.17)$$

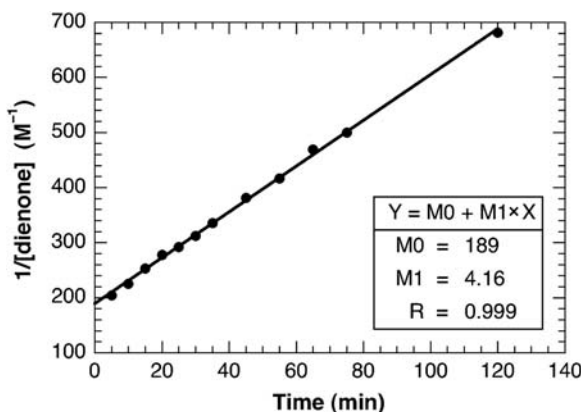


FIGURE 4.2

Relationship between the reciprocal of concentration of dienone and time for the reaction of dimerisation of a dienone.

Using, separately, the first and third members, and the second and third members of eq. (4.16), we obtain the two equations [1]:

$$\begin{aligned}\frac{d[A]}{[A]} &= -k_2[B]dt \\ \frac{d[B]}{[B]} &= -k_2[A]dt\end{aligned}\quad (4.18)$$

and subtraction of these then yields

$$\frac{d[A]}{[A]} - \frac{d[B]}{[B]} = k_2([A] - [B])dt \quad (4.19)$$

Using the mass balance eq. (4.17), we can write

$$\frac{d[A]}{[A]} - \frac{d[B]}{[B]} = k_2([A]_0 - [B]_0)dt \quad (4.20)$$

which can be integrated from time $t = 0$ to time t , to give

$$\ln\left(\frac{[A]}{[A]_0}\right) - \ln\left(\frac{[B]}{[B]_0}\right) = k_2t([A]_0 - [B]_0) \quad (4.21)$$

or, rearranging

$$\frac{1}{[A]_0 - [B]_0} \ln\left\{\frac{[B]_0[A]}{[A]_0[B]}\right\} = k_2t \quad (4.22)$$

A plot of $\log ([B]/[A])$ as a function of the time will have a slope of $([B]_0 - [A]_0)k_2/2.3$. For the case of second-order reactions in which the initial concentration can be expressed in terms of a single variable, $[A] = [B] = [A]_0 - x = [B]_0 - x$. When $x = 0$ for $t = 0$, the integration of eq. (4.16), after substitution for this variable, gives,

$$\frac{x}{[A]_0([A]_0 - x)} = k_2t \quad (4.23)$$

4.1.3 Zero-order reactions

Even though concentration of reactants has been given as one of the factors on which reaction rates depend, there are also cases of reactions that are independent of reactant concentration. In this case, the differential rate law is constant

$$-\frac{d[A]}{dt} = k_0 \quad (4.24)$$

On integrating, we obtain

$$[A] = [A]_0 - k_0 t \quad (4.25)$$

Thus a zero-order reaction gives a linear plot of change in concentration as a function of time, with slope equal to $-k_0$. The units of this rate constant are identical to those of the rate (e.g., liters per second). As with other reaction orders, we can determine the half-life, which is given by

$$\frac{[A]_0}{2} = [A]_0 - k_0 t_{1/2} \quad (4.26)$$

where

$$t_{1/2} = \frac{[A]_0}{2k_0} \quad (4.27)$$

Zero-order reactions appear in heterogeneous systems when the surface of a solid phase is saturated with a reactant, but are also seen in certain homogeneous systems.

4.1.4 Third-order reactions

In the same way that differential and integral rates can be defined for first- and second-order reactions, we can also obtain rate laws for third-order reactions of the general type



The differential rate law for this reaction is

$$-\frac{d[A]}{dt} = k_3[A][B][C] \quad (4.28)$$

The integration of this equation can be made using the method of partial fractions, which leads to

$$\frac{1}{([A]_0 - [B]_0)([B]_0 - [C]_0)([C]_0 - [A]_0)} \ln \left(\left(\frac{[A]}{[A]_0} \right)^{[B]_0 - [C]_0} \left(\frac{[B]}{[B]_0} \right)^{[C]_0 - [A]_0} \left(\frac{[C]}{[C]_0} \right)^{[A]_0 - [B]_0} \right) = k_3 t \quad (4.29)$$

The use of the expressions (4.28) and (4.29) in the determination of the partial orders of these reactions and their rate constants is not very practicable. As we will discuss later in this chapter, an alternative is to use the so-called isolation method.

However, as previously discussed, third-order reactions involving the simultaneous collision of three molecules are very unlikely in comparison with alternative reaction mechanisms involving a series of elementary second-order steps. A good example of a reaction of this type is the oxidation of vitamin C by hexacyanoferrate(III) discussed in [Chapter 3](#), Experimental Methods. Although the stoichiometry of this reaction shows the consumption of three molecules of reactants, the mechanism involves a series of simpler steps in which the reaction order is never greater than two, reactions (3.XI) and (3.XII). This is a typical example of a complex reaction whose mechanism involves a sequence of elementary steps.

The sum of these steps gives the overall stoichiometry of the reaction. The effect of ionic strength on the kinetics suggests a mechanism with a step involving the reaction between two ions of the same charge. This excludes a third order reaction as the rate-determining step in the chemical process.

4.2 Rates of complex reactions

As seen earlier, the majority of kinetic processes involves more than one elementary step. However, the fact that a mechanism is in agreement with the kinetic law does not mean that it is the correct mechanism for the reaction. The same kinetic law can, and frequently does, correspond to more than one possible mechanism. A mechanism is always a theoretical hypothesis of how a reaction occurs. We can never prove a mechanism from the kinetic behaviour, but can only eliminate certain hypotheses. A good illustration is given by the gas-phase reaction at 400 °C



studied by Bodenstein in 1894, which was considered to be an elementary process. However, even at this time he recognised that it was difficult to find chemically simple reactions in the gas phase, that is, reactions whose rates are proportional to the product of the concentrations of reactants raised to integral powers. Reaction (4.III) was presented as an example of an elementary kinetic process in all textbooks until Sullivan in 1967 detected the presence of free radicals in the system at 350 °C, and proposed an alternative mechanism



where M is an inert gas. In summary, mechanisms of the reactions are proposed on the basis of the observed kinetic behaviour but very detailed physical chemical studies are necessary before any mechanism can be considered as accepted. It is necessary to confirm the feasibility of all the steps proposed in addition to demonstrating the possible existence of the different intermediates. Because of various experimental difficulties, these tasks are difficult to carry out for the majority of the chemical reactions. In addition to kinetic studies, involving, for example, predictions of the effects of various factors on rates and product distributions, these studies must be complemented by other chemical and physical studies, in particular attempts to try to trap and characterise the intermediates.

Complex reaction mechanisms can conveniently be grouped within the following classification: parallel reactions, consecutive reactions and reversible reactions. Parallel reactions are those in which the same species participates in two or more competitive steps. Consecutive reactions are characterised by the product of the first reaction being a reactant in a subsequent process, leading to formation of the final

product. Reversible reactions are those in which the products of the initial reaction can recombine to regenerate the reactant.

As complex reactions follow a reaction mechanism involving various elementary steps, the determination of the corresponding kinetic law involves the solution of a system of differential equations, and the complete analytical solution of these systems is only possible for the simplest cases. In slightly more complicated cases it may still be possible to resolve the system of corresponding differential equations using methods such as Laplace transforms or matrix methods. However, there are systems which cannot be resolved analytically, or whose analytical solution is so complex that it is not easily applied. In the absence of information on the orders of magnitude of the rate constants involved, the treatment of these kinetic systems is made using numerical methods. These methods allow us to obtain concentrations of the reactants for discrete time intervals, which can then be represented graphically and compared with experimental data to provide an insight into the changes occurring. Further, although the results obtained numerically are inherently approximations, we can estimate and allow for the errors involved, which can be expressed as error limits when compared with experimental data. In some cases, it may also be possible to introduce some changes of a chemical nature in the system to help simplify and analyse these complex systems. For example, if we know the relative magnitudes of some of the rate constants, it may be possible to simplify the system of complex differential equations involved by modifying the initial concentrations of reactants and obtaining a rate equation that can be solved analytically. Finally, when these procedures cannot be used to resolve complex systems of differential equations, it is still possible to use stochastic treatments such as Markov chains or the Monte Carlo method.

Today, using modern equipment with enhanced time resolution and advanced spectroscopy methods, it is possible to generate large arrays of data with time-resolved spectroscopic information. Such data can be analysed in terms of the changes in one observable as a function of time (e.g., time-dependent absorption or emission at one specific wavelength), or all changes can be analysed together using global analysis. [Figures 3.29 and 3.32](#) show examples of data on time-resolved spectra constructed from the measured fluorescence or transient absorption, respectively. Global analysis of such spectra can be very informative and will be discussed separately.

4.2.1 Parallel first-order reactions

The simplest parallel reactions involve two competitive first-order steps:



The rate of disappearance of A is given by the differential equation

$$\frac{d[A]}{dt} = -k_1[A] - k_2[A] = -k_T[A] \quad (4.30)$$

where $k_T = k_1 + k_2$. Integrating this equation gives

$$[A] = [A]_0 e^{-k_T t} = [A]_0 e^{-(k_1 + k_2)t} \quad (4.31)$$

To determine the rate of formation of B, we have

$$\frac{d[B]}{dt} = k_1[A] \quad (4.32)$$

and, substituting for [A] using expression (4.31), followed by integration with the condition that for $t = 0$, $[B] = 0$, we obtain

$$[B] = \frac{k_1[A]}{k_T} (1 - e^{-k_T t}) \quad (4.33)$$

We can obtain the variation of [C] with time in the same way:

$$[C] = \frac{k_2[A]}{k_T} (1 - e^{-k_T t}) \quad (4.34)$$

From the above two expressions we see immediately that the ratio of the rate constants of parallel first-order reactions is equal to the ratio of yields of the products.

$$\frac{[B]}{[C]} = \frac{k_1}{k_2} \quad (4.35)$$

This quotient is called the branching ratio of the reaction.

Figure 4.3 shows the time evolution of [A], [B] and [C] for the cases in which $k_1 = k_2$ and $k_1 = 2k_2$.

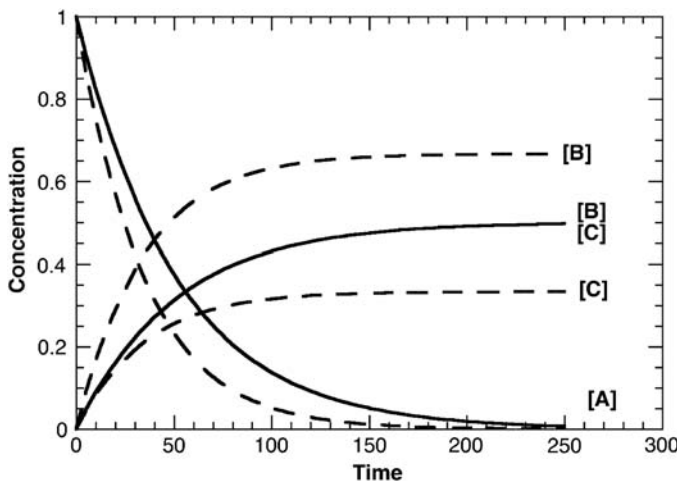
This solution can easily be extended to parallel reactions involving more than two processes. If there are n parallel reactions, then $k_T = k_1 + k_2 + \dots + k_n$, and the expression for the disappearance of A has the same form as eq. (4.30).

Parallel reactions give kinetic control over the products of the competitive reactions. More will be formed of the product that is formed faster. Optimising the yield of a desired product B with respect to by-products C formed in parallel reactions consists essentially in finding the reaction conditions that increase the ratio k_1/k_2 .

4.2.2 Consecutive first-order reactions

Another very common kinetic scheme involves a series of first-order reactions, leading first to the formation of an intermediate B, which subsequently reacts to give the final product



**FIGURE 4.3**

Variation of the concentrations of reactant and final products for parallel first-order reactions. The full lines correspond to the situation in which $k_1 = k_2$ and the dashed lines correspond to the case in which $k_1 = 2k_2$.

The differential equations describing this sequence of elementary steps are

$$\begin{aligned} \frac{d[A]}{dt} &= -k_1[A] \\ \frac{d[B]}{dt} &= k_1[A] - k_2[B] \\ \frac{d[C]}{dt} &= k_2[B] \end{aligned} \quad (4.36)$$

As we have seen, the integrated rate equation for the disappearance of A is given by

$$[A] = [A]_0 e^{-k_1 t} \quad (4.37)$$

and can be substituted for [A] in the equation describing the variation of [B] with time. After rearranging, this can be written as

$$\frac{d[B]}{dt} + k_2[B] = k_1[A]_0 e^{-k_1 t} \quad (4.38)$$

Multiplying both terms by $\exp(k_2 t)$, we obtain [2]

$$e^{k_2 t} \frac{d[B]}{dt} + k_2[B] e^{k_2 t} = k_1[A]_0 e^{(k_2 - k_1)t} \quad (4.39)$$

and as

$$e^{k_2 t} \frac{d[B]}{dt} + k_2 [B] e^{k_2 t} = \frac{d([B] e^{k_2 t})}{dt} \quad (4.40)$$

the equation can be written as the differential equation

$$d([B] e^{k_2 t}) = k_1 [A]_0 e^{(k_2 - k_1)t} dt \quad (4.41)$$

which, upon integration, leads to

$$[B] e^{k_2 t} = \frac{k_1 [A]_0 e^{(k_2 - k_1)t}}{k_2 - k_1} + I \quad (4.42)$$

where the integration constant I is obtained for the simplest case of $[B] = 0$ at $t = 0$, as

$$I = -\frac{k_1 [A]_0}{(k_2 - k_1)} \quad (4.43)$$

Substituting this value for I in eq. (4.42) and dividing by $\exp(k_2 t)$, we obtain the integrated equation for the dependence of $[B]$ upon time:

$$[B] = k_1 [A]_0 \frac{(e^{-k_1 t} - e^{k_2 t})}{k_2 - k_1} \quad (4.44)$$

which is true for the case in which $k_1 \neq k_2$. When $k_1 = k_2$, we obtain

$$d([B] e^{k_2 t}) = k_1 [A]_0 dt \quad (4.45)$$

whose solution is

$$[B] = k_1 [A]_0 e^{-k_1 t} \quad (4.46)$$

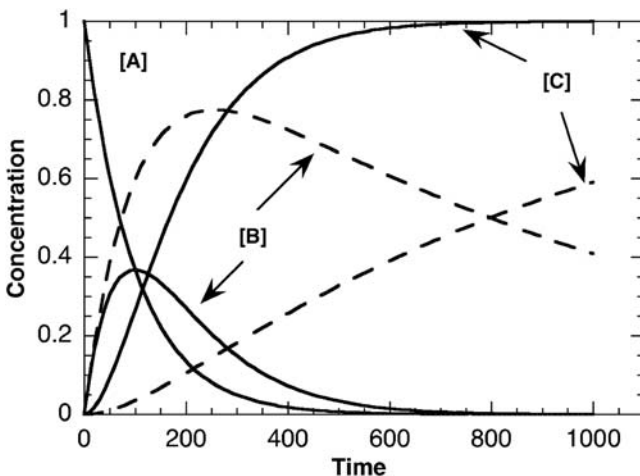
when $[B] = 0$ at $t = 0$. Figure 4.4 shows the time evolution of the concentrations of reactant, intermediate and final product for the cases in which $k_1 = k_2$ and $k_1 = 10k_2$. This figure also shows that reactive intermediates may be present at very low concentrations in the reaction mixture and may be difficult to detected, which makes the establishment of reaction mechanism very challenging.

It is tempting to assume that k_1 is responsible for the rise time of $[B]$ and k_2 for its decay. However, the symmetry of the fraction in eq. (4.44) makes the time profile exactly identical when we make $k_1 = 10k_2$ or $k_2 = 10k_1$ in Figure 4.4. Only the magnitude of $[B]$ changes because $[B]$ is directly proportional to k_1 . It is not possible to assign k_1 and k_2 just from fitting the time dependence of a property proportional to the concentration of the intermediate.

4.2.3 Reversible first-order reactions

The simplest reversible reactions are of the type



**FIGURE 4.4**

Variation of the concentrations of reactant, intermediate and final product with time for consecutive first-order reactions. The solid line shows the case in which $k_1 = k_2$, while the dashed line is for the condition $k_1 = 10k_2$.

The corresponding differential equations for this mechanism are

$$\begin{aligned}\frac{d[A]}{dt} &= -k_f[A] + k_r[B] \\ \frac{d[B]}{dt} &= k_f[A] - k_r[B]\end{aligned}\quad (4.47)$$

Assuming that at time $t = 0$ the initial concentrations of the two species are $[A]_0$ and $[B]_0$, we can write the law of conservation of mass for this system:

$$[A]_0 + [B]_0 = [A] + [B] \quad (4.48)$$

and solving in terms of $[B]$ we obtain

$$[B] = [A]_0 + [B]_0 - [A] \quad (4.49)$$

Substituting $[B]$ in the differential expression and rearranging, we can write

$$\frac{d[A]}{dt} = (k_f + k_r) \left\{ \frac{k_r([A]_0 + [B]_0)}{(k_f + k_r)} - [A] \right\} \quad (4.50)$$

where

$$\frac{k_r([A]_0 + [B]_0)}{(k_f + k_r)} = m \quad (4.51)$$

is a constant. Thus in the integration

$$\int_{[A]_0}^{[A]} \frac{d[A]}{m - [A]} = (k_f + k_r) \int_0^t dt \quad (4.52)$$

we can identify the standard integral

$$\int \frac{dx}{a + bx} = \frac{1}{b} \ln(a + bx) \quad (4.53)$$

where $b = -1$. This integration leads to

$$\ln\left(\frac{k_f[A] - k_r[B]}{k_f[A]_0 - k_r[B]_0}\right) = -(k_f + k_r)t \quad (4.54)$$

when [eqs. \(4.49\)](#) and [\(4.51\)](#) are employed.

Equilibrium is eventually reached in reversible reactions, and when this occurs the forward and reverse reactions have the same rates. This corresponds to a formulation of the principle of microscopic reversibility. Thus, at equilibrium, the concentrations of reactant and product do not change with time

$$\frac{d[A]_e}{dt} = \frac{d[B]_e}{dt} = 0 \quad (4.55)$$

that is

$$k_f[A]_e - k_r[B]_e = 0 \quad (4.56)$$

where the subscript refers explicitly to the equilibrium condition. From this, the equilibrium constant is given by

$$\frac{k_f}{k_r} = \frac{[B]_e}{[A]_e} = K_{eq} \quad (4.57)$$

[Figure 4.5](#) shows the evolution of $[A]$ and $[B]$ for the cases in which $k_f = k_r$ and $k_f = 3k_r$.

Reversible reactions are of fundamental importance in relaxation methods. A very useful form of the rate equation for such processes is obtained using the conservation of mass to re-write [eq. \(4.50\)](#) as

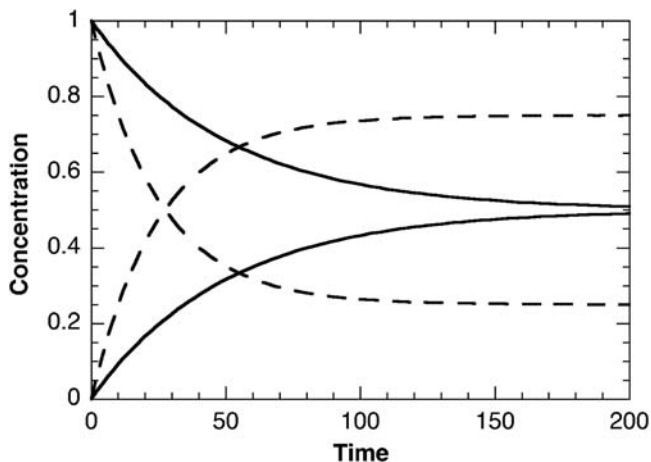
$$\frac{d[A]}{dt} = k_r([A]_0 + [B]_0) - (k_f + k_r)[A] \quad (4.58)$$

which at equilibrium leads to

$$(k_f + k_r)[A]_{eq} = k_r([A]_0 + [B]_0) \quad (4.59)$$

Replacing this equation above gives

$$\frac{d[A]}{dt} = - (k_f + k_r)([A] - [A]_{eq}) \quad (4.60)$$

**FIGURE 4.5**

Evolution of the concentrations of the species A and B for a reversible first-order system until equilibrium is reached. The full line indicates the situation in which $k_f = k_r$ and the dashed line shows the evolution of the system in which $k_f = 3k_r$.

The integration of

$$\int_{[A]_0}^{[A]} \frac{d[A]}{[A]_{eq} - [A]} = -(k_f + k_r) \int_0^t dt \quad (4.61)$$

using the integral of eq. (4.53), yields

$$\ln \frac{[A]_{eq} - [A]}{[A]_{eq} - [A]_0} = -(k_f + k_r)t \quad (4.62)$$

which emphasises the nature of the exponential decay to equilibrium of the change in $[A]$

$$[A]_{eq} - [A] = ([A]_{eq} - [A]_0) \exp[-(k_f + k_r)t] \quad (4.63)$$

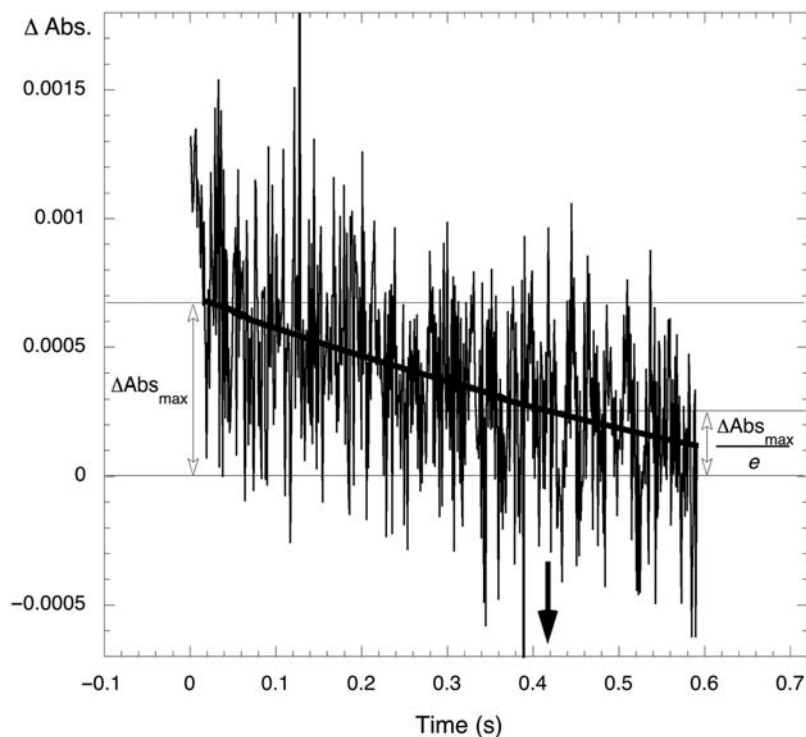
It is useful to define the relaxation time

$$\tau = \frac{1}{k_f + k_r} \quad (4.64)$$

to characterise the decay of $[A]$ to equilibrium, and realise that at $t = \tau$

$$[A] - [A]_{eq} = \frac{[A]_0 - [A]_{eq}}{e} \quad (4.65)$$

The perturbation from equilibrium, $[A]_0 - [A]_{eq}$, is experimentally accessible and can be used to obtain the relaxation time which, together with eq. (4.57), leads to the rate constants k_f and k_r . Figure 4.6 illustrates the relaxation to

**FIGURE 4.6**

Decay at 360 nm observed in the flash photolysis of $[\text{NO}_2\text{H}] = 4.3 \times 10^{-4} \text{ M}$ in 2% MeOH: H_2O , assigned to the re-protonation of the carbanion, and evaluation of the relaxation time.

nitroalkane of the carbanion generated by intramolecular proton transfer after excited-state proton transfer of naphthol to water shown in [Figure 3.15](#) [3]. The carbanion absorbs at 360 nm and the change in absorption at this wavelength reflects the kinetics of its protonation in aqueous solution (with 2% methanol) at pH 5. The decay observed by flash photolysis is very noisy because at long detection times the xenon lamp cannot be pulsed and delivers a much lower light intensity. Nevertheless, it is possible to draw an exponential decay (thick line) which allows for the estimate of $\tau \approx 0.43 \text{ sec}$. The protonation of the carbanion is a second-order reaction, $\text{C}^- + \text{H}_3\text{O}^+ \rightarrow \text{CH} + \text{H}_2\text{O}$, and the relation of its relaxation time with the rates of forward and reverse reactions is more complicated than [eq. \(4.64\)](#). Nevertheless, the principles discussed above apply similarly to this system and allows for the determination of k_f and k_r using the acidity constant of the nitroalkane, $K_a \approx 10^{-9}$.

The same ideas can be applied to reversible reactions that occur in various steps. The principle of microscopic reversibility can help resolve more complicated systems of kinetic equations when the system is in equilibrium.

4.3 Methods for solving kinetic equations

4.3.1 Laplace transforms

Classical methods of integration are used to solve many of the linear differential equations that describe the kinetic behaviour of chemical reactions. However, the methods of solving these equations can often be very complicated. In contrast, in many cases it is possible to use methods of operational calculus directly to obtain solutions that satisfy a set of given initial conditions without resorting to the manipulation of particular integrals separately, or introduction of arbitrary constants. Consequently, operational calculus can be applied profitably to these systems, since it appreciably simplifies and speeds up solution of the appropriate kinetic equations. The principle of integral calculus is based on the introduction of a definite integral, called the transformation integral that is given by the general formula

$$F(s) = \int_a^b f(t)\mathbf{K}(s,t)dt \quad (4.66)$$

where $F(s)$ is the transformation of $f(t)$ relative to the *kernel* $\mathbf{K}(s,t)$.

A kernel frequently used in chemical kinetics is $\mathbf{K}(s,t) = e^{-st}$. This kernel, integrated between the limits 0 and ∞ , corresponds to the Laplace transform. The great value of this transform stems from the fact that the exponential dependence as a function of time is similar to that encountered in the integrals needed in chemical kinetics, while in the applications of the Laplace transform, with integration between the limits $t = 0$ and $t = \infty$, the transformed function only depends on s . Thus the transform $F(s)$ of the function $f(t)$ using the Laplace treatment is defined by the integral

$$F(s) = L[f(t)] = \int_a^b f(t)e^{-st}dt \quad (4.67)$$

For the function $f(t) = a$, where a is a constant, its Laplace transform is $F(s) = a/s$. If $L[f(t)] = F(s)$ is the Laplace transform of the function $f(t)$, then we say that $f(t) = L^{-1}[F(s)]$ is the inverse of the Laplace transform of $F(s)$.

For example, for the function $f(t) = \exp(-at)$ in which a is constant, its Laplace transform is obtained using

$$\begin{aligned} F(s) &= L[f(t)] = L[e^{-at}] = \int_a^\infty e^{-at}e^{-st}dt \\ &= \int_0^\infty e^{-(a+s)t}dt = -\frac{1}{a+s} [e^{-(a+s)t}]_0^\infty \\ &= \frac{1}{s+a} \end{aligned} \quad (4.68)$$

which is restricted to the condition that $s > -a$, for which $e^{-(a+s)t}$ will be equal to zero and the integral $L[e^{-at}]$ converges.

The application of Laplace transforms to the analytical solution of complicated differential kinetic laws is simplified significantly on the basis of three of its fundamental properties:

1. The Laplace transform of a linear combination of functions is the same linear combination of the transformed functions. Thus if

$$f(t) = f_1(t) + f_2(t) + \cdots + f_n(t) \quad (4.69)$$

then its Laplace transform is

$$L[f(t)] = F_1(s) + F_2(s) + \cdots + F_n(s) \quad (4.70)$$

2. The Laplace transform of the derivative of $f(t)$, that is, $f'(t)$, can be easily obtained

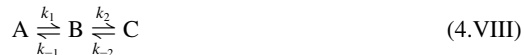
$$\begin{aligned} L[f(t)] &= \int_0^\infty f'(t)e^{-st}dt \\ &= f(t)e^{-st}\Big|_0^\infty + s \int_0^\infty f(t)e^{-st}dt \\ &= sL[f(t)] - f(0) \end{aligned} \quad (4.71)$$

3. The Laplace transform of an integral of a function $f(t)$ can be expressed as

$$L\left[\int_0^\infty f(t)dt\right] = \frac{L[f(t)]}{s} \quad (4.72)$$

Using these three properties and **Table 4.1** containing both the Laplace transforms and inverse transforms, it is possible to solve many differential kinetic equations analytically.

As an example of application of Laplace transforms to complex reaction schemes, consider the consecutive first-order reversible reactions



whose corresponding rate equations are

$$\begin{aligned} \frac{d[A]}{dt} &= -k_1[A] + k_{-1}[B] \\ \frac{d[B]}{dt} &= k_1[A] - (k_{-1} + k_2)[B] + k_{-2}[C] \\ \frac{d[C]}{dt} &= k_2[B] - k_{-2}[C] \end{aligned} \quad (4.73)$$

with the initial conditions $[A] = [A]_0$ and $[B] = [C] = 0$ at $t = 0$. Applying Laplace transforms [eq. (4.71)], and using the mass balance $[A]_0 = [A] + [B] + [C]$ to eliminate $[C]$ in the expression of the variation of $[B]$ with time, we obtain

$$\begin{aligned} \frac{d[A]}{dt} &= -k_1[A] + k_{-1}[B] \\ \frac{d[B]}{dt} &= (k_1 - k_2)[A] - (k_{-1} + k_2 + k_{-2})[B] + k_{-2}[A]_0 \end{aligned} \quad (4.74)$$

and

$$\begin{aligned} sL[A] - [A]_0 &= -k_1L[A] + k_{-1}L[B] \\ sL[B] &= (k_1 - k_{-2})L[A] - (k_{-1} + k_2 + k_{-2})L[B] + \frac{k_{-2}[A]_0}{s} \end{aligned} \quad (4.75)$$

Table 4.1 Table of Laplace transforms.

No.	$F(s)$	$f(t)$
1	$\frac{1}{s}$	1
2	$\frac{a}{s}$	a
3	$\frac{1}{s^2}$	t
4	$\frac{1}{s^n} \quad (n = 1, 2, \dots)$	$\frac{t^{n+1}}{(n-1)!}$
5	$\frac{1}{\sqrt{s}}$	$\frac{1}{\sqrt{\pi t}}$
6	$s^{-3/2}$	$2\sqrt{\frac{t}{\pi}}$
7	$\frac{1}{s-a}$	e^{at}
8	$\frac{1}{(s-a)^2}$	te^{at}
9	$\frac{1}{(s-a)^n} \quad (n = 1, 2, \dots)$	$\frac{1}{(n-1)!} t^{n-1} e^{at}$
10	$\frac{1}{(s-a)(s-b)}$	$\frac{1}{(a-b)} (e^{at} - e^{bt})$
11	$\frac{1}{(s-a)(s-b)(s-c)}$	$-\frac{(b-c)e^{at} + (c-a)e^{bt} + (a-b)e^{ct}}{(a-b)(b-c)(c-a)}$
12	$\frac{s}{(s-a)(s-b)}$	$\frac{1}{(a-b)} (ae^{at} - be^{bt})$
13	$\frac{1}{s+a}$	e^{-at} valid for complex a
14	$\frac{1}{(s+a)^2}$	te^{-at}
15	$\frac{1}{(s+a)^n} \quad (n = 1, 2, \dots)$	$\frac{1}{(n-1)!} t^{n-1} e^{-at}$
16	$\frac{1}{s(s+a)}$	$\frac{1}{a} (1 - e^{-at})$
17	$\frac{1}{s^2(s+a)}$	$\frac{1}{a^2} (e^{-at} + at - 1)$
18	$\frac{1}{(s+a)(s+b)}$	$\frac{1}{(b-a)} (e^{-at} - e^{-bt})$
19	$\frac{1}{s(s+a)(s+b)}$	$\frac{1}{ab} \left[1 + \frac{1}{(a-b)} (be^{-at} - ae^{-bt}) \right]$
20	$\frac{1}{(s+a)(s+b)(s+c)}$	$\frac{1}{(b-a)(c-a)} e^{-at} + \frac{1}{(a-b)(c-b)} e^{-bt} + \frac{1}{(a-c)(b-c)} e^{-ct}$
21	$\frac{s}{(s+a)^2}$	$(1-at)ae^{-at}$
22	$\frac{s}{(s+a)(s+b)}$	$\frac{1}{(a-b)} (ae^{-at} - be^{-bt})$
23	$\frac{s}{(s+a)(s+b)(s+c)}$	$-\frac{a}{(b-a)(c-a)} e^{-at} - \frac{b}{(a-b)(c-b)} e^{-bt} + \frac{1}{(a-c)(b-c)} e^{-ct}$
24	$\frac{1}{s^2 + \omega^2}$	$\frac{1}{a} \sin(\omega t)$
25	$\frac{s}{s^2 + \omega^2}$	$\cos(\omega t)$
26	$\frac{1}{s^2 - a^2}$	$\frac{1}{a} \sinh(at)$
27	$\frac{s}{s^2 - a^2}$	$\cosh(at)$
28	$\frac{1}{s(s^2 + a^2)}$	$\frac{1}{a^2} [1 - \cos(at)]$
29	$\frac{s+a}{s(s+b)}$	$\frac{a}{b} - \frac{(a-b)}{b} e^{-bt}$
30	$\frac{s+a}{(s+b)(s+c)}$	$\frac{1}{(c-b)} [(a-b)e^{-bt} - (a-c)e^{-ct}]$
31	$\frac{s+a}{s(s+b)(s+c)}$	$\frac{a}{bc} + \frac{a-b}{b(b-c)} e^{-bt} + \frac{a-c}{c(c-b)} e^{-ct}$
32	$\frac{s}{(s-a)^{3/2}}$	$\frac{1}{\sqrt{\pi t}} e^{at} (1 + 2at)$
33	$\sqrt{s-a} - \sqrt{s-b}$	$\frac{1}{2\sqrt{\pi t^3}} (e^{bt} - e^{at})$
34	$\ln \frac{s-a}{s-b}$	$\frac{1}{t} (e^{bt} - e^{at})$

Solving the first eq. (4.75) in the order of $L[A]$ and introducing the resulting expression into the second equation, we obtain

$$\begin{aligned} L[B] &= \frac{k_1[A]_0(s + k_{-2})}{s[s^2 + (k_1 + k_{-1} + k_2 + k_{-2})s + (k_1k_2 + k_1k_{-2} + k_{-1}k_{-2})]} \\ &= \frac{k_1[A]_0(s + k_{-2})}{s(s + a)(s + b)} \end{aligned} \quad (4.76)$$

where

$$a + b = k_1 + k_{-1} + k_2 + k_{-2} \quad (4.77)$$

and

$$ab = k_1k_2 + k_1k_{-2} + k_{-1}k_{-2} \quad (4.78)$$

We can apply the inverse Laplace transform to the previous equation to obtain the time dependence of the concentration for B. Using entry no. 31 of Table 4.1, we obtain

$$[B] = k_1[A]_0 \left[\frac{k_{-2}}{ab} + \frac{k_{-2} - a}{a(a - b)} e^{-at} - \frac{k_{-2} - b}{b(a - b)} e^{-bt} \right] \quad (4.79)$$

To obtain $L[A]$, we start by solving the second eq. (4.75) in the order of $L[B]$, substitute the value obtained in the first equation and solve for $L[A]$

$$L[A] = [A]_0 \left[\frac{k_{-1}k_{-2} + s(s + c)}{s(s + a)(s + b)} \right] \quad (4.80)$$

where

$$c = k_{-1} + k_2 + k_{-2} \quad (4.81)$$

Applying the inverse transform with the same entry of Table 4.1, we get

$$\begin{aligned} [A] &= [A]_0 \left[\frac{k_{-1}k_{-2}}{ab} + \frac{k_{-1}k_{-2} - a(c - a)}{a(a - b)} e^{-at} - \frac{k_{-1}k_{-2} - b(c - a)}{b(a - b)} e^{-bt} \right] \\ &= [A]_0 \left[\frac{k_{-1}k_{-2}}{ab} + \frac{k_{-1}(a - k_2 - k_{-2})}{a(a - b)} e^{-at} - \frac{k_{-1}(b - k_2 - k_{-2})}{b(a - b)} e^{-bt} \right] \end{aligned} \quad (4.82)$$

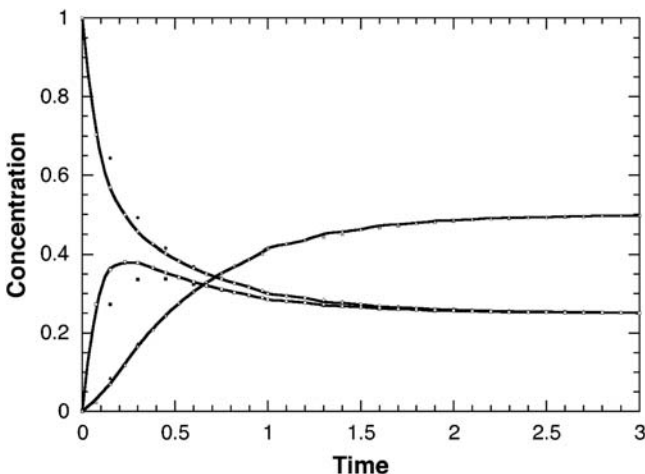
The time dependence of the concentration of C can be obtained by introducing eqs. (4.79) and (4.82) into the mass balance expression

$$[C] = k_1k_2[A]_0 \left[\frac{1}{ab} + \frac{1}{a(a - b)} e^{-at} - \frac{1}{b(a - b)} e^{-bt} \right] \quad (4.83)$$

Figure 4.7 presents the concentrations of A, B and C calculated by eqs. (4.79), (4.82) and (4.83), respectively, for the case in which $k_1 = k_{-1} = 3k_2 = 6k_{-2}$.

Another kinetic scheme conveniently solved with Laplace transforms is that of the monomer-excimer excited-state equilibrium



**FIGURE 4.7**

Calculation of the concentrations of the species involved in mechanism (4.VIII) by the method of Laplace transform (lines) and by the fourth-order Runge-Kutta method (points). Two different integration steps were used in the Runge-Kutta method, with the steps of the solid points being twice that of the others. The example presented uses $k_1 = k_{-1} = 3k_2 = 6k_{-2}$.

The rate equation for the formation of the excimer AA^* from the excited monomer A^* and ground-state monomer A is not linear with respect to the reactants and the Laplace method should not be applicable. However, experimentally $[\text{A}] \gg [\text{A}^*]$ and can be considered constant and included in the forward rate constant, that is, $k'_1 = k_1[\text{A}]$. This approximation will be discussed in detail in Section 4.4. Under this approximation, the rate equations are

$$\begin{aligned}\frac{d[\text{A}^*]}{dt} &= -(k'_1 + k_m)[\text{A}^*] + k_{-1}[\text{AA}^*] = -k_x[\text{A}^*] + k_{-1}[\text{AA}^*] \\ \frac{d[\text{AA}^*]}{dt} &= k'_1[\text{A}^*] - (k_{-1} + k_e)[\text{AA}^*] = k'_1[\text{A}^*] - k_y[\text{AA}^*]\end{aligned}\quad (4.84)$$

where we made $k_x = (k'_1 + k_m)$ and $k_y = (k_{-1} + k_e)$ to simplify the notation, and the Laplace transforms are

$$\begin{aligned}sL[\text{A}^*] - [\text{A}^*]_0 &= -k_x L[\text{A}^*] + k_{-1} L[\text{AA}^*] \\ sL[\text{AA}^*] - [\text{AA}^*]_0 &= k'_1 L[\text{A}^*] - k_y L[\text{AA}^*]\end{aligned}\quad (4.85)$$

Taking $[\text{AA}^*]_0 = 0$ at time $t = 0$, solving the first equation in order of $L[\text{A}^*]$ and replacing in the second one, gives

$$\begin{aligned}L[\text{A}^*] &= \frac{[\text{A}^*]_0 + k_{-1} L[\text{AA}^*]}{s + k_x} \\ (s + k_y)L[\text{AA}^*] &= \frac{k'_1[\text{A}^*]_0 + k'_1 k_{-1} L[\text{AA}^*]}{s + k_x}\end{aligned}\quad (4.86)$$

Rearranging

$$L[AA^*] = k'_1[A^*]_0 \frac{1}{(s + k_y)(s + k_x) - k'_1 k_{-1}} \quad (4.87)$$

In order to make the fraction in the equation above identical to entry no. 18 of **Table 4.1**, we make the following change in variables

$$\begin{aligned} \frac{1}{(s + k_y)(s + k_x) - k'_1 k_{-1}} &= \frac{1}{s^2 + (k_x + k_y)s + k_x k_y - k'_1 k_{-1}} = \frac{1}{s^2 + (\lambda_1 + \lambda_2)s + \lambda_1 \lambda_2} \\ &= \frac{1}{(s + \lambda_1)(s + \lambda_2)} \end{aligned} \quad (4.88)$$

Hence

$$\begin{aligned} \lambda_1 \lambda_2 &= k_x k_y - k'_1 k_{-1} \\ \lambda_1 + \lambda_2 &= k_x + k_y \end{aligned} \quad (4.89)$$

Using entry no. 18 of **Table 4.1**, we obtain

$$[AA^*] = \frac{k'_1 [A^*]_0}{\lambda_2 - \lambda_1} (e^{-\lambda_1 t} - e^{-\lambda_2 t}) \quad (4.90)$$

A similar approach to find the time dependence of $[A^*]$ gives, from [eq. \(4.85\)](#),

$$\begin{aligned} (s + k_x)L[A^*] &= [A^*]_0 + \frac{k_{-1} k'_1 L[A^*]}{(s + k_y)} \\ L[AA^*] &= \frac{k'_1 L[A^*]}{(s + k_y)} \end{aligned} \quad (4.91)$$

Rearranging the equation of interest

$$L[A^*] = [A^*]_0 \frac{s + k_y}{(s + k_x)(s + k_y) - k_{-1} k'_1} \quad (4.92)$$

and making evident that the fraction is equivalent to entry no. 30 of **Table 4.1**,

$$\frac{s + k_y}{s^2 + (k_x + k_y)s + k_x k_y - k'_1 k_{-1}} = \frac{s + a}{s^2 + (\lambda_1 + \lambda_2)s + \lambda_1 \lambda_2} = \frac{s + a}{(s + \lambda_1)(s + \lambda_2)} \quad (4.93)$$

the inverse transform gives

$$[A^*] = \frac{[A^*]_0}{\lambda_2 - \lambda_1} [(k_y - \lambda_1)e^{-\lambda_1 t} - (k_y - \lambda_2)e^{-\lambda_2 t}] \quad (4.94)$$

Using [eq. \(4.89\)](#)

$$[A^*] = \frac{[A^*]_0}{\lambda_2 - \lambda_1} [(\lambda_1 + \lambda_2 - k_x - \lambda_1)e^{-\lambda_1 t} - (\lambda_1 + \lambda_2 - k_x - \lambda_2)e^{-\lambda_2 t}] \quad (4.95)$$

We obtain the Birks solution [\[4\]](#) for the monomer-excimer mechanism

$$[A^*] = \frac{[A^*]_0}{\lambda_2 - \lambda_1} [(\lambda_2 - k_x)e^{-\lambda_1 t} + (k_x - \lambda_1)e^{-\lambda_2 t}] \quad (4.96)$$

Eqs. (4.90) and (4.96) predict bi-exponential decays for the exciplex and momomer, respectively, where the parameters λ_1 and λ_2 are related to the microscopic rate constants by eq. (4.89)

$$\begin{aligned}\lambda_1 &= \frac{1}{2} \left[(k_x + k_y) - \sqrt{(k_x - k_y)^2 + 4k'_1 k_{-1}} \right] \\ \lambda_2 &= \frac{1}{2} \left[(k_x + k_y) + \sqrt{(k_x - k_y)^2 + 4k'_1 k_{-1}} \right]\end{aligned}\quad (4.97)$$

From the amplitudes and time constants of the bi-exponential decays, together with the lifetime of the monomer determined by its mono-exponential decay at a sufficiently low concentrations to avoid the perturbation caused by the excimer formation, it is possible to employ Birks solution to determine all the microscopic rate constants of this system.

For rate equations that are linear with respect to the reactants, the Laplace transform method is a powerful method to solve the kinetic equations. In the case of non-linear rate laws, these can be made linear by using excess concentrations of certain reactants, leading to pseudo-first-order equations, which can be solved. Pseudo-first-order equations are discussed later in this chapter.

4.3.2 Matrix method

Systems involving first-order reversible reactions lead to groups of simultaneous linear differential equations with constant coefficients. These can be solved by using matrix methods, the same mathematical technique frequently encountered in quantum mechanics and vibrational spectroscopy.

For the general case, the concentration of the species A_i involved in a system of first-order kinetic equations involving n species is $[A_i]$. The set of these equations [5] is

$$\begin{aligned}-\frac{d[A_1]}{dt} &= k_{11}[A_1] + k_{12}[A_2] + \dots + k_{1n}[A_n] \\ -\frac{d[A_2]}{dt} &= k_{21}[A_1] + k_{22}[A_2] + \dots + k_{2n}[A_n] \\ &\vdots \\ -\frac{d[A_n]}{dt} &= k_{n1}[A_1] + k_{n2}[A_2] + \dots + k_{nn}[A_n]\end{aligned}\quad (4.98)$$

which can be expressed in terms of matrices as

$$\begin{bmatrix} -\frac{d[A]}{dt} \\ -\frac{d[A_2]}{dt} \\ \vdots \\ -\frac{d[A_n]}{dt} \end{bmatrix} = \begin{bmatrix} k_{11} & k_{12} \dots k_{1n} \\ k_{21} & k_{22} \dots k_{2n} \\ \vdots & \vdots \\ k_{n1} & k_{n2} \dots k_{nn} \end{bmatrix} \begin{bmatrix} [A_1] \\ [A_2] \\ \vdots \\ [A_n] \end{bmatrix}\quad (4.99)$$

or in the abbreviated form,

$$\frac{d\mathbf{A}}{dt} = \mathbf{KA} \quad (4.100)$$

where \mathbf{A} is the composition vector and \mathbf{K} the rate constant matrix. For this problem, in which \mathbf{K} is an $n \times n$ matrix, and n the number of components, A_n , it is possible to diagonalise \mathbf{K} and obtain n linearly independent proper vectors. The solution of the differential eq. (4.100) is similar to the corresponding scalar equation, that is

$$\mathbf{A}(t) = \mathbf{A}(0)e^{\mathbf{K}t} \quad (4.101)$$

The matrix $e^{\mathbf{K}t}$, which is designated the transition state matrix, is defined by the expansion of a Taylor series

$$e^{\mathbf{K}t} = \mathbf{U} + \mathbf{K}t + \frac{(\mathbf{K}t)^2}{2!} + \dots \quad (4.102)$$

where \mathbf{U} is the unitary matrix of order n . Eq. (4.100) can be solved by initially calculating successive powers of \mathbf{K} , followed by the application of eq. (4.102). However, although this procedure is reasonable, it is very slow. Alternatively, it is possible to reduce the previous infinite series to

$$e^{\mathbf{K}t} = \frac{1}{\Delta} [\Delta_0 \mathbf{U} + \Delta_1 (\mathbf{K}t)^2 + \dots + \Delta_{n-1} (\mathbf{K}t)^{n-1}] \quad (4.103)$$

where Δ is the Vandermonde determinant

$$\Delta = \det \begin{bmatrix} 1 & \mu_1 & \mu_1^2 & \cdots & \mu_1^{n-1} \\ 1 & \mu_2 & \mu_2^2 & \cdots & \mu_2^{n-1} \\ \vdots & & & & \\ 1 & \mu_n & \mu_n^2 & \cdots & \mu_n^{n-1} \end{bmatrix} \quad (4.104)$$

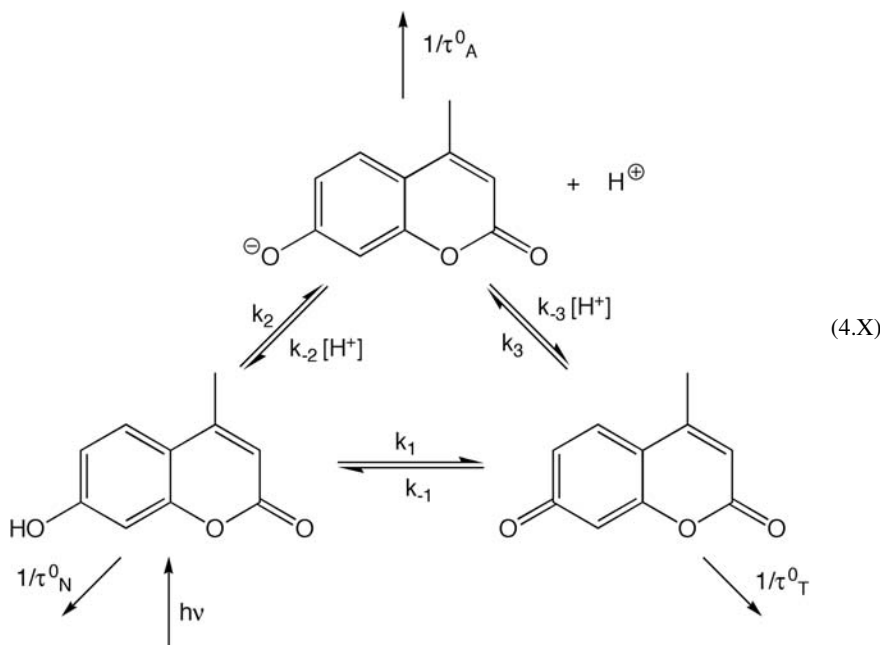
and each Δ_i is the determinant obtained from the previous equation substituting $\mu_1^i, \mu_2^i, \dots, \mu_n^i$ by $\exp(\mu_1), \exp(\mu_2), \dots, \exp(\mu_n)$. The values of μ_i are related to the proper values of \mathbf{K} through

$$\mu_i = \lambda_i t, \quad i = 1, 2, \dots, n \quad (4.105)$$

where the proper values are obtained from the equation

$$\det(\mathbf{K} - \lambda \mathbf{U}) = 0 \quad (4.106)$$

The method of matrices has been applied to the solution of reversible equilibria between the excited states of the neutral, anionic and tautomeric forms of 7-hydroxy-4-methylcoumarin [6], which in its most complex form involves equilibria between all the species, as shown in the mechanism below. The values of τ_N^0, τ_A^0 and τ_T^0 refer to the radiative lifetimes of each of the neutral, anionic and tautomeric forms. Absorption of light initially produces the excited state of the neutral form, which then participates in the above scheme. In this kinetic scheme, there are nine unknowns: six rate constants and three inverse lifetimes.



which require nine kinetic equations for complete analysis. The differential equations that determine the time dependence of concentrations of the species are

$$\frac{d}{dt} \begin{bmatrix} N^* \\ A^* \\ T^* \end{bmatrix} = \begin{bmatrix} -X & k_{-2}[H^+] & k_{-1} \\ k_2 & -Y & k_3 \\ k_1 & k_{-3}[H^+] & -Z \end{bmatrix} \begin{bmatrix} N^* \\ A^* \\ T^* \end{bmatrix} \quad (4.107)$$

where N^* , A^* and T^* are the concentrations of N , A and T in the excited state, given by

$$\begin{aligned} X &= k_1 + k_2 + \frac{1}{\tau_N^0} \\ Y &= (k_{-2} + k_{-3})[H^+] + \frac{1}{\tau_A^0} \\ Z &= k_{-1} + k_3 + \frac{1}{\tau_T^0} \end{aligned} \quad (4.108)$$

From the integration of eq. (4.107) we obtain

$$\begin{bmatrix} N^* \\ A^* \\ T^* \end{bmatrix} = \begin{bmatrix} a_{11} & a_{12} & a_{13} \\ a_{21} & a_{22} & a_{23} \\ a_{31} & a_{32} & a_{33} \end{bmatrix} \begin{bmatrix} e^{-\lambda_1 t} \\ e^{-\lambda_2 t} \\ e^{-\lambda_3 t} \end{bmatrix} \quad (4.109)$$

where the proper values λ_i are the reciprocals of the decay lifetimes and the pre-exponential factors a_{ij} the linear combinations of the proper base of vectors which obey the three initial conditions:

$$\begin{aligned}\sum_{j=1}^3 a_{ij} &= 1, \quad i = 1 \\ \sum_{j=1}^3 a_{ij} &= 0, \quad i = 2, 3\end{aligned}\tag{4.110}$$

[Eq. \(4.110\)](#) shows the situation where only the reactant $i = 1$ exists for $t = 0$. The nine equations link the values of λ_j and a_{ij} with the nine unknowns, and can be written in the following form:

$$\begin{bmatrix} -X & k_{-2}[\text{H}^+] & k_{-1} \\ k_2 & -Y & k_3 \\ k_1 & k_{-3}[\text{H}^+] & -Z \end{bmatrix} = \begin{bmatrix} a_{11} & a_{12} & a_{13} \\ a_{21} & a_{22} & a_{23} \\ a_{31} & a_{32} & a_{33} \end{bmatrix} \begin{bmatrix} -\lambda_1 & 0 & 0 \\ 0 & -\lambda_2 & 0 \\ 0 & 0 & -\lambda_3 \end{bmatrix} \begin{bmatrix} a_{11} & a_{12} & a_{13} \\ a_{21} & a_{22} & a_{23} \\ a_{31} & a_{32} & a_{33} \end{bmatrix}^{-1}\tag{4.111}$$

This equality allows us to determine the rate constants, k_i , of the system, since we know the values of the pre-exponential factors, a_{ij} , and the inverse of the decay times, λ_i . [Figure 4.8](#) presents the variations of the concentrations of the various species with time and the values of the kinetic constants determined by this method.

4.3.3 Runge-Kutta method

The fourth-order Runge-Kutta method is a numerical method which, when the initial conditions are known [in particular that $y(t_0) = y_0$], allows approximate solutions of differential equations of the type

$$y'(t) = f(t, y)\tag{4.112}$$

where the differential dy/dt is represented as y' . For this differential equation, if we divide the time interval $[t_0, t_n]$ into N equally spaced sub-intervals of size

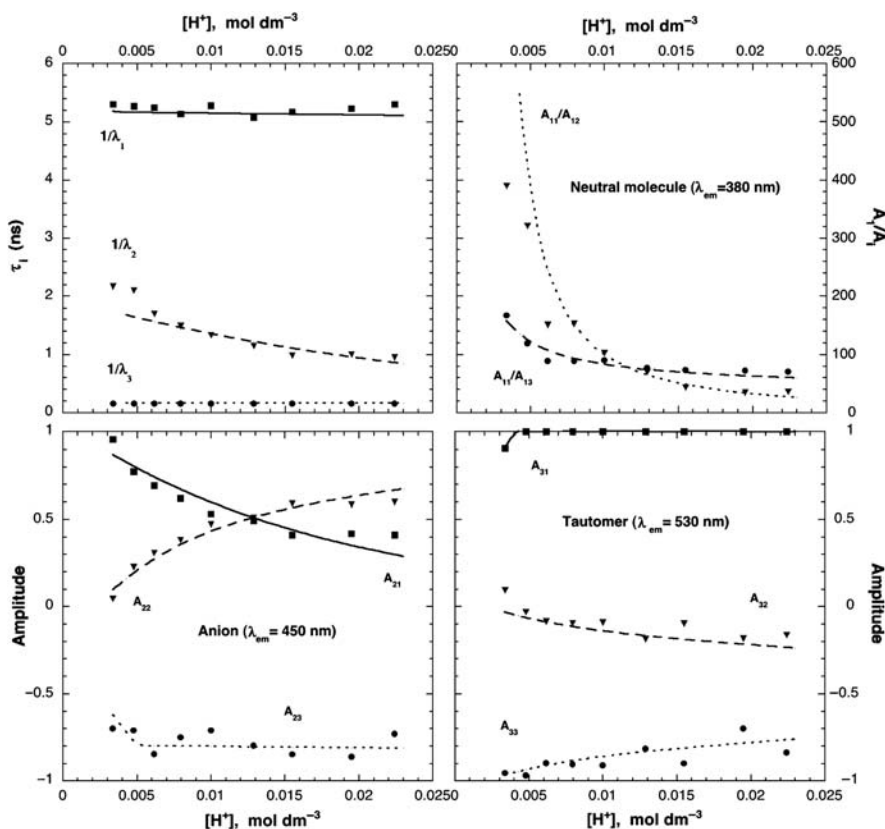
$$h = \frac{(t_N - t_0)}{N}\tag{4.113}$$

and each new independent variable increment is approximately equal to

$$t_n = t_0 + nh\tag{4.114}$$

where $n = 0, 1, 2, \dots, N$. If $y(t)$ is continuous and single valued, this can now be expanded relative to the point t_0 using a Taylor series

$$y(t_0 + h) = y(t_0) + f'(t_0, y_0)h + f''(t_0, y)\frac{h^2}{2!} + \dots\tag{4.115}$$

**FIGURE 4.8**

Kinetics of the photokinetic reversible equilibrium among neutral, anionic and tautomeric forms of 7-hydroxy-4-methylcoumarin.

When h is small, higher order terms in h can be ignored. If we truncate after the term in h in the Taylor series expansion, we get the method of Euler, where

$$y(t_0 + h) = y(t_0) + hy'(t_0) \quad (4.116)$$

From the value y_n and its derivative, this process can be continued through various steps to obtain the value of y_{n+1} .

For a more precise treatment, we can truncate the expansion after the term in h^2 , and obtain the second-order Runge-Kutta method. For this, we need to know the second derivative $y''(t_0)$, which can be estimated as a finite difference.

$$y''(t_0) = \frac{\Delta y'}{\Delta t} = \frac{y'(t_0 + h) - y'(t_0)}{h} \quad (4.117)$$

Substituting this expression into the truncated Taylor series, we obtain

$$\begin{aligned} y(t_0 + h) &= y(t_0) + hy'(t_0) + \frac{h^2}{2!} \left(\frac{y'(t_0 + h) - y'(t_0)}{h} \right) \\ &= y(t_0) + \frac{h^2}{2} [y'(t_0 + h) + y'(t_0)] \end{aligned} \quad (4.118)$$

For an even more rigorous treatment, in the third-order method, we keep the terms in the Taylor series until h^3 . For this we need to know the third derivative $y'''(t_0)$. The resulting equations are

$$y_{n+1} = y_n + \frac{h}{6} (\Delta Y_1 + 4\Delta Y_3 + \Delta Y_4) \quad (4.119)$$

where

$$\begin{aligned} \Delta Y_1 &= f(t_n, y_n) \\ \Delta Y_2 &= f(t_n + h, y_n + \Delta Y_1) \\ \Delta Y_3 &= f(t_n + h/2, y_n + \Delta Y_1/2) \\ \Delta Y_4 &= f(t_n + h, y_n + \Delta Y_2) \end{aligned} \quad (4.120)$$

Finally, the most common case in chemical kinetics involves the fourth-order Runge-Kutta method, given by the equations

$$y_{n+1} = y_n + \frac{h}{6} (\Delta Y_1 + 2\Delta Y_2 + 2\Delta Y_3 + \Delta Y_4) \quad (4.121)$$

where

$$\begin{aligned} \Delta Y_1 &= f(t_n, y_n) \\ \Delta Y_2 &= f(t_n + h/2, y_n + \Delta Y_1/2) \\ \Delta Y_3 &= f(t_n + h/2, y_n + \Delta Y_2/2) \\ \Delta Y_4 &= f(t_n + h, y_n + \Delta Y_3) \end{aligned} \quad (4.122)$$

The error associated with numerical integration using the Runge-Kutta method of order n is of the order of magnitude h^{n+1} , since the terms up to the order h^n are eliminated in the series expansion. As the error depends on the step size, the temptation is to reduce this by choosing a very small integration step. However, the use of such a small step involves the use of a lot of computer time since it requires a large number of iterations. As each calculation is affected by a rounding-up error, the use of a very small h introduces a global error determined by the sum of the rounding-up errors, which could be greater than that expected from the order-of-magnitude error associated with the order h^{n+1} .

As an example of the application of the fourth-order Runge-Kutta method, we will consider the reversible equilibria of mechanism (4.VIII), described by the differential eq. (4.73). The changes in the concentrations of the species A, B and C are illustrated in Figure 4.7 for two different integration step sizes. Note the difference between the calculated values and the exact ones obtained by the Laplace transform method for calculations using the larger step size. Since we are treating

a system that is approaching equilibrium, this difference is conspicuous at the start of these reactions. Care must be exercised in choosing the step size since the choice of a totally inadequate value for it for the rate constants under consideration can lead to completely erroneous results.

4.3.4 Markov chains

The most complex systems of kinetic equations cannot be solved analytically. In addition, when two of the differential equations of these systems describe processes that occur on drastically different timescales, their numerical integration using methods involving finite increments is unstable and unreliable. These methods are inherently deterministic, since their time evolution is continuous and dictated by the system of differential equations. Alternatively, we can apply stochastic methods to determine the rates of these reactions. These methods are based on the probability of a reaction occurring within an ensemble of molecules. This probabilistic formulation is a reflection either of the random nature of the collisions that are responsible for bimolecular reactions or of the random decay of molecules undergoing unimolecular processes. Stochastic methods allow us to study complex reactions without either solving differential equations or supplying closed-form rate equations. The method of Markov chains is a stochastic one in which the rate constants are considered as probabilities of reaction per unit time [7]. With this method, the microstates of a system change with time such that the probability, p_{ij} , that the system proceeds from state a_i at time t to state a_j at time $t + \Delta t$, depends only on the state a_i at time t , and is independent of any states of the system at times before t . The probability that the state a_i will be unchanged during the same time interval is p_{ii} .

For a chemical reaction in which there is a 1:1 relationship in the conversion of reactant to product, the probabilities of transition p_{ij} can be represented by a square matrix having only positive or zero elements with m lines or columns, such that the sum of the entries in each line is unity.

$$\sum_{j=1}^m p_{ij} = 1 \quad (4.123)$$

The relation between the representative vector for the reactants considered at time t and for the products considered at time $t + \Delta t$ can be expressed as

$$\begin{bmatrix} [A_1]_t & [A_2]_t & \dots & [A_m]_t \end{bmatrix} \begin{bmatrix} p_{11} & p_{12} & \dots & p_{1m} \\ p_{21} & p_{22} & \dots & p_{2m} \\ \vdots & & & \\ p_{m1} & p_{m2} & \dots & p_{mm} \end{bmatrix} = \begin{bmatrix} [A_1]_{t+\Delta t} & [A_2]_{t+\Delta t} & \dots & [A_m]_{t+\Delta t} \end{bmatrix} \quad (4.124)$$

Thus the concentration of the species A_i in time $t + \Delta t$ is given by

$$[A_i]_{t+\Delta t} = p_{1i}[A_1]_t + p_{2i}[A_2]_t + \dots + p_{mi}[A_m]_t \quad (4.125)$$

The values of the probabilities used in the transition matrix are related to the rate constants and to the time interval Δt . For a first-order reaction following eq. (4.1), the first term of the Taylor series expansion the exponential, leads to

$$[A] = (1 - k_1)[A]_0 \quad (4.126)$$

and for the products

$$[B] = k_1[A]_0 \quad (4.127)$$

The rate constant k_1 can thus be related to the probability with which the molecule A_i decays within one unit of time, $p_{1,i}$, while $1 - k_1$ is related to the probability that this molecule remains unchanged during the same period. It is important to note that the probability depends on the unit of time (Δt) taken into consideration. For a first-order reaction with $k_1 = 10^8 \text{ sec}^{-1}$ and $\Delta t = 10^{-9} \text{ sec}$, the transition probability is 10%, $p_{12} = 0.1$. If the time interval chosen $\Delta t = 10^{-10} \text{ sec}$, the transition probability will be only 1%, $p_{12} = 0.01$. Using smaller time intervals leads to a linear solution of the kinetic equation that approximates more closely to the exact solution. However, this requires a lengthier calculation to describe the system at any given time after the start of the reaction, and a compromise has to be made between the precision required and the computation time necessary. This relation can be extended to higher order elementary processes, since for sufficiently small time intervals, these kinetic processes can be considered to follow first-order behaviour. In a second-order reaction of the type $A + B \rightarrow \text{products}$, the probability of disappearance of A per unit time is $k_2 [B]$ and the probability of A not reacting is $1 - k_2[B]$.

As an example of the use of this treatment to construct a transition matrix, we will take the first-order decomposition reaction



and consider that $p_1 = k_1\Delta t$. For the first iteration, the transition matrix will be

$$\begin{bmatrix} [A]_0 & 0 \end{bmatrix} \begin{bmatrix} 1 - p_1 & p_1 \\ 0 & 1 \end{bmatrix} = \begin{bmatrix} (1 - p_1)[A]_0 & p_1[A]_0 \end{bmatrix} \quad (4.128)$$

where $[A]_0$ is the initial concentration of the reactant and $(1 - p_1[A]_0)$ its concentration after time interval Δt . The equations of recurrence for the disappearance of A and the formation of B are

$$\begin{aligned} [A]_{t+\Delta t} &= (1 - p_1)[A]_t \\ [B]_{t+\Delta t} &= [B]_t + p_1[A]_t \end{aligned} \quad (4.129)$$

The method of Markov chains provides a useful tool for the study of very complex kinetic systems that do not have studied analytical solutions. As an example, consider the competitive-consecutive mechanism [7]



The transition matrix, with $p_1 = k_1 \Delta t$ and $p_2 = k_2 \Delta t$, can be written

$$\begin{matrix} A & B & C & D & E \\ \left[\begin{array}{ccccc} 1 - p_1[B] - p_2[C] & 0 & p_1[B]/2 & (p_1[B] + p_2[C])/2 & p_2[C]/2 \\ 0 & 1 - p_1[A] & p_1[A]/2 & p_1[A]/2 & 0 \\ 0 & 0 & 1 - p_2[A] & p_2[A]/2 & p_2[A]/2 \\ 0 & 0 & 0 & 1 & 0 \\ 0 & 0 & 0 & 0 & 1 \end{array} \right] & (4.130) \end{matrix}$$

The probability of the formation of C, D and E is multiplied by $\frac{1}{2}$ since from the stoichiometry of the reaction, two molecules of reactant A are used up to form one molecule of C, D, or E. The expressions of recurrence for concentration as a function of time are

$$\begin{aligned} [A]_{t+\Delta t} &= [A]_t(1 - p_1[B]_t - p_2[C]_t) \\ [B]_{t+\Delta t} &= [B]_t(1 - p_1[A]_t) \\ [C]_{t+\Delta t} &= p_1[A]_t[B]_t + [C]_t(1 - p_2[A]_t) \\ [D]_{t+\Delta t} &= p_1[A]_t[B]_t + p_2[A]_t[C]_t + [D]_t \\ [E]_{t+\Delta t} &= p_2[A]_t[C]_t + [E]_t \end{aligned} \quad (4.131)$$

The change in the concentrations of A, B, C, D and E with time are shown in [Figure 4.9](#), together with the values of the initial concentrations and rate constants.

This method can also be applied to more complex cases such as flow systems involving spatially inhomogeneous systems and also to oscillating reactions in which the concentrations of the various intermediate species proceed through a

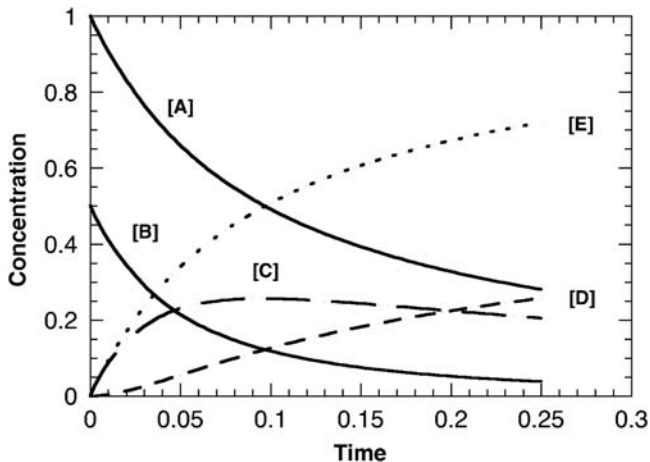


FIGURE 4.9

Change in concentrations of reactants and products with time for mechanism (4.XII) calculated using Markov chains for a maximum transition probability of 10%. $[A]_0 = 1$, $[B]_0 = 0.5$, $[C]_0 = 0$, $[D]_0 = 0$, $[E]_0 = 0$, $k_1 = 20$, $k_2 = 10$.

number of cycles [8]. An example of an oscillating reaction in a homogeneous system with constant amplitude involves the Lotka type II mechanism [9]



where $[A]$ is a constant. The transition matrix for this reaction

$$\begin{bmatrix} X & Y \\ 1 - p_2[Y] + p_1[A] & p_2[Y] \\ 0 & 1 - p_3 + p_2[X] \end{bmatrix} \quad (4.132)$$

leads to the following equations for the concentrations of X and Y

$$\begin{aligned} [X]_{t+\Delta t} &= [X]_t(1 - p_2[Y]_t + p_1[A]) \\ [Y]_{t+\Delta t} &= p_2[X]_t[Y]_t + [Y]_t(1 - p_3 + p_2[X]_t) \end{aligned} \quad (4.133)$$

Lotka showed analytically that this system oscillates with a period $T = 2\pi\sqrt{(k_1 k_2 [A])}$ and that the amplitude depends on the initial concentrations of X and Y . For oscillatory reactions of this type the computational error has to be considerably less than 10% because the propagation of errors from one transition to another has the effect that small differences in the oscillation periods ($\sim 10\%$) of X and Y , lead to a marked change in the amplitudes from cycle to cycle (20–30% when the transition probability is 10%). Results of calculations are shown in Figure 4.10 for the cases where transition probabilities of 10% and 1%

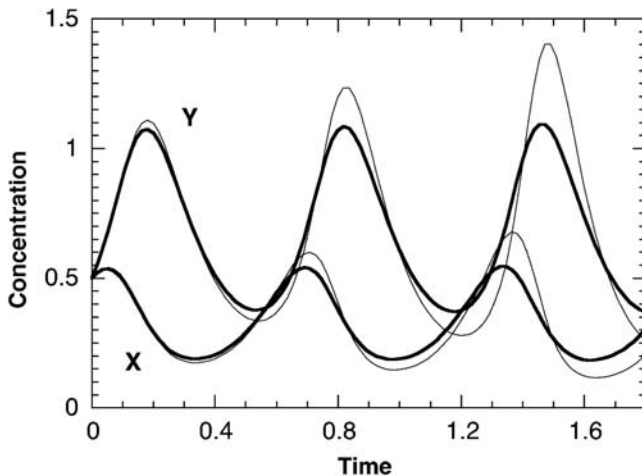


FIGURE 4.10

Calculated concentrations of intermediates in a Lotka type II reaction for maximum transition probabilities of 1% (thick line) and 10% (thin line). $[X]$ and $[Y]$ correspond to the smaller and larger amplitudes, respectively. $[A] = 1$, $[X]_0 = 0.5$, $[Y]_0 = 0.5$, $k_1 = 10$, $k_2 = 15$, $k_3 = 10$.

are used. It is obvious in this case that it is impossible to avoid carrying out a more detailed (and time-consuming) calculation.

4.3.5 Monte Carlo method

The Monte Carlo method is another stochastic procedure for the numerical determination of the change in concentrations of reactants, intermediates or products of a reaction as a function of time. This method can simulate the time evolution of any chemical system.

The major advantage of the Monte Carlo method stems from the fact that its convergence is independent of the dimension of the integral. Let us consider an integral of dimension j

$$I = \int_{x_j} \dots \int_{x_2} \int_{x_1} F(x) w(x) dx \quad (4.134)$$

where $F(x)$ is a function of the variables $x = (x_1, x_2, \dots, x_j)$ and $w(x)$ is its distribution function. Within the Monte Carlo method, we initially apply a transformation of the type $x \rightarrow \xi = (\xi_1, \xi_2, \dots, \xi_j)$ to the set of variables, with $0 \leq \xi_j \leq 1$. This transforms the above integral into

$$I = \int_0^1 \dots \int_0^1 F(\zeta) w(\zeta) J d\zeta = \int_0^1 \dots \int_0^1 F(\zeta) d\zeta \quad (4.135)$$

where J represents the Jacobian transform which is equal to $[w(\xi)]^{-1}$. Once the values are calculated of F for N randomly chosen sets of variables $(\xi_1, \xi_2, \dots, \xi_j)$, the value of the integral estimated by the Monte Carlo method, I' , is given by

$$I \cong I' = \frac{1}{N} \sum_{i=1}^N F(\eta_i) \quad (4.136)$$

where η_i represents the set of the variables $(\xi_1^i, \xi_2^i, \dots, \xi_j^i)$. This method has been extensively used in studies of reaction dynamics, where the evolution of a trajectory that leads from the reactants in a given state (electronic, vibrational, or rotational) to the products in another state requires the solution of the appropriate differential equations of motion. A minimum of 10^j trajectories for each integral of dimensionality j is needed to ensure convergence with this type of calculation.

The Monte Carlo method can also be applied to solve the differential equations describing the time evolution of reactants, intermediates and products within a reaction sequence. We start by distributing the reactant molecules within a system of N coordinates. The molar fraction of each reactant can be considered to be the number of molecules of this reactant distributed over the total number of coordinates. The reaction is simulated by randomly generating numbers between 1 and N . In a first-order reaction, each time that a number generated corresponds to

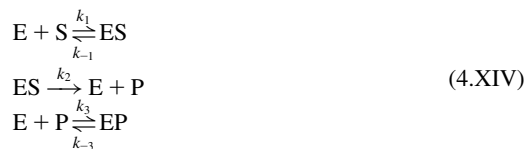
a coordinate occupied by the reactant, the reaction occurs. The rate constant, k_1 , can be obtained by relating the number of reactive selections n_1 accomplished during a cycle to the reaction time (which is the total number of selections). Each molecule has an equal and constant probability of reacting in time Δt since each position occupied by a molecule has an equal and constant probability, p , of being selected at random. Thus if m is the number of cycles carried out, the simulation of a first-order reaction can be expressed as a function of real time knowing that

$$k_1 \Delta t = p n_1 m \quad (4.137)$$

In a reaction of rate constant $k_1 = 10^7 \text{ sec}^{-1}$, if we consider a timescale with units of 1 nsec and 10 events are accomplished in each cycle, the probability of a reaction occurring in each cycle will be $p = 10^{-3}$. The description of the time evolution of the system can thus be given in terms of the dependence of the molar fraction as a function of the number of cycles or, using the previous relation and converting the initial molar fraction into the initial concentration, as the variation of concentration with time.

If the reaction is second order, the probability of a molecule occupying a coordinate is independent of another occupying another coordinate. Consequently for each cycle m , two events must be made, one for each reactant molecule. If a molecule is found in both selections, then the reaction will occur.

Particularly useful applications of the Monte Carlo method include modelling complex oscillatory reactions and studying enzyme catalysis [10,11]. As an example of the latter treatment, we will consider a system involving an initial reversible complex formation between the enzyme and the substrate, accompanied by a reversible step of inhibition of the catalyst by the product, as described by the scheme



The system of differential equations needed to describe this system is very complex:

$$\begin{aligned} \frac{d[S]}{dt} &= -k_1[E][S] + k_{-1}[ES] \\ \frac{d[E]}{dt} &= -k_1[E][S] + k_{-1}[ES] + k_2[ES] - k_3[E][P] + k_{-3}[EP] \\ \frac{d[ES]}{dt} &= k_1[E][S] - k_{-1}[ES] - k_2[ES] \\ \frac{d[P]}{dt} &= k_2[ES] - k_3[E][P] + k_{-3}[EP] \\ \frac{d[EP]}{dt} &= k_3[E][P] - k_{-3}[EP] \end{aligned} \quad (4.138)$$

A further equation is given by the mass balance

$$[E]_0 = [E] + [ES] + [EP] \quad (4.139)$$

where $[E]_0$ is the initial enzyme concentration. However, the study of this system by the Monte Carlo method avoids having to treat all these equations. Results are presented in [Figure 4.11](#) for a kinetic simulation using as starting point 100 molecules of S and 10 of E.

The simulations accomplished using the Monte Carlo method show oscillations of the order $N^{-\frac{1}{2}}$, where N is the total number of molecules in the simulation. Considering the process at the macroscopic level, it is tempting to assume that the oscillations observed in these simulations are approximations of the continuous behaviour given by the functional and integral expressions. However, events that occur on the molecular scale are discrete. Continuous macroscopic behaviour is only observed since in real chemical systems we normally consider a very large number of molecules. The Monte Carlo method clearly shows that starting from a random microscopic behaviour a deterministic macroscopic behaviour results. We should note that there is currently great interest in studying the dynamic behaviour in these systems at the level of the behaviour of single molecules, using, for example, single-molecule fluorescence. These studies are providing important insights into the link between the microscopic and macroscopic behaviour of chemical systems.

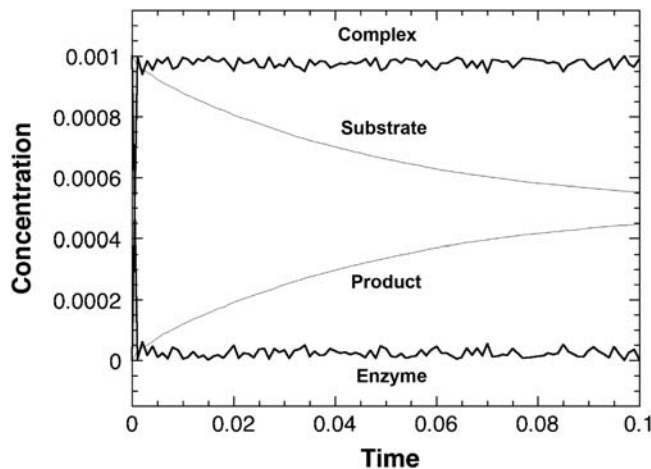


FIGURE 4.11

Application of the Monte Carlo method to mechanism (4.XIV).

4.4 Simplification of kinetic schemes

In the previous sections, we have discussed methods of solving kinetic equations based upon rigorously formulating all the elementary steps involved in the reaction mechanism in terms of the respective differential equations. In the most complex cases, the solution of the system of these differential equations obtained is possible by the use of approximate numerical methods, leading to an approximate solution to a rigorously formulated kinetic scheme. Alternatively, we can make use of our chemical knowledge of the system, and then make approximations using this knowledge that appreciably simplifies the system of differential equations, such that we can obtain an exact solution of a system that approximately describes the kinetic scheme. In both cases we obtain approximate solutions. With numerical approximations, the precision of the results obtained depends on the amount of the computational time invested. In the case of simplifying the chemical system, the quality of the result depends on how adequately the simplified model describes the real system.

Three types of fundamental simplification can be used: the method of isolation of one of the reactants, the pre-equilibrium approximation and the steady-state approximation. In addition, in many mechanisms it is possible to identify the one step that exercises a pronounced effect on the velocity of the overall reaction. This step is normally termed as the rate-determining step of the reaction, and when it exists, it allows us to obtain very simple relationships for the kinetics of the overall reaction.

4.4.1 Isolation method

An elementary reaction involving two or three reactants can, in principle, be treated as a pseudo-first-order reaction using the isolation method. In agreement with this method, if all the reactants except one are in excess, the apparent order of the reaction will be the order relative to the isolated reactant, since the concentrations of the species in excess do not vary appreciably during the reaction. Thus if a reaction is of order a relative to A, of order b relative to B and of order c relative to C, and if the concentrations of B and C are considerably greater than that of A, experimentally the order of reaction will be a and the rate constant will be k'

$$-\frac{d[A]}{dt} = k'[A]^a \quad (4.140)$$

where

$$k' = k_3[B]^b[C]^c \quad (4.141)$$

For the commonest case of $a = 1$, eq. (4.140) corresponds to a pseudo-first-order reaction.

The partial orders b and c can be obtained by the same process. The application of this method requires some caution, and it is desirable to use other methods to confirm the orders of reaction for the other components, since for complex mechanisms involving various steps, these can be influenced by changes in concentration, leading to different mechanisms under different conditions of “isolation.” In addition, when using a large excess of one of the reagents, if this contains an impurity, the concentration of the impurity under these conditions could be so great that it takes part in the rate law, leading to erroneous and frequently erratic results.

The precision with which this method can be used depends on the experimental conditions used. For example, in an elementary bimolecular reaction in which $[B] = 100[A]$, at the end of the first half-life of the reaction, there is only a 0.5% reduction in the initial value of $[B]$, while at the end of the reaction, the concentration of B is still 99% of its initial value, and changes of this order of magnitude are not significant within the current methods of analysis. If one of the reactants is H^+ or OH^- , instead of using an excess of these reactants we can achieve the same effect using a buffer solution that keeps the pH constant throughout the reaction. An alternative method involves keeping one of the reactants in solution in equilibrium with its solid phase, such that even though there is consumption of the reactant, its solution concentration will be constant.

We should note that when one of the reactants is the solvent, its participation in the mechanism of the reaction may not be noticed, since its concentration remains practically constant. The observed rate law for this reaction could, in fact, be a pseudo-first-order one.

4.4.2 Pre-equilibrium approximation

A second-order reaction in equilibrium followed by a first-order one of the type



leads to a kinetic system whose rate of formation of products can be expressed as

$$\frac{d[D]}{dt} = k_2[C] \quad (4.142)$$

but whose analytical solution is complicated. Kinetically, this problem is greatly simplified if k_1 as well as k_{-1} is significantly larger than k_2 . Under these

conditions it is possible to assume that the formation of C from A and B is in equilibrium, from which [C] can be obtained from the relationship

$$k_1[A][B] = k_{-1}[C] \quad (4.143)$$

knowing that

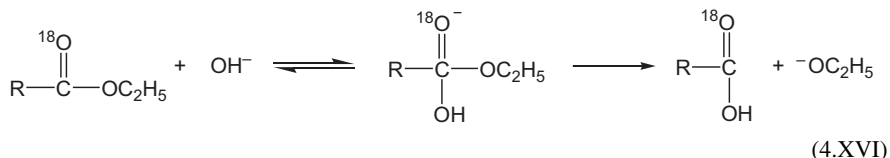
$$K = \frac{k_1}{k_{-1}} \quad (4.144)$$

and substituting $[C] = K[A][B]$ in eq. (4.142) to give

$$\frac{d[D]}{dt} = k_2 K[A][B] \quad (4.145)$$

where the rate of this reaction is described by a simple second-order kinetic equation.

A system of the above type is characterised by a rapid pre-equilibrium step. A typical example is given by the base-catalysed hydrolysis of an ester



4.4.3 Steady-state approximation

If in the kinetic scheme



described by the rate laws

$$\begin{aligned} \frac{d[\text{A}]}{dt} &= -k_1[\text{A}] + k_{-1}[\text{B}] \\ \frac{d[\text{B}]}{dt} &= k_1[\text{A}] - (k_{-1} + k_2)[\text{B}] \\ \frac{d[\text{C}]}{dt} &= k_2[\text{B}] \end{aligned} \quad (4.146)$$

the concentration [B] does not vary appreciably with time, that is, to a first approximation $d[\text{B}]/dt = 0$, we can write

$$[\text{B}] = \frac{k_1[\text{A}]}{k_{-1} + k_2} \quad (4.147)$$

which leads to the simple relationship for the rate of disappearance of A or of formation of the product C in the form

$$\frac{d[A]}{dt} = -\frac{d[C]}{dt} = -\frac{k_1 k_2}{k_{-1} + k_2} [A] \quad (4.148)$$

This is known as the steady-state approximation, since the concentration of B is assumed to be constant throughout the reaction. This is valid except at the initial and final stages of many kinetic schemes. Applying the steady-state approximation, the above kinetic scheme is reduced to a first-order rate law, where the observed pseudo-first-order constant is given by $k_1 k_2 / (k_{-1} + k_2)$.

It is reasonable that the variation of [B] with time will be small if [B] is also a small quantity. Thus the condition for application of the steady-state approximation can be given as

$$[B] = \frac{k_1 [A] - \frac{d[B]}{dt}}{k_{-1} + k_2} \quad (4.149)$$

that is

$$\frac{d[B]}{dt} \ll k_1 [A] \quad (4.150)$$

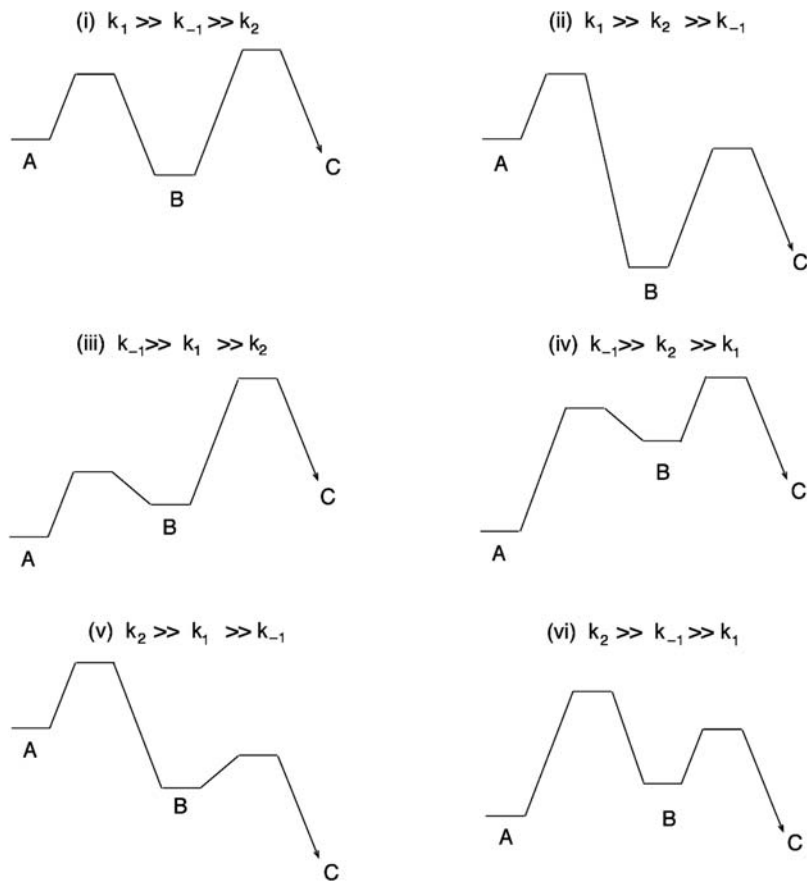
At the start of the reaction, when the intermediate B is being formed, the change in its concentration with time is not negligible, and the steady-state approximation does not hold. However, as it is assumed that the concentration of B is small, that is $[B] \ll [A]$, we can also formulate the conditions for the application of the steady-state approximation in terms of the rate constants for the formation and decay of B

$$k_{-1} + k_2 \gg k_1 \quad (4.151)$$

Thus this is valid when the disappearance of the intermediate is faster than its formation. Alternatively, it is useful to consider the validity of the steady-state approximation in terms of free-energy profiles, which are shown in Figure 4.12 for the various situations possible for mechanism (4.XVII) [12]. For profiles (iii), (iv) and (vi) the steady-state approximation is valid because the reactant is more stable than the intermediate, such that the concentration of B will always be less than that of A. Although B is more stable than A in profile (v), it does not form to any appreciable extent because its conversion into products is faster than its rate of formation. However, with profiles (i) and (ii), appreciable concentrations of B will be produced, such that the steady-state approximation is not valid.

One of the most important examples of the application of this approximation is enzyme catalysis [13]. Enzyme catalysis can be described in its simplest form by the scheme



**FIGURE 4.12**

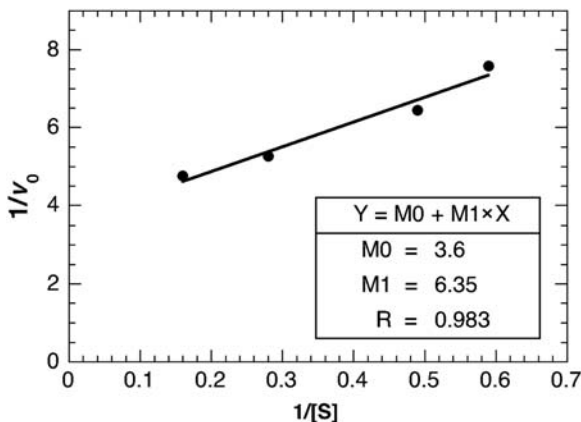
Schematic free-energy profiles illustrating the six possible relationships between the rate constants for mechanism (4.XVII).

where E represents the enzyme, S the substrate and P the catalytic product. Using the steady-state approximation, we obtain

$$\begin{aligned}\frac{d[ES]}{dt} &= k_1[E][S] - (k_{-1} + k_2)[ES] = 0 \\ [ES] &= \frac{k_1[E][S]}{k_{-1} + k_2}\end{aligned}\tag{4.152}$$

As the total concentration of enzyme present $[E]$, is normally known and can be expressed as

$$[E]_t = [E] + [ES]\tag{4.153}$$

**FIGURE 4.13**

Lineweaver-Burke plot for the hydrolysis of Azocoll by papain.

the concentration of the enzyme/substrate complex following the steady-state approximation will be

$$[ES] = \frac{k_1[E]_t[S]}{k_{-1} + k_2 + k_1[S]} \quad (4.154)$$

If we define the rate of reaction in terms of formation of the products, $v = d[P]/dt = k_2[ES]$, we obtain

$$v = \frac{k_1 k_2 [E]_t [S]}{k_{-1} + k_2 + k_1 [S]} \quad (4.155)$$

which, following Michaelis and Menten, can also be written as

$$v = \frac{V_m [S]}{K_m + [S]} \quad (4.156)$$

where V_m is the maximum velocity and K_m the Michaelis constant.

$$V_m = k_2 [E]_t \quad (4.157)$$

$$K_m = \frac{k_{-1} + k_2}{k_1} \quad (4.158)$$

The Michaelis-Menten equation can be rewritten to produce linear relationships. For example, Lineweaver-Burke plots are obtained using

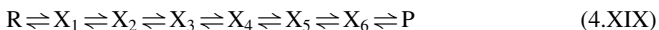
$$\frac{1}{v} = \frac{K_m}{V_m [S]} + \frac{1}{V_m} \quad (4.159)$$

In [Figure 4.13](#), a Lineweaver-Burke plot is shown for the example of enzyme catalysis discussed in [Chapter 3](#), Experimental Methods.

4.4.4 Rate-determining step of a reaction

In the solvolysis of 2-chloro-2-methylpropane, iodination of acetone in water, and ascorbic acid oxidation by hexacyanoferrate(III), discussed in [Chapter 3](#), Experimental Methods, the slowest step was identified, and was designated the rate-determining step of the reaction. In the general scheme, the subsequent fast steps do not have any influence on the kinetics of the overall reaction: the velocity of formation of the final products cannot exceed the rate of formation of the intermediate produced in the slowest step of the kinetic mechanism [14,15].

It is tempting to associate the slowest step with that which has the highest energy barrier among those involved in the reaction mechanism. However, this is not strictly true for reversible reactions, where intermediates that are more stable than the reactants are normally formed. [Figure 4.14](#) shows a complex mechanism of the type



The transition state of the highest energy in this reaction is \ddagger_2 , but the rate-determining step is not the conversion of X_1 to X_2 . It is convenient to divide the free-energy profile into sections to identify the slowest step. The end of each section is determined by the appearance of the first intermediate whose energy is less than that of the intermediate (or initial reactant) that starts the section. Within each section, it is easy to identify the highest energy transition state. In [Figure 4.14](#), these are \ddagger_2 , \ddagger_4 and \ddagger_5 . The free energies of activation of these transition states relative to the start

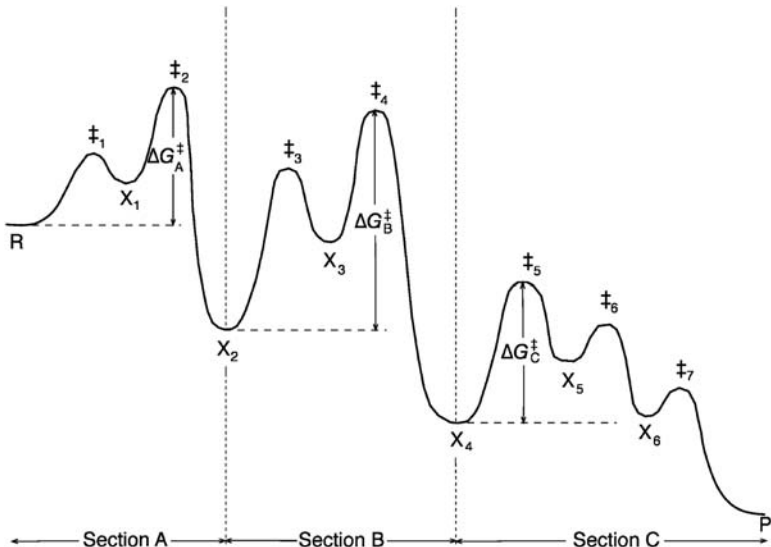


FIGURE 4.14

Changes in free energy during a reaction that follows mechanism (4.XIX).

of each section are ΔG_A^\ddagger , ΔG_B^\ddagger and ΔG_C^\ddagger . The largest of them is ΔG_B^\ddagger and X_2 is converted into X_4 more slowly than it is formed from R . Thus the rate-determining step of this reaction is the transformation of X_3 into X_4 .

4.5 Global and target analysis of kinetic data

State-of-the-art kinetic measurements often result in large and complex time-resolved spectroscopic data. It is not uncommon to obtain more than 1000 time points at 400 different wavelengths in one single experiment. The colour plots in [Figures 3.29 and 3.32](#) illustrate such data, which contain information on amplitude, wavelength and time. The model underlying the data matrix is a superposition of n_{comp} components given by the equation

$$\Psi(\lambda, t) = \sum_{l=1}^{n_{\text{comp}}} c_l(t) \varepsilon_l(\lambda) \quad (4.160)$$

where c_l and ε_l are the unknown concentration profile and spectrum of component l , respectively. The simultaneous (global) analysis of all the data should allow for the identification of the contribution of each component at each time point of the experiment, for each one of the wavelengths observed. [Figure 3.29](#) shows the kinetic trace collected for one wavelength, 615 nm, in two time scales, but taking full advantage of all the data requires the *global analysis* of the decay traces at all measured wavelengths. The combination of global analysis with testing a photochemical or photochemical model is often called *target analysis*. In chemical kinetics, such a model consists of a mechanistic proposal containing transitions between states of a species and/or between different species. This is also called a compartmental model and [Chapter 15](#), Pharmacokinetics, discusses compartmental models in the context of pharmacokinetics.

Prior to the analysis of the kinetic data, pre-processing of the data is usually carried out, including averaging, baseline subtraction and outlier detection, to avoid artefacts. When ultrafast time resolution is required, pre-processing also includes probe light chirp correction (i.e., correction for the earlier arrival in the sample of the red portion of the probe pulse) and measurement of the instrument response function (IRF, given by the convolution of pump and probe pulses).

Typical values for the number of components that can be distinguished with time-resolved spectroscopy are $1 \leq n_{\text{comp}} \leq 10$. In order to get an idea of how many components may be present in a given dataset, it is convenient to start by making a *singular value decomposition* (SVD) of the dataset [16]. The SVD technique indicates the number of independent components in the data. It shows when adding one additional component has little impact on the quality of the fit and when an additional component is too noisy or has too little structure, which indicate that it is not relevant to interpret the data.

Once the data are clean from artefacts and n_{comp} has been estimated, it is possible to separate time and wavelength properties with [eq. \(4.160\)](#). However, the

quantity estimated is $c_1\varepsilon_1$, which in itself is insufficient to obtain the absolute values of c_1 and ε_1 . Only a detailed kinetic model allows for the determination of the relative concentrations of the components.

Without *a priori* knowledge about a detailed kinetic model, the first step is to fit the data with the number of exponential decays, and their amplitudes, suggested by SVD. These constitute the *Decay Associated Spectra* (DAS) [17], and eq. (4.160) then reads

$$\Psi(\lambda, t) = \sum_{l=1}^{n_{\text{comp}}} [\exp(-k_l t) \otimes i(t)] \text{DAS}_l(\lambda) \quad (4.161)$$

where the convolution of the exponential decay with the IRF, denoted by $i(t)$, is explicitly represented. In difference absorption spectroscopy, it is more appropriate to name these spectra *Decay Associated Difference Spectra* (DADS). In the following we will not differentiate between spectra and difference spectra.

The simplest interpretation of DAS is that of a mechanism of consecutive first-order reactions with increasing lifetimes. The estimated spectra are called evolution-associated spectra (EAS). The DAS are interpreted as a loss or gain of emission or absorption with a certain lifetime, whereas the EAS represent the spectral evolution. For example, extending mechanism (4.VI) to include the decay of C, A → B → C →, the second EAS corresponds to species B which raises with the first lifetime and decays with the second lifetime, while the third EAS is that of species C, that raises with the second lifetime and decays with the third lifetime. Panels A and B of Figure 3.32 show transient spectra at different time points and panel C shows the EAS of the species initially formed, $^1\mathbf{1}$, and of the species rapidly formed from $^1\mathbf{1}$ and slowly decaying, named $^1\mathbf{1}^\pm$. When the consecutive reactions with increased lifetimes represent the correct mechanism, as is the case in Figure 3.32, the EAS correspond to true species-associated spectra (SAS). The kinetics of more complicated systems can be investigated with target analysis.

Target analysis combines global analysis with the testing of a specific kinetic mechanism. In order to find the best mechanism, typically several models with $n_{\text{comp}} = n_{\text{decay}}$ components can be tried. These models may involve combinations of consecutive, parallel and reversible first-order reactions. The hypothetical mechanisms should be based on the knowledge of the system. The quality of the fit, the physical meaning of the spectra and the microscopic rate constants obtained dictate the choice of the best mechanism. For example, the photophysics and photochemistry of molecule **1** was studied in dichloromethane (Figure 3.32) and in *n*-butyl ether (Figure 4.15). Two lifetimes between 1 psec and 20 nsec are necessary to fit the transient spectra of **1** in dichloromethane, but three lifetimes are necessary for the same quality of fit of the decays observed in *n*-butyl ether. Flash photolysis of **1** in *n*-butyl ether showed the presence of its triplet state, $^3\mathbf{1}$, but in dichloromethane no triplet was observed [18]. The charge-separated state of **1**, $^1\mathbf{1}^\pm$, is less stabilised by less polar solvents and *n*-butyl ether is less polar than dichloromethane. Hence it is reasonable to consider that in *n*-butyl ether $^1\mathbf{1}^\pm$ has a higher energy than $^3\mathbf{1}$ and may decay to this triplet state via the triplet state

of the charge-separated species, ${}^3\mathbf{1}^\pm$. However, the time window mentioned above does not allow for the observation of the triplet. This motivated target analysis of the decay of **1** in *n*-butyl ether with the mechanism of Figure 4.16. This

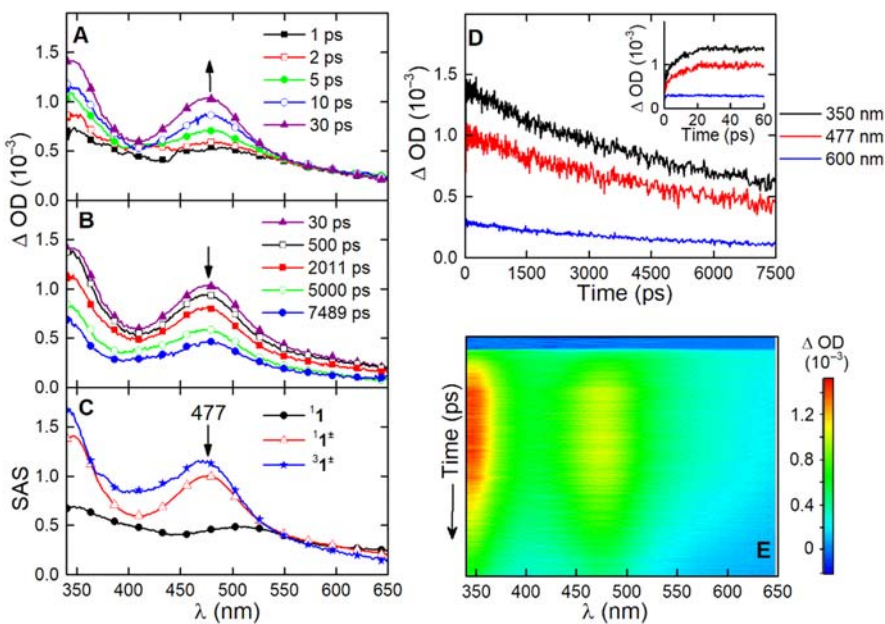


FIGURE 4.15

Transient absorption spectra of the processes illustrated in scheme (3.XIX) for molecule **1** in *n*-butyl ether at 293K, in short- (a) and long-time scales (b), and calculated species-associated spectra (c). Time profile of selected decays (d). 2D image of collected data (e). All the spectra presented were subject to the subtraction of the solvent response and chirp correction. Results obtained with the ultrafast transient absorption spectrometer in the Coimbra Chemical Centre.

Courtesy of Kamila Mentel.

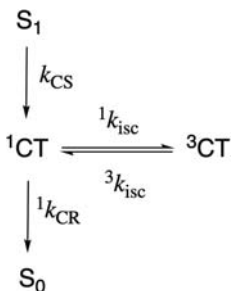


FIGURE 4.16

Kinetic mechanism employed in the target analysis of the data shown in Figure 4.15.

mechanism involves consecutive reactions with a parallel and a reversible reaction. A new species with a spectrum very similar to that of ${}^1\text{I}^\pm$ was identified and assigned to ${}^3\text{I}^\pm$ [18].

References

- [1] E Levin, JG Eberhart, *J. Chem. Educ.* **66** (1989) 705.
- [2] SC Castillo, SG Micolta, *J. Chem. Educ.* **68** (1991) 179.
- [3] RMD Nunes, M Pineiro, LG Arnaut, *J. Am. Chem. Soc.* **131** (2009) 9456.
- [4] JB Birks, DJ Dyson, IH Munro, *Proc. Royal Soc. A* **275** (1963) 575.
- [5] MN Berberan-Santos, JMG Martinho, *J. Chem. Educ.* **67** (1990) 375.
- [6] J Seixas de Melo, AL Maçanita, *Chem. Phys. Lett.* **204** (1993) 556.
- [7] SJ Formosinho, MGM Miguel, *J. Chem. Educ.* **56** (1979) 582.
- [8] SJ Formosinho, *J. Chem. Educ.* **59** (1982) 281.
- [9] AJ Lotka, *J. Am. Chem. Soc.* **42** (1920) 1595.
- [10] MR Kibby, *Nature* **222** (1969) 298.
- [11] DT Gillespie, *J. Phys. Chem.* **81** (1977) 2340.
- [12] R Raines, DE Hansen, *J. Chem. Educ.* **65** (1988) 757.
- [13] O Moe, R Cornelius, *J. Chem. Educ.* **65** (1988) 137.
- [14] JR Murdoch, *J. Chem. Educ.* **58** (1981) 32.
- [15] KJ Laidler, *J. Chem. Educ.* **65** (1988) 250.
- [16] J Snellenburg, S Laptenok, R Seger, KM Mullen, IHM Van Stokkum, *J. Stat. Software* **49** (2012) 1.
- [17] IHM van Stokkum, DL Larsen, R van Grondelle, *Biochem. Biophys. Acta* **1657** (2004) 82.
- [18] KK Mentel, A Serra, PE Abreu, LG Arnaut, *Nature Commun* **9** (2018) 2903.

Collisions and molecular dynamics

5

We can only really say that we understand any physical phenomenon when we can predict it and can calculate both its occurrence and order of magnitude using only fundamental data based on the physical and structural factors involved. This calculation must be based on a theory that relates the forces involved in the observed phenomenon and the experimental measurements on it.

The development of any such scientific theory initially involves experimental observations. Based on this experimental foundation, suppositions or hypotheses are then constructed, which provide reasonable explanations for the observed behaviour and which are able to solve problems (i.e., make predictions) related to it. The success of this is determined by the confirmation of any predictions, the possibility of explaining other related observations and, eventually, by the solution of new problems within the same area. When this process of verification is successful, we obtain one of the “hard core” of scientific laws, which are useful for explanation as well as prediction of experimental observations. However, any theoretical model is an internal representation created within the framework of the world that surrounds us, and as such can never be perfect or complete. A theory is, thus, a set of models associated with various hypotheses that relate, in a causal form, to the real-world systems.

Within scientific theories, in particular those related to chemical kinetics, there is a certain hierarchy. The simplest conceptual structure involves some statistically significant correlation between sets of experimental data, for example, relationships between rate constants of certain reactions and their corresponding equilibrium constants. This is known as an *empirical correlation*. At the opposite extreme, we can find theories that allow us to calculate reaction rate constants using only fundamental constants from the basic laws of physics (such as those given in [Appendix I](#), General Data), and, frequently, the Born-Oppenheimer approximation involving separation of nuclear and electron motions. These theories are known as *ab initio* theories, that is, based on first principles. The term *ab initio*, which to some extent is a misnomer, was first used by Parr to describe processes that had been developed since the beginning within a given research project in his laboratory. In general, the validity of such *ab initio* procedures, as with any scientific theory, can only be shown by comparison with experiments.

Between these limits of empirical correlations and *ab initio* calculations, a large number of theories of chemical kinetics are found with varying degrees of

empiricism, which depend upon how many adjustable parameters are needed to fit the calculation to the experimental data. Although they may lack the theoretical rigour of more fundamental theoretical formulations, these more empirical theories are important since, apart from their historical interest, they often act as pointers for the development of more quantitative theoretical models. These can be directed toward real systems and can help us avoid using highly sophisticated calculations to treat the wrong target. To quote the late John W. Tukey, who made major contributions to statistics, both in industrial and academic areas: “An approximate answer to the right question is worth a great deal more than a precise answer to an approximate question.” It is worth noting that John Tukey’s initial background was chemistry.

At a first glance, an *ab initio* theory would seem to be the most satisfactory way to treat theoretically the chemical kinetics of any system, since this does not need to introduce any experimental data. However, only those systems involving three to four atoms in the gas phase can be solved with chemical accuracy ($\pm 4 \text{ kJ mol}^{-1}$) by this route. For the vast majority of reactions of chemical interest, we need either to introduce major simplifications into the most sophisticated theories so that they can be applied, or to opt for a simpler theory, including empirical parameters, which can be used without *a posteriori* changes to estimate the rate constants. These approaches differ because in the first case, approximations are made when the method is applied, while with the latter approach, the approximations come within the formulation of the theory. In both cases, we hope that we can understand and interpret any discrepancies between the observed and the calculated kinetic data. The approach we use frequently depends upon the nature of the chemical system. The biggest problem is how to interpret any disagreement between experiment and calculation. This could result from experimental error, from wrong approximations when we apply the theory or incorrect assumptions in the theory itself. In the latter case, the theory is wrong and must be rejected. We must try to avoid the tendency of attributing any discrepancies between theoretical prediction and experimental observation to approximations introduced in the application of the theory, rather than to any weakness in the theory itself. The continued use of any obsolete theory past its “sell-by date,” is scientifically incorrect as well as hindering the development of more appropriate models.

A scientific theory is intended to simulate and help us understand the behaviour of part of or the whole Universe. It should be kept sufficiently simple to be understandable, and its proof should be purely operational, provided that is based in verifiable facts and does not contain errors of logic. The relevant question should then not be whether it is true or false, since this does not have any meaning from a scientific viewpoint. Instead, we should ask: “does it work”?

Even so, the answer to this question may not be completely objective. We can discard a theory based on wrong data or that contains errors of logic, but a similar decision based upon comparison between theoretical predictions and experimental data depends on how rigorous we want the agreement to be.

Based on these ideas, we will discuss the simple collision theory, which is appealing because of the relationship it provides between the orientation and the

energy of the molecules involved in collisions and their reactivity. However, it is not actually satisfactory as a theoretical hypothesis for polyatomic systems, since it cannot be used quantitatively for the calculation of rates of chemical reactions. However, for triatomic systems whose PESs are well defined, the calculation of trajectories using this approach provides an excellent method for calculating the reaction rates and is of high predictive value for elementary reactions. Such calculations apply to the molecular dynamics of individual reactive collisions. One of the chief experimental approaches to probe molecular dynamics is molecular beam scattering. This involves forming the reagent molecules into two collimated beams, each so diluted that collisions between them are negligible. The two beams intersect in a vacuum and the direction and velocity of the product molecules emitted from the collision zone are measured [1]. Molecular dynamics offer a detailed, microscopic view of a simple, elementary reaction. For polyatomic systems or reactions in solution, we are generally interested in knowing what products are obtained from what reactions under what conditions. In order to address these general interests of chemical kinetics, we will turn to other theories, to be discussed in the following chapters.

5.1 Simple collision theory

The simplest model for the rates of chemical reactions assumes that every time there is a bimolecular collision, there is a reaction. From calculations of the frequency of collisions in this system, we can then determine the rate constant.

To calculate the number of collisions per unit time, we need a model for the behaviour of molecules in these systems. The simplest approach involves a system of two gases, A and B, whose molecules behave as hard spheres, which are characterised by impenetrable radii r_A and r_B . A collision between A and B occurs when their centres approach within a distance d_{AB} , such that

$$d_{AB} = r_A + r_B \quad (5.1)$$

If we assume that the molecules of B are fixed and that those of A move with an average velocity \bar{v}_A , each molecule A sweeps a volume $\pi d_{AB}^2 v_A$ per unit time which contains stationary molecules of B. The area $\sigma_p = \pi d_{AB}^2$, is known as the *collision cross section*. If there are N_B/V molecules of type B per unit volume, the number of collisions of a molecule of type A with the stationary molecules B will be

$$z_{AB} = \frac{\pi d_{AB}^2 \bar{v}_A N_B}{V} \quad (5.2)$$

If the total number of molecules of A per unit volume is N_A/V , then the total number of collisions of A with B per unit volume is given by

$$Z_{AB} = \frac{\pi d_{AB}^2 \bar{v}_A N_B N_A}{V^2} \quad (5.3)$$

As indicated above, we have assumed that the molecules of B are stationary to obtain the above expression. In practice, Figure 5.1 shows that, for each pair of molecules, A and B, involved in a collisional trajectory, we can define a relative velocity v_{AB} , which is related to their velocities, v_A and v_B , according to

$$v_{AB} = \left(v_A^2 + v_B^2 - 2v_A v_B \cos\theta \right)^{1/2} \quad (5.4)$$

The value of $\cos\theta$ can vary between -1 and 1 . As all values of θ between 0° and 360° are equally probable, the positive and negative values of $\cos\theta$ will cancel out, and the mean value will be zero. Thus, we obtain

$$\bar{v}_{AB}^2 = \bar{v}_A^2 + \bar{v}_B^2 \quad (5.5)$$

Assuming that the molecular velocities are described by a Maxwell-Boltzmann distribution, the mean velocity of the molecules of a gas A is given by eq. (1.11). Consequently, the relative mean molecular velocity of molecules of types A and B will be

$$\bar{v}_{AB} = \sqrt{\frac{8k_B T}{\pi\mu}} \quad (5.6)$$

where the reduced mass is $\mu = m_A m_B / (m_A + m_B)$. Introducing this value for the relative velocity in eq. (5.3), we obtain

$$Z_{AB} = \frac{\pi d_{AB}^2 \bar{v}_{AB} N_B N_A}{V^2} \quad (5.7)$$

If we consider a gas that contains only molecules of type A, the total number of collisions would be

$$Z_{AA} = \frac{1}{2} \frac{\pi 4 r_A^2 \bar{v}_{AA} N_A^2}{V^2} \quad (5.8)$$

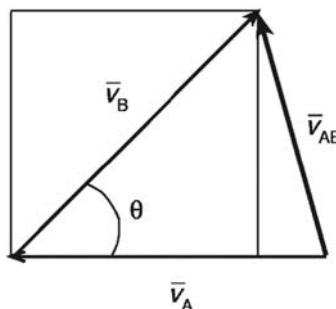


FIGURE 5.1

Relative velocities for a collisional trajectory between molecules A and B.

where the factor $\frac{1}{2}$ arises because we cannot count the same molecule twice. Since from eq. (5.5), the relative mean velocity of the molecules of a gas can be related to the mean velocity of the molecules, $\bar{v}_{AA} = \sqrt{2}\bar{v}_A$, eq. (5.8) can be rewritten as

$$Z_{AA} = \frac{2\sqrt{2}\pi r_A^2 \bar{v}_A N_A^2}{V^2} \quad (5.9)$$

The expressions for the number of collisions per unit time, also known as the collision densities, contain two factors involving the number of molecules per unit volume. These can be expressed in terms of pressures or molar concentrations, giving the rate constant for a bimolecular reaction between molecules of A and B in the experimentally more meaningful form

$$k_{AB} = \sigma_R \bar{v}_{AB} = \pi d_{AB}^2 \sqrt{\frac{8k_B T}{\pi \mu}} \quad (5.10)$$

We can test this collision theory approximation by comparing the value calculated for the elementary reaction



at 870K with the experimental value, $k_{\text{exp}} = 1.5 \times 10^2 \text{ dm}^3 \text{ mol}^{-1} \text{ sec}^{-1}$. From the van der Waals radii of N and O atoms, the reactant bond lengths, and assuming that these behave as hard spheres, we can estimate that $d_{AB} = 4 \times 10^{-10} \text{ m}$. The reduced mass can be calculated from the relative molecular masses of nitrogen dioxide and carbon monoxide

$$\mu = \frac{46 \times 28}{46 + 28} 1.661 \times 10^{-27} = 2.89 \times 10^{-26} \text{ kg} \quad (5.11)$$

where the units conversion factor in the unified atomic mass unit, from which we obtain the relative mean velocity, using the relationship $1 \text{ J} = 1 \text{ kg m}^2 \text{ sec}^{-2}$,

$$\bar{v}_{\text{NO}_2, \text{CO}} = \sqrt{\frac{8 \times 1.38 \times 10^{-23} \times 870}{3.14 \times 2.89 \times 10^{-26}}} = 1.03 \times 10^3 \text{ m sec}^{-1} \quad (5.12)$$

such that we calculate the rate constant to be $k_{AB} = 5.17 \times 10^{-16} \text{ m}^3 \text{ molecules}^{-1} \text{ sec}^{-1} = 3.11 \times 10^{11} \text{ dm}^3 \text{ mol}^{-1} \text{ sec}^{-1}$. We can see from the comparison between the experimental and calculated values that the latter are a factor of at least 10^9 greater than the former.

In this simple collision theory, there are two implicit approximations which lead to calculated values that are considerably greater than the experimental ones: (i) not all the collisions occur with a favourable orientation for reaction; (ii) we need a certain amount of energy for the conversion of the reactants into products, and not all the collisions have enough energy to produce this chemical transformation.

The first of these approximations can be corrected for by introducing a geometric factor, $g \leq 1$. This can be calculated using the molecular geometries of the

reactants and products. In the example of reaction (5.1), it is necessary that in the collision, the NO bond is extended and its oxygen atom directly approaches the carbon atom of CO for the reaction to occur (Figure 5.2). When the N–O and C–O bonds are collinear, the chemical transformation results from the stretching of these bonds, since these stretching vibrations are of high frequency and energy. In this model, the geometric factor g is given by the product of the orientation factor for the CO molecule, $\frac{1}{2}$, and that of the NO_2 molecule, which, as indicated in Figure 5.2, will be approximately $2/17$. Therefore for this reaction, $g = 1/17$.

The geometric factor may become much less than unity with increasing complexity of the reaction in the gas phase. In addition, with reactions in solution, we need to consider effects of solvent cage, which allow many collisions to occur during an encounter between the two reactants, such that the effect of the geometric factor becomes more difficult to calculate. However, as we will see, in these systems, too, it is less relevant.

The energetic factor is of fundamental importance in the determination of reaction probabilities and, hence, rate constants. Once more, we start from the Maxwell-Boltzmann distribution (eq. 1.10) to calculate this factor. In practice, in simple collision theory, we normally use the distribution function of molecular velocities in two dimensions rather than in three.

$$\frac{dN}{N_0} = \frac{m}{k_B T} \exp\left(\frac{-mv^2}{2k_B T}\right) v dv \quad (5.13)$$

Although there is no strong theoretical basis for this decrease in dimensionality, it simplifies the system, and we can rationalise it by considering that at the instant of collision between the two molecules, the velocity vectors have a common point such that they lie within a plane. Thus, the components of the velocities within the two dimensions that define this plane are sufficient to describe an effective collision. The distribution of molecular energies, based on the aforementioned equation, is

$$\frac{dN(\varepsilon)}{N_0} = \frac{1}{k_B T} \exp\left(\frac{-\varepsilon}{k_B T}\right) d\varepsilon \quad (5.14)$$

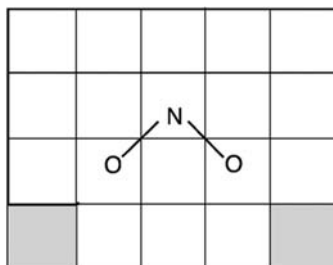


FIGURE 5.2

Sketch of the origin of the geometric factor in a collision. The favourable orientations for the attack of the carbon atom of CO are shaded.

which can be integrated to obtain the fraction of collisions with energy equal to or greater than the critical value, ε_c , for the reaction to occur.

$$\int_{\varepsilon > \varepsilon_c} \frac{dN(\varepsilon)}{N_0} = \int_{\varepsilon_c}^{\infty} \frac{1}{k_B T} \exp\left(\frac{-\varepsilon}{k_B T}\right) d\varepsilon \\ = \exp\left(\frac{-\varepsilon_c}{k_B T}\right) \quad (5.15)$$

If we include this energetic term and the geometric factor g in the expression for the rate constant, we obtain the final expression for the rate constant given by the collision theory that considers only effective collisions.

$$k_{\text{col}} = g\pi d_{AB}^2 \sqrt{\frac{8k_B T}{\pi\mu}} \exp\left(\frac{-\varepsilon_c}{k_B T}\right) \quad (5.16)$$

This expression bears an obvious resemblance to that of the Arrhenius law. In fact, the pre-exponential factor in the latter expression can be identified as

$$A = g\pi d_{AB}^2 \sqrt{\frac{8RT}{\pi\mu}} \quad (5.17)$$

The activation energy, expressed in molar terms, is given by

$$E_a = \frac{d \ln(k_{\text{col}})}{d(1/RT)} = E_c + \frac{1}{2}RT \quad (5.18)$$

The expressions (5.16)–(5.18) were first applied to bimolecular gas phase reactions by M. Trautz (1916) and W. C. McC. Lewis (1924). The terms in d_{AB} and μ in eq. (5.17) generally compensate each other, such that, if we exclude the geometric factor g , in many cases $\log A = 10.5 \pm 0.5$, with A given in $\text{dm}^3 \text{mol}^{-1} \text{sec}^{-1}$. Steric hindrance, caused by the presence of bulky groups in the positions adjacent to the point of attack, is seen mainly through an increase in the activation energies of reactions and not through a decrease in the frequency of effective collision. Thus, the simple collision theory does not lead to significant correlations between the changes in structures and the calculated values for A . Some authors have refined this theory by defining an entropy of activation for the molecular collisions, leading to

$$A = g\pi d_{AB}^2 \sqrt{\frac{8RT}{\pi\mu}} \exp(\Delta S^*/R) \quad (5.19)$$

The introduction of this extra term in the expression for the pre-exponential factor may explain values much less than those determined by the frequency of collisions. However, as in most situations it is not easy to calculate this entropy of activation, this new term is only of limited use.

The numerical value of the collision theory value rate constant, previously calculated for the $\text{NO}_2 + \text{CO}$ reaction ($3.11 \times 10^{11} \text{ dm}^3 \text{ mol}^{-1} \text{ sec}^{-1}$) corresponds to the typical values calculated for the pre-exponential factors of gas-phase

bimolecular reactions. Dividing this value by the molar volume of an ideal gas at standard temperature and pressure ($22.421 \text{ dm}^3 \text{ mol}^{-1}$), we obtain a relaxation rate, which is approximately $(p\tau)^{-1} = 10^{10} \text{ atm}^{-1} \text{ sec}^{-1}$ at 273K. This implies that the mean free time between collisions of molecules of an ideal gas is 0.1 nsec, and that the corresponding collision frequency is $\tau_{\text{coll}}^{-1} \approx 10^{10} \text{ sec}^{-1}$. Some caution must be made in using these values, since molecules interact with a range of velocities and instantaneous inter-molecular distances, such that there is no single collision frequency, but there is a distribution of time intervals between collisions. This distribution can be given in terms of a Poisson function in n

$$P(n) = e^{-\gamma} \frac{\gamma^n}{n!} \quad (5.20)$$

where the mean value of n is $\langle n \rangle = \gamma = T/\tau_{\text{coll}}$, and T is the number of collisions per unit time. With the same caveat on the distribution of time intervals between collisions, it is instructive to calculate the mean free path length between collisions

$$\lambda = \frac{\text{distance}}{\#\text{ of collisions}} = \frac{\text{distance/time}}{\#\text{of collisions/time}} = \bar{v}\tau_{\text{coll}} \quad (5.21)$$

Given eq. (5.12) and the collision frequency, the mean free path length between collisions at standard temperature and pressure is 10^{-7} m ($0.1 \mu\text{m}$).

The simple collision theory treatment shows the basic elements for a bimolecular rate constant: we need a collision to occur, a certain critical energy has to be exceeded and the particles involved in the collision have to have the correct relative orientations.

5.2 Improved collision theory

Two implicit approximations were considered in the simple collision theory, one related with the orientation and the other one with the energy of the reactants. Two additional approximations need to be addressed to improve the collision theory: (i) molecules are not hard spheres and the collision cross section is not simply related to the sum of their radii; (ii) molecules in different quantum states (e.g., different vibrational or rotational quantum number) may behave differently. We postpone the discussion on the quantum states to the section on trajectories, and start by addressing the use of more realistic cross sections.

Instead of assuming hard sphere behaviour, we can refine the collision theory by using cross sections calculated on the basis of microscopic interaction potentials of species A and B during their collision, $\sigma(v)$, which depend on their relative velocity v . The rate of conversion of A into products for a given v is then, after eq. (5.10),

$$k(v) = \sigma(v)v \quad (5.22)$$

Averaging over the speed distribution $f(v,T)$, yields the fundamental equation for improved collision theories

$$k(v) = \int_0^\infty v\sigma(v)f(v, T)dv \quad (5.23)$$

The Maxwell distribution of velocities, eq. (1.10), offers the speed distribution that can be introduced in the equation above to give

$$k_{v,j} = 4\left(\frac{\mu}{2\pi k_B T}\right)^{3/2} \int_0^\infty v^3 \sigma_{v,j}(\varepsilon_T) \exp\left(-\frac{\mu v^2}{2k_B T}\right) dv \quad (5.24)$$

We can transform velocities into translational energies according to

$$\begin{aligned} \varepsilon_T &= \frac{1}{2}\mu v^2 \\ v &= \left(\frac{2\varepsilon_T}{\mu}\right)^{1/2} \\ \frac{dv}{d\varepsilon_T} &= \left(\frac{2}{\mu}\right)^{1/2} \frac{1}{2} \left(\frac{1}{\varepsilon_T}\right)^{1/2} = \left(\frac{1}{2\mu}\right)^{1/2} \left(\frac{1}{\varepsilon_T}\right)^{1/2} \\ dv &= \left(\frac{1}{2\mu}\right)^{1/2} \left(\frac{1}{\varepsilon_T}\right)^{1/2} d\varepsilon_T \end{aligned} \quad (5.25)$$

which give

$$k(T) = \left(\frac{1}{\pi\mu}\right)^{1/2} \left(\frac{2}{k_B T}\right)^{3/2} \int_{\varepsilon_c}^\infty \varepsilon_T \sigma(\varepsilon_T) \exp\left(-\frac{\varepsilon_T}{k_B T}\right) d\varepsilon_T \quad (5.26)$$

where the integration from ε_c to ∞ takes into account that the reaction can only occur if the translational energy is higher than a certain critical value. The function $\exp[-\varepsilon_T/(k_B T)]\varepsilon_T$ describes the fraction of molecules with energy ε_T .

Eq. (5.26) can be applied using realistic microscopic interaction potentials, but the solutions are rather evolved. We will show how it can be used using two simple models: the hard sphere model and the line-of-centres model.

The reactive cross section for the hard sphere model is illustrated in Figure 5.3 and can be written as

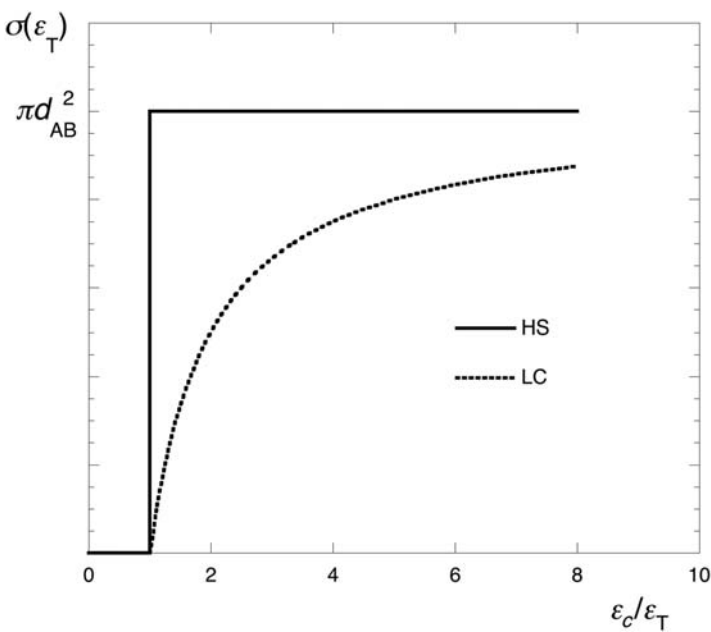
$$\sigma_{HS}(\varepsilon_T) \begin{cases} \pi d_{AB}^2 & \varepsilon_T > \varepsilon_c \\ 0 & \varepsilon_T < \varepsilon_c \end{cases} \quad (5.27)$$

which expresses the approximation that collisions with a translational energy below a certain critical energy will not be reactive. Inserting eq. (5.27) in eq. (5.26),

$$k_{HS}(T) = \left(\frac{1}{\pi\mu}\right)^{1/2} \left(\frac{2}{k_B T}\right)^{3/2} \int_{\varepsilon_c}^\infty \varepsilon_T \pi d_{AB}^2 \exp\left(-\frac{\varepsilon_T}{k_B T}\right) d\varepsilon_T \quad (5.28)$$

and using the standard integral

$$\int x e^{ax} dx = \frac{e^{ax}}{a^2} (ax - 1) \quad (5.29)$$

**FIGURE 5.3**

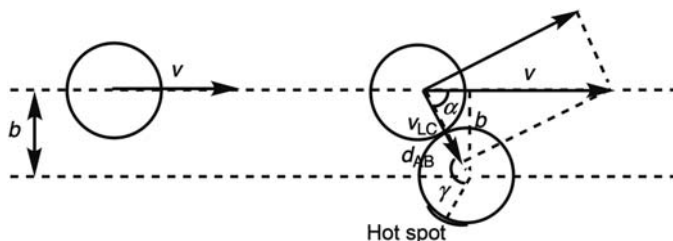
Reactive cross sections for the hard sphere model (full line) and for the line-of-centres model (dashed line).

we obtain

$$\begin{aligned}
 k_{\text{HS}}(T) &= \left(\frac{1}{\pi\mu} \right)^{1/2} \left(\frac{2}{k_B T} \right)^{3/2} \pi d_{AB}^2 (k_B T)^2 \exp\left(-\frac{\varepsilon_T}{k_B T}\right) \left(-\frac{\varepsilon_T}{k_B T} - 1 \right) \Big|_{\varepsilon_c}^\infty \\
 &= \pi d_{AB}^2 \left(\frac{8k_B T}{\pi\mu} \right)^{1/2} \left(1 + \frac{\varepsilon_c}{k_B T} \right) \exp\left(-\frac{\varepsilon_c}{k_B T}\right)
 \end{aligned} \quad (5.30)$$

It is important to note that this is different from the expression obtained with the simple collision theory, eq. (5.16). The reason for this difference can be best understood with the line-of-centres model.

Angular momentum must be conserved in all collisions. As a consequence, not the entire energy of collisions between hard spheres is available for reaction. Figure 5.4 illustrates a collision between hard spheres with a velocity component along the line-of-centres v_{LC} and *impact parameter* b . When we have a central (head-on) collision ($b = 0$), all the energy is available, $\varepsilon_{LC} = \varepsilon_T$, and the collision is most effective. However, when $b = d_{AB}$, the translational

**FIGURE 5.4**

Component of the velocity along the line-of-centres, v_{LC} , and identification of a “hot spot,” or preferential orientation, for reaction.

energy is no longer available for reaction, $\varepsilon_{LC} = 0$. Trigonometry gives $v_{LC} = v \cos(\alpha)$, or

$$\begin{aligned} v_{LC}^2 &= v^2 \cos^2 \alpha \\ &= v^2 (1 - \sin^2 \alpha) \\ &= v^2 \left(1 - \frac{b^2}{d_{AB}^2} \right) \end{aligned} \quad (5.31)$$

Hence the component of the translational energy along the line-of-centres is

$$\varepsilon_{LC} = \varepsilon_T \left(1 - \frac{b^2}{d_{AB}^2} \right) \quad (5.32)$$

The value of ε_{LC} decreases when b increases. For a sufficiently large value of b , the value of ε_{LC} becomes smaller than the critical energy required for reaction, $\varepsilon_{LC} < \varepsilon_c$. This limit can be obtained from the condition

$$\varepsilon_{LC} = \varepsilon_T \left(1 - \frac{b^2}{d_{AB}^2} \right) \geq \varepsilon_c \quad (5.33)$$

or

$$b^2 \leq d_{AB}^2 \left(1 - \frac{\varepsilon_T}{\varepsilon_c} \right) = b_c^2 \quad (5.34)$$

and the line-of-centres cross section becomes

$$\sigma_{LC}(\varepsilon_T) = \pi b_c^2 = \pi d_{AB}^2 \left(1 - \frac{\varepsilon_c}{\varepsilon_T} \right) \quad (5.35)$$

or

$$\sigma_{LC}(\varepsilon_T) = \begin{cases} \pi d_{AB}^2 \left(1 - \frac{\varepsilon_c}{\varepsilon_T} \right) & \varepsilon_T > \varepsilon_c \\ 0 & \varepsilon_T < \varepsilon_c \end{cases} \quad (5.36)$$

The dependence of ε_T on ε_c is illustrated in Figure 5.3.

The rate constant for the line-of-centres model is obtained inserting eq. (5.36) in eq. (5.26),

$$\begin{aligned} k_{LC}(T) &= \left(\frac{1}{\pi\mu}\right)^{1/2} \left(\frac{2}{k_B T}\right)^{3/2} \int_{\varepsilon_c}^{\infty} \varepsilon_T \pi d_{AB}^2 \left(1 - \frac{\varepsilon_c}{\varepsilon_T}\right) \exp\left(-\frac{\varepsilon_T}{k_B T}\right) d\varepsilon_T \\ &= \left(\frac{1}{\pi\mu}\right)^{1/2} \left(\frac{2}{k_B T}\right)^{3/2} \pi d_{AB}^2 \int_{\varepsilon_c}^{\infty} (\varepsilon_T - \varepsilon_c) \exp\left(-\frac{\varepsilon_T}{k_B T}\right) d\varepsilon_T \end{aligned} \quad (5.37)$$

which yields upon integration

$$k_{LC}(T) = \pi d_{AB}^2 \left(\frac{8k_B T}{\pi\mu}\right)^{1/2} \exp\left(-\frac{\varepsilon_c}{k_B T}\right) \quad (5.38)$$

It is interesting to note that the line-of-centres modes gives the same expression for the rate constant as the simple collision theory, eq. (5.16), when the geometric factor is included in eq. (5.38).

A convenient method to include the geometric factor in the rate constant is to consider that the sphere representing one of the reactants has a “hot spot,” or reactive centre, at a certain angle γ with the line of centres, as shown in Figure 5.4. The reaction threshold energy then becomes angle dependent

$$\varepsilon_c^* = \varepsilon_c + \varepsilon'(1 - \cos \gamma) \quad \text{with} \quad \begin{cases} \varepsilon_c^* = \varepsilon_c & \text{for } \gamma = 0 \\ \varepsilon_c^* > \varepsilon & \text{for } \gamma \neq 0 \end{cases} \quad (5.39)$$

This approach can explain geometric factors in the range $1 \leq g \leq 0.01$.

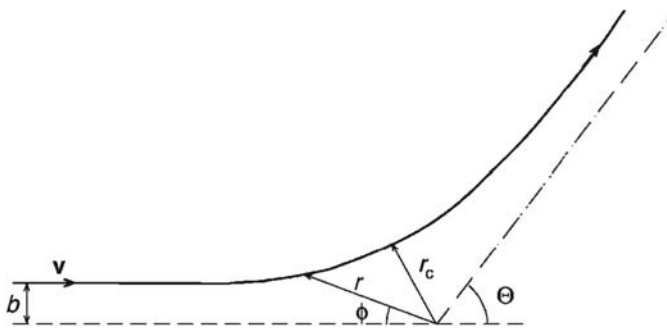
The improvements of collision theory discussed above did not consider the general case of collision between molecules in different quantum states. This will be further discussed later, in the context of trajectory calculations.

5.3 Collision cross section

Equation (5.23) reveals the importance of collision cross sections in reaction rate constants calculations. In order to further understand the role of $\sigma(v)$, we will start by treating the simpler situation of an elastic collision between two bodies subjected to a central force, which only leads to scattering.

The collision of these two bodies can be seen by a system of coordinates based on the centre of mass (Figure 5.5). In the case of a non-central collision, the kinetic energy has “translational” and “rotational” components. The total energy in centre-of-force coordinates is

$$E = \frac{1}{2} \mu \left(\frac{dr}{dt}\right)^2 + \frac{1}{2} \mu v_{\text{radial}}^2 + V(r) \quad (5.40)$$

**FIGURE 5.5**

Classical trajectory for velocity v and impact parameter b , with deflection angle θ , following a system of coordinates based on the centre of mass. The classical turning point is r_c .

Given the relation $\cos \phi = b/r = v_{\text{radial}}/v$, where v is the relative incident velocity, the equation above can be written

$$E = \frac{1}{2} \mu \left(\frac{dr}{dt} \right)^2 + \frac{1}{2} \mu \frac{v^2 b^2}{r^2} + V(r) \quad (5.41)$$

Given the angular velocity

$$\omega = \frac{d\phi}{dt} = \frac{v_{\text{radial}}}{r} = \frac{vb}{r^2} \quad (5.42)$$

and the definition of orbital angular momentum

$$L = I\omega = \mu r^2 \frac{vb}{r^2} = \mu vb \quad (5.43)$$

Eq. (5.41) can also be written

$$E = \frac{1}{2} \mu \left(\frac{dr}{dt} \right)^2 + \frac{L^2}{2\mu r^2} + V(r) \quad (5.44)$$

From the aforementioned equations, we obtain

$$d\phi = \frac{L}{\mu r^2} dt \quad (5.45)$$

and from eq. (5.44)

$$dr = - \left\{ \frac{2}{\mu} \left[E - V(r) - \frac{L^2}{2\mu r^2} \right] \right\}^{1/2} dt \quad (5.46)$$

or

$$dt = - \left\{ \frac{2}{\mu} \left[E - V(r) - \frac{L^2}{2\mu r^2} \right] \right\}^{-1/2} dr \quad (5.47)$$

Now, we can write

$$\begin{aligned}\phi(t) &= \int_{-\infty}^t \left(\frac{L}{\mu r^2} \right) dt \\ &= - \int_{\infty}^r \frac{L/\mu r^2}{\left\{ \frac{2}{\mu} \left[E - V(r) - \frac{L^2}{2\mu r^2} \right] \right\}^{1/2}} dr\end{aligned}\quad (5.48)$$

and use the relationship $L = \mu v b = b(2\mu E)^{1/2}$ to obtain

$$\phi(t) = \pm b \int_{\infty}^r \frac{dr}{r^2 \left[1 - \frac{b^2}{r^2} - \frac{V(r)}{E} \right]^{1/2}} \quad (5.49)$$

The sign must be chosen to agree with that of the radial velocity: that is positive for the species leaving and negative for those approaching.

For any collision, there will always be a maximum approach distance r_c for which $r(t)$ has its minimum value. In this classical turning point all the initial kinetic energy is converted into potential energy. It is convenient to define $t = 0$ for $r(t) = r_c$ and $\phi(0) = \phi_c$. The complete classical trajectory can be determined by integrating eq. (5.49) from infinity to r_c and then from r_c forward. However, it is unnecessary to follow the trajectory with this detail when we are only observing what happens after the collision. In this case, it is sufficient to know the total deflection, θ . As shown in Figure 5.5, this deflection is given by

$$\begin{aligned}\Theta(E, b) &= \pi - 2\phi_c \\ &= \pi - 2b \int_{r_c}^{\infty} \frac{dr}{r^2 \left[1 - \frac{b^2}{r^2} - \frac{V(r)}{E} \right]^{1/2}}\end{aligned}\quad (5.50)$$

For us to analyse the behaviour of the angle of deflection as a function of the energy and of the impact parameter, we have to define the potential. In the simplest case of the potential of hard spheres

$$\begin{aligned}V(r) &= 0, \quad r > d_{AB} \\ V(r) &= \infty, \quad r \leq d_{AB}\end{aligned}\quad (5.51)$$

it is obvious that independent of the energy of collision $r_c = d_{AB}$. Under these conditions, the integration of eq. (5.50) leads to

$$\begin{aligned}\Theta(E, b) &= \pi - 2b \int_{d_{AB}}^{\infty} \frac{dr}{r^2 \left[1 - \frac{b^2}{r^2} - 0 \right]^{1/2}} \\ &= \pi - 2b \int_{d_{AB}}^{\infty} \frac{dr}{r \sqrt{r^2 - b^2}} \\ &= \pi - 2b \left\{ \frac{1}{b} \cos^{-1} \left(\frac{b}{r} \right) \right\}_{r=d_{AB}}^{r=\infty} \\ &= \pi - 2 \left[\cos^{-1} \left(\frac{b}{\infty} \right) - \cos^{-1} \left(\frac{b}{d_{AB}} \right) \right] \\ &= \pi - \pi + 2 \cos^{-1} \left(\frac{b}{d_{AB}} \right) = 2 \cos^{-1} \left(\frac{b}{d_{AB}} \right)\end{aligned}\quad (5.52)$$

For impact parameters greater than the hard sphere diameter d_{AB} , eq. (5.52) requires the reciprocal of the cosine of a number greater than one, which is not possible. For this case, $\theta(b) = 0$. For impact parameters less than d_{AB} , the value of $\theta(b)$ varies between 0 and π (Figure 5.6).

A potential energy function that represents the interaction between two bodies in a more realistic form is the Lennard-Jones potential

$$V(r) = 4\epsilon \left[\left(\frac{\sigma_{LJ}}{r} \right)^{12} - \left(\frac{\sigma_{LJ}}{r} \right)^6 \right] \quad (5.53)$$

shown in Figure 5.7, where the attractive term in r represents the dispersion forces as well as dipole-dipole and dipole-induced dipole interactions. The purely empirical repulsive part was chosen from adjustment to a wide range of atomic potentials. The deflection function of this potential can be calculated using

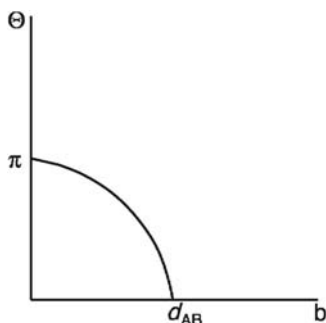


FIGURE 5.6

Deflection function $\theta(b)$ for the hard sphere potential of diameter d_{AB} .

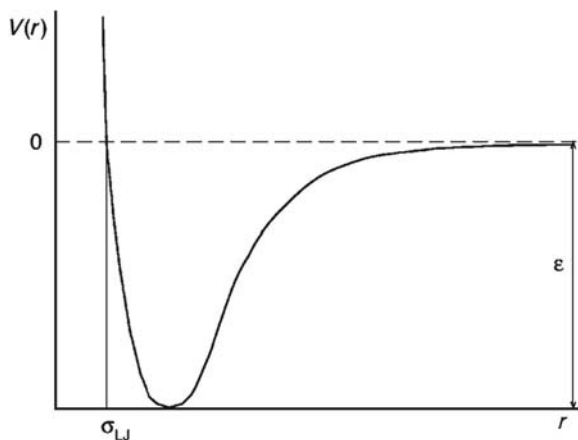


FIGURE 5.7

Lennard-Jones potential, showing the minimum at $r_m = 2^{1/6}/\sigma_{LJ}$ with an energy $V(r_m) = -\epsilon$.

eq. (5.50). The arithmetical treatment of this solution is very complicated. In Figure 5.8, we show only the results in terms of the reduced impact parameter $b^* = b/\sigma_{\text{LJ}}$ for a range of reduced energies $E^* = E/\varepsilon$. This figure shows three regions with a different dispersive behaviour.

For collisions that are almost head-on ($b \rightarrow 0$), the deflection function is very similar to that of collision between hard spheres (Figure 5.6), because the impinging particle passes through the attractive part of the potential and is repelled by the wall given by r^{-12} . This behaviour of specular reflection can be found for scattering with almost all potentials.

For very large-impact parameters, the dispersion is also similar to that for the hard sphere, that is, the impinging particle is hardly scattered in its trajectory. This is due to the rapid decay of the attractive part of the potential to zero. We should note that this limit is reached more rapidly when the energy of the incident particle increases.

In the intermediate region of b^* and E^* we find a new behaviour. The deflection angles can take considerably negative values, even less than $-\pi$. This results from the strong interaction of the incident particle with the attractive part of the Lennard-Jones potential, as is shown in Figure 5.9.

The above discussion focussed on the trajectory of a single event, specified by an initial energy and an impact parameter. From the practical point of view,

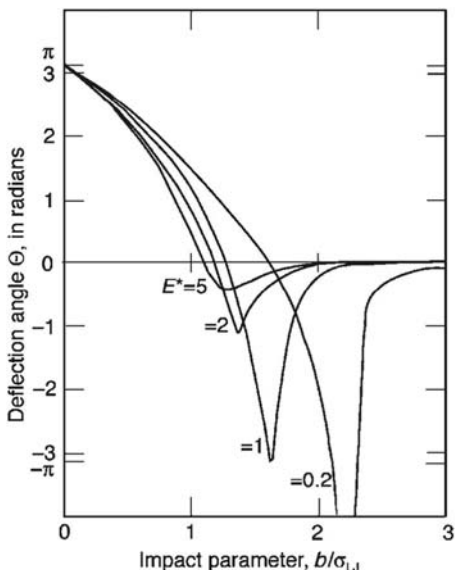
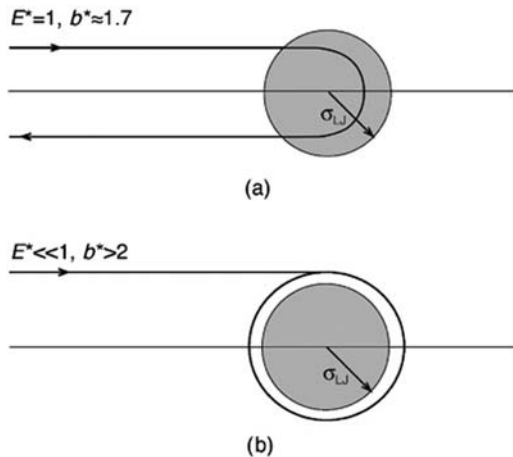


FIGURE 5.8

Deflection function $\theta(E, b)$ for the Lennard-Jones potential. The minima correspond to the “rainbow” angle discussed in the text.

**FIGURE 5.9**

Trajectories in the scattering by a Lennard-Jones potential: (a) “rainbow” scattering, $\theta(E,b) = -\pi$, so called because of the similarity between its mathematical description and that of light scattering in the atmosphere, which leads to the formation of rainbows. (b) Example of a collision captures in an orbit, which may eventually be unstable and lead to separation of the particles.

although it is possible to accurately define the initial energy in a molecular beam experiment, it is impossible to isolate a single impact parameter. Thus, the experimental results are presented in terms of collision cross sections, as shown in Figure 5.10. In the case of elastic scattering, we can distinguish between the total cross section $\sigma(E)$ and the differential cross section $d\sigma/d\Omega$. This latter parameter is defined as the intensity of scattering per solid angle unit of measurement, θ , termed the *dispersion angle*. As it is impossible to distinguish positive and negative deflections, θ is given experimentally as the modulus of the magnitude of the deflection θ of eq. (5.50) between the limits indicated:

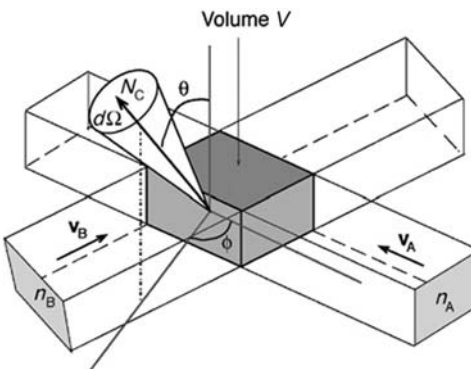
$$\theta = |\Theta|, \quad 0 < \theta < \pi \quad (5.54)$$

Figures 5.8 and 5.9 show that $\theta(E,b)$ varies continuously with b . Thus, the trajectories with an impact factor $b + db$ define an area $2\pi b \, db$ and are deflected through a solid angle corresponding to $2\pi \sin \theta \, d\theta$. The differential cross section can now be written as

$$\frac{d\sigma}{d\Omega} = I(\theta, E) = \left| \frac{2\pi b \, db}{2\pi \sin \theta \, d\theta} \right| = \left| \frac{b}{\sin \theta \frac{d\theta}{db}} \right| \quad (5.55)$$

and the total elastic section is

$$\sigma(E) = \int \frac{d\sigma}{d\Omega} d\Omega = 2\pi \int_0^\pi I(\theta, E) \sin \theta \, d\theta \quad (5.56)$$

**FIGURE 5.10**

Definition of the scattering process $A + B \rightarrow C + D$ within laboratory coordinates. The density of the particles A and B is given by n_A and n_B in units of number of cubic centimetre; $v = |v_A - v_B|$ is the relative velocity between the particles A and B; experimentally it is given as number dN_c of molecules C per unit time which emerge within the solid angle $d\Omega$ defined by the angles θ and ϕ of the centre of scattering, $d\Omega = \sin \theta d\theta d\phi$; V is the volume defined by the intersection of the molecular beams A and B.

The use of [eqs. \(5.50\), \(5.55\)](#) and [\(5.56\)](#) to show the deduction of the cross section from the form of the potential $V(r)$, can be easily obtained for the hard-sphere potential case. From [eq. \(5.52\)](#), for all the trajectories for which there is scattering

$$b = d_{AB} \cos\left(\frac{\theta}{2}\right) \quad (5.57)$$

Substituting in [eq. \(5.55\)](#), we obtain $I(\theta, E) = \frac{1}{4} d^2$ and, substituting in [eq. \(5.56\)](#) we get

$$\sigma(E) = 2\pi \int_0^\pi \frac{1}{4} d^2 \sin \theta d\theta = \pi d^2 \quad (5.58)$$

The significance of this result is that the scattering intensity is equal in all directions and is independent of the energy. The total cross section is simply the area of the cross section presented by the sphere. This result was used before, [eq. \(5.27\)](#), but the methods employed here illustrates that it is possible to obtain a cross section knowing the potential.

Ion-molecule and ion-atom reactions are governed by point-charge-induced-dipole interactions with an attractive potential

$$V_{\text{ion-dipole}} = -\frac{1}{2} \frac{\alpha_n e^2}{r^4} \quad (5.59)$$

where e is the elementary charge, α_n is the polarisability of the neutral molecule or atom. Langevin expressed the attractive potential between a point charge (the ion) and a point-polarisable neutral species (the molecule or atom), as

$$V_L(r) = -\frac{1}{2} \frac{\alpha_n e^2}{r^4} + E_T \left(\frac{b}{r} \right)^2 \quad (5.60)$$

Although there is no potential energy barrier in ion-molecule reaction, the second term of the potential energy in the expression above represents a centrifugal barrier that the reactive system must surmount. We found this term before in eqs. (5.40) and (5.41). The location of the maximum of the centrifugal barrier is given by $dV(r)/dr = 0$, which yields

$$r_c = \left(\frac{\alpha_n e^2}{E_T b^2} \right)^{1/2} \quad (5.61)$$

and the height of the barrier is $V_L(r_c) = \frac{1}{2} E_T^2 b^4 / (\alpha e^2)$. Classically, the reaction can only occur if $E_T \geq V_L(r_c)$. Taking the equality between these quantities, we can calculate the critical impact parameter at which the reaction can occur

$$b_c = \left(\frac{2\alpha_n e^2}{E_T} \right)^{1/4} \quad (5.62)$$

and obtain the expression for the Langevin cross section

$$\sigma_L = \pi b_c^2 = \pi \left(\frac{2\alpha_n e^2}{E_T} \right)^{1/2} \quad (5.63)$$

Following the procedure described before for the hard sphere and line-of-centres models, this cross section can be inserted in eq. (5.26) to obtain a very simple solution for the Langevin collisional rate constant

$$k_L = 2\pi e \left(\frac{\alpha_n}{\mu} \right)^{1/2} \quad (5.64)$$

where μ is the reduced mass of the ion-molecule pair. Typically, it is experimentally found that $k_L \approx 100 k_{HS}$.

A chemical reaction cannot be described by only two particles interacting. A minimum of three particles is necessary. Unfortunately, for such three-bodied systems, it is not possible to obtain analytical solutions and it becomes necessary to use numerical methods. Among these, the Monte Carlo method assumes particular relevance for the calculation of classical trajectories using random sampling.

5.4 Calculation of classical trajectories

By knowing the PES for a chemical reaction, it is possible to solve the classical equations of motion for a collision on this surface. In the context of classical mechanics, the movement of particles is described by Newton's second law:

$$\mathbf{F} = \frac{d\mathbf{P}}{dt} = m\mathbf{a} \quad (5.65)$$

where \mathbf{F} is the force acting on the particle, \mathbf{P} its linear momentum and \mathbf{a} the acceleration. In the calculation of trajectories we normally solve the Hamiltonian equations for each coordinate Q_j and its conjugate momentum $P_j = m_j dQ_j/dt$. For a system of N particles with generalised coordinates (q_1, q_2, \dots, q_k) , we can establish $2k$ Hamiltonian equations. When we know the initial state of the system $(q_1^0, q_2^0, \dots, q_k^0, p_1^0, p_2^0, \dots, p_k^0)$, its time evolution will be determined through the solution of these $2k$ first-order differential equations.

The simplest example of a classical trajectory is the collinear collision complex A + BC, for which there are only two independent coordinates: the A–B distance (r_1) and the B–C distance (r_2). However, even in such a simple system, a complication is introduced by transforming from internal molecular coordinates to Cartesian space. This complication can be appreciated by writing the complete Hamiltonian of the system:

$$\begin{aligned} \mathbf{H} &= T + V \\ &= \frac{1}{2m_A + m_B} \left(\frac{dr_1}{dt} \right)^2 + \frac{1}{2(m_A + m_B + m_C)} \left(\frac{dr_2}{dt} + \frac{m_A}{m_A + m_B} \frac{dr_1}{dt} \right) + V(r_1, r_2) \\ &= \frac{1}{2(m_A + m_B + m_C)} \left[m_A(m_B + m_C) \left(\frac{dr_1}{dt} \right)^2 + 2m_A m_B \frac{dr_1}{dt} \frac{dr_2}{dt} \right. \\ &\quad \left. + m_C(m_A + m_B) \left(\frac{dr_2}{dt} \right)^2 \right] + V(r_1, r_2) \end{aligned} \quad (5.66)$$

The first term in kinetic energy represents the motion of A relative to B, while the second one represents the motion of AB relative to C. When the equation is expanded, we are left with a cross term, $dr_1/dt dr_2/dt$. This term must be eliminated if the movement of any representative point on the PES occurs without friction. It is possible to do this by making a new transformation of the coordinates into a mass-weighted system, which diagonalises the kinetic energy of the system. This transformation is shown in [Figure 5.11](#). The angle between the two coordinate systems [2] is given by

$$\sin \theta = \left[\frac{m_A m_C}{(m_A + m_B)(m_B + m_C)} \right]^{1/2} \quad (5.67)$$

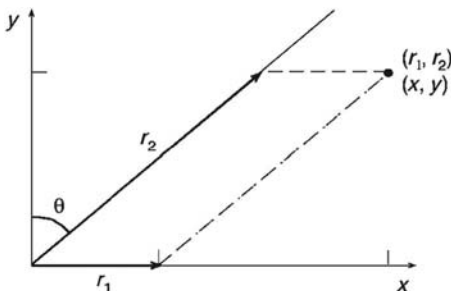


FIGURE 5.11

Transformation of Cartesian coordinates into mass-weighted coordinates.

The Hamiltonian then becomes

$$\mathbf{H} = \frac{1}{2(m_A + m_B + m_C)} \left[\left(\frac{dx}{dt} \right)^2 + \left(\frac{dy}{dt} \right)^2 \right] + V(r_1, r_2) \quad (5.68)$$

The calculation of the trajectory for this atom-diatom system requires the specification of 12 initial conditions, even after the separation of the three coordinates of motion by using the centre of mass. The six independent coordinates, together with the six respective conjugates, can be written (using the notation of Figure 5.12)

$$\begin{aligned} Q_1^0 &= R_{BC} \sin \theta \cos \phi & P_1^0 &= -P(\sin \phi \cos \eta - \cos \phi \cos \theta \sin \eta) \\ Q_2^0 &= R_{BC} \sin \theta \sin \phi & P_2^0 &= -P(\cos \phi \cos \eta - \sin \phi \cos \theta \sin \eta) \\ Q_3^0 &= R_{BC} \cos \theta & P_3^0 &= -P \sin \theta \sin \eta \\ Q_4^0 &= 0 & P_4^0 &= 0 \\ Q_5^0 &= b & P_5^0 &= 0 \\ Q_6^0 &= -\sqrt{r^2 - b^2} & P_6^0 &= \mu_{A,BC} v_r^0 \end{aligned} \quad (5.69)$$

where P is the rotational angular momentum $J(J+1)h^2/R^2$, the angles θ , ϕ and η specify the initial orientation of the molecule BC in the space and v_r^0 is the initial relative velocity. The application of the Monte Carlo method to the solution of the Hamiltonian equations of the system corresponds effectively to the calculation of a set of trajectories for which the initial conditions for each of the trajectories will be chosen at random.

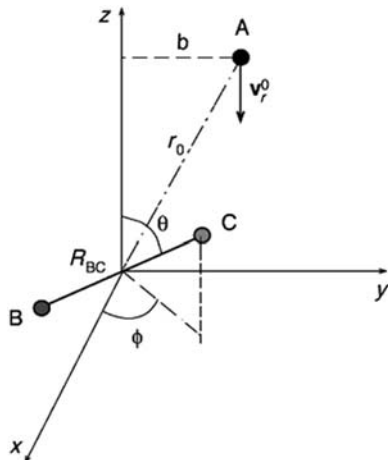


FIGURE 5.12

Classic coordinates for an atom diatom collision of the type $A + BC \rightarrow AB + C$; θ and ϕ are the angles of the polar spherical coordinates, R_{BC} the interatomic separation and the angle η specifies the plane of rotation of BC.

The fundamental parameter that is obtained in these calculations is the probability of reaction for any given relative initial velocity (i.e., initial reactive kinetic energy), roto-vibrational state of BC, impact parameter and orientation. In practice, this probability is defined as the ratio between the number of reactive trajectories and the total number of trajectories

$$P_{v,j}(v_r^0, b, \theta, \phi, R_{BC}, \eta) = \lim_{N \rightarrow \infty} \frac{N_R(v_r^0, b, \theta, \phi, R_{BC}, \eta)}{N_{\text{total}}(v_r^0, b, \theta, \phi, R_{BC}, \eta)} \quad (5.70)$$

which is only statistically correct when a very large number of trajectories have been followed. The reactive cross section, relative to the quantum state of BC, takes the following form:

$$\sigma_{v,j}(v_r^0) = \int_{b=0}^{b_{\max}} \int_{\theta=0}^{\pi} \int_{\phi=0}^{2\pi} \int_{R_{BC}=\rho_-}^{\rho_+} \int_{\eta=0}^{2\pi} P_{v,j}(v_r^0, b, \theta, \phi, R_{BC}, \eta) [H(\eta) d\eta] [G(R_{AB}) dR_{BC}] [\Phi(\phi) d\phi] [\Theta(\theta) d\theta] 2\pi b db \quad (5.71)$$

where ρ_- and ρ_+ are the interior and exterior turning points of the vibration, respectively, $G(R_{BC})$ the distribution function for R_{BC} , which depends on the roto-vibrational state of the molecule and its diatomic potential, and the normalised distribution functions of the angles take the following form:

$$\begin{aligned} \Theta(\theta) &= \frac{1}{2} \sin(\theta) \\ \Phi(\phi) &= \frac{1}{2\pi} \\ H(\eta) &= \frac{1}{2\pi} \end{aligned} \quad (5.72)$$

If we want to make a comparison between these cross sections and the experimental values for the reaction in thermal equilibrium, it is necessary to make first an average over the initial states (reactants) to obtain an expression that gives the rate of appearance of the product in a determined state, and then sum over all the states of the products to obtain the total rate of appearance of products. This procedure constitutes the basis of molecular dynamics. Normally, it is assumed that the molecular velocities are described by a Maxwell-Boltzmann distribution, and the specific rate constant is expressed relative to the quantum state of BC not in terms of the initial relative velocity v_r^0 , but in terms of the relative translational energy, $E_{\text{tr}} = \frac{1}{2} \mu_{A-BC}(v_r^0)^2$. Introducing eq. (1.10) in eq. (5.23) and transforming velocities into translational energies, we obtain

$$k_{v,j} = \left(\frac{2}{k_B T} \right)^{3/2} \left(\frac{1}{\pi \mu_{A-BC}} \right)^{1/2} \int_0^\infty \sigma_{v,j}(E_{\text{tr}}) \exp\left(-\frac{E_{\text{tr}}}{k_B T}\right) E_{\text{tr}} dE_{\text{tr}} \quad (5.73)$$

The total rate constant of the reaction is the average of $k_{v,j}$ weighted on the basis of the distribution of states (v,j)

$$k = \sum_v \sum_j F(v,j) k_{v,j} \quad (5.74)$$

where $F(v,j)$ is the normalised distribution function for the roto-vibrational states of BC

$$F(v,j) = \frac{(2j+1)\exp\left(-\frac{E_{v,j}}{k_B T}\right)}{Q} \quad (5.75)$$

with $E_{v,j}$ being the energy of the roto-vibrational state (v,j) and Q the corresponding roto-vibrational partition function

$$Q = \sum_v \sum_j (2j+1)\exp\left(-\frac{E_{v,j}}{k_B T}\right) \quad (5.76)$$

At the end of each trajectory, this is classified on the basis of the product of collision. However, other properties are equally important for the final statistical analysis, in particular the relative translational energy of the products,

$$E_{\text{tr}} = \frac{1}{2} \mu_{AB-C}(v_p)^2 \quad (5.77)$$

the scattering angle

$$\cos \theta_{\text{scatt}} = \frac{\mathbf{v}_p \cdot \mathbf{v}_R}{|\mathbf{v}_p| \cdot |\mathbf{v}_R|} \quad (5.78)$$

and the internal states of the products. The velocities indicated above refer to the relative velocities between the centres of mass of products and reactants. The angular momentum L and the moment of inertia I can be calculated from the coordinates and from the final momentum. Thus, it is possible to obtain an estimate for the vibrational and rotational energies from the following equations:

$$E_{\text{rot}} = \frac{L^2}{2I} \quad (5.79)$$

$$E_{\text{vib}} = E_{\text{int}} - E_{\text{rot}}$$

Calculations of trajectories provide details on both the state-to-state reactivity ($k_{v,j}$) and the energy distribution (translational, vibrational and rotational) of the products. The comparison between results of these calculations and data from molecular beam experiments allows one to obtain very detailed information on the PES of the reaction system. The most important role of the molecular collision theory is that of identifying the dominant characteristics of a given PES and extracting from these all the possible observable consequences.

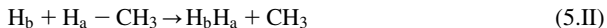
The complexity of the classical trajectory method is obvious. As the number of integrals involved increases with the number of atoms in the system, in practice the method is limited to tri- and tetra-atomic systems, always assuming that it is possible to obtain a realistic PES for these systems. Apart from this, the classical trajectory method has two intrinsic limitations: it does not consider either the zero-point energy (ZPE) or quantum mechanical tunnelling.

The ZPE of the reactants comes as one of the immediate consequences of energy quantisation in quantum mechanics. The energy of each vibrational mode is quantised and the ZPE is the quantity of energy of the lowest mode. However, the classical energy distribution is continuous for all degrees of freedom, such that the classical vibrational energy can have values much less than their quantum limit. Thus, even though the reactants are placed in their exact quantum states, during the dynamic evolution of the system the energies of the vibrational modes can decrease below the ZPE and form intermediates or products that violate the quantum restriction. This problem is particularly important for endothermic reactions, where the classical cross section can be much greater than that obtained by exact quantum calculations. A simple method of reducing the problem of the ZPE transformation in a reaction is to exclude trajectories that do not possess an internal energy equal to or greater than the ZPE in the statistical analysis. This procedure can, however, lead to deviations in the initial distributions of the dynamic variables.

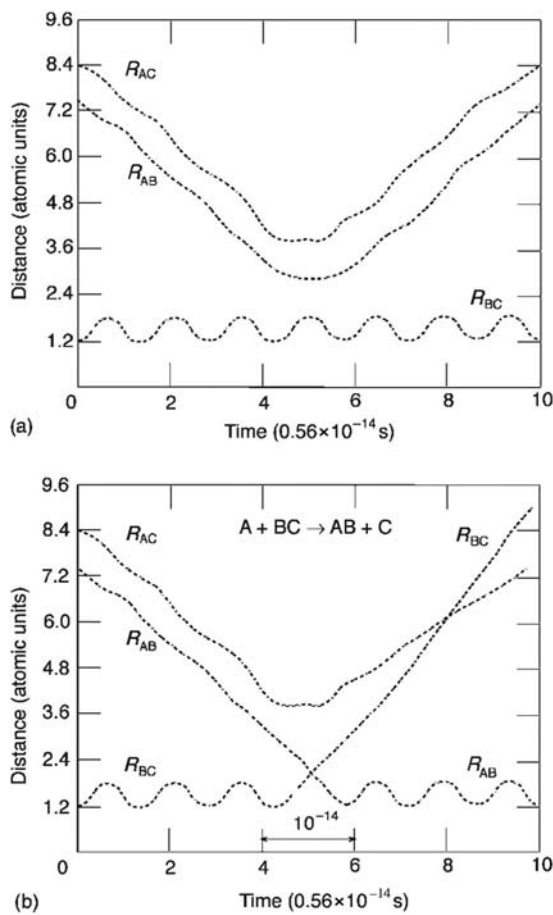
The effect of tunnelling concerns the passage of a particle through a barrier of energy greater than its kinetic energy. This means that chemical reactions can occur even though the system lacks sufficient energy to cross the reaction barrier through the minimum energy pathway. The effect of tunnelling is that the classical trajectory method underestimates the rate constant when the energy of the system is close to the classical threshold at which the reaction occurs. Other characteristics of the tunnel effect will be discussed in the next chapter.

The simplicity of the $\text{H} + \text{H}_2$ system allows us to calculate accurate PESs and use them in molecular dynamics. This system is very well characterised and it is known that there is compensation between the loss of ZPE and tunnelling. The classical trajectories calculated for this system therefore reveal some of the basic aspects of molecular dynamics.

[Figure 5.13](#) allows us to visualise the trajectories in terms of their time evolution while [Figure 5.14](#) shows a comparative analysis between the results of classical trajectories for the system $\text{H} + \text{H}_2$ and the results obtained by the simple collision theory (assuming hard spheres). In spite of the inherent difficulties of calculating PESs for polyatomic systems and the solution of the equations of motion for such surfaces, much effort is being devoted to extend molecular dynamics studies to such systems. [Figure 5.15](#) shows a PES [4] for the system



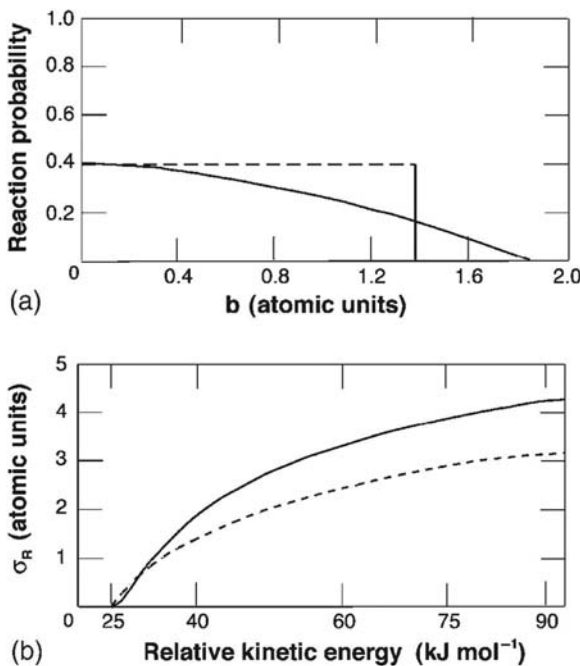
and classical trajectories calculated using the programme MARINER [5]. One of the images shows a reactive trajectory that passes very close to the saddle-point, while the other shows a non-reactive trajectory, which returns to the reactant valley after being reflected by the barrier.

**FIGURE 5.13**

Scattering trajectories ($J_1 = 0$, $v_1 = 0$, $v_r^0 = 1.32 \times 10^6 \text{ cm sec}^{-1}$) represented as changes in interatomic distance with time: (a) Non-reactive trajectory. (b) Reactive trajectory. The difference between the two trajectories appears to be due to a very small difference in the vibrational phase of the molecule BC. The crossing observed in (b) is due to the formation of rotationally excited products ($J' \approx 5$) [3].

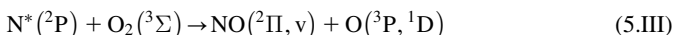
5.5 PES crossings

The scattering processes we have considered are characterised by taking place on a single electronic PES. Such processes are called adiabatic. However, if

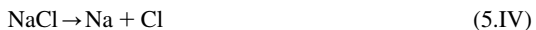
**FIGURE 5.14**

Analysis of classical trajectories on the PES for the system $\text{H} + \text{H}_2$: (a) the dashed line shows the results for simple collision theory using hard spheres with $b_{\max} = 0.98 \text{ \AA}$ and a steric factor $g = 0.4$, while the solid line shows a fit to the empirical function $P_R^\circ / \cos(\pi b / 2b_{\max})$ that approaches the value calculated for classical trajectories. (b) The solid line indicates the results of classical trajectory calculations and the dashed line that obtained using hard spheres, eq. (5.52) [3]. PES, Potential energy surface.

there are two electronic PESs, whose energies approach or cross at a particular point in configurational space, it is possible that a trajectory jumps from one PES to the other at this point. Such a chemical reaction involves a change in electronic PES and the reaction is said to be diabatic (or non-adiabatic). The most common examples of these processes involve electronically excited species, such as in the example



while other cases lead to the separation of an ion pair into atoms



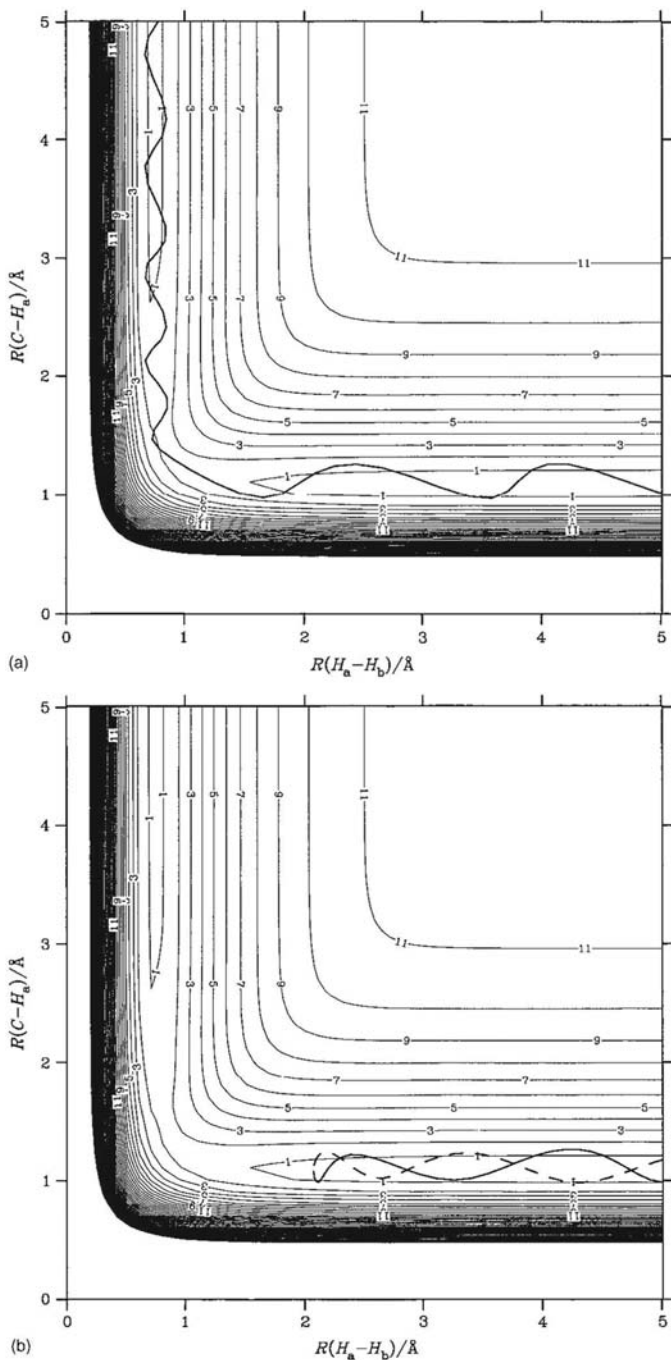


FIGURE 5.15

Classical trajectories on the PES indicated by mechanism (5.II). The contours have a separation $41.84 \text{ kJ mol}^{-1}$. The top shows a reactive trajectory while the bottom shows a non-reactive one. Trajectory calculations are courtesy of A.A.C.C. Pais. *PES*, Potential energy surface.

The interaction between PESs in diabatic reactions is shown in Figure 5.16.

The simplest description for the electronically diabatic processes was formulated independently by Landau and by Zener. Following the model of these authors, the probability of passing from one “diabatic” surface to the other, considered as unidimensional, in the avoided crossing region, is given by

$$P_{LZ} = \exp\left(-\frac{2\pi V_{12}^2}{\hbar v |s_1 - s_2|}\right) \quad (5.80)$$

where $v = dr/dt$ is the velocity at the crossing point r_0 , s_1 and s_2 the slopes $dV(r_0)/dr$ of the unperturbed surfaces and V_{12} half the energetic separation between the two surfaces at the point r_0 . When the coupling between the two surfaces is very small, $V_{12} = 0$, the system will go through the crossing point with unit probability, $P_{LZ} = 1$, and will evolve seamlessly from the higher energy diabatic surface to the lower energy diabatic surface. When the velocity at the crossing point approaches zero, then $P_{LZ} \rightarrow 0$ and the system will stay in the adiabatic surface (full lines in Figure 5.16). The probability of remaining on the adiabatic surface has a simple form when V_{12} is small and the expansion of the exponential may neglect all terms beyond that involving V_{12}^2 ,

$$1 - P_{LZ} = 1 - \exp\left(-\frac{2\pi V_{12}^2}{\hbar v |s_1 - s_2|}\right) \approx \frac{2\pi V_{12}^2}{\hbar v |s_1 - s_2|} \quad (5.81)$$

In Figure 5.16, this corresponds to a transition between $A^* + B$ to $A + B^*$ along a full line.

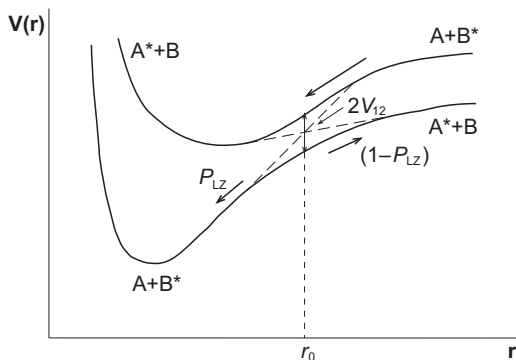
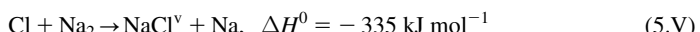


FIGURE 5.16

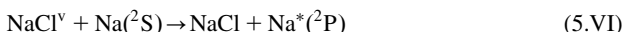
Interaction between two PESs, showing an electronically diabatic trajectory, which crosses the two PESs with a probability P_{LZ} from the higher energy surface to the lower energy surface, and stays on the lower energy surface with a probability $(1 - P_{LZ})$ when the reactants separate. *PES*, Potential energy surface.

5.6 Molecular dynamics

The first studies on molecular dynamics were made in the early 1930s by Michael Polanyi and co-workers. In these studies, very dilute flames and diffusional flames were used to study the reactions of alkali metals with halogens and halides in the vapour phase. In many cases, chemiluminescence was observed. For example, the reaction



produces a vibrationally excited molecule of sodium chloride (NaCl^{\vee}) which transfers its energy to a sodium atom. The vibrational energy content of NaCl^{\vee} is sufficiently high to produce an electronically excited sodium atom



which subsequently emits visible light as the well-known orange colour of the sodium D line



Evans and Polanyi put forward the idea that the PES of this system has the shape shown in Figure 5.17. The Na–Na bond is very long (3.1 Å) and the Na–Cl bond is formed by electron transfer at a distance much greater than the equilibrium length. This is an example of the *harpooning mechanism*, where one alkali atom tosses out its valence electron, hooks the

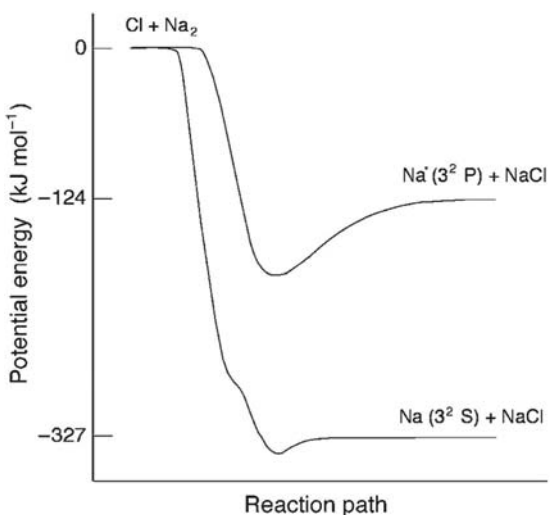


FIGURE 5.17

Attractive PES for the system $\text{Cl} + \text{Na}_2 \rightarrow \text{NaCl} + \text{Na}$ [6]. PES, Potential energy surface.

halogen atom and pulls it in with a Coulomb force. The $\text{Na}^+ - \text{Cl}^-$ bond that is formed is an ionic bond in which Na^+ , being a cation, has a very small radius. Following a small barrier (1.7 kJ mol^{-1}) on entering the PES, much of the exothermicity of the reaction will be liberated as vibrational energy of $\text{Na}^+ - \text{Cl}^-$. This mechanism explains why 85% of the collisions of Cl and Na result in vibrationally excited NaCl. This type of surface is known as an *attractive surface*.

The harpooning mechanism is often encountered when an alkali atom attacks a covalent bond involving a halogen atom, and the covalent bond is converted in an ionic bond. The PES has the same features as those of [Figure 5.16](#), where the upper curve at long distances is now that of the ionic species $\text{M}^+ + \text{X}^-$, which correlates to the lower curve at short distance of the ionic bond M^+X^- , whereas the lower curve at long distance corresponds to the neutral species $\text{M} + \text{X}$. The crossing radius r_0 may be estimated from

$$\frac{e^2}{r_0} = I_{\text{P}}(\text{A}) - E_{\text{A}}(\text{BC}) \quad (5.82)$$

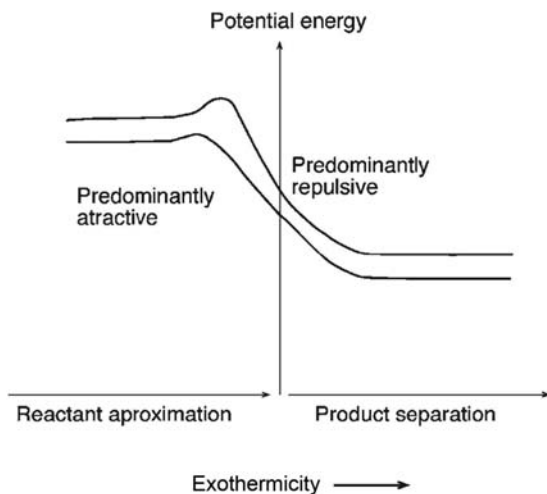
where $I_{\text{P}}(\text{A})$ represents the ionisation potential of the alkali atom and $E_{\text{A}}(\text{BC})$ is the electron affinity of the molecule with a halogen atom. This crossing radius is related to the size of the reaction cross section, which is very large ($>10 \text{ \AA}^2$) in these reactions.

It was only in the 1960s that the pioneering work of M. G. Evans, M. Polanyi and also of H. Eyring, was extended with the arrival of new techniques, which allowed experimental determination of energies of products, and the introduction of computers capable of effectively solving the equations of motion. The contributions of Dudley Herschbach, Yuan Lee and John Polanyi to the development of crossed molecular beams, in the case of the first two researchers, and of infrared chemiluminescence, in the case of the last one, led in 1986 to the award of the Nobel Prize in chemistry to these researchers.

Some experimental observations were rationalised by J. C. Polanyi in terms of localisation of the barrier in the PES topography and of the combinations of the masses involved. For example, the reactions



have repulsive PESs ([Figure 5.18](#)) because much of the energy is evolved as repulsion between the products. This liberation of repulsive energy produces a marked increase in the relative movements (i.e., translation) of the species when the combination of the masses is $\text{L} + \text{HH} \rightarrow \text{LH} + \text{H}$ (L corresponds to a light atom and H a heavy atom), while the same type of energy evolution produces a

**FIGURE 5.18**

Energy profiles along the reaction coordinate for predominantly attractive and predominantly repulsive PESs, with reactions occurring in the exothermic direction. *PESs*, Potential energy surfaces.

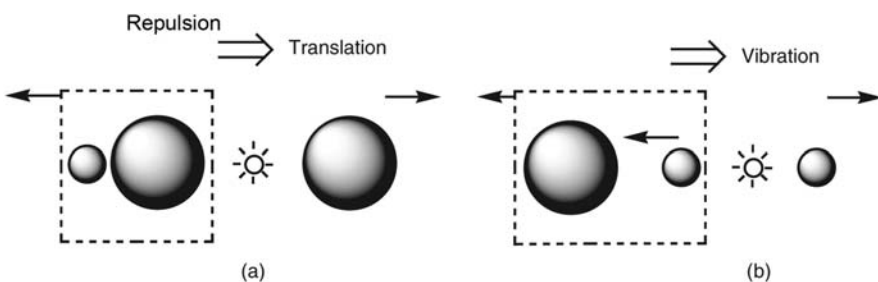
**FIGURE 5.19**

Illustration of two distinct dynamic behaviours on PES involving release of repulsive energy. The size of the spheres shows the relative masses. (a) Schematic for the system $\text{H} + \text{Cl}_2$. (b) Schematic for the system $\text{F} + \text{H}_2$. *PES*, Potential energy surface.

mainly internal motions (i.e., vibrations) in the products when the combination of masses is $\text{H} + \text{LL} \rightarrow \text{HL} + \text{L}$.

This process can be visualised through Figure 5.19 [7.8]. When the two heavy atoms repel, they are deflected with one of them carrying the light atom

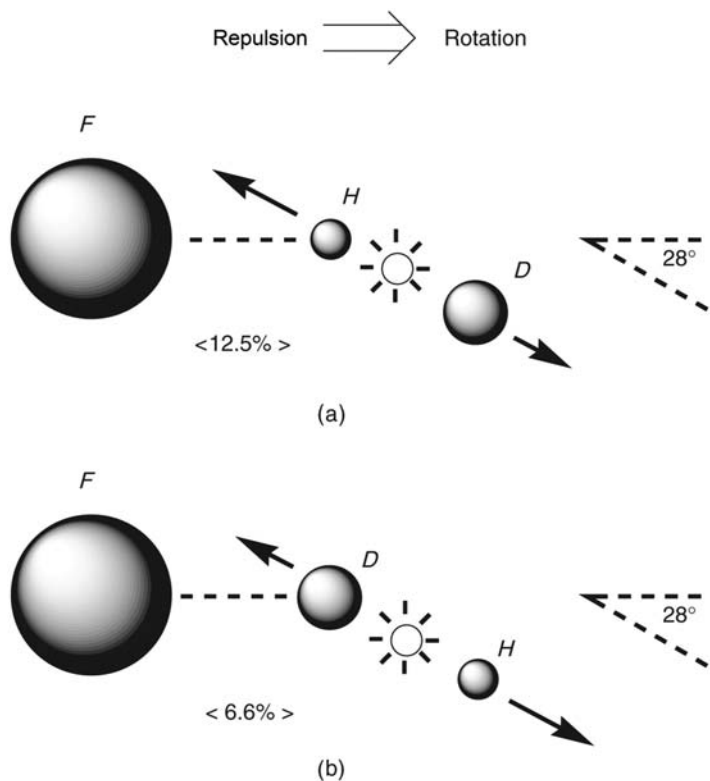
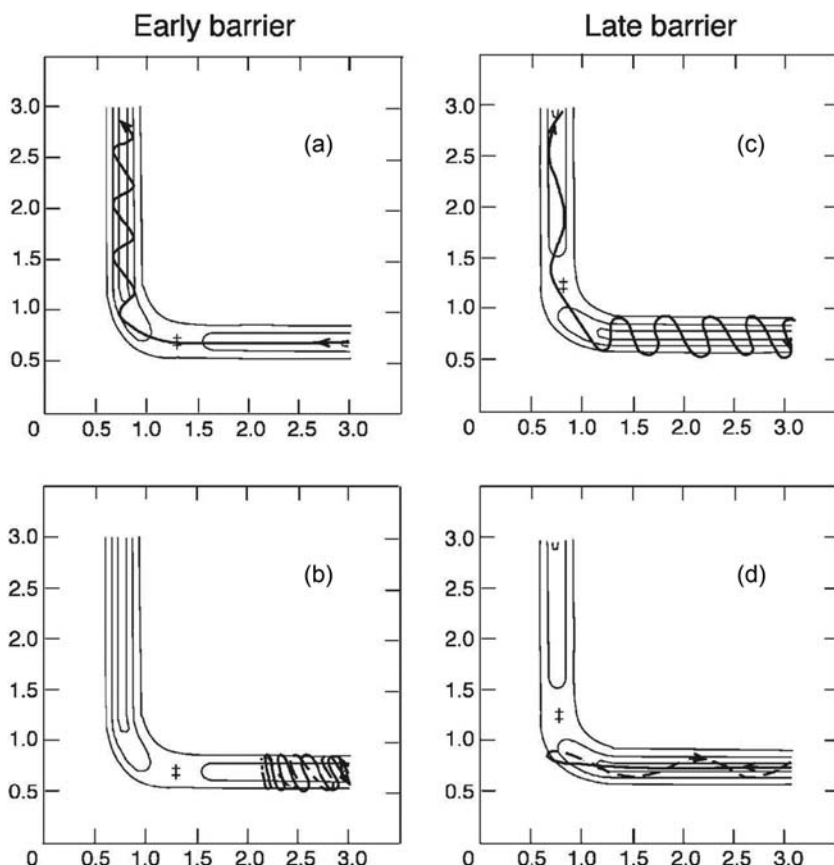
**FIGURE 5.20**

Illustration similar to the previous scheme, but considering the presence of a transition state bent by 28° . The examples shown are appropriate for the reactions (a) $F + HD \rightarrow HF + D$ and (b) $F + DH \rightarrow DF + H$. In the second case, the conversion of translational into rotational energy has half the efficiency of the first.

with it. In contrast, when the two light atoms repel, one of them can leave with a high translational energy, but the other is thrown at high velocity into the heavy atom, producing a high vibrational excitation. Figure 5.19 gives a rough sketch of the events; since in practice the transition state is slightly bent, such that the repulsion applies a torque to the leaving molecule that makes it rotate. This is clearly seen in the reaction $F + HD \rightarrow HF + D$ as compared with the process $F + DH \rightarrow DF + H$, since the product HF in the former case has about twice the rotational excitation compared with the product DF (Figure 5.20) [9].

Polanyi showed how the position of the barrier in a collinear PES is related to the way the distribution of energy in the reactants can increase the

**FIGURE 5.21**

Trajectories showing the effect of energy distribution of the reactants on the reactivity. Translational energy of reactants is effective for crossing an early barrier (a), but ineffective for late barriers (d) on the PES. In contrast, the vibrational energy of the reactants helps cross the late barriers (c), but not the early ones (b). *PES*, Potential energy surface.

reactivity. As seen in Figure 5.21, when the barrier is placed at the entrance of the PES, translational energy is much more effective than vibrational energy in making the reactants cross over the barrier to form products. The opposite is true when the barrier occurs in the latter part of the reaction coordinate. Although these ideas of J. C. Polanyi were well received at the time, it does not appear possible to make generalisations with them for all triatomic systems. For example, the reaction $\text{H} + \text{F}_2$ appears to have an anomalous behaviour being highly exothermic, but with particularly small translational energy (Table 5.1).

Table 5.1 Relative distributions of vibrational, rotational and translational energy of products in gas-phase atom abstraction reactions [10].

	$\Delta E^0/\text{kJ mol}^{-1}$	V'	R'	T'
$\text{F} + \text{H}_2 \rightarrow \text{HF} + \text{H}$	−133.3	0.664	0.083	0.260
$\text{F} + \text{HD} \rightarrow \text{HF} + \text{D}$	−130.0	0.558	0.125	0.287
$\text{F} + \text{DH} \rightarrow \text{DF} + \text{H}$	−137.1	0.626	0.066	0.309
$\text{F} + \text{D}_2 \rightarrow \text{DF} + \text{D}$	−132.9	0.665	0.076	0.259
$\text{Cl} + \text{HBr} \rightarrow \text{HCl} + \text{Br}$	−67	0.5	0.3	0.2
$\text{Cl} + \text{HI} \rightarrow \text{HCl} + \text{I}$	−137	0.68	0.14	0.18
$\text{F} + \text{HCl} \rightarrow \text{HF} + \text{Cl}$	−144	0.56	0.21	0.23
$\text{D} + \text{I}_2$	−158	0.26		
$\text{H} + \text{Br}$	−186	0.55	0.04	0.41
$\text{H} + \text{Cl}_2$	−203	0.38	0.08	0.53
$\text{H} + \text{ICl} \rightarrow \text{HCl} + \text{I}$	−219	0.59	0.21	0.20
$\text{H} + \text{BrCl} \rightarrow \text{HCl} + \text{Br}$	−213	0.55	0.09	0.39
$\text{H} + \text{BrCl} \rightarrow \text{HBr} + \text{Cl}$	−148	0.50	0.14	0.36
$\text{H} + \text{ClF} \rightarrow \text{HCl} + \text{F}$	−180	0.47	0.11	0.42
$\text{H} + \text{ClF} \rightarrow \text{HF} + \text{Cl}$	−318	0.68	0.07	0.25
$\text{H} + \text{F}_2$	−429	0.62	0.03	0.33

Note: $E_{tr} = 5.0 \text{ kJ mol}^{-1}$ except for $\text{H} + \text{F}_2$ where $E_{tr} = 3.8 \text{ kJ mol}^{-1}$ and for $\text{F} + \text{H}_2$ and its isotopic variants where $E_{tr} = 10 \text{ kJ mol}^{-1}$.

References

- [1] DR Herschbach, *Angew. Chem. Int. Ed. Engl.* **26** (1987) 1221.
- [2] BH Mahan, *J. Chem. Educ.* **51** (1974) 308.
- [3] M Karplus, RN Porter, RD Sharma, *J. Chem. Phys.* **43** (1965) 3259.
- [4] MJT Jordan, RG Gilbert, *J. Chem. Phys.* **102** (1995) 5669.
- [5] WL Hase, KF Lim, Program package MARINER. Department of Chemistry, University of Melbourne, Australia, Melbourne, 1990.
- [6] M-L Wang, K-L Han, G-Z He, N-Q Lou, *Chem. Phys. Lett.* **284** (1998) 200.
- [7] JC Polanyi, *Acc. Chem. Res.* **5** (1972) 161.
- [8] JC Polanyi, *Science* **236** (1987) 680.
- [9] JC Polanyi, in A Zewail (Ed.), *The Chemical Bond*, Academic Press, San Diego, 1992, p. 149.
- [10] MR Levy, *Prog. Reaction Kinetics* **10** (1979) 1.

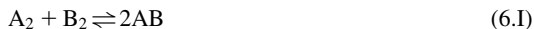
Reactivity in thermalised systems

6

6.1 Transition-state theory

“The calculation of absolute reaction rates” formulated by Eyring in 1934, was submitted in the form of a scientific paper to the well-known *J. Chem. Phys.* [1]. This paper was rejected by one referee of this journal under the impression that “the method of treatment is unsound and the result incorrect” [2]. Eventually, Eyring’s paper was accepted for publication after Eugene Wigner and Hugh S. Taylor took up the issue with the editor of *J. Chem. Phys.* [3]. Shortly after, M. Polanyi and M. G. Evans also made a significant contribution to this theory, and suggested the term “transition state” to the critical intermediate invoked by the theory for every rate process. Today, this theory is known as the TST and has become the paradigm for interpreting the rates of chemical processes and their dependence on temperature, medium, structure and other parameters.

Probably, the most important reason for the initial resistance to TST was the method presented to calculate the pre-exponential factor. Rather than the usual cross section of collision theory, Eyring calculated the pre-exponential factor of the H+H₂ reaction from a ratio of partition functions. Although the value given by this method was in good agreement with that from the cross sections, such an agreement was considered ‘purely accidental’. It is somewhat ironic that in 1941 Eyring and his co-workers choose to criticise the collision theory precisely for its procedure of calculating the frequency factor [4]. They pointed out that for a reversible reaction



the ratio of the forward and reverse reactions is equal to the equilibrium constant of the system, which, following eq. (5.16), should be written as

$$K = \frac{k_1}{k_2} = e^{-(E_1 - E_2)/RT} \quad (6.1)$$

since the cross sections and reduced masses in the two directions should not differ significantly from each other. The difference between the activation energies for

the forward and reverse reactions is equal to ΔH and the simple collision theory leads to the requirement that

$$K = \frac{k_1}{k_2} = e^{-\Delta H/RT} \quad (6.2)$$

which can only be true either at the temperature of absolute zero or if the reaction involves no entropy change. The aforementioned equations ignore the steric factors, present in eq. (5.16), which must involve an entropy term. Since the equilibrium constant is $K = \exp(-\Delta G^0/RT)$, the collision theory must be modified to include an entropy of activation, as shown in eq. (5.19). Consequently, the collision theory equation should have the form

$$k = \pi d_{AB}^2 \sqrt{\frac{8RT}{\pi\mu}} e^{\Delta S^\ddagger/R} e^{-\Delta H^\ddagger/RT} \quad (6.3)$$

where the entropy of activation assimilates the steric factor. This critique by Eyring and co-workers emphasises the fact that it is the free energy of activation, and not the heat of activation, that determines the reaction rate.

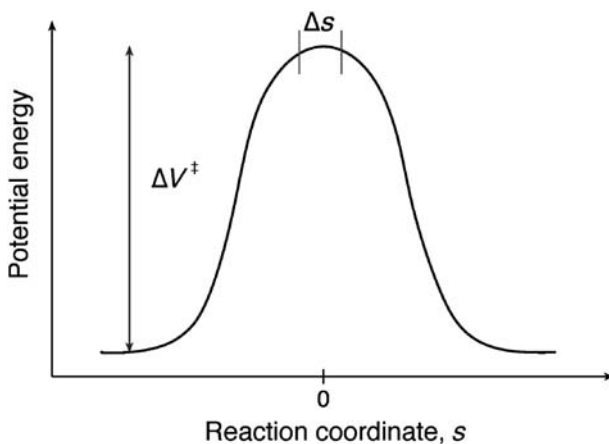
6.1.1 Classical formulation

The TST, as Eyring's theory is known, is a statistical-mechanical theory to calculate the rate constants of chemical reactions. As a statistical theory, it avoids the dynamics of collisions. However, ultimately, TST addresses a dynamical problem: the proper definition of a transition state is essentially dynamic, because this state defines a condition of dynamical instability, with the movement on one side of the transition state having a different character from the movement on the other side. The statistical mechanics aspect of the theory comes from the assumption that thermal equilibrium is maintained all along the reaction coordinate. We will see how this assumption can be employed to simplify the dynamics problem.

Let us define a reaction coordinate s , joining reactants ($s < 0$) to products ($s > 0$), and a transition state with a fixed value of s , that is, with one degree of freedom less than a stable molecule (Figure 6.1). It is possible to derive TST from one fundamental assumption: there is a quasi-equilibrium between the transition-state species (formed from the reactants) and the reactants themselves. The quasi-equilibrium state is characterised by the equilibrium between the reactants and the transition-state species, and by the fact that the concentration of these species does not vary with their disappearance to the products. This quasi-equilibrium offers a method to calculate the concentration of transition-state species using chemical equilibrium theories, and the dynamics problem is transformed into an equilibrium problem, with a known solution.

Representing the transition-state species by \ddagger , the kinetic mechanism



**FIGURE 6.1**

Potential energy curve for a reaction going through a transition state \ddagger contained in an imaginary potential box with length Δs .

leads to the bimolecular reaction rate

$$\nu = \nu^\ddagger[\ddagger] \quad (6.4)$$

This expression indicates that the number of species transformed into products, per unit time, is the product of their concentration and the frequency of their conversion. The frequency ν^\ddagger is the number of times, per unit time, that the transition-state species evolve along the reaction coordinate in the direction of the products. This movement corresponds to the conversion of an internal degree of freedom into a translational degree of freedom. Therefore, the transition state has one degree of freedom less than a normal molecule, because one of these is the reaction coordinate. The movement along this coordinate is that of the relative displacement of two atoms in opposite directions. This frequency can also be represented by the mean velocity of crossing the transition state, \bar{v}_q , over the length of the transition state at the top of the barrier, Δs . Hence, the above equation can be written as

$$\nu = \frac{\bar{v}_q}{\Delta s} [\ddagger] \quad (6.5)$$

and the mean velocity can be obtained from the Maxwell–Boltzmann distribution of molecular velocities over one dimension

$$\bar{v}_q = \frac{\int_0^{\infty} e^{-\gamma_2 m v_q / k_B T} v_q dv}{\int_{-\infty}^{\infty} e^{-\gamma_2 m v_q / k_B T} dv} = \sqrt{\frac{k_B T}{2\pi m}} \quad (6.6)$$

where the limits of integration in the denominator are taken from $-\infty$ to ∞ to allow for the fact that the complexes are moving in both directions, whereas in

the numerator the limits are zero to infinity because it is the mean velocity in the direction of the products that is required. The mass m is the effective mass of the complex in this movement.

Using the quasi-equilibrium approximation,

$$K^\ddagger = \frac{[\ddagger]}{[A][B]} \quad (6.7)$$

the reaction rate becomes

$$v = \sqrt{\frac{k_B T}{2\pi m}} \frac{1}{\Delta s} K^\ddagger [A][B] \quad (6.8)$$

The calculation of the rate constant is now focussed on the calculation of the quasi-equilibrium constant. Statistical mechanics relate the equilibrium constant with the structures and energies of the reactants and products. These relations are developed in detail in [Appendix II](#), Statistical Thermodynamics. It is shown that the equilibrium constant for the system



can be written in terms of the molar partition functions, per unit volume, of A, B and \ddagger ,

$$K^\ddagger = \frac{Q_\ddagger}{Q_A Q_B} e^{-\Delta E_0/RT} \quad (6.9)$$

The partition functions are a measure of the states that are thermally accessible to the molecule at a given temperature. In the equation above, the energetic factor

$$\Delta E_0 = E_0^\ddagger - E_0^A - E_0^B \quad (6.10)$$

is the difference between the zero-point energies (ZPEs) of the transition state and the reactants, per mole, at $T = 0$ K. It is the amount of energy that the reactants must acquire at 0 K to reach the transition state.

As discussed above, one of the vibrational degrees of freedom of \ddagger in mechanism [\(6.III\)](#) became a translation along the reaction coordinate in mechanism [\(6.II\)](#). This can be factored out of the transition state in mechanism [\(6.II\)](#), Q^\ddagger , and related to the partition functions of the normal molecule, Q_\ddagger ,

$$Q_\ddagger = Q_{\text{trans},q} Q^\ddagger \quad (6.11)$$

As will be seen below, the translational partition function along the reaction coordinate has the form

$$Q_{\text{trans},q} = \frac{(2\pi m k_B T)^{1/2} \Delta s}{h} \quad (6.12)$$

and the rate constant can be written, using [eqs. \(6.8\)](#) and [\(6.9\)](#)

$$\begin{aligned} k &= \frac{k_B T}{h} K^\ddagger \\ &= \frac{k_B T}{h} \frac{Q^\ddagger}{Q_A Q_B} e^{-\Delta E_0/RT} \end{aligned} \quad (6.13)$$

It is quite remarkable that the combination of the two terms involving the properties of the transition state, namely the velocity of crossing the transition state and the translational partition function along the reaction coordinate, gives the quantity $k_B T/h$, which is the same for reactants and reactions of all types. It represents the frequency with which any transition state becomes a product at a given temperature and its value is about $6 \times 10^{12} \text{ sec}^{-1}$ at 300 K. Additionally, the length Δs representing the transition state at the top of the barrier, is eliminated in this procedure, and there is no obvious restriction on its magnitude. The most interesting achievement of TST is that the calculation of the partition functions of reactants and transition state leads to the reaction rate, provided that the energy term is known.

The constant K^\ddagger is exactly analogous to any other equilibrium constant, and hence should be related to ΔG^\ddagger , ΔH^\ddagger and ΔS^\ddagger , the standard free energy, enthalpy and entropy changes, respectively, accompanying the formation of the transition state from the reactants by means of the familiar thermodynamic relationships. In this manner, eq. (6.13) can also be written in the form

$$k = \frac{k_B T}{h} e^{-\frac{\Delta G^\ddagger}{RT}} = \frac{k_B T}{h} e^{\frac{\Delta S^\ddagger}{R} - \frac{\Delta H^\ddagger}{RT}} \quad (6.14)$$

that satisfies the requirement that the reaction rate is determined by the free energy of activation. This is an improvement over the simple collision theory in that it gives a precise and simple significance to the frequency factor. It must be emphasised that ΔG^\ddagger , ΔH^\ddagger and ΔS^\ddagger refer to the reactants and transition state in their standard states, although the conventional zero superscript is omitted.

6.1.2 Partition functions

Statistical mechanics offers well-established methods to obtain the partition functions of simple systems. In view of their relevance to the calculation of the pre-exponential factor of eq. (6.13), they are briefly reviewed below for translational, rotational and vibrational partition functions. The electronic partition function is assumed here to be identical to the degeneracy of the electronic ground state, $Q_{\text{elec}} = g_{\text{elec}}$.

The translational partition function is conveniently derived from the energy levels accessible to a particle of mass m moving in a potential energy box of length l . According to the Schrödinger equation for this system, the allowed energy levels are

$$E_n = \frac{n^2 h^2}{8ml^2} \quad (6.15)$$

where n is the quantum number associated with the energy levels. The one-dimensional partition function is, then,

$$Q_{\text{trans}} = \sum_{n=1}^{\infty} \exp\left(\frac{-n^2 h^2}{8ml^2 k_B T}\right) \quad (6.16)$$

According to the definition of the partition function as a measure of the number of thermally accessible states at a given temperature, there are very large numbers of translational states accessible for molecular systems at typical temperatures because the energetic separation between the translational states is much smaller than the thermal energy, $3/2 k_B T$ from eq. (2.43). Therefore, the summation can be replaced by appropriate integration, with the integral having a standard form

$$\begin{aligned} Q_{\text{trans}} &= \int_0^\infty \exp\left(\frac{-n^2 h^2}{8ml^2 k_B T}\right) dn \\ &= \frac{1}{2} \left(\frac{8\pi ml^2 k_B T}{h^2}\right)^{1/2} = \frac{(2\pi m k_B T)^{1/2} l}{h} \end{aligned} \quad (6.17)$$

for each dimension. The translational energy for the three dimensions is

$$E_{\text{trans}} = E_{\text{trans},x} + E_{\text{trans},y} + E_{\text{trans},z} \quad (6.18)$$

and, consequently, the translational partition function for the three dimensions is

$$Q_{\text{trans}} = Q_{\text{trans},x} Q_{\text{trans},y} Q_{\text{trans},z} \quad (6.19)$$

or

$$Q_{\text{trans}} = \left(\frac{2\pi m k_B T}{h^2}\right)^{3/2} V \quad (6.20)$$

where $V = l^3$.

The vibrational partition function of a harmonic oscillator has equally spaced energy levels [eq. (1.5)]. Representing the separation between the energy levels by ε , the vibrational partition function can be written as a geometric progression:

$$\begin{aligned} Q_{\text{vib}} &= 1 + e^{-\varepsilon/k_B T} + e^{-2\varepsilon/k_B T} + \dots = 1 + e^{-\varepsilon/k_B T} + (e^{-\varepsilon/k_B T})^2 + \dots \\ &= \frac{1}{1 - e^{-\varepsilon/k_B T}} = \frac{1}{1 - e^{-hv/k_B T}} \end{aligned} \quad (6.21)$$

where we used the relations

$$\begin{aligned} S &= 1 + x + x^2 + \dots \\ xS &= x + x^2 + x^3 + \dots \\ S &= \frac{1}{1 - x} \end{aligned} \quad (6.22)$$

The linear, rigid rotor has energy levels given by

$$E_J = \frac{J(J+1)}{2I} \left(\frac{\hbar}{2\pi}\right)^2 \quad (6.23)$$

where $I = \sum m_i r_i^2$ is the moment of inertia (r_i is the perpendicular distance between atom i of mass m_i and the rotation axis), and $J = 0, 1, 2, \dots$ is the rotational quantum number. The linear, rigid rotor has degenerate energy levels,

and the rotational degeneracy is $2J + 1$. The corresponding rotational partition function is

$$Q_{\text{rot}} = \sum_{J=0}^{\infty} (2J+1) \exp \left[-\frac{J(J+1)}{2Ik_B T} \left(\frac{h}{2\pi} \right)^2 \right] \quad (6.24)$$

In general, at room temperature, the difference between the rotational energy levels is much smaller than $k_B T$. Under these conditions, many rotational levels are occupied and it is reasonable to replace the summation by the integral

$$\begin{aligned} Q_{\text{rot}} &= \int_0^{\infty} (2J+1) \exp \left[-\frac{J(J+1)}{2Ik_B T} \left(\frac{h}{2\pi} \right)^2 \right] dJ \\ &= \frac{8\pi^2 I k_B T}{h^2} \end{aligned} \quad (6.25)$$

The H_2 molecule is one of the rare exceptions to the conditions formulated above, because its small mass, hence the small moment of inertia, leads to relatively large energetic separations between the energy levels. Given the H–H bond length $l_{\text{HH}} = 0.741 \text{ \AA}$, we have $I = 4.5 \times 10^{-48} \text{ kg m}^2$ and $\Delta E_J = 3 \text{ kJ mol}^{-1}$, whereas at room temperature, $3/2RT = 3.7 \text{ kJ mol}^{-1}$.

For a polyatomic molecule with moments of inertia I_a , I_b and I_c along the principal axis, the rotational partition function is

$$Q_{\text{rot}} = \pi^{1/2} \left(\frac{8\pi^2 I_a k_B T}{h^2} \right)^{1/2} \left(\frac{8\pi^2 I_b k_B T}{h^2} \right)^{1/2} \left(\frac{8\pi^2 I_c k_B T}{h^2} \right)^{1/2} \quad (6.26)$$

6.1.3 Absolute rate calculations

Using eq. (6.13), together with eqs. (6.20), (6.21), (6.25) or (6.26), and knowing the ZPE difference between the transition state and the reactants, it is now possible to calculate “absolute” reaction rates. In practice, TST can only be applied if the structure of the transition state and its vibrational levels are also known, because the former is required for the calculation of the rotational partition function of the transition state, and the latter enter the transition-state vibrational partition function. These data and ΔE^0 can be obtained from *ab initio* calculations or experimental information employed in the making of potential energy surfaces (PESs). The rapid development of computers and software has made it possible to carry out accurate *ab initio* calculations of transition-state properties for many triatomic and some tetra-atomic systems in the gas phase. The best-known system is the atom exchange in the $\text{H} + \text{H}_2$ system, and the properties of its linear transition state are shown in Table 6.1.

Using the data presented in Appendix III, Parameters Employed in ISM Calculations, on the properties of stable molecules, and in Table 6.1, on the linear

Table 6.1 Data from the PES obtained by the double many-bodied expansion method for the linear transition state $\{\text{H}-\text{H}-\text{H}\}^\ddagger$ [5].

$\Delta V_{\text{cl}}^\ddagger$ (kJ mol ⁻¹)	$I_{\text{H}_1\text{H}_2} = I_{\text{H}_2\text{H}_3}^\ddagger$ (Å)	\bar{v}_{sym} (cm ⁻¹)	\bar{v}_{asym} (cm ⁻¹)	\bar{v}_{bend} (cm ⁻¹)	$\Delta V_{\text{ad}}^\ddagger$ (kJ mol ⁻¹)
40.4	0.9287	2067	1493 ^a	899	38.2

^aThis is an imaginary frequency.

transition state of the $\text{H} + \text{H}_2$ reaction, it is possible to calculate the rate constant for this reaction as the product of the partition function ratios

$$k = \frac{k_B T}{h} \left(\frac{Q^\ddagger}{Q_{\text{H}} Q_{\text{H}_2}} \right)_{\text{vib}} \left(\frac{Q^\ddagger}{Q_{\text{H}} Q_{\text{H}_2}} \right)_{\text{rot}} \left(\frac{Q^\ddagger / V}{Q_{\text{H}} / V Q_{\text{H}_2} / V} \right)_{\text{trans}} e^{-\Delta E_0 / RT} \quad (6.27)$$

that can be calculated separately. The ratio of the translational partition functions at 440 K is

$$\begin{aligned} \left(\frac{Q^\ddagger / V}{Q_{\text{H}} / V Q_{\text{H}_2} / V} \right)_{\text{trans}} &= \left(\frac{m_{\text{H}} + m_{\text{H}_2}}{m_{\text{H}} m_{\text{H}_2}} \right)^{3/2} \left(\frac{h^2}{2\pi k_B T} \right)^{3/2} \\ &= (2.683 \times 10^{40} \text{ kg}^{3/2}) (3.900 \times 10^{-71} \text{ kg}^{3/2} \text{ m}^3) \\ &= 1.05 \times 10^{-30} \text{ m}^3 \end{aligned} \quad (6.28)$$

and the ratio of the rotational partition function for the linear transition state is simply given by the ratio of the moments of inertia

$$\begin{aligned} \left(\frac{Q^\ddagger}{Q_{\text{H}_2}} \right)_{\text{rot}} &= \frac{I_{\text{H}_2}^\ddagger}{I_{\text{H}_2}} = \frac{m_{\text{H}^1} \left(l_{\text{H}^1\text{H}^2}^\ddagger \right)^2 + m_{\text{H}^3} \left(l_{\text{H}^2\text{H}^3}^\ddagger \right)^2 - \frac{\left(m_{\text{H}^1} l_{\text{H}^1\text{H}^2}^\ddagger - m_{\text{H}^3} l_{\text{H}^2\text{H}^3}^\ddagger \right)^2}{m_{\text{H}^1} + m_{\text{H}^2} + m_{\text{H}^3}}}{\frac{m_{\text{H}^2} m_{\text{H}^3}}{m_{\text{H}^2} + m_{\text{H}^3}} (l_{\text{H}_2,\text{eq}})^2} \\ &= 6.28 \end{aligned} \quad (6.29)$$

Finally, the ratio of the vibrational partition functions is

$$\left(\frac{Q^\ddagger}{Q_{\text{H}_2}} \right)_{\text{vib}} = \frac{1 - \exp\left(-\frac{\hbar\bar{v}_{\text{H}_2} c}{k_B T}\right)}{\left[1 - \exp\left(-\frac{\hbar\bar{v}_{\text{sym}} c}{k_B T}\right)\right] \left[1 - \exp\left(-\frac{\hbar\bar{v}_{\text{bend}} c}{k_B T}\right)\right]^2} = 1.12 \quad (6.30)$$

where we considered two degenerate bendings at the transition state, one in the plane, the other in and out of the plane, and the symmetric stretching. The anti-symmetric stretching has become the reaction coordinate and has an imaginary value. The vibrational frequency of H_2 , employed in the construction of its Morse curve in [Appendix III](#), Parameters Employed in ISM Calculations, is $\bar{v}_{\text{H}_2} = 4400 \text{ cm}^{-1}$.

The last parameter required for the calculation of the rate constant for the $\text{H} + \text{H}_2$ reaction is the energetic factor ΔE_0 . As mentioned before, it corresponds

to the difference between the ZPEs of the transition state and the reactants. In [Table 6.1](#), the classical potential energy difference between transition state and the reactants is represented by ΔV^\ddagger and the barrier corrected for the ZPE is represented by $\Delta V_{\text{ad}}^\ddagger$. It is often designated as the vibrationally adiabatic barrier and corresponds to ΔE_0 . The rate constant calculated at 440 K with the universal frequency of TST, $\Delta V_{\text{ad}}^\ddagger = 38.2 \text{ kJ mol}^{-1}$ and the ratio of the partition functions calculated above is $1.2 \times 10^6 \text{ dm}^3 \text{ mol}^{-1} \text{ sec}^{-1}$, fairly close to the experimental value of $5.7 \times 10^6 \text{ dm}^3 \text{ mol}^{-1} \text{ sec}^{-1}$.

6.1.4 Statistical factors

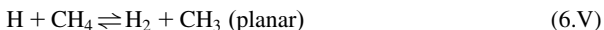
An even better agreement can be obtained considering the role of statistical effects in the transition state. The origin of such effects can be easily understood comparing the reactions



The partition functions for the two reactions are similar. However, the first reaction may result from two possible arrangements of the hydrogen molecule. This is clearer when we number each identical atom of the molecule



In contrast, reaction [\(6.IIIb\)](#) can only occur from one transition-state arrangement, because the other one leads to a different product, HD + H. It is natural that reaction [\(6.IIIa\)](#) is favoured by a statistical factor σ that is twice that of reaction [\(6.IIIb\)](#). The basis for the introduction of such statistical factors relies on the nature of the TST: the reaction rate is determined by the number of species that enter the transition state and do not return to the reactants. A simple method to obtain the statistical factors is to label the identical atoms and count the number of equivalent transition states. For example, the reaction



leads to the labelled species represented in [Figure 6.2](#). The forward reaction leads to four sets of products with different labels, thus $\sigma_f = 4$. The reverse reaction also leads to four distinct sets of products, and thus $\sigma_r = 4$. The equilibrium constant written as the ratio of forward and reverse reactions agrees with that of equilibrium thermodynamics

$$K_{\text{eq}} = \frac{k_f}{k_r} = \frac{[\text{H}_2][\text{CH}_2]}{[\text{H}][\text{CH}_4]} = \frac{\sigma_f Q_{\text{H}_2} Q_{\text{CH}_2}}{\sigma_r Q_{\text{H}} Q_{\text{CH}_4}} e^{-\Delta E_0/RT} \quad (6.31)$$

The use of statistical factors requires extra care when the reaction introduces or removes an asymmetric centre. For example, the addition of a hydrogen atom

to an asymmetric methyl radical leads to two enantiomers, because the H atom may bind to either side of the symmetry plane (Figure 6.3). In the forward direction we have $\sigma_f = 2$, but in the reverse direction, $\sigma_r = 1$ and the equilibrium constant is multiplied by a factor of two

$$K_{\text{eq}} = \frac{\sigma_f}{\sigma_r} \frac{Q_{\text{CH}_3R_1R_2R_3}}{Q_{\text{H}}Q_{\text{CR}_1R_2R_3}} e^{-\Delta E_0/RT} \quad (6.32)$$

The analyses of statistical factors may provide important information on the symmetry of the transition state. For example, the isomerisation of cyclopropane to propene may proceed via a symmetrical or an asymmetrical transition state (Figure 6.4).

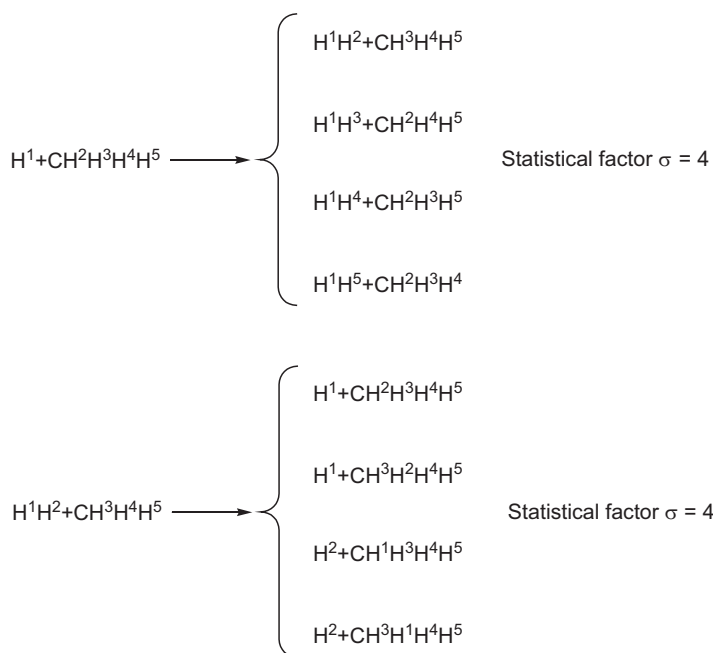


FIGURE 6.2

Distinct species present in the reaction $H + CH_4 \rightarrow H_2 + CH_3$ (planar). The methanes $CH^2H^3H^4H^5$ and $CH^3H^2H^4H^5$ as well as $CH^1H^3H^4H^5$ and $CH^3H^1H^4H^5$ are enantiomers.

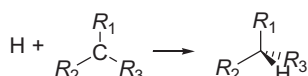
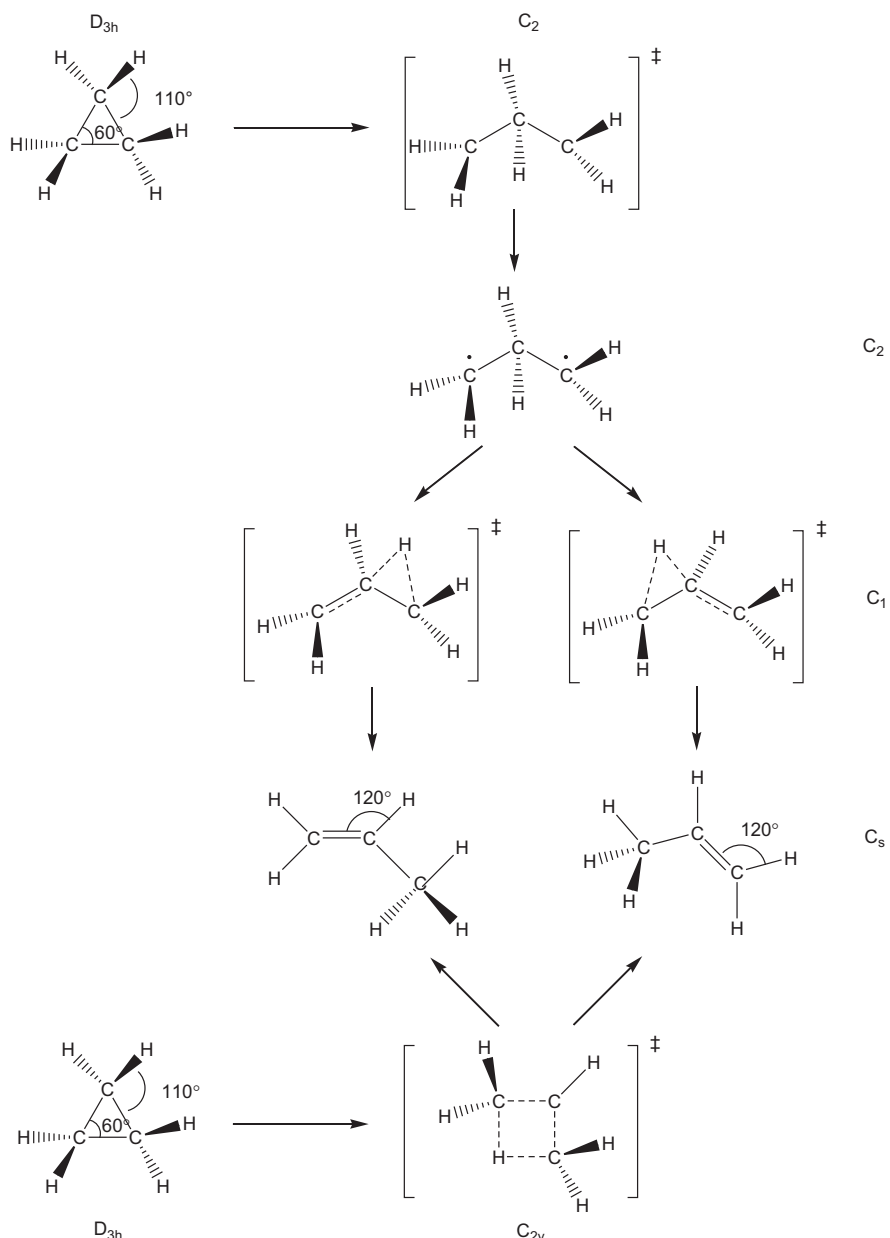


FIGURE 6.3

Addition of a hydrogen atom to an asymmetric methyl radical leading to two enantiomers. The statistical factor of the forward reaction is twice that of the reverse reaction.

**FIGURE 6.4**

Symmetrical and asymmetrical transition states in the isomerisation of cyclopropane to propene. The symmetrical transition state does not have any physical meaning because it requires the splitting of the reaction path into two paths at the transition state.

In the first case, $\sigma_f = 2$, whereas in the second case $\sigma_f = 1$. The symmetrical transition state corresponds to the generation of two reaction paths from the same transition state. This cannot happen in a PES, where one transition state can only connect one reactant's valley to one product's valley. Consequently, the symmetrical transition state is unphysical.

The consideration of statistical factors in the TST is a simple and necessary refinement of this theory. When the statistical factor is included, the classical rate constant of TST is expressed as

$$k_{\text{TST}} = \sigma \frac{k_{\text{B}}T}{h} K^0 \frac{Q_{\text{A}}^{\ddagger}}{Q_{\text{A}} Q_{\text{BC}}} e^{-\Delta V_{\text{ad}}^{\ddagger}/RT} \quad (6.33)$$

where explicit mention is made of the fact that the energetic factor is the vibrationally adiabatic barrier, $\Delta V_{\text{ad}}^{\ddagger}$. K^0 is the reaction quotient for the formation of the transition state evaluated at the standard-state concentration of each species: $K^0 = 1$ for first-order reactions and $K^0 = (c^0)^{-1}$ for second-order reactions. For gas-phase bimolecular reactions, with rate constants expressed in units of $\text{cm}^3 \text{ molecule}^{-1} \text{ sec}^{-1}$, $(c^0)^{-1}$ is $k_{\text{B}}T/p^0$, where p^0 is 1 bar, whereas for liquid-phase reactions the standard-state concentration is 1 mol dm^{-3} . The inclusion of a statistical factor in the rate formulation is not compatible with the inclusion of symmetry numbers in the rotational partition functions. Indeed, such symmetry numbers were not included in our previous calculation of the partition functions. Now that we know that $\sigma = 2$ for the $\text{H} + \text{H}_2$ reaction, we can calculate a classical rate of $2.4 \times 10^6 \text{ dm}^3 \text{ mol}^{-1} \text{ sec}^{-1}$ at 440 K. The calculated rate now approaches the uncertainty of the experimental value, $5.7 \times 10^6 \text{ dm}^3 \text{ mol}^{-1} \text{ sec}^{-1}$, but remains too slow.

6.1.5 Beyond the classical formulation

Further improvement of TST requires a critical analysis of its fundamental assumptions. The development of this theory was based on the following approximations: (1) the distribution of energy in the reactants and transition state follows the Boltzmann distribution law, (2) every system that crosses the transition state becomes a product and (3) the movement along the reaction coordinate is adiabatic and can be described by classical mechanics. Next, we analyse each one of these approximations to identify the conditions in which they fail and see how the theory can be improved in terms of both generality and accuracy.

The quasi-equilibrium assumption, that is the basis for the use of the Boltzmann distribution law, may lose its validity for rapid reactions. In such reactions, the most energetic reactant molecules may disappear very rapidly and the concentration of species at the transition state may be lesser than that for a true equilibrium. In practice, even when $E_a/RT \approx 1.3$, as in the $\text{Cl} + \text{HBr} \rightarrow \text{HCl} + \text{Br}$ hydrogen atom abstraction, internal-state non-equilibrium effects are very small [6].

The assumption that the transition state is only crossed once by every reactive system neglects several types of trajectories that the system may follow, as

illustrated in [Figure 6.5](#). In fact, the classical TST assumes that the reactive systems can only follow trajectories of type 1, illustrated in this figure. However, trajectories of types 2, 5 and 6 also cross the transition state in the direction of the products, but do not correspond to reactive systems. Furthermore, although trajectories of type 3 are reactive, they cross the transition state twice in the direction of the products, but only contribute once to the actual rate. In general, a trajectory with just the energy necessary to cross the transition state will do so at a region very close to the saddle-point, which is the point of minimum energy separating the reactants and products in the PES. It is very unlikely that such a trajectory will find a path to return to the reactants and cross the transition state again. However, trajectories with higher energies may deviate appreciably from the minimum energy path connecting the reactants to the transition state and, finally, to the products. Such trajectories have an increased probability of being reflected by the repulsive potential after the transition state, and re-cross it back to the reactants. As the energy of the trajectories increases, the bottleneck of the reaction moves from the saddle-point towards the asymptotic regions of reactants or products where the PES is usually narrower. This behaviour can be rationalised as a competition between the energetic and the entropic factors. The energetic factor is determined by the mean velocity of the trajectories, and favours the localisation of the transition state at the saddle-point. The entropic factor is related to changes in force constants and moments of inertia, and drives the transition state to the more constricted regions of the PES. As the temperature increases, the average energy of the trajectories also increases, and the location of the transition state

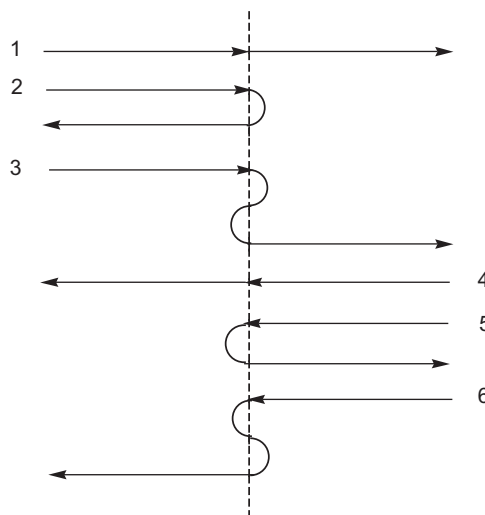


FIGURE 6.5

Schematic trajectories illustrating the re-crossing of a transition state. Trajectory 1 corresponds to the situation idealised by TST.

becomes dominated by the entropic factor, rather than by the energetic factor. These considerations suggest that it is more exact to define a variational transition state, located at the bottleneck that minimises its re-crossing. This approach was followed by Garrett and Truhlar [7], who used a variational method to locate the transition state. The variational transition state minimises the reactive flux from the reactants to the products. The variational TST (VTST) has met with considerable success, and represents a significant improvement over the classical TST at higher temperatures, where re-crossing effects are more relevant [8]. However, the rates of classical TST are an upper limit of the rates of classical VTST, and this cannot be the reason why the classical TST underestimates the $\text{H} + \text{H}_2$ reaction rate at 440 K.

The last assumption of the classical TST concerns the adiabaticity of the movement along the reaction coordinate. The term “adiabatic” has been used in many different instances and requires some explanation. Following the original suggestion by F. London, an (electronically) adiabatic transformation is one in which there is a continuous equilibrium between the electrons and the nuclei, and the whole process takes place on a single PES. This is only possible in the presence of a strong coupling between the reactant and the product states. The opposite of an (electronically) adiabatic process is a non-adiabatic (or diabatic) process that involves a jump from the initial to the final electronic state, that is, it occurs through an abrupt electronic re-arrangement. In addition to the electronic adiabaticity, the TST also assumes that the reactions are vibrationally adiabatic, that is, they occur in the vibrational ground state, with the conservation of the ZPE along the reaction coordinate. To go beyond the vibrational adiabaticity of the classical TST, it is necessary to introduce quantum corrections. Such corrections are very important for systems involving small molecular masses. The introduction of quantum correction in the classical TST leads to hybrid theories, with classical transition states and quantum effects. Such theories are called semi-classical theories.

6.2 Semi-classical treatments

The inclusion of quantum corrections in the reaction coordinate of the TST involves some conceptual and computational difficulties. Conceptually, the precise localisation of the transition state in a PES implies an absolute uncertainty in its conjugated momentum [eq. (1.8)]. This was avoided in the classical derivation of the TST, because the length of the transition state at the top of the barrier, Δs in eq. (6.5), cancelled with the translational partition function along the reaction coordinate in eq. (6.12), and the actual size of the transition state is irrelevant for the calculations.

Eyring adopted an ad hoc procedure that has been successful in including quantum effects in TST. First, the classical partition functions are replaced by

their quantum analogues. Second, the classical rate is multiplied by a transmission coefficient that takes into account the quantum effects along the reaction coordinate. The quantum partition functions assume that the transition state can be treated as a stable system. The separate quantisation of the reaction coordinate is based on the vibrational adiabaticity assumption, that is, all the other vibrational modes of the reactive system very rapidly adjust to the reaction coordinate and maintain the continuity and smoothness of the PES.

6.2.1 Kinetic isotope effects

The quantisation of the vibrational degrees of freedom offers a method of calculating the effect of isotopic substitution on the rate constants, because isotopes differ in their masses, hence in their ZPEs, but not in their electronic potential energies.

Following eqs. (1.2) and (1.5), the ZPE of a molecular vibration is given by

$$E_{v_0} = \frac{1}{2} \hbar \sqrt{\frac{f}{\mu}} \quad (6.34)$$

Under the harmonic approximation, and using a force constant of $2.90 \times 10^3 \text{ kJ mol}^{-1} \text{ Å}^{-2}$ for a C–H or a C–D bond, the ZPE difference between these two bonds is 4.7 kJ mol^{-1} . In the limiting case where they are effectively broken at the transition state, the difference in ZPEs between the C–H and C–D bonds is also their difference in activation energies. Under these circumstances, the ratio of the room-temperature rates involving the breaking of C–H and C–D bonds is $k_H/k_D = 6.7$. For higher force constants, such as those of the N–H and O–H bonds, the maximum isotope effect calculated by this minimalist model is even higher. This effect of the ZPE change on the rates of chemical reactions differing by isotopic substitution is named *primary kinetic isotope effect* (KIE).

The naive approximation described above is in conflict with the TST, because the reactive bond is never completely broken at the transition state. The existence of a bonding interaction in A···B···C is the reason why the transition state can be defined in the first place, and the ZPEs of the C–H or C–D bonds cannot be totally omitted. Thus the observed KIE should always be smaller than the calculated maximum.

Westheimer [9] pointed out a more consistent method to estimate the maximum KIE in a reaction of the type



from the vibrations of the linear transition state A···H···B. Neglecting the vibrations of species A and B, we only have to consider the $3n - 5 = 4$ vibrational modes of the linear transition state. These vibrational modes are the anti-symmetric stretching (which corresponds to the movement along the reaction coordinate), the symmetric stretching (which is perpendicular to the reaction

coordinate) and two degenerate bendings (one in the plane and the other in and out of the plane)



Neglecting the contribution of the bendings and considering that the anti-symmetric stretching is, in fact, the translational motion along the reaction coordinate, the ZPE of the transition state is determined only by the symmetric stretching. In a perfectly symmetric transition state, $\text{B} = \text{A}$, the symmetric stretching is a synchronous movement of A and B leaving H equally distant from the end atoms, and at rest. The central atom does not move in the symmetric stretching of such a transition state, and the isotopic substitution does not change the symmetric stretching frequency. Consequently, the ZPE of the transition state is the same for the symmetrical transfer of H or D atoms, and Westheimer concluded that the KIE should attain its maximum for symmetrical transfers of H or D atoms (Figure 6.6). Under these approximations, the difference in activation energy between H and D transfers is, again, equal to the ZPE difference of the reactive bonds with H or D.

If the transition state is not perfectly symmetrical, the H atom will be closer to either A or B, and will move with the symmetric stretching. This movement will produce a ZPE difference between the hydrogenated and deuterated species, which will partly offset the ZPE difference of the reactive bonds. Thus, a smaller

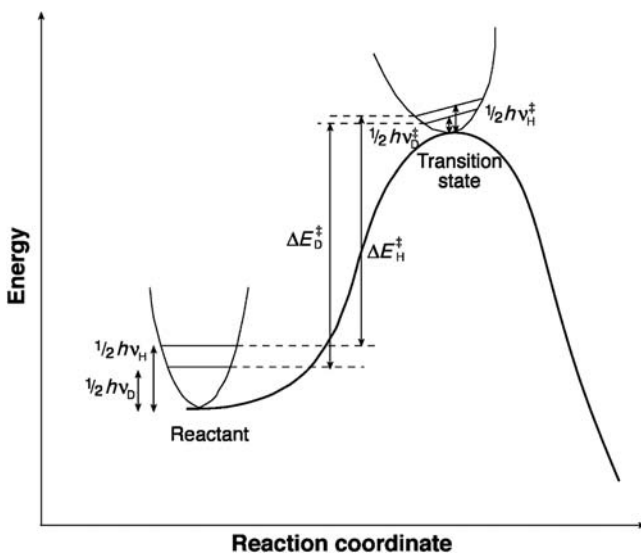


FIGURE 6.6

Difference in activation energy due to the difference in ZPE of C–H and C–D bonds, in a symmetrical transition state.

KIE should be observed when H (or D) is closer to either A or B. In [Chapter 7](#), Relationships Between Structure and Reactivity, we will see that in an exothermic reaction the structure of the transition state resembles more closely that of the reactants and in an endothermic reaction, the transition-state structure approaches that of the products. The reasoning presented earlier leads to the conclusion that in a series of H-atom or proton transfers differing mostly in their reaction energy, the KIE increases from the most exothermic reactions, reaches its maximum for the isothermal reaction and decreases as the reactions become endothermic. Although this discussion was oriented towards the relative position of the central atom, it is clear from [eq. \(6.34\)](#) that the tightness of the bonds also modulates the symmetry of the KIE dependence on the reaction energy.

Westheimer's interpretation of KIE is based on identical pre-exponential factors for H or D transfers, neglects the contribution of the bending vibrations, and assumes that classical mechanics can describe the movement along the reaction coordinate. It is, nevertheless, a useful approximation for mechanistic interpretations of KIE. For example, the observation of a sizeable KIE when a hydrogen atom is replaced by deuterium in a given compound indicates that the bond where the isotopic substitution was made is practically broken in the rate-determining step of the reaction.

It is often possible to observe a KIE even when the bond to the H or D atom is not broken in the course of the reaction. In such cases, we have *secondary KIEs*. Two reasons may concur for the observation of a secondary KIE, and both of them are related to the ZPE differences between the isotopes.

To explain the secondary KIE, we have to go beyond the simple harmonic model for a chemical bond. A more realistic model for a chemical bond is that of a Morse potential

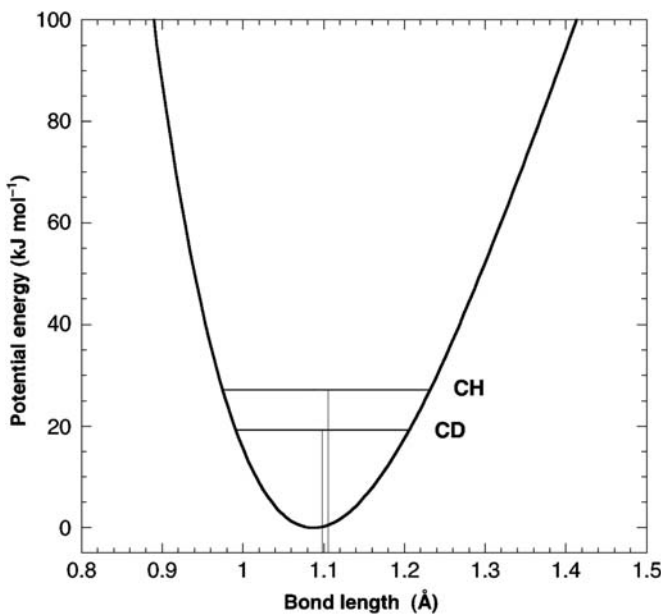
$$V = D_e \{1 - \exp[-\beta(l - l_{eq})]\}^2 \quad (6.35)$$

where D_e is the electronic dissociation energy, l_{eq} the equilibrium bond length and β the spectroscopic constant, defined as

$$\beta = \varpi_e \sqrt{\frac{2\pi^2 c \mu}{h D_e}} = 0.01332 \varpi_e \sqrt{\frac{\mu}{D_e}} \quad (6.36)$$

The numerical constant is obtained when the reduced mass of the directly bonded atoms (μ) is expressed in amu, D_e is in kilojoule per mole, the equilibrium stretching frequency (ϖ_e) is per centimetre and β is in per angstrom. The Morse potential reflects the anharmonicity of a chemical bond and reproduces its dissociation energy ([Figure 6.7](#)). It is a very convenient potential because the depth of the potential minimum is related to the bond dissociation energies tabulated at 298 K (D_{298}^0)

$$D_e = D_{298}^0 - 1.5RT + 0.5hc\varpi_e = D_{298}^0 - 1.5RT + 0.00598\varpi_e \quad (6.37)$$

**FIGURE 6.7**

Morse potential of the C–H bond in CH_4 , with indication of vibrational energy levels.

and the equilibrium stretching frequency is related to the infrared stretching frequency

$$\omega_e = \bar{\nu} + 0.5hc \frac{(\bar{\nu})^2}{D_{298}^0 - 1.5RT} = \bar{\nu} + 0.00598 \frac{(\bar{\nu})^2}{D_{298}^0 - 1.5RT} \quad (6.38)$$

Thus all the parameters of this potential can be obtained from experimental data tabulated for many bonds. The term $1.5RT$ appearing in the above expression accounts for translational motion of one additional species when the bond is broken, and should be used with $T = 298$ K, to be consistent with D_{298}^0 .

The Schrödinger equation has an analytical solution for the Morse potential and gives the following expression for its energy levels

$$E_v = \left(v + \frac{1}{2}\right)hc\omega_e - \left(v + \frac{1}{2}\right)^2 x_e hc\omega_e \quad (6.39)$$

where x_e is the anharmonicity constant. As shown in Figure 6.7, the fundamental vibrational frequencies of the C–H and C–D bonds correspond to different equilibrium bond lengths. The lighter isotopes have longer equilibrium bond lengths, although they correspond to the same potential energy curve. This leads to two consequences: (1) the longer C–H bond entails that steric effects are more

important than with the shorter C–D bond; (2) with the same electronic nature but a shorter bond, the C–D bond has a higher electron density at C than the C–H bond. In this respect, we can say that deuterium exerts a stronger electron-donating inductive effect than hydrogen. These effects are, nevertheless, very mild, and the secondary KIE, k_H/k_D , is usually < 2 and, in some cases, is even less than unity. In such cases these are named inverse KIEs.

6.2.2 Tunnel effect

We have seen that the rate of crossing the transition state leads to the classical factor $k_B T/h$ in eq. (6.13). In quantum mechanics, we must also consider the possibility that systems with less energy than the barrier height may leak to the product, and also that cases with more energy than the barrier be reflected back to the reactants. For the moment, we will consider only the classical barrier, ΔV^\ddagger , without ZPE corrections. We will defer the discussion of tunnelling through the vibrationally adiabatic barrier to a later stage. The classical probability of crossing the barrier, $P_C(E)$, in the classical factor

$$\begin{aligned}\frac{k_B T}{h} &= \frac{1}{h} \int_0^{\infty} dE e^{-E/k_B T} \\ &= \frac{1}{h} \int dE P_C(E) e^{-E/k_B T}\end{aligned}\quad (6.40)$$

must be replaced by the quantum probability, $P_Q(E)$. Whereas classically $P_C(E) = 0$ if $E < \Delta V^\ddagger$ and $P_C(E) = 1$ if $E \geq \Delta V^\ddagger$, the solution of the Schrödinger equation for the probability of a particle crossing a barrier gives $P_Q(E) > 0$ even when $E < \Delta V^\ddagger$. The crossing of a barrier with a potential energy higher than the kinetic energy of the incident particle is a quantum mechanical phenomenon called the *tunnel effect*.

The origin of the tunnel effect can be found in the wave-particle duality proposed by de Broglie

$$\lambda = \frac{h}{mv} = \frac{h}{\sqrt{2mE_c}} \quad (6.41)$$

where λ is the wavelength associated with a particle of mass m , velocity v and kinetic energy E_c . Many chemical reactions have an activation energy *ca.* 50 kJ mol⁻¹, and we can assume that the reactive systems must have a similar kinetic energy. Using the equation above with $E_c = 50$ kJ mol⁻¹, we calculate the wavelengths of particles such as the electron, hydrogen, carbon or bromine atoms and the buckminsterfullerene (footballene) molecule (C_{60}), shown in Table 6.2. It is evident that the electron has an associated wavelength that is one order of magnitude higher than a typical bond length, and only its wave-like properties will be observed in the course of chemical reactions. The bond length changes that occur as the reactant and product bond lengths extend to their configuration at the transition state are much smaller than the equilibrium bond lengths. The wavelength associated with the hydrogen atom is then similar to the sum of the reactive bond length changes and this atom may also manifest its

Table 6.2 de Broglie wavelengths of particles with a kinetic energy of 50 kJ mol⁻¹.

Particle	e ⁻	H	C	Br	C ₆₀
Mass (amu)	1/1750	1	12	80	720
λ (Å)	16.70	0.40	0.12	0.04	0.015

wave-like properties. It should be noted that the other atoms and molecules have too short associated wavelengths to manifest quantum-mechanical behaviour in the course of chemical reactions, but, under special conditions, even C₆₀ has shown wave-like properties [10].

In quantum mechanics, the wave function that describes the movement along a direction x of a system with a mass m and energy E is

$$\psi(x, t) = \psi(x)\exp(-iEt/\hbar) \quad (6.42)$$

and that wave function must obey the equation of Schrödinger for the system

$$\frac{d^2\psi(x)}{dx^2} + \frac{2m}{\hbar^2}[E - V(x)]\psi(x) = 0 \quad (6.43)$$

where $V(x)$ is the potential that the systems encounter. For some types of potentials it was possible to obtain the exact solutions for the wave function $\psi(x)$ that satisfy Schrödinger's equation, and from such solutions it was possible to obtain $P_Q(E)$. Independently and almost simultaneously, Brillouin [11], Wentzel [12] and Kramers [13] proposed a method to obtain an approximate solution to eq. (6.43), which gives the permeability of any unidimensional barrier. According to the WKB method, the transmission probability of a particle through a unidimensional barrier is

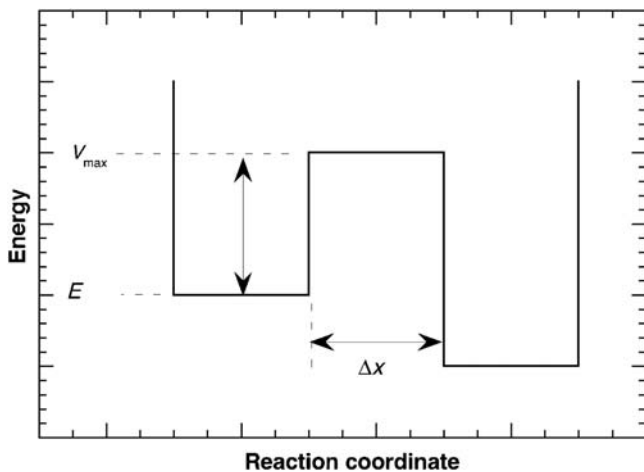
$$P_Q(E) = \frac{1}{1 + \exp\left\{\frac{2\sqrt{2m}}{\hbar}\int_{x_1}^{x_2} \sqrt{V(x) - E} dx\right\}} \quad (6.44)$$

This equation is rather precise, even for energies close to the barrier maximum, ΔV^\ddagger , and it is exact for potential barriers with the shape of an inverted parabola. When E is much smaller than ΔV^\ddagger , a case commonly found in molecular systems, the aforementioned expression can be simplified to

$$G(E) = \exp\left\{-\frac{2\sqrt{2m}}{\hbar} \int_{x_1}^{x_2} \sqrt{V(x) - E} dx\right\} \quad (6.45)$$

Eq. (6.45) has analytical solutions for several classes of potential barriers. For example, in the case of a square barrier, Figure 6.8, with a constant potential V_{\max} over a given interval of the reaction coordinate, Δx , the integral of eq. (6.45) is the area of the square $[\Delta V^\ddagger - E]^{1/2} \Delta x$, and the transmission probability becomes

$$G(E) = \exp\left\{-\frac{2\sqrt{2m}}{\hbar} \sqrt{V_{\max} - E} \Delta x\right\} \quad (6.46)$$

**FIGURE 6.8**

Square potential barrier.

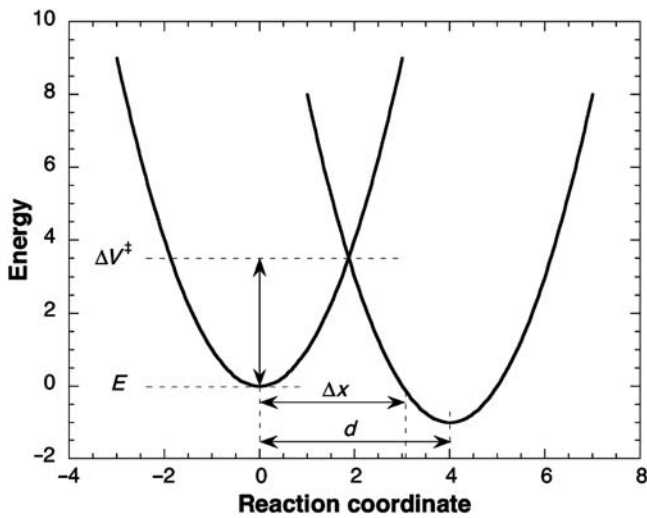
This solution can be applied to the probability of transmission of an electron, through vacuum, from a reduced to an oxidised species, or, in a scanning tunnelling microscopy experiment, the jump of an electron from the surface of the sample to the tip of the probe. In such systems, the electron escapes from the potential well of the donor to the potential well of the acceptor. The ionisation potential of the neutral donor or the work function of the metal gives the energetic factor in eq. (6.46), and the distance between the electron donor and acceptor gives Δx . Thus eq. (6.46) gives the transmission probability in a non-adiabatic electron transfer reaction.

Another analytical solution can be obtained for the case of the intersection of two parabolas separated by a distance Δx along the reaction coordinate (Figure 6.9). The parabolas are characterised by a square dependence on the displacement from the equilibrium position, eq. (1.6), and the term $[V(x) - E]^{1/2}dx$ in eq. (6.45) has the shape of a triangle. The integral is the area of a triangle with a base Δx and a height ΔV^\ddagger , and the transmission probability becomes

$$G(E) = \exp \left\{ -\frac{\sqrt{2m}}{\hbar} \sqrt{\Delta V^\ddagger - E} \Delta x \right\} \quad (6.47)$$

A popular type of barrier in the description of tunnelling in hydrogen-atom transfers is the infinite parabolic barrier $V(x) = V_0 - \frac{1}{2}(f^*)x^2$, which is an upside-down harmonic potential with an imaginary frequency $i\nu^\ddagger$, where

$$\nu^\ddagger = \frac{1}{2\pi} \sqrt{\frac{f^*}{m}} \quad (6.48)$$

**FIGURE 6.9**

Potential barrier defined by the intersection of two parabolas.

This imaginary frequency is that of the asymmetric stretch along the reaction coordinate. The WKB solution for the transmission probability through this barrier is

$$G(E) = \exp\left\{-\frac{\Delta V^\ddagger - E}{\hbar\nu^\ddagger}\right\} \quad (6.49)$$

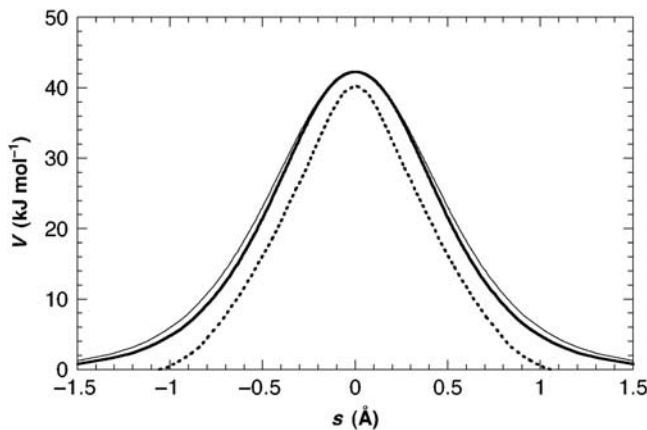
Finally, a potential barrier that closely approaches the classical reaction path of an atom-transfer reaction and that also has an analytical solution for the transmission probability, is the Eckart barrier [14]

$$\begin{aligned} V(x) &= -\frac{Ay}{1-y} - \frac{By}{(1-y)^2} \\ y &= -\exp\left(\frac{2\pi x}{l}\right) \end{aligned} \quad (6.50)$$

where

$$\begin{aligned} A &= \Delta V^\ddagger - (\Delta V^\ddagger - \Delta V^0) \\ B &= \left[\sqrt{\Delta V^\ddagger} + \sqrt{\Delta V^\ddagger - \Delta V^0} \right]^2 \\ l &= 2\pi \sqrt{-\frac{2}{f^*} \left[\frac{1}{\sqrt{\Delta V^\ddagger - \Delta V^0}} + \frac{1}{\sqrt{\Delta V^\ddagger}} \right]^{-1}} \end{aligned} \quad (6.51)$$

represented in Figure 6.10. The probability $G(E)$ of a particle of mass μ , moving towards the barrier with an energy E at $-\infty$, to cross the barrier and appear later

**FIGURE 6.10**

Eckart barrier for the $\text{H} + \text{H}_2$ reaction (thin line), fitted to the curvature of the reaction path of the ISM (full line). The accurate reaction path by the DMBE PES is shown as a dashed line. For this system, $\Delta V^0 = 0$. The reaction coordinate is defined as $s = \pm 2^{1/2} (l_{\text{HH}} - l_{\text{HH}}^\dagger)$.

at $+\infty$ with an energy E , has been obtained from the resolution of Schrödinger's equation and has the form

$$G(E) = 1 - \frac{\cosh[2\pi(\alpha - \beta)] + \cosh(2\pi\delta)}{\cosh[2\pi(\alpha + \beta)] + \cosh(2\pi\delta)} \quad (6.52)$$

where

$$\begin{aligned} \alpha &= \frac{1}{2} \sqrt{\frac{E}{C}} \\ \beta &= \frac{1}{2} \sqrt{\frac{E - A}{C}} \\ \delta &= \frac{1}{2} \sqrt{\frac{B - C}{C}} \\ C &= \frac{h^2}{8\mu l} \end{aligned} \quad (6.53)$$

In a real system, we do not have one particle with a given energy colliding with the barrier, but many molecules with a Boltzmann distribution of energies at the temperature T . Thus for real systems, we have to integrate the transmission probability $G(E)$ over all the energies

$$\kappa(T) = \exp\left(\frac{\Delta V^\ddagger}{k_B T}\right) \int_0^\infty G(E) \exp\left(-\frac{E}{k_B T}\right) d\left(\frac{E}{k_B T}\right) \quad (6.54)$$

to obtain the tunnel correction at the temperature T . The data required for this calculation are the height of the barrier (ΔV^\ddagger), the reaction energy (ΔV^0), the curvature of the reaction path at the transition state (f^*) and the reduced mass (μ).

The popularity of the upside-down harmonic potential to calculate tunnelling corrections in hydrogen-atom transfer is related both to its physical meaning and simplicity. The fact that eq. (6.49) contains the energy to the first power in the exponent allows for an analytical solution for the tunnel correction. Wigner derived a solution by treating the motion through the transition state as a vibration on an upside-down potential and expanding the quantum partition function to second order in $1/(k_B T)$. The result is the tunnel correction

$$\kappa(T) = 1 + \frac{1}{24} \left(\frac{\hbar\nu^\ddagger}{k_B T} \right) \quad (6.55)$$

which is a simple multiplicative term affecting the rate constant. Although simple and appealing, the Wigner correction tends to overestimate the tunnelling correction because the upside-down harmonic potential becomes unrealistic narrow not far below the transition-state energy.

Alternatively, using the data in Table 6.1 for the $\text{H} + \text{H}_2$ reaction, together with the relation between the frequency and the force constant in eq. (1.2), and the reduced mass

$$\mu = \frac{m_B m_C + m_A m_B}{2(m_A + m_B + m_C)} \quad (6.56)$$

we obtain a tunnelling correction with the Eckart barrier of 3.0 at 440 K, 12 at 300 K and 618 at 200 K. The Eckart barrier permeability tends to overestimate the tunnelling corrections (6.93 at 300 and 95.5 at 200 K) at lower temperatures for the $\text{H} + \text{H}_2$ reaction according to the more sophisticated methods, but it is more precise than the Wigner correction.

Introducing the tunnelling correction in the classical TST equation, we obtain the semi-classical expression

$$k_{\text{scTST}} = \kappa(T) \sigma \frac{k_B T}{h} K^0 \frac{Q^\ddagger}{Q_A Q_{BC}} e^{-\Delta V_{\text{ad}}^\ddagger / RT} \quad (6.57)$$

With the tunnelling correction at 440 K calculated from the Eckart barrier permeability discussed above, the semi-classical rate constant is $7.2 \times 10^6 \text{ dm}^3 \text{ mol}^{-1} \text{ sec}^{-1}$ at this temperature, only slightly higher than the experimental value, $5.7 \times 10^6 \text{ dm}^3 \text{ mol}^{-1} \text{ sec}^{-1}$. This excellent agreement shows that absolute rates can be calculated with great accuracy using the TST, provided that the energy and the geometry of the transition state as well as the curvature of the reaction path at this point of the PES are all known.

The unidimensional tunnelling calculations described earlier presume that movement along the reaction coordinate is electronically and vibrationally adiabatic. In real systems there are two sources of non-adiabatic effects on the reaction coordinate: (1) changes in the frequencies of the internal displacements

(perpendicular to the reaction coordinate) and (2) curvilinear effects on the reaction coordinate. Such effects are more pronounced in exothermic reactions, which may lead to vibrationally excited products, and in systems where a light atom is transferred between two heavy atoms (e.g., I–H–I), because the diagonalisation of the kinetic energy in such systems leads to a substantial curvature of the PES.

The most common and meaningful example of the breakdown of the vibrational adiabaticity is the deviation of the tunnelling path relative to the minimum energy path (MEP). Tunnelling occurs preferably along a path displaced towards the concave side of the MEP, which corresponds to the classical turning points for the vibrations perpendicular to the reaction path (Figure 6.11). This path, first described by Marcus and Coltrin [15], contracts the reaction coordinate and leads to a thinner, albeit higher, barrier. Although ΔV^* is larger along this path, Δx is smaller and compensates for the energy factor because it appears as a square root in the exponential decay, eq. (6.45). The Marcus and Coltrin path minimises the exponential dumping of the wave function in the classically forbidden region, and gives the least-action tunnelling correction.

The tunnel effect is the most important correction to the classical TST for reactions involving light particles such as H-atom transfers, proton transfers or hydride

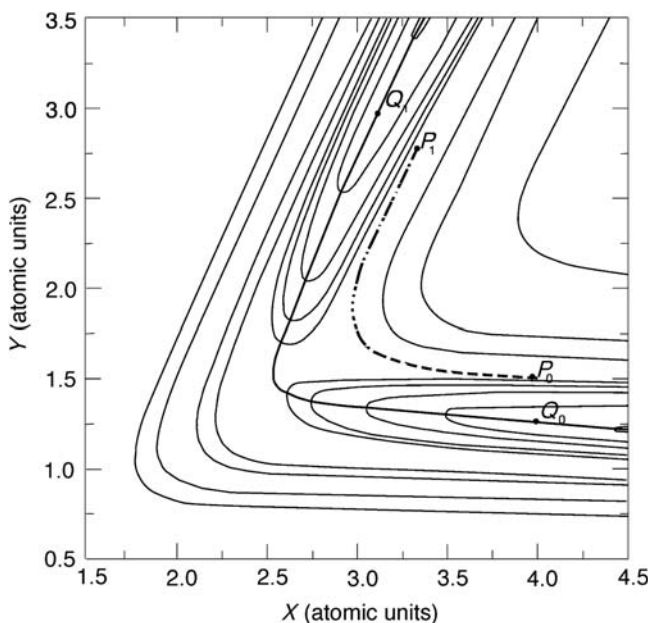
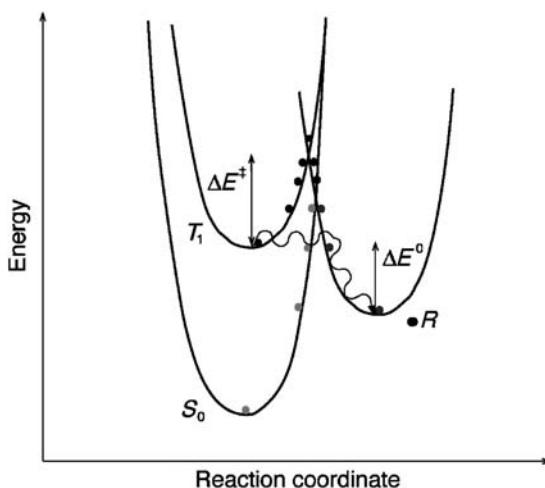


FIGURE 6.11

Marcus–Coltrin path (dashed line) and MEP (full line) in a PES for the $\text{H} + \text{H}_2$ reaction. P_0 and P_1 represent the initial and final points for tunnelling of a trajectory in the Marcus–Coltrin path, respectively; Q_0 and Q_1 have the same meaning, but for the MEP.

**FIGURE 6.12**

Increase in the reaction quantum yield owing to nuclear tunnelling. Thermal activation takes the system over the barrier and across a funnel from the product surface to the ground-state reactant surface, which may take some system back to the reactants. In contrast, nuclear tunnelling places the reactive systems in a region of the product surface beyond the funnel with the reactants, and the systems cannot return to their original state.

transfers. The importance of this correction increases as the temperature is lowered. Traditionally, the experimental evidence for nuclear tunnelling in a chemical reaction comes from: (1) sizeable deviations from the Arrhenius law, (2) isotope-dependent pre-exponential factors, (3) anomalously high KIE. Additionally, in some photochemical reactions it has been suggested that nuclear tunnelling could lead to higher product quantum yields than thermal activation (Figure 6.12).

6.3 Intersecting-state model

The collision theory and the TST offer methods to calculate the rates of chemical reactions, but both require some information on the PES of the system. The minimum information that they require is the difference in energy between the saddle-point and the reactants, which gives the critical energy necessary for the reaction, ε_c in eq. (5.15), or the difference between the ZPEs of the transition state and reactants, ΔE_0 in eq. (6.13). Just as the simple collision theory can be improved with the calculation of trajectories with a Maxwell–Boltzmann distribution of velocities that explore large regions of the PES, classical TST can also be improved by the inclusion of tunnelling, which requires the knowledge of the PES along the reaction path, or by employing a variational method to optimise

the location of the transition state, and which requires an even more detailed knowledge of the PES. Thus the practical application of these methods depends on our knowledge of the PES. With the currently available *ab initio* methods and using fast computers, it has been possible to obtain the properties of transition states with chemical accuracy (better than 1 kcal mol⁻¹) for a number of triatomic and tetra-atomic systems, and for some alkyl + alkane reactions [16,17]. However, it remains an enormous challenge to calculate, from first principles, accurate PESs for polyatomic systems without using information on the kinetics of the systems.

Density functional theory (DFT) offers the opportunity to calculate the energies of nuclear configurations of polyatomic systems with an increasing efficiency. “Direct dynamics”, where the energies of the nuclear configurations are calculated as they are reached by a trajectory, promise to bypass the need for a PES in rate calculations. However, chemists need more general and structure-motivated methods to interpret and predict reactivity. Semi-empirical methods may play a significant role in this respect, because they offer a simple, accurate and structure-related approach to chemical reactivity.

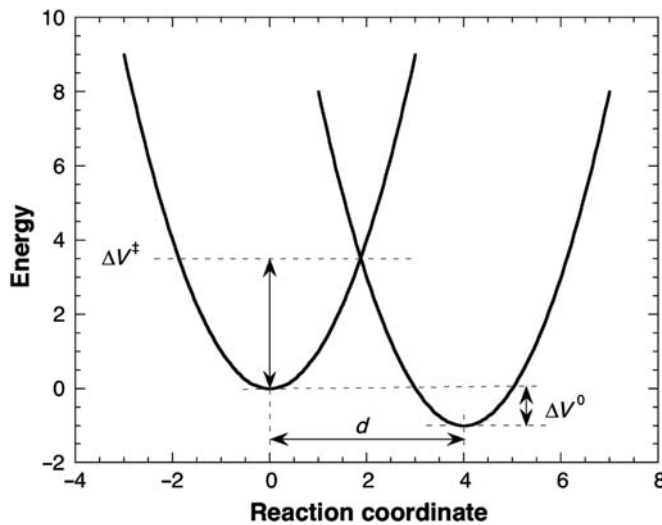
The distinctive features of semi-empirical methods are the use of experimental information on reactants and products, and simplified potential models to calculate the transition-state structure and energy. A semi-empirical model that provides useful transition-state data on bond-breaking-bond-forming reactions is the intersecting/interacting state model (ISM) [18,19].

ISM is a unidimensional reactivity model based on the diabatic method originally proposed by Evans and Polanyi [20] and on the conservation of the bond order along the reaction coordinate of the bond-energy-bond-order (BEBO) first proposed by Johnston and Parr [21]. For a reaction of the type



the diabatic method uses the potential curves of the reactive fragments, BC and AB to build the reaction coordinate and, at a later stage, includes the resonance energy between the two fragments at the transition state. The interesting feature of this method is that it employs the properties of the reactants and products, readily accessible from experiment, to obtain a first approximation for the reaction coordinate. For example, the vertical separation between the reactant and product minima is the reaction energy, and can be easily obtained from the difference of bond dissociation energies of products and reactants, or from the equilibrium constant. However, as illustrated in Figure 6.13, the diabatic method can only be applied if it is possible to calculate the separation of the reactants and products minima along the reaction coordinate, *d*.

The success of the method in calculating the horizontal separation *d* from the properties of the reactants and products ultimately determines its ability to provide reasonable estimates of the activation energy. According to the ISM, the separation *d* is the sum of the reactive bonds’ extensions from their equilibrium to their transition-state configurations. For a reaction such as that of

**FIGURE 6.13**

Relationship between the barrier height and the separation between the minima of the potential functions describing the reactant and product fragments along the reaction coordinate.

mechanism (6.VIII), this is the sum of the extension of the BC bond with that of the AB bond

$$d = \left| l_{BC}^{\ddagger} - l_{BC,eq} \right| + \left| l_{AB}^{\ddagger} - l_{AB,eq} \right| \quad (6.58)$$

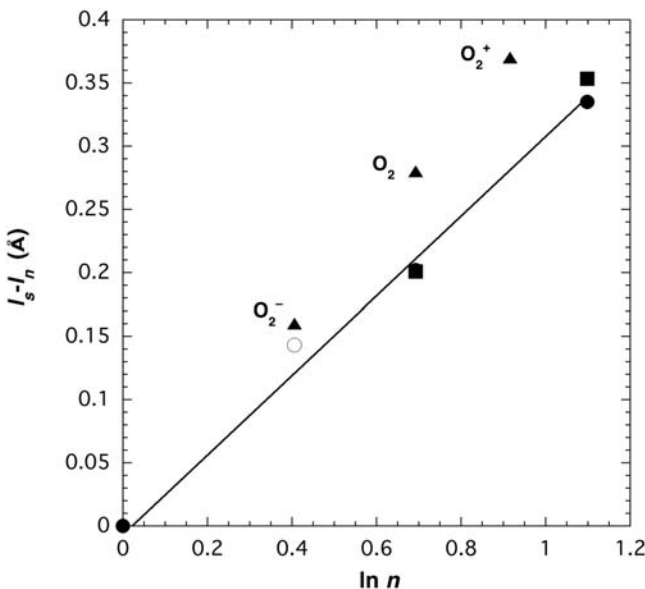
Next, the method requires a relation between the bond extensions and a parameter that can be calculated for any arbitrary bond-breaking-bond-forming reaction. A very interesting relationship involving bond lengths was found by Pauling [22], who showed that they can be related to the corresponding bond orders n ,

$$l_{n,eq} - l_{s,eq} = -0.6 \log(n) = -a \ln(n) \quad (6.59)$$

where $l_{s,eq}$ represents the length of the single bond. This relation is illustrated in Figure 6.14 for CC, NN and OO bonds.

Pauling's equation can be generalised to transition-state configurations, rather than equilibrium ones, using a different scaling

$$\begin{aligned} l_{BC}^{\ddagger} - l_{BC,eq} &= -a' (l_{BC,eq} + l_{AB,eq}) \ln\left(\frac{l_{BC}^{\ddagger}}{l_{BC,eq}}\right) \\ l_{AB}^{\ddagger} - l_{AB,eq} &= -a' (l_{BC,eq} + l_{AB,eq}) \ln\left(\frac{l_{AB}^{\ddagger}}{l_{AB,eq}}\right) \end{aligned} \quad (6.60)$$

**FIGURE 6.14**

Pauling's relationship between equilibrium bond lengths and bond orders. Circles represent CC bonds and squares represent NN bonds. The O₂ bond lengths at several oxidation states are relative to O₂²⁻ [23]. The open circle represents benzene and was not included in the correlation.

where the scaling by $a'(l_{BC,\text{eq}} + l_{AB,\text{eq}})$ rather than a is related to the fact that two bonds are involved in the transition state, and that longer bonds will extend more than shorter bonds. The value of the scaling factor a' will be discussed shortly later, but the generalisation of the Pauling relation allows the method to focus on transition-state bond orders, n^\ddagger , rather than bond extensions.

The calculation of transition-state bond orders is much facilitated by the insightful BEBO method of Johnston and Parr, where the bond order is conserved along the reaction coordinate

$$n_{BC} + n_{AB} = 1 \quad (6.61)$$

and defines the reaction coordinate

$$n = n_{AB} = 1 - n_{BC} \quad (6.62)$$

The BEBO method has been quite successful in calculating the activation energies of a large number of atom-transfer reactions, but reveals some difficulties with reactions involving dramatic ZPE differences. For example, it predicts the structure Cl–H–Cl to be a stable molecule rather than a transition state of the Cl + HCl atom exchange. We will not pursue the BEBO method any further,

but make use of its definition of the reaction coordinate to express the sum of bond extensions as

$$d = -a'(l_{BC,eq} + l_{AB,eq}) \ln [n^\ddagger(1 - n^\ddagger)] \quad (6.63)$$

For a symmetrical reaction ($\Delta V^0 = 0$), A = C, the transition-state bond order must be $n^\ddagger = 0.5$, and the bond extensions can be calculated if a' is known, or vice versa. An interesting feature of eq. (6.63) is that d is a minimum for $n^\ddagger = 0.5$. The sum of bond extensions, for the same equilibrium bond lengths, will increase for endothermic and for exothermic reactions.

6.3.1 Activation energies

The simplest method to obtain the scaling factor a' in eq. (6.63) is purely empirical. Later we will see that the scaling can also be made without using any experimental kinetic information. Representing the energy dependence of the BC and AB bonds on their bond lengths by Morse curves

$$\begin{aligned} V_{BC} &= D_{e,BC} \left\{ 1 - \exp[-\beta_{BC}(l_{BC} - l_{BC,eq})] \right\}^2 \\ V_{AB} &= D_{e,AB} \left\{ 1 - \exp[-\beta_{AB}(l_{AB} - l_{AB,eq})] \right\}^2 + \Delta V^0 \end{aligned} \quad (6.64)$$

where the classical reaction energy is

$$\Delta V^0 = D_{e,BC} - D_{e,AB} \quad (6.65)$$

For an exothermic reaction, the bond that is formed is stronger than the bond that is broken, $D_{e,AB} > D_{e,BC}$, and $\Delta V^0 < 0$.

Rewriting the Morse curves to make their relation between bond extension and energy explicit

$$\begin{aligned} l_{BC} - l_{BC,eq} &= -\frac{1}{\beta_{BC}} \ln \left[1 - \sqrt{\frac{V_{BC}}{D_{e,BC}}} \right] \\ l_{AB} - l_{AB,eq} &= -\frac{1}{\beta_{AB}} \ln \left[1 - \sqrt{\frac{(V_{AB} - \Delta E^0)}{D_{e,AB}}} \right] \end{aligned} \quad (6.66)$$

we can express d in terms of the Morse parameters just by recognising that, at the transition state, the energies of BC and AB are identical

$$V_{BC}\left(l_{BC}^\ddagger\right) = V_{AB}\left(l_{AB}^\ddagger\right) = \Delta V^\ddagger \quad (6.67)$$

which leads to

$$d = -\frac{1}{\beta_{AB}} \ln \left[1 - \sqrt{\frac{(\Delta V^\ddagger - \Delta V^0)}{D_{e,AB}}} \right] - \frac{1}{\beta_{BC}} \ln \left[1 - \sqrt{\frac{\Delta V^\ddagger}{D_{e,BC}}} \right] \quad (6.68)$$

For a symmetrical reaction, the comparison between the equation above and eq. (6.63) yields

$$a' = \frac{\ln \left(1 - \sqrt{\frac{\Delta V^\ddagger}{D_e}} \right)}{2l_{\text{eq}}\beta \ln(0.5)} \quad (6.69)$$

This equation applies only to symmetrical reactions. It is useful because it gives the scaling factor for a given barrier and Morse curve parameters of the reactants, which are identical to the products. The choice of the system that will be the reference for the ISM is restricted by the diabatic approximation followed in the derivation of this equation. This approximation does not consider the effect of resonance at the transition state. Thus, it is convenient to use as reference a system where such resonance is expected to be minimal. The obvious choice is the H + H₂ system, in view of its small number of electrons, and relatively high ionisation potentials and low electron affinities of the reactants. Replacing ΔV^\ddagger by the experimental $E_a = 31.8 \text{ kJ mol}^{-1}$, and using the Morse parameters of the H₂ presented in [Appendix III, Parameters Employed in ISM Calculations](#), the above equation gives $a' = 0.154$. Historically, the model was scaled to a different set of experimental activation energies and $a' = 0.156$ was obtained. The difference between these two values is irrelevant. With $a' = 0.156$ the model gives $E_a = 32.6 \text{ kJ mol}^{-1}$ for the H + H₂ reaction.

The adequacy of ISM to calculate the sum of bond extensions from reactant or product equilibrium bond lengths to the transition state configuration, d , can be assessed comparing the value of d with data available from potential energy surfaces of small systems, [Table 6.3](#). ISM overestimates the value of d for the O + CH₄ and OH + CH₄ systems, which are known to form precursor and successor complexes. Such complexes are very common in hydrogen-bonded systems and will be further discussed in [Chapter 13, Acid-Base Catalysis and Proton-Transfer Reactions](#), on proton transfer reactions. [Figure 6.15](#) shows that the increase of d with $|\Delta V^\ddagger|$, expected from eq. (6.63) is also observed in potential energy surfaces.

The activation energy calculated with $a' = 0.156$ accounts for the resonance of the H + H₂ system, but before the ISM can be applied to other systems, it must allow for the difference in resonance between its reference system and those of the others. In this context, resonance is defined as the stabilisation achieved when the electrons can move under the simultaneous influence of more than two nuclei. It is a measure of the electronic delocalisation present in the tri-atomic transition states of the ISM reaction coordinate. The electronic movement is facilitated by low ionisation potentials (I_P) and high electron affinities (E_A) of the transition-state fragments. In fact, the ionisation potential is defined as the energy necessary to eject an electron from a neutral species and form a mono-positive cation

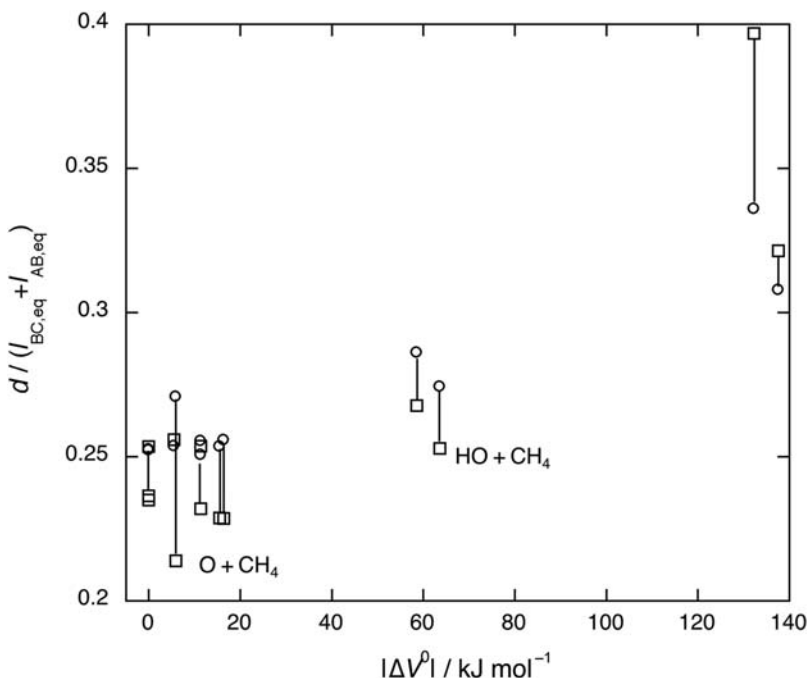


Table 6.3 Bond extensions calculated by intersecting/interacting state model (ISM) ($m = 1$) and given by *ab initio* methods of H-atom transfer reactions [24].

System	ΔV_{cl}^0 (kcal mol ⁻¹)	<i>Ab initio</i> (Å)	ISM (Å)
$H + H_2 \rightarrow H_2 + H$	0	0.376	0.374
$CH_3 + CH_4 \rightarrow CH_4 + CH_3$	0	0.514	0.549
$C_2H_5 + C_2H_6 \rightarrow C_2H_6 + C_2H_5$	0	0.514	0.552
$CH_3 + C_2H_6 \rightarrow CH_4 + C_2H_5$	-3.7	0.499	0.553
$H + CH_4 \rightarrow H_2 + CH_3$	-1.3	0.468	0.464
$NH_2 + CH_4 \rightarrow NH_3 + CH_3$	-3.9	0.480 ^a	0.537
$O + CH_4 \rightarrow OH + CH_3$	1.4	0.44	0.557
$OH + CH_4 \rightarrow H_2O + CH_3$	-15.2	0.517	0.561
$F + CH_4 \rightarrow HF + CH_3$	-32.9	0.644	0.617
$O + H_2 \rightarrow OH + H$	2.7	0.397	0.429
$NH_2 + H_2 \rightarrow NH_3 + H$	-2.7	0.445	0.448
$OH + H_2 \rightarrow H_2O + H$	-14.0	0.455	0.486
$F + H_2 \rightarrow HF + H$	-31.6	0.658	0.557

Note: The scaling factor employed in these calculations was $a'_{sc} = 0.182$, from the fitting to $H + H_2$ potential energy surface, rather than $a' = 0.156$.

^aFrom a hybrid Hartree–Fock-density functional method [25].

**FIGURE 6.15**

Increase in the sum of reduced bond extensions to the transition state according to *ab initio* calculations (squares) and to ISM (circles) as a function of $|\Delta V^0|$. The lines unite the reduced bond extension of the same system calculated by the two methods. *ISM*, Intersecting/interacting state model.

A low I_P means a weak attraction between the electron and the nucleus, and makes it easier to share the electron with other nuclei. The electron affinity is defined as the energy necessary to form a mono-negative anion from a neutral species and an electron



A high E_A corresponds to a more stable anion and a greater ability of the nucleus to interact with an additional electron.

The electron affinity is a measure of the capacity of a molecule or a radical to accept precisely one electron from an electron donor. However, in general, in a transition state we should expect to observe a partial electron delocalisation, rather than a complete electron transfer from A to BC, or from C to AB. The extent to which partial electron transfer contributes to the lowering of the binding energy by maximal flow of electrons, is measured by the electrophilicity index proposed by Parr [26]

$$m = \frac{-\mu_{\text{el}}}{\eta_{\text{el}}} = \frac{I_P + E_A}{I_P - E_A} \quad (6.70)$$

which is the ratio between the negative value of the electronic chemical potential, $\mu_{\text{el}} = -(I_{\text{P}} + E_{\text{A}})/2$, and the chemical hardness, $\eta_{\text{el}} = (I_{\text{P}} - E_{\text{A}})/2$. The electrophilicity index gives the saturation point for electron inflow at the transition state. For very large I_{P} or very small E_{A} , the electron inflow is negligible and $m \approx 1$. This should be the case of the reference system $\text{H} + \text{H}_2$. In contrast, $m > 1$ reflects an electronic stabilisation of the transition state, much in the same manner as a bond order greater than unity is associated with a stronger bond.

Many other reactivity models have incorporated electronic factors such as the ones mentioned above. A good example is the valence-bond approach to reactivity formulated by Shaik [27], which expresses the barrier height as a fraction of the chemical hardness.

Our confidence that these electronic factors are not just an *ad hoc* scheme to account for the transition-state energy comes from the fact that they are also present in the bond dissociation energies. For example, the bond dissociation energy (D_0^{298}) of a C–H bond in CH_3NH_2 is 48 kJ mol⁻¹ lower than that of CH_4 . Figure 6.16 shows how bond dissociation energies of CH_3R molecules correlate with the values of m of the corresponding CH_2R radicals.

The electrophilicity index of an atom-transfer reaction, mechanism (6.VIII), can be calculated from four different combinations of the ionisation potentials and electron affinities of the atoms or radicals involved in the reaction. Two of them make use of the properties of only one species, $I_{\text{P}}(\text{A})$ and $E_{\text{A}}(\text{A})$ or $I_{\text{P}}(\text{C})$

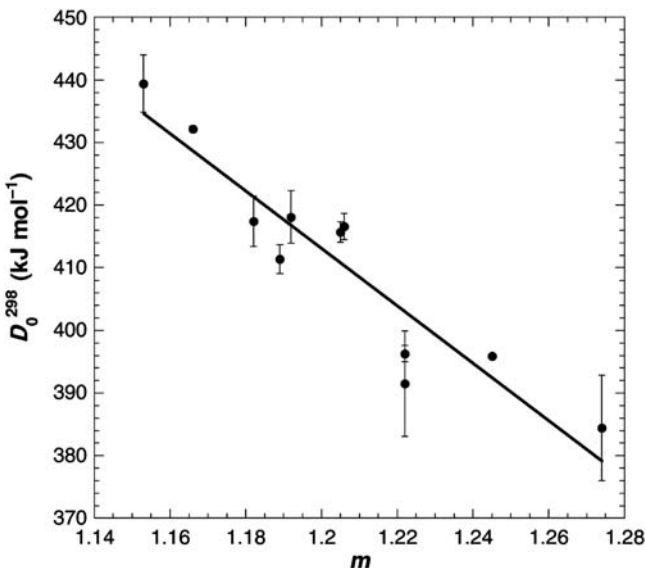


FIGURE 6.16

Correlation between the bond dissociation energies of C–H bonds in CH_3R molecules and the electrophilicity indexes of the corresponding CH_2R radicals.

and $E_A(C)$, and the other two involve cross terms, $I_P(A)$ and $E_A(C)$ or $I_P(C)$ and $E_A(A)$. These latter two cases correspond to charge transfer or polar effects in the transition state. The dominant combination is that which maximises m , because it produces a greater stabilisation of the transition state. Figure 6.17 illustrates the effect of m in the stabilisation of the transition-state energy.

With the inclusion of the electrophilicity index, the transition state given by the intersection of the Morse curves in eq. (6.64), can be obtained from

$$\begin{aligned} D_{e,BC} \left\{ 1 - \exp \left[\frac{a'(l_{AB,eq} + l_{BC,eq})\beta_{BC} \ln(1-n^\ddagger)}{m} \right] \right\}^2 \\ = D_{e,AB} \left\{ 1 - \exp \left[\frac{a'(l_{AB,eq} + l_{BC,eq})\beta_{AB} \ln(n^\ddagger)}{m} \right] \right\}^2 + \Delta V^0 \end{aligned} \quad (6.71)$$

where the relation between transition-state bond extensions and bond orders, eq. (6.60), has been included. The value of n^\ddagger that satisfies the above equation must be in the [0,1] interval and is very simple to calculate. All the other parameters involved in the calculations are given by the Morse curves or electronic parameters of the relevant species, and are experimentally accessible for a large number of species. In the special case of a symmetrical reaction, the above expression reduces to

$$\Delta V^\ddagger = D_e \left\{ 1 - \exp \left[\frac{2a' l_{eq} \beta \ln(0.5)}{m} \right] \right\}^2 \quad (6.72)$$

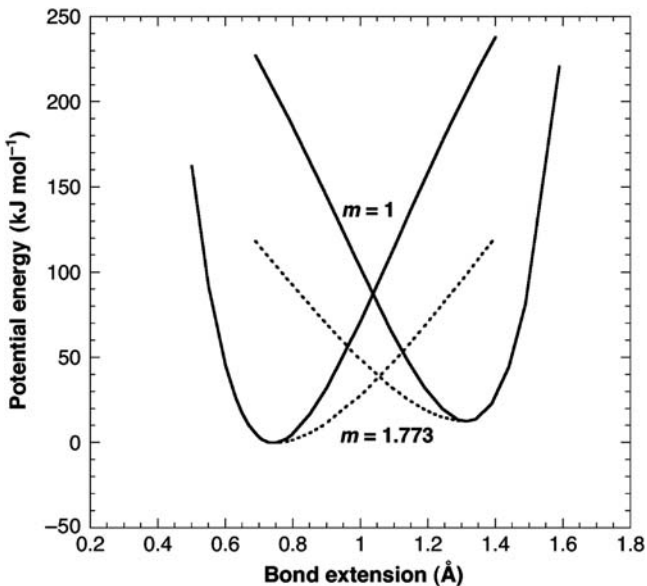


FIGURE 6.17

Lowering of the activation owing to an increase in the value of m at the transition state.

The hydrogen atom-transfer reactions of the type $R + H_2 \rightarrow RH + H$, where $R = H, F, Cl, Br, I, OH, SH, SeH, NH_2, PH_2, AsH_2, CH_3, SiH_3$ and GeH_3 , have been studied in great detail and are an important training set for reactivity models. Table 6.4 compares the activation energies of these reactions with the reaction energy barriers calculated by the ISM using the Morse curve parameters presented in Appendix III, Parameters Employed in ISM Calculations and eq. (6.71). The electrophilicity indexes were calculated with the ionisation potentials and electron affinities of Appendix III, Parameters Employed in ISM Calculations and eq. (6.70). Given the approximations involved, the agreement between the calculated and the experimental barriers is rather good.

It is very important to define precisely the energy barriers employed in chemical kinetics and explore the relations between them [37]. Figure 6.18 shows the difference, at 0 K, between the purely electronic energy barrier, ΔV^\ddagger , defined as the potential energy difference between the classical transition state and the electronic energy of the reactants, and the vibrationally adiabatic barrier, ΔV_{ad}^\ddagger , which includes the ZPE difference between the transition state and the reactants. At a given temperature T , we have to add the thermal energy to the transition state as well as to the reactants, using the respective heat capacities, and arrive at the internal energy of activation, ΔU_T^\ddagger . Furthermore, using the definition of enthalpy, $H = U + pv$, a $\Delta(pv)$ term must be added to the transition state and reactants before we obtain the enthalpy of activation, ΔH^\ddagger . For a reaction in the gas phase, assuming ideal gas behaviour,

$$\Delta H^\ddagger = \Delta U_T^\ddagger + \Delta n_g^\ddagger RT \quad (6.73)$$

where Δn_g^\ddagger is the change in the number of molecules in going from the reactants to the transition state ($\Delta n_g^\ddagger = -1$ for a bimolecular reaction and $\Delta n_g^\ddagger = 0$ for a unimolecular reaction).

It should be noted that, given the relation $d(1/T) = -dT/T^2$, the activation energy is a phenomenological quantity, defined from [38]

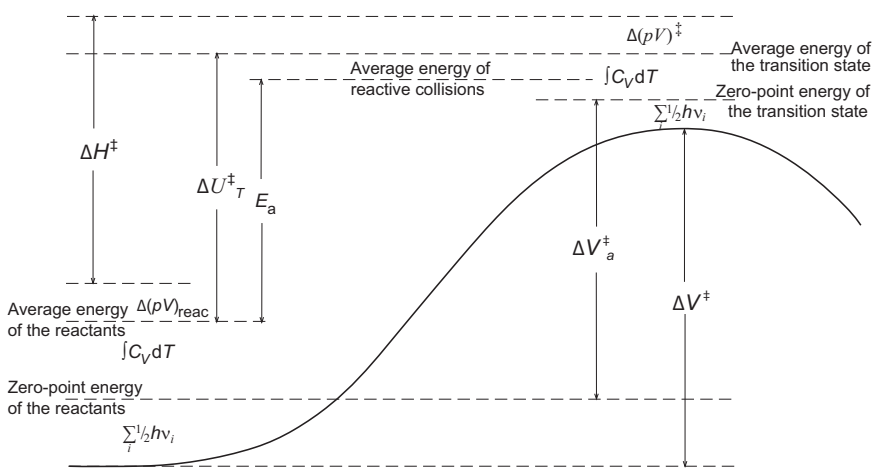
$$\begin{aligned} \frac{d \ln k}{d(1/T)} &= -\frac{E_a}{R} \\ \frac{d \ln k}{dT} &= \frac{E_a}{RT^2} \end{aligned} \quad (6.74)$$

per mole, and does not correspond to any of the barriers defined above. It depends on the range of temperatures experimentally employed. The activation energy in the mid-temperature range is the average total energy (relative translational plus internal energies) of all molecules undergoing reaction minus the average total energy of all the reactant molecules. Additionally, at low temperatures, the tunnel effect is significant and contributes to lower E_a . This effect is already present in the $H + H_2$ system and the empirical scaling of the ISM by the activation energy of this system, already accounts for some tunnelling. However, tunnelling is not transferable between different systems and this may contribute to some of the

Table 6.4 Calculation of energy barriers by intersecting/interacting state model (ISM), ΔV^\ddagger and experimental activation energies, E_a , for H-atom transfers in the gas phase.

Reaction	ISM		Experimental			Reference
	<i>m</i>	ΔV^\ddagger (kJ mol ⁻¹)	E_a (kJ mol ⁻¹)	<i>T</i> (K)	ΔE^0 (kJ mol ⁻¹)	
$H + H_2 \rightarrow H_2 + H$	1	32.6	31.8	450–750	0	[28]
$H_2 + CH_3 \rightarrow H + CH_4$	1	42.7	46 ± 2	300	-5	[29]
$H + SiH_4 \rightarrow H_2 + SiH_3$	1.418	8.2	16.0	290–660	-65	[30]
$H + GeH_4 \rightarrow H_2 + GeH_3$	1.508	3.2	9.4	210–440	-100	[31]
$H_2 + NH_2 \rightarrow H + NH_3$	1.154	32.1	36 ± 2	300	-11	[29]
$H + PH_3 \rightarrow H_2 + PH_2$	1.292	6.7	8.7	293–472	-97	[32]
$H + AsH_3 \rightarrow H_2 + AsH_2$	1.296	3.7	6.0	294–424	-130	[32]
$H_2 + OH \rightarrow H + H_2O$	1.327	8.2	17 ± 2	300	-58	[29]
$H + SH_2 \rightarrow H_2 + SH$	1.572	5.7	15	500–1000	-64	[33]
$H_2 + F \rightarrow H + HF$	1.679	1.1	4 ± 0.4	300	-132	[34]
$H + HCl \rightarrow H_2 + Cl$	1.773	14.4	17.3	298–1190	-13	[34]
$H + HBr \rightarrow H_2 + Br$	1.796	2.5	2.6	296–523	-80	[35]
$H + HI \rightarrow H_2 + I$	1.828	0.5	2.4	250–373	-150	[36]

Note: The reaction energy, ΔE^0 , contains ZPE corrections for the bond that is broken and the bond that is formed in the course of the reaction.

**FIGURE 6.18**

Comparison between the several definitions of the reaction barriers. Tunnelling was not considered, but tends to reduce the observed activation energy.

differences between the calculated and experimental barriers in [Table 6.4](#). A more exact estimate of the activation energies must take into account the tunnelling of each system, the ZPE difference between the transition state and reactants, and the heat capacities of the transition state and reactants. This will be addressed later. For the moment, it is interesting to focus on the reactivity patterns revealed by the model.

One of the older reactivity principles relates the activation energy to the reaction enthalpy (ΔH^0). This principle was formulated independently by Bell, and by Evans and Polanyi [39,40]. The Bell–Evans–Polanyi (BEP) relationship is

$$E_a = E_a^0 + \alpha \Delta H^0 \quad (6.75)$$

where α is constant for a given series of reactions and E_a^0 is the intrinsic barrier, that is, the energy of activation of the reaction of that family for which $\Delta H^0 = 0$. If we define a series of reactions as a set of systems with similar modified Morse curves, that is, with similar values for the parameters l , β and m , we may take the $H + HCl$ and $H + HBr$ reactions as examples. Indeed, these reactions obey the BEP relationship: the most exothermic reaction is also that with the lowest activation energy. This reactivity pattern is also present in the ISM: as ΔV^0 becomes more negative in [eq. \(6.71\)](#), the barrier is lowered.

The definition of similar Morse curves given above includes the parameter m , and this is why *modified* Morse curves are explicitly mentioned. The reaction series must have a constant value of m , otherwise large deviations are observed. For example, the reactions $CH_3 + H_2$ and $H + HCl$ have similar reaction energies, but the activation energy of the latter that has the highest m value is much smaller. The

importance of polar or resonance effects has been recognised by other reactivity models, but the ISM integrates this factor in a simple and quantitative manner.

Even when the reaction energies and electrophilicity indexes are similar, the activation energies may be very different. For example, the activation energy of the $\text{CH}_3 + \text{H}_2$ reaction is 50% higher than that of the $\text{H} + \text{H}_2$ reaction. Such a difference cannot be related to the reaction energy, because both reactions are nearly isothermal, or to the electronic parameters, because both have $m \approx 1$. The only significant difference between the Morse curves of the H–H and C–H bonds is the equilibrium bond length. The C–H bond is 30% longer than the H–H bond. According to eq. (6.72), the ISM predicts that longer bonds lead to higher activation energies. This is also apparent in the calculations presented in Table 6.4. This expectation is corroborated by the activation energy of the $\text{CH}_3 + \text{CH}_4$ reaction, which is 61 kJ mol^{-1} [41].

The activation energies of atom-transfer reactions in the gas phase have been collected and updated in many review articles. At present, the National Institute of Standards and Technology (NIST), maintains a database of the kinetics of such reactions that can be accessed through the site <https://kinetics.nist.gov/kinetics/index.jsp>. The vast amount of data available can be rationalised using the three reactivity factors underscored by the ISM: the reaction energy ΔE^0 , the electronic factor m and the equilibrium bond lengths.

6.3.2 Classical rate constants

The most important reactivity observable is the rate constant. The interest in calculating rate constants was already expressed in the development of the collision theory and the TST. Such calculations require a reliable estimate of the reaction barrier, which remains a difficult task for *ab initio* calculations of polyatomic systems. The simplest way to make rate calculations is to use the energy barriers calculated by ISM in eq. (6.57) of the TST. However, in this empirical version of ISM, ΔV^\ddagger was obtained from the scaling to the activation energy of a reference system, and differs from the vibrationally adiabatic barrier $\Delta V_{\text{ad}}^\ddagger$, used in the TST. An approximate relation between the activation energy and vibrationally adiabatic barrier can be obtained neglecting the tunnel effect and the minor difference between the thermal distribution of the molecules in the transition state and in the reactants. Deriving the logarithmic form of eq. (6.13) with respect to T and making it identical to eq. (6.74),

$$\frac{d \ln k}{dT} = \frac{1}{T} + \frac{d \ln K^\ddagger}{dT} = \frac{E_a}{RT^2} \quad (6.76)$$

we obtain, in concentration units,

$$\begin{aligned} E_a &= RT + \Delta U^\ddagger \\ &= RT + \Delta H^\ddagger - p\Delta v^\ddagger \end{aligned} \quad (6.77)$$

where Δv^\ddagger is the difference in volume between the transition state and the reactants.

The heat capacities that distinguish the internal energies from the vibrationally adiabatic energies in Figure 6.18, $\Delta U^\ddagger = \Delta V_a^\ddagger + C_v^\ddagger - C_v^R$, can be estimated assuming that the temperature is sufficiently high to allow the classical equipartition theorem to accurately calculate the mean translational energies and the mean rotational energies, but sufficiently low to neglect the contribution of the vibrational partition function to the internal energy. For a reaction between an atom and a diatomic molecule going through a linear tri-atomic transition state, such as that of mechanism (6.VIII), the equipartition theorem gives $C_v^\ddagger = (3/2 + 1)R$ for the translational and rotational contributions to the transition state, and $C_v^A + BC = (3/2 + 3/2 + 1)R$ for the same modes, but for the reactants. Therefore we have $\Delta C_v = -3/2 R$ and eq. (6.77), becomes

$$\begin{aligned}\Delta V^\ddagger &= RT + \Delta V_{\text{ad}}^\ddagger - \frac{3}{2}RT \\ &= \Delta V_{\text{ad}}^\ddagger - \frac{1}{2}RT\end{aligned}\quad (6.78)$$

We explicitly use ΔV^\ddagger rather than E_a in the expression above, to emphasise that it was obtained using the ISM approximations for a gas-phase A + BC reaction with a linear tri-atomic transition state, in molar concentration units. Under these approximations, and remembering that the ratio of the vibrational partition functions was assumed to be unity, we obtain a compact expression for the classical transition-state rate constants, eq. (6.33),

$$k_c = \sigma \frac{6.82 \times 10^{10}}{\sqrt{T}} \left(\frac{m_A + m_B + m_C}{m_A(m_B + m_C)} \right)^{3/2} \frac{I_{ABC}}{I_{BC}} \exp\left(-\frac{\Delta V^\ddagger}{RT} - \frac{1}{2}\right) \text{dm}^3 \text{mol}^{-1} \text{sec}^{-1} \quad (6.79)$$

for bimolecular reactions in the gas phase, where the constant is obtained when the atomic masses are expressed in amu and the moments of inertia are

$$I_{ABC} = m_A \left(l_{AB}^\ddagger \right)^2 + m_C \left(l_{BC}^\ddagger \right)^2 - \frac{\left(m_A l_{AB}^\ddagger - m_C l_{BC}^\ddagger \right)^2}{m_A + m_B + m_C} \quad (6.80)$$

and

$$I_{BC} = \frac{m_B m_C}{m_B + m_C} \left(l_{BC,\text{eq}} \right)^2 \quad (6.81)$$

The transition-state moment of inertia can only be calculated with the transition-state bond lengths. This is not a problem because the transition-state bond order, n^\ddagger , obtained with eq. (6.71), can be employed in eq. (6.60) to yield the transition-state bond extensions. In summary, classical rate constants can be calculated with eqs. (6.60), (6.71), (6.79), (6.80) and (6.81), that only require bond dissociation energies, vibrational frequencies and bond lengths of the reactive bonds, ionisation energies and electron affinities of the relevant radicals, and the masses of the atoms involved in the reaction coordinate. A few examples can make these calculations more clear.

The $\text{H} + \text{H}_2$ atom exchange is symmetrical, thus it is necessary to have $n^\ddagger = 0.5$, and we can make use of eq. (6.72), with the appropriate Morse curve parameters on Appendix III, Parameters Employed in ISM Calculations, to calculate $\Delta V^\ddagger = 32.6 \text{ kJ mol}^{-1}$. With $n^\ddagger = 0.5$, eq. (6.60) gives $l_{\text{HH}}^\ddagger = 0.901 \text{ \AA}$, and the ratio of the moments of inertia is 5.91. Using these data and $\sigma = 2$ in eq. (6.79), we obtain $k_c = 5.8 \times 10^6 \text{ dm}^3 \text{ mol}^{-1} \text{ sec}^{-1}$ at 440 K, indistinguishable from the experimental rate of $5.7 \times 10^6 \text{ dm}^3 \text{ mol}^{-1} \text{ sec}^{-1}$ at this temperature [42,43]. This excellent agreement is biased by the fact that the ISM was scaled by the activation energy of this system, and results from a compensation of factors because a tunnelling correction of 3.0 was previously calculated for this reaction. The scaling by the experimental activation energy is the cause for the empiricism of this version of the ISM. We will see later how that empiricism can be removed. Nevertheless, the empirical ISM may be very useful if it gives accurate rates for other systems.

The $\text{F} + \text{H}_2$ atom transfer is very asymmetrical and has a large electrophilicity index, $m = 1.679$. The solution of eq. (6.71) yields $n^\ddagger = 0.152$ and $\Delta V^\ddagger = 1.0 \text{ kJ mol}^{-1}$, and then eq. (6.60) gives $l_{\text{HH}}^\ddagger = 0.784 \text{ \AA}$ and $l_{\text{HF}}^\ddagger = 1.404 \text{ \AA}$. The ratio of the moments of inertia is 22.4 and with $\sigma = 2$, eq. (6.79) gives $k_c = 2.9 \times 10^{10} \text{ dm}^3 \text{ mol}^{-1} \text{ sec}^{-1}$ at 300 K. The experimental rate is $1.5 \times 10^{10} \text{ dm}^3 \text{ mol}^{-1} \text{ sec}^{-1}$ at this temperature [44]. The agreement is excellent because a small barrier is expected to have a small tunnelling correction.

The ISM can also be applied to polyatomic systems, but now the partition function ratio of eq. (6.33) does not simplify into the pre-exponential factor of eq. (6.79). For linear transition states, the ratio of the partition functions for atom + diatomic and atom + polyatomic molecule has the same form

$$\frac{Q^\ddagger}{Q_A Q_{BC}} = \left(\frac{q_v}{q_t} \right)^2 P \quad (6.82)$$

where $P = (Q_{\text{rot}})^2 / (Q_{\text{trans}})^3$ and Q_{trans} , Q_{vib} and Q_{rot} are the translational, vibrational and rotational partition functions. The electronic partition functions are equal to the degeneracy of the ground state and are not explicitly considered in this comparison. This formulation gives pre-exponential factors of the order of magnitude of $10^{10} \text{ mol}^{-1} \text{ dm}^3 \text{ sec}^{-1}$ for atom + diatomic and atom + polyatomic molecule systems, in good agreement with the experimental pre-exponential factors. Atom transfers resulting from the attack of diatomic radicals to polyatomic molecules have partition-function ratios of the type $(1/\theta)^4 P$, where $\theta = Q_{\text{rot}}/Q_{\text{vib}}$, and those involving polyatomic radicals and molecules are of the type $(1/\theta)^5 P$. Typical values are $1 \leq Q_{\text{vib}} \leq 10$ and $10 \leq Q_{\text{rot}} \leq 100$, and θ may be anywhere from 1 to 100. However, some of the vibrations in polyatomic transition states are very loose vibrations and sometimes even regarded as hindered rotations. Thus, θ should be rather close to the lower limit. Assuming that the value of the rotational partition function is three times that of the vibrational one, we expect that the pre-exponential factor of diatomic + polyatomic systems should be slightly larger than 10^9 and that of polyatomic + polyatomic systems should be close to $5 \times 10^8 \text{ mol}^{-1} \text{ dm}^{-3} \text{ sec}^{-1}$. Thus the pre-exponential factors of atom + polyatomic,

diatomic + polyatomic and polyatomic + polyatomic systems can be estimated dividing the value obtained for tri-atomic transition states by the factors 1, 9 and 27, respectively, and eq. (6.79) can be generalised to include such systems,

$$k_c = \frac{\sigma}{\theta^j} \frac{6.82 \times 10^{10}}{\sqrt{T}} \left(\frac{m_A + m_B + m_C}{m_A(m_B + m_C)} \right)^{3/2} \frac{I_{ABC}}{I_{BC}} \exp \left(-\frac{\Delta V^\ddagger}{RT} - \frac{1}{2} \right) \text{dm}^3 \text{mol}^{-1} \text{sec}^{-1} \quad (6.83)$$

where $\theta = 3$, BC is a polyatomic molecule and $j = 0, 2$ or 3 when A is an atom, a diatomic radical or a polyatomic radical, respectively.

Using this new approximation, we can also use the ISM to calculate the rates of more complex systems, such as the $\text{CH}_3 + \text{H}_2$ hydrogen atom abstraction. For this system, $m \approx 1$ and the solution of eq. (6.71) with $\Delta E^0 = -5 \text{ kJ mol}^{-1}$, yields $n^\ddagger = 0.487$ and $\Delta V^\ddagger = 43.6 \text{ kJ mol}^{-1}$, and then eq. (6.60) gives $I_{\text{HH}}^\ddagger = 0.932 \text{ \AA}$ and $I_{\text{CH}_3}^\ddagger = 1.292 \text{ \AA}$. The ratio of the moments of inertia is 20.9, $\sigma = 2$, $\theta^j = 9$ and eq. (6.83) give $k_c = 4.8 \times 10^2 \text{ dm}^3 \text{ mol}^{-1} \text{ sec}^{-1}$ at 372 K. The experimental rate is $2.7 \times 10^2 \text{ dm}^3 \text{ mol}^{-1} \text{ sec}^{-1}$ at this temperature [45], a very good agreement for such a simple method.

Figure 6.19 shows the temperature dependence of the $\text{H} + \text{H}_2$, $\text{F} + \text{H}_2$ and $\text{CH}_3 + \text{H}_2$ hydrogen abstraction rates. The classical rates tend to underestimate the lower temperature experimental rates, but the general trends are reproduced very well. The empirical ISM has an interesting pedagogical value in chemical kinetics because it makes the calculation of classical atom-transfer rate constants possible with a pocket calculator and basic information on the reactants and products.

Although appealing for their simplicity, these classical calculations have two limitations: they cannot explain KIEs and do not include tunnelling corrections.

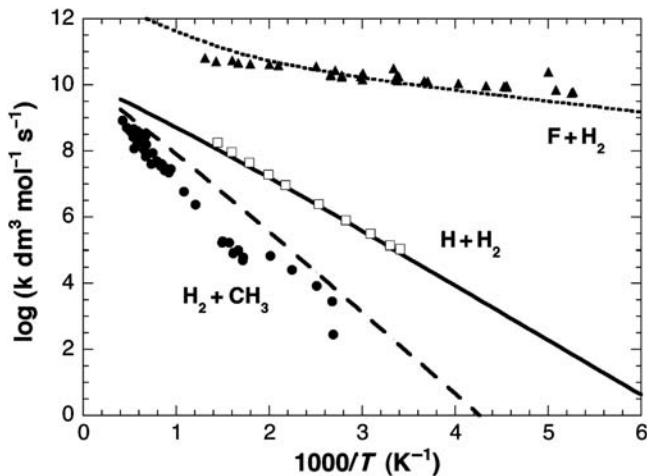


FIGURE 6.19

Temperature dependence of the $\text{H} + \text{H}_2$, $\text{F} + \text{H}_2$ and $\text{CH}_3 + \text{H}_2$ hydrogen abstraction rates, and their comparison with the classical ISM rates. /ISM, Intersecting/interacting state model.

These limitations have been overcome in a more sophisticated formulation, as will be seen below, which additionally removes the empirical scaling of this model to the activation energy of the H + H₂ reaction.

6.3.3 Absolute semi-classical rates

The empiricism of the ISM is eliminated using *ab initio* data, rather than experimental data, to obtain the value of d . The most exact *ab initio* calculations on reactive systems are those of the H + H₂ system. Varandas and co-workers [46] used such *ab initio* calculations to build a DMBE PES, which has the properties presented in Table 6.1. The *ab initio* sum of bond extensions at the transition state of this surface is $d = 0.3746 \text{ \AA}$, and eq. (6.63) with $n^\ddagger = 0.5$ leads to $a'_{\text{sc}} = 0.182$. The ISM is now scaled to structural data and does not involve kinetic information. On the other hand, the model now gives classical (electronic) potential energy barriers, free of ZPE or tunnelling corrections, rather than activation energies. They are directly comparable with the classical barriers of *ab initio* calculations, but require a method to calculate ZPE corrections along all the reaction coordinates before they can be employed in the TST to calculate tunnelling corrections and semi-classical rate constants.

The need for an analytical description of the complete reaction coordinate can be satisfied with an interpolation between the energies of the reactants and products, using the continuity of the reaction coordinate n , following earlier work by Agmon and Levine [47],

$$\begin{aligned} V_{\text{cl}}(n) &= (1 - n)V_{\text{BC}}(1 - n) + nV_{\text{AB}}(n) + n\Delta V^0 \\ &= (1 - n)D_{\text{e,BC}}\{1 - \exp[\gamma_{\text{BC}}\ln(1 - n)]\}^2 + nD_{\text{e,AB}}\{1 - \exp[\gamma_{\text{AB}}\ln(n)]\}^2 + n\Delta V^0 \\ \gamma_{\text{BC}} &= \frac{a'_{\text{sc}}(l_{\text{BC,eq}} + l_{\text{AB,eq}})\beta_{\text{BC}}}{m} \\ \gamma_{\text{AB}} &= \frac{a'_{\text{sc}}(l_{\text{BC,eq}} + l_{\text{AB,eq}})\beta_{\text{AB}}}{m} \end{aligned} \quad (6.84)$$

Equating the first derivative of the classical reaction path, above, to zero gives the location of the classical transition state

$$\begin{aligned} \frac{\partial V_{\text{cl}}(n)}{\partial n} &= -D_{\text{e,BC}}\left[1 - (1 - n^\ddagger)^{\gamma_{\text{BC}}}\right]\left[1 - (1 - 2\gamma_{\text{BC}})(1 - n^\ddagger)^{\gamma_{\text{BC}}}\right] \\ &\quad + D_{\text{e,AB}}\left[1 - (1 - n^\ddagger)^{\gamma_{\text{AB}}}\right]\left[1 - (1 - 2\gamma_{\text{AB}})(n^\ddagger)^{\gamma_{\text{AB}}}\right] + \Delta V^0 = 0 \end{aligned} \quad (6.85)$$

and eq. (6.84) gives the corresponding classical energy.

Using the parameters of the H₂ Morse curve presented in Appendix III, Parameters Employed in ISM Calculations, and knowing that a symmetrical reaction has $n^\ddagger = 0.5$, we calculate $\Delta V_{\text{cl}}^\ddagger = 42.3 \text{ kJ mol}^{-1}$ for the H + H₂ reaction. The classical reaction barrier for this reaction is 40.4 kJ mol⁻¹ according to the DMBE PES, Table 6.1, and 41.5 kJ mol⁻¹ according to the most exact *ab initio*

calculations presently available. Table 6.5 presents the classical potential energy barriers calculated with the semi-classical ISM (scISM) and compares them with the classical barriers obtained by the *ab initio* methods. The agreement is quite satisfactory for such simple calculations without adjustable parameters.

The full reaction path given by eq. (6.84) can also be compared with the MEP of the DMBE PES, Figure 6.10, using the distance along the reaction coordinate defined as

$$\begin{aligned} s = - \sqrt{\left[l_{BC}(n) - l_{BC}^* \right]^2 + \left[l_{AB}(n) - l_{AB}^* \right]^2}, & \quad l_{BC}(n) \leq l_{BC}^* \\ s = + \sqrt{\left[l_{BC}(n) - l_{BC}^* \right]^2 + \left[l_{AB}(n) - l_{AB}^* \right]^2}, & \quad l_{BC}(n) > l_{BC}^* \end{aligned} \quad (6.86)$$

The similarity of scISM and DMBE reaction paths suggests that their tunnelling corrections should be similar. The simplest realistic tunnelling correction is that of the Eckart barrier. This barrier can be fitted to the scISM reaction path using its asymptotic limits, the barrier height ΔV_{cl}^\ddagger and the curvature of this path

Table 6.5 Classical potential energy barriers calculated by *ab initio* methods (V^\ddagger) and by intersecting/interacting state model (ISM) (ΔV_{cl}^\ddagger) [17].

Reaction	Quantum mechanics	scISM	
	V^\ddagger (kJ mol ⁻¹)	m	ΔV_{cl}^\ddagger (kJ mol ⁻¹)
$H + H_2 \rightarrow H_2 + H$	41.5	1	42.3
$CH_3 + CH_4 \rightarrow CH_4 + CH_3$	73.3 ^a	1	74.6
$C_2H_5 + C_2H_6 \rightarrow C_2H_6 + C_2H_5$	69.8 ^a	1	76.4
$H + CH_4 \rightarrow H_2 + CH_3$	61.0	1	55.7
$O + CH_4 \rightarrow OH + CH_3$	55.6	1.349	50.0
$Cl + CH_4 \rightarrow HCl + CH_3$	28.9	2.161	28.4
$NH_2 + H_2 \rightarrow NH_3 + H$	39.8	1.154	44.2
$H + HCl \rightarrow H_2 + Cl$	21.0	1.773	21.7
$OH + H_2 \rightarrow H_2O + H$	23.5	1.327	25.1
$H + SH_2 \rightarrow H_2 + SH$	15.1	1.572	15.6
$H + SiH_4 \rightarrow H_2 + SiH_3$	23.2	1.418	21.5
$CH_3 + HBr \rightarrow CH_4 + Br$	4.9	2.038	11.0
$H + HBr \rightarrow H_2 + Br$	7.9	1.796	10.5
$H_2 + CN \rightarrow H + HCN$	15.1	1.793	9.2
$H + PH_3 \rightarrow H_2 + PH_2$	15.1	1.292	18.8
$H + GeH_4 \rightarrow H_2 + GeH_3$	14.8	1.508	14.0
$H_2 + CCH \rightarrow H + HCCH$	18.3	1.687	8.6
$H_2 + F \rightarrow H + HF$	6.1	1.679	9.2
$H + Cl_2 \rightarrow HCl + Cl$	9.4	1.773	7.1
$H + F_2 \rightarrow HF + F$	7.5	1.679	0.9

^aFrom Ref. [48].

at the classical transition state. This latter parameter can be obtained from the curvature of the scISM reaction path by making the second derivative of [eq. \(6.84\)](#),

$$\begin{aligned} \frac{d^2 V_{\text{cl}}(n)}{dn^2} &= 2\gamma_{\text{BC}} D_{\text{BC}} (1-n^\ddagger)^{\gamma_{\text{BC}}-1} \left[(2\gamma_{\text{BC}} + 1) (1-n^\ddagger)^{\gamma_{\text{BC}}} - \gamma_{\text{BC}} - 1 \right] \\ &\quad + 2\gamma_{\text{AB}} D_{\text{AB}} (n^\ddagger)^{\gamma_{\text{AB}}-1} \left[(2\gamma_{\text{AB}} + 1) (n^\ddagger)^{\gamma_{\text{AB}}} - \gamma_{\text{AB}} - 1 \right] \end{aligned} \quad (6.87)$$

and multiplying it by $(dn/ds)^2$, where

$$\left(\frac{ds}{dn} \right)^2 = \left[\frac{a'_{\text{sc}} (l_{\text{BC}} + l_{\text{AB}})}{m} \right]^2 \left[\frac{1}{(1-n^\ddagger)^2} + \frac{1}{(n^\ddagger)^2} \right] \quad (6.88)$$

The curvature of the scISM reaction path at the transition state

$$f^* = \left(\frac{d^2 V}{dn^2} \right) \left(\frac{dn}{ds} \right)^2 \quad (6.89)$$

gives the imaginary frequency of the transition state

$$\nu_{\text{asym}} = \frac{1}{2\pi c} \sqrt{\frac{f^*}{\mu}} \quad (6.90)$$

where μ is the reduced mass of the anti-symmetric stretch. For a symmetric transition state, $A = C$, μ is given by [eq. \(6.56\)](#). [Figure 6.10](#) also shows the Eckart barrier fitted to the scISM reaction path, which is particularly simple for calculating tunnelling corrections.

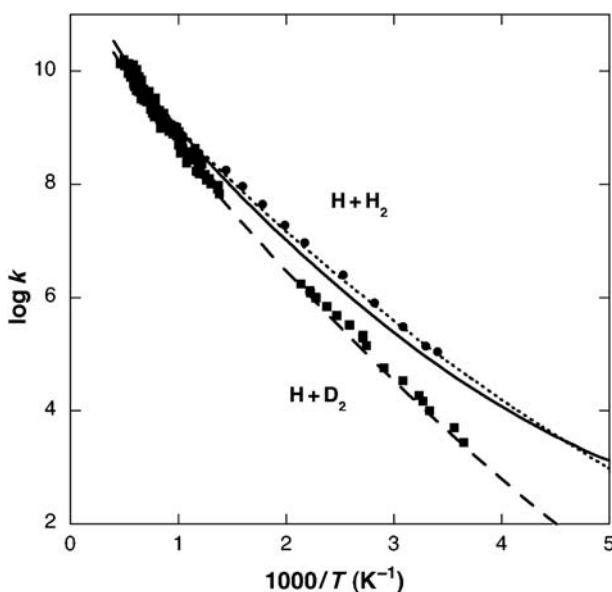
Unfortunately, the tunnelling correction involves an integral, [eq. \(6.54\)](#), and can only be evaluated numerically. Additionally, the transition rate expression for rate constant, [eq. \(6.57\)](#), requires vibrationally adiabatic barriers, and ZPEs have to be added along the classical reaction path of the ISM.

$$V_{\text{ad}}(n) = V_{\text{cl}}(n) + Z(n) \quad (6.91)$$

where $Z(n)$ represents the ZPEs along the vibrationally adiabatic path. The procedure for the calculation of $Z(n)$ is given in [Appendix IV](#), Semi-classical Interacting State Model, and can only be done efficiently using computational methods. The vibrationally adiabatic barrier is the difference between the maximum of [eq. \(6.91\)](#), and the ZPE of the reactants, Z_{BC} ,

$$\Delta V_{\text{ad}}^\ddagger = V_{\text{ad}}(n^\ddagger) - Z_{\text{BC}} \quad (6.92)$$

Thus scISM rate constants, given by the procedure described above, are not as easily accessible as their classical counterparts. In contrast, the tunnelling corrections now extend the accuracy of the calculated rates to lower temperatures, and, with the ZPE corrections, provide reasonable estimates of the KIEs. [Figure 6.20](#) illustrates the results obtained for the $H + H_2$ and $H + D_2$ systems with the ZPE corrections described in [Appendix IV](#), Semi-classical Interacting State Model and the tunnelling corrections of an Eckart barrier fitted to the classical path. This figure also presents

**FIGURE 6.20**

Comparison between the rate constants of the reactions $H + H_2$ and $H + D_2$, in units of $\text{mol}^{-1} \text{dm}^{-3} \text{sec}^{-1}$, calculated by the scISM with Eckart-barrier tunnelling corrections and by the VTST with least-action tunnelling corrections (dotted lines) with the experimental rates. scISM, Semi-classical intersecting/interacting state model.

the VTST calculations with the DMBE PES and least-action tunnelling corrections, which are presumably the most exact rate calculations within the framework of the TST. Calculation using scISM are freely available through the Internet at <http://www.ism.qui.uc.pt:8180/ism/>.

6.3.4 Relative rates

An increasing degree of sophistication has taken us to the most exact absolute rate calculations for the simplest reactive system. In chemical kinetics it is often more interesting to relate a given rate constant to others of similar systems, rather than to make a very accurate absolute rate calculation. Such a relation emphasises the factor that dominates the reactivity of a family of reactions, and is particularly useful if the activation energies are expressed as a simple function of that factor. In Sec. 6.3.1, it was shown that the activation energies of gas-phase atom transfers strongly depend on the reaction energy ΔE^0 , the electronic factor m , and the sum of equilibrium bond lengths ($l_{BC,\text{eq}} + l_{AB,\text{eq}}$). In the intuitive concept of a “family of reactions”, the equilibrium bond lengths of the reactive bonds do not change appreciably, and the first two parameters should control the reactivity.

In order to obtain simplified relations between activation energies and reaction energies, it is useful to consider the free energy of the system with respect to the free energy of the reactants

$$G(n) = [- (1 - n) \ln(1 - n) - n \ln(n)] \Omega + n \Delta G^0 \quad (6.93)$$

This formalism now employs free energies (denoted by G) of which the vibrationally adiabatic potential energy is the low temperature limit [49]. Marcus derived the aforementioned expression, using potential energies, as a Taylor approximation to the BEBO energy profile [50]. The parameter Ω is has units of energy and behaves as an intrinsic barrier, that is, it is related to the barrier of the symmetric reaction ($\Delta G^0 = 0$, $n^\ddagger = 0.5$) in the family of reactions. In fact, for the symmetric reaction,

$$\Omega_0 = \frac{\Delta G^\ddagger}{\ln(2)} \quad (6.94)$$

When the reactants and products are described by Morse curves, the value of Ω can be obtained from eq. (6.72). For simplicity, in this section we employ harmonic oscillators, and the barrier is, by analogy with eq. (6.71)

$$\begin{aligned} \Delta G^\ddagger &= \frac{1}{2} f_{BC} \left[\frac{a'(l_{BC,\text{eq}} + l_{AB,\text{eq}}) \ln(1 - n^\ddagger)}{m} \right]^2 \\ &= \frac{1}{2} f_{AB} \left[\frac{a'(l_{BC,\text{eq}} + l_{AB,\text{eq}}) \ln(n^\ddagger)}{m} \right]^2 + \Delta G^0 \end{aligned} \quad (6.95)$$

Hence for symmetrical harmonic oscillators,

$$\Omega_0 = 2 \ln(2) f_{BC} \left(\frac{a' l_{BC}}{m} \right)^2 \quad (6.96)$$

The location of the transition state for asymmetric reactions is given by the first derivative of eq. (6.93),

$$\frac{\partial G(n)}{\partial n} = \Delta G^0 - \Omega \ln \left(\frac{n^\ddagger}{1 - n^\ddagger} \right) = 0 \quad (6.97)$$

that gives

$$n^\ddagger = \left[1 - \exp \left(-\frac{\Delta G^0}{\Omega} \right) \right]^{-1} \quad (6.98)$$

The functional dependence of these parameters can be further simplified using eq. (6.98) together with eqs. (6.60) and (6.62),

$$\begin{aligned} l_{AB}^\ddagger - l_{AB,\text{eq}} &= a'(l_{AB,\text{eq}} + l_{BC,\text{eq}}) \ln \left[1 + \exp \left(-\frac{\Delta G^0}{\Omega} \right) \right] \\ l_{BC}^\ddagger - l_{BC,\text{eq}} &= -a'(l_{AB,\text{eq}} + l_{BC,\text{eq}}) \ln \left\{ 1 - \left[1 + \exp \left(-\frac{\Delta G^0}{\Omega} \right) \right]^{-1} \right\} \end{aligned} \quad (6.99)$$

to express the sum of bond extensions as

$$d = a'(l_{AB,eq} + l_{BC,eq}) \ln \frac{\left[1 + \exp\left(-\frac{\Delta G^0}{\Omega}\right)\right]}{\left\{1 - \left[1 + \exp\left(-\frac{\Delta G^0}{\Omega}\right)\right]^{-1}\right\}} \quad (6.100)$$

that gives, after a Taylor series expansion

$$d = d(0) + \left(\frac{\partial d}{\partial \Delta G^0}\right)_0 \Delta G^0 + \frac{1}{2} \left(\frac{\partial^2 d}{\partial (\Delta G^0)^2}\right) (\Delta G^0)^2 + \dots \quad (6.101)$$

where

$$d(0) = 2a'(l_{BC,eq} + l_{AB,eq}) \ln 2; \quad \frac{\partial d}{\partial \Delta G^0} = 0; \quad \frac{\partial^2 d}{\partial (\Delta G^0)^2} = \frac{a'(l_{BC,eq} + l_{AB,eq})}{\Omega^2} \quad (6.102)$$

The first three terms of the expansion give

$$d = 2a'(l_{BC,eq} + l_{AB,eq}) \left[\ln(2) + \left(\frac{\Delta G^0}{2\Omega}\right)^2 \right] \quad (6.103)$$

The simplest way to use this expression is to use the relation expressed by eq. (6.95), and represented in Figure 6.21, to obtain

$$(l^\ddagger - l_{BC,eq}) = \frac{-f_{AB}d + \sqrt{f_{AB}^2 d^2 + (f_{BC} - f_{AB})(f_{AB}d^2 + 2\Delta G^0)}}{(f_{BC} - f_{AB})} \quad (6.104)$$

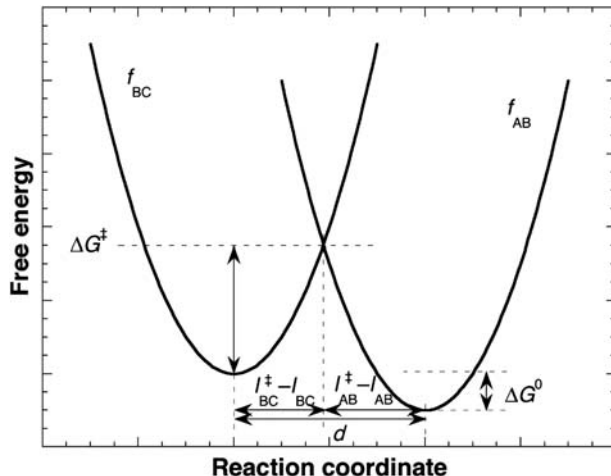


FIGURE 6.21

Representation of the reaction coordinate of the intersecting-state model using harmonic oscillators for reactant and product bonds.

and calculate the free energy of activation from

$$\Delta G^\ddagger = \frac{1}{2} f_{BC} \left[\frac{l^\ddagger - l_{BC,eq}}{m} \right]^2 \quad (6.105)$$

In earlier empirical applications of the ISM, a different nomenclature was employed, which is related to the present parameters via

$$\begin{aligned} \Lambda &= \Omega \sqrt{m} \\ n^\ddagger &= \frac{m}{2} \end{aligned} \quad (6.106)$$

and [eqs. \(6.103\)–\(6.105\)](#), respectively, become

$$d_n = \frac{a'(l_{BC,eq} + l_{AB,eq})}{n^\ddagger} \left[\ln(2) + \frac{n^\ddagger}{2} \left(\frac{\Delta G^0}{\Lambda} \right)^2 \right] \quad (6.107)$$

$$d_r = \frac{-f_{AB} d_n + \sqrt{f_{AB}^2 d_n^2 + (f_{BC} - f_{AB})(f_{AB} d_n^2 + 2\Delta G^0)}}{(f_{BC} - f_{AB})} \quad (6.108)$$

$$\Delta G^\ddagger = \frac{1}{2} f_{BC} d_r^2 \quad (6.109)$$

Both sets of [eqs. \(6.103\)–\(6.105\)](#) and [\(6.107\)–\(6.109\)](#) give the same activation free energy, but through a different reactant bond extension, $d_r = (l^\ddagger - l_{BC,eq})/m$. In principle, for reactions in solution, Ω can be estimated from [eq. \(6.96\)](#), m from [eq. \(6.70\)](#) and the rate constant from [eq. \(6.14\)](#). In practice, Ω may differ from Ω_0 , the solvent may modulate the value of m and the harmonic approximation tends to overestimate the barrier. As a result, it is better practice to use the set of [eqs. \(6.107\)–\(6.109\)](#) with n^\ddagger and Λ as the empirical parameters. In this case, such parameters characterise the electronic and thermodynamic dependences of a family of reactions. The parameter n^\ddagger is associated with an increased transition-state bond order, because the electronic stabilisation of a bond can be seen as an increase in its bond order. The parameter Λ is called a “dynamic parameter” because it is related to the dissipation of the reaction energy. This version of the ISM is not employed to analyse a reaction rate *per se*, but it rationalises structure-reactivity and energy-reactivity relationships. As a result, some order emerges from the large amounts of data on chemical reactivity and the relations between reactivity models become clearer.

References

- [1] H Eyring, *J. Chem. Phys.* **2** (1935) 107.
- [2] Editorial Comment, *New J. Chem.* **14** (1990) 257.

- [3] KJ Laidler, MC King, *J. Phys. Chem.* **87** (1983) 2657.
- [4] S Glasstone, KJ Laidler, H Eyring, *The Theory of Rate Processes*, McGraw-Hill, New York, 1941.
- [5] BC Garrett, DG Truhlar, AJC Varandas, NC Blais, *Int. J. Chem. Kin.* **18** (1986) 1065.
- [6] C Lim, DG Truhlar, *J. Phys. Chem.* **89** (1985) 5.
- [7] BC Garrett, DG Truhlar, *J. Phys. Chem.* **83** (1979) 1052.
- [8] JL Bao, DG Truhlar, *Chem. Soc. Rev.* **46** (2017) 7548.
- [9] FH Westheimer, *Chem. Rev.* **61** (1961) 265.
- [10] M Arndt, O Nairz, J Vos-Andreae, C Keller, G van der Zouw, A Zeilinger, *Nature* **401** (1999) 680.
- [11] L Brillouin, *J. Phys.* **7** (1926) 353.
- [12] G Wentzel, *Z. Phys.* **38** (1926) 518.
- [13] HA Kramers, *Z. Phys.* **39** (1926) 828.
- [14] C Eckart, *Phys. Rev.* **35** (1930) 1303.
- [15] RA Marcus, ME Coltrin, *J. Chem. Phys.* **67** (1977) 2609.
- [16] Y Zhao, N González-García, DG Truhlar, *J. Phys. Chem. A* **109** (2005) 2012.
- [17] A Dybala-Defratyka, P Paneth, J Pu, DG Truhlar, *J. Phys. Chem. A* **109** (2005) 2475.
- [18] AJC Varandas, SJ Formosinho, *J. Chem. Soc. Farad. Trans 2* (82) (1986) 953.
- [19] LG Arnaut, AAC Pais, SJ Formosinho, M Barroso, *J. Am. Chem. Soc.* **125** (2003) 5236.
- [20] MG Evans, M Polanyi, *Trans. Farad Soc* **34** (1938) 11.
- [21] HS Johnston, C Parr, *J. Am. Chem. Soc.* **85** (1963) 2544.
- [22] L Pauling, *J. Am. Chem. Soc.* **69** (1947) 542.
- [23] L Vaska, *Acc. Chem. Res.* **9** (1976) 175.
- [24] LG Arnaut, SJ Formosinho, *Chem. Eur. J* **14** (2008) 6578.
- [25] TV Albu, JC Corchado, DG Truhlar, *J. Phys. Chem.* **105** (2001) 8465.
- [26] RG Parr, LV Szentpály, S Liu, *J. Am. Chem. Soc.* **121** (1999) 1922.
- [27] A Pross, S Shaik, *Acc. Chem. Res.* **16** (1983) 363.
- [28] JA Kerr, in CH Bamford, CFH Tipper (Eds.), *Selected Elementary Reactions*, Elsevier, Amsterdam, 1975, pp. 99–109.
- [29] E Kraka, J Gauss, D Cremer, *J. Chem. Phys.* **99** (1993) 5306.
- [30] A Goumri, W-J Yuan, L Ding, Y Shi, P Marshall, *Chem. Phys.* **177** (1993) 233.
- [31] DF Nava, WA Payne, G Marston, LJ Stief, *J. Geophys. Res.* **98** (1993) 5531.
- [32] NL Arthur, IA Cooper, *J. Chem. Soc. Farad Trans* **93** (1997) 521.
- [33] M Yoshimura, M Koshi, H Matsui, K Kamiya, H Umeyama, *Chem. Phys. Lett.* **189** (1992) 199.
- [34] GY Adusei, A Fontijn, *J. Phys. Chem.* **97** (1993) 1409.
- [35] PW Seakins, MJ Pilling, *J. Phys. Chem.* **95** (1991) 9878.
- [36] K Lorenz, HG Wagner, R Zellner, *Ber. Bunsenges. Phys. Chem.* **83** (1979) 556.
- [37] PD Pacey, *J. Chem. Educ.* **58** (1981) 612.
- [38] DG Truhlar, *J. Chem. Educ.* **55** (1978) 309.
- [39] RP Bell, *Proc. R. Soc. London A* **154** (1936) 414.
- [40] MG Evans, M Polanyi, *Trans. Faraday Soc* **32** (1936) 1333.
- [41] LG Arnaut, AAC Pais, SJ Formosinho, *J. Mol. Struct.* **563/564** (2001) 1.
- [42] KA Quickert, DJ Le Roy, *J. Chem. Phys.* **53** (1970) 1325.
- [43] JV Michael, *J. Chem. Phys.* **92** (1990) 3394.
- [44] A Persky, H Kornweitz, *Int. J. Chem. Kinet.* **29** (1997) 67.

- [45] PC Kobrinsky, PD Pacey, *Can. J. Chem.* **52** (1974) 3665.
- [46] AJC Varandas, FB Brown, CA Mead, DG Truhlar, BC Garrett, *J. Chem. Phys.* **86** (1987) 6258.
- [47] N Agmon, RD Levine, *Chem. Phys. Lett.* **52** (1977) 197.
- [48] A Dybala-Defratyka, P Paneth, J Pu, DG Truhlar, *J. Phys. Chem. A* **108** (2005) 2475.
- [49] N Agmon, *Int. J. Chem. Kinetics* **13** (1981) 333.
- [50] RA Marcus, *J. Phys. Chem.* **72** (1968) 891.

This page intentionally left blank

Relationships between structure and reactivity

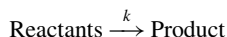
7

7.1 Quadratic free-energy relationships

The view that the ability of molecules to react rests ultimately on their own structural properties has long been dear to chemists. Although the encounter of two molecules triggers unique features which neither molecule possess alone, notably an electron inflow to the reactive bonds up to the point of saturation, the notion that molecules contain all the information necessary to understand their reactivity has proved extremely useful. In the middle of the nineteenth century, Auguste Laurent expressed the idea that ‘structure determines reactivity and is directly connected with crystalline form’ [1]. Chemical reactivity can be understood both as the ability of individual molecules to take part in various chemical reactions as well as the study of rates of such reactions, that is equilibrium and rate processes. In this textbook, we will focus upon rate constants, conscious that their value for the understanding of chemical reactivity depends largely on our ability to relate them with reaction energies and molecular structure.

Chemical reactivity depends on energy relationships along the reaction coordinate. While some features are specific for particular reactions, others are common to series of reactions, which in some sense constitute a *family of reactions*. Those relations are the ones that allow the establishment of structure–reactivity relationships and can be classified into some broad categories.

It is one of the fundamental assumptions of our chemical knowledge that like substances react similarly and that similar changes in structure produce similar changes in reactivity. This is a qualitative and intuitive notion, which can be addressed in a quantitative way in terms of chemical kinetics, that is in terms of the rate constant k



In an ideal situation, one would wish that the changes in k in a series of chemical reactions would be dominated by the changes in a single structural factor. In such a case, other structural factors do not change along the reaction series, or such changes are not significant. Under such conditions, we can say that these processes constitute a reaction family.

Owing to the exponential dependence of the rate upon energy, the rate problem reduces mainly to the determination of the lowest energy barrier that has to be surmounted. The ISM model, which was presented in the previous chapter, points, in general terms, to some structural factors that control the barriers of chemical reactions

and, as a consequence, the rate constants. These relevant factors are (1) *reaction energy*, ΔE^0 , ΔH^0 or ΔG^0 ; (2) the *electrophilicity index* of Parr, m , a measure of the electron inflow to the reactive bonds at the transition state (TS); (3) when the potential energy curves for reactants and products can be represented adequately by harmonic oscillators, the relevant structural parameters are the *force constants* of reactive bonds, f_r and f_p in reactants and products, respectively; and (4) equilibrium *bond-lengths* of reactive bonds, l_r and l_p , in reactants and products, respectively.

Let us represent the course of reaction (7.I) by the intersection of potential energy curves of the reactant BC and the product AB as



When the potential energy of the molecular species is represented by harmonic oscillators, the common energy of the distended configurations of BC and AB at the TS is represented by the following expression:

$$\frac{1}{2}f_r x^2 = \frac{1}{2}f_p(d-x)^2 + \Delta E^0 \quad (7.1)$$

where x is the bond extension of the reactant molecule BC to the TS, and d represents the sum of the bond extensions of BC and AB on going to the TS. In eq. (7.1), $d-x$ represents the bond extension of the product molecule as illustrated in Figure 7.1. This equation expresses reaction energy in terms of a thermodynamic quantity, the internal energy, ΔE^0 , rather than in terms of a difference in the potential energies of products and reactants, ΔV^0 .

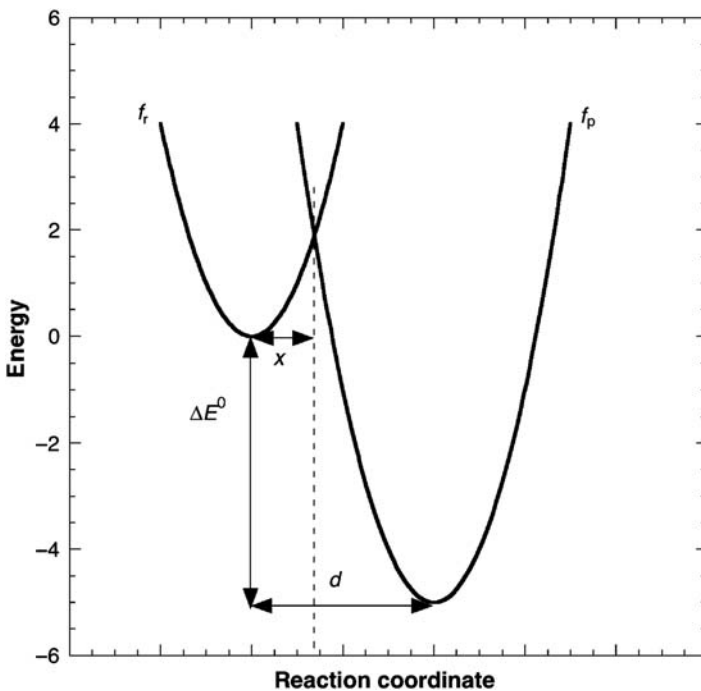
Before pursuing further, a word of caution is necessary. Chemical thermodynamics deals with macroscopic observations but aims to build a bridge between macroscopic variables and events at the microscopic level by specifying the composition of the system in molecular terms. Potential energy, V , is a microscopic variable defined for all configurations of the reacting system. Thus V varies in a continuous manner along the progress variable and defines a reaction path. But thermodynamic energies are not continuous functions along this path. They are only valid for stable or metastable states, i.e., for elementary reactions they are only valid for reactants, products and the TS. Although eq. (7.1), defined in terms of ΔV^0 , possesses a physical meaning for all the points $0 \leq x \leq d$, the same mathematical expression defined in terms of ΔE^0 , or in terms of any other thermodynamic quantity, has no physical meaning for the points interpolated between reactants, TS and products.

The energy barrier for the prototype reaction, measured with respect to reactants, is expressed by the equation

$$\Delta E^\ddagger = \frac{1}{2}f_r x^2 \quad (7.2)$$

Under the particular condition of almost equal force constants for reactant and product, $f=f_r=f_p$, eq. (7.1) becomes

$$\frac{1}{2}fx^2 = \frac{1}{2}fd^2 - fdx + \frac{1}{2}fx^2 + \Delta E^0 \quad (7.3)$$

**FIGURE 7.1**

Reaction coordinate of a bond-breaking–bond-forming reaction in terms of intersecting harmonic oscillators. The reaction coordinate d represents the sum of the reactant and product bond extensions, from equilibrium to transition state configurations.

Solving this equation for the reactant distension, x , yields

$$x = \frac{d}{2} + \frac{\Delta E^0}{fd} \quad (7.4)$$

This expression can also take the more convenient form

$$x = \frac{1}{2}d \left(1 + \frac{2\Delta E^0}{fd^2} \right) \quad (7.5)$$

If we make the substitution of x in the expression of the energy barrier, eq. (7.2), we have

$$\Delta E^\ddagger = \Delta E^\ddagger(0) \left(1 + \frac{\Delta E^0}{4\Delta E^\ddagger(0)} \right)^2 \quad (7.6)$$

where $\Delta E^\ddagger(0)$ represents the *intrinsic barrier* of reaction (7.1).

$$\Delta E^\ddagger(0) = \frac{1}{8}fd^2 \quad (7.7)$$

The intrinsic barrier represents the barrier of the reaction taking it as an isoenergetic process, that is with $\Delta E^0 = 0$.

In the past, Evans and Polanyi [2] have introduced the concepts of *chemical driving force* and *chemical inertia*. By chemical inertia, they meant the work that must be done to produce reaction, partly in breaking BC bond and in placing the atom A sufficiently close to B. In the present formulation, this can be represented by the intrinsic barrier, $\Delta E^\ddagger(0)$. By chemical driving force they meant the contribution that the energy of formation of the new bond AB makes towards overcoming the inertia, which is represented by the reaction energy ΔE^0 . Eq. (7.6) reveals that under certain approximations, one can separate the *thermodynamic contribution*, ΔE^0 , and the *kinetic contribution*, $\Delta E^\ddagger(0)$, for the energy barrier of the reaction ΔE^\ddagger . Seminal ideas for such a separation go back to Jean-Auguste Muller in 1886, but the correct quantitative formulation was proposed by Rudolph Marcus [3] in the 1960s.

We adopt here the formalism of ISM presented in eqs. (6.106)–(6.109) of Chapter 6, to calculate the sum of bond extensions to the TS, d , as

$$d = a'(l_r + l_p) \left[\frac{2\ln(2)}{m} + \frac{1}{2} \left(\frac{\Delta E^0}{\Lambda} \right)^2 \right] \quad (7.8)$$

When the dynamic parameter Λ is, in absolute terms, much greater than the reaction energy, $\Lambda \gg |\Delta E^0|$, then d is independent of the reaction energy. Under such conditions, d has a constant value that is the sum of bond extensions of reactants and products at thermoneutrality, $d(0)$

$$d(0) = a'(l_r + l_p) \frac{2\ln(2)}{m} \quad (7.9)$$

with $a' = 0.156$. Under this set of approximations, the separation between the intrinsic and thermodynamic contributions for the energy barrier, ΔE^\ddagger , is valid (see eq. (7.6)). Thus the intrinsic barrier can be expressed in terms of several molecular factors, specifically force constant, transition-state bond order and the sum of the equilibrium bond lengths of reactant and product.

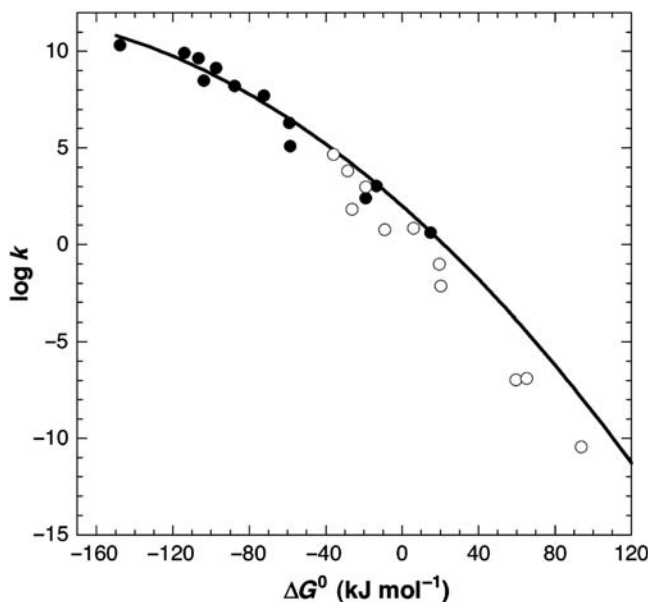
$$\Delta E^\ddagger(0) = \frac{1}{2} f \left[\frac{a'\ln(2)}{m} (l_r + l_p) \right]^2 \quad (7.10)$$

Eq. (7.6), known as the equation of Marcus, leads to a quadratic relationship between the barrier of reaction and the reaction energy, which shows up also in the modified form

$$\Delta E^\ddagger = \Delta E^\ddagger(0) + \frac{\Delta E^0}{2} + \frac{(\Delta E^0)^2}{16\Delta E^\ddagger(0)} \quad (7.11)$$

For reactions in solution, one tends to use Gibbs energy, G , instead of internal energy, E . For this reason, eqs. (7.6) and (7.11) are called (Gibbs) *free-energy relationships*. In this particular case, such equations represent *quadratic free-energy relationships* (QFER).

Figure 7.2 illustrates a QFER for the proton-transfer reactions between enolate anions and water molecules [4]. The experimental data can be reproduced by the equation of Marcus with an intrinsic barrier of $\Delta G^\ddagger(0) = 57 \text{ kJ mol}^{-1}$ and a pre-exponential factor of $k_{\text{dif}} = 10^{11} \text{ mol}^{-1} \text{ dm}^3 \text{ sec}^{-1}$. This is a good illustration of a

**FIGURE 7.2**

Rate constants of proton transfers from enolate ions and water. The curve represents an application of the Marcus quadratic relationship, with $\Delta G^\ddagger(0) = 57 \text{ kJ mol}^{-1}$ and $k_{\text{dif}} = 10^{11} \text{ mol}^{-1} \text{ dm}^3 \text{ sec}^{-1}$.

family of reactions which have similar behaviour throughout a very extensive energy range, $\Delta\Delta G^0 = 200 \text{ kJ mol}^{-1}$ and $\Delta\Delta G^\ddagger = 85 \text{ kJ mol}^{-1}$ and covering reaction rates over 14 orders of magnitude. Changes in reactivity are controlled entirely by changes in ΔG^0 . This means that the bonds to be broken and formed, OH and CH, have the same force constants and bond lengths throughout the reaction series and that n^\ddagger is also constant. This implies that the electrophilicity is quite invariant for the different enolates employed in this study.

7.2 Linear free-energy relationships

Eq. (7.11) can be further simplified if the intrinsic barrier is much higher than the range of reaction energies, such that $16(\Delta E^\ddagger(0)) \gg (\Delta E^0)^2$. Inserting this condition into eq. (7.11) leads to

$$\Delta E^\ddagger \approx \Delta E^\ddagger(0) + \frac{\Delta E^0}{2} \quad (7.12)$$

This expression reveals the existence of a linear relation between energy barrier and reaction energy. When expressed in terms of Gibbs energy, this represents a *linear free-energy relationship* (LFER).

The equation of Marcus was developed in 1956 and ISM in 1986. Predictions on the effects of substituents on the rate constants and the equilibrium constants are not due to such developments but due to the rich history of empiricism. Nevertheless, many of those historical paths can now be encompassed by the Marcus equation and ISM.

7.2.1 Brönsted equation

In the acid–base reaction (7.II), it appeared reasonable to Brönsted and Pederson that if the rates k at which proton is removed by a particular basis B were compared for various acids HA



then the base might remove the proton more rapidly from the stronger acids. In fact, relationships between the rate of an acid–base reaction and equilibrium have been observed in many cases and frequently obey an equation known as the Brönsted catalysis law

$$k = GK^\alpha \quad (7.13)$$

where G and α are empirical constants, k is the rate for reaction (7.II) and K is the acid dissociation equilibrium constant. In logarithmic form, the Brönsted equation can be written as

$$\log k = \alpha \log K + \text{constant} \quad (7.14)$$

The value of α can be estimated from a plot of the second-order catalytic constant $\log k$ for the reaction catalysed by the acid HA, against the pK_{HA} . Equivalent procedures can also be performed for base catalysed reactions. [Figure 7.3](#)

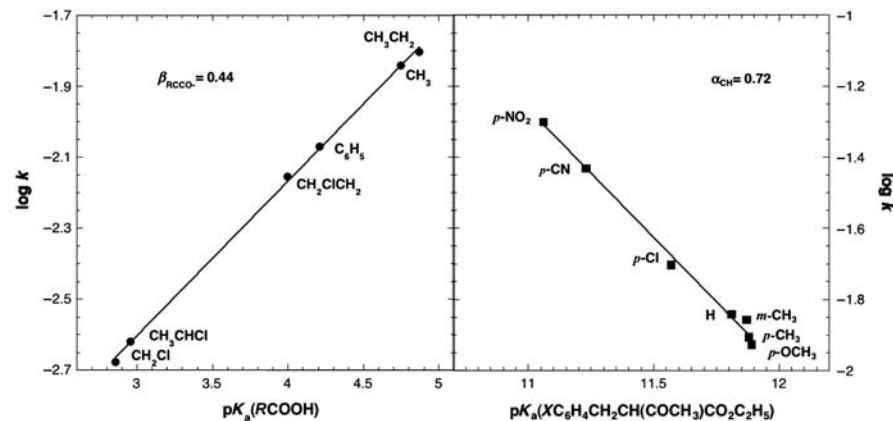
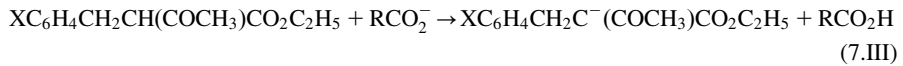


FIGURE 7.3

Correlation between the ionisation constants of carboxylic acids RCOOH or carbon acids R_3CH , and the second-order rate constant of the reactions in mechanism (7.III).

illustrates the application of Brönsted relationship for the proton-transfer reactions [5].



In one set of the reactions, the substituent X of the carbon acid was varied and the same base, CH_3COO^- , was used; this allows one to estimate the Brönsted constant for the acid catalysis, α . In another set of experiments the base was varied, but the acid was kept constant; this allows the estimation of the Brönsted β parameter for base catalysis.

Taking into consideration the relations between rate constants k and ΔG^\ddagger and equilibrium constants K and ΔG^0 ,

$$k = \frac{k_B T}{h} \exp\left(-\frac{\Delta G^\ddagger}{RT}\right)$$

$$K = \exp\left(-\frac{\Delta G^0}{RT}\right)$$

(7.15)

the Brönsted equation takes the form

$$\Delta G^\ddagger = \alpha \Delta G^0 + \text{constant}$$

(7.16)

showing that, at a constant temperature, this equation reflects an LFER.

Following a suggestion of Leffler [6], chemists have tried for a number of years to use the Brönsted coefficient, $\alpha = \partial(\Delta G^\ddagger)/\partial(\Delta G^0)$, as a measure of the position of the TS along the reaction coordinate, since usually $0 < \alpha < 1$, with $\alpha = 0$ for reactants, and $\alpha = 1$ for products. As a consequence, $\alpha = 0.5$ would imply that the TS is exactly half way between reactants and products.

As illustrated in Figure 7.4 for a thermoneutral reaction, α is not always a measure of the position of TS. When $f_r = f_p$, one has for this kind of reaction

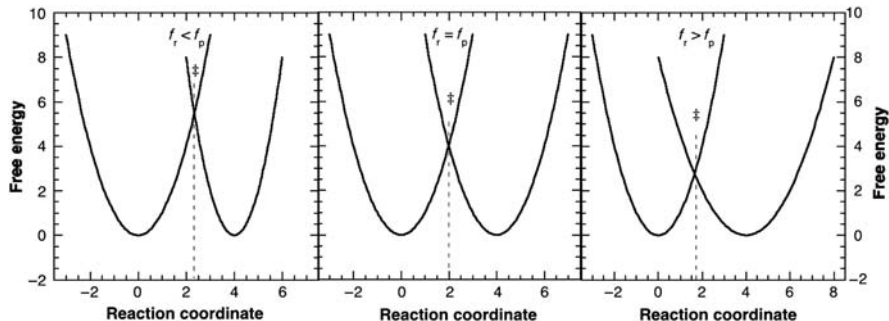


FIGURE 7.4

Effect of the force constants of the reactive bonds on the position of the transition state for an isothermal reaction.

$\alpha = 0.5$, reflecting correctly the position of the TS. But if $f_r > f_p$, the TS is before the measure provided by α ; if $f_r < f_p$ the TS is ahead of the measure of α .

The Marcus equation, now expressed in terms of Gibbs energy, can be written as

$$\frac{\delta \Delta G^\ddagger}{\delta \Delta G^0} = \frac{1}{2} + \frac{1}{8} \frac{\Delta G^0}{\Delta G^\ddagger(0)} \quad (7.17)$$

This equation does not give full support to the empirical equation of Brönsted, because the relation is a quadratic one, while that of Brönsted is linear, such that under the relevant approximations, α would be constant and always equal to 0.5. ISM, which is more general than the equation of Marcus, accommodates LFER with values of $\alpha \neq 0.5$ ($0 < \alpha < 1$) when the force constants do not have a common value, $f_r \neq f_p$. In empirical terms, there are cases with $\alpha > 1$ and < 0 , but these are anomalous situations which will be discussed later on in [Chapter 13](#), devoted to proton-transfer reactions. Identical considerations are valid for the β coefficients.

7.2.2 Bell–Evans–Polanyi equation

In the mid-1930s of the twentieth century, Bell, Evans, and Polanyi correlated energies of activation, E_a , for several reactions in the vapour phase with heats of reaction, ΔH^0 , according to the following expression:

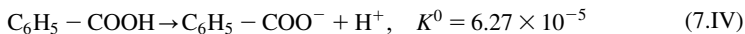
$$E_a = \alpha \Delta H^0 + \text{constant} \quad (7.18)$$

which is also an LFER. The additive constant in this relationship will be taken to assume, according to Rudolph Marcus, the presence of an intrinsic barrier.

Both free-energy relationships, expressed by [eqs. \(7.6\)](#) and [\(7.18\)](#), would imply that reactions which have a strong driving force thermodynamically will also proceed rapidly. However, if we consider this more deeply, we will see that such an implication does not hold generally. For example, the energetically favourable oxidation of hydrocarbons in the presence of air may not take place for years, whereas the energetically unfavourable hydration of carbon dioxide takes place in seconds. For elementary reactions, the correct interpretation rests on the values of the intrinsic barriers.

7.2.3 Hammett and Taft relationships

In January 1937, Hammett published *Effects of Structure Upon the Reactions of Benzene Derivatives*. Let us consider the dissociation of benzoic acid



Hammett realised that the addition of a substituent in the aromatic ring has a quantitative effect on the dissociation constant K . For *para*-nitrobenzoic acid the dissociation constant



increases, indicating an increment in the stabilisation of the negative charge generated by dissociation. If the substituent is an ethyl group in *para* position, the opposite effect is observed with respect to the unsubstituted reaction



indicating that the ethyl group destabilises the negative charge generated in dissociation.

Hammett found, for example, that the nitro group has a stabilising effect on other dissociation reactions such as those of phenylacetic acid. He then proposed a quantitative relationship to account for such findings

$$\log K = \log K^0 + \rho\sigma \quad (7.19)$$

The same kind of expression is also valid for the rate constants, k

$$\log k = \log k^0 + \rho\sigma \quad (7.20)$$

K^0 and k^0 denote the corresponding constants for the ‘parent’ or ‘unsubstituted’ compound.

The *substituent constant* σ is a measure of the electronic effect of replacing H by a given substituent (in the *para*- or *meta*-position) and is, in principle, independent of the nature of reaction. The *reaction constant* ρ depends on the nature of the reaction, including conditions such as solvent and temperature; ρ is a measure of the susceptibility of the reaction to the electronic effects of substituents. The reference reaction is the ionisation of unsubstituted benzoic acid in water at 25 °C, with $\rho = 1$.

Thus it is clear that just a few values of σ and ρ can summarise a large body of equilibrium and rate measurements and can help to predict rate coefficients and equilibrium constants for reactions which have not yet been studied. The *substituent constant* σ is a positive or negative number (Table 7.1; Figure 7.5). For example, $\sigma_p = 0.71$ for $-\text{NO}_2$ indicates that this group has an electron-removing effect higher than H-atom, whereas $\sigma_p = -0.66$ for $-\text{NH}_2$ indicates that this group has an electron-donating effect stronger than H-atom. Electron-withdrawing substituents facilitate the ionisation of benzoic acid (stabilise the benzoate anion) and thus have positive values of σ , whereas electron-donating substituents destabilise the benzoate ion relative to benzoic acid and have negative values of σ . Reactions with $\rho > 0$ are facilitated by electron-removing substituents.

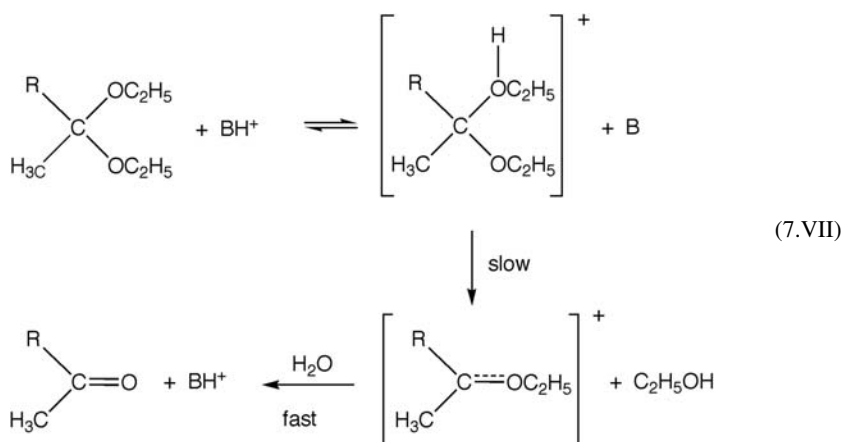
Although the Hammett relationship works well for *meta*- and *para*-substituted aromatic compounds, it frequently fails for either *ortho*-aromatic (due to steric effects) or aliphatic compounds, and other scales have been proposed, such as that of Taft.

$$\log k - \log k_0 = \rho^* \sigma^* \quad (7.21)$$

Figure 7.6 compares the performance of the equations of Hammett and Taft with respect to the hydrolysis of ketals that proceeds according to the mechanism (7.VII) [7].

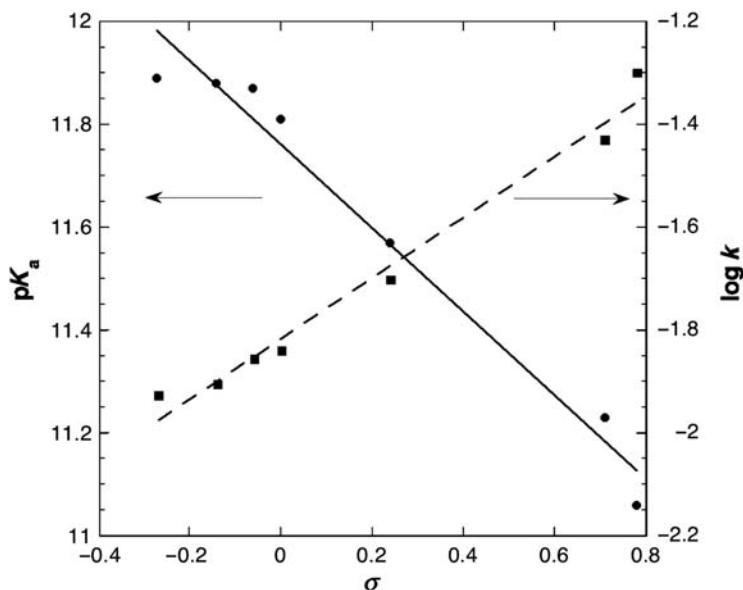
Table 7.1 Hammett (σ_m , σ_p) and Taft (σ^*) coefficients of common substituents in organic molecules.

Substituents	σ_m	σ_p	$\sigma^*(\text{CH}_2\text{Y})$
$-\text{NH}_2$	-0.16	-0.66	
$-\text{NMe}_2$	-0.10	-0.32	
$-\text{OH}$	0.02	-0.22	0.555
$-\text{OMe}$	0.12	-0.27	0.52
$-\text{OAc}$	0.39	0.31	
$-\text{SMe}$	0.14	0.06	
$-\text{H}$	0	0	
$-\text{Me}$	-0.06	-0.14	-0.10
$-\text{Et}$	-0.10		
$-\text{n-Pr}$	-0.13		
$-\text{t-Bu}$	-0.09	-0.15	-0.165
$-\text{C}_6\text{H}_5$	0.05	0.05	0.215
$-\text{COMe}$	0.36	0.47	0.60
$-\text{F}$	0.34	0.15	1.1
$-\text{Cl}$	0.37	0.24	1.05
$-\text{Br}$	0.37	0.26	1.00
$-\text{I}$	0.34	0.28	0.85
$-\text{CN}$	0.62	0.71	1.30
$-\text{NO}_2$	0.71	0.78	1.40
$-\text{CF}_3$	0.46	0.53	0.92

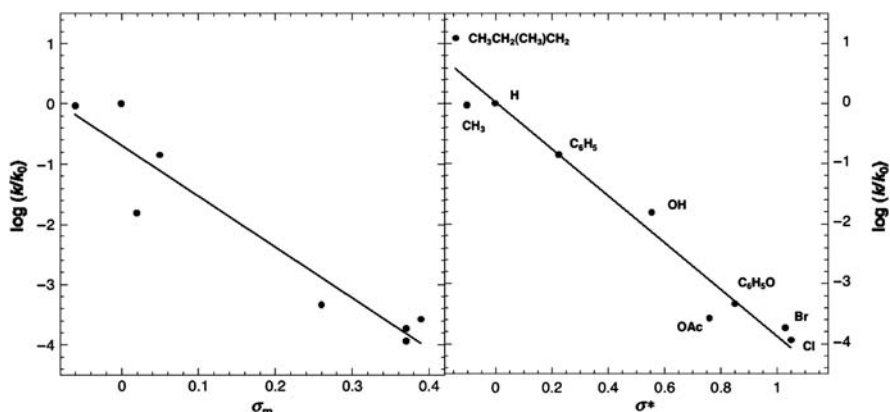


These empirical correlations call for an explanation, by which we mean a theoretical basis, however profound or modest. From eq. (7.20) we can write

$$\Delta G^{\ddagger 0} = \Delta G_0^{\ddagger 0} - 2.3RT\sigma\rho \quad (7.22)$$

**FIGURE 7.5**

Application of the Hammett equation to the reactions following mechanism (7.III).

**FIGURE 7.6**

Application of Hammett and Taft equations to the rate of the hydrolysis of ketals that proceed according to mechanism (7.VII).

where $\Delta G_0^{\ddagger 0}$ corresponds to the Gibbs activation energy of the reference reaction. For other homologous reactions, with the same set of substituents, one has

$$\Delta G^{\ddagger 0'} = \Delta G_0^{\ddagger 0} - 2.3RT\sigma'\rho \quad (7.23)$$

Those two equations can be written in a different form

$$\begin{aligned}\frac{\Delta G^{\ddagger 0}}{\rho} &= \frac{\Delta G_0^{\ddagger 0}}{\rho} - 2.3RT\sigma \\ \frac{\Delta G^{\ddagger 0'}}{\rho'} &= \frac{\Delta G_0^{\ddagger 0'}}{\rho'} - 2.3RT\sigma\end{aligned}\quad (7.24)$$

and if one subtracts the other, we obtain

$$\frac{\Delta G^{\ddagger 0}}{\rho} - \frac{\Delta G^{\ddagger 0'}}{\rho'} = \frac{\Delta G_0^{\ddagger 0}}{\rho} - \frac{\Delta G_0^{\ddagger 0'}}{\rho'} \quad (7.25)$$

We can, therefore, write a linear equation between the free energies of activation of one set of reactions and those of a corresponding set

$$\Delta G^{\ddagger 0} - \frac{\rho}{\rho'} \Delta G^{\ddagger 0'} = \text{constant} \quad (7.26)$$

where the coefficient ρ/ρ' has the same value for all reactions in the set. Hammett equations are, thus, another kind of LFER.

The equations of Hammett and Taft apply reasonably well to Gibbs free energies but it is interesting to note that a change in σ by $\Delta\sigma = 0.7$ from benzoic to *m*-nitrobenzoic acid changes ΔG^0 by only $\Delta\Delta G^0 = -4.2 \text{ kJ mol}^{-1}$. In fact, the change in enthalpy is even smaller, $\Delta\Delta H^0 = -1.1 \text{ kJ mol}^{-1}$, and most of the effect comes from the change in entropy $\Delta\Delta S^0 = 18 \text{ J mol}^{-1} \text{ K}^{-1}$ [8].

One might anticipate that changes in enthalpies or in entropies might give relations similar to those of free-energy relationships, in view of the equation

$$\Delta G^\ddagger = \Delta H^\ddagger - T\Delta S^\ddagger \quad (7.27)$$

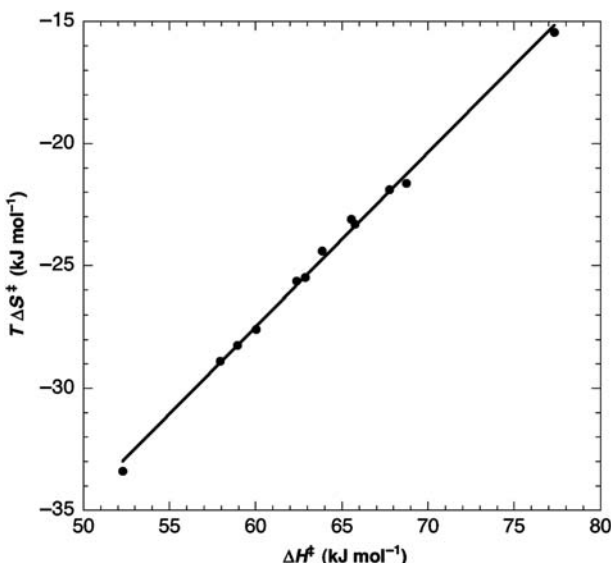
However, this is not the case. The changes in ΔH^\ddagger and in ΔS^\ddagger show a considerable scatter when compared with ΔG^\ddagger , and there is a compensating effect between ΔH^\ddagger and ΔS^\ddagger . A substituent group that induces a strong interaction of the solute with solvent molecules and decreases ΔH^\ddagger also decreases ΔS^\ddagger . Figure 7.7 illustrates this effect of compensation in the alkaline hydrolysis of ethyl benzoate in water/alcohol and water/dioxane mixtures [9], which can be translated by the linear relationship

$$\delta\Delta H^\ddagger = \beta_{\text{iso}} \delta\Delta S^\ddagger \quad (7.28)$$

when a parameter of the reaction (solvent, substituent, etc.) is changed,

$$\delta\Delta G^\ddagger = \delta\Delta H^\ddagger - T\delta\Delta S^\ddagger = (\beta_{\text{iso}} - T)\delta\Delta S^\ddagger \quad (7.29)$$

The parameter β_{iso} represents the *isokinetic temperature*, the real or virtual temperature for which all members of the series have the same rate constant (Figure 7.8). Equivalent considerations are also valid for equilibrium constants.

**FIGURE 7.7**

Enthalpy-entropy compensation in the alkaline hydrolysis of ethyl benzoate in water/alcohol and water/dioxane mixtures.

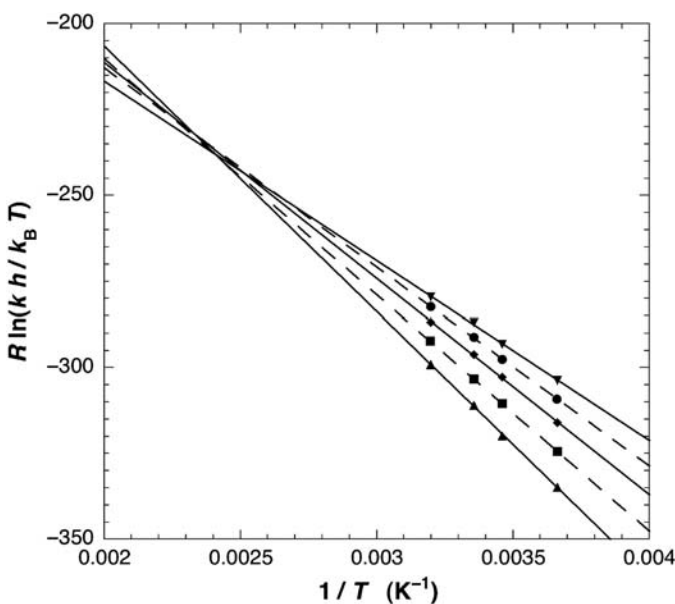
7.3 Other kinds of relationships between structure and reactivity

7.3.1 The Hammond postulate

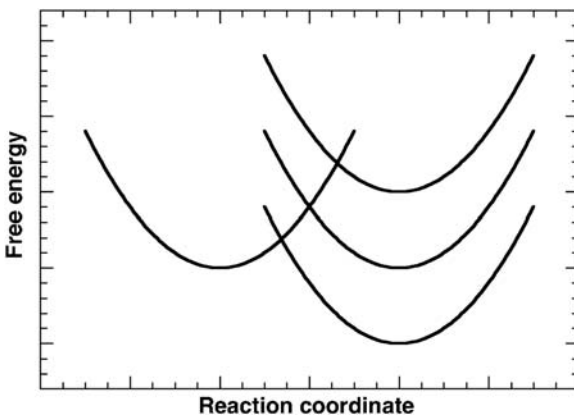
The equation of Bell–Evans–Polanyi (see eq. (7.18)) implies that exothermic reactions will have lower barriers than the endothermic ones. The view that an TS has structural and energy features that are intermediate between those of starting materials and products is due to George Hammond [10], who resurrected the view implied by those three authors in 1955. The aim of Hammond was that of mechanistic interpretations, postulating that the changes in structure of the TS are affected by the manner in which the substituents affect the energies of intermediates on alternate pathways from reactants to products. Since then, this assumption has been known as the Hammond postulate.

In an elementary reaction with a significant energy difference between products and reactants, where is the TS located? The TS is viewed as changing gradually from reactant-like in highly exergonic reactions to intermediate in character for ergoneutral reactions, to product-like for endergonic reactions, as illustrated in Figure 7.9. This is expressed quantitatively in a free-energy relationship

$$\Delta\Delta G^\ddagger = \alpha\Delta G_P + (1 - \alpha)\Delta G_R \quad (7.30)$$

**FIGURE 7.8**

Isokinetic relationship in the alkaline hydrolysis of ethyl benzoate in water/alcohol and water/dioxane mixtures. The enthalpies and entropies of activation of the previous figure were obtained from the slope and intercept of each of the straight lines in this figure.

**FIGURE 7.9**

Change in the location of the transition state with the reaction free energy.

which relates changes in TS energy brought about by substituents, to the free-energy changes brought about by those same substituents in reactants (R) and products (P). If $\alpha \approx 0$, then $\Delta\Delta^\ddagger G \approx \Delta G_R$ and the TS responds to changes in

substituents in the same manner as the reactants, a characteristic of exoenergetic elementary steps. The TS is closer to the reactants and, in consequence, the structural rearrangements to achieve the activated complexes are minimised and the activation barrier is small.

Conversely, if $\alpha \approx 1$, $\Delta\Delta^{\ddagger}G \approx \Delta G_p$ and the TS responds to changes in substituents in a similar fashion to the products, a characteristic of highly endoenergetic elementary reaction. The TS is closer to the products and its structural features are similar to those of the final materials. Large structural rearrangements are required to attain the TS and the activation barrier is high.

These considerations have also been expressed as the *principle of least nuclear motion*, which claims that elementary reactions that involve the least change in atomic position and electronic configurations will be favoured over related elementary reactions that involve more extensive changes in nuclei and electronic configurations.

These considerations are essentially valid when the force constants of reactants and products are similar. However, when $f_r \gg f_p$ there is a general tendency for the TS to be closer to reactants, even for endothermic reactions. The inverse is valid, that is when $f_r \ll f_p$ the TS has a tendency to be closer to the product configuration.

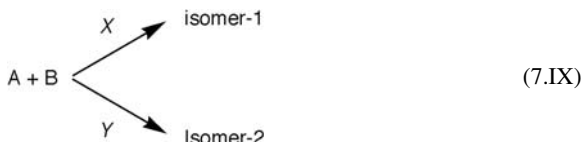
7.3.2 The reactivity–selectivity principle

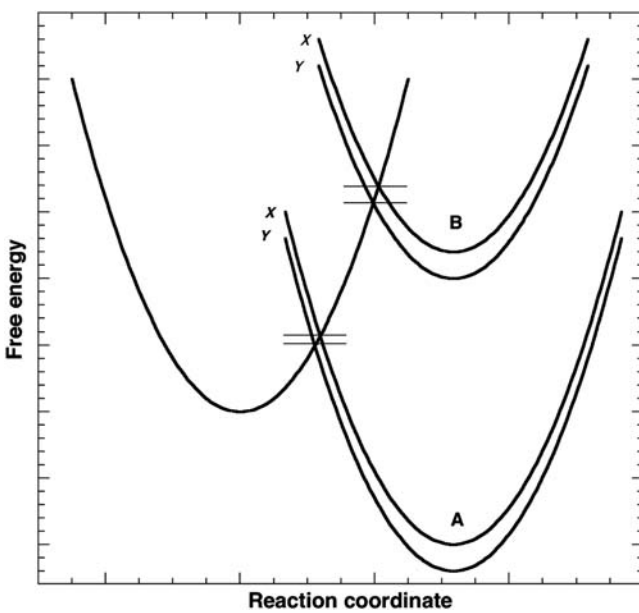
Consider the reaction of halogen (X_2) with propane



where we represent $CH_2XCH_2CH_3$ as isomer **1** and CH_3CHXCH_3 as isomer **2**. If the X_2 were not selective, the monohalogenated product would be expected to contain 75% of isomer **1** and 25% of **2**, according to the number of positions of primary- and secondary-H. Experimentally it is found that with Cl_2 at 25 °C, 45% of **1** is produced and 55% of **2**, while with Br_2 at 125 °C, 5% of **1** and 95% of **2** results. These data are commonly taken to indicate that the less reactive bromine is more selective in the reaction [11].

The question of the relationship between *reactivity* and *selectivity* is usually discussed in terms of the reactivity–selectivity principle (RSP); in a series of related reactions, the more reactive species tend to be less selective in their reactivity than less reactive ones. Let us consider two substances A and B that follow the same type of reaction by two different pathways X and Y; for example, one leading to an isomer **1** and the other to an isomer **2**.



**FIGURE 7.10**

Schematic illustration of the RSP.

The selectivity S of the reaction is defined as follows:

$$S = \log\left(\frac{k_X}{k_Y}\right) \quad (7.31)$$

an expression that essentially corresponds to a difference in energy barriers, $S = \Delta G_Y^\ddagger - \Delta G_X^\ddagger$. The two substances A and B that undergo the same kind of reaction, A is more reactive than B. As illustrated in Figure 7.10, the more reactive reactant A is less selective, because the energy differences are smaller and their difference is also smaller, $S(A) = \Delta G_Y^\ddagger(A) - \Delta G_X^\ddagger(A) < S(B) = \Delta G_Y^\ddagger(A) - \Delta G_X^\ddagger(A)$. Following eq. (7.30), it is important to note that α can also be regarded as a selectivity parameter.

Table 7.2 presents the selectivity of several radicals (R^\bullet) for H-abstraction from alkanes: primary, secondary, and tertiary hydrogen atoms. Selectivity is measured with respect to the reaction



When one compares the selectivity of Br^\bullet and Cl^\bullet , the more reactive species (Cl^\bullet) is clearly the less selective one. For example, bromine atoms abstract tertiary H-atoms 1700 times faster than the primary H-atom. By comparison, chlorine radical is only 7 times faster. In fact, the electronic factor m for those two radicals has almost identical values (m close to 2) and RSP is obeyed. When changes in reactivity are not due only to changes in reaction energy (ΔE^0 , ΔH^0 or ΔG^0), the

Table 7.2 Experimental selectivity in the abstraction of hydrogen atoms from alkanes at 350 K.

Radical	Primary	Secondary	Tertiary	ΔE^0	ΔE^\ddagger
Cl [•] ($m \approx 1$)	1	4.3	7.0	0	16
Br [•] ($m \approx 1$)	1	80	1700	67	75
CH ₃ [•] ($m = 0.5$)	1	10	80	-4	73

postulates of physical organic chemistry are no longer verified. For example, Br[•] and CH₃[•] have almost the same reactivity with respect to CH₄. According to RSP, one would expect that both radicals should have identical selectivities for H-atom abstractions. Nevertheless, Br[•] is much more selective, because the electrophilicity parameter is also much higher for bromine radical ($m(\text{Br}) \approx 2$ and $m(\text{CH}_3) = 1$). Owing to an increase in m , the most reactive species is also the most selective one. Thus, basically, the RSP can be expected to apply to reaction series in which ΔG^\ddagger is only dependent on ΔG^0 and not on the electrophilicity parameter m .

7.3.3 Relationships of the electronic effect: nucleophilicity and electrophilicity

Structure–reactivity relationships in chemistry have been dominated by LFER. However, the kinetics of several cation–anion recombinations,

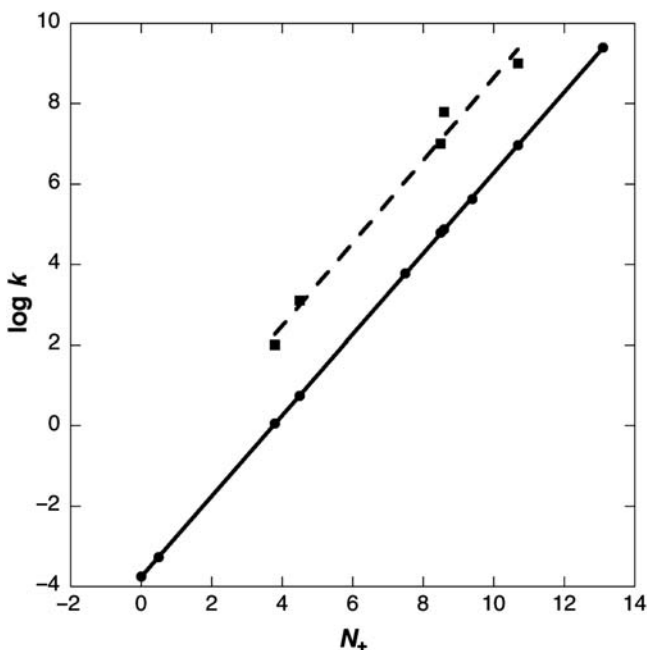


have been described by Calvin Ritchie using the simple empirical relation

$$\log k_{\text{X},\text{C}^+} = \log k_{\text{H}_2\text{O},\text{C}^+} + N_+ \quad (7.32)$$

where k_{X,C^+} is the rate of recombination of the nucleophile X[−] with the cation C⁺ in a given solvent, and $k_{\text{H}_2\text{O},\text{C}^+}$ is the pseudo-first-order rate constant for the reaction of C⁺ with water in pure form. N_+ is a simple property of the anionic nucleophile and of the solvent. Surprisingly, the last equation has no term describing the normal effect of the reaction energy on the rate constant, i.e., it does not describe a free-energy relationship, in spite of the fact that ΔG^0 can change by *ca.* $\delta\Delta G^0 = 30 \text{ kJ mol}^{-1}$. Figure 7.11 illustrates the application of this equation to cation–anion recombinations [12,13].

A rationale for such a relationship can be provided by ISM in terms of a curve-crossing model. One would wish to find the conditions for which the effect of ΔG^0 on rate constants is minimised and that of m is maximised. Table 7.3 studies such conditions for harmonic oscillators and reveals that they are verified when $f_r \ll f_p$ and correlated changes are occurring in the bond lengths. This is precisely the situation with cation–anion recombinations, where the force constants of the cation and anion bonds with the solvent molecules are much weaker and have lower force

**FIGURE 7.11**

Correlation of cation–anion recombinations by eq. (7.32). Circles: malachite green; squares: *p*-tolyl diazonium. The reaction of malachite green with water in pure water was taken as the reference, and the N_+ scale is defined as the difference between the logarithms of the rate constants of the other Malachite Green reactions and this reference reaction.

Table 7.3 Electronic and thermodynamic effects in the reaction barriers as a function of the reactant and product force constants, for $\Delta G^0 = 0$.^a

$I_r + I_p$ (Å)	f_r (kJ mol ⁻¹ Å ⁻¹)	f_p (kJ mol ⁻¹ Å ⁻¹)	$\partial \Delta G^\ddagger / \partial n^\ddagger$ ^b	$\partial \Delta G^\ddagger / \partial \Delta G^0$
3	3×10^3	3×10^3	-628	0.5
4.7 ^c	0.5×10^3	3×10^3	-518	0.29

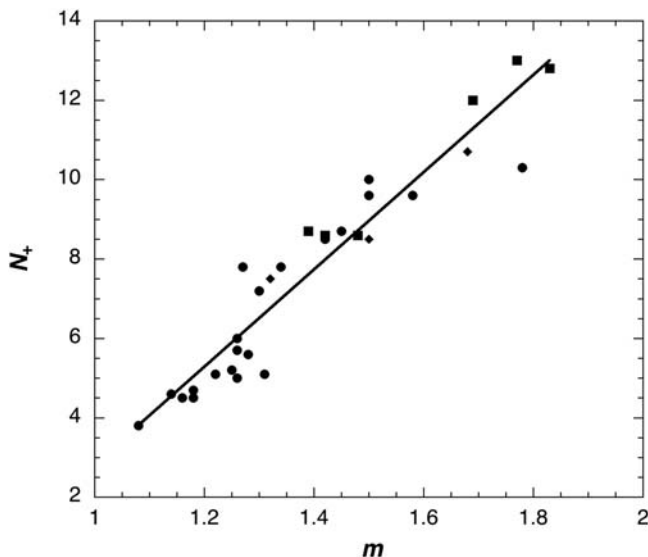
^aFrom Ref. [14].

^bBy definition $n^\ddagger = m/2$.

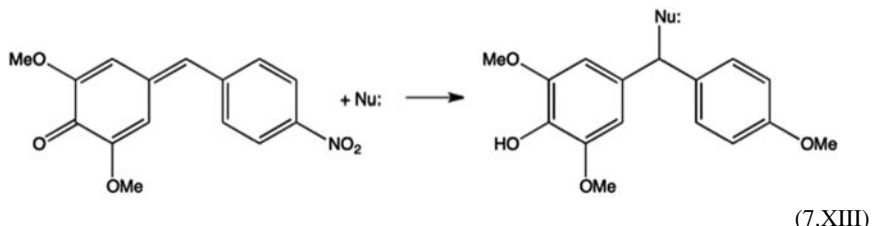
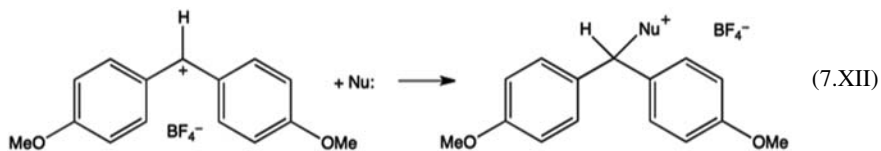
^cThe bond length increase is correlated to the force constant decrease using typical values and correlations expressed in the literature.

constants than the normal chemical X–R bond. The nucleophilicity parameter N_+ is directly proportional to the electrophilicity index, m (see Figure 7.12).

Nucleophilicity scales have been constructed for a large variety of nucleophiles using benzhydrylium ions and structurally related quinone methides as reference electrophiles

**FIGURE 7.12**

Correlation between Ritchie parameter N_+ for nucleophiles and the electrophilicity index m in cation–anion recombinations. These recombinations were studied in water (circles), dimethylsulphoxide (squares) and methanol (lozenges) [14].



The quinone methide in the reaction above can also be written in a zwitterionic resonance structure with the quinone written as a phenolate ion and a positive charge in the carbon binding the two aromatic moieties. Ritchie's equation was generalised to reference electrophiles mentioned above by the Mayr–Patz equation [15,16]

$$\log k = s_N(E + N) \quad (7.33)$$

where E characterises the electrophiles, and the nucleophiles are characterised by the nucleophilicity parameter N and by the nucleophile-specific sensitivity parameter s_N . Both N and s_N are solvent dependent. This equation defines nucleophilicity as the intercept of the correlation lines with the abscissa, i.e., if $\log(k) = 0$ then $N = -E$. Each electrophile has a characteristic E value and the change in electrophile gives a LFER. Hence, eq. (7.33) gives a series of LFERs because the intrinsic barrier changes with the nucleophile. As pointed out for Ritchie's equation, the intrinsic barrier changes because the electrophilicity index is changing.

7.3.4 An empirical extension of the Bell–Evans–Polanyi relationship

So far we have considered only the effect of reaction energy and of the electronic electrophilicity parameter on chemical reactivity. ISM implies that other structural factors, such as force constants and bond lengths, can also play a significant role. Although this may be found in very specific cases, it does not have the generality of the factors previously discussed.

The empirical approach continues to be a useful source of knowledge, particularly in complex systems such as many of those involved in chemical reactivity. This can be extended to employ powerful statistical methods (chemometrics), such as Partial Least Squares and multivariate analysis, to retrieve useful information and predict system response. It has been shown that activation energies of several atom-transfer reactions can be described mainly in terms of reaction energy and Parr electrophilicity parameter, according to the expression [17]

$$E_a = A + B\Delta H^0 + Cm^{-3/2} \quad (7.34)$$

where A , B and C are constants. This expression expands the previous Bell–Evans–Polanyi relationship and shows that the intrinsic barrier has an inverse dependence on m ; an increase in m decreases the barrier for the reaction. In this electronically extended Bell–Evans–Polanyi relationship, electronic and reaction energy factors appear now to be dominant for the control of chemical reactivity.

References

- [1] TH Levere, *Ambix* **17** (1970) 112.
- [2] MG Evans, M Polanyi, *Trans. Faraday Soc.* **34** (1938) 11.
- [3] RA Marcus, *Ann. Rev. Phys. Chem.* **15** (1964) 155.
- [4] J Wirz, *Pure Appl. Chem.* **70** (1998) 2221.
- [5] RP Bell, S Grainger, *J. Chem. Soc. Perkin II* (1976) 1367.
- [6] JE Leffler, *Science* **117** (1953) 340.
- [7] MM Kreevoy, RW Taft, Jr., *J. Am. Chem. Soc.* **77** (1955) 5590.
- [8] T Matsui, HC Ko, LG Hepler, *Can. J. Chem.* **52** (1974) 2906.

- [9] RA Fairclough, CN Hinshelwood, *J. Chem. Soc.* (1937) 538.
- [10] GS Hammond, *J. Am. Chem. Soc.* **77** (1955) 334.
- [11] E Buncel, H Wilson, *J. Chem. Educ.* **64** (1987) 475.
- [12] CD Ritchie, *Acc. Chem. Res.* **5** (1972) 348.
- [13] CD Ritchie, *Can. J. Chem.* **64** (1986) 2239.
- [14] SJ Formosinho, LG Arnaut, *J. Mol. Struct. (Theochem)* **371** (1996) 133.
- [15] H Mayr, M Patz, *Angew. Chem. Int. Ed. Engl.* **33** (1994) 938.
- [16] H Mayr, AR Ofial, *Pure Appl. Chem.* **89** (2017) 729.
- [17] M Barroso, JC Pereira, AACC Pais, LG Arnaut, SJ Formosinho, *Mol. Phys.* **104** (2006) 731.

This page intentionally left blank

Unimolecular reactions

8

8.1 Lindemann–Christiansen mechanism

In principle, unimolecular reactions should be one of the most conceptually simple reactions in chemistry. However, the history of the understanding of simple decomposition processes, such as



or



has been one of considerable debate, controversy and complexity, even till our own days. The decomposition of N_2O_5 , originally believed to be unimolecular, was eventually shown to occur by a composite mechanism, involving different kinds of radicals, notably NO_2 , NO_3 and NO . On another level, one might imagine that even a true elementary reaction such as the decomposition of Br_2 , although it shows a first-order rate law, cannot possibly have a simple collisional explanation. The reactant molecule must acquire some amount of energy before it decomposes. Obviously, such an amount of energy can be obtained through ultraviolet or visible light of appropriate wavelength (see Chapter 16: Transitions Between Electronic States). However, under thermal conditions what is the source of such energy?

In 1919, Perrin proposed that unimolecular gas reactions would acquire the energy for the reaction through the radiation from the walls of the reaction vessels. Later, during a Faraday Society meeting in 1921, Lindemann [1] (later Lord Cherwell) expressed strong opposition to this radiation hypothesis and proposed an activation collision mechanism that was explicitly described in more detail a few days later by Christiansen in his Ph.D. thesis. The mechanism of Lindemann–Christiansen, the basis for all the modern theories of unimolecular reactions [2], considers the formation of a metastable molecule A^* having sufficient energy to undergo reaction. The energisation process involves collisions between two molecules of A



The energised molecule may undergo de-energisation by collisions with a normal molecule, or it may undergo a reaction of molecularity equal to one to form

products. There are, therefore, three distinct processes in this mechanism with their own rates: (i) the rate of energisation is $k_1[A]^2$, (ii) A^* can be de-energised at a rate $k_{-1}[A^*][A]$ and (iii) A^* can be converted into products at a rate $k_2[A^*]$.

The rate of product formation depends on the $[A^*]$, which can be found from a steady approximation for A^*

$$\frac{d[A^*]}{dt} = k_1[A]^2 - k_{-1}[A^*][A] - k_2[A^*] \quad (8.1)$$

From the condition of $d[A^*]/dt = 0$ one obtains

$$[A^*] = \frac{k_1[A]^2}{k_2 + k_{-1}[A]} \quad (8.2)$$

and subsequently

$$v = \frac{d[P]}{dt} = k_2[A^*] = \frac{k_1 k_2 [A]^2}{k_2 + k_{-1}[A]} \quad (8.3)$$

In the vapour phase, at high pressures, one has $k_{-1}[A] \gg k_2$, and the rate of reaction assumes the more simple form

$$v_\infty = \frac{k_1 k_2}{k_{-1}} [A] \quad (8.4)$$

At high pressures, the reaction is a first-order process. Under those conditions, the rate of energisation and de-energisation are relatively fast steps, which can be treated as a fast pre-equilibrium. Thus the rate-determining step is the transformation of A^* into products.

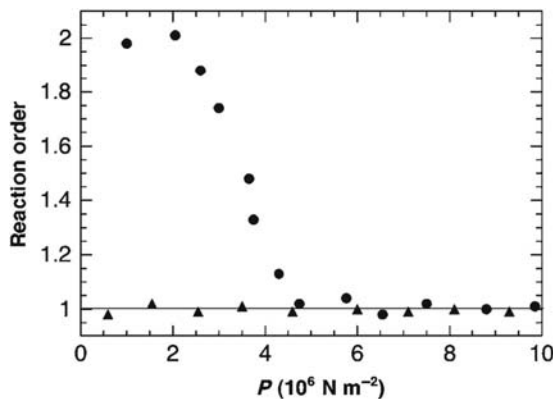
At low pressures, when $k_{-1}[A] \ll k_2$, a new expression for the rate of product formation is obtained.

$$v = k_1[A]^2 \quad (8.5)$$

The rate law is second order. At low $[A]$ de-energisation is much less rapid than the rate at which A is converted into products. There is no longer equilibrium involving A^* . The rate of product formation is effectively equal to the rate at which the species A^* are formed, since now these molecules nearly always become products.

After Lindemann and Christiansen put forward their mechanism, experimental work was carried out to verify if the unimolecular reactions did become second order at sufficiently low pressures. Figure 8.1 illustrates the order of dimethyl ether decomposition in the vapour phase as a function of the addition of a foreign gas. In qualitative terms, the mechanism of Lindemann–Christiansen gives a good account of the experimental observations, since the order of the reaction varies from second- to first-order when the overall pressure increases.

In spite of this apparent success, another important aspect of this mechanism is the concentration of A at which one should observe a transition from first- towards

**FIGURE 8.1**

Change in the reaction order in the decomposition of dimethyl ether, in the presence or absence of a foreign gas. Circles: dimethyl ether alone; triangles: dimethyl ether with a large excess of H₂ or N₂.

second-order kinetics. Defining a rate constant for the first-order process at high pressures, k_{∞}^1 ,

$$v = k_{\infty}^1 [A] \quad (8.6)$$

Eq. (8.4) allows one to write

$$k_{\infty}^1 = \frac{k_1 k_2}{k_{-1}} \quad (8.7)$$

This rate constant can be estimated experimentally at high pressures. Furthermore, eqs. (8.3) and (8.4) allow the determination of the concentration, [A]_{1/2}, at which the rates of de-energisation and product formation are equal

$$k_{-1}[A^*][A]_{1/2} = k_2[A^*] \quad (8.8)$$

Under such conditions, the rate is half of the maximum value

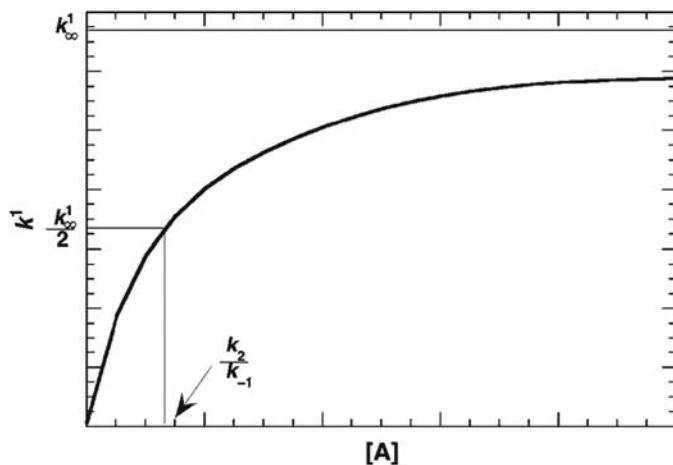
$$v_{1/2} = \frac{1}{2} k_2 \frac{k_1}{k_{-1}} [A]_{1/2} = \frac{1}{2} k_{\infty}^1 [A]_{1/2} \quad (8.9)$$

A first-order rate coefficient, k^1 , can be defined under any condition by

$$v = k^1 [A] \quad (8.10)$$

Such a coefficient can be studied experimentally as a function of pressure, as shown in Figure 8.2. However, the experimental values of [A]_{1/2} are always much smaller than those expected from the expression

$$[A]_{1/2} = \frac{k_2}{k_{-1}} = \frac{k_{\infty}^1}{k_1} \quad (8.11)$$

**FIGURE 8.2**

Dependence of the first-order rate coefficient, k^1 , on the concentration of the reactant, $[A]$.

when k_1 is estimated on the basis of a simple collision theory, $k_1 = Z_1 e^{-E_1/RT}$, where Z_1 is the collision frequency and E_1 the activation energy. Thus a modification must be contemplated to allow k_1 to be much larger than $Z_1 e^{-E_1/RT}$ and to account for the increase in that discrepancy with the increase in complexity of the reactants, for example, C_3H_6 versus N_2O or HI .

The second difficulty with the Lindemann–Christiansen mechanism becomes apparent when experimental data are plotted in another way

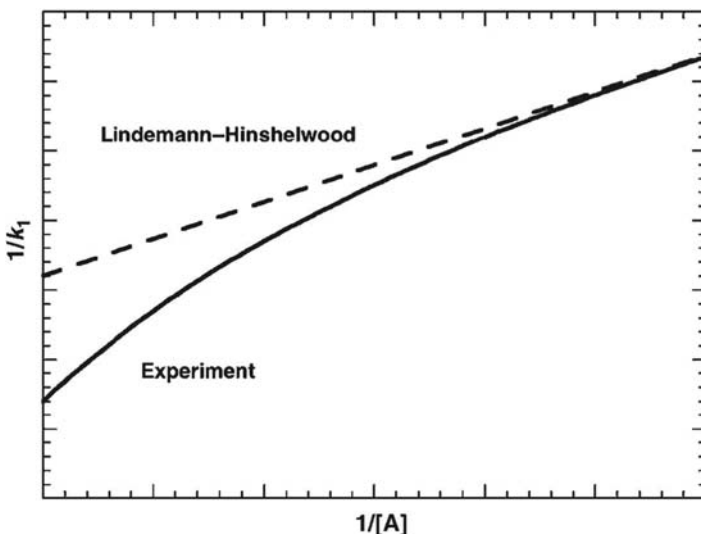
$$\frac{1}{k^1} = \frac{k_{-1}}{k_1 k_2} + \frac{1}{k_1 [A]} \quad (8.12)$$

A plot of $1/k^1$ against the reciprocal of $[A]$ should give a straight line. However, deviations from linearity of the kind shown in Figure 8.3 have been found.

8.2 Hinshelwood's treatment

The first difficulty of the Lindemann–Christiansen mechanism is associated with the fact that on the basis of simple collision theory, first-order rates are predicted to change to second order at higher pressures than was found experimentally in a number of cases. This difficulty was successfully overcome by Hinshelwood [3], taking into account the fact that the energy of activation is distributed between n degrees of freedom in the molecule.

Maxwell and Boltzmann, in their treatment of the distribution of molecular speeds and energies, demonstrated that the fraction of molecules having energies between ε_x and $\varepsilon_x + d\varepsilon_x$ is

**FIGURE 8.3**

Predicted and observed behaviour when $1/k^1$ against the reciprocal of $[A]$.

$$\frac{dN_x}{N} = \frac{1}{\sqrt{\pi\varepsilon_x k_B T}} \exp\left(-\frac{\varepsilon_x}{k_B T}\right) d\varepsilon_x \quad (8.13)$$

This relationship applies to a molecule moving in the x direction.

The fraction of molecules, f^* , that have energies above a certain specified quantity ε^* is given by

$$f^* = \frac{1}{\sqrt{\pi k_B T}} \int_{\varepsilon^*}^{\infty} \frac{1}{\sqrt{\varepsilon}} \exp\left(-\frac{\varepsilon}{k_B T}\right) d\varepsilon \quad (8.14)$$

The result of the integration cannot be expressed in a closed form. However, if one considers molecular motions along two directions, x and y , the probability of finding the molecule with a translational energy between ε_x and $\varepsilon_x + d\varepsilon_x$ in the x direction and ε_y and $\varepsilon_y + d\varepsilon_y$ along the y direction is

$$\frac{dN}{N} = \frac{1}{\pi k_B T \sqrt{\varepsilon_x \varepsilon_y}} \exp\left(-\frac{\varepsilon_x}{k_B T}\right) \exp\left(-\frac{\varepsilon_y}{k_B T}\right) d\varepsilon_x d\varepsilon_y \quad (8.15)$$

Within a kinetic point of view, what is relevant is the total energy of the molecule, ε , independent of how this is distributed along the two degrees of motion. With $\varepsilon = \varepsilon_x + \varepsilon_y$, we can estimate the probability of finding the molecule with a total energy between ε and $\varepsilon + d\varepsilon$. One can obtain such a probability by writing $\varepsilon_y = \varepsilon - \varepsilon_x$, and integrating with respect to ε_x from 0 to ε .

$$\frac{dN}{N} = \frac{1}{\pi k_B T} \int_0^{\varepsilon} \frac{1}{\sqrt{\varepsilon_x}} \frac{1}{\sqrt{\varepsilon - \varepsilon_x}} \exp\left(-\frac{\varepsilon_x}{k_B T}\right) \exp\left(-\frac{\varepsilon - \varepsilon_x}{k_B T}\right) d\varepsilon_x d\varepsilon_y \quad (8.16)$$

$$\frac{dN}{N} = \frac{\exp(-\varepsilon/k_B T)}{\pi k_B T} d\varepsilon \int_0^\varepsilon \frac{1}{\sqrt{\varepsilon_x}} \frac{1}{\sqrt{\varepsilon - \varepsilon_x}} d\varepsilon_x \quad (8.17)$$

The value of the integral is π , and the final result takes the simple form

$$\frac{dN}{N} = \frac{1}{k_B T} \exp\left(-\frac{\varepsilon}{k_B T}\right) d\varepsilon \quad (8.18)$$

The fraction of molecules having energy in excess of the critical value ε_0^*

$$f^* = \frac{1}{k_B T} \int_{\varepsilon_0^*}^{\infty} \exp\left(-\frac{\varepsilon}{k_B T}\right) d\varepsilon \quad (8.19)$$

is obtained by integrating between the limits ε_0^* and infinity

$$f^* = \exp\left(-\frac{\varepsilon_0^*}{k_B T}\right) \quad (8.20)$$

Hinshelwood correctly pointed out that the expression $Z_1 e^{-E_l/RT}$ only applies if the energy is distributed among two degrees of freedom. For some unimolecular reactions, however, the number of internal degrees of freedom, s , is much greater than two. The activation energy is distributed initially among these s degrees, and there are many ways in which such a distribution can occur. Under such conditions, Hinshelwood has demonstrated that the fraction of molecules with energy above ε_0^* is then given by the expression

$$f^* = \frac{1}{(s-1)!} \left(\frac{\varepsilon_0^*}{k_B T}\right)^{s-1} \exp\left(-\frac{\varepsilon_0^*}{k_B T}\right) \quad (8.21)$$

and the rate constant, k_1 , no longer has an exponential dependence multiplied by simple collision frequency.

$$k_1 = Z_1 \frac{1}{(s-1)!} \left(\frac{\varepsilon_0^*}{k_B T}\right)^{s-1} \exp\left(-\frac{\varepsilon_0^*}{k_B T}\right) \quad (8.22)$$

Thus a new additional factor is present

$$\frac{1}{(s-1)!} \left(\frac{\varepsilon_0^*}{k_B T}\right)^{s-1} \quad (8.23)$$

that can be greater than unity by many powers of 10, when s is sufficiently high. For example, with $s = 5$ and $\varepsilon_0^*/k_B T = 5$ the factor of eq. (8.23) is 25, but if $s = 5$ and $\varepsilon_0^*/k_B T = 10$ the factor is much larger, for example, 1.5×10^4 .

The activation energy predicted by the formulation of Hinshelwood differs from that predicted by simple collision theory

$$\varepsilon_a = \varepsilon_0^* - \left(s - \frac{3}{2}\right) k_B T \quad (8.24)$$

In spite of the progress that the treatment of Hinshelwood has brought to the field, some difficulties remain. One that persisted was the reciprocal dependence of

$1/k^1$ versus the reciprocal of concentration, which as we have seen is not found at high pressures. However, there are other problems, such as the fact that the number of degrees of freedom required to reproduce experimental data is one-half of the total number of vibrational modes. In addition, according to eq. (8.23), one would also expect a strong temperature dependence of the pre-exponential factor, especially for large values of s . There is no experimental evidence for this prediction.

8.3 Rice–Ramsperger–Kassel–Marcus treatment

In more advanced treatments of unimolecular reactions, the previous mechanism is modified in order to distinguish *energised* molecules, A^* , from *activated* molecules, A^\ddagger . An activated molecule A^\ddagger is defined as one that is passing directly through the diving part on the product side of the potential-energy surface from the reactants to the products. An energised molecule, A^* is one that has acquired all the energy it needs to become an activated molecule, but, nevertheless, must undergo vibrations before it does so, and consequently its rate of conversion into A^\ddagger may depend on the critical energy for the conversion, ε_0^* . The mechanism for the general case of the presence of a foreign gas has the following scheme:

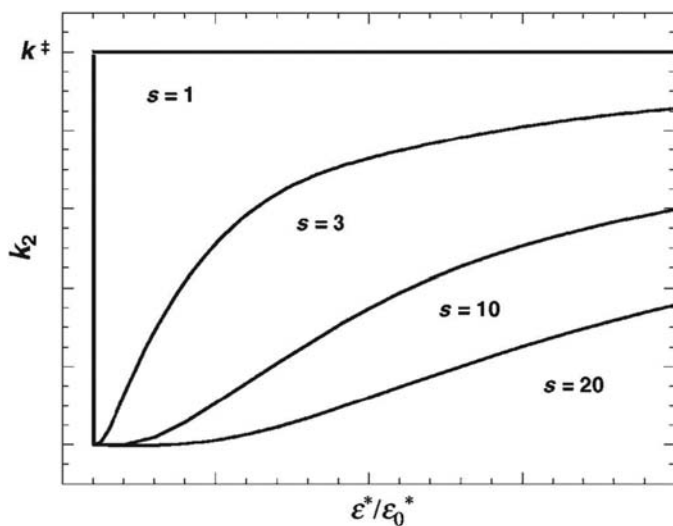


The highly energised molecule A^* has a metastable nature due to reasons associated with the slowness of the internal energy flow or, with the insight provided by the Rice–Ramsperger–Kassel–Marcus (RRKM) theory, to an entropy barrier arising from the improbability of concentrating vibrational energy into a few degrees of freedom prior to reaction. For this new treatment, the rate of conversion into products, k_2 , was found to be

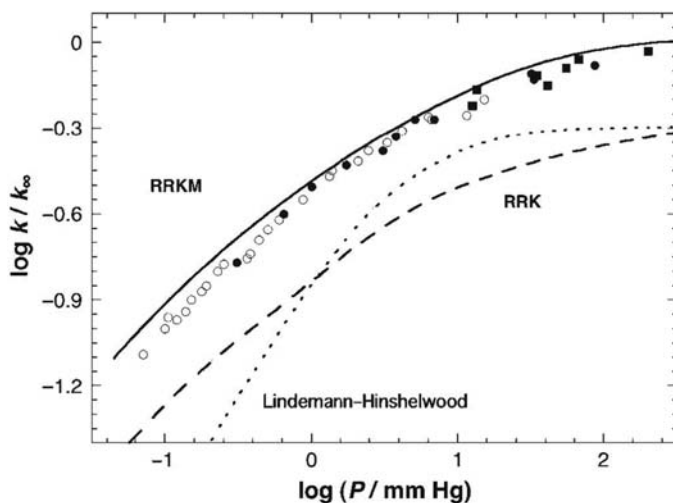
$$k_2 = k^\ddagger \left(\frac{\varepsilon^* - \varepsilon_0^*}{\varepsilon^*} \right)^{s-1} \quad (8.25)$$

where ε^* is the amount of energy for the energised species and ε_0^* the critical energy value for the conversion into products. This expression is the result of the statistics of a randomly distribution of energy among the various normal modes of vibration. Rice and Ramsperger used classical statistical mechanics, whereas Kassel introduced a quantum treatment in addition to the statistical one. In general, the s value of the classical formulation that reproduces experimental data ranges between $1/4$ and $2/3$ of the total number of the normal vibrational modes, but the results from the quantum-mechanical formulation are closer to the total number of modes.

When ε^* is sufficiently high, every energised molecule A^* is essentially an activated species A^\ddagger , but this condition depends on the value of s as shown in Figure 8.4. Figure 8.5 illustrates the application of Lindemann–Christiansen–Hinshelwood, RRK mechanisms to the isomerisation of cyclopropane as a function of pressure [4].

**FIGURE 8.4**

Dependence of k_2 on ϵ^*/ϵ_0^* for different values of s , that is, of the number of degrees of freedom.

**FIGURE 8.5**

Isomerisation rates of cyclopropane at 765 K, as a function of its pressure. The circles represent experimental data from several authors, and the curves represent the results of calculations with the theories indicated in the plot.

In the limit of high pressures, the theory RRK leads to the limiting high-pressure first-order rate constant of the conventional transition-state theory

$$k_{\infty}^1 = k^{\ddagger} \exp\left(-\frac{\varepsilon_0^*}{k_B T}\right) = \frac{k_B T}{h} \frac{Q^{\ddagger}}{Q_i} \exp\left(-\frac{\varepsilon_0^*}{k_B T}\right) \quad (8.26)$$

where Q_i and Q^{\ddagger} are the partition functions for activated and initial states. Since both partition functions refer to the same molecule, albeit in different configurations, one can expect that $Q_i \approx Q^{\ddagger}$ and the pre-exponential factor will be close to the average of the normal-mode frequencies, that is, *ca.* 10^{13} – 10^{14} sec⁻¹. This is found in some reactions, but others present much higher values.

Marcus extended the RRK formalism in such a way that the individual vibrational frequencies of the energised species and activated complexes are considered explicitly [5,6]: account is taken of the way that the rotations and different normal modes of vibration, together with zero-point energies, contribute to the reaction. The energised species possess vibrational energy ε_v^* and rotation ε_r^* . Along the reaction coordinate, the activated species has a translational energy ε_t^{\ddagger} together with vibrational energies (ε_v^{\ddagger}), and both contribute to the activation energy, ε^{\ddagger} . Conservation of angular momentum requires that the external rotational modes with energy ε_r^{\ddagger} do not contribute for the activation energy, ε^{\ddagger} . These are called *adiabatic modes* and, conversely, the other ones are considered to be the *active modes*. Figure 8.6 illustrates the energy scheme

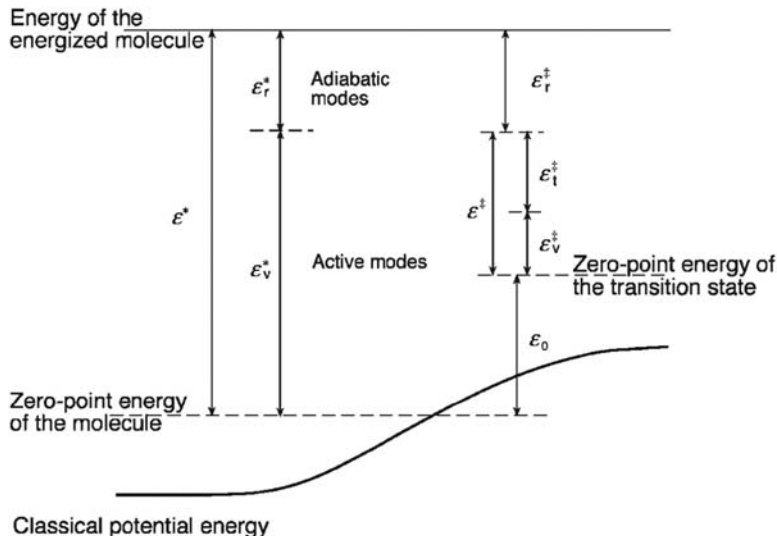


FIGURE 8.6

Energy diagram in the RRKM theory. *RRKM*, Rice–Ramsperger–Kassel–Marcus.

for the RRKM mechanism, while the expression for the rate of conversion into products, k_2 , is

$$k_2(\varepsilon^*) = \frac{s^\ddagger}{h} \frac{\sum P(\varepsilon_{\text{active}}^*)}{N(\varepsilon_{\text{active}}^*) F_r} \quad (8.27)$$

s^\ddagger is a statistical factor similar to those presented in [Section 6.1](#) and $\sum P(\varepsilon_{\text{active}}^*)$ the number of vibration-rotational quantum states of the activated molecules, corresponding to all energies up to and including $\varepsilon_{\text{active}}^\ddagger$. $N(\varepsilon_{\text{active}}^*)$ is the density of states having energy between ε^* and $\varepsilon^* + d\varepsilon^*$, that is, the number of states per unit energy range. Finally, F_r is a factor introduced to correct for the fact that rotations may not be the same in the activated molecule as in the energised molecule.

Under such conditions, pre-exponential factors greater than 10^{14} sec^{-1} can be estimated. This is usually interpreted in terms of weakly bonded activated molecules, which have a density of states much higher than the reagents. [Figure 8.5](#) also illustrates the application of RRKM theory to the isomerisation of cyclopropane as a function of pressure. Data were reproduced with a pre-exponential factor of $A^\infty = 2.82 \times 10^{15} \text{ sec}^{-1}$ and an activation energy $E_a^\infty = 274 \text{ kJ mol}^{-1}$.

8.4 Local random matrix theory

Efficiencies of energisation and de-energisation are not entirely independent of the nature of molecules. Noble gas and other simple molecules tend to be rather ineffective in transferring energy; complex molecules are more effective. Molecules that are able to react chemically transfer more energy than non-reactive molecules. This finding is interpreted in terms of some distortion of the potential-energy surfaces when there is chemical interaction. These matters are relevant for inter-molecular energy transfer.

Intra-molecular energy transfer is also more complex than the above theories contemplate. RRKM is based on the assumption that when a molecule is energised, the vibrational energy is exchanged rapidly between the normal modes. Details of such modes are relatively unimportant. Progress in this field has revealed, however, that the phenomenological energy flow is much richer than earlier thought and can depend on the local structure of molecular vibrational states. The slowness of energy flow in energised molecules causes substantial deviations from statistical RRKM theory, notably for unimolecular reactions with low reaction barriers.

The harmonic picture of forces in a molecule is a good approximation because nuclei are much heavier than the electron, so the low-energy wave functions for nuclear motion can be more precisely localised than electron clouds. A pure harmonic system can represent a molecule for kinetics. According to Slater, one waits for classical motions of the modes to be in phase with each other. Reaction occurs when a particular superposition of these modes causes the reaction

coordinate to reach the top of the reaction barrier. The anharmonicity of the bonds, however, limits this approach because it allows energy to flow between modes.

However, even for the harmonic level of approximation one can contemplate that certain paths of motion are more facile than others. Such paths follow resonances in which a few quanta in one mode are converted into quanta of other modes, such that the total mode energy is nearly conserved.

Molecules which are not high in symmetry—the vast majority—have many localised normal modes. For ordinary covalently bonded molecules, normal or local modes, supplemented by torsional modes for conformational isomerisations, represent slow varying degrees of freedom and can be used to label privileged quantum states. Figure 8.7 presents a schematic view of the *state space* of a molecule, adapted from the work of Gruebele and Wolynes [7]. Most of the states have excitations in many modes, the so-called *interior states*. Interior states have a rich set of possible non-linear connections, allowing the energy to flow in many ways. If the molecule is sufficiently energised, many of these possible flow paths can be realised. Motion in the interior can be viewed as a sequential hopping to nearby states, limited to states differing by changes of only a few quanta numbers in a few modes. For interior states, the flow to nearby states proceeds first.

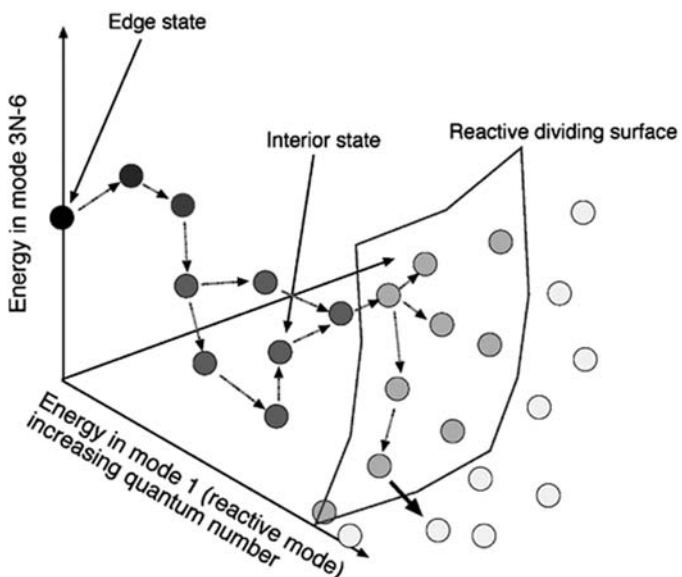


FIGURE 8.7

Three of the $3N-6$ dimensions of the molecular quantum state space. The energy of interior states flows in many ways, as opposed to the edge states. When the energy is localised in a reactive mode, the molecule can directly react as indicated by the thick arrow.

The local ways of hopping are quantified through a *local density of states*. This local density is crucial in determining the rate and manner of energy flow in the interior states. It measures the likelihood that a resonance local transfer can occur.

At the periphery of the state space, the picture for energy flow is altogether a different one. The so-called *edge states* have nearly all their energy concentrated in a single mode. The direct paths for energy flow from edge states are limited. Instead these states decay by “dynamical tunnelling”, in which intermediate states are never populated but facilitate hopping to energy states that are nearly resonant and which are found in the interior with very different quantum numbers.

The assumptions of the limits of no randomisation and that of total randomisations are too strong, because either IVR is slow compared to the unimolecular rate for reactions with low-energy barriers and the molecule simply does not have the time to explore all the available phase space before the reaction occurs, or the motion is constrained to a subset of the available phase space. Therefore real molecules required intermediate pictures between no randomisation and full randomisation. A model that captures this transition from facile energy flow throughout the phase space at high energies to strictly localised energy flow at low excitation is based on the local random matrix theory (LRMT) due to Logan and Wolynes. One of its predictions is that near the intra-molecular vibrational redistribution (IVR) threshold, either a state is very prone to IVR, or it is not. Therefore LRMT accommodates facts such as that nearly isoenergetic states in propyne molecule could have different IVR properties, depending on how close they are to the edge of the state space; the total density in these cases is nearly identical, but the local densities of states differ. If energy flow is slower than the reaction coordinate vibration itself, the simple RRKM rate will be in error because states depleted by reaction must be repopulated via IVR, and diffusion through the state space becomes rate determining. Such a feature shows up in the pressure dependence of the rates because rate space diffusion is facilitated by collisions.

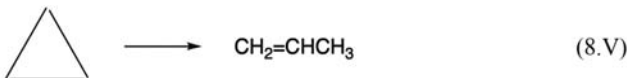
Freed, Rice and Jortner among others have argued that the density of levels in the state space can be treated as a continuum, allowing the use of the *golden rule* formalism to describe this IVR in the intra-molecular energy transfer processes. Such an approach will be presented later in [Chapter 16](#), Transitions Between Electronic States.

8.5 Energy barriers in the isomerisation of cyclopropane

In the early days of the transition-state theory, there was great hope that this theory would allow quantitative predictions of rate constants, although this requires adequate pre-exponential factors and energy barriers for the reactions. The theories previously discussed are essentially concerned with the pre-exponential factors of Arrhenius-type equations. Currently energy barriers for unimolecular reactions are estimated by ab initio methods or by density functional theory. Such

quantum-mechanical methods are particularly useful for small systems, but the numerical solution they offer are not easily related to processes of a similar kind.

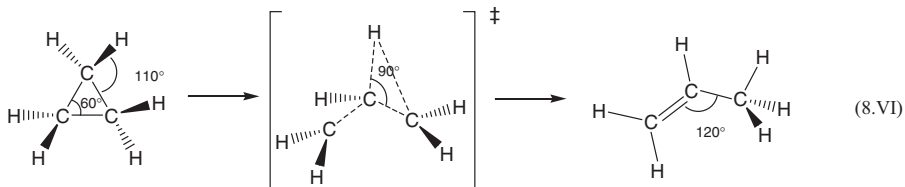
The Intersecting-State Model (ISM) can also be employed to provide some insight for unimolecular reactions. We will consider the case of the isomerisation of cyclopropane to propene.



In the high-pressure region ($P > 10$ Torr) for the temperature range of $470\text{ }^\circ\text{C}$ – $520\text{ }^\circ\text{C}$, the rate constant obeys the following expression:

$$k = 1.5 \times 10^{15} \exp\left(-\frac{272}{RT}\right) \text{ s}^{-1} \quad (8.28)$$

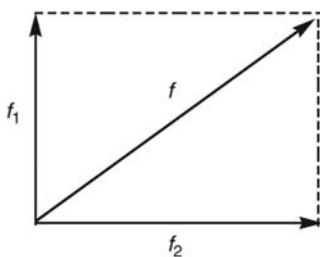
with the energies expressed in kJ mol^{-1} and $\Delta E^0 = -40.5 \text{ kJ mol}^{-1}$. When this unimolecular reaction is considered to follow the mechanism



one recognises that there is breaking of a C–C bond and of a C–H bond and the formation of a new C–H bond and a π carbon–carbon bond. More than one reactive mode is involved in the reactants or in the products, and the reaction coordinate must be a combination of the changes occurring in all the reactive bonds.

Although the concept of reaction coordinate is central to chemical reactivity studies, we must recall that, in the absence of PES information, the definition of “the reaction coordinate” of a given reaction largely remains an educated guess based on chemical intuition. In order to define simple reaction coordinate for a multi-dimensional problem, it is convenient to define an effective force constant, f_{eff} , for the stretching of the reactive bonds up to the transition state. When changes in the different reactive bonds define a normal mode of vibration, the current procedure is to define a common force constant, for example, for a ring, as the arithmetic average of the force constants of the individual bonds. Alternatively, when the reactive modes have local mode behaviour, simple procedure to obtain the effective force constant is to make a vectorial addition of the individual reactive bonds force constants (Figure 8.8).

We will assume the harmonic approximation for the stretching reactive modes for the isomerisation of cyclopropane. Additionally, we assume that the CCC angle at the transition state is intermediate ($\theta^\ddagger = 90$ degrees) between the value in the reactants (60 degrees) and that in the products (120 degrees), as illustrated

**FIGURE 8.8**

Vectorial addition of two local modes to obtain the effective force constant for a unidimensional reaction coordinate.

in [Scheme \(8.VI\)](#). If such modes have a local character, with force constants f_i , the effective force constant is just the result of a vectorial addition as shown in [Figure 8.8](#). Generalising for three bonds, in order to encompass the CH bond perpendicular to the CC bonds, one obtains the following expression:

$$f_{\text{eff}} = \sqrt{f_{\text{CC}}^2 + f_{\text{CC}}^2 + f_{\text{CH}}^2} \quad (8.29)$$

Relying on the values known for the relevant force constants, $f_{\text{C-C}} = 2.7 \times 10^3 \text{ kJ mol}^{-1} \text{ \AA}^{-2}$ and $f_{\text{C-H}} = 2.9 \times 10^3 \text{ kJ mol}^{-1} \text{ \AA}^{-2}$, [eq. \(8.29\)](#) leads to $f_{\text{eff}} = 4.8 \times 10^3 \text{ kJ mol}^{-1} \text{ \AA}^{-2}$. For consistency, the effective structural data are estimated as $l_r + l_p = (2 l_{\text{C-C}} + l_{\text{C-H}})(2/3)$; the factor (2/3) is required to impose the equivalent to the sum of two bond lengths. The equilibrium bond length data to be employed is $l_{\text{C-C}} = 1.54 \text{ \AA}$, $l_{\text{C-H}} = 1.1 \text{ \AA}$. This leads to $l_r + l_p = 2.79 \text{ \AA}$. From [eqs. \(6.96\), \(6.106\) and \(6.109\)](#) with $\Delta E^0 = -40.5 \text{ kJ mol}^{-1}$ and a total bond order at the TS of $m = 2n^\ddagger = 1$, one obtains the contribution for the energy barrier due to the reactive stretching modes, $\Delta E_{\text{stretch}}^\ddagger = 200 \text{ kJ mol}^{-1}$.

The isomerisation process also requires changes in the bending modes of CCC and CCH. The minimum energy required for harmonic bending motions is

$$\Delta E_{\text{bend}}^\ddagger = \frac{1}{2} f_{\text{CCC}} (\theta^\ddagger - \theta_0)^2 \quad (8.30)$$

where θ_0 and θ^\ddagger are the angles for reactants and transition state, respectively. The estimate of this contribution for the energy barrier is made under thermoneutral conditions, since the exothermicity of the reaction was taken into due account in the stretching contribution for the energy barrier. With the relevant data $f_{\text{CCC}} = 0.146 \text{ kJ mol}^{-1} \theta^{-2}$, $f_{\text{CCH}} = 0.1 \text{ kJ mol}^{-1} \theta^{-2}$ and for the CCC angle, $\theta_0 = 60$ degrees and $\theta^\ddagger = 90$ degrees, [eq. \(8.30\)](#) leads to a bending contribution of $\Delta E_{\text{CCC}}^\ddagger = 66 \text{ kJ mol}^{-1}$ for the changes in the CCC angle. For the CCH angle, one has $\theta_0 = 110$ degrees and $\theta^\ddagger = 90$ degrees, and the contribution for the energy barrier is $\Delta E_{\text{CCH}}^\ddagger = 20 \text{ kJ mol}^{-1}$.

The estimated overall barrier for the isomerisation of cyclopropane is, consequently, the sum of these three contributions, $\theta E^\ddagger = 286 \text{ kJ mol}^{-1}$. It is not so

much the close agreement of the estimated barrier with experiment that is important, but the insight that the ISM methodology provides for understanding mechanistic details of this unimolecular reaction.

References

- [1] FA Lindemann, *Trans. Faraday Soc* **17** (1922) 598.
- [2] MC King, KJ Laidler, *Arch. Hist. Exact. Sci.* **30** (1983) 45.
- [3] CN Hinshelwood, *Proc. R. Soc. A* **113** (1927) 230.
- [4] HO Pritchard, RG Sowden, AF Trotman-Dickenson, *Proc. R. Soc. A* **217** (1953) 563.
- [5] RA Marcus, *J. Chem. Phys.* **20** (1952) 364.
- [6] GM Wieder, RA Marcus, *J. Chem. Phys.* **37** (1962) 1835.
- [7] M Gruebele, PG Wolynes, *Acc. Chem. Res.* **37** (2004) 261–267.

This page intentionally left blank

Elementary reactions in solution

9

9.1 Solvent effects on reaction rates

With reactions in solution, the solvent is generally present at a much higher concentration than the reactants and its concentration is approximately constant during the course of a reaction. If the solvent is also one of the reactants, as with water in hydrolyses or in the example of recombination of carbocations with water molecules we discussed previously, the order with which the solvent participates in the reaction rate cannot be obtained by kinetic studies in this solvent. To get this, we need kinetic studies with solvent mixtures or isotopically labelled molecules, spectroscopic studies, etc.

In other systems, the solvent only acts as an inert medium where reaction occurs without affecting the mechanism. This appears to be the case of the decomposition of nitrogen pentoxide, in which the pre-exponential factor and the activation energy are very similar in the gas phase and in solvents of various types, as shown in [Table 9.1](#).

A more subtle effect of solvent is seen in the reactions first studied by Menschutkin [\[1\]](#), and which take his name. An example is the reaction



whose rate and equilibrium constants have been studied in a wide range of solvents [\[2\]](#).

The results shown in [Table 9.2](#) indicate that the rate constants decrease by a factor of 140 times on going from acetonitrile to benzene. This solvent effect occurs without any change in mechanism, but what causes it? Note that there is also an effect in the same solvents on the free energy of reaction, ΔG^0 , which is seen as a decrease in the equilibrium constant by a factor of 2.5×10^4 . However, as shown in [Figure 9.1](#), this does not correspond to a linear correlation between kinetic and thermodynamic parameters.

What seems to be happening is that, though the solvent does produce an effect on ΔG^0 , at the same time there is a change in the electrophilicity index, m . According to [Figure 9.2](#), this can be correlated with the Kamlet–Taft solvent parameter β_{KT} , which is an empirical measure of the capacity of the solvent to coordinate via the donation of a pair of non-bonding electrons, that is, the solvent acts as a Lewis base.

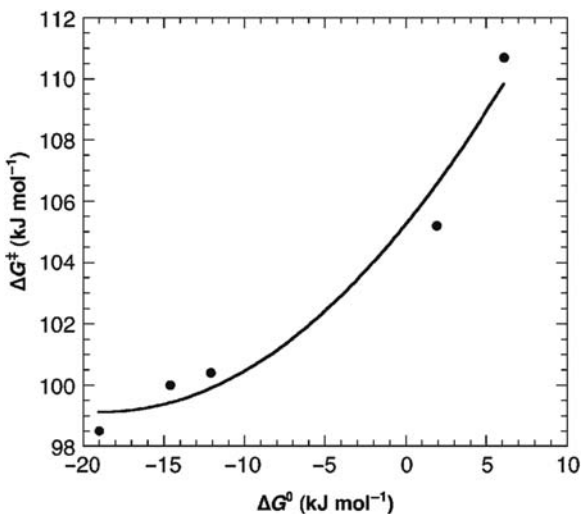
Table 9.1 Decomposition of N₂O₅.

Reaction medium	$\log A$ (dm ³ mol ⁻¹ sec ⁻¹)	E_a (kJ mol ⁻¹)
Gas phase	13.6	103.3
Chloroform	13.7	102.7
Nitromethane	13.5	102.5
Pentachloroethane	14.0	104.6

Table 9.2 Effect of solvent on the Menschutkin reaction.

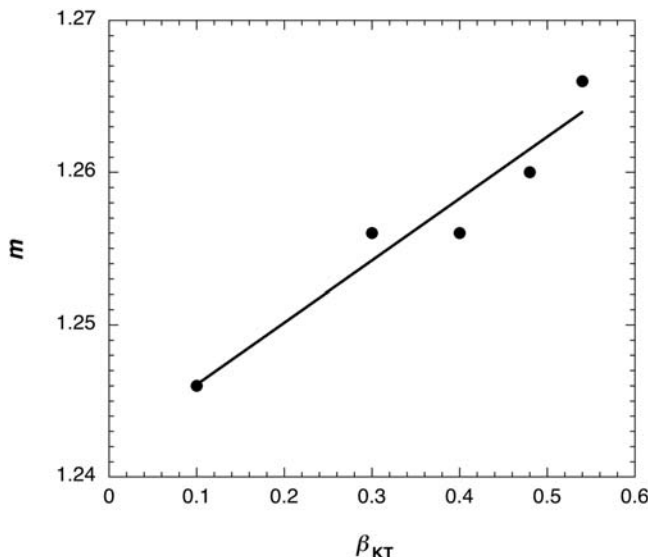
Solvent	ΔG^\ddagger (kJ mol ⁻¹)	ΔG^0 (kJ mol ⁻¹)	m^a	β_{kT}
Acetonitrile	98.5	-19.0	1.256	0.40
Nitrobenzene	100.0	-14.6	1.256	0.30
Acetone	100.4	-12.1	1.260	0.48
Tetrahydrofuran	105.2	1.9	1.266	0.54
Benzene	110.7	6.1	1.246	0.10

^aValue which reproduces the activation energy using harmonic oscillators to describe the C—I bond ($f_{CI} = 1.6 \times 10^3 \text{ kJ mol}^{-1} \text{ Å}^{-2}$ and $l_{CI} = 2.207 \text{ Å}$) in the reactants and the NC bond ($f_{NC} = 2.95 \times 10^3 \text{ kJ mol}^{-1} \text{ Å}^{-2}$ and $l_{NC} = 1.472 \text{ Å}$) in the products.

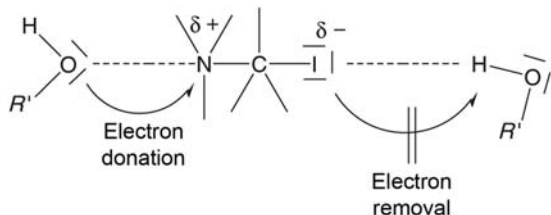
**FIGURE 9.1**

Variation of activation energy with reaction energy, for the Menschutkin reaction (data from Table 9.2).

This effect of the solvent lone pair can be rationalised in terms of attraction by the positive part of the amine dipole, which leads to an increase in m , due to an increase in electron density in the N—C bond, as indicated diagrammatically in Figure 9.3.

**FIGURE 9.2**

Correlation of the electrophilicity index (m) with the Kamlet–Taft β_{KT} parameter for the Menschutkin reaction (data from Table 9.2). The intercept has a value $m = 1.24$.

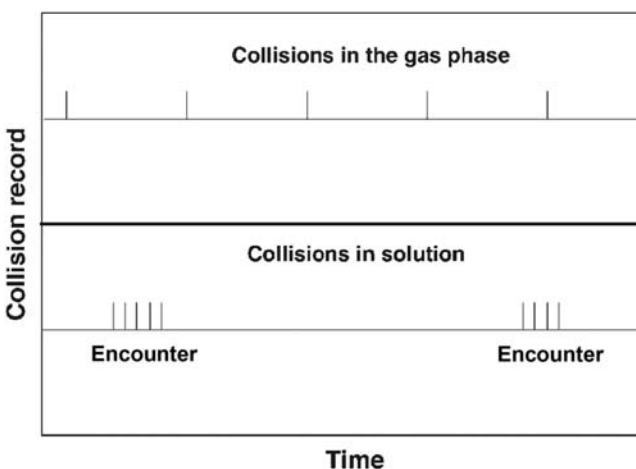
**FIGURE 9.3**

Changes in electron density produced by electron donation and withdrawal by the solvent.

In addition to these limits of a solvent acting as an inert medium or as an active chemical or electronic species in the transition state, we will see a number of other effects of a more physical nature can occur, as will be discussed in the following sections.

9.2 Effect of diffusion

With reactions in solution, even when the medium is chemically inert, the solvent will exert an effect as a consequence of it being a condensed phase, with its

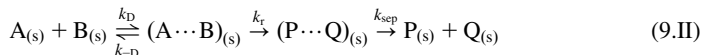
**FIGURE 9.4**

Contrast between collisions in the gas phase and encounters between the same two reactants in the solvent cage in a liquid.

molecules very close together. As a consequence, the distribution of collisions is much more important than their frequency, which is comparable, but generally two to three times greater in liquids than in gases. As seen in a simulation in [Figure 9.4](#), due to Rabinowitch and Wood [3], while collisions between molecules in the gas phase are separated by reasonable time intervals; in liquids, collisions occur in groups of rapid sequences, known as encounters.

In each encounter between two reactants, the molecules undergo at least four collisions, until they manage to escape the cage of solvent molecules that surround them. However, the frequency of these encounters is about 100 times lower than that for collisions of the same molecules in the gas phase.

Based on this, a reaction in solution can be broken down into three steps: (1) diffusion of reactants from bulk solution to the collision distance; (2) chemical reaction of the reacting species within the solvent cage and (3) diffusion of the products from the solvent cage to bulk solution. We can represent these processes in the following kinetic scheme:



The rate of reaction, measured by the decrease in concentration of species A, is given by the expression:

$$-\frac{d[A]}{dt} = k_D[A][B] - k_{-D}[A \cdots B] \quad (9.1)$$

and the formation of the encounter pair or complex, $(AB)_s$, between reactants A and B is

$$\frac{d[A \cdots B]}{dt} = k_D[A][B] - k_{-D}[A \cdots B] - k_r[A \cdots B] \quad (9.2)$$

Assuming steady-state conditions for $(AB)_s$, $d[(AB)_s]/dt = 0$, such that from the previous equation

$$[A \cdots B] = \frac{k_D[A][B]}{k_{-D} + k_r} \quad (9.3)$$

Substitution for $[(AB)_s]$ into eq. (9.1) leads to the reaction rate

$$-\frac{d[A]}{dt} = k_D[A][B] - k_{-D}k_D \frac{[A][B]}{k_{-D} + k_r} \quad (9.4)$$

which, on rearranging, gives

$$-\frac{d[A]}{dt} = \frac{k_r k_D}{k_{-D} + k_r} [A][B] \quad (9.5)$$

Eq. (9.5) shows two limiting conditions in the reaction kinetics, $k_r \ll k_{-D}$ and $k_r \gg k_{-D}$. In the first case, the reaction rate is given by the expression:

$$-\frac{d[A]}{dt} = k_r \frac{k_D}{k_{-D}} [A][B] \quad (9.6)$$

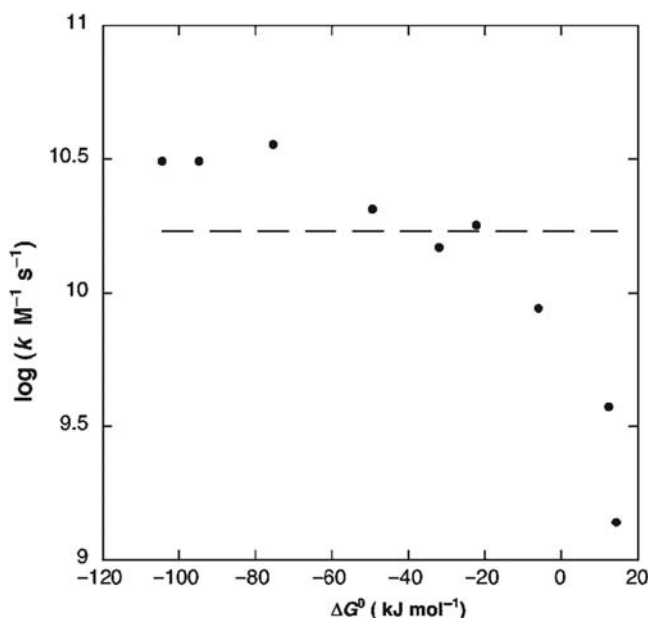
This is the limit of reaction (or activation) control; the rate in solution is controlled by the activation-controlled reaction between the reactants, k_r . The second limit corresponds to diffusional control, where the rate of reaction is controlled by the rate of diffusion of the reactants, k_D .

$$-\frac{d[A]}{dt} = k_D[A][B] \quad (9.7)$$

An example of the transition of a process controlled by chemical reaction to one controlled by diffusion is found in the electron transfer between excited aromatic hydrocarbons (D^*), and various nitriles A in heptane



The aromatic hydrocarbons are stronger reducing agents when electronically excited than in the ground state, and can donate an electron to a species A. The rate of this electron transfer depends on the ease with which A is reduced, and the reaction follows a free-energy relationship. When ΔG^0 is sufficiently small, such that $k_r \gg k_{-D}$, then the reaction is diffusion controlled, with a rate constant which is constant and is independent of the reaction energy. These effects are indicated in Figure 9.5.

**FIGURE 9.5**

The change from diffusional control to reaction control in electron transfer between electronically excited aromatic hydrocarbons and nitriles in heptane at room temperature. The dashed line is diffusion rate constant calculated with eq. (9.23) using the viscosity of heptane. (Courtesy Carlos Serpa.)

Another example, also involving a photochemical reaction in solution, is the decomposition of molecular iodine and the reverse process of recombination of iodine atoms within the solvent cage.



This is a *primary recombination* process, which can be distinguished from *secondary recombination* reactions, which occur after the two atoms have separated.

The yield of formation of atomic iodine is twice that of disappearance of molecular iodine. Under steady-state conditions for $(\text{I:I})_{\text{s}}$, the reaction rate takes the form

$$v = \frac{k_{\text{abs}} k_r}{k_{-\text{D}} + k_r} [\text{I}_2] \quad (9.8)$$

The yield of I_2 loss is the ratio of the rate of formation of 2I to the total rate of dissociation of $(\text{I:I})_{\text{s}}$

$$\phi_{2\text{I}} = -\phi_{\text{I}_2} = \frac{k_r}{k_{-\text{D}} + k_r} \quad (9.9)$$

Table 9.3 Yield of decomposition of molecular iodine in a photo-induced reaction.

Solvent	$-\phi_{12}$	η_s/cP
Hexane	0.5	0.30
Carbon tetrachloride	0.11	0.91
Hexachlorobuta-1,3-diene	0.0042	2.5

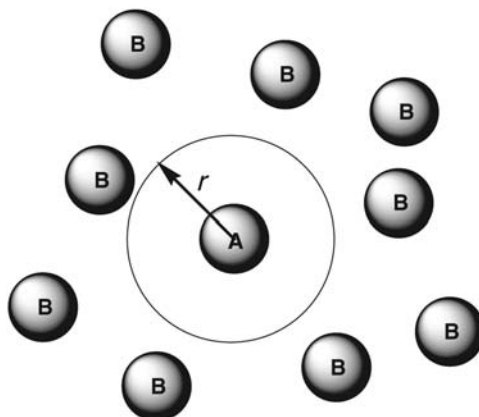


FIGURE 9.6

Molecules A in solution surrounded by B.

When the process is diffusion controlled, this yield depends on the solvent viscosity, η_s , and, as we will see shortly, the diffusion constants present an inverse relation with η_s . Data for this reaction are given in **Table 9.3**. This cage effect becomes more significant when the solvents have a high viscosity, and in this case, the highest primary recombination yields are observed. This cage effect is known as the *Franck–Rabinowitch effect*.

To obtain a more detailed understanding of the kinetics of these reactions, we will now see how we can estimate the diffusion constants of reactants.

9.3 Diffusion constants

We will start by considering an uncharged molecule A surrounded by a statistically symmetrical distribution of B molecules ([Figure 9.6](#)). The flow, J , of B molecules in the direction towards A can be considered to be the flow of B molecules which cross a sphere centred on A, with radius r .

This flow is defined in terms of Fick's first law of diffusion as

$$J \equiv \frac{dn}{dt} = -DA \frac{dc}{dx} \quad (9.10)$$

where dn represents the number of moles of substance which diffuses across a surface of area A , D the diffusion coefficient and dc/dx the concentration gradient. For the moment we will consider that molecule A is stationary. The negative sign is due to diffusion being in the direction of lower concentration. The surface of the sphere centred on A, radius r is $A = 4\pi r^2$, such that from eq. (9.10), we have

$$J \equiv \frac{dn_B}{dt} = 4\pi r^2 D_B \frac{dc_B}{dr} \quad (9.11)$$

Here the concentration gradient, dc_B/dr , takes the increase of the radius as reference, such that the negative sign disappears. Thus the concentration gradient becomes

$$\frac{dc_B}{dr} = \frac{J_B}{4\pi r^2 D_B} \quad (9.12)$$

Integrating this equation with the limits of concentration of B at the distance r from A, c_{B_0} , and the concentration of B in the bulk solution ($r = \infty$), represented as [B]

$$\int_{C_{B_0}}^{[B]} dc_B(r) = \frac{J_B}{4\pi D_B} \int_r^\infty \frac{1}{r^2} dr \quad (9.13)$$

gives

$$c_B|_{C_{B_0}}^{[B]} = -\frac{J_B}{4\pi D_B} \frac{1}{r} \Big|_r^\infty \quad (9.14)$$

which leads to

$$c_{B_0} = -\frac{J_B}{4\pi D_B r} + [B] \quad (9.15)$$

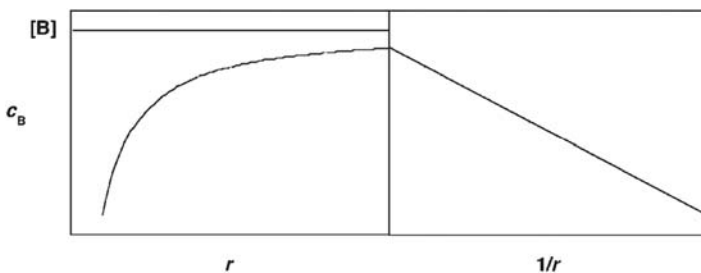
This result is valid for the conditions where A is stationary. However, as in practice this species also diffuses, the equation should be modified to include the two diffusion coefficients

$$c_{B_0} = -\frac{J_B}{4\pi(D_B + D_A)r} + [B] \quad (9.16)$$

When the reaction is totally controlled by diffusion at the microscopic level, B reacts very rapidly with A when they are separated by a critical distance, d_{AB} . Therefore when $r = d_{AB}$ the concentration $c_{B_0} = 0$. This is because there is reaction between A and B on every encounter. Therefore from eq. (9.16), we obtain

$$J_B = 4\pi(D_B + D_A)d_{AB}[B] \quad (9.17)$$

The graph of concentration of B as a function of distance is shown in Figure 9.7.

**FIGURE 9.7**

Concentration B as a function of distance from A for a reaction completely controlled by diffusion, following eq. (9.16).

The rate of reaction involving all molecules of A becomes

$$v = 4\pi(D_B + D_A)d_{AB}[A][B] \quad (9.18)$$

and the diffusion-controlled rate constant is

$$k_D = 4\pi(D_B + D_A)d_{AB} \quad (9.19)$$

The *Système International* (SI) units for D_A and D_B are $\text{m}^2 \text{ sec}^{-1}$, such that k_D will have the units $\text{m}^3 \text{ sec}^{-1}$. Normally in chemical kinetics we use molar quantities and litres, which requires multiplying $k_D/\text{m}^3 \text{ sec}^{-1}$ by the Avogadro number N_A and by 10^3 to give

$$k_D = 4\pi 10^3 N_A (D_B + D_A) d_{AB} \text{ dm}^3 \text{ mol}^{-1} \text{ sec}^{-1} \quad (9.20)$$

When the diffusion coefficients are not known, we can determine them from the Stokes–Einstein equation

$$D = \frac{k_B T}{6\pi\eta_s r} \quad (9.21)$$

where η_s is the solvent viscosity. The Stokes–Einstein equation is valid when the solute molecules are much bigger than those of the solvent. The sum of the diffusion coefficients is approximately

$$D_A + D_B = \frac{k_B T}{6\pi\eta_s} \left(\frac{1}{r_A} + \frac{1}{r_B} \right) \quad (9.22)$$

And, taking $d_{AB} = r_A + r_B$, substitution of eq. (9.22) into eq. (9.20) leads to the diffusion-controlled rate constant

$$k_D = \frac{2k_B T (r_A + r_B)^2}{3\eta_s r_A r_B} \quad (9.23)$$

If the molecules have the same size (i.e., $r_A = r_B$), we obtain

$$k_D = \frac{8k_B T}{3\eta_s} \quad (9.24)$$

The rate constant k_{-D} is the reciprocal of the time in which A and B remain as nearest neighbours, which, in the absence of any specific interactions between A and B will be

$$k_{-D} = \frac{6(D_A + D_B)}{d_{AB}^2} \quad (9.25)$$

When the reactions are controlled by diffusion, the rate will be proportional to the reciprocal of the solvent viscosity, as shown by eqs. (9.7) and (9.24), and Table 9.4. The typical activation energy of diffusion in solution is fairly small, *ca.* 15 kJ mol⁻¹. Figure 9.8 shows an Arrhenius plot of one of the systems in Figure 9.5 under the diffusion-controlled regime, but measured in isopropyl ether. The experimental activation energy for this system in this solvent is 11 kJ mol⁻¹ and is entirely due to the temperature dependence of the viscosity.

Although from eq. (9.23) the diffusion-controlled constant, k_D , depends on the size of molecules, according to

$$\frac{(r_A + r_B)^2}{r_A r_B} = 2 + \frac{r_A}{r_B} + \frac{r_B}{r_A} \quad (9.26)$$

With the normal range of sizes of molecules of interest, this only shows a modest change with r_A/r_B . For example, the ratio of eq. (9.26) will be 4.5 for $r_A/r_B = 2$ and 4.0 with $r_A/r_B = 1$. However, dramatic effects can be seen when one of the species is a polymer, and the other is a small molecule. For example, with the case given in Chapter 3, Experimental Methods, of triplet energy transfer in benzene from biphenyl to the polymer MEH–PPV, of molecular weight

Table 9.4 Diffusion controlled rate constants calculated from eq. (9.24) and viscosities for some common solvents at 25 °C.

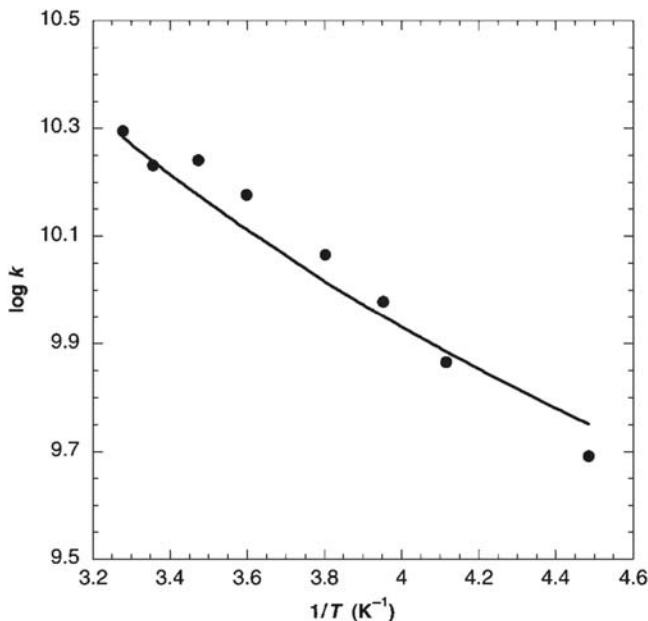
Solvent	Viscosity ^a (η)(mPa sec)	$k_{\text{diff}}^{\text{b}}$ (M ⁻¹ sec ⁻¹)
Carbon dioxide	0.0577 ^c	1.2×10^{11}
Diethyl ether	0.222	3.0×10^{10}
Hexane	0.294	2.2×10^{10}
Acetone	0.316	2.1×10^{10}
Toluene	0.558	1.2×10^{10}
Decane	0.861	7.7×10^9
Water	0.890	7.4×10^9
Ethanol	1.083	6.1×10^9
Propan-2-ol	2.044	3.2×10^9
Ethylene glycol	19.9 ^d	3.3×10^8
Glycerol	945	7.0×10^6

^aFrom Handbook of Chemistry and Physics. 59th Edn. (ed. RC Weast), CRC Press, West Palm Beach, FA, 1979.

^bUsing viscosities in mPa sec, it is necessary to multiply by 10^6 to get values in M⁻¹ sec⁻¹.

^cAt 35 °C and 10 MPa, in the supercritical phase, from <http://webbook.nist.gov/>.

^dAt 20 °C.

**FIGURE 9.8**

Temperature dependence of electron transfer between electronically excited naphthalene and fumaronitrile in isopropyl ether. The line is the diffusion rate constant calculated at the different temperatures [4].

$1.5 \times 10^6 \text{ Da}$, the experimental rate constant is $1.97 \times 10^{11} \text{ dm}^3 \text{ mol}^{-1} \text{ sec}^{-1}$ [5], which can be compared with the normal diffusion-controlled rate constant in benzene at 25°C ($1.1 \times 10^{10} \text{ dm}^3 \text{ mol}^{-1} \text{ sec}^{-1}$) [6]. Using eq. (9.23) and reasonable estimates for the polymer and biphenyl size, we can calculate a value $k_D = 1.2 \times 10^{11} \text{ dm}^3 \text{ mol}^{-1} \text{ sec}^{-1}$ for this system.

For reactions between species of similar size in water at 25°C , eq. (9.24) leads to a value of the diffusion-controlled rate constant for neutral species of $7 \times 10^9 \text{ dm}^3 \text{ mol}^{-1} \text{ sec}^{-1}$. This is probably an underestimate, and in Table 9.5, some experimental rate constants are given for diffusion-controlled reactions in water.

For reactions between species of charge $Z_1 e$ and $Z_2 e$, eq. (9.24) needs to be modified to allow for the electrostatic attraction or repulsion between ions

$$k_D = \frac{8k_B T}{3\eta_s} \frac{\delta}{\exp(\delta) - 1} \quad (9.27)$$

with

$$\delta = \frac{Z_A Z_B e^2}{4\pi\epsilon k_B T d_{AB}} \quad (9.28)$$

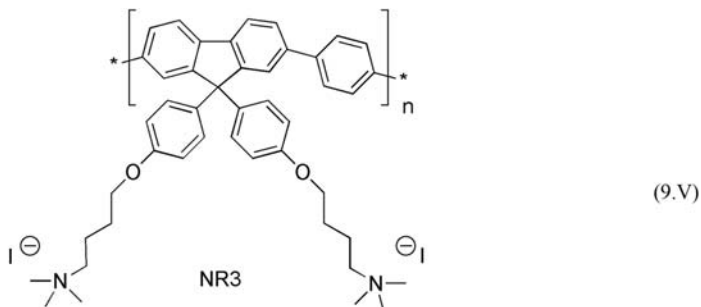
Table 9.5 Experimental rate constants for some typical diffusion controlled reactions in aqueous solutions^a.

Reaction	k ($10^9 \text{ M}^{-1} \text{ sec}^{-1}$)
$\text{H} + \text{H}\cdot \rightarrow \text{H}_2$	7.75
$\text{H} + \cdot\text{OH} \rightarrow \text{H}_2\text{O}$	7.0
$\cdot\text{OH} + \cdot\text{OH} \rightarrow \text{H}_2\text{O}_2$	5.5
$\cdot\text{OH} + \text{OH}^- \rightarrow \text{O}^{2-} + \text{H}_2\text{O}$	13
$\text{H} + \text{O}_2 \rightarrow \text{HO}_2\cdot$	21
$\text{H}\cdot + \text{Fe}(\text{CN})_6^{3-} \rightarrow \text{H}^+ + \text{Fe}(\text{CN})_6^{4-}$	6.3
$\text{C}_6\text{H}_6(\text{benzene}) + \cdot\text{OH} \rightarrow \text{C}_6\text{H}_6\text{OH}\cdot$	7.8

^aData selected from Ref. [7].

where ε is the relative permittivity of the solvent. This equation shows that reactions between oppositely charged species will have diffusion-controlled rate constants greater than those for uncharged neutral molecules. For example, with $Z_1Z_2 = -2$ in water, rate constants are about three times faster than those involving uncharged species. In contrast, with ions of the same charge, the diffusion-controlled rate constants will be less than with neutral molecules; for $Z_1Z_2 = 2$ in water, $k_D(\text{ions})/k_D(\text{neutral molecules}) \approx 1/5$. Some typical values for reaction of hydrated electrons with charged species are given in Table 9.6.

A particularly dramatic example of the effect of charge on diffusion-controlled reaction is seen with the conjugated polyelectrolyte NR3 and the solvated electron,



where the rate constant is $5.4 \times 10^{12} \text{ dm}^3 \text{ mol}^{-1} \text{ sec}^{-1}$. From this, the charge NR3 is calculated to be +13, which is in reasonable agreement with that expected from the size of the polymer, assuming complete ionisation.

Table 9.6 Rate constants for reactions of hydrated electrons (e_{aq}^-) with charged and uncharged species in aqueous solution^a.

Reaction	k ($10^{10} \text{ M}^{-1} \text{ sec}^{-1}$)
$e_{\text{aq}}^- + \text{H}^\cdot \rightarrow \text{H}_2 + \text{OH}^-$	2.5
$e_{\text{aq}}^- + e_{\text{aq}}^- \rightarrow \text{H}_2 + 2\text{OH}^-$	0.55
$e_{\text{aq}}^- + \text{OH}^\cdot \rightarrow \text{OH}^-$	3.0
$e_{\text{aq}}^- + \text{H}^+ \rightarrow \text{H}^\cdot$	2.3
$e_{\text{aq}}^- + \text{O}_2 \rightarrow \text{O}_2^\cdot$	1.9
$e_{\text{aq}}^- + \text{O}_2^\cdot \rightarrow \text{O}_2^{2-}$	1.3
$e_{\text{aq}}^- + \text{Ag}^+ \rightarrow \text{Ag}(0)$	3.7
$e_{\text{aq}}^- + \text{Cu}^{2+} \rightarrow \text{Cu}^+$	3.3
$e_{\text{aq}}^- + \text{UO}_2^{2+} \rightarrow \text{UO}_2^+$	1.7
$e_{\text{aq}}^- + \text{Co}(\text{NH}_3)_6^{3+} \rightarrow \text{Co}(\text{NH}_3)_6^{2+}$	8.8
$e_{\text{aq}}^- + \text{Au}(\text{CN})_2^- \rightarrow \text{Au}(0) + 2\text{CN}^-$	0.35
$e_{\text{aq}}^- + \text{Al}(\text{OH})_4^- \rightarrow \text{Al}(\text{OH})_4^{2-}$	0.00055
$e_{\text{aq}}^- + \text{Fe}(\text{CN})_6^{3-} \rightarrow \text{Fe}(\text{CN})_6^{4-}$	0.31
$e_{\text{aq}}^- + \text{C}_6\text{H}_6(\text{benzene}) \rightarrow \text{C}_6\text{H}_7^\cdot$	0.0009
$e_{\text{aq}}^- + \text{coenzyme B12} \rightarrow \text{reduced form}$	3.2

^aData selected from Ref. [7].

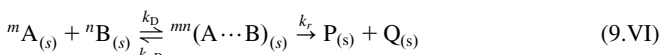
We should note that for very fast reactions produced by either photoexcitation or high-energy radiation, the initial distribution of reactants is not homogeneous, and that the diffusional rate constants are time dependent.

9.4 Spin-statistical factors in diffusion-controlled reactions

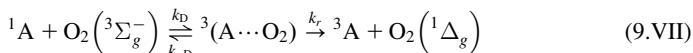
There are circumstances in which a diffusion-controlled reaction occurs with a rate constant lower than k_D . For example, the quenching of the singlet state fluorescence of tetracene by O_2 in benzene takes place with a rate constant $k_q = 2.2 \times 10^{10} \text{ dm}^3 \text{ mol}^{-1} \text{ sec}^{-1}$ to yield the triplet state of tetracene with unit quantum yield, and this rate constant is indistinguishable from the diffusion-controlled rate constant in benzene. However, the triplet state of tetracene is also quenched by O_2 in benzene but returns to the ground state with a rate constant $k_q = 3.9 \times 10^9 \text{ dm}^3 \text{ mol}^{-1} \text{ sec}^{-1}$. The energy difference between the first excited singlet state of tetracene and its lowest triplet state, $\Delta E_{\text{ST}} = 130 \text{ kJ mol}^{-1}$, is almost identical to its triplet state energy, $E_T = 123 \text{ kJ mol}^{-1}$, and both energy transfers to oxygen are sufficiently exothermic to be diffusion controlled because they lead to the excited singlet state of oxygen, $\text{O}_2^1\Delta_g$, which has an electronic energy of 94 kJ mol^{-1} [8]. Although both singlet and triplet quenching by O_2 should have

rate constants limited by diffusion, the quenching of the triplet state of tetracene is 5.6 times slower than the corresponding singlet quenching.

The highest occupied molecular orbitals of molecular oxygen are degenerate and two of them are occupied by one electron each. These two electrons have the same spin ($+1/2$, $+1/2$), which give a total spin quantum number $S = 1/2 + 1/2 = 1$ for O_2 . Molecular oxygen is paramagnetic. The spin multiplicity is defined as $M = 2S + 1$, and the values $S = 0$, $1/2$ and 1 give spin multiplicities named singlet, doublet and triplet. In terms of spin multiplicity, the ground state of molecular oxygen is a triplet, $O_2^3\Sigma_g^-$. The spin multiplicity is the number of distinct states (sub-levels) that exist in the atomic or molecular species in the presence of an external magnetic field. The transitions between states of different multiplicities are relatively slow when compared with the lifetimes of encounter pairs of reactive species in solution. Hence, spin multiplicity must be taken into account in scheme (9.II). When this is done

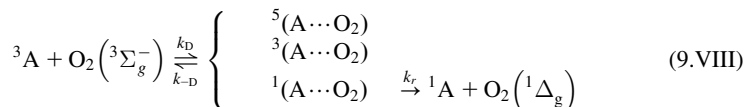


we realise that the spin states of the encounter pair can have a multiplicity of $m \times n$. In the absence of an external magnetic field these spin states are degenerate and equally populated. Consequently, the probability of formation of each encounter pair is given by the spin-statistical factor $(m \times n)^{-1}$. If both reactants are singlets, as is usually the case in reactions between organic molecules, $m \times n = 1$ and we do not have to consider spin statistics. The reaction between singlet tetracene and $O_2^3\Sigma_g^-$



proceeds along a spin-allowed path with conservation of the total spin. However, Porter and Wright showed that there are spin-statistical consequences in the quenching of triplet states by molecular oxygen [9].

When two triplets interact, they give $m \times n = 9$ encounter pairs with sublevels of quintet, triplet and singlet multiplicities. For example, the reaction of triplet tetracene and $O_2^3\Sigma_g^-$



there are nine encounter-pair spin states. Five of them are quintet states and are formed with a rate constant ${}^5/9 k_D$. Three of them are triplets formed with a rate constant ${}^3/9 k_D$ and one of them is a singlet formed with a rate constant ${}^1/9 k_D$. Only the singlet channel can lead to a multiplicity-allowed product. The quintet and triplet channels are unproductive and give back the reactants. Therefore when spin-conservation rules are strictly followed, diffusion-controlled quenching of triplet states by $O_2^3\Sigma_g^-$ takes place with a rate constant ${}^1/9 k_D$. Such rules are followed when inter-system crossing in the encounter pair is slow relative to k_{-D} (diffusion apart is faster than intersystem crossing) and all singlet encounter pairs give quenching (the quantum yield of singlet oxygen is unity, $\Phi_\Delta = 1$).

In practice, when the quenching of triplet states of organic molecules by molecular oxygen occurs with $k_q \approx 1/9k_D$, we observe $\Phi_\Delta \approx 1$, but in systems with $4/9k_D \geq k_q \geq 1/9k_D$ we typically obtain $\Phi_\Delta < 1$. Wilkinson assigned this deviation from strict spin conservation rules to the presence of charge transfer in the encounter pair [10]. Although spin statistics in diffusion-controlled reactions may seem to be rather exotic phenomena, they have consequences in the generation of singlet oxygen by photosensitisers employed in photodynamic therapy (PDT). PDT is a therapeutic approach employed in oncology and infectious diseases that uses light, a photosensitiser that absorbs that light and the oxygen present in body tissues, to generate reactive oxygen species (such as singlet oxygen) that produce oxidative stress capable of triggering cell death in target tissues. Photosensitisers that are involved in charge-transfer interactions with O_2 will give lower yields of singlet oxygen but may generate other reactive oxygen species [11].

9.5 Reaction control

Reactions in solution that are not controlled by diffusion can be addressed with the chemical considerations presented in Chapter 6, Reactivity in Thermalised Systems, and again we resort to TST. However, because of problems, in particular, of standard states and activities, there are difficulties in formulation of partition functions for species in solution. The best way of applying TST in this case involves the thermodynamic formulation of conventional transition state theory (CTST). Within this, the reaction rate is directly proportional to the concentration of the activated complexes.

$$\nu = \frac{k_B T}{h} [X^\ddagger] \quad (9.29)$$

For a bimolecular reaction



the activation equilibrium constant is given by the expression

$$K_s^\ddagger = \frac{\gamma_\ddagger^\ddagger [X^\ddagger]}{\gamma_A [A] \gamma_B [B]} \quad (9.30)$$

in which γ_A and γ_B are the activity coefficients for the reactants and γ_\ddagger^\ddagger for the activated complex. Substituting eq. (9.30) into eq. (9.29) gives

$$\nu = \frac{k_B T}{h} K_s^\ddagger \frac{\gamma_A \gamma_B}{\gamma_\ddagger^\ddagger} [A][B] \quad (9.31)$$

from which, the rate constant will be

$$k_s = \frac{k_B T}{h} K_s^\ddagger \frac{\gamma_A \gamma_B}{\gamma_\ddagger^\ddagger} \quad (9.32)$$

The activity coefficient of the transition state γ_{\ddagger} enters into the expressions for the reaction rate and rate constant since the concentration of activated complexes comes from the activation equilibrium constant. If the reaction rate depends on the activity of the transition state, $a_{\ddagger} = \gamma_{\ddagger}[X^{\ddagger}]$, then the overall rate of reaction will depend on the activity coefficients of the reactants.

As with ideal gases in the gas phase the activity coefficients are equal to one, we get

$$k_g = \frac{k_B T}{h} K_g^{\ddagger} \quad (9.33)$$

and

$$k_s = k_g \frac{\gamma_A \gamma_B}{\gamma_{\ddagger}} \quad (9.34)$$

When rate constants are equal in the gas phase and solution, this implies $(\gamma_A \gamma_B)/\gamma_{\ddagger} = 1$. For unimolecular reactions where this is true, such as the decomposition of N_2O_5 , this is due to the structures of the activated complexes being similar in the two media. However, in the closely related case of decomposition of nitric acid, the reaction rate is significantly lower in solution than in the gas phase, probably as a result of complexation between the reactant and solvent.

We will compare now the behaviour in two different solvents. The activity coefficients are based on a convenient standard state, usually infinite dilution of the solutes. With this reference state, the rate constant is given by

$$k_0 = \frac{k_B T}{h} K_0^{\ddagger} \quad (9.35)$$

Applying CTST for first-order reactions, with

$$E_a = \Delta H^{\ddagger 0} + RT \quad (9.36)$$

and

$$k = \frac{k_B T}{h} \exp\left(\frac{\Delta S^{\ddagger 0}}{R}\right) \exp\left(-\frac{E_a - RT}{RT}\right) \quad (9.37)$$

or

$$k = e^{\frac{k_B T}{h}} e^{\Delta S^{\ddagger 0}/R} e^{-E_a/RT} \quad (9.38)$$

The estimation of various activation entropies for non-polar molecules in solution showed that the pre-exponential factors are about three times greater than in the gas phase. This is close to the ratios of the collision frequencies in the two media.

9.5.1 Internal pressure

Attractive forces between molecules vary inversely with the intermolecular separation, r , with a dependence r^{-6} , such that their magnitude is appreciable when distances are close to molecular diameters. This is true for liquids, and such

cohesion forces are responsible for many of the properties of this state of matter. Cohesion forces are also present in the gas phase and are responsible for the van der Waals (a/V^2) correction to the *internal pressure*.

However, in liquids, repulsive forces also operate at short intermolecular distances to balance the attractive, cohesive intermolecular forces. This leads to

$$P_i dV = \left(\frac{\partial E}{\partial V} \right)_T dV \quad (9.39)$$

or

$$P_i = \left(\frac{\partial E}{\partial V} \right)_T \quad (9.40)$$

From these equations, an internal pressure P_i can be defined in terms of its effect on the internal energy of the liquid. For any substance, we can show

$$\left(\frac{\partial E}{\partial V} \right)_T = T \left(\frac{\partial P}{\partial T} \right)_V - P \quad (9.41)$$

in which P is the *external pressure*, and given that this is, in general, much less than the internal pressure. So we can also write

$$P_i = T \left(\frac{\partial P}{\partial T} \right)_V \quad (9.42)$$

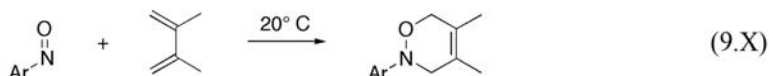
The internal pressure can be estimated experimentally by studying the increase in pressure with the temperature. If we take α as the coefficient of thermal expansion of the liquid and β its compressibility coefficient, given by

$$\left(\frac{\partial P}{\partial T} \right)_V = \left(\frac{\partial P}{\partial V} \right)_T \left(\frac{\partial V}{\partial T} \right)_P \quad (9.43)$$

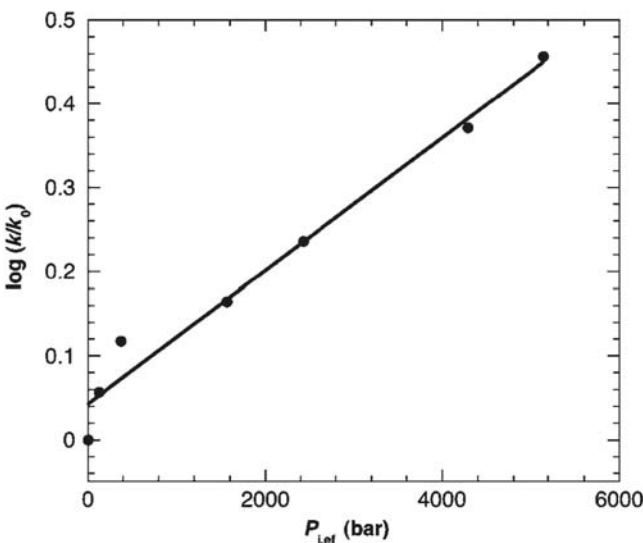
then

$$P_i = T \frac{\alpha}{\beta} \quad (9.44)$$

The solvent internal pressure can induce changes in the reaction kinetics when specific solvent-solute interactions are weak, and the activation volumes involved, which we will discuss later, are substantial. An example involves the kinetics of the Diels–Alder reaction between 4-bromonitrosobenzene and 2,3-dimethylbutadiene in solutions of various inorganic perchlorates in acetone [12]



where rates correlate linearly with the effective internal pressure of the solutions (Figure 9.9). Here, the increase in the effective internal pressure depends on the nature of the cation [13].

**FIGURE 9.9**

Dependence of the kinetics of reaction (9.X) on the effective internal pressure in acetone solutions of inorganic perchlorates.

Hildebrand and Scott developed expressions for the activity coefficients of non-electrolytes in terms of molar volumes, V_x , and energies of vaporisation, L_x . These are related to average internal pressure through

$$P_{i,x} = \frac{L_x}{V_x} \quad (9.45)$$

If we take k_0 as the rate constant under ideal conditions, we can write the expression for a bimolecular reaction between A and B

$$\ln k = \ln k_0 + \frac{V_A}{RT} (\sqrt{P_{i,s}} - \sqrt{P_{i,A}})^2 + \frac{V_B}{RT} (\sqrt{P_{i,s}} - \sqrt{P_{i,B}})^2 - \frac{V_{\ddagger}}{RT} (\sqrt{P_{i,s}} - \sqrt{P_{i,\ddagger}})^2 \quad (9.46)$$

in which $P_{i,A}$ and $P_{i,B}$ are the internal pressures of the solutes, $P_{i,\ddagger}$ is that of the activated complex, $P_{i,s}$ that of the solvent, while V_A and V_B are the molar volumes of the solutes and V_{\ddagger} that of the activated complex, all taken in the liquid phase. We assume that the internal pressure of the activated complex will be intermediate between that of reactants and products.

From eq. (9.46), we see that when the internal pressures of A, B and the transition state are similar, the solvent behaves as ideal and $k \approx k_0$. However, when $P_{i,\ddagger}$ is greater than $P_{i,s}$ and different from that of the solutes, the term $(P_{i,s}^{1/2} - P_{i,\ddagger}^{1/2})^2$ will be dominant, and k will be smaller than under ideal conditions. In contrast, if the internal pressure of the solvent is similar to that of the activated complex, but markedly different from those of the reactants, the

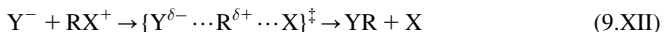
internal pressure terms of these will be dominant in eq. (9.46), and k will be greater in solution than under ideal conditions.

With these ideas, in the Menschutkin reaction:



the activated complexes are partially ionised and will be more strongly solvated than the reactants in a polar solvent, such as nitrobenzene. This lowers the activity coefficient γ_\ddagger more than γ_A and γ_B , such that, from eq. (9.32), the rate will be greater than under ideal conditions.

However, if we consider the case



the activated complex is less solvated than the reactants, such that $\gamma_\ddagger > \gamma_A \gamma_B$, and the rate will be lower than under ideal conditions.

9.5.2 Reactions between ions

We will base our discussion of reactions between ions in solution on the effects of electrostatic interactions between species of charges $Z_A e$ and $Z_B e$ in a solvent of dielectric constant, ϵ . Initially we consider the ions at an infinite distance, and then calculate the energy needed to bring them together to a contact distance, d_{AB} , forming the double sphere as shown in Figure 9.10.

When the ions are separated by a distance r , the force f between them is given by Coulomb's law

$$f = \frac{Z_A Z_B e^2}{4\pi\epsilon_0\epsilon r^2} \quad (9.47)$$

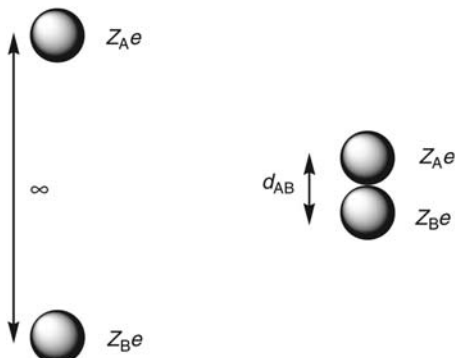


FIGURE 9.10

Approach of two ions to a contact distance.

where ϵ_0 is the permittivity of vacuum ($\epsilon_0 = 8.854 \times 10^{-12} \text{ C}^2 \text{ N}^{-1} \text{ m}^{-2}$, one of the basic quantities for all electrostatic equations using SI units). The work done when the ions approach through a separation distance dr will be

$$dw = -\frac{Z_A Z_B e^2}{4\pi\epsilon_0\epsilon r^2} dr \quad (9.48)$$

Integrating between the limits of the initial position and the contact distance

$$w = -\int_{\infty}^{d_{AB}} \frac{Z_A Z_B e^2}{4\pi\epsilon_0\epsilon r^2} dr \quad (9.49)$$

gives

$$w = \frac{Z_A Z_B e^2}{4\pi\epsilon_0\epsilon d_{AB}} \quad (9.50)$$

The work w is positive if the charges of the ions are the same and negative if they are different.

This work corresponds to the contribution of the electrostatic interactions, when the two ions form an activated complex, to the free energy of activation, $\Delta G_{\text{es}}^{\ddagger 0}$. Multiplying by Avogadro's constant gives this in molar quantities

$$\Delta G_{\text{es}}^{\ddagger 0} = \frac{N_A Z_A Z_B e^2}{4\pi\epsilon_0\epsilon d_{AB}} \quad (9.51)$$

The free energy of activation $\Delta G^{\ddagger 0}$ is the sum of the contributions which are not due to electrostatic effects, $\Delta G_{\text{nes}}^{\ddagger 0}$, with the electrostatic contribution

$$\Delta G^{\ddagger 0} = \Delta G_{\text{nes}}^{\ddagger 0} + \frac{N_A Z_A Z_B e^2}{4\pi\epsilon_0\epsilon d_{AB}} \quad (9.52)$$

Using CTST, the expression for the rate constant is

$$k = \frac{k_B T}{h} \exp\left(-\frac{\Delta G^{\ddagger 0}}{RT}\right) = \frac{k_B T}{h} \exp\left(-\frac{\Delta G_{\text{nes}}^{\ddagger 0}}{RT}\right) \exp\left(-\frac{Z_A Z_B e^2}{4\pi\epsilon_0\epsilon d_{AB} k_B T}\right) \quad (9.53)$$

where $R/N_A = k_B$, the Boltzmann constant. In logarithmic form

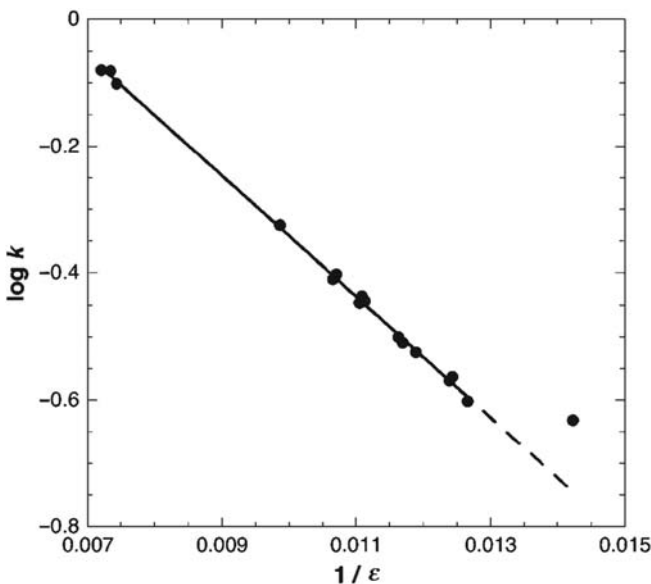
$$\ln k = \ln \frac{k_B T}{h} - \frac{\Delta G_{\text{nes}}^{\ddagger 0}}{RT} - \frac{Z_A Z_B e^2}{4\pi\epsilon_0\epsilon d_{AB} k_B T} \quad (9.54)$$

which is more conveniently given as

$$\ln k = \ln k_0 - \frac{Z_A Z_B e^2}{4\pi\epsilon_0\epsilon d_{AB} k_B T} \quad (9.55)$$

where k_0 is the rate constant for a medium of infinite dielectric constant.

Eq. (9.55) predicts that if we study a reaction in various solvents, $\ln k$ will vary linearly with $1/\epsilon$. The slope of such a plot, $Z_A Z_B e^2 / (4\pi\epsilon_0 d_{AB} k_B T)$ allows us

**FIGURE 9.11**

Study of the dependence of rate constant on solvent dielectric constant for the reaction between $\text{BrCH}_2\text{CO}_2^-$ and $\text{S}_2\text{O}_3^{2-}$ [14].

to estimate the contact distance between the ions. Figure 9.11 shows this type of study for the reaction between $\text{BrCH}_2\text{CO}_2^-$ and $\text{S}_2\text{O}_3^{2-}$, from which we can calculate $d_{AB} = 5.1 \text{ \AA}$.

For reactions between ions, eq. (9.52) allows us to estimate the electrostatic contribution to the entropy of activation, $\Delta S_{es}^{\ddagger 0}$, given that

$$S = \left(\frac{\partial G}{\partial T} \right)_P \quad (9.56)$$

From eqs. (9.52) and (9.56) we obtain

$$\Delta S_{es}^{\ddagger 0} = - \frac{N_A Z_A Z_B e^2}{4\pi\epsilon_0 d_{AB}} \left(\frac{\partial (1/\epsilon)}{\partial T} \right)_P \quad (9.57)$$

which can be expressed as

$$\Delta S_{es}^{\ddagger 0} = + \frac{N_A Z_A Z_B e^2}{4\pi\epsilon_0 d_{AB} \epsilon^2} \left(\frac{\partial \epsilon}{\partial T} \right)_P \quad (9.58)$$

or

$$\Delta S_{es}^{\ddagger 0} = + \frac{N_A Z_A Z_B e^2}{4\pi\epsilon_0 d_{AB} \epsilon} \left(\frac{\partial \ln \epsilon}{\partial T} \right)_P \quad (9.59)$$

For aqueous solutions, $\varepsilon = 78.5$ and $(\partial \ln \varepsilon / \partial T)_P = -0.0046 \text{ K}^{-1}$, and taking a typical value $d_{AB} = 2 \text{ \AA}$, we obtain

$$\Delta S_{es}^{\ddagger 0} \approx -40Z_A Z_B \text{ J K}^{-1} \text{ mol}^{-1} \quad (9.60)$$

This is interesting, because it shows us that the pre-exponential factor, $A \propto \exp(\Delta S_{es}^{\ddagger 0}/R)$, changes by a factor of 100 for each change of one unit in the product, $Z_A Z_B$.

The results in [Table 9.7](#) are qualitatively in agreement with this prediction, although there are some quantitative differences, probably due to the sum of reactant radii being different from $d_{AB} = 2 \text{ \AA}$.

The physical basis of this effect is shown schematically in [Figure 9.12a](#) for the case of two positively charged ions. Each ion is surrounded by a certain number of solvent molecules. With ions of the same charge, when the activated complex is formed, the charge increases, which results in the attraction of more solvent molecules ([Figure 9.12a](#)). This restriction in the motion of solvent molecules in the activated complex, relative to the reactants, leads to a decrease in the entropy of activation $\Delta S^{\ddagger 0}$ and, hence, the pre-exponential factor. The restriction of the movements of the solvent molecules becomes greater with increasing charge of the ions. This effect is known as *electrostriction* or *solvent bonding*. Note that the dependence with the reciprocal of ε expressed by [eq. \(9.59\)](#), which is more important than the change in $(\partial \ln \varepsilon / \partial T)_P$, which means that the effect of the electrostriction on the activation entropy will be more significant in solvents of low polarity. In polar solvents, the high value of ε rapidly attenuates any effect due to the charges of the ions and electrostriction only has a small effect on the pre-exponential factor or activation entropy.

With oppositely charged ions ([Figure 9.12b](#)), electrical charge decreases when the activated complex is formed. Therefore, there is a decrease in the electrostriction, and there are fewer molecules of solvent in the activated complex. This leads to an increase in the entropy of activation and the pre-exponential factor. These will be much greater than typical values of uncharged species (e.g., $A = 10^{13} \text{ mol}^{-1} \text{ dm}^3 \text{ sec}^{-1}$).

9.5.3 Effect of ionic strength

Ionic strength, I , is a measure of the concentration of electrically charged species in solution

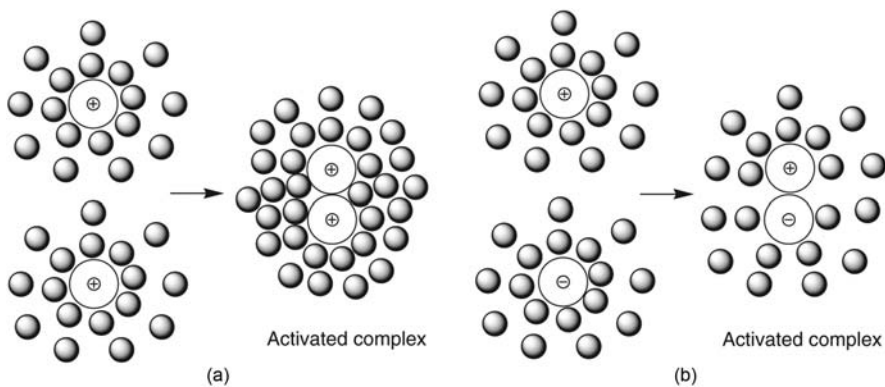
$$I = \frac{1}{2} \sum_i c_i Z_i^2 \quad (9.61)$$

in which c_i is the concentration of ion i of charge Z_i . In a solution in which the ionic strength is not zero, the interactions involved between many ions have rather different effects from those between pairs of ions we have just considered. For solutions of relatively low ionic strength, the activity coefficient of an ion can be estimated by the Debye–Hückel theory. This uses a model with each ion surrounded by an atmosphere of ions of the same charge, but which is opposite to

Table 9.7 Some predicted and observed pre-exponential factors and entropies of activation^a.

Reactants	Experimental		Estimated	
	A (dm ³ mol ⁻¹ sec ⁻¹)	ΔS ^{‡0} (J K ⁻¹ mol ⁻¹)	A (dm ³ mol ⁻¹ sec ⁻¹)	ΔS ^{‡0} (J K ⁻¹ mol ⁻¹)
Cr(HO) ₆ ³⁺ + CNS ⁻	≈ 10 ¹⁹	≈ 126	10 ¹⁹	126
Co(NH ₃) ₅ Br ²⁺ + OH ⁻	5 × 10 ¹⁷	92	10 ¹⁷	84
CH ₂ BrCOOCH ₃ + S ₂ O ₃ ²⁻	1 × 10 ¹⁴	25	10 ¹³	0
CH ₂ ClCOO ⁻ + OH ⁻	6 × 10 ¹⁰	-50	10 ¹¹	-42
ClO ⁻ + ClO ₂ ⁻	9 × 10 ⁸	-84	10 ¹¹	-42
CH ₂ BrCOO ⁻ + S ₂ O ₃ ²⁻	1 × 10 ⁹	-71	10 ⁹	-84
Co(NH ₃) ₅ Br ²⁺ + Hg ²⁺	1 × 10 ⁸	-100	10 ⁵	-167
S ₂ O ₄ ²⁻ + S ₂ O ₄ ²⁻	2 × 10 ⁴	-167	10 ⁵	-167
S ₂ O ₃ ²⁻ + S ₂ O ₃ ²⁻	2 × 10 ⁶	-126	10 ⁵	-167

^aFrom Refs. [15, 16].

**FIGURE 9.12**

Model of electrostriction. (a) The approach of two ions with the same charge leads to an increase in the electrostriction of the solvent. (b) The approach of oppositely charged ions decreases the electrostriction of the solvent.

that of the central ion. The ionic atmosphere lowers the chemical potential of the central ion by neutralising its charge. If A and B have charges of the same sign, a high ionic strength favours the formation of encounter pairs having a higher charge and, consequently, increases the rate of reaction. The Debye–Hückel theory expression for the activity coefficient is

$$\log \gamma_i = -AZ_i^2 \sqrt{I} \quad (9.62)$$

The parameter A in water at 25 °C has the value $A = 0.51 \text{ mol}^{-1/2} \text{ dm}^{3/2}$.

For a reaction of the type



[Eq. \(9.32\)](#) gives the expression for the rate constant

$$k = k_0 \frac{\gamma_A \gamma_B}{\gamma_\ddagger} \quad (9.63)$$

relative to the value in an ideal medium, k_0 ,

$$\log k = \log k_0 + \log \gamma_A + \log \gamma_B - \log \gamma_\ddagger \quad (9.64)$$

Introducing activity coefficients from [eq. \(9.62\)](#) we get

$$\log k = \log k_0 - A [Z_A^2 + Z_B^2 - (Z_A + Z_B)^2] \sqrt{I} \quad (9.65)$$

which can be written as

$$\log k = \log k_0 + 2AZ_A Z_B \sqrt{I} \quad (9.66)$$

Using the numerical value of A for aqueous solutions at 25 °C, this becomes

$$\log \frac{k}{k_0} \approx 1.02 Z_A Z_B \sqrt{I} \quad (\text{mol dm}^{-3})^{1/2} \quad (9.67)$$

Figure 9.13 shows the confirmation of these predictions of ionic strength effects in solution for the following group of reactions between ions [15,16]:

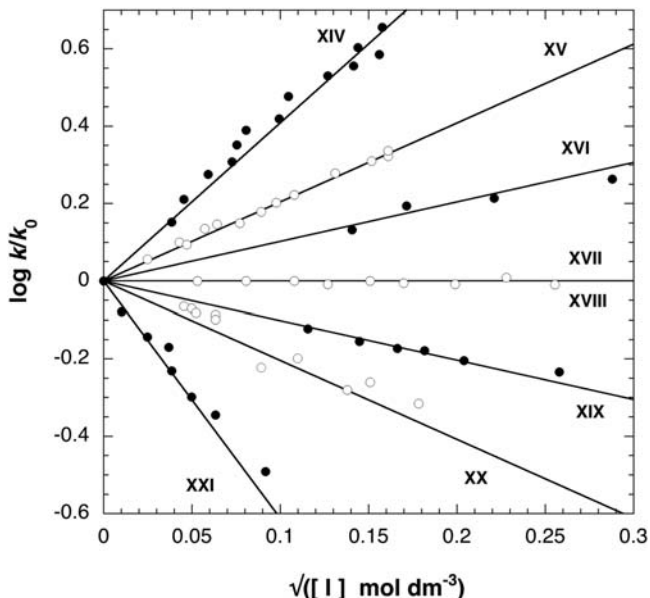
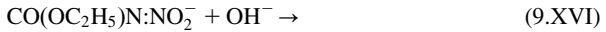


FIGURE 9.13

Effect of ionic strength on the kinetics of ionic reactions in aqueous solutions. Reactions (9.XIV)–(9.XXI) are given in the text. Slopes are equal to $1.02 Z_A Z_B$.

The increase in I increases the rate constant for reactions between ions of the same charge and decreases it when the ions are oppositely charged. This kinetic effect of addition of a salt to the solutions, when the salt is not involved in the reaction, was studied in detail by Brönsted [17] and Bjerrum [18] and the expression, which it represents, is known as the *Brönsted–Bjerrum equation*.

For reactions in which one of the species is neutral, ionic strength should not have any effect. In practice, there are often small effects of changing ionic strength when reactions are catalysed by acids or bases. These are known as secondary salt effects and are due to effects of ionic strength on acid–base equilibria.

9.5.4 Effect of hydrostatic pressure

Because the rates of reaction are much less sensitive to the effect of pressure than of temperature, studies of the effects of external pressure for reactions in solution are more difficult to carry out, and need pressures of several thousand atmospheres (kilobars). However, they do yield important information on the transition state, which helps understanding mechanisms. The theory of pressure effects was initially formulated by van't Hoff in terms of the effect of pressure on equilibrium constants

$$\left(\frac{\partial \ln K_c}{\partial P} \right)_T = - \frac{\Delta V^0}{RT} \quad (9.68)$$

where ΔV^0 is the change in the standard volume, which is the difference between the standard volumes of the products and the reactants

$$\Delta V^0 = V_p - V_r \quad (9.69)$$

If V_{\ddagger} is volume of the activated complex, then

$$\Delta V^0 = (V_{\ddagger} - V_r) - (V_{\ddagger} - V_p) \quad (9.70)$$

Since for an elementary reaction

$$K_c = \frac{k_1}{k_{-1}} \quad (9.71)$$

we get the relationship

$$\left(\frac{\partial \ln k_1}{\partial P} \right)_T - \left(\frac{\partial \ln k_{-1}}{\partial P} \right)_T = - \frac{\Delta V_1^{\ddagger 0}}{RT} + \frac{\Delta V_{-1}^{\ddagger 0}}{RT} \quad (9.72)$$

where $\Delta V_1^{\ddagger 0}$ is the change in the standard volume in the forward direction and $\Delta V_{-1}^{\ddagger 0}$ for the reverse reaction. These quantities are known as the *volumes of activation*.

The simplest way of separating this into the effects on the forward and back reactions is

$$\left(\frac{\partial \ln k_1}{\partial P} \right)_T = - \frac{\Delta V_1^{\ddagger 0}}{RT} \quad (9.73)$$

and

$$\left(\frac{\partial \ln k_{-1}}{\partial P} \right)_T = - \frac{\Delta V_{-1}^{\ddagger 0}}{RT} \quad (9.74)$$

In terms of volumes of activation, we can write

$$\ln k = \ln k_0 - \frac{\Delta V^{\ddagger 0}}{RT} P \quad (9.75)$$

in which k_0 is the rate constant for zero hydrostatic pressure (in practice usually taken as atmospheric pressure). A study of the change in $\ln(k)$ with pressure, P , will give a linear relationship, whose slope, $\Delta V^{\ddagger 0}/RT$, allows us to determine the volume of activation of the reaction [19]. Figure 9.14 gives data from studies of the effect of pressure on the reactions

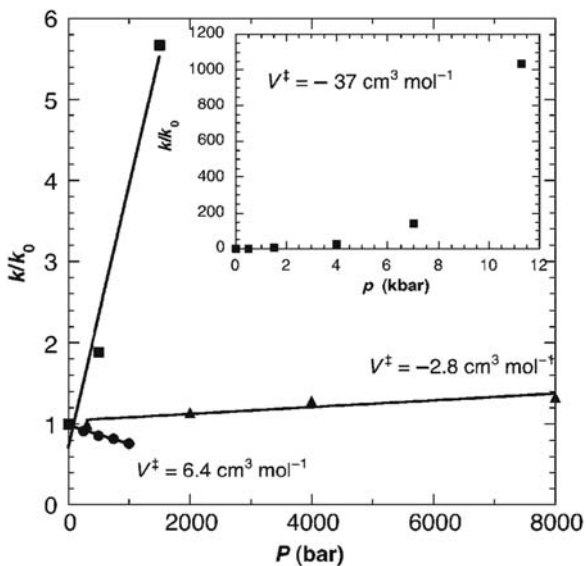
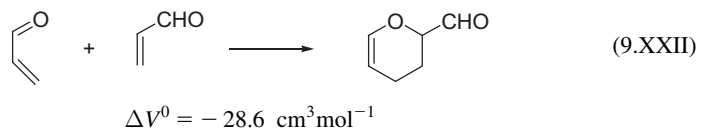
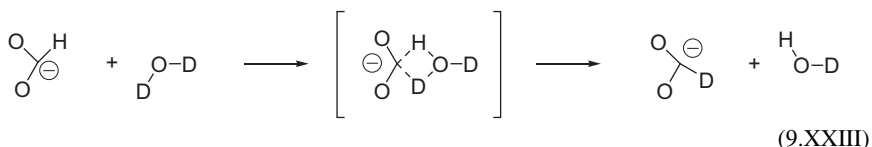


FIGURE 9.14

Effect of external pressure on the kinetics of reactions (9.XXII) (squares) [20], (9.XXIII) (triangles) [21] and (9.XXIV) (circles) [22].



$$\Delta V^0 = 0$$



In interpreting volumes of activation, we need to consider both structural variations in reactants and activated complexes and also contributions due to the solvent. For a reaction in the gas phase, such as



in which M is an inert or non-reactive molecule, the structural effects due to the involvement of M lead to $\Delta V^{\ddagger 0} > 0$, or for the reverse reaction $\Delta V^{\ddagger 0} < 0$. With reactions in solution, with neutral species $\Delta V^{\ddagger 0}$ is dominated by structural effects, while for reactions between ions in general the effects of solvent dominate. In agreement with the model of electrostriction (Figure 9.10), for ions of the same sign, it is predicted that there will be a decrease in both $\Delta V^{\ddagger 0}$ and $\Delta S^{\ddagger 0}$. For oppositely charged ions, we expect an increase in $\Delta V^{\ddagger 0}$ and $\Delta S^{\ddagger 0}$.

Table 9.8 presents some values for $\Delta V^{\ddagger 0}$ for water exchange reactions involving hydrated metal ions. Two extreme types of mechanisms that are considered are an *associative mechanism* in which the central ion increases the coordination number in the activated complex

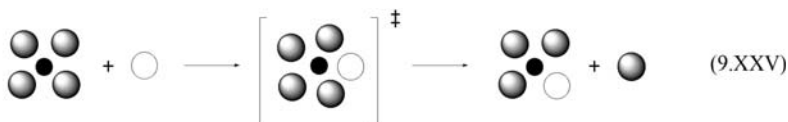
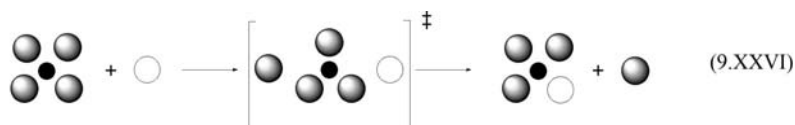


Table 9.8 Volumes and entropies of activation for water exchange reactions of metal cations.

	ΔV^\ddagger ($\text{cm}^3 \text{ mol}^{-1}$)	ΔS^\ddagger ($\text{J mol}^{-1} \text{ K}^{-1}$)
$\text{Ni}_{(\text{aq})}^{2+}$	+7.7	+32
$\text{Co}_{(\text{aq})}^{2+}$	+6.1	+21
$\text{V}_{(\text{aq})}^{3+}$	-10.0	-67
$\text{Cr}_{(\text{aq})}^{3+}$	-9.3	+20
$\text{Fe}_{(\text{aq})}^{2+}$	+3.8	-
$\text{Fe}_{(\text{aq})}^{3+}$	-5.4	+12

and a *dissociative* one, in which in the transition state shows a decrease in metal coordination



For an associative mechanism the change in the volume of activation is

$$\Delta V_A^\ddagger = [V^\ddagger(\text{solvated ion})] - [V^\ddagger(\text{solvated ion} + V_{\text{H}_2\text{O}})] \approx -10 \text{ cm}^3 \text{ mol}^{-1} \quad (9.76)$$

Knowing that the molar volume of water is $10 \text{ cm}^3 \text{ mol}^{-1}$, and assuming that the molar volumes of the hydrated ions and complexes are approximately equal, a value of $\Delta V_A^{\ddagger 0} = -10 \text{ cm}^3 \text{ mol}^{-1}$ can be estimated for a purely associative mechanism of water exchange. Similarly, for the dissociative case we have

$$\Delta V_D^\ddagger = [V^\ddagger(\text{solvated ion} + 2V_{\text{H}_2\text{O}})] - [V^\ddagger(\text{solvated ion} + V_{\text{H}_2\text{O}})] \approx 10 \text{ cm}^3 \text{ mol}^{-1} \quad (9.77)$$

9.5.5 Transient volume changes

Volume changes of chemical reactions taking place in water can be studied without resorting to very high hydrostatic pressures using photoacoustic calorimetry (PAC). As explained in [Chapter 3](#), Experimental Methods, PAC gives a signal that is proportional to the volume change of a photo-initiated reaction. In the absence of a structural volume change (i.e., reactant and product molecules have approximately the same volume), the PAC signal is essentially the pressure pulse produced by the thermoelastic expansion associated with the heat released by an exothermic reaction

$$P_i \propto \frac{H_i}{V_{\text{irr}}} \frac{\alpha}{C_p \rho \kappa_T} \quad (9.78)$$

where P_i is the contribution to the PAC signal due to the heat release H_i (in Joule) of reaction i of a sequence of consecutive reactions. Given the irradiated volume V_{irr} (m^3), the thermal expansion coefficient α (K^{-1}), the specific heat constant C_p ($\text{J K}^{-1} \text{ kg}^{-1}$), the density ρ (kg m^{-3}) and the adiabatic compressibility κ_T ($\text{m}^2 \text{ N}^{-1}$), P_i is in units of pressure (Pascal). PAC measures fractions of thermal energy released in consecutive reactions when volume changes are neglected. For consecutive reactions, it is more convenient to express the contribution of the thermoelastic expansion in terms of fractions of energies

$$Q_i \propto \frac{\alpha}{C_p \rho \kappa_T} \frac{H_i}{E_\lambda} \quad (9.79)$$

where E_λ is the energy of 1 mol of photons at the excitation wavelength.

Pure water has the peculiar property of having the highest density at 3.98 °C. This means that at this temperature $\alpha = 0$ and all $Q_i = 0$. Thermoelastic expansion at this temperature does not give a photoacoustic signal. However, structural volume changes can still contribute to the PAC signal. At temperatures slightly above 3.98 °C, the contributions of structural volume changes are, in terms of energy,

$$S_i \propto \frac{\Delta V_i}{E_\lambda} \left(\frac{C_p \rho}{\alpha} \right)_{\alpha \neq 0} \quad (9.80)$$

In general, the contributions of thermoelastic expansion and of structural volume change to the fraction of excitation energy release associated with each one of the i consecutive reactions initiated by the absorption of light with a wavelength λ , are

$$\phi_i E_\lambda \propto Q_i + \Delta V_i \left(\frac{C_p \rho}{\alpha} \right)_{\alpha \neq 0} \quad (9.81)$$

The factor $(C_p \rho / \alpha)$ changes rapidly when the temperature of water increases above 3.98 °C. Measuring PAC signals at various temperatures and calculating the value of this factor at each temperature, it is possible to obtain the linear dependence expressed by eq. (9.81) and obtain transient volume changes ΔV_i associated with consecutive reactions. Figure 9.15 shows data on the protonation

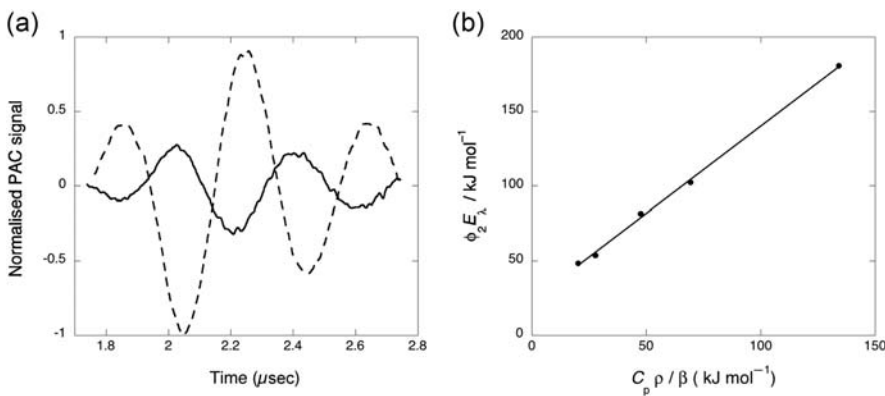


FIGURE 9.15

Photoacoustic calorimetry of a pH jump experiment with *o*-nitrobenzaldehyde (*o*NB) and 500 μM Ac-Glu-NH₂ in aqueous solution at a pre-pulse pH 5.3, using the third harmonic of a nanosecond Nd:YAG laser. (a) Photoacoustic waves of bromocresol purple at 6.0 °C (dashed line), employed as photoacoustic reference, and of *o*NB and Ac-Glu-NH₂ at 1.8 °C, at which temperature this solution has $\alpha = 0$. (b) Plot of the energy content for the reaction of the released protons with Ac-Glu-NH₂ as a function of the solution thermoelastic properties for temperatures between 6.0 and 20.0 °C.

of the negatively charged amino acid Ac-Glu-NH₂ measured in water at various temperatures [23]. In this experiment, a photoacid was employed to rapidly release a proton ($\text{H}_3\text{O}_{(\text{aq})}^+$) upon excitation and trigger the protonation of the carboxylate group of glutamic acid, which is in large excess in solution. The deconvolution of the PAC signal gives two fractions of energy released, $\phi_1 E_\lambda$ and $\phi_2 E_\lambda$, assigned to the deprotonation of the photoacid (<10 nsec) and to the protonation of glutamic acid (~200 nsec). This second-order protonation occurs with a rate constant $9.5 \times 10^9 \text{ M}^{-1} \text{ sec}^{-1}$ and has an associated volume change of $\Delta V = +3.9 \text{ mL mol}^{-1}$. The volume change associated with the fast deprotonation of the photoacid is $\Delta V = -4.0 \text{ mL mol}^{-1}$.

PAC allows for determination of volume changes of very reactive intermediates and has been employed to study fast processes with difficult to measure spectral changes, such as protein folding.

References

- [1] NA Menschutkin, *Z. Phys. Chem. Neue Folge* **5** (1890) 589.
- [2] T Matsui, N Tokura, *Bull. Chem. Soc. Jpn.* **43** (1970) 1751.
- [3] E Rabinowitch, WC Wood, *Trans. Faraday Soc* **32** (1936) 1381.
- [4] C Serpa, PJS Gomes, LG Arnaut, JS de Melo, SJ Formosinho, *ChemPhysChem* **7** (2006) 2533.
- [5] HD Burrows, J Seixas de Melo, C Serpa, LG Arnaut, MG Miguel, AP Monkman, I Hamblett, S Navaratnam, *Chem. Phys.* **285** (2002) 3.
- [6] SL Murov, I Carmichael, GL Hug, *Handbook of Photochemistry*, Marcel Dekker, New York, 1993.
- [7] GV Buxton, CL Greenstock, WP Helman, AB Ross, *J. Phys. Chem. Ref. Data* **17** (1988) 513.
- [8] J Saltier, BW Atwater, *Adv. Photochem.* **14** (1988) 1.
- [9] G Porter, MR Wright, *Discuss. Faraday Soc* **27** (1959) 18.
- [10] F Wilkinson, AA Abdel-Shafi, *J. Phys. Chem. A* **101** (1997) 5509.
- [11] EFF Silva, C Serpa, JM Dabrowski, CJP Monteiro, SJ Formosinho, G Stochel, K Urbanska, S Simões, MM Pereira, LG Arnaut, *Chem. Eur. J.* **16** (2010) 9273.
- [12] G Faita, PP Righetti, *Tetrahedron* **51** (1995) 9091.
- [13] A Kumar, *J. Org. Chem.* **59** (1994) 4612.
- [14] KJ Laidler, *Chemical Kinetics*, HarperCollins, New York, 1987.
- [15] CT Burris, KJ Laidler, *Trans. Faraday Soc* **15** (1955) 1497.
- [16] DTY Chen, KJ Laidler, *Can. J. Chem.* **37** (1959) 599.
- [17] JN Brönsted, *Z. Phys. Chem.* **102** (1922) 169.
- [18] N Bjerrum, *Z. Phys. Chem.* **108** (1924) 1924.
- [19] R van Eldik, T Asano, W Le Noble, *Chem. Rev.* **89** (1989) 549.
- [20] J Rimmelin, G Jenner, H Abdi-Oskoui, *Bull. Soc. Chim. Fr* (1977) 341.
- [21] SD Hamann, M Linton, *Aust. J. Chem.* **30** (1977) 1883.
- [22] R van Eldik, DA Palmer, *J. Solution Chem.* **11** (1982) 340.
- [23] CSH Jesus, PF Cruz, LG Arnaut, RMM Brito, C Serpa, *J. Phys. Chem. B* **122** (2018) 3790.

This page intentionally left blank

Reactions on surfaces

10

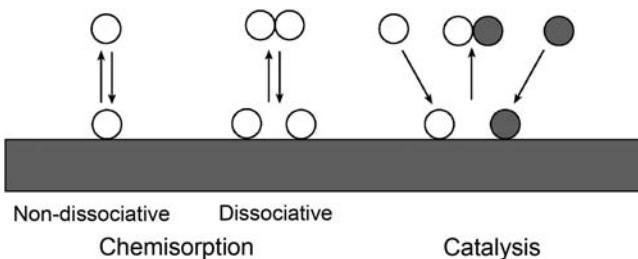
Several reactions of industrial interest occur at inconveniently slow rates in the absence of a catalyst, but can be accelerated considerably by the solid surface of a metal. These include the Haber process for the synthesis of ammonia, the cracking of petroleum, the Fischer–Tropsch synthesis and others. Catalytic surface chemistry is also particularly important to remove the poisonous products of fossil fuel combustion in vehicles, namely to convert CO in CO_2 and NO_x in N_2 and H_2O . The emission of these deadly products is strictly regulated and the finding of “defeat-devices” to bypass regulations with less-performing catalytic systems and fuel economy have led to the highest indemnities of the automobile industry. Originally, the main effect of the solid catalyst was thought to be the presentation of reactants at considerably higher local concentrations than in the gas phase. However, this is not generally true, since in some cases, different surfaces cause a substance to react in different ways. We will analyse some of these.

As illustrated in [Figure 10.1](#), a surface reaction may be regarded as requiring five consecutive steps:

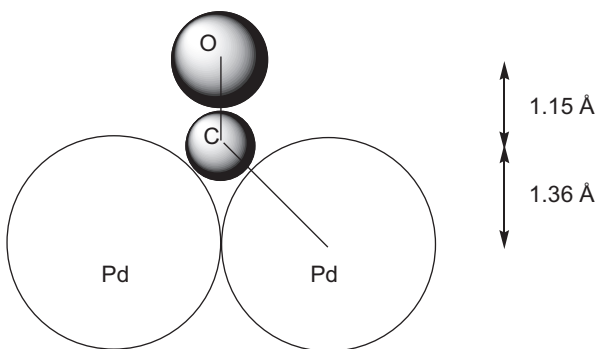
1. diffusion of the reactant molecules to the surface;
2. adsorption of the gases on the surface;
3. reaction of the adsorbed reactants on the surface;
4. desorption of the products formed;
5. diffusion of the desorbed products into the main body of the gas phase.

10.1 Adsorption

A fundamental understanding of the great diversity of chemistry occurring at surfaces requires familiarity with the molecule–surface interaction. Two main types of adsorption may be distinguished. One is relatively weak and arises mainly through van der Waals interactions, with heats of adsorption ΔH_{ad}^0 typically in the range from -20 to -30 kJ mol^{-1} . This is called *physical adsorption*, or physisorption. Physical adsorption equilibria are usually established very rapidly, except when limited by gaseous diffusion. The other type of adsorption is of a much stronger nature, typically with ΔH_{ad}^0 in the range from -50 to -400 kJ mol^{-1} . When the molecules are bound to a surface, chemical bonds can be established between the adsorbed molecule and the surface in the so-called *chemisorption*. A relevant

**FIGURE 10.1**

Reactive processes at the surface of a solid.

**FIGURE 10.2**

Adsorption of a CO molecule onto the surface of palladium. For simplicity, only two palladium atoms on the surface are illustrated in this scheme.

example is the adsorption of carbon monoxide (CO) molecules on a palladium surface. As illustrated in Figure 10.2, the CO molecules are bonded to the metal through the carbon atom, with a Pd–C bond length of 1.93 Å, a Pd–CO vibrational frequency of 236 cm^{-1} and $\Delta H_{\text{ad}}^0 = -150\text{ kJ mol}^{-1}$.

Another good example showing that chemisorbed molecules possess structures and chemical properties substantially different from those of the isolated species is benzene (C_6H_6) adsorbed on Pt(111). The aromaticity of adsorbed C_6H_6 is somewhat reduced, the planar and six-fold symmetries of the molecule are broken as the H atoms distort away from surface, and the carbon-carbon bonds have alternating lengths [1]. At the same time, adsorbate binding causes changes in the substrate geometry, leading to surface reconstruction. Until about 1970 there was little direct evidence as to the detailed structure of surfaces. Now, several surface analysis techniques such as HREELS (high-resolution electron energy loss spectroscopy), XPS (X-ray and ultraviolet photoemission spectroscopy), LEED (low-energy electron diffraction), FIM (field-ion microscopy), STM (scanning tunnelling microscopy), scanning electron microscopy (SEM), and scanning

transmission electron microscopy (STEM) are available that provide information at the molecular level of molecule–surface interactions. Figure 10.3 illustrates cases of Pt surface reconstructions occurring in the presence of CO.

Molecules that dissociate upon adsorption can act as intermediates in surface-catalysed chemical reactions. A good example is the catalytic formation of biphenyl ($C_6H_5-C_6H_5$) from adsorption of iodobenzene on metal surfaces. The reaction has been studied on well-defined single-crystal surfaces in vacuum. With the Cu(111) surface, the reaction proceeds via a number of steps. First, iodobenzene adsorbs to the copper surface, dissociating above 180 K to form surface-bound iodine atoms (an *adatom*, i.e., adsorbed atom) and phenyl intermediates. Subsequently, between 180 and 300 K, phenyl moieties diffuse on the surface,

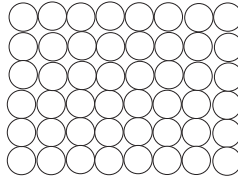
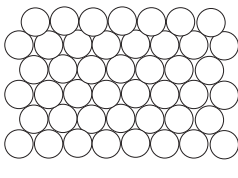
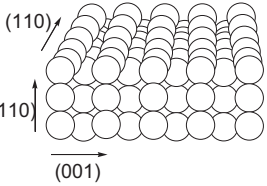
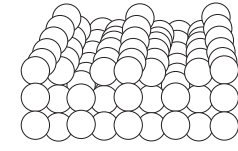
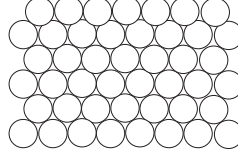
	1x1 surface	Reconstructed surface
(100)		 Hex
(110)		 1x2
(111)		

FIGURE 10.3

Structural models of the three low-index planes of Pt surfaces. Of the three, only the closed-packed Pt(111) surface is stable in its bulk-like 1×1 termination, while the more open (100) and (110) surfaces reconstruct into a quasi-hexagonal (hex) and a 1×2 “missing-row” geometry, respectively. Certain adsorbates such as CO can reversibly lift these reconstructions [2].

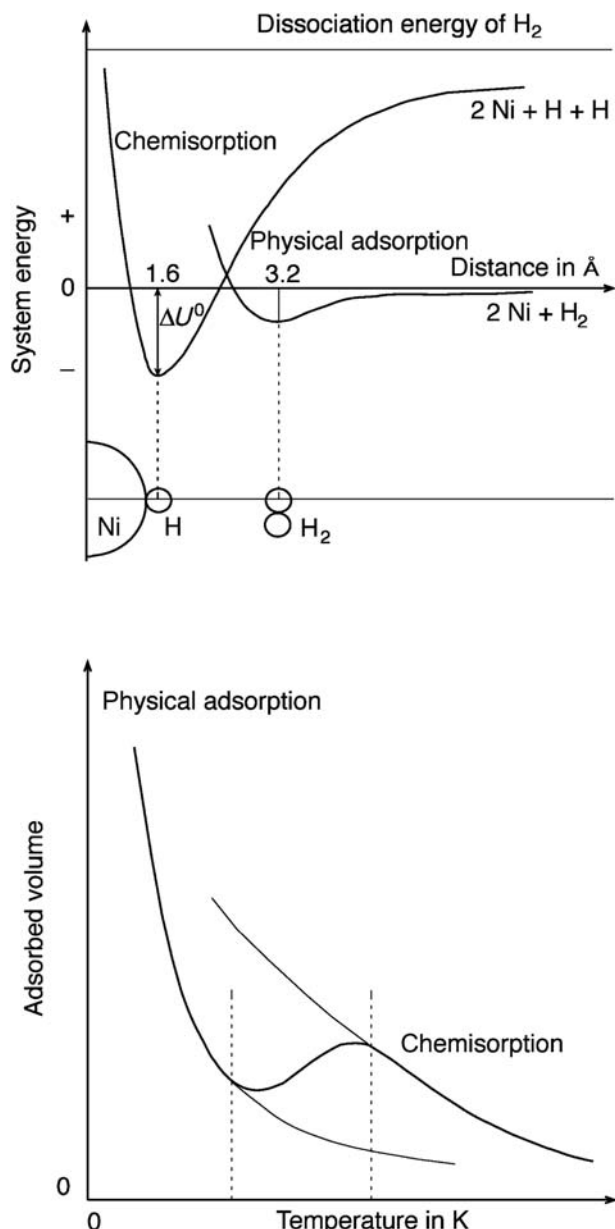
while above 300 K they react to form biphenyl, which subsequently desorbs upon its formation between 300 and 400 K. Finally, removal of iodine as CuI occurs at temperatures *ca.* 950 K. The role of the surface in this reaction is two-fold. The surface creates the C₆H₅ intermediates via dissociation of iodobenzene. Additionally, the phenyl species on the surface experience inter-molecular forces, resulting in the formation of loosely bound complexes bringing the phenyl radicals into close proximity, leading to the correct orientation for eventual biphenyl formation [2]. A schematic view of an example of activated chemisorption with dissociation is illustrated in Figure 10.4 [3].

The surface of a solid material, even of a well-defined crystalline metal, is not entirely uniform. Some of the main features of a solid surface are illustrated in Figure 10.5. There are various kinds of surface sites. These include atoms in *terraces*, atoms at *steps*, atoms at *kinks* and *adatoms*, which project out of the surface. Atoms in terraces have several neighbouring atoms, whereas adatoms have none. On most surfaces, there are a few adatoms, together with many more atoms in different surface sites until the limit of surface densities *ca.* 10¹⁴ – 10¹⁵ atoms cm⁻² of those atoms in terraces is reached. The various types of surface atoms differ very markedly in their properties, and in particular their ability to chemisorb and to catalyse chemical reactions.

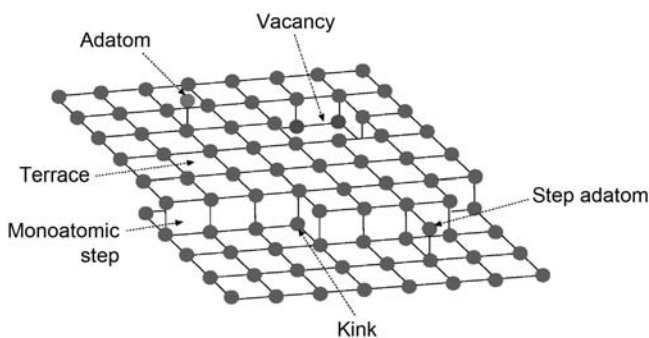
Benzene, for example, adsorbed on Pt(111) surface binds more strongly at defect sites and at step edges. The STM images of adsorbed C₆H₆ display three distinct molecular shapes that are attributed to the C₆H₆ bonds at different types of surface sites. In one of these, the C₆H₆ molecule appears as a protrusion on the surface, with a threefold symmetry and a central depression. Additionally, three small but pronounced depressions appear symmetrically about the periphery of the molecule. These depressions indicate that the perturbation of the surface electronic structure or local density of states is significantly larger than the molecule, extending up to 6–10 Å away from the centre of the C₆H₆ molecule.

On Cu(111), C₆H₆ interacts weakly with the surface forming disordered monolayers, while it desorbs from terrace sites at <250 K. The C₆H₆ molecules present a high mobility on terraces and at 77 K they can be observed by STM only when bound at step edges or in clusters with high coverage. Benzene can act as a nucleophile and thus donate electrons to the surface. Consequently it has a higher affinity for binding at the upper step edges where the electron density is smoothed. The filled surface electronic-state density is decreased above step edges, while it is increased near the lower edges of the steps (the so-called Smoluchowski effect).

In contrast, tetracyanoquinonedimethane (TCNQ) is a strong electrophile and is known to form charge-transfer complexes with copper. TCNQ is thus expected to perturb the electronic structure of the surface strongly. Whereas C₆H₆ was observed to bind preferentially at the electron-poor region above step edges, TCNQ, which is an electron acceptor, binds at electron-rich sites such as the bottom of the steps.

**FIGURE 10.4**

Upper panel: potential energy curves for physisorption and chemisorption. Lower panel: adsorption isobars illustrating the presence of the two types of adsorption, one involving stronger binding forces than the other.

**FIGURE 10.5**

Types of structures and defects found at the surfaces of metals.

Electronic effects on surfaces can generate preferential adsorption sites, as illustrated for step edges. However, a necessary condition for this to occur on surfaces is the availability of free charge as well as states for the free charge to occupy. The closed-packed (111) surfaces allow for a greater orbital overlap of the surface atoms. This greater electron freedom leads to a two-dimensional free-electron gas confined to the surface. However, such surface states do not exist for the (110) and (100) surfaces. Studies on C₆H₆ adsorbed on Ag(110) reveals that the terraces and the (001) steps remain completely free of molecules.

10.2 Adsorption isotherms

10.2.1 Langmuir isotherm

The simplest situation for the mechanism of adsorption is to consider that gas atoms or molecules occupy single sites on the surface and are not dissociated. The process can be represented by



Langmuir employed a kinetic approach to derive the isotherm under such ideal conditions [4]. Let θ be the fraction of surface that is covered; $1 - \theta$ will then be the fraction that is not covered. The rate of adsorption, v_{ad} , will then be that for the bimolecular process between the reactant, A, and an active site of the surface,

$$v_{\text{ad}} = k_{\text{ad}}[A](1 - \theta) \quad (10.1)$$

Here k_{ad} is the rate constant of adsorption. Such a rate law assumes that k_{ad} is independent of θ , that is, that ΔH_{ad}^0 is independent of θ . The rate of desorption,

v_{-ad} , will be that for the unimolecular dissociation process with the concentration at surface equivalent to the coverage θ ,

$$v_{-2} = k_{-ad}\theta \quad (10.2)$$

At equilibrium these rates are equal such that

$$k_{ad}[A](1 - \theta) = k_{-ad}\theta \quad (10.3)$$

or

$$\frac{k_{ad}[A]}{k_{-ad}} = \frac{\theta}{1 - \theta} \quad (10.4)$$

If we represent the equilibrium constant for the adsorption process by $K = k_{ad}/k_{-ad}$, we can express the coverage as

$$\theta = \frac{K[A]}{1 + K[A]} \quad (10.5)$$

The variation of θ with $[A]$, known as the Langmuir adsorption isotherm [eq. (10.5)], is shown in Figure 10.6a. Eq. (10.5) represents an isotherm since K is dependent on temperature, such that the curves of Figure 10.6 must be determined at a constant T . At sufficiently low concentrations (or pressures), $K[A]$ is small in comparison with unity, and θ is then proportional to $[A]$.

The bare fraction of surface is given by

$$1 - \theta = \frac{1}{1 + K[A]} \quad (10.6)$$

and at sufficiently high concentrations this will be given by

$$1 - \theta \approx \frac{1}{K[A]} \quad (10.7)$$

A distinctive feature of this isotherm is that the surface becomes saturated ($\theta \approx 1$) with adsorbed molecules at high concentrations of A.

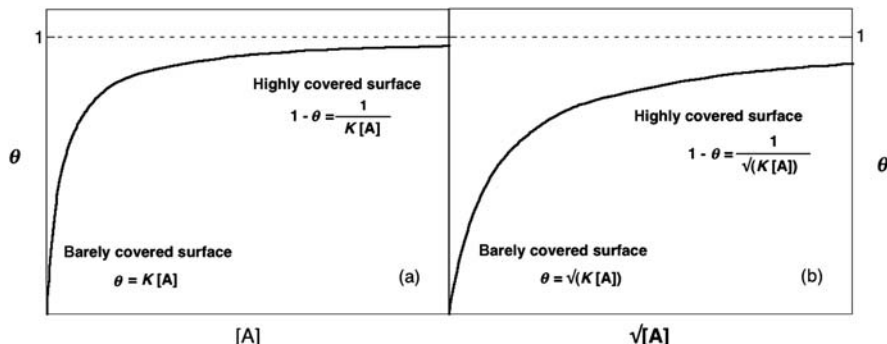
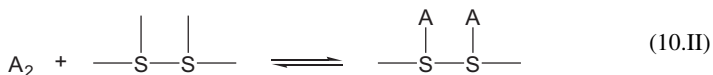


FIGURE 10.6

Langmuir isotherms, without dissociation (a), and with dissociation (b).

10.2.2 Adsorption with dissociation

In certain cases there is evidence that the process of adsorption is accompanied by the dissociation of the molecule on the surface, as shown in mechanism (10.II)



Since the process of adsorption can be viewed as a reaction between a gas molecule A_2 and two reaction sites, the rate of adsorption will be

$$v_{\text{ad}} = k_{\text{ad}}[\text{A}_2](1 - \theta)^2 \quad (10.8)$$

The desorption process involves a bimolecular reaction between two adsorbed atoms, and the rate is

$$v_{-\text{ad}} = k_{-\text{ad}}\theta^2 \quad (10.9)$$

At equilibrium these rates are equal and therefore

$$\frac{\theta}{1 - \theta} = \left(\frac{k_{\text{ad}}[\text{A}_2]}{k_{-\text{ad}}} \right)^{1/2} \quad (10.10)$$

So one can write

$$\theta = \frac{\sqrt{K[\text{A}_2]}}{1 + \sqrt{K[\text{A}_2]}} \quad (10.11)$$

At low concentrations of A_2 , θ is proportional to $[\text{A}_2]^{1/2}$. This can then be written as

$$1 - \theta = \frac{1}{1 + \sqrt{K[\text{A}_2]}} \quad (10.12)$$

such that at high concentrations, $K^{1/2}[\text{A}_2]^{1/2} \gg 1$, the fraction of the bare surface is inversely proportional to the square root of the concentration or pressure. Figure 10.6b illustrates the Langmuir isotherm with dissociation.

10.2.3 Competitive adsorption

When two substances A and B adsorb on the same surface and compete for the same sites, inhibition can occur. Let the fraction of coverage by substance A be represented by θ_A and that for B by θ_B . The uncovered fraction is $(1 - \theta_A - \theta_B)$. If both species are adsorbed without dissociation, the rate of adsorption of A will be

$$v_{\text{ad}}^A = k_{\text{ad}}^A[\text{A}](1 - \theta_A - \theta_B) \quad (10.13)$$

and an equivalent expression will be given for B. The corresponding rates of desorption are

$$v_{-\text{ad}}^A = k_{-\text{ad}}^A \theta_A \quad (10.14)$$

and similarly an equivalent expression for B can be written. At equilibrium, the rates of adsorption and desorption for each substance are equal and consequently we can write

$$\frac{\theta_A}{1 - \theta_A - \theta_B} = K_A[A] \quad (10.15)$$

and

$$\frac{\theta_B}{1 - \theta_A - \theta_B} = K_B[B] \quad (10.16)$$

Here, $K_A = k_{\text{ad}}^A/k_{-\text{ad}}^A$ and $K_B = k_{\text{ad}}^B/k_{-\text{ad}}^B$. Solving the two eqs. (10.15) and (10.16) for the surface coverages leads to

$$\theta_A = \frac{K_A[A]}{1 + K_A[A] + K_B[B]} \quad (10.17)$$

$$\theta_B = \frac{K_B[B]}{1 + K_A[A] + K_B[B]} \quad (10.18)$$

Eq. (10.17) shows that the coverage of A, θ_A , diminishes when there is an increase in [B]; the opposite is true for θ_B when there is an increase in [A]. This competition exists because A and B are competing for a limited number of active sites, hence the term competitive adsorption. There is evidence that sometimes two substances are adsorbed on two different sets of adsorption sites, for example, at steps and at terraces, and in such cases there is no such competition.

10.3 Kinetics on surfaces

10.3.1 Unimolecular surface reactions

Surface reactions that involve a single molecule can be classified as unimolecular reactions. When the adsorption follows a Langmuir isotherm, the rate of reaction, v , will be proportional to the surface coverage, θ , and can be written as

$$v = k\theta = \frac{kK[A]}{1 + K[A]} \quad (10.19)$$

where k is the rate constant. At high concentrations of the reactant, $K[A] \gg 1$, the rate of reaction is constant,

$$v = k \quad (10.20)$$

since all the active sites are occupied with adsorbed molecules. This is a zero-order reaction. At low concentrations, however, the rate law is

$$v = kK[A] \quad (10.21)$$

and we are dealing with a first-order process.

The decomposition of NH_3 on a surface of platinum follows this kind of behaviour. One of the reaction products, H_2 , poisons the catalyst. From eq. (10.17) the surface coverage can be expressed by

$$\theta = \frac{K_A[A]}{1 + K_A[A] + K_I[I]} \quad (10.22)$$

where I represents the *inhibitor* and K_I is the adsorption constant for the same. The rate of the reaction is given by

$$v = \frac{kK_A[A]}{1 + K_A[A] + K_I[I]} \quad (10.23)$$

When $K_I[I] \gg 1 + K_A[A]$ the rate law simplifies to the form

$$v = \frac{kK_A[A]}{K_I[I]} \quad (10.24)$$

This behaviour arises from the fact that since the surface is covered sparsely by A, the coverage is proportional to [A]. However, under these conditions the surface is almost fully covered by the inhibitor, I, and as a consequence the bare fraction is inversely proportional to [I].

The rate law for the decomposition of ammonia is $v = k[\text{NH}_3]/[\text{H}_2]$. Since hydrogen is a product of the reaction, there is progressive inhibition as the reaction proceeds.

10.3.2 Activation energies of unimolecular surface reactions

The dependence of the rate constant of eq. (10.19) on the temperature should take the form of the Arrhenius equation,

$$\frac{d \ln k}{dT} = \frac{E_2}{RT^2} \quad (10.25)$$

where E_2 is the activation energy corresponding to the reaction of the adsorbed species, that is, to



The temperature dependence of the equilibrium constant K will follow the van't Hoff relationship

$$\frac{d \ln k}{dT} = \frac{\Delta U^0}{RT^2} \quad (10.26)$$

Here ΔU^0 is the standard molar internal energy change in the adsorption process. At low pressures, since the rate of reaction is $v = kK[A]$, the overall rate constant for this process is simply

$$k^1 = kK \quad (10.27)$$

and it follows that

$$\frac{d \ln v}{dT} = \frac{d \ln k^1}{dT} = \frac{d \ln k}{dT} + \frac{d \ln K}{dT} \quad (10.28)$$

or, in equivalent terms,

$$\frac{d \ln k^1}{dT} = \frac{E_2 + \Delta U^0}{RT^2} \quad (10.29)$$

The apparent activation energy, E_a , for this first-order reaction is thus

$$E_a = E_2 + \Delta U^0 \quad (10.30)$$

At high concentrations of the reactant, the rate follows eq. (10.20), and the observed activation energy is simply

$$E_a = E_2 \quad (10.31)$$

The energy diagram for a unimolecular surface reaction of Figure 10.7 reveals that initially the reactant has to surmount a small energy barrier, but stays

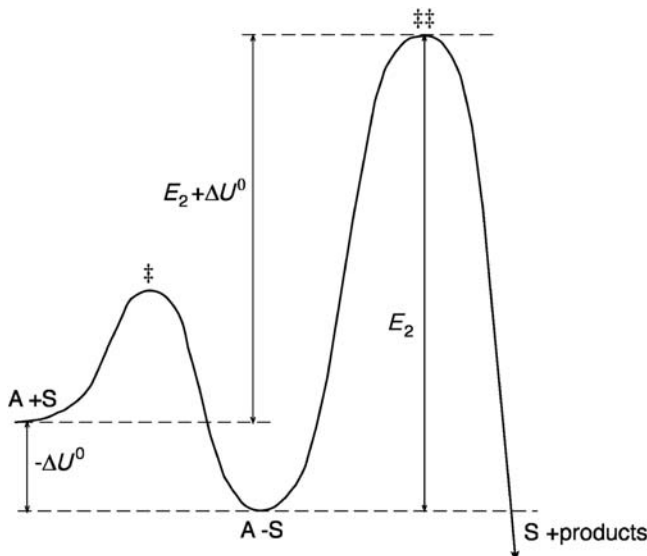


FIGURE 10.7

Energy diagram for a unimolecular surface reaction.

adsorbed in a well, either to be converted into products or to revert somewhat more easily to the desorbed condition.

At low concentrations, the majority of the molecules are not adsorbed, such that they have to surmount the energy barrier, $E_2 + \Delta U^0 (\Delta U^0 < 0)$. However, at high concentrations, equilibrium favours the adsorbed molecules and the barrier to be surmounted is even higher, E_2 .

When there is inhibition, according to eq. (10.24),

$$\frac{d \ln K_I}{dT} = \frac{\Delta U_I^0}{RT^2} \quad (10.32)$$

and the apparent activation energy is thus

$$E_a = E_2 + \Delta U_A^0 - \Delta U_I^0 \quad (10.33)$$

which is greater than $E_2 = \Delta U_A^0$ for the uninhibited reaction since ΔU_I^0 is negative. The reason for this increase in activation energy is that a molecule of the inhibitor must be desorbed (an endothermic process) when a reactant molecule is adsorbed and undergoes reaction.

10.3.3 Reaction between two adsorbed molecules

For a surface bimolecular reaction to occur, the reactants or intermediates must have enough energy, usually through thermal activation, to surmount an activation barrier.

Additionally, the reactants or intermediates must be in close proximity to react, while for molecular (as opposed to atomic) species, the relative orientation can also be critical. The frequency with which all of these conditions are met determines the reaction rate.

For a surface reaction between two reactants A and B, there are two distinct mechanisms: Langmuir–Hinshelwood and Rideal–Eley. In the former mechanism, the reaction occurs between A and B when both are adsorbed on the surface. In the latter, the reaction occurs between an adsorbed molecule and a molecule in the gas phase. These mechanisms may be distinguished on the basis of the corresponding kinetic equations.

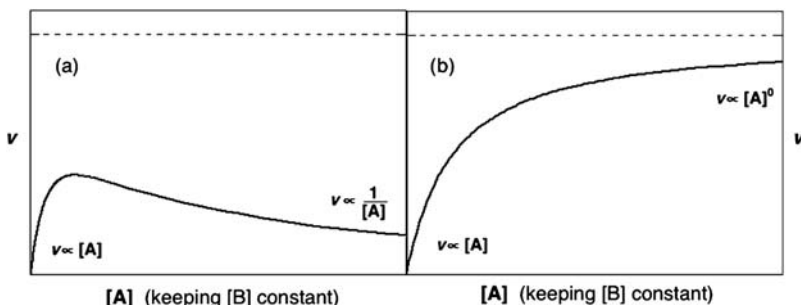
The rate of reaction of the Langmuir–Hinshelwood mechanism is proportional to the fractions of the molecules of A and B that are adsorbed,

$$v = k\theta_A\theta_B \quad (10.34)$$

These fractions are given by eqs. (10.17) and (10.18), such that the rate is therefore

$$v = \frac{kK_A K_B [A][B]}{(1 + K_A[A] + K_B[B])^2} \quad (10.35)$$

Figure 10.8 illustrates the variation of the rate of reaction as a function of [A], keeping [B] constant. The rate first increases in a manner proportional to [A],

**FIGURE 10.8**

Surface bimolecular reaction rate as a function of one of the reactants.
(a) Langmuir–Hinshelwood mechanism; (b) Rideal–Eley mechanism.

then passes through a maximum and subsequently decreases. The decline in the rate at high [A] can be explained in terms of the displacement of one of the reactants, B, when the concentration of A increases.

Eq. (10.35) can be employed for the study of special cases such as the regime of sparsely covered surface at low concentrations of both reactants ($K_A[A] + K_B[B] \ll 1$), the case when one of the reactant is very weakly adsorbed, ($K_A[A] \ll 1 + K_B[B]$) or strongly adsorbed ($K_B[B] \gg 1$), etc. For the latter situation the rate is

$$v = \frac{kK_A[A]}{K_B[B]} \quad (10.36)$$

The activation energies can be established under the experimental conditions for which eq. (10.35) is valid,

$$E_a = E_2 + \Delta U_A^0 + \Delta U_B^0 \quad (10.37)$$

and under the conditions of the validity of eq. (10.36),

$$E_a = E_2 + \Delta U_A^0 - \Delta U_B^0 \quad (10.38)$$

These two examples reveal that, within the same mechanism, the observed activation energy is strongly dependent upon the experimental conditions of surface coverage.

10.3.4 Reaction between a molecule in the gas phase and an adsorbed molecule

When the reaction follows the Rideal–Eley mechanism, where reactant A is in the gas phase and B is adsorbed, the rate is given by

$$v = k\theta_B[A] \quad (10.39)$$

or

$$\nu = \frac{kK_B[A][B]}{1 + K_A[A] + K_B[B]} \quad (10.40)$$

The rate of reaction tends to a plateau with an increase in [A], because reactant A occupies sites that are no longer available for B. Figure 10.8b displays the variation of the rate with [A], keeping [B] constant. The rate no longer passes through a maximum in contrast to its behaviour in the Langmuir–Hinshelwood mechanism.

10.4 Transition-state theory for reactions on surfaces

10.4.1 Unimolecular reactions

The statistical mechanical formulation of the transition-state theory (TST) can also be applied to the kinetics of reactions on surfaces. Let us consider the following reaction:



The equilibrium between the activated complex and the reactant can be expressed by the equation

$$\frac{c^\ddagger}{c_g c_s} = \frac{Q_\ddagger}{Q_g Q_s} \exp\left(-\frac{\varepsilon_0}{k_B T}\right) \quad (10.41)$$

Here c_g represents the concentration of the reactant in the gas phase, $c_g = N_g/V$ where N_g is the number of molecules in the gas phase and V the volume of the gas; c_{ad} the concentration of adsorbed molecules in molecules per unit area, $c_{ad} = N_{ad}/S$ and S is the area of the surface; c_s the concentration of bare sites per unit area, $c_s = N_s/S$, where N_s is the number of sites at adsorption equilibrium; c_\ddagger the concentration per unit area of activated complexes, $c_\ddagger = N_\ddagger/S$ where N_\ddagger is the number of activated complexes. The partition functions Q_\ddagger and Q_s are for unit area and Q_g for unit volume. The energy ε_0 represents the molecular energy of activation at absolute zero.

The rate of reaction is estimated in terms of the product of the frequency of transformation, ν_\ddagger , of the activated complexes and the concentration of the same complexes, $\nu = \nu_\ddagger c_\ddagger$. As previously discussed, one of the vibrational factors in the partition function corresponds to a very loose vibration expressed usually by $k_B T/h\nu$, where ν is its vibrational frequency. If we define a new partition function that lacks the contribution of such loose vibration, $Q'_\ddagger = Q^\ddagger (k_B T/h)$, the rate of the reaction is given by

$$\nu = c_g c_s \frac{k_B T}{h} \frac{Q'_\ddagger}{Q_g Q_s} \exp\left(-\frac{\varepsilon_0}{k_B T}\right) \quad (10.42)$$

The value of the partition function Q^\ddagger may be taken as unity, $Q^\ddagger = 1$, since the activated state consists of a molecule immobilised on the surface.

Two limiting cases of eq. (10.42) are of interest. The first is that of a sparsely covered surface. The concentration of bare surface sites c_s is approximately equal to L_s the total number of sites per unit area of completely bare surface. Under such conditions, c_s is approximately independent of c_g , such that the rate is directly proportional to c_g . Therefore we are dealing with a first-order process,

$$v = c_g L_s \frac{k_B T}{h} \frac{Q^\ddagger}{Q_g Q_s} \exp\left(-\frac{\varepsilon_0}{k_B T}\right) \quad (10.43)$$

The second limiting case involves the surface covered almost completely by the adsorbed molecules. The concentration of active sites c_s can be estimated from the isotherm equation, now written as

$$\frac{c_{ad}}{c_s} = c_g \frac{Q_{ad}}{Q_g Q_s} \exp\left(-\frac{\varepsilon}{k_B T}\right) \quad (10.44)$$

where ε represents the adsorption energy, which is the difference between the zero-point energy (ZPE) of the adsorbed and the free molecule. Substituting this equation in the rate expression, we obtain

$$v = c_{ad} \frac{k_B T}{h} \frac{Q^\ddagger}{Q_{ad}} \exp\left(-\frac{\varepsilon_0 - \varepsilon}{k_B T}\right) \quad (10.45)$$

When the surface is almost completely covered by the adsorbed molecules, c_{ad} may be considered to be constant, and the rate is independent of the pressure of the reactant. The kinetics are therefore zero order.

The partition function of the adsorbed species involves only vibrational factors, because the adsorbed molecules do not possess translation or rotational degrees of freedom. For the vibrational partition function we can assume $Q_{ad} \approx 1$, and since $Q^\ddagger = 1$, the expression for the rate will be

$$v = c_{ad} \frac{k_B T}{h} \exp\left(-\frac{E_0}{RT}\right) \quad (10.46)$$

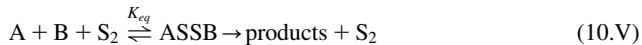
where E_0 is the molar activation energy at 0 K.

Eq. (10.46) can be employed to estimate the rate of the catalysed decomposition of NH_3 on a tungsten surface under zero-order conditions at 904 K. The experimental activation energy is known, $E_0 = 159 \text{ kJ mol}^{-1}$. Employing typical values for a smooth surface of $10^{15} \text{ atoms cm}^{-2}$ gives $c_{ad} \approx L_s = 10^{15} \text{ cm}^{-2}$. The estimated reaction rate is $4 \times 10^{17} \text{ cm}^{-2} \text{ sec}^{-1}$ at 904 K, which should be compared with the experimental value of $8 \times 10^{18} \text{ cm}^{-2} \text{ sec}^{-1}$. The cross-section of a molecule is πr^2 , and can be estimated using a typical radius of $r = 1.5 \text{ \AA}$. When the entire surface of a catalyst is covered with a monolayer of adsorbed molecules, one molecule per active site, the number of covered sites is the reciprocal of the cross-section, thus $L_s = 10^{15} \text{ cm}^{-2} = 10^{19} \text{ m}^{-2}$. With this L_s value and the

thermal frequency factor $k_B T/h = 10^{13} \text{ sec}^{-1}$, the pre-exponential factor typical for a unimolecular reaction on a surface is $10^{28} \text{ cm}^{-2} \text{ sec}^{-1}$.

10.4.2 Bimolecular reactions

Let us assume that a reaction on a surface follows the Lindemann–Hinshelwood mechanism



S_2 represents an active dual site. The rate of reaction is then given by

$$v = c_g c'_g c_{\text{S}_2} \frac{k_B T}{h} \frac{Q^*}{Q_g Q'_g Q_{\text{S}_2}} \exp\left(-\frac{\varepsilon_0}{k_B T}\right) \quad (10.47)$$

where c_g and c'_g are the molecular concentrations of A and B, respectively, in the gas phase, Q_g/V and Q'_g/V are the corresponding partition functions per unit volume, c_{S_2} is the concentration of the dual sites where the species A and B can be adsorbed in contiguous positions.

The concentration of bare dual sites is related to the concentration of bare single sites. Each single site has a certain number of available adjacent sites. For a random distribution this is $s(1 - \theta)$ where s is the coordination number of the surface and $(1 - \theta)$ represents the bare surface which is available to adsorb the reactant species. Thus the concentration of dual sites is given by

$$c_{\text{S}_2} = \frac{c_s s (1 - \theta)}{2} \quad (10.48)$$

If the number of dual sites was evaluated by counting s for each single site, the result would be $s c_s$, but in such a procedure, each pair is counted twice: one as a central site, the other as an adjacent one. In eq. (10.48), the division by two takes this fact into account.

If the concentration of covered single sites is c_{ad} , θ is then given by

$$\theta = \frac{c_{\text{ad}}}{c_{\text{ad}} + c_s} \quad (10.49)$$

taking into consideration eq. (10.48), the concentration of bare dual sites is

$$c_{\text{S}_2} = \frac{s c_s^2}{2(c_{\text{ad}} + c_s)} \quad (10.50)$$

or

$$c_{\text{S}_2} = \frac{s c_s^2}{2 L_s} \quad (10.51)$$

where $L_s = c_{\text{ad}} + c_s$ is the total concentration of single sites per unit area when the surface is completely bare. By introducing eq. (10.51) into eq. (10.47), we obtain

$$v = \frac{1}{2} s \frac{c_g c'_g c_s^2}{L_s} \frac{k_B T}{h} \frac{Q^*}{Q_g Q'_g Q_s} \exp\left(-\frac{\varepsilon_0}{k_B T}\right) \quad (10.52)$$

This equation may be presented in a more general form using the equilibrium expressions for the adsorption of A and B

$$K = \frac{c_{\text{ad}}}{c_g c_s} \quad (10.53)$$

$$K' = \frac{c'_{\text{ad}}}{c_g c_s} \quad (10.54)$$

where c_{ad} and c'_{ad} are the concentrations of adsorbed A and B, respectively, by unit area. Since in addition

$$c_{\text{ad}} + c'_{\text{ad}} + c_s = L_s \quad (10.55)$$

from eqs. (10.53) and (10.54) one obtains

$$c_s = \frac{L_s}{1 + Kc_g + K'c'_g} \quad (10.56)$$

Inserting this expression into eq. (10.52) gives

$$\nu = \frac{1}{2} s \frac{c_g c'_g L_s}{(1 + Kc_g + K'c'_g)^2} \frac{k_B T}{h} \frac{Q^{\ddagger}}{Q_g Q'_g Q_s} \exp\left(-\frac{\varepsilon_0}{k_B T}\right) \quad (10.57)$$

as a general rate expression for a bimolecular reaction on a surface.

When the surface is covered sparsely, $Kc_g + K'c'_g \ll 1$, and as a consequence the rate equation becomes

$$\nu = \frac{1}{2} s c_g c'_g L_s \frac{k_B T}{h} \frac{Q^{\ddagger}}{Q_g Q'_g Q_s} \exp\left(-\frac{\varepsilon_0}{k_B T}\right) \quad (10.58)$$

This type of expression can be applied quantitatively for the catalysed reaction of NO and O₂ on a glass surface. The reaction is second order and the rate at 85 K follows the expression:

$$\nu = 9.4 \times 10^{-27} c_{\text{NO}} c_{\text{O}_2} \exp\left(-\frac{E_0}{RT}\right) \quad \text{cm}^4 \text{ sec}^{-1} \quad (10.59)$$

Eq. (10.58) with $Q^{\ddagger}/Q_s = 1$, $L_s = 10^{15} \text{ cm}^{-2}$ and a coordination number $s = 4$ leads to a pre-exponential factor of $15 \times 10^{-27} \text{ cm}^4 \text{ sec}^{-1}$, in good agreement with the experimental data.

Without resorting to the calculation of the partition functions, the equations presented above can provide order of magnitude values of the pre-exponential factor, $(1/2)sL_s(k_B T/h)(1/Q_g Q'_g)$, using the orders of magnitude of the partition functions for the different types of motion involved, given in Chapter 6, Reactivity in Thermalised Systems (partition functions: translation, $Q_{\text{trans}} = 10^{25} - 10^{26} \text{ cm}^{-3}$; rotation of a linear molecule, $Q_{\text{rot}} = 10 - 10^2$, and a non-linear molecule, $Q_{\text{rot}} = 10^4 - 10^5$, vibration, $Q_{\text{vib}} = 1 - 10$). As the temperature is not very high, let us assume that $Q_{\text{vib}} = 1$ for both the reactants and take the geometric mean values

for Q_{trans} and Q_{rot} . Under these assumptions we obtain a pre-exponential factor of $10^{-26} \text{ cm}^4 \text{ sec}^{-1}$ that is not far from the experimental value.

When one of the reactants is strongly adsorbed, we can have $Kc_g \gg 1 + K'c'_g$ and as a consequence the rate is

$$v = \frac{1}{2} s \frac{L_s}{K^2 c_g} \frac{k_B T}{h} \frac{Q^*}{Q_g Q'_g Q_s} \exp\left(-\frac{\varepsilon_0}{k_B T}\right) \quad (10.60)$$

We can express the equilibrium constant K in terms of the partition functions as

$$v = \frac{1}{2} s L_s \frac{c'_g}{c_g} \frac{k_B T}{h} \frac{Q^* Q_g Q_s}{Q'_g Q_{\text{ad}}^2} \exp\left(-\frac{\varepsilon_0 + 2\varepsilon}{k_B T}\right) \quad (10.61)$$

The activation energy is greater by 2ε than the value for a sparsely covered surface; the underlying reason is that two molecules of A must be adsorbed before the activated complex is formed.

This equation is valid for the reaction between CO and O₂ on a platinum surface. At 527 K the empirical rate was found to be [5]

$$v = 7.1 \times 10^{-14} \frac{c_{\text{CO}_2}}{c_{\text{CO}}} \text{ cm}^{-2} \text{ sec}^{-1} \quad (10.62)$$

with an activation energy of 139 kJ mol⁻¹. The rate estimated by the TST [eq. (10.61)] is $4.3 \times 10^{-14} \text{ cm}^{-2} \text{ sec}^{-1}$, once again in good agreement with the experimental data.

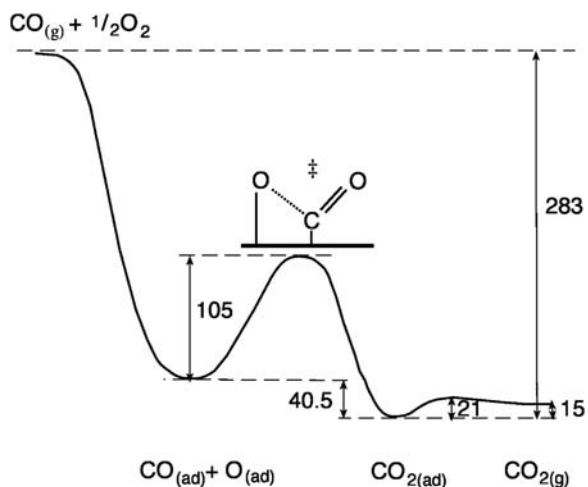
10.5 Model systems

10.5.1 Langmuir–Hinshelwood mechanism

The catalytic oxidation of CO on a Pt surface has been extensively studied in view of its relevance to automotive gas pollution. Moreover, its relative simplicity motivated its extensive use as a model system for heterogeneous catalysis. Molecular beam studies of the catalytic oxidation of CO on the plane (111) on platinum indicate that the reaction follows a Langmuir–Hinshelwood mechanism [6],



where O_{ad} represents the adatoms of atomic oxygen. The rate of CO₂ product formation at the surface is, by definition, the flux corresponding to the number of CO₂ molecules produced per second per cm². An energy diagram for the reaction was constructed on the basis of experimental data, and is illustrated in Figure 10.9 [7,8]. The energy barrier for the reaction of the CO_{ad} and O_{ad}

**FIGURE 10.9**

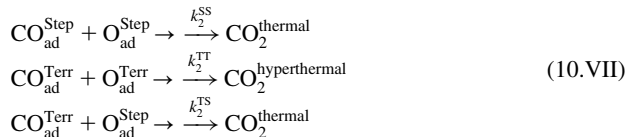
Potential energy diagram for the catalytic oxidation of CO on a Pt(111) surface. Energies are in kJ mol^{-1} .

adsorbed species is $\Delta E^\ddagger = 105 \text{ kJ mol}^{-1}$ and the reaction energy is $\Delta E^0 = -40.5 \text{ kJ mol}^{-1}$.

Mechanism (10.VI) emphasises that the reactive components of the catalytic oxidation of CO on a Pt surface are the adsorbed O and CO. The Pt surface plays an essential role in the dissociation of O_2 , but the CO molecules on the surface preserved its integrity. A very fast chemical reaction occurs between O_{ad} and CO_{ad} in neighbouring adsorption sites of the surface, followed by the immediate release of the CO_2 produced. The CO oxidation reaction of a Pt(111) surface proceeds via a Langmuir–Hinshelwood mechanism whereby a chemisorbed CO molecules combines with an adsorbed oxygen atom. The experimental activation energy for this combination when both species are in low concentrations is $E_{\text{LH}} = 101 \text{ kJ mol}^{-1}$, but at high oxygen concentration this barrier decrease to about 46 kJ mol^{-1} [9]. Although the Langmuir–Hinshelwood mechanism is well established, it is evident that there are subtleties in this reaction that are not explained by mechanism (10.VI). Another interesting piece of this puzzle is that the CO_2 products are formed in a bimodal kinetic energy distribution: thermal (the products fit to a Maxwell–Boltzmann distribution) and hyperthermal (the mean particle velocity is displaced to much higher kinetic energies) products are observed [10].

Although this catalytic oxidation has been studied for more than a century, it was only recently that a study employing molecular beams to controllably introduce reactants and synchronized pulsed-laser ionisation of CO_2 to obtain the CO_2 flux as a function of time, provided a clear relation between the bimodal distribution and the reactions taking place at different sites of the Pt(111) surface. Recalling Figure 10.5, we can consider the presence of two major sites on this surface: terraces

and steps. O_2 dissociates more easily at steps than at terraces and oxygen atoms are bound 5 kJ mol^{-1} more strongly at steps than at terraces. However, the Pt(111) step density is only 0.25% and more than 99% of the CO adsorbs initially at terraces. The reaction between adsorbed species may follow three different routes:



where the superscripts Step and Terr identify in which sites the reacting adsorbed molecules are located.

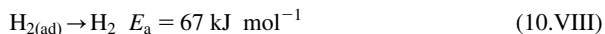
At experimentally accessible temperatures, the conversion of $\text{CO}_{\text{ad}}^{\text{Terr}}$ to $\text{CO}_{\text{ad}}^{\text{Step}}$ is much faster than k_2^{TT} , but at high temperatures the CO desorption becomes much faster than CO diffusion and reaction preferentially occurs at the terrace sites where most CO is present. However, at low temperatures the reaction is dominated by the more active sites. The activation energies for k_2^{SS} , k_2^{TT} and k_2^{TS} are 63, 58 and 39 kJ mol^{-1} , respectively. The reaction of $\text{CO}_{\text{ad}}^{\text{Terr}}$ with $\text{O}_{\text{ad}}^{\text{Step}}$ becomes dominant at low temperatures. The hyperthermal channel disappears at low oxygen coverage because then the oxygen adatoms are bond to steps. This means that the hyperthermal channel is due to the reaction $\text{CO}_{\text{ad}}^{\text{Terr}}$ with $\text{O}_{\text{ad}}^{\text{Terr}}$ [11].

Ab initio molecular dynamics simulations suggest that CO_2 formed on the Pt(111) terrace desorbs directly, with a high translational energy and narrow angular distribution, which explain the hyperthermal channel [10]. In contrast, CO_2 formed on a step site is temporarily trapped in a shallow chemisorption well and its translational energy has time to thermalise with the surface, giving rise to the thermal reaction channel.

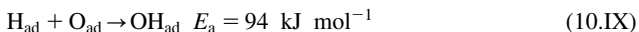
In general, low-concentration, high-reactivity defects on surfaces are expected to be important in low-temperature surface reactions in which reactant diffusion is faster than desorption.

10.5.2 Eley–Rideal mechanism

Reaction of gas-phase atomic hydrogen with dissociatively chemisorbed oxygen on Ru(001) can be taken as a model reaction for the Eley–Rideal mechanism. The Langmuir–Hinshelwood reaction between co-adsorbed hydrogen H_{ad} and O_{ad} atoms does not occur on the Ru(001) surface. The reason for this is simple. The activation energy for recombinative desorption of molecular hydrogen



is approximately 27 kJ mol^{-1} less than that for the reaction



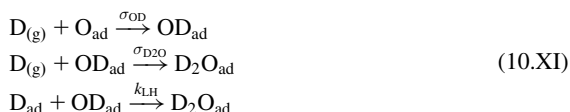
Therefore the reaction occurs between the hydrogen molecules (or atoms) in the vapour phase and the adsorbed oxygen atoms.

The reaction



on Ru(001) is estimated to be exothermic by approximately 230–270 kJ mol⁻¹ (depending on the exact value of the Ru–OH) and is expected to have only a small barrier [12].

Weinberg reports studies with an ordered $p(1 \times 2)$ oxygen adatom overlayer corresponding to a fractional area of $\theta_{\text{O}} = 0.5$. The metal surface was bombarded with deuterium atoms with a flux $\Xi_{\text{D}} = 1.2 \times 10^{13} \text{ cm}^{-2} \text{ sec}^{-1}$. D and H atoms produce identical results within experimental uncertainties. The elementary reactions taken into consideration were



where σ represents the reaction cross-section, and k_{LH} is the competing Langmuir–Hinshelwood reaction rate coefficient that is negligible under the surface temperature of 90 K employed in the experiments. According to this mechanism, in general terms we can write

$$\begin{aligned} \frac{d\theta_{\text{O}}}{dt} &= -\sigma_{\text{OD}}\Xi_{\text{D}}\theta_{\text{O}} \\ \frac{d\theta_{\text{OD}}}{dt} &= -\sigma_{\text{OD}}\Xi_{\text{D}}\theta_{\text{O}} - \sigma_{\text{D}_2\text{O}}\Xi_{\text{D}}\theta_{\text{OD}} - k_{\text{LH}}\theta_{\text{D}}\theta_{\text{OD}} \\ \frac{d\theta_{\text{D}_2\text{O}}}{dt} &= \sigma_{\text{D}_2\text{O}}\Xi_{\text{D}}\theta_{\text{OD}} + k_{\text{LH}}\theta_{\text{D}}\theta_{\text{OD}} \end{aligned} \quad (10.63)$$

On neglecting the terms involving k_{LH} , and based on the surface coverage of water on Ru(001), Weinberg reported cross-section values of $\sigma_{\text{OD}} = 6.8 \times 10^{-17} \text{ cm}^2$ and $\sigma_{\text{D}_2\text{O}} = 2.2 \times 10^{-15} \text{ cm}^2$. The product water remains adsorbed at the reaction temperature and acts as an inhibitor of the direct reaction when $\theta_{\text{D}_2\text{O}} > 0.3$.

References

- [1] S Lehwald, H Ibach, JE Demuth, *Surf. Sci.* **78** (1978) 577–590.
- [2] ECH Sykes, P Han, SA Kandel, KF Kelly, GS McCarty, PS Weiss, *Acc. Chem. Res.* **36** (2003) 945–953.
- [3] B Frémaux, *Éléments de Cinétique et de Catalyse, Technique et Documentation*, Lavoisier, Paris, 1989.
- [4] I Langmuir, *J. Am. Chem. Soc.* **38** (1916) 2221.

- [5] I Langmuir, *Trans. Farad. Soc* **17** (1922) 621.
- [6] R Imbihl, G Ertl, *Chem. Rev.* **95** (1995) 697.
- [7] G Ertl, PR Norton, J Rustig, *Phys. Rev. Lett.* **49** (1982) 177.
- [8] MJ Hei, HB Chen, YJ Lin, YZ Lin, G Wei, DW Liao, *Surf. Sci* **417** (1998) 82.
- [9] CT Campbell, G Ertl, H Kuipers, J Segner, *J. Chem. Phys.* **173** (1980) 5862.
- [10] GB Park, TN Kitsopoulos, D Borodin, K Golibrzuch, J Neugebohren, DJ Auerbach, CT Campbell, AM Wadtke, *Nature Rev. Chem* **3** (2019) 723.
- [11] J Neugebohren, D Borodin, HW Hahn, J Altschäffel, A Kandratsenka, DJ Auerbach, CT Campbell, D Schwarzer, DJ Harding, AM Wadtke, TN Kitsopoulos, *Nature* **558** (2018) 280.
- [12] WH Weinberg, *Acc. Chem. Res.* **29** (1996) 479.

Substitution reactions

11

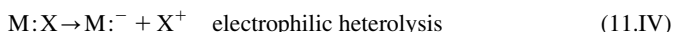
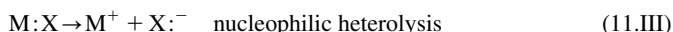
11.1 Mechanisms of substitution reactions

A substitution reaction is characterised by the replacement of a molecule (or ion) from the coordination shell of a reactive centre by another molecule (or ion) from the reaction medium, irrespective of whether it is a gas or a liquid. During the substitution, the bond between the ligand and the reactive centre is broken, while a new bond is formed between that centre and the new species entering the coordination shell. Le Bel suggested in 1911 that aliphatic substitutions



could occur in a synchronous process where the bond to the entering group (the nucleophile), Y^- , is gradually formed while the bond to the leaving group (the nucleofuge, or leaving group), X^- , is gradually broken [1]. In 1933, Christopher (later Sir Christopher) Ingold with Patel [2,3] introduced a classification for substitution reactions on carbon atoms that was subsequently popularised by Ingold and E.D. Hughes. This classification is based on the type of bond breaking between the leaving group and the reactive centre, which can be either homolytic or heterolytic. In homolytic reactions, the two electrons of the chemical bond are separated, with one remaining in the reactive centre, while the other goes to the leaving group. This leads to the chemistry of systems with unpaired electrons, commonly referred to as free radicals, which will be addressed in Chapter 12, Chain Reactions. In heterolytic reactions, the electron removal or addition to the reactive centre occurs in pairs. This is the chemistry of diamagnetic charged species, that is, cations and anions.

In the latter case, a subdivision of this classification is made by considering the site of the electron pair after the heterolytic scission. When the electron pair remains in the reactive centre, it is named electrophilic heterolysis and when it accompanies the leaving group, it is called nucleophilic heterolysis.



“Nucleophilic substitution” is now the commonly accepted designation of a substitution reaction by a nucleophilic reactant, and is usually represented by S_N followed by

a number that represents the molecularity of the rate-determining reaction step. For example, bimolecular nucleophilic substitution is represented as S_N2 , whereas first-order nucleophilic substitution is described as S_N1 . Similarly, for electrophilic heterolysis, the processes are described as S_E2 and S_E1 reactions, while for the homolytic reactions, they are referred to as S_H2 and S_H1 reactions. As we will see shortly, these may be considered as the limits in a spectrum of reaction mechanisms.

Nucleophilic substitution reactions are one of the most important classes of reactions in organic chemistry. In particular, S_N2 reactions are among the most extensively studied chemical processes in solution and in the gas phase, both theoretically and experimentally. The history of the study of these reactions closely parallels (and is sometimes responsible for) the development of concepts such as structure–reactivity relationships, linear free-energy relationships, steric inhibition, kinetics as a probe of mechanism, stereochemistry as a probe of mechanism and solvent effects.

11.2 S_N2 and S_N1 reactions

When the nucleophilic substitution reaction of mechanism (11.I) occurs as a concerted R–X bond-breaking and R–Y bond-making process, the reaction rate of this elementary reaction is

$$v = k_2[RX][Y^-] \quad (11.1)$$

where k_2 is a bimolecular rate constant, usually expressed in units of $M^{-1} \text{ sec}^{-1}$. This reaction is described as an S_N2 reaction.

Ingold and co-workers considered another reaction mechanism, where the rate-limiting step is the heterolytic dissociation of the RX substrate



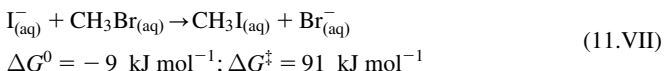
The reaction rate is now determined by the rate of the slow step, heterolytic dissociation of the C–X bond,

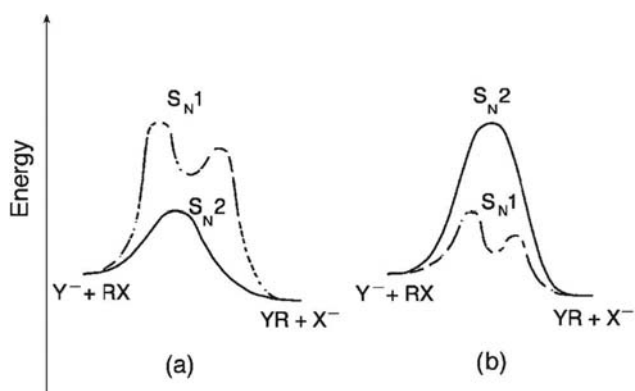
$$v = k_1[RX] \quad (11.2)$$

where k_1 is a first-order rate constant.

The difference between S_N2 and S_N1 reactions can be rationalised by the reaction energy profiles shown in Figure 11.1. The nucleophilic substitutions of bromomethane and of tertiary butyl bromide in aqueous solution illustrate some of the factors that determine the size of the energy barriers and the stability of the intermediate in these mechanisms.

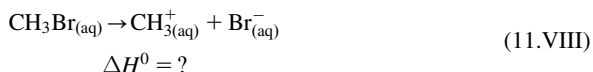
The nucleophilic substitution of bromomethane by iodine



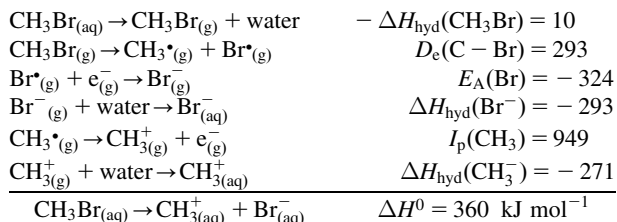
**FIGURE 11.1**

Energy profiles characterising S_N2 and S_N1 reactions. (a) Reaction proceeding through the S_N2 mechanism. (b) Reaction proceeding through the S_N1 mechanism.

can be decomposed in a thermodynamic cycle to obtain the enthalpy of the first step, the heterolytic cleavage



using the data from the literature [4,5], in kJ mol⁻¹,



A more accurate estimate for the enthalpy of the heterolytic cleavage of CH₃Br must include an electrostatic term for the stabilisation of the (CH₃⁺ Br⁻) ion pair. However, the stabilisation for a 2.5 Å charge separation in water ($\varepsilon = 78.5$) is only $-10.5 \text{ kJ mol}^{-1}$, and does not change the fact that the enthalpy for the heterolytic bond cleavage is much higher than the activation free energy of reaction (11.VII). Thus the barrier of the S_N1 mechanism is much higher than that observed for the reaction, showing that it must proceed through the alternative S_N2 mechanism.

However, estimation of the enthalpy of dissociation of tertiary butyl bromide in water

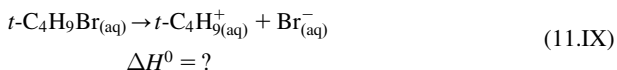
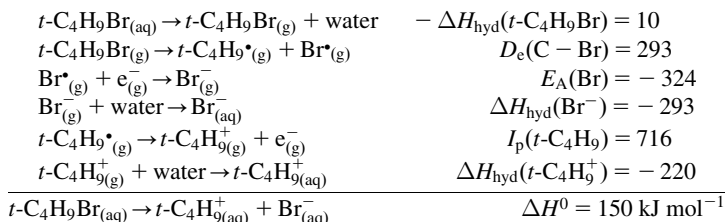


Table 11.1 Comparison of the energies of the steps in the thermodynamic cycle for the heterolytic dissociation of CH₃Br and *t*-C₄H₉Br in water.

Steps	CH ₃ Br (kJ mol ⁻¹)	<i>t</i> -C ₄ H ₉ Br (kJ mol ⁻¹)	ΔH(CH ₃ Br) – ΔH(<i>t</i> -C ₄ H ₉ Br) (kJ mol ⁻¹)
–ΔH _{hydr} (RX)	10	10	0
D _e (C–Br)	293	263	30
E _A (Br)	–324	–324	0
ΔH _{hyd} (Br [–])	–293	–293	0
I _P (R [•])	949	716	233
ΔH _{hyd} (R ⁺)	–271	–220	51

leads to strikingly different results. The same thermodynamic cycle, using identical data sources,



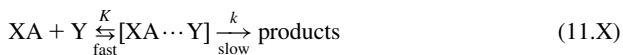
shows that the enthalpy of this heterolytic dissociation is 200 kJ mol^{–1} lower than that of the bromomethane heterolytic dissociation. The dramatic stabilisation of the (*t*-C₄H₉⁺ Br[–]) ion pair offers an alternative to the S_N2 mechanism. The rate of reaction (11.IX) was studied in 80% ethanol and ΔG[‡] = 91 kJ mol^{–1} was obtained at 55°C. An approximate estimate for the enthalpy of this reaction in 80% ethanol is ΔH⁰ ≈ 110 kJ mol^{–1}, including the ion-pair stabilisation. If we consider that the entropy change is relatively unimportant, this compares reasonably well with the experimental ΔG[‡] and strongly suggests that this reaction follows the S_N1 mechanism.

The comparison between the contributions to the thermodynamic cycle is presented, step-by-step, in Table 11.1. This comparison assigns most of the difference between the enthalpies of reactions (11.VIII) and (11.IX) to the ionisation potentials of the radical R[•]. Minor contributions also come from the hydration of the R⁺ carbocation and from the C–X bond dissociation energy. The factor that controls the mechanism of nucleophilic substitution appears then to be I_P(R[•]). A low I_P(R[•]) favours the S_N1 mechanism because it lowers the enthalpy of its rate-determining step, while a high I_P(R[•]) favours the S_N2 mechanism.

11.3 Langford–Gray classification

The mechanisms of substitution reactions at carbon atoms lead to a direct relation between the order of the reaction and its molecularity. This may cause the

impression that S_N1 and S_N2 mechanisms encompass all possible substitution reaction mechanisms. However, the most general case is



and the reaction rate can be obtained using the same kinetic analysis presented for enzyme catalysis, eq. (4.156). Writing $k_1 = k_{-1}K$, dividing both the numerator and denominator by k_{-1} , and assuming that $k_2/k_{-1} \ll 1$, gives

$$-\frac{d[XA]}{dt} = \frac{kK[XA][Y]}{1 + K[Y]} \quad (11.3)$$

independent of the nature of the interaction in the $XA \cdots Y$ species (ion-pair, solvation or complexation). When $K[Y] \gg 1$, the rate law becomes

$$v = k[XA] \quad (11.4)$$

and one can, apparently, consider that the reactant Y is not present in the transition state (TS) of the rate-determining step. This is misleading and does not contribute to the correct understanding of the reaction mechanism. Under these conditions, the reaction order is not a good criterion for the molecularity of the reaction, and S_N1 and S_N2 mechanisms should be regarded as limiting cases.

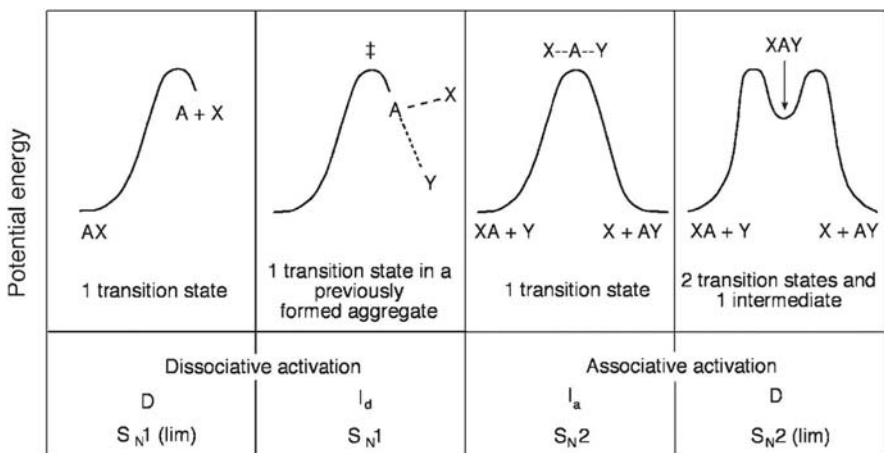
Langford and Gray presented another classification for the mechanism of substitution reactions that is particularly appropriate for metal complexes [6], but also englobes the classification of Ingold and co-workers for organic substitutions. This classification makes a distinction between the stoichiometric mechanism and the activation mechanism. The stoichiometric mechanism concerns the nature of the intermediate. It distinguishes between:

1. An *associative* mechanism (A), where an intermediate has a higher coordination number than that of the reactants.
2. A *dissociative* mechanism (D), where an intermediate has a lower coordination number than that of the reactants.
3. An *interchange* mechanism (I), where the bond-breaking–bond-making processes occur in a previously formed aggregate.

The activation mechanism is related to the nature of the activation step. It distinguishes between:

1. *Dissociative* activation, identified by the subscript d, when the TS of the rate-determining step does not have an interaction between the reactive centre and the entering group.
2. *Associative* activation, identified by the subscript a, when the TS of the rate-determining step has an interaction between the reactive centre and the entering group.

Figure 11.2 presents the relation between the classification of Ingold–Hughes and that of Langford–Gray. An example of a dissociative mechanism, D, which

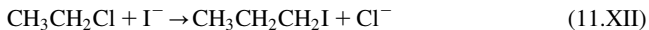
**FIGURE 11.2**

Relationship between the mechanisms of substitution reactions and their energy profiles, and the classifications of Hughes–Ingold and Langford–Gray.

corresponds to the S_N1 mechanism in the classification of Ingold–Hughes, is reaction (11.VII) and



An example of an interchange mechanism, I, which is essentially an S_N2 mechanism, is the reaction



that can be more exactly classified as I_a .

The transition between an I_a mechanism and an associative mechanism occurs when a single TS is replaced by one intermediate and two TSs. In one of these TSs the bond making is more advanced than the bond breaking, whereas in the other, the converse is true. Figure 11.3 illustrates the energy profiles for associative mechanisms.

The associative mechanism can also be illustrated by the kinetic mechanism



which leads to the reaction rate

$$-\frac{d[XR]}{dt} = \frac{k_a k_b}{k_{-a} + k_b} [XR][Y] = k_2[XR][Y] \quad (11.5)$$

where

$$k_2 = \frac{k_a k_b}{k_{-a} + k_b} \quad (11.6)$$

This rate law has two limiting cases. If $k_{-a} \gg k_b$, then

$$k_2 = \frac{k_a k_b}{k_{-a}} \quad (11.7)$$

and if $k_b \gg k_{-a}$ then

$$k_2 = k_a \quad (11.8)$$

Good examples of the associative mechanism are substitution reactions in complexes with a square planar geometry, which proceed via a trigonal bipyramidal geometry, as shown in [Figure 11.4](#).

IUPAC has recommended a more systematic system of nomenclature for substitution reactions [7]. Rather than representing the molecularity of the reaction, the IUPAC system describes the reaction mechanism in terms of bond making

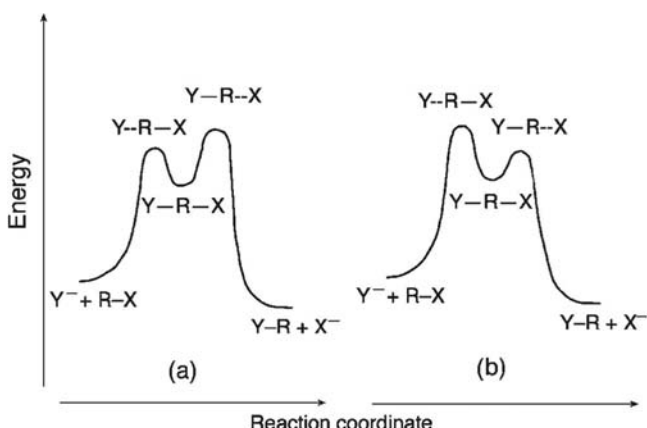


FIGURE 11.3

Energy profiles for the associative mechanism of substitution reactions, A in the Langford–Gray classification, showing the relation between the intermediate and the two TSs: (a) The bond-breaking TS has higher energy. (b) The bond-making TS has higher energy.

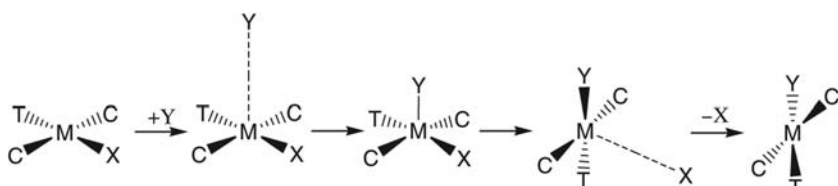


FIGURE 11.4

Nucleophilic substitution in a complex with a square planar geometry proceeding through a TS with a trigonal bipyramidal geometry.

(symbolised by A for “attachment”) and breaking (D, “detachment”), with subscripts and other symbols to indicate the pattern of electron movement. For example, $A_N D_N$ describes a single concerted process involving nucleophilic bond making and nucleofugic bond breaking (such as the S_N2 Ingold mechanism), and $A_N + D_N$ represents a two-step process (such as S_N1). This was severely criticised because mechanisms are not measurable quantities, but the best rationalisation of the reaction path based on available data. Clearly, there is a mechanistic continuum between limiting S_N1 and S_N2 reactions. Although recognising limitations in the classification of Ingold, the scientific community by and large continues to use the original Ingold classification.

11.4 Symmetrical methyl group transfers in the gas-phase

The high ionisation potential of the $\text{CH}_3\cdot$ radical makes methyl group transfers undergo the S_N2 mechanism



This class of reactions has been extensively studied, both experimentally and using *ab initio* methods and is one of the archetypal reactions of physical–organic chemistry. Table 11.2 shows that the gas-phase internal barriers (ΔE_i^\ddagger) of symmetrical methyl group transfers are strongly dependent on the nature of the reactants. Additionally, the rates of the asymmetric reactions may change by ten orders of magnitude with the polarity of the solvent [8].

It is convenient to start considering the study of methyl transfers with the reactions in the gas phase, which are free from solvent effects. However, there is a price to be paid for this simplification. In the gas phase these reactions proceed through the formation of a precursor ion–dipole complex in the absence of a

Table 11.2 Central barriers of ion–molecule complexes (upper row) and complexation energies (lower row), in kJ mol^{-1} , of gas-phase identity methyl transfer reactions of the type: $X^- + \text{CH}_3\text{X}$ ($\text{X} = \text{CH}_3\text{CH}_2, \text{CH}_3\text{NH}, \text{CH}_3\text{O}, \text{F}, \text{CH}_3\text{SiH}_2, \text{CH}_3\text{PH}, \text{CH}_3\text{S}, \text{Cl}, \text{CH}_3\text{GeH}_2, \text{CH}_3\text{AsH}, \text{CH}_3\text{Se}, \text{Br}, \text{CH}_3\text{SnH}_2, \text{CH}_3\text{SbH}, \text{CH}_3\text{Te}, \text{I}$).

C	187 ^a	N	123 ^a	O	81.6 ^a	F	55.6 ^b
Si	192 ^a	P	125 ^a	S	91.6 ^a	Cl	-57.2 ^b
Ge	159 ^a	As	103 ^a	Se	74.5 ^a	Br	56.9 ^b
Sn	128 ^a	Sb	82.4 ^a	Te	60.0 ^a	I	-44.1 ^b

^aHoz et al. [15].

^bParthiban et al. [36].

barrier, followed by the actual methyl transfers and the formation of a successor ion–dipole complex, and the subsequent separation of the final products [9,10].

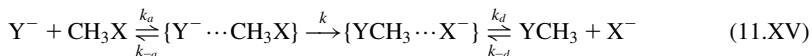


Figure 11.5 represents the energy changes involved in this mechanism for the case of the $\text{Cl}^- + \text{CH}_3\text{Cl} \rightarrow \text{ClCH}_3 + \text{Cl}^-$ reaction using the data from Ziegler and co-workers [11]. The ion–dipole complex is stabilised both by electrostatic and donor–acceptor orbital interactions. Hydrogen-bonded complexes may also be formed when the nucleophile is OH^- or NH_2^- , but rearrangement to the ion–dipole complex occurs before the TS of the substitution reaction is reached.

Table 11.2 uncovers a very interesting relation between ΔE_1^\ddagger and the position of the entering or leaving group in the Periodic Table. There is a trend towards lower internal barriers along the rows of the periodic table and also along the columns, although this latter trend is much less pronounced. These trends are correlated with the stabilisation energy (ΔE_c) of the ion–dipole complex. The

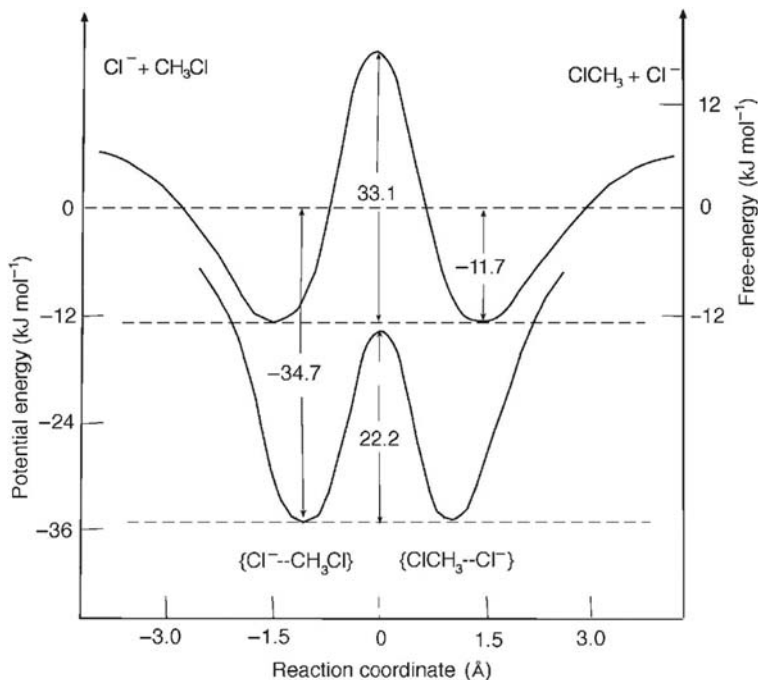


FIGURE 11.5

Energy profiles of the gas-phase $\text{Cl}^- + \text{CH}_3\text{Cl} \rightarrow \text{ClCH}_3 + \text{Cl}^-$ reaction. The upper line corresponds to the free-energy changes at 300 K and the lower line represents the classical potential energy.

formation of the ion–dipole complexes is associated with a decrease in the entropy of the systems, and compensates for the decrease in entropy also expected for the TSs. For example, the entropy change upon formation of the ion–dipole complex from the separated reactions in the $\text{Cl}^- + \text{CH}_3\text{Cl}$ methyl exchange is $-64.0 \pm 4.2 \text{ J K}^{-1} \text{ mol}^{-1}$ [10]. Thus when free-energy changes are calculated, the thermodynamic stabilisation of the complexes decreases significantly, but the internal (free-energy) barriers remain very high. For this reaction, the calculated entropy changes for the formation at 300 K of the complex and of the TS are -76.6 and $-104.6 \text{ J K}^{-1} \text{ mol}^{-1}$, respectively, and the internal free-energy barrier is only 10.9 kJ mol^{-1} higher than the classical internal barrier [11].

The traditional interpretation of $\text{S}_{\text{N}}2$ reactions considers that the ten valence electrons of reaction (11.XIV) are accommodated in a trigonal bipyramidal TS where the entering (Y) and leaving (X) groups occupy axial positions and the central carbon atom has an sp^2 hybridisation with the spectator (H) ligands in the equatorial positions. The σ bonds with the hydrogen atoms are maintained by the sp^2 -hybridised carbon atom, and the axial p_z orbital of the carbon atom interacts with the p orbitals of σ symmetry (p_z) of X and Y. Figure 11.6 illustrates this interaction, and the resulting bonding, non-bonding and anti-bonding orbitals. The four electrons left out of the C–H bonds occupy the bonding and non-bonding orbitals. The total bond order is unity and is maintained along the reaction coordinate.

Figure 11.6 also shows that for energetic and symmetry reasons the highest occupied molecular orbital (HOMO) is mostly localised in the X and Y groups. This leaves the carbon atom with an eight-electron valence shell and the attack on the tetrahedral carbon is directed towards a facial attack, with the entering group occupying the opposite position to the leaving group. The result is an inversion of configuration at the carbon atom, as illustrated in Figure 11.7.

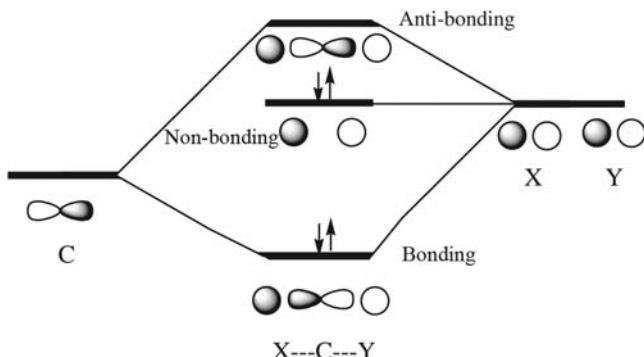
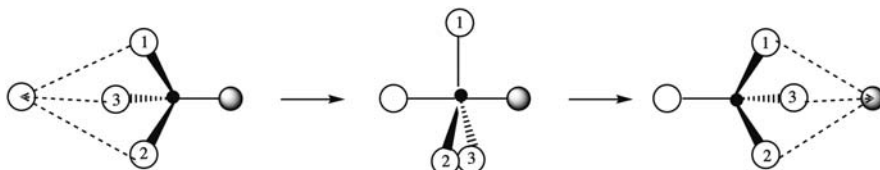


FIGURE 11.6

Molecular orbital diagram of an $\text{S}_{\text{N}}2$ reaction, illustrating the interaction between the central carbon atom and the axial ligands of the trigonal bipyramidal TS. This is also an I_a mechanism.

**FIGURE 11.7**

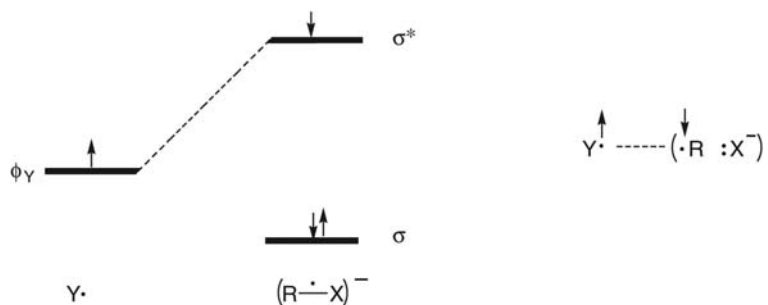
Inversion of configuration at the carbon atom following an S_N2 (or an I_a) reaction.

This traditional view explains the inversion of configuration observed experimentally in methyl transfers. However, it gives no leads to the motifs of the internal barriers reported in Table 11.2. Moreover, this view does not capture the driving force for the reaction: how is it possible that the C–X bond breaks if all the electrons have bonding or non-bonding character?

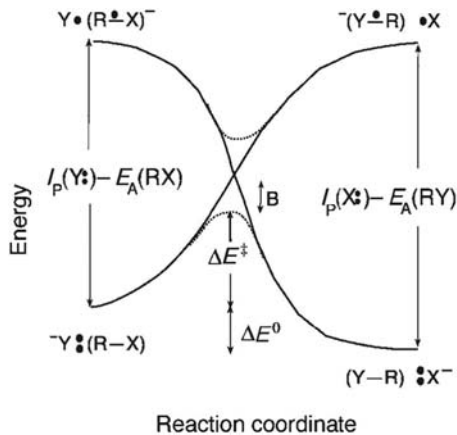
11.5 State correlation diagrams of Pross and Shaik

Pross and Shaik developed a model based on the valence-bond configurations of the reactive bonds that offers a conceptual understanding of the energy variations along the reaction coordinate of S_N2 reactions [12]. The key feature of this model is the representation of the reactants and products by valence-bond wave functions Ψ_R and Ψ_P , respectively, and the recognition that they are incorporated into well-defined excited states of the products and reactants. The only excited states considered in this work are charge-transfer states in which the nucleophiles (Y^- and X^-) transfer one single electron to their respective substrates ($R-X$ and $Y-R$). The choice of the charge-transfer excited states is motivated by their correlation with the ground-state reactants or products. For example, the $Y^*(R\ddot{X}^-)$ charge-transfer state can either be described by the molecular-orbital or valence-bond representations shown in Figure 11.8. According to the molecular-orbital representation, this charge-transfer state contains a $\phi_Y-\sigma^*$ bond pair, indicated by the dashed line, which accounts for one inter-molecular bond between the Y^- and $R-X$ reactants. This is also the interaction that promotes the cleavage of the $R-X$ bond. The electronic distribution of this charge-transfer state contains that of the products ($Y-R$): X^- , but in the geometry of the reactants. Therefore $Y^*(R\ddot{X}^-)$ qualifies as a unique excited state that will correlate with the ground state of the products, ($Y-R$): X^- .

More insight into the nature of the $Y^*(R\ddot{X}^-)$ charge-transfer state is given by the valence-bond representation of Figure 11.9. It emphasises the fact that this excited state mirrors the electronic distribution of the ground-state products, ($Y-R$): X^- , at the reactants' geometry. As the geometry is varied along the reaction coordinate, $Y^*(R\ddot{X}^-)$ will be gradually stabilised and will eventually correlate with ($Y-R$): X^- , as illustrated in Figure 11.9 [13]. Analogous arguments apply to the $Y^-:(R-X)\rightarrow(^-Y\ddot{R})^*X$ correlation line in this figure. The energy

**FIGURE 11.8**

Molecular orbital and valence-bond representations of the ground-state reactants in S_N2 reactions.

**FIGURE 11.9**

Shaik and Pross state correlation diagram for S_N2 reactions.

gaps in Figure 11.9 are the vertical electron transfer energies, $I_p(Y\cdot) - E_a(RX)$ and $I_p(X\cdot) - E_a(RY)$, where I_p and E_a are the ionisation potentials and electron affinities, respectively. They reflect the essence of the electronic reshuffle in S_N2 reactions, where a single electron shift is concomitant with the bond-breaking–bond-forming process. It follows that the barrier for the reaction can be expressed as a fraction (f) of the vertical electron transfer energy, from which the crossing avoidance (B) has been subtracted,

$$\Delta E^\ddagger = f[I_p(Y\cdot) - E_a(RX)] - B \quad (11.9)$$

Eq. (11.9) contains the physical essence of the activation process. The energy of activation arises from the molecular distortions that must attend the single electron shift ($Y \rightarrow X$) characterising the S_N2 reaction. The only manner by which such a

shift can take place is when energy equality between $\text{Y}^-(\text{R}-\text{X})$ and $\text{Y}^\bullet(\text{R}^\bullet-\text{X}^-)$ is attained. Since these two states are initially separated by an energy $I_p(\text{Y}^:) - E_A(\text{RX})$, their crossing must be achieved at the expense of molecular distortions that stabilise $\text{Y}^\bullet(\text{R}^\bullet-\text{X}^-)$ and simultaneously destabilise $\text{Y}^-(\text{R}-\text{X})$. The activation energy will then reflect the size of the vertical electron transfer energy and the resistance to molecular distortions, with the latter parameter being reflected by the value of f .

The value of the curvature factor f depends on the energy curve employed to derive eq. (11.9). For example, when straight lines are employed to connect the appropriate states of a symmetrical reaction, then $f = 0.5$. In contrast, if two identical parabolas are employed, then $f = 0.25$. In this case, a Marcusian-type (quadratic) expression is obtained, where the energy gap $I_p(\text{Y}^:) - E_A(\text{RX})$ replaces the intrinsic barrier $\Delta E^\ddagger(0)$ in the Marcus expression, eq. (7.6). Shaik associated the value of f to the extent of the “extra delocalisation” of the bonding odd electrons in the charge-transfer states. The extra delocalisation of the odd electrons causes a sluggish descent of the charge-transfer states towards their intersection point, and increases the f factor [13].

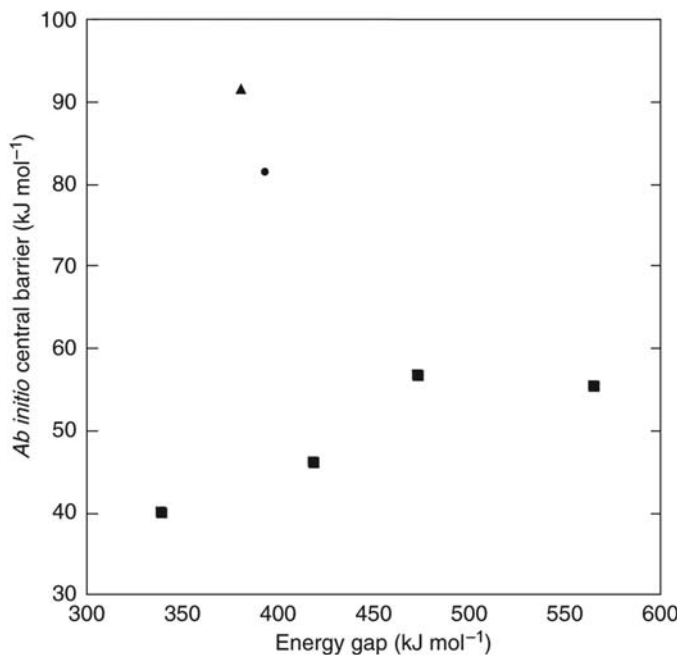
The state correlation diagrams of Pross and Shaik provide a very interesting insight into the nature of the reaction coordinate of $\text{S}_{\text{N}}2$ reactions. However, they cannot be used for quantitative estimates of the reaction rates. In fact, the simplest expectation from eq. (11.9), a correlation between the energy gap and the energy barrier, is not verified (Figure 11.10). More recently, Shaik and Shurki reproduced the intrinsic barriers of the halide series in calculations where the resonance term B was assumed to be dependent on the HOMO–LUMO orbital splitting and on the charge distribution at the TS [14]. The success of the Shaik–Pross state correlation diagram in predicting correctly the barriers of halide–methyl halide $\text{S}_{\text{N}}2$ identity reactions cannot be, at the moment, reduced to a simple, easy-to-use model or explanation [15].

11.6 Intersecting-state model

The formalism of the intersecting-state model (ISM) previously applied to atom-transfer reactions in Chapter 6, Reactivity in Thermalised Systems, can also be employed to interpret the trends observed in central barriers of gas-phase identity methyl transfer reactions [16]. The symmetry of such reactions offers the opportunity to use the simplest version of ISM. For harmonic oscillators and symmetric reactions, eq. (6.95) gives

$$l_{\text{XC}}^\dagger - l_{\text{XC}} = -2a'l_{\text{XC}}\ln(2) \quad (11.10)$$

$$\Delta V^\ddagger = 2 \frac{f}{m^2} [a'l_{\text{XC}}\ln(2)]^2 \quad (11.11)$$

**FIGURE 11.10**

Correlation between the energy gap [$I_P(Y:) - E_A(RX)$] and the central barrier of methyl transfers in the gas phase. The energy gap values were taken from Table 11.2 of Ref. [11], and the central barriers are from Table 11.2. (Squares: X = halogen atom; circles: X = CH_3O ; triangle: X = CH_3S .)

where $l_{\text{XC}}^{\ddagger} - l_{\text{XC}}$ represents the extension of the XC bond length from equilibrium to the TS, $a' = 0.183$, the electrophilicity index of Parr is

$$m = \frac{I_P + E_A}{I_P - E_A} \quad (11.12)$$

and the force constant is

$$f = 2D_e\beta^2 \quad (11.13)$$

with the spectroscopic constant β related to electronic dissociation energy of the CH_3-X bond, to the vibrational energy and to the reduced mass

$$\beta = \varpi_e \sqrt{\frac{2\pi^2 c \mu}{h D_e}} = 0.01332 \varpi_e \sqrt{\frac{\mu}{D_e}} \quad (11.14)$$

where the numerical value applied corresponds to the case when the masses are expressed in amu, the frequencies in per centimetre and energies in kJ mol^{-1} .

The data on the ionisation potentials (I_P) and electron affinities (E_A) of X and on the $\text{CH}_3\text{--X}$ bonds dissociation energies, bond lengths and vibrational frequencies of the systems represented in Table 11.2 can be found in Tables 11.1 and 11.3 of Appendix III, Parameters Employed in ISM Calculations [16]. Figure 11.11 compares the TS bond lengths calculated with eq. (11.10) with those obtained by *ab initio* calculations [17–19] for symmetrical reactions. The $\text{H}^- + \text{H}_2$ reaction is obviously not a methyl transfer reaction but it is the simplest $\text{S}_{\text{N}}2$ reaction and fits remarkably well with the other reactions. Moreover, the PES of this system has a central barrier of 48.4 kJ mol^{-1} [19] and eq. (11.11) gives 48.1 kJ mol^{-1} . This barrier is slightly higher than that calculated by ISM for the $\text{H} + \text{H}_2$ hydrogen-abstraction reaction presented in Table 6.5, 42.3 kJ mol^{-1} , because the present calculations employ the harmonic approximation rather than Morse curves to represent the reactive bonds. It seems that steric effects play a minor role in methyl transfers, but such effects increase with increasing methyl substitution at the central carbon. The reaction rates decrease when R in mechanism (11.I) changes in order methyl > ethyl > *iso*-propyl > *tert*-butyl. The steric effect of a *tert*-butyl group was calculated to raise the activation energy by 26 kJ mol^{-1} relative to methyl [20]. The scaling parameter $a' = 0.183$ is appropriate for H and CH_3 transfers but needs to be increased by 0.012 every time that an hydrogen atom in CH_3 is replaced by a methyl group [16]. It is interesting to note that in such cases, where the central carbon atom is bond to an alkyl group, base-induced elimination leading to a double CC bond, HY and X^- , competes with the $\text{S}_{\text{N}}2$ reaction.

Unfortunately, the values of I_P and E_A are not readily available for all the systems of Table 11.2. Nevertheless, Figure 11.12 presents the results obtained for a larger set of data than Figure 11.10, and shows that the ISM presents a good account of the central barriers in the gas phase. More importantly, these simple calculations reproduce the trends of the *ab initio* barriers: the central barriers change modestly along the last column and dramatically along the second row of the Periodic Table.

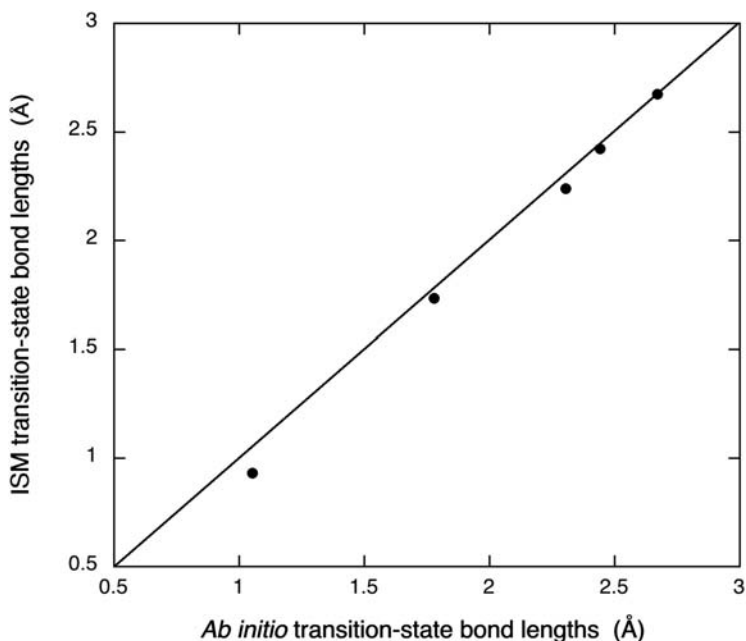
Table 11.3 Energies of activation for symmetrical exchange reactions in different media, in kJ mol^{-1} .

Reaction	ΔG^\ddagger (water)	ΔG^\ddagger (methanol)	ΔG^\ddagger (DMF)	ΔG^\ddagger (acetone)	$\Delta V_{\text{cl}}^\ddagger$ (gas) ^a	ΔG^\ddagger (gas) ^b
$\text{F}^- + \text{CH}_3\text{F}$	133				56	
$\text{Cl}^- + \text{CH}_3\text{Cl}$	111	118	95	91	57	
$\text{Br}^- + \text{CH}_3\text{Br}$	99	96	77	71	42	
$\text{I}^- + \text{CH}_3\text{I}$	97	88	67	68	40	
$\text{OH}^- + \text{CH}_3\text{OH}$	175					

Note: From Ref. [29] unless otherwise noted. DMF represents dimethylformamide.

^aCentral barriers from Ref. [15], without (ZPE) corrections.

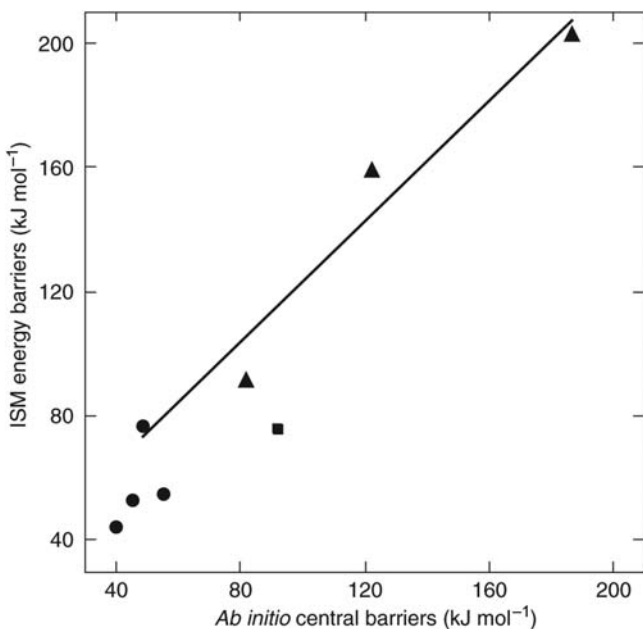
^bCentral free-energy barrier, obtained from the ZPE-corrected (G3 method) central barrier with the addition of the calculated (DFT method) entropy changes upon formation of ion–dipole complex, and TS, from the separated reactants, from Ref. [11].

**FIGURE 11.11**

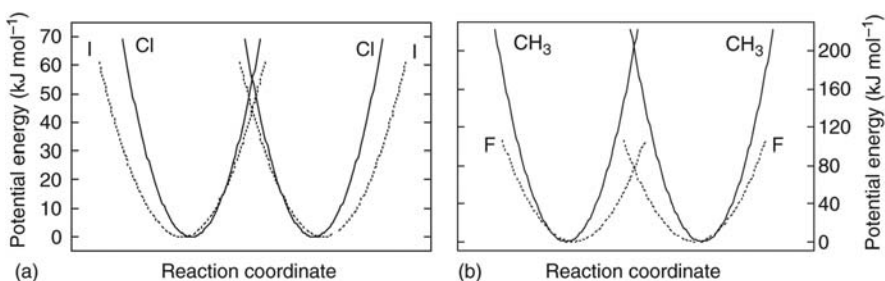
Comparison between ISM [16] and *ab initio* transition-state bond lengths [17–19] of symmetrical nucleophilic substitutions. The line is the ideal correlation.

The relative constancy of the central barrier within a column of the Periodic Table has a simple explanation in the framework of the ISM. As the atomic number increases along the series of halogens, the X–C bond lengths increase (1.351, 1.764, 1.951 and 2.027 Å), the corresponding force constants decrease (2950, 1740, 1410 and 1130 kJ mol⁻¹ Å⁻¹), while the electrophilicity indices remain approximately constant (1.493, 1.773, 1.796 and 1.828). Eq. (11.11) shows that, for a constant m , the decrease in f_{XC} is compensated by the increase in l_{XC} and the barriers remains approximately constant [13,16]. This compensation is illustrated in Figure 11.13.

The ISM also accommodates the decrease in central barrier along the second row of the Periodic Table. In this case the decrease in l_{XC} (1.512, 1.474, 1.404 and 1.351 Å) is not accompanied by a systematic trend in the corresponding force constants (2450, 3110, 2610 and 2950 kJ mol⁻¹ Å⁻¹), and the relative reactivity is dominated by the increase in m (0.938, 1.163, 1.343 and 1.493). Figure 11.13 offers a simple view of the effect of m on the energy barrier, by dividing f_{XC} by m^2 . It should always be remembered that this is only a schematic view, because the force constants near the minima are given by the spectroscopic properties of the bonds, while the full effect of m is only manifested at the TS.

**FIGURE 11.12**

Correlation between the central barriers of *ab initio* calculations given in Table 11.2, and the barriers of the ISM calculations under the harmonic approximation. (Triangles: X = halogen atom; circles: X = CH₃CH₂, CH₃NH, CH₃O; square: CH₃S. The line is the correlation between the barriers of the second row of the Periodic Table.)

**FIGURE 11.13**

- (a) Compensation between decreases in force constants and increases in bond lengths.
- (b) Effect of the electrophilicity index m on the TS, schematically represented by the division of the force constant by m^2 .

The beauty of this explanation undoubtedly lies in its straightforwardness and simplicity. Moreover, similar trends have been calculated for the transfer of the N(CH₃)₂ group [21] and confirmed by other authors [22], in support of the reactivity factors described above. At this level of simplicity, the ISM cannot provide

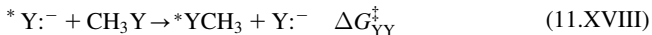
a complete explanation for all the observations, and its success is probably due to a compensation of errors. For example, the central barriers tend to be underestimated when Morse curves, rather than harmonic oscillators, are employed in the calculations. The harmonic oscillators compensate for the original scaling of the ISM to the H + H₂ atom abstraction.

11.7 Cross-reactions in methyl group transfers in the gas phase

The separation between the intrinsic contribution to the reaction barrier of a symmetric reaction ($\Delta G^0 = 0$) and the thermodynamic contribution that is present when $\Delta G^0 \neq 0$ was initially formulated by Rudolph Marcus in the context of electron transfer reactions, to be discussed in Chapter 17, Electron Transfer Reactions. This separation was shown in Chapter 7, Relationships between Structure and Reactivity, to yield quadratic free-energy relationships. It has also been used in substitution reactions to relate the free energy of activation of the cross-reaction



to the free energies of activation of the symmetrical exchanges



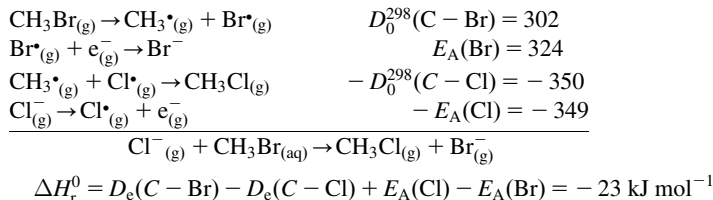
according to the expression

$$\Delta G_{\text{YX}}^\ddagger = \Delta G_{\text{YX}}^{\ddagger 0} \left(1 + \frac{\Delta G_{\text{YX}}^0}{4\Delta G_{\text{YX}}^{\ddagger 0}} \right)^2 \quad (11.15)$$

where

$$\Delta G_{\text{YX}}^{\ddagger 0} = \frac{1}{2} \left(\Delta G_{\text{XX}}^\ddagger + \Delta G_{\text{YY}}^\ddagger \right) \quad (11.16)$$

The reaction energy of a cross-reaction can be obtained from the difference in bond dissociation energies and electron affinities of the two reaction partners. For example,



However, this is not the directly relevant reaction energy for the central barrier, because the energetic separation between the minima of the precursor and successor complexes may not correspond to the energetic separation between the isolated reactants and the products. For the case of the reaction illustrated above, the complexation energies of $\text{Cl}^- \cdots \text{CH}_3\text{Br}$ and $\text{Br}^- \cdots \text{CH}_3\text{Cl}$ are 52 and 46 kJ mol^{-1} , respectively, and the energetic separation between the complexes is only 6 kJ mol^{-1} less exothermic than ΔH_r^0 . When the difference between complexation energies is small, as in the case of alkylhalide–halide ions [10,23], it is legitimate to expect that the global free energy of the reaction is reflected by the central barrier, and that the free-energy relationships discussed in Chapter 7, Relationships between Structure and Reactivity, may apply. This is approximately the case for the cross-reactions between halide ions such as $\text{Cl}^-/\text{CH}_3\text{Br}$ and $\text{F}^-/\text{CH}_3\text{Cl}$, where the reaction exothermicity increases from -23 to -147 kJ mol^{-1} , with a concomitant decrease of the experimental central barrier from 45 kJ mol^{-1} [23] to a value estimated to be between 24 and 33 kJ mol^{-1} [24]. ISM calculations using the harmonic approximation and the global reaction energy reproduce these barriers relatively well, giving 41 and 21 kJ mol^{-1} , respectively, when the average value of m of the halogens involved is employed, $m_{YX} = (m_{YY} + m_{XX})/2$ [16].

The success of this approach to gas-phase methyl transfers is very limited. For example, Figure 11.14 illustrates the reaction energy profile of the $\text{F}^- + \text{CH}_3\text{SH}$ methyl transfer and shows that the overall reaction is exothermic, $\Delta H_r^0 = -48$ kJ mol^{-1} , but the central barrier is placed between the two minima corresponding to ion–molecule complexes whose endothermic conversion requires $\Delta V_{ad}^0 = 75$ kJ mol^{-1} [25]. Although the reaction energy, measured for the separated products to the separated reactants, is moderately exothermic, the actual reaction involves a precursor and successor complex that must be regarded as the reaction intermediates. The conversion between these two intermediates is an elementary reaction, and is endothermic because the electrostatic stabilisation in

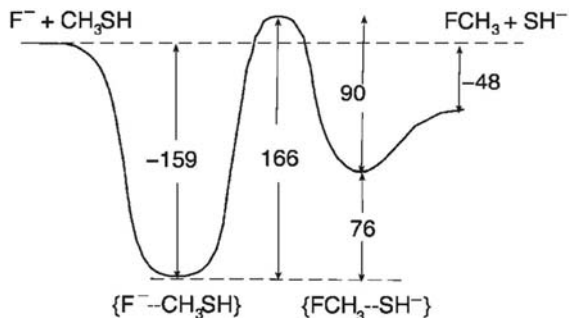


FIGURE 11.14

Reaction energy profile of the $\text{F}^- + \text{CH}_3\text{SH}$ methyl transfer in the gas phase. The energies were obtained by *ab initio* methods by Schaefer and co-workers, and include zero-point energy (ZPE) corrections [25].

the $\text{F}^- + \text{CH}_3\text{SH}$ complex is stronger than in the $\text{HS}^- + \text{CH}_3\text{F}$ complex. The barrier calculated for the elementary reaction is high, $\Delta V_{\text{ad}}^\ddagger = 166 \text{ kJ mol}^{-1}$ [25], as expected for an endothermic reaction, but the energy of the TS is only 18 kJ mol^{-1} above that of the separated reactants. Marcus cross-relation gives a better prediction of net barriers (i.e., the difference between TS and isolated reactants energies) than of central barriers (i.e., the difference between TS and precursor complex energies) [26].

There are several lessons to be learnt from this example. First, free-energy relationships can only be applied to elementary reactions; otherwise they will fail or fortuitously give the correct results owing to compensation of factors. Second, the presence of a stable intermediate may reduce the experimental activation energy, and may even lead to a negative activation energy, but that does not mean that high-energy barriers do not exist along the reaction path in the conversion between the intermediates. Finally, the presence of two complexes separated by a barrier suggests that their conversion resembles that of a unimolecular reaction and that the experimental data corresponding to this mechanism should be evaluated with the Rice–Rampsberger–Kassel–Marcus (RRKM) theory. In fact, RRKM calculations have been remarkably successful in describing the kinetics of three-bodied ion–molecule association reactions [27], but non-statistical behaviour, where the vibrational energy is not rapidly and randomly distributed among the vibrational modes, is also known [28]. In such cases, the deep attractive well is “flown over” and the well is irrelevant in computing rate constants.

The mechanistic complexity of $\text{S}_{\text{N}}2$ reactions is removed in aqueous solutions. The solvation of the attacking nucleophile reduces the energy of the reactants below that of the complex, and the reaction occurs in a single step, with concerted bond breaking and bond making.

11.8 Solvent effects in methyl group transfers

The rate constant for the symmetrical methyl transfer between I^- and CH_3I varies with change of solvent, and has values at 298 K (in $\text{M}^{-1} \text{ sec}^{-1}$) ranging from 5.1×10^{-4} in water to 3.2×10^{-3} in methanol and 8.0 in acetone, and is expected to exceed 10^9 in the gas phase [29]. This change in the rate is clearly related to the polarity of the solvent. Another way of looking at this effect is to consider the free energies of activation, ΔG^\ddagger , in the different media (Table 11.3; [29]). It is important to emphasise that the energy data in solution are not (adiabatic or electronic) potential energies, but free energies. Such free energies are estimated from the rate constants using the pre-exponential factor of the transition state theory in its thermodynamic formulations, $k_{\text{B}}T/h$. They are not directly comparable with the potential energies presented for gas-phase reactions, which do not include entropy changes. Fortunately, the entropy changes along the reaction path of the $\text{Cl}^- + \text{CH}_3\text{Cl}$ have been calculated with high accuracy by *ab initio* methods [9], and provide a term for comparison.

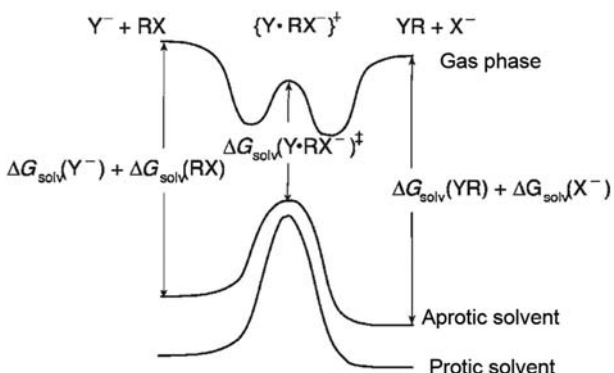


FIGURE 11.15

Solvent effect on the energy profiles of methyl transfer reactions.

The effect of the solvent on methyl group transfers is illustrated in Figure 11.15. In Figure 11.5, we had already shown that the consideration of entropy changes reduces the energy difference between the reactants and the precursor complex, as well as between the products and the successor complex. Now, we also have to consider that the ionic nature of the reactants and products facilitates their solvation to higher degree than in these complexes. As a result, in a sufficiently polar solvent such as water, these complexes disappear from the reaction coordinate, and the methyl group transfer becomes an elementary reaction.

The TS is of lower polarity than the reactants and the products. Thus in polar solvents, it rises in energy with respect to the reactants, and to a higher degree than the precursor and the successor complexes. This can be verified for the $\text{Cl}^- + \text{CH}_3\text{Cl}$ reaction, where the internal free-energy barrier in the gas phase is smaller than the free-energy barrier in solution. For identity transfers, where $\Delta G^0 = 0$, the changes in solvation energy are relatively independent of the nature of the reactants, and the reactivity trends observed for gas-phase reactions are also observed in solution. In fact, from $\text{Cl}^- + \text{CH}_3\text{Cl}$ to $\text{I}^- + \text{CH}_3\text{I}$ there is a *ca.* 20% decrease in the free-energy barrier, similar to that calculated for $\Delta V_{\text{cl}}^\ddagger$ in the gas phase. Also, the free energy of activation of the $\text{OH}^- + \text{CH}_3\text{OH}$ exchange in water is much higher than the self-exchanges involving halide ions, a trend also observed in the gas phase. The recognition of the same reactivity patterns in symmetrical methyl transfers in the gas phase and in solution, suggests that the explanation offered by the ISM for such patterns in the gas phase is also applicable to solution. However, a quantitative account of the free-energy barriers in different solvents requires a solvent-dependent parameter in the model, because the rate of a given reaction may change by several orders of magnitude with a change in solvent.

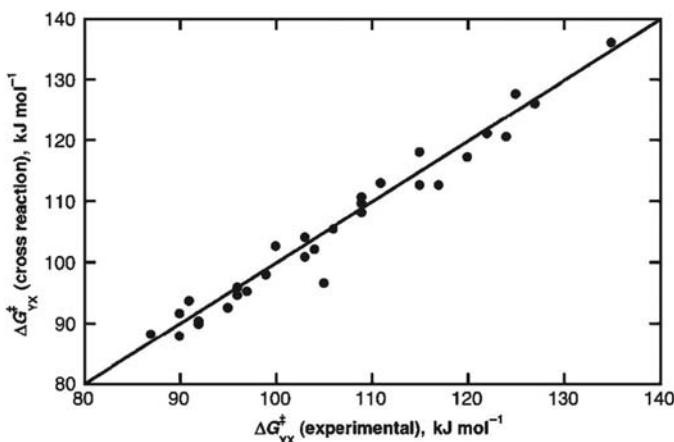
The comparison between gas phase and solution becomes even more convoluted when cross-reactions are considered. For example, the rate of the $\text{Cl}^- + \text{CH}_3\text{Br}$ reaction, at 298 K (in $\text{M}^{-1} \text{ sec}^{-1}$), decreases from 8×10^9 in the gas phase, to 0.4

in dimethylformamide (DMF), 6×10^{-6} in methanol, and reaches 5×10^{-6} in water [30]. We have seen that this reaction is exothermic in the gas phase. The difference in free energies of formation in aqueous solution, at 298 K in kJ mol^{-1} , of CH_3Cl (-57) and CH_3Br (-24), almost compensates those of Cl^- (-131) and Br^- (-104), and the exothermicity of this reaction in aqueous solution, $\Delta G^0 = -6 \text{ kJ mol}^{-1}$, is comparable with the value given previously for the gas phase [29]. Clearly, the minor decrease in exothermicity for the gas phase to solution cannot justify the 15 orders of magnitude change in the methyl transfer rate.

In addition to the striking difference in absolute rates in different media, there are differences and reversals in relative rates. For instance, the halogen nucleophilic order is changed from $\text{F}^- > \text{Cl}^- > \text{Br}^- > \text{I}^-$ in the gas phase and polar aprotic solvents such as acetone and DMF, to $\text{I}^- > \text{Br}^- > \text{Cl}^- > \text{F}^-$ in protic solvents such as methanol and water [30]. The enthalpies of transfer from dimethylsulphoxide (polar aprotic solvent) to methanol are, at 298 K in kJ mol^{-1} , Cl^- (-10.4), Br^- (-0.4) and I^- (11.3). The increase in the relative solvation of the smaller halides in methanol is enough to reverse their order of reactivity, since the solvation of the TSs is not as sensitive to solvent changes as the solvation of the reactant anions [30].

The fact that methyl transfers in water are elementary reactions suggests that they should be a better ground to test the applicability of free-energy relationships in $\text{S}_{\text{N}}2$ reactions. Albery and Kreevoy made an extensive study of methyl transfers having the ions PhSO_3^- , NO_3^- , F^- , Cl^- , Br^- , I^- , CN^- , OH^- as nucleophiles as well as leaving groups, and attempted to interpret their free-energy dependence using the Marcus cross-reaction scheme. They also considered the substitution by the water molecule, which is involved in the hydrolysis of halogenomethanes. In the absence of information in most of the identity exchange reactions, they fitted the values of $\Delta G_{\text{XX}}^\ddagger$ and $\Delta G_{\text{YY}}^\ddagger$, to obtain the best agreement with $\Delta G_{\text{YX}}^\ddagger$, given the experimental reaction free energies, ΔG^0_{YX} . Some of the activation energies included in Table 11.3 were in fact obtained by this method. Figure 11.16 shows that the activation free energies calculated with the cross-relation are in good agreement with the experimental cross-reaction activation free energies. Such a good agreement is not totally expected because Marcus originally proposed the cross-reaction scheme for electron-transfer reactions, where the reaction coordinate involves the two reactants and the two products. In $\text{S}_{\text{N}}2$ reactions, this scheme is equivalent to saying that the properties of the C–X bond in the reactants and of the C–Y bond in the product are similar to the average of the C–X and C–Y bond properties. The assumption that the free-energy dependence is quadratic rather than linear is also reasonably followed in the exothermicity range of 200 kJ mol^{-1} covered by the systems selected by Albery and Kreevoy.

ISM calculations of $\text{S}_{\text{N}}2$ reaction rates in solution require the inclusion of solvent dependence in the model and an estimate of the pre-exponential factor of such bimolecular reactions. Pearson discussed the values of ionisation potentials and electron affinities in the gas phase and in solution, and concluded that gas-phase values should be used even in solution [4]. Although this applies reasonably

**FIGURE 11.16**

Comparison between the activation free energies calculated by the cross-reaction scheme and the experimental values, using data from Albery and Kreevoy [29].

well to neutral molecules, Contreras and co-workers showed that continuum solvent effects tend to attenuate the electrophilicity index of charged and ionic electrophiles [31]. Thus on going from the gas phase to a polar solvent, the parameters m should decrease. The extent of the attenuation is appropriately taken into account by the solvent acceptor number ($AN = 0$ for the gas phase), which measures the ability of solvents to interact with electron pairs from suitable donors [32]. A correlation was found between AN and the values of m that reproduce the Arrhenius activation energy of ${}^{\circ}\text{I}^- + \text{CH}_3\text{I}$ exchanges in solution and the central barrier in the gas phase [16]

$$m' = m \exp(-\delta AN) \quad (11.17)$$

where $\delta = 0.004$ is an empirical parameter. ISM with m' in the place of m becomes an empirical model capable of accounting for solvent effects.

The pre-exponential factor of bimolecular hydrogen-atom transfers was discussed in Chapter 6, Reactivity in Thermalised Systems, and, following the relation of eq. (6.82), it was shown to be $A_0 \approx 10^{10} \text{ M}^{-1} \text{ sec}^{-1}$ for atom + polyatomic systems. This factor is reduced by a power of the ratio of vibrational (q_v) to rotational (q_r) partition functions for diatomic + polyatomic and polyatomic + polyatomic systems. In general, the rate constant can be written with a simplified notation for the pre-exponential factor

$$k = A_0 \left(\frac{q_v}{q_r} \right)^j \exp \left(-\frac{\Delta V^{\ddagger}}{RT} \right) \quad (11.18)$$

where $(q_v/q_r) \approx 1/3$ and $j = 0, 2, 3$ when the nucleophile is an atom (or monoatomic ion), a diatomic or a polyatomic species.

The calculation of S_N2 reaction rates when reactant and product bonds are represented by harmonic oscillators, is conveniently made using the relations

$$V_{\text{CX}}(1-n) = V_{\text{CY}}(n) + \Delta V_0 \quad (11.19)$$

$$V_{\text{CX}}(1-n) = \frac{1}{2}f_{\text{CX}} \left[\frac{a'(l_{\text{CX}} + l_{\text{CY}})\ln(1-n)}{m'_{YX}} \right]^2$$

$$V_{\text{CY}}(n) = \frac{1}{2}f_{\text{CY}} \left[\frac{a'(l_{\text{CX}} + l_{\text{CY}})\ln(n)}{m'_{YX}} \right]^2 \quad (11.20)$$

Figure 11.17 compares rate constants calculated with eqs. (11.17)–(11.20) [16] with experimental data at 25 °C. The calculations assumed $\Delta V^0 = \Delta G^0$ and employed the reaction energies reported by Albery and Kreevoy [33] or estimated from the ratios of forward and reverse reactions [34,35]. The agreement is remarkably good but it must be remembered that the value of m' benefits from an empirical correlation with the donor number of the water and acetone.

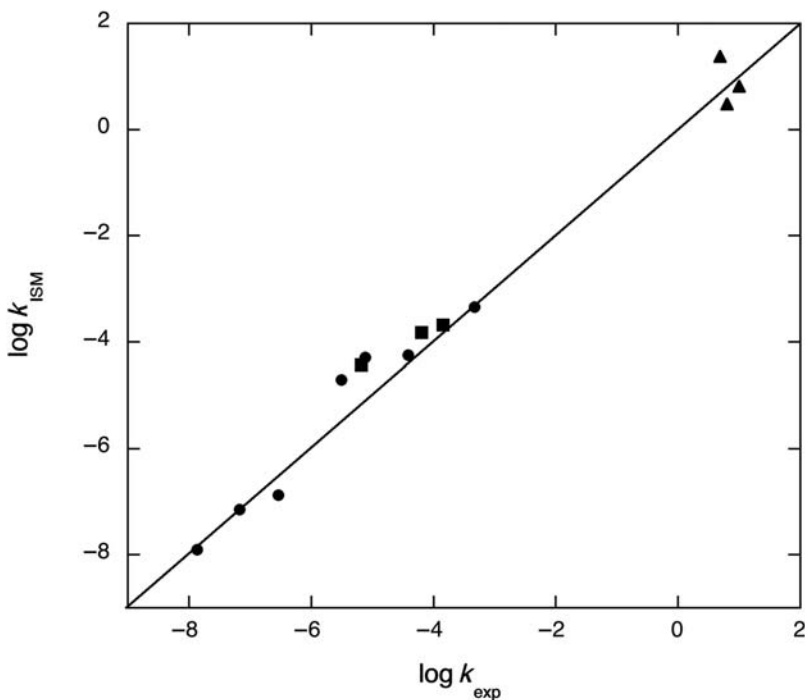


FIGURE 11.17

Comparison between ISM and experimental methyl transfers rate constants in water (squares and circles) and in acetone (triangles) at 298 K. Circles and triangles: $\text{X}^- + \text{CH}_3\text{X}$; squares: $\text{OH}^- + \text{CH}_3\text{X}$; in all cases, $\text{X} = \text{F}, \text{Cl}, \text{Br}, \text{I}$. The line is the ideal correlation.

It is interesting to illustrate the calculated solvent effect with an example. The rate constant of the $\text{Cl}^- + \text{CH}_3\text{I}$ methyl exchange increase from $3.2 \times 10^{-6} \text{ M}^{-1} \text{ sec}^{-1}$ in water to $5.1 \text{ M}^{-1} \text{ sec}^{-1}$ in acetone [35] while the reaction energies change from $\Delta G^0 = 4.6$ to $-20.5 \text{ kJ mol}^{-1}$. The corresponding ISM rates are $1.9 \times 10^{-5} \text{ M}^{-1} \text{ sec}^{-1}$ in water to $24 \text{ M}^{-1} \text{ sec}^{-1}$ in acetone [16]. Hence ISM reproduces the 6 order of magnitude increase in the rates. However, changing the reaction energy without changing m' only gives a two-fold increase in the rate in acetone relative to water. The increase from $m' = 1.446$ in water to 1.712 in acetone is responsible for four orders of magnitude increase in the rate. A similar sensitivity to changes in the electrophilicity parameter was identified in the context of the Ritchie relation, eq. (7.32), for the recombination of a nucleophile with a carbon cation. When the AN is high (e.g., water), the electron inflow at the TS saturates at a lower point because part of the electron density of the nucleophile is coupled to the solvent, leading to a lower value of m . The result is less resonance at TSs in solvents with high AN, hence higher barriers. This is a static solvent effect that in $\text{S}_{\text{N}}2$ reactions is more important than the thermodynamic effect of the solvent in the reaction energy.

References

- [1] JA Le Bel, *J. Chim. Phys.* **9** (1911) 323.
- [2] ED Hughes, CK Ingold, CS Patel, *J. Chem. Soc.* (1933) 526.
- [3] CK Ingold, *Structure and Mechanism in Organic Chemistry*, Cornell University Press, Ithaca, NY, 1969.
- [4] RG Pearson, *J. Am. Chem. Soc.* **108** (1986) 6109.
- [5] RC Weast (Ed.), *CRC Handbook of Chemistry and Physics*, CRC Press, Boca Raton, FL, 1983.
- [6] CH Langford, HB Gray, *Ligand Substitution Processes*, Benjamin, New York, 1965.
- [7] RD Guthrie, *Pure Appl. Chem.* **61** (1989) 23.
- [8] S Wolfe, DJ Mitchell, MT Bowers, *J. Am. Chem. Soc.* **103** (1981) 7694.
- [9] ST Gravel, MT Bowers, *J. Am. Chem. Soc.* **113** (1991) 9696.
- [10] RC Dougherty, JD Roberts, *Org. Mass Spectrom.* **8** (1974) 81.
- [11] S-Y Yang, P Fleurat-Lessard, I Hristov, T Ziegler, *J. Phys. Chem. A* **108** (2004) 9461.
- [12] SS Shaik, A Pross, *J. Am. Chem. Soc.* **104** (1982) 2708.
- [13] SS Shaik, *Prog. Phys. Org. Chem.* **15** (1985) 197.
- [14] SS Shaik, A Shurki, *Angew. Chem. Int. Ed.* **38** (1999) 586.
- [15] S Hoz, H Basch, JL Wolk, T Hoz, E Rozental, *J. Am. Chem. Soc.* **121** (1999) 7724.
- [16] LG Arnaut, SJ Formosinho, *Chem. Eur. J.* **13** (2007) 8081.
- [17] E Uggerud, *Chem. Eur. J.* **12** (2006) 1127.
- [18] MN Glukhovtsev, A Pross, L Radom, *J. Am. Chem. Soc.* **117** (1995) 2024.
- [19] M Ayouz, O Dulieu, R Guérout, J Robert, V Kokouline, *J. Chem. Phys.* **132** (2010) 194309.
- [20] TA Hamlin, M Swart, FM Bickelhaupt, *ChemPhysChem* **19** (2018) 1315.
- [21] R Yi, H Basch, S Hoz, *J. Org. Chem.* **67** (2002) 5891.

- [22] E Uggerud, *Adv. Phys. Org. Chem.* **51** (2017) 1.
- [23] C Li, P Ross, JE Szulejko, TB McMahon, *J. Am. Chem. Soc.* **118** (1996) 9360.
- [24] MJ Pellerite, JI Brauman, *J. Am. Chem. Soc.* **105** (1983) 2672.
- [25] JM Gonzales, RS Cox, III, ST Brown, WD Allen, HF Schaefer, III, *J. Phys. Chem. A* **105** (2001) 11327.
- [26] JM Gonzales, WD Allen, HF Schaefer, III, *J. Phys. Chem. A* **109** (2005) 10613.
- [27] BD Wladkowski, KF Lim, WD Allen, JI Brauman, *J. Am. Chem. Soc.* **114** (1992) 9136.
- [28] L Sun, K Song, WL Hase, *Science* **296** (2002) 875.
- [29] J Albery, MM Kreevoy, *Adv. Phys. Org. Chem.* **16** (1978) 87.
- [30] WN Olimstead, JI Brauman, *J. Am. Chem. Soc.* **99** (1977) 4219.
- [31] P Pérez, A Toro-Labbé, R Contreras, *J. Am. Chem. Soc.* **123** (2001) 5527.
- [32] AJ Parker, U Mayer, R Schmid, V Gutmann, *J. Org. Chem.* **43** (1978) 1843.
- [33] J Albery, MM Kreevoy, *Adv. Phys. Org. Chem.* **16** (1978) 1333.
- [34] EA Moelwyn-Hughes, *The Chemical Statics and Kinetics of Solutions*, Academic Press, London, 1971.
- [35] AJ Parker, *Chem. Rev.* **69** (1969) 1.
- [36] S Parthiban, G De Oliveira, JML Martin, *J. Phys. Chem. A* **105** (2001) 895.

Chain reactions

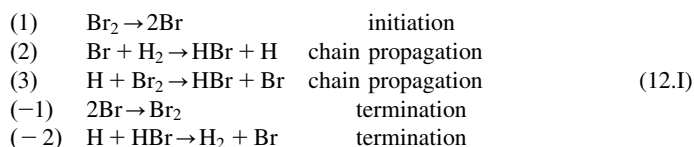
12

Open shell atoms and other molecular species that act as *free radicals* play a special role as intermediates in reaction mechanisms. Because they have incomplete electron shells they are usually highly reactive, even with stable molecules at ordinary temperatures. The concentrations of such free radicals in these reaction systems are usually low and the application of the *steady-state hypothesis* to them is valid.

In *chain reactions*, free radicals bring about chemical processes such as abstraction when they react with a molecule, producing new atoms and radicals, which can then bring about further reactions. Figure 12.1 displays a sequence of steps for chain reactions involving halogens and molecular hydrogen: (1) *initiation* step which produces the chain carriers, R_i ; (2) *propagation* steps in which chain carriers recycle and thus catalyse the conversion of reactants, Q , to products; (3) *termination* steps which remove the intermediates [1].

12.1 Hydrogen–bromine reaction

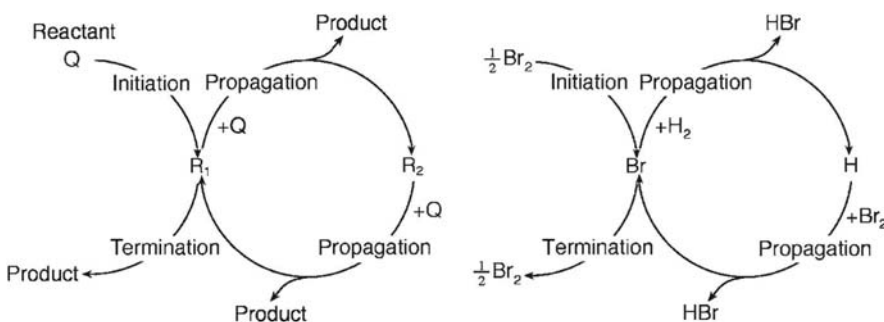
The mechanism for the reaction between Br_2 and H_2 was proposed in 1916 independently by Christiansen [2], Herzfeld [3,4] and Polanyi [5]. The basic steps are



This mechanism has an initiation step (1) one termination step (−1) and a pair of propagation steps (2) and (3). There is an additional step of termination (−2), which accounts for the inhibition by HBr seen experimentally.

As shown in Table 12.1 the rates of the propagation steps are much greater than those of the initiation or the termination processes, which have negligible contributions to the overall rate. In the propagation steps, atoms are formed and consumed. One needs to obtain expressions for their concentrations, which is most frequently done through the steady-state hypothesis.

As we have seen for the reaction between Br_2 and H_2 , once a mechanism is postulated for a chain reaction, the sequential nature of the different steps, in closed cycles, leads to some repetition of the rate laws in the differential equations

**FIGURE 12.1**

Reaction between halogens and molecular hydrogen.

Table 12.1 Experimental rate constants for the different elementary steps of the reaction between $\text{H}_2 + \text{Br}_2$, at 1 atm, 500 K and $[\text{M}] \approx 0.025 \text{ M}$.

Reaction	Step	k ($\text{dm}^3 \text{ mol}^{-1} \text{ sec}^{-1}$)	Step no.
$\text{Br}_2 + \text{M} \rightarrow 2\text{Br} + \text{M}$	Initiation	$3.8 \times 10^{-8} [\text{M}]$	(1)
$2\text{Br} + \text{M} \rightarrow \text{Br}_2 + \text{M}$	Termination	$4.2 \times 10^{-13} [\text{M}]$	(-1)
$\text{Br} + \text{H}_2 \rightarrow \text{HBr} + \text{H}$	Propagation	960	(2)
$\text{H} + \text{HBr} \rightarrow \text{H}_2 + \text{Br}$	Inhibition	7.2×10^9	(-2)
$\text{H} + \text{Br}_2 \rightarrow \text{HBr} + \text{Br}$	Propagation	9.6×10^{10}	(3)

established for each atom or radical. This means that mathematical simplifications, involving addition or subtraction, can be introduced into these equations.

By applying the steady-state hypothesis to the two intermediates Br and H, both of which are present at very low concentrations, we can write

$$\frac{d[\text{H}]}{dt} = k_2[\text{Br}][\text{H}_2] - k_3[\text{H}][\text{Br}_2] - k_{-2}[\text{H}][\text{HBr}] = 0 \quad (12.1)$$

$$\frac{d[\text{Br}]}{dt} = 2k_1[\text{Br}_2] - k_2[\text{Br}][\text{H}_2] + k_3[\text{H}][\text{Br}_2] + k_{-2}[\text{H}][\text{HBr}] - 2k_{-1}[\text{Br}]^2 = 0 \quad (12.2)$$

By adding these two equations, a solution for [Br] is obtained

$$2k_1[\text{Br}_2] - 2k_{-1}[\text{Br}]^2 = 0 \quad (12.3)$$

and therefore

$$[\text{Br}] = \left(\frac{k_1}{k_{-1}} \right)^{1/2} [\text{Br}]^{1/2} \quad (12.4)$$

Substituting [Br] in eq. (12.1) gives

$$k_2 \left(\frac{k_1}{k_{-1}} \right)^{1/2} [\text{Br}_2]^{1/2} [\text{H}_2] - k_3 [\text{H}] [\text{Br}_2] - k_{-2} [\text{H}] [\text{HBr}] = 0 \quad (12.5)$$

which can be rearranged mathematically to give

$$[\text{H}] = \frac{k_2(k_1/k_{-1})^{1/2}[\text{Br}_2]^{1/2}[\text{H}_2]}{k_3[\text{Br}_2] + k_{-2}[\text{HBr}]} \quad (12.6)$$

The rate of reaction, in terms of the disappearance of H_2 , is

$$v = \frac{d[\text{H}_2]}{dt} = k_2[\text{Br}][\text{H}_2] - k_{-2}[\text{H}][\text{HBr}] \quad (12.7)$$

Subtracting this expression from eq. (12.1) leads to

$$v = k_3[\text{H}][\text{Br}_2] \quad (12.8)$$

Rewriting eq. (12.6) in the light of eq. (12.8), we have the expression for the rate of reaction

$$v = \frac{k_3k_2(k_1/k_{-1})^{1/2}[\text{Br}_2]^{3/2}[\text{H}_2]}{k_3[\text{Br}_2] + k_{-2}[\text{HBr}]} \quad (12.9)$$

or

$$v = \frac{k_2(k_1/k_{-1})^{1/2}[\text{Br}_2]^{1/2}[\text{H}_2]}{1 + (k_{-2}[\text{HBr}]/k_3[\text{Br}_2])} \quad (12.10)$$

This is in good agreement with the empirical rate law [6]

$$v = \frac{k[\text{Br}_2]^{1/2}[\text{H}_2]}{1 + (c[\text{HBr}]/[\text{Br}_2])} \quad (12.11)$$

where k and c are constants; the value of c is *ca.* 10 and is virtually independent of temperature. The circumstance that Br_2 and HBr are both in competition for the H atoms accounts for the fact that the inhibitory effect of HBr decreases with an increase of $[\text{Br}_2]$. This provides a good rationale for the appearance of $[\text{HBr}]/[\text{Br}_2]$ in the denominator of the rate law.

This mechanism has a unique feature for chain reactions. $[\text{Br}]$ is identical to the equilibrium concentration, $\text{Br}_2 \rightleftharpoons 2\text{Br}$ ($\Delta H^0 = 194 \text{ kJ mol}^{-1}$). In contrast, for example, in the decomposition reaction of ethane, $[\text{C}_2\text{H}_5]$ is much higher than the concentration of the equilibrium $\text{C}_2\text{H}_6 \rightleftharpoons \text{C}_2\text{H}_5 + \text{H}$ ($\Delta H^0 = 410 \text{ kJ mol}^{-1}$), since the initiation of the decomposition of ethane is much more endothermic than the equivalent step for bromine. The circumstance that $[\text{Br}]$ is an equilibrium concentration implies that the overall rate of reaction is independent of the presence of any catalyst or of a foreign body, M , present in the activation or in the deactivation steps of bromine, $\text{Br}_2 + M \rightleftharpoons 2\text{Br} + M$.

Eq. (12.10) reveals that at the beginning of the reaction, when $[\text{HBr}]$ is low, the following rate law is valid

$$v = k_2 \left(\frac{k_1}{k_{-1}} \right)^{1/2} [\text{Br}_2]^{1/2} [\text{H}_2] \quad (12.12)$$

Table 12.2 Activation energies, in kJ mol^{-1} , for the elementary reactions between halogens and hydrogen, at 500 K.

Reaction	Cl	Br	I
(1) $X_2 \rightarrow 2X$	245	195	154
(−1) $2X \rightarrow X_2$	0	0	0
(2) $X + H_2 \rightarrow HX + H$	18.8	72.5	135.5
(−2) $H + HX \rightarrow H_2 + X$	14.6	3.0	5.5
(3) $H + X_2 \rightarrow HX + X$	2.9	2.4	2.3
(4) $X_2 + H_2 \rightarrow 2HX$	170	178	205
$E_a = E_2 + (\frac{1}{2})(E_1 - E_{-1})$	141	170	213
$E_4 - E_a$	29	8	-8

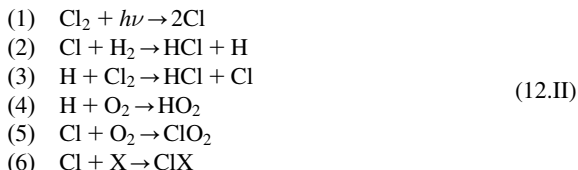
Under such conditions the activation energy is

$$E_a = E_2 + \frac{1}{2}(E_1 - E_{-1}) \quad (12.13)$$

As will be discussed in [Section 12.4](#), the activation energies of the different elementary steps of the mechanism calculated through the intersecting-state model (ISM), and displayed in [Table 12.2](#), give a value of E_a ($E_a = 170 \text{ kJ mol}^{-1}$) extremely close to that reported by Laidler for this reaction, $E_a = 168 \text{ kJ mol}^{-1}$ [7].

12.2 Reaction between molecular hydrogen and chlorine

The thermal and photochemical reactions between molecular hydrogen and chlorine show some resemblance to the hydrogen–bromine reactions, but the mechanisms are more complex. Since it is easier to understand its main features, we will consider first the photochemical reaction. The mechanism has to account for the profound effect of oxygen on the rates [8],



where X is a species capable of removing the chlorine atoms. The chain ending step $2\text{Cl} \rightarrow \text{Cl}_2$ is not taken into consideration, because the chlorine radicals are removed more effectively by reactions (5) and (6). In fact, since chlorine recombination is a second-order process with respect to Cl, the rate is very low when $[\text{Cl}]$ is low, which is the general case within the present mechanism.

The concentration of chlorine atoms $[\text{Cl}]$ in this mechanism is much lower than that of $[\text{Br}]$ in the H_2/Br_2 reaction. This is a direct consequence of the lower

activation energy of $\text{Cl} + \text{H}_2 \rightarrow \text{HCl} + \text{H}$ when compared with E_a of $\text{Br} + \text{H}_2 \rightarrow \text{HBr} + \text{H}$, as will be discussed in [Section 12.4](#).

The rate of Cl formation in step (1) is $2I$, where I is the intensity of the absorbed light in appropriate units, because two radicals are formed for each absorbed photon. This rate has the following expression:

$$\frac{d[\text{Cl}]}{dt} = 2I - k_2[\text{Cl}][\text{H}_2] + k_3[\text{H}][\text{Cl}_2] - k_5[\text{Cl}][\text{O}_2] - k_6[\text{Cl}][\text{X}] = 0 \quad (12.14)$$

Under stationary conditions for H atom we have

$$\frac{d[\text{H}]}{dt} = k_2[\text{Cl}][\text{H}_2] - k_3[\text{H}][\text{Cl}_2] - k_4[\text{H}][\text{O}_2] = 0 \quad (12.15)$$

from which it follows that

$$[\text{Cl}] = \frac{k_3[\text{H}][\text{Cl}_2] + k_4[\text{H}][\text{O}_2]}{k_2[\text{H}_2]} \quad (12.16)$$

Introduction of this expression into [eq. \(12.14\)](#), neglecting the small quadratic term in $[\text{O}_2]$, leads to

$$[\text{H}] = \frac{2Ik_2[\text{H}_2]}{k_3k_6[\text{Cl}_2][\text{X}] + [\text{O}_2](k_2k_4[\text{H}_2] + k_3k_5[\text{Cl}_2] + k_4k_6[\text{X}])} \quad (12.17)$$

The rate of formation of the product HCl is then

$$v = \frac{d[\text{HCl}]}{dt} = k_2[\text{Cl}][\text{H}_2] + k_3[\text{H}][\text{Cl}_2] \quad (12.18)$$

Subtraction of [eq. \(12.15\)](#) from [eq. \(12.18\)](#) leads to an expression for the rate law for the H_2/Cl_2 photochemical reaction that can be inserted into [eq. \(12.17\)](#) to give

$$v = \frac{2Ik_2k_3[\text{H}_2][\text{Cl}_2]}{k_3k_6[\text{Cl}_2][\text{X}] + [\text{O}_2](k_2k_4[\text{H}_2] + k_3k_5[\text{Cl}_2] + k_4k_6[\text{X}])} \quad (12.19)$$

The thermal reaction has some additional complications owing to the fact that the decomposition of Cl_2 can take place on the surface of the reaction vessels. The rate law assumes the general form

$$\frac{d[\text{HCl}]}{dt} = \frac{k'[\text{H}_2][\text{Cl}_2]^2}{c_1[\text{Cl}_2] + [\text{O}_2]([\text{H}_2] + c_2[\text{Cl}_2])} \quad (12.20)$$

Here k' , c_1 and c_2 are constants. This expression can be rationalised in terms of a preferential termination step on the surface vessel. This is no longer valid in the presence of O_2 .

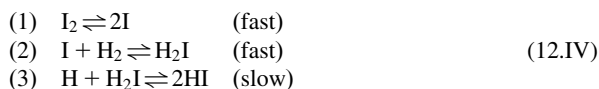
12.3 Reaction between molecular hydrogen and iodine

The reaction between H_2 and I_2 was extensively studied by Bodenstein [9–11] at the end of the nineteenth century. For many years, it was considered to be a true

bimolecular reaction. However, in 1959, Sullivan showed the presence of free radicals in the system above 600 K, leading to the proposed mechanism [12–14]



that is, a chain reaction. Once the intermediate HI is formed, it can be deactivated through the reverse process of step (2). In addition, it is also plausible that there is the formation of a linear transition state $\{\text{I}\cdots\text{H}\cdots\text{H}\cdots\text{I}\}^{\ddagger}$, which relates I and H_2I with the products, HI. The following mechanism includes the formation of intermediates of this type:



where the rate-determining step is step (3) and thus

$$v = k_3[\text{I}][\text{H}_2\text{I}] \quad (12.21)$$

Inserting the expressions for $[\text{I}]$ and $[\text{H}_2\text{I}]$, obtained from the equilibrium processes (1) and (2), one gets

$$v = k[\text{H}_2][\text{I}_2] \quad (12.22)$$

Here, $k = k_3K_2/K_1$. This mechanism, together with mechanism (12.III) and a few others, all appear to make contributions to the overall reaction. Another process that is almost certainly involved proceeds via the elementary step $\text{I}_2 + \text{H}_2 \rightarrow 2\text{HI}$, which proceeds via a transition state with a trapezoidal configuration.

This illustrates that a single reaction can often occur by more than one mechanism proceeding simultaneously. In general, there is no unique mechanism corresponding to a given empirical law, although under certain experimental conditions one may be dominant.

12.4 Calculation of energy barriers for elementary steps in hydrogen–halogen reactions

The calculation of the energy barriers for the elementary reactions between X and H_2 , H and HX and H and X_2 , which are involved in the mechanisms (12.I)–(12.III) has been presented in Chapter 6, Reactivity in Thermalised Systems. Using the ISM formalism and the structural parameters of Appendix III, Parameters Employed in ISM Calculations, data have been calculated for chlorine, bromine and iodine and are presented in Table 12.2.

The calculation of the energy barrier for the elementary reaction between molecular halogens and hydrogen,



presents some new challenges for a formal treatment, because one has to deal with the simultaneous breaking and formation of two chemical bonds. Figure 12.2 presents a transition state with a trapezoidal geometry for this kind of reaction.

The extension of each reactive bond from its equilibrium length up to the transition state can be estimated through a generalisation of eq. (6.60)

$$\begin{aligned} l_{AB}^* - l_{AB} &= -a'(l_{AB} + l_{CD} + l_{AC} + l_{BD}) \ln(n_{AB}^*) \\ l_{CD}^* - l_{CD} &= -a'(l_{AB} + l_{CD} + l_{AC} + l_{BD}) \ln(n_{CD}^*) \\ l_{AC}^* - l_{AC} &= -a'(l_{AB} + l_{CD} + l_{AC} + l_{BD}) \ln(n_{AC}^*) \\ l_{BD}^* - l_{BD} &= -a'(l_{AB} + l_{CD} + l_{AC} + l_{BD}) \ln(n_{BD}^*) \end{aligned} \quad (12.23)$$

Here one considers the sum of four equilibrium bond lengths, since this is the number of the reactive bonds in the transition state.

Making the assumption that the bond-forming–bond-breaking processes have a concerted nature, we can use the bond order of any one of the formed bonds as the reaction coordinate. As a consequence, we can write

$$n = n_{AC} = n_{BD} = 1 - n_{AB} = 1 - n_{CD} \quad (12.24)$$

The variation of the classical potential energy along the reaction coordinate can be obtained through generalisation of eq. (6.84) for the case of four reactive bonds, each one described by a Morse curve

$$V_{\text{MEP}}(n) = (1 - n)(V_{AB} + V_{CD}) + n(V_{AC} + V_{BD}) + n\Delta V^0 \quad (12.25)$$

where

$$\Delta V^0 = (D_{AB} + D_{CD}) - (D_{AC} + D_{BD}) \quad (12.26)$$

The modified functional form for each of the molecules of reactants and products is

$$V_{AB} = D_{AB}\{1 - \exp[-\beta(l - l_{AB})/m]\}^2 \quad (12.27)$$

In the same fashion, the electrophilicity index of the same molecules is obtained as given earlier [see eq. (6.70)]

$$m = \frac{I_p + E_A}{I_p - E_A} \quad (12.28)$$

Since the electron affinities of the atomic halogens are higher and the ionisation energies are lower than the corresponding values for H₂, the value of *m* is

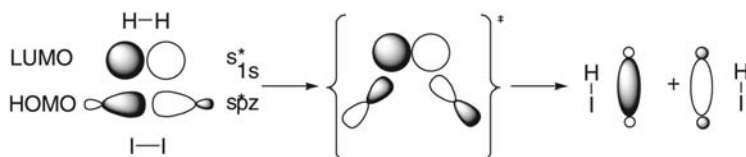


FIGURE 12.2

Reaction coordinate of reaction (12.15), illustrating the changes in the frontier orbitals.

determined by the electronic properties of the atomic halogen species (see [Appendix III](#), Parameters Employed in ISM Calculations).

The expression in [eq. \(12.25\)](#) can be calculated for all the values of n between 0 and 1, employing the Morse curve parameters for X_2 , H_2 and HX and the ionisation potentials and electronic affinities of X . The structural and electronic data required for the calculations are also given in [Appendix III](#), Parameters Employed in ISM Calculations. The maximum value of m allows one to estimate the classical potential energy barriers for the molecular reactions ([12.V](#)), without the use of any adjustable parameters. The results are compiled in [Table 12.2](#).

The energy barrier for the reactions $X_2 \rightarrow 2X$ is simply taken as the dissociation energy of the molecular species. Morse curves use potential energies at 0 K; hence we subtract the zero-point energy values from D_e and add $(3/2)RT$ to account for the differences in heat capacities between two atoms and a diatomic molecule. The final result is also given for each reaction in [Table 12.2](#).

We consider that the association processes $2X \rightarrow X_2$ with atoms have no activation barrier, as illustrated in [Figure 12.3](#). With more complex species such as free radicals where the translational energy can be converted into energy of some internal modes, the de-energisation of X_2^* can occur without the need for termolecular collisions with a foreign body (such as an inert gas, M).

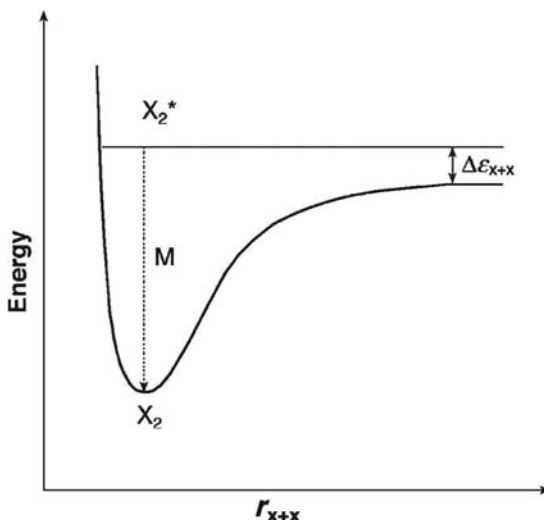


FIGURE 12.3

Potential energy curve for the recombination between atoms; $\Delta\epsilon_{x+x}$ is the kinetic energy of the collision between the atoms, and M represents a molecule that deactivates the vibrational energy of X_2^* .

12.5 Comparison of the mechanisms of the hydrogen–halogen reactions

Although chlorine, bromine and iodine are homologous, there are significant differences in the way they react with hydrogen. The first main difference is:

1. *The reaction between H₂ and I₂ is largely a molecular reaction whereas the others are almost entirely chain reactions.* If the reaction between H₂ and I₂ were entirely a chain reaction [eq. (12.13)] analogous to that for the H₂/Br₂ reaction, the activation energy would be given by eq. (12.13). To understand what is really happening, it is necessary to compare the activation energies of the chain reaction with those of the molecular process. With the data given in Table 12.2 we have

$$E_a(H_2/I_2) = 135.5 + (154 - 0)/2 = 212.5 \text{ kJ mol}^{-1} \quad (12.29)$$

However, we have estimated a lower energy barrier for the molecular process, 205 kJ mol⁻¹. Therefore the molecular process occurs more rapidly. In contrast, for the H₂/Br₂ and H₂/Cl₂ reactions, which have much lower E₂, the chain reaction mechanisms have much lower activation energies than the molecular process (see Table 12.2). Although the comparison established between the activation energies, E_a, and the classical potential-energy barrier of the molecular process, V₄, only provides a simple qualitative analysis of the relative reactivities of the different systems, it does fulfil the present objectives.

2. *In the H₂/Br₂ reaction there is a significant inhibition by the product, HBr; in the H₂/Cl₂ reaction there is no noticeable inhibition by HCl.* The activation energies of the relevant elementary processes



and



are low and extremely close; consequently both reactions have high and comparable rates. In such a situation, Br₂ and HBr compete for the H atoms, with the product HBr having a very small advantage at high temperatures owing to a higher pre-exponential factor. The homologous processes with chlorine



and



have very different activation energies. The reaction with the product HCl is *ca.* 100 times slower at 300 K and, consequently, is unable to compete with the reagent, Cl₂, for the hydrogen atoms.

3. The rate of the thermal H_2/Br_2 reaction is proportional to $[Br_2]^{1/2}$. For the H_2/Cl_2 , the reaction rate is proportional to $[Cl_2]$. The termination step that dominates in the H_2/Br_2 reaction is



because $[Br]$ is relatively high owing to the very low rate for the removal of bromine atoms through the reaction with molecular hydrogen



as a consequence of its relatively high activation energy. In contrast, the formation of bromine atoms through the step



is a very fast process. Thus we have both fast formation of bromine atoms and slow removal of the same species, such that $[Br]$ is high. This contrasts markedly with the H_2/Cl_2 system,



Here the chlorine (Cl) atoms are removed much more rapidly than the Br atoms in the earlier case, and $[Cl]$ is around 9 orders of magnitude lower than $[Br]$. Under such circumstances, the rate of bimolecular Cl–Cl recombination will be an extremely slow process.

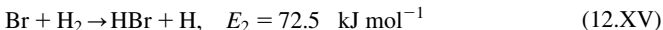
4. The chain lengths for the reaction H_2/Cl_2 are much greater than for the case with H_2/Br_2 . The length of a chain reaction, γ , can be defined as the average number of times the closed cycle of reactions, comprised of the chain-propagation steps, is repeated. Thus γ is given by the ratio of two rates: the rate of the overall reaction divided by that of the initiation step, $\gamma = v/v_i$. In the absence of the product HBr, from eq. (12.12) one can write

$$\gamma = \frac{k_2(k_1/k_{-1})^{1/2}[H_2][Br_2]^{1/2}}{k_1[Br_2]} \quad (12.30)$$

and thus

$$\gamma = k_2 \left(\frac{1}{k_1 k_{-1}} \right)^{1/2} [H_2][Br_2]^{-1/2} \quad (12.31)$$

The chain length γ is directly proportional to k_2 for the H_2/Br_2 as well as the H_2/Cl_2 reactions. If we compare the activation energies of the two elementary steps



one immediately realises that $k_2(\text{H}_2/\text{Cl}_2) >> k_2(\text{H}_2/\text{Br}_2)$ and consequently, $\gamma(\text{H}_2/\text{Cl}_2) >> \gamma(\text{H}_2/\text{Br}_2)$.

This comparative study in a family of complex reactions illustrates the levels of complexity of the field of chemical kinetics. Even with such homologous species, minor differences in activation energies may modify drastically the reaction mechanisms of the reacting systems. Simple models, such as the ISM, that provide estimates of E_a from structural and electronic parameters, help to rationalise such complex kinetic behaviour.

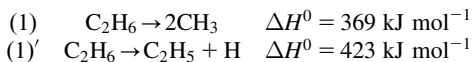
12.6 Pyrolysis of hydrocarbons

A linear chain reaction is one in which chain carriers react with no net gain in the number of carriers. Although the rate laws obtained can be as complex as those seen earlier for the reaction between H_2 and Br_2 , this is not necessarily the case. The thermal decomposition of hydrocarbons in the gas phase involves homolytic bond cleavage at the weakest chemical bond to produce two free radicals. In general, free radicals lead to chain reactions. However, the rate laws are often simple as was shown in 1934 by Rice and Herzfeld [15].

12.6.1 Pyrolysis of ethane

The pyrolysis of ethane yields ethene (i.e., ethylene). It is the major chemical utilisation of ethane, and ethylene is one of the most fundamental chemicals of the petrochemical industry, with *ca.* 150 million tons of ethylene produced annually worldwide. Ethylene is the raw material for the production of polyethylene, ethylene oxide and styrene, among other highly valuable materials.

Two possible unimolecular reactions can be considered as the initiation step



Because the second reaction is more endothermic, the first reaction dominates ethane decomposition. The homolytic cleavage of ethane is a typical unimolecular reaction, such as those discussed in Chapter 8, Unimolecular Reactions, with an interval of pressure for which the reaction rate is dependent on C_2H_6 pressure. There is low-pressure rate constant k^0 and a limiting high-pressure rate constant k_∞^1 . For limiting high pressure, the frequency factor of the Arrhenius equation is $A_{1\infty} = 5.2 \times 10^{16} \text{ sec}^{-1}$, and the activation energy is $E_{a1\infty} = 372 \text{ kJ mol}^{-1}$.

The very endothermic initiation step of the pyrolysis of ethane requires high temperatures ($>800^\circ\text{C}$). In the industrial production of ethylene, this is achieved diluting ethylene with heated steam in the absence of oxygen and briefly heating the mixture in a furnace.

The mechanism proposed by Rice and Herzfeld for the pyrolysis of ethane is as follows:

- | | | | |
|-----|---|------------------|-----------|
| (1) | $\text{C}_2\text{H}_6 \rightarrow 2\text{CH}_3$ | initiation step | (12.XVII) |
| (2) | $\text{CH}_3 + \text{C}_2\text{H}_6 \rightarrow \text{CH}_4 + \text{C}_2\text{H}_5$ | initiation step | |
| (3) | $\text{C}_2\text{H}_5 \rightarrow \text{C}_2\text{H}_4 + \text{H}$ | propagation step | |
| (4) | $\text{H} + \text{C}_2\text{H}_6 \rightarrow \text{H}_2 + \text{C}_2\text{H}_5$ | propagation step | |
| (5) | $\text{H} + \text{C}_2\text{H}_5 \rightarrow \text{C}_2\text{H}_6$ | termination step | |

The chain carriers are the radicals C_2H_5 and H. The free radical CH_3 does not propagate the chain reaction, since it is formed in step (1), deactivates in step (2), and is not to be regenerated. The stationary conditions for CH_3 , C_2H_5 and H lead to the following set of differential equations:

$$2k_1[\text{C}_2\text{H}_6] - k_2[\text{CH}_3][\text{C}_2\text{H}_6] = 0 \quad (12.32)$$

$$k_2[\text{CH}_3][\text{C}_2\text{H}_6] - k_3[\text{C}_2\text{H}_5] + k_4[\text{H}][\text{C}_2\text{H}_6] - k_5[\text{H}][\text{C}_2\text{H}_5] = 0 \quad (12.33)$$

$$k_3[\text{C}_2\text{H}_5] - k_4[\text{H}][\text{C}_2\text{H}_6] - k_5[\text{H}][\text{C}_2\text{H}_5] = 0 \quad (12.34)$$

Adding these three equations, we obtain

$$2k_1[\text{C}_2\text{H}_6] - 2k_5[\text{H}][\text{C}_2\text{H}_5] = 0 \quad (12.35)$$

from which the concentration of hydrogen atoms is

$$[\text{H}] = \frac{k_1[\text{C}_2\text{H}_6]}{k_5[\text{C}_2\text{H}_5]} \quad (12.36)$$

This expression can be inserted into eq. (12.34), leading, after some mathematical rearrangement, to

$$k_3k_5[\text{C}_2\text{H}_5]^2 - k_1k_5[\text{C}_2\text{H}_6][\text{C}_2\text{H}_5] - k_1k_4[\text{C}_2\text{H}_6]^2 = 0 \quad (12.37)$$

The general solution of this quadratic equation is

$$[\text{C}_2\text{H}_5] = \left(\frac{k_1}{2k_3} + \left[\left(\frac{k_1}{2k_3} \right)^2 + \left(\frac{k_1k_4}{k_3k_5} \right) \right]^{1/2} \right) [\text{C}_2\text{H}_6] \quad (12.38)$$

The constant k_1 is very small since the initiation reaction has a very high activation energy. The terms involving $k_1/2k_3$ are therefore very small in comparison with k_1k_4/k_3k_5 and therefore

$$[\text{C}_2\text{H}_5] = \left(\frac{k_1k_4}{k_3k_5} \right)^{1/2} [\text{C}_2\text{H}_6] \quad (12.39)$$

The rate of production of ethene is

$$\frac{d[\text{C}_2\text{H}_4]}{dt} = k_3[\text{C}_2\text{H}_5] \quad (12.40)$$

or

$$v = \left(\frac{k_1k_3k_4}{k_5} \right)^{1/2} [\text{C}_2\text{H}_6] \quad (12.41)$$

The reaction is thus first order. Inserting the corresponding Arrhenius expressions for the individual rate constants leads to

$$v = \left[\frac{A_1 \exp(-E_1/RT) A_3 \exp(-E_3/RT) A_4 \exp(-E_4/RT)}{A_5 \exp(-E_5/RT)} \right]^{1/2} [\text{C}_2\text{H}_6] \quad (12.42)$$

or

$$v = \left(\frac{A_1 A_3 A_4}{A_5} \right)^{1/2} \exp\left(-\frac{E_1 + E_3 + E_4 + E_5}{2RT} \right) [\text{C}_2\text{H}_6] \quad (12.43)$$

The activation energy for the overall reaction is

$$E_a = \frac{1}{2}(E_1 + E_3 + E_4 - E_5) \quad (12.44)$$

The hydrogen-atom abstraction of ethane by methyl, step (2), is slightly exothermic, $\Delta H^0 = -16 \text{ kJ mol}^{-1}$, and deviates from the Arrhenius equation. Its activation energy is $E_{a2} = 60 \text{ kJ mol}^{-1}$. The rate of this H-atom transfer reaction is conveniently calculated with ISM (51 kJ mol^{-1}) as described before and in [Chapter 6](#), Reactivity in Thermalised Systems. The thermal decomposition of the ethyl radical, step (3), is also a unimolecular reaction and from the temperature dependence of the extrapolated high-pressure rate constant it is possible to obtain $A_{3\infty} = 2.7 \times 10^{14} \text{ sec}^{-1}$, and $E_{a3\infty} = 171 \text{ kJ mol}^{-1}$. The hydrogen-atom abstraction of ethane by a hydrogen atom, step (4), also slightly exothermic $\Delta H^0 = -12 \text{ kJ mol}^{-1}$, and its temperature dependence between 350 and 1250 K gives $A_4 = 1.3 \times 10^{11} \text{ sec}^{-1}$, and $E_{a4} = 40 \text{ kJ mol}^{-1}$ ($E_a = 38 \text{ kJ mol}^{-1}$ according to ISM). Finally, the termination step (5) has the exothermicity of the C–H bond energy in ethane and proceeds without a barrier. Overall, the barrier is, according to [eq. \(12.44\)](#), $E_a = 292 \text{ kJ mol}^{-1}$, which is much lower than the activation energy of the initiating step. The enthalpy of the dehydrogenation of ethane to generate ethene and molecular hydrogen is $\Delta H^0 = +138 \text{ kJ mol}^{-1}$. Since E_3 and E_4 are much smaller than E_1 , the activation energy of the reaction is much lower than that of the initiating step.

The chain length is given by

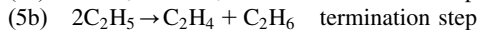
$$\gamma = \frac{v}{v_i} = \frac{(k_1 k_3 k_4 / k_5)^{1/2} [\text{C}_2\text{H}_6]}{k_1 [\text{C}_2\text{H}_6]} \quad (12.45)$$

or

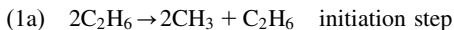
$$\gamma = \left(\frac{k_3 k_4}{k_1 k_5} \right)^{1/2} \quad (12.46)$$

Since k_1 is very small, the chain length is often very large.

Although the above mechanism explains the first-order dependence, other termination steps have been suggested such as



that account for the production of a small amount of butane. However, a mechanism with steps (1), (2), (3), (4), (5a) and (5b) should lead to a rate law of order 1/2. Therefore, to explain the experimental kinetic behaviour, a second-order initiation reaction was proposed,



However, evidence has been presented that the production of methane, in small amounts, shows a first-order dependence and this indicates that the initiation reaction is first order. This reaction mechanism is still the object of much interest.

12.6.2 Pyrolysis of acetic aldehyde

The Rice–Herzfeld mechanism for the decomposition of acetaldehyde involves the following steps:

- (1) $\text{CH}_3\text{CHO} \rightarrow \text{CH}_3 + \text{CHO}$
 - (2) $\text{CH}_3 + \text{CH}_3\text{CHO} \rightarrow \text{CH}_4 + \text{CH}_3\text{CO}$
 - (3) $\text{CH}_3\text{CO} \rightarrow \text{CH}_3 + \text{CO}$
 - (4) $2\text{CH}_3 \rightarrow \text{C}_2\text{H}_6$
- (12.XVIII)

The radical CHO gives other decomposition products that will not be considered here. Applying the steady-state condition, we obtain

$$k_1[\text{CH}_3\text{CHO}] - k_2[\text{CH}_3][\text{CH}_3\text{CHO}] + k_3[\text{CH}_3\text{CO}] - 2k_4[\text{CH}_3]^2 = 0 \quad (12.47)$$

and for the CH_3CO radicals

$$k_2[\text{CH}_3][\text{CH}_3\text{CHO}] - k_3[\text{CH}_3\text{CO}] = 0 \quad (12.48)$$

Addition of these equations gives

$$k_1[\text{CH}_3\text{CHO}] - 2k_4[\text{CH}_3]^2 = 0 \quad (12.49)$$

which can be rearranged to

$$[\text{CH}_3] = \left(\frac{k_1}{2k_4}\right)^{1/2} [\text{CH}_3\text{CHO}]^{1/2} \quad (12.50)$$

The rate of formation of methane is

$$\frac{d[\text{CH}_4]}{dt} = k_2[\text{CH}_3][\text{CH}_3\text{CHO}] \quad (12.51)$$

$$\frac{d[\text{CH}_4]}{dt} = k_2 \left(\frac{k_1}{2k_4}\right)^{1/2} [\text{CH}_3\text{CHO}]^{3/2} \quad (12.52)$$

The mechanism explains correctly the three-halves order. The overall activation energy is

$$E_a = E_2 + \frac{1}{2}(E_1 - E_4) \quad (12.53)$$

which is again usually much lower than E_1 .

The chain length is given by

$$\gamma = k_2(k_1 2k_4)^{-1/2} [\text{CH}_3\text{CHO}]^{1/2} \quad (12.54)$$

and depends on the concentration of the reactant.

To obtain a 3/2 order the initiation step can be a first-order process, but the termination step requires the combination of the same two radicals. If in the same mechanism instead of step (4) we have the reaction



as the termination step, the rate law becomes

$$\frac{d[\text{CO}]}{dt} = k_3 \left(\frac{k_1}{2k_4} \right)^{1/2} [\text{CH}_3\text{CHO}]^{1/2} \quad (12.55)$$

12.6.3 Goldfinger–Letort–Niclause rules

The above examples show that the order of the overall reaction depends on the manner in which the chains are broken as well as the nature of the radicals. Goldfinger, Letort and Niclause [16] have treated this problem in a systematic manner by distinguishing between two types of radicals:

1. Radicals that are involved in second-order propagation steps; these are referred to as β radicals. In the above cases, the H and CH_3 radicals are examples of this type.
2. Radicals that are involved in first-order reactions in the propagation steps; these are referred to as μ radicals. The radicals C_2H_5 and CH_3CO are of this type.

The order of the overall reaction depends on the kinetic type of the radicals that carry the chains and on the presence or absence of a third body M in the termination steps. The presence of a foreign body reduces the overall order by 1/2. Table 12.3 displays the overall orders of reactions for thermal

Table 12.3 Reaction orders for chain reactions in the pyrolysis of hydrocarbons.

First-order initiation		Second-order initiation		
Simple termination	Termination with third body	Simple termination	Termination with third body	Reaction order
$\beta\beta$		$\beta\beta$		2
$\beta\mu$	$\beta\beta\text{M}$	$\beta\mu$	$\beta\beta\text{M}$	3/2
$\mu\mu$	$\beta\mu\text{M}$	$\mu\mu$	$\beta\mu\text{M}$	1
			$\mu\mu\text{M}$	1/2
				0

decompositions of hydrocarbons. The same order, n , can also be estimated through the expression

$$n = \frac{i + \rho_1 + \rho_2 - t}{2} \quad (12.56)$$

Here i is the order of the initiation step and ρ_i the orders of the propagation steps: $\rho = 1$ for the μ radicals and $\rho = 2$ for the β radicals; t the order of the termination step. For example, for the decomposition of ethane we have $i = 1$, $\rho_1 = 1$, $\rho_2 = 2$ and $t = 2$ and thus $n = 1$.

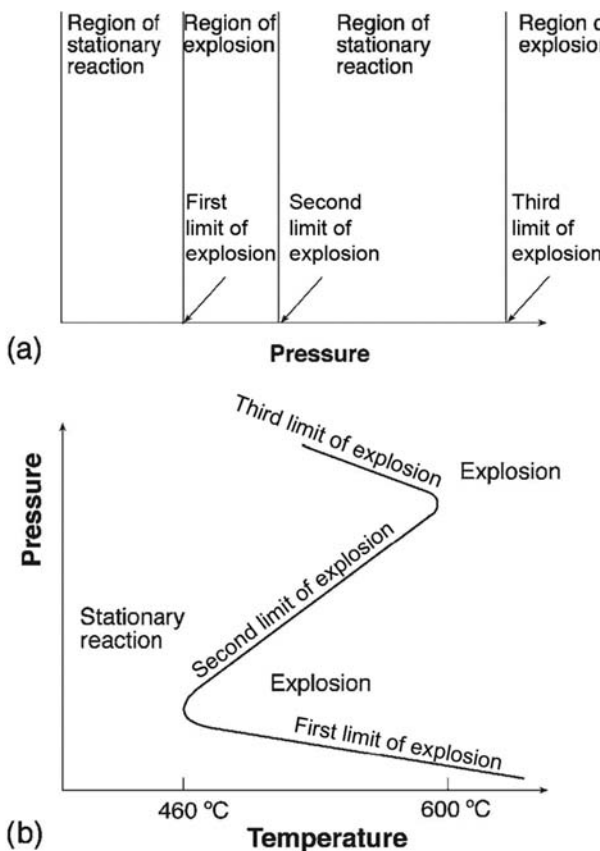
12.7 Explosive reactions

The gas-phase reactions between oxygen and various substances such as hydrogen, carbon monoxide and phosphorus have a special characteristic: under certain conditions of temperature, T , and pressure, P , they occur normally, but a slight change in T or P may cause the mixture to explode. An explosion is a sudden and violent release of energy, in general associated with emission of light, a violent burst and a large release of heat. Often there is a sudden pressure change, and one speaks of a *detonation*. Detonations have typical speeds of 2 km sec^{-1} , while detonations for military purposes may have speeds of $6\text{--}8 \text{ km sec}^{-1}$. This is much faster than the speed of sound in air, 0.34 km sec^{-1} , which is characteristic of shock waves. The manner in which a detonation travels through a gas mixture was first investigated by Dixon [17]. Later Chapman [18], based on such results, developed a theory of gaseous detonations. We are going to study the reaction between H_2 and O_2 as an example of this behaviour.

12.7.1 Combustion between hydrogen and oxygen

A stoichiometric mixture of the two gases explodes spontaneously at any pressure above 600°C . Below about 460°C there is no explosion at any pressure, unless a spark passes through the gaseous mixture or a flame is introduced into it. Between 460 and 600°C , however, a stoichiometric mixture explodes spontaneously at certain pressures but not at others, as displayed in Figure 12.4. In this figure, there are three limits of explosion as a function of pressure. The first one occurs at very low pressures, around 10^{-3} atm (260 Pa); a second one in the range of 10^{-1} atm and, finally, a third limit of explosion at higher pressures at *ca.* 10 atm .

To explain the kinetic behaviour of such systems Semenov [19,20] and Hinshelwood and Thompson [21,22] have proposed the concept of *branching chains*. When a pair of ordinary propagation steps occurs, there is no change in the number of chain carriers. When a branching chain occurs,

**FIGURE 12.4**

(a) Regions of stationary and explosive reactions for a typical combustion in the gas phase such as the hydrogen/oxygen reactions. (b) Change in the limits of explosion with the temperature: the temperatures indicated correspond to the stoichiometric mixture $2\text{H}_2 + \text{O}_2$.

however, there is an increase in the number of carriers. Let us consider the pair of reactions:



In both cases, two chain carriers have been formed from one. When the two reactions are added together, the net result is



so that the H atom is regenerated, but has produced two OH radicals which can undergo further reactions. When such chain branching happens, the number of

atoms and free radicals can increase rapidly in the system (see Table 12.4), and an explosion may result. Suppose the steps (1) and (2) are associated with step (3)



in the formation of water molecules. Each time the pair of reactions (1) and (2) occurs, reaction (3) occurs twice, so that the overall reaction is



Thus in the first cycle of reactions, one H atom produces 3H atoms together with two molecules of water. The numbers produced in subsequent cycles are shown in Table 12.4. After 50 cycles, the number of H radicals and water molecules is of the order of the Avogadro constant. The reactions are very fast, and 50 cycles can occur in a fraction of a second.

In more general terms, a branching chain reaction, with initiation and termination steps, can be considered with reference to the following mechanism:

- | | |
|---|---|
| (1) $\rightarrow \text{R}$ | initiation step (rate r_i) |
| (2) $\text{R} \rightarrow \alpha\text{R}$ | branching chain ($\alpha > 1$, generally $\alpha \approx 2$) |
| (3) $\text{R} + \text{Q} \rightarrow \text{Z} + \text{R}$ | propagation step |
| (4) $\text{R} \rightarrow$ | termination step |
- (12.XXIV)

Here, no distinction is made between the different kinds of radicals, R; Q represents a reactant and Z a product. The termination step can be the ending of the chain at a surface or in the gas phase. The rates of the four reactions are:

$$(1) \quad r_i = \frac{d[\text{R}]}{dt}$$

$$(2) \quad r_b = k'_b[\text{R}] = \frac{1}{\alpha - 1} \frac{d[\text{R}]}{dt} \quad (12.57)$$

$$(3) \quad r_p = k'_p[\text{R}]$$

$$(4) \quad r_t = k'_t[\text{R}] = - \frac{d[\text{R}]}{dt}$$

Table 12.4 Increase in the number of reactive species in the branching chain reaction between H atoms and H_2O molecules.

y	Number of H atoms reacting	Number of H atoms produced	Number of H_2O formed
1	1	3	2
2	3	9	6
3	9	27	18
4	27	81	54
10	19,683	59,049	39,366
20	1.16×10^9	3.49×10^9	2.32×10^9
30	6.9×10^{13}	2.05×10^{14}	1.4×10^{14}
49	4.1×10^{18}	1.2×10^{19}	8.1×10^{18}
50	2.4×10^{23}	7.2×10^{23}	4.8×10^{23}

where r_b and r_t are rates of first-order processes with respect to the active radicals and the rate constants k'_b and k'_t are usually functions of the concentrations of other reactants. The net rate of the formation of radicals is independent of the rate of the propagation step and can be written as

$$\frac{d[R]}{dt} = r_i + r_b(\alpha - 1) - r_t \quad (12.58)$$

or

$$\frac{d[R]}{dt} = r_i + \{k'_b(\alpha - 1) - k'_t\}[R] \quad (12.59)$$

If one defines a *net branching factor*, ϕ , in terms of the expression

$$\phi = k'_b(\alpha - 1) - k'_t \quad (12.60)$$

then eq. (12.59) can be written in the form

$$\frac{d[R]}{dt} = r_i + \phi[R] \quad (12.61)$$

which shows that the rate of radical formation follows a first-order law. If the net branching factor is $\phi < 0$, a stationary condition can be found for $[R]$, $[R]_{ss} = r_i/|\phi|$. Under such conditions the branching chain behaves as a normal chain reaction, because there is no significant net accumulation of active radicals; the termination step dominates over the branching step.

However, if $\phi > 0$ (see Figure 12.5), $[R]$ increases exponentially and approaches infinity at large values of t ,

$$[R] = \frac{r_i}{\phi} [\exp(\phi t) - 1] \quad (12.62)$$

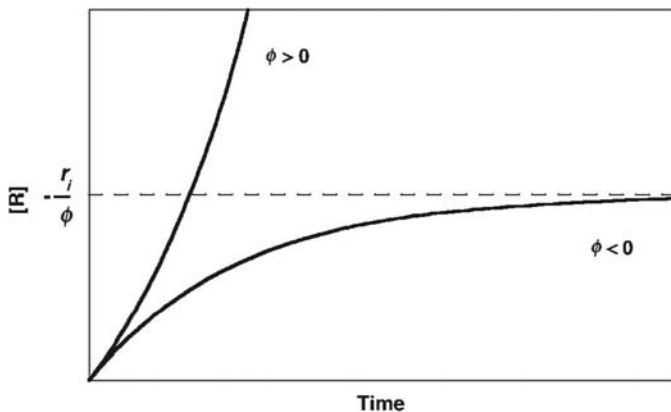


FIGURE 12.5

Increase in the concentration of the radical that propagates the chain reaction $[R]$, for different values of the net branching factor, ϕ .

Then the rate of reaction will be

$$v = k'_p[R] = \frac{r_i k'_p}{\phi} [\exp(\phi t) - 1] \quad (12.63)$$

After the initial instants, the rate increases exponentially with time. The branching processes dominate the termination process; there is an autocatalytic effect that leads eventually to an explosion. The primary cause of such an explosion is the increase in active chain carriers, and not the increase in temperature that is also present in an exothermic reaction. The rate of reaction tends to infinity, but above a certain limit, the reaction develops the characteristics of the explosive reactions.

In the gas phase, there are two explosion limits. At low pressures, the reaction has a low rate with $\phi < 0$. At low pressure, the removal of the radicals occurs primarily at the surface of the vessel. However, at a certain temperature, an increase in pressure reduces the rate at which radicals can reach the walls of the vessel, reducing k_t . Such a decrease occurs up to a certain pressure p_1 for which we arrive at the condition $\phi = 0$. Thus one reaches the first explosion limit.

At much higher pressures, $p \gg p_1$, the termination step occurs in the gas phase, with sufficient efficiency so that $\phi < 0$. Lowering this pressure, a new decrease in k_t occurs since the termination step is a kind of a third-order process,



and, thus, $\phi > 0$. At a pressure p_u ($p_u > p_1$) we reach once again the condition $\phi = 0$, and hence the second explosion limit. Keeping the temperature constant, between p_u and p_1 is the condition $\phi > 0$ and the reaction is always explosive (see [Figure 12.5](#)). Above p_u is the condition $\phi < 0$ and the combustion occurs in a smooth manner till one reaches a third explosion limit whose origin is discussed in the next section.

12.7.2 Thermal explosions

A thermal explosion is one where the primary cause is the auto-catalysis produced by the self-heating effect of the reaction mixtures. For an exothermic reaction, the heat evolved during the course of the reaction raises the temperature of the reacting mixtures, thereby accelerating the reaction rates, leading to further heating and further reaction, until an explosion occurs. Such a thermal reaction stabilises when the rate of generation of heat is compensated by thermal dissipation through thermal convection and conductivity or by radiation.

The rate of production of a certain amount of heat, Q_R , in a system of volume V and with a reaction rate, v , is given by

$$Q_R = -Vv|\Delta H| \quad (12.64)$$

where $-|\Delta H|$ represents the change of the enthalpy of the reaction. If we assume for simplicity that the rate law has the form

$$v = kC^x \quad (12.65)$$

where C is the concentration of the reactant, x the order of the reaction and k the rate constant, which follows the Arrhenius expression

$$k = A \exp\left(-\frac{E_a}{RT}\right) \quad (12.66)$$

under such conditions we obtain

$$Q_R = -VC^x A \exp\left(-\frac{E_a}{RT}\right) |\Delta H| \quad (12.67)$$

Let us assume that the rate of the dissipation of heat follows the empirical law of Newton,

$$Q_C = Sh(T - T_{ext}) \quad (12.68)$$

Here T is the temperature of the gaseous mixture, T_{ext} the temperature of the surroundings, S the surface of the vessel and h the thermal coefficient per unit area of the reaction vessel.

Figure 12.6 illustrates three possible conditions for Q_R at three concentrations of the reagent, $C_1 > C_C > C_2$. At C_2 , the system is at a temperature T_s where the

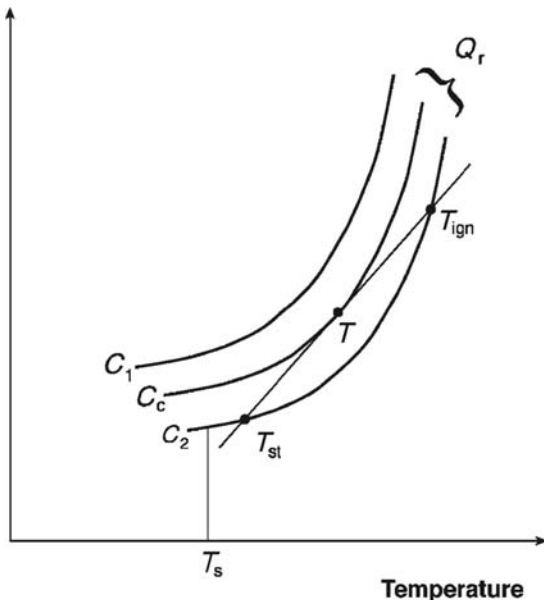


FIGURE 12.6

Variation of Q_R with the temperature for three concentration values.

rate of generation of heat is higher than that of heat dissipation, $Q_R > Q_C$. The temperature of the system rises up to T_{st} where $Q_R = Q_C$. Around this temperature, the system reveals some stability to small perturbations. When the system is heated to a temperature well above T_{st} the rate of cooling is higher compared to the rate of heat production and the temperature drops down to T_{st} . However, when the system is heated to the temperature of ignition, T_{ign} , it is no longer stable because $Q_R > Q_C$ always.

There is a critical concentration, C_C , where the temperature of ignition and that of stationary conditions have the same value, and then

$$Q_C = Q_R \quad (12.69)$$

or

$$\frac{dQ_C}{dt} = \frac{dQ_R}{dt} \quad (12.70)$$

Hence

$$\frac{RT_C^2}{E_a} = T_C - T_{ext} \quad (12.71)$$

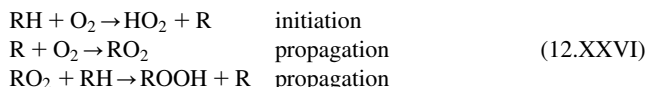
and from this equation we obtain

$$Sh(T_C - T_{ext}) = -VC_C^n A \exp\left(-\frac{E_a}{RT}\right) |\Delta H| \quad (12.72)$$

Above such a limiting condition, one reaches the limit of thermal explosion. This corresponds to the third explosion limit of the reaction $O_2/2H_2$. The explosions in the reactive system Cl_2/H_2 are also primarily of a thermal nature, because the chain is not a branching one and owing to the high activation energy, $E_a = 141 \text{ kJ mol}^{-1}$, the rate of formation of the chain carriers is sufficiently low to be the source of any isothermal explosion.

12.7.3 Combustion of hydrocarbons

The combustion of hydrocarbons has some features in common with reactions such as that between hydrogen and oxygen, in that explosion occurs between certain limits of temperature and pressure. But the mechanism involves what Semenov [19,20] has designated as *degenerated branching*. This type of branching is brought about by some intermediate that has a relatively long lifetime compared with the ordinary free radicals. Let us take as example the combustion of hydrocarbon RH,



In the vapour phase, below 100 °C, the hydroperoxides ROOH are the only products for many oxidation reactions of hydrocarbons. These hydroperoxides can decompose into new branching chain carriers in reactions that are much slower than the above ones.



Thus these oxidation reactions present quite substantial *induction periods*, periods of time needed for free radicals such as RO and HO to reach some concentration values.

During the first instants of the reaction $\phi < 0$ and the oxidation reaction is a slow process. For high temperatures ϕ is high, $\phi > 0$, and the combustion process is accompanied by ordinary *hot flames*. However, under certain conditions (see Figure 12.7) the so-called *cold flames* are also observed. Several of these blue flames are associated with sharp temperature increases (*ca.* 100 °C) and the corresponding rate acceleration. Nevertheless, quenching processes do occur before the reaction is complete. Not much reactant is consumed during the passage of a cold flame. As a consequence, the net branching factor ϕ must change sign during these pulses, so that only a degenerated explosion occurs. A full explanation of these reactions in the cold-flame regions is still awaited.

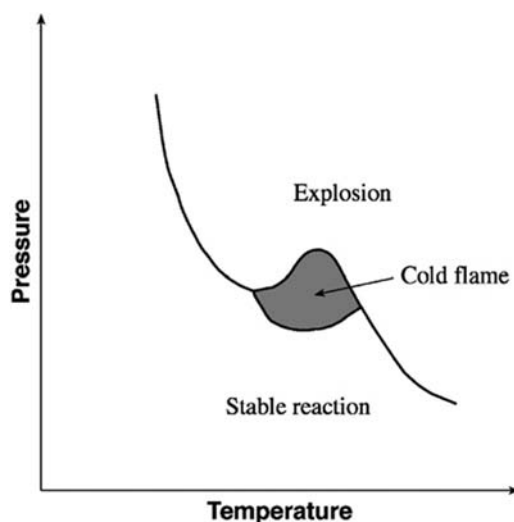
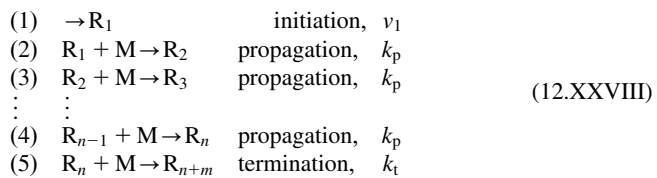


FIGURE 12.7

Illustration of the temperature and pressure conditions necessary to obtain a cold flame.

12.8 Polymerisation reactions

Gas-phase polymerisations occur by composite mechanisms that may be of a molecular type or of a radical type. In liquid solutions and emulsions, again both ionic and radical polymerisation mechanisms are important, depending upon whether one is dealing with condensation or addition polymerisation. In this section, we will consider the formation of macromolecules M_n made by a repetition of a certain number of identical monomers M by a free-radical mechanism, as follows:



where R_1 is a radical that initiates the polymerisation and R_n is a radical R_1 linked to a chain of $(n - 1)$ monomers. All the propagation steps are considered to have the same rate constant k_p ; the termination step has a rate constant k_t .

The steady-state condition for species R_1 leads to

$$v_1 - k_p[R_1][M] - k_t[R_1]([R_1] + [R_2] + \dots + [R_n]) = 0 \tag{12.73}$$

The termination step considers the removal of radical R_1 by reaction with R_1, R_2, \dots, R_n and this leads to

$$v_1 - k_p[R_1][M] - k_t[R_1] \sum_1^n [R_n] = 0 \tag{12.74}$$

Similarly, for R_2 , one has

$$k_p[R_1][M] - k_p[R_2][M] - k_t[R_2] \sum_1^n [R_n] = 0 \tag{12.75}$$

while for R_n the expression is

$$k_p[R_{n-1}][M] - k_p[R_n][M] - k_t[R_n] \sum_1^n [R_n] = 0 \tag{12.76}$$

The sum of all such equations simply states that the rate of initiation is equal to the sum of the rates of all the termination steps

$$v_1 - k_t \left(\sum_1^n [R_n] \right)^2 = 0 \tag{12.77}$$

or

$$\sum_1^n [R_n] = \left(\frac{v_1}{k_t} \right)^{1/2} \tag{12.78}$$

The rate of consumption of monomer is

$$-\frac{d[M]}{dt} = k_p[M] \sum_1^n [R_n] \quad (12.79)$$

which reduces to

$$-\frac{d[M]}{dt} = k_p \left(\frac{v_1}{k_t} \right)^{1/2} [M] \quad (12.80)$$

This is a set of general equations that can be made explicit for different kinds of mechanisms. For example, if the initiation step is a second-order process,

$$v_1 = k_1[M]^2 \quad (12.81)$$

then from eq. (12.80) we get

$$-\frac{d[M]}{dt} = k_p \left(\frac{k_1}{k_t} \right)^{1/2} [M]^2 \quad (12.82)$$

If initiation has a photochemical nature, then

$$v = I \quad (12.83)$$

where I is the intensity of the absorbed light, and subsequently, the rate of monomer consumption can be written as

$$-\frac{d[M]}{dt} = k_p \left(\frac{I}{k_t} \right)^{1/2} [M] \quad (12.84)$$

If the initiation step involves catalysis, where Cat represents the catalyst, then

$$v_1 = k_1[\text{Cat}][M] \quad (12.85)$$

and

$$-\frac{d[M]}{dt} = k_p \left(\frac{k_1}{k_t} \right)^{1/2} [M]^{3/2} [\text{Cat}]^{1/2} \quad (12.86)$$

The length of the chain is given by the general expression

$$\gamma = -\frac{d[M]/dt}{v_1} \quad (12.87)$$

which for a second-order initiation step [eq. (12.81)] leads to

$$\gamma = \frac{k_p (k_1/k_t)^{1/2} [M]^2}{k_1 [M]} \quad (12.88)$$

or

$$\gamma = k_p \left(\frac{1}{k_1 k_t} \right)^{1/2} [M] \quad (12.89)$$

References

- [1] MG Neuman, *J. Chem. Educ.* **63** (1986) 684.
- [2] JA Christiansen, *Vidensk. Selsk. Mat.-Fys. Medd.* **1** (1919) 14.
- [3] KF Herzfeld, *Z. Elektrochem.* **25** (1919) 301.
- [4] KF Herzfeld, *Ann. Phys.* **59** (1919) 635.
- [5] M Polanyi, *Z. Elektrochem.* **26** (1920) 50.
- [6] M Bodenstein, SC Lind, *Z. Phys. Chem.* **57** (1907) 108.
- [7] KJ Laidler, *Chemical Kinetics*, HarperCollins, New York, 1987.
- [8] M Bodenstein, W Unger, *Z. Phys. Chem. B* **11** (1930) 253.
- [9] M Bodenstein, *Z. Phys. Chem.* **13** (1894) 56.
- [10] M Bodenstein, *Z. Phys. Chem.* **22** (1897) 23.
- [11] M Bodenstein, *Z. Phys. Chem.* **29** (1899) 295.
- [12] JH Sullivan, *J. Chem. Phys.* **30** (1959) 1291.
- [13] JH Sullivan, *J. Chem. Phys.* **36** (1962) 1925.
- [14] JH Sullivan, *J. Chem. Phys.* **39** (1963) 300.
- [15] FO Rice, KF Herzfeld, *J. Am. Chem. Soc.* **56** (1934) 284.
- [16] P Goldfinger, M Letort, M Niclause, Contribution à l'étude de la structure moléculaire, Liège V. Henri Commemorative Volume (1948) 283.
- [17] HB Dixon, *Philos. Trans.* **175** (1884) 617.
- [18] DL Chapman, *Philos. Mag.* **47** (1899) 90.
- [19] NN Semenov, *Z. Phys.* **46** (1927) 109.
- [20] NN Semenov, *Chemical Kinetics and Chain Reactions*, Clarendon Press, Oxford, 1935.
- [21] CN Hinshelwood, HW Thompson, *Proc. R. Soc. London* **118** (1928) 171.
- [22] CN Hinshelwood, HW Thompson, *Kinetics of Chemical Change in Gaseous Systems*, Clarendon Press, Oxford, 1933.

Acid–base catalysis and proton-transfer reactions

13

Proton-transfer (PT) reactions lie at the heart of the mechanistic definition of what is an acid and what is a base in the concept initially proposed by Brönsted. Remember that, according to Brönsted, an acid is a molecular entity capable of donating a proton, and a base is another molecular entity with a tendency to accept that proton. The equilibrium



represents the transfer of a proton from an acid HA to a base B^- , or, for the reverse reaction, the transfer of a proton from the conjugate base A^- (of the AH acid) to the conjugate acid BH (of the B^- base). Such reactions are present in catalysis by acids or bases in solution, and are also particularly relevant in enzyme-catalysed processes in biological systems.

13.1 General catalytic mechanisms

Following Laidler [1], we first consider a mechanism that is sufficiently general to encompass most homogeneous catalysis. Designating the catalyst as C and the substrate as S (i.e., the reactant subject to the catalytic reaction), the mechanism can be written



where X and Y represent intermediates, one of which (X) reacts with another substance (W), to yield the final product (P) and an additional substance (Z), which may subsequently react, but which is not involved in kinetically significant reactions. For simplicity, we will consider that only the first step is reversible. This is also equivalent to the case where the products are rapidly removed from the reaction.

13.1.1 Fast pre-equilibrium: Arrhenius intermediates

When the first step of the mechanism, step (13.II), is a fast equilibrium, the intermediate X is in equilibrium with the reactants, and corresponds to Arrhenius's concept of an equilibrium intermediate. This step leads to

$$\frac{[X][Y]}{[C][S]} = \frac{k_1}{k_{-1}} = K \quad (13.1)$$

In this expression, the concentrations of C and S, [C] and [S], are their equilibrium concentrations and not their initial concentrations. For initial concentrations, $[C]_0$ and $[S]_0$, we can write

$$[C]_0 = [C] + [X] \quad (13.2)$$

$$[S]_0 = [S] + [X] \quad (13.3)$$

Introducing these expressions in eq. (13.1), we obtain

$$\frac{[X][Y]}{([C]_0 - [X])([S]_0 - [X])} = K \quad (13.4)$$

which is a quadratic equation in X. The reaction rate, expressed in terms of the formation of the product P in step (13.III), is given by

$$v = k_2[X][W] \quad (13.5)$$

The intermediate X can be eliminated from this expression using eq. (13.4).

It is often more useful to consider the relative concentrations of the catalyst and substrate and obtain limiting cases for the rate law, rather than carry out all the algebra with the quadratic equation. Because [X] cannot be larger than $[C]_0$, we can obtain a first limiting case when the initial concentration of the substrate is relatively high, $[S]_0 \gg [C]_0$, and, consequently, $[S]_0 - [X] \approx [S]_0$. Under this approximation eq. (13.4) becomes

$$\frac{[X][Y]}{([C]_0 - [X])[S]_0} = K \quad (13.6)$$

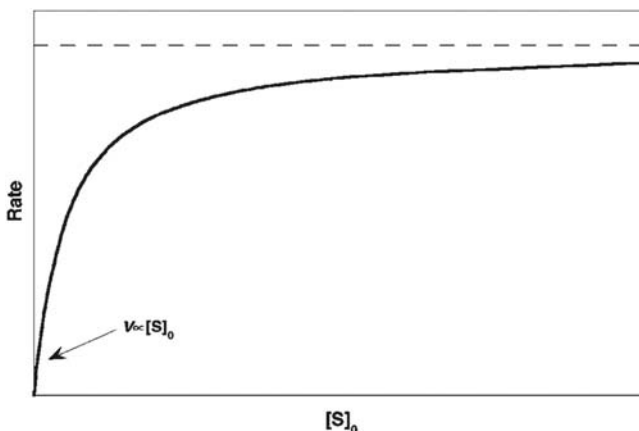
or

$$[X] = \frac{K[C]_0[S]_0}{K[S]_0 + [Y]} \quad (13.7)$$

and the rate law can be written as

$$v = \frac{k_2 K [C]_0 [S]_0 [W]}{K [S]_0 + [Y]} \quad (13.8)$$

This expression shows that the reaction rate changes with $[S]_0$, as illustrated in Figure 13.1. For low substrate concentration, the rate resembles a first-order process with respect to the substrate. However, for higher

**FIGURE 13.1**

Rate of a catalysed reaction as a function of the initial concentration of substrate, $[S]_0$, observed when $[S]_0 \gg [C]_0$.

substrate concentrations, the rate may attain a plateau and become independent of the substrate concentration, just like a zero-order reaction with respect to S. As long as $[S]_0 \gg [C]_0$, the reaction rate is first order with respect to the catalyst.

We have seen this behaviour before in [Chapter 10](#), Reactions on Surfaces, in single-substrate reactions on the surface of solids, and will discuss it again in [Chapter 14](#), Enzymatic Catalysis, in the context of enzyme catalysis. For both cases of surface reactions and enzyme catalysis, the species Y and W do not exist and [eq. \(13.8\)](#) becomes

$$v = \frac{k_2 K [C]_0 [S]_0}{K [S]_0 + 1} \quad (13.9)$$

this equation is equivalent to [eq. \(10.19\)](#) of surface reactions, which is defined per unit area, and to the Michaelis–Menten equation of enzyme catalysis, [eq. \(4.156\)](#).

Another limiting case is obtained when the catalyst is in excess relative to the substrate, $[C]_0 \gg [S]_0$, and [eq. \(13.4\)](#) becomes

$$\frac{[X][Y]}{[C]_0([S]_0 - [X])} = K \quad (13.10)$$

leading to

$$v = \frac{k_2 K [C]_0 [S]_0 [W]}{K [C]_0 + [Y]} \quad (13.11)$$

Now the reaction is always first order with respect to the substrate, independent of $[S]$, provided that $[S]_0 \ll [C]_0$, but the partial order with respect to the catalyst may vary between zero and unity.

Additionally, when $K[C]_0$ is much greater than $[Y]$, the rate of reaction is simply given by

$$v = k_2[S]_0[W] \quad (13.12)$$

and the activation energy is

$$E_a = E_2 \quad (13.13)$$

where E_a is the activation energy of reaction (13.III).

The activation energies associated with the rates expressed by eqs. (13.8) and (13.11) can also be obtained when only a very small quantity of the substrate S is present. In such cases, the rate of reaction is

$$v = k_2 \frac{k_1}{k_{-1}} [C]_0 [S]_0 [W] [Y]^{-1} \quad (13.14)$$

and the activation energy becomes

$$E_a = E_1 + E_2 - E_{-1} \quad (13.15)$$

where E_1 and E_{-1} represent the activation energy of reaction (13.II) and its reverse, respectively.

13.1.2 Steady-state conditions: van't Hoff intermediates

If $k_2[W] \gg k_{-1}[Y]$ in mechanisms (13.II) and (13.III), then $[X]$ is small and the steady-state approximation can be applied to this mechanism. Laidler called X under these conditions a van't Hoff intermediate. The energy profiles corresponding to Arrhenius and van't Hoff intermediates are illustrated in Figure 13.2.

Under steady-state conditions, $[X]$ does not change appreciably with time

$$\frac{d[X]}{dt} = k_1[C][S] - k_{-1}[X][Y] - k_2[X][W] = 0 \quad (13.16)$$

Replacing eqs. (13.2) and (13.3) in this expression gives

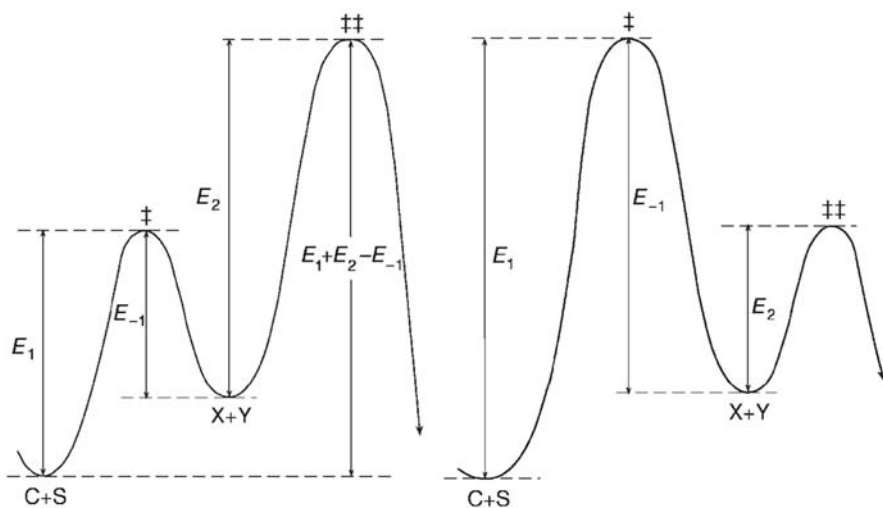
$$k_1([C]_0 - [X])([S]_0 - [X]) - k_{-1}[X][Y] - k_2[X][W] = 0 \quad (13.17)$$

The low concentration of X justifies ignoring the quadratic term in $[X]$, and leads to

$$[X] = \frac{k_1[C]_0[S]_0}{k_1([C]_0 + [S]_0) + k_{-1}[Y] + k_2[W]} \quad (13.18)$$

The rate is therefore

$$v = \frac{k_1 k_2 [C]_0 [S]_0 [W]}{k_1([C]_0 + [S]_0) + k_{-1}[Y] + k_2[W]} \quad (13.19)$$

**FIGURE 13.2**

Potential-energy profiles for catalysed reactions. (a) The rate-determining step is the second step, occurring after the formation of an Arrhenius intermediate. (b) The rate-determining step is the first step, which leads to a van't Hoff intermediate.

As mentioned before, Y and W do not exist in surface and enzyme catalysis, and eq. (13.19) simplifies to

$$v = \frac{k_1 k_2 [C]_0 [S]_0}{k_1 ([C]_0 + [S]_0) + k_{-1} + k_2} \quad (13.20)$$

At high catalyst concentrations, eq. (13.19) reduces to eq. (13.12), and the activation energy is given by eq. (13.13). For low substrate and catalyst concentrations, eq. (13.20) becomes

$$v = \frac{k_1 k_2}{k_{-1} + k_2} [C]_0 [S]_0 \quad (13.21)$$

The Arrhenius equation, and consequently the definition of activation energy, does not apply to this system, except if $k_2 \gg k_{-1}$ or $k_{-1} \gg k_2$. In the first case,

$$v = k_1 [C]_0 [S]_0 \quad (13.22)$$

and the activation energy is

$$E_a = E_1 \quad (13.23)$$

In the second case,

$$v = \frac{k_1 k_2}{k_{-1}} [C]_0 [S]_0 \quad (13.24)$$

and the activation energy is that of eq. (13.15).

13.2 General and specific acid–base catalysis

Arrhenius and Ostwald played very important roles in the early studies on acid–base catalysis, one century ago. Arrhenius contributed to the definition of acids and bases, and established the dependence between the rate constants and the temperature. Additionally, he also formulated an electrolytic theory of dissociation that ultimately led to him receiving the 1903 Nobel Prize in Chemistry. Ostwald proposed useful definitions of catalysis and classifications of catalysts, but he was unable to develop a satisfactory theory of these effects. This is not surprising, in view of the very limited knowledge of the mechanisms of catalysis at his time, and of the lack of understanding of how molecular properties can influence the rates of reactions. Nevertheless, his seminal work on catalysis was rewarded by him receiving the 1909 Nobel Prize in Chemistry.

Ostwald recognised that a catalysed reaction proceeds by an alternative reaction pathway, made possible by the addition of a new species. For a process that in the absence of catalysts proceeds with a rate constant k_0 , the general acid–base-catalysed reaction follows the rate expression:

$$v = (k_0 + k_{\text{H}^+}[\text{H}^+] + k_{\text{OH}^-}[\text{OH}^-] + k_{\text{HA}}[\text{HA}] + k_{\text{A}^-}[\text{A}^-])[\text{S}] \quad (13.25)$$

involving the sum of the rates for all the alternative pathways. In this expression, k_{H^+} and k_{OH^-} are the rate constants for catalysis by proton and hydroxide ion, and k_{HA} and k_{A^-} are the catalytic rate constants for the acid HA and the base A^- . In aqueous solutions, the proton is strongly hydrated and, as will be discussed below, it is not present in the form of the free H^+ ion. However, for simplicity, except where required to illustrate PT to water, we will continue to use the representation H^+ for the proton in the equations, and will also continue to represent the hydroxide ion, OH^- .

[Eq. \(13.25\)](#) indicates that the reaction is catalysed by an acid, HA, or a base, A^- , present in the solution, in addition to catalysis by H^+ and OH^- . We refer to catalysis in the former case (by HA and A^-) as general acid–base catalysis. However, in many catalytic mechanisms, particularly in aqueous solutions, only H^+ and OH^- significantly influence the rate of the reaction. In this case, we are in the presence of specific acid–base catalysis.

In the general catalytic mechanism represented by [\(13.II\)](#) and [\(13.III\)](#), an acid catalysis corresponds to replacing X by SH^+ , the catalyst C by the acid AH and Y by that catalyst without a proton. In the second step, SH^+ transfers a proton to the species, W, for example, a water molecule, and gives the product P



This example, where W is a solvent molecule, corresponds to a protolytic transfer. When W is the conjugate base of the catalyst, $\text{W} = \text{A}^-$, the mechanism

is called prototropic. **Table 13.1** presents the four possible combinations for acid and base catalysis that correspond to the possible identities of species involved in the general catalytic mechanism.

The mechanism of each of the four possible combinations may involve an Arrhenius or a van't Hoff intermediate. This leads to eight possible mechanisms, schematically presented in **Table 13.2**. Each of these mechanisms can be developed using either the pre-equilibrium or the steady-state approximation to arrive at the corresponding rate law. The lessons that can be learnt from the treatment of these mechanisms are also indicated in **Table 13.2**; some mechanisms lead exclusively to specific acid or base catalysis, while others lead to general acid or base catalysis. Furthermore, the specific catalysis is associated with the existence of a limiting rate, that is the rate that will not increase indefinitely with the H^+ , or OH^- , concentration, but attain a limiting value equal to $k_2[\text{S}]_0$.

For specific acid–base catalysis at low pH, [eq. \(13.25\)](#) simplifies to

$$v = (k_0 + k_{\text{H}^+}[\text{H}^+])[S] \quad (13.26)$$

Table 13.1 Nature of the reacting species in general acid–base catalysis in aqueous solutions.

Catalysis	C	Y	W	Z
Acid	HA	A^-	H_2O	H_3O^+
Acid	H_2O	OH^-	B	BH^+
Base	B	BH^+	H_2O	OH^-
Base	H_2O	H_3O^+	HA	A^-

Table 13.2 Summary of mechanisms for acid–base catalysis.

Acid catalysis	Arrhenius intermediates	van't Hoff intermediates
H^+ transferred to solvent $\text{BH}^+ + \text{S} \rightleftharpoons \text{SH}^+ + \text{B}$ $\text{SH}^+ + \text{H}_2\text{O} \rightarrow \text{P} + \text{H}_3\text{O}^+$	$k_2 \ll k_{-1}[\text{B}]$ Specific H^+ catalysis With limiting rate	$k_2 > k_{-1}[\text{B}], k_2 > k_1[\text{BH}^+]$ General catalysis No limiting rate
H^+ transferred to solute $\text{BH}^+ + \text{S} \rightleftharpoons \text{SH}^+ + \text{B}$ $\text{SH}^+ + \text{B} \rightarrow \text{P} + \text{BH}^+$	$k_2 \ll k_{-1}$ General catalysis No limiting rate	$k_2 > k_{-1}$ General catalysis No limiting rate
H^+ transferred from solvent $\text{B} + \text{SH} \rightleftharpoons \text{S}^- + \text{BH}^+$ $\text{S}^- + \text{H}_2\text{O} \rightarrow \text{P} + \text{OH}^-$	$k_2 \ll k_{-1}[\text{BH}^+]$ Specific OH^- catalysis With limiting rate	$k_2 > k_{-1}[\text{BH}^+], k_2 > k_1[\text{B}]$ General catalysis No limiting rate
H^+ transferred from solute $\text{B} + \text{SH} \rightleftharpoons \text{S}^- + \text{BH}^+$ $\text{S}^- + \text{BH}^+ \rightarrow \text{P} + \text{B}$	$k_2 \ll k_{-1}$ General catalysis No limiting rate	$k_2 > k_{-1}$ General catalysis No limiting rate

As the pH increases, the participation of the hydroxide ion in the catalysis becomes increasingly important, and the reaction rate for specific acid–base catalysis becomes

$$v = (k_0 + k_{\text{H}^+}[\text{H}^+] + k_{\text{OH}^-}[\text{OH}^-])[S] \quad (13.27)$$

It is convenient to define a pseudo-first-order rate constant

$$k_\Psi = \frac{v}{[S]_T} \quad (13.28)$$

where $[S]_T$ is the total concentration of the substrate, and express the reaction rate constant in terms of

$$k_\Psi = k_0 + k_{\text{H}^+}[\text{H}^+] + k_{\text{OH}^-}[\text{OH}^-] \quad (13.29)$$

In aqueous solutions, the equilibrium



where $[\text{H}^+][\text{OH}^-] = K_w$, leads to

$$k_\Psi = k_0 + k_{\text{H}^+}[\text{H}^+] + \frac{k_{\text{OH}^-}K_w}{[\text{H}^+]} \quad (13.30)$$

Usually, it is possible to consider a region of sufficiently low pH where the catalysis is dominated by the H^+ ion, and eq. (13.30) simplifies to

$$k_\Psi = k_{\text{H}^+}[\text{H}^+] \quad (13.31)$$

or

$$\log k_\Psi = \log k_{\text{H}^+} - \text{pH} \quad (13.32)$$

It may also be possible to find a region of sufficiently high pH where the catalysis is dominated by the OH ion, and eq. (13.30) becomes

$$k_\Psi = \frac{k_{\text{OH}^-}K_w}{[\text{H}^+]} \quad (13.33)$$

or

$$\log k_\Psi = \log k_{\text{OH}^-} - \text{p}K_w + \text{pH} \quad (13.34)$$

Another special case is that of a small spontaneous reaction, in the absence of catalysis, that is, $k_0 \ll (K_w k_{\text{H}^+} k_{\text{OH}^-})^{1/2}$, and the rate of reaction as a function of the pH goes through a minimum. The value of that minimum can be obtained differentiating eq. (13.30):

$$\frac{dk_\Psi}{d[\text{H}^+]} = k_{\text{H}^+} - \frac{k_{\text{OH}^-}K_w}{[\text{H}^+]^2} \quad (13.35)$$

equating the derivative to zero and expressing the H^+ concentration as

$$[\text{H}^+]_{\min} = \sqrt{\frac{k_{\text{OH}^-}K_w}{k_{\text{H}^+}}} \quad (13.36)$$

This expression allowed Wijs [2,3], at the end of the nineteenth century, to measure the catalytic rate constants for the hydrolysis of ethyl acetate at low and high pHs and obtain the ionic product of water, K_w .

13.3 Mechanistic interpretation of the pH dependence of the rates

The above discussion shows that the dependence of the reaction rate upon the pH contains very important information on the reaction mechanism. Each rate must be measured at constant pH, which usually involves measuring it in a buffer solution. In addition, usually an inert salt is added to maintain ionic strength constant to avoid the salt effects discussed in [Chapter 9](#), Elementary Reactions in Solution. In fact, experimentally, the rates are measured at different buffer concentrations, keeping the pH and the ionic strength constant. Under these conditions, and for a constant substrate concentration, there is a linear dependence between the rate and the buffer concentration, as illustrated in [Figure 13.3](#). Extrapolating to zero buffer concentration, one obtains the rate for a constant pH. When general acid–base catalysis is present, the rate depends on the nature of the buffer, and the extrapolation gives different rates for different buffers. Such cases of general acid–base catalysis will be discussed in the next section. Here, we focus on the mechanistic interpretation of the pseudo-first-order rate constants measured as a function of the pH in aqueous solutions.

There are five fundamental types of pH dependence, and they are illustrated in [Figure 13.4](#) by the dependence of the logarithm of the rate as a

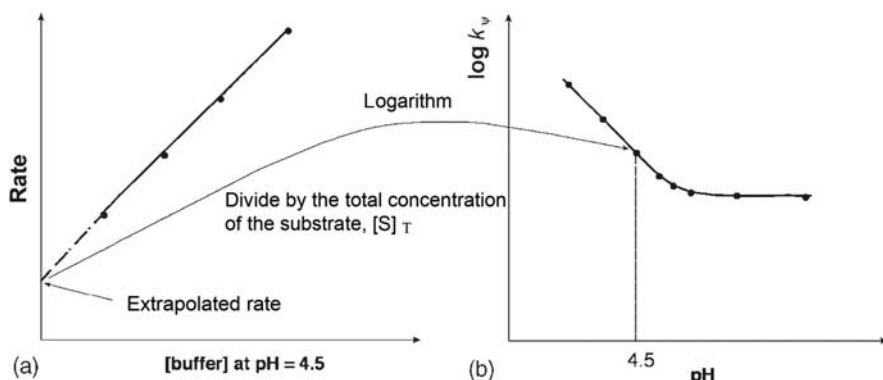
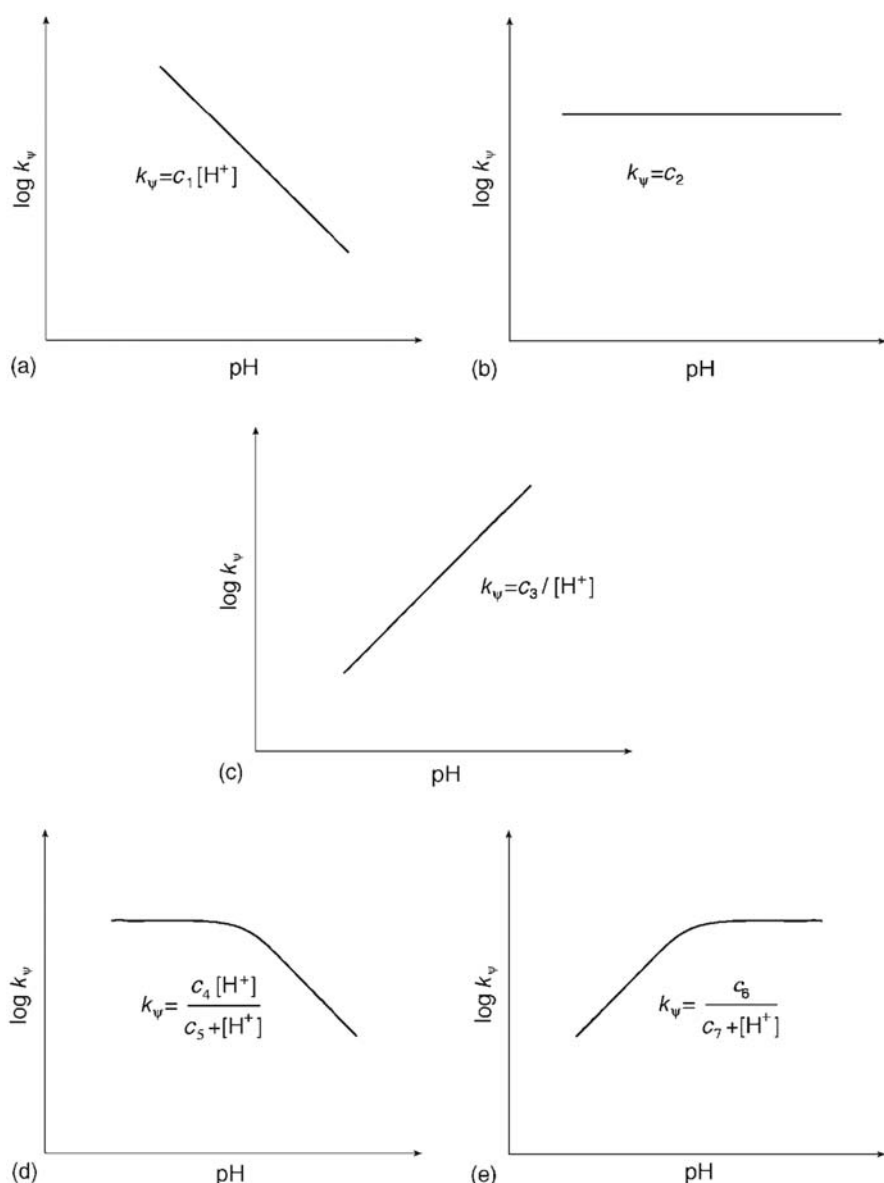


FIGURE 13.3

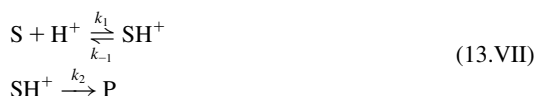
Representation of the method employed to obtain the pH dependence of the pseudo-first-order rates (k_p) as a function of the pH. (a) Rates measured for different buffer concentrations at pH 4.5. (b) Pseudo-first-order rates at different pHs.

**FIGURE 13.4**

Fundamental curves representing the dependence of the logarithm of the pseudo-first-order rate of acid–base catalysis on the pH of the solution, without involving a change in the reaction mechanism.

function of pH (to a first approximation, the negative of the logarithm of the hydrogen ion concentration) [4]. The experimentally observed pH dependences can be divided in sections that correspond to these fundamental types. Types (a), (b) and (c) correspond to reactions that are catalysed by H^+ , not catalysed, and catalysed by OH^- , respectively. The catalysis by H^+ is described by eq. (13.32), which explains the origin of the slope -1 , corresponding to a linear dependence of rate upon hydrogen ion concentration. The absence of significant acid–base catalysis occurs when k_0 dominates all the other terms in the right-hand side of eq. (13.30), and leads to a rate that is independent of the pH of the solution. The catalysis by OH^- is described by eq. (13.34), which shows the origin of the slope $+1$. The other two types, (d) and (e), correspond to cases where the rate constant decreases, case (d), or stops increasing, case (e), after a certain pH. These cases cannot correspond to a change in mechanism because such a change is always associated with the predominance of a competitive reaction, after a certain pH, and that necessarily leads to an increase in the rate. This is not the case, because the trends followed by the downward trend of the curves represented in (d) and (e) reflect a decrease in the rates after a given pH. Thus each of these curves with a downward trend must be associated with a single mechanism. There are two alternative mechanisms that may lead to such breaks followed by downward trends; the presence of a fast pre-equilibrium or a change in the rate-determining step.

In the case of a mechanism of acid catalysis involving a fast pre-equilibrium



where the acidity constant is $K_a = k_{-1}/k_1$, it is convenient to express the rate constant in terms of the fraction of protonated substrate

$$f_{\text{SH}} = \frac{[\text{SH}^+]}{[\text{SH}^+] + [\text{S}]} = \frac{[\text{H}^+]}{K_a + [\text{H}^+]} \quad (13.37)$$

because $[\text{SH}^+] = f_{\text{SH}}[\text{S}]_T$ and the rate constant is $v = k_2[\text{SH}^+] = k_2 f_{\text{SH}}[\text{S}]_T$. Using these relations and eq. (13.28), gives

$$k_\Psi = k_2 f_{\text{SH}} = \frac{k_2 [\text{H}^+]}{K_a + [\text{H}^+]} \quad (13.38)$$

This expression is equivalent to

$$k_\Psi = \frac{c_4 [\text{H}^+]}{c_5 + [\text{H}^+]} \quad (13.39)$$

where c_4 and c_5 are constants, which is the equation of the curve represented in Figure 13.4d.

In contrast, the rate constant of a mechanism of base catalysis involving a fast pre-equilibrium



where the acidity constant is $K_a = k_1/k_{-1}$, is conveniently expressed in terms of the fraction of un-protonated substrate

$$f_S = \frac{[\text{S}]}{[\text{SH}^+] + [\text{S}]} = \frac{K_a}{K_a + [\text{H}^+]} \quad (13.40)$$

because

$$k_\Psi = k_2 f_S = \frac{k_2 K_a}{K_a + [\text{H}^+]} \quad (13.41)$$

and has a clear analogy with the mathematical expression of the curve represented in [Figure 13.4e](#)

$$k_\Psi = \frac{c_6}{c_7 + [\text{H}^+]} \quad (13.42)$$

where c_6 and c_7 are constants.

It is interesting to note that in curves (d) and (e) of [Figure 13.4](#), the two segments of the curve intersect at $K_a = [\text{H}^+]$, and the K_a of the substrate is given by the pH at that intersection ([Figure 13.5](#)). At this pH, $k_\Psi = k_2/2$.

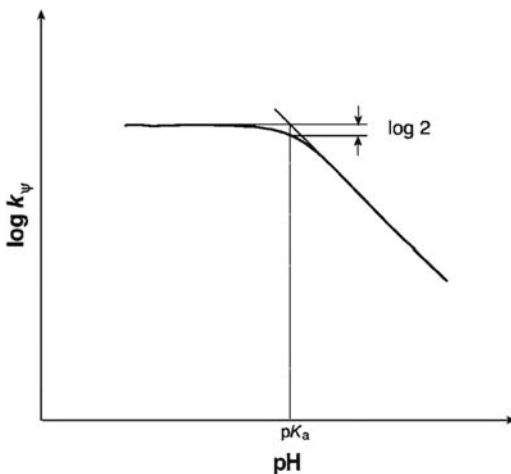


FIGURE 13.5

Estimation of the K_a for deprotonation of a substrate from the dependence of its pseudo-first-order rate constant on the pH of the solution.

There are other mechanisms that also lead to mathematical expressions identical to eq. (13.39) or eq. (13.42). Such mechanisms are kinetically indistinguishable, and require additional information to decide which actually applies to the reaction. For example, the mechanism



where X is a van't Hoff intermediate, has a first step that is independent of the pH followed by a second step where the reaction rate increases with the pH. For sufficiently acidic solutions, the second step is slow and becomes rate determining. However, for basic solutions, the second step is fast and the rate is determined by the first step, which is independent of the pH. Thus we can expect to find pH dependences such as that in Figure 13.4e. This can be verified using the steady-state approximation to find the concentration of the van't Hoff intermediate, and then replace it in the rate law. The result is

$$k_\Psi = \frac{k_1 k_2 [\text{OH}^-]}{k_{-1} + k_2 [\text{OH}^-]} = - \frac{k_1 k_2 K_w / [\text{H}^+]}{k_{-1} + k_2 K_w / [\text{H}^+]} = \frac{(k_1 k_2 / k_{-1}) K_w}{(k_2 K_w / k_{-1}) + [\text{H}^+]} \quad (13.43)$$

Another mechanism of this type is



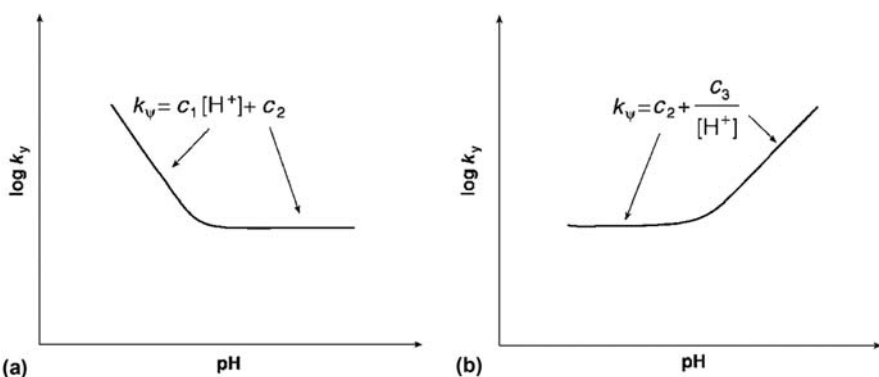
that gives the pseudo-first-order rate constant

$$k_\Psi = \frac{k_1 k_2 [\text{H}^+]}{k_{-1} + k_2 [\text{H}^+]} = \frac{k_1 [\text{H}^+]}{\frac{k_{-1}}{k_2} + [\text{H}^+]} \quad (13.44)$$

which is mathematically equivalent to eq. (13.39). Note that the change in the rate-determining step exemplified by mechanisms (13.IX) and (13.X) requires the presence of an intermediate and, conversely, a change in the rate-determining step suggests the presence of an intermediate.

The distinction between mechanisms (13.VII) and (13.IX), or between mechanisms (13.VII) and (13.X), cannot be made exclusively on the grounds of their kinetic behaviour. However, the presence, or absence, of a substituent with a pK_a that may correspond to the pH where the slope of the curve changes, as indicated in Figure 13.5, may help to assign the correct mechanism.

The most important conclusion of this discussion is that only the observation of a curve with a bend followed by an upward trend reveals a change in mechanism with a change in pH (Figure 13.6). Such a curve indicates that, at a certain pH, the rate constant becomes higher than expected, and that a new mechanism has been triggered by the change in pH. Consequently the number of independent terms that describe the rate of a reaction as a function of the pH is equal to the number of upward bends plus one.

**FIGURE 13.6**

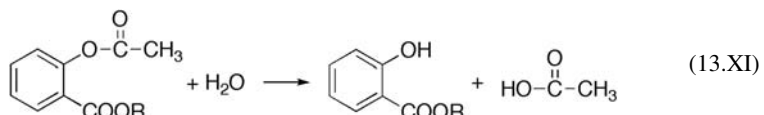
Examples of the dependence of the pseudo-first-order rate of acid–base catalysis on the pH of the solution with upward curvature, which require a change in the reaction mechanism with the pH.

Each one of these terms can be expressed in the form of the fundamental curves of Figure 13.4. Each independent term of the rate equation corresponds to a different mechanism and its predominance can be observed in a specific pH range.

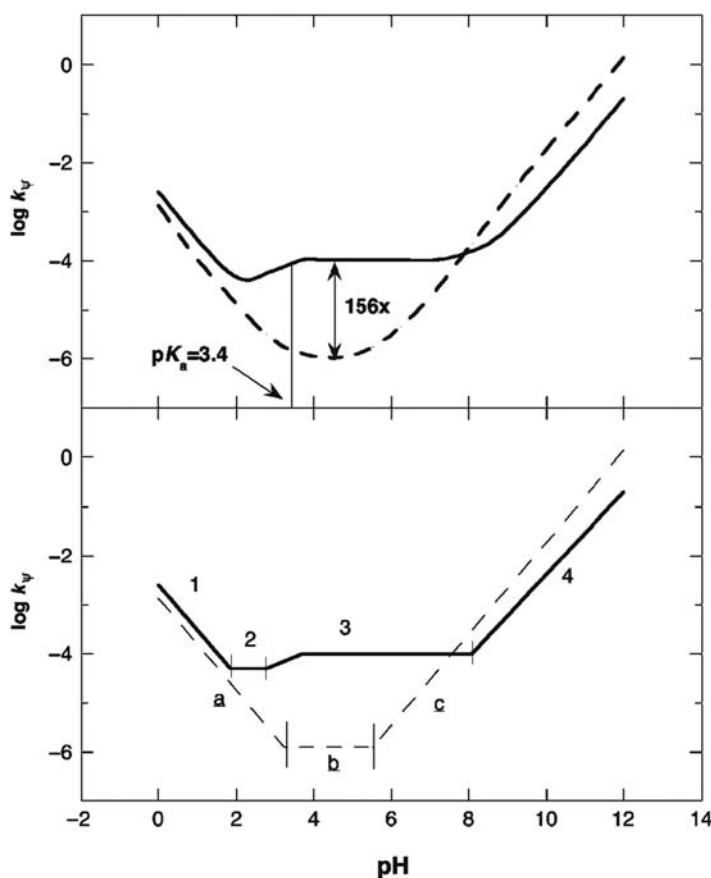
Very complex pH-rate profiles can be interpreted using a sequence of five steps [4]:

1. Divide the pH-rate profile into regions separated by upward curvature.
2. Note each pH value at which a downward curvature occurs, and evaluate whether the substrate may have a group, which may undergo acid–base dissociation at this value. If so, postulate that the downward bend corresponds to substrate dissociation. If not, postulate that it corresponds to a change in the rate-determining step.
3. Use the empirical equations of Figure 13.4 to represent the pH dependence in each region. Multiply each term less than two pH units to the left (lower pH) of a pK_a by f_{SH} , and all terms less than two pH units to the right (higher pH) of that pK_a by f_s .
4. Fit the empirical rate law to the data.
5. Propose a mechanism consistent with the rate law to each region of the pH-rate profile.

The application of this sequence of steps is conveniently illustrated by the hydrolysis of aspirin and its methyl ester,



which exhibit the pH-rate profiles illustrated in Figure 13.7. Figure 13.7b represents the idealised profiles, which identify more clearly the regions separated by upward curvatures.

**FIGURE 13.7**

(Upper panel) The pH-rate profiles of aspirin (full line) and its methyl ester (dashed line).

(Lower panel) Idealised profiles with the identification, by number in aspirin and by letters in its methyl ester, of the different regions that correspond to different terms of the rate law.

The pH-rate profile of the methyl ester of aspirin has three regions, with slopes -1 , 0 and $+1$, and the molecule does not contain ionisable groups. By analogy with Figure 13.4, the pseudo-first-order rate constant must have the form

$$k_p + c_1[H^+] + c_2 + \frac{c_3}{[H^+]} \quad (13.45)$$

Region a must be an acid catalysis, and its mechanism can be written as



where E represents the methyl ester of aspirin and a water molecule was explicitly included because it is an hydrolysis reaction. The corresponding rate law in this region is

$$k_{\Psi} = k_1[\text{H}_2\text{O}][\text{H}^+] \quad (13.46)$$

Region b does not involve acid–base catalysis and its mechanism must be



with the rate law

$$k_{\Psi} = k_2[\text{H}_2\text{O}] \quad (13.47)$$

Finally, region c is the region of base catalysis, and its mechanism can be written as



expressed by the rate law

$$k_{\Psi} = k_3[\text{OH}^-] = k_3 \frac{K_w}{[\text{H}^+]} \quad (13.48)$$

The pH-rate profile of aspirin is more complex, with four regions, and involves a molecule with an ionisable group, the carboxylic acid group. The downward curvature of region 3 may correspond to the titration of this group because the pH of the intersection between the two arms of this region is typical of an aromatic carboxylic acid, $pK_a = 3.4$. Additionally, region 2 is less than 2 pH units from the postulated pK_a and its rate law must be multiplied by f_{SH} . On the other hand, region 4 does not have to be multiplied by f_S because it is more than 2 pH units from that pK_a . Putting together all the contributions to the rate laws yields:

$$k_{\Psi} = c_1[\text{H}^+] + \frac{c_2[\text{H}^+]}{K_a + [\text{H}^+]} + \frac{c_3 K_a}{K_a + [\text{H}^+]} + \frac{c_4}{[\text{H}^+]} \quad (13.49)$$

This rate law can be fitted to the experimental pH-rate profile very well using the following parameters: $c_1 = 2.8 \times 10^{-3} \text{ M}^{-1} \text{ min}^{-1}$, $c_2 = 1.89 \times 10^{-5} \text{ min}^{-1}$, $c_3 = 1.55 \times 10^{-4} \text{ min}^{-1}$, $c_4 = 19.7 \text{ M}^{-1} \text{ min}^{-1}$ and $K_a = 4.17 \times 10^{-4} \text{ M}$.

In region 1, aspirin is predominantly in the protonated form (SH) and the mechanism of hydrolysis in this region is



The corresponding rate law is given by eq. (13.46). In region 2, aspirin remains in the protonated form and the un-catalysed hydrolysis follows the mechanism



with the rate law

$$k_{\Psi} = k_2 f_{\text{SH}}[\text{H}_2\text{O}] = \frac{k_2 [\text{H}^+] [\text{H}_2\text{O}]}{K_a + [\text{H}^+]} \quad (13.50)$$

The value of k_2 for aspirin is about 20 times greater than for its methyl ester. This suggests a special role for the carboxylic acid group, which may be formulated in terms of intra-molecular acid catalysis (Figure 13.8a).

The mechanism of region 3 may be expressed as the attack of a water molecule on the aspirin anion



for which the rate law is

$$k_{\Psi} = k_3 f_{\text{S}}[\text{H}_2\text{O}] = \frac{k_3 K_a [\text{H}_2\text{O}]}{K_a + [\text{H}^+]} \quad (13.51)$$

The rate constant for this reaction is 156 times larger than that of the analogous reaction in the methyl ester of aspirin and suggests a special role for the carboxylate group of aspirin. A molecular structure for the postulated intra-molecular base catalysis is presented in Figure 13.8b. There are other kinetically indistinguishable mechanisms that are possible for regions 2 and 3. The distinction between such mechanisms requires additional information of the system, such as isotope effects comparing behaviour in water and D_2O , or studies of substituent effects using related compounds. Finally, region 4 suggests the mechanism



with the rate law

$$k_{\Psi} = k_4 [\text{OH}^-] = k_4 \frac{K_w}{[\text{H}^+]} \quad (13.52)$$

This procedure leads to mechanisms of specific acid–base catalysis that are compatible with the kinetic data. However, it should always be remembered that

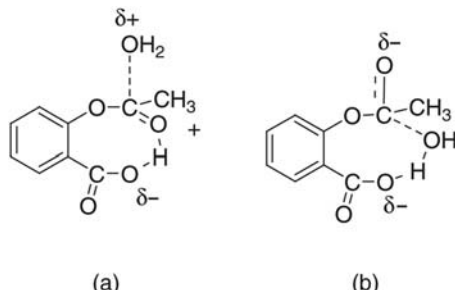


FIGURE 13.8

- (a) Intra-molecular acid catalysis by the carboxylic acid group of aspirin.
- (b) Intra-molecular base catalysis by the carboxylate group of aspirin.

kinetically indistinguishable mechanisms may exist and that the proposal of a mechanism should always be based on all the information available for the system, and not only the kinetic data.

13.4 Catalytic activity and acid–base strength

The search for relationships between molecular structure and chemical reactivity, presented in [Chapter 7](#), Relationships Between Structure and Reactivity, was instrumental for the development of chemical kinetics in the beginning of the twentieth century. One of the early successes in this area was the relationship suggested by Brönsted and Pedersen for the acid catalysis,



according to which the catalytic constant of an acid HA is related to the acid dissociation constant K_{HA} , by [5]

$$k_f = G_f(K_{\text{AH}})^\alpha \quad (13.53)$$

where G_f is a constant that depends on the temperature, medium and substrate, whereas α is a parameter that remains constant for the same type of acid. This parameter is called the Brönsted coefficient for acid catalysis. The reverse reaction in mechanism (13.XIX) can be regarded as a base catalysis, where A^- is the base catalyst. For this reaction a similar relationship applies

$$k_r = G_r \left(\frac{1}{K_{\text{AH}}} \right)^\beta \quad (13.54)$$

and β is the Brönsted coefficient for base catalysis.

Brönsted relationships can only be observed for a limited range of acid dissociation constants K_{HA} , because as they become larger the reaction eventually becomes diffusion controlled and α must tend to be zero. On the other hand, given the equilibrium constant $K_{\text{eq}} = (k_f/k_r)$, when $\alpha = 0$ the reaction rate for the reverse reaction must vary inversely with K and, consequently, be proportional to $(K_{\text{HA}})^{-1}$. Then, $\beta = 1$. In general, the sum of the Brönsted coefficients must be equal to unity

$$\alpha + \beta = 1 \quad (13.55)$$

When the acid has more than one equivalent proton that can be transferred and the conjugate base has more than one equivalent basic site to be protonated, the above equations can be generalised to

$$\frac{k_f}{p} = G_f \left(\frac{q}{p} K_{\text{AH}} \right)^\alpha \quad (13.56)$$

$$\frac{k_r}{q} = G_r \left(\frac{p}{q} \frac{1}{K_{\text{AH}}} \right)^\beta \quad (13.57)$$

where p is the number of equivalent dissociable protons and q the number of equivalent basic sites in the conjugate base. These relations have the same nature as the statistical correction for equivalent hydrogen atoms discussed in Chapter 6, Reactivity in Thermalised Systems.

Figure 13.9 illustrates the reversible abstraction of a proton of 2,2',4,4'-tetranitrophenylmethane by a series of bases in 50% water/50% dimethyl sulfoxide, where this acid has a dissociation constant of $pK_a^{CH} = 10.90$, and that may proceed by general acid–base catalysis [6]. The general expression for the rate constant of this reaction is, according to eq. (13.25),

$$k_{\text{obs}} = k_p^{\text{H}_2\text{O}} + k_p^{\text{OH}}[\text{OH}^-] + k_p^B[\text{B}^-] + k_{-p}^{\text{H}}[\text{H}^+] + k_{-p}^{\text{BH}}[\text{BH}] + k_{-p}^{\text{H}_2\text{O}} \quad (13.58)$$

This reaction can be studied under conditions where some of the terms of the general equation can be neglected. For example, in the presence of an excess of OH^- , eq. (13.58) reduces to

$$k_{\text{obs}} = k_p^{\text{OH}}[\text{OH}^-] + k_{-p}^{\text{H}_2\text{O}} \quad (13.59)$$

and a plot of k_{obs} as a function of $[\text{OH}]$ is linear. In this case, k_p^{OH} can be obtained from the slope ($k_p^{\text{OH}} = 46.6 \text{ M}^{-1} \text{ sec}^{-1}$) and $k_{-p}^{\text{H}_2\text{O}}$ is given by the intercept or by $k_{-p}^{\text{H}_2\text{O}} = k_p^{\text{OH}}/K_p^{\text{OH}}$ ($k_{-p}^{\text{H}_2\text{O}} = 3.31 \times 10^{-4} \text{ sec}^{-1}$), where K_p^{OH} is the equilibrium constant for the system represented in Figure 13.9 in the absence of a buffer solution and at high pH. In contrast, in HCl solutions, eq. (13.58) becomes

$$k_{\text{obs}} = k_{-p}^{\text{H}}[\text{H}^+] \quad (13.60)$$

and $k_{-p}^{\text{H}} = 1.75 \times 10^4 \text{ M}^{-1} \text{ sec}^{-1}$ has been measured. From the relation $k_p^{\text{H}_2\text{O}} = k_{-p}^{\text{H}} K_a^{CH}/K_p^{\text{H}_2\text{O}}$, where $K^{H_2O} = -1.44$ ($[\text{H}_2\text{O}] = 27.5 \text{ M}$) in this medium, $k_p^{\text{H}_2\text{O}} = 7.92 \times 10^{-9} \text{ M}^{-1} \text{ sec}^{-1}$.

The values of k_{-p}^{BH} and k_p^B can be measured in experiments run at different values of the ratio $[\text{BH}]/[\text{B}^-]$. For buffers with $\text{pH} < 5$, eq. (13.58) simplifies to

$$k_{\text{obs}} = k_{-p}^{\text{H}}[\text{H}^+] + k_{-p}^{\text{BH}}[\text{BH}] \quad (13.61)$$

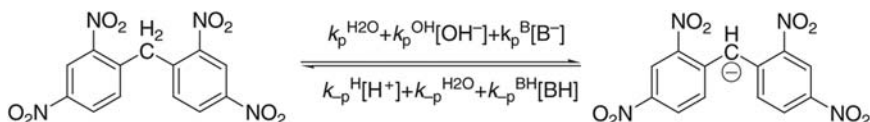


FIGURE 13.9

Reversible abstraction of a proton of 2,2',4,4'-tetranitrophenylmethane in 50% water—dimethylsulphoxide at 25°C.

and the rate constant for the general acid catalysis is given by the slope of the plot of k_{obs} as a function of $[\text{BH}]$. Several parallel lines of this type are obtained when the experiments are done at different pH values. In the case of phenol and methoxyphenol buffers, the slope of k_{obs} as a function of $[\text{BH}]$ depends on the pH, as illustrated in Figure 13.10. In this case eq. (13.58) becomes

$$k_{\text{obs}} = k_p^{\text{B}}[\text{B}] + k_{-p}^{\text{BH}}[\text{BH}] \quad (13.62)$$

because $k_p^{\text{OH}}[\text{OH}^-]$ and $k^{\text{H}_2\text{O}}$ are negligible, as shown by the intercepts of Figure 13.10. The rate constants k_{-p}^{BH} and k_p^{B} can be obtained from experiments at different values of the $[\text{BH}]/[\text{B}^-]$ ratio. Table 13.3 presents the rate constants for general acid and base catalysis for the systems represented in Figure 13.9 when the catalysts are phenols. Figure 13.11 illustrates the Brønsted plots for the base catalysis of the ionisation reaction and for the acid catalysis of the re-protonation reaction. The sum of the experimental Brønsted coefficients is only slightly in excess of unity.

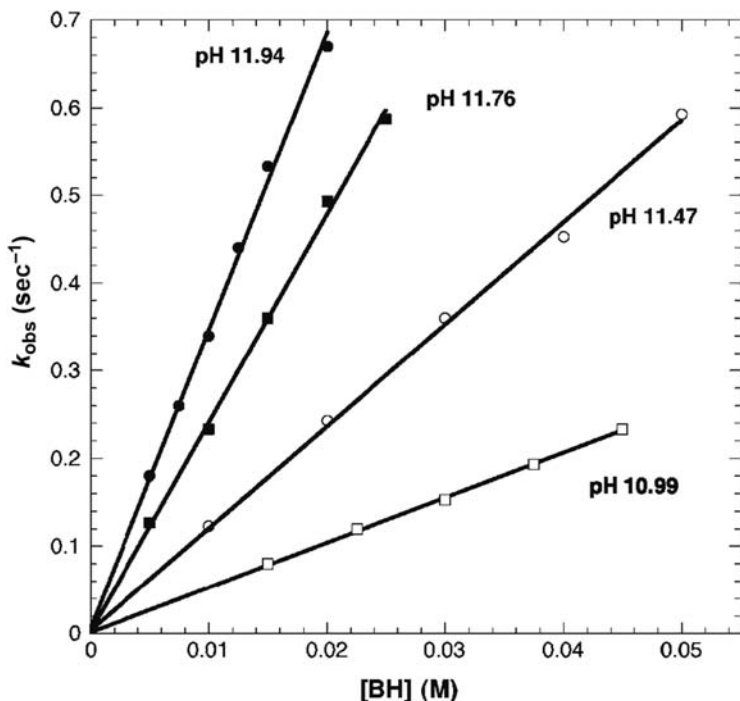


FIGURE 13.10

pH and buffer concentration effect on the PT rates of 2,2',4,4'-tetrinitrophenylmethane in 50% water—dimethylsulphoxide at 25°C. (PT, Proton transfer).

Table 13.3 Rate constants for the acid and base catalysis of PT in 2,2',4,4'-tetranitrophenylmethane in 50% water—dimethylsulphoxide at 25°C ($pK_a^{CH} = 10.90$).

Buffer (acid form)	pK_a^{BH}	k_{-p}^{BH} (M ⁻¹ sec ⁻¹)	k_p^{BH} (M ⁻¹ sec ⁻¹)
2-Cyanophenol	7.97	180	0.21
4-Cyanophenol	8.45	49.1	0.174
2-Bromophenol	9.52	29.4	1.23
4-Chlorophenol	10.18	11.13	2.13
Phenol	11.21	1.62	6.05
4-Methoxyphenol	11.47	1.20	10.87

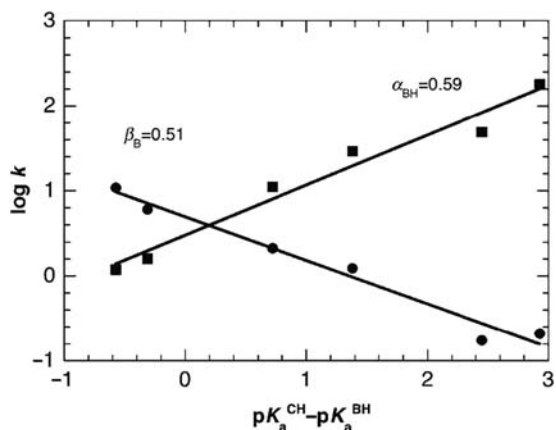


FIGURE 13.11

Brønsted plots for the base catalysis (circles) and acid catalysis (squares) of 2,2',4,4'-tetranitrophenylmethane PT in 50% water—dimethylsulphoxide at 25°C. (PT, Proton transfer)

13.5 Salt effects

The addition of 0.1 M lithium perchlorate increases the ionisation rate of a sulphonic acid ester by a factor of 10^5 when the reaction takes place in a non-polar solvent. The empirical relation between the rate and the salt concentration is

$$k = k_0 + b[\text{salt}] \quad (13.63)$$

where k_0 is the rate constant in the absence of salt and b a constant that depends on the nature of the salt. This remarkably high salt effect is due to the formation of ion pairs. In polar solvents, the salt effect is usually much lower.

In acid–base catalysis, it is convenient to distinguish between a primary salt effect and a secondary salt effect. The primary effect is related to the dependence of the rate constant on the activity coefficients of the species entering the rate law

$$v = k_0[A][B] \frac{\gamma_A \gamma_B}{\gamma_{\ddagger}} \quad (13.64)$$

As the addition of a salt changes the activity coefficient γ , it also changes the reaction rate. This effect was discussed in [Chapter 9](#), Elementary Reactions in Solution and was expressed in [eq. \(9.67\)](#).

The secondary effect is related to the changes introduced by the salt in the ionisation constant of a weak acid HB,

$$K_{HB} = \frac{[H^+][B^-]}{[HB]} \frac{\gamma_{H^+} \gamma_{B^-}}{\gamma_{AB}} \quad (13.65)$$

where K_{HB} is the true dissociation constant of the acid. The addition of a salt changes the ionic strength, hence the activity coefficients, and the concentrations of HB and H^+ . Some examples of positive secondary salt effects are illustrated in [Table 13.4](#). They refer to an increase in $[H^+]$, and decrease in $[HB]$, with addition of salt. Different effects are expected for charged acids or bases. For strong acids and bases the secondary salt effects are negligible.

13.6 Acidity functions

The simplest relationships between rate constants and the pH, which is an acidity function, were illustrated in [Figure 13.4](#). However, the concept of pH is in general only valid in the region $0 < \text{pH} < 14$. For very concentrated acid solutions, these relationships break down and alternative acidity functions have been proposed. The first to meet with some success was proposed by Hammett and Deyrup [7] and was based on equilibria of the type



found in anilines.

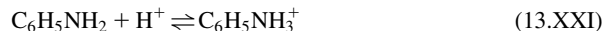


Table 13.4 Secondary salt effects on the decomposition of diazoacetic ester in 0.05 M acetic acid, at 15°C.

$[KNO_3]$ (mol dm $^{-3}$)	$[H^+]$ (10 $^{-4}$ mol dm $^{-3}$)	k (min $^{-1}$)
0.00	9.53	1.27
0.02	10.3	1.37
0.10	10.9	1.46

The equilibrium constant of such reactions is

$$K = \frac{[\text{BH}^+]}{[\text{H}^+][\text{B}]} \frac{\gamma_{\text{BH}^+}}{\gamma_{\text{B}} \gamma_{\text{H}^+}} \quad (13.66)$$

and may also be written as

$$\log K - \log \frac{[\text{BH}^+]}{[\text{B}]} = -\log \left(a_{\text{H}^+} \frac{\gamma_{\text{B}}}{\gamma_{\text{BH}^+}} \right) \quad (13.67)$$

If $[\text{BH}^+]$ and $[\text{B}]$ can be distinguished spectroscopically, as is the case for the anilines, and if K can be measured in more dilute solutions, then all the quantities in the left-hand side of eq. (13.67) are experimentally accessible. The right-hand side, where a_{H^+} is the activity of H^+ , is defined as the acidity function H_0

$$H_0 \equiv -\log \left(a_{\text{H}^+} \frac{\gamma_{\text{B}}}{\gamma_{\text{BH}^+}} \right) \quad (13.68)$$

This acidity function can be measured in any acidic solution by introducing a suitable indicator and measuring the concentration of $[\text{BH}^+]$ and $[\text{B}]$. For example, the mechanism



where the second step is the rate-determining step,

$$v = k^\ddagger [(\text{SH}^+)^\ddagger] \quad (13.69)$$

and the transition states are in quasi-equilibrium with the species SH^+

$$K_S^\ddagger = \frac{a_\ddagger}{a_{\text{SH}^+}} = \frac{[(\text{SH}^+)^\ddagger] \gamma_\ddagger}{[\text{SH}^+] \gamma_{\text{SH}^+}} \quad (13.70)$$

where a_\ddagger and γ_\ddagger are the activity and activity coefficient of the activated complex, respectively, leads to the rate

$$v = k^\ddagger K_S^\ddagger [\text{SH}^+] \frac{\gamma_{\text{SH}^+}}{\gamma_\ddagger} \quad (13.71)$$

This rate law can be expressed in terms of the reactant concentrations using the pre-equilibrium approximation:

$$\frac{a_{\text{SH}^+}}{a_{\text{S}} a_{\text{H}^+}} = \frac{[\text{SH}^+]}{[\text{S}]} \frac{\gamma_{\text{SH}^+}}{\gamma_{\text{S}} a_{\text{H}^+}} = K_S \quad (13.72)$$

that yields

$$v = k^\ddagger K_S^\ddagger K_S \frac{\gamma_{\text{S}}}{\gamma_\ddagger} a_{\text{H}^+} [\text{S}] \quad (13.73)$$

Table 13.5 Hydrolysis of β -propiolactone in concentrated perchloric acid solution [8].

$[\text{HClO}_4]$ (mol dm $^{-3}$)	k (10^{-3} min $^{-1}$)	$-\log_{10} k$ (min $^{-1}$)	$-H_0$
1.83	3.65	2.44	0.58
2.60	5.38	2.27	0.94
4.53	32.2	1.49	1.84
5.36	69.9	1.16	2.28

The first-order rate constant

$$k = k^\ddagger K_S^\ddagger K_S \frac{\gamma_S}{\gamma_\ddagger^*} a_{\text{H}^+} \quad (13.74)$$

can be written in logarithmic terms as

$$\log k = \log(k^\ddagger K_S^\ddagger K_S) + \log\left(\frac{\gamma_S}{\gamma_\ddagger^*} a_{\text{H}^+}\right) \quad (13.75)$$

to emphasise the similarity between the last term and the acidity function H_0 . Accordingly, there must be a linear correlation between $\log(k)$ and H_0 , with a slope of -1 . The hydrolysis of β -propiolactone in concentrated acid solution presents this type of behaviour, as illustrated in Table 13.5.

Just as with pH, the function H_0 is a logarithmic function. It is convenient to define its anti-logarithm as

$$H_0 = -\log h_0 \quad (13.76)$$

where h_0 is equal to the activity of H^+ in diluted aqueous solution.

13.7 Hydrated proton mobility in water

The proton in water, represented above by H^+ or H_3O^+ , is strongly hydrated. Eigen argued that the symmetrical distribution of the excess positive charge among the three protons in the hydronium ion allows for the formation of very stable hydrogen bonds to three neighbouring H_2O molecules and the complex ion $\text{H}_3\text{O}^+(\text{H}_2\text{O})_3$ should be remarkably stable and observable in aqueous solution. Direct evidence for the existence of the “Eigen ion” in solution was obtained in the X-ray and neutron scattering studies of Triolo and Narten [9], who measured a nearest-neighbour oxygen–oxygen distance of $l_{\text{OO}}(\text{H}_3\text{O}^+\cdots\text{OH}_2) = 2.52 \text{ \AA}$. This is much shorter than the near-neighbour $\text{H}_2\text{O}\cdots\text{OH}_2$ distance in the tetrahedral network of pure water, $l_{\text{OO}} = 2.85 \text{ \AA}$, also measured by these authors. Although the enthalpy of the hydrogen bond in liquid water is known rather precisely, $10.6 \pm 0.4 \text{ kJ mol}^{-1}$ [10], the strength of the H bonds in the Eigen ion is

not known but must be greater than this because shorter H-bonds distances correspond to stronger H bonds. For example, the calculated gas-phase O···O distance of H_5O_2^+ is $l_{\text{OO}} = 2.38 \text{ \AA}$ [11] and its experimental H-bond enthalpy is 133 kJ mol^{-1} [12]. A good estimate for the strength of the H bond in the Eigen ion can be obtained with the Lippincott–Schroeder [13] potential. This potential, presented in detail in [Appendix V](#), The Lippincott–Schroeder Potential, gives a quantitative relation between H-bond strengths, distances and frequencies. A comparison between H-bond lengths and strengths is presented in [Figure 13.12](#).

For low degrees of hydration, Zundel proposed that the $(\text{H}_2\text{O} - \text{H}^+ \cdots \text{OH}_2)$ ion should also be relatively stable. In fact, the X-ray and neutron diffraction measurements of Kameda and co-workers on aqueous 21% HCl solutions, revealed the existence of a species with a nearest-neighbour O···O distance of $2.37 \pm 0.02 \text{ \AA}$, consistent with the Zundel ion. This is an exceptionally short distance, comparable with that obtained by *ab initio* calculations for this ion in the gas phase. According to the Lippincott–Schroeder potential, the H-bond strength

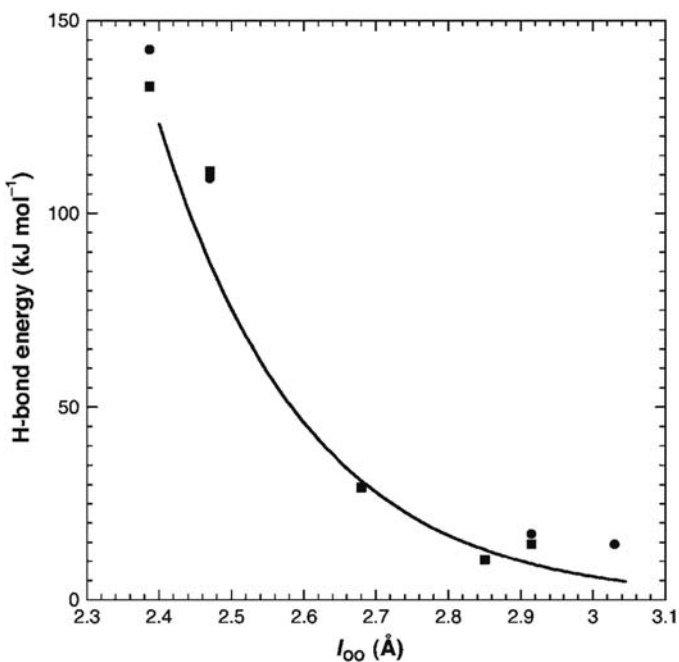


FIGURE 13.12

Relation between the H-bond lengths and strengths involving oxygen acids and bases. The circles are classical potential energies from *ab initio* calculations, the squares are experimental H-bond enthalpies and the line is the relation given by the Lippincott–Schroeder potential described in [Appendix V](#), The Lippincott–Schroeder Potential.

of the Eigen ion is 33 kJ mol^{-1} and that of the Zundel ion is 92 kJ mol^{-1} . In spite of this difference, the Eigen ion is the predominant species in dilute acid solutions, because it involves three hydrogen bonds. Other theoretical and experimental data also indicate that the Eigen ion is slightly more stable than the Zundel ion in dilute acid solutions, by *ca.* 3 kJ mol^{-1} [14].

The identification of both Eigen and Zundel ions in acidic solutions helps to understand the anomalously high mobility of protons in liquid water, which is approximately five times that of ions of similar size to H_3O^+ . An early explanation for this high mobility is known as the Grotthuss mechanism. This involves a proton shuttling between successive water molecules, such that rather than involving the transport of the larger H_3O^+ species, protons move by a relay in the H-bonded water network. This picture must be refined to accommodate the very fast dynamics of the aqueous proton transport, which approach 1 psec [15]. The proton changes positions between H-bonded oxygen atoms nearly 10^{12} times every second, equivalent to vibration in a shallow potential well. The current view on this process is that the Zundel ion is almost always an intermediate in the conversion between two Eigen ions. This process is illustrated in Figure 13.13 and should be associated with a very small barrier. The actual rate-determining step may be a change in the second hydration layer, and proton mobility is facilitated by cooperative many-molecule effects [16,17].

The very small barrier associated with the transfer of the proton in water is a consequence of the strong hydrogen bonds involved. This is not exclusive to the excess proton in water. When AH and B in reaction (13.I) can form H bonds stronger than 4 kJ mol^{-1} , the barrier for PT is significantly reduced and the PT rate is significantly enhanced at room temperature. This is always the case for PT between oxygen, nitrogen and halogen acid and bases. In such cases, the mechanism for PT between strong acids and bases involves hydrogen-bonded intermediates. According to the mechanism proposed by Eigen [18], we have to consider a precursor and a successor complex along the reaction coordinate

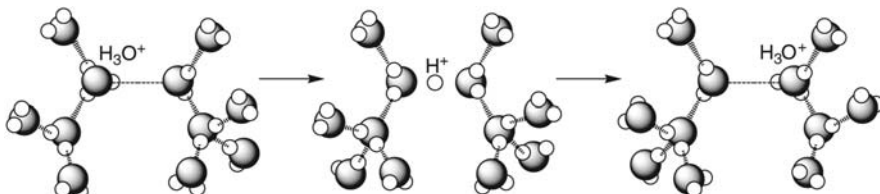


FIGURE 13.13

From left to right, a proton in an Eigen ion migrates to form a Zundel ion, and then proceed to form another Eigen ion. Only the hydration shell of the lower water molecules is shown.

The hydrogen bond involves an incipient PT because it corresponds to an advancement of the PT coordinate with respect to the separated reactants. Using the bond order of the product bond as the reaction coordinate, it changes from 0 in the reactants, to $n_{\text{H}\cdots\text{B}}$ in the precursor complex, to n^{\ddagger} in the transition state, to $n_{\text{A}\cdots\text{H}}$ in the successor complex and finally to 1 in the products. Using the definition of the bond order given by the ISM in Chapter 6, Reactivity in Thermalised Systems, which relates bond orders to bond extensions, and given the relation between bond lengths and bond strengths shown in Figure 13.12, it is not surprising that ISM and the LS potential give an approximately linear relation between the bond order in the H-bonded complex $\text{AH}\cdots\text{B}$ and the corresponding H-bond strength (Figure 13.14). When the bond strength exceeds 140 kJ mol^{-1} , $n_{\text{H}\cdots\text{B}}$ reaches 0.5. At this point, the barrier for PT disappears and the proton is symmetrically placed between A and B. This is the case of the FHF^- ion, that is formed in water with an association constant of 4 M^{-1} [19], and in the gas phase is a symmetrical ion with an H-bond enthalpy of 203 kJ mol^{-1} , the highest ever measured. The high stability of this species is likely to be one of the reasons that, in

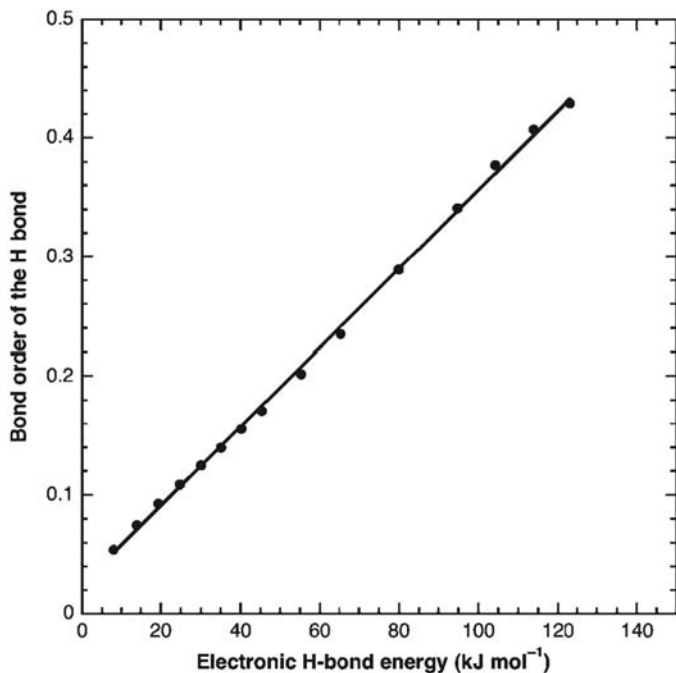


FIGURE 13.14

Relation between hydrogen-bond orders ($n_{\text{H}\cdots\text{O}}$) and electronic H-bond energies ($D_{\text{e(OHO)}}$), according to the LS potential and ISM. (LS, Lippincott–Schroeder; ISM, intersecting-state model).

contrast to the other hydrohalic acids (HI $pK_a = 9$; HBr $pK_a = 8$, HCl $pK_a = 6.1$), HF is a weak acid in water ($pK_a = 3.18$).

The three steps of mechanism (13.XXIV) correspond to the diffusion of the reactants in solution until an H-bonded complex is formed, followed by the PT step between precursor and successor complexes, and the diffusion of the products to their equilibrium separations. The rate constant for the forward transfer is

$$v = k_f[\text{AH}][\text{B}^-] \quad (13.77)$$

and the forward rate constant can be expressed in terms of the actual rate constants of the three steps using the steady-state approximation for the concentration of the two complexes.

$$k_f = \frac{k_a k_p k_s}{k_p k_s + k_{-a} k_s + k_{-p} k_{-a}} \quad (13.78)$$

Similarly, for the reverse rate constant

$$v = k_r[\text{A}^-][\text{HB}] \quad (13.79)$$

the reverse rate constant can also be expressed within the same approximation as

$$k_r = \frac{k_{-a} k_{-p} k_{-s}}{k_p k_s + k_{-a} k_s + k_{-p} k_{-a}} \quad (13.80)$$

In acid catalysis, the nature of AH changes while the substrate B^- is maintained constant. The Brønsted coefficient for the forward process is α_A and for the reverse process it is β_A . In base catalysis, B varies while AH remains constant along the reaction series; now β_B is the Brønsted coefficient in the forward direction and the α_B coefficient for the reverse direction. Table 13.6 summarises these relationships.

Acids centred on oxygen, nitrogen and halogen atoms have rapid PT, $k_p \gg k_a, k_s$. Additionally, for exothermic forward reactions, $k_p > k_{-p}$. When these conditions are met, eqs. (13.78) and (13.80) simplify to

$$\begin{aligned} k_f &= k_a \\ k_r &= \frac{k_{-s} k_{-p}}{k_s k_p} k_{-a} \end{aligned} \quad (13.81)$$

and the forward rate constant is independent of the acidity of AH and of the basicity of B^- , that is, $\alpha_A = 0$ and $\beta_B = 0$. In this case there is no catalysis by the

Table 13.6 Brønsted coefficients for PT reactions.

Catalysis	Catalyst (changing along the series)	Substrate (constant along the series)	Brønsted coefficient	
			Forward	Reverse
Acid	HA_i	B^-	α_A	β_A
Base	B^-_i	HA	β_B	α_B

acid AH, or by the base B^- , and the value of k_f approaches that of the diffusion rate constant, *ca.* $10^{10} \text{ dm}^3 \text{ mol}^{-1} \text{ sec}^{-1}$ in aqueous solution. For the reverse reaction, the rate constant k_r depends on the acidity constant of the acid and is directly proportional to $-\Delta pK = -(pK_{\text{HA}} - pK_{\text{HB}})$, because $(k_{-p}/k_p) = (pK_{\text{HB}} - pK_{\text{HA}})$. Although there is no acid catalysis in the forward direction, in the reverse direction there is base catalysis and the Brønsted coefficient which will affect k_r is $\beta_A = 1$. This behaviour is illustrated in Figure 13.15.

Another limiting condition for eqs. (13.78) and (13.80) is $k_p \gg k_a, k_s$, but $k_p < k_{-p}$. In this case, the forward PT is an endothermic process. The rate constants are simplified to

$$\begin{aligned} k_f &= \frac{k_a}{k_{-a}} \frac{k_p}{k_{-p}} k_s \\ k_r &= k_{-s} \end{aligned} \quad (13.82)$$

The forward rate constant depends on the equilibrium constant of the PT, and k_f is directly proportional to $(pK_{\text{HA}} - pK_{\text{HB}})$. The consequences are similar to those discussed above for the first limiting condition: forward direction, acid catalysis gives $\alpha_A = 1$ and base catalysis gives $\beta_B = 1$. The reverse reaction is diffusion controlled and is not catalysed.

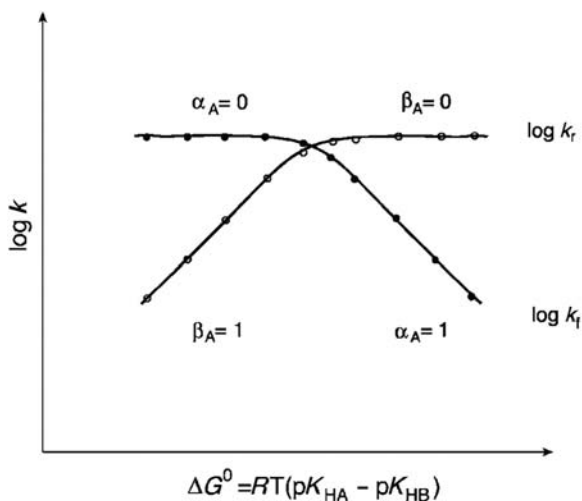


FIGURE 13.15

Eigen plots for the acid–base catalysis of strong acids following mechanism (13.XXIV). In acid catalysis in the forward direction, HA is the catalyst and varies along the reaction series, while the substrate B^- is kept constant. In the forward direction, the change in HA gives the Brønsted coefficient α_A for acid catalysis, and for the reverse direction the change in A^- gives the Brønsted coefficient β_B for base catalysis.

In summary, when the barrier for PT is small in the forward direction, the exothermic rate constants are diffusion controlled and catalysis is not observed. On the other hand, the barriers in the reverse direction are high and increase in the same fashion as their endothermicity. The rates vary in the same proportion as the pH (specific acid catalysis) or the pOH (specific base catalysis).

A third limiting condition occurs when $k_p < k_{-a}$ and $k_{-p} < k_s$. The rate-determining step is now the transfer of the proton, and

$$\begin{aligned}k_f &= \frac{k_a \cdot k_p}{k_{-a}} \\k_r &= \frac{k_{-s} \cdot k_{-p}}{k_s}\end{aligned}\quad (13.83)$$

This condition is often met in carbon acids. In this case, it is possible to observe general acid–base catalysis and the values of α and β are in between 0 and 1.

13.8 Proton-transfer rates in solution

The protolysis of acids of similar strength spans an extraordinary range of reaction rates. For example, the rate of the acid-catalysed de deuteration of azulene-1-*d* ($pK_a = -1.76$) is $0.45 \text{ M}^{-1} \text{ sec}^{-1}$ [20], whereas the deprotonation rate of electronically excited 5-cyano-1-naphthol ($pK_a = -2.8$) is $1.3 \times 10^{11} \text{ sec}^{-1}$ [21], when both of them are measured in water ($pK_a = -1.74$). The nature of the reactants also has a profound effect on the kinetic isotope effects (KIEs). For example, the de tritiation of toluene ($pK_a = 41.2$) by caesium cyclohexylamine ($pK_a = 41.6$) in cyclohexylamide has $k_H/k_D = 11$ [22], whereas for the deprotonation of 5-cyano-1-naphthol in water k_H/k_D is only 1.6 [21].

The free-energy dependence of many PT rates follows the Brönsted relationship described above, but the success of this free-energy linear relationship is unexpected. In principle, it should not be valid over a large range of acidity constants, because the Brönsted coefficient for acid catalysis should vary dramatically from $\alpha_A = 0$ to 1 when the reaction becomes endothermic, as shown in Figure 13.15, where acid–base catalysis is not observed. This was assigned to the small size of the barrier for the forward PT, but an explanation for the size of the barriers based on molecular structure of the reactants is still lacking.

In the remainder of this chapter, the rates of PT reactions in solution are quantitatively related to the molecular structures of the reactants and to their hydrogen-bonding ability. This relation uses ISM, previously employed to calculate the rates of atom transfers and S_N2 reactions, thus providing a general account of the rates of the most important bond-breaking–bond-making reactions. In the next chapter, the principles applied to these reactions in gas phase and in solution are also applied to some cases of enzyme catalysis.

13.8.1 Classical PT rates

The most important difference between the application of ISM to H-atom transfers in the gas phase and PT in solution is the calculation of the reaction energy. In the first case, the classical potential energy of the H-atom transfer, ΔV^0 , is obtained as the difference between the classical potential energies of the HA bond in the reactants and the HB bond in the products. Then the vibrationally adiabatic potential energy is obtained by adding the difference in zero-point energies between reactants and products. For PT in solution the reaction free energy is directly obtained from the difference in acidity constants.

$$\Delta G^0 = -RT \left[2.303pK_{BH} + \ln\left(\frac{p_B}{q_B}\right) - 2.303pK_{AH} - \ln\left(\frac{p_A}{q_A}\right) \right] \quad (13.84)$$

The reaction free energy is simple to obtain experimentally for most PTs of interest. However, its decomposition in enthalpy and entropy contributions requires the measurement of acidity constants as a function of temperature. The entropies of reaction are not usually known, but, for the calculation of PT rates, the participation of the entropy in the reaction coordinate can be limited to the determination of the partition functions. In the simplest approximation, it can be assumed that the ratio of the transition state versus reactant vibrational partition functions is close to unity. Ignoring tunnelling corrections and vibrational frequency changes along the reaction coordinate, the classical rate for PT is, following eq. (6.83)

$$k_{cl} = \sigma \left(\frac{1}{3} \right)^3 \frac{6.82 \times 10^{10}}{\sqrt{T}} \left(\frac{m_A + m_B + m_C}{m_A(m_B + m_C)} \right)^{3/2} \frac{I_{BHA}}{I_{HA}} \exp\left(-\frac{\Delta V_{cl}^\ddagger}{RT}\right) \quad (13.85)$$

where σ is a statistical factor ($\sigma = p_A q_B$), the scaling factor $(1/3)^3$ was obtained from the typical ratio of vibrational to rotational partition functions in polyatomic systems, and the value of the constant gives the rate in units of $M^{-1} \text{ sec}^{-1}$ when the masses are expressed in atomic mass units. The moment of inertia of the reactants is

$$I_{HA} = \frac{m_H m_A}{m_H + m_A} (l_{HA,eq})^2 \quad (13.86)$$

and that of the transition state is

$$I_{BHA} = m_B (l_{HB}^\ddagger)^2 + m_A (l_{HA}^\ddagger)^2 - \frac{(m_B l_{HB}^\ddagger - m_A l_{HA}^\ddagger)^2}{m_B + m_H + m_A} \approx m_B (l_{HB}^\ddagger)^2 + m_A (l_{HA}^\ddagger)^2 \quad (13.87)$$

These equations have a simple solution for nearly symmetrical reactions, when $\Delta V^0 \approx 0$ and $n^\ddagger \approx 0.5$. In this case, following ISM, the transition state bond lengths are given by

$$\begin{aligned} l_{HA}^\ddagger &= l_{HA,eq} - a'_{sc} (l_{HA,eq} + l_{HB,eq}) \ln(0.5) \\ l_{HB} &= l_{HB,eq} - a'_{sc} (l_{HA,eq} + l_{HB,eq}) \ln(0.5) \end{aligned} \quad (13.88)$$

and the classical energy barrier is

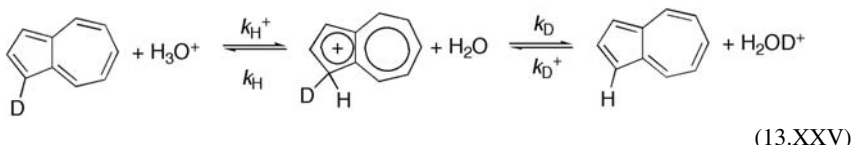
$$\begin{aligned}\Delta V_{\text{cl}} &= D_{e,\text{HA}} \left\{ 1 - \exp[\beta_{\text{HA}} a'_{\text{sc}} (2l_{\text{HA,eq}}) \ln(0.5)/m] \right\}^2 \\ &= D_{e,\text{HB}} \left\{ 1 - \exp[\beta_{\text{HB}} a'_{\text{sc}} (2l_{\text{HB,eq}}) \ln(0.5)/m] \right\}^2\end{aligned}\quad (13.89)$$

where the electronic dissociation energy ($D_{e,\text{HA}}$, $D_{e,\text{HB}}$), spectroscopic constant (β_{HA} , β_{HB}) and equilibrium bond length ($l_{\text{HA,eq}}$, $l_{\text{HB,eq}}$) are readily available from bond-dissociation energies, vibrational frequencies and structural data. Some examples are given in Table 13.7. The “universal” constant of ISM, $a'_{\text{sc}} = 0.182$, and the electrophilicity index of Parr

$$m = \frac{I_p + E_A}{I_p - E_A} \quad (13.90)$$

complete all the data required to calculate the $\Delta V_{\text{cl}}^\ddagger$, provided that the ionisation potential (I_p) and the electron affinity (E_A) of B (or A) are also known.

This simple method to calculate classical rates is conveniently illustrated by the deprotonation of the conjugated acid of azulene in aqueous solution, mechanism (13.XXV).



In the absence of data on the radical ion of azulene, we take the ionisation potential and electron affinity of the molecule, $I_p = 7.42$ eV and $E_A = 0.79$ eV, to

Table 13.7 Bond lengths, bond-dissociation energies, vibrational frequencies of the molecules and ionisation potentials and electron affinities of the radicals employed in the calculation of the energy barriers of PT reactions^a.

	I_{eq} (Å)	D_e (kJ mol ⁻¹)	β (Å ⁻¹)	I_p (eV)	E_A (eV)
C ₆ H ₆	1.101	488.7	1.8415	8.32	1.096
CH₃C₆H₅	1.111	390.4	1.9894 ^b	7.242	0.912
CH ₃ COCH ₃	1.103	425.9	1.9005	9.703 ^c	1.76 ^d
CH ₃ NO ₂	1.088	64.6	2.5447	11.08 ^c	0.50 ^c
CH ₃ NH ₂	1.010	270.3	2.1717		
H ₂ O	0.9575	517.1	2.1697	13.017	1.8277
CH ₃ COOH	0.97	461.5	2.2581	10.65 ^c	3.29 ^d
C ₆ H ₅ OH	0.956	381.2	2.5617	8.56	2.253

^aBoldface letters indicate where the radical is centred after the bond to the hydrogen atom is broken; bond lengths and bond-dissociation energies from ref. [23]; ionisation potentials and electron affinities from webbook.nist.gov, except where noted.

^bZavitsas [24].

^cFor the molecule.

^dPearson [25].

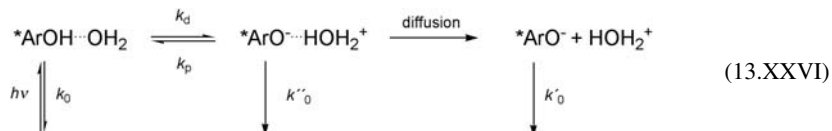
calculate $m = 1.238$. The $D_{e,HA}$, β_{HA} and l_{HA} values of the two acidic C–H bonds of azulene can be taken from those of benzene. Using these parameters and eq. (13.89), we obtain $\Delta V_{cl}^\ddagger = 56.1 \text{ kJ mol}^{-1}$. With $D_{e,HA}$, β_{HA} and $l_{HA,eq}$ values of water a similar calculation gives $\Delta V_{cl}^\ddagger = 61.5 \text{ kJ mol}^{-1}$. The model is very forgiving, provided that a consistent set of data are employed. Using $\Delta V_{cl}^\ddagger = 58.6 \text{ kJ mol}^{-1}$, the classical rate is $1.5 \times 10^{-2} \text{ M}^{-1} \text{ sec}^{-1}$. Table 13.8 compares this and other calculated rates with the corresponding experimental data.

The approximate calculation of classical PT barriers in H-bonded systems is slightly more complicated, because hydrogen bonding reduces the PT barrier. As mentioned earlier, the H bond corresponds to a progress along the PT reaction coordinate. This is taken into account by replacing n^\ddagger by $(n^\ddagger - n_{H\dots B})$, where $n_{H\dots B}$ is the bond order associated with the hydrogen bond. The ISM classical barrier is now

$$\Delta V_{cl}^\ddagger = [1 - (n^\ddagger - n_{H\dots B})]D_{e,HA}\{1 - \exp[\beta_{HA}d'_{sc}(2l_{HA,eq})\ln(1 - n^\ddagger + n_{H\dots B})/m]\}^2 + (n^\ddagger - n_{H\dots B})D_{e,HB}\{1 - \exp[\beta_{HB}d'_{sc}(2l_{HB,eq})\ln(n^\ddagger - n_{H\dots B})/m]\}^2 \quad (13.91)$$

The bond order associated with the H bond is given by the LS potential, provided the H-bond strength or length is known. The simplest method to obtain $n_{H\dots B}$ is to use the linear correlation between this parameter and the H-bond strength illustrated in Figure 13.14 for oxygen acids and bases, $n_{H\dots B} \approx 0.0253 + 0.0033D_{0(AHB)}$. For energies below 50 kJ mol⁻¹, a good linear correlation is also found with the vibrationally adiabatic H-bond energies, $n_{H\dots B} = 0.0427 + 0.0039D_{0(AHB)}$.

The procedure to calculate the barrier for PT in an H-bonded system is conveniently illustrated with the excited-state deprotonation of 5-cyano-1-naphthol (5CN1N) in water, mechanism (13.XXVI). The H-bond energies of precursor and successor complexes are 8 and 17 kJ mol⁻¹, respectively. We will use $D_{0(AHB)} = 12.5 \text{ kJ mol}^{-1}$ to have the symmetry required by the simplified formulation. This gives $n_{H\dots B} = 0.0915$. The excited-state I_P is the ground state I_P minus the excited state energy (E_e). Using $I_P(C_6H_5O) = 8.56 \text{ eV}$ and $E_e(5CN1N) = 3.444 \text{ eV}$, together with $E_A(C_6H_5O) = 2.253 \text{ eV}$, we obtain $m = 2.574$. With the D_e , l_{eq} and β values of the O–H bonds in naphthol and water, eq. (13.91) gives $\Delta V_{cl}^\ddagger = 6.3 + 11.3 = 17.6 \text{ kJ mol}^{-1}$.



The transfer of a proton in an H-bonded system corresponds to the movement of the proton along its hydrogen bond. This movement is limited by the frequency of approach between the A and B atoms in the H-bonded precursor complex, which is the H-bond vibrational frequency, \bar{v}_{AB} . It is related to the H-bond

Table 13.8 Parameters employed in the ISM reaction coordinate of $\text{AH} + \text{B}^- \rightarrow \text{A}^- + \text{HB}$, and corresponding ISM classical (k_{cl}) and semi-classical (k_{sc}) rates^a.

AH, pK_a	HB, pK_a	Reactant model	Product model	m	D_{0(AHB)} (kJ mol⁻¹)	k_{cl}	k_{sc}	k_{exp}
H_3O^+ , -1.74	Azulene H^+ , -1.76	C_6H_6	H_2O	1.238	—; —	1.5×10^{-2}	1.2	1.5^{b}
$5\text{CN}1\text{N}^*$, -2.8	H_3O^+ , -1.74	$\text{C}_6\text{H}_6\text{OH}$	H_2O	2.574	8; 17	5.2×10^9	1.7×10^{11}	$1.3 \times 10^{11\text{c}}$
Nitromethane, 10.22	Water, 15.74	CH_3NO_2	H_2O	1.095	—; —	8.8×10^{-2}	6.5	9.2^{d}
Acetylacetone, 9.0	Water, 15.74	CH_3COCH_3	H_2O	1.443	—; —	1.4×10^1	6.0×10^3	$2 \times 10^{4\text{e}}$
Acetic acid, 4.76	Propionic acid, 4.88	CH_3COOH	CH_3COOH	1.894	17; 17	4.0×10^6	1.3×10^9	$3.9 \times 10^{8\text{f}}$
Toluene, 41.2	Li c-hexylamide, 41.6	$\text{C}_6\text{H}_6\text{CH}_3$	CH_3NH_2	1 ^g	—; —	7.5×10^{-4}	1.1×10^{-2}	$6.3 \times 10^{-2\text{h}}$

^aRates at 25°C per equivalent proton in M^{-1} sec⁻¹, except for italicised rates, which are in sec⁻¹.

^bGruen and Long [20].

^cPines and co-workers [21].

^dBell and Goodall [26].

^eAt 12°C, [18].

^fRates at 20°C, [27].

^gFor H bonded to sp^3 carbon atoms the standard value of unity is always employed by ISM.

^hStreitwieser, Jr. [22].

distance and strength through the LS potential. For an H-bond strength of 12.5 kJ mol^{-1} between oxygen atoms, this frequency is $\bar{v}_{AB} = 236 \text{ cm}^{-1}$. PT is now a first-order reaction and the classical rate constant expressed in terms of this vibrational frequency is

$$k_{\text{cl}} = K_c c \bar{v} \exp\left(-\frac{\Delta V_{\text{cl}}^{\ddagger}}{RT}\right) \quad (13.92)$$

where K_c represents the fraction of acid species H bonded to the base. For 5CN1N in aqueous solution all acid species are H bonded to water, $K_c = 1$, and $k_{\text{cl}} = 5.9 \times 10^9 \text{ sec}^{-1}$ at 298 K. The comparison with the experimental rate is presented in [Table 13.8](#).

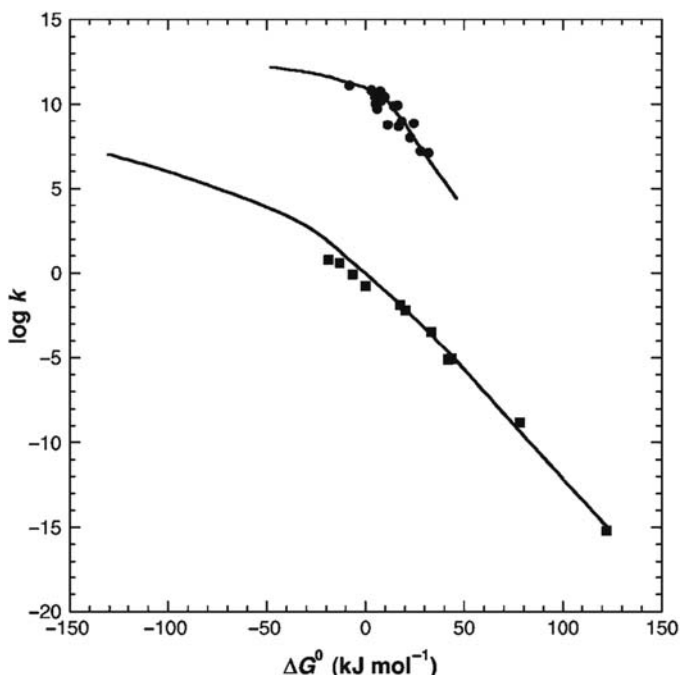
The classical rates necessarily underestimate the experimental rates because the zero-point energy corrections reduce the barrier by 5–10 kJ mol⁻¹ (a factor of 5–30 at room temperature) and tunnelling further increases the rates by another factor of 5–10 at room temperature. Thus the symmetrical classical rates are one to two orders of magnitude too small. The underestimate of k_{cl} is more severe in exothermic reactions, because the reaction energy was not taken into account in these very simple calculations. The systems presented in [Table 13.8](#) confirm this expectation.

Although the simple calculations using a classical model tend to underestimate the rates, classical ISM does explain the 11 orders of magnitude difference between the excited-state deprotonation of 5CN1N and the acid-catalysed dedeuteration of azulene without adjustable parameters. According to ISM, the molecular factors that control the rates of nearly isothermal PT are the electrophilicity index m and the hydrogen-bonding ability. Low values of m ($m \rightarrow 1$) correspond to “hard molecules” [28], and lead to high barriers. Electronic excitation increases the value of m , leads to “softer” acids and faster reactions. Strong hydrogen bonds appreciably decrease the barriers and correspond to “normal”, or rapidly reacting acids.

13.8.2 Semi-classical absolute rates

The similarity between classical calculations of atom and PT rates can be extended to the semi-classical calculations. The methods employed for the semi-classical calculations are those of [Section 6.3.3](#). They require zero-point energy corrections along the reaction coordinate, as well as tunnelling corrections. Such corrections can only be done efficiently with the aid of a computer programme. However, the calculations remain so simple that can be done using programs freely available over the Internet [29] at www.ism.qui.uc.pt:8180/ism/3. Representative semi-classical rate constants are presented in [Table 13.8](#) [30]. As expected, they are a significant improvement over the classical calculations. Additionally, with the aid of a computer, the rates of asymmetrical systems are easily calculated and the free-energy dependence of the rates can be explored.

[Figure 13.16](#) shows the free-energy dependence calculated for the protonation of aromatic hydrocarbons, such as azulene discussed above, and for the excited-state

**FIGURE 13.16**

Free-energy relationships in the protonation of aromatic hydrocarbons and methoxybenzenes (squares) and in the excited-state PT from aromatic naphthols (circles), in water. (PT, Proton transfer).

PT from aromatic alcohols, such as 5CN1N also discussed above. The calculations employed the parameters of azulene and water, for the first family of reactions, and of naphthol and water, for the second family of reactions, and only the reaction free energy was changed within each series of reactions. The calculated and experimental free-energy dependence are in excellent agreement and illustrate the change from a Brønsted type of relationship for the aromatic hydrocarbons, to an Eigen-type of relationship for the excited naphthols. The dramatic increase in the curvature of the free-energy dependence is closely associated with the increase in electrophilicity index. A value of m close to unity leads to a free-energy dependence that looks linear over a wide range of free energies, whereas a large value of m leads to a strong dependence of the free energy for endothermic reactions, changing rapidly to nearly free-energy independent rates for exothermic reactions. The Brønsted- and Eigen-type of free-energy dependences can also be related to the size of the “intrinsic barriers” of each family of reactions. With low values of m , the Brønsted plots correspond to high “intrinsic barriers”, and the location of the transition state changes slowly with the free-energy originating “constant” Brønsted coefficients for acid and base catalysis. On the other hand,

the large values of m give the low barriers characteristic of the Eigen plots, and the location of the transition state changes from very close to the structure of the successor complex to that of the precursor complex, as the reaction free energy changes from slightly positive to slightly negative.

One of the most interesting features of the semi-classical calculations is their ability to predict and rationalise KIE. The most significant isotope effects arise from the replacement of the proton by a deuteron. As shown in Figure 6.6, this replacement increases the zero-point energy difference between the transition state and the reactants when the bond to proton, or deuteron, is partially broken at the transition state. Assuming identical pre-exponential factors for proton and deuteron transfers and neglecting all changes in the bending vibrational frequencies along the reaction coordinate, Westheimer predicted a maximum KIE for symmetrical transfers, where the symmetric stretching at the transition state is independent of the mass of the central atom [31]. Figure 13.17 shows the ratio

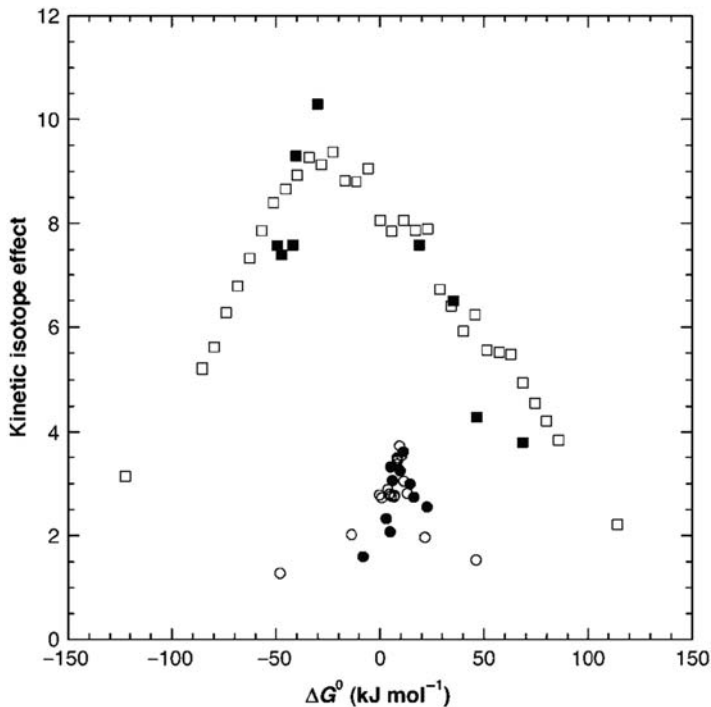


FIGURE 13.17

KIE in the ionisation of nitroalkanes to water, hydroxide and carboxylate ions (squares), and in the excited-state PT of naphthols to water (circles). ISM-LC/scTST calculations (open symbols) employed the data for nitromethane or excited naphthols and water. (ISM-LC/scTST, intersecting-state model with Lippincott-Schroeder potential/semi-classical Transition State Theory; KIE, Kinetic isotope effect; PT, proton transfer).

between the rates of proton (k_H) and deuteron (k_D) transfer as a function of the reaction free energy of nitroalkane ionisations to bases such as H_2O , OH^- , RCOO^- or PhO^- [32–35], and of excited-state PT of naphthols to water [36,37]. These systems were selected for the structural homogeneity of the reactants in each family of reactions. The experimental data do not follow very closely Westheimer's postulate. The maximum KIE of PT between carbon and oxygen atoms is displaced towards the endothermic reactions, and an opposite asymmetry is observed in the transfer between oxygen atoms. Moreover, the maximum KIE in the nitroalkane ionisation exceeds $k_H/k_D = 6.7$, that is the value expected from the difference in the zero-point energies of C–H and C–D bonds, 4.7 kJ mol^{-1} . An opposite anomaly is observed in the transfer between oxygen atom, where the experimental KIE is much lower than $k_H/k_D = 7.9$, calculated from the zero-point energy differences of O–H and O–D bonds, 5.1 kJ mol^{-1} .

The semi-classical calculations using the ISM-LS reaction coordinate and TST with tunnelling corrections, but otherwise identical pre-exponential factors for proton and deuteron transfers are in good agreement with the experimental data of Figure 13.17. The success of these calculations comes from the incorporation of the tunnelling corrections and, in the case of excited naphthols, hydrogen bonding. The tunnelling correction for a PT in a nitroalkane with $\Delta G^0 = 0$ is 14, whereas for a deuteron transfer in this system it is only 4. Thus the tunnelling correction contributes with a factor of 3.5 to the KIE, and the calculated KIE is “only” 8 because the difference in zero-point energies is 2 kJ mol^{-1} , rather than the maximum value of 4.7 kJ mol^{-1} . The asymmetry of the KIE as a function of the reaction free energy is due to asymmetry of the reactive bonds: a C–H is broken and an O–H bond is formed. The excited-state PT of the naphthols is not symmetrical either. The hydrogen bond formed between the ionic products is stronger than that formed between the neutral reactants, and the maximum KIE now occurs in the endothermic reactions. The hydrogen bond is also responsible for the progress of the reactants along the reaction coordinate and for a further reduction in zero-point energies differences between proton and deuteron transfers. The calculated vibrationally adiabatic barriers differ only by 0.8 kJ mol^{-1} for a naphthol ionisation with $\Delta G^0 = 0$, which contribute with a factor of 1.4 to the KIE at 298 K. The low barriers of these reactions give small tunnelling corrections at this temperature, 2.5 for the proton and 1.5 for the deuteron, and the calculated KIE is only 2.3.

13.9 Proton-transfer model system

Many interesting features of PT reactions were combined in the design of a photo-acid capable of long-lived and reversible pH jumps, 1-(2-nitro-ethyl)-naphthalene-2-ol (NO_{2n}H) [38], presented in Figure 3.15. In the electronic ground state, the first ionisation constant of NO_{2n}H in 2% methanol:water is $\text{p}K_a = 9.7$

and leads to an anion exchanging a proton between naphthalate and carbanion moieties. At pH 7 NO_{2n}H is a neutral species. However, the naphthol moiety of NO_{2n}H becomes a strong acid in the excited singlet state ($\text{p}K_{\text{a}}^* = 1.9$) and ionises rapidly and completely when the 2% methanol:water solution is initially neutral. The decay of the naphthalate singlet state to its ground state competes with intra-molecular PT from the nitroalkane moiety, which is a non-adiabatic reaction that leads to the ground state of the carbanion. Finally, the carbanion slowly re-protonates to regenerate neutral NO_{2n}H .

These reversible PT reactions occur in widely different time scales. As discussed before for 5CN1N, excited-state deprotonations of naphthols to water molecules are extremely fast, occurring with rate constants $>10^9 \text{ sec}^{-1}$, as shown in [Table 13.8](#). The intra-molecular PT that neutralises the excited naphthalate occurs in a favourable geometry and is a non-adiabatic reaction that takes advantage of the excited-state energy of naphthalate to be very exothermic ($\Delta G^0 < -300 \text{ kJ mol}^{-1}$). [Figure 13.16](#) shows that the rate of this first-order reaction can compete with the 20 nsec lifetime of excited naphthalate to yield a carbanion. PT reactions at the α carbon of nitroalkanes are notoriously slow, as shown in [Table 13.8](#), which mean that the protonation of the nitrocarbanion to regenerate NO_{2n}H at a pH close to 7 may occur in the time scale of seconds, as shown in [Figure 4.6](#). The rate constants calculated with ISM for the various PT steps were presented in [Figure 3.15](#). The experimental rate constants follow very closely the theoretical predictions [38]. The excited state lifetime of NO_{2n}H is predicted to be 0.5 nsec, and the experimental lifetime is *ca.* 4 nsec at pH 6.4. The intra-molecular PT is calculated to be $3 \times 10^8 \text{ sec}^{-1}$ and the measured value is *ca.* 10^8 sec^{-1} . The relaxation time of the carbanion is expected to be 2 sec at pH 5 and the relaxation time observed was 0.6 sec. Theoretical design was decisive to guide the synthesis of a photo-acid capable of persistent pH jumps.

References

- [1] KJ Laidler, *Chemical Kinetics*, HarperCollins, New York, 1987.
- [2] JJA Wijs, *Z. Phys. Chem.* **11** (1893) 492.
- [3] JJA Wijs, *Z. Phys. Chem.* **12** (1893) 415.
- [4] GM Loudon, *J. Chem. Educ.* **68** (1991) 973–983.
- [5] JN Brönsted, KL Pederson, *Z. Phys. Chem.* **108** (1924) 185.
- [6] F Terrier, J Lelievre, A-P Chatrousse, P Farrell, *J. Chem. Soc. Perkin 2* (1985) 1479.
- [7] LP Hammett, AJ Deyrup, *J. Am. Chem. Soc.* **54** (1932) 2721.
- [8] LA Long, M Purcham, *J. Am. Chem. Soc.* **72** (1950) 3267.
- [9] R Triolo, AH Narten, *J. Chem. Phys.* **63** (1975) 3624–3631.
- [10] DM Carey, GM Korenowski, *J. Chem. Phys.* **108** (1998) 2669–2675.
- [11] P Salvador, M Duran, JJ Dannenberg, *J. Phys. Chem. A* **106** (2002) 6883–6889.
- [12] M Meot-Ner (Mautner), CV Speller, *J. Phys. Chem.* **90** (1986) 6618–6624.
- [13] ER Lippincott, R Schroeder, *J. Chem. Phys.* **23** (1955) 1099–1106.
- [14] N Agmon, *Isr. J. Chem.* **39** (1999) 493–502.

- [15] Z Luz, S Meiboom, *J. Am. Chem. Soc.* **86** (1964) 4768–4769.
- [16] D Marx, ME Tuckerman, J Hutter, M Parrinello, *Nature* **397** (1999) 601.
- [17] H Lapid, N Agmon, MK Petersen, GA Voth, *J. Chem. Phys.* **122** (2005) 014506.
- [18] M Eigen, *Ang. Chem. Int. Ed. Engl.* **3** (1964) 1.
- [19] RL Scott, *J. Phys. Chem.* **75** (1971) 3843–3845.
- [20] LC Gruen, FA Long, *J. Am. Chem. Soc.* **89** (1967) 1287–1291.
- [21] E Pines, D Pines, T Barak, B-Z Magnes, LM Tolbert, JE Haubrich, *Ber. Bunsenges. Phys. Chem.* **102** (1998) 511–517.
- [22] A Streitwieser, Jr., PH Owens, G Sonnichsen, WK Smith, GR Ziegler, HM Niemeyer, TL Kruger, *J. Am. Chem. Soc.* **95** (1973) 4254.
- [23] DR Lide, *Handbook of Chemistry and Physics*, CRC Press Inc., 2001.
- [24] AA Zavitsas, *J. Am. Chem. Soc.* **94** (1972) 2779–2789.
- [25] RG Pearson, *J. Am. Chem. Soc.* **108** (1986) 6109.
- [26] RP Bell, DM Goodall, *Proc. R. Soc. London A* **294** (1966) 273–297.
- [27] M-L Ahrens, G Maass, *Angew. Chem. Int. Ed.* **7** (1968) 818–819.
- [28] RG Pearson, *Acc. Chem. Res.* **26** (1993) 250–255.
- [29] LG Arnaut, M Barroso, D Oliveira, *ISM_APT*, University of Coimbra, Coimbra, 2006.
- [30] M Barroso, LG Arnaut, SJ Formosinho, *J. Phys. Chem. A* **111** (2007) 591–602.
- [31] FH Westheimer, *Chem. Rev.* **61** (1961) 265.
- [32] RP Bell, JE Crooks, *Proc. R. Soc. London A* **286** (1965) 285.
- [33] DJ Barnes, RP Bell, *Proc. R. Soc. London A* **318** (1970) 421–440.
- [34] FG Bordwell, WJ Boyle, Jr., *J. Am. Chem. Soc.* **97** (1975) 3447–3452.
- [35] M Amin, WH Saunders, Jr., *J. Phys. Org. Chem.* **6** (1993) 393–398.
- [36] LG Arnaut, SJ Formosinho, *J. Photochem. Photobiol. A: Chem.* **75** (1993) 1–20.
- [37] M Barroso, L Arnaut, SJ Formosinho, *J. Photochem. Photobiol. A: Chem.* **154** (2002) 13–21.
- [38] RMD Nunes, M Pineiro, LG Arnaut, *J. Am. Chem. Soc.* **131** (2009) 9456.

Enzymatic catalysis

14

Enzymes are the best catalysts known. They mediate a vast array of chemical transformations in all living organisms and do so very efficiently under mild conditions. Most enzymatic mechanisms of catalysis have ample precedents in organic catalytic reactions. Yet reactions that are very fast in the presence of enzymes, become extremely slow in their absence, and some have half-lives approaching the age of the Earth. For example, the half-life for the spontaneous decarboxylation of amino acids is 1100 million years, but in the presence of arginine decarboxylase, the rate constant of the catalysed reaction is in the vicinity of $100\text{--}1000 \text{ sec}^{-1}$ [1]. This, as many other enzyme-catalysed reactions, demonstrates the excellent kinetic efficiency of these catalysts. In general, enzymes produce rate enhancements that range from 10^7 -fold to 10^{21} -fold. Table 14.1 presents rate constants of enzyme-catalysed reactions and, for each of the examples, presents also in the row immediately below, the rate of the analogous uncatalysed reaction. The rate enhancement reaches a factor of 10^{21} for the hydrolysis of phosphodiester linkages by staphylococcal nuclease when compared with the uncatalysed hydrolysis of the same type of linkage in dimethylphosphate [2].

In addition to their efficiency, enzymes are also remarkable for their specificity. Each enzyme usually catalyses one specific reaction, and sometimes, only one specific reactant, called substrate, is converted into products. For example, succinate dehydrogenase is an enzyme that exclusively catalyses the oxidation of succinic acid, and not any other carboxylic acid. One of the other important aspects of enzyme catalysis is their stereospecificity. For example, proteases only hydrolyse the derivatives of L-amino acids and not the corresponding D-amino acids. This can be extremely valuable in understanding enzyme mechanisms. At the other extreme, are the enzymes that catalyse families of reactions, such as the esterases, which are enzymes that catalyse the hydrolysis of esters independent of the molecular groups attached to the ester linkage.

14.1 Terminology

All known enzymes are proteins. They are made of covalently linked amino acids residues that form very long, unbranched chains. The amino acid residues are consecutively numbered, starting from the N-terminus. The DNA code specifies the amino acid sequence of the proteins, but before they can carry out their functions, in particular as enzymes, they must take on a particular shape or a “fold”.

Table 14.1 Rate constants of enzyme-catalysed and corresponding uncatalysed reactions, where the uncatalysed analogue is shown in the row below the catalysed reaction^a.

Enzyme or uncatalysed reaction	Enzyme substrate	k_1^b (sec ⁻¹)	k_2^c (M ⁻¹ sec ⁻¹)
Staphylococcal nuclease	DNA phosphodiester linkages	95	1.0×10^7
Hydrolysis of dimethyl phosphate		1.7×10^{-13}	3.1×10^{-15}
Carbonic anhydrase $\text{CO}_2 + \text{H}_2\text{O} \rightarrow \text{H}_2\text{CO}_3$	CO_2	1.0×10^6 0.13	1.2×10^8 2.4×10^{-3}
Triosephosphate isomerase	Dyhydroxyacetone phosphate	4.3×10^3	2.4×10^8
Intramolecular deprotonation of dyhydroxyacetone phosphate		1.7×10^{-6}	
Catalase $\text{H}_2\text{O}_2 \rightarrow \text{H}_2\text{O} + \frac{1}{2}\text{O}_2$	H_2O_2	7.3×10^7 7×10^{-9}	6.6×10^7 1.3×10^{-10}
Ketosteroid isomerase	5(10)-Estrene-3,17-dione	9.0	5.4×10^5
	Acetate ion + 5(10)-estrene-3,17-dione		1.1×10^{-6}

^aFrom ref. [2] except for catalase, which is from refs. [3] and [4], and for ketosteroid isomerase, which is from ref. [5].

^bRepresents k_{cat} for enzyme-catalysed reactions or the rate constant for the analogous uncatalysed first-order reaction presented in the row immediately below.

^cRepresents k_{cat}/K_M , where K_M is the Michaelis constant, for enzyme-catalysed reactions or the rate constant for the analogous bimolecular reaction presented in the row immediately below, using $[\text{H}_2\text{O}] = 55 \text{ M}$.

This usually results from relatively weak non-covalent interactions such as hydrogen bonding, electrostatic attractions or repulsions and hydrophobic interactions. In addition, some cross-linking may occur owing to S–S bonding involving cysteine residues. At temperatures above 60–70 °C, most proteins denature, that is, over a relatively narrow temperature range their native structure unfolds in a cooperative manner, and they become inactive.

The specificity of an enzyme is closely related to the three-dimensional arrangement of its amino acid residues, the tertiary structure. The polypeptide chain follows a complicated path that is unique to each protein. In the complex structure of a protein, it is possible to identify regularities associated with the local conformation of its backbone, its secondary structure. A frequently encountered regularity is a right-handed α -helix of the polypeptide conformation that enables conformational changes and favourable hydrogen-bonding patterns. Another common regularity is the β -pleated sheet, which corresponds to favourable hydrogen bonding between adjacent polypeptide chains, rather than within one chain as in the α -helix.

An enzyme's tertiary structure strictly defines the geometry and charge distribution around a substrate-binding site. This site is largely preformed, waiting for

the substrate to bind, but also exhibits at least some degree of induced fit upon binding of the substrate. The lock-and-key hypothesis, formulated by Emil Fischer in 1894, captures the essence of the enzyme specificity for its substrate: the enzyme is like a lock with a complementary geometry to that of the substrate, which is the key. The binding of the substrate to the enzyme is due to hydrogen bonding, electrostatic and van der Waals interactions (Figure 14.1). The active sites correspond to 10–20% of the total volume of the enzyme.

In addition to the backbone, involving the amino acid residues, many enzymes are strongly associated with small molecules or transition metal ions, called cofactors. Sometimes the cofactors are organic molecules transiently associated with a given enzyme, but in other cases, they are permanently associated with their protein. In both cases, these organic molecules are known as coenzymes, but when they are permanently associated, they are called prosthetic groups. For example, the haem prosthetic group of haemoglobin is tightly bound to its protein through extensive hydrophobic and hydrogen-bonding interactions, together with a covalent bond between the haem Fe^{2+} ion and the imidazole group of a histidine residue of the protein.

A catalytically active enzyme-cofactor complex is called a holoenzyme. When the cofactor can be separated from the enzyme, for example, using dialysis, the enzymatically inactive protein is referred to as an apoenzyme.

Enzymes are classified and named according to the nature of the chemical reactions they catalyse. The six major classes of reactions that enzymes catalyse are (with the enzyme classification in parentheses): oxidation-reduction reactions (oxidoreductases), transfer of functional groups (transferases), hydrolysis reactions (hydrolases), group elimination to form double bonds (lyases), isomerisation (isomerasers) and bond formation coupled with ATP hydrolysis (ligases). There are sub-classes and sub-sub-classes within these classes, and systematic names have been given to minimise ambiguity, but for the purpose of the study of enzyme kinetics, it is not necessary to go into these details.

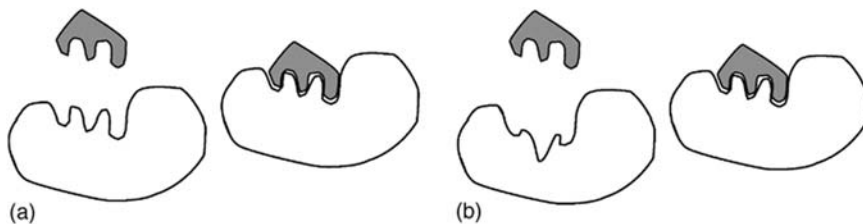


FIGURE 14.1

Binding of a substrate to the active site of an enzyme, owing to the favourable interaction with the functional groups present in the active site: (a) lock-and-key hypothesis, where the shape of the active site is complementary to that of the substrate; (b) induced fit model, where the complementarity of the shapes is induced by the interactions between the enzyme and the substrate.

Enzymes exert thousands of different biological functions and activate hundreds of chemical mechanisms. They accelerate the right reactions to outpace natural dissipative forces, so that living systems can create and maintain conditions for their survival. Moreover, millions of years of evolution and competition between organisms, led enzymes to optimise processes that enable faster growth, more efficient reproduction and faster responses to changing conditions. Given their centrality in Biology, they became preferential drug targets and play a very important role in the drug design of Medicinal Chemistry.

14.2 Factors that accelerate enzymatic action

The velocities of reactions catalysed by enzymes depend on the same factors as all other chemical reactions: nature of reactants, concentrations, temperature and medium. The main reason for the enormous rate enhancements achieved by enzymes is the very special role played by the enzyme as the “medium” for the reaction.

Over half a century ago, Pauling [6] formulated the hypothesis that “enzymes are molecules that are complementary in structure to the activated complexes (transition states) of the reactions that they catalyse”. Today this is more precisely understood as the active sites of enzymes presenting complementary in shape and in electrostatic properties to the transition states of the reactions of their substrates. This view of enzyme catalysis was highly influential and was corroborated by the first structural characterisations of enzyme active sites, which occurred many years later. It is now widely recognised that enzyme catalysis involves very specialised molecular recognition, and that this accounts for a major part of the efficiency of enzyme catalysis. Molecular recognition is due to the complementarities of non-covalent forces. The active site of the enzyme stabilises the transition state through steric effects, proximity, desolvation, entropic effects, electrostatic forces and van der Waals forces. Additionally, molecular recognition is enforced by partially covalent interactions such as hydrogen bonding and general acid–base catalysis. In extreme cases, the transient formation of an enzyme–substrate covalent bond also takes place. All these forces contribute to high enzyme–substrate association constants and to lower the energy of the transition state with respect to the isolated enzyme and substrate. They work cooperatively and most often it is not possible, or useful, to separate the contributions of the various factors. Nevertheless, it is interesting to explore the role played by the factors that contribute to enzyme efficiency using simple molecular models.

14.2.1 Tension and distortion

The binding of the substrate to the active site is energetically favoured by the complementarity of non-covalent forces, but such forces can also be used by the

enzyme to produce distortions in the substrate structure that make its geometry closer to that of the transition state. The strong effect of tension and distortion is illustrated in Figure 14.2 with the alkaline hydrolysis of phosphoesters [7]. Considerable ring strain is released in the alkaline hydrolysis of the cyclic ester and its rate of hydrolysis is a factor of 10^8 faster than that of the corresponding acyclic phosphodiester. The distortion of the functional groups of the reactants into the geometry of the transition state is a major driving force in chemical reactivity and can play an important role in many enzymatic catalysis.

14.2.2 Proximity

Intramolecular and enzymatic catalysis reactions require conformations in which the orbitals of reactants are properly aligned and van der Waals surfaces are set in a near-attack conformation. A convenient method to quantify catalytic efficiency is to compare the rate constant for the intra-molecular reaction with that for the corresponding inter-molecular process. In this context, it is useful to define the effective molarity (EM) as the (first-order) rate constant for the intra-molecular reaction divided by the (second-order) rate constant for the equivalent inter-molecular process. The EM is nominally the concentration of the equivalent external catalyst needed to make the inter-molecular rate match that of the intra-molecular reaction [8].

Figure 14.3 presents EMs of intra-molecular carboxyl group nucleophilic catalysis of the hydrolysis of a series of monophenyl esters [9]. The rate enhancements in this series were assigned to the probability of formation of ground state conformers where the reacting groups are held in conformation to enter the

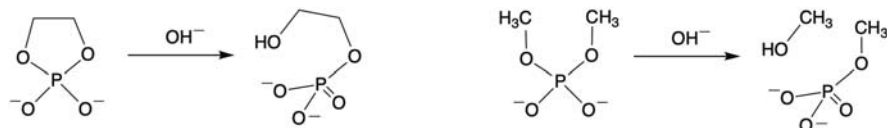


FIGURE 14.2

Alkaline hydrolysis of phosphoesters.

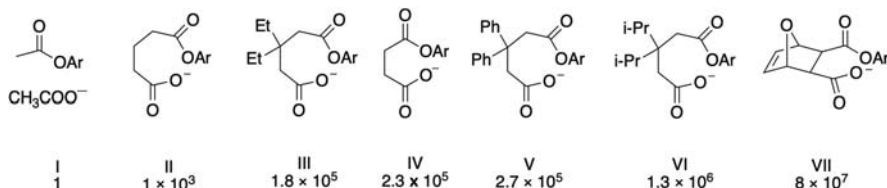


FIGURE 14.3

Carboxyl group nucleophilic catalysis of the hydrolysis of monophenyl esters and their effective molarities.

transition state. This probability was calculated as the mole fraction of conformers with near-attack conformations, based on the stabilisation energy of each conformation. Enthalpy differences, rather than entropic changes, drive rate enhancements in this system. The rate constants increase by about 230-fold upon removal of each single rotatable bond in the sequence II → IV → VII.

14.2.3 Desolvation

The removal of water molecules from charged groups of the substrate upon binding at the active site of the enzyme binding will destabilise the charged groups because enzymes have lower dielectric constants than water. Desolvation will also expose a water-bonded charged group and make it more available for reaction. Similar effects are also found in other host-guest interactions such as cyclodextrins binding organic guests or drug-receptor interactions.

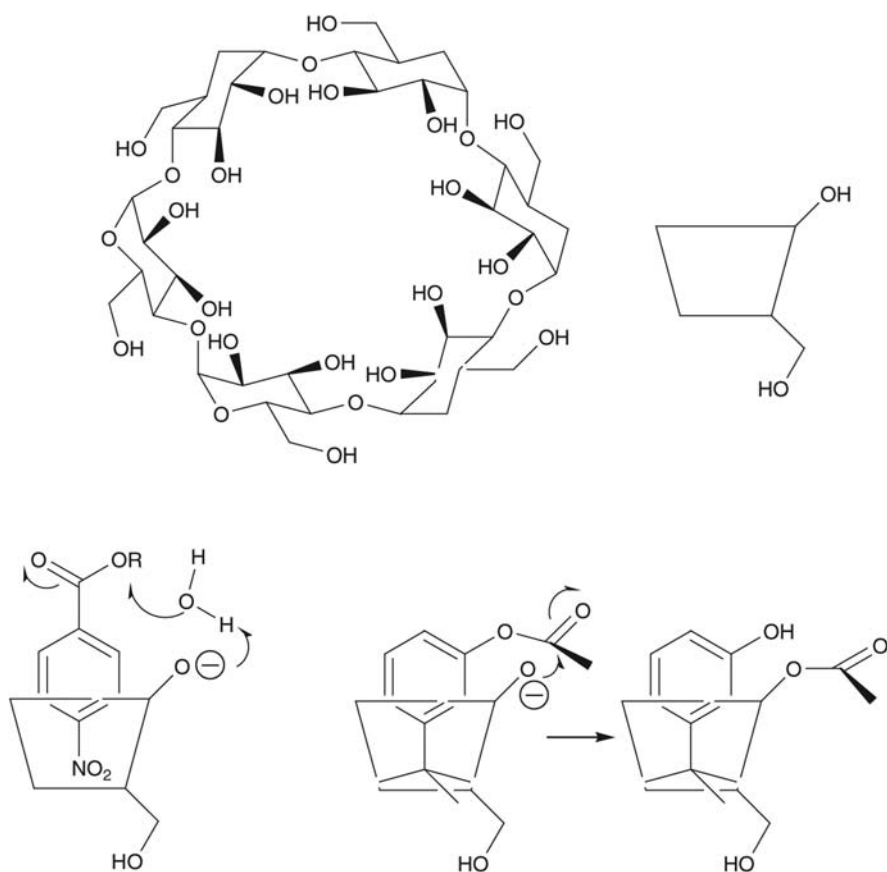
Cyclodextrins are a class of α -D-glucose oligomers with a hydrophobic cavity surrounded by OH groups on the upper and lower edges (Figure 14.4). The hydrophobic pocket favours desolvation and proximity, since it provides a trap for the less-polar moieties of the substrate. Additionally, cyclodextrins lower the local dielectric constant (ϵ) and may enhance the roles of hydrogen bonding and electrostatic forces. For example, the rates of acylation reactions are accelerated in the presence of cyclodextrins [10].

14.2.4 Entropy

There is a translational energy loss associated with bringing reactants into proximity at the transition state. Bimolecular reactions are considered to be intrinsically associated with more negative activation entropies than the unimolecular ones, disregarding possible solvent contributions. There is also a rotational entropy loss to reach the specific angular requirements of the transition state, which may already be present in the enzyme–substrate complex. It has been considered that part of the translational and rotational entropies lost to reach the transition state, is compensated by the enzyme–substrate binding free energy. However, detailed calculations on entropy changes in enzymatic reactions compared with the analogous uncatalysed reactions in water revealed that the lower entropy penalty paid by enzymatic reactions is not related to the “freezing” of reactant motions [11]. The entropy advantage of the studied cases was related to the elimination of solvent reorganisation and to changes in mechanism in the enzyme.

14.2.5 Hydrogen bonding

The strength of the hydrogen bonds increases as the static dielectric constant decreases, and this effect is particularly notable when charged species are involved [12]. Additionally, the electrostatic interaction between two atomic

**FIGURE 14.4**

Molecular models for enzyme catalysis based on cyclodextrins.

charges on the donor and acceptor atoms, q_1 and q_2 , has a reciprocal dependence upon both their distance d_{AB} and ε , eq. (9.50),

$$E = \frac{q_1 q_2 e^2}{4\pi \varepsilon_0 \varepsilon d_{AB}} \quad (14.1)$$

where ε_0 is the vacuum permittivity. The dielectric constant at the surface of a protein, where many polar groups can be found, is *ca.* 30–40. In the most hydrophobic regions of the protein, this value drops to a value closer to that of chloroform ($\varepsilon = 4.8$). In the active site of an enzyme, it is assumed that $\varepsilon \approx 15$ [13]. The energetic stabilisation calculated for an ion pair at a distance of 2.7 Å is presented in Table 14.2 for several values of ε .

When chymotrypsin, a proteolytic enzyme, binds a substrate, Ser195 nucleophilically attacks the scissile carbonyl bond of the peptide to form a tetrahedral

Table 14.2 Energetic stabilisation of an ion-pair ($q_1 = 1$, $q_2 = -1$) at a distance $d_{AB} = 2.7 \text{ \AA}$, as a function of the dielectric constant of the medium.

ϵ	$\Delta(\Delta G^0)$ (kJ mol $^{-1}$)
4.8	106.7
15	34.2
30	17.1
40	12.8
78.5	6.5
∞	0

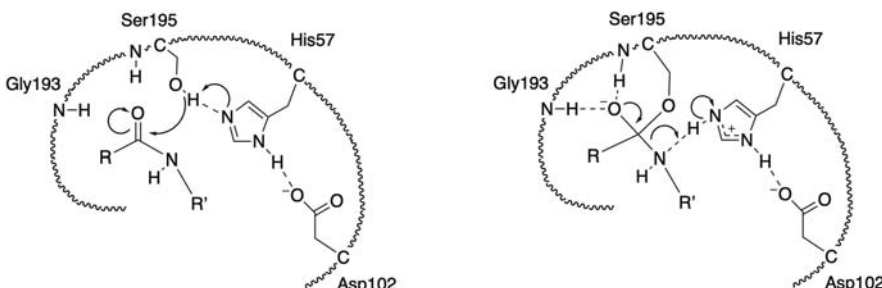


FIGURE 14.5

Transition-state stabilisation of chymotrypsin. (a) Binding of the substrate with conformation appropriate for nucleophilic attack of the peptide bond. (b) Tetrahedral intermediate with a low-barrier hydrogen bond to Ser195.

intermediate, as shown in [Figure 14.5 \[14\]](#). The oxyanion generated can form an unusually short and strong hydrogen bond with Ser195. Such bonds cannot exist in aqueous solutions because of the high dielectric constant of water and its ability to form hydrogen bonds, as discussed in [Chapter 13](#), Acid–Base Catalysis and Proton-Transfer Reactions. Chymotrypsin converts a weak hydrogen bond in the initial enzyme–substrate complex into a strong hydrogen bond in the transition state, thereby facilitating proton transfer while applying the difference in free energy between normal and strong hydrogen bonds to stabilise the transition state.

14.2.6 General acid–base catalysis

The hydrolysis of aspirin, presented in [Figure 13.8a](#), is a good example of intra-molecular acid catalysis. In this case, the acid catalysis is enhanced by the presence of an intra-molecular hydrogen bond. The H bond in the salicylate anion is worth $17\text{--}21 \text{ kJ mol}^{-1}$, and raises the pK_a of the phenolic OH to 13. Other molecular models showed that EMs for intra-molecular general acid–base catalysis can be at least 10^4 M , if favourable intra-molecular H bonds are formed [\[8\]](#).

This is also the factor that separates the typical pre-exponential factor of a bi-molecular reaction in solution, $10^9 \text{ M}^{-1} \text{ sec}^{-1}$, from that of an intra-molecular reaction between the hydrogen-bonded reactants, 10^{13} sec^{-1} . The basis for this change has been discussed in the context of the intersecting-state model (ISM) applications to proton transfers [eqs. (13.85) and (13.92)]. The EM can exceed this value because another factor contributes to accelerate the intra-molecular rate: the strength of the H bond. A hydrogen bond of energy 17 kJ mol^{-1} corresponds to 20% advance of the bond order along the reaction coordinate (Figure 13.14). Using the data for phenol in Table 13.7 ($m = 1.714$), eq. (13.91) gives a 5 kJ mol^{-1} decrease in $\Delta V_{\text{cl}}^\ddagger$, relative to the same system in the absence of the H bond, which corresponds to a factor of 50 in the rate constant at room temperature, and increases the EM to $5 \times 10^5 \text{ M}$.

The lower dielectric constant of enzymes can change the pK_a values of amino acid sidechain groups in the active site. For example, if a carboxylic acid is in a weakly polar micro-environment, the anion form will be unstabilised and the pK_a will rise. However, if the carboxylate ion forms a salt bridge, it will be stabilised and the pK_a will lower. Likewise, the deprotonation of a basic group will be disfavoured in a lower polarity environment and its pK_a will be decreased, but it will rise if the protonated base is in a salt bridge. Such pK_a changes can be used to promote general acid–base catalysis. Moreover, as illustrated in Figure 14.6 enzymes can utilise acid and base catalysis simultaneously, in contrast with reaction in solution.

14.2.7 Metal ions

Nearly one third of all known enzymes require metals for catalytic activity. The most common metal ion cofactors are transition metal ions such as Fe^{+2} , Fe^{3+} , Cu^{2+} , Mn^{2+} or Co^{2+} . They participate in the catalytic process in the following ways: (1) bind to substrates to orient them properly for reaction; (2) mediate oxidation–reduction reactions through reversible changes in their oxidation states; (3) stabilise developing negative charge on a leaving group; (4) shield negative charges on a substrate group that otherwise repel nucleophilic attack; (5) increase the rate of a hydrolysis reaction by forming a complex with a water molecule that increases its acidity. The roles played in (3), (4) and (5) are illustrated in Figure 14.7.

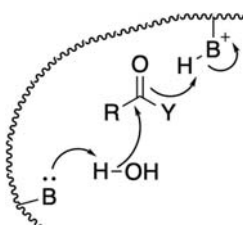
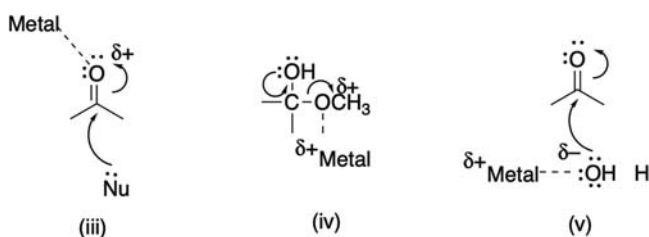


FIGURE 14.6

Simultaneous acid and base enzyme catalysis.

**FIGURE 14.7**

Metal ion stabilising a developing negative charge (iii), shielding a negative charge on a substrate group (iv) and forming a complex with a water molecule to increase its acidity (v).

14.2.8 Transient covalent binding

The binding free energies achieved by non-covalent and partially covalent forces are usually below 65 kJ mol^{-1} [15]. This sets the maximum of 10^{11} M^{-1} for the efficiency of enzyme catalysis. It is an extraordinarily large number, but not quite enough for all the rate enhancements observed in the presence of enzymes. Houk proposed that the maximum efficiency is only achieved when direct covalent bonding between the enzyme or cofactor and the reacting substrate is involved in the reaction mechanism. This is the case of the acyl-enzyme intermediate involved in the catalytic mechanism of serine proteases shown in Figure 14.5 and discussed further in the section on mechanisms involving two enzyme–substrate complexes. In covalent catalysis, the enzyme actually reacts with the substrate, for example, through electrophilic or nucleophilic reactions, and forms a transient enzyme–substrate bond. The more stable the covalent bond formed, the less easily it breaks in the final steps of the catalysis. A good covalent catalyst forming reversible bonds must therefore combine two seemingly contradictory properties: high nucleophilicity and good leaving group properties.

14.3 Michaelis–Menten equation

In 1902 Adrian Brown proposed an explanation for the rate of hydrolysis of sucrose to glucose and fructose catalysed by the yeast enzyme β -fructofuranosidase, based on the formation of a complex between the enzyme and its substrate [16]. Today, the mechanism involving such an intermediate is expressed as



where E and S represent the enzyme and the substrate, respectively, ES is the enzyme–substrate complex and P the final product. In 1913 Michaelis and Menten [17] proposed a simple equation to describe the kinetics of this mechanism on the basis of the steady-state approximation for the complex ES,

$$k_1[E][S] - k_{-1}[ES] - k_2[ES] = 0 \quad (14.2)$$

In general, the concentrations of free enzyme and of the enzyme–substrate complex are not known, but the total concentration of enzyme is equal to its initial concentration, $[E]_0$, and

$$[E]_0 = [E] + [ES] \quad (14.3)$$

The value of $[E]$ can be eliminated from the above two equations to give

$$k_1([E]_0 - [ES])[S] - (k_{-1} + k_2)[ES] = 0 \quad (14.4)$$

or

$$[ES] = \frac{k_1[E]_0[S]}{k_{-1} + k_2 + k_1[S]} \quad (14.5)$$

Following the definition of reaction rate

$$v = k_2[ES] \quad (14.6)$$

and substituting for $[ES]$ gives the reaction rate in terms of the initial enzyme concentration and the concentration of the substrate

$$v = \frac{k_1 k_2 [E]_0 [S]}{k_{-1} + k_2 + k_1 [S]} \quad (14.7)$$

This can be presented in a more convenient form dividing the numerator and the denominator of the fraction by k_1 ,

$$v = \frac{\frac{k_2 [E]_0 [S]}{k_{-1} + k_2 + k_1 [S]}}{\frac{k_1}{k_1} + \frac{k_2}{k_1} + \frac{[S]}{k_1}} \quad (14.8)$$

and representing the ratio of rate constants by the Michaelis constant

$$K_M = \frac{k_{-1} + k_2}{k_1} \quad (14.9)$$

K_M represents the dissociation constant of the enzyme–substrate complex when $k_{-1} \gg k_2$. Low values of K_M thus correspond to strong enzyme–substrate complexes. The reaction rate in terms of the Michaelis constant, is

$$v = \frac{k_2 [E]_0 [S]}{K_M + [S]} \quad (14.10)$$

When the concentration of the substrate is sufficiently small, $[S] \ll K_M$ and the reaction rate is first order with respect to the substrate

$$v = \frac{k_2}{K_M} [E]_0 [S] \quad (14.11)$$

For high substrate concentrations, $[S] \gg K_M$ and the reaction rate is zero order with respect to the substrate

$$v = k_2[E]_0 \quad (14.12)$$

The enzyme is saturated and an increase in $[S]$ is not reflected in the effects on the reaction rate. This behaviour resembles that of surface catalysis on solids described in Chapter 11, Substitution Reactions. Figure 14.8 represents the initial rate of enzyme catalysis as a function of substrate concentration.

Eq. (14.10) can be represented in another form, using the maximum rate V_{\max} that occurs for very high substrate concentrations, when the enzyme is saturated, that is, it is entirely in the ES form. This is the reaction rate expressed by eq. (14.12), which can also be written as

$$v_{\max} = k_2[E]_0 \quad (14.13)$$

The Michaelis–Menten equation uses both K_M and V_{\max} to simplify the expression of the reaction rate of this mechanism

$$v = \frac{V_{\max}[S]}{K_M + [S]} \quad (14.14)$$

This expression gives another meaning to the Michaelis constant. When $K_M = [S]$ then $v = V_{\max}/2$. Using these parameters, it is also useful to define the catalytic constant of an enzyme as

$$k_{\text{cat}} = \frac{V_{\max}}{[E]_0} \quad (14.15)$$

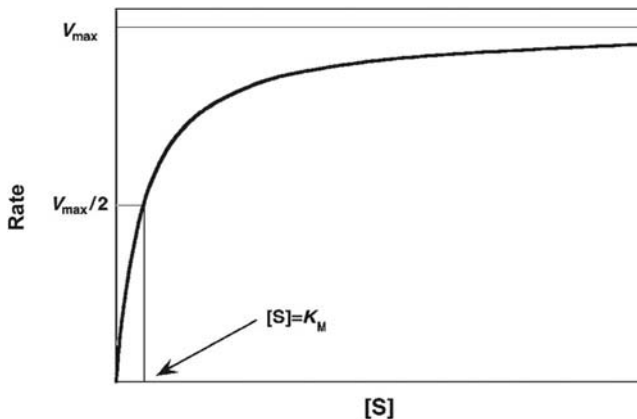
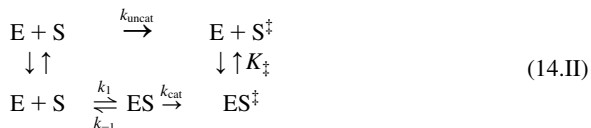


FIGURE 14.8

Dependence of the initial reaction rate of a simple Michaelis–Menten scheme on the substrate concentration.

This quantity is also known as the turnover number of an enzyme because it is the number of reaction processes (turnovers) that each active site catalyses per unit time. For the Michaelis–Menten mechanism it is obvious from eq. (14.13) that $k_{\text{cat}} = k_2$. However, for more complex mechanisms, k_{cat} may be a function of several rate constants. Table 14.1 presents representative values of k_{cat} , in units of sec^{-1} , and of k_{cat}/K_M , in units of $\text{M}^{-1} \text{ sec}^{-1}$, from which it is possible to extract the values of the Michaelis constant, in molar units.

The ratio k_{cat}/K_M in the Michaelis–Menten mechanism represents the apparent second-order rate constant, which can be taken as a measure of the efficiency of the catalysis when compared with the analogous uncatalysed bimolecular reaction in solution. When divided by the rate constant for the uncatalysed reaction in water, k_{uncat} , this defines the efficiency of enzyme catalysis, $(k_{\text{cat}}/K_M)/k_{\text{uncat}}$. When the uncatalysed reaction involves water, its concentration must be included in the calculation of k_{uncat} : $[\text{H}_2\text{O}] = 55 \text{ M}$. The efficiency is formally the equilibrium constant for the conversion of the transition state of the uncatalysed reaction in water and the enzyme in water into the transition state of the enzyme–substrate complex,



Prior to the development of rapid methods for data treatment, Hans Lineweaver and Dean Burk proposed a simple method using the reciprocals of eq. (14.14) to obtain experimentally the values of V_{max} and K_M [18],

$$\frac{1}{v} = \frac{K_M}{V_{\text{max}} [\text{S}]} + \frac{1}{V_{\text{max}}} \quad (14.16)$$

and their work has become, rather unexpectedly, the one of the most cited work in biochemistry. The double-reciprocal plot, illustrated in Figure 14.9, shows that enzyme catalysis following the Michaelis–Menten mechanism gives a linear dependence of $1/v$ as a function of $1/[\text{S}]$, with an extrapolated intercept of $-1/K_M$ and a slope of K_M/V_{max} .

Most experimental measurements involve relatively high $[\text{S}]$. A better separation between the experimental points can be achieved using Eadie plots, which results from another mathematical rearrangement of eq. (14.14),

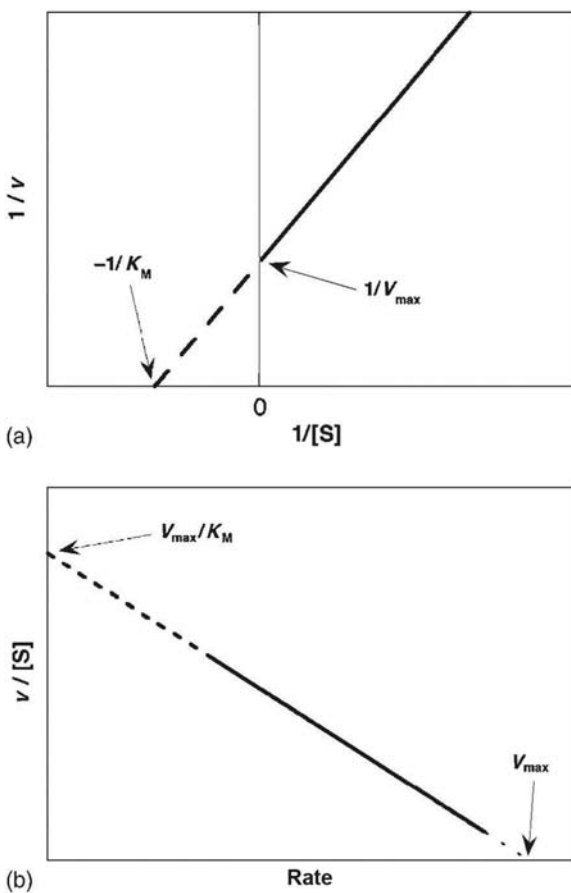
$$vK_M + v[\text{S}] = V_{\text{max}}[\text{S}] \quad (14.17)$$

or

$$\frac{v}{[\text{S}]} K_M + v = V_{\text{max}} \quad (14.18)$$

and finally

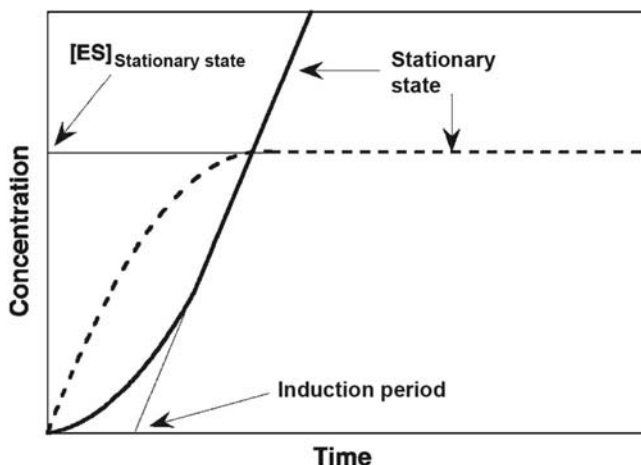
$$\frac{v}{[\text{S}]} = -\frac{1}{K_M} v + \frac{V_{\text{max}}}{K_M} \quad (14.19)$$

**FIGURE 14.9**

(a) Lineweaver–Burk plot. (b) Eadie plot.

Eadie plots represent $v/[S]$ as a function of the reaction rate itself. The plot is also linear for a Michaelis–Menten mechanism, but the slope is $-1/K_M$ and the intercept at the origin is V_{\max}/K_M , as illustrated in Figure 14.9. Although, where the quality of the experimental data permits, with the development of efficient computer software packages, the Eadie, Lineweaver–Burk and related treatments should be considered as starting points for more sophisticated treatments of data within the Michaelis–Menten scheme, these simple plots are still widely used.

Steady-state studies cannot give the values of the three rate constants, k_1 , k_{-1} and k_2 . Only using techniques with fast time resolution, such as the stopped-flow technique, is it possible to study experimentally the initial

**FIGURE 14.10**

Variations in the initial concentration of the enzyme–substrate complex (dashed line) and concentration of the reaction product (full line) for a reaction following the Michaelis–Menten mechanism.

moments of enzyme catalysis. As shown in Figure 14.10, there is an induction period, given by

$$\tau = \frac{1}{k_{-1} + k_2 + k_1[S]_0} \quad (14.20)$$

where $[S]_0$ is the initial concentration of the substrate, when steady-state conditions do not apply. Measuring τ as a function of $[S]_0$ gives the values of k_1 and $(k_{-1} + k_2)$. Associating these values with the value of K_M , obtained under steady-state conditions, it is thus possible to obtain all the rate constants for the elementary steps of the Michaelis–Menten mechanism.

14.4 Mechanisms with two enzyme–substrate complexes

Sometimes the mechanism of enzyme catalysis involves more than one enzyme–substrate complex. A representative example is chymotrypsin, one of the most-studied enzymes. Chymotrypsin can act as an esterase and a protease, because the chemical mechanisms of ester and amide hydrolases are almost identical. The catalytic mechanism when chymotrypsin acts as a serine protease involves the following steps.

First, chymotrypsin binds the polypeptide substrate to form the Michaelis complex. The substrate is held in the correct configuration for the subsequent reaction by non-covalent interactions. In the rate-determining step, it is suggested that there is a nucleophilic attack of the serine in position 195 of chymotrypsin (Ser195) on the carbonyl

group of the peptide to form a tetrahedral intermediate. In this process, the imidazole ring of histidine in position 75 (His75) accepts a proton forming an imidazolium ion. Next, the tetrahedral intermediate decomposes to form the acyl-enzyme intermediate, under the driving force of proton donation from N3 of His75. The amine product, which is the new N-terminal portion of the cleaved polypeptide chain, is released from the protein and replaced by a water molecule from the solvent. The acyl-enzyme intermediate is now subject to nucleophilic attack by water and a second tetrahedral intermediate is formed. Finally, the deacylation of this intermediate leads to the release of the resulting product with a free carboxylate group, which is the new C-terminal portion of the cleaved polypeptide chain, and the active enzyme is regenerated. These steps are illustrated in [Figure 14.11](#), adapted from Voet and Voet [19], and the kinetics can be schematically represented by the mechanism



where P_1 and P_2 are the amine and carboxylate products, respectively, and ES_1 and ES_2 represent the Michaelis complex and the acyl-enzyme intermediate, respectively. Applying the steady-state approximation to both complexes ES_1 and ES_2 , it is possible to show that the reaction rate still obeys Michaelis–Menten kinetics, [eq. \(14.14\)](#), but now

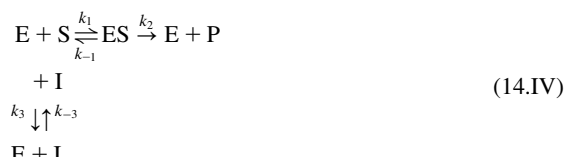
$$K_M = \frac{k_3(k_{-1} + k_2)}{k_1(k_2 + k_3)} \quad (14.21)$$

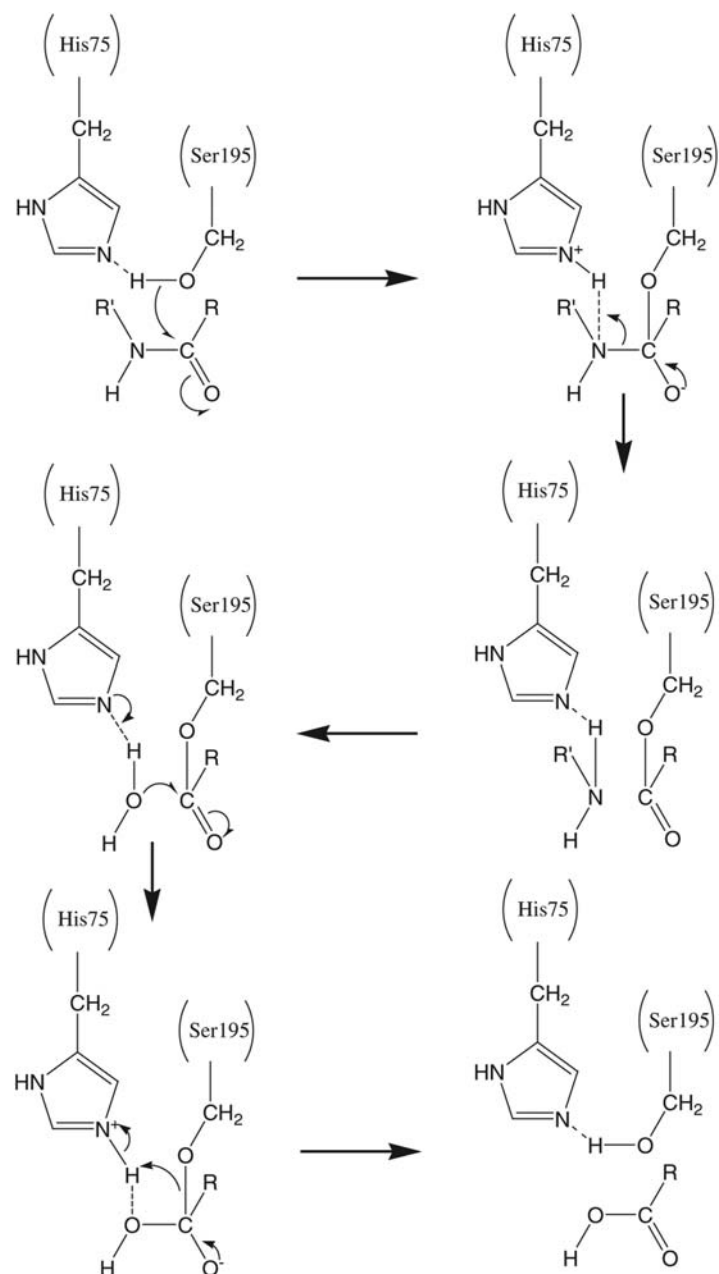
and

$$V_{\max} = \frac{k_2 k_3 [E]_0}{k_2 + k_3} \quad (14.22)$$

14.5 Inhibition of enzymes

The efficiency of an enzyme can be reduced or can even become negligible in the presence of certain substances, known as inhibitors. Many inhibitors have structural resemblances with the substrates and compete with them for the formation of complexes with the enzyme. This is the case of the inactivation of cytochrome *c* oxidase by the cyanide ion, which blocks the mitochondrial electron-transport chain to oxygen. Similarly, the inactivation of the succinate dehydrogenase by malonate involves its inhibition of the conversion of succinate to fumarate in the citric acid cycle. In the latter case, the mechanism for competitive inhibition is



**FIGURE 14.11**

Steps involved in the catalytic mechanism of serine proteases, represented by chymotrypsin.

where S is the succinate ($\text{^-OOCCH}_2\text{CH}_2\text{COO}^-$) and I is the malonate ($\text{^-OOCCH}_2\text{COO}^-$). Assuming that the inhibitor binds reversibly to the enzyme and is in rapid equilibrium,

$$K_I = \frac{[E][I]}{[EI]} \quad (14.23)$$

and using the definition of the Michaelis constant, eq. (14.9), together with the steady-state approximation for the ES complex, eq. (14.2), gives

$$[E] = \frac{K_M [ES]}{[S]} \quad (14.24)$$

When the concentrations of the enzyme-inhibitor complex and of the free enzyme, which can be obtained from eqs. (14.23) and (14.24), are substituted in the expression for the conservation of the total enzyme concentration

$$[E]_0 = [ES] + [EI] + [E] \quad (14.25)$$

the following equation is obtained:

$$[E]_0 = [ES] \left\{ \frac{K_M}{[S]} \left(1 + \frac{[I]}{K_I} \right) + 1 \right\} \quad (14.26)$$

which can be solved for [ES]

$$[ES] = \frac{[E]_0 [S]}{K_M \left(1 + \frac{[I]}{K_I} \right) + [S]} \quad (14.27)$$

so that the initial reaction rate defined by eq. (14.6), is expressed as

$$v = \frac{k_2 [E]_0 [S]}{K_M \left(1 + \frac{[I]}{K_I} \right) + [S]} \quad (14.28)$$

or

$$v = \frac{V_{\max} [S]}{K + [S]} \quad (14.29)$$

where the apparent Michaelis constant is

$$K = K_M \left(1 + \frac{[I]}{K_I} \right) \quad (14.30)$$

The corresponding Lineweaver–Burk plot has the form

$$\frac{1}{v} = \frac{1}{V_{\max}} + \frac{K_M}{V_{\max}} \left(1 + \frac{[I]}{K_I} \right) \frac{1}{[S]} \quad (14.31)$$

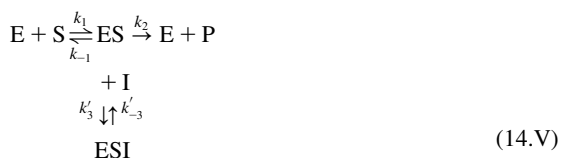
or

$$\frac{1}{v} = \frac{1}{V_{\max}} + \frac{\kappa K_M}{V_{\max}} \frac{1}{[S]} \quad (14.32)$$

with $\kappa = 1 + [I]/K_I$.

This shows that in competitive catalysis the maximum rate V_{max} is not changed. Rather, the presence of the inhibitor has the effect of making [S] appear more dilute than it actually is, and the effect of the inhibitor can be overcome for sufficiently high substrate concentrations.

In uncompetitive inhibition, the inhibitor binds to the enzyme, but not to its active site, and an ESI complex can be formed.



where now

$$K'_I = \frac{[ESI]}{[ES][I]} \quad (14.33)$$

When the binding of the inhibitor in this complex changes the conformation of the active site, as illustrated in Figure 14.12, such changes produce a decrease in the V_{max} . The corresponding double-reciprocal plot is

$$\frac{1}{v} = \frac{\kappa'}{V_{max}} + \frac{K_M}{V_{max}} \frac{1}{[S]} \quad (14.34)$$

where $\kappa' = 1 + [I]/K'_I$. The lines of the Lineweaver–Burk plot have now the same slope, K_M/V_{max} , as shown in Figure 14.13. Uncompetitive inhibition requires that the inhibitor binds only after the substrate has bound to the enzyme. This is not

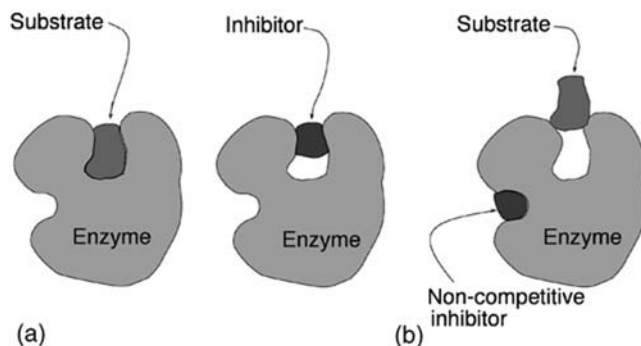
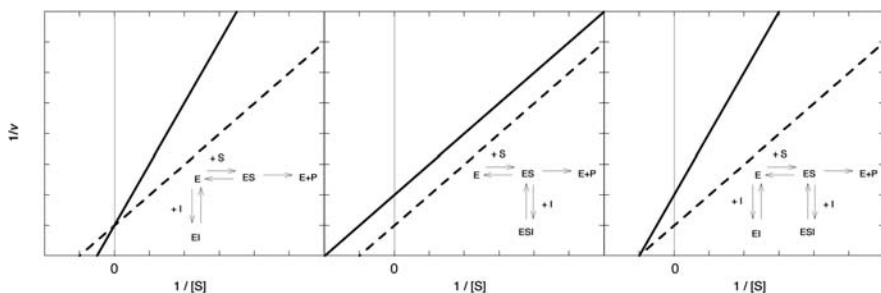


FIGURE 14.12

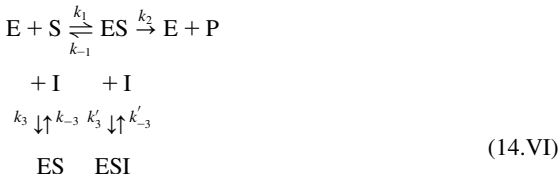
Changes in the active site of an enzyme resulting from binding to an inhibitor in:
(a) competitive inhibition, where the active site is blocked; (b) uncompetitive inhibition, where binding of the inhibitor to the enzyme–substrate complex induces conformational changes in the active site; (c) mixed inhibition where the inhibitor binds both the enzyme and the enzyme–substrate complex.

**FIGURE 14.13**

Lineweaver–Burk plots for (left) competitive inhibition, (centre) uncompetitive inhibition and (right) mixed inhibition for the case where $K_I = K'_I$, that is, pure non-competitive inhibition. The absence of competition is shown as a full line.

expected to occur for single-substrate enzymes but may occur for multi-substrate enzymes. Although it is a rare situation, it was observed for inosine 5'-monophosphate dehydrogenase (IMPDH). IMPDH catalyses hydride transfer from C2 of inosine 5'-monophosphate (IMP) to the cosubstrate nicotinamide adenine dinucleotide (NAD^+) and xanthosine monophosphate (XMP) is produced by addition of water to IMP. The rate-limiting step is the hydrolysis of a covalent thioimide complex formed between the nascent XMP and an active site cysteine. The natural product mycophenolic acid binds to the IMPDH-IMP complex in uncompetitive inhibition.

The kinetics of mixed inhibition (also called non-competitive inhibition)



can be obtained with the same procedures and lead to

$$\frac{1}{v} = \frac{\kappa'}{V_{\max}} + \frac{\kappa K_M}{V_{\max}} \frac{1}{[S]} \tag{14.35}$$

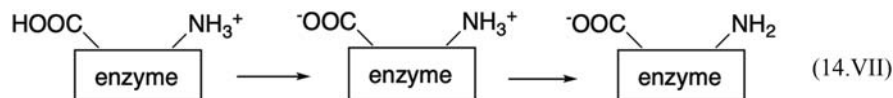
The particular case of $K'_I = K_I$ (i.e., $\kappa' = \kappa$), called pure non-competitive inhibition, is illustrated in Figure 14.13. In this case, K_M is the same as for the reaction in the absence of inhibitor and V_{\max} is decreased. In the general case of $K'_I \neq K_I$, the apparent Michaelis constant may increase or decrease with respect to the K_M of the reaction without inhibitor, depending on the relative values of K'_I and K_I .

Competitive, uncompetitive and mixed inhibitions can be kinetically distinguishable under steady-state conditions. Figure 14.13 shows that in competitive inhibition changes in $[I]$ do not change V_{\max} (the same $1/v$ at infinite $[S]$), whereas in uncompetitive inhibition both the apparent V_{\max} and apparent K_M are decreased although the slope K_M/V_{\max} is maintained (parallel lines). The mixed

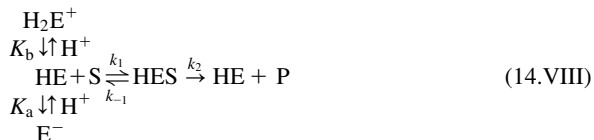
inhibition for the conditions illustrated in the same figure (pure non-competitive inhibition) does not change K_M with respect to the reaction without inhibitor (same value of $[S]$ for $1/v = 0$).

14.6 Effects of pH

Most proteins, including enzymes, are only effective within a narrow pH range, typically from 5 to 9. The pH effect in the rates of enzyme catalysis, illustrated in [Figure 14.14](#), gives rise to a bell-shaped dependence with a maximum close to pH 7.4, the physiological pH. This is due to the presence of ionisable groups in the amino acid chain, namely NH_3^+ and CO_2H , which must be in appropriate ionisation states in the vicinity of the active site for enzyme catalysis to be observed. Michaelis interpreted the pH effects on the basis of the mechanism



where the zwitterion was considered the active form. The concentration of the zwitterion goes through a maximum as a function of the pH, and its actual position depends on the acidity constants of these two groups. The simplest situation is represented by the mechanism



Assuming that the steady-state approximation applies to the concentration of the HES complex, the reaction rate is

$$v = \frac{k_2[\text{E}]_0[\text{S}]}{K_M(1 + K_a/\text{[H}^+]) + [\text{H}^+] / K_b + [\text{S}]} \quad (14.36)$$

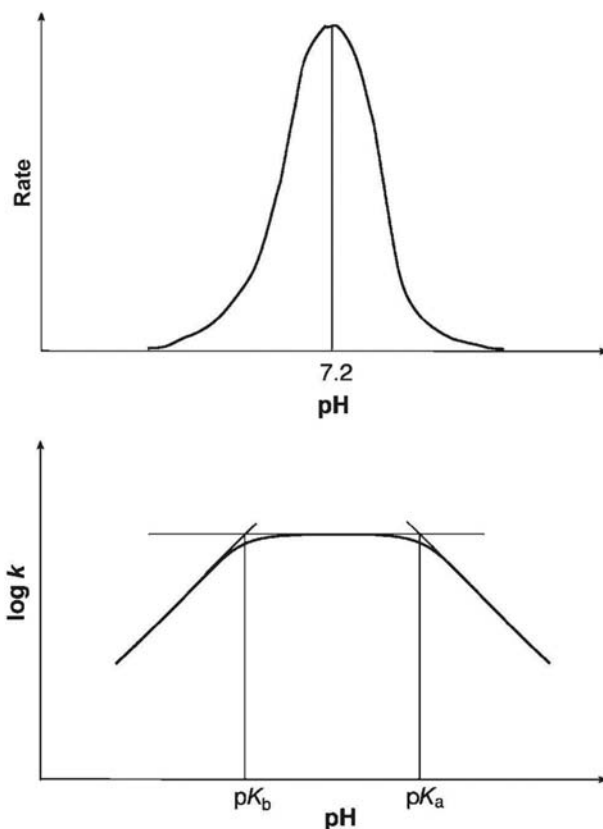
Note that at any given pH, [eq. \(14.36\)](#) behaves as a simple Michaelis–Menten equation.

For low substrate concentrations and at low pH values, $([\text{H}^+]/K_b) \gg (K_a/[\text{H}^+])$ and the above equation is simplified to

$$v = \frac{K_b k_2 [\text{E}]_0 [\text{S}]}{K_M [\text{H}^+]} \quad (14.37)$$

or

$$\log v = \text{constant} - \log [\text{H}^+] = \text{constant} + \text{pH} \quad (14.38)$$

**FIGURE 14.14**

(a) The effect of pH on the initial rate of a reaction catalysed by an enzyme. (b) Profile of the pH dependence of the catalytic constant of an enzyme.

At high pH, the corresponding equation is

$$v = \frac{k_2[E]_0[S][H^+]}{K_M K_a} \quad (14.39)$$

and

$$\log v = \text{constant} + \log[H^+] = \text{constant} - \text{pH} \quad (14.40)$$

The slope of the plots of $\log(v)$ as a function of the pH changes from 1 to +1. The maximum of this function occurs at $(pK_a + pK_b)/2$. Typical pK_s found in enzymes are 4 for the RCOO_2H group in Asp or Glu residues, 6 for histidine and 10 for the RNH_3^+ group of lysine. However, the pK_a of a given acid–base group in a protein residue may vary by several pH units from its expected value as a consequence of the electrostatic influence of the nearby charged groups and the polarity

of its environment. It is interesting to note that this simple approach to the pH dependence of enzymatic activity is consistent with a maximum efficiency at pH *ca.* 7 for enzymes with RCOO_2H and RNH_3^+ groups in the vicinity of the active site.

14.7 Temperature effects

As mentioned before, at temperatures above 60°C most enzymes lose their tertiary structure and, consequently, become inactive. The denaturation of proteins and DNA at high temperatures is the fundamental mechanism by which bacteria in boiling water are killed. However, a few bacteria are fit to live at relatively high temperatures. A good example is the bacterium *Thermus aquaticus*, first identified in the Lower Geyser Basin of the Yellowstone hot springs, a habitat where the temperature ranges from 50 to 80°C . This thermophilic bacterium produces a DNA polymerase enzyme that is widely used to replicate DNA in high-temperature polymerase chain reactions.

With thermophilic enzymes, the study of catalysis as a function of temperature has often demonstrated the biphasic Arrhenius behaviour, with an increased enthalpy of activation at lower temperatures, assigned to an increase in protein rigidity [20]. However, in general, at temperatures below 60°C , a temperature increase leads to an increase in the rate of the enzyme-catalysed reaction, often in agreement with the Arrhenius equation. As a consequence, the activity of enzymes as a function of the temperature goes through a maximum, and the study of the temperature dependence of enzyme activity must be carried out at relatively low temperatures.

For lower substrate concentrations, the reaction rate from eq. (14.10) is

$$v = \frac{k_2}{K_M} [\text{E}]_0 [\text{S}] \quad (14.41)$$

or

$$v = \frac{k_1 k_2}{k_{-1} + k_2} [\text{E}]_0 [\text{S}] \quad (14.42)$$

The corresponding temperature dependence is relatively complicated, but becomes more informative when $k_{-1} \gg k_2$, that is, for a fast equilibrium between the substrate and the enzyme. Under these conditions, the reaction rate can be written as

$$v = \frac{k_1 k_2}{k_{-1}} [\text{E}]_0 [\text{S}] \quad (14.43)$$

and the global activation energy has contributions from the activation energies of the three elementary reactions

$$E_a = E_{a1} + E_{a2} - E_{a-1} \quad (14.44)$$

In typical enzyme catalysis, the rate-determining step is the second step, as illustrated in Figure 14.15. The alternative, $k_{-1} \ll k_2$, would correspond to a reaction kinetically controlled by the formation of the enzyme–substrate complex, rather than by the product formation.

For higher substrate concentrations, the reaction rate attains its maximum, $V_{\max} = k_2[E]_0$. The study of the reaction rate as a function of the temperature under these conditions gives directly the activation energy for the transformation of the ES complex into products, E_a2 .

The free-energy changes in enzyme-catalysed and uncatalysed reactions can be compared using the free-energy profile of Figure 14.15. According to this figure

$$\Delta G_{\text{ncat}}^{\ddagger} + \Delta G_{\text{ES}}^0 = \Delta G_{\text{cat}}^{\ddagger} + \Delta G_{\text{cat}}^0 \quad (14.45)$$

where ΔG_{ES}^0 is the free-energy change in the formation of the enzyme–substrate complex by the forces of molecular recognition, and $\Delta G_{\text{ncat}}^{\ddagger}$ and $\Delta G_{\text{cat}}^{\ddagger}$ are the free energies of activation of the non-catalysed and catalysed reactions, respectively. The efficiency of the catalysis comes from the value of $\Delta G^{0\ddagger}$.

The enthalpies of activation of enzyme-catalysed reactions are typically *ca.* 45 kJ mol⁻¹ and the corresponding $T\Delta S^{\ddagger}$ values are concentrated around -20 kJ mol⁻¹ [21]. These values combine to give rate constants of the catalysed reaction of the order of 100–1000 sec⁻¹, as mentioned earlier. The extraordinary rate

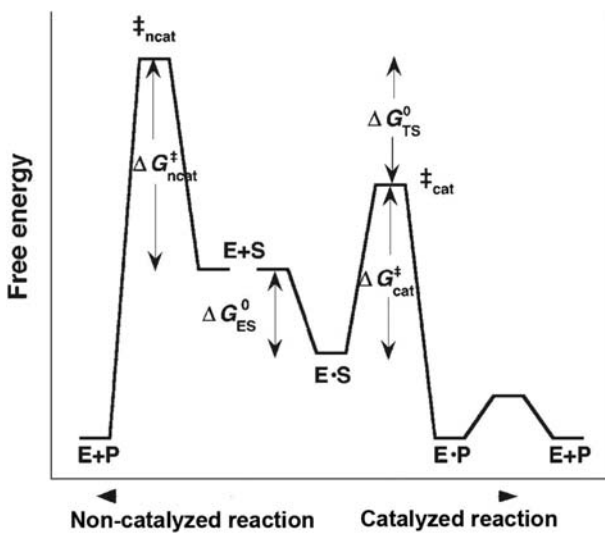


FIGURE 14.15

Free-energy profiles for an enzyme-catalysed reaction controlled by the formation of the product (from centre to right) and for a non-catalysed reaction (from centre to left). The reaction path going through the formation of the ES complex is the minimum-energy path.

enhancements achieved in the presence of enzymes are mainly related to the decrease in ΔH^\ddagger with respect to the uncatalysed reactions. The key to the understanding of enzyme catalysis is in the explanation for the energetic stabilisation of their transition states of the catalysed reactions. The factors that contribute to such stabilisation were discussed above but their cooperative action is best understood with some examples.

14.8 Isomerisation of dihydroxyacetone phosphate to glyceraldehyde 3-phosphate catalysed by triose-phosphate isomerase

A representative example of how enzymes stabilise reactive intermediates is the loss of a proton from the α -position of a carbonyl compound, a rate-limiting step in carbon–carbon bond formations and racemisations, which proceeds via an unstable enol or enolate intermediate. A particularly interesting illustrative case is that of triose-phosphate isomerase (TIM) and how it catalyses the isomerisation between dihydroxyacetone phosphate (DHAP) and glyceraldehyde 3-phosphate (GAP) (Figure 14.16). The uphill direction from DHAP to GAP is essential for optimal throughput in the glycolytic pathway, since only GAP can proceed further along this pathway. Thus the TIM reaction ensures efficient catabolism of all the six carbons in glucose. TIM is at a branch point in sugar metabolism, from which various biodegradative pathways emanate. Consequently there is a strong evolutionary pressure for efficient catalysis by the

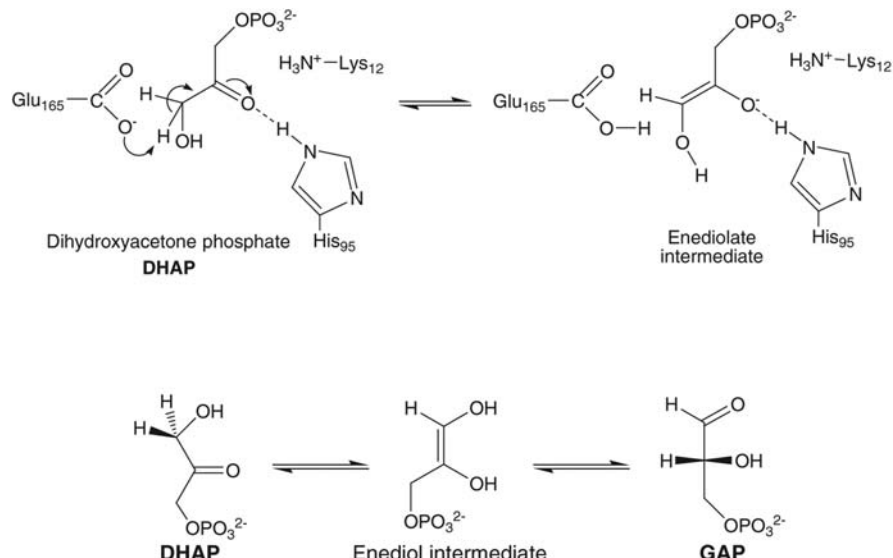


FIGURE 14.16

Isomerisation of DHAP to GAP catalysed by TIM.

enzyme under *in vivo* conditions. Viscosity-dependence studies have established that TIM is diffusion-controlled, that is, the rate of the reaction is limited by the diffusion of the substrate and product to and from the active site, and all the purely chemical steps are faster [22].

The key chemical step is a proton transfer where the general base catalyst is Glu165 ($pK_a^{\text{Glu165}} = 6$) [23]. The nature of the (enediol or enediolate) intermediates in this type of reaction remains a subject of lively debate. The pK_a^K of DHAP has not been measured, but from the similarity in the rate constants for hydroxide-catalysed elimination of DHAP ($0.56 \text{ M}^{-1} \text{ sec}^{-1}$ at 37°C [24]) and hydroxide-catalysed deprotonation of acetone ($0.22 \text{ M}^{-1} \text{ sec}^{-1}$ at 25°C [25]), it was deduced that both reactions proceeded through an enediolate intermediate, and that DHAP ionising at carbon-3 should have an acidity constant slightly lower than that of acetone, $pK_a^K(\text{acetone}) = 19$. The reaction energy estimated from the ΔpK_a ($\Delta G^0 = 75 \text{ kJ mol}^{-1}$) is not compatible with the high turnover number of the TIM-catalysed isomerisation of DHAP ($k_{\text{cat}} \approx 10^4 \text{ sec}^{-1}$ [24]).

The explanation by Gerlt and Gassman [23,26] of electrophilic catalysis extends the model of enzyme catalysis beyond the classical view that rate enhancements result because they provide a better fit for the intermediate than for the substrate. Proton abstraction by the general base catalyst was assumed to be concerted with the protonation of the carbonyl group by an acidic (electrophilic) catalyst, the His95, generating an enediol. According to this view, it is not the exact nature of the “enolate intermediate” that is relevant for the stabilisation of the intermediate, but its ability to establish “short, strong hydrogen bonds” to the electrophilic catalyst. According to Gerlt and Gassman, such bonds could stabilise the intermediate by $29\text{--}33 \text{ kJ mol}^{-1}$. A more dramatic stabilisation of $40\text{--}80 \text{ kJ mol}^{-1}$ owing to the formation of “low-barrier hydrogen bonds” in enzyme-intermediate complexes was proposed by Cleland and Kreevoy [27] and by Frey and co-workers [28]. Such proposals met with considerable criticism [29,30], because H bonds of this strength are usually typical of charged groups in the gas phase. Fersht and co-workers [31] showed that the differential stabilisation of charged versus uncharged H-bond donors or acceptors in proteins is typically of the order of 13 kJ mol^{-1} . As DHAP is converted into the enediolate intermediate, a negative charge accumulates in this oxygen atom and leads to a very strong interaction with the adjacent RNH_3^+ group of Lys12. The QM/MM calculations of Cui and Karplus [32] show that the presence of Lys12 merely 3.0 \AA from the carbonyl group of DHAP [33], leads to a 73.6 kJ mol^{-1} stabilisation of the intermediate. This is a realistic distance, because the transition-state analogue phosphoglycolohydroxamate of the DHAP interconversion to GAP, forms a complex with TIM where the $\text{N}\zeta$ of Lys12 is $2.797\text{--}2.84 \text{ \AA}$ from the O^2 of PGH [32]. A distance of 2.68 \AA between the $\text{N}\zeta$ of the Lis13 residue of *Leishmania mexicana* TIM and the carbonyl oxygen of 2-phosphoglycolate, another transition-state analogue, has also been measured [34].

Simple electrostatics, eq. (14.1), gives a stabilisation energy of 34.2 kJ mol^{-1} for two opposing charges at a 2.7 \AA separation in a medium of $\varepsilon = 15$

(Table 14.2). This is the electrostatic stabilisation energy expected for the charged oxygen atom of the intermediate in the presence of the Lys12 residue. Adding the 13 kJ mol^{-1} differential stabilisation of charged versus uncharged H-bond donors or acceptors, and subtracting the total stabilisation from the free energy associated to the ΔpK_a of DHAP and Glu-165, the endergonicity of the proton transfer in the enzyme drops to $\Delta G^0 = 29 \text{ kJ mol}^{-1}$. Cui and Karplus arrived at $\Delta V^0 = 26 \text{ kJ mol}^{-1}$, but the structure used as input was criticised by Friesner and co-workers, that obtained $\Delta V^0 = 48 \text{ kJ mol}^{-1}$ [35].

Transition-state theory (TST) rate calculations using the reaction path of the ISM, discussed in the previous chapter for proton-transfer reactions, assume that the reactions in enzymes are intra-molecular, but otherwise identical to the reactions in solution. Using the data for acetone and acetic acid in Table 13.7 to calculate the reaction coordinate of the ISM, together with $\Delta G^0 = 38 \text{ kJ mol}^{-1}$ and the classical TST formalism for an intra-molecular reaction gives $k_{ISM} = 3 \times 10^4 \text{ sec}^{-1}$ at 25°C [36], consistent with the value of k_{cat} measured for the TIM-catalysed conversion of DHAP to GAP. This agreement is favoured by the choice of ΔG^0 but nevertheless shows that the enzymatic rate can be calculated with reasonable values for the reaction energy and reactants properties. ISM calculations include a tunnelling correction factor of 10 and give a kinetic isotope effect (KIE) of *ca.* 4, in good agreement with the experimental value [37].

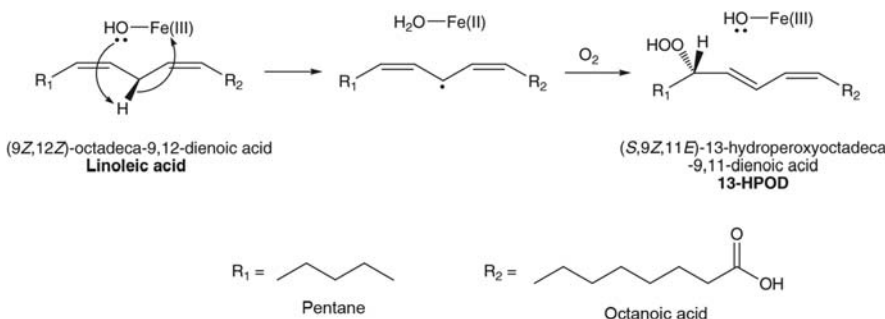
TIM catalysis is a case where the electrostatic forces and the differential hydrogen bonding are decisive in stabilising the intermediate to the loss of a proton from the α -position to a carbonyl compound, and, together with the proximity effect, lead to an increase in the rate of the reaction by 15 orders of magnitude.

14.9 Hydroperoxidation of linoleic acid catalysed by soybean lipoxygenase-1

Soybean lipoxygenase-1 (SLO) is often used as the prototype for studying the family of lipoxygenases from tissues of different species. They are non-haem iron dioxygenases that catalyse the conversion of unsaturated fatty acids to hydroperoxides. Plant lipoxygenases aid in germination and participate in the synthesis of fatty acid-derived products involved in wound response and pest determent. Mammalian lipoxygenase plays a role in the synthesis of hormones that act in the inflammation of the respiratory and nervous systems [38].

The interest in the hydroperoxidation of linoleic acid catalysed by SLO, which involves formally the abstraction of a hydrogen atom from the C11 position of the substrate by the Fe(III)-OH cofactor, stems from the fact that it exhibits nearly temperature-independent rates and KIEs close to 80 [39]. This KIE is much higher than that observed in other H-atom abstractions; for example, that of the $\text{H} + \text{H}_2$ versus $\text{H} + \text{D}_2$ hydrogen (deuterium) transfer is only 9.5 ± 1.4 at 30°C [40]. Such high KIEs were claimed to be inconsistent with the TST view of catalysis [41].

The formal H-atom abstraction of linoleic acid by SLO is a proton-coupled electron transfer, where the electron is transferred from the π -system of the linoleic acid (π_D) to the iron (Fe_A) and promotes the transfer of the proton from the C11 carbon atom of linoleic acid to the oxygen atom of the Fe-bound OH ligand (Figure 14.17). The $\pi_D\text{-Fe}_A$ distance is 5.69 Å and the $\text{Fe}_A\text{-O}$ bond length is 1.86 Å [42], which lead to an electron donor–acceptor distance $\Delta r \approx 4$ Å. According to the square-potential barrier expressed by eq. (6.46) and applied in detail to electron tunnelling in Chapter 16, Transitions between Electronic States, it is possible to calculate the electron-tunnelling probability using the barrier height and the donor–acceptor distance. The barrier height is determined by the energy of the relevant electron level in the donor (2.3 V vs NHE [42]), and that in the NHE reference relative to the electron energy at rest in vacuum, 4.44 eV. This gives a barrier height $V_{\max} - E = 6.74$ eV and an electron-tunnelling probability of 3×10^{-4} for electron tunnelling through the dielectric medium [43]. This probability multiplied by the frequency of the electron in the donor, typically 10^{15} sec $^{-1}$, gives a reaction frequency 2 orders of magnitude smaller than that of the TST. When the electronic reorganisation cannot accompany the nuclear reorganisation, the reaction becomes non-adiabatic and the reaction frequency is that of the electronic factor [44]. The energy barrier associated with the transfer of the proton is calculated with $m = 1$ and the data for H_2O and benzene (see Table 13.7). These species were chosen because they represent the OH and CH bonds involved in the reaction coordinate and give the reaction energy of -23 kJ mol $^{-1}$, identical to the experimental ΔG^0 [42]. Finally, the ($\text{CH}\cdots\text{O}$) distance was estimated as $l_{\text{CO}} = 2.95$ Å [45]. According to the relation between H-bond lengths and strengths in Figure 13.12, $l_{\text{CO}} = 2.96$ Å corresponds to $D_{0(\text{CHO})} = 7.8$ kJ mol $^{-1}$ and the Lippincott–Scroeder potential gives and a H-bond stretching frequency of 167 cm $^{-1}$, in good agreement with the available data. Such a significant H-bond energy involving a CH bond has been explained by the strong electron withdrawal effect of the nearby Fe(III) ion [46]. The frequency factor 3×10^{11} sec $^{-1}$, the data for benzene and water in Table 13.7 and $l_{\text{CO}} = 2.9$ Å, give $k_{\text{ISM}} = 540$ sec $^{-1}$ and

**FIGURE 14.17**

Proton-coupled electron transfer in the hydroperoxidation of linoleic acid catalysed by SLO.

$k_H/k_D = 44$ at 25 °C [43]. This rate and the large KIE include a hydrogen-tunnelling correction of 100 at 25 °C, owing to the thin and high-energy barrier of this reaction. The barrier topography of this atom transfer is determined by the repulsive part of the Morse potential, calculated from the LS potential for the (CH···O) H bond, which is absent in a typical proton transfer [47]. The calculated rate and KIE are in good agreement with the experimental values, $k_{\text{cat}} = 327 \pm 14 \text{ sec}^{-1}$ and $k_H/k_D = 76$ [41], corroborating that the ISM reaction path and TST calculations capture the most important factors that contribute to the enhancement of the rates of enzyme-catalysed reactions.

The isomerisation catalysed by TIM and the hydroperoxidation catalysed by SLO follow very different mechanisms and are subject to different stabilisation factors. Nevertheless, they show that Pauling's view of enzyme catalysis remains very influential, in particular his implication of the role of the enzyme in the stabilisation of the transition state of the rate-determining step. In modern words, this has been stated as "the entire and sole source of the catalytic power of enzymes is due to the lowering of the free energy of activation and any increase in the generalised transmission coefficient, as compared to that of the uncatalysed reaction" [48]. Of the factors contributing to the transmission coefficient, tunnelling is decidedly a most important one.

14.10 Enzymes in drug design

Almost all drugs used today were discovered and developed in the last 50 years. Enzyme inhibitors and inactivators comprise roughly half of all marketed drugs and more than one third of the discrete drug targets found within the portfolios of large pharmaceutical companies [49]. Enzymology plays an important role in the rational design of enzyme inhibitors or inactivators in drug discovery campaigns. Drug discovery and development is a very lengthy and expensive process. It is estimated that only one out of one thousand compounds showing activity against a validated drug target actually reaches the stage of development compound and enters clinical trials. Moreover, only *ca.* 1% of the compounds that enter clinical trials obtain approval for clinical use and are successful in the pharmaceutical market. The failures of the vast majority of the molecules tested are the major contributor to the cost of bringing a new drug to the market, currently estimated at *ca.* 1000 million euros per successful innovative drug. The improvement of the dramatic drug attrition in the discovery stage requires better understanding of kinetic mechanisms, namely on the chemical mechanism of catalysis of an enzyme target. The attrition on the clinical development stage is often related to the poor pharmacokinetics of the development compound. This subject is discussed in Chapter 15, Pharmacokinetics.

A drug discovery campaign aiming at a novel enzyme inhibitor, usually integrates isolated enzyme assay with cell-based assays and, ultimately, metabolic pathways and systems knowledge. The most common method to quantify the efficacy

of a tested inhibitor is the determination of its half-maximum inhibitory concentration, IC_{50} . This is the inhibitor concentration that gives a 50% decrease in rate under the specific assay conditions employed. IC_{50} values are readily related to the equilibrium between inhibitor and enzyme in competitive inhibition equating the rate in eq. (14.28) to half of the rate in eq. (14.10) for $[I] = IC_{50}$, which gives

$$IC_{50} = K_I \left(1 + \frac{[S]}{K_M} \right) \quad (14.46)$$

Identically, for uncompetitive inhibition

$$IC_{50} = K'_I \left(1 + \frac{K_M}{[S]} \right) \quad (14.47)$$

and for pure non-competitive inhibition

$$IC_{50} = K_I \quad (14.48)$$

Hence inhibition assays can provide useful information on the mechanism of inhibition and, vice versa, the knowledge of the inhibition mechanism informs on IC_{50} behaviour.

Given the definition of K_I in eq. 14.23, lower values of IC_{50} reflect enzyme-inhibitor equilibria strongly displaced to the enzyme-inhibitor complex. This is evidence for high affinity between the inhibitor and the enzyme. Very low concentrations of inhibitor are expected to produce a strong inhibition and, eventually, a strong therapeutic effect. Moreover, if low concentrations of inhibitor can be used, the effective drug dose can be low and it is less likely that off-target effects will be found. Low drug doses are expected to have lower side effects. Today it is common to find development compounds with nanomolar, and sometimes picomolar, EC_{50} values.

An enzyme target inside a cell will experience frequent exposure to its substrate but, owing to pharmacokinetics, only temporary exposure to an added inhibitor. The role of pharmacokinetics in drug bioavailability is discussed in the next chapter.

References

- [1] R Wolfenden, MJ Snider, *Acc. Chem. Res.* **34** (2001) 938.
- [2] A Radzicka, R Wolfenden, *Science* **267** (1995) 90.
- [3] P Jones, A Suggett, *Biochem. J.* **110** (1968) 617.
- [4] CC Lin, FR Smith, N Ichikawa, T Baba, M Itow, *Int. J. Chem. Kinetics* **23** (1991) 971.
- [5] JP Schwans, DA Kraut, D Herschlag, *Proc. Natl. Acad. Sci. U. S. A.* **109** (2009) 14271.
- [6] L Pauling, *Chem. Eng. News* **24** (1946) 1375.
- [7] T Covitz, FH Westheimer, *J. Am. Chem. Soc.* **85** (1963) 1773.
- [8] AJ Kirby, *Acc. Chem. Res.* **30** (1997) 290.
- [9] FC Lightstone, TC Bruice, *J. Am. Chem. Soc.* **118** (1996) 2595.
- [10] R Breslow, SD Dong, *Chem. Rev.* **98** (1998) 1997.

- [11] J Åqvist, M Kazemi, GV Isaksen, BO Brandsdal, *Acc. Chem. Res.* **50** (2017) 199.
- [12] J Chen, MA McAllister, JK Lee, KN Houk, *J. Org. Chem.* **63** (1998) 4611.
- [13] JP Guthrie, R Kluger, *J. Am. Chem. Soc.* **115** (1993) 11569.
- [14] JD Robertus, J Kraut, RA Alden, JJ Birktoft, *Biochemistry* **11** (1972) 4302.
- [15] X Zhang, KN Houk, *Acc. Chem. Res.* **38** (2005) 379.
- [16] A Brown, *J. Chem. Soc.* **81** (1902) 373.
- [17] L Michaelis, ML Menten, *Biochem. Z.* **49** (1913) 333.
- [18] H Lineweaver, D Burk, *J. Am. Chem. Soc.* **56** (1934) 658.
- [19] D Voet, JG Voet, *Biochemistry*, Wiley, New York, 1995.
- [20] A Kohen, R Cannio, S Bartolucci, JP Klinman, *Nature* **399** (1999) 496.
- [21] R Wolfenden, M Snider, C Ridgway, B Miller, *J. Am. Chem. Soc.* **121** (1999) 7419.
- [22] RC Davenport, PA Bash, BA Seaton, M Karplus, GA Petsko, D Ringe, *Biochemistry* **30** (1991) 5821.
- [23] JA Gerlt, PG Gassman, *J. Am. Chem. Soc.* **115** (1993) 11552.
- [24] IA Rose, W-J Fung, JVB Warms, *Biochemistry* **29** (1990) 4312.
- [25] Y Chiang, AJ Kresge, YS Tang, J Wirz, *J. Am. Chem. Soc.* **106** (1984) 460.
- [26] JA Gerlt, PG Gassman, *Biochemistry* **32** (1993) 11943.
- [27] WW Cleland, MM Kreevoy, *Science* **264** (1994) 1887.
- [28] PA Frey, SA Whitt, JB Tobin, *Science* **264** (1994) 1927.
- [29] A Warshel, A Papazyan, PA Kollman, *Science* **1995** (1995) 102.
- [30] CN Schutz, A Warshel, *Proteins* **55** (2004) 711.
- [31] AR Fersht, J-P Shi, J Knill-Jones, DM Lowe, AJ Wilkinson, DM Blow, P Brick, P Carter, MMY Waye, G Winter, *Nature* **314** (1985) 235.
- [32] Q Cui, M Karplus, *J. Phys. Chem. B* **106** (2002) 1768.
- [33] G Jogi, S Rozovsky, AE McDermott, L Tong, *Proc. Natl. Acad. Sci. U. S. A.* **100** (2003) 50.
- [34] I Kursula, RK Wierenga, *J. Biol. Chem.* **278** (2003) 9544.
- [35] V Guallar, M Jacobson, A McDermott, RA Friesner, *J. Mol. Biol.* **337** (2004) 227.
- [36] M Barroso, LG Arnaut, SJ Formosinho, *J. Phys. Org. Chem.* **22** (2009) 254.
- [37] TK Harris, RN Cole, FI Comer, AS Mildvan, *Biochemistry* **37** (1998) 16828.
- [38] MH Glickman, JP Klinman, *Biochemistry* **35** (1996) 12882.
- [39] A Kohen, JP Klinman, *Acc. Chem. Res.* **31** (1998) 397.
- [40] LG Arnaut, AAC Pais, SJ Formosinho, M Barroso, *J. Am. Chem. Soc.* **125** (2003) 5236.
- [41] MJ Knapp, K Rickert, JP Klinman, *J. Am. Chem. Soc.* **124** (2002) 3865.
- [42] E Hatcher, AV Soudackov, S Hammes-Schiffer, *J. Am. Chem. Soc.* **126** (2004) 5763.
- [43] M Barroso, LG Arnaut, SJ Formosinho, *J. Phys. Org. Chem.* **21** (2008) 659.
- [44] LG Arnaut, in *Proton-Coupled Electron Transfers: A Carrefour of Chemical Reactivity Traditions*, Eds. S. J. Formosinho, M. Barroso, RSC Catalysis Book Series, 2012, p. 32.
- [45] G Tresadern, JP McNamara, M Mohr, H Wang, NA Burton, IH Hillier, *Chem. Phys. Lett.* **358** (2002) 489.
- [46] W Siebrand, Z Smedarchina, *J. Phys. Chem. B* **108** (2004) 4185.
- [47] M Barroso, LG Arnaut, SJ Formosinho, *ChemPhysChem* **6** (2005) 363.
- [48] M Garcia-Viloca, J Gao, M Karplus, DG Truhlar, *Science* **303** (2004) 186.
- [49] GA Holdgate, TD Meek, RL Grimley, *Nat. Rev. Drug Discov.* **17** (2018) 115.

This page intentionally left blank

Pharmacokinetics

15

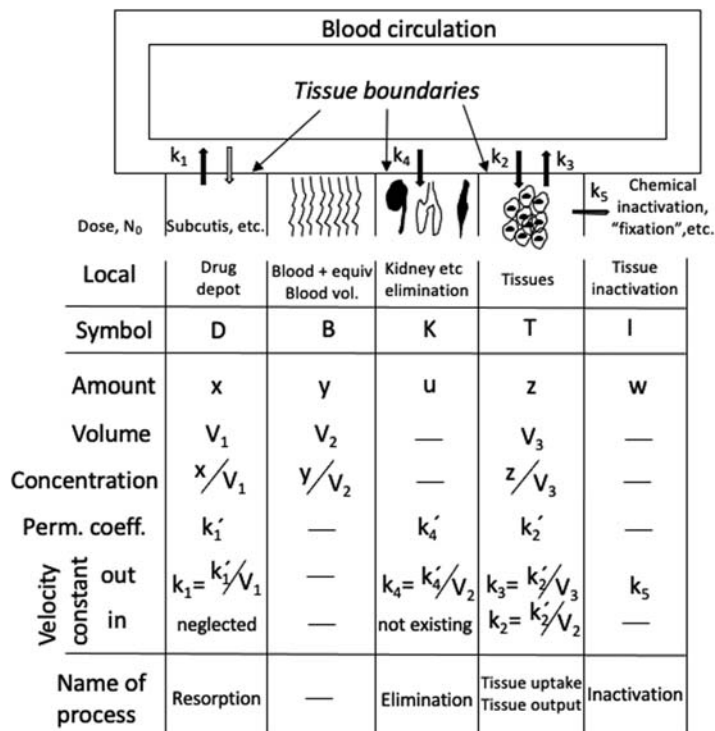
15.1 Origins and current use of pharmacokinetics

Literally, the word “pharmacokinetics” means the application of kinetics to “pharmacon”, the Greek word for drugs and poisons. Pharmacokinetics studies the time course of medicines and their metabolites in biological fluids, tissues and excreta. Traditionally, it covers aspects related to the absorption of pharmaceutical compounds, their distribution in the body, metabolism and excretion, often represented by the abbreviation ADME. Nowadays, the concerns with the toxicity of compounds led to the inclusion of a fifth dimension—toxicity—in pharmacokinetics, and the abbreviation was extended to ADME-Tox.

This subject of application of kinetics is of great interest to Pharmacy and Medicine but it is uncommon to consider it in chemical kinetics. Indeed, the time course of a pharmaceutical compound in the body is not necessarily ruled by the rates and mechanisms of chemical reactions. However, as will be seen in this chapter, the rate laws of pharmacokinetics and chemical kinetics are based on essentially the same mathematical descriptions and much can be learnt from each other. In the past, the lack of understanding of pharmacokinetics, especially by medicinal chemists, was a major contributor to the early termination of drug development programs. A joint benchmark study conducted in 1991 by the Food and Drug Administration and the Pharmaceutical Manufacturers Association (now PhRMA) concluded that inappropriate pharmacokinetics was the leading reason (40%) for the failure of innovative drugs, followed by lack of efficacy (30%), pre-clinical toxicity (11%) and adverse events in man (10%) [1]. The tremendous attrition in drug discovery, with 1 in 30,000 compounds investigated in pre-clinical studies reaching clinical trials, and in drug development, with 1 in 30 compounds initiating clinical trials reaching the market, is responsible for the very high cost of innovative medicines. Considering the annual investment in new pharmaceutical compounds and the number of new medicines approved every year, it is currently estimated that each new medication approved came with an investment of 1,000,000,000 euros in drug discovery and development. This highlights the relevance of ADME-Tox for medicinal chemists.

Buchanan was one of the precursors of pharmacokinetics. In 1847, he related the depth of narcosis to the brain content in ether, which depended on the arterial concentration of ether, which in turn he recognised to depend on the strength of the inhaled mixture [2]. The first equations describing the time course of a drug

in the blood were published in 1924 by Widmark and Tandberg [3], and remain valid today for the so-called one-compartment model, to be described below. Also in 1924 Haggard published a series of landmark papers on the absorption, distribution and elimination of ethyl ether in the body [4], using his own method to analyse ethyl ether in the blood and in the air. In 1934, Dominguez and Pomerene introduced the concept of volume of distribution, defined as “the hypothetical volume of body fluid dissolving the substance at the same concentration as the plasma” [5], which is now widely used in pharmacokinetics. Shortly after, in 1937, Teorell published two papers that are considered the foundations of modern pharmacokinetics [6]. Teorell proposed to derive general mathematical relations from which it would be possible to describe the kinetics of distribution of substances in the body. He proposed the scheme shown in [Figure 15.1](#) where the drug is administered via the sub-cutaneous route, blood transports the drug and distributes it to several organs and tissues, organs such as the kidneys can eliminate the drug, inactivation/metabolism can take place in some tissues and, very importantly, rate constants are included to account for the kinetics of

**FIGURE 15.1**

Pharmacokinetics according to Teorell [6].

“resorption”, elimination and reversible exchange of the drug between the blood and the tissues. Teorell’s mathematical model involved five compartments: the drug depot, the blood, the kidney and other organs contributing to elimination, the target tissues and the tissues contributing to inactivation. Toerell was able to find the solutions for the differential equations that describe this kinetic system and presented drug distributions in the blood and tissues. Teorell became Chair in Physiology at the Uppsala University in 1940 but the reviewers of his application did not appreciate his work on pharmacokinetics [7]. It was only two decades later that the contributions of Teorell to pharmacokinetics were recognised.

From the viewpoint of chemical kinetics, the models that describe the kinetics of a drug through the body are of greater interest than the mechanisms of absorption, distribution, metabolism or excretion. Hence only a brief overview is given below on the routes of drug administration and absorption, on drug distribution in the body, and on drug metabolism and elimination. The understanding of these routes of entry, distribution and exit of the drugs sets the stage for a mathematical description of the kinetics of a drug in the body, and more specifically in the plasma because in a clinical setting this is the most accessible compartment for drug sampling.

15.2 Drug administration and absorption

The most common and preferred route of drug administration is oral administration. It is painless, easy to administer, adequate for self-administration, portable, inexpensive, does not require sterilisation, is appropriate for repeated administrations, and oral drug formulations may allow for fast or slow release of the drug. Most drugs taken through this route are meant for absorption by the duodenum, which is the major site of entry in the systemic circulation because of its large absorptive surface. Such drugs must resist the acidity of the stomach and when absorbed from the gastrointestinal tract enter the portal circulation and encounter the liver before they are distributed into the general circulation. Gastric acidity as low as pH 1.5, passive diffusion or active transport across the cell membranes of epithelial cells in the duodenum, and the first-pass metabolism in the liver, limit the amount of drug that reach the circulation. Hence the fraction F of the administered drug that reaches the systemic circulation—that is, the bioavailability—of drugs taken orally is often low and variable. Additionally, the whole process is slow and oral administration is not adequate for emergencies.

Lipinski studied the physicochemical properties of a very large number of orally administered drugs and found that the vast majority of them had the following properties [8]: (1) a molecular mass less than 500 dalton, (2) a logarithm of the octanol:water partition coefficient less than 5, $\log P_{ow} < 5$, (3) not more than 5 hydrogen-bond donors, (4) not more than 10 hydrogen-bond acceptors.

This simple rationalisation of the properties that a drug must have to be adequate for oral administration became known as Lipinski's rule of five, because the number 5 appears often in the desired properties. It must be emphasised that this rule is based on a statistical treatment of a database, and many exceptions are known. Nevertheless, it is a most influential rule in the design of oral medications.

The most important alternative to the oral administration of a drug is its intravenous administration. It avoids the gastro-intestinal tract, offers maximum bioavailability, allows for fast administration and is precise. For many drugs and for biopharmaceuticals it is often the only possible route of administration. However, it is painful, may induce adverse events due to fast and high drug concentrations in the body, requires trained healthcare professionals, may lead to opportunistic infections, requires sterility and is expensive. The fast injection of a given volume of medication is named bolus injection. The dangers of rapidly increasing the concentration of the drug in the plasma can be reduced making an infusion of the drug over an extended period of time, usually more than 30 minutes, rather than a bolus injection.

In view of the importance of oral and intravenous administrations in Medicine, the pharmacokinetics models discussed later will only consider these two types of administrations. However, there are other alternatives for administration that are very common in clinical practise.

Intra-arterial and intravenous administrations are the two types of intra-vascular administration. Intra-arterial administration is less used because arteries are found deeper than veins, which makes the administration more difficult and more painful, and puncturing an artery leads to much bleeding. Intra-vascular together with intra-muscular and sub-cutaneous administrations are named parenteral administrations. Intra-muscular administration leaves a drug depot in the body that can subsequently dissolve slowly and provide a sustained dose over an extended period of time. However, it is very painful and the volume that can be administered is very limited. It also requires trained personnel to perform the administration. Sub-cutaneous administration is less painful and easier to perform, which makes it more suitable for self-administration. Insulin is self-administered using this route. However, the volumes that can be administered are even smaller than in the intra-muscular administration.

Oral administration is one of the three options for enteral administration. The other two options are buccal/sub-lingual and rectal administrations. Placing the drug formulation under the tongue offers the opportunity for local drug absorption by a dense capillary network without the challenges of the absorption in the gastro-intestinal tract. However, it is limited to small doses and by the taste of medications. Rectal administration also avoids the low pH of the stomach and intestinal enzymes, but has low patient compliance and erratic absorption.

Inhalation is a very appealing route of administration because the large surface area of the lungs and the good pulmonary epithelium permeability enable very

fast absorptions. The outcome is an administration almost as fast as an intravenous injection. However, unless the drug is a gas, there are challenges in preparing aerosol formulations for pulmonary delivery. Aerosol particles with an aerodynamic diameter of about 1–2 µm, if slowly and deeply inhaled, can be deposited in the lungs with efficiencies as high as 90% [9]. However, if the particles are too large, they will deposit on the mouth, throat and upper airways, and if they are too small, they risk exhalation. Furthermore, if the patients inhale too forcefully, the particles will deposit as if they were too large. Developments in the fabrication nanoparticles and in inhaler technology are expected to increase the use of pulmonary administration.

Topical and transdermal administrations are also very appealing because the skin is the largest and most accessible human organ. Skin evolved to become a remarkable protection against chemicals and pathogens. The main contributor to the skin barrier is its outermost layer, called stratum corneum, although it is only 10–20 µm thick. It is made by a dozen layers of hardly packed non-living corneocyte cells embedded in a mixture of lipids with high spatial organisation. Most molecules penetrate the skin by diffusion through the inter-cellular lipids, a narrow and tortuous path around the corneocytes that is highly constrained by structural and solubility requirements [10]. As a result, the physicochemical properties of the molecules that permeate the skin effectively are even more restrictive than those described by Lipinski's rule of 5 for oral administration. In particular, the molecular weight of drugs intended for transdermal delivery should be lower than 500 dalton and the logarithm of the octanol:water partition coefficient should be between –2 and 3 [11]. Topical formulations may include permeation enhancers, such as surfactants or organic solvents, to increase skin permeation, but most often an increase in skin permeation is associated with an increase in skin irritation. Alternatively, various active methods have been developed to deliver drugs through the skin. They include microneedles, ablation of the stratum corneum (including laserporation), iontophoresis, electroporation, ultrasound, photoacoustic waves and many more. The grand challenge of transdermal drug delivery is not just to bypass the efficient protection of our skin. Transdermal delivery aims at painless and fast transport of drugs through the skin without damaging it, such that the skin recovers its protective function and original appearance shortly after the treatment. In this respect, photoacoustic waves seem to be a promising transdermal drug delivery method [12].

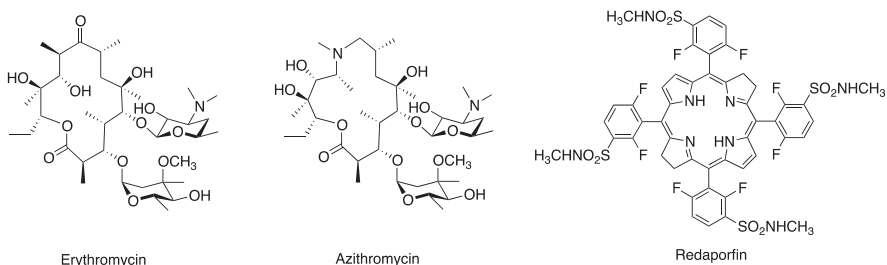
15.3 Drug distribution

Once the drug reaches the systemic circulation, it can be distributed to the tissues and organs eventually reaching its target. Drug distribution is relatively rapid. Well-perfused organs and tissues, such as the heart, liver or the kidneys, in which the drug distributes very rapidly, are considered together with the blood as the

central compartment. Poorly perfused organ and tissues, such as the adipose tissue and skeletal muscle, take longer to equilibrate the drug concentration with the systemic circulation and are part of the peripheral compartment. There are about 10 billion capillaries in the body, with a total surface area of 200 m^2 . They probe every part of the body such that no cell is more than $20\text{--}30\text{ }\mu\text{m}$ away from the nearest capillary. The walls of the capillaries are made of a thin layer of cells packed tightly together, but have pores with a diameter of $9\text{--}15\text{ nm}$. Such pores are too small to allow the plasma proteins to escape the capillaries but large enough for most drugs to escape to the aqueous fluid surrounding the tissues and the organs. Once in the extra-vascular fluid, many drugs still have to cross the cell membrane to find their targets. The entry of drugs into cerebrospinal fluid and the central nervous system is limited by the blood–brain barrier. This is a highly specialised barrier, less porous and with an extra fatty layer that protects the brain from most xenobiotics and drugs. It is convenient to consider the brain separately from the peripheral compartment.

The extent of drug distribution in the body is reflected by its volume of distribution. It is currently defined as the apparent volume needed to account for the total amount of drug in the body if the drug was evenly distributed throughout the body and in the same concentration as the site of sample collection, which normally is the peripheral venous plasma. V_d is usually employed to represent the volume of distribution and is normalised to body weight because it is reasonable to expect that volumes of distribution increase with body weight. The meaning of V_d can be understood with reference to physiological tissue volumes. Blood is present in the body at 0.08 L kg^{-1} and plasma is about half that volume. The tradition in pharmacokinetics is to express the unit of litre by a capital L. The interstitial fluids contribute with 0.16 L kg^{-1} and are part of the extravascular fluid that has a total volume of 0.56 L kg^{-1} . The total body water is 0.6 L kg^{-1} . When a drug has a V_d less than total body water, it is considered to exhibit a low volume of distribution. Drugs with V_d between 0.6 and 5 L kg^{-1} are termed to be of moderate volume of distribution and $V_d > 6\text{ L kg}^{-1}$ is considered high [13]. A drug with $V_d \leq 0.08\text{ L kg}^{-1}$ is essentially contained in the vascular compartment. Drugs with $0.05 \leq V_d \leq 0.7\text{ L kg}^{-1}$ are more extensively bound to plasma proteins than to tissues. Although there is no upper limit, it is rare to find $V_d > 10\text{ L kg}^{-1}$.

The most important physico-chemical properties that influence volumes of distribution are the acid/base character and the lipophilicity of drugs. Basic molecules exhibit a tendency to bind to albumin and a great tendency to partition into phospholipid membranes. They tend to be drawn from the systemic circulation and have volumes of distribution around $1\text{--}25\text{ L kg}^{-1}$ [13]. The volumes of distribution of neutral molecules are mostly determined by their lipophilicity and typically cover the range of $0.7\text{--}4\text{ L kg}^{-1}$. Acids have very low membrane affinity and very high affinity for albumin. Given that albumin is too large to escape through the holes in the capillaries and is mostly present in plasma, acids generally have volumes of distribution between 0.1 and 0.4 L kg^{-1} [13].

**FIGURE 15.2**

Molecular structures of erythromycin, azithromycin and redaporfin.

As an example, Figure 15.2 shows erythromycin and azithromycin, which are antibiotics used in the treatment of a number of bacterial infections. Erythromycin, with one basic centre, has $V_d = 0.95 \text{ L kg}^{-1}$ and a half-life of 2 h [14], whereas azithromycin, with two basic centres, has $V_d = 33 \text{ L kg}^{-1}$ and a half-life of 69 h [15]. An apparently small structural change on a large macrolide enabled increases in V_d and half-life that changed the administration from several times a day for erythromycin to once a day for azithromycin. This figure also shows redaporfin, which will be used later in an example of intravenous administration.

15.4 Drug metabolism and excretion

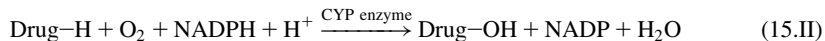
The drug in the body is subject to transformations induced by a relatively aggressive medium, in particular due to the efficiency and specificity of metabolic enzymes. As discussed in the previous chapter, enzymes can accelerate the rates of chemical reactions by factors of 10^7 – 10^{21} . As a result, most drugs undergo some form of metabolite reaction. In some cases, the metabolite has a higher toxicity or a higher activity than the drug. When very toxic metabolites are formed, this is a reason for concern and molecular modifications of the drug may be required. On the other hand, when the metabolism leads to a more active drug, the parent (inactive) drug can be regarded as a pro-drug. Administering a compound without pharmacological activity that is metabolised to produce an active metabolite, which is actually the effective drug, is a very useful strategy. An early example of the use of metabolites was the initial treatment of syphilis with arsphenamine (better known by the trade name Salvarsan), introduced by Ehrlich in the 1910s. Later Voegtlin showed that the activity of arsphenamine was due to its metabolite oxphenarsine



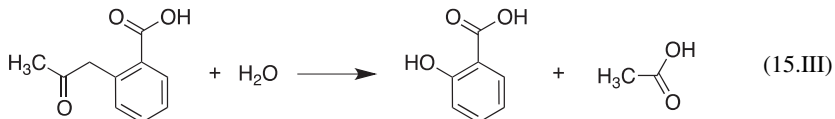
and oxophenarsine eventually replaced arsphenamine in the treatment of syphilis since it was less toxic at the dose required for effective treatment.

Polar drugs are usually hydrophilic and can be quickly excreted by the kidneys. However, non-polar drugs have to be metabolised to more polar molecules before they can be excreted. The liver is the main drug-metabolising organ, and hepatic clearance is a major determinate of total clearance. In general, drugs with high hepatic clearance have low oral bioavailability because of the first-pass metabolism. The relevance of hepatic metabolism is directly related to the content of cytochrome P450 (CYP) enzymes present in the liver. CYP is a family of enzymes that collectively are involved in the metabolic clearance of nearly 75% of the 200 most prescribed therapeutic drugs in the United States [16].

CYP enzymes can add polar groups to a wide variety of drugs. A typical oxidation reaction catalysed by CYP enzymes can be represented by

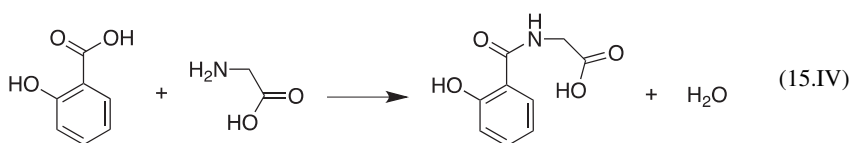


where NAPDH/NADP is the coenzyme nicotinamide adenine dinucleotide phosphate in the reduced/oxidised form. Alternatively, enzymes may reveal masked polar functional groups already present in a drug. For example, the de-methylation of methyl ether present in a drug will reveal the more polar hydroxyl group. This is illustrated by the metabolism of aspirin (2-ethanoyloxybenzoic acid)



Another group of metabolic enzymes present in liver cells are the flavin-containing mono-oxygenases. These enzymes are specialised in metabolic reactions involving oxidation at nucleophilic nitrogen, sulphur and phosphorous atoms rather than carbon. Either adding or de-masking polar groups will result in a more polar and water-soluble molecule more likely to be excreted when it passes through the kidneys. These metabolic reactions are classed as phase I reactions and generally involve oxidation, reduction or hydrolysis.

There is another class of metabolic reactions that also occur mainly in the liver, named phase II reactions. Most of these reactions are conjugation reactions, catalysed by transferase enzymes, where a polar molecule is attached to a suitable substituent present in the drug or that has been introduced in phase I reactions. For example, 2-hydroxybenzoic acid, produced in reaction (15.III) conjugates with glycine using coenzyme A and energy from reactions using ATP



The resulting polar molecule is excreted in the urine.

Drugs and their metabolites can be excreted from the body by a number of routes. The most important is their filtration in the kidneys and excretion in the urine. However, volatile and gaseous drugs may be more easily excreted through the lungs and exhaled. It is possible that 10% of a drug is lost through the skin as sweat. The bile travels from the liver to the intestines carrying bile acids and salts that are important for digestion. Some of the drug administered may be diverted into the bile and travel to the intestines, where it has another chance of being absorbed. In this case, a delayed drug concentration peak may be found in the plasma due to the enterohepatic circulation of the drug.

15.5 Pharmacokinetics models

15.5.1 One-compartment model

The simplest model to represent the time course of a drug in the body is the one-compartment model. It assumes that the drug achieves a homogenous distribution in the body immediately after the administration, and equilibrates instantaneously with the tissues. In this case, the drug concentration in the plasma (C_p) attains its maximum (C_{p0}) immediately after time $t = 0$ and then decays as the drug is eliminated from the body. This simple model can describe cases of intravenous bolus administration where the drug is eliminated without substantial re-equilibration between the drug in the plasma and in the peripheral tissues. [Figure 15.3](#) illustrates compartment models.

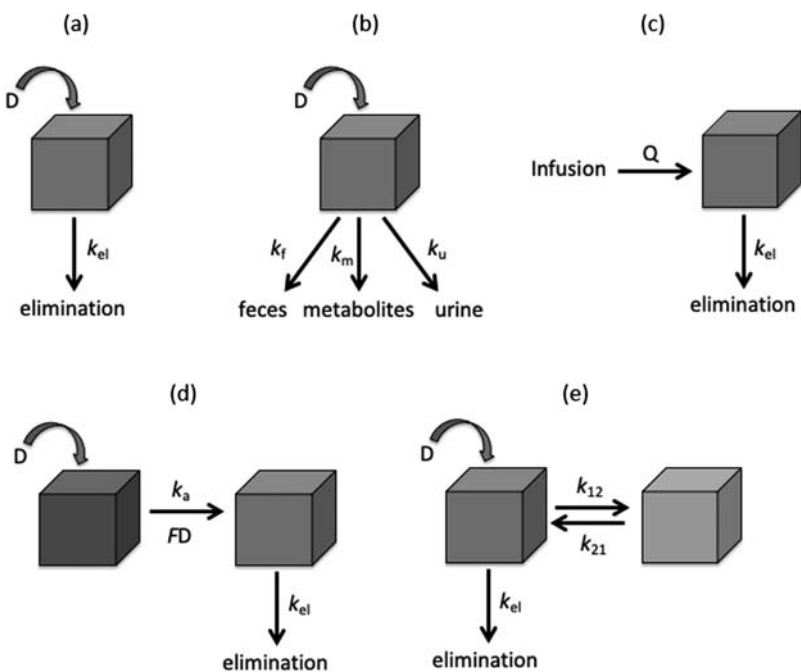
The kinetics of the drug elimination from the body is described by

$$\frac{dC_p}{dt} = k_{el}C_p \quad (15.1)$$

which has exactly the same form as the rate equation of first-order kinetics, [eq. \(4.1\)](#). Hence it is possible to write the concentration of the drug in the plasma as

$$C_p = C_{p0} \exp(-k_{el}t) \quad (15.2)$$

C_p is usually expressed in units of mg of drug per ml of plasma or, for very potent drugs, in units of $\mu\text{g ml}^{-1}$.

**FIGURE 15.3**

Compartment models. (a) One-compartment model for intravenous bolus administration. (b) Same as previous model but with explicit representation of various drug elimination mechanisms from the central compartment. (c) One-compartment model for intravenous infusion under a constant rate Q . (d) One-compartment model for oral administration. (e) Two-compartment model for intravenous bolus administration.

In an intravenous bolus administration, the total amount of drug in the body is the dose D that was administered, which is usually expressed in units of mg of drug per kg of body-mass. It is convenient to use the volume of distribution to express the initial plasma concentration of the drug in terms of the dose D ,

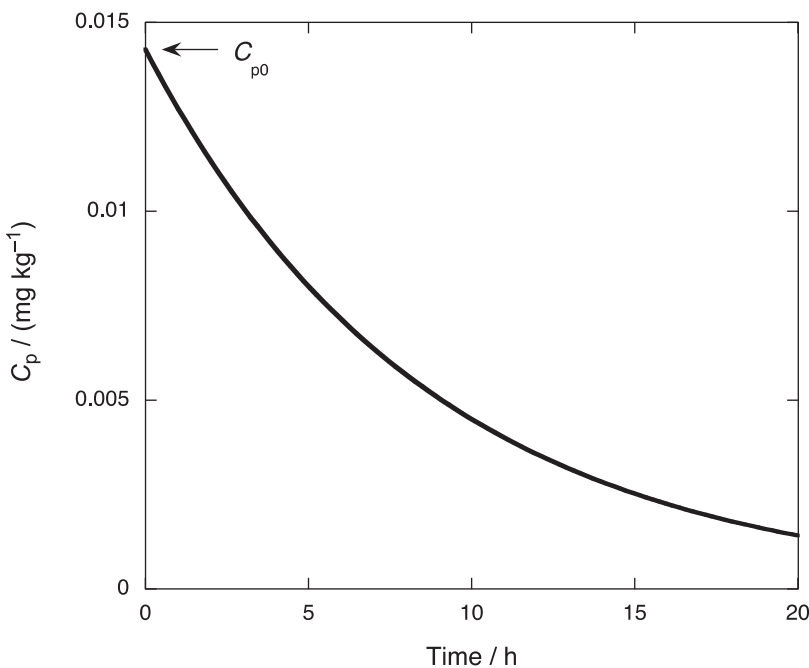
$$C_{p0} = \frac{D}{V_d} \quad (15.3)$$

V_d is in units of ml kg^{-1} .

The exponential decay described by eq. (15.2) is represented in Figure 15.4. Similarly to first-order reactions, it is convenient to define the half-life

$$t_{1/2} = \frac{\ln 2}{k_{el}} \quad (15.4)$$

to characterise the time it takes for the drug concentration in the plasma to decay to $C_{p0}/2$. Another parameter of interest to describe the elimination of the drug, is

**FIGURE 15.4**

Simulation of the decay of drug concentration in the plasma after intravenous bolus injection using the one-compartment model with $D = 1 \text{ mg kg}^{-1}$, $V_d = 70 \text{ ml kg}^{-1}$ and $t_{1/2} = 6 \text{ h}$.

the volume of the plasma in the vascular compartment cleared of drug per unit time, which is named drug clearance

$$CL = k_{el} V_d \quad (15.5)$$

The total exposure of the body to the drug is reflected by the area under the plasma concentration-time curve (AUC), which is usually expressed in $(\text{mg h}) \text{ L}^{-1}$. According to this definition, AUC is the integral of the decay in Figure 15.4, which is calculated from $t = 0$ to a given endpoint. When the endpoint is $t = \infty$, the integral becomes

$$AUC_{\infty} = C_{p0} \int_0^{\infty} \exp(-k_{el}t) dt = C_{p0} \left(\frac{0 - 1}{-k_{el}} \right) = \frac{C_{p0}}{k_{el}} = \frac{D}{V_d k_{el}} \quad (15.6)$$

It is also useful to define the area under the first moment of the plasma concentration-time curve

$$AUMC_{\infty} = C_{p0} \int_0^{\infty} t \exp(-k_{el}t) dt = \frac{C_{p0}}{k_{el}^2} \quad (15.7)$$

where the standard integral

$$\int_0^\infty xe^{-ax}dx = \frac{1}{a^2} \quad (15.8)$$

was employed. Finally, it is important to define the mean residence time

$$MRT = \frac{AUMC}{AUC} \quad (15.9)$$

[Figure 15.3](#) also illustrates the case of a one-compartment model where various mechanisms of clearance of the drug from the plasma are discriminated. This is similar to the case of parallel first-order reactions presented in [Section 4.2.1](#). The kinetics of the elimination remains mono-exponential and the contribution of each mechanism of elimination is proportional to its rate: k_f , k_m or k_u .

15.5.2 Intravenous infusion

Intravenous bolus of large drug doses may have acute adverse effects that can be avoided with the slow infusion of the drug over a long period of time. Usually, when the intravenous administration is prolonged for more than 30 minutes, its kinetics is modelled as those of an infusion.

The time course of the drug in the body under infusion can be divided in three phases. In the beginning, the drug concentration in the body is low and the elimination rate is also low. In this first phase, the drug concentration in the body increases with infusion time. After some time, the drug concentration in the body is sufficiently high to make the elimination rate equal to the infusion rate (assumed constant). After this time, the drug in the body attains a steady-state concentration and remains constant (for a constant infusion rate) until the infusion is stopped. When the infusion is stopped, the kinetics of the drug elimination is identical to that of a bolus injection.

During the infusion, the drug is entering the body at a constant rate, which means that its kinetics is that of a zero-order reaction. Given this and the elimination rate, the concentration of the drug in the plasma is described by

$$\frac{dC_p}{dt} = Q - k_{el}C_p \quad (15.10)$$

where Q is the zero-order infusion rate constant. For consistency with the other units, in the equation above it must be expressed in units of $\text{mg ml}^{-1} \text{ h}^{-1}$. The infusion rate can also be expressed as the dose administered over the time interval ($\Delta\tau$) of its administration, making use of V_d ,

$$Q = \frac{D}{V_d \Delta\tau} \quad (15.11)$$

The best method to solve [eq. \(15.10\)](#) is that of Laplace transforms, presented in [Section 4.3.1](#). Using the fact that the Laplace transform of the function $f(t) = a$

where a is a constant, is $F(p) = a/s$, together with the properties 1 and 2 of Laplace transforms, eq. (15.10) can be written

$$sL[C_p] - C_p^0 = \frac{Q}{s} - k_{el}L[C_p] \quad (15.12)$$

where C_p^0 is the concentration of the drug in the plasma at the beginning of the infusion, that is, $C_p^0 = 0$, and $L[C_p]$ represents the Laplace transform of C_p . Rearranging this equation gives

$$L[C_p] = \frac{Q}{s(s + k_{el})} \quad (15.13)$$

The time course of the drug in the body during continuous infusion can now be expressed as an integrated rate law using the inverse transform found in the table of Laplace transforms in Table 4.1,

$$C_p = \frac{Q}{k_{el}}(1 - \exp(-k_{el}t)) \quad (15.14)$$

Figure 15.5 presents the plasma concentration of a drug administered by intravenous infusion. This figure also shows that when the infusion is stopped, the

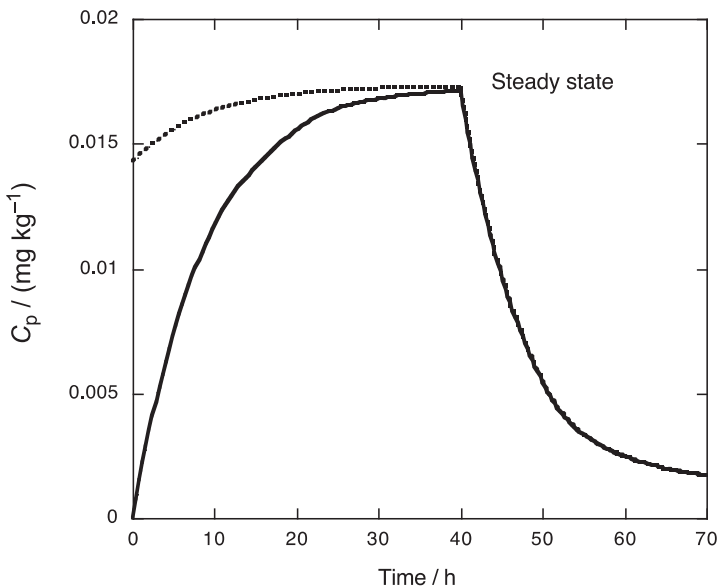


FIGURE 15.5

Simulation of the decay of drug concentration in the plasma after drug infusion using the one-compartment model with $Q = 0.002 \text{ mg kg}^{-1} \text{ h}^{-1}$ and $t_{1/2} = 6 \text{ h}$. The dashed line represents simulations with the addition of a loading dose $D_L = 1 \text{ mg kg}^{-1}$ and $V_d = 70 \text{ ml kg}^{-1}$.

decay of the drug concentration in the plasma is exponential, as discussed above for the bolus injection.

It can be appreciated in [Figure 15.5](#) that the steady-state concentration of the drug in the plasma is only approached after a relatively long time, which depends on the drug half-life in the plasma. This is often undesirable in clinical cases and can be solved with an intravenous bolus administration of a loading dose (D_L) immediately before starting the infusing. The plasma concentration following a loading dose and maintenance infusion is the sum of the exponential decay of the bolus injection with the profile of continuous infusion

$$C_p = \frac{D_L}{V_d} \exp(-k_{el}t) + \frac{D}{CL\Delta\tau}(1 - \exp(-k_{el}t)) \quad (15.15)$$

where [eqs. \(15.5\)](#) and [\(15.11\)](#) were also used. The corresponding drug concentration in the plasma is presented in [Figure 15.4](#).

15.5.3 Single oral dose

The absorption in oral administration takes some time and as the drug enters the circulation, its elimination begins. However, this case differs from intravenous infusion because the rate of absorption in oral administration most often follows first-order kinetics

$$\frac{dC_p}{dt} = k_a C_a - k_{el} C_p \quad (15.16)$$

where C_a is the amount of drug at the absorption site. This model is closely related to that of consecutive first-order reactions presented in [Section 4.2.2](#), where the intermediate B plays the role of C_p . Hence the solution to this differential equation is

$$C_p = k_a C_a^0 \frac{[\exp(-k_a t) - \exp(-k_{el} t)]}{k_{el} - k_a} \quad (15.17)$$

where C_a^0 refers to the initial amount of drug at the absorption site.

In intravenous administration all drug administered reaches the systemic circulation. However, in oral administration, part of the drug is not absorbed and another part is lost in the first pass through the liver. The fraction of the dose that ultimately reaches the systemic circulation defines the absolute bioavailability

$$F = \frac{AUC(\text{oral})/D(\text{oral})}{AUC(\text{iv})/D(\text{iv})} \quad (15.18)$$

This can be taken into account in the expression for the drug concentration in plasma in oral administration to obtain

$$C_p = \frac{FD}{V_d} \frac{k_a}{k_{el} - k_a} [\exp(-k_a t) - \exp(-k_{el} t)] \quad (15.19)$$

where eq. (15.3) was used to express C_p as a function of the oral dose. Figure 15.6 presents the plasma concentration of a drug after oral administration. The time it takes to reach the maximum concentration of the drug in the plasma is given by the time derivative of the equation above, which yields

$$t_{\max} = \frac{\ln(k_{el}/k_a)}{k_{el}/k_a} \quad (15.20)$$

15.5.4 Multiple doses

It is rare that a drug is given only once. Most often, a treatment will require multiple doses of several days duration, if not several years. After some time, steady-state maximum and minimum concentrations will be reached, and the drug concentration in the plasma is maintained in a range situated above the therapeutic dose but below the toxic dose.

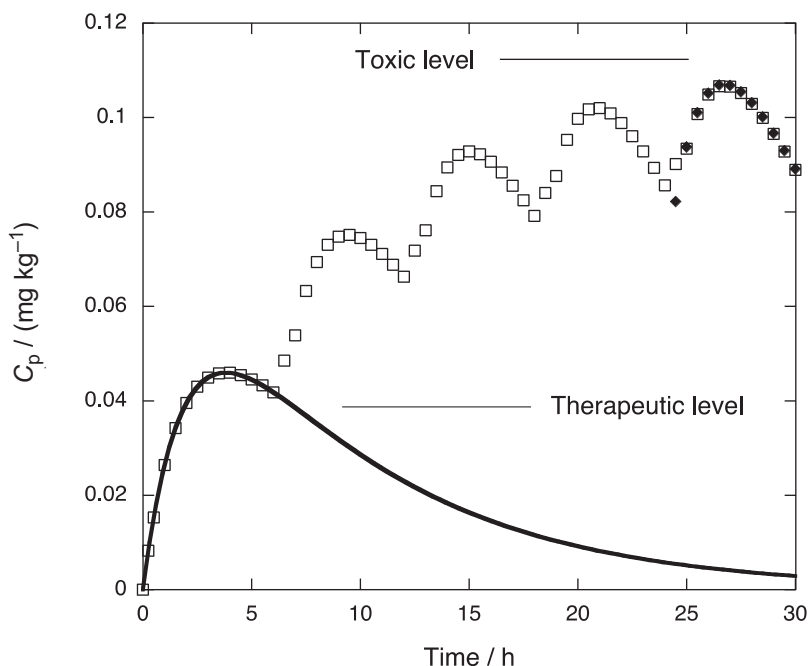


FIGURE 15.6

Simulation of the decay of drug concentration in the plasma after a single oral dose (line) or multiple oral doses (squares) using the one-compartment model with $D = 10 \text{ mg kg}^{-1}$, $V_d = 70 \text{ ml kg}^{-1}$, $F = 0.5$, $k_a = 0.5 \text{ h}^{-1}$, $t_{1/2} = 6 \text{ h}$ and $\Delta t = 6 \text{ h}$. The lozenges represent the calculations using eq. (15.23) with $n = 5$.

The kinetics of the drug in the plasma can be calculated as the sum of contributions of each dose, allowing for a time interval Δt for the calculation of subsequent doses. [Figure 15.6](#) illustrates the cumulative effect of each dose until the steady state is reached. The kinetics of the n th dose can be described making the replacement

$$\exp(-kt) \rightarrow \left[\frac{1 - \exp(-nk\Delta t)}{1 - \exp(-k\Delta t)} \right] \exp(-kt) \quad (15.21)$$

For bolus intravenous administration [eq. \(15.2\)](#) with [eq. \(15.3\)](#) is transformed into

$$C_{pn} = \frac{D}{V} \left[\frac{1 - \exp(-nk_{el}\Delta t)}{1 - \exp(-k_{el}\Delta t)} \right] \exp(-k_{el}t) \quad (15.22)$$

and for oral administration [eq. \(15.19\)](#) is transformed into

$$C_{pn} = \frac{FD}{V} \frac{k_a}{k_{el} - k_a} \left\{ \left[\frac{1 - \exp(-nk_a\Delta t)}{1 - \exp(-k_a\Delta t)} \right] \exp(-k_a t) - \left[\frac{1 - \exp(-nk_{el}\Delta t)}{1 - \exp(-k_{el}\Delta t)} \right] \exp(-k_{el}t) \right\} \quad (15.23)$$

The equations above assume that the time interval between subsequent doses, Δt , is constant. They also assume that the elimination and absorption rates are independent of the dosing. [Figure 15.6](#) also shows the kinetics of the fifth dose calculated with [eq. \(15.23\)](#).

15.5.5 Two-compartment model

All the models discussed above ignored a possible competitive equilibrium between the drug in the central (vascular) compartment and in peripheral (tissues/organs) compartments. Very often, the vasculature and the tissues do not exchange the drug rapidly. The drug in peripheral compartments cannot normally be sampled and sampling of the drug in the plasma may give a bi-exponential decay when the equilibrium between the compartments is slow. Bi-exponential decays are characterised by an initial phase and a terminal phase. The challenge of pharmacokinetics is to interpret these decays without information on what is happening in the tissues.

[Figure 15.3](#) illustrates this case for an intravenous bolus administration. The kinetics of this case are described by

$$\begin{aligned} \frac{dC_1}{dt} &= -k_{el}C_1 - k_{12}C_1 + k_{21}C_2 \\ \frac{dC_2}{dt} &= k_{12}C_1 - k_{21}C_2 \end{aligned} \quad (15.24)$$

where the indexes 1 and 2 are employed to represent the drug in the central and the peripheral compartments, respectively. Making use of Laplace transforms as before, these equations can be written

$$\begin{aligned} sL[C_1] - C_1^0 &= -k_{el}L[C_1] - k_{12}L[C_1] + k_{21}L[C_2] \\ sL[C_2] - C_2^0 &= k_{12}L[C_1] - k_{21}L[C_2] \end{aligned} \quad (15.25)$$

$t = 0$, $C_2^0 = 0$, and the Laplace transform of the drug in the peripheral compartment can be written

$$L[C_2] = \frac{k_{12}L[C_1]}{s + k_{21}} \quad (15.26)$$

This can now be substituted in the Laplace transform of the drug in the vascular compartment where C_1^0 is the dose D/V_d ,

$$sL[C_1] - \frac{D}{V_d} = \frac{k_{12}k_{21}[C_1]}{s + k_{21}} - (k_{el} + k_{12})[C_1] \quad (15.27)$$

Developing and rearranging yields

$$L[C_1] = \frac{(s + k_{21})D/V_d}{s^2 + s(k_{el} + k_{12} + k_{21}) + k_{el}k_{21}} \quad (15.28)$$

Further simplification of the denominator of the equation above requires substitution of variables.

In order to make an inverse Laplace transform using [Table 4.1](#), it would be useful to have

$$s^2 + s(\alpha + \beta) + \alpha\beta = (s + \alpha)(s + \beta) \quad (15.29)$$

This can be achieved making the substitutions

$$\begin{aligned} k_{el} + k_{12} + k_{21} &= \alpha + \beta \\ k_{el}k_{21} &= \alpha\beta \end{aligned} \quad (15.30)$$

which lead to

$$L[C_1] = \frac{(s + k_{21})D/V_d}{(s + \alpha)(s + \beta)} \quad (15.31)$$

Using the Laplace transform table, the drug concentration in the plasma becomes

$$C_1 = \frac{D}{V_d(\beta - \alpha)} [(k_{12} - \alpha)e^{-\alpha t} - (k_{12} - \beta)e^{-\beta t}] \quad (15.32)$$

or

$$C_p = \frac{D(\alpha - k_{12})}{V_d(\alpha - \beta)} e^{-\alpha t} + \frac{D(k_{12} - \beta)}{V_d(\alpha - \beta)} e^{-\beta t} \quad (15.33)$$

which is usually presented as

$$C_p = A e^{-\alpha t} + B e^{-\beta t} \quad (15.34)$$

where, by definition, α is greater than β .

In a clinical setting, it is possible to collect plasma samples at different times after bolus injection and plot C_p values as a function of time. [Eq. \(15.34\)](#) can be fitted to the experimental data and obtain the values of A , B , α and β . Unfortunately, it is not always evident that the best fitting is a bi-exponential and not a mono-

exponential or a tri-exponential. Moreover, collecting data using analytical methods with better sensitivity and over a longer period of time may change the drug decay from a mono- to a bi-exponential, or from bi to a tri-exponential. Assuming that the data is properly collected and fitted, the values of A , B , α and β can be obtained and related to the micro-constants using the equations

$$\begin{aligned} C_{p0} &= A + B \\ k_{21} &= \frac{A\beta + B\alpha}{C_{p0}} \\ k_{el} &= \frac{\alpha\beta}{k_{21}} \\ k_{12} &= (\alpha + \beta) - (k_{21} + k_{el}) \end{aligned} \quad (15.35)$$

Bi-exponential decays are characterised by two phases, each one of them with a lifetime. By definition, the shortest lifetime is the initial or distribution half-life defined as

$$t_{1/2\alpha} = \frac{\ln 2}{\alpha} \quad (15.36)$$

and the longest half-life is the terminal or elimination half-life

$$t_{1/2\beta} = \frac{\ln 2}{\beta} \quad (15.37)$$

Generalising the definitions of the quantities defined for the one-compartment bolus injection, the total exposure to the body to the drug is given by

$$AUC_{\infty} = \int_0^{\infty} Ae^{-\alpha t} dt + \int_0^{\infty} Be^{-\beta t} dt = \frac{A}{\alpha} + \frac{B}{\beta} \quad (15.38)$$

and the first moment of the plasma concentration-time curve is

$$AUMC_{\infty} = A \int_0^{\infty} te^{-\alpha t} dt + B \int_0^{\infty} te^{-\beta t} dt = \frac{A}{\alpha^2} + \frac{B}{\beta^2} \quad (15.39)$$

Together they define the mean residence time

$$MRT = \frac{AUMC_{\infty}}{AUC_{\infty}} \quad (15.40)$$

This is the geometrical mean time that the drug stays in the body.

The apparent volume of the central or vascular compartment, which represents the apparent volume of distribution immediately following an intravenous bolus dose, is given by

$$V_1 = \frac{D}{C_{p0}} = \frac{D}{A + B} \quad (15.41)$$

The apparent volume of the peripheral compartment is

$$V_2 = \frac{CL}{\beta} = \frac{V_1 k_{el}}{\beta} = \frac{D}{\beta AUC_{\infty}} \quad (15.42)$$

where it was made use of the definition of systemic clearance and of the relations in eq. (15.35) to express V_2 in terms of the parameters obtained in the fit to the experimental data. This also shows that V_2 is not a pure measure of the distribution because it is a function of the clearance rate. It is also useful to define a “steady-state” volume related to the apparent distribution volume associated with the steady-state dosing paradigm

$$V_{ss} = V_1 \frac{k_{12} + k_{21}}{k_{21}} = D \frac{AUCM_{\infty}}{(AUC_{\infty})^2} = CL \cdot MRT \quad (15.43)$$

V_{ss} is typically larger than V_1 but smaller than V_2 . Differences in V_{ss} are primarily related to differences in protein binding and/or nonspecific partitioning in plasma and tissues [13].

The concepts of two-compartment models become clearer with an example of the pharmacokinetics of a specific drug. Figure 15.7 shows the plasma concentrations of redaporfin (Figure 15.2), a drug in clinical trials for the photodynamic therapy (PDT) of advanced head and neck cancer [17], after intravenous bolus

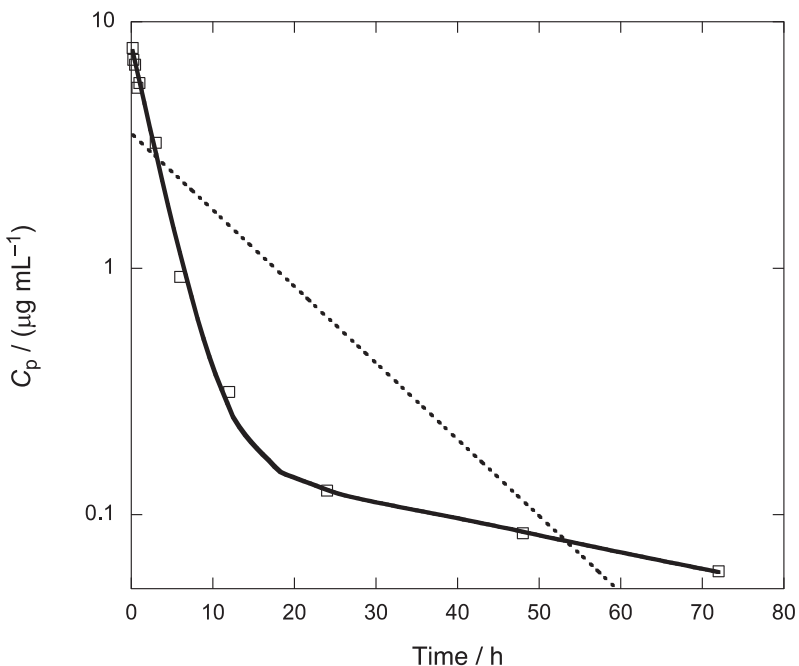


FIGURE 15.7

Plasma concentrations of redaporfin in a patient following intravenous injection of a 0.5 mg kg^{-1} dose for 10 minutes. The dashed line represents a mono-exponential decay, whereas the full line is the fit of eq. (15.34) with $A = 7.907 \mu\text{g ml}^{-1}$, $B = 0.181 \mu\text{g ml}^{-1}$, $\alpha = 0.348 \text{ h}^{-1}$ and $\beta = 0.0157 \text{ h}^{-1}$.

administration of 0.5 mg kg^{-1} [18]. PDT employs a drug, also called photosensitiser, and light to electronically excite that drug. When the drug is electronically excited, it transfers its excess energy (or an electron) to molecular oxygen and generates singlet oxygen (or superoxide ion) [19]. These reactive oxygen species, and other formed subsequently, have short lifetimes but are very cytotoxic, killing the cells in the volume where they were generated. When the photosensitiser is electronically excited shortly after the intravenous administration, most of the photosensitiser molecules are in the vascular compartment and the protocol is named vascular-PDT. On the other hand, selecting a drug-to-light interval of a few hours or days may allow the photosensitiser to distribute to the tissues and be internalised by the cells, in a protocol named cellular-PDT.

Figure 15.7 employs a logarithmic scale, where a mono-exponential function becomes a straight line. It is evident that a mono-exponential function cannot fit the pharmacokinetic data. Eq. (15.34) gives a very good fit to the data, supporting the use of a two-compartment model to interpret the results. The data in Figure 15.7 lead to $t_{1/2\alpha} = 2.0 \text{ h}^{-1}$ and $t_{1/2\beta} = 44 \text{ h}^{-1}$, for the distribution and terminal half-lives, respectively. This means that vascular-PDT should be performed with a drug-to-light interval less than 1 h, to ensure that the drug is still mostly in the vasculature, and cellular PDT may be performed with drug-to-light intervals between 24 and 72 h, before the drug is extensively cleared from the tissues. The first experimental point corresponds to the maximum concentration of redaporfin in the plasma, as expected from an intravenous administration closer to the definition of bolus rather than infusion. The total exposure of the body to redaporfin is $AUC_\infty = 34 \text{ h mg L}^{-1}$. Extrapolation to $t = 0$ gives $C_{p0} = A + B = 8.088 \mu\text{g mL}^{-1}$. Considering that $D = 0.5 \text{ mg kg}^{-1}$, these parameter give $V_1 = 0.062 \text{ L kg}^{-1}$ and $V_2 = 0.937 \text{ L kg}^{-1}$ for the apparent volumes of the vascular and peripheral compartments, respectively. The value of V_2 indicates that after distribution into the tissues, redaporfin is partly sequestered in body fat, which is not surprising for an amphiphilic molecule with a $\log P_{\text{ow}} = 1.9$ [20]. However, the most significant parameter to describe the volume of distribution in a two-compartment model is the steady-state volume V_{ss} . It is both a function of the physiologic volume of the plasma and of tissues. For redaporfin, $V_{ss} = 0.34 \text{ L kg}^{-1}$. This is a relatively low V_{ss} but it does not mean that the drug cannot reach remote sites of action. The micro-constants can be calculated from the data fitted with eq. (15.35), and give the following results: $k_{12} = 0.104 \text{ h}^{-1}$, $k_{21} = 0.023 \text{ h}^{-1}$ and $k_{el} = 0.236 \text{ h}^{-1}$. The clearance rate is now calculated as $CL = 0.015 \text{ L kg}^{-1} \text{ h}^{-1}$. It is also possible to calculate $MRT = 23 \text{ h}$.

The concepts and applications discussed above for the two-compartment model referred to bolus injection of a drug. Oral administration involves the additional process of drug absorption. The drug concentration in the plasma after oral administration has the same form as eq. (15.34) but with one additional term related to drug absorption

$$C_p = Ae^{-\alpha t} + Be^{-\beta t} + Ce^{-k_{at}} \quad (15.44)$$

The fitting of the plasma concentration-time curve now requires six parameters.

15.5.6 Non-compartmental models

Compartmental models become increasingly difficult to use when six or more parameters are required to fit the plasma concentration-time curve. Very detailed information can be extracted from such fittings, but often this goes beyond the interests of the pharmaceutical industry. Alternatively, it is possible to use a model-independent approach to extract the most important information from the plasma concentration-time curve, namely AUC , $AUMC$, MRT and V_{ss} .

Numerical methods can be employed to calculate AUC and $AUMC$ in the time interval of the plasma sampling. Then AUC_∞ and $AUMC_\infty$ are estimated making extrapolations of the area from the last time point sampled to infinity. Eq. (15.40) is then employed to calculate MRT , which is a representative measure of the lifetime of the drug in the body. The total clearance is given by

$$CL = \frac{D}{AUC_\infty} \quad (15.45)$$

and V_{ss} can be obtained from eq. (15.43).

This approach does not require the choice of a model and is available in software packages. However, it does not allow for visualisation or prediction of plasma concentration-time curves for other dosing regimens.

One last comment should be made about drug formulations. The presentation above may have given the impression that the pharmacokinetics of a drug is entirely dictated by its molecular structure. Although this is indeed a most important determinant of pharmacokinetics, drug formulations also play a significant role in the time course of a medicine. Such formulations may accelerate or delay absorption, and may protect the drug from metabolism or early excretion.

References

- [1] TA Baillie, PG Pearson, in AL Burlingame, SA Carr, MA Baldwin (Eds.), *The Impact of Drug Metabolism in Contemporary Drug Discovery: New Opportunities and Challenges for Mass Spectrometry*, Humana Press, Totowa, NJ, 2000.
- [2] JG Wagner, *Pharmacol. Therap.* **12** (1981) 537–562.
- [3] E Widmark, J Tandberg, *Biochem. Z.* **147** (1924) 358–369.
- [4] HW Haggard, *J. Biol. Chem.* **59** (1924) 771–781.
- [5] R Dominguez, E Pomerene, *J. Biol. Chem.* **104** (1934) 449–471.
- [6] T Toerell, *Arch. Int. Pharmacodyn. Ther.* **57** (1937) 205–255.
- [7] LK Paalzow, *Upsala J. Med. Sci* **100** (1995) 41–46.
- [8] CA Lipinski, F Lombardo, BW Dominy, PJ Feeney, *Adv. Drug Deliv. Rev.* **46** (2001) 3–26.
- [9] JS Patton, PR Byron, *Nat. Rev. Drug Discovery* **6** (2007) 67–74.

- [10] GFF Sa, C Serpa, LG Arnaut, *J. Control. Release* **167** (2013) 290–300.
- [11] BM Magnusson, YG Anissimov, SE Cross, MS Roberts, *J. Invest. Dermatol.* **122** (2004) 993–999.
- [12] a GFF Sa, C Serpa, LG Arnaut, in N Dragicevic-Curic, HI Maibach (Eds.), *Photoacoustic Waves as a Skin Permeation Enhancement Method*, Springer, Heidelberg, 2017, pp. 175–191.
b MJ Freire dos Santos, R Carvalho, LG Arnaut, *Aesth. Plast. Surg.* **42** (2018) 1655–1663.
- [13] DA Smith, K Beaumont, TS Maurer, L Di, *J. Med. Chem.* **58** (2015) 5691–5698.
- [14] P Welling, WA Craig, *J. Pharm. Sci.* (1978) 1057–1059.
- [15] DR Luke, G Foulds, SF Cohen, B Levy, *Antimicrob. Agents Chemother.* **40** (1996) 2577–2581.
- [16] B Achour, J Barber, A Rostami-Hodjegan, *Drug Metab. Dispos.* **42** (2014) 1349–1356.
- [17] LL Santos, J Oliveira, E Monteiro, J Santos, C Sarmento, *Case Rep. Oncol.* **11** (2018) 769–776.
- [18] J Oliveira, E Monteiro, J Santos, JD Silva, L Almeida, LL Santos, *J. Clin. Oncol.* **35** (2017) e14056.
- [19] JM Dabrowski, LG Arnaut, *Photochem. Photobiol. Sci.* **14** (2015) 1765–1780.
- [20] LG Arnaut, MM Pereira, JM Dabrowski, EF Silva, FA Schaberle, AR Abreu, LB Rocha, MM Barsan, K Urbanska, G Stochel, CM Brett, *Chem. Eur. J.* **20** (2014) 5346–5357.

Transitions between electronic states

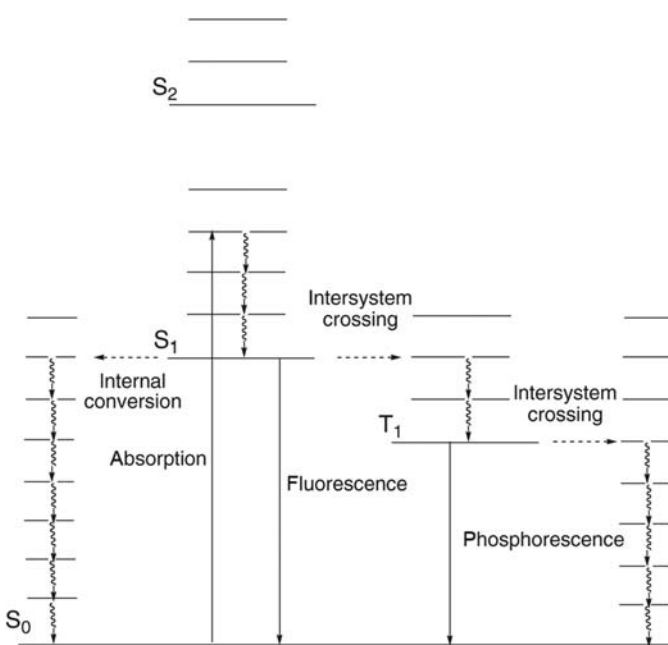
16

16.1 Mechanisms of energy transfer

The previous chapters dealt with reactions triggered by a strong interaction during the collision between the reactants, manifested in the transfer of thermal energy and in the reorganisation of molecular bonds. The bond-breaking–bond-making process resulting from that interaction leads to the transformation of the reactants into products. The relative nuclear motion in the course of the collision can be associated with the “reaction coordinate” connecting reactants to products. Additionally, it is possible to locate a maximum of energy along that reaction coordinate and identify it as the transition state. The transition state was characterised by an imaginary frequency, which corresponds to the curvature of the reaction path. The finite value of the imaginary frequency ensures that the transition between reactants and products is “smooth”, that is, is described by a continuous function of nuclear coordinates. When these properties are confirmed, the reaction can be described by a single potential energy surface and is termed adiabatic. Adiabatic reactions can be described in considerable detail by the transition-state theory. Pharmacokinetics does not deal directly with the rates of chemical reactions but the underlying principles are the same. However, chemical kinetics is not limited to such strong interactions between molecular species.

The methods of chemical kinetics can also be applied to the study of transitions between different electronic states. This study must now be guided by different principles, because the initial (reactant) and final (product) states cannot be described by the same potential energy surface. Such transitions may occur either with the absorption or emission of light, designated as radiative transitions, or with the conversion of the energy difference between the two states into heat, which are termed radiationless transitions. In photochemistry and spectroscopy the transitions between electronic states are conveniently illustrated by the so-called Jablonski diagram [1], where radiative transitions are represented by vertical arrows and radiationless transitions by wavy and/or by dashed lines, [Figure 16.1](#).

Radiative transitions correspond to either absorption or emission of light. When the emission of light occurs between states of the same multiplicity, usually between singlet states in typical organic systems, it is called fluorescence. The emission of light associated with the transition between states of different

**FIGURE 16.1**

Jablonski diagram illustrating the transitions between electronic states in a polyatomic molecule, in a condensed phase. The vibrational levels in each electronic state are only schematically represented, because there are likely to be a very large number of vibrational modes that exist in a multi-dimensional surface. The wavy lines represent the vibrational relaxation within the electronic states.

multiplicity, usually between a triplet and a singlet state, is called phosphorescence. When the absorption of radiative energy exceeds the energy of the excited electronic state, the molecule is left in an excited vibrational level of the excited electronic state. If this molecule is in a condensed state, the collision with neighbouring molecules rapidly relaxes it to the lowest vibrational level of that excited state, the excess vibrational energy is converted into heat, and thermal equilibrium is obtained. Under these conditions, the vibrational relaxation is faster than any other process represented in Figure 16.1, and all the subsequent processes occur from the lowest vibrational level of the lowest excited state. According to Kasha and following earlier suggestions of Vavilov, “The emitting level of a given multiplicity is the lowest excited level of that multiplicity” [2]. However, if the molecule is in the gas phase at low pressures, vibrational relaxation is much slower and reversible inter-system crossing may occur. This is more likely for small molecules, with more spaced vibrational states, but has also been observed for anthracene in the gas phase [3]. Exceptions to Kasha’s rule are known and the most noteworthy of them is that of azulene. Azulene has absorption bands centred

near 300 nm and near 585 nm, corresponding to transitions from the ground (S_0) to the second (S_2) or to the first (S_1) excited state, respectively. When excited at 300 nm, azulene fluoresces at 374 nm. This emission from the S_2 state is possible because the energy gap between the S_2 and S_1 states is very large (130 kJ mol⁻¹), comparable to that between the S_1 and S_0 states (170 kJ mol⁻¹). One important aspect of this chapter is to relate the rate of transition between two electronic states to their energetic difference.

Exceptions to Kasha's rule are rare. Most often, in condensed phases, the electronically excited molecule rapidly relaxes to the lowest vibrational state of the lowest electronically excited state. From this state it will undergo an electronic transition to the ground state with conservation of spin that can either be radiative (fluorescence emission) or non-radiative (internal conversion), or may involve a spin flip of one of the electrons in an electronic transition to an isoenergetic vibrationally excited level of the lowest triplet state (inter-system crossing). In the triplet state the molecule undergoes rapid vibrational relaxation to its lowest vibrational level, and from here it will return to the ground state either radiatively (phosphorescence emission) or nonradiatively (inter-system crossing to a high vibrational level of the ground state, followed by vibrational relaxation).

Excited electronic states can be formed as the result of high temperatures, very exothermic chemical reactions (chemiluminescence), radiative recombination of electrons and holes (electroluminescence), or, more commonly, absorption of radiation. In this last case, if the monochromatic light of intensity I_0 is incident normal to a sample of homogeneous coloured solution, the intensity of the transmitted light will be

$$I_t = I_0 10^{-\varepsilon l C} \quad (16.1)$$

where C is the concentration (in M = mol dm⁻³) of the molecules that absorb light, ε their molar absorption coefficient (sometimes called extinction coefficient) in M⁻¹ cm⁻¹ at the wavenumber (inverse of the wavelength) of the incident light, and l is the length (in cm) of the optical path in the solution. The molar absorption coefficient at a given wavenumber, $\varepsilon(\bar{\nu})$, is used to obtain the absorption cross section, which is a parameter frequently used in optics

$$\sigma(\bar{\nu}) = \frac{2303\varepsilon(\bar{\nu})}{N_A} = 3.81 \times 10^{-19} \varepsilon(\bar{\nu}) \text{ (cm}^2\text{)} \quad (16.2)$$

Both the molar absorption coefficient and the absorption cross sections are measures of the electronic transition probability. A further important measure of this is the oscillator strength, f , given for transition between a lower state 1 and an upper state 2, which is proportional to the area of the absorption band,

$$f_{12} = \frac{2303m_e c^2}{\pi e^2 N_A n_D} \int \varepsilon(\bar{\nu}) d\bar{\nu} \quad (16.3)$$

Here m_e is the mass and e is the charge of an electron, and n_D is the refractive index of the solution.

An excited atom may decay spontaneously to the ground state with the emission of a photon of energy

$$E_2 - E_1 = h\nu_{21} = \hbar\omega_{21} \quad (16.4)$$

where the angular oscillation frequency is $\omega = 2\pi\nu$. Einstein represented the transition probability for spontaneous emission for our system of two states, 1 and 2, by A_{21} . However, the excited atom in the presence of a radiation field may also relax to the ground state by interaction with the incident radiation in the process termed stimulated emission. This is the process that is the basis of the light amplification by stimulated emission of radiation (LASER). Einstein called the corresponding transition probability B_{21} . Microscopic reversibility requires that the transition probability for stimulated emission must be equal to the transition probability for absorption

$$B_{21} = B_{12} \quad (16.5)$$

Einstein obtained a relation between spontaneous and stimulated emission, using the relation between the number of atoms in the two states

$$\frac{n_1}{n_2} = e^{-\frac{E_1 - E_2}{k_B T}} = e^{\frac{h\nu_{21}}{k_B T}} \quad (16.6)$$

and Planck's expression for the radiation density of a black body at temperature T

$$I(\nu) = \frac{8\pi h\nu^3}{c^3} \frac{1}{e^{h\nu/k_B T} - 1} \quad (16.7)$$

When an atomic system is in equilibrium with the radiation field, as many transitions occur in the direction $1 \rightarrow 2$ as in the opposite direction, $2 \rightarrow 1$. In this case, the equilibrium condition will be

$$I(\nu)(n_1 B_{12} - n_2 B_{21}) - A_{21} n_2 = 0 \quad (16.8)$$

Using eqs. (16.5)–(16.7) in eq. (16.8), gives

$$A_{21} = \frac{8\pi h\nu^3}{c^3} B_{21} = 8\pi h\nu^3 B_{21} \quad (16.9)$$

Assuming that at time $t = 0$, the external radiation field is removed and that all atoms are in the excited state, the decay to the ground state follows the (first-order) radiative decay law

$$n_2(t) = n_2(0)e^{-A_{21}t} \quad (16.10)$$

and the radiative (sometimes termed natural) lifetime of fluorescence is $\tau_F = 1/A_{21}$.

The distinction between electronic transitions involving states of the same spin multiplicity (fluorescence and internal conversion) and states of different spin multiplicity (phosphorescence and inter-system crossing) is due to the existence of selection rules for electronic transitions. Wigner expressed the spin conservation rule stating that the total spins of α (\uparrow) or β (\downarrow) type in the combined initial and final states of the system must be the same. One of the most important

consequences of this rule is that the change of the spin of an electron during a spectroscopic transition is forbidden, that is, $\Delta S = 0$. The electron is a fermion with spin quantum numbers $s = +\frac{1}{2}$ or $s = -\frac{1}{2}$, whereas the photon is a boson with $s = 1$. A photon absorption or emission does not change the spin state of the electron directly, and phosphorescence is a spin-forbidden process. Inter-system crossing also involves a change in the spin of an electron and consequently, it is also a spin-forbidden transition. The spin-forbidden nature of these processes is of electronic origin, but can be circumvented by interaction with the medium, especially when heavy atoms or paramagnetic species are present. Under these conditions, spin is no longer a pure quantum number and significant spin-orbit coupling occurs, due largely to relativistic effects. Heavy atoms also facilitate inter-system crossing and phosphorescence when they are present in the molecule—the internal heavy-atom effect. The simplest way to account for the spin-forbidden nature of these processes is to introduce a spin-forbidden factor $\chi_0 < 1$ in the expression for the rate of electronic transition between states of different spin multiplicity. This accounts for the fact that such transitions are much slower than internal conversion and fluorescence. In view of these spin restrictions and given that the ground state of organic molecules is a singlet state (S_0), the lowest excited singlet state of such molecules (S_1) has a much shorter lifetime than the corresponding triplet state (T_1). Kasha suggested a value of $\chi_0 = 10^{-6}$ for the inter-system crossing from T_1 to S_0 in aromatic hydrocarbons.

Chemical reactions between two reactants in different electronic states, leading to two products in electronic states that preserve the total spin multiplicity, can also be called radiationless transitions. Two frequently encountered examples are electron and electronic-energy transfers. Here, electron transfers are understood as processes where only one electron is transferred from one molecule or ion to another molecule or ion, without breaking or making of any bonds. These processes are also termed outer-sphere electron transfers. They will be discussed in detail in the next chapter. Electronic-energy transfers may occur through three mechanisms: radiatively (the so-called “trivial mechanism”, involving emission of one molecule followed by re-absorption by another), nonradiatively through coulombic (mainly dipole-dipole) interaction (the Förster mechanism [4]) or nonradiatively through electron exchange (the Dexter mechanism [5]).

The radiative, or trivial, mechanism of inter-molecular energy transfer can be expressed as a sequence of two independent steps



where D' represents the excited energy donor and A is the acceptor. The rate of this mechanism is proportional to the fluorescence rate constant of the donor, the concentration of excited molecules and the probability of absorption by A

$$\nu_{\text{rad}} \propto k_f^D [D'] P_{\text{abs}}^A \quad (16.11)$$

From the above discussion on the spin selection rule, it is implicit in this formulation that the states D and D', A and A' involved in radiative energy transfer will have the same spin multiplicity. However, the pair A, A' may have different spin multiplicity from the pair D, D'. The probability of light absorption by A is proportional to its concentration and to the spectral overlap between the donor emission and the acceptor absorption. The most distinct features of this mechanism are its long range, its dependence of the overlap between the fluorescence of the donor and the absorption of the acceptor, its dependence on the size and shape of the vessel utilised, and the fact that it leaves the lifetime of the donor unchanged. Radiative energy transfer is observed mainly in optically thick samples.

The two mechanisms of non-radiative electronic energy transfer differ in the nature of the interaction between the energy donor and the energy acceptor. In the Förster, or Coulombic, mechanism there is an electrostatic interaction between the transition dipole moment corresponding to the electronic de-excitation of the donor and that corresponding to the electronic excitation of the acceptor, and the two transitions occur simultaneously. The energy lost by the donor molecule is acquired by the acceptor molecule in a resonant fashion, and can take place at distances much larger than molecular sizes because the interaction between two point dipoles falls off with their distance R as R^{-6} [6]. This process corresponds to the coupling of two oscillators of electromagnetic field by a “virtual” rather than a “real” photon. It is the dominant energy transfer mechanism except when the dipole strength of the acceptor transition is low or the fluorescence yield of the donor is vanishingly small. Figure 16.2 illustrates the change in donor and acceptor electronic configurations taking place in the course of the Förster energy transfer mechanism.

Triplet states do not meet the requirements for efficient Förster energy transfer. Yet, triplet-triplet energy transfers, where the donor is initially in a triplet state A($\uparrow\uparrow$) and the acceptor is initially in the ground (singlet) state B($\downarrow\uparrow$) and

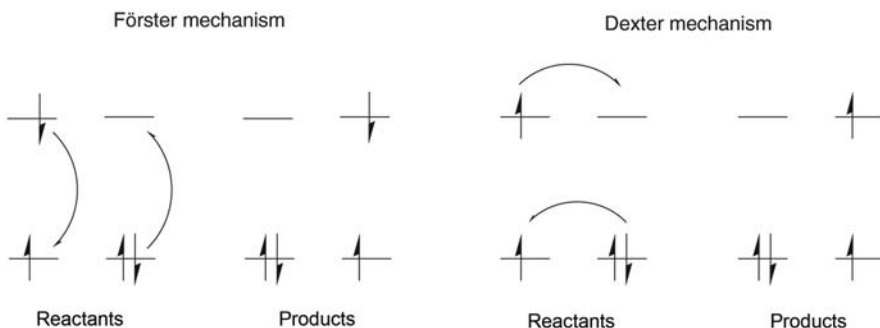


FIGURE 16.2

Electronic configurations in (a) Förster energy transfer and (b) Dexter energy transfer.

lead to the donor in the ground (singlet) state $A(\downarrow\uparrow)$ and the acceptor in a triplet state $B(\uparrow\uparrow)$, are relatively common in the photochemistry of organic molecules. Triplet-triplet energy transfer requires the acceptor to have a triplet state of lower energy than the donor. Wigner's spin rule allows for energy transfer between two triplet states, for example, between species $A(\uparrow\uparrow)$ and $B(\downarrow\downarrow)$, to give two species in the singlet state, $A(\uparrow\downarrow)$ and $B(\downarrow\uparrow)$. A particularly important case of triplet energy transfer is the transfer of energy from the triplet state of an organic molecule to molecular oxygen, whose ground state is a triplet (${}^3\Sigma_g^-$) and whose first singlet (${}^1\Delta_g$) state is 94 kJ mol^{-1} above the ground state. In this case, the two reactants are triplets and the two products are singlets. Interestingly, singlet oxygen is a cytotoxic species and this process is employed in the photodynamic therapy (PDT) of cancer to kill tumour cells.

This is an example of a process called triplet-triplet annihilation. This designation is more commonly associated with the case when two identical organic molecules in their triplet states (T_1) meet and yield a singlet ground state (S_0) and a highly excited singlet state (S_n^*), which collects the excitation energies of both partners. This process frequently leads to delayed fluorescence (known as P-type delayed fluorescence from its observation with the aromatic hydrocarbon pyrene). Here the emission has the same spectrum as normal fluorescence but has the lifetime of the triplet state. The transfer still follows Wigner's spin rule, and is governed by spin statistics. Initially it can be characterised by the formation of an intermediate pair state $T_1 + T_1 \leftrightarrow {}^{1,3,5}(T_1\dots T_1)$, that subsequently decays to $S_0 + S_n^*$. The reverse process, where a highly excited singlet state dissociates into two triplets is also known, and is termed singlet fission. In singlet fission, the initial localisation of the singlet exciton in a suitable chromophore rapidly leads, through radiationless decay, to the production of two triplet-excited states. This requires the triplet excitation energy to be less than, or close to, one-half of the corresponding excited-singlet state. This situation has been demonstrated for molecular crystals, concentrated solutions and isolated bichromophores in fluid solution. The mechanism for exciton multiplication is under intense investigation because it is a possible route to increase charge densities in organic opto-electronic devices [7].

Triplet-triplet energy transfers can be conceptualised as the tunnelling of an electron from one partner to the other, while another electron tunnels in the opposite direction, leaving the overall spin multiplicity intact, [Figure 16.2](#). This mechanism, first described by Dexter, requires the overlap of the wave functions of the two partners in space and is triggered by the electron-exchange interaction. Dexter energy transfer is also possible for singlet-singlet energy transfers, but it takes place at shorter distances than Förster energy transfer.

Electron and triplet energy transfers have certain features in common. For example, such reactions may occur with relatively high rates even when the electron (or energy) donor is physically separated from the electron (or energy) acceptor by distances of 10 \AA . However, rather than the concerted transfer of two

electrons pictured for triplet energy transfers in [Figure 16.2](#), electron transfers involve the transfer of one electron only. The understanding of the factors that govern the rates of energy and electron transfers rests on the resolution of the time-dependent Schrödinger equation.

16.2 The “Golden Rule” of quantum mechanics

Quantum mechanics establishes a simple expression for the rate constant of a transition between an initial and a final state when these states are only subject to a weak interaction. The formalism of weak interactions was originally developed for spectroscopic transitions but later found application in energy and electron transfers.

The time-dependent Schrödinger equation, for a time-independent Hamiltonian, has the form

$$\mathbf{H}\Psi(x, y, z, t) = i\hbar \frac{d\Psi(x, y, z, t)}{dt} \quad (16.12)$$

and its more familiar application is to represent the motion of a particle as the motion of a wave packet. Here, [eq. \(16.12\)](#) is employed to describe the time development of the system from its initial state to its final state. The general solution for this equation of motion is a linear superposition of the stationary states

$$\Psi(x, y, z, t) = \sum_n a_n \Psi_n = \sum_n a_n \psi_n \exp\left(-\frac{i}{\hbar} E_n t\right) \quad (16.13)$$

where ψ_n is a function of the space coordinates. When the system is subject to a perturbation, the coefficients a_n become functions of time during the perturbation, and remain constant in the unperturbed system. For example, if the system is initially in a stationary state defined by $n = 1$ and undergoes a transition to the stationary state defined by $n = 3$, then, during the transition, a_1 will decrease from unity to zero, while a_3 will increase from zero to unity, inverting the weight of the contributions ψ_1 and ψ_3 . The rate of change from a_1 to a_3 is a measure of the rate of transition from the first to the third stationary state. The calculation of this rate is one of the central problems of theories of spectroscopic and radiationless transitions.

In the most relevant cases for these transitions, the perturbing interaction is limited in time and space. For example, the system is unperturbed before it interacts with an electromagnetic wave, and it is free again from the perturbation after sufficient time has elapsed. This suggests that the total Hamiltonian can be considered as the sum of two terms

$$\mathbf{H} = \mathbf{H}_0 + V \quad (16.14)$$

where the time-independent operator \mathbf{H}_0 describes the unperturbed system, and V is the perturbation. This perturbation may be explicitly time dependent, as in the case of a transient electromagnetic field, or not, as in the case of an applied field.

Replacing eq. (16.14) into eq. (16.12) and omitting the coordinates to simplify the form of the equation,

$$(\mathbf{H}_0 + V)\Psi = i\hbar \frac{d\Psi}{dt} \quad (16.15)$$

and the solutions can be written

$$\Psi = \sum_j c_j \psi_j \exp\left(-\frac{i}{\hbar} E_j t\right) \quad (16.16)$$

where ψ_j represents the full set of eigenfunctions with the associated eigenvalues E_j of the unperturbed system hamiltonian \mathbf{H}_0 , when the coefficients c_j are time-dependent. Replacing eq. (16.16) in eq. (16.15) and exchanging the left and right sides

$$\sum_j \left(c_j E_j \psi_j + i\hbar \frac{dc_j}{dt} \psi_j \right) \exp\left(-\frac{i}{\hbar} E_j t\right) = \sum_j c_j (\mathbf{H}_0 \psi_j + V \psi_j) \exp\left(-\frac{i}{\hbar} E_j t\right) \quad (16.17)$$

which can be reduced to

$$\sum_j i\hbar \frac{dc_j}{dt} \psi_j \exp\left(-\frac{i}{\hbar} E_j t\right) = \sum_j c_j V \psi_j \exp\left(-\frac{i}{\hbar} E_j t\right) \quad (16.18)$$

because each term $\mathbf{H}_0 \psi_j$ on the left-hand side of eq. (16.17) cancels with the corresponding $E_j \psi_j$ term on the right-hand side of that equation. An expression for dc_j/dt can be obtained taking the inner product of $\mathbf{H}\Psi$ with one of the stationary states. Representing this other stationary state by the index k , the inner product corresponds to

$$\int \sum_j i\hbar \frac{dc_j}{dt} \psi_k^* \exp\left(\frac{i}{\hbar} E_k t\right) \psi_j \exp\left(-\frac{i}{\hbar} E_j t\right) d\tau = \int \sum_j c_j \psi_k^* \exp\left(\frac{i}{\hbar} E_k t\right) V \psi_j \exp\left(-\frac{i}{\hbar} E_j t\right) d\tau \quad (16.19)$$

where ψ_k^* is the complex conjugate of ψ_k , and the integration is over all the space, represented by τ . Given that the stationary states of the Hamiltonian are orthogonal

$$\int \psi_k^* \psi_j d\tau = \delta_{kj} \quad (16.20)$$

as well as adopting the shorthand notation for the matrix element of the perturbation between unperturbed eigenstates

$$V_{kj} = \int \psi_k^* V \psi_j d\tau \quad (16.21)$$

and defining the transition frequency

$$\omega_{kj} = \frac{E_k^{(0)} - E_j^{(0)}}{\hbar} \quad (16.22)$$

gives a set of coupled first order differential equations

$$i\hbar \frac{dc_k}{dt} = \sum_j V_{kj} c_j e^{i\omega_{kj} t}; \quad k = 1, 2, 3, \dots \quad (16.23)$$

In matrix notation, this is equivalent to

$$i\hbar \frac{d}{dt} \begin{pmatrix} c_1 \\ c_2 \\ \vdots \\ \vdots \end{pmatrix} = \begin{pmatrix} V_{11} & V_{12} e^{-i\omega_{12} t} & \dots & \dots \\ V_{21} e^{-i\omega_{21} t} & V_{22} & \dots & \dots \\ \vdots & \vdots & \ddots & \dots \\ \vdots & \vdots & \vdots & \ddots \end{pmatrix} \begin{pmatrix} c_1 \\ c_2 \\ \vdots \\ \vdots \end{pmatrix} \quad (16.24)$$

No approximations have yet been made and eq. (16.24) is exact. The values of c_j determined by that equation are related to the probability of finding the system in any particular state at any later time. Unfortunately, it is not generally possible to find exact solutions to this equation. The solution of this complicated linear system invokes the perturbation approximation, and the method is called *time-dependent perturbation theory*.

The solution of eq. (16.23) depends critically on the initial conditions. Assuming, for simplicity, that the system at the initial time $t_0 = -\infty$ is in one of the stationary states of the unperturbed Hamiltonian, and that \mathbf{H}_0 possesses only discrete energy levels, the following initial conditions are introduced

$$c_s(-\infty) = 1, \quad c_k(-\infty) = 0 \quad \text{if } k \neq s \quad (16.25)$$

The index s represents the initial stationary state. A successive approximation method can be used to solve eq. (16.23) subject to these initial conditions. The initial values of the coefficients c_k are introduced in the right-hand side of eq. (16.23). For $k \neq s$, the approximate equations

$$i\hbar \frac{dc_k}{dt} = V_{ks} e^{i\omega_{ks} t} \quad k \neq s \quad (16.26)$$

are thus obtained. These equations are only valid for values of t such that $c_k(t) \ll c_s(t) \approx 1$, if $k \neq s$.

Eq. (16.26) can be immediately integrated when the perturbation V does not itself depend on time, although the time development of the system with the Hamiltonian eq. (16.14) is, nevertheless, conveniently described in terms of transitions between eigenstates of the unperturbed Hamiltonian \mathbf{H}_0 . Taking the initial time as $t_0 = 0$

$$i\hbar \int_0^t dc_k = V_{ks} \int_0^t e^{i\omega_{ks} t} dt \quad k \neq s \quad (16.27)$$

and using eq. (16.22), the coefficients

$$c_k(t) = V_{ks} \frac{1 - e^{i\omega_{ks} t}}{E_k^{(0)} - E_s^{(0)}} \quad (16.28)$$

are obtained for $k \neq s$, if $c_k(0) = 0$ and $c_s(0) = 1$.

If the system is known to have been in the initial discrete state s at $t = 0$, the probability that it will be in the unperturbed final eigenstate $k \neq s$ at time t is given by

$$|c_k(t)|^2 = 2|V_{ks}|^2 \frac{1 - \cos(\omega_{ks}t)}{(E_k^{(0)} - E_s^{(0)})^2} \quad (16.29)$$

where the relation

$$\cos(x) = \frac{1}{2}(e^{ix} + e^{-ix}) \quad (16.30)$$

was employed. The total probability of transition to all the final states, labelled f , which form a quasi-continuum of states per unit energy interval, is given by

$$\sum_{k \in f} |c_k(t)|^2 = 2 \int |V_{ks}|^2 \frac{1 - \cos(\omega_{ks}t)}{(E_k^{(0)} - E_s^{(0)})^2} \rho_f(E_k^{(0)}) dE_k^{(0)} \quad (16.31)$$

where $\rho_f(E)$ represents the density of final unperturbed states. The assumption that the final states form a quasi-continuum justified the use of an integral rather than sums on the right-hand side of eq. (16.31). Within this approximation, it is of interest to formulate the time rate of change of the total transition probability

$$w = \frac{d}{dt} \sum_{k \in f} |c_k(t)|^2 = \frac{2}{\hbar^2} \int |V_{ks}|^2 \frac{\sin(\omega_{ks}t)}{\omega_{ks}} \rho_f(E_k^{(0)}) dE_k^{(0)} \quad (16.32)$$

It is usual practice to assume that both $|V_{ks}|^2$ and $\rho_f(E_k^{(0)})$ are approximately constant over an energy range ΔE in the neighbourhood of E_s . Additionally, the function $\sin(\omega_{ks}t)/\omega_{ks}$ has a pronounced peak at $E_k^{(0)} = E_s^{(0)}$ for t values which satisfy the relation

$$t \gg \hbar/\Delta E \quad (16.33)$$

as illustrated in Figure 16.3. This expresses the fact that the transitions that tend to conserve the unperturbed energy are dominant. If the right-hand side of eq. (16.33) corresponds to a very short time, there is a considerable range of t values, such that the inequality is fulfilled and yet the initial state s is not appreciably depleted. For such a range of t values, eq. (16.32) can be simplified to

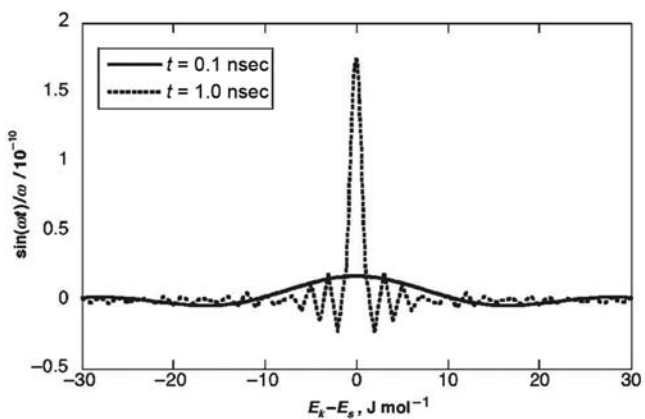
$$w = \frac{2}{\hbar} |V_{ks}|^2 \rho_f(E_s^{(0)}) \int_{-\infty}^{+\infty} \frac{\sin(\omega_{ks}t)}{\omega_{ks}} d\omega_{ks} \quad (16.34)$$

where the condition of eq. (16.33) was employed to replace the limits of the integral by $-\infty$ and $+\infty$. Given the standard integral

$$\int_{-\infty}^{+\infty} \frac{\sin(ax)}{x} dx = \pi \quad \text{when } a > 0 \quad (16.35)$$

the transition probability per unit time becomes

$$w = \frac{2\pi}{\hbar} |V_{ks}|^2 \rho_f(E_s^{(0)}) \quad (16.36)$$

**FIGURE 16.3**

Dependence of the function $\sin(\omega_{ks}t)/\omega_{ks}$ on the energy difference between unperturbed initial and final states, calculated for the values of t indicated in the plot.

Fermi called eq. (16.36) the *Golden Rule of time-dependent perturbation theory*, because of its prevalence in radiationless transitions. Sometimes it is referred to as Fermi's Golden Rule.

The matrix element of the perturbation between the eigenstates V_{ks} is expressed in units of energy, the density of states $\rho_f(E_k^{(0)})$ is expressed in reciprocal energy units, and w is used in sec^{-1} . A typical case where the Golden Rule is applicable is the internal conversion of a large molecule, following its electronic excitation. For example, the energy of the first excited singlet state (S_1) of anthracene relative to that of its ground state (S_0) is 316 kJ mol^{-1} . At this energy, the density of vibrational states in S_0 is extremely high. Typically, for such molecules, this is in the range of 10^{11} – 10^{17} states per J mol^{-1} , and the S_1 state will relax into an isoenergetic level of the manifold of highly excited vibrational states of S_0 , a process already defined as internal conversion. Subsequent vibrational relaxation in the S_0 state converts the electronic excitation into heat. It must be recalled that this is not the only decay process available to the S_1 state. It may also decay radiatively by fluorescence, or undergo inter-system crossing to the manifold of the triplet states.

16.3 Radiative and radiationless rates

Classically, charged particles radiate when they are accelerated. The strength of radiation is proportional to the square of the electric dipole moment, which is

$$\vec{\mu}_{21} = \int \Psi_2 [\vec{e}\vec{r}_{21}] \Psi_1 d\tau = e \langle \Psi_2 | \vec{r}_{21} | \Psi_1 \rangle \quad (16.37)$$

where \vec{r}_{21} stands for the electron position vector. The absorption oscillator strength, that describes the strength of the coupling between the electric dipole and the electromagnetic field, is defined as

$$f_{12} = \frac{8\pi^2 m_e c \bar{\nu}}{3h} \frac{|\mu_{12}|^2}{e^2} = 1.085 \times 10^{-5} \bar{\nu}_{\max} \left(\frac{\mu_{12}}{e} \right)^2 \quad (16.38)$$

where the numerical value applies when $\bar{\nu}$ is expressed in per centimetre and $|\mu_{12}|/e$ is in angstrom. The oscillator strength is a dimensionless quantity.

The absorption of light is mainly the result of the interaction between the oscillating electric vectors of the electromagnetic radiation with the charged particles within the molecules. The transition probability coefficient in the absorption from a lower electronic state 1 to an upper electronic state 2 corresponds to Einstein's coefficient of absorption

$$B_{12} = \frac{8\pi^3}{3h^2} |\mu_{12}|^2 \quad (16.39)$$

Eliminating μ_{12} and f_{12} using eqs. (16.3) and (16.38) in the above expression gives the absorption probability in the gas phase ($n_D = 1$) in terms of experimentally accessible quantities

$$B_{12} = \frac{2303c}{hN_A} \int_0^\infty \frac{\varepsilon(\bar{\nu})d\bar{\nu}}{\bar{\nu}} \quad (16.40)$$

The radiative rate can now be expressed in terms of these quantities using eq. (16.9),

$$k_r = A_{21} = \frac{64\pi^4 \nu^3}{3hc^3} |\langle \Psi_2 | e\vec{r}_{21} | \Psi_1 \rangle|^2 = \frac{8 \times 2303\pi c}{N_A} \nu^2 \int_0^\infty \varepsilon(\bar{\nu}) d\bar{\nu} \quad (16.41)$$

This relation is only strictly applicable to two-level systems, such as atomic systems, where the transitions have sharp lines, and in a medium of refractive index $n_D = 1$. The electric dipole radiation dominates the mechanism of radiative decay in molecular systems. For molecular systems in solution, Strickler and Berg proposed a modified equation that gives good results for the radiative rate [8]

$$k_{\text{SB}} = \frac{8 \times 2303\pi c}{N_A} n_D^2 \langle \bar{\nu}^{-3} \rangle^{-1} \int \frac{\varepsilon(\bar{\nu}) d\bar{\nu}}{\bar{\nu}} = 2.88 \times 10^{-9} n_D^2 \langle \bar{\nu}^{-3} \rangle^{-1} \int \frac{\varepsilon(\bar{\nu}) d\bar{\nu}}{\bar{\nu}} \quad (16.42)$$

where

$$\langle \bar{\nu}^{-3} \rangle^{-1} = \frac{\int F(\bar{\nu}) d\bar{\nu}}{\int F(\bar{\nu}) \bar{\nu}^{-3} d\bar{\nu}} \quad (16.43)$$

and $F(\bar{\nu})$ is the molecular fluorescence intensity distribution (i.e., its spectrum). When the fluorescence is the mirror image of the absorption, the radiative rates calculated with the Strickler-Berg equation compare well with the experimental

rates obtained from the fluorescence quantum yield and lifetime of the donor molecules

$$k_F = \frac{\Phi_F}{\tau_D} \quad (16.44)$$

[Eq. \(16.42\)](#) predicts that the radiative rate depends on the absorption coefficient. An interesting example is given by *meso*-tetra(2-fluoro-5-*N*-methylsulfamoylphenyl)porphyrin and chlorin, that differ only in one double versus single bond in the tetrapyrrolic macrocycle. This small difference makes the lowest energy absorption band increase from 639 nm ($\varepsilon_{639} = 790 \text{ M}^{-1} \text{ cm}^{-1}$) in the porphyrin to 652 nm ($\varepsilon_{652} = 34,000 \text{ M}^{-1} \text{ cm}^{-1}$) in the chlorin. The fluorescence bands are concomitantly shifted to 644 and 657 nm, respectively. Using [eq. \(16.42\)](#) with the integrated absorption spectra and normalised and integrated fluorescence spectra, the calculated radiative rate constants for the porphyrin and chlorin are $k_{SB} = 3 \times 10^6 \text{ sec}^{-1}$ and $16 \times 10^6 \text{ sec}^{-1}$, respectively. The fluorescence rate constants of the porphyrin and chlorin obtained from their experimental lifetimes (9.8 and 9.3 nsec) and fluorescence quantum yields (0.096 and 0.396) are $k_F = 9.8 \times 10^6$ and $43 \times 10^6 \text{ sec}^{-1}$, respectively [9]. This is a quite reasonable agreement and the relative rates are very well reproduced ([Figure 16.4](#)).

[Eq. \(16.42\)](#) relates the radiative energy transfer rate constant to molecular properties. The corresponding rate, [eq. \(16.11\)](#), involves the probability of absorption by A, which can be expressed as

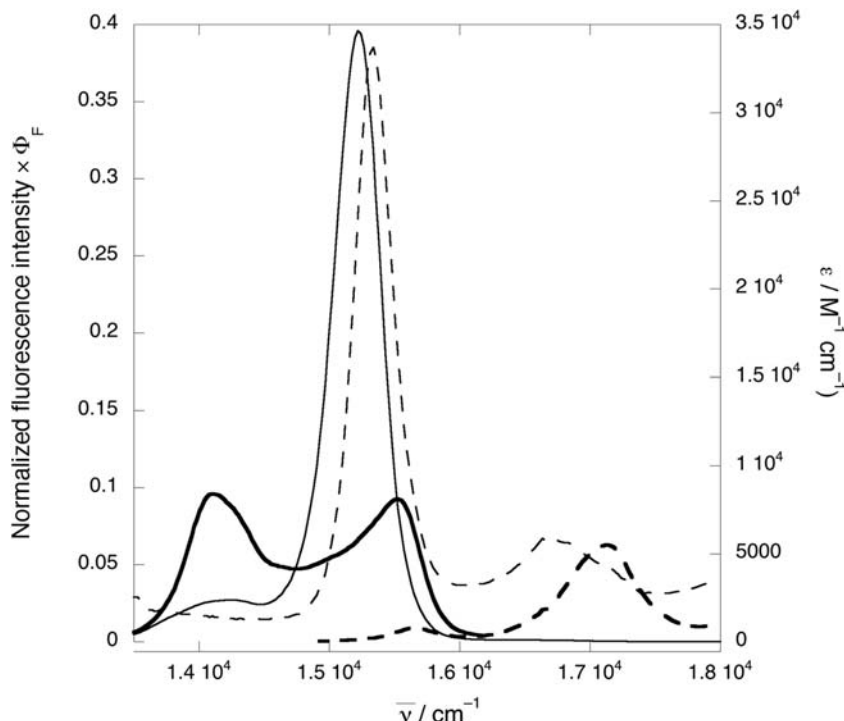
$$P_{\text{abs}}^A \propto [\text{A}]l \int_0^\infty F'_D(\bar{\nu})\varepsilon_A(\bar{\nu})d\bar{\nu} \quad (16.45)$$

where l is the path length of absorption, and the spectral overlap involves the normalised spectral distribution of the donor emission $F'_D(\bar{\nu})$ and the molar absorption coefficient of the acceptor $\varepsilon_A(\bar{\nu})$. The normalisation of the donor emission is given by

$$F'_D(\bar{\nu}) = \frac{F_D(\bar{\nu})}{\int_0^\infty F_D(\bar{\nu})d\bar{\nu}} \quad (16.46)$$

As mentioned before, radiative energy transfer originates from the interaction between the oscillating electric vector of the electromagnetic radiation and the charged particles within the molecules. Another possible interaction between the excited donor and the ground state acceptor molecule is the electric dipole-dipole interaction, which is the basis of the Förster mechanism, schematically presented in [Figure 16.2](#). The dipole-dipole interaction energy in the vacuum between two dipoles $\vec{\mu}_1$ and $\vec{\mu}_2$ at a distance R between their centres, has the form

$$V_{12} = \frac{1}{R^3} \left[\vec{\mu}_1 \otimes \vec{\mu}_2 - \frac{3(\vec{\mu}_1 \otimes \vec{R})(\mu_2 \otimes \vec{R})}{R^2} \right] \quad (16.47)$$

**FIGURE 16.4**

Absorption (dashed lines) and fluorescence (full lines) of *meso*-tetra(2-fluoro-5-*N*-methylsulfamoylphenyl) porphyrin (thick lines) and chlorin (thin lines) in methanol, where the fluorescence was normalised and scaled by the fluorescence quantum yields of each molecule.

A quantitative treatment using the Golden Rule with this interaction energy leads to the following expression for the rate of Förster energy transfer

$$k_F = \frac{9000(\ln 10)\kappa^2\Phi_f}{128\pi^5 n_D^4 N_A R^6 \tau_D} \int_0^\infty \frac{F_D(\bar{\nu})\varepsilon_A(\bar{\nu})d\bar{\nu}}{\bar{\nu}^4} = \frac{1}{\tau_D} \left(\frac{R_0}{R} \right)^6 \quad (16.48)$$

where κ is an orientation factor (for a random directional distribution the average value is $\kappa^2 = 2/3$), the donor fluorescence intensity F_D is normalised to unit area on a wavenumber scale, and the decadic molar absorption coefficient of the acceptor ε_A is in the usual units ($M^{-1} \text{ cm}^{-1}$). The reason why the emission shape needs to be normalised to unity, while the absorption shape does not, is the presence of the term τ_D^{-1} that already contains information on the absolute magnitude of the emitting transition moment. The above expression emphasises the fact that the probability of energy transfer is proportional to the square of the interaction energy and decreases, therefore, with the sixth power of the distance. The critical transfer distance R_0 is the distance at which the energy transfer and

the spontaneous decay of the excited donor are equally probable. Typically, values between 30 and 100 Å are calculated for aromatic donors.

Electric dipole–dipole coupling is strongest if the corresponding optical transitions in both molecules are allowed for electric dipole radiation. This is not the case of triplet energy transfer, Figure 16.2, which must follow an alternative mechanism. Dexter proposed that for such cases it is necessary to include explicitly the spin wave functions in the matrix element of the perturbation, eq. (16.21). The molecular wavefunction ψ is expressed as the product between a spatial $\varphi(\vec{r})$ and a spin $\xi(\vec{s})$ electronic wave function

$$\begin{aligned} \langle V_{12} \rangle = & \int \varphi_D^{''*}(\vec{r}_1) \varphi_A^*(\vec{r}_2) V_{12} \varphi_D(\vec{r}_1) \varphi_A'(\vec{r}_2) \times \xi_D^{''*}(\vec{s}_1) \xi_A^*(\vec{s}_2) \xi_D(\vec{s}_1) \xi_A'(\vec{s}_2) - \\ & - \int \varphi_D^{''*}(\vec{r}_1) \varphi_A^*(\vec{r}_2) V_{12} \varphi_D(\vec{r}_2) \varphi_A'(\vec{r}_1) \times \xi_D^{''*}(\vec{s}_1) \xi_A^*(\vec{s}_2) \xi_D(\vec{s}_2) \xi_A'(\vec{s}_1) \end{aligned} \quad (16.49)$$

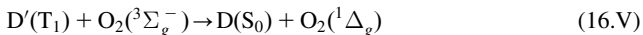
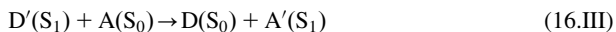
where \vec{r}_1 and \vec{r}_2 denote the spatial coordinates of the electrons involved and the apostrophe denotes an excited state. The first integral is the Coulomb term with V_{12} given by eq. (16.47), and is different from zero when the spins of the electrons remain unchanged. The second integral is an exchange integral with $V_{12} = e^2/r_{12}$ in the vacuum, where r_{12} is the distance between the two electrons. This second integral represents the electrostatic interaction between the two charged clouds, and dies off exponentially with the distance between the donor and the acceptor. Unless $\xi'_D = \xi'_A$ and $\xi_D = \xi_A$, the integral vanishes, but ξ' is not necessarily equal to ξ . If s'_D and s_A are the initial spin quantum numbers of the two participating molecules, the resultant spin quantum number of the two species taken together must have one of the values

$$s'_D + s_A, s'_D + s_A - 1, s'_D + s_A - 2, \dots |s'_D - s_A| \quad (16.50)$$

It follows that the spin quantum numbers of the resulting species can only have values s_D and s'_A if at least one of the values

$$s_D + s'_A, s_D + s'_A - 1, s_D + s'_A - 2, \dots |s_D - s'_A| \quad (16.51)$$

is common to the series above. Thus processes such as



are spin allowed by an exchange mechanism. This is also an expression of Wigner's spin rule.

The treatment of this perturbation with the Golden Rule, gives an exchange transfer rate of the form

$$k_D = \frac{2\pi}{\hbar} \Gamma \exp(-2R/\ell) \int_0^\infty F_D(\bar{\nu}) A_A(\bar{\nu}) d\bar{\nu} \quad (16.52)$$

where Γ and ℓ reflect the ease of electron tunnelling between the donor and the acceptor and are not simply related to measurable quantities. They will be further discussed in this chapter, under Sections 16.6 and 16.8. The donor emission F_D and the acceptor absorption A_A spectra are normalised to unity, such that the integral of F_D and the integral of A_A are both equal to unity. The most salient features of eq. (16.52) are the exponential dependence on the inter-molecular distance and the normalisation of both emission and absorption, which makes the exchange transfer rates independent of the oscillator strengths of the two transitions.

The overlap integrals appearing in eqs. (16.45), (16.48) and (16.52) reflect the spatial overlap between the wavefunctions of the initial unperturbed state s and the final unperturbed state k , and have their origin in the first of the two factors entering the Golden Rule, $|V_{ks}|^2$ in eq. (16.36). The calculation of the spatial overlap almost invariably employs the Born–Oppenheimer approximation, which, based on the difference of masses between electrons and nuclei, treats the nuclei as stationary points with the electrons moving around them. In practice, this consists in expressing the molecular wavefunction ψ as the product between an electronic (φ_e) and a nuclear (v_v) wavefunction. The simplest case is that of a diatomic molecule with translational and rotational motions that give rise to a continuum of energies at the temperatures under consideration, and with a vibrational motion described by a harmonic oscillator. Representing the distance between the two nuclei by R , the Born–Oppenheimer approximation is expressed as

$$\psi(x, R) = \varphi_e(x; R)v_v(R) \quad (16.53)$$

The representation $(x; R)$ denotes the parametric dependence of the electronic wavefunction on the inter-nuclear distance.

Substituting eq. (16.53) in eq. (16.21) and assuming that only the electronic distribution is perturbed, gives

$$\int \psi_k^* V \psi_j d\tau = \int \varphi_k^* v_{v'}^* V \varphi_s v_v d\tau_e d\tau_n = \int \varphi_k^* V \varphi_s d\tau_e \int v_{v'}^* v_v d\tau_n \quad (16.54)$$

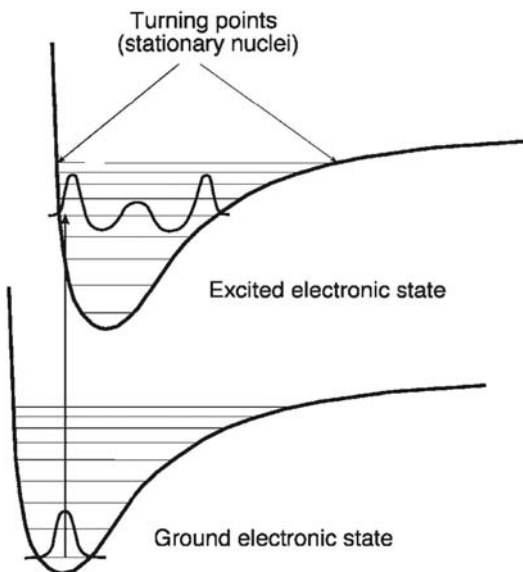
The first factor

$$V_{ks}^e = \int \varphi_k^* V \varphi_s d\tau_e \quad (16.55)$$

measures the extension of the electronic redistribution induced by the transition from the initial state s to the final state k . The second factor

$$J_{v', v} = \int v_{v'}^* v_v d\tau_n \quad (16.56)$$

is the overlap integral between the vibrational wavefunctions of the initial (v) and final (v') states, which is called the *Franck–Condon factor* for the $k, v' \leftarrow s, v$ transition. According to eq. (16.36), the transition probability, or intensity, is

**FIGURE 16.5**

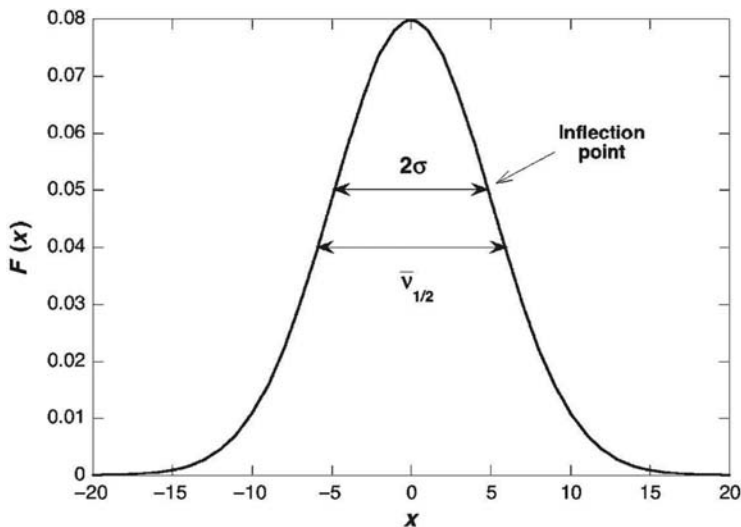
Electronic transition corresponding to the absorption of light by the ground state of a diatomic molecule. The final state, reached immediately after the electronic transition, is the vibrational state of the electronically excited state that has the largest overlap with the lowest vibrational state of the electronic ground state.

proportional to $|J_{v,v'}|^2$. Figure 16.5 represents an electronic transition that takes place at a fixed nuclear geometry, following the Franck–Condon principle. The vibrational relaxation takes place entirely in the excited state, after the electronic transition, and takes the system to the lowest vibrational state of the electronically excited state.

16.4 Franck–Condon factors

The Franck–Condon factor of an electronic transition from the vibrational level $v = 0$ of the electronic ground state to the corresponding level $v' = 0$ of the electronic excited state has a simple analytical solution when the vibrational motion is described by a harmonic oscillator. In this case, the vibrational wavefunctions of the ground vibrational levels is described by a normal (Gaussian) distribution function

$$F(x) = \frac{1}{\sqrt{2\pi}\sigma_x} \exp\left[-\frac{1}{2}\left(\frac{x-x_e}{\sigma_x}\right)^2\right] \quad (16.57)$$

**FIGURE 16.6**

Normal (Gaussian) distribution function, centred in its average, $x_e = 0$.

illustrated in [Figure 16.6](#). As shown in the figure, the Gaussian is centred in its average x_e and the variance σ^2 is given by the inflection points of the distribution function. It is also convenient to characterise this distribution by its full width at half-maximum

$$\Delta\bar{v}_{1/2} = 4\sigma\sqrt{\ln 2} \quad (16.58)$$

More specifically, the wavefunction of the ground vibrational state of a harmonic oscillator with a force constant f and a reduced mass μ , has the form

$$v_0 = \left(\frac{1}{\alpha\sqrt{\pi}} \right)^{1/2} \exp \left[-\frac{(R-R_e)^2}{2\alpha^2} \right] \quad \alpha^2 = \hbar/\sqrt{f\mu} \quad (16.59)$$

$$v'_0 = \left(\frac{1}{\alpha\sqrt{\pi}} \right)^{1/2} \exp \left[-\frac{(R-R'_e)^2}{2\alpha^2} \right]$$

The overlap integral between these identical but displaced oscillators is

$$J_{0,0} = \int_{-\infty}^{+\infty} v_0^* v_0 dR = \frac{1}{\alpha\sqrt{\pi}} \int_{-\infty}^{+\infty} \exp \left[-\frac{(R-R_e)^2 + (R-R'_e)^2}{2\alpha^2} \right] dR \quad (16.60)$$

The integral can be evaluated making the substitution of variables

$$\alpha z = R - \frac{1}{2}(R_e + R'_e) \quad (16.61)$$

which yields

$$J_{0',0} = \frac{1}{\sqrt{\pi}} \exp \left[-\frac{(R_e - R'_e)^2}{4\alpha^2} \right] \int_{-\infty}^{+\infty} e^{-z^2} dz \quad (16.62)$$

where the integral now has a standard form and gives $\sqrt{\pi}$. Thus the overlap is

$$J_{0',0} = \exp \left[-\frac{(R_e - R'_e)^2}{4\alpha^2} \right] \quad (16.63)$$

Considering that the intensity of the $0' \leftarrow 0$ transition is proportional to $|J_{v',v}|^2$, it attains its maximum when the bond lengths of the ground and excited state are identical, and diminishes as $(R_e - R'_e)^2$ increases. This effect is illustrated in [Figure 16.7](#), where it is also shown that the intensities of the transitions to higher vibrational states of the electronically excited state attain their maxima for $R_e \neq R'_e$ and may dominate the absorption spectrum. The $0 \leftarrow 0$ transition is a purely electronic transition, while the $v' \leftarrow 0$ transitions are vibronic (electronic + vibrational) transitions, subject to selection rules.

At room temperatures, the molecules are generally in their lowest vibrational state of the electronic ground state. Upon light absorption, the electron is promoted from the vibrational level $v = 0$ of the ground state to a vibrational level v' of the excited state. For parabolas with the same force constant f but minima displaced by $d = |R_e - R'_e|$, as shown in [Figure 16.8](#), the progression of the vibronic bands follows a Poisson distribution, already presented in [eq. \(5.20\)](#),

$$J_{v',0} = \exp[-S] \frac{S^{v'}}{v'!} \quad (16.64)$$

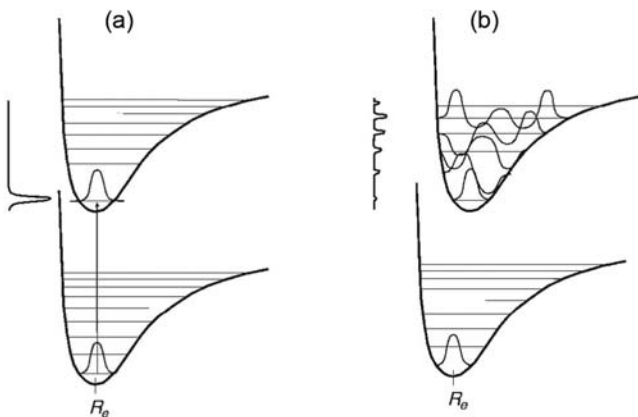
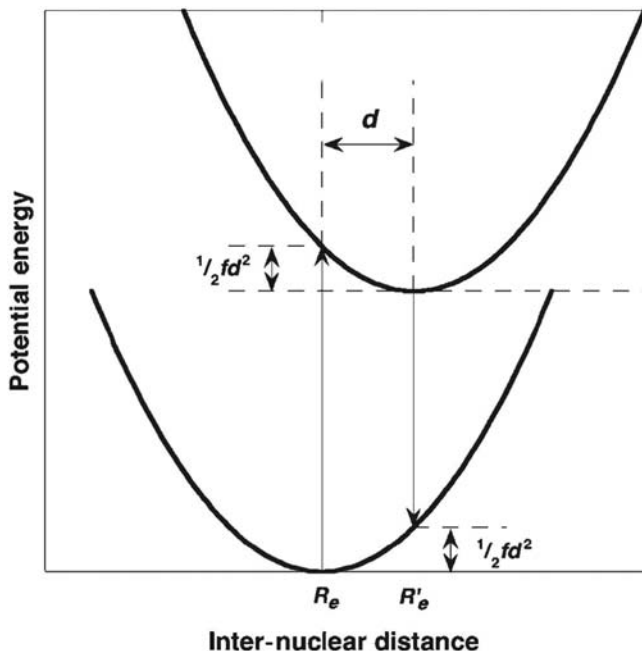


FIGURE 16.7

Electronic transitions illustrating the intensity expected for the vibronic band of the absorption spectrum. (a) Totally allowed transition following the Franck–Condon principle. (b) Partially allowed transition according to the Franck–Condon principle.

**FIGURE 16.8**

Schematic representation of light absorption and fluorescence emission between electronic states described by identical (same force constant f) but displaced ($R_e \neq R'_e$) parabolas. The absorption is, necessarily, at higher energies than the fluorescence.

where S is a reduced displacement,

$$S \equiv \left(\frac{d}{2\sigma_R} \right)^2 \quad (16.65)$$

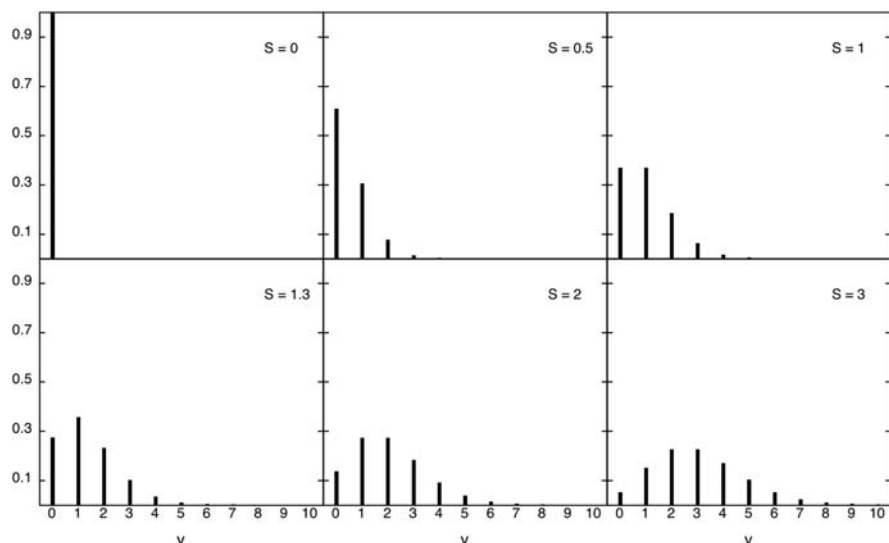
and σ_R , the root mean square amplitude of the zero-point oscillation in the electronic ground state, is defined as

$$\sigma_R^2 \equiv \langle (R - R_e)^2 \rangle_0 = \frac{1}{2} \frac{\hbar}{\sqrt{\mu f}} = \frac{\alpha^2}{2} \quad (16.66)$$

Within the harmonic oscillator approximation, the force constant and the reduced mass are related to the angular frequency of the classical oscillator (ω , expressed in sec^{-1}) and to the wavenumber of the vibration ($\bar{\nu}$, expressed in cm^{-1}) by

$$\omega = 2\pi c \bar{\nu} = \sqrt{\frac{f}{\mu}} \quad (16.67)$$

[Figure 16.9](#) illustrates the progression of the peaks expected for different values of S .

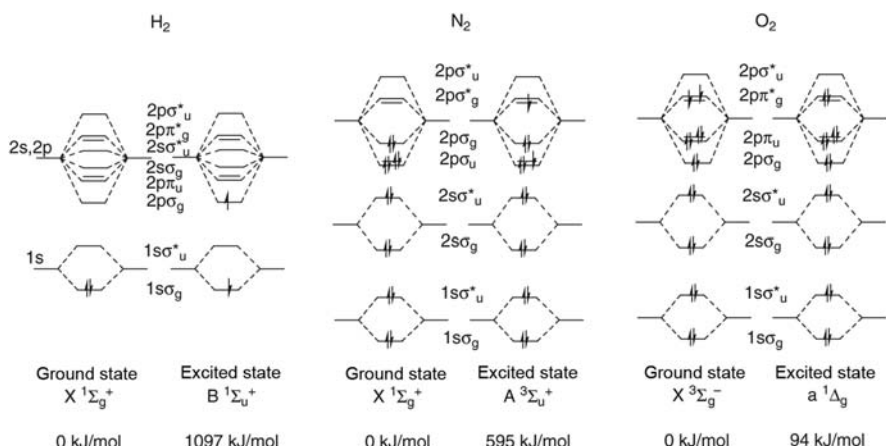
**FIGURE 16.9**

Poisson distribution for different values of the parameter S . The number of peaks in the spectrum increases when the geometry of the excited state differs more significantly from that of the ground state.

Table 16.1 Spectroscopic constants of oxygen ($\mu = 8.000$), nitrogen ($\mu = 7.004$) and hydrogen ($\mu = 0.5041$).

Molecule	Electronic state	$\bar{\nu}$ (cm $^{-1}$)	R_e (Å)	F (kJ mol $^{-1}$ Å $^{-2}$)
O ₂	X $^3\Sigma_g^-$	1580	1.2074	7.086×10^3
O ₂	a $^1\Delta_g$	1509	1.2155	6.463×10^3
N ₂	X $^1\Sigma_g^+$	2358	1.0976	13.817×10^3
N ₂	A $^3\Sigma_u^+$	1460	1.293	5.296×10^3
H ₂	X $^1\Sigma_g^+$	4395	0.7416	3.455×10^3
H ₂	B $^1\Sigma_u^+$	1357	1.2927	0.329×10^3

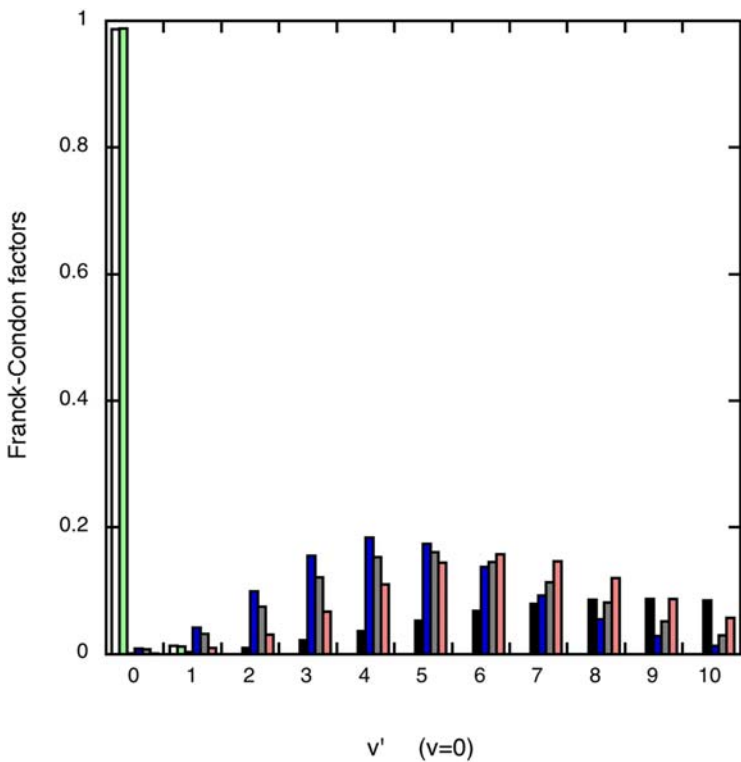
The Franck–Condon factors given by eq. (16.64) for the transfer from the lowest vibrational level of the initial electronic state to the v' vibrational levels of the final electronic state are particularly simple to calculate for diatomic molecules, in view of the straightforward relation between the observed frequencies and the parameters involved in the calculation of S . Table 16.1 presents the spectroscopic constants of O₂, N₂ and H₂, in different electronic states. They represent the cases of small (O₂), medium (N₂) and large (H₂) changes in bond lengths upon electronic excitation from the ground state to the excited state. The adjustments of the bond lengths minimise the energies of the systems in their electronic states, which have the electronic

**FIGURE 16.10**

Electronic configurations of the electronic states indicated for O_2 , N_2 and H_2 .

configurations illustrated in Figure 16.10. Pauling's relation between bond lengths and bond orders can also be employed to evaluate the chemical bond order of these excited states. As usual, for bonds between the same atoms, a longer bond corresponds to a lower bond order and, consequently to a weaker bond. Although all the examples presented in the table correspond to longer bonds in the excited state, it is possible to find excited states with shorter bonds, when the electronic transition corresponds to the excitation of an anti-bonding electron. The table also reveals that changes in bond lengths are associated with changes in force constants, and that the approximations used to obtain eq. (16.64) are not very realistic. However, Figure 16.11 shows that, using the average value for S obtained with the data for the two electronic states and eq. (16.64), the Franck–Condon factors calculated with the harmonic model are in reasonable agreement with the more exact values calculated with Morse oscillators [10]. The largest discrepancies are observed for the transition between the electronic states of N_2 considered in this example.

The same principles can be used to simulate the absorption, fluorescence and phosphorescence spectra of polyatomic molecules. In such cases, the changes of the bond lengths are not generally known and the progression of the vibronic bands is used to extract the value of S . It then represents the collective relative change in the bond lengths associated with the electronic excitation. An additional difficulty is that the absorption spectrum in condensed phases, at room temperature, is not a series of narrow peaks. Rather, it is made of absorption bands with an appreciable width. The width of these bands (described as the inhomogeneous broadening) is related to the distribution of molecular energies within each electronic level, as well as to interactions with the medium (or solvent). It can be assumed that the translational and rotational motions originate a continuum of energy at the temperatures under consideration. Under this assumption, it is

**FIGURE 16.11**

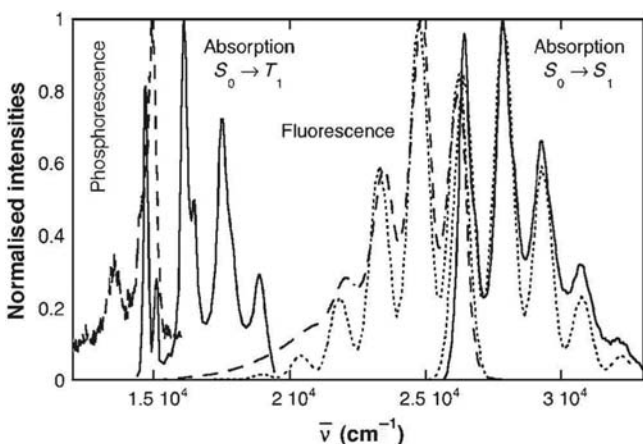
Franck–Condon factors calculated using Morse or harmonic oscillators for the $X^3\Sigma_g^-$ to $a^1\Delta_g$ transition in O_2 white and light shade $X^1\Sigma_g^+$ to A^+ transition in N_2 black and darker shade, and $X^1\Sigma_g^+$ to $B^1\Sigma_u^+$ transition in H_2 right pair of bars. In each set, the first bar refers to the Morse oscillator and the second (in colour) to the harmonic oscillator.

reasonable to describe the energy distribution by a Gaussian function. Thus the absorption spectrum can be simulated by a sum of the peaks corresponding to the vibronic transitions, each one of them multiplied by a Gaussian that reflects the continuous distribution of energy ε within each vibrational level, and fitted to the experimental bandwidth,

$$\alpha(\varepsilon) = \sum_{v'=0}^{\infty} \exp[-S_A] \frac{S_A^{v'}}{v'!} \frac{1}{\sqrt{2\pi\sigma_A^2}} \exp\left\{-\frac{[(E'_0 - E_0) + v'\hbar\omega_A - \varepsilon]^2}{2\sigma_A^2}\right\} \quad (16.68)$$

Identically, for the emission from $v' = 0$ of an electronically excited state to the vibronic levels of the ground electronic state

$$\iota(\varepsilon) = \sum_{v=0}^{\infty} \exp[-S_D] \frac{S_D^v}{v!} \frac{1}{\sqrt{2\pi\sigma_D^2}} \exp\left\{-\frac{[(E'_0 - E_0) - v\hbar\omega_D - \varepsilon]^2}{2\sigma_D^2}\right\} \quad (16.69)$$

**FIGURE 16.12**

Absorption and emission spectra of anthracene. These are at room temperature, except for the phosphorescence, that was measured at 77 K. The singlet–triplet absorption is the triplet excitation spectrum in single-crystal anthracene. The dotted lines are the simulated absorption ($E_S = 26,400 \text{ cm}^{-1}$, $\sigma_A = 350 \text{ cm}^{-1}$, $S_A = 1.18$, $\bar{v}_A = 1450 \text{ cm}^{-1}$) and fluorescence ($E_S = 26,200 \text{ cm}^{-1}$, $\sigma_D = 350 \text{ cm}^{-1}$, $S_D = 1.18$, $\bar{v}_D = 1450 \text{ cm}^{-1}$) spectra.

where E_0 and E'_0 are the energies of the ground state and excited state in their lowest vibrational levels, respectively.

Figure 16.12 illustrates the simulation of normalised anthracene absorption and fluorescence spectra using eqs. (16.68) and (16.69), respectively. This figure also illustrates the singlet–triplet absorption of anthracene measured as the triplet excitation spectrum of a single crystal of the anthracene [11]. The excitation spectrum was obtained by observing the intensity of blue fluorescence as a function of the wavelength of the exciting light, because the direct singlet–triplet absorption is strongly forbidden. For the same reason, the phosphorescence was measured in a hydrocarbon matrix at 77K, although a room temperature spectrum of anthracene has also been measured in ultra-pure and de-oxygenated cyclohexane [12]. The energies of the excited states ($E'_0 - E_0$), the frequencies of the vibrational progressions ω , the widths of the vibronic bands 2σ , and the values of S , that reflects the relative intensities of the vibronic bands, were adjusted to fit both the absorption and the fluorescence spectra. The best fit to the experimental spectra requires a higher excited state energy for the absorption ($E_S = 316 \text{ kJ mol}^{-1}$) than for the fluorescence ($E_S = 313 \text{ kJ mol}^{-1}$).

In condensed phases, it is very frequent to observe a difference between the spectral positions of the band maxima (or the band origin) of the absorption and fluorescence arising from the same electronic origin. The fluorescence maximum occurs at a lower wavenumber than the absorption, and their difference is called Stokes shift. Anthracene is amenable to the treatment of its vibronic progressions using a single vibrational frequency whose value is much greater than the width

of the vibronic bands. Under these conditions, it is possible to identify both the $0' \leftarrow 0$ transition in absorption and the corresponding $0 \leftarrow 0'$ band in fluorescence. The Stokes shift measured as the difference between these band maxima, 200 cm^{-1} , is probably due to the solvent relaxation. However, in many systems, several vibrational progressions are associated with the electronic excitation, and their overlap leads to the observation of only one broad band for the absorption, and another for the fluorescence, in transitions between the same electronic states. In such cases, the Stokes shift has quantum contributions from the vibrational progressions and classical contributions from the solvent relaxation.

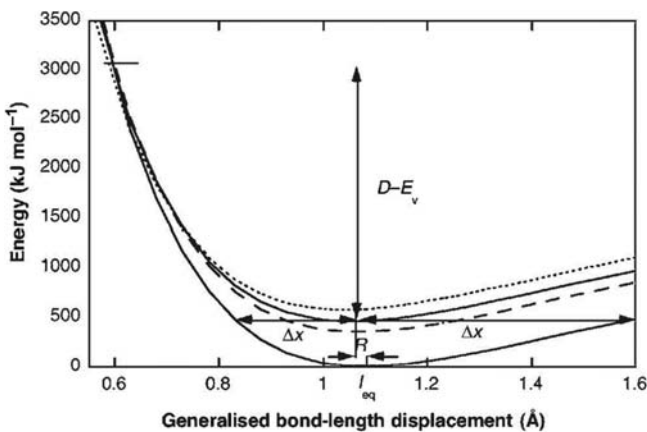
Empirically, the singlet-state energy is best determined from the intersection between normalised absorption and fluorescence spectra. The same principle could be applied to the triplet energy, but this is not usually feasible because the singlet-to-triplet absorption is very difficult to observe. Alternatively, the triplet energy is estimated from the origin of the phosphorescence spectrum or from the maximum of the phosphorescence band plus half of the Stokes shift observed for fluorescence. Non-spectroscopic techniques, such as photoacoustic calorimetry, often provide a better estimate of the triplet energies.

16.5 Radiationless transition within a molecule

The Franck–Condon factors discussed above are relevant for radiative transitions from the lowest vibrational level of the initial state to a series of vibrational levels of the final state. In each radiative transition, the exact energy difference between the two states is either supplied or released by photons. Radiationless transitions must also conserve energy but cannot use photons for their energy balance. Internal conversion takes place from the lowest vibrational level of the S_1 state to isoenergetic, very high vibrational levels of the S_0 state. It has already been indicated that there is a very large density of vibrational states of S_0 at the energy of S_1 . The same applies to the inter-system crossing from T_1 to S_0 . Radiationless transition rates can be treated using the methods of quantum mechanics to obtain closed-form expressions for the rates in some limiting cases. [Appendix VI](#), Quantum-Mechanical Radiationless Transition Theory, presents derivations of various expressions of radiationless transition rates and discusses the limits of their validities. Jortner and Ulstrup showed that for very exo-energetic transitions between electronic states of the same molecule, neglecting the contribution of the low-frequency lattice/solvent modes and assuming that only the lowest vibrational level of the high-frequency mode is populated, the radiationless transition rate takes the form [13]

$$k = \frac{2\pi}{\hbar^2\omega} |V|^2 \exp\left[-\frac{d\sqrt{2\mu E_A}}{\hbar}\right] \exp\left[-(\gamma + 1)\frac{\Delta E}{\hbar\omega}\right] \quad (16.70)$$

where the value of $(\gamma - 1)$ under these conditions is a small negative quantity and the second exponential is close to unity. Under these conditions, the radiationless

**FIGURE 16.13**

Anharmonic potential energy curves of the generalised CH vibrational modes of benzene in the ground state, first singlet state (solid line), second singlet state (dotted line) and first triplet state (dashed line). The tunnelling barrier width, Δx , is indicated both for the repulsive and the attractive sides. The height of the tunnelling barrier in the repulsive side, $D - E_v$, is measured from the bottom of the S_1 state to its crossing with the S_0 state. The tunnelling barrier in the attractive side is the generalised CH bond dissociation energy.

transition rate is analogous to the tunnelling transmission probability through a barrier formed by intersecting parabolas, eq. (6.47).

The first calculation of Franck–Condon factors in terms of nuclear tunnelling preceded this formal demonstration [14]. Using the WKB approximation for tunnelling through intersecting parabolas, Formosinho expressed the tunnelling rate as

$$k_{\text{WKB}} = \chi \nu \exp \left[-\frac{\sqrt{2\mu}}{\hbar} \sqrt{D - E_v} \Delta x \right] \quad (16.71)$$

where χ is the electronic forbidden factor ($\chi \ll 1$ for non-adiabatic transitions), ν is the frequency of the vibrational mode attempting the transition, μ its reduced mass, $D - E_v$ is the barrier height and Δx the barrier width illustrated in Figure 16.13. This figure represents the generalised CH vibrational modes of benzene. In the process of converting a polyatomic molecule into a diatomic molecule, C_1H_1 , it is convenient to define the relative number of atoms involved in the transition as $\eta = n_H/(n_H + n_C)$, where n_H and n_C are the number of hydrogen and carbon atoms, respectively [15]. As a first approximation, the contribution of the CC bonds to the internal conversion or inter-system crossing is neglected, and the effective vibration is $\eta/0.5$ times smaller than the CH stretching mode. The corresponding barrier width is $0.5/\eta$ times smaller and, according to the tunnel effect theory [14,16], eq. (16.71) is modified to

$$k_{\text{TET}} = \chi \nu \exp \left[-\frac{\sqrt{2\mu_{\text{CH}}}}{\hbar} \sqrt{D - E_v} \frac{\Delta x}{2\eta} \right] \quad (16.72)$$

Clearly, for benzene eq. (16.72) is identical to eq. (16.71) but for the other aromatic hydrocarbons the relative number of CH modes is somewhat lower and the rate is reduced.

The minima of the CH bonds represented in this figure in their S_0 and S_1 states are displaced because each CH bond contracts by $\Delta r \approx 0.01 \text{ \AA}$ upon electronic excitation. This contraction directs the crossing of the curves to their repulsive side. McCoy and Ross expressed the electronic transitions in polycyclic aromatic hydrocarbons in terms of a bond-length displacement coordinate ΔR [17],

$$\Delta R = \left(\sum_j \Delta r_j^2 \right)^{1/2} \quad (16.73)$$

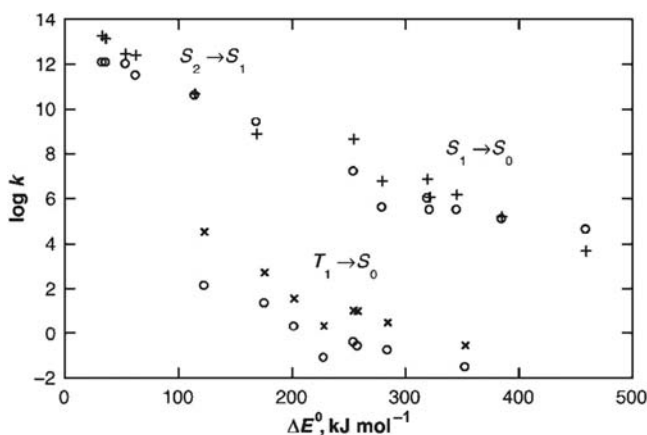
where Δr_j denotes the change in the length of the j th bond. This gives approximately $\Delta R = 0.025 \text{ \AA}$ for benzene, which is representative of other aromatic hydrocarbons because the increase in the number of bonds is probably associated with a smaller CH bond contraction of each bond. The crossing between the generalised CH vibrational modes can now be calculated from the intersection of their Morse curves

$$D_{e,\text{CH}} \{1 - \exp[-\beta(l - l_{\text{eq,CH}})]\}^2 = D_{e,\text{CH}} \{1 - \exp[-\beta(l - (l_{\text{eq,CH}} - R))]\}^2 + E_{S1} \quad (16.74)$$

knowing the excitation energy and the CH Morse curve parameters of Appendix III, Parameters Employed in ISM Calculations. The width of the barrier is given by the displacement of the ground-state curve at the energy of S_1 . The reaction frequency, for a fully allowed process ($\chi = 1$) is just that of the CH frequency, $\nu = 9.0 \times 10^{13} \text{ sec}^{-1}$. However, there is one final detail before the internal conversion rates of aromatic hydrocarbons can be calculated: the Morse curve must be adapted to describe the generalised mode.

It has long been recognised that the role played by CH stretching vibrations in radiationless transitions of aromatic molecules is better described in terms of local rather than normal modes of vibration [18]. The concept of a normal mode arises from the analysis of vibrational motions for infinitesimal amplitudes. However, reactivity is most often associated with large vibrational amplitudes. The concept of local modes derives from an analysis of vibrational motion for such large amplitudes. For higher energies, the molecules oscillate according to a pattern that is closer to a local mode than a normal mode. The vibrational energy of polyatomic molecules is evenly distributed among a number of equivalent chemical bonds and the bond-dissociation energy is much greater than the dissociation energy of one of these bonds. Henry and Siebrand showed that the stretching overtone spectrum of benzene is accurately reproduced assuming that the six local CH bonds of benzene vibrate independently [19]. Additionally, Formosinho showed that in the treatment of local modes as independent oscillators, the generalised CH vibration is expressed by a force constant $f_{\text{CH}}/(n_{\text{H}})$ [20], as shown in eq. (8.29) and Figure 8.8. Given the relation between the force constant and the Morse parameter, $f = 2D_e\beta^2$, the generalised CH bond-dissociation energy can be written

$$D_{e,\text{CH}} = \sqrt{n_{\text{H}} D_e} \quad (16.75)$$

**FIGURE 16.14**

Calculated (crosses and plus signs) and experimental (open symbols) internal conversion rates in benzene, naphthalene, phenanthrene, anthracene, pyrene, coronene, tetracene and azulene. The calculated inter-system crossing rates from T_1 to S_0 were multiplied by $\chi = 10^{-6}$.

where D_e is the bond-dissociation energy of a CH bond, given in [Appendix III, Parameters Employed in ISM Calculations](#). With the Morse parameters for the CH bond of benzene, its singlet-state energy and $\Delta R = 0.025 \text{ \AA}$, the intersection of the curves in [eq. \(16.74\)](#) occurs at $D - E_v = 2.63 \times 10^3 \text{ kJ mol}^{-1}$. The width of the barrier at $E_{S1} = 459 \text{ kJ mol}^{-1}$ is $\Delta x = 0.247 \text{ \AA}$ and the Franck–Condon factor for [eq. \(16.72\)](#) is 3×10^{-11} . Assuming a fully allowed transition, $\chi\nu = 9.0 \times 10^{13} \text{ sec}^{-1}$, the calculated internal conversion rate is $3 \times 10^3 \text{ sec}^{-1}$. The contribution of tunnelling in the repulsive side is lower than the experimental value, $4 \times 10^4 \text{ sec}^{-1}$ [21], because the internal conversion in benzene has an equally important contribution from the attractive side. This is not seen for the other aromatic hydrocarbons represented in [Figure 16.14](#), because of their higher $D_{e,\text{CH}}$ values and lower excited state energy. [Figure 16.14](#) also shows the results obtained with similar calculations for the internal conversions from S_2 to S_1 states and inter-system crossing from T_1 to S_0 [16a]. The displacements between these curves are expected to be smaller than that between S_1 and S_0 . Consequently $\Delta R = 0.015 \text{ \AA}$ was employed. The inter-system crossing rate was calculated with the non-adiabatic factor suggested by Kasha ($\chi = 10^{-6}$). However, the calculations show that the nonadiabaticity is even stronger, $\chi < 10^{-6}$.

Internal conversion and inter-system crossing rates exhibit a free-energy dependence that is remarkably different from those of the reactions discussed in the previous chapters. As the exothermicity of the internal conversion increases, its rate becomes smaller. This is known as the *energy-gap law* of radiationless transitions [22]. [Appendix VI, Quantum-Mechanical Radiationless Transition Theory](#), presents the formal demonstration on the energy gap law

$$FCWD = \frac{1}{\hbar\omega} \exp\left(-\frac{\Delta E}{\hbar\omega_M}\gamma\right) \quad (16.76)$$

16.6 Triplet energy (or electron) transfer between molecules

Whereas in internal conversions and inter-system crossings only one molecule is involved, in energy (or electron) transfers one species donates energy (or an electron) while another accepts it. Each of these species must be represented by curves such as those of [Figure 16.7](#), describing its initial and final electronic states. For simplicity, the discussion below addresses directly the case of a triplet energy transfer through the Dexter mechanism, but the same reasoning also applies to electron transfers.

The transfer of energy is subject to the restrictions of the Franck–Condon principle (a vertical transition, where the nuclei remain in their initial positions as the electron is transferred) and to the conservation of energy (the energy decrease in one molecule is identical to the simultaneous energy increase in the other one). [Figure 16.15a](#) shows that for two identical molecules, which necessarily have the same triplet energy, these conditions are only met for a small fraction of the donor and acceptor molecules. This was also illustrated by the experimental data for anthracene in [Figure 16.12](#). As the triplet energy of the acceptor decreases, and the triplet energy transfer becomes more exothermic, there is a better overlap

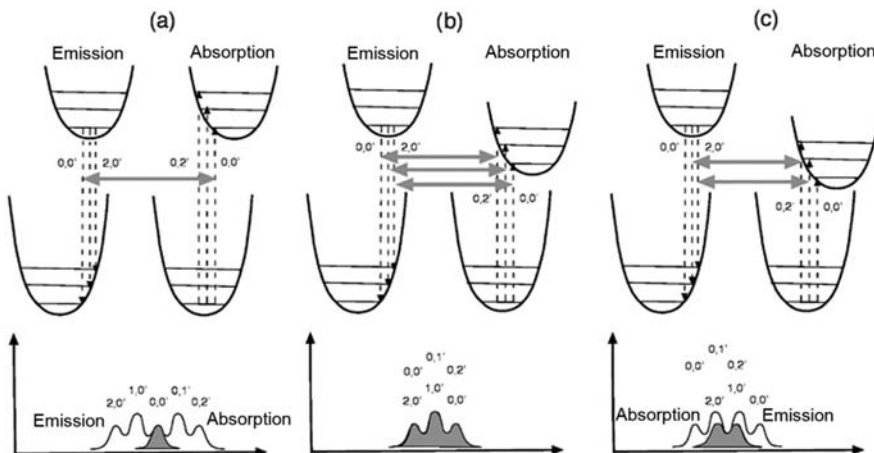


FIGURE 16.15

Correspondence between the transfer of energy from an electronically excited donor to an acceptor in its ground state (upper diagrams) and the corresponding emission and absorption spectra. Only the coupled transitions identified in the upper diagrams conserve energy and may occur. (a) Transfer between identical molecules. (b) Exothermic transfer that maximises the spectral overlap. (c) Very exothermic transfer, beyond the optimal spectral overlap.

between the donor emission and the acceptor absorption spectra. This overlap goes through a maximum, shown in Figure 16.15b, and then decreases for even more exothermic reactions, Figure 16.15c. This latter situation is similar to that of the energy gap law.

The simplest way to calculate the transfer rate from the initial state s to the final state k is to use the classical expression for the transfer rate at a given energy E such that $E > \Delta E^\ddagger$, where ΔE^\ddagger is the energy of the crossing point between the two states. Such an expression is the product between the probability of conversion at the crossing point (P_{ks}) and the frequency of passage over the crossing point

$$w(E) = 2\nu P_{ks} \quad (16.77)$$

There is a factor of 2 in this expression because the energetic condition $E > \Delta E^\ddagger$ requires that the turning point of the vibration exceeds the distortion to attain the crossing point, $|x_v| > |x^\ddagger|$, such that the conversion between the two states is attempted twice during each vibrational motion.

The classical probability of transition probability was first formulated by Landau and Zener [23], and was presented in eq. (5.55). Using the notation of this chapter

$$P_{ks} = \frac{2\pi}{\hbar} |V_{ks}^e|^2 \frac{1}{r|s_s - s_k|} \quad (16.78)$$

where $r = dx/dt$ is the velocity of passage over the crossing point at x^\ddagger , and s_s and s_k are the slopes of the potential energy curves describing the initial and final states at that point, $dV(x^\ddagger)/dx$, respectively. For the specific case of electronic states represented by unidimensional harmonic oscillators with the same force constant f , the difference between the slopes is

$$|s_s - s_k| = \left| \frac{d}{dx} \left(\frac{1}{2}fx^2 \right) - \frac{d}{dx} \left[\frac{1}{2}f(d-x)^2 - \Delta E^0 \right] \right| = fd \quad (16.79)$$

The velocity of the vibrational motion of this oscillator is defined as the length travelled per unit time. Given the classical amplitude of the oscillation with an energy E

$$x_v = \sqrt{\frac{2E}{\mu\omega^2}} \quad (16.80)$$

the velocity of passage over x^\ddagger is

$$r = \omega \sqrt{(x_v)^2 - (x^\ddagger)^2} \quad (16.81)$$

Rearranging the above expressions leads to the expression for the rate of transfer at an energy $E > \Delta E^\ddagger$

$$w(E) = \frac{2}{\hbar} |V_{ks}|^2 \frac{1}{\sqrt{fd^2} \sqrt{f[(x_v)^2 - (x^\ddagger)^2]}} \quad (16.82)$$

The actual classical transfer rate at a given temperature T , requires averaging over a Boltzmann distribution of energies

$$w = \frac{\int_{E^\ddagger}^{\infty} w(E) e^{-E/k_B T} dE}{\int_0^{\infty} e^{-E/k_B T} dE} \quad (16.83)$$

This procedure yields a compact result because

$$\int_0^{\infty} e^{-E/k_B T} dE = k_B T \quad (16.84)$$

and eq. (16.80) can be used with eq. (16.67) to express the other integral as

$$\int_{\Delta E^\ddagger}^{\infty} (E - \Delta E^\ddagger)^{-1/2} e^{-E/k_B T} dE = \sqrt{\pi k_B T} e^{-\Delta E^\ddagger/k_B T} \quad (16.85)$$

The resulting expression

$$w = \frac{2\pi}{\hbar} |V_{ks}|^2 \frac{1}{\sqrt{2\pi f d^2 k_B T}} \exp\left(-\frac{\Delta E^\ddagger}{k_B T}\right) \quad (16.86)$$

can be further modified using the quadratic relation between energy barriers and reaction energies, discussed in Chapter 7, Relationships between Structure and Reactivity, eq. (7.6),

$$(\Delta E^0 - \lambda)^2 = 4\lambda\Delta E^\ddagger \quad (16.87)$$

and associating the reorganisation energy with the displacement between the curves representing the electronic states, Figure 16.8,

$$\lambda = \frac{1}{2} f d^2 \quad (16.88)$$

The final expression for the *classical rate for triplet-triplet (or electron) transfer*,

$$w = \frac{2\pi}{\hbar} |V_{ks}^e|^2 \frac{1}{\sqrt{4\pi\lambda k_B T}} \exp\left[-\frac{(\Delta E^0 - \lambda)^2}{4\lambda k_B T}\right] \quad (16.89)$$

must be regarded with the caution which follows from the numerous approximations involved in its derivation. Firstly, the problem of energy transfer between molecules is multi-dimensional, whereas the in deriving the above expression only one effective frequency was used. Secondly, the Landau–Zener probability is only valid when $|V_{ks}^e| < \sqrt{1/2\mu r^2}$, that is for an electronic coupling of 5 kJ mol^{-1} the reorganisation energy must exceed 20 kJ mol^{-1} , which involves a difficult balance between having enough adiabaticity and at the same time a transfer rate which is competitive with the radiative lifetime. Thirdly, the quadratic relation between energy barriers and reaction energies must be obeyed. Finally, the classical model assumes that the electronic states cross at a given energy, used to define the activation energy ΔE^\ddagger , but in fact there are two molecules (and four electronic states) in the reactants, and as many in the products. The crossing point is not rigorously defined and is replaced by the reorganisation energy defined in eq. (16.88), where

it is assumed that all the electronic states have the same frequency ω . However, the value of λ is not calculated from the energy of the crossing point but from the displacement of the electronic states in each species, [Figure 16.8](#). A derivation of [eq. \(16.89\)](#) as the high-temperature limit of a quantum-mechanical treatment of the transition rate is presented in [Appendix VI](#), Quantum-Mechanical Radiationless Transitions Theory.

A more fundamental approach to the problem of energy transfer can be made by writing the classical probability distribution for the donor in the excited state that takes the form at R

$$\nu(R) = \left(\frac{f}{2\pi k_B T} \right)^{1/2} \exp\left(-\frac{f(R-R_e)^2}{2k_B T} \right) \quad (16.90)$$

This has a clear analogy with the wavefunction of the harmonic oscillator at its ground vibrational state, [eq. \(16.59\)](#). The energy transfer involves a vertical transition between the two energy curves of the donor. Given $\nu(R)$, the distribution of energies associated with the donor, $\iota(\varepsilon')$, which represents the energies required to transfer the triplet energy from the donor, is

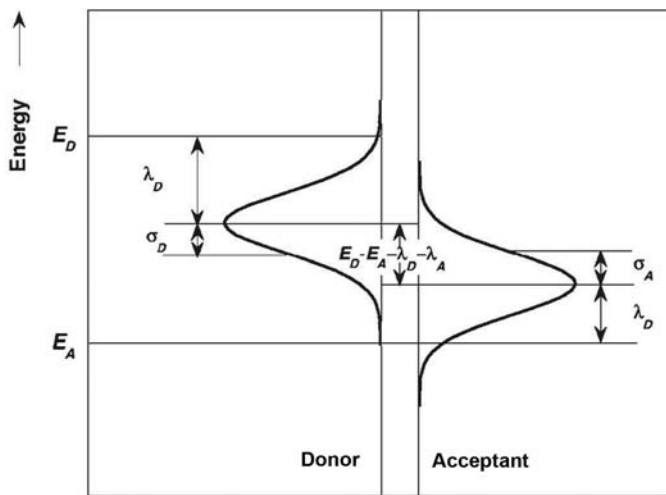
$$\iota(\varepsilon') = \frac{1}{\sqrt{2\pi\sigma_D^2}} \exp\left[-\frac{(\varepsilon' + E_D - \lambda_D)^2}{2\sigma_D^2} \right] \quad (16.91)$$

where E_D is the triplet energy of the donor, $\sigma_D^2 = k_B T/f$ is the square of the standard deviation of the respective Gaussian distribution, and λ_D is the difference between the energy of the triplet state in its equilibrium geometry and the energy it would have in that state at the equilibrium configuration of the ground state, [eq. \(16.88\)](#). The centre of the Gaussian distribution is placed at the ground-state equilibrium configuration of the donor, with an energy $E_D - \lambda_D$ which is lower than its triplet energy, [Figure 16.16 \[24\]](#). This displacement is related to the difference between the nuclear configuration of the initial triplet state and the final ground state of the donor. This energy difference, λ_D , is the reorganisation energy of the donor. A similar spectrum can be formulated for the ground-state acceptor,

$$\alpha(\varepsilon) = \frac{1}{\sqrt{2\pi\sigma_A^2}} \exp\left[-\frac{(\varepsilon + E_A + \lambda_A)^2}{2\sigma_A^2} \right] \quad (16.92)$$

where E_A is the triplet energy of the acceptor and λ_A its reorganisation energy.

Mathematically, the possibility that the energy taken from the donor is between ε' and $\varepsilon' + d\varepsilon'$, is $\iota(\varepsilon')d\varepsilon'$, and the possibility that the energy given to the acceptor is between ε and $\varepsilon + d\varepsilon$, is $\alpha(\varepsilon)d\varepsilon$. To conserve energy in the process, the transfer from a particular energy ε' in the donor distribution $\iota(\varepsilon')$ must be paired with the transfer in the acceptor distribution $\alpha(\varepsilon)$ of the same energy. In [Figure 16.16](#) this corresponds to a horizontal process. The probability of transition with ε' between ε' and $\varepsilon' + d\varepsilon'$ and ε between ε and $\varepsilon + d\varepsilon$, is $\iota(\varepsilon')d\varepsilon'\alpha(\varepsilon)d\varepsilon$, with $\varepsilon' = \varepsilon$. The density of states in [eq. \(16.36\)](#) is this probability per unit of

**FIGURE 16.16**

Probability distribution of energies required for triplet energy transfer from a donor to an acceptor. Conservation of energy requires that the transfer is a horizontal process in this diagram, and the nuclear coordinates must pre-organise accordingly.

energy. Thus dividing the probability of transition by one of the energy intervals, and integrating over the other one, gives the total density of states

$$J = \int_{-\infty}^{+\infty} \iota(\varepsilon) \alpha(\varepsilon) d\varepsilon = \frac{1}{2\pi\sigma_D^2\sigma_A^2} \int_{-\infty}^{+\infty} \exp\left[-\frac{(\varepsilon+E_D-\lambda_D)^2}{2\sigma_D^2} - \frac{(\varepsilon+E_A+\lambda_A)^2}{2\sigma_A^2}\right] d\varepsilon \quad (16.93)$$

If we make the substitution

$$\begin{aligned} a &= -\lambda_A - E_A \\ d &= \lambda_D - E_D \end{aligned} \quad (16.94)$$

the exponential term can be rewritten

$$\exp\left\{-\frac{[\varepsilon-a]^2}{2\sigma_A^2} - \frac{[\varepsilon-d]^2}{2\sigma_D^2}\right\} = \exp\left[\frac{\sigma_A^2 a + \sigma_D^2 d}{\sigma_A^2 \sigma_D^2} \varepsilon - \frac{\sigma_A^2 + \sigma_D^2}{2\sigma_A^2 \sigma_D^2} \varepsilon^2\right] \exp\left(-\frac{\sigma_A^2 a^2 + \sigma_D^2 d^2}{2\sigma_A^2 \sigma_D^2}\right) \quad (16.95)$$

to indicate the presence of the standard integral

$$\int_{-\infty}^{+\infty} e^{c_1 x - c_2 x^2} dx = \sqrt{\pi/c_2} \exp\left[\frac{c_1^2}{4c_2}\right] \quad (16.96)$$

and express the overlap integral in a more compact form

$$J = \int_{-\infty}^{+\infty} \iota(\varepsilon) \alpha(\varepsilon) d\varepsilon = \frac{1}{\sqrt{4\sigma^2\pi}} \exp\left\{-\frac{[\Delta E^0 - \lambda]^2}{4\sigma^2}\right\} \quad (16.97)$$

where $\sigma^2 = (\sigma_D^2 + \sigma_A^2)/2$, $\lambda = \lambda_D + \lambda_A$, and reaction energy is the difference between the triplet energies of donor and acceptor $\Delta E^0 = E_D - E_A$.

Introducing this Franck–Condon weighted density of states in the Golden Rule, gives

$$w = \frac{2\pi}{\hbar} |V_{ks}^e|^2 \frac{1}{\sqrt{4\sigma^2\pi}} \exp\left[-\frac{(\Delta E^0 - \lambda)^2}{4\sigma^2}\right] \quad (16.98)$$

This expression for the Golden Rule is identical to the classical expression, eq. (16.89), when $\sigma^2 = \lambda k_B T$. However, it was initially formulated as $\sigma^2 = k_B T/f$. This difference can be solved with the transformation

$$\sigma^2 = \frac{\hbar\omega}{2f} \coth\left(\frac{\hbar\omega}{2k_B T}\right) \quad (16.99)$$

which approaches $\lambda k_B T$ at high temperatures ($k_B T \gg \hbar\omega/2$) and $k_B T/f$ at low temperatures ($k_B T \ll \hbar\omega/2$). In view of this connection between a classical behaviour at high temperatures and the temperature independence at low temperatures, eq. (16.98) is a *semi-classical rate for triplet-triplet energy (or electron) transfer* [25]. This formulation takes the reorganisation energy of the donor as the difference in its energy when in the triplet state but having the same geometry as the ground state. This is the Stokes shift between the maxima of the emission and absorption envelopes of the donor, without specific consideration of the vibronic bands. The same applies to the acceptor. Hence this reorganisation energy includes both vibrational and solvent contributions to the Stokes shift.

The semi-classical rate is a significant improvement in the definition of the reaction coordinate for triplet energy transfer. It relates the reorganisation energy of each reactant to the displacement of the corresponding initial and final states along the reaction coordinate, without having to assume the presence of a crossing between the reactive states. It is also less restrictive on the size of the electronic coupling. However, the connection between high and low temperatures was introduced in an *ad hoc* fashion, and does not recognise that vibronic transitions change the overlap substantially. Further improvement in the treatment of the quantum effects can be achieved with a quantum-mechanical formulation.

The full quantum-mechanical treatment of radiationless transitions is rather sophisticated. Appendix VI, Quantum-Mechanical Radiationless Transition Theory presents a detailed quantum-mechanical description of a system where, for the purpose of obtaining closed-form expressions, the vibrational modes were segregated in two categories, namely low-frequency medium modes representing the lattice/solvent and high-frequency molecular modes representing intramolecular vibrations. It is convenient to use the classical approximation to describe the low-frequency modes when their frequencies are $\hbar\omega_s \ll k_B T$. For example, $\bar{\nu} < 10 \text{ cm}^{-1}$ corresponds to a spacing $< 0.1 \text{ kJ mol}^{-1}$ between the vibrational levels, which is much less than the thermal energy at room temperature, $RT = 2.5 \text{ kJ mol}^{-1}$. For such low frequencies, the classical treatment is

accurate. When only one intra-molecular vibrational mode is used for the donor, ω_D , and another one for the acceptor, ω_A , and the low frequencies are treated as classical modes, the Franck–Condon factor for triplet energy transfer can be obtained combining the description of the vibrational levels done by eqs. (16.68) and (16.69), with the reorganisation energies included in eqs. (16.91) and (16.92). Integrating as in eq. (16.93), gives

$$J_{v',v} = \frac{1}{\sqrt{4\pi\sigma^2}} \sum_{v=0}^{\infty} \sum_{v'=0}^{\infty} e^{-S_D} e^{-S_A} \frac{S_D^{v'} S_A^v}{v'! v!} \exp\left[-\frac{(\Delta E^0 - \lambda + v'\hbar\omega_D + v\hbar\omega_A)^2}{4\sigma^2}\right] \quad (16.100)$$

where

$$\sigma^2 = \frac{\sigma_D^2 + \sigma_A^2}{2} = (\lambda_D + \lambda_A)k_B T = \lambda k_B T \quad (16.101)$$

as a consequence of the approximation made for the low-frequency modes. The overlap integral $J_{v',v}$ is also known as the Franck–Condon weighted density of states. The corresponding triplet energy transfer rate is

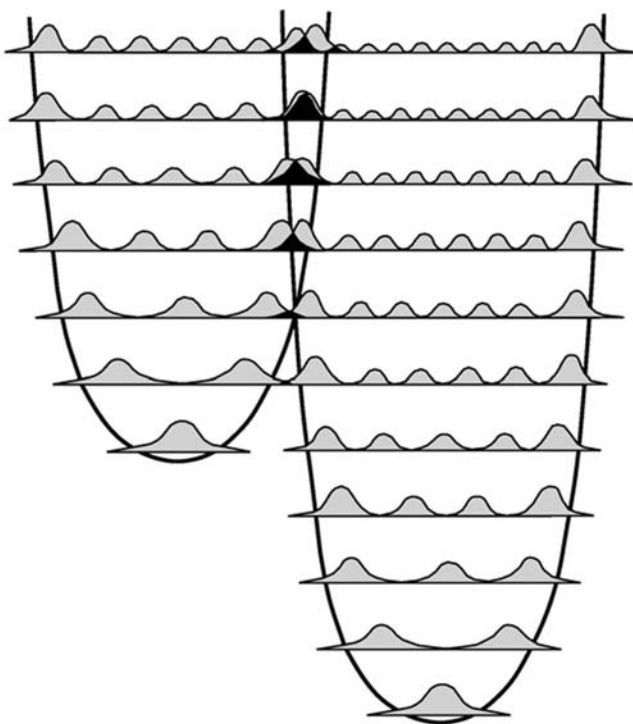
$$w = \frac{2\pi}{\hbar} |V_{ks}^e|^2 \frac{1}{\sqrt{4\pi\sigma^2}} \sum_{v=0}^{\infty} \sum_{v'=0}^{\infty} e^{-S_D} e^{-S_A} \frac{S_D^{v'} S_A^v}{v'! v!} \exp\left[-\frac{(\Delta E^0 - \lambda + v'\hbar\omega_D + v\hbar\omega_A)^2}{4\sigma^2}\right] \quad (16.102)$$

Setting $\omega_D = \omega = \omega_A$, $\sigma_D = \sigma = \sigma_A$ and $S = S_D + S_A$ gives, after some algebraic manipulations, the result is

$$w = \frac{2\pi}{\hbar} |V_{ks}^e|^2 \frac{1}{\sqrt{4\pi\lambda k_B T}} \sum_{v=0}^{\infty} e^{-S} \frac{S^v}{v!} \exp\left[-\frac{(\Delta E^0 - \lambda + v\hbar\omega)^2}{4\lambda k_B T}\right] \quad (16.103)$$

This expression for the *quantum-mechanical rate for triplet energy (or electron) transfer* remains numerically indistinguishable from eq. (16.102) even when ω_D and ω_A differ by as much as 10% [26]. Appendix VI, Quantum-Mechanical Radiationless Transition Theory, offers a formal derivation of eq. (16.103) and discusses the approximations involved.

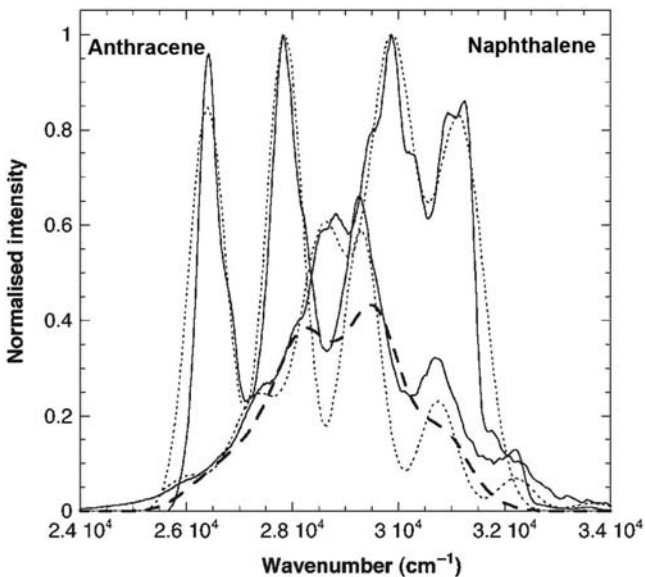
The overlap between the vibronic bands of reactants and products is illustrated in Figure 16.17 [24]. This representation is inspired by the model developed by Marcus for electron transfer [27], which will be discussed in detail in Chapter 17, Electron Transfer Reactions. The curve for the reactants represents the potential energy of the system when the donor is in the triplet state and the acceptor in the ground state. The product curve represents the system when the donor is in the ground state and the acceptor is in the triplet state. The Franck–Condon principle requires that the nuclear configuration is the same immediately after the transfer, that is, the transfer is vertical. Conservation of energy requires that the transfer is horizontal. The only possible way to meet both requirements is at the crossing point. However, the reaction coordinate should have as many dimensions as there are degrees of freedom for nuclear motion in the system, and the crossing point is, in fact, a large ensemble of nuclear configurations. Some of these are

**FIGURE 16.17**

Nuclear motion accompanying triplet energy transfers, emphasising the quantum nature of the vibrational modes. The vibrational energy levels are shown with the squares of the vibrational wavefunctions superimposed on them. The reaction coordinate represents a combination of the positions of all the nuclei disturbed by the electronic transition, as it evolves from the reactants (excited donor and ground-state acceptor) to the products (ground-state donor and excited acceptor).

represented in [Figure 16.15](#), which gives a more exact microscopic description of the energy transfer process.

The expression obtained for the quantum-mechanical rate is based on the description of the initial and final states of the electronic transition as displaced harmonic oscillators. Additionally, the derivation was based on a single vibrational mode for each reactant. It was assumed that an average vibrational frequency could describe the modes that promote the electronic transition and accept the excess energy released in the course of that transition. However, a more detailed analysis of the absorption and emission bands of the aromatic hydrocarbons, which are most amenable to simulations with displaced harmonic oscillators, reveals that even these systems have “shoulders” in the main progression bands, which are probably associated with other vibrational modes. [Figure 16.18](#)

**FIGURE 16.18**

Normalised fluorescence of naphthalene ($E_S = 31,150 \text{ cm}^{-1}$) and absorption of anthracene ($E_S = 26,400 \text{ cm}^{-1}$), modelled by two vibrational modes. Naphthalene: $\bar{\nu}_D = 1420 \text{ cm}^{-1}$, $\sigma_D = 150 \text{ cm}^{-1}$, $S_D = 0.82$, and $\bar{\nu}_D = 500 \text{ cm}^{-1}$, $\sigma_D = 150 \text{ cm}^{-1}$, $S_D = 0.50$. Anthracene: $\bar{\nu}_A = 1450 \text{ cm}^{-1}$, $\sigma_A = 150 \text{ cm}^{-1}$, $S_A = 0.70$, and $\bar{\nu}_A = 400 \text{ cm}^{-1}$, $\sigma_{DA} = 150 \text{ cm}^{-1}$, $S_{DA} = 0.50$). Solid lines: experimental spectra; dotted lines: simulated spectra; dashed line: calculated spectral overlap.

shows the overlap between the fluorescence of naphthalene and the absorption of anthracene modelled with high-frequency progression band discussed above and a subsidiary medium-frequency band, probably associated with CCC bending vibrations.

Multi-mode processes can be treated as single-mode employing the average-mode approximation [26,28]. S is taken as the sum of the S_j values for the coupled high and medium frequency vibrations

$$S = \sum_j S_j \quad (16.104)$$

and $\hbar\omega$ as the weighted average of the quantum spacing

$$\hbar\omega = \frac{\sum_j S_j \hbar\omega_j}{\sum_j S_j} \quad (16.105)$$

The average-mode approximation combines the vibrational progressions needed for a better simulation of absorption and emission spectra. Unfortunately, for triplet energy (and electron) transfers the relevant singlet–triplet absorption

and phosphorescence (or charge-transfer bands) are rarely available for such simulations. It should also be noted that bimolecular transfer rates tend to be controlled by diffusion when the overlap is large, and that for small overlaps minor errors in the simulation of the spectra lead to large errors in $J_{v,v}$. Moreover, when the reaction energies exceed 60 kJ mol⁻¹, the higher frequency modes, such as the CH stretching vibrations become better energy acceptors than the CC modes, and the information carried by the absorption and fluorescence spectra is of little use. Finally, very exothermic reactions result in the population of highly excited vibrational levels, as illustrated in Figure 16.15, and these are strongly anharmonic. The participation of additional accepting modes in the reaction coordinate, the increased anharmonicity of the accepting modes as the reactions become more exothermic and the change in entropy of reaction, make it very challenging to use eq. (16.103) without adjustable parameters. Moreover, the relevance of some of accepting modes may change with the reaction energy, making the reorganisation energy dependent of the reaction energy.

The observation of large deuterium isotope effects is a good diagnostic for the participation of CH, or other bonds to hydrogen, in the reaction coordinate for energy or electron transfer. The paradigmatic example is the quenching of O₂(¹Δ_g) in solution. The bimolecular rate constant of radiationless deactivation of singlet oxygen drops from 4.3×10^3 M⁻¹ sec⁻¹ in H₂O to 2.6×10^2 M⁻¹ sec⁻¹ in D₂O, a KIE of 16.5. The rate is further reduced to 0.75 M⁻¹ sec⁻¹ in perfluorodecalin, a solvent without carbon-hydrogen bonds. This spectacular effect is due to the deactivation by coupled vibronic O₂(¹Δ_g, v' = 0 → v' = m) and vibrational X–H(v = 0 → v = n) transitions [29]. Charge recombinations between aromatic hydrocarbons and tetracyanoethylene have much smaller KIE, usually not exceeding a factor of two, with the particularity that the deuteration of methyl hydrogens in methylated benzene donors gives a larger KIE than deuteration of phenyl hydrogens [30].

Absorption and fluorescence are usually registered using a continuous irradiation of the sample, that is, in steady-state conditions. It is also possible to measure both absorption and fluorescence intensities at different wavelengths as a function of time. Ware and co-workers followed the fluorescence spectra after excitation on the nanosecond time scale, and observed a red shift of the fluorescence maxima as a function of time [31]. Ultra-fast techniques have more recently been employed to measure the time-dependence of absorption and fluorescence spectra, and confirmed the generality of this phenomenon for charge-transfer transitions in condensed phases, known as the “dynamic Stokes shift”.

The time evolution of the fluorescence spectrum of a suitable probe molecule, following excitation by an ultra-short optical pulse, can be used to monitor the dynamic Stokes shift response function

$$S(t) = \frac{\bar{\nu}(t) - \bar{\nu}(\infty)}{\bar{\nu}(0) - \bar{\nu}(\infty)} \quad (16.106)$$

where $\overline{v}(x)$ represents the peak of the fluorescence spectrum at times t , zero and infinity. Expressed in this way, the frequencies need not be referenced to their (usually unknown) gas phase values. This function carries information on the polar solvation dynamics. The fastest processes occur on the tens of femtoseconds time scale and correspond to the intra-molecular relaxation of high-frequency modes from the vertically excited Franck–Condon state towards a relaxed configuration, the so-called inertial response. Subsequently, in the time scale from a few hundreds of femtoseconds to nanoseconds, collective motion with diffusive character develops. Hence in the scale of hundreds of femtoseconds and extending to a few hundreds of picoseconds, there is a continuous shift of the fluorescence spectrum to the red as solvent relaxation proceeds. Solvation is nonexponential in time, and cannot be interpreted with only one time constant. This is in conflict with the description of the dielectric constant of polar solvents by the frequency dependence of the Debye dispersion [32]

$$\varepsilon(\omega) = \varepsilon_{\text{op}} + \frac{\varepsilon - \varepsilon_{\text{op}}}{1 - i\omega\tau_D} \quad (16.107)$$

where ε and $\varepsilon_{\text{op}} (=n_D^2)$ are the static and optical (infinite) frequency dielectric constants and τ_D is the Debye relaxation time. This simple model of a polar solvent as a dielectric continuum predicts a single exponential shift of the fluorescence spectrum with a time constant approximately equal to the solvent longitudinal relaxation time $\tau_L = (\varepsilon_{\text{op}}/\varepsilon)\tau_D$, whereas the dynamic Stokes shifts reveal several time constants, some of them much shorter than τ_L . Water is a particularly “fast” solvent, with more than 50% of the solvation response happening within the first 50 fsec [33], which corresponds roughly to 660 cm^{-1} in frequency. This should be compared with $\tau_D = 8.2\text{ psec}$, $\varepsilon_{\text{op}} = 4.21$, $\varepsilon = 78.3$, and $\tau_L = 440\text{ fsec}$ for water. The ultra-fast relaxation of water was assigned to the librational (rotational) motions of the water molecule. It has a particular incidence on preventing the re-crossing of the reaction free-energy barrier, because it shows that water can stabilise the reaction products before they may re-cross to the reactants that would reduce the reaction rate. However, the description of the full range of $S(t)$ requires additional frequencies. In water, some of these frequencies are associated with the hindered translation of the hydrogen-bonded network (180 cm^{-1}), the hydrogen-bonding bend (60 cm^{-1}), and the diffusive motions ($2\text{--}10\text{ cm}^{-1}$). In fact, the entire dielectric dispersion spectrum of $\varepsilon(\omega)$ must be considered in the simulation of $S(t)$, including the low-frequency part, which is well described by the Debye formula, and the high-frequency part, which contains various contributions from inter- and intra-molecular vibrational modes of the solvent. Fleming and co-workers employed seven frequencies in the range indicated above, to reproduce the dynamic Stokes shift that they observed in water [34].

The subsequent processes take place from the lowest vibrational level of the first singlet state and have already been discussed. One additional point to take into consideration is that internal conversion leaves the ground state with an excess of heat, which may correspond to temperatures in excess of 1000 K. Its

cooling occurs within 1–10 psec, with the shorter times associated with polar molecules in polar environments [35].

Another experimental method to probe the Franck–Condon excited state is resonance Raman spectroscopy. Recall that Raman scattering is an inelastic process entailing a transition to a virtual or real molecular state (or sum of states), and a nominally instantaneous return to the ground state, but in a higher or lower vibrational state. In resonance Raman, the incident radiation nearly coincides with the frequency of the electronic transition of the sample. Only a few vibrational modes contribute to the scattering of the radiation, which simplifies the Raman spectrum and enhances its intensity. The modes that show resonance Raman activity are the same as those that are Franck–Condon active in the electronic transition, and their degree of enhancement is related to their displacement upon formation of the excited state. Consequently the analysis of vibrational Raman lines obtained in resonance with charge-transfer transitions can, in principle, reveal the complete set of mode-specific reorganisation energies associated with the charge separation or recombination attending the electronic transition [36]. This technique has been applied to many charge transfers, in particular in transition metal complexes and in organic donor–acceptor complexes. A widely used transition-metal complex that has been studied using resonance Raman is the $\text{Ru}(\text{bpy})_3^{2+}$ complex in water. Fourteen totally symmetric vibrational modes were found to be active in the metal-to-ligand charge transfer, with frequencies ranging from 283 to 1608 cm^{-1} . The total reorganisation energy was divided among these modes, including metal–ligand stretching and bending modes, and ligand (bipyridine) localised modes. The hexamethylbenzene-tetracyanoethylene (HMB/TCNE) complex is a typical example of organic donor–acceptor complexes studied by resonance Raman. There are some differences in reported results between the several groups that have studied this system, but more than 10 vibrational modes are associated with the electronic transition [30,37]. The high-frequency modes seem to be most populated, but the very low-frequency donor–acceptor mode at 165 cm^{-1} is also strongly populated. The contribution of the solvent and of each vibrational mode to the total reorganisation energy λ remains unsettled. In CCl_4 , where the contribution of the solvent to the reorganisation energy should be very small, λ values between 45 and 56 kJ mol^{-1} were proposed [30,37a]. These values of λ do not include the contributions from CH bonds that are necessary to explain the KIE mentioned above but could not be assessed from the resonance Raman spectra.

The picture emerging from ultra-fast techniques and resonance Raman is that a large spectrum of solvent frequencies, extending to 1000 cm^{-1} in water, and a large number of vibrational frequencies, down to 165 cm^{-1} in donor–acceptor complexes, contribute to the energy barrier of electron and triplet energy transfers in solution. A detailed description of these transfers requires the quantum treatment of a very large number of vibrational modes and a wide dielectric dispersion spectrum for the solvent. Jortner presented a multi-mode formalism and compared its results for the HMB/TCNE complex using nine modes, with the average-mode approximation and with a model using a high single-mode with the same reorganisation

energy as the multimode [38]. The average-mode approximation underestimates the Franck–Condon factor when the reaction exothermicity exceeds 85 kJ mol^{-1} . On the other hand, a high-frequency single mode combined with the correct reorganisation energy gives a good account of the Franck–Condon factors. The lesson to be learnt is that an incomplete model that is good enough to reproduce the relevant absorption and emission spectra, is can also be used to calculate the Franck–Condon factors but may require the fitting of some of its parameters to compensate for the missing information. The calculation of the electron or triplet energy transfer rates additionally requires an estimate of the electronic coupling.

16.7 Electronic coupling

The factor $(4\sigma^2\pi)^{-1/2}$ included in eq. (16.102) is associated with the coupling between electronic and nuclear motions. Consequently it cannot be exclusively assigned to the nuclear or to the electronic factor. This factor has the units of $(\text{energy})^{-1}$ and, when associated with $|V_{ks}^e|^2$ and with $2\pi/\hbar$, gives the electronic factor in units of sec^{-1} , that is, as a frequency.

In order to relate the electronic coupling to molecular parameters, it is necessary to return to eq. (16.37) and express the wavefunction of the ground (Ψ_1) and excited (Ψ_2) states in terms of the wavefunctions of the initial and final unperturbed states, ψ_s and ψ_k , respectively. The resolution of this simple two-state problem captures the physics of the electronic coupling. The interaction between the unperturbed wavefunctions is expressed as two linear combinations of ψ_s and ψ_k , corresponding to the ground and excited states Ψ_1 and Ψ_2 , of energies E_1 and E_2 , where $E_1 < E_2$,

$$\begin{aligned}\Psi_1 &= c_s\psi_s + c_k\psi_k \\ \Psi_2 &= c_s\psi_s - c_k\psi_k\end{aligned}\quad (16.108)$$

The coefficients of the linear combinations are normalised ($c_s^2 + c_k^2 = 1$). When the overlap integral is zero ($S_{ks} = \langle \psi_k | \psi_s \rangle = 0$), the energies of the adiabatic states are given by the secular determinant

$$\begin{vmatrix} V_{ss} - E & V_{ks} \\ V_{ks} & V_{kk} - E \end{vmatrix} = 0 \quad (16.109)$$

where V_{ss} and V_{kk} are the energies of the initial and final unperturbed states, and the V_{ks}^e is electronic matrix element coupling the two nonadiabatic states. The roots of this determinant are

$$\begin{aligned}E_1 &= \frac{V_{ss} + V_{kk}}{2} - \frac{[\Delta_{ks}^2 + 4(V_{ks}^e)^2]^{1/2}}{2} \\ E_2 &= \frac{V_{ss} + V_{kk}}{2} + \frac{[\Delta_{ks}^2 + 4(V_{ks}^e)^2]^{1/2}}{2}\end{aligned}\quad (16.110)$$

where $\Delta_{ks} = (V_{kk} - V_{ss}) \geq 0$. The difference between adiabatic and nonadiabatic energies is

$$(E_2 - E_1)^2 = \Delta_{ks}^2 + 4(V_{ks}^e)^2 \quad (16.111)$$

Knowing the adiabatic energies E_1 and E_2 , the coefficients c_s and c_k can be calculated from the equations

$$\begin{aligned} \begin{pmatrix} V_{ss} - E_1 & V_{ks}^e \\ V_{ks}^e & V_{kk} - E_1 \end{pmatrix} \begin{pmatrix} c_s \\ c_k \end{pmatrix} &= 0 \\ \begin{pmatrix} V_{ss} - E_2 & V_{ks}^e \\ V_{ks}^e & V_{kk} - E_2 \end{pmatrix} \begin{pmatrix} -c_k \\ c_s \end{pmatrix} &= 0 \end{aligned} \quad (16.112)$$

These equations give, following the convention that $E_2 \geq E_1$,

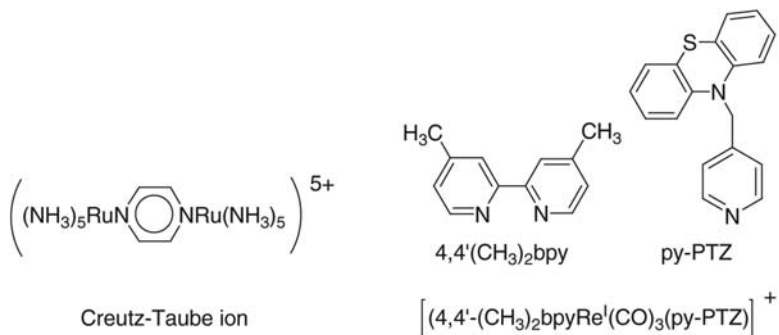
$$\begin{aligned} E_1 &= V_{ss} - \left| \frac{c_k}{c_s} V_{ks}^e \right| = V_{kk} - \left| \frac{c_s}{c_k} V_{ks}^e \right| \\ E_2 &= V_{ss} + \left| \frac{c_s}{c_k} V_{ks}^e \right| = V_{kk} + \left| \frac{c_k}{c_s} V_{ks}^e \right| \end{aligned} \quad (16.113)$$

and the product between the mixing coefficients is related to the electronic coupling matrix element

$$|c_s c_k| = \frac{|V_{ks}^e|}{E_2 - E_1} \quad (16.114)$$

This is an important relation because it is possible to express the factor $|c_s c_k|$ as a function of spectroscopic parameters of charge-transfer reactions. When the degree of charge transfer approaches unity, these are effectively the electronic couplings of electron transfer reactions. The electronic couplings of electrons transfers can later be related to those of triplet energy transfers, and complete the kinetic description of such processes in terms of molecular parameters. The only approximation involved in the derivation of this relation for a two-state system, is the orthonormality of the electronic states involved ($S_{ks} = 0$).

There are two important classes of spectroscopic transitions where an electronic transition is associated with a full charge transfer within a molecule or a complex: inter-valence absorption bands and charge-transfer (exciplex with full charge transfer) emission. The most pronounced inter-valence bands are found in mixed-valence complexes and were first described by Taube, who received the Nobel prize in 1983 for his work on the mechanisms of electron transfer reactions. Mixed-valence complexes are characterised by the presence of two metal centres in different oxidation states separated by a bridging ligand. One of the earliest examples of a stable mixed-valence complex is the Creutz-Taube ion illustrated in [Figure 16.19](#). Its inter-valence band is observed at 1570 nm. [Figure 16.19](#) also shows a rhenium complex where a similar optical electron transfer occurs. In this case the inter-valence band is associated with the optical transfer of an electron from the py-PTZ ligand to the 4,4'-(CH₃)₂bpy ligand separated by ~ 6 Å. Its

**FIGURE 16.19**

Complexes that show inter-valence bands and ligand-to-ligand charge transfer absorption bands.

inter-valence band is characterised by $\bar{\nu}_{\max} = 1.99 \times 10^4 \text{ cm}^{-1}$, $\varepsilon_{\max} = 2.4 \text{ M}^{-1} \text{ cm}^{-1}$ and $\Delta\bar{\nu}_{1/2} = 3.50 \times 10^3 \text{ cm}^{-1}$ [39].

The other type of charge-transfer band is fluorescence from an exciplex, when it has a high degree of charge transfer. An exciplex is a complex formed between an electron donor and an electron acceptor, normally with one of them in the S₁ state. The fingerprint of exciplex formation is the observation of a broad and structureless emission, red-shifted relative to the emission of the molecular components of the exciplex. The stability of the exciplex comes from the mixture of pure locally excited, pure charge transfer and pure ground states

$$\Psi_{ex} = c_{le}\Psi_{le}[\text{A D}^*] + c_{ct}\Psi_{ct}[\text{A}^\bullet\text{---D}^\bullet\text{---}] + c_{gs}\Psi_{gs}[\text{A D}] \quad (16.115)$$

where c_{le} , $c_{ct} \gg c_{gs}$. A high degree of charge separation, $c_{ct} \gg c_{le}$, requires that the following conditions are met: the exciplex fluorescence is weak ($\Phi_F < 0.15$), the separation between exciplex and molecular emission ($> 5000 \text{ cm}^{-1}$) and the dipole moment of the exciplex (μ_{ex}) are large. The magnitude of μ_{ex} depends on the charge-separation distance. For example, exciplexes formed between aromatic hydrocarbons and other planar molecules typically have a separation of 3.3 Å between their planes, and for this separation, a full charge separation has $\mu_{ex} = 16 \text{ D}$. These conditions are met, for example, in the exciplex formed between excited pyrene and fumaronitrile, which is characterised by $\Phi_F = 0.10$, $\bar{\nu}_{ex} = 2.2 \times 10^4 \text{ cm}^{-1}$, $\mu_{ex} = 19 \text{ D}$, and a lifetime of 18 nsec in heptane [40].

The intensity of the absorption bands is given by eq. (16.38), and the electric dipole moment by eq. (16.37). Replacing the wavefunctions of this equation by those of eq. (16.108), yields

$$\begin{aligned} \vec{\mu}_{12} &\equiv c_s c_k (\vec{\mu}_k - \vec{\mu}_s) \\ \vec{\mu}_s &\equiv -e \langle \psi_s \sum \vec{r}_i \psi_s \rangle \\ \vec{\mu}_k &\equiv -e \langle \psi_k \sum \vec{r}_i \psi_k \rangle \end{aligned} \quad (16.116)$$

when $S_{ks} = 0$ and $\vec{\mu}_{ks} = 0$. Under this approximation and recognising that the difference between the dipole moments of the unperturbed states is

$$(\vec{\mu}_k - \vec{\mu}_s) = e\Delta r \quad (16.117)$$

where Δr is the distance separating the electron donor and acceptor moieties, eqs. (16.114) and (16.22) lead to

$$\frac{\vec{\mu}_{12}}{e} = \frac{|V_{ks}^e| \Delta r}{h\nu_{\max}} \quad (16.118)$$

The oscillator strength defined in eq. (16.38) can now be expressed as

$$f_{ks} = 1.085 \times 10^{-5} \frac{|V_{ks}^e|^2 (\Delta r)^2}{\nu_{\max}} \quad (16.119)$$

Its relation with the absorption bands was established in eq. (16.3). When the shape of such band can be described by a Gaussian curve, as is approximately the case of intra-valence bands, the integral can be obtained analytically

$$\int \varepsilon(\bar{\nu}) d\bar{\nu} = \sqrt{\frac{\pi}{4\ln(2)}} \varepsilon_{\max} \Delta\bar{\nu}_{1/2} \quad (16.120)$$

and the expression for the oscillator strength is reduced to

$$f_{ks} = 4.61 \times 10^{-9} \varepsilon_{\max} \Delta\bar{\nu}_{1/2} \quad (16.121)$$

The numerical values of the expressions above apply when ε_{\max} is expressed in $M^{-1} \text{ cm}^{-1}$, the bandwidth at half-height is expressed in cm^{-1} and Δr is in Å.

It is now possible to relate the electronic coupling with the properties of the absorption band combining eqs. (16.119) and (16.121),

$$|V_{ks}^e|^2 = \frac{4.3 \times 10^{-4} \varepsilon_{\max} \Delta\bar{\nu}_{1/2} \bar{\nu}_{\max}}{(\Delta r)^2} \quad (16.122)$$

Using the data obtained by Meyer and co-workers for the ligand-to-ligand charge transfer absorption bands of the complex represented in Figure 16.19, gives $V_{ks}^e = 45 \text{ cm}^{-1}$ ($= 0.53 \text{ kJ mol}^{-1}$). This value of the electronic coupling is within the limits required by radiationless transitions theories

Combining eq. (16.118) with eqs. (16.37) and (16.41) leads to a compact expression relating the electronic coupling to the charge transfer emission band

$$|V_{ks}^e|^2 = \frac{3h^3 c^3 k_F}{64\pi^4 \nu_{\max} (\Delta\mu)^2} \quad (16.123)$$

This expression is more useful when it explicitly includes the factors associated with the refractive index of the medium n_D , and the vacuum permittivity $(4\pi\varepsilon_0)^{-1}$,

$$|V_{ks}^e|^2 = \frac{3\varepsilon_0 h^3 c^3 k_F}{16\pi^3 n_D^3 \bar{\nu}_{\max} (\Delta\mu)^2} = 3.0 \times 10^6 \frac{k_F}{n_D^3 \bar{\nu}_{\max} (\Delta\mu)^2} \quad (16.124)$$

where the numerical value applies when the frequency of the maximum emission is expressed in cm^{-1} , the fluorescence rate is in sec^{-1} , and the change in dipole moment is in debye. Using the data for the pyrene/fumaronitrile exciplex emission in heptane ($n_D = 1.385$) mentioned earlier and using eq. (16.44) to estimate the fluorescence rate constant, gives $V_{ks}^e = 890 \text{ cm}^{-1}$ ($= 10.6 \text{ kJ mol}^{-1}$). The value of V_{ks}^e for the emission of an exciplex ($\Delta r = 3.3 \text{ \AA}$) with a nearly complete charge transfer is 20 times larger than that of V_{ks}^e for the ligand-to-ligand ($\Delta r = 6 \text{ \AA}$) charge transfer absorption. The increase in the donor–acceptor separation by 2.7 \AA decreases the electronic coupling by a factor of 400 and the rate should decrease by a factor of 1.6×10^5 .

The distance dependence of the electronic factor was explored in detail by Closs and co-workers [41]. Using a 4-biphenyl or a 4-benzophenyl group as donor, connected via a rigid spacer with a 2-naphthyl group, as illustrated in Figure 16.20, it was possible to demonstrate that the rate constants of intra-molecular long-range electron, hole and triplet energy transfers can be written in the form

$$k = k_0 \exp[-\beta(\Delta r)] \quad (16.125)$$

where Δr is the edge-to-edge separation between donor and acceptor, and the rate constant at contact k_0 includes the contribution of the Franck–Condon factors, presumed constant along the reaction series. Additionally, the distance-dependent coefficient for triplet energy transfers was shown to be equal to the sum of the corresponding coefficients for electron and hole transfers, $\beta_{te} = \beta_{el} + \beta_{hl}$. This is the experimental confirmation that the Dexter mechanism of triplet energy transfer can be viewed as a simultaneous double-electron exchange.

The problem of electron or triplet energy transfer through a rigid spacer is similar to that of a particle in a double-well potential, Figure 16.21, which has an exact quantum-mechanical solution. The resolution of the Schrödinger equation for that system gives a splitting of the energy levels in the two potential wells due to the tunnelling of the electron through the barrier. The splitting is

$$E_2 - E_1 = 8 \frac{E\Phi}{E + \Phi} \frac{1}{1 + \Gamma l} \exp[-\Gamma(\Delta r)] \quad (16.126)$$

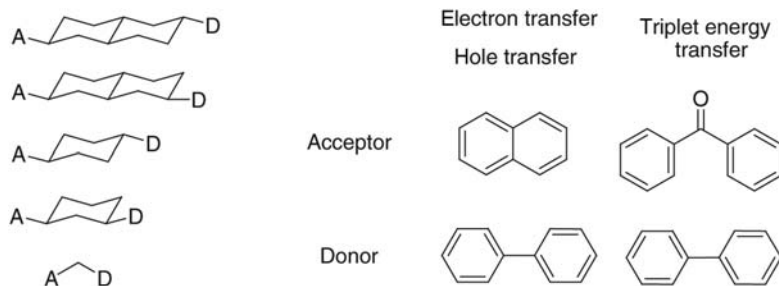
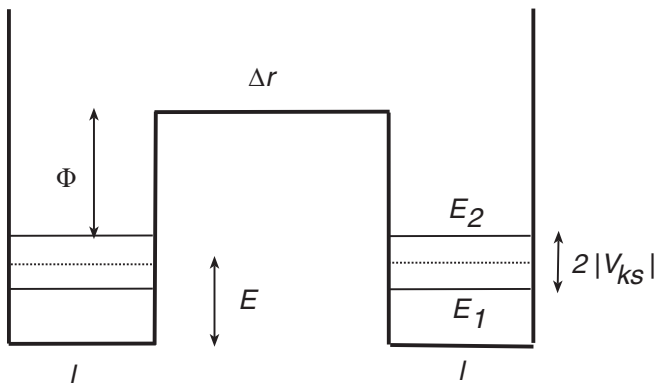


FIGURE 16.20

Molecular structures of some covalently linked donor–acceptor systems.

**FIGURE 16.21**

Double square-potential well, with symmetrical wells of length l separated by a barrier of height Φ and edge-to-edge distance Δr .

where l is the size of the potential well, E the energy of the electron, Φ the height of the barrier and

$$\Gamma = \frac{1}{\hbar} \sqrt{2m_e \Phi} \quad (16.127)$$

The size of the potential well and the energy of the electron are related. For cata-condensed aromatic hydrocarbons, Platt proposed a simple relation [42]

$$E = \frac{\hbar^2}{2ml} n^2, \quad n = 0, 1, 2, \dots \quad (16.128)$$

where l is the perimeter of the aromatic system. For example, the triplet state energy of anthracene, 228 kJ mol^{-1} , corresponds to a perimeter $l = 23.9 \text{ \AA}$, which is a rather realistic value.

The electronic coupling of the symmetric wells is related to the splitting

$$|V_{ks}^e| = \frac{E_2 - E_1}{2} \quad (16.129)$$

and gives

$$|V_{ks}^e|^2 = \left(4 \frac{E\Phi}{E + \Phi} \frac{1}{1 + \Gamma l} \right)^2 \exp[-2\Gamma(r - r_0)] \quad (16.130)$$

Typically, the electronic barrier is $\Phi = 3 \pm 1 \text{ eV}$. This, together with the parameters of naphthalene calculated above and factor $2\pi/\hbar$ of the Golden Rule, gives a relatively constant pre-exponential factor, which is typical for aromatic hydrocarbons,

$$\frac{2\pi}{\hbar} \left(4 \frac{E\Phi}{E + \Phi} \frac{1}{1 + \Gamma l} \right)^2 = (5.4 \pm 0.1) \times 10^{14} \text{ eV sec}^{-1} \quad (16.131)$$

The Franck–Condon factor can be expressed in eV^{-1} and the resulting transfer rate is in sec^{-1} . This pre-exponential factor is approximately equal to the frequency of the electronic movement in an aromatic hydrocarbon, $\nu_{el} = 10^{15} \text{ sec}^{-1}$, and another way of arriving at essentially the same formulation is to describe the distance dependence of electron transfer as the tunnelling of the electron from the donor to the acceptor, through a square-potential barrier, eq (6.46).

$$\nu = \nu_{el} \exp[-\beta(\Delta r)] \quad (16.132)$$

where $\beta = 2\Gamma$.

In the gas phase, the height of the barrier in eq. (16.127) is the ionisation energy of the donor, or, in the original scanning transmission microscopy experiments [43], the average work functions of the metal surface and probe. In an electron transfer between rigidly linked donor–acceptor systems, the height of the barrier is the difference between the energy of the electron in the donor and in the medium separating it from the acceptor, because the electron tunnels through matter and the decay of its wavefunction with the distance from the edge of the classically allowed region depends on the properties of that matter. The energy difference between the electron at rest in a vacuum and the electron in the donor (Φ_0) is simple to calculate from the reduction potential of the donor versus NHE or versus SCE, knowing that the absolute potentials of NHE and SCE are $\Phi_0(\text{NHE}) = 4.44 \text{ eV}$ and $\Phi_0(\text{SCE}) = 4.71 \text{ eV}$. Some examples of such calculations are shown in Figure 16.22. A simple correction for the stabilisation of the energy of the electron tunnelling through matter is [44]

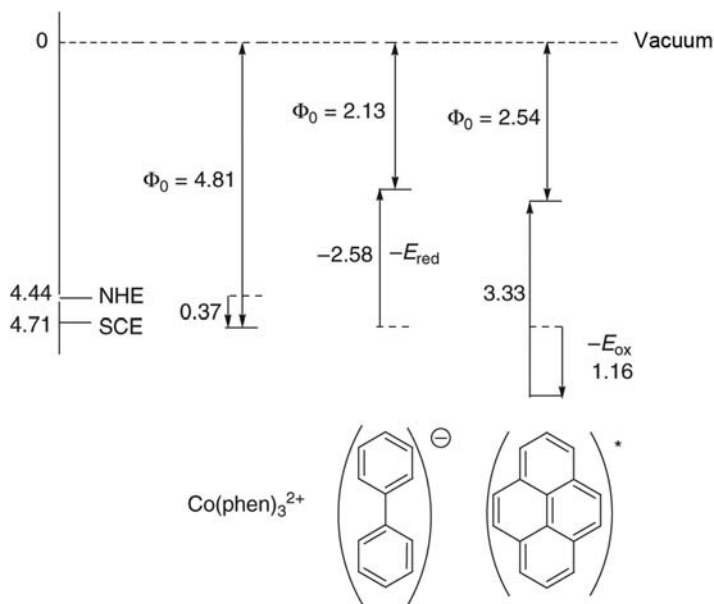
$$\Phi = \frac{\Phi_0}{\varepsilon_{op}} \quad (16.133)$$

since the optical dielectric constant of the medium separating electron donor and acceptor, $\varepsilon_{op} = (n_D)^2$, responds to the electronic movement. The refractive index n_D is defined as the ratio between the speed of light in vacuum and in the medium. These equations together lead to

$$\nu = \nu_{el} \exp \left[-\frac{2}{\hbar} \sqrt{2m_e \frac{\Phi_0}{n_D^2}} \Delta r \right] = \nu_{el} \exp \left[-1.025 \frac{\sqrt{\Phi_0}}{n_D} \Delta r \right] \quad (16.134)$$

where the constant applies when the electron barrier is expressed in eV and the distances in Å.

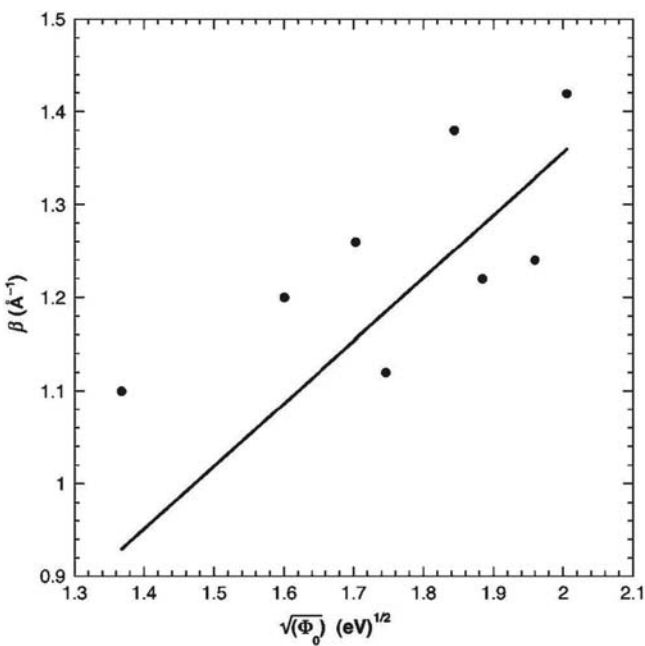
The relation of the electron tunnelling decay coefficient to molecular properties of the reactants and, in particular, to the energy of the electron in the donor, is often obscured by the difficulty of separating the Franck–Condon factors from the electronic factors. Changing the donor with the purpose of changing the energy of the electron and testing the energy dependence of the electronic factor also changes the Franck–Condon factor of the reaction. However, Figure 16.15 shows that there is a reaction energy that maximises the Franck–Condon factor. Krongauz used the free-energy dependence of the Franck–Condon factors to select, from a variety of acceptors, the species that maximise the Franck–Condon factor of each donor [45].

**FIGURE 16.22**

Calculation of the barrier height for electron tunnelling through vacuum, using $E^0 = 0.37$ V versus NHE for $\text{Co}(\text{phen})_3^{2+/3+}$, $E^{\text{red}} = -2.58$ V versus SCE for biphenyl, and $E^{\text{ox}} = 1.16$ V versus SCE for pyrene together with $E_{\text{S}1} = 3.33$ eV.

The couples of optimised nuclear factors were then selected for the distance-dependence study in 2-methyltetrahydrofuran (MTHF) glass at 77 K. The results are shown in Figure 16.23, together with the electron tunnelling decay coefficient of eq. (16.134) calculated with $n_D = 1.5$. The square root dependence on the binding energies of the electrons is reasonably well obeyed, and the optical dielectric constant is found to be an appropriate scaling factor.

The example above considered that the height of the tunnelling-energy barrier was measured from the vacuum to the energy of the electron in the donor, Φ_0 . However, the donor and acceptor may be separated by a medium with low energy vacant orbitals that offer a lower energy channel to conduct the electron from the donor to the acceptor. Then, the energy difference between the electronic origins of the lowest medium absorption and the lowest donor absorption band becomes the tunnelling-energy barrier [46]. For intra-molecular transfers involving donor-spacer-acceptor moieties, this “superexchange” mechanism for electron transfer was shown to depend on the energy difference between the LUMO orbitals of donor and spacer. For hole tunnelling, the same reasoning suggests that the tunnelling-energy barrier is given by the difference between the oxidation potentials of the donor and of the spacer [46]. Superexchange mechanisms lead to distance dependences with the form of eq. (16.132) but with lower attenuation coefficients β .

**FIGURE 16.23**

Experimental and calculated distance dependence of the electronic factor as a function of the energy of the electron in the donor, in MTHF at 77 K.

16.8 Triplet energy transfer rates

The expectation arises that accurate Franck–Condon factors could be calculated by a model incorporating a suitable high frequency and a good estimate of the reorganisation energy. In terms of the relations presented above

$$\lambda = \frac{1}{2} \sum_{i=1}^m f_i d_i^2 = \frac{1}{2} f_{\text{eff}} d_{\text{eff}}^2 \quad (16.135)$$

The effective force constant of the high frequency (f_{eff}) is determined by the dominant vibronic progression. In the spectra of aromatic hydrocarbons this corresponds to $\hbar \omega \approx 1400 \text{ cm}^{-1}$, which with $\mu_{\text{CC}} = 6 \text{ amu}$, gives $f = 4.2 \times 10^3 \text{ kJ mol}^{-1} \text{ \AA}^{-2}$, close to the force constant of the breathing mode of an aromatic ring obtained by normal mode analysis of aromatic hydrocarbons. Resonance Raman spectroscopy shows that in polyatomic systems there are many modes that contribute to λ . However, for diatomic molecules the Stokes shift reports on the effective displacement, and thus these are particularly appropriate to test the validity of the methods employed to calculate λ because there is no ambiguity in the calculation of f_{eff} or d_{eff} . Table 16.2 presents some

Table 16.2 Bond lengths and displacements (in Å) of diatomic molecules and ions with bond order differences of 0.5.

System elect. conf.	H_2^+/H_2 $X\ 2\Sigma_g^+ / X\ 1\Sigma_g^+$	F_2/F_2^- $X\ 1\Sigma_g^+ / X\ 2\Sigma_u^+$	O_2/O_2^- $X\ 3\Sigma_g^- / X\ 2\Pi_{g,i}$	O_2^+/O_2 $X\ 2\Pi_g / X\ 3\Sigma_g^-$	N_2/N_2^- $X\ 1\Sigma_g^- / X\ 2\Pi_g$
l_{ox}/l_{red}	1.052/0.7414	1.4119/1.88	1.2075/1.35	1.1164/1.2075	1.0977/1.19
$l_{ox} - l_{red}$	0.311	-0.47	-0.14	-0.0911	-0.09
Bond orders	0.5/1.0	1.0/0.5	2.0/1.5	2.5/2.0	3.0/2.5
d_{eff}	0.259	0.475	0.158	0.112	0.090

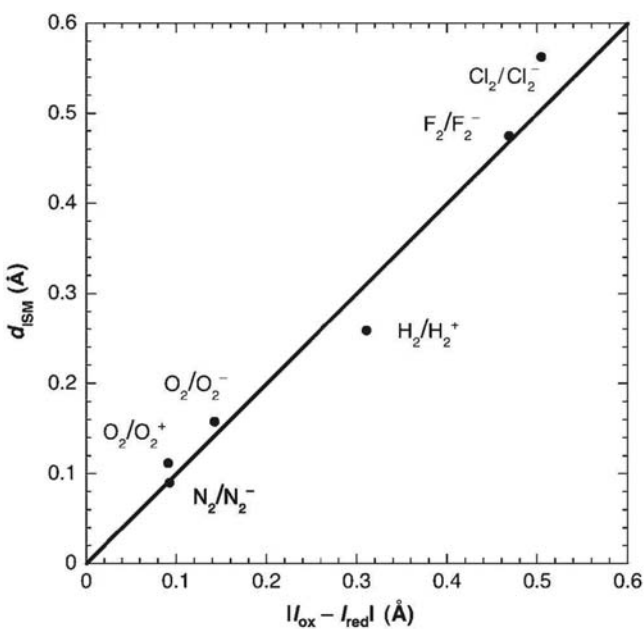
homonuclear diatomic molecules and ions, presented in pairs that differ only in one bonding or anti-bonding electron. They are also a good testing ground for the calculation of λ for electron transfer reactions because the change in the electronic configuration corresponds to a change in bond order by 0.5 and Pauling's relation is obeyed. In fact, [Figure 6.14](#), illustrating Pauling's relation between bond orders and bond lengths, also includes some of these systems.

The comparison between the bond length changes of the systems indicated in [Table 16.2](#) requires some reference state. Considering that these systems follow Pauling's relation, the reference state can be found multiplying $|l_{ox} - l_{red}|$ by the respective bond orders, or, better, the average of the bond order n_{av} , because the effective displacement is independent of the choice of initial and final states. This takes into account the fact that smaller bond orders are more sensitive to bond order changes than large bond orders. For the same reason, the product $n_{av}|l_{ox} - l_{red}|$ must be divided by the sum of the equilibrium bond lengths. The success of this procedure of reducing the effective displacement to a common reference state can be assessed from the average and standard deviation of the reduced bond length changes: 0.106 ± 0.016 . A similar procedure was followed by intersecting-state model (ISM) to obtain the reduced bond length changes of bond-breaking–bond-making reactions. It was shown in [Chapter 7](#), Relationships between Structure and Reactivity, that the fundamental equation obtained for isothermal processes was, [eq. \(7.9\)](#),

$$d_{eff} = \frac{a' \ln(2)}{n^\ddagger} (l_D + l_A) = \frac{0.108}{n^\ddagger} (l_D + l_A) \quad (16.136)$$

where n^\ddagger is now n_{av} , because no bonds are broken in the electronic transitions involved in [Tables 16.1](#) and [16.2](#).

The scaling factor $a' = 0.156$ of hydrogen-atom and proton transfers seems to be transferable to triplet energy and electron transfers. This is not totally unexpected because the reference system chosen for bond-breaking–bond-making reaction, $H + H_2$, does not have significant steric effects and the resonance at the transition state is minimal. These are also properties of triplet energy and electron transfers. The effective displacements calculated with [eq. \(16.136\)](#) are presented in [Table 16.2](#) and compared with the spectroscopic data in [Figure 16.24](#). For the systems selected for this test, the performance of [eq. \(16.136\)](#) is particularly encouraging. However, it must be emphasised that these systems were selected

**FIGURE 16.24**

Correlation between the effective displacements calculated by ISM and the experimental data on the diatomic molecules of Table 16.2. ISM, Intersecting-state model.

for their adherence to Pauling's relation in discrete increments of 0.5 in the bond order. For example, the electronic transition from the ${}^3\Sigma_g^-$ state to the ${}^1\Delta_g$ state of molecular oxygen, shown in Table 16.1, does not involve the same type of change in bond order and its effective displacement cannot be calculated from eq. (16.136).

The generalisation of this method to polyatomic systems is straightforward. For example, benzene formally has three double bonds and three single bonds, that is $n = 1.5$. Its cation has one bonding electron less and the total bonding is reduced to $n = 1.42$, thus $n_{\text{av}} = 1.44$. The CC bond length of benzene is 1.397 Å and normal mode analysis gives $f = 3.87 \times 10^3 \text{ kJ mol}^{-1} \text{ \AA}^{-2}$. With these values eq. (16.136) gives $d_{\text{eff}} = 0.207 \text{ \AA}$ and $\lambda(\text{benzene}) = 82.7 \text{ kJ mol}^{-1}$. Another example is tetracyanoethylene, with its four triple bonds, one double bond and four single bonds, which lead to $n = 2.0$. Its anion has $n = 1.94$ and, consequently, $n_{\text{av}} = 1.97$. With the average bond length of 1.301 Å for the neutral and 1.291 Å for the anion, and the corresponding average force constants of 6.42×10^3 and $6.19 \times 10^3 \text{ kJ mol}^{-1} \text{ \AA}^{-2}$, respectively, the reorganisation energy for this redox couple is $\lambda(\text{TCNE}) = 63.7 \text{ kJ mol}^{-1}$. The charge transfer in the HMB/TCNE charge-transfer complex should be intermediate between these two values. As mentioned before, resonance Raman suggests that the total reorganisation energy

is between 45 and 56 kJ mol⁻¹ for this system, which may be increased upon consideration of the role of the CH bonds. Again, this is an encouraging agreement between eq. (16.136) and the experimental data.

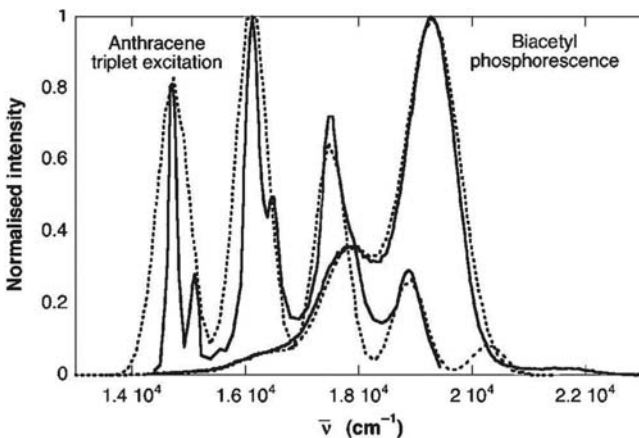
The heuristic validation of eq. (16.136) for the calculation of effective displacements for triplet energy and electron transfers under the specified conditions has interesting consequences. The isomorphism of eqs. (16.136) and (7.9), suggests that the energy dependence of the effective displacement should have the form of eq. (7.8), or, more precisely,

$$d_{\text{eff}} = \frac{a'}{2n^{\ddagger}} \ln \left\{ \frac{1 + \exp(\sqrt{2n^{\ddagger}} \Delta E^0 / \Lambda)}{1 - [1 + \exp(\sqrt{2n^{\ddagger}} \Delta E^0 / \Lambda)]^{-1}} \right\} (l_D + l_A) \quad (16.137)$$

where Λ is a parameter that accounts for the coupling of the reaction energy with vibrational modes other than the high-frequency mode selected for the reaction coordinate. An empirical choice of Λ , guided by the best fit to the energy dependence of a series of reactions, gives the correct reorganisation energy and, together with the high-frequency mode and the electronic coupling, leads to good estimates of the reaction rates. A detailed interpretation of eq. (16.137) is postponed to Chapter 17, Electron Transfer Reactions, where it is applied to electron transfer reactions. For the moment, it is just emphasised that d_{eff} increases with ΔE^0 for finite values of Λ , which means that the *reorganisation energy tends to increase with the driving force* of the reaction. For $\Lambda \gg \Delta E^0$, eq. (16.137) tends to eq. (16.136). Only this limit will be considered for the examples of triplet energy transfer reactions presented below.

The most convincing argument for the relation between molecular structure, spectroscopy and kinetics developed in this chapter, is to calculate triplet energy transfer rates using the Franck–Condon factors and electronic couplings given by the molecular models. An interesting system to test these relations is the triplet energy transfer from a biacetyl molecule trapped inside a hemicarcerand cage to aromatic hydrocarbons in free solution. This system has two very convenient features: firstly, biacetyl is one of the few organic molecules phosphorescing at room temperature, and secondly it is possible to study experimentally an extended range of reaction energies [47]. The fluorescence of biacetyl overlaps with its phosphorescence in steady-state emission spectra, but registering the spectrum with a 10 µsec delay gives enough time for the biacetyl fluorescence to disappear, as illustrated in Figure 16.25 [26]. This figure also shows the phosphorescence of anthracene at 77 K in ethanol with ethyl iodide to enhance the inter-system crossing and facilitate the observation of phosphorescence. The simulation of anthracene phosphorescence requires at least two modes, with frequencies 1450 and 400 cm⁻¹ [26]. The phosphorescence of biacetyl can be simulated with only one mode with a large width at room temperature, which probably buries the contribution of lower frequency modes.

Golden Rule calculations using eq. (16.103) with the average single mode approximation of eqs. (16.104) and (16.105), and the parameters indicated in

**FIGURE 16.25**

Phosphorescence spectra of biacetyl and anthracene. The simulated spectra (thin lines and dotted lines) used $E_D = 19,300 \text{ cm}^{-1}$, $\bar{\nu}_D = 1470 \text{ cm}^{-1}$, $\sigma_D = 480 \text{ cm}^{-1}$ and $S_D = 0.35$ for biacetyl, and $E_A = 14,950 \text{ cm}^{-1}$, $\bar{\nu}_A = 1450 \text{ cm}^{-1}$, $\sigma_A = 150 \text{ cm}^{-1}$ and $S_A = 0.70$ (thin lines) together with $\bar{\nu}_A = 400 \text{ cm}^{-1}$, $\sigma_A = 150 \text{ cm}^{-1}$ and $S_A = 0.50$ (dotted lines) for anthracene.

Figure 16.25 for anthracene, give the rates presented in Figure 16.26, when the electronic coupling is fitted ($V_{ks}^e = 0.3 \text{ cm}^{-1}$) to place the fastest rate within the experimental range observed for triplet energy transfer rate from biacetyl, through a hemicarcerand cage, to an aromatic hydrocarbon in solution by two independent laboratories [47]. Only the parameters of anthracene were employed in eqs. (16.104) and (16.105) because the low-frequency contributions to the biacetyl spectrum are not identifiable in the room-temperature phosphorescence spectrum. However, the rates were measured at room temperature and it is more realistic to calculate the reorganisation energy of the medium with eq. (16.101) using $\sigma_D = 480 \text{ cm}^{-1}$ from biacetyl at room temperature, that is, $\lambda_s = 13.5 \text{ kJ mol}^{-1}$. The Golden Rule reproduces quite well the general energy dependence of the rates, although this formulation tends to overestimate the rates in the range of reaction energies where the energy-gap law is followed.

Figure 16.26 also presents calculations with ISM in the limit of very high Λ , that is, using eq. (16.136) with the sum of the average bond lengths of biacetyl and anthracene ($l_D + l_A = 2.7 \text{ \AA}$) and the average bond order of biacetyl and anthracene ($n^\ddagger = 1.5$) [26]. The distance d between the parabola representing initial and final states was kept constant and their intersection was calculated with the force constant estimated with the average mode approximation ($\hbar\omega_s = 1017 \text{ cm}^{-1}$ leads to $f = 2.44 \times 10^3 \text{ kJ mol}^{-1} \text{ \AA}^{-2}$)

$$x_r = \frac{d}{2} + \frac{\Delta G^0}{fd} \quad (16.138)$$

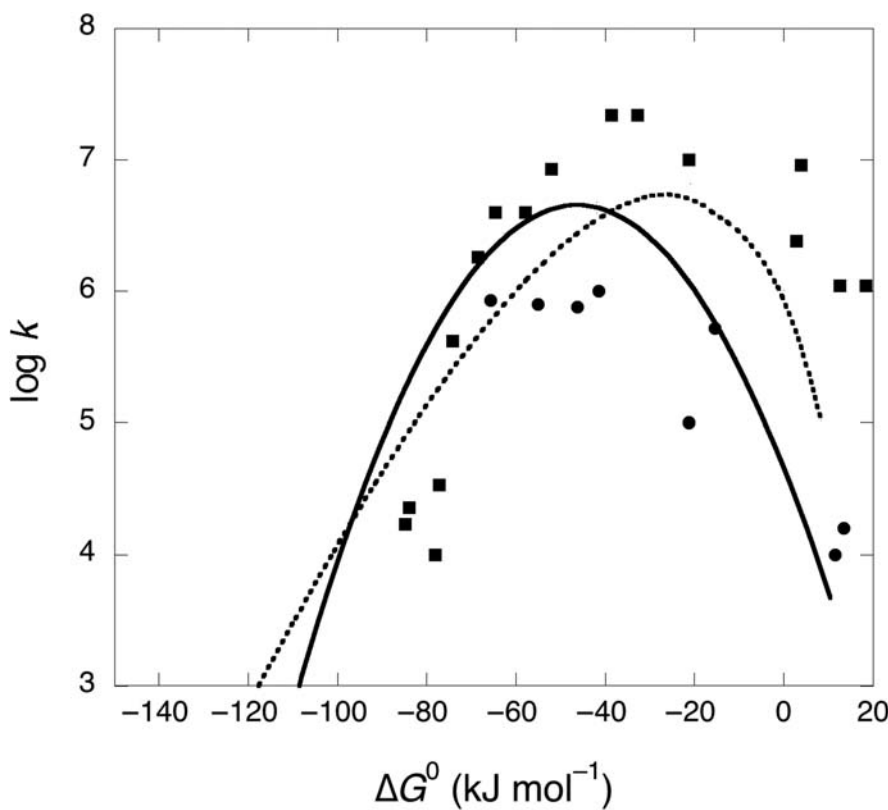


FIGURE 16.26

Rate constants for the triplet energy transfer from biacetyl, through a hemicarcerand cage, to aromatic hydrocarbons in solution [47]. The dotted line represents Golden Rule calculations employing eq. (16.103) with $\hbar\omega = 1017 \text{ cm}^{-1}$, $S_A = 1.2$, $\lambda = 13.5 \text{ kJ mol}^{-1}$, and the full line are thermal rate constants calculated with ISM calculations using eq. (16.136) with $I_B + I_A = 2.7 \text{ \AA}$, $n^\ddagger = 1.5$ and $f = 2.44 \times 10^3 \text{ kJ mol}^{-1} \text{ \AA}^{-2}$. *ISM*, Intersecting-state model.

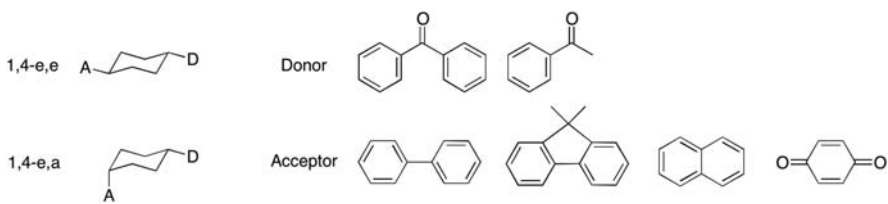
This allows for the calculation of the energy barrier

$$\Delta G^\ddagger = \frac{1}{2} f x^\ddagger \quad (16.139)$$

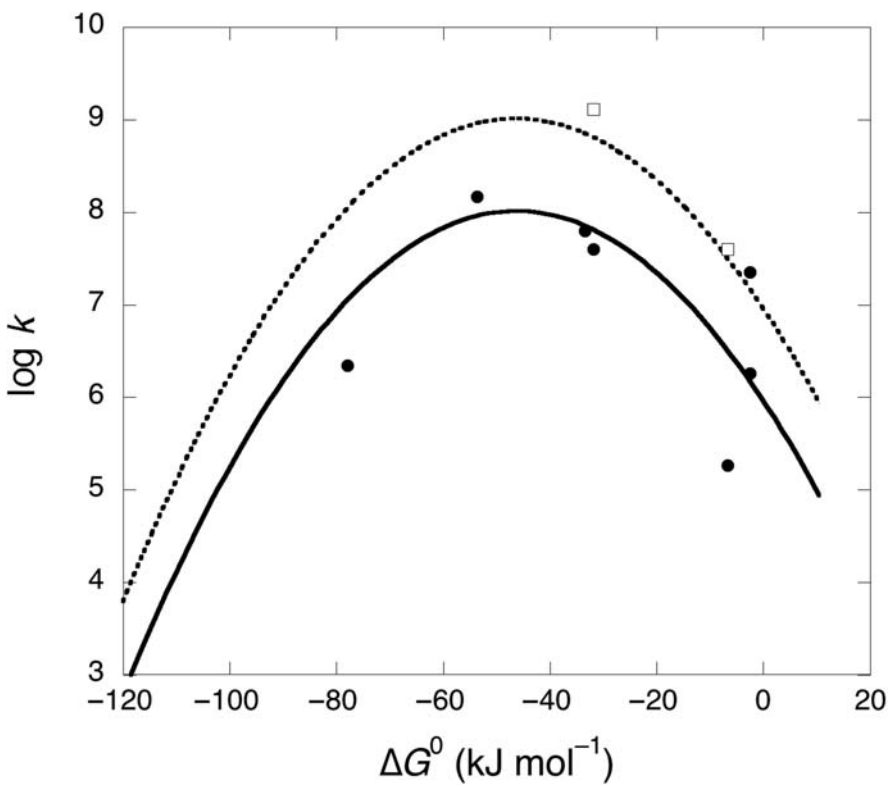
and, consequently for the thermal rate

$$k_{th} = \nu \exp\left(\frac{\Delta G^\ddagger}{RT}\right) \quad (16.140)$$

The tunnelling rate, eq. (16.71), requires an estimate of the reduced mass, which will be discussed in Chapter 17, Electron Transfer Reactions. The thermal rate was scaled by a pre-exponential ν factor to yield a maximum rate within the

**FIGURE 16.27**

Molecular structures of rigid donor–spacer–acceptor systems employed in triplet energy transfer studies.

**FIGURE 16.28**

Rate constants for intra-molecular triplet energy transfer from 4-benzophenonyl or 4-acetophenonyl moieties through 1,4-cyclohexanediyl spacers to aromatic acceptors [48]. The squares and circles are conformations 1,4-e,e and 1,4-e,a, respectively. The dashed line are ISM calculations without adjustable parameters and the full line is the dashed line multiplied by 0.1 to account for the angle of the acceptor group in 1,4-e,a conformers. *ISM*, Intersecting-state model.

experimental range. This scaling is similar to that described above for the Golden Rule calculations. Although this is a simple model and only the pre-exponential factor was fitted to the kinetic data, the fundamental features of the energy gap law are reproduced within the experimental uncertainty.

The calculated rates in Figure 16.26 have absolute values close to the experimental ones because the electronic coupling (or pre-exponential factor) was selected to favour their agreement. It is possible to use eq. (16.134) to calculate the frequency factor, but this requires the choice of a system with a fixed distance between triplet donors and acceptors. Sigman and Closs studied intramolecular triplet energy transfers in the rigid systems presented in Figure 16.27 [48]. The edge-to-edge distance in the 1,4-e,e conformation is 4.4 Å [41a]. The frequency factor for this system can be calculated with eq. (16.134) and the aid of Figure 16.22 using the oxidation potential of benzophenone, $E_{\text{ox}} = 2.37$ eV versus SCE, its triplet energy, $E_T = 3.00$ eV, and taking $n_D = 1.4$ for the spacer. Given the electronic frequency, $\nu_{\text{el}} = 5 \times 10^{14} \text{ sec}^{-1}$, and remembering that triplet energy transfer can be regarded as a double electron transfer, $\beta_{\text{TT}} = 2\beta$, this yields $\nu = 1.1 \times 10^9 \text{ sec}^{-1}$. In view of the structural similarities of this system with the biacetyl-anthracene system discussed above, the nuclear factor can be calculated with the same parameters: $l_D + l_A = 2.7$ Å, $n^\ddagger = 1.5$, $f = 2.44 \times 10^3 \text{ kJ mol}^{-1} \text{ Å}^{-2}$. Eq. (16.136) and the crossing of donor and acceptor surfaces give the triple energy transfer rates shown in Figure 16.28. The agreement with the experimental rates for the configurations 1,4-e,e is striking for a “back-of-the-envelope” calculation. The rates for the conformations 1,4-e,a where donor and acceptor are not properly oriented required the multiplication of the electronic frequency calculated above by 0.1 to account for the angle of the acceptor group in 1,4-e,a conformers.

References

- [1] A Jablonski, *Z. Phys.* **94** (1935) 38–46.
- [2] M Kasha, *Discuss. Faraday Soc.* **9** (1950) 14–19.
- [3] SJ Formosinho, AM da Silva, *Mol. Photochem.* **9** (1979) 257–275.
- [4] T Förster, *Ann. Phys.* **2** (1948) 55.
- [5] DL Dexter, *J. Chem. Phys.* **21** (1953) 836–850.
- [6] T Förster, *Discuss. Faraday Soc.* **27** (1959) 7–17.
- [7] BJ Walker, AJ Musser, D Beljonne, RH Friend, *Nat. Chem.* **5** (2013) 1019–1024.
- [8] SJ Strickler, RA Berg, *J. Chem. Phys.* **37** (1962) 814–822.
- [9] CJP Monteiro, J Pina, MM Pereira, LG Arnaut, *Photochem. Photobiol. Sci.* **11** (2012) 1233–1238.
- [10] (a) M Halmann, I Laulicht, *J. Chem. Phys.* **43** (1965) 438–448.
 (b) M Halmann, I Laulicht, *J. Chem. Phys.* **44** (1966) 2398–2405.
- [11] P Avakian, E Abramson, RG Kepler, JC Caris, *J. Chem. Phys.* **39** (1963) 1127–1128.
- [12] KH Grellmann, H-G Scholz, *Chem. Phys. Lett.* **62** (1979) 64–71.

- [13] J Jortner, J Ulstrup, *Chem. Phys. Lett.* **63** (1979) 236–239.
- [14] SJ Formosinho, *J. Chem. Soc. Faraday Trans. 2* **70** (1974) 605.
- [15] W Siebrand, The Triplet State. AB Zehalan (Ed.), Cambridge University Press, 1967, p. 31.
- [16] (a) SJ Formosinho, LG Arnaut, *Adv. Photochem.* **16** (1991) 67.
(b) EG Azenha, AC Serra, M Pineiro, MM Pereira, J Seixas de Melo, LG Arnaut, SJ Formosinho, AMdAR Gonsalves, *Chem. Phys.* **280** (2002) 177–190.
- [17] EF McCoy, IG Ross, *Aust. J. Chem* **15** (1962) 573–590.
- [18] OS Mortensen, W Siebrand, AW Tarr, *Chem. Phys.* **125** (1988) 231–245.
- [19] BR Henry, W Siebrand, *J. Chem. Phys.* **49** (1968) 5369–5376.
- [20] SJ Formosinho, *J. Chem. Soc. Faraday Trans.* **72** (1976) 1313–1331. 2.
- [21] JB Birks, *Photophysics of Aromatic Molecules*, Wiley, London, 1970.
- [22] R Engelman, J Jortner, *Mol. Phys.* **18** (1970) 145–164.
- [23] (a) L Landau, *Phys. Z. Sowjetunion* **1** (1932) 88.
(b) C Zener, *Proc. Roy. Soc. A* **137** (1932) 696. *London*.
- [24] D DeVault, *Q. Rev. Biophys.* **13** (1980) 387–564.
- [25] JJ Hopfield, *Proc. Natl. Acad. Sci. U.S.A.* **71** (1974) 3640–3644.
- [26] C Serpa, LG Arnaut, SJ Formosinho, KR Naqvi, *Photochem. Photobiol. Sci* **2** (2003) 616.
- [27] (a) RA Marcus, *J. Chem. Phys.* **24** (1956) 966–978.
(b) RA Marcus, *Faraday Discuss. Chem. Soc.* **29** (1960) 21.
- [28] JP Claude, KM Omberg, DS Williams, TJ Meyer, *J. Phys. Chem. A* **106** (2002) 7795–7806.
- [29] R Schmidt, *J. Photochem. Photobiol. A: Chem* **80** (1994) 1–5.
- [30] K Kulinowski, IR Gould, NS Ferris, AB Myers, *J. Phys. Chem.* **99** (1995) 17715–17723.
- [31] WR Ware, P Chow, SK Lee, *Chem. Phys. Lett.* **2** (1968) 356–358.
- [32] PY Chen, TJ Meyer, *Chem. Rev.* **98** (1998) 1439–1477.
- [33] R Jimenez, GR Fleming, PV Kumar, M Maroncelli, *Nature* **369** (1994) 471–473.
- [34] MJ Lang, XJ Jordanides, X Song, GR Fleming, *J. Chem. Phys.* **110** (1999) 5884–5892.
- [35] SA Kovalenko, R Schanz, VM Farztdinov, H Hennig, NP Ernsting, *Chem. Phys. Lett.* **323** (2000) 312–322.
- [36] (a) AB Myers, *Chem. Rev.* **96** (1996) 911–926.
(b) JT Hupp, RD Williams, *Acc. Chem. Res.* **34** (2001) 808–817.
- [37] (a) K Wynne, C Galli, RM Hochstrasser, *J. Chem. Phys.* **100** (1994) 4797–4810.
(b) BM Britt, JL McHale, DM Friedrich, *J. Phys. Chem.* **99** (1995) 6347–6355.
- [38] M Bixon, J Jortner, J Cortes, H Heitele, ME Michel-Bayerle, *J. Phys. Chem.* **98** (1994) 7289–7299.
- [39] NE Katz, SL Mecklenburg, DK Graff, P Chen, TJ Meyer, *J. Phys. Chem.* **98** (1994) 8959–8961.
- [40] C Serpa, PJS Gomes, LG Arnaut, SJ Formosinho, J Pina, J Seixas de Melo, *Chem. Eur. J.* (2006) 12.
- [41] (a) GL Closs, LT Calcaterra, NJ Green, KW Penfield, JR Miller, *J. Phys. Chem.* **90** (1986) 3673.
(b) GL Closs, MD Johnson, JR Miller, P Piotrowiak, *J. Am. Chem. Soc.* **111** (1989) 3751.
(c) GL Closs, P Piotrowiak, JM MacInnis, GR Fleming, *J. Am. Chem. Soc.* **110** (1988) 2652.

- [42] JR Platt, *J. Chem. Phys.* **17** (1949) 481.
- [43] (a) G Binnig, H Rohrer, *Angew. Chem. Int. Ed. Engl.* **26** (1987) 606.
(b) G Binnig, H Rohrer, C Gerber, E Weibel, *Physica* **109 & 110B** (1982) 2075.
- [44] LG Arnaut, LG Formosinho, *J. Photochem. Photobiol. A: Chem.* **100** (1996) 15.
- [45] VV Krongauz, *J. Phys. Chem.* **96** (1992) 2609.
- [46] OS Wenger, *Acc. Chem. Res.* **44** (2011) 25–35.
- [47] (a) F Pina, AJ Parola, E Ferreira, M Naestri, N Armaroli, R Ballardini, V Balzani, *J. Phys. Chem.* **99** (1995) 12701–12703.
(b) ZS Romanova, K Deshayes, P Piotrowiak, *J. Am. Chem. Soc.* **123** (2001) 11029–11036.
- [48] ME Sigman, GL Closs, *J. Phys. Chem.* **95** (1991) 5012–5017.

This page intentionally left blank

Electron-transfer reactions

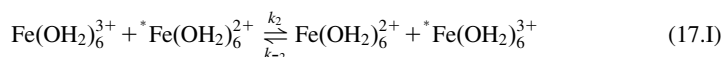
17

17.1 Rate laws for outer-sphere electron exchanges

Electron transfer (ET) is another prototype of chemical reactions as paradigmatic as H-atom or proton transfer reactions. Furthermore, they are chemical processes ubiquitous in chemistry and biology. They are important from a historical point of view in the development of chemical kinetics, and are scientifically relevant in many physical, chemical, biological and technological processes.

The field of electron-transfer reactions has developed only since World War II and initially was centred around inorganic processes. Two kinds of mechanisms are invoked for ET reactions in transition-metal complexes. One, the *inner-sphere mechanism*, where the two reactants share one or more ligands in their first coordination shell in the activated complex and the ET is considered to occur via the bridging ligand. This requires bond breaking followed by bond forming. The other is the *outer-sphere mechanism*, where the first coordination shells of the two reactants remain intact with respect to the number and kind of ligands present. The latter mechanism is the focus of this chapter.

Let us consider the isothermal process for the transfer of one electron between hydrated iron (II) and (III) species



This is a *self-exchange* reaction, where the products are identical to the reactants. For it to be followed experimentally, the iron species were marked radioactively (represented by *). If the reaction is followed, for example, in terms of ${}^*\text{Fe}^{3+}_{(\text{aq})}$, the rate law can be written as

$$\frac{d[{}^*\text{Fe}^{3+}]}{dt} = k_2 [\text{Fe}^{3+}] [{}^*\text{Fe}^{2+}] - k_{-2} [\text{Fe}^{2+}] [{}^*\text{Fe}^{3+}] \quad (17.1)$$

by simplifying the representation of the ionic species in terms of the chemical symbol of the metallic element and of the electric charge. Since second-order rate constants in the direct and reverse directions are equal, $k = k_2 = k_{-2}$, representing by a the initial concentration of reactants and by x the concentration of products, one can write

$$\frac{dx}{dt} = k(a-x)^2 - kx^2 \quad (17.2)$$

which can be rearranged to

$$\frac{dx}{dt} = ka^2 - 2kax \quad (17.3)$$

or

$$\frac{dx}{dt} = ka(a - 2x) \quad (17.4)$$

As a consequence, this yield

$$\frac{dx}{a - 2x} = kadt \quad (17.5)$$

This equation can be integrated

$$\int_0^x \frac{dx}{a - 2x} = \int_0^t kadt \quad (17.6)$$

The result requires knowledge of the value of the standard integral

$$\int_0^x \frac{dx}{a - bx} = \frac{1}{b} \ln(a + bx) \quad (17.7)$$

and thus

$$-\frac{1}{2} \ln(a - 2x) = kat + \text{constant} \quad (17.8)$$

The value of the constant of integration is obtained by solving eq. (17.8) for $t = 0$, where $x = 0$,

$$\ln \frac{a - 2x}{a} = -2kat \quad (17.9)$$

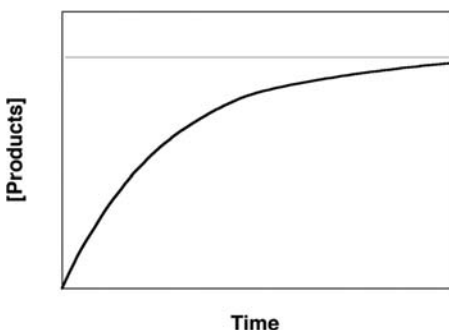
or

$$\frac{a - 2x}{a} = \exp(-2kat) \quad (17.10)$$

Figure 17.1 displays the profile of the concentration of the products as a function of time in a self-exchange reaction, according to eq. (17.9).

Table 17.1 lists typical values of rate constants for self-exchange reactions of transition-metal complexes with different kinds of ligands, in water; the rates cover 14 orders of magnitude. The collection of the vast majority of such data became experimentally feasible only through the availability of several metal radioactive isotopes due to the Manhattan project. The surprising result for the chemists at the end of the 1940s and beginning of the 1950s of twentieth century was the slowness of such processes.

In contrast, in the beginning of the 1980s, Gray and collaborators [3] have shown that electrons can be transferred in proteins over distances of 15–20 Å on a biologically relevant timescale of milliseconds to microseconds. This appears to be consistent with a significant effect producing slow rates for ETs due to bulk

**FIGURE 17.1**

Change in the concentration of the products with time in a reaction following mechanism (17.1). The concentration of the products tends to half of the initial concentration of the reactants, if the concentrations of the two reactants are identical.

solvent. Anticipating an alternative view, one should be aware that the electronic nature of the reactive bonds in hydrated transition-metal ions and in donor and acceptor complexes in proteins are entirely different. As it will be shown in due course, such a direct comparison is therefore not meaningful from a theoretical point of view.

17.2 Theories of electron-transfer reactions

17.2.1 Classical theory of Marcus

ET reactions between molecular species in cases where no bond-breaking–bond-forming processes occur are usually considered to be very different in nature from atom-transfer reactions. For the latter case, Born–Oppenheimer adiabatic potential-energy surfaces are used because of the strong interaction with the attacking atom, which effectively determines the barrier for the reaction. In contrast, for the former processes the interaction between the electron donor and its acceptor is very weak, the nuclear configuration of the products resembles that of the reactants and, in retrospect with a certain naivety, chemists expected that ET would be in general fast processes and would mainly be diffusion controlled.

The current view is that the electron-transfer event itself is a fast activationless process; the barrier for the reaction stems from the necessity to adjust the orientation of the solvent dipoles around ions and the lengths of some bond in the inner-coordination shells prior to the transfer stage. According to such a view, which was largely due to Rudolph Marcus, for the solvent [4], and to Noel Hush, for the metal–ligand-bond lengths [5], there are no proper transition states in electron-transfer reactions, because the solvent molecules are not in equilibrium distribution with the charges of the oxidised and reduced species.

Table 17.1 Rate constants of electron self-exchange reactions in transition-metal complexes, measured in water at room temperature, and parameters used by models (MT-1 and ISM) to calculate such rates^a.

Complexes	Electronic config.	k (mol ⁻¹ dm ³ s ⁻¹)	Force constants (kJ mol ⁻¹ Å ⁻² /10 ³)		Bond lengths (Å)		r (Å)	n^*	v (sec ⁻¹)
			f_{red}	f_{ox}	l_{red}	l_{ox}			
Fe(CN) ₆ ^{4-/3-}	π^6/π^5	19	1.38	1.44	1.88	1.88	8.80	1	10^{13}
V(OH ₂) ₆ ^{2+/3+}	π^3/π^2	1.0×10^{-2}	0.96	1.53	2.13	1.99	6.50	1	10^{13}
Cr(OH ₂) ₆ ^{2+/3+}	$\pi^3\sigma^{*1}/\pi^3$	$\leq 2 \times 10^{-5}$	0.96	1.53	2.15	1.98	6.50	1	4×10^{10}
Mn(OH ₂) ₆ ^{2+/3+}	$\pi^3\sigma^{*2}/\pi^3\sigma^{*1}$	≤ 4	0.99	1.53	2.18	1.99	6.50	1	5×10^9
Fe(OH ₂) ₆ ^{2+/3+}	$\pi^4\sigma^{*2}/\pi^3\sigma^{*2}$	1.1	0.96	1.53	2.10	1.98	6.50	1	10^{13}
Co(OH ₂) ₆ ^{2+/3+}	$\pi^5\sigma^{*2}/\pi^6$	2.4	0.96	1.53	2.08	1.87	6.50	1	10^{13}
Fe(phen) ₆ ^{2+/3+}	π^6/π^5	3.3×10^8	1.44	1.42	1.97	1.97	13.60	2	10^{13}
Co(phen) ₃ ^{2+/3+}	$\pi^5\sigma^{*2}/\pi^6$	12	0.68	1.38	2.11	1.91	13.60	2	6×10^3
Fe(Cp) ₂ ^{0/+}	e_g^4/e_g^3	b	1.90	1.75	1.65	1.68	7.60	1.25	6×10^3

^aData from Ref. [1] except where noted. Ligands: phen = 1,10-phenanthroline; Cp = cyclopentadienyl.

^bIn acetonitrile from Ref. [2].

The first theoretical formalism proposed to estimate the rates of ET reactions that gained general acceptance is known as the theory of Marcus (TM) [4,6]. However, it is relevant to make a distinction between two components of the theory. One component is concerned with the estimation of the intrinsic barrier, ΔG_0^* , for homo-nuclear reactions in terms of molecular parameters of the reactants, which is called here TM-1. The other component of the theory addresses the effect of the reaction energy, ΔG^0 , on the reaction rates, presented in Chapter 7, Relationships between Structure and Reactivity, in terms of the quadratic expression of Marcus [eq. (7.6)] and is called here TM-2. It is currently employed to estimate the rates of cross-reactions when the reaction energies of the heteronuclear reactions are known together with the rates of the corresponding homo-nuclear reactions.

In general terms, Marcus proposed a model for ET reactions based on the approximation that the inner-coordination sphere energy is independent of the outer-sphere reorganisation. In its classical formulation, [6a] TM provides the rate for a self-exchange reaction such as reaction (17.I)

$$k_{\text{TM}} = \kappa_{\text{el}} Z \exp[-(w_r + \Delta G_v^* + \Delta G_s^*)/RT] \quad (17.11)$$

expressed in terms of a collision frequency factor, Z (taken as $Z = 10^{11} \text{ M}^{-1} \text{ sec}^{-1}$); κ_{el} is an electronic transmission factor ($\kappa_{\text{el}} = 1$ for adiabatic reactions and $\kappa_{\text{el}} < 1$ for non-adiabatic reactions). The reaction energy barrier is made up of three contributions: (1) a small electrostatic term, w_r , the electrostatic work required to bring the two reactants together; (2) an external reorganisation of the solvent dipoles, ΔG_s^* and (3) an internal reorganisation of the metal–ligand bonds in the inner-coordination shell, ΔG_v^* . Within the framework of TM-1, the explicit formulae of these terms, for energies in kJ mol^{-1} and radii in \AA , are the following:

$$w_r = \frac{e^2 z_{\text{ox}} z_{\text{red}}}{\varepsilon r \left[1 + r \sqrt{\frac{8\pi N_A^2 e^2 I}{10^{33} \varepsilon RT}} \right]} = \frac{1389 z_{\text{ox}} z_{\text{red}}}{\varepsilon r \left[1 + 50.3r \sqrt{\frac{I}{\varepsilon T}} \right]} \quad (17.12)$$

$$\Delta G_s^* = \frac{e^2}{4} \left(\frac{1}{2r_{\text{ox}}} + \frac{1}{2r_{\text{red}}} - \frac{1}{r} \right) \left(\frac{1}{n_D^2} - \frac{1}{\varepsilon} \right) = 347.3 \left(\frac{1}{r_{\text{av}}} - \frac{1}{r} \right) \left(\frac{1}{n_D^2} - \frac{1}{\varepsilon} \right) \quad (17.13)$$

$$\Delta G_v^* = \frac{1}{2} c_n \frac{f_{\text{ox}} f_{\text{red}}}{f_{\text{ox}} + f_{\text{red}}} (l_{\text{ox}} - l_{\text{red}})^2 \quad (17.14)$$

$$e^2 = \frac{e_0^2 N_A}{4\pi\varepsilon_0} \quad (17.15)$$

In the above expressions e_0 is the elementary charge, N_A is the Avogadro constant, ε_0 is the permittivity of the vacuum, n_D and ε are the refractive index and the static dielectric constants of the solvent, respectively, I is the ionic strength of the solution and r is the distance between the centres of the reactants in the collisional complex, assumed to be equal to $2r_{\text{av}} = (r_{\text{ox}} + r_{\text{red}})$; f_{ox} and f_{red} are the stretching vibration for the two reactants in the oxidised and reduced forms, and l_{ox} and l_{red} are the equilibrium lengths of the metal–ligand bonds in the same

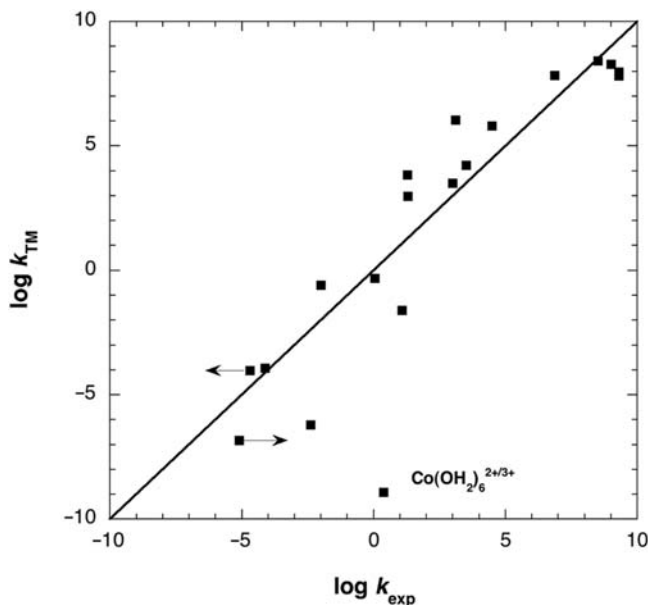
species. The parameter r corresponds to the diameter of the spherical symmetric transition-metal complexes which can be estimated from the relation $r = (r_x r_y r_z)^{1/3}$. Finally, c_n is the coordination number, that is, the number of metal–ligand bonds in the reaction coordinate.

By end of the 1950s, the experimental data on ET in transition-metal complexes was insufficient for a reliable confrontation with the theoretical ideas of Marcus and Hush. However, by the beginning of the 1960s Norman Sutin [7] had obtained a considerable amount of kinetic data on such systems and was able to test the theoretical ideas available. The idea to account for an internal reorganisation is due to N. Hush but eq. (17.14), in fact, is not the one originally proposed. Instead, Sutin employed another expression available from spectroscopy to account for the minimal energy rearrangement for bond length changes and this expression was empirically found to be more convenient to express ΔG_v^* .

The rates were calculated according to TM-1 assuming the following approximations: (1) near adiabaticity ($\kappa_{\text{el}} \approx 1$); (2) dielectric continuum model for the solvent; (3) intermediate distortions between oxidised and reduced species for the internal modes and (4) separation between internal modes and medium modes (either higher frequency vibrational modes or low-frequency modes). This last approximation is implicit in eqs. (17.12)–(17.15). The separation between the inner-sphere, ΔG_v^* , and the outer-sphere, ΔG_s^* , reorganisation energies distinguishes between high-frequency vibrational modes associated to the reactants and products, and low-frequency solvent modes. The low-frequency modes must have much larger vibrational amplitudes to give a comparable contribution for the energy barrier.

The success of such ideas can be judged from the excellent agreement of the theoretical calculations with the experimental self-exchanges rates in transition-metal complexes (Figure 17.2). The parameters required to calculate these self-exchanges rates with eqs. (17.11)–(17.15) in water are $\kappa_{\text{el}} \approx 1$, $n_D = 1.33$, $\varepsilon = 78$ and force constants, bond lengths and distance r is the collisional complex presented in Table 17.1. Although very simple, such calculations reproduce rather well the widely different experimental rates known, with the exception of the reaction $\text{Co}(\text{OH}_2)_6^{2+}/\text{Co}(\text{OH}_2)_6^{3+}$. ΔG_v^* is very sensitive to changes in bond lengths, leading to low rates for systems such as $\text{Cr}(\text{OH}_2)_6^{2+}/\text{Cr}(\text{OH}_2)_6^{3+}$, $\text{Co}(\text{OH}_2)_6^{2+}/\text{Co}(\text{OH}_2)_6^{3+}$ or $\text{Co}(\text{phen})_3^{2+}/\text{Co}(\text{phen})_3^{3+}$, where the number of σ^* electrons is changed and large variations in bond lengths are observed. On the other hand systems where $l_{\text{red}} \approx l_{\text{ox}}$ have $\Delta G_v^* \approx 0$, and their rates are differentiated by the decrease in ΔG_s^* with the increase in size of the complexes, as in $\text{Fe}(\text{CN})_6^{4-/3-}$ and $\text{Fe}(\text{phen})_6^{2+/3+}$. This initial success was very encouraging, but the $\text{Co}(\text{OH}_2)_6^{2+}/\text{Co}(\text{OH}_2)_6^{3+}$ anomaly persisted. TM-1 underestimates this exchange rate by *ca.* 8 orders of magnitude. Rudolph Marcus called it “the soldier marching the wrong way”.

Two alternative mechanisms were proposed to account for the anomaly: (1) rather than following the outer-sphere mechanism, this reaction would proceed through a water-bridging mechanism, (2) a low-spin excited state $(\pi d)^6(\sigma^* d)^1$ of $\text{Co}(\text{OH}_2)_6^{2+}$ or a high-spin excited state $(\pi d)^4(\sigma^* d)^2$ of $\text{Co}(\text{OH}_2)_6^{3+}$ of

**FIGURE 17.2**

Comparison between electron self-exchange rates of transition-metal complexes calculated by TM-1 and experimental data, in water at room temperature, from Ref. [1].

sufficiently low electronic energy would be formed as an intermediate. In the first case, the water bridge between the two cobalt centres could increase the electronic coupling in the inner-sphere complex. In the latter case, a much smaller difference between l_{red} and l_{ox} would be expected, and the rate could be higher, because the population of the (σ^*d) orbital would not change by two electrons.

The water-bridging mechanism was tested synthesising cobalt clusters with hexa-aqua-like O-atom ligand fields surrounding Co(II) or Co(III) cores, but a secondary structure that precludes ET by an inner-sphere pathway [8]. The self-exchange rate for this system is $1.5 \times 10^{-3} \text{ M}^{-1} \text{ sec}^{-1}$ at 40°C in acetonitrile. The large decrease in rate relative to the $\text{Co}(\text{OH}_2)_6^{2+/3+}$ system was taken as evidence in favour of the water-bridging mechanism in the faster system. However, the rate calculated with MT-1 for the exchange in these cobalt clusters, using $\kappa_{\text{el}} \approx 1$, is 5 orders of magnitude higher than the observed value. The discrepancy here was assigned to anion effects, but such effects cannot account for more than 1 order of magnitude [9]. It is clear that other factors play a role in the exchange between cobalt clusters. Rather than solving one anomaly, such cobalt clusters revealed a second anomaly.

Marcus further developed the theory, TM-2, to relate self-exchange rates ($\Delta G^0 = 0$) to cross-reaction rates ($\Delta G^0 \neq 0$)



In TM-2 Marcus represented the reactants ($\text{Red}_1 + \text{Ox}_2$) by one single parabola and did the same for the products. The parabolas are vertically separated by ΔG^0 , and horizontally displaced by a distance that yields the activation energy as the crossing point between reactants and products curves, as illustrated in Figure 17.3. When the work terms are neglected, the parabolas illustrated in this figure lead to the following relation between self-exchange and cross-reaction rate constants:

$$k_{12} = (k_{11}k_{22}K_{12}f_{12})^{1/2} \quad (17.16)$$

$$\ln f_{12} = \frac{(\ln K_{12})^2}{4} \left[\ln \left(\frac{k_{11}k_{22}}{(k_B T/h)^2} \right) \right]^{-1} \quad (17.17)$$

These predictions of the theory have also met with a remarkable success.

TM-1 and TM-2 are collectively known as the TM. However, the approximations involved in the derivation of the two formalisms are different. The approximations involved in TM-2 have already been discussed with respect to Figure 16.16.

Another great success of TM was the prediction of new pattern of reactivity for very exothermic ETs: the existence of an *inverted region*, to be discussed later in Section 17.5. The prediction of such pattern of reactivity against the scientific consensus at the time reveals how those simple ideas of Marcus, based on his quadratic equation, grasped one of the essential features of physical reality in this field, one that has important implications for fundamental biological processes

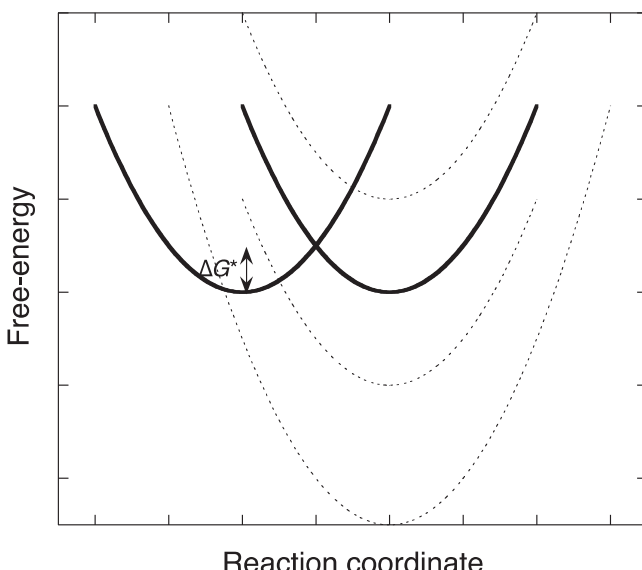


FIGURE 17.3

Intersecting parabola representing reactants and products in an electron-transfer reaction according to Marcus theory.

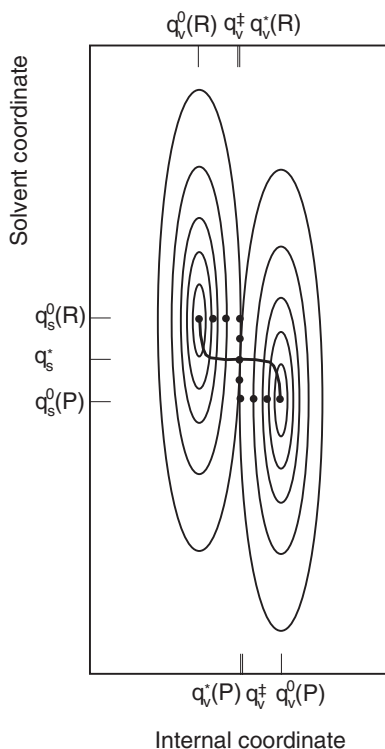
such as photosynthesis. In 1992, Rudolph Marcus was awarded the Nobel Prize in Chemistry for his contributions to the theory of electron-transfer reactions.

17.2.2 Solute-driven and solvent-driven processes

In order to assess the solvent contribution for the electron-transfer processes in solution, it is useful to represent the potential energy surface (PES) for an electron self-exchange reaction in solution by a bi-dimensional diagram. One dimension is for the internal coordinate of reactants and products and the other for the solvent, an ill-described average for the distance approach and orientation with respect to reactants and products. Two extreme limits can be considered for such PES. In the first limit, the overall force-constant for motions of solvent molecules, f_s , is much lower than that for reactants and products, f_v ($f_v/f_s \geq 5$). [Figure 17.4](#) illustrates such a surface and the reaction path for ETs. Solvent motion is relatively slow, after a fast initial reorientation of the solvent molecules that requires very little energy. There is also some solvent relaxation after the electron-transfer event, close to the products configuration. Nevertheless, the main part of the reaction path is due to rearrangements of the internal coordinate, and this type of diagram represents a *solute-driven* reaction. The “transition-state” configuration of those processes is very close to that of the “diabatic path” of Evans and Polanyi, as illustrated in the same figure.

When the energy barriers provided by internal motions are extremely low, the force constant for solvent interactions becomes significant and a large contribution to the reaction coordinate is due to solvent motions. Molecules spend a long time in this transition-state region and dynamic motions of solvent molecules can determine the kinetics. Those are the *solvent-driven* reactions. The role of the dynamic effect of solvents can be excluded for the vast majority of ET reactions considered here. Exceptions are the virtually “activationless processes”, that is, cases where $\Delta G^* < 5 \text{ kJ mol}^{-1}$. In the limits of solute-driven and solvent-driven reactions, a one-dimensional representation of the reaction is reasonable. However, the electron-transfer reaction is better represented by a bi-dimensional diagram when the force constants of solvent and of reactants/products are within a factor of 2 of each other.

The second type of effect, which solvent molecules can induce, is of a static nature. Solvent molecules may modify the rearrangements in the internal coordinate of a solute-driven reaction through non-specific (dipole moment, polarisability, etc.) or specific (hydrogen bonding) effects. In the context of self-exchange reactions, the solvent cannot produce changes on the reaction energy, ΔG^0 . Non-specific interactions with solvent molecules can cause small changes in force constants and bond lengths, but in general, these effects tend to compensate each other and have small impact on the rates. In general, such contributions to the energy barrier, together with some external reorganisation of the solvent molecules, are of the order of $\Delta G^* < 5 \text{ kJ mol}^{-1}$ and can be neglected.

**FIGURE 17.4**

Equipotential curves representing reactant and product in an electron-exchange reaction as a function of a solvent reorganisation coordinate and an internal coordinate, both treated as harmonic. The heavy line represents the classical reaction path (path of steepest descent from the top of the barrier). The dotted line represents the Evans–Polanyi “diabatic path”, whose energy dependence is determined by the generalised internal coordinate q_v . In this plot, $f_v/f_s = 5$ and the energy change from $q_v^0(R)$ to $q_v^‡$ is very close to the energy change from $[q_v^0(R), q_s^0(R)]$ to $[q_v^*, q_s^*]$.

17.2.3 Critique of the classical theory of Marcus

The approximations in which the classical TM is based have been mentioned above. They require a balance between the effects of having enough interaction between the reactants in the collisional complexes to achieve adiabaticity, but not enough as to decrease the barrier. The near-adiabaticity assumed for ET reactions, may not be applicable to all molecular systems, in particular when spin changes are involved or when the redox-active orbitals of the two reactants cannot approach each other very closely. On the other hand, if the redox partners interact very strongly, the electron coupling will increase to a point where its value reduces the energy barrier appreciably.

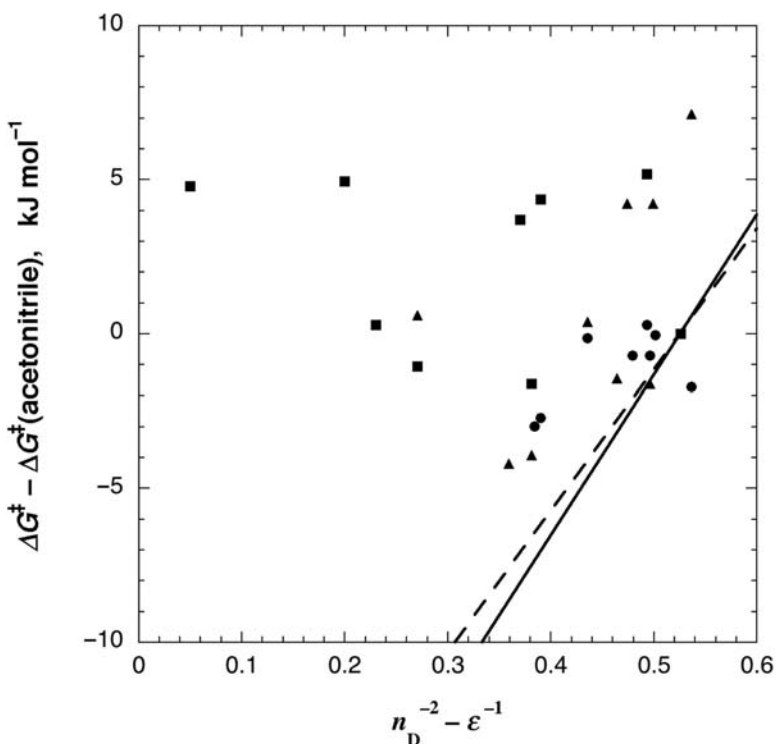
As far as the total reorganisation energy barrier, $\Delta G_{\text{total}}^*$, is concerned, TM-1 makes a separation between internal and medium modes. In hydrated transition-metal ions the first hydration sphere is treated as a static medium with an optical dielectric constant $\varepsilon_{\text{op}} = n_D^{-2}$, and the second hydration shell is regarded as a dielectric continuum characterised by the bulk dielectric constant of water. ET of hydrated transition-metal ions is, in general, a very slow processes and this is thought to be due mainly to the water-molecule dipole reorientation around the ions. However, the ratio of the force constants for hydrated metal ions in the first (internal contribution) and second coordination (external contribution) shells, is *ca.* $f_v/f_s \approx 8$. From the previous arguments, one would expect for such a regime the ET to be a predominantly solute-driven. In addition, in the presence of hydrated metal ions there is almost no free volume for expansion in the second hydration shell and the large difference in force constants cannot be compensated by a larger difference in configurational changes [10].

The most effective way to assess empirically the role of solvent reorganisation on electron-transfer reactions is to study self-exchange reactions involving one uncharged partner, in various solvents. Under such conditions the work term is zero ($w_r = 0$), the decrease in the solvent dielectric constant should lead to a decrease of ΔG_s^* in eq. (17.13), and to a logarithmic dependence of the rates on $\gamma = n_D^{-2} - \varepsilon^{-1}$. The results presented in Figure 17.5 argue against the effect of the solvent reorganisation on electron-transfer reactions proposed by the TM. A compensation of effects due to solvent dynamics has been excluded, at least for the ferrocene self-exchange [14]. According to Li *et al.*, TM currently overestimates ΔG_s^* by a factor of 2 in polar media and the source of error is due to the fact that during the Born charging of an ion the dielectric constant of the solvent is considered to be invariable [15].

The limiting case to assess the role of solvent reorganisation for an electron-transfer reaction is the absence of bulk solvent, that is, the gas phase. The study of gas phase ETs has the same simplifying and complicating features as the study of S_N2 reactions in the gas phase, discussed in detail in Chapter 11, Substitution Reactions. The reaction coordinate can be defined more precisely, but, on the other hand, the formation of precursor and successor complexes makes the interpretation of the kinetics more elaborate. For very negative enthalpies of formation of such complexes, which are identical for self-exchanges, the rates may be very fast even when the central barrier is high (Figure 11.14). The maximum rate of a bi-molecular ion-molecule reaction for a small molecule exchanging an electron with the corresponding ion, is very well described by the Langevin collision rate

$$k_L = 2\pi e \sqrt{\frac{\alpha}{\mu}} = 2.34 \times 10^{-9} \sqrt{\frac{\alpha'}{\mu}} \quad (17.18)$$

where α is the polarisability of the neutral and α' its polarisability volume. When the polarisability volume is expressed in Å³ and the reduced mass in amu, the numerical constant gives the collision rate in cm³ molecule⁻¹ sec⁻¹. For example, the Langevin

**FIGURE 17.5**

Solvent dependence of the free energy of activation of self-exchanges as a function of the solvent optical and static dielectric constants. The free energies were obtained from the experimental rates using the frequency factor of transition state theory, and are relative to those in acetonitrile. Tetraethoxyethylene^{0/-}: squares [11] and solid line, calculated with eq. (17.14) using $r = 6.7 \text{ \AA}$; ferrocene^{0/+}: circles [12] and dashed line, calculated with eq. (17.14) using $r = 7.6 \text{ \AA}$; sesquibicyclic hydrazine 22/u22: triangles [13].

collision rate of the electron exchange O_2/O_2^- ($\alpha' = 1.56 \text{ \AA}^3$, $\mu = 8.00 \text{ amu}$) is $k_L = 1.03 \times 10^{-9} \text{ cm}^3 \text{ sec}^{-1}$, or $6.2 \times 10^{11} \text{ M}^{-1} \text{ sec}^{-1}$. The self-exchange rate constant experimentally obtained for the gas-phase reaction of $^{18}\text{O}_2^+$ with $^{16}\text{O}_2$ is $(2.5 \pm 0.2) \times 10^{11} \text{ M}^{-1} \text{ sec}^{-1}$ [16]. This is almost half of k_L , which is the maximum expected for a symmetric charge-transfer reaction at thermal energy, since on each collision the system has essentially an equal probability to form the products or to go back to the reactants. Similar results have been obtained for other gas-phase self-exchanges such as DBr^+/HBr ($\alpha' = 3.61 \text{ \AA}^3$, $\mu = 40.5 \text{ amu}$, $k_L = 4.2 \times 10^{11} \text{ M}^{-1} \text{ sec}^{-1}$), which has a very similar thermal rate constant, $2.4 \times 10^{11} \text{ M}^{-1} \text{ sec}^{-1}$ [17]. These examples illustrate that the gas-phase self-exchange rates of small molecules and their ions are very fast, and show the relation with their polarisability and reduced mass, but indicate that they are unrelated to the respective Franck–Condon factors.

The apparent contradiction between the principles of the Golden Rule developed in Chapter 16, Transitions Between Electronic States, and the fast gas-phase electron self-exchanges can be resolved taking a closer look at the electronic couplings of these reactions. The formation of stable ion-molecule complexes and the small size of the reactants favours the electronic coupling between the two reactants. Detailed calculations for the H_2^+/H_2 system reveal that the electronic interaction leads to a very large energy splitting, and that it can be considered as an H_4^+ system with an energy splitting of 533 kJ mol^{-1} between ground and excited states at the equilibrium geometry of the ground state (1.59 \AA between the parallel axis defined by the two sets of nuclei, with a bond-dissociation energy of 76 kJ mol^{-1}) [18]. The electronic coupling in the O_2/O_2^- system is smaller, but it is still 56 kJ mol^{-1} , in agreement with the larger distance between the two moieties (3.18 \AA for the same geometry as described above, and a complexation energy of 12 kJ mol^{-1}) [19]. For such large electronic couplings, Morokuma expressed doubts that the non-adiabatic approach to ETs should be preferred over the adiabatic approach with a proper transition state [19]. The electronic couplings of self-exchanges involving small molecules in the gas phase are very high and such systems are not good models for self-exchanges in solution.

This difficulty can be overcome studying larger systems in the gas phase. For example, the exchange of one electron between ferrocene, $\text{Fe}(\text{Cp})_2$, and ferricinium ion, $\text{Fe}(\text{Cp})_2^+$, has been studied in many different solvents and in the gas phase. The symmetry of equilibrium conformation of $\text{Fe}(\text{Cp})_2$ in the gas phase is D_{5h} . Figure 17.6. The most stable complex formed between $\text{Fe}(\text{Cp})_2$ and $\text{Fe}(\text{Cp})_2^+$ in the gas phase maintains this symmetry, with the centres of the four cyclopentadienyl rings and the two metals along the same straight line. The complexation energy in this configuration is 24.3 kJ mol^{-1} and the distance between the two irons is 6.75 \AA [20]. At such a distance the calculated electronic coupling is only 135 cm^{-1} (1.6 kJ mol^{-1}) and the self-exchange can be regarded as a slightly non-adiabatic reaction, both in solution and in the gas phase. In fact, this electronic coupling is such as to place the reaction in the limit between adiabaticity and non-adiabaticity ($\kappa_{\text{el}} \approx 1$). The Langevin collision rate of the electron exchange $\text{Fe}(\text{Cp})_2/\text{Fe}(\text{Cp})_2^+$ ($\alpha' = 19 \text{ \AA}^3$, $\mu = 93 \text{ g mol}^{-1}$) is $k_L = 6.4 \times 10^{11} \text{ M}^{-1} \text{ sec}^{-1}$, but the experimental self-exchange rate is only $1.5 \times 10^{11} \text{ M}^{-1} \text{ sec}^{-1}$ at 350 K [21]. The experimental rate is

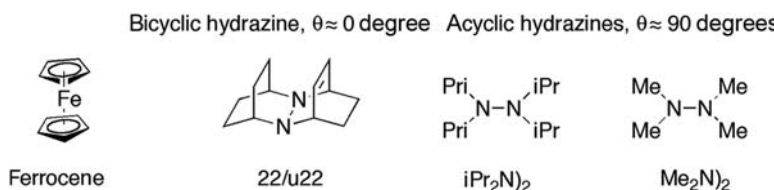


FIGURE 17.6

Molecular structures of species studied for their self-exchanges in different solvents and in the gas phase. The angle θ is lone pair/lone pair dihedral angle.

significantly less than half the Langevin rate, which is the maximum anticipated for an efficient electron exchange during the lifetime of each ion–molecule encounter pair. The actual observed efficiency is 0.2 ± 0.1 . The branching fraction for a precursor with energy E is defined as

$$BF(E) = \frac{k_{\text{et}}(E)}{k_{\text{et}}(E) + k_{\text{d}}(E)} \quad (17.19)$$

where k_{et} is the self-exchange between precursor and successor complex and k_{d} is the dissociation of the precursor complex in the isolated ion + molecule reactants. The microscopic efficiency at a given temperature can be expressed as a function of the canonical branching fraction

$$\Phi(T) = \frac{k_{\text{obs}}(T)}{k_{\text{L}}(T)} = \frac{BF(T)}{1 + BF(T)} \quad (17.20)$$

In the simplest approximation where the first-order k_{et} and k_{d} rate constants have the same frequency factors, the difference between the rates can be assigned to the difference in activation energies. The activation energy of k_{d} is the complexation energy, 24.3 kJ mol^{-1} . The efficiency of 0.2 ± 0.1 can be obtained when, under these approximations, the activation energy of the self-exchange is $28.0 \pm 2.5 \text{ kJ mol}^{-1}$. It is of interest that the temperature dependence of the $\text{Fe}(\text{Cp})_2/\text{Fe}(\text{Cp})_2^+$ self-exchange in acetonitrile gave an enthalpy of activation of 24 kJ mol^{-1} [22], very similar to the gas-phase value and consistent with the solvent independence illustrated in Figure 17.5.

The solvent independence and the large gas-phase barrier required to explain the inefficiency of the $\text{Fe}(\text{Cp})_2/\text{Fe}(\text{Cp})_2^+$ self-exchange is not compatible with the ΔG_s^* and ΔG_v^* values of eqs. (17.13) and (17.14), respectively. Using the refractive index ($n_D = 1.341$) and static dielectric constant ($\varepsilon = 37$) of acetonitrile together with a metal-metal distance of 7.6 \AA , eq. (17.13) gives $\Delta G_s^* = 24 \text{ kJ mol}^{-1}$. Using the metal-ring centre distances and associated force constants for $\text{Fe}(\text{Cp})_2$ and $\text{Fe}(\text{Cp})_2^+$ given in Table 17.1, eq. (17.14) leads to $\Delta G_v^* = 1 \text{ kJ mol}^{-1}$, when $c_n = 4$ because of the presence of two vibrating bonds in each reactant. The success of TM on estimating the self-exchange barrier of $\text{Fe}(\text{Cp})_2/\text{Fe}(\text{Cp})_2^+$ in acetonitrile but not in the gas-phase substantiates the suspicion that it overestimates the solvent contribution ΔG_s^* in polar media and that is compensated by an underestimate of the internal reorganisation ΔG_v^* . In the gas phase, this compensation cannot take place and the model fails to reproduce the experimental barrier of the $\text{Fe}(\text{Cp})_2/\text{Fe}(\text{Cp})_2^+$ exchange.

An interesting case study involving organic molecules is the self-exchange of alkylhydrazines^{0/+}, some of which are illustrated in Figure 17.6. These self-exchanges are particularly interesting because the molecules are approximately spherical, the active orbitals in the electron-transfer process are centred in the nitrogen atoms, and these are isolated from the other partner by a “hydrocarbon layer”. The sphere centred in the NN bond has a radius of 3.93 \AA for $22/\text{u}22$ and 4.34 \AA for $i\text{Pr}_2\text{N}_2$. In addition, the self-exchanges of alkylhydrazines are much slower than those

of the more common aromatic molecules, and, in solution, they can be studied far from the limit of diffusion-controlled rates.

The solvent independence of the 22/u22 self-exchanges was presented in [Figure 17.5](#). The gas-phase electron exchange in the $\text{Me}_2\text{N}_2)_2/\text{Me}_2\text{N}_2)_2^+$ complex was also studied by Nelsen and co-workers. The heat of association of the complex is -54 kJ mol^{-1} and the activation energy is 23 kJ mol^{-1} , which means that the central barrier for the self-exchange in the complex is 77 kJ mol^{-1} [23]. This barrier is very close to that obtained in acetonitrile, 72 kJ mol^{-1} , and similar results were obtained for eight other compounds, which lead Nelson to conclude that “There is apparently a closer correspondence of ET barriers in the presence and absence of solvent than most people expected” [24]. In fact, [eq. \(17.13\)](#) with $r = 8 \text{ \AA}$ and the data of acetonitrile gives $\Delta G_s^* = 23 \text{ kJ mol}^{-1}$, but the barrier in the gas phase is not less than in the acetonitrile. These data indicate that ETs in organic systems also involve a completely solute-driven processes.

The success of TM on the estimation of self-exchange rates in [Figure 17.2](#) now becomes a matter of concern. If the rates are properly calculated and the solvent contribution ΔG_s^* in polar media is overestimated, then it seems that this is compensated by an underestimate of the internal reorganisation ΔG_v^* .

17.2.4 Intersecting-state model as a criterion for solute-driven electron transfers

The energy barrier of the $\text{Fe}(\text{Cp})_2/\text{Fe}(\text{Cp})_2^+$ self-exchange can also be explored with the intersecting-state model (ISM), under the approximations discussed in [Chapter 16](#), Transitions Between Electronic States, for the use of this model in the calculation of Franck–Condon factors. According to ISM, the sum of bond distortions from the equilibrium to the “transition-state” configuration is, for a self-exchange reaction,

$$d_0 = |l_r^* - l_r| + |l_p^* - l_p| = \frac{0.108}{n^*} (l_{\text{ox}} + l_{\text{red}}) \quad (17.21)$$

where the term “transition state” is employed to describe the activated nuclear configuration that the reactants must reach to transfer an electron. The bond orders are preserved along the reaction coordinate of an ET, and n^* represents the average bond order of the two reactants. For $\text{Fe}(\text{Cp})_2$ this requires an analysis of its electronic configuration, shown in [Figure 17.7](#).

The principal bonding interaction occur between the d_{xz} and d_{yz} orbitals (transforming together as e'_1) and the e''_1 symmetry-adapted linear combinations of ligand orbitals. Their excellent overlap gives delocalised π -type metal-ring bonds. The $d_{x^2-y^2}$ and d_{xy} (e'_2) orbitals interact with e'_2 symmetry-adapted linear combinations of ligand orbitals. The d_{z^2} (a'_1) orbital, although of the same symmetry as the Cp π orbitals and strongly directed towards the ligands, has a nodal surface that coincides with that of the Cp π orbitals and their interaction is weak. The bonding character of the e'_2 and a'_1 orbitals (LUMO: lowest unoccupied

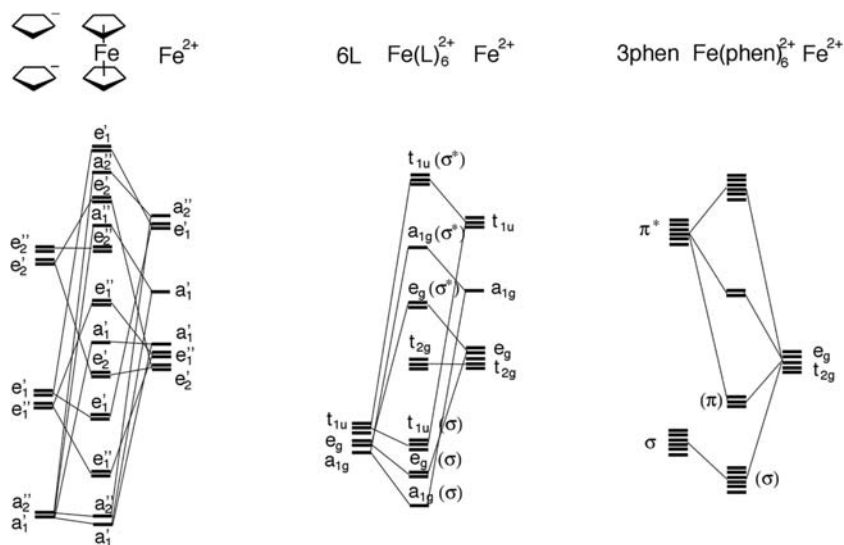


FIGURE 17.7

Molecular orbitals of transition-metal complexes, employed to estimate metal–ligand-bond orders. Left: ferrocene on the assumption of a D_{5h} symmetry; in ferrocene and the other 18-electrons bis(cyclopentadienyl) complexes the a_1' orbital and all the other lower orbital are full, but the e_1'' and higher energy orbitals are empty. Centre: $\text{Fe}(\text{OH}_2)_6^{2+}$ with a O_h symmetry. Right: $\text{Fe}(\text{phen})_6^{2+}$ with O_h symmetry, emphasising the role of the ligands π^* orbitals in π -back bonding.

molecular orbital) can be assessed by removing one of their electrons to yield $\text{Fe}(\text{Cp})_2^+$. This process is accompanied by an increase in the bond length and a decrease in the force constant, which are consistent with a decrease in M–Cp bonding. Thus the bond order of $\text{Fe}(\text{Cp})_2$ must be greater than 1.0, but probably less than 1.5. In contrast, the bond order of $\text{Fe}(\text{Cp})_2^+$ is reduced with respect to $\text{Fe}(\text{Cp})_2$, and should be close to 1.0. A reasonable estimate for the $\text{Fe}(\text{Cp})_2/\text{Fe}(\text{Cp})_2^+$ self-exchange is $n^* = 1.25$, which gives $d_0 = 0.287 \text{ \AA}$.

The transition-state energy of a self-exchange is given by

$$\Delta G_0^* = \frac{1}{2} f_{\text{eff}} \left(\frac{d_0}{2} \right)^2 \quad (17.22)$$

where the value of the effective force constant depends on the use of a normal or local mode treatment of the reactive modes, as discussed in Chapter 16, Transitions Between Electronic States. The Cp–M stretch force constants of $\text{Fe}(\text{Cp})_2$ and $\text{Fe}(\text{Cp})_2^+$ are obtained from

$$f_{\text{sym}} = 4\pi^2 \bar{\nu}_{\text{sym}}^2 c^2 \mu = 3.548 \times 10^{-4} \bar{\nu}_{\text{sym}}^2 \mu \quad (17.23)$$

where the constant involves the symmetric stretching frequency expressed in cm^{-1} , the reduced mass in amu and the force constant is in $\text{kJ mol}^{-1} \text{\AA}^{-2}$. These values for the force constants rely on a simple three-body model where the central atom does not move within the symmetrical stretching regime and each Cp ring is approximated by a point mass equal to 65 amu, that is, $\mu = 65$ amu. The Cp–M–Cp symmetric stretching occur at $\bar{\nu}_{\text{sym}} = 303 \text{ cm}^{-1}$ for $\text{Fe}(\text{Cp})_2$ and at a slight lower frequency for $\text{Fe}(\text{Cp})_2^+$, consistent with its longer Cp–M bond. The anti-symmetric mode is observed at a higher frequency, $\bar{\nu}_{\text{asym}} = 478 \text{ cm}^{-1}$. Chapter 16, Transitions Between Electronic States, presented the difference between local and normal mode behaviour, and concluded that CH bonds in aromatic hydrocarbons are best described as a local modes. Local mode behaviour is expected from small inter-bond coupling constants between anharmonic vibrational modes. The inter-bond coupling constant is related to the vibrational splitting between symmetric and anti-symmetric stretching vibrations. For example, the CH symmetric stretching of benzene (a_{1g} symmetry, $\bar{\nu}_1$ in the Herzberg notation) occurs at 3062 cm^{-1} , whereas the CH anti-symmetric stretching (b_{1u} symmetry, $\bar{\nu}_5$) occurs at 3068 cm^{-1} , an inter-bond coupling of $\xi = |\bar{\nu}_{\text{sym}} - \bar{\nu}_{\text{asym}}|/2 = 3 \text{ cm}^{-1}$. This is in contrast with the a_{1g} symmetry ring-breathing mode ($\bar{\nu}_2 = 992 \text{ cm}^{-1}$) and b_{2u} symmetry alternate elongation-contraction CC mode ($\bar{\nu}_9 = 1310 \text{ cm}^{-1}$), which have a coupling $\xi = 159 \text{ cm}^{-1}$ and are best described as normal modes. The splitting between symmetric ($\bar{\nu}_1$) and anti-symmetric ($\bar{\nu}_3$) metal–ligand-stretching vibrations in octahedral hexa-ammine or hexa-aqua complexes is also small ($\xi = 10–20 \text{ cm}^{-1}$) and these have to be treated as local modes. However, the values observed for metallocenes ($\xi = 90–60 \text{ cm}^{-1}$) are intermediate between those of typical local and normal mode behaviour. Using a local mode behaviour, the calculated barrier is $\Delta G^* = 26.5 \text{ kJ mol}^{-1}$, intermediate between the value inferred from the gas-phase efficiency and the enthalpy of activation in acetonitrile.

The Franck–Condon factor of the $(\text{Me}_2\text{N}_2)_2/\text{Me}_2\text{N}_2)_2^+$ exchange is principally associated with changes in the NN bond. The X-ray geometries of the similar $i\text{Pr}_2\text{N}_2)_2$ and $i\text{Pr}_2\text{N}_2)_2^+$ compounds are known, and reveal a decrease in the NN bond length from 1.394 to 1.333 Å when the neutral [25] is oxidised to the cation [26], concomitant with the change in the lone pair/lone pair dihedral angle θ from *ca.* 90 degrees to *ca.* 0 degrees. Clearly, the removal of a non-bonding electron from a nitrogen atom leads to an increase in bonding, and the N–N bond acquires some three-electron-bond character. For simplicity, this bond can still be characterised with $n^* = 1$, which is probably an underestimate but compensates for the neglect of changes in the other bonds. With $n^* = 1$, the N–N-bond lengths discussed above and the corresponding force constants given in Appendix III, Parameters Employed in ISM Calculations, eq. (17.21) gives $d_0 = 0.2945 \text{ \AA}$, which, using eq. (17.22), leads to $\Delta G^* = 78 \text{ kJ mol}^{-1}$. In this case, there is no ambiguity as to the nature of the local or normal mode behaviour of the N–N mode, because only one bond is involved in the reaction coordinate, and the force constant is the average of the neutral and cation N–N force constants. The barrier calculated by this model is in excellent agreement with the barriers observed in the gas phase and in solution.

It seems that the kinetics of self-exchange reactions can be explained within the ISM formalism. However, reducing the role of the solvent to a thermodynamic effect, which is reflected in ΔG^0 , and, occasionally, to specific interactions (hydrogen bonding, heat sink) with the redox centres, is a major departure from the paradigm shared by most practitioners of this field. Figure 17.5 and the similarity between electron-transfer barriers in solution and in the gas phase do not leave much room for the solvent in self-exchanges. From the theoretical point of view, it is also increasingly clear that regarding the solvent as a dielectric continuum, as done in TM, leads to an overestimate of ΔG_s^* in polar media [27]. In contrast with TM, ISM employs a common theoretical formalism for many important types of chemical transformations, which stresses the role of the electronic properties of reactive bonds and also of reaction energy in chemical reactivity. This formalism was discussed in detail in the previous chapters, and will be pursued further in this chapter in the interpretation of the rates of electron-transfer reactions.

17.3 ISM and electron-transfer reactions

17.3.1 Representing electron-transfer reactions by the crossing of two potential-energy curves

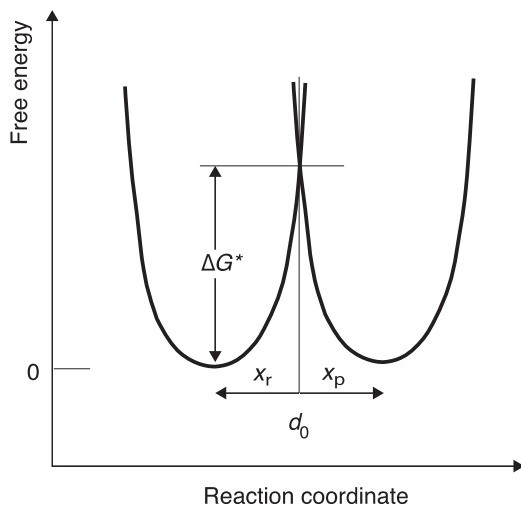
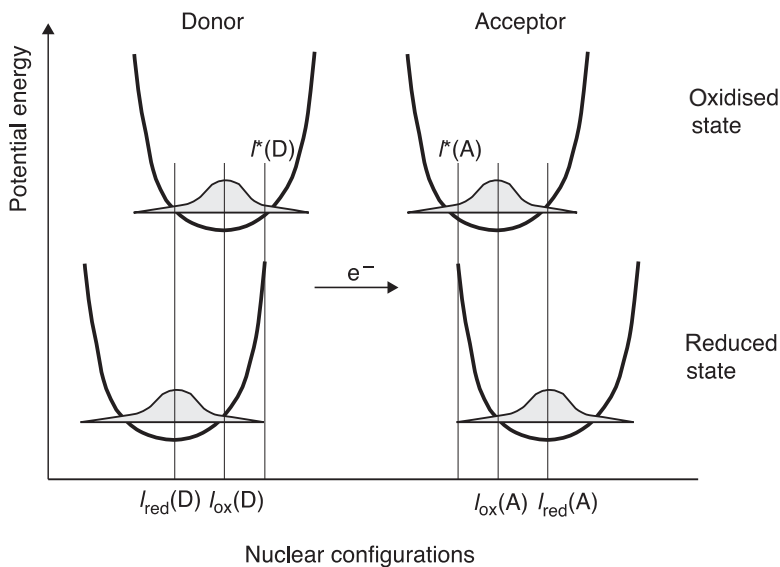
ET reactions, such as the $\text{Fe}(\text{OH}_2)_6^{3+/2+}$ self-exchange, mechanism (17.I), do not involve any bond breaking. In this specific case, the Fe–O bonds between the iron ion and the six water molecules of the first coordination shell remain intact. However, this does not mean that there is not a substantial distortion of the Fe–O bonds in the electron-transfer process. In fact, such bond rearrangement must occur to trigger the electron-transfer event.

The molecular orbitals for the σ metal–ligand bonds in $\text{Fe}(\text{OH}_2)_6^{2+}$ arise from the interaction of metal $4s\ 4p_x\ 4p_y\ 4p_z\ 3d_{x_2-y_2}\ 3d_{z_2}$ orbitals with ligand σ orbitals sharing the same symmetry (Figure 17.7). When one considers the distribution of electron spins in the d orbitals of the ligand fields of $\text{Fe}(\text{OH}_2)_6^{3+}$ and $\text{Fe}(\text{OH}_2)_6^{2+}$, it becomes evident that the electron to be transferred is one from a t_{2g} (type π) orbital to an orbital of the same symmetry in the other ion. This means that the bond order of each bond is preserved, $n = 1$, and that no electronic restriction exists for such a transfer. In this ET, the spin changes by $1/2$, $S(\text{Fe}^{3+}) = 5/2$ and $S'(\text{Fe}^{2+}) = 4/2$, where S and S' are the spin quantum numbers of oxidised and reduced species, respectively.

Let us assume, for simplicity, that the hydrated iron ions are bonded to a single water molecule each and, therefore, have a single Fe–O bond



Figure 17.8 represents in qualitative terms the potential-energy curves of the two metal–water bonds of the oxidised and reduced species of reactants. According to the Franck–Condon principle, the $\text{Fe}^{3+}-\text{O}$ and $\text{Fe}^{2+}-\text{O}$ bonds of

**FIGURE 17.8**

Transformation of the reaction coordinate according to ISM. The shaded areas in the upper panel reflect the probabilities of finding the reactants in the reduced and oxidised states in the nuclear configurations. The ISM reaction coordinate is the sum of the two reactants bond distortions from equilibrium to transition state configurations.

this self-exchange have to reach a common configuration, loosely called “transition state”, before the electron is transferred. The products then relax from their configuration at the “transition state” to their equilibrium bond lengths. This process is illustrated in the top panel of [Figure 17.8](#). The bottom panel of that figure shows the more common representation of the electron-transfer process in terms of intersecting free-energy curves representing reactants and products.

A word of caution must be said on the crossing between the reactants and products curves in [Figure 17.8](#). The crossing is represented as weakly avoided, assuming a weak electronic coupling between reactants and products curves. This is consistent with non-adiabatic ETs, where the energy of the crossing point corresponds to the activation energy. The limit between adiabatic and non-adiabatic reactions can be defined, rather arbitrarily, as an electronic coupling of 4 kJ mol^{-1} (330 cm^{-1}), which is enough to let the electronic factor approach unity, but not as much as to reduce the barrier appreciably. A stronger non-adiabaticity ($|V_{\text{ks}}| < < 4 \text{ kJ mol}^{-1}$) does not change meaningfully the energy of the crossing point, but reduces the reaction frequency. This word of caution relates to the designation of the crossing point as the “transition state”. A proper transition state, defined in [Chapter 6](#), Reactivity in Thermalised Systems, is a critical intermediate where one of its degrees of freedom is the reaction coordinate. This is not the case represented in [Figure 17.8](#). In an electron-transfer reaction, the two reactants maintain the integrity of their bonds at the “transition state”. In order to emphasise the difference between this case and that of a bond-breaking–bond-forming reaction, where the bond order of the reactive bond tends to zero as the reaction proceeds along the reaction coordinate, [Figure 17.8](#) represents the bond lengths at the “transition state” by l^* rather than by l^\ddagger .

The contributions of donor (D) and acceptor (A) to the reaction barrier of a self-exchange can be explicitly written

$$\Delta G_0^* = \frac{1}{2} f_{\text{red}} [l_{\text{red}}^*(\text{D}) - l_{\text{red}}(\text{D})]^2 + \frac{1}{2} f_{\text{ox}} [l_{\text{ox}}^*(\text{A}) - l_{\text{ox}}(\text{A})]^2 \quad (17.24)$$

The calculation of the barrier requires a criterion to determine l^* . [Eq. \(17.14\)](#) of Marcus theory was obtained making $l^* = l_{\text{red}}^* = l_{\text{ox}}^*$, and minimising [eq. \(17.24\)](#) with respect to l^* . This procedure gives

$$l^* = \frac{f_{\text{red}} l_{\text{red}}(\text{D}) + f_{\text{ox}} l_{\text{ox}}(\text{A})}{f_{\text{red}} + f_{\text{ox}}} \quad (17.25)$$

which replaced in [eq. \(17.24\)](#) gives [eq. \(17.14\)](#). This procedure leads to the prediction that for systems with $l_{\text{red}} \approx l_{\text{ox}}$, such as $\text{Fe}(\text{Cp})_2^{0/+}$, $\Delta G_v^* \approx 0$ and the energy barrier in the gas phase should be zero. As discussed above, this is not substantiated by the barrier deduced for the ferrocene/ferrocenium self-exchange in the gas phase.

An alternative to this energy minimisation procedure, and to the consequent $\Delta G_v^* = 0$ for $l_{\text{red}} = l_{\text{ox}}$, is to use the relations between the bond lengths and bond extensions in [Figure 17.8](#)

$$\begin{aligned} d_0 &= x_r + x_p \\ x_r &= |l_{\text{red}}^*(\text{D}) - l_{\text{red}}(\text{D})| + |l_{\text{ox}}^*(\text{A}) - l_{\text{ox}}(\text{A})| \\ x_p &= |l_{\text{ox}}^*(\text{D}) - l_{\text{ox}}(\text{D})| + |l_{\text{red}}^*(\text{A}) - l_{\text{red}}(\text{A})| \end{aligned} \quad (17.26)$$

which can be simplified using the Franck–Condon principle, that is, $l_{\text{red}}^*(\text{D}) = l_{\text{ox}}^*(\text{D}) = l_{\text{D}}^*$ and $l_{\text{ox}}^*(\text{A}) = l_{\text{red}}^*(\text{A}) = l_{\text{A}}^*$, and for the explicit case of a self-exchange, that is, $l_{\text{red}}(\text{D}) = l_{\text{red}}(\text{A}) = l_{\text{red}}$ and $l_{\text{ox}}(\text{D}) = l_{\text{ox}}(\text{A}) = l_{\text{ox}}$,

$$d_0 = |l_{\text{D}}^* - l_{\text{red}}| + |l_{\text{A}}^* - l_{\text{ox}}| + |l_{\text{D}}^* - l_{\text{ox}}| + |l_{\text{A}}^* - l_{\text{red}}| \quad (17.27)$$

These bond extensions can be expressed in terms of one reference state, arbitrarily chosen as the reduced state of the donor,

$$d_0 = |l_{\text{D}}^* - l_{\text{red}}| + |l_{\text{A}}^* - l_{\text{ox}}| + |l_{\text{D}}^* - l_{\text{red}} + \Delta l| + |l_{\text{A}}^* - l_{\text{ox}} - \Delta l| \quad (17.28)$$

where $\Delta l = l_{\text{red}} - l_{\text{ox}}$. Rearranging

$$|l_{\text{A}}^* - l_{\text{ox}}| = \frac{d_0}{2} - |l_{\text{D}}^* - l_{\text{red}}| \quad (17.29)$$

[Eq. \(16.57\)](#) can be used to describe the classical probability distribution of the donor in the reduced state by

$$\iota(\text{D}) = \frac{1}{\sqrt{2\pi}\sigma_l} \exp\left\{-\frac{[l_{\text{red}}^*(\text{D}) - l_{\text{red}}(\text{D})]^2}{2\sigma_l^2}\right\} \quad (17.30)$$

and that of the acceptor in the oxidised state

$$\alpha(\text{A}) = \frac{1}{\sqrt{2\pi}\sigma_l} \exp\left\{-\frac{[l_{\text{ox}}^*(\text{A}) - l_{\text{ox}}(\text{A})]^2}{2\sigma_l^2}\right\} \quad (17.31)$$

Using [eq. \(17.29\)](#) these equations can now be expressed in terms of a common variable, $x = l_{\text{D}}^* - l_{\text{red}}$, and the transfer from a particular extension x in the donor distribution can be paired with the transfer in the acceptor distribution with the same extension x . Following the development of [eqs. \(16.90\)–\(16.96\)](#), gives

$$J_0 = \int_{-\infty}^{+\infty} \iota(\text{D})\alpha(\text{A})dx = \frac{1}{2\pi\sigma_x^2} \int_{-\infty}^{+\infty} \exp\left[-\frac{(x)^2}{2\sigma_x^2} - \frac{(\delta-x)^2}{2\sigma_x^2}\right] dx \quad (17.32)$$

where $\delta = d_0/2$, and

$$J_0 = \frac{1}{\sqrt{4\pi}\sigma_x^2} \exp\left[-\frac{\delta^2}{4\sigma_x^2}\right] \quad (17.33)$$

Given that $\sigma^2 = k_{\text{B}}T/f$, and assuming that all the oscillators have the same force constant f , the numerator in the exponential term is an energy

$$\Delta G_0^*(\text{paired}) = \frac{1}{4}f\left(\frac{d_0}{2}\right)^2 \quad (17.34)$$

that corresponds to the contribution of each oscillator for the intrinsic barrier of the self-exchange, ΔG_0^* . This procedure defines a reaction coordinate for ET that is characterised by a common bond distortion of both reactants in a self-exchange reaction.

The bond-length distortions proceed without breaking the bonds and the identical nuclear configurations of the Fe–O bonds can be regarded as having the

same bond order n^* at the “transition state”. This principle is also at the foundation of ISM, and the nuclear distortion from equilibrium to the “transition state” of a self-exchange reaction should have the form of eq. (17.21).

According to eq. (17.22), the energy of the crossing point depends on the value of the effective force constant. In TM-1, eq. (17.14), the force constant is obtained from a symmetrisation procedure and then multiplied by the number of bonds in the reaction coordinate. In ISM, the transformation in Figure 17.8 corresponds to placing the two reactants in an average energy position, to obtain a thermo-neutral process for a self-exchange, and their effective force constant is also the average of the force constants of the oxidised and reduced species,

$$f_r = \frac{f_{\text{ox}} + f_{\text{red}}}{2} \quad (17.35)$$

The same treatment is used to obtain the effective force constant of products, f_p . Eq. (17.35) is an effective way to calculate the reaction barrier in eq. (17.24) using the common bond-distortion procedure. For consistency, the same averaging procedure is also applied to equilibrium bond lengths

$$l_r = \frac{l_{\text{ox,eq}} + l_{\text{red,eq}}}{2} \quad (17.36)$$

It must be emphasised that eq. (17.21) accounts for the existence of two reactants (and two products) in the reaction coordinate, because it gives the sum of the bond extensions in the two species.

17.3.2 Adiabatic self-exchanges of transition-metal complexes

Following ISM, the sum of bond lengths extensions to the transition state in a self-exchange is given by eq. (17.21). Since the bond order of $\text{Fe}^{3+}-\text{OH}_2$ and $\text{Fe}^{2+}-\text{OH}_2$ can be approximated as a single bond (bond order $n = 1$), the “transition-state”—bond-order is unity, $(n_{\text{ox}} + n_{\text{red}})/2 = n^* = 1$. The real molecular system contains six single bonds in each reactant, mechanism (17.1), because each Fe ion has six water molecules in the first coordination shell. In view of the small inter-bond coupling of the $\text{Fe}^{3+}-\text{OH}_2$ bonds in these complexes, the six iron–oxygen bonds behave as local modes, and their effective force constant is

$$f = f_r = f_p = \sqrt{6} \frac{f_{\text{ox}} + f_{\text{red}}}{2} \quad (17.37)$$

The energy barrier, ΔG^* , will be given by

$$\Delta G^* = \frac{1}{2} \sqrt{6} \frac{f_{\text{ox}} + f_{\text{red}}}{2} \left(\frac{d}{2} \right)^2 \quad (17.38)$$

or taking into consideration eq. (17.21),

$$\Delta G^* = \frac{\sqrt{6}}{16} (f_{\text{ox}} + f_{\text{red}}) \left[\frac{0.108}{n^*} (l_{\text{ox}} + l_{\text{red}}) \right]^2 \quad (17.39)$$

With the relevant structural data listed in [Table 17.1](#), one estimates

$$\Delta G^* = \frac{\sqrt{6}}{16} (1.53 + 0.96) \times 10^3 \text{ kJ mol}^{-1} \text{ Å}^{-2} \left[\frac{0.108}{1} (1.98 + 2.10) \text{ Å} \right]^2 \quad (17.40)$$

and $\Delta G^* = 74 \text{ kJ mol}^{-1}$.

The frequency for conversion of the reactants species to the activated common configuration is that of the stretching frequency modes of the Fe–O bonds in the hydrated metal ions: $\bar{\nu}_{\text{ox}} = 490 \text{ cm}^{-1}$ and $\bar{\nu}_{\text{red}} = 389 \text{ cm}^{-1}$. With an average frequency $\bar{\nu}_N = 440 \text{ cm}^{-1}$, the frequency factor for the process, ν , is that of the nuclear motions, ν_n ,

$$\nu = \nu_n = \bar{\nu}_N c = 1.3 \times 10^{13} \text{ sec}^{-1} \quad (17.41)$$

when the effective electronic frequency is higher than this value. This is true when $|V_{ks}^e| > 300 \text{ cm}^{-1}$ (3.6 kJ mol^{-1}) for $\lambda = 4\Delta G^* = 296 \text{ kJ mol}^{-1}$, as discussed in [Section 16.7](#). Under these conditions, which are in the borderline region between non-adiabatic and adiabatic processes, the rate constant is given by

$$k_{\text{ISM}} = K_c \nu_n \exp\left(-\frac{\Delta G^*}{RT}\right) \quad (17.42)$$

where K_c is the equilibrium constant for the formation of reactant pairs separated by a distance r . According to the Eigen–Fuoss model, the stability constant of the precursor complex is

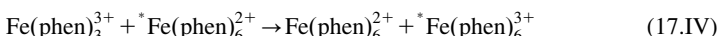
$$K_c = \frac{4\pi N_A r^3}{3000} \exp\left(-\frac{w_r}{RT}\right) \quad (17.43)$$

and its numerical value ranges from 0.1 M^{-1} for the $\text{Fe}(\text{OH}_2)_6^{3+/2+}$ exchange when the ionic strength is 0.55 M , to 0.8 M^{-1} for the $\text{Fe}(\text{Cp})_2^{+0}$ exchange. Lower values of r decrease K_c but increase $|V_{ks}^e|$. For the small range of $|V_{ks}^e|$ that corresponds to nearly adiabatic reactions where $\nu \approx \nu_n$ these effects tend to compensate each other and the neglect of $|V_{ks}^e|$ in the lowering of ΔG^* , can be offset with the assumption of $K_c \approx 1$. Thus for bimolecular electronic transfers in solutions with a high ionic strength or involving one uncharged partner, it is reasonable to assume that $K_c \approx 1 \text{ M}^{-1}$. Under these approximations, the rate constant estimated by ISM for the reaction $\text{Fe}(\text{OH}_2)_6^{3+/2+}$ at 298 K , is $k_{\text{ISM}} = 1.2 \text{ M}^{-1} \text{ sec}^{-1}$, in very good agreement with the experimental rate constant, $k_{\text{exp}} = 1.1 \text{ M}^{-1} \text{ sec}^{-1}$.

Given the approximate nature of these calculations, the frequency factor for bi-molecular ETs in transition-metal complexes can be taken as $K_c \nu_n = 10^{13} \text{ M}^{-1} \text{ sec}^{-1}$. With this pre-exponential factor and the barrier calculated above for the $\text{Fe}(\text{Cp})_2/\text{Fe}(\text{Cp})_2^+$ exchange, $\Delta G^* = 26.5 \text{ kJ mol}^{-1}$ with $n^* = 1.25$, ISM calculations give $k_{\text{ISM}} = 2.1 \times 10^8 \text{ M}^{-1} \text{ sec}^{-1}$. The experimental rate in acetonitrile, extrapolated to zero ionic strength, is $9.3 \times 10^6 \text{ M}^{-1} \text{ sec}^{-1}$ [22]. It could be anticipated that the calculated rate would be an upper limit to the experimental values in solution because the bonding character of the e'_2 and a'_1 orbitals was over-emphasised. With $n^* = 1$, a lower bound for this parameter, the calculated rate is $k_{\text{ISM}} = 5.0 \times 10^5 \text{ M}^{-1} \text{ sec}^{-1}$.

17.3.3 Outer-sphere electron transfers with characteristics of an inner-sphere mechanism

Another representative class of outer-sphere ETs is the exchange between iron (II/III)–phenanthroline complexes



The metallic centres in the collisional complex are quite far apart, at a minimum distance of $r_{\text{Me,Me}} = 13.6 \text{ \AA}$, due to the size of the ligands. In contrast, for the $\text{Fe(OH}_2)_6^{3+/2+}$ complexes such distance is much smaller, and an electron can jump between the two iron atoms leading to a nearly adiabatic reaction, as illustrated in Figure 17.9. In $\text{Fe(phen)}_3^{3+/2+}$ complexes the distance is too large for a nearly adiabatic electron jump from one metal centre to the other. However, although the electron is exchanged between $d(\pi)$ orbitals centred in metal ions 13.6 Å far apart, the ligand π^* (LUMO) has a good overlap with the $d(\pi)$ iron orbital and provides a conductive *bridge* for the transfer of the electron from metal to the other. This orbital connection, also illustrated in Figure 17.9, favours a nearly adiabatic ET between iron–phenanthroline complexes.

In addition to providing a conducting bridge for the transfer of an electron, the good overlap between the π^* (LUMO) orbitals of the ligands and the t_{2g} (d_{xy} , d_{xz} , d_{yz}) orbitals of the metal also allows for the possibility of π bonding. Pi bonding in coordination complexes is most relevant when the ligand has

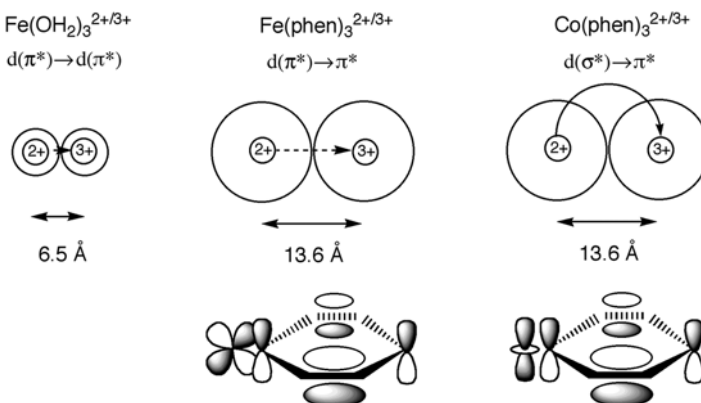


FIGURE 17.9

Schematic illustration of the distances involved in electron transfers between metal centres, with the emphases on the favourable orbital overlap between the active redox orbitals of iron and the phenanthroline π^* (LUMO) orbital, and the zero overlap between the redox active orbitals of cobalt and the same ligand orbital.

empty π^* orbitals, or π acceptor ligands. In this case, the ligand π^* orbitals have energies greater than, but near those of the metal t_{2g} orbitals, with which they overlap. As a result, they form molecular orbitals, with the bonding orbitals being lower in energy than the initial metal t_{2g} orbitals. The corresponding anti-bonding orbitals are higher in energy than the e_g σ anti-bonding orbitals. Metal ion d electrons occupy the bonding orbitals, resulting in increased bonding strength and bond orders. This metal-to-ligand π bonding is also called π back bonding, with electrons from d orbitals of the metal donated to the ligands [28]. In the first approximation, the number of bonding orbitals increases to 9, and the average bond order of the $\text{Fe}(\text{phen})_3^{2+}$ complex is $n = 1.5$. The barrier calculated with the data on the Fe–N bonds listed in Table 17.1, the local-mode approximation for the six modes involved in the reaction coordinate and $n^* = 1.5$, is $\Delta G^* = 35 \text{ kJ mol}^{-1}$. This barrier together with $K_c \nu_n = 10^{13} \text{ M}^{-1} \text{ sec}^{-1}$ gives $k_{\text{ISM}} = 7.3 \times 10^6 \text{ M}^{-1} \text{ sec}^{-1}$, smaller than the experimental value, $k_{\text{exp}} = 3.3 \times 10^8 \text{ M}^{-1} \text{ sec}^{-1}$. This difference indicates the need for modification of the assumptions used to derive the parameters employed in the calculation. Figure 17.10 shows that a resonance effect in the transition state of an ET involving metal–ligand π back bonding may shift of electronic density around the metal–ligand bonds in the activated common configuration such that $n^* = 2$. This effect is equivalent to the maximum electron inflow inside the transition state provided by the electrophilicity index of Parr. The importance of resonance in ETs was emphasised earlier for gas phase reactions, and Eberson and Shaik have argued that it also plays an important role in solution when there is a good overlap between the two LUMO of the two reactants [29]. With $n^* = 2$ and the data in Table 17.1, eq. (17.40) gives $\Delta G^* = 20 \text{ kJ mol}^{-1}$ and eq. (17.42) gives $k_{\text{ISM}} = 3 \times 10^9 \text{ M}^{-1} \text{ sec}^{-1}$. Since this value is very close to the rate of diffusion in water, $k_{\text{diff}} = 3 \times 10^9 \text{ M}^{-1} \text{ sec}^{-1}$, the comparison with the experiment should be made using the calculated “observed” rate constant, k_{obs} , that accounts for the effect of diffusion the expression

$$\frac{1}{k_{\text{obs}}} = \frac{1}{k_{\text{diff}}} + \frac{1}{k_{\text{ISM}}} \quad (17.44)$$

This leads to a rate, $k_{\text{obs}} = 1.5 \times 10^9 \text{ M}^{-1} \text{ sec}^{-1}$, in good agreement with experiment.

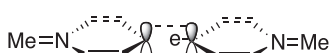


FIGURE 17.10

Electronic interaction between metal–ligand complexes when the ligands have empty π^* orbitals, leading to transition state bond orders $n^* = 2$.

17.4 Non-adiabatic self-exchanges of transition-metal complexes

17.4.1 A source of non-adiabaticity: orbital symmetry

An important example of non-adiabatic ET is the self-exchange process of the phenanthroline complex of cobalt ions (II and III),



Although this appears to be identical to the reaction (17.IV), the rate of ET is considerably slower, *ca.* seven orders of magnitude, $k = 12 \text{ M}^{-1} \text{ sec}^{-1}$. This dramatic difference is related to the nature of the orbitals involved. In contrast to the reactions of $\text{Fe}(\text{phen})_3^{3+/2+}$, where the transfer of the electron occurs from a d (t_{2g}) orbital, of π symmetry, the active redox orbitals of $\text{Co}(\text{phen})_3^{2+}$ are d(e_g) orbitals, of σ^* symmetry. The overlap of this orbital with the LUMO orbital of the ligand is zero by symmetry reasons, as illustrated in Figure 17.9. Therefore the π^* LUMO orbital of the ligand cannot operate as a conducting wire between the two Co-metal centres that are 13.6 Å apart. The only way that the electron can be transferred from one ion to the other is through quantum mechanical tunnelling.

17.4.2 Electron tunnelling at a distance

The expressions for quantum mechanical tunnelling were presented in Chapter 6, Reactivity in Thermalised Systems, and the application to ETs was discussed in Chapter 16, Transitions Between Electronic States. Briefly, the electron tunnelling probability through a square-potential barrier can be calculated when the height and width of the barrier are known. In ET between the cobalt centres presented above, the width of the tunnelling barrier is the metal-to-metal distance, $r = 13.6 \text{ \AA}$. In aromatic hydrocarbons, where the LUMO is delocalised over all the conjugated bonds, it is more appropriate to define the tunnelling barrier as the distance between the edges of the aromatic systems. The distance dependence of tunnelling probability is

$$\chi_r = \exp(-\beta r) \quad (17.45)$$

where β is an electronic decay coefficient, also called a *distance-dependence factor*, which is given by the expression

$$\beta = \frac{4\pi}{h} \sqrt{2m_e \Phi} = 1.025 \sqrt{\Phi} \quad (17.46)$$

where the numerical value corresponds to the barrier height Φ expressed in eV and β in \AA^{-1} . Chapter 16, Transitions Between Electronic States related the barrier height to the energy difference between the electron at rest in the vacuum

and in the highest occupied molecular orbital (HOMO) of the donor, Φ_0 , and to the refractive index of the material separating the donor and acceptor

$$\Phi = \frac{\Phi_0}{n_D^2} \quad (17.47)$$

Φ_0 is also the absolute potential of the electron in the donor, and can be estimated from the electrode potential of the metal complex, E^0 , measured with respect to the normal hydrogen electrode (NHE). Taking $\Phi_0(\text{NHE}) = 4.44 \text{ eV}$, the absolute potential of the electron in the donor is

$$\Phi_0 = 4.44 + E^0 \quad (17.48)$$

In this example, the reduction potential of $\text{Co}(\text{phen})_3^{3+}$ is $E^0 = 0.37 \text{ eV}$, and for the phenanthroline spacer, $n_D(\text{phen}) = 1.62$. With the relevant set of data one obtains: $\Phi_0 = 4.81 \text{ eV}$, $\Phi = 1.833 \text{ eV}$ and $\beta = 1.388 \text{ \AA}^{-1}$. From eq. (17.45) with a separation distance of the metal centres of $r = 13.6 \text{ \AA}$, the probability for the tunnelling of the electron is quite low, $\chi_r = 6.3 \times 10^{-9}$.

The calculations of non-adiabaticity of ETs require the assessment of the frequency of the ET under the effect of the separation distance. The reaction frequency is the product of an electronic frequency, $\nu_{\text{el}} = 10^{15} \text{ sec}^{-1}$ and the probability of transfer at a distance r , that is, $\nu_{\text{el}}\chi_r$. The ET is a nearly adiabatic process when it is controlled by the nuclear motion, $\nu_n > \nu_{\text{el}}\chi_r$, but becomes strongly non-adiabatic when it is controlled by the effective electronic frequency motion, $\nu_n < \nu_{\text{el}}\chi_r$.

17.4.3 Non-adiabaticity due to spin-forbidden processes

Some electron exchanges of cobalt complexes involve changes in spin configuration, from low-spin to high-spin such that $S' \neq S \pm 1/2$, and this can lead to another source of non-adiabaticity. The spin forbidden factor, χ_s , is entirely empirical within the present formalism, as well as within the TM formalism. For the complexes $\text{Co}(\text{phen})_3^{3+/2+}$ experimental evidence, also supplemented by quantum mechanical calculations, suggest that $\chi_s \approx 10^{-3}$. As a rule of thumb, it is assumed that $\chi_s \approx 10^{-3}$ for spin-forbidden ETs in transition-metal complexes. However, when no heavy metals or paramagnetic species are involved, the spin-forbidden factor can be $\chi_s \ll 10^{-3}$, as shown in Chapter 16, Transitions Between Electronic States, for aromatic hydrocarbons.

Finally, when the reaction barrier is estimated, the rate constant will be given by

$$k = K_c \nu_{\text{el}} \chi_r \chi_s \exp\left(-\frac{\Delta G^\ddagger}{RT}\right) \quad (17.49)$$

For the self-exchange reaction of $\text{Co}(\text{phen})_3^{3+/2+}$ the frequency factor will be $\nu = (10^{15})(6.3 \times 10^{-9})(10^{-3}) = 6.3 \times 10^3 \text{ sec}^{-1}$ and $K_c \approx 1 \text{ M}^{-1}$, as usual. The structural data in Table 17.1 lead to $\Delta G^* = 15 \text{ kJ mol}^{-1}$ and a rate constant

$k_{ISM} = 14 \text{ M}^{-1} \text{ sec}^{-1}$, which compares very well with the experimental data at room temperature, $k_{exp} = 12 \text{ M}^{-1} \text{ sec}^{-1}$.

Figure 17.11 illustrates the results from applications of ISM for self-exchange rates in transition-metal complexes. These are at least as good as that provided by TM-1, but can also treat the “anomalous” case of the $\text{Co}(\text{OH}_2)_6^{3+/2+}$ system. This reveals that ISM provides an alternative view for the electron-transfer self-exchange reactions in transition-metal complexes. It is a view not in terms of solvent- and solute-driven reactions as in the formalism of Marcus, but entirely in terms of solute-driven reactions. The relevant factors are force constants, the sum of the equilibrium bond lengths of oxidised and reduced species and the electronic properties of the same bonds (*bond orders*).

17.5 Electron self-exchanges of organic molecules

Electron-transfer reactions occur frequently between organic molecules and their radical cations or anions. A good example is the reaction between naphthalene in a neutral form and the radical anion

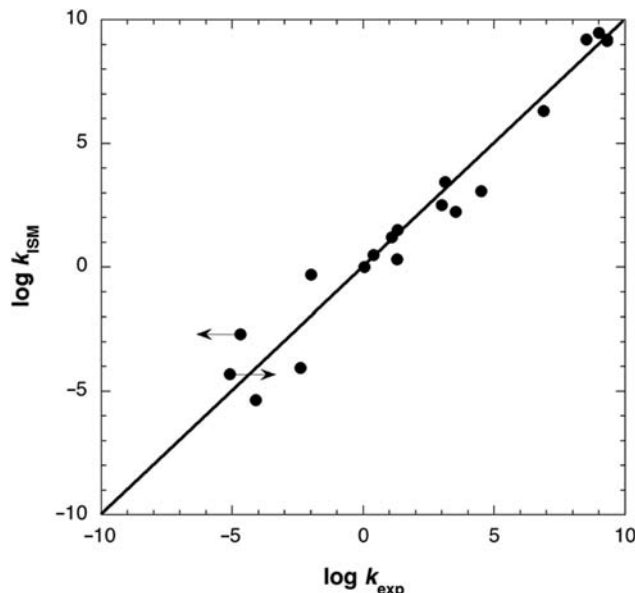


FIGURE 17.11

Comparison between electron self-exchange rates of transition-metal complexes calculated by ISM and experimental data, in water at room temperature, from Ref. [1].

One electron is transferred from a π orbital. The bond extensions occur on the carbon skeleton and do not significantly involve the CH bonds. The reactive bonds are therefore considered to be the CC bonds of the aromatic ring. Assuming that the carbon–carbon stretching modes behave as normal modes, the effective force constant for naphthalene is given by

$$f_{\text{ox}} = \frac{\sum_{i=1}^n f_i}{n} \quad (17.50)$$

Vibrational data are available from normal mode analysis of vibrational spectra, notably from the symmetric stretching modes that employs valence force field. For naphthalene one has $f_{\text{ox}} = 3.81 \times 10^3 \text{ kJ mol}^{-1} \text{ Å}^{-2}$. Using the same averaging manner, the average bond length are estimated as

$$l_{\text{ox}} = \frac{\sum_{i=1}^n l_i}{n} \quad (17.51)$$

From the structural data the result is $l_{\text{ox}} = 1.398 \text{ Å}$. The same procedure can be employed for the radical anion data, but for the majority of the cases such experimental data are not available. Therefore the data employed for the neutral and ionic species will be the same, without any significant error, since quantum-mechanical calculations show that the changes in CC bond lengths are very small between neutral and mono-charged aromatic species. Additionally, the changes in the bond lengths tend to be compensated by opposing changes in the force constants. In contrast, changes in n^* quite significantly affect the energy barriers, and require a more detailed consideration of the bond orders in the neutral and radical ion species.

For the neutral naphthalene molecule the average bond order of the carbon–carbon bonds is

$$n_{\text{ox}} = \frac{5 \times 2 + 6}{11} = 1.455 \quad (17.52)$$

resulting from to the five C=C and six C–C bonds of the naphthalene aromatic ring. For the radical anion the extra electron has an anti-bonding character, π , and the bond order can be written as

$$n_{\text{red}} = n_{\text{ox}} - \frac{0.5}{11} = 1.409 \quad (17.53)$$

The reactants bond order is then

$$\frac{1}{n^*} = \left(\frac{1}{2n_{\text{red}}} + \frac{1}{2n_{\text{ox}}} \right) \quad (17.54)$$

and yields $n^* = 1.43$.

The energy barrier for local mode behaviour is given by eq. (17.38). For normal modes, the equivalent expression is

$$\Delta G^* = \frac{1}{2} f_{\text{ox}} + \frac{f_{\text{red}}}{2} \left(\frac{d}{2} \right)^2 \quad (17.55)$$

With the structural data mentioned above and $n^* = 1.43$, eqs. (17.21) and (17.55) lead to $\Delta G^* = 21.2 \text{ kJ mol}^{-1}$.

The frequency nuclear factor for ET in these organic systems is the frequency of the CC stretching vibration of 1600 cm^{-1} , or $\nu_n = 4.8 \times 10^{13} \text{ sec}^{-1}$. The separation distance between the planes defined by the aromatic rings is typically the van der Waals contact distance of 3.5 \AA . For a typical distance parameter of $\beta = 1.2 \text{ \AA}^{-1}$, this leads to a probability of ET $\chi_r \approx 1.5 \times 10^{-2}$. Thus the electronic frequency factor, for a spin allowed process, is $\nu = \nu_{el} \chi_r = (10^{15} \text{ sec}^{-1}) (1.5 \times 10^{-2}) = 1.5 \times 10^{13} \text{ sec}^{-1}$ and since $\nu_{el} \chi_r < \nu_n$ are of comparable magnitude, the ET has a slight non-adiabatic character. As usual, $\nu = 10^{13} \text{ sec}^{-1}$ and $K_c = 1 \text{ M}^{-1}$.

The rate constant for the exchange of an electron between naphthalene and its radical anion is $k_{ISM} = 1.8 \times 10^9 \text{ M}^{-1} \text{ sec}^{-1}$ at $T = 298 \text{ K}$. Using the diffusion-controlled rate in acetonitrile, $k_{dif} = 1.9 \times 10^{10} \text{ M}^{-1} \text{ sec}^{-1}$, eq. (17.44) allows the estimation of $k_{obs} = 1.6 \times 10^9 \text{ M}^{-1} \text{ sec}^{-1}$, that is within one order of magnitude of the experimental value in the absence of the effects of ion pairing, $k_{exp} = 6.2 \times 10^8 \text{ M}^{-1} \text{ sec}^{-1}$. Somewhat dramatically, the electron exchange between $iPr_2N_2)_2$ and $iPr_2N_2)_2^+$ is much slower, $k_{exp} = 3.0 \times 10^{-3} \text{ M}^{-1} \text{ sec}^{-1}$ at 298 K in acetonitrile. Using the barrier calculated in Section 17.2.4, $\Delta G^* = 78 \text{ kJ mol}^{-1}$, and the experimental contact distance of 8.68 \AA , it is possible to calculate with $\beta = 1.2 \text{ \AA}^{-1}$, $\nu_{el} \chi_r = 3.0 \times 10^{10} \text{ M}^{-1} \text{ sec}^{-1}$ and $k_{ISM} = 6.4 \times 10^{-4} \text{ M}^{-1} \text{ sec}^{-1}$ at $T = 298 \text{ K}$, in good agreement with the experimental value. Figure 17.12 compares the rates estimated for several organic self-exchange reactions by ISM and the experimental rates.

17.6 Inverted regions

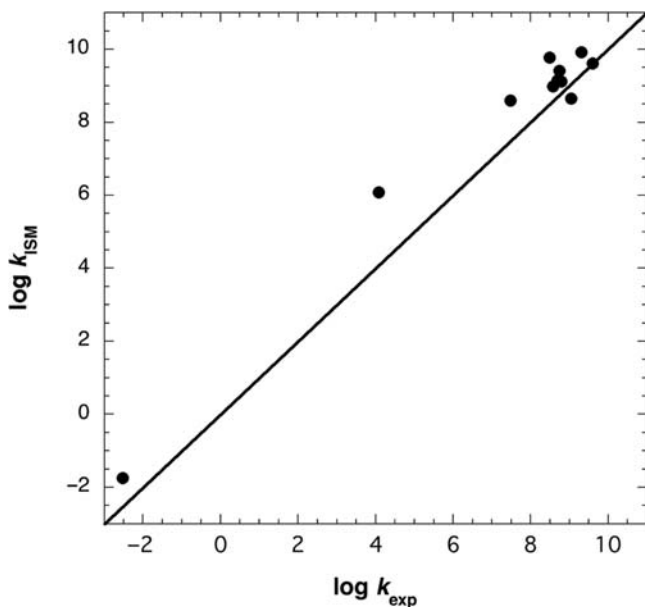
In a family of reactions with a constant intrinsic barrier, ΔG_0^* , the quadratic equation of Marcus led this scientist to predict the existence of an inversion on the effect of reaction energy, ΔG^0 , on energy barriers, ΔG^* , for very exothermic reactions [30]. From eq. (7.11) one can formulate the quadratic equation as

$$\Delta G^* = \Delta G_0^* + \frac{\Delta G^0}{2} + \frac{(\Delta G^0)^2}{16\Delta G_0^*} \quad (17.56)$$

This equation can be differentiated to give

$$\frac{d\Delta G^*}{d\Delta G^0} = \frac{1}{2} + \frac{1}{8} \frac{\Delta G^0}{\Delta G_0^*} \quad (17.57)$$

Usually the derivative $(d\Delta G^*/d\Delta G^0)$ has a positive sign and this means that a decrease in ΔG^0 leads also to a decrease in ΔG^* and, consequently, promotes an increase in the rate constants. However, when $\Delta G^0 < -4\Delta G_0^*(0)$, eq. (17.57) shows that $(d\Delta G^*/d\Delta G^0)$ becomes negative. This means that a decrease in ΔG^0

**FIGURE 17.12**

Comparison between electron self-exchange rates of organic species calculated by ISM and experimental data, in acetonitrile at room temperature, from Ref. [1].

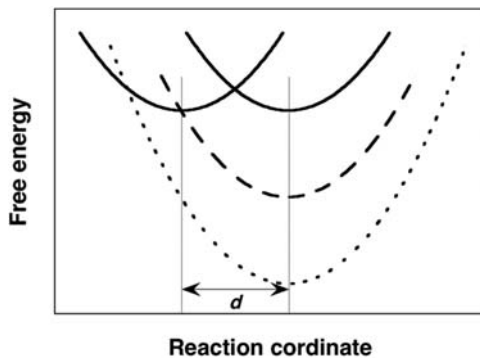
leads to an increase in ΔG^* and, consequently, leads to a decrease in the rate constants. Figure 17.13 illustrates the appearance of an *inverted region* in terms of a curve-crossing model. A considerable advantage for the use of uni-dimensional representations for ET processes is the representation of the inverted regions. Such regions are not amenable to any physical representation for multi-dimensional PESs.

In spite of the fact that such a prediction of Marcus was in contradiction with the scientific consensus at the time, several researchers persistently searched for this effect. A convenient way to produce very exothermic reactions is by preparation of electronic excited states, A^* , as reacting species using ultraviolet or visible light. Excited states are better oxidants and reductants than the same species in their ground states, and as a consequence photochemical reactions often lead to electron-transfer processes. Let us consider an acceptor of electron, A, that is subsequently excited by light,



where I_{abs} represents the intensity of the light absorbed. In the presence of a donor molecule, D, an electron-transfer reaction can occur,



**FIGURE 17.13**

Crossing of potential energy curves representing the reactants and products of increasingly exothermic electron transfers. For a sufficiently exothermic reaction, the barrier vanishes (dashed curve) and the rate attains its maximum. In even more exothermic reactions, the crossing of the curves moves up from the minimum of the reactants curve, a reaction barrier reappears (dotted curve) and the rate decreases. This decrease in the rate in very exothermic electron transfers is the “inverted region”.

Such a photo-induced reaction can be followed experimentally through the competition with the fluorescence emission of A^*



and with non-radiative decay processes



with rate constants k_F and k_{nr} , respectively.

Under steady-state conditions for A^*

$$\frac{d[A^*]}{dt} = I_{\text{abs}} - (k_F + k_{nr})[A^*] - k_{\text{et}}[D][A^*] \quad (17.58)$$

from which

$$[A^*] = \frac{I_{\text{abs}}}{k_F + k_{nr} + k_{\text{et}}[D]} \quad (17.59)$$

The intensity of the fluorescence emission, I_F , in the presence of donor molecules is

$$I_F = k_F[A^*] = \frac{k_F I_{\text{abs}}}{k_F + k_{nr} + k_{\text{et}}[D]} \quad (17.60)$$

while that in the absence of the donor is

$$I_F^0 = \frac{k_F I_{\text{abs}}}{k_F + k_{nr}} \quad (17.61)$$

From these two equations, it results that a study of the ratio of intensities, I_F^0/I_F ,

$$\frac{I_F^0}{I_F} = \frac{k_F + k_{nr} + k_{et}[D]}{k_F + k_{nr}} \quad (17.62)$$

as a function of the [D] leads to the familiar Stern–Volmer equation [see also eq. (3.21) and Figure 9.4]

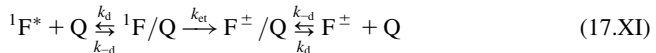
$$\frac{I_F^0}{I_F} = 1 + \frac{k_{et}}{k_F + k_{nr}}[D] \quad (17.63)$$

The quenching of fluorescence of A^* expressed by the ratio I_F^0/I_F is a linear function of the concentration of the quencher, that is, the donor in the present case. The intercept of the plot is one, and the slope is $k_{et}\tau$, where k_{et} is the rate of ET and τ the lifetime of A^* in the absence of quencher,

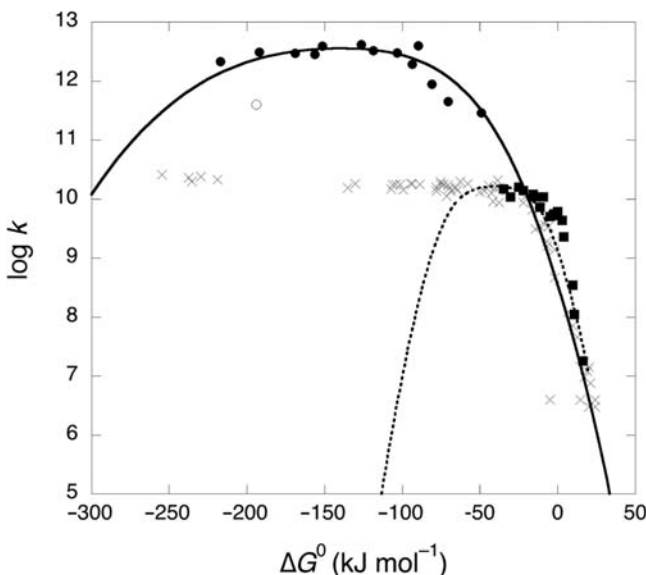
$$\tau^{-1} = (k_F + k_{nr})^{-1} \quad (17.64)$$

The lifetime of A^* is obtained through independent measurements under non-stationary conditions as described in Chapter 3, Experimental Methods.

Weller pioneered the use of photo-induced ETs to test the prediction of the inverted region. Rate constants in acetonitrile were measured in his laboratory for a range of reaction energies ΔG^0 between +25 and −250 kJ mol^{−1}. This polar solvent stabilises the charges of the products in a charge-separation reaction and enables the measurement of very exergonic reactions. The photo-induced charge separation was presumed to involve a full ET in a collision complex according to the mechanism



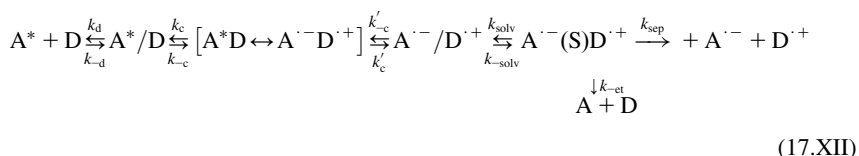
where F is the fluorophore and Q the quencher and the charges represent both case where F is an electron donor or an electron acceptor. Most of the donors studied were aromatic molecules with amine or methoxy substituents, and most of the acceptors were nitriles or aromatic molecules with carboxylic substituents. Figure 17.14 presents the data published by Rehm and Weller [31]. In contrast with the predictions of Marcus, no inverted region was observed. All the rates of very exothermic reactions ($\Delta G^0 < -50$ kJ mol^{−1}) are constant and indistinguishable from the diffusion rate constant expected for the systems in acetonitrile: 2×10^{10} M^{−1} sec^{−1}. Subsequently, the so-called Rehm–Weller plateau of diffusion-controlled reactions was observed literally thousands of times in photo-induced bimolecular electron-transfer reactions in solution and exerted a very strong influence in this field. The conflict between the predicted Marcus inverted region and the observed Rehm–Weller plateau motivated various hypothesis to reconcile theory with observation. The most relevant of them was the suggestion that these bi-molecular reactions could take place when the donor and acceptor were separated by more than one solvent molecule (donor–acceptor distance $r > 700$ pm), which in eq. (17.13) increases ΔG_s^* and displace the onset of the inverted region to more exothermic reactions. As discussed above, ETs can occur at long

**FIGURE 17.14**

Bi-molecular photo-induced electron transfer in acetonitrile. Crosses: original data from Rehm and Weller [31], squares: revised data from Ref. [32], circles: revised rate constants from Ref. [33] with revised energies from Ref. [32]; open circle: perylene*/tetracyanoethylene; dashed line: MT-2, eq. (17.56), with $\Delta G^*_0 = 10 \text{ kJ mol}^{-1}$; full line: ISM calculations with $f_r = f_p = 3.8 \times 10^3 \text{ kJ mol}^{-1} \text{ Å}^{-2}$, $l + l_p = 2.8 \text{ Å}$, $n^* = 1.41$ and $\Lambda = 160 \text{ kJ mol}^{-1}$.

distances, but in such cases the non-adiabatic factor is very low and difficult to reconcile with the observation of diffusion-controlled reactions at $\Delta G^0 = -250 \text{ kJ mol}^{-1}$.

The Rehm–Weller systems were recently revisited using techniques with higher sensitivity and better time resolution. It was found that for moderately endergonic and moderately exergonic reactions ($\Delta G^0 \approx -10 \text{ to } +10 \text{ kJ mol}^{-1}$) exciplexes with varying charge-transfer character are likely to be formed to interconvert with the excited fluorophore, and the mechanism of these reactions was revised to [32]



The rate constants k_c and k_{-c} refer to conformational alignment of the components to form the exciplexes and reversion to the A^*/D encounter pair, respectively. Analogously, k'_c and k'_{-c} refer to the interchange between the exciplex and

an $A^{\bullet-}/D^{\bullet+}$ encounter pair. The mechanism also includes the solvation to form a solvent-separated radical ion pair, $A^{\bullet-}(S)D^{\bullet+}$, and its decay by return ET or dissociation to free ions. The critical aspect of this mechanism is that ET proceeds through the formation of an intermediate, that is, the exciplex, and does not occur in a single step in this ΔG^0 range. The mechanism was substantiated by the observation of a very weak exciplex emission, previously unnoticed, and bi-exponential decays in single-photon counting. Moreover, accurate measurements of the redox potentials shifted the rates to more positive values of ΔG^0 and it was shown that the lower rates were biased by impurities. The revised free-energy dependence, shown in [Figure 17.14](#), is steeper in the endergonic region and has few points below the diffusion limit in the exergonic region. It was interpreted in terms of rapid inter-conversion between the encounter pairs and the exciplex and unrelated with elementary full-electron-transfer kinetics.

Shortly after, the more exergonic Rehm–Weller systems were re-investigated with femtosecond fluorescence up-conversion [33]. It was found that the quenching rate constant is time-dependent in the ultra-fast regime, being faster immediately after the excitation, because reactants at optimal distances react faster, and then becoming diffusion controlled in the nanosecond regimen. As a consequence, the decay of the fluorescence intensity in non-exponential, especially when followed with high time resolution. It is possible to model such decays to extract the “intrinsic” bi-molecular photo-induced charge-separation rates and such rates are shown in [Figure 17.14](#). The method to obtain rates higher than the diffusion limit requires modelling of the distribution function of F^* and Q , and of the rate constants. Although this introduces uncertainties in the rate constants, it seems that the most exothermic systems have minor rate restrictions. Of note, the system with a clearly lower rate is perylene*/tetracyanoethylene, and in this case it was possible to show that the primary product is an excited state of the ionic product, that is, the reaction is less exothermic than shown in the plot.

The first lesson to learn from Rehm–Weller systems is that they are a remarkable example of how a mechanistic proposal may have to be revised when technological developments enable studies with higher precision and resolution. Rehm and Weller authored a landmark publication and their data inspired many developments in electron-transfer theory and applications. However, their mechanistic proposal had to be revised.

The second aspect to emphasise is that Marcus inverted region is virtually absent from bi-molecular charge-separation reactions. Fitting Marcus inverted parabola to the moderately endergonic and moderately exergonic reactions, as shown in [Figure 17.14](#), yields a strongly inverted region that is not observed. Allowing the most exothermic reactions to occur over a range of long distances r to increase ΔG_s^* in [eq. \(17.13\)](#) and displace the maximum rate to *ca.* -150 kJ mol^{-1} , requires the use of a low electronic decay coefficient, $\beta = 0.775\text{ \AA}^{-1}$ [33], unexpected for ETs across acetonitrile molecules.

Alternatively, ISM can be used to explain the weak free-energy dependence of Rehm–Weller systems. The general expression for the calculation of the sum of bond extensions is, from eq. (16.137),

$$d = \frac{a'}{2n^*} \ln \left[\frac{1+g}{1-1/(1+g)} \right] (l_{\text{ox}} + l_{\text{red}}), \quad g = \exp \left(\sqrt{2n^* \Delta G^0 / \Lambda} \right) \quad (17.65)$$

This relation between d and ΔG^0 offers a method to estimate energy barriers for very exothermic reactions. This method differs from the Marcus cross-relation, TM-2, expressed by eqs. (17.16) and (17.17), or, in free-energy terms, eq. (17.56), and illustrated in Figure 17.13. TM-2 is based on a constant d , independent of the value of ΔG^0 , whereas ISM contemplates an increase of d with an increase in the absolute value of the reaction energy, $|\Delta G^0|$. TM-2 corresponds to the limiting situation of $\Lambda > > |\Delta G^0|$ in ISM. This is important because the Rehm–Weller pattern of reactivity can now be reproduced with the structural data of naphthalene and aromatic amines and a dynamic parameter $150 < \Lambda < 280$, in kJ mol^{-1} . Figure 17.14 shows the rates calculated with ISM using $\Lambda = 160 \text{ kJ mol}^{-1}$ to calculate d in eq. (17.65) and taking the energy barrier ΔG^* from the crossing point between harmonic reactant and product curves in Figure 17.8 with the relation

$$\frac{1}{2} f_r(x_r)^2 = \frac{1}{2} f_p(x_p)^2 + \Delta G^0 \quad (17.66)$$

and finally calculating the rate constant with eq. (17.42). The ET is adiabatic and Λ is the only parameter adjusted to the experimental data.

Instead of dealing with systems where the donor and acceptor molecules have to diffuse and collide for the electron-transfer process to occur, in 1986 Closs, Miller and collaborators have studied long-distance intra-molecular ETs in molecular systems where the donor and the acceptor species are covalently linked by a rigid hydrocarbon spacer. The system designed by Closs and Miller is the ET from the 4-biphenyl anion to a series of aromatic molecules, with the anion being prepared by electron addition using pulse radiolysis. This system insures that the distance between donor and acceptor is known with precision. In the cases represented in Figure 17.15, the spacer imposes a donor–acceptor edge-to-edge distance $r_e = 10.3 \text{ \AA}$. The electronic decay coefficient can be calculated with eqs. (17.46) and (17.47) using the reduction potential of biphenyl ($E_{\text{red}} = -2.58 \text{ V vs SCE}$) and the refractive index of the hydrocarbon spacer ($n_D = 1.4$). These data give $\beta = 1.07 \text{ \AA}^{-1}$ which compares reasonable well with the experimental value, obtained using different spacers with naphthalene and biphenyl in edge positions, $\beta = 1.22 \text{ \AA}^{-1}$ [34]. The frequency of the electron in the donor ($\nu_{\text{el}} = 5 \times 10^{14} \text{ sec}^{-1}$), together with distance-dependent non-adiabatic factor and the energy barriers ΔG^* discussed above, suffice to calculate the electron-transfer rates with eq. (17.49). Eqs. (17.65) and (17.66) employing the average force constants and bond lengths of the CC bonds in naphthalene and biphenyl. Figure 17.15 presents the rates calculated with the value of Λ that best

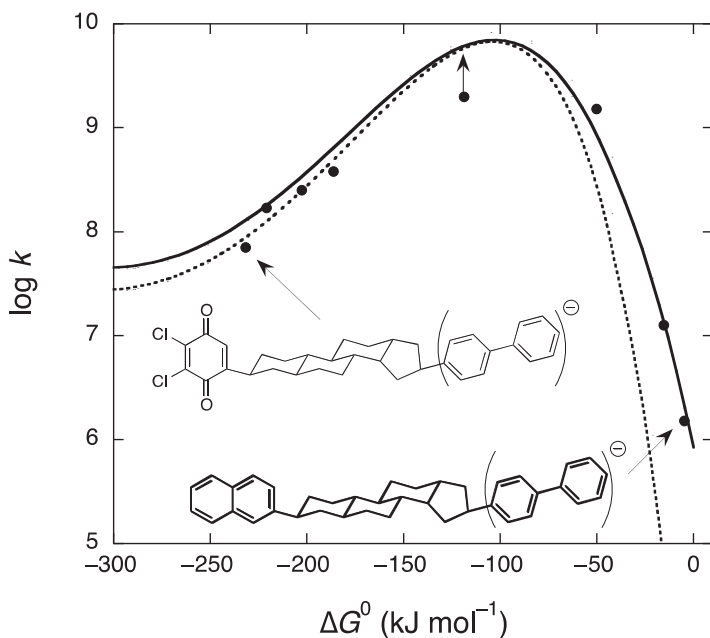


FIGURE 17.15

Intra-molecular electron transfer in methyltetrahydrofuran [34]. ISM calculations employed $f_r = f_p = 4.1 \times 10^3 \text{ kJ mol}^{-1} \text{ Å}^{-2}$, $l_r + l_p = 2.78 \text{ Å}$, $n^* = 1.45$, $\Lambda = 290 \text{ kJ mol}^{-1}$, $\beta = 1.07 \text{ Å}^{-1}$ and $r_e = 10.3 \text{ Å}$. Full line: thermal activation rates; dashed line: nuclear tunnelling rates.

fits the experimental data, $\Lambda = 290 \text{ kJ mol}^{-1}$. This figure also shows nuclear tunnelling rates calculated with eq. (16.71) setting

$$\sqrt{\mu} = \sqrt{\mu_D} + \sqrt{\mu_A} \quad (17.67)$$

where the reduced mass of the donor are the six CC oscillators of biphenyl, $\mu_D = 36 \text{ amu}$, and that of the acceptor are the three CC oscillators of the aromatic ring, $\mu_A = 18 \text{ amu}$. Under these approximations, the tunnelling rates are slightly lower than the thermal activation rates. An interesting feature of the calculations is the asymmetry of the inverted region, hinting that the Marcus inverted region may come to an end for very exergonic reactions.

The system developed by Closs and Miller provided the first clear evidence of Marcus inverted region and contributed to the decision to award the 1992 Nobel Prize in Chemistry to Rudolph Marcus for his contributions to the theory of electron-transfer reactions in chemical systems. Inverted regions have been observed in very exothermic inter-molecular ETs and in other systems where the relative motions of donor and acceptor are somewhat restricted. In such conditions, the kinetics of the electron-transfer step are not masked by diffusion and a

wider kinetic window is open for the observation of the inverted region. The ability to explore the free-energy dependence of ETs with $\Delta G^0 < -300 \text{ kJ mol}^{-1}$, often believed to be deep in the Marcus inverted region and slow, depends on the design of systems that can be investigated over wide ΔG^0 and T ranges without changes in reaction mechanism or electronic coupling. Very recently, this became possible with the synthesis of rigid donor–acceptor systems using benzene derivatives as donors and a dicyanoethene moiety as acceptor [35]. Figure 17.16 presents the charge-separation and charge-recombination rates in such systems measured in weakly polar solvents using picosecond single-photon counting and femtosecond transient absorption techniques.

ISM calculations presented in Figure 17.16 employed a non-adiabatic factor calculated as described above for the Closs–Miller system, but using the reduction potential of isopropylidenemalononitrile ($E_{\text{red}} = -1.69 \text{ eV}$ vs SCE) and the edge-to-edge distance of this system ($r_e = 5.9 \text{ \AA}$). The force constants, bond length and bond order were taken as averages of those of the benzene and dicyanoethene moieties. The reduced mass of the system was taken from the three CC oscillators of the benzene moiety ($\mu_D = 18 \text{ amu}$) and the two CN and one CC oscillators of the

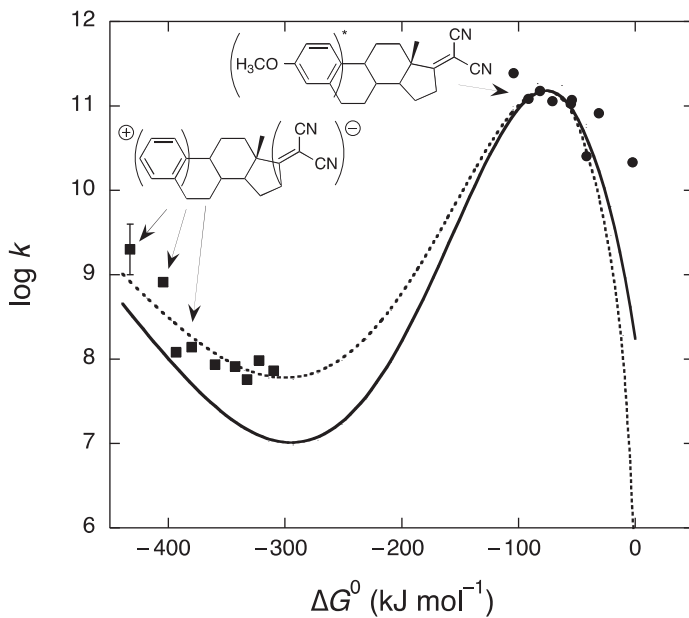


FIGURE 17.16

Intra-molecular charge separation (circles) and charge recombination (squares) as a function of the driving force at $T = 293 \text{ K}$ for various weakly polar solvents. ISM calculations employed $f_r = f_p = 4.8 \times 10^3 \text{ kJ mol}^{-1} \text{ \AA}^{-2}$, $l_r + l_p = 2.74 \text{ \AA}$, $n^* = 1.75$, $\Lambda = 290 \text{ kJ mol}^{-1}$, $\beta = 1.27 \text{ \AA}^{-1}$ and $r_e = 5.9 \text{ \AA}$. Full line: thermal activation rates; dashed line: nuclear tunnelling rates.

dicyanoethene moiety ($\mu_A = 19$ amu). Remarkably, in this case, with the parameters employed, the tunnelling rate is higher than the thermal activation rate in the inverted region. This leads to nearly temperature-independent rates in the inverted region. Moreover, the “inverted region” does not extend indefinitely. When the reaction exergonicity exceeds -300 kJ mol^{-1} , the charge-recombination rates increase again. It was shown that this is not due to a change in the decay mechanism [35,36]. Rather, it is a consequence of eq. (17.65). The existence of a “double-inverted region” had been predicted for ultra-exothermic ETs [37], and can be rationalised with Figure 17.17. The increase in the reorganisation energy with the increase in $|\Delta G^0|$ reflects the increased participation of other reactant modes in the reaction coordinate as more energy has to be dissipated by the reactants. The dynamic parameter Λ depends on the nature of the reactants and of the solvent. It is expected to be lower for the activated configurations with a small number of degrees of freedom. For example, charge recombinations in contact ion-pairs require $\Lambda = 300 \text{ kJ mol}^{-1}$, but in solvent separated

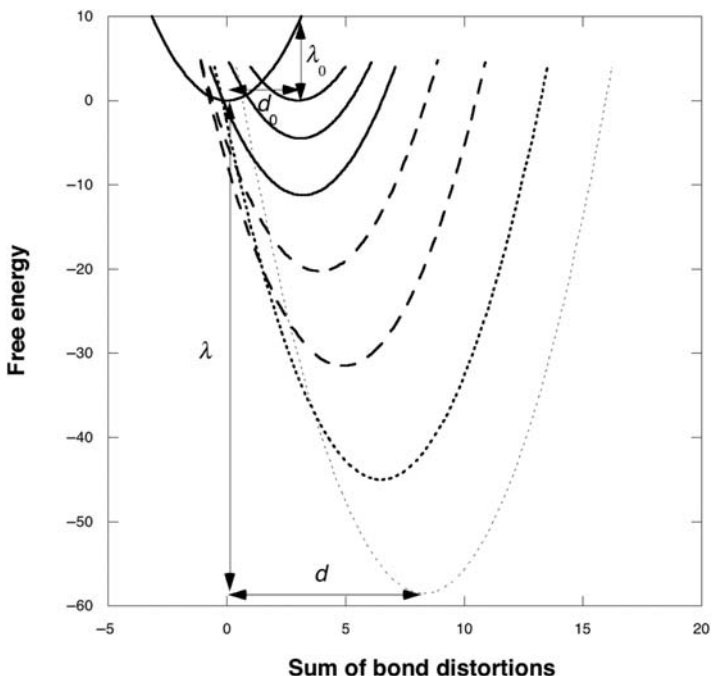


FIGURE 17.17

The sum of reactant and product bond distortions from equilibrium to transition state configurations (d) increases with the free-energy of the reactions (ΔG^0). This increase in d leads to an increase in the total reorganisation energy (λ). The activation energy, given by the crossing between reactant and product curves, first decreases with ΔG^0 (full lines), goes through a minimum, increases in the inverted region (dashed lines), goes through a maximum, and decreases again in double-inverted region (dotted lines).

ion-pairs they can be fitted with $\Lambda = 350 \text{ kJ mol}^{-1}$. Figure 17.18 illustrates the diversity of free-energy relationships that result from the values of Λ discussed above.

Finally, inverted regions have also been observed in ETs between redox centres embedded in proteins. This is both the case of modified intra-protein ETs briefly mentioned before [3,38], and of the reaction centres of photosynthetic bacteria [39].

17.7 Electron transfer at electrodes

17.7.1 The equation of Tafel

Electrochemistry deals primarily with chemical and physical phenomena at interfaces between an electronic conductor (typically a metal or a semiconductor) and an ionic conductor such an electrolyte solution, as affected by the electric potential of the solid conductor. An electrochemical reaction involves a current going through the interface, hence the passing of either electrons or ions. However, even if the current is carried through by ions, an electron-transfer step occurs within the ions, which must be either generated or discharged by an exchange of electrons.

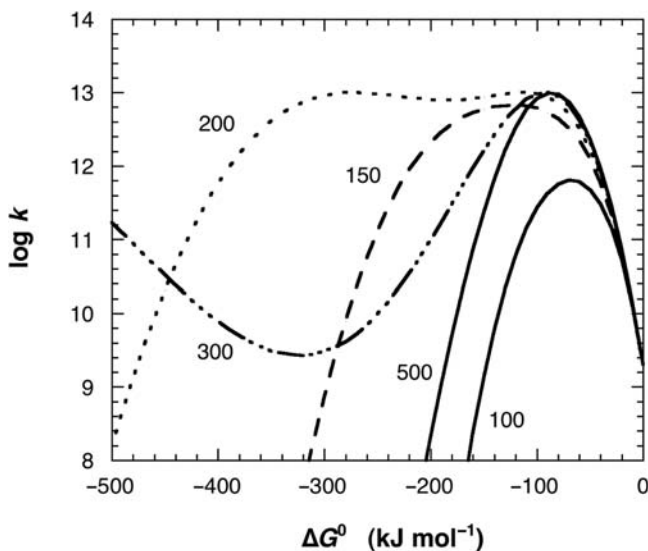


FIGURE 17.18

Free-energy dependences of adiabatic electron transfers according to ISM. The calculations employed $\nu = 10^{15} \text{ sec}^{-1}$, $f_r = f_p = 3.77 \times 10^3 \text{ kJ mol}^{-1} \text{ Å}^{-2}$, $l_r + l_p = 2.80 \text{ Å}$, $n^* = 1.435$, and the values of Λ indicated in the plot.

Figure 17.19 illustrates pictorially some of the relevant features of a solid/liquid interface [40]. For simplicity, we will consider mainly metal electrodes. The ET occurs between the solid surface layer and the dissolved species. Beneath this surface layer, for metals there is a constant potential in which no electron localisation is possible.

In an electrochemical cell, there are usually two electrodes: one, the *reference electrode*, at a constant potential and the other, the *working electrode*, where more positive or negative potentials are applied to produce electrochemical reactions through the transfer of electrons. If more negative potentials are applied to the working electrode, the energy of the electrons in the metal is increased such that the energy can be higher than that of the LUMO of any oxidant species present in solution and, consequently, at the metal/liquid interface. Under these circumstances, a flow of electrons can occur from the metal electrode to the solution, the so-called reduction current. Alternatively, more positive potentials, E , can be applied to the working electrode. The energy level of the electrons in the metal is lowered, and an electron can be transferred from the HOMO of a species in solution to the metal. Hence an oxidation electric current is generated. The creation of these reduction and oxidation currents is illustrated in Figure 17.20. The critical potential for such processes depends on the standard potential, E^0 , of the reactant.

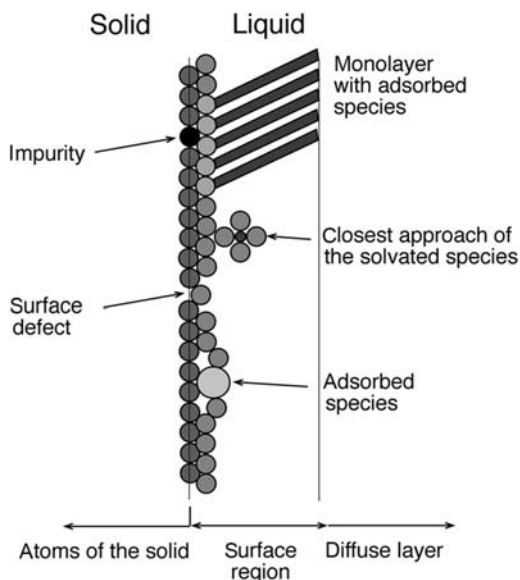
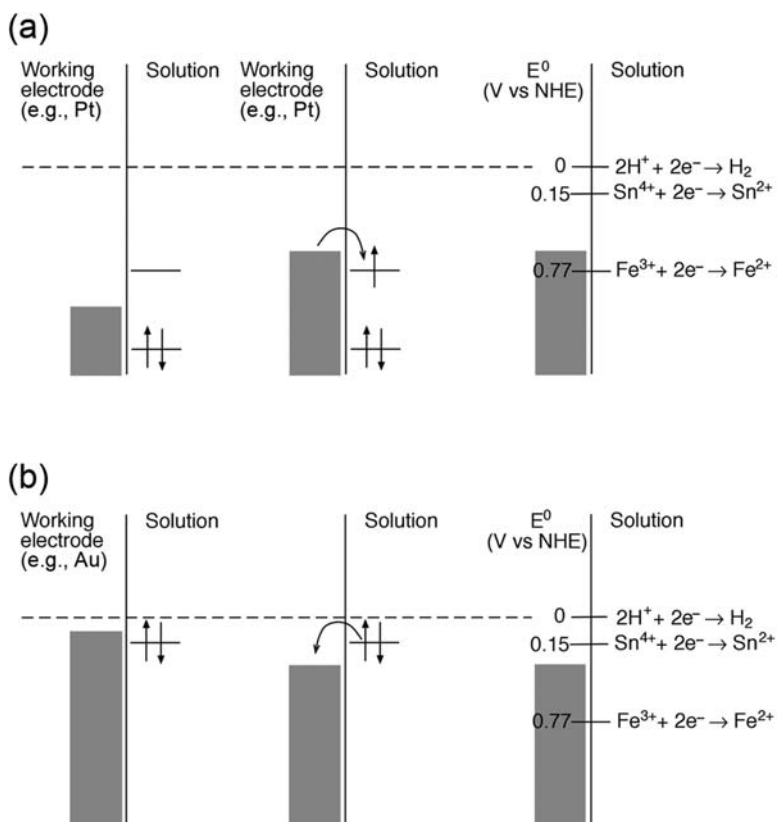


FIGURE 17.19

Representation of the electrode/solution interface, illustrating some of the species that can be found in this region.

**FIGURE 17.20**

(a) Reduction: initially (left) the energy of the electrons in the working electrode is too low to reduce the species in solution, but on increasing the energy of these electrons (centre) an ET to the LUMO of that species will occur; the right panel shows the reduction potentials of Fe^{3+} and Sn^{4+} , and an energy level of the electrons in the electrode that allows for the reduction of Fe^{3+} but not of Sn^{4+} . (b) Oxidation: initially (left) the energy of the electrons in the working electrode is too high to oxidise the species in solution, but decreasing the energy of these electrons (centre) an ET from the HOMO of that species will occur; the right panel shows the oxidation potentials of Fe^{2+} and Sn^{2+} , and an energy level of the electrons in the electrode that allows for the oxidation of Sn^{2+} but not of Fe^{2+} . The initial potential of the electrodes corresponds to their equilibrium in solution (no current).

The driving force for these heterogeneous reactions can be achieved by varying the electrode potential as

$$\Delta G_{\text{het}}^0 = F(E - E^0) \quad (17.68)$$

where F is the Faraday constant ($F = 96\,485\,C\,mol^{-1}$). This equation reveals that kinetic processes at electrodes can be drastic and continuously modified by

changing the electrode potential. This is a unique feature of electrochemical processes. For metals, which contain a large concentration of mobile electrons in thermal equilibrium, any change in the potential of the metal is communicated to the energy levels in the metal that, in turn, communicate with the electrolyte to follow the electrode potential. This situation is unlike that at semiconductor-electrolyte interfaces, where the change in the electrode potential may not result in a change in the energy level of charge carriers available to the electrolyte. For metals, at interfaces, the induced charge resides on the surface. For semiconductors, owing to their low free-carrier density, the induced charge can be distributed over relatively large distances from surfaces. The potential, which the reactant species experience in solution is less than the real potential energy difference between the electrode and the solution, because of the presence of solvent molecules and other molecular species (including counter ions) adsorbed at the surface of the metal electrode.

The rate of the electronic transfer is associated with the intensity, i , of the electric current that goes through the electrode, where i represents the number of electrons which react with the active species by unit of time,

$$i(A) = \frac{dQ}{dt} (\text{C sec}^{-1}) \quad (17.69)$$

Since electrode reactions are heterogeneous process, the rates are defined by mol sec^{-1} by unit area,

$$v = \frac{i}{nFA} \text{ mol sec}^{-1} \text{cm}^{-2} \quad (17.70)$$

Here n is the number of electrons transferred on each elementary process and A is the active surface of the electrode.

The kinetics of ETs at electrodes is usually studied in terms of the current intensity as a function of the potential. When $i = 0$, the potential of the electrode is that of the equilibrium, E_{eq} . The application of a potential different from E_{eq} corresponds to a polarisation of the electrode, whose magnitude is called the *over-potential*, η ,

$$\eta = E - E_{\text{eq}} \quad (17.71)$$

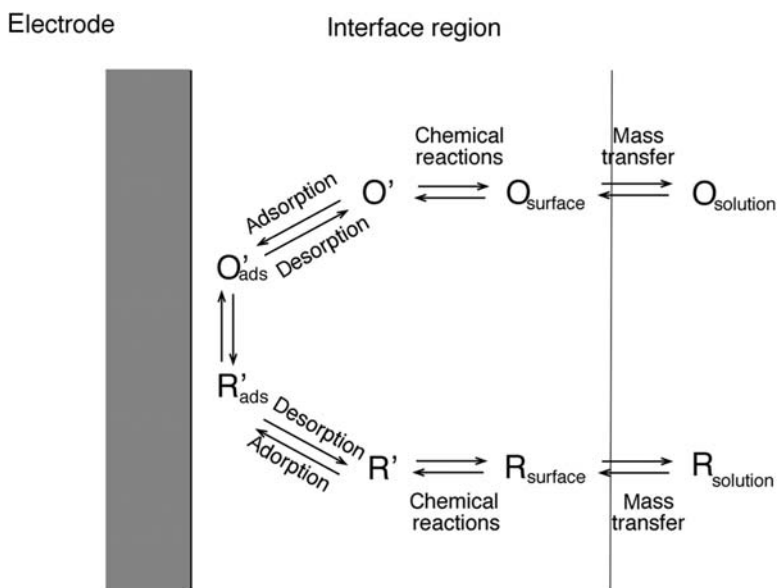
The measurement of a certain i is always associated with the presence of over-potential. However, the dependence of i upon η is complicated by the existence of several elementary steps displayed in Figure 17.21 and associated with the effect of the electrical double-layer [41]. This *double-layer effect* is due to the electrostatic work necessary to bring the electroactive ion to a charged interface.

For a low intensity regime, Tafel in 1905 showed that the over-potential is linearly related to the intensity,

$$\eta = a + b \log i \quad (17.72)$$

where a and b are constants. To understand the empirical equation of Tafel, consider the reaction



**FIGURE 17.21**

Pathway of a general electrode reaction.

The rate of reduction is proportional to the concentration of the oxidant species at the surface of the electrode, $[Ox]_s$, at a certain instant of time

$$v_{\text{red}} = k_{\text{red}} [Ox]_{0,t} = \frac{i_c}{nFA} \quad (17.73)$$

Here i_c is the intensity of the cathodic current. In an analogous manner for the oxidation reaction,

$$v_{\text{ox}} = k_{\text{ox}}[R]_{0,t} = \frac{i_a}{nFA} \quad (17.74)$$

where i_a is the anodic current. The net rate of the reaction is the difference between the rates of reduction (cathodic reaction) and oxidation (anodic reaction)

$$v = v_{\text{red}} - v_{\text{ox}} = k_{\text{red}}[O]_{0,t} - k_{\text{ox}}[R]_{0,t} = \frac{i}{nFA} \quad (17.75)$$

where

$$i = i_c - i_a = nFA(k_{\text{red}}[O]_{0,t} - k_{\text{ox}}[R]_{0,t}) \quad (17.76)$$

Assuming that the rates follow Arrhenius behaviour,

$$\begin{aligned} k_{\text{red}} &= k^0 e^{-\alpha n f(E-E^\circ)} \\ k_{\text{ox}} &= k^0 e^{(1-\alpha)n f(E-E^\circ)} \end{aligned} \quad (17.77)$$

where $f = F/RT$. To obtain the Tafel equation, one needs to relate the activation energies of the reduction and of the oxidation reactions with the reaction energy as shown in Figure 17.22 [41]. The model displayed in the figure is the Butler–Volmer model for kinetics at electrodes. A change on the electrode potential, E , leads to a change in the energy of the electron relative to the electrode, and the curve relative to the process $\text{Ox} + ne^- \rightarrow$ moves up or down on the vertical scale of that figure. For an increase variation in E , that curve moves up, the barrier for the oxidation decreases, and this decrease is proportional to the energy of the reaction. The proportionality factor is $(1 - \alpha)$, where α is called the cathodic *transfer coefficient*. Thus one can write for the anodic barrier

$$\Delta G_a^* = \Delta G_{0a}^* - (1 - \alpha)nFE \quad (17.78)$$

and the corresponding expression

$$\Delta G_c^* = \Delta G_{0c}^* + \alpha nFE \quad (17.79)$$

for the cathodic barrier.

The coefficient α is usually taken as the fraction of the electron residing on the activated complex and $(1 - \alpha)$ that fraction still in the metal at the transition-state configuration. The parameter α is also called the *Tafel coefficient*.

Substituting eqs. (17.78) and (17.79) in eq. (17.77) leads to

$$\begin{aligned} k_{\text{red}} &= A_{\text{red}} e^{-\Delta G_{0c}^*/RT} e^{-\alpha nFE} \\ k_{\text{ox}} &= A_{\text{ox}} e^{-\Delta G_{0a}^*/RT} e^{(1-\alpha)nFE} \end{aligned} \quad (17.80)$$

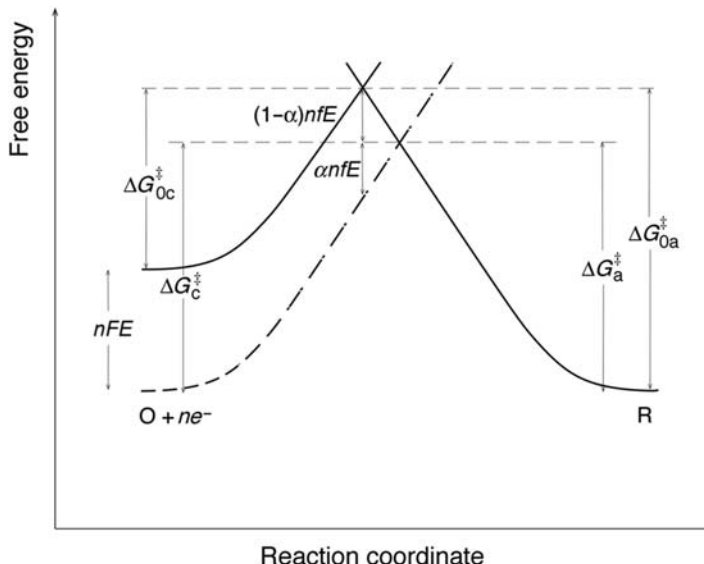


FIGURE 17.22

Effects of a potential change on the free energy of activation for oxidation and reduction.

When there is equilibrium at the interface with a solution of an equal amount of Ox and Red, the rates in the forward and reverse directions are equal, and an intrinsic rate constant, k^0 , can be defined

$$k^0 = A_{\text{red}} e^{-\Delta G_{\text{oc}}^*/RT} = A_{\text{ox}} e^{-\Delta G_{\text{od}}^*/RT} \quad (17.81)$$

and

$$\begin{aligned} k_{\text{red}} &= k^0 e^{-\alpha n f(E-E^{\circ'})} \\ k_{\text{ox}} &= k^0 e^{(1-\alpha) n f(E-E^{\circ'})} \end{aligned} \quad (17.82)$$

where $E^{\circ'}$ is the formal potential of the electroactive species. Further, substituting these expressions in eq. (17.76) one gets

$$i = nFAk^0 \left([O]_{0,t} e^{-\alpha n f(E-E^{\circ'})} - [R]_{0,t} e^{(1-\alpha) n f(E-E^{\circ'})} \right) \quad (17.83)$$

Tafel equation is a particular case of eq. (17.83)

17.7.2 Calculations of rate constants

The transfer of electrons between a metal or a semiconductor electrode and a dissolved or surface-bound reactant is of the same nature as the homogenous processes, previously described. In the model proposed by Marcus the electrochemical rate constant, k_{het} , is given by

$$k_{\text{het}} = Z \chi \exp \left(-\frac{\Delta G_{\text{het}}^*}{RT} \right) \quad (17.84)$$

where Z is the frequency factor for the electrode reaction and χ is an electronic transmission factor.

Several expressions have been proposed for the pre-exponential factor. In terms of a translational partition function, Z is

$$Z = \sqrt{\frac{RT}{2\pi\mu}} \quad (17.85)$$

where μ is the reduced mass of the reactant. For a hydrated metal ion this leads to typical values of $Z = 5 \times 10^3 \text{ cm sec}^{-1}$. Another expression for Z is

$$Z = (\delta r_e) \nu_N \quad (17.86)$$

where δr_e is the reaction zone thickness within which ET with the electrode surface occurs, and ν_N is the effective nuclear activation frequency. It is common to take $\delta r_e = 1 \text{ \AA}$, but differences of opinion exist on the appropriate value for ν_N , with some authors taking it as the typical nuclear frequency $\nu_N = 10^{13} \text{ sec}^{-1}$ and others as the reciprocal of the solvent longitudinal relaxation time $\nu_N = (\tau_L)^{-1}$ [42]. For reactions in aqueous solutions these two approaches give $Z = 1 \times 10^5 \text{ cm sec}^{-1}$ and $Z = 2 \times 10^4 \text{ cm sec}^{-1}$, respectively. When eqs. (17.85) and (17.86) are employed, it is

usually assumed that the electrochemical reaction is adiabatic, $\chi \approx 1$. An alternative expression, where adiabaticity is not implicit, is

$$Z\chi = \Gamma \nu_{\text{el}} e^{-\beta(r-r_0)} \quad (17.87)$$

where Γ , a factor that converts bulk to surface concentration of the reactant, is of the order of 10^{-7} cm [43]; Γ represents the precursor complex equilibrium constant K_c and is also called the “reactive thickness”. The other parameters have their usual meaning; r represents the distance of a metal-ion to the electrode and r_0 the width of the internal Helmholtz plane, because at this distance ET can be considered a tunnelling process from the electrode to the ion, with a unity probability. The interaction of the adsorbed solvent molecules with the electrode allows a conductive pathway for the electron through an empty anti-bonding orbital of the solvent molecules. The distance dependence of the electronic transmission factor in eq. (17.87) is similar to that expressed by eq. (17.45). The value of the pre-exponential factor given by eq. (17.87) for the reduction of $\text{Fe}(\text{OH}_2)_6^{3+}$ in aqueous solution can be estimated from its reduction potential with respect to NHE, $E_{\text{red}} = 0.38$ V, which following eq. (17.48), gives $\Phi_0 = 4.82$ eV. If one considers that in the diffuse double-layer the refractive index of water is that of the bulk, $n_D = 1.33$, then $\beta = 1.692 \text{ \AA}^{-1}$. With $\Gamma = 10^{-7}$ cm, $r - r_0 = 3 \text{ \AA}$, which is the van der Waals diameter of a water molecule [44], and $\nu_{\text{el}} = 10^{15} \text{ sec}^{-1}$, eq. (17.87) gives $Z\chi \approx 6 \times 10^5 \text{ cm sec}^{-1}$. Thus depending on the approximations assumed, a safe guess for the value of the pre-exponential factor in adiabatic electrochemical reactions ranges from 5×10^3 to $6 \times 10^5 \text{ cm sec}^{-1}$ [45].

A positive charge placed at the interface near a metallic electrode induces a negative charge in the metal. This effect, equivalent to an *image force*, leads to a decrease in the width and a sharpening of the barrier for the electron to tunnel from the metal to the transition-metal ion. Instead of the usual rectangular barrier, the image-force effect barrier can be approximated by a kind of parabolic potential [46]. However, for solutions in the 0.1–1 M concentration range typically employed in kinetic experiments, the image force interaction will be reduced and can be neglected. Thus the probability of tunnelling given by eq. (17.45) also applies to electrochemical processes.

Marcus has pointed out that the energy barrier for a heterogeneous process should be half of that for the homogeneous process in solution, ΔG^*_{hom} , described above,

$$\Delta G^*_{\text{het}} = \frac{1}{2} \Delta G^*_{\text{hom}} \quad (17.88)$$

because the response of the metal electrode to the transfer of the electron with the redox species does not involve energy changes [47], and the reactions can be effectively described as if only one reactant is present.

Curtiss *et al.* [48] have carried out measurements for reaction rates of the electrochemical oxidation of $\text{Fe}(\text{OH}_2)_6^{2+}$ to $\text{Fe}(\text{OH}_2)_6^{3+}$ at a gold electrode in a 0.5 M HClO_4 aqueous solution. The experimental design of a pressurised flow-system allowed electrochemical studies in the range of temperatures from 25 to 75 °C.

A good Arrhenius behaviour was found with $E_a = 56.8 \pm 1.5 \text{ kJ mol}^{-1}$, a frequency factor of $Z = 6 \times 10^5 \text{ cm sec}^{-1}$ and a Tafel coefficient $\eta = 0.425 \pm 0.01$ independent of the temperature. The measured standard rate constant at 25 °C is $k_{\text{het}} = 6 \times 10^{-5} \text{ cm sec}^{-1}$.

The activation energy of the electrochemical oxidation of $\text{Fe(OH}_2)_6^{2+}$ can be calculated with the structural and electronic data in Table 17.1 for $\text{Fe(OH}_2)_6^{3+/2+}$, $f_r = \sqrt{6}$, $f_{\text{ox}} = 3.75 \times 10^3 \text{ kJ mol}^{-1} \text{ Å}^{-2}$, $f_p = \sqrt{6}$, $f_{\text{red}} = 2.35 \times 10^3 \text{ kJ mol}^{-1} \text{ Å}^{-2}$, $l_{\text{ox}} + l_{\text{red}} = 4.08 \text{ Å}$, together with $n^* = 1$, valid for a normal outer-sphere process. The barrier for the heterogeneous reaction is, using eqs. (17.40) and (17.88), $\Delta G_{\text{het}}^* = 36 \text{ kJ mol}^{-1}$, which is 20 kJ mol⁻¹ lower than the experimental activation energy. Using an intermediate value for the pre-exponential factor, $Z\chi \approx 5 \times 10^4 \text{ cm sec}^{-1}$, the calculated rate 25 °C, $k_{\text{het}} = 2 \times 10^{-2} \text{ cm sec}^{-1}$, is much higher than the experimental value. However, the estimated Tafel coefficient ($\eta_{\text{ox}} = 0.44$) at $\Delta G^0 = 0$ is in close agreement with experiment, provided one considers the asymmetry of the potential energy curves [see eq. (17.66)].

Part of the discrepancy between the calculated and experimental electrochemical oxidation rates of $\text{Fe(OH}_2)_6^{2+}$ is due to electrostatic double-layer effects upon the apparent rate constants for electrochemical exchange. The “standard” rate constants measured at the formal potential for the redox couple concerned must be corrected for double-layer effects to obtain the “corrected” rate [49]. Such corrections depend on the electrode, electrolyte, Tafel coefficient, potential and charge of the redox couple. For the electrochemical exchange of the $\text{Fe(OH}_2)_6^{2+/3+}$ couple at the mercury/aqueous surface at 25 °C, the correction for the double-layer effects increase the rate from 2×10^{-5} to $1 \times 10^{-4} \text{ cm sec}^{-1}$ [42a]. Thus the discrepancy noted above is reduced to a factor of 200.

The double-layer effects are significantly reduced when one of the partners in the redox couple is uncharged. This is the case of ferrocene, treated in detail before for gas and homogenous solution exchanges. The standard rate constants for the electro-oxidation of ferrocene at a platinum electrode in acetonitrile range from 0.02 to 220 cm sec⁻¹ [50]. Some of the observed scatter is related to differences in electrolyte nature and concentration, or in temperature, but also reflects the experimental errors of some of the techniques employed. Fawcett and Opallo reviewed these data and recommended a rate between 1 and 4 cm sec⁻¹ [50]. Using the data for Fe(Cp)_2^{0+} in Table 17.1 and assuming the local mode behaviour, ISM calculations with $n^* = 1$ give $\Delta G_{\text{het}}^* = 21 \text{ kJ mol}^{-1}$. Taking $Z\chi \approx 5 \times 10^4 \text{ cm sec}^{-1}$, this gives $k_{\text{het}} = 10 \text{ cm sec}^{-1}$ at 25 °C, in good agreement with the experimental rate.

17.7.3 Asymmetry in Tafel plots

Hupp and Weaver [51] have extended the usual Tafel plots to strong overpotential in the anodic and cathodic regions for the system $\text{Cr(OH}_2)_6^{2+}/\text{Cr(OH}_2)_6^{3+}$ and have found a significant asymmetry in the plots. Under exothermic conditions, the plot is virtually linear in the cathodic region over a 500 mV range according to the Butler–Volmer model, but has a strong downward curvature in

the anodic region. For example, at an over-potential of 700 mV the cathodic reduction of $\text{Cr}(\text{OH}_2)_6^{3+}$ at Hg-electrode is 200 times faster than the anodic oxidation of $\text{Cr}(\text{OH}_2)_6^{2+}$ at the same over-potential.

The asymmetry of the plots is related first to the asymmetry of reactants and products. In the anodic oxidation the reactant is $\text{Cr}(\text{OH}_2)_6^{2+}$ and the product is $\text{Cr}(\text{OH}_2)_6^{3+}$, hence $f_r = \sqrt{6} f_{\text{red}}$ and $f_p = \sqrt{6} f_{\text{ox}}$. On the other hand, in the cathodic reduction the reactant is $\text{Cr}(\text{OH}_2)_6^{3+}$ and the product is $\text{Cr}(\text{OH}_2)_6^{2+}$, hence $f_r = \sqrt{6} f_{\text{ox}}$ and $f_p = \sqrt{6} f_{\text{red}}$. The potential-energy curves of reactant and product are asymmetric for each reaction, and this asymmetry is reversed between electrochemical oxidation and reduction. With the data available in Table 17.1, this contribution to the asymmetry of the cathodic reduction of the $\text{Cr}(\text{OH}_2)_6^{2+}/\text{Cr}(\text{OH}_2)_6^{3+}$ couple system can be shown to be given by $f_r = \sqrt{6} f_{\text{ox}} = 3.75 \times 10^3 \text{ kJ mol}^{-1} \text{ Å}^{-2}$ and $f_p = \sqrt{6} f_{\text{red}} = 2.35 \times 10^3 \text{ kJ mol}^{-1} \text{ Å}^{-2}$.

The pre-exponential factor is another source of asymmetry. The barrier for tunnelling is raised by the application of an anodic over-potential and lowered by applying a cathodic one. Where there is over-potential the barrier for tunnelling varies according to the expression

$$\Phi = \frac{\Phi_0 - \Delta G_{\text{het}}^0}{n_D^2} \quad (17.89)$$

However, these two contributions are not enough to account for the full asymmetry in the Tafel plots. They can account for a factor of *ca.* 40 times faster rates for the anodic process when compared with the cathodic ones. Further corrections are needed to account for the experimental data. An additional contribution may be due to a difference in entropy change for the cathodic and anodic processes.

Using the force constants mentioned above, $l_r + l_p = 4.13 \text{ Å}$ and $n^* = 1$, ISM calculations give $\Delta G_{\text{het}}^* = 36.4 \text{ kJ mol}^{-1}$. The frequency factor for the electrochemical exchange must be smaller than that employed for the $\text{Fe}(\text{OH}_2)_6^{2+/3+}$ and $\text{Fe}(\text{Cp})_2^{0/+}$ exchanges, because the $\text{Cr}(\text{OH}_2)_6^{2+/3+}$ couple exchanges a σ^* electron and it was shown that this is a non-adiabatic process. In homogeneous self-exchanges, the frequency of the $\text{Cr}(\text{OH}_2)_6^{2+/3+}$ exchange is a factor of 240 lower than that of the $\text{Fe}(\text{OH}_2)_6^{2+/3+}$ exchange. Assuming that the same factor applies to electrochemical exchanges, then $Z\chi \approx 2 \times 10^2 \text{ cm sec}^{-1}$ and $k_{\text{het}} = 8 \times 10^{-5} \text{ cm sec}^{-1}$ for the $\text{Cr}(\text{OH}_2)_6^{2+/3+}$ exchange at 25°C . At this temperature, the standard rate constant is $2 \times 10^{-5} \text{ cm sec}^{-1}$ and the double-layer corrected rate constant is $2 \times 10^{-6} \text{ cm sec}^{-1}$ [49]. In this case, the double-layer correction decreases the rate because the potential drop across the diffuse layer is negative. In view of all the approximations and corrections involved, the calculations provide a reasonable estimate of the experimental rate.

17.7.4 Electron transfer at surfaces through a blocking layer

An outer-sphere electron-transfer process should be independent of the nature of the electrode and of the electrolyte medium. Nevertheless, experimental electron-transfer

rates are strongly dependent on the nature of the electrodes and of their surface history.

Long-distance electron-transfer processes at metal/electrolyte interfaces have been studied with ferrocene groups positioned at a fixed distance from a gold electrode by the self-assembly monolayers of a mixed ferrocene-substituted alkyl thiol, $(C_5H_5)Fe(C_5H_4)CO_2(CH_2)_{16}SH$ diluted with unsubstituted alkane thiols, $CH_3(CH_2)_{15}SH$. Monolayers at Au appear to be reasonably homogeneous and the kinetic electrochemical data obtained by Chidsey and co-workers [52] under those conditions appear to be free from heterogeneities and double-layer effects that lead to kinetic dispersions as found by other authors. Figure 17.23 shows this system. The inferred structure for the C-16 alkyl layer employed in these experiments corresponds to an estimated distance from the surface of 19 Å. In these systems, ET has the characteristics of an intra-molecular process and, therefore the rate constants are in units of sec⁻¹; at the standard potential the rate is $k_{het} = 1.25 \text{ sec}^{-1}$ at 298 K.

The pre-exponential factor for this electrochemical exchange can be calculated with eq. (17.87) making $\Gamma = 1$. Assuming the monolayer has a refractive index

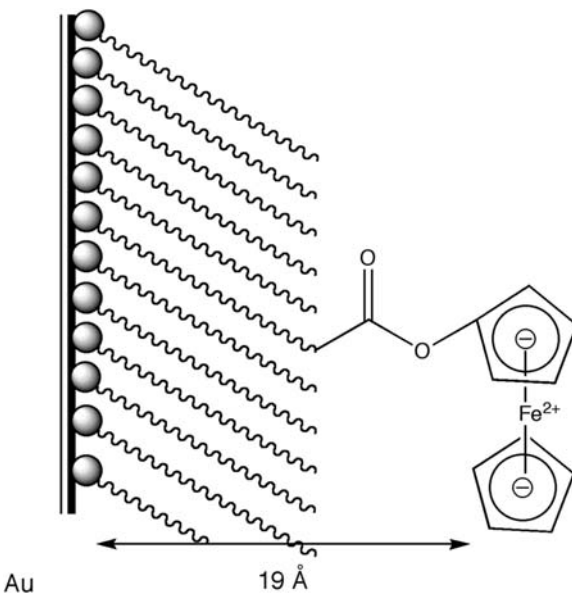


FIGURE 17.23

Ferrocene covalently linked to an alkanethiol adsorbed to the surface of a gold electrode. The ferrocene-substituted alkyl thiol is diluted in other alkanethiols to minimise the interactions between ferrocenes and favour a homogenous coverage of the electrode. The stability of the monolayer is due to the strong adsorption of the sulphur atom at the surface of the gold electrode.

$n_D = 1.6$, making $r - r_0 = 19 \text{ \AA}$ and taking the absolute potential of ferrocene $\Phi_0 = 5.17 \text{ eV}$, the frequency factor becomes 10^3 sec^{-1} . This with the activation free-energy already calculated for the $\text{Fe}(\text{Cp})_2^{0/+}$ couple, $\Delta G^*_{\text{het}} = 21 \text{ kJ mol}^{-1}$, gives $k_{\text{het}} = 0.2 \text{ sec}^{-1}$ at 298 K. It is rewarding to see that in this system, free from double-layer effects and uncertainties in the pre-exponential factor, the calculate rate is in good agreement with the experiment.

A more rigorous treatment must consider that in a metal electrode there is a continuum of energy levels and, therefore, a manifold of activated complexes for ETs, Figure 17.24. In the previous approach, the sum over activated complexes was replaced by a *single activated complex* with properties corresponding to the Fermi level. For the present kinetic data, it is worth avoiding such a simplification.

The density of electronic states in the electrode, ρ , close to the Fermi level of the metal, is dependent on the Fermi energy (ε_F) and on the number of conducting electrons provided by each atom (N), and can be estimated within the model of a free electronic gas

$$\rho(\varepsilon_F) = \frac{3N}{2\varepsilon_F} \quad (17.90)$$

For gold, each atom contributes with $N = 1$ for the electronic gas and $\varepsilon_F = 5.51 \text{ eV}$. Hence the density of states for gold at the Fermi level is $\rho(\varepsilon_F) = 0.27 \text{ states eV}^{-1} \text{ atom}^{-1}$.

The distribution of the electrons in a metal follows the Fermi–Dirac statistics

$$f_{\text{red}}(\varepsilon) = \frac{1}{1 + \exp(\varepsilon/k_B T)} \quad (17.91)$$

$$f_{\text{ox}}(\varepsilon) = \frac{\exp(\varepsilon/k_B T)}{1 + \exp(\varepsilon/k_B T)}$$

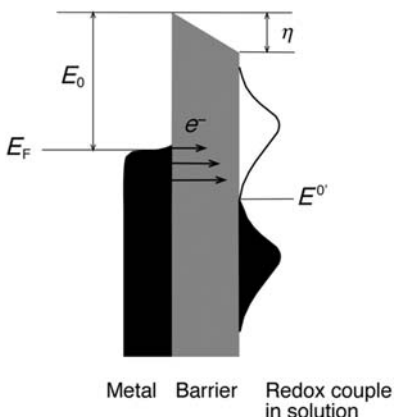
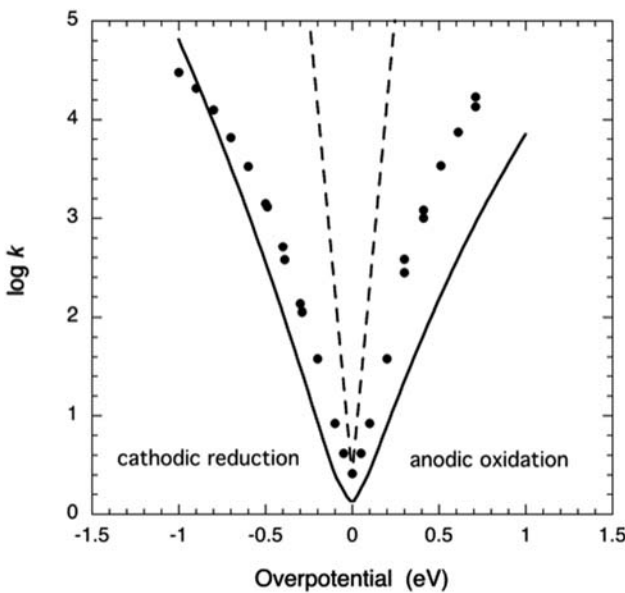


FIGURE 17.24

Representation of the electron transfers for the several electronic levels of the metal.

**FIGURE 17.25**

Tafel plots for a first-order electron-transfer rate, at 298 K, on a gold electrode covered with a monolayer of *n*-alkylthiols, some of them covalently linked to ferrocenes. The points are the experimental data of Chidsey [52], the dashed line represents the Butler–Volmer model calculated with $k_0 = 1.25 \text{ sec}^{-1}$ and $\alpha = 0.5$, and the full line was calculated with ISM [2].

For reduction, such a statistical distribution favours the energy levels of lower energy, since the high-energy levels are less populated. Nevertheless the barrier for the ET decreases with an increase in the energy levels of the electrons to be transferred. Consequently the rate for the reduction process is proportional to

$$\rho(\varepsilon_F) f_{\text{red}}(\varepsilon) \exp\left(-\frac{\varepsilon^*}{k_B T}\right) \quad (17.92)$$

where ε^* is the energy barrier for the level of energy ε . The probability of ET attains a maximum for the electrochemical potential of the electrons in the metal.

The probability of ET from an ion or molecule to an electrode follows the same formalism, and also attains a maximum for the electrochemical potential of the electrons in the metal,

$$\rho(\varepsilon_F) f_{\text{ox}}(\varepsilon) \exp\left(-\frac{\varepsilon^*}{k_B T}\right) \quad (17.93)$$

The experimental electron-transfer rate is given by the integral for all the elementary rates from each energy level. The factor of non-adiabaticity needs also to be taken into account and the overall rate is given by

$$k_{\text{ele}} = \nu_{\text{el}} \rho(\varepsilon_F) RT \int \chi_r f(\varepsilon) \exp\left(-\frac{\varepsilon^*}{k_B T}\right) d\left(\frac{\varepsilon}{k_B T}\right) \quad (17.94)$$

Here the integral is carried out for all the levels thermally populated.

Figure 17.25 presents the ISM calculations for the system of Chidsey together with the results for the Butler–Volmer model; the monolayer is described as before with a refractive index $n_D = 1.6$ and the absolute potential of ferrocene is $\Phi_0 = 5.17$ eV. The calculations incorporated the correction of the images forces for tunnelling of the electrons. All the models interpret well the rates at the standard potential.

The Butler–Volmer model overestimates the effect of the over-potential on the rates and has a symmetric behaviour. The more complete calculations with ISM rates with $\Lambda = 350$ kJ mol⁻¹, are in fair agreement with experiment for the cathodic reduction and, with respect to the Butler–Volmer approach, present some asymmetry due to a more favourable non-adiabatic factor for tunnelling of the electrons in reduction. There is no close agreement for data in the anodic region. Incorporating a correction with a lower Λ for the Butler–Volmer model does not appear to be valid, because it would decrease the rate constants even more, which would increase the disagreement still further. A possible solution would be the incorporation of the transfer of holes from the electrode to the molecular species in the oxidation region of the process.

References

- [1] SJ Formosinho, LG Arnaut, R Fausto, *Prog. React. Kinet.* **23** (1998) 1–90.
- [2] LG Arnaut, AAC C Pais, SJ Formosinho, *J. Mol. Struct.* **563/564** (2001) 1–17.
- [3] JR Winkler, HB Gray, *Chem. Rev.* **92** (1992) 369–379.
- [4] RA Marcus, *J. Chem. Phys.* **24** (1956) 966–978.
- [5] NS Hush, *J. Chem. Phys.* **28** (1958) 962.
- [6] (a) RA Marcus, N Sutin, *Biochim. Biophys. Acta* **811** (1985) 265.
(b) RA Marcus, *Angew. Chem. Int. Ed. Engl.* **32** (1993) 1111–1121.
- [7] N Sutin, *Annu. Rev. Nucl. Sci.* **12** (1962) 285.
- [8] AM Ullman, DG Nocera, *J. Am. Chem. Soc.* **135** (2013) 15053–15061.
- [9] MT Nielsen, KA Moltved, KP Kepp, *Inorg. Chem.* **57** (2018) 7914–7924.
- [10] SJ Formosinho, LG Arnaut, *J. Mol. Struct. (Theochem)* **130** (1994) 105–124.
- [11] G Grampp, A Kapturkiewicz, W Jaenicke, *Ber. Bunsenges. Phys. Chem.* **94** (1990) 439.
- [12] GE McManis, RM Nielson, A Gochev, MJ Weaver, *J. Am. Chem. Soc.* **111** (1989) 5533.
- [13] SF Nelsen, Y Kim, SC Blackstock, *J. Am. Chem. Soc.* **111** (1989) 2045.

- [14] A Zahl, R van Eldik, M Matsumoto, TW Swaddle, *Inorg. Chem.* **42** (2003) 3718–3722.
- [15] H-S Ren, M-J Ming, J-Y Ma, X-Y Li, *J. Phys. Chem. A* **117** (2013) 8017–8025.
- [16] R Derai, PR Kemper, MT Bowers, *J. Chem. Phys.* **82** (1985) 4517.
- [17] J Xie, RN Zare, *J. Chem. Phys.* **96** (1992) 4293.
- [18] C-Y Lee, AE DePristo, *J. Am. Chem. Soc.* **105** (1983) 6775–6781.
- [19] K Ohta, K Morokuma, *J. Phys. Chem.* **91** (1987) 401–406.
- [20] MD Newton, K Ohta, E Zhong, *J. Phys. Chem.* **95** (1991) 2317–2326.
- [21] DE Richardson, JR Eyler, *Chem. Phys.* **176** (1993) 457–466.
- [22] K Kirchner, S-Q Dang, M Stebler, HW Dodgen, S Wherland, JP Hunt, *Inorg. Chem.* **28** (1989) 3604–3606.
- [23] SF Nelsen, DT Rumack, M Meot-Ner, Mautner *J. Am. Chem. Soc.* **109** (1987) 1373–1379.
- [24] SF Nelsen, A Konradsson, TL Jentzsch, JJ O'Konek, JR Pladziewicz, *J. Chem. Soc. Perkin Trans 2* (2001) 1552–1556.
- [25] SF Nelsen, MT Ramm, RF Ismagilov, MA Nagy, DA Trieber, DR Powell, X Chen, JJ Gengler, Q Qu, JL Brandt, JR Pladziewicz, *J. Am. Chem. Soc.* **119** (1997) 5900.
- [26] SF Nelsen, L-J Chen, DR Powell, FA Neugebauer, *J. Am. Chem. Soc.* **117** (1995) 11434–11440.
- [27] (a) MD Newton, MV Basilevsky, IV Rostov, *Chem. Phys.* **232** (1998) 201–210.
(b) X-Y Li, *Int. J. Quantum Chem.* **115** (2015) 700–721.
- [28] GL Miessler, DA Tarr, *Inorganic Chemistry*, 327, Prentice Hall, New Jersey, 1998.
- [29] L Eberson, SS Shaik, *J. Am. Chem. Soc.* **112** (1990) 4484.
- [30] RA Marcus, *Faraday Discuss. Chem. Soc.* **29** (1960) 21.
- [31] D Rehm, A Weller, *Isr. J. Chem.* **8** (1970) 259.
- [32] S Farid, JP Dinnocenzo, PB Merkel, RH Young, D Shukla, G Guirado, *J. Am. Chem. Soc.* **133** (2011) 11580–11587.
- [33] A Rosspeintner, G Angulo, E Vauthey, *J. Am. Chem. Soc.* **136** (2014) 2026–2032.
- [34] GL Closs, LT Calcaterra, NJ Green, KW Penfield, JR Miller, *J. Phys. Chem.* **90** (1986) 3673.
- [35] KK Mentel, A Serra, PE Abreu, LG Arnaut, *Nat. Commun.* **9** (2018) 2903.
- [36] C Serpa, PJS Gomes, LG Arnaut, SJ Formosinho, J Pina, J Seixas de Melo, *Chem. Eur. J.* **12** (2006) 5014–5023.
- [37] LG Arnaut, SJ Formosinho, *J. Mol. Struct. (Theochem)* **233** (1991) 209.
- [38] LG Arnaut, SJ Formosinho, *J. Photochem. Photobiol. A: Chem.* **118** (1998) 173.
- [39] LG Arnaut, SJ Formosinho, *J. Photochem. Photobiol. A: Chem.* **111** (1997) 111.
- [40] AJ Bard, HD Abruña, CE Chidsey, LR Faulkner, SW Feldberg, K Itaya, M Majda, O Melray, RW Murray, MD Porter, MP Soriano, HS White, *J. Phys. Chem.* **97** (1993) 7147.
- [41] AJ Bard, LR Faulkner, *Electrochemical Methods*, J. Wiley & Sons, Nova Iorque, 1980, p. 4.
- [42] (a) JT Hupp, MJ Weaver, *Inorg. Chem.* **22** (1983) 2557.
(b) DK Phelps, AA Kornyshev, MJ Weaver, *J. Phys. Chem.* **94** (1990) 1454.
- [43] RJD Miller, G McLendon, A Nozik, W Schmickler, F Willig, *Surface Electron Transfer Processes*, 75, Wiley, New York, 1995.
- [44] RA Pierotti, *J. Phys. Chem.* **69** (1965) 281.
- [45] Z-D He, Y-X Chen, E Santos, W Schmickler, *Angew. Chem. Int. Ed.* **57** (2018) 7948–7956.

- [46] JG Simmons, *J. Appl. Phys.* **34** (1963) 1793.
- [47] RA Marcus, *Ann. Rev. Phys. Chem.* **15** (1964) 155.
- [48] LA Curtiss, JW Halley, J Hautman, NC Hung, Z Nagy, Y-J Rhee, RM Yonco, *J. Electrochem. Soc.* **138** (1991) 2023.
- [49] MJ Weaver, *J. Electroanal. Chem. Interfacial Electrochem* **93** (1978) 231.
- [50] WR Fawcett, M Opallo, *Angew. Chem. Int. Ed. Engl.* **33** (1994) 2131.
- [51] JT Hupp, MJ Weaver, *J. Phys. Chem.* **88** (1984) 6128.
- [52] CED Chidsey, *Science* **251** (1991) 919.

This page intentionally left blank

Oscillatory reactions

18

18.1 Non-linear systems

The description of the rate of a chemical reaction



as the time derivative of the concentration of a reactant or a product (i.e., a differential equation)

$$\frac{d[A]}{dt} = -k[A][B] \quad (18.1)$$

creates the impression that it is always possible to predict a monotonic decrease of the concentration of reactants, or increase in the concentration of products, from the initial state of the reactants to the final state of the products. Indeed, the previous chapters emphasised the ability to predict the concentrations of reactants, products and intermediates at any instant during the reaction based on the initial conditions and the rate constants. The expectation of a monotonic behaviour is deeply rooted in the definition of entropy (S) and the formulation of the second law of thermodynamics: in an isolated system, exchanging neither energy nor matter with the outside world, the entropy increases monotonically until it reaches its maximum at the state of thermodynamic equilibrium,

$$\frac{dS}{dt} \geq 0 \quad (18.2)$$

The second law of thermodynamics prohibits the construction of a *perpetuum mobile*.

The monotonic approach to equilibrium is a characteristic of systems described exclusively by first-order reaction rates. The rates of such reactions have the form $dx/dt = f(x)$ and can be regarded as the flow on a line. It is not possible to return to the initial state and periodic solutions are impossible. On the other hand, chemical systems with second- or higher-order reactions are described by non-linear differential equations involving powers, products or other functions of the concentrations of the chemical species, such as $[A][B]$, $[A]^2$ or $[A]^{3/2}$. Such non-linear systems are very difficult to solve analytically but can give rise to very interesting phenomena.

A non-linear system with oscillatory reactions was encountered in [Section 4.3.4](#). The Lotka type II mechanism



where A is a constant, is described by the equations

$$\begin{aligned} \frac{d[X]}{dt} &= k'_1[X] - k_2[X][Y] \\ \frac{d[Y]}{dt} &= k_2[X][Y] - k_3[Y] \end{aligned} \quad (18.3)$$

where $k'_1 = k_1[A]$, and [Figure 4.9](#) shows that the concentrations of X and Y exhibit persistent oscillations. This system does not violate the second law of thermodynamics because it is an open system: the only way of keeping A constant is to have a constant influx of A in the system. Moreover, the oscillations are observed for the intermediates, and not for the reactants or products.

The Lotka type II mechanism is also known as the Lotka–Volterra predator–prey model. It is a simple approach to understand a system with unlimited food supply (constant A), an exponential reproduction of preys (e.g., X represents rabbits and $k'_1[X]$ their exponential growth), a rate of predation $k_2[X][Y]$ proportional to the encounter between predators (e.g., Y represents foxes) and preys (X are rabbits), a rate of predator population growth $k_2[X][Y]$, and an exponential decay $k_3[Y]$ of the predator population in the absence of preys. In a more refined version, the rate of predation does not have to be equal to the rate of predator population growth, but it nevertheless leads to cycles in the population of both species for a wide range of initial conditions. This is not considered very realistic because real predator–prey cycles typically have one characteristic amplitude, that is, one single periodic orbit, or at most a few characteristic amplitudes, whereas the Lotka type II mechanism will lead to oscillations with different amplitudes and frequencies for different initial concentrations of the intermediates.

Another interesting model used in ecosystems is the Lotka–Volterra model of competition between two species, such as rabbits and sheep [\[1\]](#). Again we represent rabbits by X and we now represent sheep by Y, each with a characteristic population growth dependent of the availability of food, but now the encounter between sheep and rabbits leads to a conflict due to competition for the same resources, that reduces the growth rate for each species. This model can be represented by the equations



where the last two steps represent the decay of the species in the absence of pasture. The step $X + Y \rightarrow$ written above assumes that both rabbits and sheep are equally competitive for pasture. This is not very realistic. It is more reasonable to assume that when rabbits and sheep compete for the same space, the larger animals can push the smaller ones aside. Eq. (18.III) are represented by the set of non-linear differential equations

$$\begin{aligned}\frac{d[X]}{dt} &= k'_1[X] - k_3[X][Y] - k_4[X]^2 = (k'_1 - k_3[Y] - k_4[X])[X] \\ \frac{d[Y]}{dt} &= k'_2[Y] - k_3[X][Y] - k_5[Y]^2 = (k'_2 - k_3[X] - k_5[Y])[Y]\end{aligned}\quad (18.4)$$

where $k'_1 = k_1[A]$ and $k'_2 = k_2[A]$. The change in the population of each species in the absence of inter-species competition can be written in the form

$$\begin{aligned}\frac{d[X]}{dt} &= [X](k'_1 - k_4[X]) \\ \frac{d[Y]}{dt} &= [Y](k'_2 - k_5[Y])\end{aligned}\quad (18.5)$$

It is more usual to express population (N_a , N_b) dynamics of organisms a and b in terms of the logistic equations

$$\begin{aligned}\frac{dN_a}{dt} &= r_a N_a \left(1 - \frac{N_a}{K_a}\right) \\ \frac{dN_b}{dt} &= r_b N_b \left(1 - \frac{N_b}{K_b}\right)\end{aligned}\quad (18.6)$$

which are equivalent to eq. (18.5) when $r_a = k'_1$ and $K_a = r_a/k_4$, and identically for species b . The parameter r_a (r_b) has the meaning of the growth rate of species a (b), and K_a (K_b) is the carrying capacity of the species a (b) that determines when the death rate becomes larger than the birth rate.

The equations for the population dynamics incorporating the inter-species competition have the form

$$\begin{aligned}\frac{dN_a}{dt} &= r_a N_a \left(1 - \frac{N_a}{K_a} - \alpha \frac{N_b}{K_a}\right) \\ \frac{dN_b}{dt} &= r_b N_b \left(1 - \frac{N_b}{K_b} - \beta \frac{N_a}{K_b}\right)\end{aligned}\quad (18.7)$$

where $r_b\beta/K_b$ may be different from $r_a\alpha/K_a$ and we do not have to assume that the two species are equally competitive. The behaviour of eq. (18.7) is more conveniently studied when the system is non-dimensionalised.

The parameters N_a , N_b , K_a and K_b have the same dimensions. A possible approach is to divide the first of eq. (18.7) by K_a and the second by $(K_a)^2$, and define $x = N_a/K_a$ and $y = N_b/K_a$.

$$\begin{aligned}\frac{dx}{dt} &= r_a x(1 - x - \alpha y) \\ \frac{1}{K_a} \frac{dy}{dt} &= r_b y \frac{1}{K_b} \left(\frac{K_b}{K_a} - y - \beta x \right)\end{aligned}\quad (18.8)$$

because $dN_a = K_a dx$ and $dN_b = K_a dy$. Defining the dimensionless time τ as $\tau = r_a t$, that is, $dt = d\tau/r_a$, gives

$$\begin{aligned}\frac{dx}{d\tau} &= x(1 - x - \alpha y) \\ \frac{dy}{d\tau} &= \frac{r_b}{r_a} \frac{K_a}{K_b} y \left(\frac{K_b}{K_a} - y - \beta x \right)\end{aligned}\quad (18.9)$$

or

$$\begin{aligned}\frac{dx}{d\tau} &= x(1 - x - \alpha y) \\ \frac{dy}{d\tau} &= y(\rho - \gamma x - \kappa y)\end{aligned}\quad (18.10)$$

where

$$\rho = \frac{r_b}{r_a} \quad \kappa = \frac{r_b}{r_a} \frac{K_a}{K_b} \quad \gamma = \frac{r_b}{r_a} \frac{K_a}{K_b} \beta \quad (18.11)$$

The equations above can be applied to the competition for pasture between rabbits and sheep with simple assumptions. The faster reproduction ability of rabbits is taken into account making $r_a = 2r_b$. The strength of sheep in pushing the rabbits aside given by $\alpha = 3\beta$. The larger carrying capacity of rabbits for the same extent of pasture is translated by $K_a = 2K_b$. Setting $r_b = 1$, $\beta = 1$ and $K_b = 100$, eq. (18.10) becomes

$$\begin{aligned}\frac{dx}{d\tau} &= x(1 - x - 3y) \\ \frac{dy}{d\tau} &= y(0.5 - x - y)\end{aligned}\quad (18.12)$$

As it is most often the case, it is unpractical to look for an analytical solution to these non-linear differential equations. Even when an analytical solution exists, it is much too complicated to inform on the behaviour of the system without calculations. On the other hand, it is possible to study the behaviour of this two-dimensional non-linear system in the phase plane (x, y) that is accessible to the functions. The procedure for this study requires finding the fixed points of the system and the calculation of the eigenvalues of the matrix corresponding to the set of differential equations.

The fixed points are obtained solving $dx/dt = 0$ and $dy/dt = 0$ simultaneously. For eq. (18.12), the fixed points are the solutions of the system

$$\begin{aligned} x(1 - x - 3y) &= 0 \\ y(0.5 - x - y) &= 0 \end{aligned} \quad (18.13)$$

which are $(0,0)$, $(0,0.5)$, $(1,0)$ and $(0.25, 0.25)$.

The calculation of the eigenvalues is based on linear algebra that is briefly recalled here. The eigenvalues of a matrix A

$$A = \begin{pmatrix} a & b \\ c & d \end{pmatrix} \quad (18.14)$$

are given by the characteristic equation

$$\det(A - \lambda I) = 0 \quad (18.15)$$

where I is the identity matrix. For the matrix above, the characteristic equation becomes

$$\det\begin{pmatrix} a - \lambda & b \\ c & d - \lambda \end{pmatrix} = 0 \quad (18.16)$$

and expanding the determinant yields

$$\lambda^2 - \tau\lambda + \Delta = 0 \quad (18.17)$$

where

$$\begin{aligned} \tau &= \text{trace}(A) = a + d \\ \Delta &= \det(A) = ad - bc \end{aligned} \quad (18.18)$$

which gives the solutions

$$\lambda_1 = \frac{\tau + \sqrt{\tau^2 - 4\Delta}}{2} \quad \lambda_2 = \frac{\tau - \sqrt{\tau^2 - 4\Delta}}{2} \quad (18.19)$$

The behaviour in the phase plane is conveniently studied when the phase portrait near a fixed point (x^*, y^*) is approximated to that of a corresponding linear system. In this case, the small disturbance u from the fixed point x^* , $u = x - x^*$, or the small disturbance v from the fixed point y^* , $v = y - y^*$, evolves according to

$$\begin{pmatrix} \frac{du}{dt} \\ \frac{dv}{dt} \end{pmatrix} = \begin{pmatrix} \frac{\partial f}{\partial x} & \frac{\partial f}{\partial y} \\ \frac{\partial g}{\partial x} & \frac{\partial g}{\partial y} \end{pmatrix}_{(x^*, y^*)} \begin{pmatrix} u \\ v \end{pmatrix} \quad (18.20)$$

where

$$J_{x^*, y^*} = \begin{pmatrix} \frac{\partial f}{\partial x} & \frac{\partial f}{\partial y} \\ \frac{\partial g}{\partial x} & \frac{\partial g}{\partial y} \end{pmatrix}_{(x^*, y^*)} \quad (18.21)$$

is the Jacobian matrix at the fixed point (x^*, y^*) . It is important to realise that the partial derivatives $\partial f/\partial x$, $\partial f/\partial y$, $\partial g/\partial x$ and $\partial g/\partial y$ are evaluated at the fixed point (x^*, y^*) . Hence they are numbers, not functions. When the fixed point is the origin, $(x^*, y^*) = (0,0)$, then $u = x - x^* = x$ and $v = y - y^* = y$; hence the non-linear terms in x and y can be omitted.

Often, much is learnt from the stability of the fixed points, although more information can be obtained from the detailed geometry of the trajectories in the phase plane. From the point of view of the stability, the fixed points can be classified in: *repellers* (also called *sources*) when both eigenvalues have positive real part, *attractors* (or *sinks*) when both eigenvalues have negative real part, or *saddles* when one eigenvalue is positive and the other is negative. There are also marginal cases when at least one real eigenvalue is zero, which are named *higher-order and non-isolated* fixed points [1]. It is also possible to find eigenvalues of the Jacobian matrix that are complex numbers. When the eigenvalues are complex numbers with a positive real part, the behaviour near the fixed point is a spiral source, and when they are complex numbers with a negative real part, the behaviour near the fixed point is a spiral sink.

Using these tools, it is possible to study eq. (18.12) and obtain information without sophisticated calculations. The fixed points were already calculated. The Jacobian matrix is

$$J_{x^*,y^*} = \begin{pmatrix} 1-2x-3y & -3x \\ -y & 0.5-x-2y \end{pmatrix}_{(x^*,y^*)} \quad (18.22)$$

and at $(0,0)$ takes the value

$$J_{0,0} = \begin{pmatrix} 1 & 0 \\ 0 & 0.5 \end{pmatrix} \quad (18.23)$$

where the eigenvalues are $\lambda_1 = 1$ and $\lambda_2 = 0.5$. Both eigenvalues are positive, hence this fixed point is a *repeller*. At the fixed point $(0,0.5)$

$$J_{0,0.5} = \begin{pmatrix} -0.5 & 0 \\ 0.5 & -0.5 \end{pmatrix} \quad (18.24)$$

with eigenvalues are $\lambda_1 = -0.5$ and $\lambda_2 = -0.5$. Both eigenvalues are negative hence this fixed point is an *attractor*. For the fixed point $(1,0)$

$$J_{1,0} = \begin{pmatrix} -1 & -3 \\ 0 & -0.5 \end{pmatrix} \quad (18.25)$$

the eigenvalues are complex numbers with a negative real part, and correspond to exponentially decaying oscillations to an *attractor*. Finally, for the fixed point $(0.25,0.25)$

$$J_{0.25,0.25} = \begin{pmatrix} -0.25 & -0.75 \\ -0.25 & -0.25 \end{pmatrix} \quad (18.26)$$

the eigenvalues are $\lambda_1 > 0$ and $\lambda_2 < 0$, which mean that this fixed point is a *saddle point*.

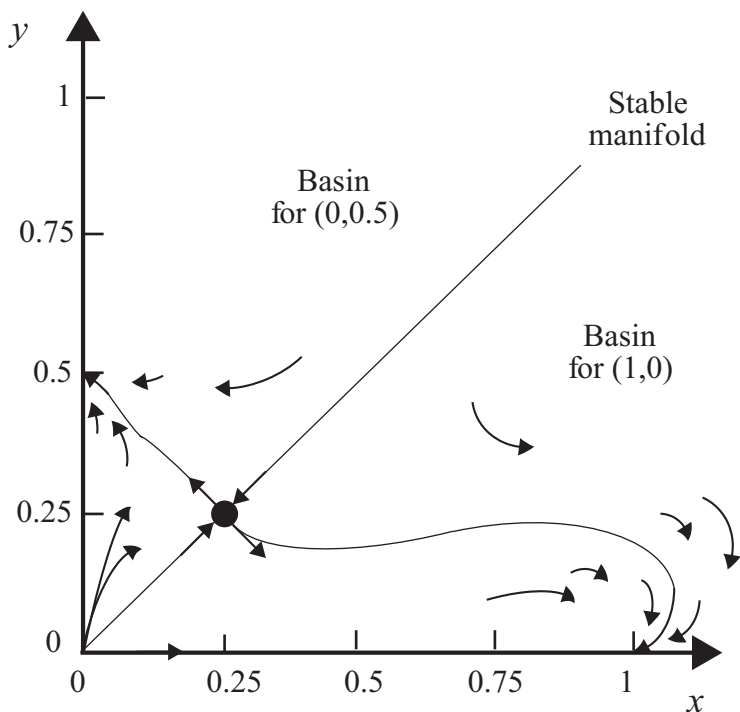
The phase portrait can be sketched plotting the nullclines, defined as the curves where either $dx/d\tau$ or $dy/d\tau$ are equal to zero. They indicate the flow in the phase portrait. For a *repeller* point, the nullclines indicate the direction out of that point. For an *attractor*, the nullclines point into the point, with the subtlety that when they are associated with a complex number, the decaying oscillation takes the form of a spiral. Finally, the saddle point is represented with nullclines pointing into and out of the stable point in perpendicular directions. [Figure 18.1](#) illustrates the phase portrait for rabbits and sheep under the assumptions described above.

[Figure 18.1](#) is very schematic and was obtained without actual calculations with [eq. \(18.12\)](#). Nevertheless, it allows for interesting biological interpretations. It shows that, in the conditions established, one species generally drives the other one to extinction. Trajectories below the stable manifold lead to the extinction of the sheep, whereas those above the manifold will lead to the extinction of the rabbits. The initial populations determine the fate of the species. This led biologists to the principle of competitive exclusion: two species competing for the same limited resources typically cannot co-exist.

It is interesting to implement a spreadsheet calculation of [eq. \(18.7\)](#) to complement the qualitative view of [Figure 18.1](#) with quantitative examples. The calculations can be conveniently made for successive generations of rabbits and sheep assuming that each new generation of both species appears at the same time. [Table 18.1](#) presents the population of the successive generations using the parameters discussed above. The calculations were started at two different initial conditions: the population of rabbits was two and the population of sheep was either six or eight. The data of [Table 18.1](#) are represented in [Figure 18.2](#).

[Table 18.1](#) and [Figure 18.2](#) show that 16 generations rabbits drive sheep to extinction when the initial populations are rabbits = 2 and sheep = 6. However, sheep drive rabbits to extinction in 12 generations when the initial populations are rabbits = 2 and sheep = 8. This remarkable sensitivity to initial conditions is observed in many non-linear systems. This example illustrates the relevance of non-linear systems and the type of graphical and numerical results that can be obtained. However, it should not be taken literally. Different choices of the parameters will lead to different results. Most often, one species competing for the same resources will lead the other one to extinction, either driven by a higher relative strength of by a higher relative growth rate. However, it is also possible to find conditions that enable coexistence.

Non-linear differential equations have found many diverse applications. An interesting case is that of the extinction of Neanderthals 40,000 years ago after a presence in Europe over a period of 400,000 years, including at least two cycles of glacial and inter-glacial conditions. The modern *Homo sapiens sapiens* (HSS) arrived in Europe *ca.* 45,000 years ago and 5000 years later Neanderthals died out. Both groups of humans were among the top carnivores and competed for the same resources. A first study of population dynamics using a competition term and the Lotka–Volterra model with the same birth rate for both hominids showed that a tiny difference in the rate of mortality unfavourable for the Neanderthals

**FIGURE 18.1**

Phase portrait for rabbits and sheep in competition for the same pasture. The thick line dividing the phase space is the stable manifold that contains the saddle point and defines two basins of attraction, one for rabbits and the other one for sheep.

could explain the observed extinction [2]. The higher rate of mortality is supported by evidence for a relatively short Neanderthal lifecycle [3]. The classical hypothesis for the extinction of Neanderthals invokes climate change. More recently, the hypothesis of some inter-breeding with HSS gained support and suggested some absorption of the Neanderthals by HSS. Recent modelling of the disappearance of Neanderthals using logistic equations and a modification of Lotka–Volterra model to account for the changes in the populations of Neanderthals, HSS and of the resources available to them, showed that neither climate alone nor a higher minimal death rate of Neanderthals can explain their extinction. On the other hand, a small advantage of HSS for resource usage or for interference between the two hominids slightly detrimental to Neanderthals could explain the extinction [4]. A reasonable hypothesis is that HSS had an advantage in learning ability relative to Neanderthals [5]. Although more archaeological evidence is needed before arriving at definitive conclusions concerning the extinction of Neanderthals, modelling such complex systems with non-linear differential equations is becoming an indispensable tool to guide research.

Table 18.1 Simulation of the population of rabbits (N_a) and sheep (N_b) according to eq. (18.7), using $N_{t+1} = N_t + dN/dt$, with $r_a = 2r_b$ ($r_b = 1$), $\alpha = 3\beta$ ($\beta = 1$) and $K_a = 2K_b$ ($K_b = 100$), for initial populations $N_a = 2$ and $N_b = 6$ or $N_a = 2$ and $N_b = 8$.

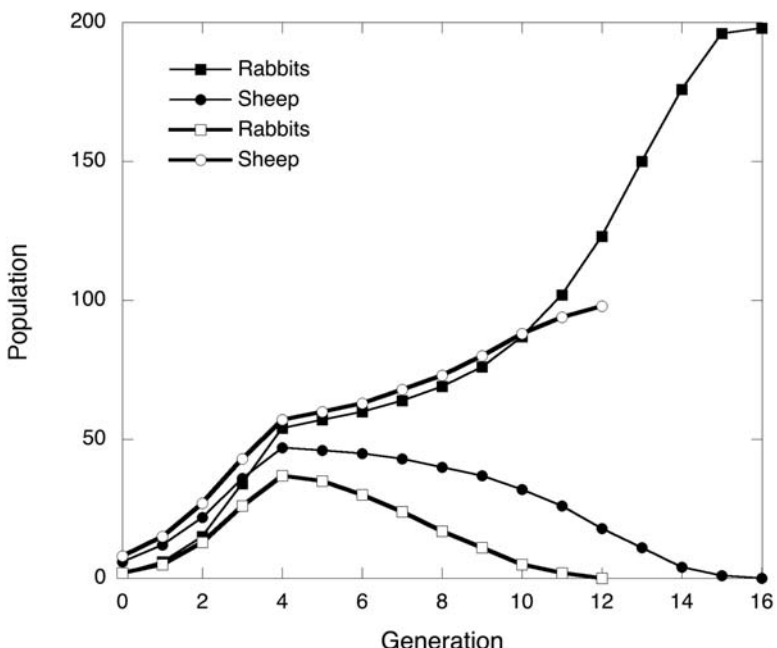
Generation	dN_a/dt	N_a	dN_b/dt	N_b	dN_a/dt	N_a	dN_b/dt	N_b
0		2		6		2		8
1	3.6	6	5.52	12	3.48	5	7.2	15
2	9	15	10	22	8	13	12	27
3	18	34	14	36	13	26	16	43
4	20	54	11	47	11	37	13	57
5	3	57	0	46	-3	35	3	60
6	2	60	-2	45	-5	30	3	63
7	4	64	-2	43	-6	24	5	68
8	5	69	-3	40	-7	17	6	73
9	8	76	-4	37	-7	11	7	80
10	11	87	-5	32	-5	5	7	88
11	15	102	-6	26	-4	2	6	94
12	21	123	-7	18	-1	0	4	98
13	27	150	-8	11				
14	26	176	-7	4				
15	20	196	-3	1				
16	2	198	-1	0				

18.2 Chaos

The sensitivity of non-linear systems to the initial conditions is at the origin of even more dramatic examples than those discussed above. The measurement of every variable is necessarily associated with a certain error. The effect of the uncertainty on the measurement is not a major problem in linear systems, but in non-linear system, the error may propagate and become larger than the value of the variable. This can be seen using a very simple non-linear equation that is a discrete-time analogue of the logistics eq. (18.6) for population growth [6]

$$x_{n+1} = ax_n(1 - x_n) \quad (18.27)$$

This equation relates the value of a population in the n th generation (x_n) to its value in the next generation (x_{n+1}). For $a \leq 1$ or $a \geq 4$ the iterations eventually lead to $x = 0$, but when $0 \leq x \leq 1$ and $1 \leq a \leq 4$, the value of x after a large number of iterations depends on the precision of the calculation. Every calculation is made with a specific precision that depends on the software and the hardware of the computer. Currently spreadsheets follow specifications that offer a precision of 15 significant digits. In order to evaluate the impact of the number of

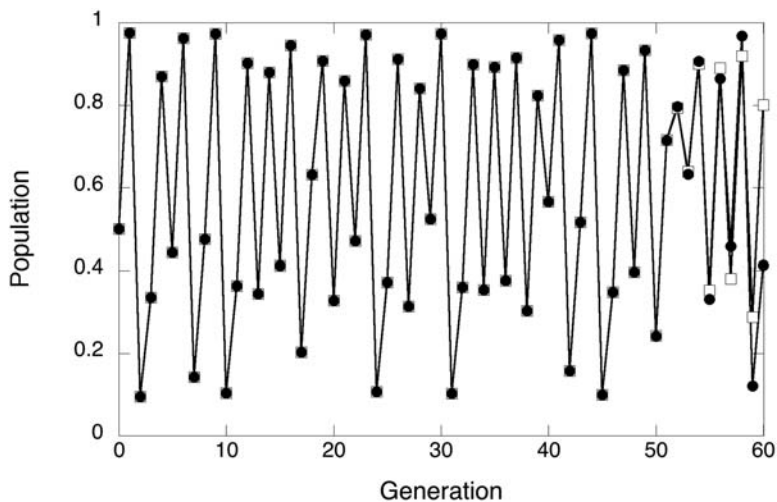
**FIGURE 18.2**

Changes in populations of rabbits and sheep competing for the same pasture as a function of their generations, according to the data in Table 18.1.

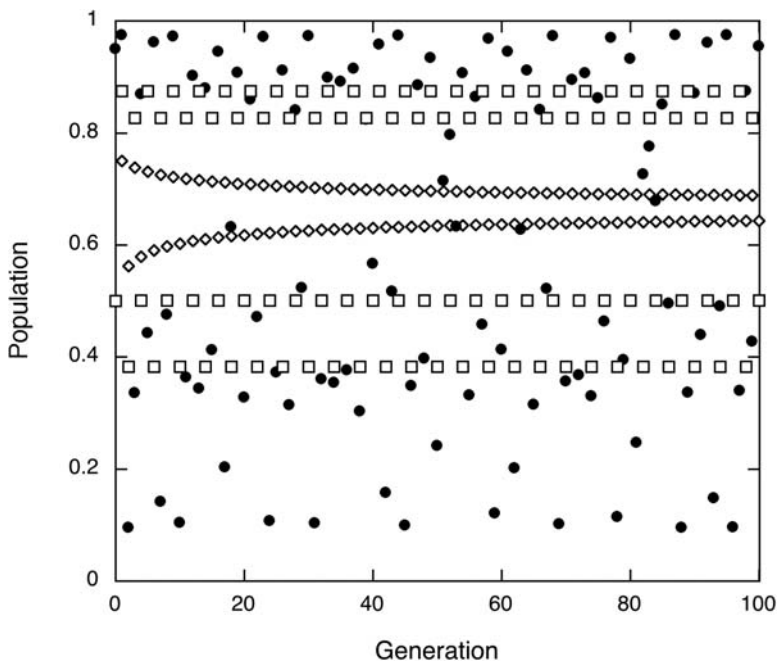
significant digits in the results of calculations with eq. (18.27), the preferences of spreadsheets may be changed to set the precision as displayed in the spreadsheet. Figure 18.3 shows that the value of x calculated with 12 significant digits becomes appreciably different from that calculated with 15 significant digits after 50 iterations, and after 60 iterations they seem to be unrelated. Identically, it can be seen that the results after a few iterations change dramatically for small changes in the initial value of a (e.g., 0.2%) even with a precision of 15 significant digits.

The sensitivity of the quadratic iteration of eq. (18.27) to the precision of the initial measurement depends on the value of a . Nevertheless, there are stable solutions for values of a between 1 and 4. For $1 < a < 3$ the population grows and eventually reaches a non-zero steady state. For example, it is possible to see that when $a = 1.5$ then $x \rightarrow 1/3$, $a = 2.0$ leads to $x \rightarrow 0.5$ and $a = 2.5$ makes $x \rightarrow 0.6$. New phenomena are observed when $a \geq 3$. Figure 18.4 shows that $a = 3$ leads to an oscillation between two states—a bifurcation. A second bifurcation, now with an oscillation between four states, is observed at $a = 3.449\dots$, and a third bifurcation is seen at $a = 3.54409\dots$ Successive bifurcations become faster and faster. In general, given $d_{k-1} = a_k - a_{k-1}$ and $d_k = a_{k+1} - a_k$,

$$d_k \approx \frac{d_{k-1}}{\delta} \quad (18.28)$$

**FIGURE 18.3**

Changes in the population according to eq. (18.27) for $x_0 = 0.5$ and $a = 3.9$ using either a precision of 12 digits (open squares) or of 15 digits (filled circles).

**FIGURE 18.4**

Bifurcations of the quadratic iterator for $a = 3.0$ (open lozenges) and $a = 3.5$ (open squares), and chaotic behaviour for $a = 3.9$.

where $\delta = 4.669$ is a constant known as Feigenbaum constant. Amazingly, this is a universal constant. It is not just the constant for period doubling in the logistic map of eq. (18.27). The same constant appears in other one-dimensional maps of quadratic equations and transcendental equations. The period-doubling regimen of the quadratic iterator converges to a point $a = 3.5699456\dots$, the Feigenbaum point, after which chaos emerges.

Chaos is aperiodic long-term behaviour in a deterministic system that exhibits sensitivity dependence on initial conditions [1]. This means that when $t \rightarrow \infty$, the system does not evolve to fixed points or periodic (quasi-periodic) orbits. However, the system remains deterministic because there are no random inputs or noise: it is defined by exact conditions and strictly obeys the non-linear equations. Nevertheless, the evolution of the systems is very sensitive to the precision of the initial conditions and nearby trajectories separate exponentially fast.

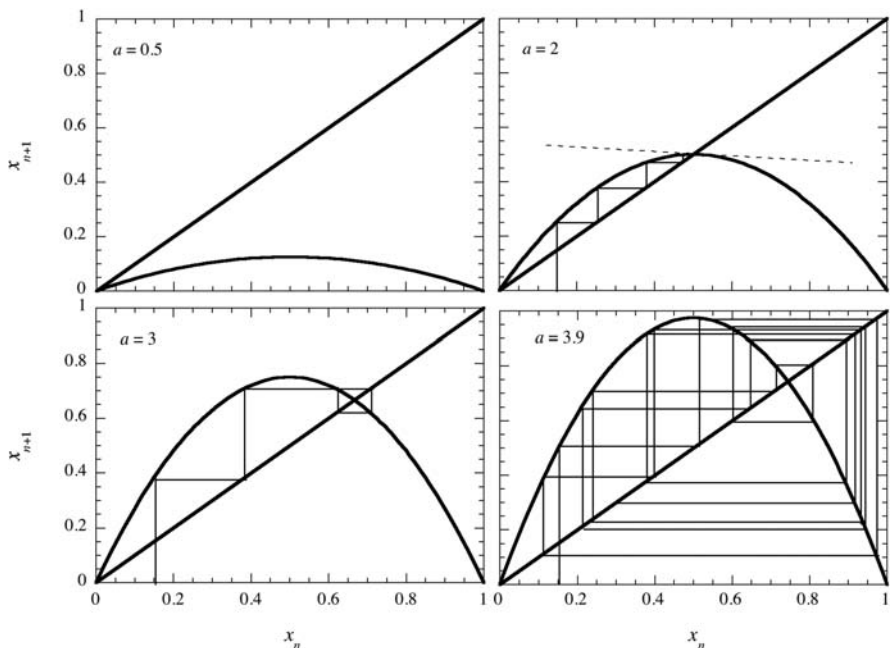
It is convenient to make a graphical study the behaviour of the quadratic iterator to understand better the changes between stable solutions, bifurcations and chaos. The graphical solution for eq. (18.27) is the intersection between the line $x_{n+1} = x_n$ and the parabola $f(x) = ax(1 - x)$. There are two fixed points that satisfy this solution: the trivial solution $x = 0$ and the non-trivial solution $x^* = 1 - 1/a$. The stability of the fixed point x^* depends on the slope of the tangent to the curve $f(x)$ at x^* . By definition, this slope, illustrated by a dashed line in Figure 18.5b, is given by

$$\frac{df(x)|_{x=x^*}}{dx} = a(1 - 2x^*) \quad (18.29)$$

The slope at $x = x^*$ is obtained making the derivative of $f(x)$ and then replacing x by its non-trivial solution. Hence the slope is given by $2 - a$. When the slope is between 45 degrees and -45 degrees (i.e., the tangent is between 1 and -1 , or $-1 < 2 - a < 1$), the fixed point x^* is locally stable and attracts all trajectories originating in the interval $0 < x < 1$ if and only if $1 < a < 3$.

Figure 18.5a shows that for $a < 1$ the parabola lies below the diagonal and the origin is the only fixed point. At $a = 1$, the parabola becomes tangent to the diagonal. For $1 < a < 3$, a fixed point x^* can be found starting from any initial value of x . This is illustrated by stating a vertical line from the initial value of x (x_0) until the intersection with the parabola. At that point a horizontal line is drawn to the line $x_{n+1} = x_n$. The intersection with this line is the value of the first iteration (x_1). The process is followed, as shown in Figure 18.5b, and converges to a fixed point x^* that is stable. Figure 18.5c illustrates the case for $a = 3$ where successive iterations lead to possible solutions, that is, the $x_n = x_{n+2}$ and $x_{n+1} = x_{n+3}$. This is called a flip bifurcation and is associated with period doubling [1]. Figure 18.5d shows that for a value of a larger than the Feigenbaum point it is not possible to find a stable solution. Successive iterations lead to different values of x_n and the graphical representation eventually resembles a black shadow that covers all the space of the possible solutions.

The emergence of chaos for certain conditions of non-linear systems is not just an exotic mathematical finding. Deterministic chaos plays an important role

**FIGURE 18.5**

Graphical study of the quadratic iterator. (a) Only the origin is the solution. (b) The solution is the fixed point $x^* = 0.5$. (c) A bifurcation occurs and yields oscillations between two solutions. (d) There is no stable solution.

in many natural systems. In fact, the first landmark paper in the study of chaos is the description offered by Lorenz for convection in the atmosphere, which is important for weather prediction. The Lorenz equations are

$$\begin{aligned}\frac{dx}{d\tau} &= -\sigma x + \sigma y \\ \frac{dy}{d\tau} &= \rho x - y - xz \\ \frac{dz}{d\tau} &= xy - \beta z\end{aligned}\tag{18.30}$$

where $\sigma, \rho, \beta > 0$ are parameters, x is proportional to the intensity of the convective motion, while y is proportional to the temperature difference between the ascending and descending currents and z is proportional to the distortion of the vertical temperature profile from linearity [7]. The derivative is with respect to the dimensionless time. All the solutions for eq. (18.30) are unstable and almost all of them are non-periodic. Numerical solutions to the convection equations are extremely sensitive to the initial conditions: slightly different initial states can

evolve into considerably different states. This observation was later popularised by the metaphor that the flap of a butterfly's wings in Brazil may set off a tornado in Texas.

18.3 Oscillatory reactions

Adding feedback to non-linearity leads to mechanisms where the intensity of the effect influences the intensity of the action that generated the effect. In chemical systems, this is translated by participation of an intermediate, or a product, in the reaction that synthesises that intermediate, or product. This is exemplified by the mechanism proposed by Prigogine and co-workers [8]



The overall reaction is $A + B \rightarrow C + D$ and feedback is provided by the third-order autocatalytic step. This mechanism is unrealistic because of the tri-molecular step. Nevertheless, it played an important role in demonstrating the possibility of having oscillatory reactions. Prigogine was awarded the 1977 Nobel Prize in Chemistry for his work on the theory of dissipative structures. At the time mechanism (18.IV) was proposed, Prigogine was working in Brussels, and this mechanism became known as the *Brusselator*.

Experimental work on oscillatory reactions preceded the *Brusselator* but was regarded with suspicion. Boris Belousov (1893–1970) found that the oxidation of citric acid could occur in conditions where intermediates oscillated for long periods of time. Over the period of 1950–1956, Belousov tried to publish this work, but it was systematically rejected by peer-reviewed journals on the basis that such oscillations were “impossible”. Belousov abandoned science before having his work recognised, but Zhabotinsky followed his laboratory notes and pursued the study of this system. In 1964 the first articles on this subject were published in Russian journals and in 1970 full recognition was achieved [9]. The so-called Belousov–Zhabotinsky (BZ) reaction involves the oxidation of an organic species such as citric acid or malonic acid with an acidic solution of bromate in the presence of metal catalysts. The metal ions more frequently used are the redox pairs $\text{Ce(II)}/\text{Ce(III)}$ and $[\text{Fe(II)}\text{phenanthroline}^{2+}/\text{Fe(III)}\text{phenanthroline}^{3+}]$. This reaction has a short induction period followed by an oscillatory phase in which, for the iron-phenanthroline pair, red and blue colours alternate in time. The oscillations may last over 2 h and only after 100 oscillations, the colours attenuate and eventually disappear when the final equilibrium state is achieved.

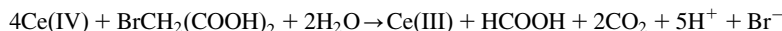
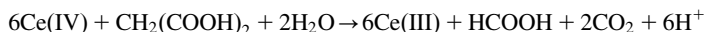
A simple protocol may be followed to observe the BZ reaction in a chemistry laboratory [10]: (1) prepare 500 mL of 1 M H_2SO_4 and 0.025 M of iron-phenanthroline indicator (add 1.485 g of 1:10-phenanthroline and 0.695 g of

$\text{FeSO}_4 \cdot 7\text{H}_2\text{O}$ to 100 mL of water); (2) add 1 or 2 mL of the indicator solution, 14.3 g of malonic acid, 5.22 g of KBrO_3 and 0.548 g of $\text{Ce}(\text{NH}_4)_2(\text{NO}_3)_6$ to the 500 mL of H_2SO_4 ; (3) pour some of this mixture to cover the bottom of a Petri dish and observe the development of chemical waves. This system has an induction period of a few minutes, which can be reduced if the H_2SO_4 solution is freshly prepared and is still warm when the reactants are mixed in.

Field, Körös and Noyes (FKN) offered a rather detailed explanation of the BZ reaction mechanism [11,12]. According to these authors, there are two different overall processes that can occur in this system, named Process A and Process B. These systems are presented in Table 18.2. The critical features of the FKN mechanism are the competition of bromide and bromate ions for bromous acid and the autocatalytic nature of the G component of Process B. When $[\text{Br}^-]$ is sufficiently high, all HBrO_2 reacts with Br^- by step (R2) and Process A describes the kinetics of the system. The consumption of Br^- leads for a critical $[\text{Br}^-]$, $[\text{Br}^-]_{\text{cr}}$, to a situation where Br^- in (R2) cannot compete with BrO_3^- in step (R5) for the reaction with HBrO_2 . According to FKN, that critical concentration is given by

$$[\text{Br}^-] = \frac{k_{\text{R5}}}{k_{\text{R2}}} [\text{BrO}_3^-] \quad (18.31)$$

The Ce(IV) produced by Process B reacts with malonic acid or with bromomalonic acid to regenerate Ce(III)



Br^- is then produced after Process B and its concentration will raise to cause step (R2) to become again dominant to determine the fate of HBrO_2 . The cycle is restarted and will continue until malonic acid is no longer present in sufficient quantities to regenerate Ce(III) and Br^- .

Table 18.2 Processes taking place in the BZ system according to the original FKN numbering scheme.

Process A	
$\text{Br}^- + \text{BrO}_3^- + 2\text{H}^+ \rightarrow \text{HBrO}_2 + \text{HOBr}$	(R3)
$\text{Br}^- + \text{HBrO}_2 + \text{H}^+ \rightarrow 2\text{HOBr}$	(R2)
$(\text{Br}^- + \text{HOBr} + \text{H}^+ \rightarrow \text{Br}_2 + \text{H}_2\text{O}) \times 3$	(R1)
$(\text{Br}_2 + \text{CH}_2(\text{COOH})_2 \rightarrow \text{BrCH}(\text{COOH})_2 + \text{Br}^- + \text{H}^+) \times 3$	(R8)
$2\text{Br}^- + \text{BrO}_3^- + 3\text{H}^+ + 3\text{CH}_2(\text{COOH})_2 \rightarrow 3\text{BrCH}(\text{COOH})_2 + 3\text{H}_2\text{O}$	(A)
Process B	
$\text{BrO}_3^- + \text{HBrO}_2 + \text{H}^+ \rightarrow 2\text{BrO}_2^\bullet + \text{H}_2\text{O}$	(R5)
$(\text{Ce}(\text{III}) + 2\text{BrO}_2^\bullet + \text{H}^+ \rightarrow \text{Ce}(\text{IV}) + \text{H}_2\text{O} + \text{HBrO}_2) \times 2$	(R6)
$2\text{Ce}(\text{III}) + \text{BrO}_3^- + \text{HBrO}_2 + 3\text{H}^+ \rightarrow 2\text{Ce}(\text{IV}) + \text{H}_2\text{O} + 2\text{HBrO}_2$	(G)
$2\text{HBrO}_2 \rightarrow \text{HOBr} + \text{BrO}_3^- + \text{H}^+$	(R4)

The typical experimental behaviour of BZ reactions is illustrated in Figure 18.6. The experimental results when $[BrO_3^-] = 0.06\text{ M}$ and $[H^+] = 0.8\text{ M}$ led to the estimation of the rate constants presented in Table 18.3. The reaction mechanism in Table 18.2 suggested a general kinetic scheme, named *Oregonator*, that represents the critical steps of the FKN mechanism. When all the steps of the model are assumed to be irreversible, the *Oregonator* takes the form

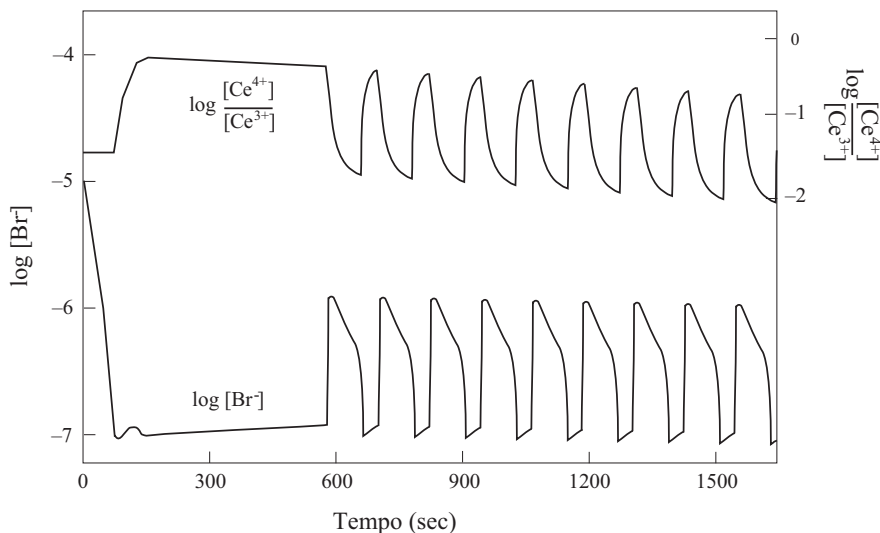
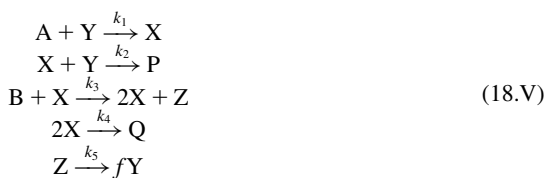


FIGURE 18.6

Typical results observed for the BZ reaction illustrating the oscillations of the potentials measured with a Pt electrode or with a Br^- electrode, both relative to the standard calomel electrode [11].

Table 18.3 Rate constants used in the simulation of the BZ reaction presented in Figure 18.6 [12].

Mechanism in Table 18.2	Mechanism (18.V)	$[BrO_3^-] = 0.06\text{ M}$, $[H^+] = 0.8\text{ M}$
$K_{R3} [H^+]^2$	k_1	$1.34\text{ M}^{-1}\text{ sec}^{-1}$
$K_{R2} [H^+]$	k_2	$1.6 \times 10^9\text{ M}^{-1}\text{ sec}^{-1}$
$K_{R5} [H^+]$	k_3	$8 \times 10^3\text{ M}^{-1}\text{ sec}^{-1}$
K_{R4}	k_4	$4 \times 10^7\text{ M}^{-1}\text{ sec}^{-1}$

The simplest stoichiometric combination of equations that leads to no net production or destruction of the intermediates X, Y and Z, is $f(1) + f(2) + 2(3) + (4) + 2(5)$ and leads to



The stoichiometric factor f adds generally to the kinetic scheme and is important for its application to the BZ reaction. The *Oregonator* can be related to the FKN mechanism of the BZ reaction when $X \equiv \text{HBrO}_2$, $Y \equiv \text{Br}^-$, $Z \equiv \text{Ce(IV)}$, the acidity effects are included in the rate constants (Table 18.3) and $A \equiv B \equiv \text{BrO}_3^-$. The stoichiometric factor f is $\frac{1}{4}$ if Ce(IV) reacts only with bromomalonic acid and still smaller if the reaction with malonic acid also takes place.

The kinetic behaviour of the intermediates in the *Oregonator*, as expressed above as a set of irreversible reactions, is

$$\begin{aligned} \frac{dX}{dt} &= k_1AY - k_2XY + k_3BX - 2k_4X^2 \\ \frac{dY}{dt} &= -k_1AY - k_2XY + fk_5Z \\ \frac{dZ}{dt} &= k_3BX - k_5Z \end{aligned} \quad (18.32)$$

This set of equations can be more easily handled, and the solution presented in a more general form, casting the concentrations and time in dimensionless variables. Making [12]

$$\begin{aligned} [\text{HBrO}_2] \equiv X &= \frac{k_1A}{k_2}x = 5.025 \times 10^{-11}x \\ [\text{Br}^-] \equiv Y &= \frac{k_3B}{k_2}y = 3.000 \times 10^{-7}y \\ [\text{Ce(IV)}] \equiv Z &= \frac{k_1k_3}{k_2k_5}ABz = 2.412 \times 10^{-8}z \\ t &= \frac{\tau}{\sqrt{k_1k_3AB}} = 0.1610\tau \end{aligned} \quad (18.33)$$

leads to the equivalent of eq. (18.32) in dimensionless variables

$$\begin{aligned} \frac{dx}{d\tau} &= \sigma(y - xy + x - \rho x^2) \\ \frac{dy}{d\tau} &= \sigma^{-1}(-y - xy + fz) \\ \frac{dz}{d\tau} &= \gamma(x - z) \end{aligned} \quad (18.34)$$

where

$$\begin{aligned}\sigma &= \sqrt{k_3B/k_1A} = 77.27 \\ \rho &= \frac{2k_1k_4A}{k_2k_3B} = 8.375 \times 10^{-6} \\ \gamma &= \frac{k_5}{\sqrt{k_1k_3AB}} = 0.1610\end{aligned}\quad (18.35)$$

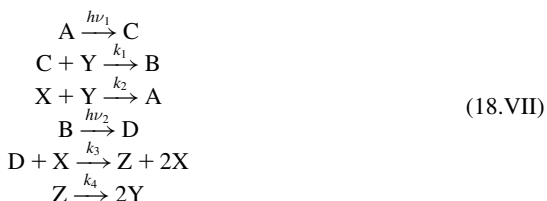
Eq. (18.34) are a “stiff” system of ordinary differential equations that is intractable to analytical approaches. However, the system can be solved numerically using commercial software [13]. This closed system of chemical reactions cannot oscillate indefinitely, that is, does not converge to a limit cycle. It is possible to obtain a limit cycle making $[BrO_3^-]$ and $[H^+]$ constant, which effectively corresponds to an open system, exchanging mass with the surroundings. Field and Noyes showed numerically that in these conditions there is a true limit cycle with sustained oscillatory behaviour and ergodic [12]. This means that the system will evolve to the same periodic trajectory regardless of the initial condition, which is not the case of the Lotka type II mechanism.

18.4 The Coimbrator

It would be of interest to conceive a closed system with sustained oscillatory behaviour and ergodic. This seems to contradict the second law of thermodynamics as it is well known that a closed chemical system at constant temperature and pressure should attain equilibrium [14]. However, such a system is not isolated: it can absorb UV/Vis light and undergo photochemical reactions. A closed chemical reaction system where a net product of other steps is photochemically transformed back in the reactant may have sustained oscillations [15]. A simple demonstration of this possibility is the replacement of the cerium catalysed step of the BZ reaction by photochemical reaction involving $Ru(bpy)_3^{2+}$ [16]. Horváth, Nagypál and Epstein were able to detect oscillations in the thiosulphate-chlorite reaction system under illumination, which were assigned to the photodecomposition of the tetrathionate formed in one step of the reaction and the presence of an autocatalytic step involving thiosulfate [17]. The impetus for the oscillations is the continuous illumination.

It has been speculated that a closed system with sustained oscillations of some of its components under constant illumination may have the ability to transform the energy of sunlight into mechanical energy, that is, to be a solar engine [18]. If this system is to be a realistic chemical system, each step must be at the most bi-molecular. Additionally, in order to have limit cycle oscillations, the system must have at least three intermediates and an auto-catalytic reaction [19]. Finally, this closed system must include at least one step where net product of other steps

is photochemically transformed back in the reactant. These conditions are met by the system



where the steps identified by $h\nu$ correspond to photochemical reactions. [Figure 18.7](#) shows an illustration of this system that emphasises that this is a closed system with no net consumption of reactants or generation of products.

The time dependence of all the chemical species involved in the system is described by

$$\begin{aligned}
 \frac{dA}{dt} &= -h_1 + k_2XY & \frac{dC}{dt} &= h_1A - k_1CY \\
 \frac{dB}{dt} &= -h_2 + k_1CY & \frac{dD}{dt} &= h_2B - k_3DX \\
 \frac{dX}{dt} &= k_3DX - k_2XY & & \\
 \frac{dY}{dt} &= -k_1CY - k_2XY + 2k_4Z & & \\
 \frac{dZ}{dt} &= k_3DX - k_4Z & &
 \end{aligned} \quad (18.\text{36})$$

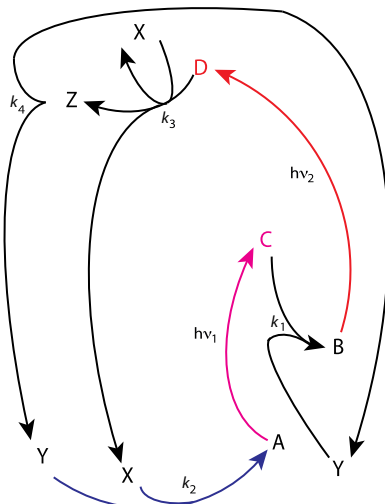


FIGURE 18.7

Representation of the reactions taking place in the closed system, where C is obtained from A by electronic excitation with $h\nu_1$, and D is obtained from B by electronic excitation with $h\nu_2$.

In a physically meaningful system all the concentrations C , D , X , Y and Z and all the constants k_1 , k_2 , k_3 and k_4 are positive. If dyes A and B are sufficiently concentrated and absorb more than 99% of different spectral ranges of the Sun, under daylight the concentrations of their electronic excited states C and D will remain approximately constant (steady state) even when A and B drop to 1/10 of their initial value at the lowest of the oscillation cycle. Under these conditions, A, B, C and D can be treated as constants and the system can be simplified and decoupled from the variations of X, Y and Z,

$$\begin{aligned}\frac{dX}{dt} &= k_3DX - k_2XY \\ \frac{dY}{dt} &= -gY - k_2XY + 2k_4Z \\ \frac{dZ}{dt} &= k_3DX - k_4Z\end{aligned}\tag{18.37}$$

where we defined $g = k_1C$. This is a pseudo-first-order rate under continuous irradiation if A is not depleted from the system. Thus the quotient g/k_2 has the dimensions of a concentration and can be defined as the characteristic concentration. This is used to make the following dimensionless measures of the species:

$$x = \frac{k_2}{g}[X] \quad y = \frac{k_2}{g}[Y] \quad z = \frac{k_2}{g}[Z] \quad \tau = gt\tag{18.38}$$

The characteristic time $1/g$ and the characteristic concentration g/k_2 allow for the definition of dimensionless constants. After the appropriate replacements, the simplified system of differential equations is, in dimensionless units,

$$\begin{aligned}\frac{dx}{d\tau} &= \alpha x - xy \\ \frac{dy}{d\tau} &= -y - xy + 2\beta z \\ \frac{dz}{d\tau} &= \alpha x - \beta z\end{aligned}\tag{18.39}$$

where $\alpha = (k_3D)/(k_1C)$ and $\beta = k_4/(k_1C)$. Following the tradition of naming oscillators from geographical origin, the system described by the ordinary differential eq. (18.39) is named *Coimbrator*.

The equilibrium (fixed) points of this three-dimensional system are obtained solving $dx/dt = 0$, $dy/dt = 0$ and $dz/dt = 0$ simultaneously. It is immediately apparent that the equilibrium points are

$$O = (0, 0, 0) \quad P = \left(1, \alpha, \frac{\alpha}{\beta} \right) \quad (18.40)$$

The Jacobian matrix is

$$J_{x^*, y^*, z^*} = \begin{bmatrix} \alpha - y & -x & 0 \\ -y & -1 - x & 2\beta \\ \alpha & 0 & -\beta \end{bmatrix}_{(x^*, y^*, z^*)} \quad (18.41)$$

and the characteristic polynomials at points O and P are

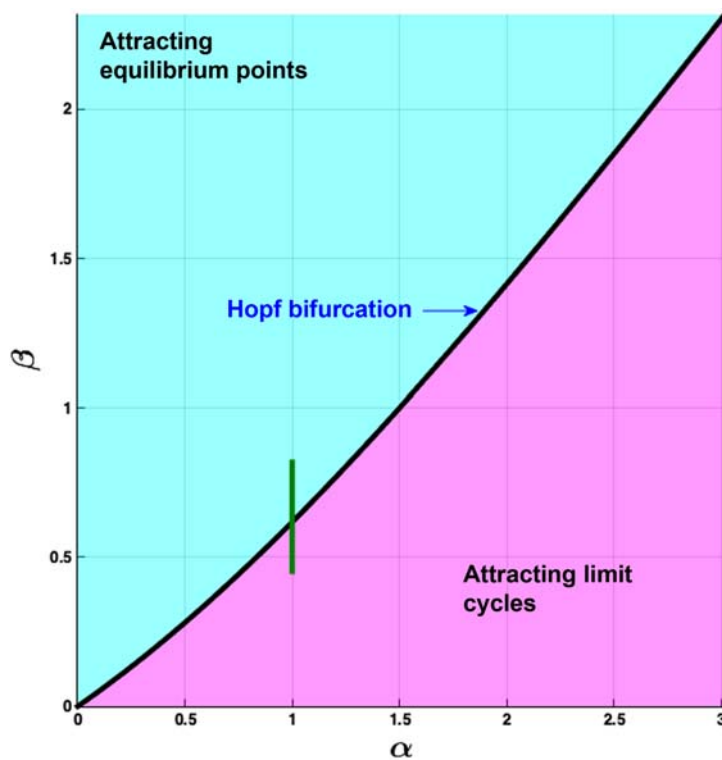
$$\begin{aligned} p_O(\lambda) &= \det \begin{pmatrix} \alpha - \lambda & 0 & 0 \\ 0 & -1 - \lambda & 2\beta \\ \alpha & 0 & -\beta - \lambda \end{pmatrix} \\ p_P(\lambda) &= \det \begin{pmatrix} 0 - \lambda & -1 & 0 \\ -\alpha & -2 - \lambda & 2\beta \\ \alpha & 0 & -\beta - \lambda \end{pmatrix} \end{aligned} \quad (18.42)$$

which yield the characteristic equations

$$\begin{aligned} \text{Point } O: \quad &\lambda^3 + (1 - \alpha + \beta)\lambda^2 + (-\alpha + \beta - \alpha\beta)\lambda - \alpha\beta = 0 \\ \text{Point } P: \quad &\lambda^3 + (\beta + 2)\lambda^2 + (2\beta - \alpha)\lambda + \alpha\beta = 0 \end{aligned} \quad (18.43)$$

The treatment of these equations to obtain the eigenvalues and their interpretation become very laborious and it is preferable to resort to calculations. [Figure 18.8](#) shows the relation between the parameters α and β that eventually leads to equilibrium points or to limit cycles [20]. The set of parameters $\alpha = 1$ and $\beta = 0.7$ falls on the domain where an equilibrium point is reached, while the set of parameters $\alpha = 1$ and $\beta = 0.6$ lead to a periodic orbit. The convergence either to equilibrium or to a limit cycle is illustrated in [Figure 18.9](#).

The *Coimbrator* may be more than just a curiosity. It is very well established that Earth experienced five glaciation cycles with a period of *ca.* 100,000 years over the last half million years. The current interpretation for this phenomenon is based on the hypothesis formulated by Milankovitch one century ago. According to Milankovitch, variations in the Earth's orbit result in cyclic changes in insolation. The orbit approximates an ellipse and departures from that ellipse, due to the gravitational pull of Jupiter and Saturn, correspond to changes in eccentricity. There are components with 95,000 and 125,000-year cycles in eccentricity changes that have been associated with 100,000 years period of glaciation. In addition, there are changes in the Earth's axial tilt (obliquity), with a cycle of 41,000 years, and in its axial precession with a period of 25,000 years. Hence insolation forcing is very appealing to explain cyclic changes in a closed system

**FIGURE 18.8**

Bifurcation diagram of the *Coimbrator* where the curve separates the sets of (α, β) values that lead to an equilibrium from the sets that lead to limit cycles. This type of bifurcation is called a Hopf bifurcation.

such as Earth. The relatively small changes in insolation may have been amplified first by greenhouse gases and then by deglaciation and the ice-albedo feedback. However, the major change in isolation comes from obliquity. Eccentricity changes are much less intense. Insolation forcing, mostly due to obliquity changes, should lead to a dominant cycle of 41,000 years and not to the glaciation cycle of 100,000 years. This anomaly of the astronomical forcing hypothesis is widely recognised [21–23]. It is becoming increasingly clear that there is no significant causal association between orbital variables (e.g., insolation) and global temperature, and that internal Earth system mechanisms rather than orbital forcing controlled climate dynamics over the Pleistocene cycles [24]. The *Coimbrator* shows that it is possible to have sustained oscillations in a closed system under continuous illumination, such as the Earth system, and is a good starting point to understand how internal mechanisms may enable sustained oscillation. The analogy between the *Coimbrator* and the Earth system has been

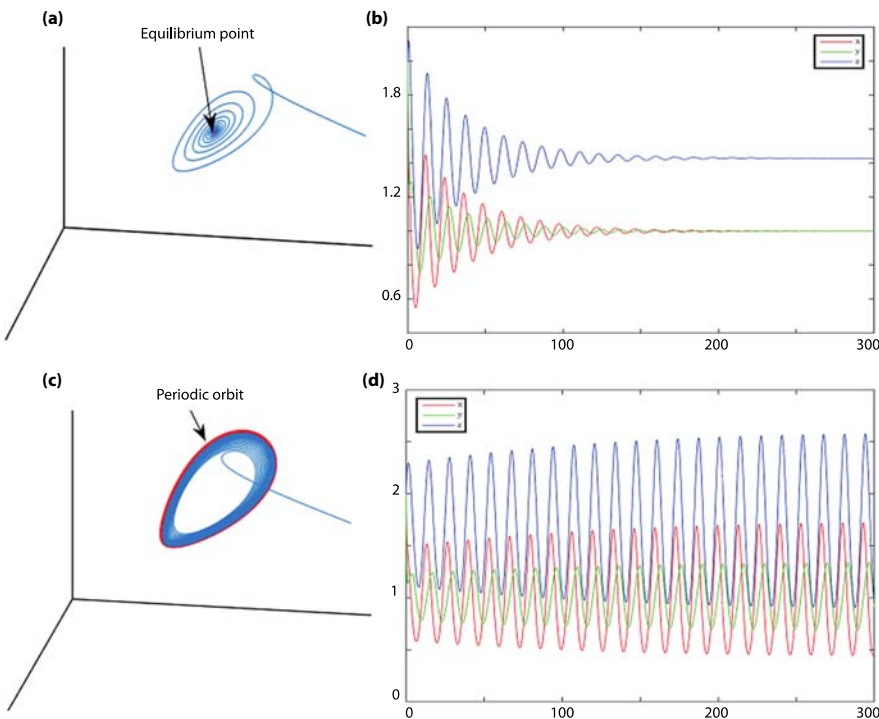


FIGURE 18.9

Phase space plots obtained by numerical integration of the xyz time dependences.

- (a) Dynamics with $\alpha = 1$ and $\beta = 0.7$ make the system evolve to equilibrium and
- (b) corresponding damped oscillations of the xyz variables. (c) Dynamics with $\alpha = 1$ and $\beta = 0.6$ lead to a periodic orbit and (d) corresponding sustained oscillations of the xyz variables.

explored to show that photosynthesis may provide the driving force represented in Figure 18.7 by the absorption of two photons, to drive glaciations [20].

References

- [1] SH Strogatz, *Nonlinear Dynamics and Chaos: With Applications to Physics, Biology, Chemistry, and Engineering*, Perseus Books, Boulder, Colorado, 1994.
- [2] JC Flores, A mathematical model for Neanderthal extinction, *J. Theoret. Biol.* **191** (1998) 295–298.
- [3] PB Pettitt, Neanderthal lifecycles: developmental and social phases in the lives of the last archaics, *World Archeol.* **31** (2000) 351–366.
- [4] MF Roberts, SE Bricher, Modeling the disappearance of the Neanderthals using principles of population dynamics and ecology, *J. Archeol. Sci.* **100** (2018) 16–31.

- [5] W Gilpin, MW Feldman, K Aoki, An ecocultural model predicts Neanderthal extinction through competition with modern humans, *Proc. Natl. Acad. Sci.* **113** (2016) 2134–2139.
- [6] RM May, Simple mathematical models with very complicated dynamics, *Nature* **261** (1976) 459–467.
- [7] EN Lorenz, Deterministic nonperiodic flow, *J. Atm. Sci.* **20** (1963) 130–141.
- [8] I Prigogine, R Lefever, Symmetry breaking instabilities in dissipative systems. II, *J. Chem. Phys.* **48** (1968) 1695–1700.
- [9] AN Zaikin, AM Zhabotinsky, Concentration wave propagation in two-dimensional liquid-phase self-oscillating system, *Nature* **225** (1970) 535–537.
- [10] SK Scott, *Oscillations, Waves and Chaos in Chemical reactions*, Oxford University Press, Oxford, 1994.
- [11] RJ Field, E Körös, RM Noyes, Oscillations in chemical systems, *J. Am. Chem. Soc.* **94** (1972) 8649.
- [12] RJ Field, RM Noyes, Oscillations in chemical systems. IV. Limit cycle behavior in a model of a real chemical reaction, *J. Chem. Phys.* **60** (1974) 1877–1884.
- [13] S Lynch, *Dynamical Systems with Applications Using Mathematica®*, Birkhäuser, Cham, 2017.
- [14] RM Noyes, Effects of global constraints on permissible local behavior, *Ber. Bunsenges. Phys. Chem.* **89** (1985) 620–629.
- [15] R-S Li, J Ross, Chemical instabilities in closed systems with illumination, *J. Phys. Chem.* **95** (1991) 2426–2430.
- [16] L Kuhnert, A new optical photochemical memory device in a light-sensitive chemical active medium, *Nature* **319** (1986) 393–394.
- [17] AK Horváth, I Nagypál, IR Epstein, Oscillatory photochemical decomposition of tetrathionate ion, *J. Am. Chem. Soc.* **124** (2002) 10956–10957.
- [18] J Maddox, Mechanical energy from light, *Nature* **342** (1989) 13.
- [19] T Wilhelm, R Heinrich, Smallest chemical reaction system with Hopf bifurcation, *J. Math. Chem.* **17** (1995) 1–14.
- [20] LG Arnaut, S Ibáñez, Self-sustained oscillations and global climate changes, *Sci. Rep.* **10** (2020) 11200.
- [21] P Huybers, Early Pleistocene glacial cycles and the integrated summer insolation forcing, *Science* **313** (2006) 508–511.
- [22] ME Raymo, P Huybers, Unlocking the mysteries of the ice ages, *Nature* **451** (2008) 284–285.
- [23] MA Maslin, CM Brierley, The role of orbital forcing in the Early Middle Pleistocene Transition, *Quat. Int.* **389** (2015) 47–55.
- [24] EH van Nes, M Scheffer, V Brovkin, TM Lenton, H Ye, E Deyle, G Sugihara, Causal feedbacks in climate changes, *Nat. Clim. Change* **2015** (2015) 445–448.

General data

1

Table A1.1 Fundamental physical constants.

Name	Symbol	Value	Units (SI)
Speed of light <i>in vacuo</i>	c	2.998×10^8	m sec^{-1}
Elementary charge	e	1.602×10^{-19}	C
Vacuum permittivity	ϵ_0	8.854×10^{-12}	$\text{C}^2 \text{N}^{-1} \text{m}^2$
Avogadro's number	N_A	6.022×10^{23}	mol^{-1}
Faraday constant	F	9.648×10^4	C mol^{-1}
Gas constant	R	8.314	$\text{J K}^{-1} \text{mol}^{-1}$
Planck constant	h	6.626×10^{-34}	J sec
Boltzmann constant	k_B	1.381×10^{-23}	J K^{-1}
Atomic mass unit ^a	amu	1.661×10^{-27}	kg
Electron rest mass	m_e	9.109×10^{-31}	kg
Proton rest mass	m_p	1.673×10^{-27}	kg

^aIUPAC recommends the name “unified atomic mass unit” and its representation by the symbol u.

Table A1.2 Conversion factors.

Length					
m	μm	nm	\AA	pm	bohr
1	10^{-6}	10^{-9}	10^{-10}	10^{-12}	1.8897×10^{-10}
Energy					
J mol^{-1}	cal mol^{-1}	erg	eV	cm^{-1}	hartree
1	0.2390	10^7	1.0365×10^{-5}	8.361×10^{-2}	3.809×10^{-7}
Pressure					
N m^{-2}	Pa	bar	atm	psi	mm Hg
1	1	10^{-5}	9.899×10^{-6}	1.450×10^{-4}	7.501×10^{-3}

Note: $1 \text{ N m}^{-1} = 1 \text{ kg sec}^{-2} = 0.6022 \text{ J mol}^{-1}$ $\text{pm}^{-2} = 6.022 \text{ kJ mol}^{-1} \text{\AA}^{-2} = 10^{-3} \text{ dyn cm}^{-1}$.

1 Debye = $3.336 \times 10^{-30} \text{ C m}$.

This page intentionally left blank

Statistical thermodynamics

2

In this appendix, we will use statistical thermodynamics to relate the equilibrium constant of a chemical reaction to the microscopic properties of the molecules involved. Our strategy will be to define functions for the microscopic properties of molecules and then to connect these to the change in the free energy of a reaction. The relationship between this property and the equilibrium constant is well known.

We will consider a system of molecules with ideal gas behaviour characterised by fixed values of temperature (T), composition (total number of molecules N) and volume (V). This system is called the canonical ensemble. In this system, there will be, on average, n_0 molecules in the state of given energy ε_0 , n_1 molecules in the state ε_1 , or in general, n_j molecules in the state ε_j . The molecules will be in equilibrium with a thermal bath, but the energy of each molecule can fluctuate. The value of T is a measure of the average energy of the molecules of the canonical ensemble. Thus the population of the energetic states is kept practically constant, but the identity of the molecules in each state can change due to molecular collisions.

As the total number of molecules has to remain constant

$$\sum_j n_j = N \quad (\text{A2.1})$$

If we also fix the energy of the system

$$\sum_j n_j \varepsilon_j = E \quad (\text{A2.2})$$

this is described as a micro-canonical ensemble. The number n_i of molecules having energy ε_i is given by Boltzmann's distribution law

$$\frac{n_i}{N} = \frac{e^{-\varepsilon_i/k_B T}}{\sum_j e^{-\varepsilon_j/k_B T}} \quad (\text{A2.3})$$

which can also be expressed as a sum over the number of energy levels (or group of states with the same energy)

$$\frac{n_i}{N} = \frac{g_i e^{-\varepsilon_i/k_B T}}{\sum_j g_j e^{-\varepsilon_j/k_B T}} \quad (\text{A2.4})$$

where g_j is a statistical factor which takes account of the number of states with the same energy level ε_j . The denominator of this expression

$$Q = \sum g_j e^{-\varepsilon_j/k_B T} \quad (\text{A2.5})$$

is called the molecular partition function, and is an indication of the average number of states which are thermally accessible to a molecule at the temperature of the system. As $T \rightarrow 0$ only the ground state will be thermally accessible, such that $Q \rightarrow g_0$, which is the degeneracy for $\varepsilon_0 = 0$. Also, as $T \rightarrow \infty$, all the levels will become accessible and $Q \rightarrow \infty$.

Until this point, we have specified the energy levels relative to an arbitrarily chosen zero energy level. In practice, the energies are normally represented as the difference between the level j and the level of lowest energy of the molecule, $\varepsilon_0 = 0$. Thus the energy E must be taken as the value of the internal energy relative to its value at $T = 0$

$$U = U(0) + E \quad (\text{A2.6})$$

where $U(0)$ is the internal energy at $T = 0$.

In addition to the relation between the energy of the system and the molecular partition functions, we must also consider the relationship between the entropy, S , and the number of configurations, which the molecules can take in this system. If we consider N molecules, the first of these can be arranged in N different ways, the second in $(N - 1)$ ways and we can continue in the same fashion until the N th molecule, which can only be arranged in one way. Thus the total number of arrangements is

$$N(N - 1)(N - 2) \cdots 1 = N! \quad (\text{A2.7})$$

However, the arrangements in which the molecules have the same energy are equivalent. We only obtain a new distribution when the particles change to different energy levels. When changes are made within the n_0 molecules which exist in the state of energy ε_0 , we do not produce any new distribution. In the same fashion it can be shown that the possible distributions of the n_1 molecules of the state of energy ε_1 are indistinguishable, and we can carry on with the other levels in exactly the same way. Consequently the total number of different distributions of N molecules having the configuration $\{n_0, n_1, \dots\}$ is given by the ratio between the total number of permutations and the number of permutations within each energy level

$$W_n = \frac{N!}{n_0! n_1! n_2! \dots} \quad (\text{A2.8})$$

where the symbol n indicates that this distribution refers exclusively to the given configuration, and that the other configurations can be considered within the conditions imposed by eqs. (A2.1) and (A2.2). The above equation allows us to obtain the weight of any given configuration. Taking logarithms, this weight can also be written as

$$\begin{aligned} \ln W_n &= \ln N! - \ln(n_0! n_1! n_2! \dots) \\ &= \ln N! - \sum_j \ln n_j! \end{aligned} \quad (\text{A2.9})$$

Using Stirling's approximation, that $\ln x! \approx x \ln x - x$, we obtain

$$\begin{aligned}\ln W_n &= N \ln N - N - \sum_j (n_j \ln n_j - n_j) \\ &= N \ln N - \sum_j (n_j \ln n_j) \\ &= \sum_j (n_j \ln N) - \sum_j (n_j \ln n_j) \\ &= \sum_j \left(n_j \ln \frac{N}{n_j} \right)\end{aligned}\quad (\text{A2.10})$$

The quantitative relationship between the statistical entropy and the molecular disorder is given by the Boltzmann relationship

$$S = k_B \ln W \quad (\text{A2.11})$$

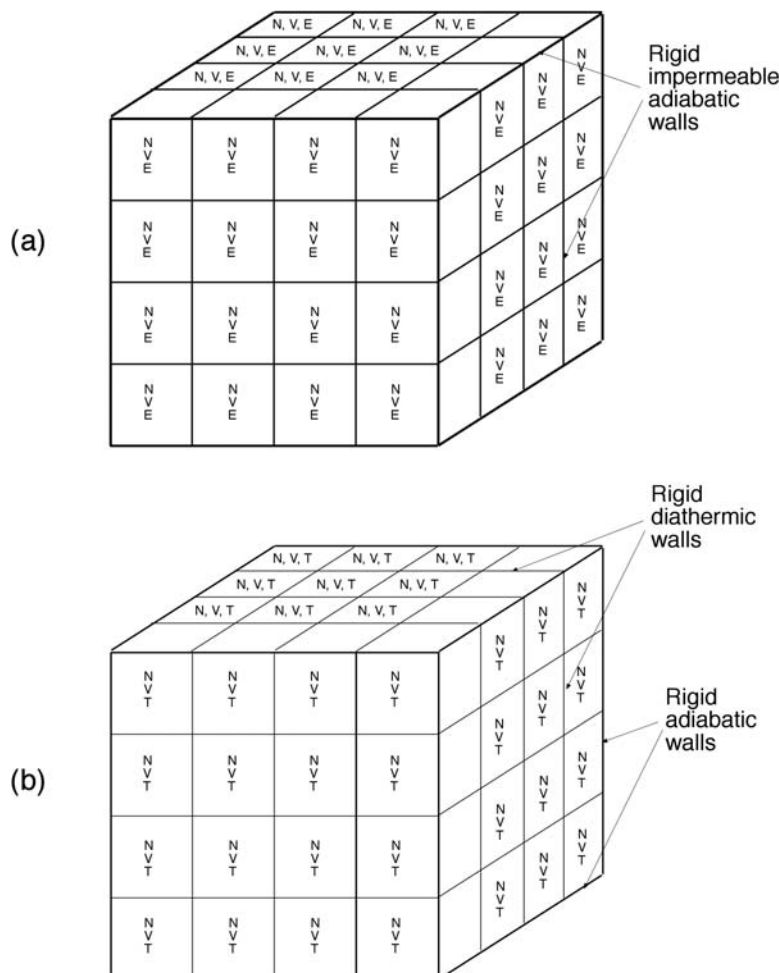
where W is the weight of the most probable configuration of the system. It should be noted that as $T \rightarrow 0$ all the molecules are in the lowest energy level, and $e^{N!} = n_0!$, from which $\ln W = 0$. Substituting eq. (A2.10) into (A2.11), we obtain

$$\begin{aligned}S &= -k_B \sum_j \left(n_j \ln \frac{n_j}{N} \right) \\ &= -k_B \sum_j n_j \left(-\frac{\varepsilon_j}{k_B T} - \ln Q \right) \\ &= \frac{1}{T} \sum_j n_j \varepsilon_j + k_B N \ln Q \\ &= \frac{1}{T} E + k_B N \ln Q\end{aligned}\quad (\text{A2.12})$$

Now, by using eq. (A2.6) we obtain

$$S = \frac{U - U(0)}{T} + k_B N \ln Q \quad (\text{A2.13})$$

The energy and entropy, which are related in this equation to the molecular partition function, are statistical entities, defined by particles which do not interact except to maintain the equilibrium conditions. To obtain similar relationships for real systems, it is necessary to apply statistical mechanics to the calculation of the thermodynamic entities, which correspond to the molar quantities of particles, or that is N approaches N_A . In this treatment it is convenient to use the canonical ensemble already discussed and presented in Figure A2.1. This ensemble consists of a very large number of systems, N , each containing 1 mol of molecules and separated from the others by diathermic walls, which allow heat conduction but do not allow particles to pass. The set of all the systems is isolated from the outside and has a fixed energy E , which is the energy of the canonical ensemble.

**FIGURE A2.1**

Schematic representations of ensembles of systems. (a) Micro-canonical ensemble of $N = 64$ systems each with the same N, V, E . (b) Canonical ensemble of $N = 64$ systems with the same N, V, T ; the systems are in thermal contact and the total energy E of the 64 replicas is a constant, although it fluctuates from one system to the other.

Each particular system within the ensemble can occupy the energy states $E_0, E_1, E_2, \dots, E_j$, and the total energy of the state j of the system is given by

$$E_j = \varepsilon_j(1) + \varepsilon_j(2) + \dots + \varepsilon_j(N) \quad (\text{A2.14})$$

where $\varepsilon_j(s)$ is the energy of molecule s in the state j , etc. We should note that the canonical ensemble, with fixed values of N, V and E , is a member of a micro-canonical ensemble.

If, at any one time, we have n_0 systems in the state of energy E_0 , n_1 in the state of energy E_1 , and, in general, n_j systems in the state E_j , the weight of the distribution $\{n_0, n_1, n_2, \dots\}$ is now given by

$$W_n = \frac{N!}{n_0!n_1!n_2!\dots} \quad (\text{A2.15})$$

and the canonical distribution is

$$\frac{n_i}{N} = \frac{e^{-E_i/k_B T}}{Q} \quad (\text{A2.16})$$

where Q is the canonical partition function which can be related to the molecular partition function given the relationship between the sum over the states of the system and the sum over molecular states

$$\begin{aligned} Q &= \sum_j e^{-E_j/k_B T} \\ &= \sum_j e^{-\varepsilon_j(1)/k_B T - \varepsilon_j(2)/k_B T - \dots - \varepsilon_j(N)/k_B T} \\ &= \left(\sum_j e^{-\varepsilon_j(1)/k_B T} \right) \left(\sum_j e^{-\varepsilon_j(2)/k_B T} \right) \dots \left(\sum_j e^{-\varepsilon_j(N)/k_B T} \right) \\ &= \left(\sum_j e^{-\varepsilon_j/k_B T} \right)^N = Q^N \end{aligned} \quad (\text{A2.17})$$

Eq. (A2.16) represents the probability that a member of the canonical ensemble has a given energy, E_j . This is given by the product of two functions, one which decreases exponentially with the energy and another, which gives the number of permitted states with a particular energy, and which increases very strongly with energy. The result of these two opposing effects is a distribution strongly centred on the average energy of the members of the ensemble.

$$E = \frac{\mathbf{E}}{N} \quad (\text{A2.18})$$

In the thermodynamic limit of $N \rightarrow \infty$ there is always one configuration of the canonical ensemble which becomes clearly dominant, from which it is possible to calculate the thermodynamic properties of the ensemble. In fact, we can ignore configurations in which the energy E is only present in one or a few systems. In this limit, the internal energy of one system of the ensemble can be written in the form

$$U = U(0) + E = U(0) + \frac{\mathbf{E}}{N} \quad (\text{A2.19})$$

On the other hand, it is only of interest to consider the weight of the most probable distribution of the ensemble, which is given by the product of the average weights of the most probable distributions of each system of the ensemble.

$$W = W^N \quad (\text{A2.20})$$

Using this equation in conjunction with the Boltzmann formula for the entropy, eq. (A2.11), we obtain

$$S = k_B \ln W^{1/N} = \frac{k_B}{N} \ln W \quad (\text{A2.21})$$

Following the arguments which led to expression (A2.13), for the canonical ensemble we can obtain

$$S = \frac{U - U(0)}{T} + k_B \ln Q \quad (\text{A2.22})$$

If it is possible to identify all the molecules, such as in case of a solid, where the positions in the crystal lattice can be defined in terms of the coordinate positions, eq. (A2.17) can be used. However, for the case where the molecules cannot be differentiated, for example, with an ideal gas, it is necessary to count over all the sums of the molecular states of indistinguishable molecules, and weigh the result by the number of possible permutations, AH. For this case

$$Q = \frac{Q^N}{N!} \quad (\text{A2.23})$$

As we already know the relationship between the canonical partition functions, the internal energy and entropy of a system, it is possible to connect the thermodynamic functions with the partition functions, which in turn are related to the spectroscopic data for the individual molecules.

The Helmholtz free energy

$$A = U - TS \quad (\text{A2.24})$$

for $T = 0$ leads to $A(0) = U(0)$. Substituting into eq. (A2.22), we obtain

$$A - A(0) = -k_B T \ln Q \quad (\text{A2.25})$$

As the Gibbs free energy is given by

$$G = A + pV \quad (\text{A2.26})$$

and for perfect gases $pV = nRT$, eq. (A2.25) can be used to write

$$\begin{aligned} G - G(0) &= A - A(0) + nRT \\ &= -k_B T \ln Q + nRT \end{aligned} \quad (\text{A2.27})$$

As ideal gases consist of indistinguishable molecules, we obtain

$$\begin{aligned} G - G(0) &= -Nk_B T \ln Q + k_B T \ln N! + nRT \\ &= -nN_A k_B T \ln Q + k_B T(N \ln N - N) + nRT \\ &= -nRT \ln \left(\frac{Q}{N} \right) \end{aligned} \quad (\text{A2.28})$$

since $N = nN_A$ and $R = k_B N_A$. Also, as the standard Gibbs free energy of a reaction $A + B \rightleftharpoons \ddagger$ is related to its equilibrium constant

$$\Delta G^0 = -RT \ln K_{\text{eq}} \quad (\text{A2.29})$$

it is also possible to express the equilibrium constant of a reaction in terms of partition functions of reactants and products. Since, for an ideal gas at $T = 0$ we obtain $G(0) = A(0) = U(0)$, it can be shown that, for any reaction at equilibrium, the difference of molar free energy between products and reactants is equal to their difference in molar internal energy, and this is given by the difference in zero-point energy between the products and reactants. This energy difference is normally given as

$$\Delta E^0 = U_{\ddagger}^0(0) - U_A^0(0) - U_B^0(0) \quad (\text{A2.30})$$

The remaining free-energy difference between reactants and products can be related to their standard molar partition functions

$$Q_A^0 = \frac{Q_A}{n}, \quad Q_B^0 = \frac{Q_B}{n}, \quad Q_{\ddagger}^0 = \frac{Q_{\ddagger}}{n} \quad (\text{A2.31})$$

where these refer to 1 mol of ideal gas in the standard state of $p^0 = 1 \text{ atm}$, such that the standard molar volume $V_m^0 = RT/p^0$. Thus

$$\Delta G^0 = \Delta E^0 - RT \ln \left(\frac{Q_{\ddagger}^0/N_A}{(Q_A^0/N_A)(Q_B^0/N_A)} \right) \quad (\text{A2.32})$$

from which

$$\ln K_{\ddagger} = \ln \left(\frac{Q_{\ddagger}^0/N_A}{(Q_A^0/N_A)(Q_B^0/N_A)} \right) - \frac{\Delta E^0}{RT} \quad (\text{A2.33})$$

and

$$K_{\ddagger} = \frac{Q_{\ddagger}^0 N_A}{Q_A^0 Q_B^0} e^{-\Delta E_0/RT} \quad (\text{A2.34})$$

This page intentionally left blank

Parameters employed in ISM calculations

3

Table A3.1 Morse curve parameters, ionisation potentials and electron affinities for the calculation of atom and proton-transfer rates^a.

	I_{eq} (Å)	D^0_{298} (kJ mol ⁻¹)	ω_e (cm ⁻¹)	I_p (eV)	E_A (eV)
H ₂	0.74144	435.99	4161	13.598	0.75419
CH ₄	1.0870	438.9	2917	9.843	0.08
CH ₃ CH ₃	1.0940	423.0	2954	8.117	-0.26
CH ₃ CH ₂ CH ₃	1.107	409.1	2887	7.37	-0.321
(CH ₃) ₃ CH	1.122	404.3	2890	6.70	-0.156
CH ₃ COCH ₃	1.103	411.3	2939		
CH ₃ OCH ₃	1.121	402.2	2817	6.90	-0.017
CH ₃ OH	1.0936	401.8	2844	7.562	
CH ₃ CHO	1.128	373.8	2822	7.00	0.423
CH ₂ O	1.116	368.5	2783	8.14	0.313
CH ₃ C ₆ H ₅	1.111	375.7	2934	7.2488	0.912
CH ₂ =CH ₂	1.087	465.3	3026	8.25	0.667
C ₆ H ₆	1.101	473.1	3062	8.32	1.096
HCN	1.0655	527.6	3311	14.170	3.862
CH≡CH	1.060	556.1	3374	11.610	2.969
CH ₃ NH ₂	1.099	390.4	2820	6.29	
(CH ₃) ₃ SiH	1.485	377.8	2107	7.03	0.971
SiH ₄	1.4798	384.1	2187	8.135	1.405
(CH ₃) ₃ SnH	1.700	322	1815	7.10	1.70
GeH ₄	1.5251	349.0	2106	7.948	1.61
NH ₃	1.012	452.7	3337	10.780	0.771
PH ₃	1.4200	351.0	2323	9.824	1.25
AsH ₃	1.511	319.2	2116	9.85	1.27
H ₂ O	0.9575	498	3657	13.017	1.8277
OH	0.96966	427.6	3737.76	13.618	1.4611
CH ₃ OH	0.9451	436.0	3681	10.720	1.57
H ₂ S	1.3356	381.6	2615	10.422	2.317
H ₂ Se	1.47	334.9	2345	9.845	2.2125

(Continued)

Table A3.1 Morse curve parameters, ionisation potentials and electron affinities for the calculation of atom and proton-transfer rates^a. *Continued*

	I_{eq} (Å)	D^0_{298} (kJ mol ⁻¹)	ω_e (cm ⁻¹)	I_P (eV)	E_A (eV)
CH ₃ SH	1.340	365.3	2610	9.262	1.867
C ₆ H ₅ SH	1.36	348.5	2597	8.6	2.26
HF	0.9169	569.87	3962	17.423	3.448
HCl	1.27455	431.62	2886	12.968	3.6144
HBr	1.41444	366.35	2559	11.814	3.3636
HI	1.60916	298.41	2230	10.451	3.059
CF ₃ H	1.098	449.5	3036	8.76	1.869
F ₂	1.41193	158.78	892	17.423	3.448
Cl ₂	1.988	242.58	557	12.968	3.6144
Br ₂	2.281	192.81	317	11.814	3.3636
I ₂	2.666	151.09	213	10.451	3.0590

^aData from LG Arnaut, AACC Pais, SJ Formosinho, M Barroso, J. Am. Chem. Soc. 125 (2003) 5236.

Table A3.2 Harmonic oscillator parameters for the simplified calculation of atom and proton-transfer rates.

Bond	f_{XH} (kJ mol ⁻¹ Å ⁻²)	I_{XH} (Å)
CH	2.90×10^3	1.07
NH	3.82×10^3	1.01
ROH	4.21×10^3	0.97
HOH	4.21×10^3	0.958
HF	5.80×10^3	0.917

Table A3.3 Morse curve parameters employed in ISM calculations of S_N2 reaction rates^a.

Molecule	D_e (kJ mol ⁻¹)	ω (cm ⁻¹)	I_{eq} (Å)
CH ₃ —CH ₂ CH ₃	368 ^b	1054 ^b	1.512
CH ₃ —SiH ₂ CH ₃	368 ^c	770 ^d	1.873
CH ₃ —GeH ₂ CH ₃	314	651	1.957
CH ₃ —SnH ₂ CH ₃	205	541	2.177
CH ₃ —NHCH ₃	259	1143	1.474
CH ₃ —PHCH ₃	264	664	1.868
CH ₃ —AsHCH ₃	234	607	1.973
CH ₃ —SbHCH ₃	201	597	2.162
CH ₃ —OCH ₃	276	1014 ^b	1.405
CH ₃ —SCH ₃	280	723	1.801

(Continued)

Table A3.3 Morse curve parameters employed in ISM calculations of S_N2 reaction rates^a. *Continued*

Molecule	D _e (kJ mol ⁻¹)	ω (cm ⁻¹)	I _{eq} (Å)
CH ₃ —SeCH ₃	280	648	1.948
CH ₃ —TeCH ₃	146	470	2.200
F—CH ₃	452 ^b	1049 ^b	1.351
Cl—CH ₃	347 ^b	732 ^b	1.764
Br—CH ₃	293 ^b	611 ^b	1.951
I—CH ₃	234 ^b	533 ^b	2.027

^aAll data were calculated by the PM3 method in ref. LG Arnaut, AACC Pais, SJ Formosinho, J. Mol. Struct., 563/564 (2001) 1, except where indicated.

^bFrom NIST Standard Reference Database # 69 (Feb. 2000).

^cFrom DF McMillen, DM Golden, Ann. Rev. Phys. Chem., 33 (1982) 493.

^dFrom similar compounds in AA Zavitsas, C Chatgilialoglu, J. Am. Chem. Soc. 117 (1995) 10645.

Table A3.4 Harmonic oscillator parameters for the calculation of electron-transfer rates^a.

Complex or molecule ^b	Electronic configuration	f _{red} (kJ mol ⁻¹ Å ⁻²)	f _{ox} (kJ mol ⁻¹ Å ⁻²)	I _{red} (Å)	I _{ox} (Å)
Fe(CN) ₆ ^{4-/3-}	(π) ⁶ /(π) ⁵	1.38 × 10 ³	1.44 × 10 ³	1.88	1.88
Cr(OH ₂) ₆ ^{2+/3+}	(π) ³ (σ*) ¹ /(π) ³	0.96 × 10 ³	1.53 × 10 ³	2.15	1.98
Mn(OH ₂) ₆ ^{2+/3+}	(π) ³ (σ*) ² /(π) ³ (σ*) ¹	0.96 × 10 ³	1.53 × 10 ³	2.177	1.991
V(OH ₂) ₆ ^{2+/3+}	(π) ⁶ /(π) ⁵	0.96 × 10 ³	1.53 × 10 ³	2.131	1.992
Fe(OH ₂) ₆ ^{2+/3+}	(π) ⁴ (σ*) ² /(π) ³ (σ*) ²	0.96 × 10 ³	1.53 × 10 ³	2.10	1.98
Co(OH ₂) ₆ ^{2+/3+}	(π) ⁵ (σ) ² /(π) ⁶	0.96 × 10 ³	1.53 × 10 ³	2.081	1.873
Ru(OH ₂) ₆ ^{2+/3+}	(π) ⁶ /(π) ⁵	1.16 × 10 ³	1.82 × 10 ³	2.11	2.03
Co(NH ₃) ₆ ^{2+/3+}	(π) ⁵ (σ*) ² /(π) ⁶	0.78 × 10 ³	1.48 × 10 ³	2.19	1.97
Ru(NH ₃) ₆ ^{2+/3+}	(π) ⁶ /(π) ⁵	1.23 × 10 ³	1.52 × 10 ³	2.14	2.12
Co(phen) ₃ ^{2+/3+}	(π) ⁵ (σ*) ² /(π) ⁶	0.68 × 10 ³	1.38 × 10 ³	2.11	1.91
Fe(phen) ₃ ^{2+/3+}	(π) ⁶ /(π) ⁵	1.44 × 10 ³	1.42 × 10 ³	1.97	1.97
Ru(bpy) ₃ ^{2+/3+}	(π) ⁶ /(π) ⁵	1.32 × 10 ³	1.32 × 10 ³	2.056	2.034
Fe(Cp) ₂ ^{0/+}	(a _{1g}) ² (e _{2g}) ⁴ / (a _{1g}) ² (e _{2g}) ³	1.90 × 10 ³	1.75 × 10 ³	1.649	1.677
Anthracene ^{0/-}			3.77 × 10 ³		1.406
22/u22 ⁺⁰		1.92 × 10 ³	1.40 × 10 ³	1.497	1.349
iPr ₂ N) ₂ ⁺⁰		4.50 × 10 ³	9.95 × 10 ³	1.394	1.333

^aData from SJ Formosinho, LG Arnaut, R Fausto, Prog. React. Kinet. 23 (1998) 1, except Fe(Cp)₂^{0/+} which are from E Diana, R Rossetti, PL Stanghellini, SFA Kettle, Inorg. Chem. 36 (1997) 382 and TN Doman, CR Landis, B Bosnich, J. Am. Chem. Soc. 114 (1992) 7264.

^bphen: 1,10-phenanthroline; bpy: 2,2'-bipyridyl; Cp: cyclopentadienyl; anthracene data are representative of most aromatic molecules, and the differences between f_{ox} and f_{red} are compensated using the differences between I_{ox} and I_{red}. For the structures of the hydrazines 22/u22 and iPr₂N)₂, see Figure 16.5.

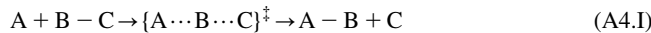
This page intentionally left blank

Semi-classical interacting state model

4

A4.1 Vibrationally adiabatic path

The classical reaction path of an atom transfer reaction



given by the intersecting/interacting state model (ISM) in [Chapter 6](#), Reactivity in Thermalised Systems, [eq. \(6.81\)](#)

$$\begin{aligned} V_{\text{cl}}(n) &= (1-n)V_{\text{BC}}(1-n) + nV_{\text{AB}}(n) + n\Delta V^0 \\ &= (1-n)D_{e,\text{BC}}\left\{1-\exp\left[\gamma_{\text{BC}}\ln(1-n)\right]\right\}^2 + nD_{e,\text{AB}}\left\{1-\exp\left[\gamma_{\text{AB}}\ln(n)\right]\right\}^2 + n\Delta V^0 \\ \gamma_{\text{BC}} &= \frac{a'_{\text{sc}}(l_{\text{BC},\text{eq}} + l_{\text{AB},\text{eq}})\beta_{\text{BC}}}{m} \\ \gamma_{\text{AB}} &= \frac{a'_{\text{sc}}(l_{\text{BC},\text{eq}} + l_{\text{AB},\text{eq}})\beta_{\text{AB}}}{m} \end{aligned} \quad (\text{A4.1})$$

must be augmented by zero-point energy corrections along the reaction coordinate n , $Z(n)$, to yield the vibrationally adiabatic path

$$V_{\text{ad}}(n) = V_{\text{cl}}(n) + Z(n) \quad (\text{A4.2})$$

This, together with a procedure to calculate tunnelling corrections, transforms classical ISM into semi-classical ISM. This appendix presents the background material necessary for such a treatment.

The zero-point energy of the reactants is directly calculated from the Morse curve of the BC bond

$$\bar{v}_{\text{BC}} = \frac{1}{2\pi c} \sqrt{\frac{f_{\text{BC}}}{\mu_{\text{BC}}}} = \frac{1}{2\pi c} \sqrt{\frac{2\beta_{\text{BC}}^2 D_{\text{BC}}}{\mu_{\text{BC}}}} = 2.3738 \times \beta_{\text{BC}} \sqrt{\frac{D_{\text{BC}}}{\mu_{\text{BC}}}} \quad (\text{A4.3})$$

where c is the speed of light, f_{BC} the force constant of the BC bond, and the numerical conversion factor is included to give the result in cm^{-1} when the spectroscopic constant β is expressed in \AA^{-1} , the reduced mass μ_{BC} in amu and the

electronic dissociation energy D_{BC} in J. The zero-point energy of the reactants is then

$$Z_{BC} = \frac{1}{2} h c \bar{v}_{BC} \quad (\text{A4.4})$$

while similar expressions give the zero-point energy of the products, Z_{AB} . These expressions ignore the very small anharmonic correction of the Morse curves associated with the fundamental vibrational level.

The normal modes of vibration of the linear tri-atomic transition state $\{A \cdots B \cdots C\}^\ddagger$ are the symmetric stretching, the anti-symmetric stretching and two degenerate bending modes. For a stable tri-atomic molecule, the symmetric and anti-symmetric stretchings are calculated from Wilson's equation

$$w^\pm = \frac{f_{ab}(\mu_A + \mu_B) + f_{bc}(\mu_C + \mu_B) \pm \sqrt{(f_{ab}\mu_A + f_{bc}\mu_C)^2 + (f_{ab} + f_{bc})^2 \mu_B^2 + 2(f_{ab} - f_{bc})(f_{ab}\mu_A - f_{bc}\mu_C)\mu_B}}{2} \quad (\text{A4.5})$$

where, using the nomenclature of Wilson, $\mu_i = m_i^{-1}$, f_{ij} are the force constants of the fragments ij , and the cross terms and bendings were neglected. The solution obtained with the subtraction of the square root term, w_- is associated with the symmetric stretch, and that obtained with the addition, w_+ , with the asymmetric stretch. The latter has an imaginary frequency and corresponds to the curvature of the classical reaction coordinate. If we make $f_{ab} = f_{bc}$, we obtain

$$\mu = \frac{2}{\mu_A + 2\mu_B + \mu_C + \sqrt{(\mu_A - \mu_C)^2 + 4\mu_B^2}} \quad (\text{A4.6})$$

We note that this equation has the correct limits: if all the masses are identical, then $\mu = m/3$; if A and C are much heavier than B, then $\mu = m_B/2$. The reduced mass μ is that of the anti-symmetric stretch of a tri-atomic molecule with $D_{\infty h}$ symmetry, as expected for a linear transition state. As will be seen below, the tunnelling correction employs eq. (A4.6) for calculating the reduced mass.

The symmetric and anti-symmetric stretching frequencies along the reaction path are obtained from

$$\begin{aligned} \bar{v}_{\text{sym}}(n) &= \frac{1}{2\pi} \sqrt{w_-} [1 - y(n)] \\ \bar{v}_{\text{asym}}(n) &= \frac{1}{2\pi} \sqrt{w_+} y(n) \end{aligned} \quad (\text{A4.7})$$

using eq. (A4.5) and the fractional force constants $f_{ab}(n)$ given by the equation of Bürgi and Dunitz [1]

$$\begin{aligned} f_{bc}(n) &= 2D_{BC}(\beta_{BC})^2 (1-n)^{2\alpha\beta_{BC}} \\ f_{ab}(n) &= 2D_{AB}(\beta_{AB})^2 n^{2\alpha\beta_{AB}} \end{aligned} \quad (\text{A4.8})$$

where $a = 0.26$ is Pauling's constant, and $y(n)$ is the switching function

$$\begin{aligned} y(n) &= \cosh \left[\frac{l_{BC}}{l_{BC} + l_{AB}} \frac{\ln(n^\dagger)}{\ln(n/0.5)} \right]^{-1} && \text{for } n < 0.5 \\ y(n) &= 0 && \text{for } n = 0.5 \\ y(n) &= \cosh \left[\frac{l_{AB}}{l_{BC} + l_{AB}} \frac{\ln(1-n^\dagger)}{\ln((1-n)/0.5)} \right]^{-1} && \text{for } n > 0.5 \end{aligned} \quad (\text{A4.9})$$

The switching function attenuates the frequencies to provide the correct asymptotic limits: when $n \rightarrow 0$ then $\bar{v}_{\text{asym}}(n) \rightarrow \bar{v}_{BC}$ and $\bar{v}_{\text{sym}}(n) \rightarrow 0$, when $n \rightarrow 0.5$ then $\bar{v}_{\text{asym}}(n) \rightarrow 0$ and $\bar{v}_{\text{sym}}(n) \rightarrow 1/2\pi\sqrt{w_-}$, when $n \rightarrow 1$ then $\bar{v}_{\text{asym}}(n) \rightarrow \bar{v}_{AB}$ and $\bar{v}_{\text{sym}}(n) \rightarrow 0$.

ISM is a uni-dimensional reactivity model and cannot offer a method to calculate the two degenerate bending frequencies. However, there is a good linear correlation between the symmetric stretching and bending frequencies of many

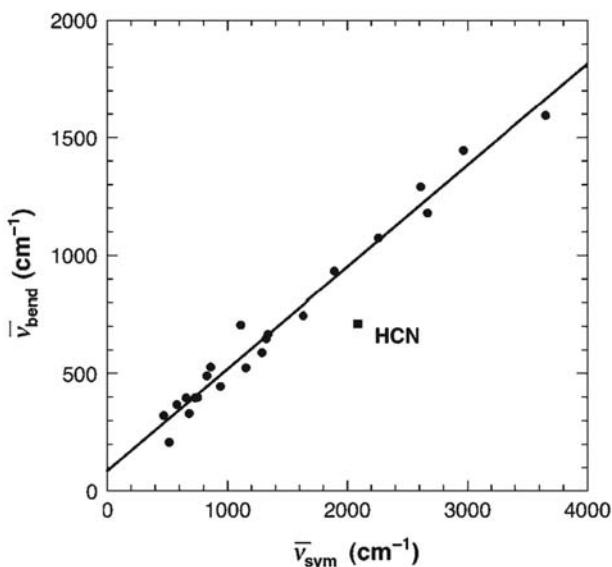


FIGURE A4.1

Correlation between bending and symmetric stretching frequencies of tri-atomic molecules. Systems included in the correlation are H_2O , D_2O , H_2S , D_2S , H_2Se , D_2Se , CH_2CO , SO_2 , NO_2 , CO_2 , CS_2 , F_2O , Cl_2O , CICN , BrCN , ICN , SCN^- , SCO , NNO , O_3 , ClO_2 and SCl_2 from references [4] and [5]. The correlation coefficient is 0.989 and the slope is 0.43. The HCN system does not fit the correlation, presumably because the force constants of the two bonds and the masses of the end atoms are very different.

tri-atomic systems (Figure A4.1). From the slope of the empirical relation (slope = 0.43), we obtain the bending frequency from the symmetric stretching frequency and get, for the transition state

$$Z_{\ddagger} = \frac{1}{2}hc \left[\bar{v}_{\text{sym}}^{\ddagger} + 2(0.43\bar{v}_{\text{sym}}^{\ddagger}) \right] \quad (\text{A4.10})$$

The above equation emphasises the fact that we are calculating the bending contribution from the symmetric stretching, and that we assume a linear transition state, that is, there are two degenerate bending vibrations.

Now we have all the elements to calculate the zero-point energy corrections along the reaction coordinate

$$Z(n) = \frac{1}{2}hc \left\{ \bar{v}_{\text{sym}}(n) + 2[0.43\bar{v}_{\text{sym}}(n)] + \bar{v}_{\text{asym}}(n) \right\} \quad (\text{A4.11})$$

and include them in eq. (A4.2) to obtain the vibrationally adiabatic path.

The asymptotic limits of the stretching frequencies are closely related to those of the electrophilicity index m . In the reactants we have $m_{\text{BC}} = 1$ and the Morse curve of BC is from the spectroscopy of the isolated molecule. Also for the products $m_{\text{AB}} = 1$, for the same reasons. At the transition state, $m(n)$ attains its maximum value, given by eq. (6.67)

$$m^{\ddagger} = \frac{I_{\text{P}} + E_{\text{A}}}{I_{\text{P}} - E_{\text{A}}} \quad (\text{A4.12})$$

Thus, we may consider that $m(n)$ varies along the reaction coordinate much in the same manner as the stretching frequencies, and it is possible to calculate this from.

$$m(n) = \frac{I_{\text{P}} + E_{\text{A}}}{I_{\text{P}} - E_{\text{A}}} [1 - y(n)] \quad (\text{A4.13})$$

The energy of the maximum point along the vibrationally adiabatic path, eq. (A4.2), minus the zero-point energy of the reactants is the vibrationally adiabatic barrier.

$$\Delta V_{ad}^{\ddagger} = V_{ad}^{\ddagger}(n) - Z_{\text{BC}} \quad (\text{A4.14})$$

In practise, this maximum is found numerically, using steps of $\Delta n = 0.01$ or smaller. Note that the maximum of the vibrationally adiabatic barrier may not coincide with that of the classical reaction path, n^{\ddagger} .

A4.2 Tunnelling corrections

A very accurate method to calculate tunnelling correction along a unidimensional reaction path involves the semi-classical approximation [2]. The transmission coefficient and the transmission probabilities are

$$\kappa(T) = 1 + \frac{2}{k_B T} \int_{\varepsilon_0}^{\Delta V_{ad}^\ddagger} \sinh \left(-\frac{\Delta V_{ad}^\ddagger - \varepsilon}{k_B T} \right) G(\varepsilon) d\varepsilon \quad (\text{A4.15})$$

$$\begin{aligned} G(\varepsilon) &= \left\{ 1 + \exp[2\gamma(\varepsilon)] \right\}^{-1} & \varepsilon_0 \leq \varepsilon \leq \Delta V_{ad}^\ddagger \\ &= 1 - G(2\Delta V_{ad}^\ddagger - \varepsilon) & \Delta V_{ad}^\ddagger \leq \varepsilon \leq 2\Delta V_{ad}^\ddagger - \varepsilon_0 \\ &= 1 & 2\Delta V_{ad}^\ddagger - \varepsilon_0 < \varepsilon \end{aligned} \quad (\text{A4.16})$$

respectively, while the barrier penetration integral is

$$\gamma(\varepsilon) = \frac{2\pi}{h} \int_{s_<}^{s_>} \sqrt{2\mu[V_{ad}(s) - \varepsilon]} ds \quad \varepsilon < \Delta V_{ad}^\ddagger \quad (\text{A4.17})$$

the threshold energy ε_0 is the limiting value of the vibrationally adiabatic potential energy for exothermic or endothermic reactions

$$\varepsilon_0 = \max[V_a(S = -\infty), V_a(S = +\infty)] \quad (\text{A4.18})$$

the reduced mass is given by eq. (A4.6), and $s_>$ and $s_<$ are the classical turning points, that is, the locations at which $V_a(s) = \varepsilon$.

Hydrogen-atom or proton-transfer transfers between heavy atoms often lead to vibrationally adiabatic paths with two maxima. Formally, the resolution of this problem should be made in the framework of the canonically unified theory [3]. In practice, given the approximate nature of our treatment, it suffices to use TST with ΔV_{ad}^\ddagger equal to the value for the maximum point. For these cases, the tunnelling correction of the particles with energies between that of the highest of the two maxima and the minimum between these is calculated for the highest barrier only.

A4.3 Semi-classical rate constants

The semi-classical expression for the reaction rate constant given by transition-state theory

$$k_{\text{scTST}} = \kappa(T) \sigma \frac{k_B T}{h} \frac{Q^\ddagger}{Q_A Q_{BC}} e^{-\Delta V_{ad}^\ddagger / RT} \quad (\text{A4.19})$$

can be calculated with the tunnelling correction and vibrationally adiabatic barrier described above, and the partition functions given by eqs. (6.20), (6.21) and (6.25). Here, σ is the statistical factor that accounts for the degeneracy of the reaction path. For a linear tri-atomic transition state, this expression can be simplified to

$$\begin{aligned} k_{\text{sc}} &= A \exp \left(-\frac{\Delta V_{ad}^\ddagger}{RT} \right) \\ A &= \sigma \kappa(T) \frac{6.82 \times 10^{10}}{\sqrt{T}} \left(\frac{m_A + m_B + m_C}{m_A(m_B + m_C)} \right)^{3/2} \\ &\times \frac{I_{ABC}}{I_{BC}} \frac{1 - \exp(\bar{v}_{BC} hc/k_B T)}{\left[1 - \exp(\bar{v}_{\text{sym}} hc/k_B T) \right] \left[1 - \exp(0.43 \bar{v}_{\text{sym}} hc/k_B T) \right]^2} \text{dm}^3 \text{mol}^{-1} \text{sec}^{-1} \end{aligned} \quad (\text{A4.20})$$

where I_{ABC} and I_{AB} are the moments of inertia of the transition state and of the reactants, respectively.

In summary, the partition functions are calculated assuming that the system involves a linear tri-atomic transition-state, a di-atomic reactant molecule and an atom. The classical transition-state geometry is obtained at the maximum of eq. (A4.1). The zero-point energy corrections are calculated with eq. (A4.11). The tunnelling correction is calculated using the semi-classical approximation, which requires numerical quadratures of eqs. (A4.15) and (A4.17). The total computational effort of calculating one rate constant at one given temperature is less than 1 sec in any modern personal computer. This efficiency of the calculations makes it possible to perform semi-classical ISM calculations on-line, through the Internet. Such calculations can be made, free of charge, at the site: <http://www.ism.qui.uc.pt:8180/ism/>.

References

- [1] H-B Bürgi, JD Dunitz, *J. Am. Chem. Soc.* **109** (1987) 2924.
- [2] BC Garrett, DG Truhlar, *J. Phys. Chem.* **83** (1979) 2921.
- [3] BC Garrett, DG Truhlar, RS Grev, GS Schatz, RB Walker, *J. Phys. Chem.* **85** (1981) 3806.
- [4] G Herzberg, *Molecular Spectra and Molecular Structure. II. Infrared and Raman Spectra of Polyatomic Molecules*, Van Nostrand, New York, 1945.
- [5] K Nakamoto, *Infrared Spectra of Inorganic and Coordination Compounds*, Wiley, New York, 1963.

The Lippincott–Schroeder potential

5

A5.1 Lippincott–Schroeder potential

The presence of a hydrogen bond along the reaction coordinate is included in the intersecting-state model (ISM) reaction path using the Lippincott–Schroeder (LS) potential [1]. This empirical potential relates the H-bond binding energies (D_{AB}) to the AB equilibrium distances ($l_{AB,eq}$) and to the AB stretching frequency (\bar{v}_{AB}) in the $B \cdots H - A$ hydrogen-bonded complex (charges omitted).



The LS potential is expressed as a sum of four terms

$$V_{\text{LS}} = V_{\text{HA}} + V_{\text{HB}} + V_{\text{rep}} + V_{\text{el}} \quad (\text{A5.1})$$

where the first two terms represent covalent interactions and have the form

$$\begin{aligned} V_{\text{HA}} &= D_{\text{HA}}[1 - \exp(-\alpha_{\text{LS}})] \\ V_{\text{HB}} &= D_{\text{H}\cdots\text{B}}[1 - \exp(-\beta_{\text{LS}})] - D_{\text{H}\cdots\text{B}} \end{aligned} \quad (\text{A5.2})$$

D_{HA} and $D_{\text{H}\cdots\text{B}}$ are the bond-dissociation energies of the unperturbed HA and $H \cdots B$ bonds, and

$$\begin{aligned} \alpha_{\text{LS}} &= \frac{\kappa_{\text{HA}}(l_{\text{HA}} - l_{\text{HA},\text{eq}})^2}{2l_{\text{HA}}} \\ \beta_{\text{LS}} &= \frac{\kappa_{\text{H}\cdots\text{B}}(l_{\text{H}\cdots\text{B}} - l_{\text{H}\cdots\text{B},\text{eq}})^2}{2l_{\text{H}\cdots\text{B}}} \\ \kappa_{\text{HA}} &= f_{\text{HA}}l_{\text{HA},\text{eq}}/D_{\text{HA}} \\ \kappa_{\text{H}\cdots\text{B}} &= f_{\text{H}\cdots\text{B}}l_{\text{H}\cdots\text{B},\text{eq}}/D_{\text{H}\cdots\text{B}} \end{aligned} \quad (\text{A5.3})$$

In these expressions, l (or f) are the bond lengths (or the harmonic force constants) of the unperturbed HA and $H \cdots B$ bonds. The data for the unperturbed $H \cdots B$ bond are not usually known. However, Lippincott and Schroeder introduced the approximation

$$\kappa_{\text{H}\cdots\text{B}} = g\kappa_{\text{HA}} \quad (\text{A5.4})$$

where $g = 1.45$, and showed that g is transferable to all $B \cdots H - A$ systems [2]. Additionally they assumed that

$$\begin{aligned} D_{H \cdots B} &= D_{HA}/g \\ l_{H \cdots B,eq} &= l_{HB} \end{aligned} \quad (\text{A5.5})$$

which provide all the approximations necessary to calculate the covalent contributions. The covalent contributions for a hydrogen bond between two oxygen atoms are indicated in [Figure A5.1](#).

Lippincott and Schroeder expressed the repulsive term as a negative exponential and the electrostatic one as a negative power of the AB distance. Both these terms involve empirical constants. They were modified to reduce the number of constants and the following expression was obtained:

$$V_{\text{rep}} + V_{\text{el}} = A \left[\exp(-bl_{AB}) + \frac{l_{AB,eq}}{2l_{AB}} \exp(-bl_{AB,eq}) \right] \quad (\text{A5.6})$$

The first derivative of the potential expresses the parameter A as a function of the repulsion constant b , and the set of parameters defined above

$$A = \frac{\frac{D_{H \cdots B} \kappa_{H \cdots B}}{2} \left[1 - \left(\frac{l_{H \cdots B}}{l_{AB,eq} - l_{HA}} \right)^2 \right] \exp(-\beta)}{\exp(-bl_{AB,eq}) (b - 1/2l_{AB,eq})} \quad (\text{A5.7})$$

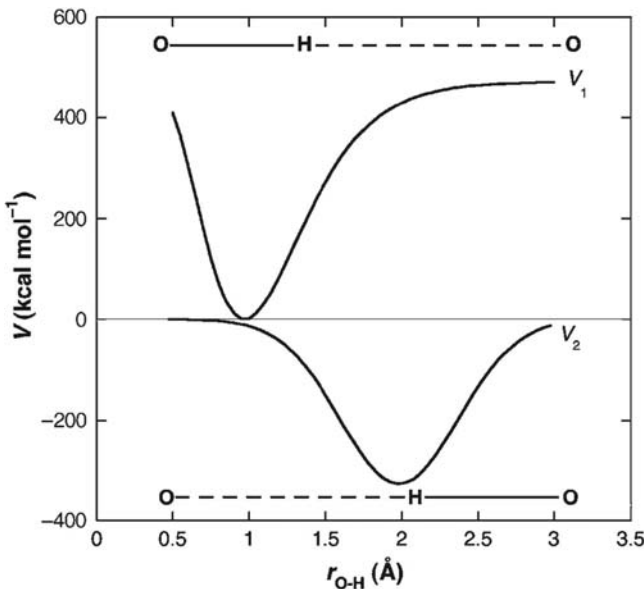


FIGURE A5.1

Covalent contributions to the LS potential for a hydrogen bond between two oxygen atoms.

The only parameter left to be fitted to the experimental data is the repulsion constant b . Lippincott and Schroeder chose the value $b = 4.8 \text{ \AA}$. Figure A5.2 illustrates the covalent, electrostatic and repulsive contributions to hydrogen bonds between two oxygen atoms, as a function of the distance between the oxygen atoms. With the data presently available on the H-bond lengths and strengths, a better description of the relation between these two quantities can be achieved with $b = 9 \text{ \AA}$. This was the value employed in the simulations presented in Figure 13.12, but the original value was implemented in the LS–ISM reaction path because the differences in the calculated rates are negligible.

Another important quantity in the LS potential is the force constant of the AB hydrogen bond. This can be obtained from the second derivative of the potential.

$$f_{AB} = B + A \exp(-bl_{AB,eq}) \frac{(bl_{AB,eq})^2 - 1}{(l_{AB,eq})} \\ B = \frac{D_{H\cdots B} \kappa_{H\cdots B}}{(l_{H\cdots B})^3} \exp(-\beta) \left[(l_{H\cdots B,eq})^2 - \frac{\beta}{2} (l_{H\cdots B} + l_{H\cdots B,eq})^2 \right] \quad (\text{A5.8})$$

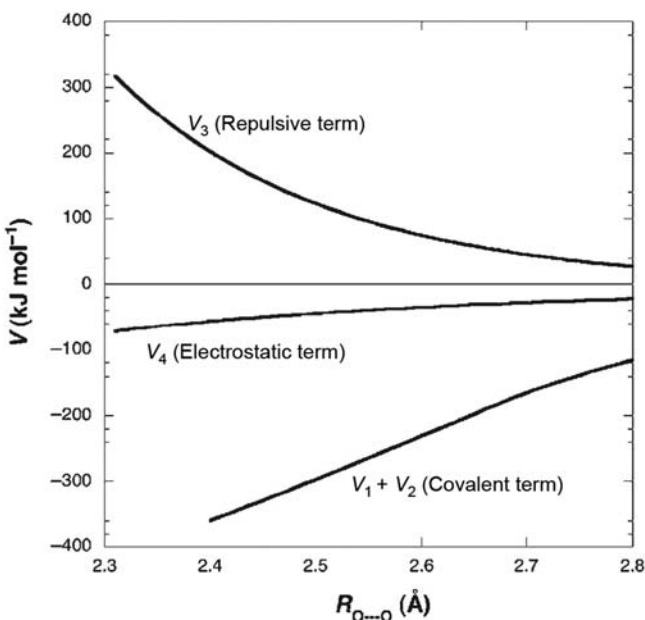


FIGURE A5.2

Covalent, electrostatic and repulsive contributions to LS potentials representing hydrogen bonds between two oxygen atoms, as a function of the distance between the oxygen atoms.

The importance of this force constant results from its relation to the AB vibrational frequency

$$\bar{v}_{AB} = \frac{1}{2\pi c} \sqrt{\frac{f_{AB}}{\mu_{AB}}} \quad (A5.9)$$

The LS potential does not include a correction for the change of translational and rotational degrees of freedom on dissociation of the hydrogen bond. Such corrections are small and have been neglected. However, the experimental H-binding energies, D_{AB} , are corrected for the zero-point energy of the AB vibration, Z_{AB} , to obtain the electronic binding energy of the H bond, $D_{e,AB}$. This is done calculating \bar{v}_{AB} from D_{AB} , to obtain a first approximation for Z_{AB} , and then recalculating the LS potential and its properties with $D_{AB} + Z_{AB}$.

A5.2 The LS–ISM reaction path

The vibrationally adiabatic path of ISM and the LS potential are combined to reflect the fact that a hydrogen-bonded complex brings the structure of the reactants closer to that of the transition state, as shown in mechanism (A5.1). A hydrogen bond can be regarded as an incipient proton transfer, and the bond order at the precursor complex is no longer $n = 0$, but the bond order of the B…H bond in that complex, $n_{H\dots B}$. Similarly, for the products, the bond order is not $n = 1$ but the bond order of the H…A bond in the successor complex, $(1 - n_{H\dots A})$. Thus for a proton transfer in condensed media, the reaction coordinate n is only defined in the interval $[n_{H\dots B}(1 - n_{H\dots A})]$. The precursor and successor complexes are included in the classical reaction path of ISM with a simple transformation of the reaction coordinate [3]

$$V_{cl}(n) = (1 - j)V_{HA}(1 - j) + jV_{HB}(j) + k\Delta V_{cl}^0 - D_{e,AB} \quad (A5.10)$$

where

$$\begin{aligned} j &= n - n_{H\dots B} && \text{for } n_{H\dots B} \leq n \leq n^\ddagger \\ j &= n - (1 - n_{H\dots A}) && \text{for } n^\ddagger < n \leq (1 - n_{H\dots A}) \\ k &= (n - n_{H\dots B})/(1 - n_{H\dots B} - n_{H\dots A}) && \text{for } n_{H\dots B} \leq n \leq (1 - n_{H\dots A}) \end{aligned} \quad (A5.11)$$

and ΔV_{cl}^0 will be given by eq. (13.84), after correction for the difference in zero-point energies between reactants and products (Z_{BC} and Z_{AB}).

The LS–ISM vibrationally adiabatic path is then calculated adding the zero-point energies along the reaction path, as indicated in eq. (A5.2), but including also Z_{AB} .

A5.3 Rate constants for proton transfer along a H bond

The rate of the reaction illustrated by mechanism (A5.1) is the product between the concentration of the transition states at the top of the barrier

$[\ddagger] = [B \cdots H \cdots A]$, and the frequency at which they pass over the barrier. Since the transition states are in thermal equilibrium with the hydrogen-bonded reactants, so

$$[\ddagger] = [B^\ddagger \cdots H - A] e^{-\Delta^\ddagger V_{ad}/RT} \quad (\text{A5.12})$$

and these can be related to the concentration of the separated reactants

$$K_c = \frac{[B^- \cdots H - A]}{[B^-][H - A]} \quad (\text{A5.13})$$

this rate can be expressed as:

$$k_{\text{H bond}} = \kappa(T) \bar{v}_{\text{TST}} K_c e^{-\Delta^\ddagger V_{ad}/RT} \quad (\text{A5.14})$$

where the tunnelling correction is included as usual. In the spirit of the transition-state theory, we assume that the reaction frequency is the “universal” transition-state frequency

$$\bar{v}_{\text{TST}} = \frac{k_B T}{h} \quad (\text{A5.15})$$

but we note that other choices are also possible. For example, the AB hydrogen-bond frequency \bar{v}_{AB} has been described as a restricted translation of the H_2O molecules along the O – H \cdots O direction [4], and is also a sensible choice for the reaction frequency. From weakly H-bonded systems such as $H_2O \cdots HCN$ ($D_{0AB} = 4 \text{ kJ mol}^{-1}$) to strongly H-bonded systems such as $H_2O \cdots HOH_2^+$ ($D_{0AB} = 29 \text{ kJ mol}^{-1}$), \bar{v}_{AB} ranges from 80 to 500 cm^{-1} , and correspond to reaction frequencies between 2×10^{12} and $1.5 \times 10^{13} \text{ sec}^{-1}$. Eq. (A5.15) gives $6 \times 10^{12} \text{ sec}^{-1}$ at room temperature. The numerical results are very similar, but the use of the frequency factor in H-bonded systems has a stronger physical motivation. This is the frequency employed in LS–ISM/semi-classical transition-state theory calculations. Proton transfers in enzymes have the properties of intramolecular reactions and are also calculated with this frequency factor.

The LS–ISM reaction path can also be implemented in the calculations offered at the site: <http://www.ism.qui.uc.pt:8180/ism/>.

References

- [1] ER Lippincott, R Schroeder, *J. Chem. Phys.* **23** (1955) 1099–1106.
- [2] R Schroeder, ER Lippincott, *J. Phys. Chem.* **61** (1957) 921.
- [3] M Barroso, LG Arnaut, SJ Formosinho, *Chem. Phys. Chem.* **6** (2005) 363–371.
- [4] GE Walrafen, MR Fisher, MS Hokmabadi, W-H Yang, *J. Chem. Phys.* **85** (1986) 6970–6982.

This page intentionally left blank

Quantum-mechanical radiationless transition theory

6

The rates of energy transfer or electron transfer between reactant and product states can be expressed as the product between the electronic coupling strength between initial and final states (V) and a Franck–Condon weighted density of states (FCWD)

$$k = \frac{2\pi}{\hbar} |V|^2 \text{FCWD} \quad (\text{A6.1})$$

The cases of interest in this context have low values of the electronic coupling, $V < 5 \text{ kJ mol}^{-1}$, and the processes are non-adiabatic. Such processes can be described as radiationless transfers between the vibronic levels $\varphi_i v_{iv}(\mathbf{R})$ of the initial state and the vibronic levels $\varphi_f v_{fv}(\mathbf{R})$ of the final state, which are characterised by the electronic wavefunctions φ_i and φ_f , and by the nuclear wavefunctions $v_{iv}(\mathbf{R})$ and $v_{fv}(\mathbf{R})$, respectively. For the case of displaced harmonic nuclear potential energy surfaces characterised by normal modes $\mathbf{R} \equiv R_1, R_2, \dots, R_k, \dots$, where the frequencies ω_k and reduced masses μ_k are identical in the initial and final states, the Franck–Condon factor of this multidimensional system takes the form [1]

$$\begin{aligned} \text{FCWD} &= \frac{1}{2\pi\hbar} \exp(-G) \int_{-\infty}^{+\infty} \exp[G_+(t) + G_-(t)] \exp\left(-\frac{i\Delta Et}{\hbar}\right) dt \\ G_+(t) &= \sum_k S_k (\bar{n}_k + 1) \exp(i\omega_k t) \\ G_-(t) &= \sum_k S_k \bar{n}_k \exp(-i\omega_k t) \\ G &= G_+(0) + G_-(0) = \sum_k S_k (2\bar{n}_k + 1) \\ \bar{n}_k &= \left[\exp\left(\frac{\hbar\omega_k}{k_B T}\right) - 1 \right]^{-1} \quad \frac{\bar{n}_k + 1}{\bar{n}_k} = \exp\left(\frac{\hbar\omega_k}{k_B T}\right) \end{aligned} \quad (\text{A6.2})$$

where ΔE is the energy gap between the minima of the initial and final nuclear potential energy surfaces ($\Delta E > 0$ or exo-energetic processes), \bar{n}_k is the number of excited vibrations with frequency ω_k at thermal equilibrium, and the mode-specific electron-vibration coupling strength

$$S_k = \frac{\Delta_k^2}{2} = \frac{\mu_k \omega_k}{2\hbar} d_k^2 \quad (\text{A6.3})$$

is related to the dimensionless displacements Δ_k of the equilibrium positions of the minima of the potential surfaces, and to the coordinate distance d_k between the minima of the potential surfaces shown in Figure 16.8. This figure represents only one vibrational mode but the subscripts k in the equations above designate the different modes of a multi-oscillatory system, and the summations are over all modes. The only restriction imposed on the vibrational modes is that they do not change frequencies from the initial to the final states. G_+ represents the absorption, and G_- the release, of one vibrational mode by each oscillator.

The energy gap ΔE is appropriately used to describe the difference of energy between initial and final states in radiationless transfers within a molecule (internal conversion or intersystem crossing) or between molecules (energy transfer). However, in electron-transfer reactions the rates are related to the free energy of reactions $\Delta G = \Delta H - T\Delta S$. Eq. (A6.2) with equal frequencies in both electronic states necessarily gives vanishing entropies of reactions ΔS . Only a multi-mode system with redistribution of the entropy of reaction among different modes supports the replacement of ΔE by ΔG . The incorporation of entropy changes in the application of eq. (A6.2) to electron-transfer reactions remains an open question and the current approach is just the use of ΔE as the driving force of the (energy/electron-transfer) reaction.

The treatment of eq. (A6.2) with the generality of the multi-mode description is very complex. However, some mathematical manipulations and the segregation of the vibrational modes in two categories, namely low-frequency medium modes and high-frequency molecular modes, simplifies dramatically the calculations and offer physical insight into limiting cases. The low-frequency medium modes $\{\omega_s\}$ may refer to the solvent contribution to the reorganisation energy, to the contribution of glasses with frequencies in the $10\text{--}100\text{ cm}^{-1}$ range, or to a protein medium with frequencies *ca.* 100 cm^{-1} [1e]. These contributions are usually represented by a single mode with frequency ω_s or a group of modes with the same frequency ω_s . The high-frequency modes are regarded as intra-molecular modes with frequencies in the range $100\text{--}3000\text{ cm}^{-1}$. The intra-molecular modes correspond to intra-molecular vibrations of the donor and acceptor centres and in many cases just one “representative” mode with a frequency between 1000 and 1500 cm^{-1} is used to represent the high-frequency modes.

The separation of the contributions from the low-frequency modes of the medium- and the high-frequency modes of the intra-molecular vibration in the initial and final nuclear potential energy surfaces can be accomplished expressing the phonon generators in terms of a superposition of the two classes of modes

$$\begin{aligned} G_+(t) &= G_+^v(t) + G_+^s(t) \\ G_-(t) &= G_-^v(t) + G_-^s(t) \\ G &= G^s + G^v \end{aligned} \quad (\text{A6.4})$$

The Franck–Condon factor is then

$$\text{FCWD} = \frac{1}{2\pi\hbar} \exp(-G^s - G^v) \int_{-\infty}^{+\infty} \exp[G_+^s(t) + G_-^s(t)] \exp[G_+^v(t) + G_-^v(t)] \exp\left(-\frac{i\Delta Et}{\hbar}\right) \quad (\text{A6.5})$$

In order to simplify eq. (A6.2) it is useful to write the sum of the phonon generators as

$$\begin{aligned}\exp[G_+(t) + G_-(t)] &= \exp\left\{\sum_k S_k \sqrt{\bar{n}_k(\bar{n}_k + 1)} \left[\sqrt{\frac{\bar{n}_k + 1}{\bar{n}_k}} \exp(i\omega_k t) + \sqrt{\frac{\bar{n}_k}{\bar{n}_k + 1}} \exp(-i\omega_k t) \right] \right\} \\ &= \exp\left\{\sum_k S_k \sqrt{\bar{n}_k(\bar{n}_k + 1)} \left[\sqrt{\frac{\bar{n}_k + 1}{\bar{n}_k}} \exp(i\omega_k t) + \frac{1}{\sqrt{\frac{\bar{n}_k + 1}{\bar{n}_k}} \exp(i\omega_k t)} \right] \right\}\end{aligned}\quad (\text{A6.6})$$

and recognise the similarity with the formula

$$\exp\left[\frac{x}{2}\left(y + \frac{1}{y}\right)\right] = \sum_{n=-1}^{\infty} y^n I_n(x) \quad (\text{A6.7})$$

where $I_n(x)$ is the modified Bessel function

$$I_p(z) = \sum_{k=0}^{\infty} \frac{(z/2)^{p+2k}}{k!(p+k)!} \quad (\text{A6.8})$$

Hence the sum of the phonon generators is

$$\exp[G_+(t) + G_-(t)] = \sum_{m_k=-\infty}^{\infty} \left(\frac{\bar{n}_k + 1}{\bar{n}_k}\right)^{\frac{m_k}{2}} e^{m_k i \omega_k t} I_{m_k}(2S_k \sqrt{\bar{n}_k(\bar{n}_k + 1)}) \quad (\text{A6.9})$$

This manipulation places the time dependence in an exponential factor that can be combined with the exponential factor for the time dependence already present in eq. (A6.5).

A further simplification is to represent the low- and high-frequency modes by one single frequency each, ω_s and ω_v , respectively. This is a rather dramatic approximation, because modes with a variety of frequencies often contribute, with an extent weighted by their S_k , to the transition. Sacrificing the accuracy of the multi-mode model, it is possible to obtain a formula of relatively simple implementation

$$\begin{aligned}\text{FCWD} &= \frac{1}{2\pi\hbar} \exp(-G^s - G^v) \sum_{n=-\infty}^{\infty} \left(\frac{\bar{n}_s + 1}{\bar{n}_s}\right)^{\frac{p(n)}{2}} I_{p(n)} \left[2S_s \sqrt{\bar{n}_s(\bar{n}_s + 1)}\right] \left(\frac{\bar{n}_v + 1}{\bar{n}_v}\right)^{\frac{n}{2}} I_n \left[2S_v \sqrt{\bar{n}_v(\bar{n}_v + 1)}\right] \\ &\times \int_{-\infty}^{+\infty} \exp[ip(n)\omega_s t + in\omega_v t] \exp\left(-\frac{i\Delta E t}{\hbar}\right) dt\end{aligned}\quad (\text{A6.10})$$

where m_v is represented by n and m_s was replaced by $p(n)$. The exponentials can now be expressed together to give a definite integral

$$\int_{-\infty}^{+\infty} \exp\left[i\left[p(n)\omega_s + n\omega_v - \frac{\Delta E}{\hbar}\right]t\right] dt = \frac{2\pi}{\omega_s} \delta\left(p(n) + \frac{n\omega_v}{\omega_s} - \frac{\Delta E}{\omega_s \hbar}\right) \quad (\text{A6.11})$$

where the value of $p(n)$ is selected from the solution of

$$p(n) = \frac{\Delta E}{\hbar\omega_s} - n \frac{\omega_v}{\omega_s} \quad (\text{A6.12})$$

to drop the δ -function and retain the factor $2\pi/\omega_s$. The value of n is the net change in quantum number for each oscillation. The sum over n from $-\infty$ to $+\infty$ covers all possible changes in quantum number, to lower or higher values of the final state relative to the initial state, for each oscillator. Eq. (A6.2) ensures the conservation of energy in the transition: for each net change in quantum number n , the value of p for the medium energy level is selected to accommodate the reaction energy. In practice, the value of p is the closest integer given by eq. (A6.12) for each value of n . The factor $2\pi/\omega_s$ together with the pre-exponential factor in eq. (A6.10), gives

$$\begin{aligned} \text{FCWD} &= \frac{1}{\hbar\omega_s} \exp[-S_s(2\bar{n}_s + 1) - S_\nu(2\bar{n}_\nu + 1)] \sum_{n=-\infty}^{+\infty} \left(\frac{\bar{n}_s + 1}{\bar{n}_s} \right)^{p(n)/2} \\ &\times I_{|p(n)|} (2S_s \sqrt{\bar{n}_s(\bar{n}_s + 1)}) \left(\frac{\bar{n}_\nu + 1}{\bar{n}_\nu} \right)^{n/2} I_{|n|} (2S_\nu \sqrt{\bar{n}_\nu(\bar{n}_\nu + 1)}) \end{aligned} \quad (\text{A6.13})$$

and the transition rate is

$$\begin{aligned} k &= \frac{2\pi}{\hbar^2\omega_s} |V|^2 \exp[-S_s(2\bar{n}_s + 1) - S_\nu(2\bar{n}_\nu + 1)] \sum_{n=-\infty}^{+\infty} \left(\frac{\bar{n}_s + 1}{\bar{n}_s} \right)^{p(n)/2} \\ &\times I_{|p(n)|} (2S_s \sqrt{\bar{n}_s(\bar{n}_s + 1)}) \left(\frac{\bar{n}_\nu + 1}{\bar{n}_\nu} \right)^{n/2} I_{|n|} (2S_\nu \sqrt{\bar{n}_\nu(\bar{n}_\nu + 1)}) \end{aligned} \quad (\text{A6.14})$$

Eq. (A6.14), and some of its limiting cases, has been applied to the calculation of energy and electron-transfer rates. It is important to realise that it was derived making substantial approximations, namely: (i) the initial and final states are represented by displaced but identical harmonic nuclear potential energy surfaces; (ii) reaction entropy changes in electron-transfer reactions are not accommodated by the model; (iii) only one low-frequency mode ω_s and one high-frequency mode ω_ν are considered, although they may be a representative average of low- and high-frequency modes with the same ω_s and S_s or ω_ν and S_ν , respectively.

Eq. (A6.14) can be applied to intra-molecular radiationless processes (internal conversion or inter-system crossing) or energy and electron-transfer reactions between independent molecules. These processes fall into different limits that are convenient to separate defining the molecular nuclear relaxation energy

$$E_M = \sum_k \hbar\omega_k S_k \quad (\text{A6.15})$$

which is half the Stokes shift, and the mean vibrational frequency

$$\langle \omega \rangle = N^{-1} \sum_k \omega_k \quad (\text{A6.16})$$

There are two coupling limits: $E_M \leq \hbar\langle\omega\rangle$ or $E_M > > \hbar\langle\omega\rangle$. In the first limit, the relative displacement of each normal mode is relatively small and the weak coupling limit is encountered. This limit is illustrated in [Figure 16.8](#). The limit of strong coupling corresponds to large displacements of the potential energy surfaces such that the surfaces may intersect in the vicinity of the minimum of the initial state (for $\Delta E > 0$). This limit is illustrated in [Figure 16.17](#).

Following the notations used by most authors, and also in this work, and making use of the relations and definitions given above, it is convenient in the following discussion to express the electron–phonon couplings (Huang–Rhys parameters) in terms of the reorganisation energies of the medium (or solvent) and of the intra-molecular vibrations

$$S_s = \frac{\lambda_s}{\hbar\omega_s}, \quad S_v = \frac{\lambda_v}{\hbar\omega_v} \quad (\text{A6.17})$$

A6.1 The strong coupling limit

In the limit where the coupling of the reactive system to the low-frequency “lattice” is negligible and the major contributions come from the high-frequency intramolecular modes of the electron (or energy) donor and acceptor centres, that is, when $S_s \rightarrow 0$ (or $\lambda_s \rightarrow 0$), G^s , G_-^s and G_+^s can be neglected and the transition is due to one single mode. In this one mode approximation of identical and displaced oscillators, only $n = 0$ contributes to the Franck–Condon factor, [eq. \(A6.12\)](#) simplifies to

$$p = \frac{\Delta E}{\hbar\omega} \quad (\text{A6.18})$$

and a simple relation is derived from [eq. \(A6.13\)](#)

$$\text{FCWD} = \frac{1}{\hbar\omega} \exp[-S(2\bar{n} + 1)](\bar{n} + 1\bar{n})^{p/2} I_p\left(2S\sqrt{\bar{n}(\bar{n} + 1)}\right) \quad (\text{A6.19})$$

where the subscripts of the modes were dropped because there is only one mode.

At the low temperature limit, $k_B T < < \hbar\omega$ and $\bar{n} \rightarrow 0$, the limiting form of the Bessel function for small values of the argument is

$$I_p(z) \rightarrow \frac{1}{p!} \left(\frac{z}{2}\right)^p \quad (\text{A6.20})$$

and the Franck–Condon factor becomes

$$\text{FCWD} = \frac{1}{\hbar\omega} \exp[-S] \frac{S^p}{p!} \quad (\text{A6.21})$$

This has the same form as the Poisson distribution presented in [eq. \(16.64\)](#). The validity of this approximation depends on the vibrational frequency selected

to represent the system. For intra-molecular vibrational frequencies of 1500 cm^{-1} , this limit applies to temperatures lower than 2000 K.

A simple solution can be obtained when one low-frequency and one high-frequency modes are present, eq. (A6.13), and the temperature is extremely low, such that

$$\begin{aligned} k_B T &<< \hbar\omega_s &<< \hbar\omega_v \\ \bar{n}_s &\rightarrow 0 \\ \bar{n}_v &\rightarrow 0 \end{aligned} \quad (\text{A6.22})$$

These conditions also insure that the limit of eq. (A6.20) is reached and eq. (A6.13) transforms into

$$\text{FCWD} = \frac{1}{\hbar\omega_s} \exp(-S_s - S_\nu) \sum_{n=0}^{+\infty} \frac{S_s^{p(n)} S_\nu^n}{[p(n)]! n!} \quad (\text{A6.23})$$

where the limits of the sum acknowledge the fact that at such low temperatures the quantum number can only change to higher values of the final state because the initial state is at its lowest level. This solution includes the low frequency from the lattice/solvent, which can be as low as 10 cm^{-1} . Now, in order to meet the conditions of eq. (A6.22), the temperature must be lower than 10 K. Eq. (A6.23) may be relevant for energy or electron-transfer reactions in cryogenic matrixes but not for reactions in solution.

The most physically meaningful limit is that where $\hbar\omega_s \ll k_B T \ll \hbar\omega_v$. As discussed above, when the low frequencies are $\leq 10\text{ cm}^{-1}$ and the high frequencies are $\sim 1500\text{ cm}^{-1}$, this case covers temperatures between 20 K and 2000 K. This case allows for the treatment of the high frequency in eq. (A6.13) using the low-temperature limit

$$\text{FCWD} = \frac{1}{\hbar\omega_s} \exp[-S_s(2\bar{n}_s + 1)] \exp(-S_\nu) \sum_{n=0}^{\infty} \left(\frac{\bar{n}_s + 1}{\bar{n}_s} \right)^{p(n)/2} I_{|p(n)|} \left(2S_s \sqrt{\bar{n}_s(\bar{n}_s + 1)} \right) \frac{S_\nu^n}{n!} \quad (\text{A6.24})$$

where eq. (A6.20) was employed together with the assumption that only the lowest vibrational state of the high-frequency mode is populated. Furthermore the low frequency can be treated in the high-temperature limit where

$$\begin{aligned} \sqrt{\bar{n}_s(\bar{n}_s + 1)} &\rightarrow k_B T / \hbar\omega_s \\ 2\sqrt{\bar{n}_s(\bar{n}_s + 1)} - (2\bar{n}_s + 1) &\rightarrow -\hbar\omega_s / 4k_B T \\ I_p(z) &\rightarrow \frac{1}{\sqrt{2\pi z}} \exp\left(z - \frac{p^2}{2z}\right) \end{aligned} \quad (\text{A6.25})$$

and eq. (A6.24) is transformed in

$$\begin{aligned} \text{FCWD} &= \frac{1}{\hbar\omega_s} \exp[-S_s(2\bar{n}_s + 1)] \exp(-S_\nu) \sum_{n=0}^{\infty} \exp\left[\frac{p(n)\hbar\omega_s}{2k_B T}\right] \\ &\times \frac{\sqrt{\hbar\omega_s}}{\sqrt{4\pi S_s k_B T}} \exp\left[2S_s \sqrt{\bar{n}_s(\bar{n}_s + 1)}\right] \exp\left[-\frac{\hbar\omega_s p(n)^2}{4S_s k_B T}\right] \frac{1}{n!} S_\nu^n \end{aligned} \quad (\text{A6.26})$$

that can be rearranged to

$$\text{FCWD} = \frac{1}{\sqrt{4\pi S_s \hbar \omega_s k_B T}} \exp(-S_v) \sum_{n=0}^{\infty} \frac{S_v^n}{n!} \exp\left[\frac{\hbar \omega_s p(n)}{2k_B T} - \frac{S_s \hbar \omega_s}{4k_B T} - \frac{\hbar \omega_s p(n)^2}{4S_s k_B T}\right] \quad (\text{A6.27})$$

or

$$\text{FCWD} = \frac{1}{\sqrt{4\pi \lambda_s k_B T}} \exp(-S_v) \sum_{n=0}^{\infty} \frac{S_v^n}{n!} \exp\left[-\frac{\hbar \omega_s}{4S_s k_B T} (\hbar \omega_s p(n)^2 - 2S_s p(n) + S_s^2)\right] \quad (\text{A6.28})$$

Recognising the presence of the square of a difference and using eq. (A6.12), gives

$$\text{FCWD} = \frac{1}{\sqrt{4\pi \lambda_s k_B T}} \exp(S_v) \sum_{n=0}^{\infty} \frac{S_v^n}{n!} \exp\left[-\frac{(\Delta E - \lambda_s - n\hbar\omega_v)^2}{4\lambda_s k_B T}\right] \quad (\text{A6.29})$$

This equation is often used to calculate the Franck–Condon factor of electron-transfer rates using the best experimental estimate of the free energy of reaction in place of ΔE . It is a valuable equation over a broad temperature domain, provided that the system can be represented by one classical low-frequency mode and one quantised high-frequency mode, and entropy changes can be neglected.

For completeness, in the high-temperature limit, which is valid for $k_B T \gg \hbar\omega_v \gg \hbar\omega_s$, the approximations in eq. (A6.25) apply to both low- and high-frequency modes. In this case, both modes are treated as classical modes and lead to

$$\text{FCWD} = \frac{1}{\sqrt{4\pi \lambda k_B T}} \exp\left[-\frac{(\Delta E - \lambda)^2}{4\lambda k_B T}\right] \quad (\text{A6.30})$$

where $\lambda = \lambda_s + \lambda_v$. Thus in the limit of very high temperature the quantum mechanical approach reproduces the classical rate constant for electron transfer in eq. (15.89).

In the classical rate equation

$$k_{cl} = \frac{\sqrt{\pi}}{\hbar \sqrt{\lambda k_B T}} |V|^2 \exp\left[-\frac{(\Delta E - \lambda)^2}{4\lambda k_B T}\right] = A \exp\left(\frac{E_a}{k_B T}\right) \quad (\text{A6.31})$$

the activation energy is given by

$$E_a = \frac{(\Delta E - \lambda)^2}{4\lambda} \quad (\text{A6.32})$$

It is important to note that E_a is the height of the energy barrier, measured as the energy difference from the crossing point between the initial and final states and the energy of the initial state. These states were described by different potential energy surfaces. The expressions above for the Franck–Condon factor did not make assumptions about the adiabaticity of the energy or electron transfers. The “strong coupling” limit followed here refers to the value of electron-vibration coupling strength S_k and not to the value of the electronic coupling between initial and final states $|V|^2$.

A6.2 The weak coupling limit

In the weak coupling limit, $E_M \approx \hbar\langle\omega\rangle$, the molecular nuclear relaxation energy is small relative to the vibrational frequency and the limit of eq. (A6.21) applies, where p is defined by eq. (A6.18) or, more generally

$$p = \frac{|\Delta E|}{\hbar\omega} \quad (\text{A6.33})$$

When $|\Delta E| \gg 0$, large values of p are obtained and it is possible to use Stirling's approximation

$$p! = \exp[p(\ln p - 1)] \quad (\text{A6.34})$$

Eq. (A6.21) then becomes

$$\text{FCWD} = \frac{1}{\hbar\omega} \exp[-S] S^p \exp[-p \ln(p - 1)] \quad (\text{A6.35})$$

Using the relation

$$x^y = e^{y \ln x} \quad (\text{A6.36})$$

It is possible to write

$$\text{FCWD} = \frac{1}{\hbar\omega} \exp[-S] \exp[p \ln S] \exp[-p \ln(p - 1)] \quad (\text{A6.37})$$

or

$$\text{FCWD} = \frac{1}{\hbar\omega} \exp[-S] \exp\left[-p\left(\ln\frac{p}{S} - 1\right)\right] \quad (\text{A6.38})$$

From eqs. (A6.3), (A6.15) and (A6.33)

$$\text{FCWD} = \frac{1}{\hbar\omega} \exp\left(-\frac{E_M}{\hbar\langle\omega\rangle}\right) \exp\left\{-\frac{\Delta E}{\hbar\omega} \left[\ln\left(\frac{\Delta E}{S\hbar\omega}\right) - 1\right]\right\} \quad (\text{A6.39})$$

or, making

$$\gamma = \ln\left(\frac{\Delta E}{m\epsilon_M}\right) - 1 \quad (\text{A6.40})$$

and recalling that $E_M \approx \hbar\langle\omega\rangle$ for the weak coupling limit

$$\text{FCWD} = \frac{1}{\hbar\omega} \exp\left(-\frac{\Delta E}{\hbar\omega_M} \gamma\right) \quad (\text{A6.41})$$

This is the expression for the energy gap law of radiationless transitions first derived by Englman and Jortner in 1970 [1b]. It predicts that internal conversion rates (or inter-systems crossing rates when spin-forbidden factors are included in the electronic factor) increase when the energetic difference between the initial and final electronic states decreases. This explains Kasha's rule: the energy difference between higher electronic states is smaller than between the S_0 and S_1 states

and the radiationless transitions between the higher states are so fast that radiative rates cannot compete with them.

Eq. (A6.38) with eq. (A6.40) can also be written as

$$\text{FCWD} = \frac{1}{\hbar\omega} \exp \left[-S - \frac{\Delta E}{\hbar\omega} \gamma + \frac{\Delta E}{\hbar\omega} - \frac{\Delta E}{\hbar\omega} \right] = \frac{1}{\hbar\omega} \exp \left[-\frac{S\hbar\omega - \Delta E}{\hbar\omega} \right] \exp \left[-(\gamma + 1) \frac{\Delta E}{\hbar\omega} \right] \quad (\text{A6.42})$$

to emphasise the presence of a factor that can be related with the activation energy in eq. (A6.32)

$$E_a = \frac{(S\hbar\omega - \Delta E)^2}{4S\hbar\omega} \quad (\text{A6.43})$$

Using eq. (A6.3), it is possible to write

$$\text{FCWD} = \frac{1}{\hbar\omega} \exp \left[-\frac{d\sqrt{2\mu E_A}}{\hbar} \right] \exp \left[-(\gamma + 1) \frac{\Delta E}{\hbar\omega} \right] \quad (\text{A6.44})$$

and obtain the expression for the rate constant of a radiationless transition in the weak coupling

$$k = \frac{2\pi}{\hbar^2\omega} |V|^2 \exp \left[-\frac{d\sqrt{2\mu E_A}}{\hbar} \right] \exp \left[-(\gamma + 1) \frac{\Delta E}{\hbar\omega} \right] \quad (\text{A6.45})$$

Jortner arrived at this expression in 1979 and noted that the second exponent in eq. (A6.45) should be of minor importance since $(\gamma + 1)$ is a small negative quantity for the conditions where the expression applies [2]. Under such conditions, the rate for radiationsless transitions bears a close formal relationship to the WKB solution for the tunnelling probability through a barrier formed by intersecting parabola, eq. (6.47). Formosinho had already formulated radiationsless transitions rates in terms of a similar tunnelling equation in 1974 but based on different principles [3], eq. (16.72).

A6.3 Energy and electron-transfer rates

The quantum-mechanical treatment of energy and electron-transfer processes described above was based on the work initiated by Jortner and co-workers in the 1970s. It allows for the calculation of intra-molecular radiationless transitions, and energy or electron transfer between donor and acceptor states.

The most general and accurate rate expression can be derived from eq. (A6.1) with the multi-mode expression in eq. (A6.2). Such an expression is valid for displaced harmonic nuclear potential energy surfaces with identical frequencies in the initial and final state. However, in view of the complexity of the calculations and absence of information on the vibrational modes to include in the reaction coordinate, in general the best compromise for the calculation of energy or

electron-transfers rates in the 100 K–300 K range to is use eq. (A6.29) with eq. (A6.1) [4]

$$k_{ET} = \frac{\sqrt{\pi}}{\hbar\sqrt{\lambda_s k_B T}} |V|^2 \exp(S_v) \sum_{n=0}^{\infty} \frac{S_v^n}{n!} \exp\left[-\frac{(\Delta G^0 + \lambda_s + n\hbar\omega_v)^2}{4\lambda_s k_B T}\right] \quad (\text{A6.46})$$

where the free energy of reaction ($\Delta G^0 < 0$ for an exothermic reaction) was used in place of the difference of energy between initial and final states ($\Delta E > 0$ for an exo-energetic reaction) because it is the quantity experimentally available for electron-transfer reactions. This expression treats the low-frequency lattice/solvent mode classically and assumes that only the lowest vibrational level of one high-frequency mode is populated. Figure A6.1 shows various simulations with eq. (A6.46) that illustrate the effect on free-energy relationships of changing the vibrational frequency ω_v , the solvent reorganisation energy λ_s , or the electron-vibration coupling strength S_v . The temperature changes are illustrated in Figure A6.2.

The increase in S_v , which reflects a larger displacement between the potential energy curves representing the initial and the final states, shifts the onset of the inverted region to higher exothermicities. This can also be regarded as an increase of the contribution of reorganisation energy associated with the high-frequency intramolecular modes, λ_v , eq. (A6.17). When $S_v \rightarrow 0$, the free-energy dependence tends to the perfect inverted parabola of the classical Marcus theory for electron transfer. The contribution of the high-frequency modes increases very substantially the rates in the inverted region. As will be seen below in Figure A6.2, this contribution is due to nuclear tunnelling of such modes.

The increase in the frequency of the high-frequency mode leads to even more dramatic increase in the rates in the inverted region. High frequencies lead to higher force constants, which mean that the parabolas are thinner and, for the

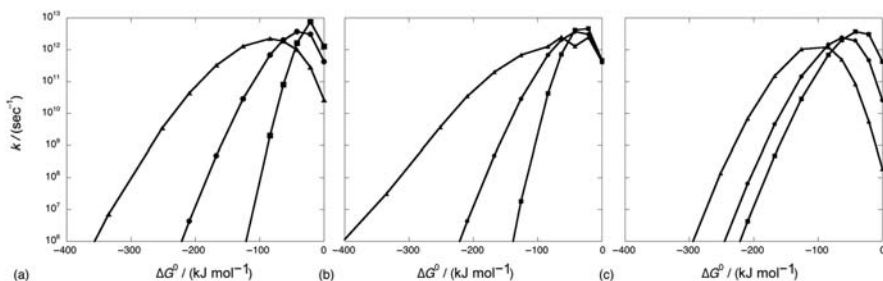
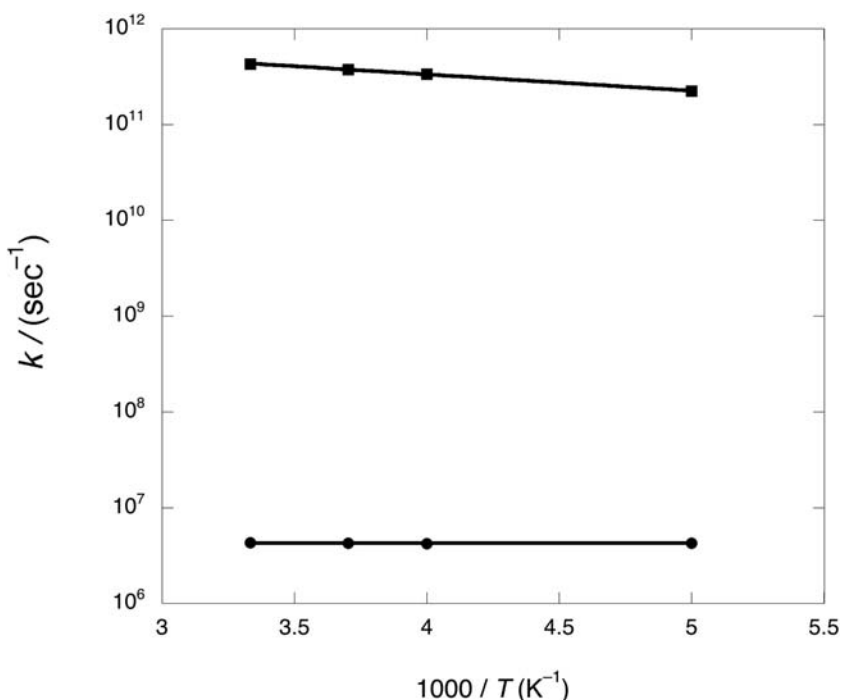


FIGURE A6.1

Free-energy relationships at $T = 298\text{K}$ calculated with eq. (A6.42). (a) $\hbar\omega_v = 1500\text{ cm}^{-1}$, $\lambda_s = 21\text{ kJ mol}^{-1}$, and $S_v = 0.1$ (squares), 1.2 (circles) or 4 (triangles). (b) $\lambda_s = 21\text{ kJ mol}^{-1}$, $S_v = 1.2$ and $\hbar\omega_v = 800$ (squares), 1500 (circles) or 3000 cm^{-1} (triangles). (c) $\hbar\omega_v = 1500\text{ cm}^{-1}$, $S_v = 1.2$ and $\lambda_s = 21$ (squares), 42 (circles) or 84 kJ mol^{-1} (triangles).

**FIGURE A6.2**

Temperature dependence in the 200K – 300K range calculated with eq. (A6.42) using $\hbar\omega_v = 1500 \text{ cm}^{-1}$, $\lambda_s = 5 \text{ kcal mol}^{-1}$ and $S_v = 1.2$, for $\Delta G^0 = 0$ (squares) and -209 (circles) kJ mol^{-1} .

same S_v , intersect at higher energies. The logarithm of nuclear tunnelling rates depends only on the square root of the height of the reaction barrier, eq. (A6.45), which makes it even more important for thin and high barriers.

The increase of the solvent (or medium) reorganisation energy λ_s adds to the total reorganisation energy and displaces the onset of the inverted region to more exothermic reactions. As the contribution of λ_s to the reaction coordinate increases, its classical behaviour is accentuated and the Marcus inverted parabola is observed over an extended free-energy region.

Figure A6.2 reveals that the temperature dependence of the rates of isothermal reactions follows Arrhenius equation, eq. (A6.31), with activation energy $E_a = 3.3 \text{ kJ mol}^{-1}$ in the conditions described in the figure. This classical behaviour is typical of the “normal” free-energy region where the reaction rates increase with the exothermicity. However, deep in the inverted region the rates are independent of the temperature. This is the signature of nuclear tunnelling. It indicates that the rates are dominated by the Franck–Condon factors of the high-frequency modes.

It is interesting to compare the calculations presented above with the two-mode approximation featuring one classical mode and one high-frequency mode,

[eq. \(A6.46\)](#), with simulations employing the multi-mode approach. Numerical simulations with nine modes comprising frequencies between 150 and 2200 cm⁻¹ revealed that the use of a single averaged mode underestimates the rate by 9 orders of magnitude at $\Delta G = -240 \text{ kJ mol}^{-1}$ [5]. Using one single mode with the frequency of 1500 cm⁻¹ reduces this discrepancy to 4 orders of magnitude. However, it is possible to use one single high-frequency mode and obtain a good agreement with experimental data in the inverted region by a trial-and-error method, that is, fitting the value of S_v . Another interesting issue pertaining to the contribution of very high-frequency vibrational modes, such as the C–H vibration at 3000 cm⁻¹, is that they may enhance the rate by 1 order of magnitude at $\Delta G = -240 \text{ kJ mol}^{-1}$ and 2 orders of magnitude at $\Delta G = -360 \text{ kJ mol}^{-1}$ relative to the numerical calculations with nine modes [5]. The contribution of C–H modes to the reaction coordinate may be assessed using deuterated molecules.

It must be recalled that the multi-mode approach was based on a harmonic model system with displaced nuclear potential surfaces characterised by the same frequencies. Hence this model still ignores entropy changes and anharmonic effects, which are relevant for electron-transfer reactions. A harmonic model can only accommodate entropy changes as changes in the vibrational frequencies resulting from the new charge distribution in the system after electron transfer. For positive entropy of reaction, the potential energy surface of the final state is shallower than that of the initial state [6]. It is possible to use asymmetric free-energy surfaces to overcome the limitations of the harmonic model but the simulations become rather elaborate [7]. The main lesson learnt from such simulations is that the asymmetry in the free-energy surfaces is manifested as an asymmetry in the free-energy dependence of the electron-transfer rates, which becomes more linear than quadratic for very exothermic reactions [7].

One final remark should be made on anharmonicity. The harmonic approximation is generally appropriate for describing the low-frequency solvent modes but it is unrealistic for quantum modes far from their equilibrium positions. It was seen in [Chapter 6](#), Reactivity in Thermalised Systems, that potential energy curves of diatomic molecules deviate appreciably from harmonic behaviour for relatively low vibrational excitations, and Morse curves, [eq. \(6.64\)](#), must be employed to describe bond-breaking–bond-forming reactions. This issue is not as critical in electron-transfer reactions when normal modes (e.g., the skeletal symmetric stretching) are involved, but it remains of interest to evaluate the effect of anharmonicity in energy and electron-transfer reactions. The anharmonicity of the molecular mode can be addressed substituting the Morse Franck–Condon overlap integral and energies into the analogous relations for harmonic oscillators given above [8]. The Morse stretching and compression modes affect differently the reaction rates. In the inverted region, the Morse compression mode is expected to give a much higher transition rate than the harmonic mode or the Morse stretching mode [8].

In summary, the quantum-mechanical formulation of radiationless transition rates advanced very substantially in the 1970s and offers today a set of closed

formulae to describe limiting cases of such rates. The calculation of the rates with one classical low-frequency mode and one quantum-mechanical high-frequency mode with a representative frequency, can account for the free energy and temperature dependences observed experimentally. However, the approximations required to obtain closed equations, namely the neglect of other high-frequency modes and of changes in entropy, give calculated rates that tend to underestimate the experimental rates deep in the inverted region.

References

- [1] (a) KF Freed, J Jortner, *J. Chem. Phys.* **52** (1970) 6272–6291.
(b) R Englman, J Jortner, *Mol. Phys.* **18** (1970) 145–164.
(c) SH Lin, *J. Chem. Phys.* **53** (1970) 3766–3767.
(d) D DeVault, *Q. Rev. Biophys.* **13** (1980) 387–564.
(e) M Bixon, J Jortner, *Adv. Phys. Chem.* **106** (1999) 35–202.
- [2] J Jortner, J Ulstrup, *Chem. Phys. Lett.* **63** (1979) 236–239.
- [3] SJ Formosinho, *J. Chem. Soc. Faraday Trans. 2* **70** (1974) 605.
- [4] (a) NR Kestner, J Logan, J Jortner, *J. Phys. Chem.* **78** (1974) 2148.
(b) SF Fischer, RP Van Duyne, *Chem. Phys.* **26** (1977) 9.
- [5] M Bixon, J Jortner, J Cortes, H Heitele, ME Michel-Bayerle, *J. Phys. Chem.* **98** (1994) 7289–7299.
- [6] O Weintraub, M Bixon, *J. Phys. Chem.* **98** (1994) 3407–3411.
- [7] DW Small, DV Matyushov, GA Voth, *J. Am. Chem. Soc.* **125** (2003) 7470–7478.
- [8] S Yeganeh, MA Ratner, *J. Chem. Phys.* **124** (2006) 044108.

This page intentionally left blank

Problems

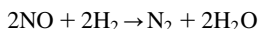
7

1. What are the orders of the following reactions, given the corresponding reaction half-lives:

- (a) The decomposition of ammonia on a tungsten filament, with the following half-lives, $t_{1/2}$, at different initial pressures, p_0 :

p_0 (mmHg)	12	48	72	120
$t_{1/2}$ (s)	52.5	210	315	525

- (b) The reaction



at the stoichiometric composition, for which the following $t_{1/2}$ values have been measured at 826°C for the initial pressure of the reactants p_0 :

p_0 (mmHg)	251	288	340
$t_{1/2}$ (s)	180	140	100

- (c) The pyrolysis of acetaldehyde at 518°C and at the initial pressure of 360 mmHg, which has the fractional lifetimes $t_{1/2}$ and $t_{3/4}$ of 420 and 1220 s, respectively.
2. The initial rates, v_0 , for the reaction $2\text{A} + \text{B} = \text{C} + \text{D}$ are shown in the following table:

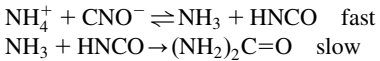
$[\text{A}]_0$ (mol dm $^{-3}$)	$[\text{B}]_0$ (mol dm $^{-3}$)	v_0 (mol dm $^{-3}$ s $^{-1}$)
0.025	0.100	0.01
0.050	0.100	0.02
0.100	0.100	0.04
0.100	0.050	0.01
0.100	0.025	0.0025

What is the rate law and what is the value of the rate constant?

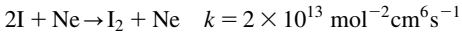
3. A live plant has some radioactivity owing to the presence of ^{14}C that shows 15.3 counts per minute per gram of carbon. In the cave of Lascaux in France some samples of coal have a radioactivity of 2.25 counts per minute per

gram of carbon. What is the age of the samples of coal, knowing that the ^{14}C half-life is 5669 years?

4. The rate constant for the reaction: $\text{H}^+ + \text{OH}^- \rightarrow \text{H}_2\text{O}$ is $1.3 \times 10^{11} \text{ dm}^3 \text{ mol}^{-1} \text{ s}^{-1}$. Nonequilibrium concentrations of protons and hydroxide ions can be induced in temperature jump experiments.
 - (a) Calculate the half-life for the neutralisation process if (i) $[\text{H}^+] = [\text{OH}^-] = 10^{-3} \text{ M}$ and (ii) $[\text{H}^+] = [\text{OH}] = 5 \times 10^{-5} \text{ M}$.
 - (b) Under the same conditions, calculate the half-life of the hydroxide ion if $\text{pH} = 6$.
5. The initial rate of formation of urea increases by a factor of 2 when one doubles the concentration of ammonium cyanate. The suggested mechanism of urea formation is

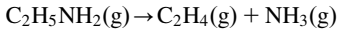


- (a) What is the rate law for this mechanism?
- (b) Is the mechanism in agreement with the effect of $[\text{NH}_4\text{CNO}]$?
6. What fast reaction technique could you choose to follow the recombination



at 333K?

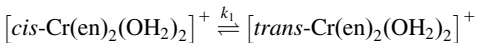
7. The rate of the reaction



was measured in terms of the total pressure P_t at 500°C as follows:

P_t (mmHg)	55	60	79	89	102	105
Time (s)	0	60	360	600	1200	1500

- (a) Verify that the decomposition follows a first-order process.
- (b) Calculate the rate constant and the half-life of the reaction.
8. The reaction



is first order in both directions with $k_1 = 3.3 \times 10^{-4} \text{ s}^{-1}$ and $K_e = 0.16$ at 25°C.

- (a) Show that

$$k_1 t = \frac{x_e}{a_0} \ln \left(\frac{x_e}{x_e - x} \right)$$

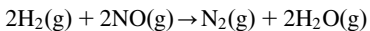
where a_0 is the initial amount of the *cis*-form and x the amount converted into the *trans*-form; the amount of the *trans*-form at equilibrium is x_e .

- (b) Starting with pure *cis*-form, how long would it take for 75% of the equilibrium amount of the *trans*-form to be formed?
9. *N*-Methylnicotinamide (NcMe^+) is a model of the biologically important electron transport agent nicotinamide adenine dinucleotide (NAD^+). One

electron reduction of NcMe^+ produces the corresponding pyridinyl radical, $\text{NcMe}\cdot$, whose decay can be monitored spectrophotometrically at 400 nm. Data from a study of absorbance against time are given below for the reaction of this pyridinyl radical in buffered aqueous solution (pH 7.2).

Time (μs)	20	100	200	400	600	800	1200	1600	∞
Absorbance at 400 nm	0.0273	0.0186	0.0128	0.0081	0.0060	0.0047	0.0026	0.0022	0.0

- (a) Determine the order of this reaction.
 (b) Derive an expression that you can use to determine the rate constant. Given the value $\varepsilon_{400 \text{ nm}} = 8900 \text{ dm}^3 \text{ mol}^{-1} \text{ cm}^{-1}$ for the molar absorption coefficient of the pyridinyl radical, and that the measurements were made in 1-cm cuvettes, calculate the rate constant for the decay of this species.
10. In aqueous solutions, the following decarboxylation reaction:
- $$\text{CO}(\text{CH}_2\text{COOH})_2 \rightarrow \text{CO}(\text{CH}_3)_2 + 2\text{CO}_2$$
- is a first-order process with an activation energy of $192.9 \text{ kJ mol}^{-1}$. At 10°C the half-life of the reaction is 107 min. What is the rate constant at 50°C ?
11. The rate constant for the elementary reaction
- $$\text{I} + \text{H}_2 \rightarrow \text{H} + \text{HI}$$
- is
- $$k = 1014.1 \text{ e}^{-140/RT} \text{ mol}^{-1} \text{ dm}^3 \text{ s}^{-1}$$
- (Note: E_a is in kJ mol^{-1}). What is the activation energy for the reaction in the reverse direction if $\Delta H = 137.3 \text{ kJ mol}^{-1}$ for the above reaction?
12. The decomposition of nitrogen oxide
- $$2\text{NO}_2 \rightarrow 2\text{NO} + \text{O}_2$$
- occurs at high temperatures, via the activated complex $\{\text{NO}_2\cdot\text{Ar}\}^\ddagger$ in a sequence of two elementary steps. The net change in the first of these is
- $$\text{Ar} + \text{NO}_2 \leftrightarrow \text{NO} + \text{O} + \text{Ar} \quad (\text{A7.i})$$
- (a) What is the second reaction, which when combined with reaction (A7.i), gives the complete reaction?
 (b) At temperatures around 600K the rate law is second order and proceeds via a different activated complex $\{\text{NO}_2\cdot\text{NO}_2\}^\ddagger$. Which one of the activated complexes is expected to lead to a lower activation energy?
13. The rate law for the reaction



is

$$v = k[\text{NO}]^2[\text{H}_2]$$

Which of the following mechanisms is in agreement with the rate law?



14. The initial rate of reaction between iodate and iodide ions



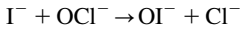
has been measured at 298K at constant ionic strength and pH:

Experiment number	1	2	3	4	5
$10^2 [\text{IO}_3^-]$ (mol dm ⁻³)	3.8	4.5	5.0	3.8	4.5
$10^2 [\text{I}^-]$ (mol dm ⁻³)	3.0	3.0	3.6	5.0	7.0
$10^8 v_0$ (mol dm ⁻³ s ⁻¹)	0.84	1.17	3.00	6.46	34.8

Data: Barton et al., J. Chem. Soc. Faraday Trans. I (1976) 72 568.

- (a) Estimate the partial orders of the reaction and the pseudo-rate constant.
 (b) From the rate law, what can be deduced about the composition of the activated complex for the rate-determining step?

15. The reaction between hypochlorite ion and iodide ion in alkaline solutions

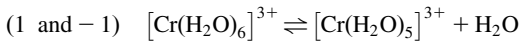


has a rate law

$$\frac{d[\text{OI}^-]}{dt} = k[\text{I}^-][\text{OCl}^-][\text{OH}^-]^{-1}$$

- (a) What can be said about the composition of the activated complex in the rate-determining step?
 (b) Propose a mechanism for the reaction.

16. (a) Propose a rate law which is consistent with the following mechanism:



- (b) Under what conditions can the reaction be considered to be a first-order process?

17. Chlorine water is used in water treatment and in the destruction of dissolved organic matter. In this system, a fast equilibrium is established between dissolved chlorine $\text{Cl}_2 (+ \text{H}_2\text{O})$ and hypochlorous acid (HOCl),



In the oxidation of propan-2-ol by chlorine water, two possible rate-determining steps can be considered:

- (a) $\text{Cl}_2 (\text{aq}) + \text{propan-2-ol} \rightarrow \text{products}$
 (b) $\text{HOCl} (\text{aq}) + \text{propan-2-ol} \rightarrow \text{products}$

At pH 1 and room temperature, with the initial concentration of $[Cl_2 \text{ (aq)}]_0 = 1.5 \times 10^{-3} \text{ mol dm}^{-3}$, and $[propan-2-ol]_0 = 2.01 \times 10^{-2} \text{ mol dm}^{-3}$, the alcohol was oxidised with the initial rate law

$$-\frac{d[\text{oxidant}]}{dt} = k_{\text{obs}}[\text{oxidant}]$$

where oxidant refers to a combination of Cl_2 and HOCl. Addition of chloride ions ($> 10^{-2} \text{ mol dm}^{-3}$) accelerated the oxidation rate and a plot of $(k_{\text{obs}})^{-1}$ versus $[Cl^-]^{-1}$ was linear. On the basis of the above, suggest kinetic methods for distinguishing between the two possible mechanisms.

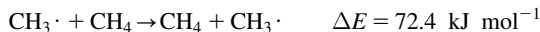
(Data: Venkatasubramanian and Srinivasan, *Indian J. Chem.* (1972) **10** 1085).

- 18.** In 1867 the Austrian chemist Leopold Pfaundler proposed that for reactions in the vapour phase at high temperatures only molecules that possess energy close to the dissociation limit could react. Using his ideas, it would appear that the internal energy of complexes, such as HDD in the reaction

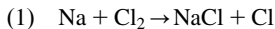


would be sufficient to keep the atoms bonded together for a certain period, even though it is close to the dissociation energy of D_2 , *ca.* 422 kJ mol^{-1} . However, 70 years later chemists found that the activation energy of the above reaction is much lower than this (close to 50 kJ mol^{-1}).

- (a) Explain why the reaction barriers of elementary chemical steps are actually considerably lower than the dissociation energies of the reactant molecules.
- (b) Interpret, in structural terms, the relative energy barriers for the two reactions:

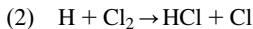


- 19.** In the 1930s Michael Polanyi studied the sodium–chlorine reaction in highly dilute flames:



The gases were mixed by diffusion and the product NaCl (which is a solid) was deposited on the walls of the vessel. An emission of sodium-*D* radiation was observed; such an emission requires an energy of 202 kJ mol^{-1} .

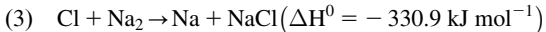
- (a) What can be the source of energy for the formation of electronically excited $Na^*(^2P)$ which leads to chemiluminescence?
- (b) In the 1950s his son, John Polanyi, studied another highly exothermic reaction



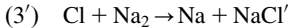
However, in this case, the emission was in the infrared region. How can one interpret such contrasting behaviours?

Relevant bond dissociation energies in kJ mol^{-1} : $\text{Na} - \text{Na} = 77$; $\text{Cl} - \text{Cl} = 242.7$; $\text{H} - \text{Cl} = 431.4$; $\text{Na} - \text{Cl} = 407.9$.

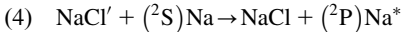
Polanyi concluded that another reaction must occur:



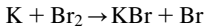
Although this energy release would be sufficient to produce $\text{Na}^*(^2\text{P})$, quenching experiments show that the energy released in reaction (3) does not pass into the sodium atom but produces vibrationally excited NaCl' ,



The vibrationally excited NaCl' molecule then transfers its energy to a sodium atom, which becomes electronically excited



- (c) The energy release in $\text{H} + \text{Cl}_2 \rightarrow \text{HCl}' + \text{Cl}$ ($\Delta H^0 = -188.7 \text{ kJ mol}^{-1}$) passes into the vibrational energy of the products, a large part going into translational and rotational energy since the potential energy surface [PES] is repulsive.
- 20.** (a) According to the hard-sphere collision theory, what is the frequency factor for the elementary reaction $\text{D} + \text{H}_2 \rightarrow \text{H}_2 + \text{H}$ at 300K, with a collision molecular diameter of 2.5 \AA ?
- (b) Relate the collision diameter of 1.0 \AA with the reaction cross section, σ , of an elementary reaction.
- (c) The collision theory was developed by Trautz and Lewis. In 1918 Lewis calculated a preexponential factor of $3.5 \times 10^{-7} \text{ dm}^3 \text{ mol}^{-1} \text{ s}^{-1}$ for the reaction $2\text{HI} \rightarrow \text{H}_2 + \text{I}_2$ at 556K in excellent agreement with the experimental value. However, this agreement was somewhat unfortunate, since it led to undue confidence in the theory and delayed the development of the subject for some years. Would that be the case if the calculation had been carried out for the reaction



- 21.** For a Maxwell–Boltzmann distribution show that the activation energy, E_a , of an elementary reaction can be related with the collision cross section, $\sigma(E)$, by the expression

$$E_a = \frac{\int_{E_0}^{\infty} \sigma(E) E^2 \exp\left[-\frac{E}{RT}\right] dE}{\int_{E_0}^{\infty} \sigma(E) E \exp\left[-\frac{E}{RT}\right] dE} - \frac{3}{2} RT$$

where E is the total energy of the molecular system and E_0 is the onset energy for a reactive collision ($\sigma(E) = 0$ for $E < E_0$)

- (a) What is the meaning of the two terms in the previous equation?
 (b) Show that for a collision cross section of the kind $\sigma = \sigma_0 \frac{\sqrt{(E - E_0)}}{E}$ the activation energy is almost independent of the energy.

- (c) Show that for a hard sphere model one has $\frac{E_a}{E_0} = 1 + \frac{RT}{2E_0}$. For values of $E_0 = 50 \text{ kJ mol}^{-1}$ discuss the experimental possibilities to investigate the change of E_a with temperature in the range 200–1000 K.
- 22.** The elementary reaction
- $$\text{H} + \text{Cl}_2 \rightarrow \text{HCl} + \text{Cl}$$
- has the following distribution of energies in the products: $f_{\text{vib}} = 39\%$, $f_{\text{rot}} = 7\%$ and $f_{\text{trans}} = 54\%$. Represent the most relevant features of the PES along the reaction valley.
- 23.** Estimate the equilibrium constant for the dissociation reaction in the vapour phase
- $$\text{Na}_2 \rightleftharpoons 2\text{Na}$$
- at 1000K. The relevant data to estimate the partition functions are: $B = 0.1546 \text{ cm}^{-1}$; $\bar{v} = 159.2 \text{ cm}^{-1}$; $D_0 = 70.4 \text{ kJ mol}^{-1}$. The ground state is a triplet electronic state.
- 24.** The reaction $2\text{HI} \rightarrow \text{H}_2 + \text{I}_2$ has a second-order rate constant that depends on temperature as follows:
- | $T \text{ (K)}$ | 556 | 629 | 647 | 700 | 716 | 781 |
|---|----------------------|-----------------------|-----------------------|-----------------------|-----------------------|-----------------------|
| $k_2 \text{ (dm}^3 \text{ mol}^{-1} \text{ s}^{-1}\text{)}$ | 3.5×10^{-7} | 3.02×10^{-6} | 8.59×10^{-5} | 1.16×10^{-3} | 1.16×10^{-3} | 3.95×10^{-2} |
- Calculate the enthalpy and the entropy of activation for the standard state 1 mol dm^{-3} .
- 25.** The thermal decomposition of F_2O in the vapour phase has an experimental rate law
- $$-\frac{d[\text{F}_2\text{O}]}{dt} = k_{\text{I}}[\text{F}_2\text{O}]^2 + k_{\text{II}}[\text{F}_2\text{O}]^{3/2}$$
- (a) Show that this law is consistent with the mechanism
- (i) $\text{F}_2\text{O} + \text{F}_2\text{O} \rightarrow \text{F} + \text{OF} + \text{F}_2\text{O}$
 - (ii) $\text{F} + \text{F}_2\text{O} \rightarrow \text{F}_2 + \text{OF}$
 - (iii) $\text{OF} + \text{OF} \rightarrow 2\text{F} + \text{O}_2$
 - (iv) $2\text{F} + \text{F}_2\text{O} \rightarrow \text{F}_2 + \text{F}_2\text{O}$
- (b) Derive the rate law for the disappearance of F_2O .
- (c) Under what reaction conditions is the decomposition of F_2O a reaction of order 3/2 in relation to this reagent?
- (d) Under the above conditions, how is the overall activation energy of the reaction related to those of the corresponding elementary processes?
- 26.** The decomposition of nitrogen pentoxide



is suggested to follow the mechanism:

- (a) $\text{N}_2\text{O}_5 \rightarrow \text{NO}_2 + \text{NO}_3$
 (b) $\text{NO}_2 + \text{NO}_3 \rightarrow \text{N}_2\text{O}_5$

- (c) $\text{NO}_2 + \text{NO}_3 \rightarrow \text{NO}_2 + \text{O}_2 + \text{NO}$
 (d) $\text{NO} + \text{N}_2\text{O}_5 \rightarrow 3\text{NO}_2$

Step (b) has activation energy close to zero, while step (c) is a reasonably endothermic process. Step (d) is also a fast process.

1. What is the rate-determining step?
2. What is the rate law?

27. For the isomerisation of bicyclooct-7-ene, the following kinetic data were obtained:

T (K)	508.7	517.1	521.5	529.1	535.5	551.8	558.1
$k (\times 10^{-4} \text{ s}^{-1})$	0.376	0.763	1.08	1.93	3.32	10.5	16.6

- (a) Calculate the activation energy for the reaction.
 (b) Calculate the preexponential factor (A) and comment on its value.
 (c) What is the rate constant for the reaction at 239°C?

28. The table below presents relevant data for the sigmatropic-shift reaction of hexa-1,5-diene, which is illustrative of pericyclic reactions. Substituents can cause changes in the reaction energy and/or in the bond order at the transition state, n^\ddagger . Select reaction series where linear free-energy relationships (LFER) can be established.

No.	Substituent	ΔG^\ddagger	ΔG^0	n^\ddagger
1	H	174.1	0	0.49
2	Allylvinyl ether	137.9	-71.1	0.40
3	2-Phenyl	148.4	0	0.524
4	2,5-Diphenyl	129.6	0	0.560
5	3,4-Dimethyl	163.0	-18	0.490
6	3,3-Dicyano	133.8	-18.8	0.534
7	3,4-Diphenyl	129.6	-18.8	0.542
8	3-Phenyl	150.0	-9.5	0.514

Energies in kJ mol^{-1} .

Data: Formosinho, Tetrahedron (1986) 42 4557–4562.

29. (a) In the quadratic equation of Marcus

$$\Delta G^\ddagger = \Delta G(0)^\ddagger \left(1 + \frac{\Delta G^0}{4\Delta G(0)^\ddagger} \right)^2$$

what is the meaning of the symbols ΔG^\ddagger , $\Delta G(0)^\ddagger$ and ΔG^0 ?

- (b) In a family of reactions under what conditions can this Marcus equation lead to an LFER?
 (c) Relate $\Delta G(0)^\ddagger$ to structural factors of force constants, f , bond lengths, l and bond-order at the transition state, n^\ddagger .

30. Use the quadratic equation of Marcus to verify the Reactivity–Selectivity Principle for a reaction with an intrinsic barrier of 10 kJ mol^{-1} .

Hint: estimate the corresponding values indicated in the following table for the energies ΔG^0 and selectivities S .

Reactant	Reactant	ΔG^0 (kJ mol $^{-1}$)	ΔG^\ddagger (kJ mol $^{-1}$)	S
A	X	-10		
	Y	-12		
B	X	10		
	Y	12		

31. The following first-order rate constants k_1 were obtained for the isomerisation of cyclopropane:

P (mmHg)	84.1	11.0	2.89	0.569	0.120	0.067
$10^4 k_1$ (s $^{-1}$)	2.98	2.23	1.54	0.857	0.392	0.303

Data: Pritchard et al., Proc. Roy. Soc. London A (1953) 217 563.

Use the data to verify the simple Lindemann equation.

32. The photodissociation of pure diazo-*n*-propane vapour ($\text{CH}_3\text{CH}_2\text{CHN}_2$) with a mercury lamp ($\lambda > 300$ nm) yields propylene (represented by S), resulting from collisional stabilisation



and products such as ethane and ethylene (represented by D) from the direct dissociation of the vibrationally hot nascent propylene Pr^*



The ratio of the decomposition products varies with pressure as follows:
What would be predicted if the Lindemann approach was verified?

[D]/[S]	0.344	0.182	0.123	0.0854	0.072	0.0452	0.033
P (kPa)	0.123	0.330	0.664	1.07	1.33	2.26	3.06

Data: Figuera et al., J. Phys. Chem. (1974) 78 1348.

33. A substance A_2 decomposes in the vapour phase



and presents the following values of concentration as function of time, at atmospheric pressure:

At constant pressure:

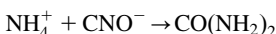
[A_2] (mol dm $^{-3}$)	1.00	0.67	0.47	0.37	0.24	0.16	0.10
t (min)	0	5	10	15	20	30	40

As can be seen, $\log[A_2]$ does not vary in a linear fashion with time. However, when the kinetics of the reaction are studied at a constant volume, the following data is obtained: at constant volume:

[A ₂] (mol dm ⁻³)	1.0	0.79	0.62	0.50	0.42	0.26	0.15
t (min)	0	5	10	15	20	30	40

In these experimental conditions, $\log[A_2]$ is a linear function of time, revealing that the reaction is a first-order process with $k = 0.046 \text{ min}^{-1}$. How can one interpret such findings?

34. The synthesis of urea



was studied at 30°C in mixtures of water/glycol. The rate constant of the reaction depends on the dielectric constant of the medium as follows:

$10^3 k (\text{dm}^3 \text{ mol}^{-1} \text{ min}^{-1})$	6.25	11.3	14.1	19.1	26.5	38.4
ε	76.7	63.5	60	55	50	45

- (a) Interpret the influence of the dielectric constant of the medium on the rates?
 (b) What would be the effect of ε if the reaction involved CO_2 rather than CNO^- ?

35. Predict the effects of

- (a) increasing ionic strength
 (b) increasing dielectric constant of the medium on the rates of the following reactions in aqueous solutions:

- (i) $[\text{Fe}(\text{H}_2\text{O})_6]^{3+} + [\text{Fe}(\text{CN})_6]^{4-} \rightarrow [\text{Fe}(\text{H}_2\text{O})_6]^{2+} + [\text{Fe}(\text{CN})_6]^{3-}$
- (ii) $\text{CH}_3\text{CH}(\text{OCH}_3)_2 + \text{H}_3\text{O}^+ \rightarrow \text{CH}_3\text{CHO} + 2\text{CH}_3\text{OH} + \text{H}^+$
- (iii) $[\text{Co}(\text{NH}_3)_5\text{Br}]^{2+} + \text{H}_2\text{O} \rightarrow [\text{Co}(\text{NH}_3)_5(\text{H}_2\text{O})]^{3+} + \text{Br}^-$
- (iv) $\text{SO}_3^{2-} + \text{ClO}^- \rightarrow \text{SO}_4^{2-} + \text{Cl}^-$

36. The diffusion coefficient for iodine atoms in carbon tetrachloride solution at 25°C is $D = 2 \times 10^{-9} \text{ m}^2 \text{ s}^{-1}$. Given that the atomic radius of iodine is 0.2 nm, calculate the maximum rate constant predicted for the recombination of iodine atoms under these conditions.

37. Radiolysis of water produces a reducing species, z, in addition to hydrogen atoms, hydroxyl radicals and various other species



The second-order rate constants for the reaction of z with Ag^+ ions in water show the following variation with ionic strength:

Ionic strength (mmol dm ⁻³)	0	0.625	3.60	10.4	16.3	29.8	38.5	44.6	56.2
$k (10^{10} \text{ dm}^3 \text{ mol}^{-1} \text{ s}^{-1})$	3.20	3.05	2.85	2.67	2.37	2.16	1.91	1.82	1.62

What is the charge of z? Also, suggest a structure for this species.

- 38.** The rate constant of the reaction between persulphate ion and iodide ion varies with ionic strength I as follows:

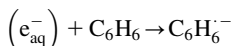
$I \times 10^3$ (mol dm $^{-3}$)	2.45	3.65	4.45	6.45	8.45	12.45
k (mol $^{-1}$ dm $^{-3}$ s $^{-1}$)	1.05	1.12	1.16	1.18	1.26	1.39

- (a) Estimate the product of the charge of the two ions, $Z_A Z_B$.
 (b) Given the kinetic data below for reaction of the muonium, Mu , with ions at 25°C, what is the electric charge of Mu ?

Reaction	k (10 8 mol dm $^{-1}$ dm 3 s $^{-1}$)	
	$I < 0.02$ mol dm $^{-3}$	$I = 0.9$ mol dm $^{-3}$
$Mu + Cu^{2+}$	65	63.5
$Mu + SCN^-$	0.62	0.74

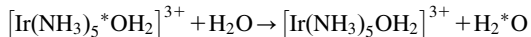
Data: Yean *et al.*, Hyperfine Interaction (1979) 6 409.

- 39.** In a study of the reactions of the hydrated electron (e_{aq}^-) at 298K, a half-life ($t_{1/2}$) in pure water of 1.2 ms was observed, while in the presence of benzene (5 mmol dm $^{-3}$), this was reduced to 9.9 μ s. Assuming that the concentration of benzene is much greater than that of the hydrated electron and that the decay in the presence of benzene is due to the bimolecular reaction



calculate the second-order rate constant for this reaction and show if this is diffusion controlled (viscosity of water is 0.890 mPa s).

- 40. (a)** Calculate the volume of activation ΔV^\ddagger of the reaction



studied at 60.5°C, using data on the variation of the rate constant k as a function of the hydrostatic pressure P given below:

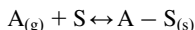
P (kPa)	1	59	1027	2020	3310
$10^5 k$ (dm 3 mol $^{-1}$ s $^{-1}$)	2.82	4.01	4.56	4.59	5.80

*Labelling with ^{18}O .

Data: Tong and Swaddle, Inorg. Chem. (1974) 13 1538.

- (b)** Interpret in terms of structural changes and solvent effects the observed effect of P on the rates.

- 41.** A reaction catalysed on a metal surface



shows the following data for the volume of the gas adsorbed as a function of pressure at 298K:

P (Pa)	25.3	129.3	253.3	540
V (cm^3)	0.042	0.163	0.221	0.321

- (a) Is the data consistent with a Langmuir adsorption isotherm?
- (b) What is the volume adsorbed, V_∞ when all the active sites are occupied?

42. The adsorption of CO on platinum



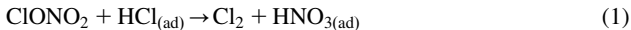
has a rate, v_d , given by the expression

$$v_d = \frac{d \Gamma_{\text{CO}_{\text{ads}}}}{dt} = \frac{k_B T}{h} \frac{q_\ddagger}{q_0(\text{CO}_{\text{ads}})} \Gamma_{\text{CO}_{\text{ads}}} \exp\left(-\frac{E_a}{RT}\right)$$

- (a) At 600K, $v_d = 0.0012 \text{ mol m}^{-2} \text{ s}^{-1}$, $\sigma = 0.5$, $E_a = 134 \text{ kJ mol}^{-1}$ and $N_s = 10^{19} \text{ m}^{-2}$. What can be said about the ratio of the partition functions q_\ddagger and $q_0(\text{CO}_{\text{ads}})$ for the activated complexes for CO desorption and adsorbed CO, respectively?

- (b) Explain the meaning of the symbols employed above.

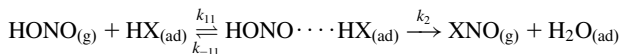
43. In the atmosphere, the halogen reservoir compound, ClONO₂ is converted to Cl₂ on polar stratospheric cloud surfaces by heterogeneous reactions. This leads to the destruction of polar ozone through reactions on ice surfaces such as



Reaction (1) is the most important heterogeneous reaction to convert photochemically inert ClONO₂ and HCl into photochemical active chlorine.

As with reaction (1), reaction with HONO on the ice surface is a nucleophilic reaction.

A possible mechanism for the reaction is the following:



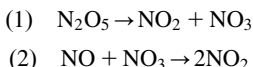
- (a) write the rate of reaction $\xi = -d[\text{HONO}]/dt$ in terms of the pressure of HONO, P_{HONO} .
- (b) If one defines the reaction probability, $\gamma = \xi/\phi$, where ϕ_{HONO} is the flux of HONO impinging on the HX-treated ice surface, show that $\gamma = \xi \sqrt{(2\pi m k_B T)/P_{\text{HONO}}}$; m_w is the molecular weight of HONO.

- 44.** Nitrogen is adsorbed on activated charcoal. The adsorbed volumes per gram of charcoal as function of the gas pressure at 196K are as shown:

$P(N_2)$ (atm)	3.5	10.0	16.7	25.7	33.5	39.2
$V(N_2)$ (mL g ⁻¹)	101	136	153	162	165	166

Verify that the data follow a Langmuir isotherm.

- 45.** The reaction $\text{NO} + \text{N}_2\text{O}_5 \rightarrow 3\text{NO}_2$ is suggested to follow the mechanism:



- (a) What is $[\text{NO}_3]$ under steady-state conditions?
 (b) What are the rate laws for the disappearance of nitrogen pentoxide and for the formation of nitrogen dioxide?

- 46.** Peroxynitric acid (HO_2NO_2 , PNA) plays an important role in atmospheric chemistry as a gas-phase reservoir for NO_x (NO and NO_2) and HO_x in the stratosphere as well as the troposphere. The lifetime of PNA at the middle latitudes in the upper troposphere and lower stratosphere is in the range of 10–12 h. However, at the higher temperatures found in the lower troposphere and even in the middle of the upper stratosphere, HO_2NO_2 degradation can be dominated by thermal decomposition (reaction –1)

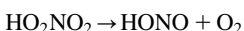


The standard enthalpy of reaction is $\Delta_f H_{298\text{K}}^0 = -100.4 \pm 2.1 \text{ kJ mol}^{-1}$. The rate coefficients vary with temperature as indicated in the following table.

T (K)	$k_{-1} (\text{s}^{-1})$
331.3	0.21
334.4	0.37
341.6	1.06
342.4	1.87
343.2	1.1
347.3	1.47
349.9	3.18

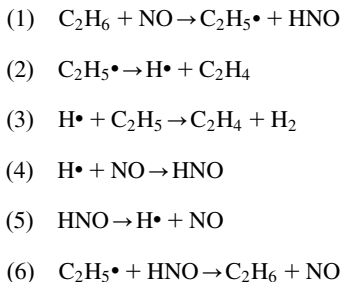
Data: T Gierczak et al., J. Phys. Chem. A (2005) 109 586–596.

- (a) Is the Arrhenius equation verified?
 (b) PNA can also thermally dissociate to give

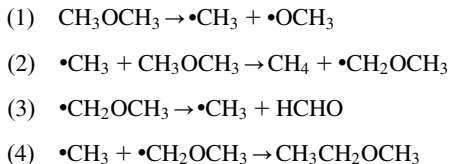


This reaction which is exothermic, $\Delta_f H_{298\text{K}}^0 = -26.8 \text{ kJ mol}^{-1}$, is believed not to compete with the thermal decomposition of PNA to yield only NO_2 and HO_2 [reaction (–1)]. Why?

- 47.** The decomposition of ethane into ethene and hydrogen in the presence of nitrous oxide is suggested to follow the mechanism:

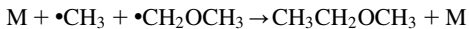


- (a) What is the role of NO?
 (b) Assuming that a fast equilibrium is established between the pairs of reaction steps 1 and 6 (K_1) and 4 and 5 (K_2), write the rate law for the decomposition.
- 48.** The decomposition of dimethylether follows the mechanism

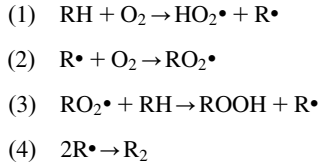


Radicals are indicated by the symbol (\bullet).

- (a) Establish the rate law of this decomposition.
 (b) What is the order of the reaction if the termination step is



- 49.** The oxidation of a hydrocarbon RH can occur via the following chain reaction mechanism:



- (a) Predict the order of the reaction.
 (b) Relate the activation energy, E_a , of the oxidation with that of the individual steps.
- 50.** The termolecular reactions for removal of oxygen atoms in the presence of an inert gas



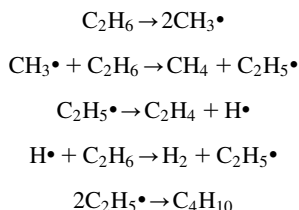
have the following rates k_3 for the cases M = Ar and M = CO₂.

	T (K)	213	298	335	386
Ar	$10^{-8}k_3 \text{ (dm}^6 \text{ mol}^{-2} \text{ s}^{-1}\text{)}$	5.39	1.86	1.38	1.01
CO ₂	$10^{-8}k_3 \text{ (dm}^6 \text{ mol}^{-2} \text{ s}^{-1}\text{)}$	34.9	12.0	8.96	6.55

Data: Mulcahy and Williams, Trans. Faraday Soc. (1968) 64 59.

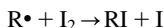
Show that the k_3 values conform to the Arrhenius equation, with negative activation energy values.

51. By applying the steady-state hypothesis to the species CH₃ and C₂H₅ show that a mechanism:



would lead to an overall rate law of one-half order.

52. In free radical polymerisation reactions, iodine, I₂, can destroy the active centres because it reacts with radicals as follows:



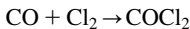
and the iodine atoms produced in these reactions do not initiate further polymerisations. Thus iodine inhibits polymerisation by acting as a radical scavenger. Propose an explanation for such behaviour.

53. The polymerisation of styrene in toluene, with benzoyl peroxide acting as a catalyst, shows the following initial rates of reaction as a function of the concentration of the monomer at 25°C:

[Styrene] (mol dm ⁻³)	0.86	2.59	4.33	6.04	7.78
v_0 (mol dm ⁻³ h ⁻¹)	3.5	15.5	31.0	47.0	64.0

What is the order of the reaction?

54. Propose a mechanism for the reaction



with an experimental rate law

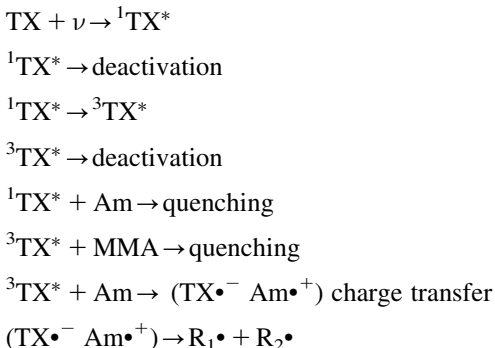
$$v = k[\text{Cl}_2]^{3/2}[\text{CO}]$$

Hint: consider that one is leading with a stoichiometric rate law.

- 55.** Photopolymerisation of methyl methacrylate (MMA) can be photoinitiated by thioxanthone (TX). The polymerisation rate, R_p , can be expressed by the equation

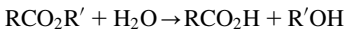
$$R_p = \frac{k_p}{\sqrt{k_t}} \sqrt{\phi_i} \sqrt{I_a} [M]$$

- (a) Propose a simple mechanism that accounts for such a rate expression.
- (b) Photopolymerisation can be initiated by TX in the presence of an amine (Am), but does not occur in the absence of amine. Interpret these findings.
- (c) A possible mechanism for photoinitiation is the following:



Radicals $\text{R}_1\cdot$ and $\text{R}_2\cdot$ can initiate polymerisation. The absence of photopolymerisation in the absence of amine indicates that the interaction of TX triplets with the monomer does not lead to polymerisation).

- 56.** The hydrolysis of an ester, $\text{RCO}_2\text{R}'(5 \times 10^{-5} \text{ mol dm}^{-3})$, in 9.5% ethanol–water at pH 12.50 and at 30°C was followed spectrophotometrically by observing the formation of the product $\text{R}'\text{OH}$. Absorbance values for the product at its maximum are given below at various times after the start of the reaction.



Time t (h)	0	2	5	9	26	48	81	144	$t = \infty$
Absorbance	0.022	0.038	0.064	0.098	0.233	0.348	0.424	0.462	0.472

- (a) Assuming pseudo-first-order kinetics, calculate the rate constant for this reaction.
- (b) The pseudo-first-order rate constants for this reaction at the same temperature at various pH values are

pH	12.67	12.80	12.90	13.71
$k (10^{-5} \text{ s}^{-1})$	1.42	4.35	5.53	40.8

What is the overall rate law for the hydrolysis and the specific rate constant?

- 57.** The mutarotation of glucose in water follows first-order kinetics, but the reaction is catalysed by acids.
(a) Calculate the rate constants for the catalysed and the noncatalysed reaction for the experimental data in aqueous solutions of HClO_4 .

[Acid] (mol dm ⁻³)	$k_{\text{obs}} (10^{-3} \text{ min}^{-1})$
10^{-4}	5.4
0.0048	6.0
0.0247	8.92
0.0325	10.02

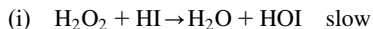
- (b)** Predict the effect of using a carbon acid on the catalysed rate constant k_{cat} .
58. Under certain experimental conditions the rate law of the reaction



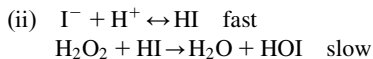
is

$$\frac{d[\text{I}_3^-]}{dt} = k[\text{H}_2\text{O}_2][\text{I}^-][\text{H}^+]$$

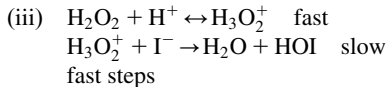
- (a)** Verify whether any of the following mechanisms interprets the experimental rate law:



followed by fast steps



followed by fast steps slow



- (b)** Propose possible steps that follow the rate-determining step in mechanism (i).
(c) Propose structures for the activated complexes in the rate-determining steps of the proposed mechanisms.

- 59.** The reaction of formation of monoiodoacetone in aqueous solution



has a rate law

$$-\frac{d[\text{I}_2]}{dt} = k[\text{CH}_3\text{COCH}_3][\text{H}^+]$$

that is zero order in iodine. Propose a mechanism for the reaction.

- 60.** The iodation of acetone is catalysed by acids. The catalytic rate constant, k_{cat} , has the following values according to the nature of the acid HA (K_a , acid dissociation constant):

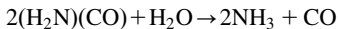
Acid catalyst	K_a	$k_{\text{cat}} (10^6 \text{ mol}^{-1} \text{ dm}^3 \text{ s}^{-1})$
Dichloroacetic	5.7×10^{-2}	220
Monochloroacetic	1.4×10^{-3}	34
Glycolic	1.54×10^{-4}	8.4
Acetic	1.8×10^{-5}	2.4
Trimethylacetic	9.1×10^{-6}	1.9

- (a) Are we dealing with a general or a specific acid–base catalysis?
 (b) Calculate the Brönsted coefficient.
61. The initial rate of hydrolysis of adenosine triphosphate catalysed by myosin at constant enzyme concentration, varies as shown:

$r_0 (\text{mmol dm}^{-3} \text{ s}^{-1})$	0.080	0.114	0.154	0.174	0.189
$[S_0] (\text{mmol dm}^{-3})$	0.01	0.02	0.05	0.1	0.25

Calculate the Michaelis constant and $r_{0,\text{max}}$.

- 62.** The hydrolysis of urea is catalysed by the enzyme urease



The dependence of the rate on the substrate concentration is given in the following table:

$v (\text{mol dm}^{-3} \text{ s}^{-1})$	0.120	0.226	0.362	0.600	0.846
$[\text{urea}] (\times 10^3 \text{ mol dm}^{-3})$	0.32	0.65	1.29	3.27	8.30

- (a) Derive the Michaelis–Menten equation.
 (b) Show whether the hydrolysis of urea obeys this equation, and if so determine the appropriate kinetic parameters.
63. Benzene absorbs ultraviolet light at $\lambda = 258 \text{ nm}$. With normal irradiation sources a molecule is excited by a single photon. Under such conditions can one carry out the reaction $\text{C}_6\text{H}_6 \xrightarrow{h\nu} \text{C}_6\text{H}_5 + \text{H}$, $\Delta H_r = 468 \text{ kJ mol}^{-1}$?
 On photoirradiation with high-intensity lasers, each molecule can absorb two or more photons at the same time. For biphotonic absorptions what is the absorption wavelength required to produce the dissociation of benzene?
64. Planck radiation formula Eq. (16.7) gives the distribution of energy per unit volume per unit frequency. The same formula for the distribution of energy per unit volume per wavelength is

$$I(\lambda) = \frac{8\pi hc}{\lambda^5} \frac{1}{e^{hc/\lambda k_B T} - 1}$$

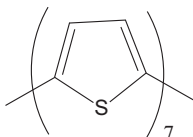
- (a) From this expression obtain Wien's displacement law for the change in the wavelength of maximum black-body irradiance with temperature, making $\partial I(\lambda)/\partial \lambda = 0$ and $\exp(hc/\lambda k_B T) - 1 \approx \exp(hc/\lambda k_B T)$.
- (b) Obtain the Stefan–Boltzmann law for the total power per unit area from a black-body radiator, using the radiated power per unit area as a function of wavelength

$$\frac{dP}{d\lambda A} = \frac{2\pi hc^2}{\lambda^5} \frac{1}{e^{hc/\lambda k_B T} - 1}$$

that differs from the expression above by the factor $c/4$ which involves an integration over all angles. The integration from $\lambda = 0$ to $\lambda = \infty$ is conveniently made with the substitutions $x = hc/\lambda k_B T$ and $dx = -hc/\lambda^2 k_B T d\lambda$, and using the standard form integral

$$\int_0^\infty \frac{x^3}{(e^x - 1)} dx = \frac{\pi^4}{15}$$

- (c) The amount of incoming solar radiation on the outer surface of Earth's atmosphere, the solar constant, can be calculated from Stefan–Boltzmann law, knowing that the surface temperature of the Sun is 6000K and that the irradiance from a sphere of radius R is proportional to R^{-2} . Calculate the solar constant using the radius of the Sun = 6.5×10^5 km and the average Earth–Sun distance = 1.5×10^8 km.
- (d) The Earth intercepts radiation passing through a disc of area πR_E^2 . Calculate the absorbed solar radiation taking as the fraction of incident radiation that is reflected back into space, called the albedo, $\alpha = 0.31$ and $R_E = 6370$ km.
- (e) Consider the equilibrium between the absorbed solar radiation, calculated above, and the emitted terrestrial radiation, given by $4\pi R_E^2 \sigma T_E^4$ and calculate the radiative equilibrium temperature of the Earth, T_E .
- (f) The Earth's surface temperature is 300K. Calculate the wavelength of its maximum irradiance, and the wavelength of the maximum absorbance of the Sun.
- (g) Provide an explanation for the difference between the radiative equilibrium temperature of the Earth and its surface temperature.
65. Oligothiophenes are conjugated polymers that have been investigated as materials for molecular electronics, including organic light-emitting diode displays (Seixas de Melo *et al.*, *J. Chem. Phys.* 2001 **115** 5625).
- (a) Use the Strickler–Berg equation to calculate the radiative rate of decay of the excited singlet state of



in dioxane ($n_D = 1.422$), knowing that $\langle \bar{v}^{-3} \rangle^{-1} = 5.59 \times 10^{12} \text{ cm}^{-3}$ and $\int \varepsilon(\bar{v}) \bar{v}^{-1} d\bar{v} = 1.19 \times 10^4 \text{ M}^{-1} \text{ cm}^{-1}$.

- (b) Compare the calculated value with the experimental radiative rate knowing that the observed lifetime and fluorescence quantum yield are 0.85 ns and 0.336, respectively.
- (c) How does the radiative rate of the singlet state change when the molar absorption coefficient increases?
66. Ruthenium (II) polypyridyl complexes have been extensively employed in solar cells. Their decadic molar extinction coefficients ε are *ca.* $104 \text{ M}^{-1} \text{ cm}^{-1}$ in the visible range.
- (a) Calculate the corresponding light capture cross sections in square nanometre.
- (b) The radius of Ru(bpy)_3^{2+} is 0.68 nm. Using the area occupied by this dye on the surface of an electrode, calculate the percentage of the incident light with a wavelength matching the maximum absorption of Ru(bpy)_3^{2+} that is absorbed.
- (c) Although it is tempting to overlay multilayers of the dye on the electrode to increase its light absorption, this is generally a mistaken tactic because the energy transfer between sensitiser molecules is rarely efficient and the outer dye layers act only as a light filter. Alternatively, using nanocrystalline particles with diameters of 10–20 nm, it is possible to reach dye surface concentrations of $\Gamma = 3 \times 10^{16} \text{ cm}^{-2}$. Calculate the percentage of the incident light absorbed by a film with this concentration of Ru(bpy)_3^{2+} , knowing that the absorbance is given by $A = \Gamma \sigma$ (Grätzel and Moser, *Electron Transfer in Chemistry*, (Ed.) I. Gould, vol. 5 (2001), Wiley-VCH, p. 587).
67. Iodide ions quench the fluorescence of anthracene (A) in aqueous solutions in the scheme



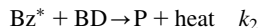
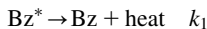
- (a) Derive an equation relating the fluorescence intensities in the presence (I) and absence (I^0) of iodide to $[\text{I}^-]$.
- (b) Given the following experimental results for the quenching of anthracene fluorescence by iodide ion:

$[\text{I}^-] (\text{mol dm}^{-3})$	0	0.001	0.003	0.005	0.010
Relative fluorescence intensity	100	94.8	86.1	78.8	64.8

and the experimental fluorescence lifetime of anthracene in water ($\tau = 1/(k_f + k_{nr}) = 4.9 \text{ ns}$), calculate k_q .

- (c) Is the quenching diffusion controlled?

- 68.** The resin matrix of dental materials has important influence on the chemical and physical properties of light cure resins. The organic formulations also include photoinitiating systems that absorb light. From there free radicals start the conversion of the oligomer blend to a polymeric cross-linked network. Camphorquinone (CQ) is widely used in dental resin mixed with an amine. However, CQ is a solid, yellow compound with an unbleachable chromophore.
- (a) How can one reduce the amount of CQ to be used in the resin formulations?
- (b) Assuming that the potential of photoactivation to initiate the polymerisation reaction is proportional to the number of photons available at each wavelength, what are the two main factors that will influence photopolymerisation efficiency?
- (c) For dentistry it seems very desirable to have some parameter that takes into account the spectral properties of the photoinitiators as well as the spectral output of the dental light curing units (LCUs). Such a parameter has been defined by Miguel Neumann and co-workers in terms of photon absorption efficiency (PAE). Other authors have defined such a parameter in terms of energy. What kind of parameter should one employ?
- (d) **Table 7A** presents the normalised PAE for four dental photoinitiators irradiated with different light sources and **Table 7B** presents the properties of the photoinitiators and the concentrations employed. Why is phenylpropanedione (PPD) the most efficient initiator? Why is it that for all initiators the light emission device UBIS is always better than UBI? The initiator lucirin is very inefficient with LED, why?
- 69.** Benzophenone in an electronically excited state, Bz^* , in a solution of benzhydrol, BD, is quenched at room temperature according to the following kinetic scheme:



P is a product of the reaction.

Table 7A PAEs of dental photoinitiators and light curing units.

Photoinitiators	Quartz–tungsten lamp Optilux ($\lambda_{\max} = 493 \text{ nm}$)	LED ultrablue I (UBI) ($\lambda_{\max} = 467 \text{ nm}$)	LED ultrablue IS (UBIS) ($\lambda_{\max} = 454 \text{ nm}$)
CQ	2.7	4.4	4.5
PPD	10.9	7.8	11.3
Irgacure 819	2.6	0.8	0.9
LucirinTPO	2.7	0.2	0.3

CQ, camphorquinone; PPD, phenylpropanedione.

Table 7B Properties and experimental conditions of the photoinitiators.

Photoinitiators	λ_{\max} (nm)	ϵ_{\max} (L mol ⁻¹ cm)	Concentration (wt.%)
CQ	470	28	0.15
PPD	398	150	0.039
Irgacure 819	370	300	0.046
LucirinTPO	381	520	0.037

CQ, camphorquinone; PPD, phenylpropanedione.

Data: Neumann *et al.*, J. Dentistry 33 (2005) 525–532.

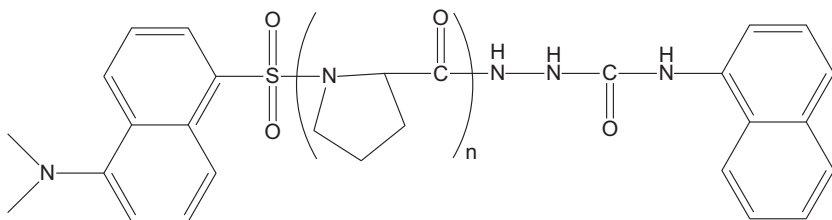
- (a) For the set of conditions $[BD] > [{}^*Bz]$ show how $[Bz^*]$ and $[P]$ vary with time.
- (b) Determine the quantum yield of product formation, ϕ_P , with $k_1 = 2.6 \times 10^5$ s⁻¹ and $k_2 = 5.0 \times 10^6$ M⁻¹ s⁻¹ when $[BD] = 10^{-2}$ M.
70. Aminoaromatic carbonyl compounds, such as Michler's ketone (MK) (4,4'-bis(*N,N*-dimethylamino)benzophenone), are ideally suited as photoinitiators since they have large extinction coefficients, charge-transfer states and relatively long triplet lifetimes in solution. MK derivatives are also unique in that they can photoproduce two different types of free-radical intermediates R_1^\bullet and R_2^\bullet .

The experimentally determined order of reaction with respect to photoinitiator concentration dependence, monomer and light intensity for the photopolymerisation of MMA deviate from normal photopolymerisation kinetics. McGinniss *et al.* (McGinniss *et al.*, *Macromolecules* 1978 11 393) reported a rate for photopolymerisation of MMA photoinitiated by 4,4'-bis(diethylamino)benzophenone (DEABP), measured by the rate of conversion of MMA to polymer (PMMA),

$$R_p = k I_a^{0.3-0.5} [\text{DEABP}]^{0.2-0.4} [\text{MMA}]^{1.2-1.3}$$

Propose mechanistic interpretations for the above observations of low order for the initiator, higher order for the monomer and lower order for light intensity.

71. Electronic excitation energy transfer following the Förster mechanism can be used as a spectroscopic ruler. Verify the prediction of the R^6 donor–acceptor distance dependence using the oligomers of poly-L-proline substituted with an α -naphthyl group as the energy donor and a dansyl group as the energy acceptor knowing the transfer efficiencies E



R (Å)	21	25	27	30	33	36	40	42	46
E	0.97	0.83	0.72	0.62	0.50	0.40	0.28	0.26	0.13

Data: Stryer and Haugland, PNAS (1967) 58 719.

72. Using the harmonic approximation calculate the Franck–Condon factor $J_{0,v''}$, with $v'' = 0–19$, for the $A^3\Sigma_u^+$ to $X^1\Sigma_g^+$ transition in Br_2 , knowing that for the excited state $R_e = 2.695 \text{ \AA}$ and $\bar{v} = 153 \text{ cm}^{-1}$, whereas for the ground state $R_e = 2.281 \text{ \AA}$ and $\bar{v} = 325.32 \text{ cm}^{-1}$.
(Data: Coxon, *J. Mol. Spectrosc.* (1971) **41** 566).
73. The electron self-exchange reaction for $[\text{Co}(\text{OH}_2)_6]^{3+/2+}$ in water has an experimental rate constant for electron transfer $k_{\text{exp}} = 2.4 \text{ M}^{-1} \text{ s}^{-1}$. There is a low-lying electronic state that bypasses the spin-forbidden character of the reaction from the ground state, and the electron transfer can be considered adiabatic. The relevant structural data for the reaction is as follows:

Complex	Electronic configuration	Force constant (kJ mol ⁻¹ Å ⁻²)		Bond lengths (Å)	
		f_{red}	f_{ox}	I_{red}	I_{ox}
$[\text{Co}(\text{OH}_2)_6]^{3+/2+}$	$(\pi)^5(\sigma^*)^2/(\pi)^6$	9.6×10^2	1.53×10^3	2.081	1.873

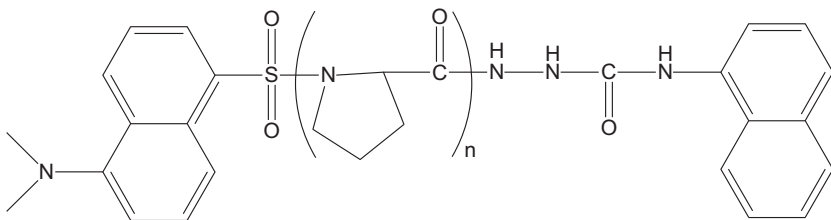
Estimate the rate constant for the reaction at 298 K:

- (a) Using Marcus Theory with the radius of each reactant $r_{\text{av}} = 6.5 \text{ \AA}$ and the collision frequency factor $Z = 10^{11} \text{ M}^{-1} \text{ s}^{-1}$.
- (b) Using ISM with a reaction frequency of $K_c \nu_N = 10^{13} \text{ s}^{-1}$.
74. The experimental rate of electron transfer for the reaction of the iron-cyclopentadienyl complex has been measured through NMR line broadening as described in Section 3.2.2. The rate constant at 298 K in acetone is $k_{\text{exp}} = 8 \times 10^6 \text{ M}^{-1} \text{ s}^{-1}$ at an ionic strength 0.15 M.
- (a) From the structural data listed in Table 16.2 estimate the energy barrier, ΔG^\ddagger , assuming a coordination number for iron of 2; the bond lengths listed are the distance from the Fe atom to the centre of the cyclopentadienyl ring.
- (b) Calculate the theoretical rate constant for a typical value of $\nu_N = 10^{13} \text{ s}^{-1}$.

- 75.** The paramagnetic encounter complex between tetracyanoethylene acceptor (TCNE) and its radical anion ($\text{TCNE}^{\cdot-}$) has a donor–acceptor separation of 2.9 \AA . The complex $(\text{TCNE})_2^{\cdot-}$ has an inter-valence absorption band with an absorption maximum at 1515 nm in dichloromethane. Calculate its electronic coupling matrix element knowing that, in this solvent, the extinction coefficient is $1.2 \times 10^3 \text{ M}^{-1} \text{ cm}^{-1}$ and that the full-width at half-maximum is $3 \times 10^3 \text{ cm}^{-1}$, assuming a Gaussian band shape.

(Data: Rosoka et al., *Chem. Phys.* (2006) **324** 117).

- 76.** In the first scanning transmission microscopy experiment, a logarithmic dependence of the tunnel current on tip-sample separation was found. Calculate the tunnelling decay coefficient of this distance dependence, knowing that the sample was in platinum and the tip was made of tungsten, and that their work functions are 5.03 and 4.55 eV , respectively.
- 77.** High-level ab initio calculations were employed to calculate the PES for electron transfer in bis(methylene) adamantyl radical cation



where the electron transfer is symmetrical, with the change in bond orders from 1.5 to 2 in one bond associated with the change from 2 to 1.5 in the other bond. Depending on the level of theory, the reorganisation energy was estimated to be 76 or 55 kJ mol^{-1} .

(Data: Blancafort et al., *J. Am. Chem. Soc.* (2005) **127** 3391).

Estimate the reorganisation energy for this electron transfer using the effective displacement of ISM and representing the double bond by the parameters of ethylene ($l_D = 1.342 \text{ \AA}$, $f_D = 5.77 \times 10^3 \text{ kJ mol}^{-1} \text{ \AA}^{-2}$) and the radical cation moiety by the parameters of benzene ($l_A = 1.397 \text{ \AA}$, $f_A = 3.87 \times 10^3 \text{ kJ mol}^{-1} \text{ \AA}^{-2}$).

Answers

1. (a) Zero order; (b) second order; (c) second order—the ratio between $t_{3/4}$ and $t_{1/2}$ is 3 times for a second-order reaction; 2 times for a first-order reaction; and 1.7 times for a one-half order reaction.
2. $v = k [A] [B]^2$; $k = 40 \text{ mol}^{-2} \text{ dm}^6 \text{ s}^{-1}$.
3. 15,700 years.

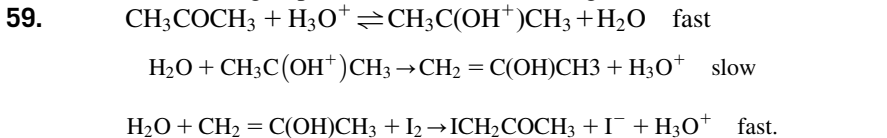
4. (a) $t_{1/2} = 0.78$ ns; (b) $t_{1/2} = 154$ ns.
5. (a) $v = k K[\text{NH}_4^+] [\text{CNO}^-]$; K is the equilibrium constant of the first step and k the rate constant of the slow process; (b) the addition of salt to water leads to complete dissociation into NH_4^+ and CNO^- .
6. Flash photolysis.
7. $k = 1.56 \times 10^{-3} \text{ s}^{-1}$; $t_{1/2} = 442$ s.
8. 580 s.
9. (a) Second-order $2\text{NcMe}\bullet \rightarrow$ products (a plot of 1/absorbance against time is linear); (b) the slope of the plot of 1/absorbance against time is $2k/\varepsilon_{400 \text{ nm}} l$. Using the above molar absorption coefficient and $l = 1$ cm gives $k = 1.2 \times 10^9 \text{ dm}^3 \text{ mol}^{-1} \text{ s}^{-1}$.
10. $k = 166.8 \text{ min}^{-1}$.
11. 2.7 kJ mol^{-1} .
12. (a) $\text{O} + \text{NO}_2 \rightarrow \text{NO} + \text{O}_2$; (b) $\{\text{NO}_2 \cdot \text{NO}_2\}^\ddagger$.
13. Mechanism III.
14. (a) $v = k [\text{IO}_3^-]^2 [\text{I}^-]^4$; $k = 7.2 \text{ dm}^{15} \text{ mol}^{-5} \text{ s}^{-1}$; (b) the experimental rate law demonstrates that the activated complex for the rate-determining step contains one iodate ion *plus* one iodide ion, *plus* an undefined number of protons because the reaction is carried out at constant pH, *plus* an undefined number of water molecules because the reaction takes place in aqueous solutions. Kinetic data seldom reveal what happens after the rate-determining step.
15. (a) $\{\text{ClOH}(\text{OH}_2)_n\}^\ddagger$; (b) one possible mechanism is
 - (i) $\text{OCl}^- + \text{H}_2\text{O} \rightleftharpoons \text{HOCl} + \text{OH}^-$ fast
 - (ii) $\text{HOCl} + \text{I}^- \rightarrow \text{ICl} + \text{OH}^-$ slow
 - (iii) $\text{ICl} + 2\text{OH}^- \rightarrow \text{OI}^- + \text{Cl}^- + \text{H}_2\text{O}$ fast
 while another possibility is:
 - (i) $\text{OCl}^- + \text{H}_2\text{O} \rightleftharpoons \text{HOCl} + \text{OH}^-$ fast
 - (ii) $\text{I}^- + \text{HOCl} \rightarrow \text{HOI} + \text{Cl}^-$ slow
 - (iii) $\text{OH}^- + \text{HOI} \rightleftharpoons \text{H}_2\text{O} + \text{OI}^-$ fast.
16. (a) $(d[[\text{Cr}(\text{H}_2\text{O})_5\text{NCS}]^{2+}]/dt) = k_1 k_2 [[\text{NCS}^-][\text{Cr}(\text{H}_2\text{O})_6]^{3+}]/(k_{-1} + k_2[\text{NCS}^-])$;
 (b) $[\text{NCS}^-] \gg (k_{-1}/k_2)$.
17. For the first mechanism where Cl_2 (aq) is the coreactant with the alcohol: $(k_{\text{obs}})^{-1} = \{k_1[\text{Cl}_2(\text{aq})]_0 + K/(k_1[\text{Cl}_2(\text{aq})]_0 [\text{H}^+])\} (1/[\text{Cl}^-])$; when HOCl (aq) is the coreactant with the alcohol a plot of $(k_{\text{obs}})^{-1}$ should be linear with $[\text{Cl}^-]$.
18. (b) The length of the CH bond is greater than that of the HH bond.
19. (a) The reaction $\text{Na} + \text{Cl}_2 \rightarrow \text{NaCl} + \text{Cl}$ ($\Delta H^0 = -165.2 \text{ kJ mol}^{-1}$) does not release enough energy to form the electronically excited Na^* .
20. (a) $7.8 \times 10^{-5} \text{ m}^3 \text{ mol}^{-1} \text{ s}^{-1}$; (b) $\sigma = 3.1 \text{ \AA}^2$; (c) the calculation would underestimate considerably the experimental value, since this a harpoon reaction.
21. The first term represents the average energy of molecules undergoing reaction and the second term represents the average energy of colliding molecules.

- 22.** This corresponds to a repulsive or late downhill surface.
- 23.** $V = 8.2 \times 10^{-2} \text{ m}^3 \text{ mol}^{-1}$; some of the partition functions are:
 $q_{\text{Na}}^{\text{el}} = 2$; $q_{\text{Na}^2}^{\text{rot}} = 2246$; $q_{\text{Na}^2}^{\text{vib}} = 4.88$; $K = 2.42$.
- 24.** $\Delta H^\ddagger = 181 \text{ kJ mol}^{-1}$; $\Delta S^\ddagger = -48 \text{ J K}^{-1} \text{ mol}^{-1}$.
- 25.** (a) $-d[F_2O]/dt = 2k_1 [F_2O]^2 + k_2 [F] [F_2O]$; the steady state for F leads to the following relations for the rates of the elementary step:
 $0 = R_1 - R_2 + 2R_3 - 2R_4$ and for OF is $0 = R_2 - 2R_3$. Then, we obtain $[F] = (k_1[F_2O]/k_4)^{1/2}$ and $k_1 = 2k_1$ and $k_{\text{II}} = k_2(k_1/k_4)^{3/2}$.
- 26.** (a) Step 3; (b) $v = k_3(k_1/(k_2 + k_3)) [\text{N}_2\text{O}_5] \approx (k_3k_1/k_2) [\text{N}_2\text{O}_5]$.
- 27.** (a) $E_a = 180 \text{ kJ mol}^{-1}$; (b) $A = 14.1$; (c) $5.5 \times 10^{-5} \text{ s}^{-1}$.
- 28.** Substituents 1, 3 and 4 have a zero reaction energy and the series of substituents 5, 6 and 7 have $\Delta G^0 \approx -18.5 \text{ kJ mol}^{-1}$. In each of these series one verifies an LFER between ΔG^\ddagger and ΔG^0 .
- 29.** $\Delta G(0)^\ddagger$ is constant throughout the family; (b) for harmonic oscillators $\Delta G(0)^\ddagger = (1/8)f [(0.108)/n^\ddagger] (2I)^2$.
- 30.** The ratio of the exothermic, and faster, rates at room temperature is 0.75, whereas that of the endothermic, and slower, reactions is 0.59. The slower rates are more different and, consequently, more selective.
- 31.** $1/k^1$ versus $1/P$ is not linear.
- 32.** For the Lindemann approach the rates k_S and k_D would be independent of energy. In terms of ideal gas law one would have $[D]/[S] k_D/k_S[M] = RTk_D/k_S P$ and one should expect a linear relation of $[D]/[S]$ versus P^{-1} . This is not verified; the plot has a pronounced downward curvature. The rate of decomposition should increase with an increase in the vibrational energy.
- 33.** In terms of the general definition of the rate, v , as a function of the amount of the reactant, $dn_{A2} = V d[A_2] + [A_2]dV$, where V is the volume, one has $v = d[A_2]/dt + [A_2]/V dV/dt$. This becomes the usual rate expression when the volume remains constant. At constant pressure the volume increases with time, since the total number of molecules is $(1 - x)n_{A2} + 2xn_{A2}$, where x is the fraction of decomposition.
- 34.** (a) $\log k$ varies linearly with the reciprocal of ε . The slope is positive because the ions in the rate-determining step have electric charges of opposite signs; (b) the rates would be independent of ε .
- 35.** With increases in both ionic strength and dielectric constant the rate of reaction (i) decreases while that of reaction (iv) increases while reactions (ii) and (iii), in principle, are unaffected.
- 36.** $3.0 \times 10^6 \text{ m}^3 \text{ mol}^{-1} \text{ s}^{-1} = 3.0 \times 10^9 \text{ dm}^3 \text{ mol}^{-1} \text{ s}^{-1}$.
- 37.** -1 ; the species is the hydrated electron.
- 38.** (a) $Z_A Z_B \approx 2$; (b) muonium is electrically neutral.
- 39.** $1.4 \times 10^7 \text{ dm}^3 \text{ mol}^{-1} \text{ s}^{-1}$; from the viscosity of water, assuming that benzene and the hydrated electron have comparable sizes the diffusion-controlled rate constant is $7.4 \times 10^9 \text{ dm}^3 \text{ mol}^{-1} \text{ s}^{-1}$, so the rate is considerably lower than diffusion control.
- 40.** $\Delta V^\ddagger = -4.8 \text{ cm}^3 \text{ mol}^{-1}$; (b) with the approach of the ions of the same charge sign, there is an intensification of the electric field, leading to an

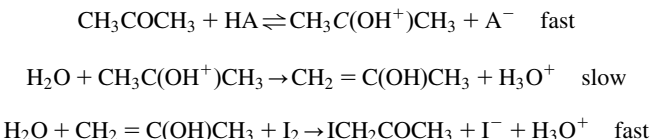
increase in electrostriction and a resulting decrease in volume. These effects tend, in general, to be more important than the volume changes owing to the change in the volume of the reactant molecules themselves as they pass into the activated complex. In the present case the structural effects dominate since one of the species is neutral.

41. The adsorption follows a Langmuir isotherm because $1/V$ is a linear function of $1/P$; (b) $V_\infty = 0.475 \text{ cm}^3$.
42. (a) The ratio $q_\ddagger/q_0(\text{CO}_{\text{ads}}) = 53.6$. Usually $q_\ddagger/q_0 > 1$ is interpreted in terms of a mobile activated complex. (b) σ is the fraction of occupied sites; N_s is the number of sites per square metre on the platinum surface; E_a is the energy barrier for desorption; Γ_{COads} is the concentration of the adsorbed CO per unit area, $\Gamma_{\text{COads}} = \sigma N_s/L = 0.5 \times 10^{19}/L = 8.3 \times 10^{-6} \text{ mol m}^{-2}$, where L is the Avogadro constant. The partition function q_\ddagger differs from q^\ddagger by $k_B T/h$.
43. (a) Rate $\xi = k P_{\text{HONO}}[\text{HX}_{(\text{ad})}]$ with $k = k_{11} k_2/(k_{11} + k_2)$; (b) this is an application of the Hertz–Knudsen equation.
44. The surface coverage “Greek letter theta” is proportional to the adsorbed volume V , and $1/V$ is directly proportional to $1/P$.
45. (a) $[\text{NO}_3]_{\text{st}} = (k_1/k_2) ([\text{N}_2\text{O}_5]/[\text{NO}])$; (b) $(-\text{d}[\text{N}_2\text{O}_5]/\text{dt}) = k_1[\text{N}_2\text{O}_5]; (\text{d}[\text{NO}_2]/\text{dt}) = 3k_1[\text{N}_2\text{O}_5]$.
46. Reaction (–1) is a more exothermic process by *ca.* 73.6 kJ mol^{–1}.
47. A catalyst; $\text{d}[\text{H}_2]/\text{dt} = (k_3 K_1/K_2)[\text{C}_2\text{H}_6]$.
48. (a) $r = k [\text{CH}_3\text{OCH}_3]$; initiation first-order, $\bullet\text{CH}_3$ β -radical, $\bullet\text{CH}_2\text{OCH}_3$ μ -radical, termination $\beta\mu$; (b) $r = k' [\text{CH}_3\text{OCH}_3]^{1/2}$.
49. (a) The fate of the less reactive radical $\text{HO}_2\bullet$ is not indicated and can be ignored in the kinetic treatment, which only uses steady-state conditions for $\text{R}\bullet$; $[\text{R}\bullet] = (k_1 [\text{RH}] [\text{O}_2]/2k_4)^{1/2}$; $\text{d}[\text{ROOH}]/\text{dt} = k_2 (k_1/2k_4)^{1/2} [\text{RH}]^{1/2} [\text{O}_2]^{3/2}$; (b) $E_a = E_2 + \frac{1}{2}E_1 - \frac{1}{2}E_4$.
50. For both examples $E_a = -6.6 \text{ kJ mol}^{-1}$.
51. $\text{d}[\text{C}_2\text{H}_4]/\text{dt} = k_3 (k_1/k_5)^{1/2} [\text{C}_2\text{H}_6]^{1/2}$.
52. A prototype reaction such as $\text{CH}_3 + \text{I}_2 \rightarrow \text{CH}_3\text{I} + \text{I}$ is a fast process, $k = 8.4 \times 10^9 \text{ mol}^{-1} \text{ dm}^3 \text{ s}^{-1}$ at 300 K. However, a possible subsequent step for the propagation of the chain such as $\text{CH}_4 + \text{I} \rightarrow \text{CH}_3\text{I} + \text{H}$ is so endothermic that the rate constant is *ca.* $k = 8.4 \times 10^{-29} \text{ mol}^{-1} \text{ dm}^3 \text{ s}^{-1}$ and the chain is quenched. Rates estimation on Java programme at <http://www.ism.quebec.pt:8180/ism/>. Termination reactions $\text{R}\bullet + \text{I} \rightarrow \text{RI}$ are fast processes.
53. 1.32.
54. $\text{Cl}_2 \rightleftharpoons 2\text{Cl}$ fast equilibrium
 $\text{Cl} + \text{CO} \rightleftharpoons \text{ClCO}$ fast equilibrium
 $\text{ClCO} + \text{Cl}_2 \rightarrow \text{COCl}_2 + \text{Cl}$ slow.
55. (a) The mechanism is identical to that proposed in the text. In the rate of polymerisation expression k_p is the rate constant of the propagation step, k_t is the rate constant of the termination step, ϕ_i is the photoinitiation quantum yield, I_a is the intensity of the light absorbed and $[\text{M}]$ is the concentration of the monomer.

- 56.** (a) $k = 2.78 \times 10^{-2} \text{ h}^{-1} = 7.76 \times 10^{-6} \text{ s}^{-1}$; from the increase in rate with pH, rate = $k [\text{RCO}_2\text{R}'][\text{OH}^-]$, and $k = 8.2 \times 10^{-4} \text{ dm}^3 \text{ mol}^{-1} \text{ s}^{-1}$.
- 57.** $k_{\text{cat}} = 0.145 \text{ mol}^{-1} \text{ dm}^3 \text{ min}^{-1}$; $k_{\text{non-cat}} = 5.3 \times 10^{-3} \text{ min}^{-1}$; (b) since a carbon acid would have a transition state bond order closer to $n^\ddagger \approx 0.5$, $k_{\text{cat}} < 0.145 \text{ mol}^{-1} \text{ dm}^3 \text{ min}^{-1}$ and eventually there is no acid catalysis.
- 58.** The composition of the activated complex is $\{\text{H}_2\text{O}_2\text{HI}\}^\ddagger$. Mechanism (i) is a termolecular process, which is more likely if some collision complex is formed, either between H_2O_2 and H^+ or between I^- and H^+ , and during the lifetime of such a complex a collision with the other reactant occurs. However, the presence of such complexes corresponds effectively to the other proposed mechanisms. Mechanism (iii) is the one that leads to products from the activated complex of the rate-determining step with the minimum rearrangement.



- 60.** (a) General acid–base catalysis; the mechanism presented in the previous question can be rewritten in general terms:



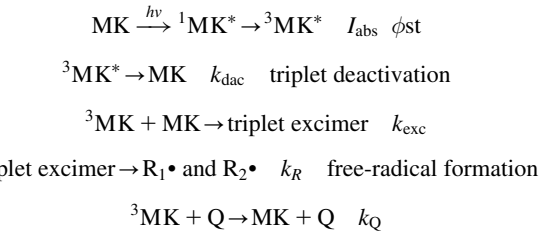
(b) $\alpha = 0.6$. If the reaction was a specific acid catalysis, the rate law would be $v = kK_a[\text{acetone}] ([\text{HA}]/[\text{A}^-])$.

- 61.** $K_M = 0.0145$; $r_0 = 0.196 \text{ mmol dm}^{-3} \text{ s}^{-1}$.
- 62.** $K_M = 2.6 \times 10^{-3} \text{ mol dm}^{-3}$.
- 63.** No; $\lambda = 510 \text{ nm}$.
- 64.** (a) $T\lambda_{\text{max}} = hc/5k_B = 2.88 \times 10^6$ when T is in Kelvin and λ in nanometre.
(b) $\frac{P}{A} = \frac{2\pi^5 k^4}{15h^3 c^2} T^4 = \sigma T^4 = [5.670 \times 10^{-8} \text{ W m}^{-2} \text{ K}^{-4}] T^4$.
(c) $S = 5.67 \times 10^{-8} (6000)^4 (6.5 \times 10^5 / 1.5 \times 10^8)^2 = 1380 \text{ W m}^{-2}$.
(d) $(1 - 0.31) 1380 \pi (6,370,000)^2 = 1.214 \times 10^{17} \text{ W}$.
(e) $T_E = 255 \text{ K}$.
(f) $\lambda_{\text{max}}(\text{Earth}) = 9600 \text{ nm}$ and $\lambda_{\text{max}}(\text{Sun}) = 480 \text{ nm}$.
(g) The infrared radiation emitted by the Earth is absorbed by H_2O , CO_2 and O_3 present in the atmosphere, which are transparent to the visible radiation of the Sun, contributing to the “greenhouse effect.”
- 65.** (a) $3.9 \times 10^8 \text{ s}^{-1}$.
(b) the value from the quantum yield and lifetime is $4.0 \times 10^8 \text{ s}^{-1}$ and the agreement is excellent.
(c) the radiative rate increases.

- 66.** (a) $\sigma = 0.0038 \text{ nm}^2$.
 (b) $A = \pi r^2 \sigma$; incident photons absorbed = $1 - 10^{-A}$; incident light absorbed = 1.3%.
 (c) incident light absorbed = 93%.
- 67.** (b) $k_q = 1.1 \times 10^{10} \text{ dm}^3 \text{ mol}^{-1} \text{ s}^{-1}$; this is very close to the calculated value for the diffusion-controlled rate constant in water ($7.4 \times 10^9 \text{ dm}^3 \text{ mol}^{-1} \text{ s}^{-1}$), and the quenching is diffusion controlled.
- 68.** (a) Since CQ has an unbleachable chromophore, large amounts will lead to undesirable yellowing, affecting the final aesthetic appearance of cured material. A possible strategy is to include other photoinitiators that act synergistically with CQ. An addition of an amine might also reduce the amount of CQ; (b) (i) the spectral properties of the photolysing reaction, which should ideally overlap with the absorption spectrum of the photoinitiator and (ii) the mechanism by which the polymerisation process is triggered by the excited photoinitiating species. For example, for CQ the mechanism for photoinitiation is an electron/proton transfer process whereas for PPD it is photocleavage. (c) The number of photons is more relevant for photoinitiation; PAE can thus be used to identify the best mechanism for photochemical process with specific photoinitiators. (d) PPD is the most efficient initiator, mainly owing to its low molecular weight, the good overlap with the LCU's emission spectra and an extinction coefficient *ca.* 5 times higher than CQ. The LCU UBIS is always somewhat more efficient owing to the shift of the output to shorter wavelengths where the photoinitiators have their absorption maxima. The narrow spectral irradiance of the LEDs employed is not appropriate for curing Lucirin that has maximum absorption well within the ultraviolet region.
- 69.** Bz^* decays in a first-order process with a rate constant $k = k_1 + k_2[\text{BD}]$; $\phi_P = 0.16$.
- 70.** Deviations from normal kinetic orders might be attributable to primary radical or photoproduct termination interactions with growing polymer radicals or formation of relatively inactive transfer radicals. The low-order kinetic for the initiator is consistent with primary initiator radical competition for the monomer and other deactivation pathways. A following simplified mechanism can be proposed:
- (1) $\text{R}\cdot + \text{M} \rightarrow \text{M}\cdot$
 - (2) $\text{M}\cdot + \text{M} \rightarrow \text{P}\cdot$
 - (3) $\text{R}\cdot + \text{R}\cdot \rightarrow \text{absorbing photoproducts}$
 - (4) $\text{R}\cdot + \text{photoproducts} \rightarrow \text{termination}$
 - (5) $\text{R}\cdot + \text{P}\cdot \rightarrow \text{termination}$
 - (6) $\text{P}\cdot + \text{photoproducts}\cdot \rightarrow \text{termination}$

Variations in light intensity are also consistent with screen effects owing to photoproduct formation.

The following mechanism has been proposed:



Show that the rate of the ketone disappearance is given by

$$-\frac{d[\text{MK}]}{dt} = I_{\text{abs}} \phi_{\text{st}} - k_{\text{dac}} [{}^3\text{MK}] + k_{\text{exc}} [{}^3\text{MK}][\text{MK}][\text{Q}] - [{}^3\text{MK}][\text{Q}].$$

- 71.** The straight line of a plot of $\ln(E^{-1}-1)$ versus $\ln(R)$ has a slope of 6.1, very close to the theoretical slope.

72. .

v''	0	1	2	3	4	5	6	7	8	9
$J_{0,v''}/1000$	0.0	0.0	0.0	0.1	0.4	1.4	3.6	7.9	15.3	26.4
v''	10	11	12	13	14	15	16	17	18	19
$J_{0,v''}/1000$	40.9	57.7	74.5	88.8	98.3	101.6	98.4	89.7	77.3	63.0

- 73.** (a) $k_{\text{Marcus}} = 1.2 \times 10^{-9} \text{ M}^{-1} \text{ s}^{-1}$.

(b) $k_{\text{ISM}} = 6 \text{ M}^{-1} \text{ s}^{-1}$.

- 74.** (a) $\Delta G^\ddagger = 38 \text{ kJ mol}^{-1}$.

(b) $k_{\text{ISM}} = 2 \times 10^6 \text{ M}^{-1} \text{ s}^{-1}$.

- 75.** $V^e = 1100 \text{ cm}^{-1}$.

- 76.** $\beta = 2.24 \text{ \AA}^{-1}$.

- 77.** $\lambda = 69 \text{ kJ mol}^{-1}$.

Index

Note: Page numbers followed by ‘*f*’ and ‘*t*’ refer to figures and tables, respectively.

A

Ab initio theories, 139–140
Absolute-rate theory. *See* Transition-state theory
Abstraction reactions, 32
Acetaldehyde decomposition, 356
Acetone iodination, 43–44, 45*f*, 46*f*
Acetonitrile, 555–556
Acid–base catalysis, 369–407, 417
and acid–base strength, 386–388
general, 369, 374–377, 412
mechanisms of, 46, 369, 385
salt effects, 389–390
specific, 374–377
Acidity functions, 390–392
Hammett, 390–391
Activated complex, 237–239, 255–256,
277–278, 280–282, 284, 308–309, 312, 391,
412, 523, 567, 573
Activation
enthalpy of, 173–174, 208, 431–432, 538–539
entropy of, 145, 278, 282, 284
Gibbs free energy of, 228, 234–236, 282
volume of, 288, 290
Activation energy, 3, 11–12, 20, 28, 47–49, 187,
188*f*, 191–192, 199–200, 208–210, 252,
255–256, 263, 264*f*, 272, 312, 314,
328–329, 331, 336, 338, 354, 356, 372–373,
530, 542
calculation of, 4, 47
of catalyzed reactions, 33–34, 372, 431–432
empirical, 47–49, 213–215, 234–236
and ISM, 213
temperature dependence, 208–210, 212, 304
Active centres, 300–301
Activity coefficients, 278, 280–281, 284–287,
390–391
Adatom, 297–298, 314–315
Adiabatic energy, 212, 504–505
Adiabaticity, 186–187, 197, 494–495, 528, 532,
554
Adsorption, 295–300
activated, 297–298
active centres, 295–300
associative chemisorption, 299*f*
competitive, 302–303
with dissociation, 302, 314–315
ideal, 300–301
isotherms, 300–303

nonideal, 298
rates, 302
statistical mechanics treatment, 308–310
van der Waals, 295–296
Aerosol particles, 444–445
Alkali metal reactions, 167
Ammonia decomposition on surfaces, 304
Analysis of kinetic results, 94–96, 99–100
Anthracene, 463–465, 474, 487–488, 487*f*, 491*f*,
492–493, 499–500, 500*f*, 509, 515–517,
516*f*
Anthraquinone, 72, 72*f*, 73*f*
Arrhenius activation energy, 338–339
Arrhenius equation, 4, 28, 304, 373, 431
Arrhenius intermediate, 370–372, 373*f*
Arsphenamine, 447–448
Ascorbic acid, oxidation, 53–54
Aspirin, 382–385, 383*f*, 385*f*, 416–417, 448
Associative mechanism, 290–291, 321–323, 323*f*
Atom combinations, on surfaces, 300, 314–315
Atom-molecule complex mechanism, 343–346
Attractor, 584–585
Autocatalysis, 32
Azithromycin, 447
molecular structure of, 447*f*
Azocoll papain, 51–52, 52*f*, 133*f*

B

Beer–Lambert law, 30
Bell–Evans–Polanyi (BEP) relationship, 210
Belousov, Boris, 592
Belousov–Zhabotinsky (BZ) reaction, 592
Benzhydrol, 78, 79*f*
Benzophenone, 78, 79*f*
 β -barium borate (BBO) crystal, 84–85
Biacetyl, 68–69, 69*f*, 70*f*, 515–517, 516*f*, 517*f*
Bi-exponential decays, 458
Bimolecular reactions, 121, 129
in gas phase, 145–146, 212
on surfaces, 310–312
Blood–brain barrier, 445–446
Bodenstein, M., 99–100, 347–348
Boltzmann formula, 610
Boltzmann relationship, 607
Boltzmann’s distribution law, 605–606
Bolus injection, 444
Bond dissociation energy, 189–190, 206,
334–335, 490–491, 535

- Bond-energy-bond-order (BEBO) method, 199
 Born–Oppenheimer approximation, 479, 525
 Bovine serum albumin, 59*f*
 Branching chains, 358–359
 degenerate, 364–365
 Branching factor, 361, 365
 Bromine atoms, reaction with H₂, 343–346, 348, 352
 Bromine–hydrogen reaction, 343–346
 Brönsted equation, 230–232, 386, 396–397
 Brönsted relationships, 230–231, 386, 398
 Brönsted–Bjerrum equation, 288
 Brusselsator, 592
 Buccal/sub-lingual administration, 444
- C**
- Cage effect, 269
 Canonical ensemble, 605
 Catalysis
 acid-base, 230, 369–407, 412
 activation energies, 372–373
 of chain reactions, 367–368
 enzyme, 51–53, 126, 131–132, 320–321, 371, 373, 398, 409–438
 of hydrogenations (heterogeneous and homogeneous), 32–33
 intramolecular, 383*f*, 385
 by ions, 376
 of polymerisation, 366–367
 surface, 420
 Catalytic constant, 230–231, 386
 Catalytic hydrogenation, 32–33
 Catalytic constant, 420–421, 430*f*
 Chain ending step, 346
 Chain length, 352–353, 355, 357
 Chain reactions, catalysis of, 367
 Chain-propagating step, 343, 352–353
 Chaos, 587–592
 Charge-coupled device (CCD) camera, 84–85
 Chemiluminescence, 167, 465
 Chemisorption, 295–298, 299*f*, 314
 Chlorine, reaction with alkali metals, 167
 with Hydrogen, 346–347, 351
 2-Chloro-2-methylpropane, 40
 Christiansen’s theory of unimolecular reactions, 247–250
 Chymotrypsin, 415–416, 416*f*, 423–424, 425*f*
 Closs–Miller system, 560–562
 Coimbra upconversion spectrometer, 85
 Coimbrator, 596–601
 bifurcation diagram of, 600*f*
 Collision cross section, 141, 150–157, 643
 Collision frequency factor, 4, 141, 177, 249–250, 252, 527
- Collision theory, 4, 140–146, 161–162, 164*f*, 173–174, 177, 198–199, 211, 249–250, 252
 improved, 146–150
 Collisions, strong, 463
 Collisions in solution, 266
 Combustion, 358–362, 364–365
 Compartment models, 135, 450*f*
 non-compartmental models, 461
 one-compartment model, 441–443, 449–452
 two-compartment model, 456–461
 Compensation effects, 236
 Competition, 54–56, 62–69, 184–186, 303, 412, 554
 Complex reactions, 20, 43–47
 mechanisms classification, 100–108
 rate equations, 100–108
 Cone cells, 29
 Cone opsins, 29
 Consecutive reactions, 100–101
 Constant fraction discriminator (CFD), 80
 Continuous flow, 56–57
 Continuum solvent effects, 338–339
 Conventional transition-state theory.
 See Transition-state theory
 Conversion factors, 603*t*
 Cool flames, 365, 365*f*
 Coulombic energy, 467
 Cross section, reaction, 141, 162, 309–310, 315
 Crossing, PES, 163–166, 184–186, 493
 Cross-reactions, 334–336, 338, 527, 529–530
 Cyclodextrins, 414
 Cyclopentadienyl iron, complexes, 535–536
 Cyclopropane isomerisation, 182–184, 183*f*, 253, 254*f*, 256, 258–261
 Cytochrome P450 (CYP) enzymes, 448
- D**
- Decay Associated Difference Spectra (DADS), 136
 Decay Associated Spectra (DAS), 136
 Degenerated branching, 364–365
 Degrees of freedom, 162, 176, 187, 252–253, 254*f*, 257, 309, 498–499, 542, 560–562, 626
 Density of states, 255–256, 258, 298, 474, 495–498, 573
 Desolvation, 414
 Desorption rates, 300–303
 Detonation, 358
 Deuterium-hydrogen exchange, 189, 435
 Deuterium-methane exchange, 501
 Dexter mechanism, 467, 468*f*, 469, 478, 492, 508
 Dielectric constant, effect on rates, 281–282, 283*f*, 414–415, 501–502, 510–511
 Difference-frequency generation (DFG), 83–84
 Differential method, 93

Diffusion-controlled reactions, 265–269, 272–273, 275–277, 555–556
 ionic reactions, 273–274
 3,4-Dimethylanisole (dMA), 81–83
 2,5-Dimethyl-3,4-diphenylcyclopentadienone, 41–42
 Diphenylcyclopentadienone, 41–42, 96
 Dipole-dipole reactions, 153–154, 476–478
 Direct reaction, 315
 Dispersion angle, 154–155
 Displacement, 175–176, 193, 196–197, 490–491, 494–495, 497, 503, 512–515, 513*f*, 514*f*
 ISM (*d*ISM), 513–514
 reduced (*s*), 482–483
 Disproportionation, 24
 Dissociative mechanism, 321–322
 Distance dependence factor, 548–549
 Distortion, 412–413
 Distribution, volume of, 441–443
 Distribution of collisions in solution, 265–266
 Distribution of energy, 4, 170–171, 184, 195–196, 253, 485–486
 Dividing surface, 253
 Double inverted region, 560–562, 561*f*
 Double-sphere model, 281
 Drug administration and absorption, 443–445
 Drug concentration in plasma, 452
 Drug design, enzymes in, 437–438
 Drug distribution, 445–447
 Drug elimination, kinetics of, 449
 Drug excretion, 449
 Drug metabolism, 447–449
 Dynamic parameter, 221, 228, 558, 560–562

E

Effective molarity (EM), 413, 416–417
 Eigen, M., 58–59, 392–394, 403–405
 Einstein, A., 466, 475
 Elastic scattering, 154–155
 Electric field jumps, 60–61
 Electron, hydrated, 273–274, 275*t*
 Electron transfer reactions, 65–67, 436–437, 505–506, 512–513, 515
 spin forbidden, 466–467
 Electron tunnelling, 436–437, 478–479, 510–511, 511*f*, 548–549
 Electronic coupling, 494–495, 497, 503–511, 515–516, 519
 Electron-jump mechanism, 546
 Electron–phonon couplings, 633
 Electron-transfer reactions, 523–575
 adiabatic, 525, 544–545
 electrodes, at, 562–575

Marcus theory, 525–537, 542
 non-adiabatic, 527, 542, 548
 self-exchanges, 523–524, 544, 548, 550–552
 spin forbidden, 549
 Electrophilicity index, 205–208, 206*f*, 211, 225–226, 241–242, 329–330, 338–339, 349, 399–400, 403–405, 546–547
 Electrostriction, 284, 286*f*, 290
 Elementary reactions, 4, 13–14, 23–26, 93, 232, 237–239, 263–293, 315, 318, 335–338, 346*f*, 348–349, 431–432
 Eley–Rideal mechanism, 314–315
 Encounters, 265–266
 Energisation, 247–248, 256
 Energy and electron-transfer rates, 637–641
 Energy distribution, 10–11, 161–162, 171*f*, 485–486
 Energy flow, 256, 258
 Energy gap, 630
 Energy gap law, 491–493, 515–519
 Energy of activation. *See* Activation energy
 Energy transfer, 59*f*, 63–64, 68, 70*f*, 75–76, 463–470, 476–478, 492–495, 496*f*, 497–499, 499*f*, 503–505, 508–509, 512–519
 inter-molecular, 256, 467–468
 intra-molecular mechanisms, 256, 258
 triplet-triplet, 74*f*, 468–469, 494–495, 497
 Enterohepatic circulation of drug, 449
 Enthalpy of activation, 208, 431, 536, 538–539
 Entropy, 414
 Entropy of activation, 145, 283–284, 414
 Enzymatic action, factors accelerating, 412–418
 desolvation, 414
 entropy, 414
 general acid–base catalysis, 416–417
 hydrogen bonding, 414–416
 metal ions, 417
 proximity, 413–414
 tension and distortion, 412–413
 transient covalent binding, 418
 Enzyme catalysis, 51–53, 126, 131–132, 320–321, 371, 409–438
 influence of pH, 429–431
 influence of temperature, 431–433
 transient-phase kinetics, 422–423
 Enzymes in drug design, 437–438
 Enzyme–substrate binding free energy, 414
 Enzymology, 437
 Equilibrium, statistical mechanics, 174, 176
 Erythromycin, 447
 molecular structure of, 447*f*
 Ester hydrolysis, 130, 409
 Ethane decomposition, 345, 353

2-Ethanoxybenzoic acid, 448
 Ethene, 353
 Ethyl radical, 355
 Ethylene, 353
 Evolution-associated spectra (EAS), 136
 Exchange reactions, 19–20, 290, 290*t*, 331*t*, 338, 524
 Excitation, 10–11, 32, 67–68, 72, 75–76, 78–80, 169–170, 257–258, 403, 468–469, 474, 484–488, 487*f*, 490, 501–502, 557
 Excited state intramolecular proton transfer (ESIPT), 85
 Explosion limits, 362, 364
 Extent of reaction, 17–19, 27, 44–46
 Eyring, H., 173–174

F

Family of reactions, 218–219, 221, 225, 228–229, 403–406, 552
 Fast reactions, 20, 54–90, 275
 Feigenbaum constant, 588–590
 Feigenbaum point, 590
 Femtochemistry, 86–87
 Femtosecond transient absorption spectrometer, 88–90, 88*f*
 Ferrocene, 65–67, 67*t*, 533, 535–536, 538*f*, 542, 570, 572–573, 572*f*, 575
 Fick, law, 270
 Field, Körös and Noyes (FKN) mechanism, 593
 Flames, 167, 365
 Flash photolysis, 69–72, 71*f*, 76
 Flavin-containing mono-oxygenases, 448
 Flow systems, 54–58
 Fluorescence, 67–68, 465, 487
 Fluorescence decays, 80–81
 Fluorescence spectroscopy, time-resolved, 78–80, 85*f*
 Fluorescence upconversion, 83–86, 84*f*
 Force constant, 8, 225–228, 231*f*, 232, 239, 241–242, 244, 259–260, 544, 551
 Foreign-gas effect, 248, 249*f*, 253
 Förster mechanism, 467, 476–477
 Franck–Condon factors, 31, 479–491, 497–498, 503–504, 508, 510–512, 515, 533–534, 537, 539, 630–631, 633, 635
 Franck–Condon principle, 31, 479–480, 482*f*, 492–493, 498–499, 540–543
 Franck–Condon weighted density of states (FCWD), 629
 Franck–Rabinowitch effect, 269
 Free radical combinations, 206–207, 343, 353
 Frequency factor. *See* Pre-exponential factor
 Full width at half-maximum (FWHM), 80–81

G

Gas-phase reactions, 34, 100, 336–337, 358, 533–534, 546–547
 General acid–base catalysis, 374–375, 375*t*, 377, 387–388, 398, 416–417
 Gibbs energy of activation, 234–236
 Golden rule, 258, 470–474, 477–479, 497, 509–510, 515–519, 517*f*, 535
 Goldfinger–Letort–Niclause rules, 357–358
 Grotthuss mechanism, 394

H

H bond, 416–417
 Halcyone Fire spectrometer, 84–85
 Half-life, 95–97, 99, 129, 409
 Halides, reaction with alkali metals, 167
 Halogenation of acetone, 43–44, 46*f*
 Halogens reactions, 239
 with alkali metals, 167
 with nitric oxide, 396–397
 Hamiltonian, 157–159, 470–472
 Hammett relationship, 233
 Hammond, postulate of, 237–239
 Harmonic oscillator parameters, 614*t*, 615*t*
 Harpooning mechanism, 161–162
 HELIOS pump-probe femtosecond transient absorption spectrometer, 89–90
 Heterogeneity of surfaces, 572
 Heterogeneous reactions, comparison with homogeneous reactions, 564–565. *See also* Surface reactions
 Higher-order fixed point, 584
 Hinshelwood, treatment of unimolecular reactions, 250–253
Homo sapiens sapiens (HSS), 585–586
 Huang–Rhys parameters, 633
 Hydrated electron, 273–274, 275*t*
 Hydration shell, 394*f*, 533
 Hydrazines, 536–537
 Hydrocarbon decompositions, 353
 Hydrocarbon oxidation, 232
 Hydrogen atoms, 32, 240, 326, 331, 339, 351, 354
 reaction with HBr, 351
 reaction with I₂, 351
 Hydrogen bonds, 61, 392–396, 398, 401–403, 406, 414–416, 623–624
 Hydrogen ion catalysis. *See* proton transfer reactions
 Hydrogen ions, combination with OH[−] ions, 377–379
 Hydrogen-atom abstraction of ethane
 by hydrogen atom, 355
 by methyl, 355

Hydrogen-bromine reaction, 343–346
 Hydrogen-chlorine reaction, 346–347
 Hydrogen-deuterium exchange, 189, 435
 Hydrogen-iodine reaction, 347–348
 Hydrogen-oxygen reaction, 358–362

I

Image force, 569
 Impact parameter, 152–155, 157, 160
 Induction period, 365, 422–423
 Inelastic scattering, 503
 Inert-gas effect, 100, 350
 Inhalation, 444–445
 Initiation of oxidation, 365
 of polymerisation, 366
 Inner-sphere reactions, 523, 529, 546–547
 Inosine 5'-monophosphate dehydrogenase (IMPDH), 427–428
 Inosine-5'-monophosphate (IMP), 427–428
 Instrument response function (IRF), 135
 Instrumental response function (IRF), 80–81, 83
 Insulin, 444
 Integration, method of, 109
 Laplace transforms, 109–115
 Markov chains, 121–125
 matrix method, 115–118
 Monte Carlo method, 125–127
 Runge-Kutta method, 118–121
 Interacting-state model. *See* ISM
 Interchange mechanism, 321–322
 Inter-molecular energy transfer, 256, 467–468
 Internal conversion of energy, 465–467, 474, 488–492, 491*f*, 502–503
 Internal pressure. *See* Pressure, influence on rates
 Intersecting-state model. *See* ISM
 Intra-arterial administration, 444
 Intra-molecular energy transfer, 256, 258
 Intra-muscular administration, 444
 Intravenous administration, 444
 Intravenous infusion, 452–454
 Intrinsic barrier, 210, 219, 227–229, 232, 243–244, 329, 403–405, 527, 543, 552
 Inverted region, 530–531, 552–562
 Iodine-acetone reaction, 44, 45*f*
 Iodine-atom combination, 268
 Iodine-hydrogen reaction, 347–348
 Ion-dipole reactions, 324–325
 Ionic reactions
 diffusion control, 272–274, 546–547
 Ionic recombinations, 562
 Ionic strength, effects, 35, 54, 99–100, 284–288
 Ion-molecule reaction, 324*t*, 336, 533–534

Ion-pair (ionic) yield, 319–321, 389, 416*t*, 560–562
 ISM, 199, 203, 225–226, 259, 329–330, 338–339, 340*f*, 341, 348, 399–400, 406, 416–417, 513, 516–517, 537, 543–544, 560–562, 574*f*, 619–620, 623
 Isokinetic temperature, 236
 Isolation method, 99, 128–129
 Isomerization of cyclopropane, 182–184, 183*f*, 253, 254*f*, 256, 258–261
 Isopropylidene malononitrile, 560–562
 Isotope effects, 187, 385, 405–406, 435
 primary, 187
 secondary, 189–191
 Isotope exchange reactions, 187, 189, 405–406

J

Jablonski diagram, 463, 464*f*
 Jacobian matrix, 584, 599
 Jortner, J., 258, 488–489, 503–504

K

Kasha, rule of, 463–465
 Kinetic data, 135–138
 Kinetic isotope effects, 187–191
 Kinetic results, analysis of, 37, 94–95, 320–321
 Kinetic theory of collisions, 139

L

Laidler, K., 346, 369, 372
 Landau and Zener, transition probability, 493–495
 Langevin collision rate, 533–536
 Langevin collisional rate constant, 157
 Langford–Gray classification of mechanisms, 320–324
 Langmuir isotherm, 300–301
 Langmuir–Hinshelwood mechanisms, 306, 307*f*, 308, 310, 312–314
 Laplace transforms, 452–453, 456–457
 Laser-induced reactions, 76
 Lennard-Jones potential, 153–154, 153*f*, 154*f*, 155*f*
 Lifetime, 10–11, 31, 62–65, 67–69, 77–81, 116–118, 469, 475–476, 494–495
 Light intensity, 30, 49–51, 71
 actinometry, 49–51
 ferrioxalate, 49–51
 Lindemann–Christiansen hypothesis, 247–250
 Linear Gibbs-energy relationships (LFER), 229, 231–232, 236, 241, 243–244, 404*f*
 Lineweaver–Burk plot, 421–422, 426–428
 Linewidth, 80–81

- Lipinski's rule, 445
 Lippincott-Schroeder (LS) potential, 392–394, 393*f*, 623–626
 Local random matrix theory (LRMT), 258
 Lorenz equations, 590–592
 Lotka, reaction, 123–124, 124*f*
 Lotka type II mechanism, 579–580
 Lotka–Volterra model, 580–581, 585–586
 Luminescence quenching, 67–69
- M**
 Marcus and Coltrin path, 197, 197*f*
 Marcus equation, 230, 232, 338, 553–554
 Marcus (RRKM) theory of unimolecular reactions, 253, 255*f*, 256, 258
 Marcus theory. *See* Electron transfer reactions
 Maxwell–Boltzmann distribution, 142, 144, 175–176, 250–251, 313
 Menschutkin reactions, 33–34, 263, 264*f*, 264*t*, 265*f*, 281
 Metal ions, 417
 Methane, reaction with H atoms, 182*f*
 Methyl radical reactions, 20–22, 181–182, 182*f*
 Methyl transfer reactions, 324*t*, 329–331, 337*f*
 Methylcoumarin, 116–117, 119*f*
 Methylpropane, 38–40, 39*t*, 40*f*, 41*f*, 93
 Michaelis–Menten equation, 133, 371, 418–423, 429
 Microscopic reversibility, 23–24, 106, 466
 Minimum-energy path (MEP), 7, 11–12, 162, 197, 197*f*, 216
 Molecular beams, 140–141, 154–155, 156*f*, 161, 168, 312–314
 Molecular dynamics, 5, 139–171
 Molecular partition function, 605–606
 Molecularity, 3–4, 247–248
 of reactions, 13–14, 317–318, 320–321
 Mono-exponential function, 460
 Mono-oxygenases, flavin-containing, 448
 Morse compression mode, 640
 Morse curve parameters, 613*t*, 614*t*
 Morse potential, 189–191, 190*f*, 484–485
 Multi-channel analyser (MCA), 80
 Multiple doses, 455–456
- N**
 Naphthalene, 68–69, 69*f*, 70*f*, 273*f*, 491*f*, 499–500, 500*f*, 509–510, 550–552, 558
 Naphtholate, 407
 2-Naphtolates, 61–62
 Nicotinamide adenine dinucleotide (NAD⁺), 427–428
 Nitric oxide, 143–144, 247, 311
- Nitrobenzoic acid, 232–233
 1-(2-Nitro-ethyl)-naphthalene-2-ol (NO₂nH), 406–407
 Non-compartmental models, 461
 Non-competitive inhibition, 428
 Non-covalent forces, 412–413
 Non-isolated fixed point, 584
 Non-linear differential equations, 585–586
 Non-linear systems, 579–586
 sensitivity of, 587
 Non-polar drugs, 448
 Normal modes, 253, 255–257, 259, 490–491, 538–539, 551–552, 618
 Norrish, R., 69–70
 Nuclear magnetic resonance (NMR), 63–67
- O**
 One-compartment model, 441–443, 449–452
 Opposing reactions, 2, 104–106
 Optical parametric amplifier (OPA), 84–85, 88*f*
 Oral administration, 443–444
 Order of reaction, 3–4, 26, 44–47, 46*f*, 93, 96, 98
 Oregonator, 594–595
 Oscillatory reactions, 592–596
 chaos, 587–592
 Coimbrator, 596–601, 600*f*
 non-linear systems, 579–586
 oscillatory reactions, 592–596
 Outer-sphere reactions, 523–525, 528–529, 546–547, 571–572
 Oxidation, gas-phase
 of hydrocarbons, 364–365
 of hydrogen, 314–315, 359*f*
 Oxophenarsine, 447–448
- P**
 Parallel reactions, 100–102
 Parr, electrophilicity index, 205–206, 225–226, 329–330, 399–400, 546–547
 Partition functions, 173–174, 176–181, 184, 186–187, 196, 212–214, 255, 277–278, 308, 310–312, 399, 605–606, 610–611, 621–622
 Pauling relationship, 200–201, 201*f*, 484–485, 512–514
 Pericyclic reactions, 31
 Perpetuum mobile, 579
 Persulphate ions, reactions, 47
 pH dependence of rates, 377–386
 pH effects in enzyme kinetics, 429–431
 pH jump, 61–62
 Pharmacokinetics, 442*f*
 drug administration and absorption, 443–445
 drug distribution, 445–447
 drug excretion, 449

- drug metabolism, 447–449
 intravenous infusion, 452–454
 multiple doses, 455–456
 non-compartmental models, 461
 one-compartment model, 441–443, 449–452
 origins and current use of, 441–443
 single oral dose, 454–455
 two-compartment model, 456–461
- Phase II reactions, 448–449
- Phosphoesters, 412–413
- Phosphorescence, 67–68, 463–467, 485–488, 487*f*, 500–501, 515–516, 516*f*
- Photoacoustic calorimetry (PAC), 76–78, 291–293, 488
- Photochemical reactions, 68, 197–198, 268, 346–347, 553–554
- Photocuring of polymers, 29
- Photodissociation, 86–87
- Photodynamic therapy (PDT), 29, 277, 459–460
- Photolysis, 50–51
 flash, 69–72
- Photopolymerisation, 29
- Photoreceptor cells, 29
- Photosensitiser, 459–460
- Physical constants, 603*t*
- Plasma, drug concentration in, 452
- Pleistocene cycles, 599–601
- Poisoning of surfaces, 304
- Poisson distribution, 145–146, 482–483, 484*f*
- Polanyi, J., 168, 170–171
- Polanyi, M., 4, 167–169, 173
- Polar drugs, 448
- Polymerisation, 366–367
- Porter, G., 69–70
- Potential-energy surfaces (PES), 4, 140–141, 163–166, 179, 253, 256, 463, 525, 531, 552–553
 attractive, 167*f*
 calculation of, 4, 11–12
 DMBE, 195*f*, 215–218
 early barrier, 171*f*
 empirical, 162, 164*f*
 late barrier, 171*f*
 profile, 34, 34*f*, 373*f*
 repulsive, 169*f*
- Pre-equilibrium approximation, 128, 130
- Pre-exponential factor, 3–4, 145, 173–174, 177, 189, 197–198, 213–214, 278, 284, 336, 338–339, 405–406, 416–417, 545, 568–573
 for solution reactions, 263
 temperature dependence, 28
- Pressure, influence on rates
 external, 279, 288–291
 internal, 76–77, 278–281
- Pressure jump, 60
- Probability of reaction, 160
- Pro-drug, 447–448
- Pross and Shaik diagrams, 327–329, 328*f*
- Protolytic mechanisms, 374–375
- Proton mobility, 392–398
- Proton transfer reactions, 369–407, 435
- Proton-transfer model system, 406–407
- Prototropic mechanisms, 374–375
- Proximity, 413–414
- Pulse radiolysis, 73–76
- Pulsed lasers, 61, 70, 73–74, 76, 80, 86
- Pump pulse, 88*f*
- Pyrolysis, 353–358
- Q**
- Q-switched Nd:YAG laser, 77*f*
- Quantum effects, 186–187, 497
- Quantum mechanical tunnelling, 161, 191–198, 403, 488–491, 548–549
- Quantum yield, 50–51, 67–68, 78, 197–198, 198*f*, 475–476
- Quantum-mechanical radiationless transition theory, 629
 energy and electron-transfer rates, 637–641
 strong coupling limit, 633–635
 weak coupling limit, 636–637
- Quasi-equilibrium, 174, 176, 184, 391
- Quenching, 43–44, 67–69, 69*f*, 501, 555, 557
- Quinone methide, 243–244
- R**
- Radiation hypothesis, 4, 258
- Radiationless transitions, 463, 467, 470, 474, 488–491, 497–498, 507
- Radiative rates, 475–476
- Radioactive decay, 96
- Rate-determining step, 14, 25–26, 38, 44–46, 93, 128, 134–135, 320–321, 373*f*, 377–379, 381–382, 391, 394, 423–424, 432, 437
- Reaction cross-section, 168, 315
- Reaction dynamics, 125, 139, 170*f*
- Reaction path, 7, 31, 194–196, 226, 323–324, 336, 432*f*, 435–437, 463, 617–622, 626
- Reaction probability, 121, 144
- Reaction threshold energy, 150
- Reactive oxygen species (ROS), 29
- Reactivity-selectivity principle (RSP), 239–241, 240*f*
- Recombination of radicals, 268, 352
- Re-crossing, 184–186, 185*f*, 501–502
- Rectal administration, 444
- Redaporfin, 460
 molecular structure of, 447*f*

- Reduced mass, 9–10, 142–143, 173–174, 189–190, 195–196, 217, 329–330, 481, 483, 489–490, 517–519, 533–534, 538–539, 558–562, 568–569
 Refractive index, 465, 475–476, 507–508, 510, 527–528, 536, 548–549, 558–559, 572–573, 575
 Rehm–Weller plateau, 555–558
 Relationships. *See* structure-reactivity relationships
 Relaxation, vibrational, 76, 463–465, 464f, 474, 479–480
 Relaxation methods, 58–62
 Relaxation time, 59, 63–64, 501–502, 568–569
 Reorganisation energy, 494–495, 497–498, 500–501, 503–504, 512, 514–516, 528, 533, 560–562, 561f
 Repellers, 584–585
 Resorption, 441–443
 11-*cis*-Retinal, 29
 Reversible reactions, 22–24, 58–59, 100–101, 104–108, 110–112, 115, 134, 173–174
 Reynolds number, 56–57
 Rhodopsin, 29
 Rice–Herzfeld mechanisms, 354, 356
 Rice–Ramsperger–Kassel–Marcus (RRKM) treatment, 253, 255f, 256
 Rideal–Eley mechanisms, 306–308, 307f
 Ritchie equation, 243–244, 243f
 Ritchie relation, 341
 Rod cells, 29
- S**
 Saddle point, 7–8, 162, 184–186
 Saddles, 584
 Salt effects, 35, 288, 377, 389–390
 Scattering, 80–81, 150, 154, 155f, 161, 163–166 rainbow, 155f
 Secondary recombination, 268
 Semi-classical rate constants, 621–622
 Semi-empirical calculations, 199
 Separability of motions, 6–7, 139
 Ser195, 415–416
 Serine proteases, 418, 423, 425f
 Shikinin, 85
 Shortest lifetime, 458
 Single oral dose, 454–455
 Single photon counting (SPC), 78–83
 Singular value decomposition (SVD), 135
 Slater’s treatment of unimolecular reactions, 256–257
 Sodium reactions, 167
 Solvent effects, 33–34, 263–265, 324–325, 329, 336–341, 337f
 Soybean lipoxygenase, 435–437
 Species-associated spectra (SAS), 136
 Specific acid-base catalysis, 374–377
 Spectra Physics Solstice Ace HP, 84–85
 Spectra-Physics Solstice-100F laser, 89–90
 Spin multiplicity, 276
 Spin-statistical factors, 275–277
 State-to-state kinetics, 161
 Statistical factors, 181–184
 Steady-state hypothesis, 130–131, 248, 267–268, 343–344, 356, 366, 372–373, 381, 396
 Steric effect of *tert*-butyl group, 331
 Steric factor, 164f, 173–174
 Stern–Volmer equation, 68, 555
 Stimulated emission, 466
 Stirling’s approximation, 607
 Stopped-flow method, 58–59, 422–423
 Stratum corneum, 445
 Strong coupling limit, 633–635
 Structure-reactivity relationships
 Bell-Evans-Polanyi, 210, 232, 237, 244
 electronic effect (Ritchie), 233, 241–244
 linear (LFER), 229–236
 quadratic (QFER), 225–229
 Sub-cutaneous administration, 444
 Substituent effects, 385
 Substitution reactions
 S_N1 mechanism, 318–320
 S_N2 mechanism, 318–320
 Successive (consecutive) reactions, 100–104
 Sum-frequency generation (SFG), 83–85
 Superexchange mechanisms, 511
 Surface heterogeneity, 572
 Surface reactions
 activation energies, 304–306
 bimolecular, 310–312
 inhibition, 302–304, 306
 mechanisms, 312–315
 on nonuniform surfaces, 298
 poisoning, 304
 transition-state theory, 308–312
 Surface structure, 298
 Surface Xplorer PRO programme, 89–90
 Sutin, N., 528
 Symmetry number, 184
- T**
 Tafel coefficient, 567
 Tafel equation, 562–568, 570–571, 574f
 Taft relationship, 232–236
 Target analysis, 135–138
 Temperature, and reaction rates, 27–29
 Temperature-jump method, 59–60

Tension and distortion, 412–413
Ter-Butyl group, steric effect of, 331
 Tetracene, 275–276
 Thermodynamic formulation of rates, 277–278
 Time-correlated single photon counting (TCSPC), 78–81, 81*f*, 82*f*, 83, 85, 89–90
 Time-resolved fluorescence spectroscopy, 78–80, 85*f*
 Time-to-amplitude converter/analogue-to-digital converter principle (TAC/ADC), 80
 TOPAS Prime-F optical parametric amplifier, 84–85
 Topical administration, 445
 Trajectory, 23–24, 125, 142, 142*f*, 150, 151*f*, 154, 158, 160–166, 163*f*, 164*f*, 165*f*, 184–186, 185*f*, 199
 Transdermal administration, 445
 Transfer coefficient, 566–567
 Transfer of energy, 468–469, 492–493, 492*f*
 Transferase enzymes, 448–449
 Transient covalent binding, 418
 Transient enzyme–substrate bond, 418
 Transient pump–probe spectroscopy, 87–90
 Transient volume changes, 291–293
 Transition state, 524, 543–544
 Transition state bond order, 200–202, 212, 221, 226, 228, 241–242, 265*f*, 546–547, 547*f*
 principle of least nuclear motion, 239
 Transitions, between states, 463–519
 Transition-state theory
 adiabatic, 186
 assumptions, 174
 conventional, 174–177, 255
 thermodynamic, 177
 variational, 184–186
 Transmission coefficient, 186–187, 437, 620–621
 Triose-phosphate isomerase, 433–435

Tunnel effect theory, 191–198, 488–491
 Tunnelling. *See* Quantum mechanical tunnelling
 Tunnelling corrections, 620–621
 Two-compartment model, 456–461

U

Ultrasonic absorption, 61
 Unimolecular reactions, 247–261, 303–304

V

Van der Waals surfaces, 413
 Van't Hoff equation, 27–28, 59, 304–305
 Van't Hoff intermediate, 372–373, 373*f*, 375, 381
 Vibrational relaxation. *See* Relaxation, vibrational
 vibrationally adiabatic path, 217, 617–620
 Volume of activation, 288, 290, 336
 Volume of distribution, 441–443

W

Water-bridging mechanism, 529
 Weak coupling limit, 636–637
 Wilson's equation, 618

X

Xanthosine monophosphate (XMP), 427–428

Z

Zero-order kinetics, 98–99, 309–310, 370–371
 Zero-order reaction, 452
 Zero-point energy, 161, 208, 309, 350, 403, 405–406
 and isotope effects, 187–191, 501
 of reactants, 617–618
 Zewail, A., 86
 Zundel ion, 393–394, 394*f*

CHEMICAL KINETICS

Luís Arnaut

Presents a rational path from the observation of molecular changes to the understanding of chemical reaction rates

Chemical Kinetics: From Molecular Structure to Chemical Reactivity, Second Edition, explains how molecular structures change with time. It offers a comprehensive and coherent coverage of the rates of chemical transformations.

The book is written for both undergraduate chemistry students, and for the specialist. The newcomer will find the fundamental concepts, the simple experiments, and the underlying theories. For the seasoned specialist, it presents sophisticated experimental and theoretical methods, offering a panorama of time-dependent molecular phenomena connected by a new rationale. The gap between the two is bridged by a logical path that leads the reader from a phenomenological approach of molecular changes, to the formalism of chemical reaction rates, and then to state-of-the-art calculations of rate constants of the most prevalent reactions: atom transfers, catalysis, proton transfers, substitution reactions, energy transfers and electron transfers. In the process, the reader is presented with the details of collision and transition state theories. The coverage includes unimolecular reactions in the gas phase, reactions in solution and reactions on surfaces.

Key Features

- All first edition chapters are revised and most are extended
- Features two new chapters, one on Pharmacokinetics and the other on Oscillatory Reactions and Chaos
- Includes practical examples, detailed theoretical calculations, and cross-relations between reactions throughout the text to underscore key concepts
- Provides a state-of-the-art presentation on the kinetics of reactions implicated in the most active research fields
- The rigor of mathematical description of phenomena is combined with simple and profusely-illustrated concepts

Luís G. Arnaut, PhD is Professor of Chemistry in the Chemistry Department at the University of Coimbra in Coimbra, Portugal.

Science / Chemistry
Physical and Theoretical



elsevier.com/books-and-journals

